Collected Reprint Series

Granites and Rhyolites

American Geophysical Union
Washington, DC

Copyright 1989 by the American Geophysical Union
2000 Florida Avenue, N.W.
Washington, DC 20009

Figures, tables and short excerpts may be reprinted in scientific books and journals if the source is properly cited.

Authorization to photocopy items for internal or personal use, or the internal or personal use of specific clients, is granted by the American Geophysical Union for libraries and other users registered with the Copyright Clearance Center (CCC). This consent does not extend to other kinds of copying, such as copying for creating new collective works or for resale.The reproduction of multiple copies and the use of full articles or the use of extracts, including figures and tables, for commercial purposes requires permission from the American Geophysical Union.

CONTENTS

Chapter 1: Introduction to special issue on Granites and Rhyolites: A commentary for the nonspecialist
Fred Barker 10131

Chapter 2: A summary of the geology and petrology of the Sierra La Primavera, Jalisco, Mexico
Gail A. Mahood 10137

Chapter 3: Gradients in silicic magma chambers: Implications for lithospheric magmatism
Wes Hildreth 10153

Chapter 4: Partitioning of rare earths and other trace elements between sanidine and coexisting volcanic glass
William P. Leeman and David W. Phelps 10193

Chapter 5: Volcanic ash beds: Recorders of Upper Cenozoic silicic pyroclastic volcanism in the western United States
Glen A. Izett 10200

Chapter 6: Pleistocene high-silica rhylolites of the Coso Volcanic Field, Inyo County, California
Charles R. Bacon, Ray Macdonald, Robert L. Smith, and Philip A. Baedecker 10223

Chapter 7: The mineralogy and chemistry of the anorogenic Tertiary silicic volcanics of the SE Queensland and NE New South Wales, Australia
A. Ewart 10242

Chapter 8: Petrogenesis of oceanic andesites
Sven Maaløe and Tom Svane Petersen 10273

Chapter 9: Gravity and thermal models of the Twin Peaks Silicic Volcanic Center, southwestern Utah
Daniel L. Carrier and David S. Chapman 10287

Chapter 10: Late Cenozoic volcanism at Twin Peaks, Utah: Geology and Petrology
H. R. Crecraft, W. P. Nash, and S. H. Evans Jr. 10303

Chapter 11: Geochemistry and petrology of mid-Tertiary ash flow tuffs from the Sierra el Virulento Area, Eastern Chihuahua, Mexico
Elizabeth J. Moll 10321

Chapter 12: Three S-type volcanic suites from the Lachlan Fold Belt, southeast Australia
D. Wyborn, B. W. Chappell, and R. M. Johnston 10335

Chapter 13: Calderas in the Precambrian terrane of the St. Francois Mountains, southeastern Missouri
J. Ronald Sides, M. E. Bickford, R. D. Shuster, and R. L. Nusbaum 10349

Chapter 14: Chemical evolution of magmas in the Proterozoic terrane of the St. Francois Mountains, southeastern Missouri, 1, Field, petrographic, and major element data
M. E. Bickford, J. R. Sides, and R. L. Cullers 10365

Chapter 15: Chemical evolution of magmas in the Proterozoic terrane of the St. Francois Mountains, southeastern Missouri, 2, Trace element data
R. L. Cullers, R. J. Koch, and M. E. Bickford 10388

Chapter 16: Contrasting eolution of calc-alkalic volcanic and plutonic rocks of Western Chihuahua, Mexico
W. C. Bagby, K. L. Cameron, and M. Cameron 10402

Chapter 17: Phase relationships of I-type granite with H_2O to 35 kilobars: The Dinkey Lakes biotite-granite from the Sierra Nevada Batholith
Charles R. Stern and Peter J. Wyllie 10412

Chapter 18: The Redskin Granite: Evidence for thermogravitational diffusion in a Precambrian granite batholith
Steve Ludington 10423

Chapter 19: Chemistry of rock-forming minerals of the Cretaceous-Paleocene batholith in southeastern Japan and implications for magma genesis
Gerald K. Czamanske, Shunso Ishihara, and Stevan A. Atkin 10431

Chapter 20: A neodymium and strontium isotopic study of the Mesozoic calc-alkaline granite batholiths of the Sierra Nevada and Peninsular Ranges, California
Donald J. DePaolo 10470

Chapter 21: Petrology and geochronology of metamorphosed volcanic rocks in a Middle Cretaceous volcanic neck in the east-central Sierra Nevada, California
Ronald W. Kistler and Samuel E. Swanson 10489

Chapter 22: Caledonian plutonism in Britian: A summary
G. C. Brown, J. Cassidy, C. A. Locke, J. A. Plant, and P. R. Simpson 10502

Chapter 23: Phase relationships of S-type granite with H_2 to 35 kbar: Muscovite granite from Harney Peak, South Dakota
W. L. Huang and P. J. Wyllie 10515

Chapter 24: The New England Batholith, eastern Australia: Geochemical variations in time and space
S. E. Shaw and R. H. Flood 10530

Chapter 25: Manaslu Leucogranite: A collision signature of the Himalaya, a model for its genesis and emplacement
Patrick Le Fort 10545

Chapter 26: Hybrid granodiorites intruding the accretionary prism, Kodiak, Shumagin, and Sanak Islands, southwest Alaska
Malcolm Hill, Julie Morris, and Joseph Whelan 10569

Chapter 27: Petrogenesis of garnet two-mica granites in the Ruby Mountains, Nevada
R. W. Kistler, E. D. Ghent, and J. R. O'Neil 10591

Chapter 28: Two-mica granites of northeastern Nevada
Donald E. Lee, Ronald W. Kistler, Irving Friedman, and Richard E. Van Loeren 10607

Chapter 29: The Late Archaean Qôrqut Granite Complex of southern west Greenland
Michael Brown, C. R. L. Friend, V. R. McGregor, and W. T. Perkins 10617

Chapter 30: Seismic reflections from the basal contacts of batholiths
Heloise B. Lynn, Laura D. Hale, and George A. Thompson 10633

JOURNAL OF GEOPHYSICAL RESEARCH, VOL. 86, NO. B11, PAGES 10131–10135, NOVEMBER 10, 1981

Introduction to Special Issue on Granites and Rhyolites: A Commentary for the Nonspecialist

FRED BARKER

U.S. Geological Survey, Denver Federal Center, Denver, Colorado 80225

WHY GRANITES AND RHYOLITES?

The siliceous, potassic igneous rocks that contain more than ~69% SiO_2 and typically 3.5–5.5% K_2O—the granites and rhyolites—now follow basalts in their importance to earth scientists. Though the 1970's could best be termed a 'Decade of Basalts' [*Hart and Allegre,* 1980], an increasing number of earth scientists are now turning their attention to the more siliceous rocks. The present collection of papers on granites and rhyolites includes geological and geophysical field studies, physical and chemical experimental studies, analysis of both rocks and the constituent minerals for major and minor elements and various isotopic ratios, and consideration of pertinent plate tectonic processes and environments. Processes which generate granitic-rhyolitic melts and mechanisms of emplacement of these melts in the upper crust or at the earth's surface are of paramount interest here. This special issue is a sample of modern research and concepts about granites and rhyolites.

NOMENCLATURE

Because the definitions of granite and rhyolite have been changed recently, terminology is discussed first.

Almost all granites are intrusive and most rhyolites are extrusive. However, a classification that is independent of mode of occurrence is preferred and so granite is defined petrographically. It is a wholly crystalline rock whose major mineral constituents are 1–25 mm in average dimension (finer-grained varieties are termed felsite or aplite; coarser varieties are pegmatite) and it contains essential alkali feldspar, quartz, and plagioclase. Commonly it also contains one or more varietal minerals such as biotite, hornblende, muscovite, sodic, amphibole, or others and accessory phases such as magnetite, ilmenite, apatite, zircon, allanite, garnet, or others. The history of rock classifications, definitions of a multitude of petrographic terms, and a now little-used but internally consistent system of classification are given by *Johannsen* [1939, 1932, 1937, 1938]. Many modern workers, however, use the more recent International Union of Geological Sciences (IUGS) classification [*Streckeisen,* 1976]. The IUGS definition of granite and similar holocrystalline, SiO_2-saturated rocks is shown in Figure 1.

The IUGS classification allows granite to contain as much as 90% of minerals other than quartz and feldspars. Few granites, though, contain more than about 20% of other minerals. The reader should keep in mind that in this scheme the proportions of the three defining minerals are relative and that their absolute contents in a given granite vary inversely with total content of other, nonessential (varietal and accessory) minerals. Thus a granite comprised of only the two feldspars and quartz must contain at least 20% quartz, whereas a granite containing 25% of other minerals need contain only 15% quartz to fall into the granite field (Figure 1). This petrographic definition of granite thus precludes exact chemical definitions.

Rhyolites pose a different problem in terminology because most are partly to largely glassy and so cannot be classified by proportions of mineral phases. A chemical classification is necessary. A useful yet simple one, shown here as Figure 2, is based on SiO_2 and K_2O abundances and was proposed by *Peccerillo and Taylor* [1976] and modified by *Ewart* [1979]. As the reader would judge, the correspondence of chemically defined rhyolite and of granite defined by proportions of minerals is haphazard. Classification of these rocks remains a minor problem.

Many petrologists and geochemists further separate granites, rhyolites and related rocks into the following three groups by molar proportions of several major constituents [*Shand,* 1951]:

peraluminous:	$Al_2O_3 > Na_2O + K_2O + CaO$
metaluminous:	$Na_2O + K_2O < Al_2O_3 < Na_2O + K_2O + CaO$
peralkaline:	$Al_2O_3 < Na_2O + K_2O$

Two other classification schemes of igneous rock suites deserve mention. The CIPW rock norm classification [*Cross et al.,* 1902; *Johannsen,* 1939] is based on the calculation (by weight proportions) of a complete set of hypothetical normative 'minerals' that include quartz (SiO_2), orthoclase ($KAlSi_3O_8$), albite ($NaAlSi_3O_8$), anorthite ($CaAl_2Si_2O_8$), corundum (Al_2O_3), enstatite ($MgSiO_3$), and others. The CIPW classification generally is better applied to volatile-poor basaltic systems [see *Morse,* 1980] than to most granite or rhyolite suites, but it has proven very useful to experimental petrologists in describing relatively simple artificial systems, such as the classic investigation by *Tuttle and Bowen* [1958] of the granite-H_2O system at low to moderate water pressures. Some workers also use the CIPW scheme to describe granites or rhyolites as corundum-normative or diopside-normative (i.e., showing corundum or diopside as a calculated normative 'mineral').

Another notable descriptive scheme is that of *Peacock* [1931], which is used to classify suites of igneous rocks that range from mafic or intermediate to siliceous compositions. Plots of $Na_2O + K_2O$ versus SiO_2 and of CaO versus SiO_2 are superposed. The SiO_2 content at which the two lines intersect is termed the alkali-lime index (ALI). Peacock distinguishes four groups of rock series on this index: ALI < 51 = alkalic (alkaline), 51 < ALI < 56 alkali-calcic, 56 < ALI < 61 = calc-alkalic (calc-alkaline), and ALI > 61 calcic. Peacock's classification is more applicable to rock suites formed by closed-system crystal-liquid fractionation of a basaltic or andesitic parental magma. The terms 'calc-alkaline' and 'alkaline' still are

This paper is not subject to U.S. copyright. Published in 1981 by the American Geophysical Union.

Paper number 1B1015.

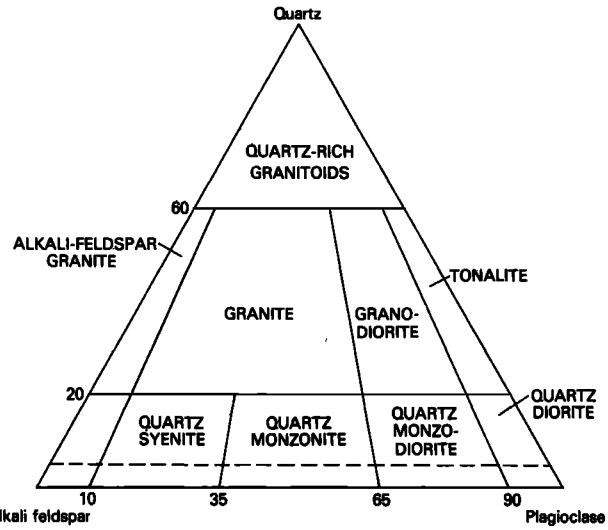

Fig. 1. Ternary diagram in volumetric proportions after *Streckeisen* [1976] showing compositional fields of granite and other rock types. Proportions of other minerals, not shown here, may range from 0 to 90% of the rock.

widely used. These terms and others are used in the extended chemical classifications in the papers of *Irvine and Baragar* [1971] and *Miyashiro* [1974].

Generation of Granitic-Rhyolitic Magmas

Granitic-rhyolitic magmas typically are generated in response to thermal and tectonic processes in the mantle. To date no one has demonstrated that such magmas may form in the mantle. Indeed, much experimental and geochemical work indicates that such siliceous liquids cannot originate there (e.g., Stern and Wyllie, Huang and Wyllie, this issue). Therefore, such magmas must be generated in the crust, although some may contain material of immediate mantle derivation (see, e.g., DePaolo, this issue). Furthermore, though rhyolite does occur in oceanic environments, such as the low-K rhyolites of some island arcs and the normal to alkaline rhyolites located near some oceanic spreading centers (*Sigurdsson* [1977] makes an excellent case for generation of Icelandic rhyolite by partial melting of plagiogranite of the oceanic crust)—they are miniscule in amount as compared to the granites and rhyolites of the continents. The latter occur in environments ranging from accretionary prisms at continental margins to continental margin magmatic arcs and fold belts to extensional regions and hotspots in continental interiors.

The origin of granite and rhyolite has been debated for the last two centuries. Three general processes have been suggested, as shown in Table 1. These are: (1) partial melting of pre-existing solid rocks; (2) closed-system crystal-liquid fractionation; and (3) coupled fractionation-melting, or open-system fractionation in which a mafic or intermediate liquid may extensively react with, or incorporate, the immediate wallrocks or roof. A subsidiary process—liquid state differentiation—may operate to produce significant compositional gradients in many magma chambers (Hildreth, Bacon et al., Mahood, this issue).

Partial Melting

The concept of partial to complete melting of crustal rocks to produce granitic-rhyolitic magmas was extensively discussed early in this century. It was approached from two very different points of view. One considered the Precambrian crystalline complexes of granitic to tonalitic gneisses, mica schists, amphobolites, and other intensely deformed and metamorphosed rocks intruded by siliceous magmas ranging from quartz diorite to granite. *Sederholm* [1907] gave us a classic example of such a complex in the mid-Proterozoic rocks of southern Finland and coined the word 'anatexis' for the partial to complete (?) melting of a siliceous gneiss to produce granitic magma. The second approach to partial melting involved the geosyncline or fold belt. *Loewinson-Lessing* [1911] described folding of a 10- to 15-km-thick filling of a large sedimentary basin wherein sufficient crustal thickening occurred that the lower parts of the basin reached melting temperatures. Fusion of shale, sandstone, and other sediments produced granitic magmas. These rise diapirically or stope their way into the overlying rocks.

Modern studies of crustal melting use the pressure-temperature constraints established by experimental petrology. *Hart and Allegre* [1980] summarize much recent work, emphasizing the use of O, Sr, Nd, and Pb isotopes in evaluating both source rocks and processes. Partial melting in this issue is discussed by Bickford et al., Cullers et al., Czamanske et al., Hill et al., Le Fort, Shaw, and Flood, and Wyborn et al.

Australian workers led by *Chappell and White* [1974] have given a large impetus to consideration of partial melting processes. In the Lachlan fold belt, southeastern Australia, they distinguish two major types of granite by source material—S type and I type. The S type is derived from sedimentary rocks (actually metamorphosed shale or pelitic schist for all Australian S type granites), and the I type granites are derived from igneous rocks that may range from gabbroic to granitic compositions. Both types are intruded as magma or mush consisting of various proportions of melt and residuum (or 'restite'). S type granites are biotite-muscovite-bearing and chemically are strongly peraluminous. I types, by contrast, are metaluminous, biotite or biotite-hornblende granites. The S type designation applies to similar granites in other parts of the world (see, e.g., Kistler et al., Le Fort, Lee et al., this issue), typically with only minor changes in *Chappell and White*'s [1974] original definition. However, there are other, far more voluminous granites of sedimentary origin, mostly in the Precambrian shields, that do not fit Chappell and White's classification. These granites are derived from graywackes—

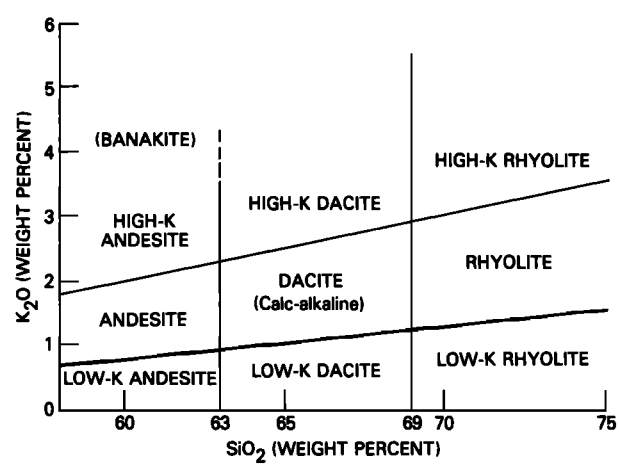

Fig. 2. Classification of andesite, dacite, and rhyolite by K_2O and SiO_2 contents [after *Ewart*, 1979].

TABLE 1. A Hypothetical Scheme for the Generation of Granitic-Rhyolitic Magmas

	General Process		
	Partial Melting	Crystal-Liquid Fractionation	Combined Melting-Fractionation
Geological environment	Fold belts, accretionary prisms(?), Precambrian greenstone belts, old metamorphic and plutonic complexes.	Midocean ridges, oceanic and continental intraplate magmatism or hotspots, island arcs, oceanic and continental rifts, other environments.	Continental margin magmatic arcs, continental rifts, continental hotspots, locally in accretionary prisms, probably in other environments.
Source materials	Graywacke, pelite (S type liquids), volcanic rocks, metamorphic complexes, plutonic complexes.	Basaltic liquid of olivine- or quartz-tholeiitic type, or andesitic liquid in some environments.	Mafic melt plus crustal melt less precipitated liquidus phases and less precipitated refractory crustal material; crustal melt from any crustal rock containing K_2O, Na_2O, SiO_2 (other components are incidental).
Heat source	Depression of source rocks into higher geotherms.	(Self-contained.)	Heats of crystallization of magmatic (liquidus) phases of mantle-derived mafic magma, locally (or commonly?) superheat of mantle-derived magma, crustal rocks initially about 200°–600°C.
Derivation of liquid	Partial melting of source rock and then (1) separation of liquid from refractory residue or (2) ascent of liquid-residue mush.	Separation of olivine, pyroxenes, plagioclase, and other phases from increasingly siliceous liquid: e.g., 100 parts basaltic liquid yield 8–10 parts granitic liquid.	Mantle-derived mafic magma pools in crust at deep to shallow levels and (1) while precipitating liquidus phases reacts directly with crustal rocks, partly melting and incorporating them, partly reacting with and precipitating their refractory parts, or (2) simply heating and melting nearby crustal rocks, or (3) mixing of liquids produced in 1 and 2.
Types of rocks produced	S type from pelite only; trondhjemite from metabasalt; minimum melt to calc-alkaline-trend type from other sources.	Granophyric-textured, high Fe/Mg types common; syenitic-trachytic types also common.	Metaluminous (approaching peralkaline) and peralkaline types of high Fe/Mg, low H_2O activity from 1 and 3 above; 2 above produces types as under 'partial melting' at left.

See text for details and references.

often of volcanogenic type—and so yield partial melts of metaluminous to mildly peraluminous character. An excellent example is given by *Arth and Hanson* [1975] in their chemical modelling of the late Archean Vermilion and Giants Range Granites of northeastern Minnesota. The I type designation of Chappell and White, however, has not met with similar widespread application (see discussion in Czamanske et al., this issue).

Closed-System Crystal-Liquid Fractionation

The second major mode of origin of siliceous magmas is by crystal-liquid fractionation or differentiation in which the magma does not interact with any of the enclosing rocks or fluids. In this process minerals that are less siliceous than the liquid crystallize and either settle or float out of the magma and thereby cause the remaining liquid to become more siliceous. This mechanism was first suggested by *Darwin* [1851] and has since been applied extensively to many crystal-liquid systems of mafic to intermediate composition. There is little doubt that basaltic liquids fractionate to yield granitic compositions: examples include the interstitial rhyolitic glasses (SiO_2 75.0–75.9%, K_2O 5.5–6.0%) formed by crystallization of basalt (SiO_2 50–51%, K_2O = 0.5–0.6%) of the Makaopuhi and Alae lava lakes, Hawaii [*Wright and Okamura,* 1977]; the worldwide occurrence of a few percent of scattered dikelets and pods of granophyre or intergrowths of alkali feldspar and quartz in diabase dikes and sills; and the soda rhyolites that are found with trachyte and other moderately alkaline lavas of some near-ridge oceanic islands (e.g., as at Easter Island [*Baker et al.,* 1974]). Many years ago *Grout* [1926] calculated that a moderately potassic basalt (K_2O = 1.52%) could yield a maximum of about 10% granite by crystal-liquid fractionation.

Controversy arises as to the scale of the fractionation of basalt to granite and rhyolite. Can granite stocks and batholiths several to many cubic kilometers in volume or continental rhyolitic ash flows of similar volume form by the closed-system fractionation of basaltic liquid? *Bowen* [1922*a*, 1928] proposed a 'reaction series' of minerals that successively crystallized and separated from a primary or mantle-derived basaltic liquid. This series commenced with olivine and calcic plagioclase and terminated with potash feldspar, muscovite and quartz, and led to production of calc-alkaline granitic-rhyolitic liquid. *Bowen* [1948] further suggested that most granites were produced by such fractionation and that assimilation of crustal rocks by the liquid was of minor extent. Bowen's influence was pervasive and a generation of geologists—except for the quasi-rational granitizers who contended that fluids or clouds of ions formed granites—tacitly agreed with him. To date, however, no one has demonstrated that any granite or rhyolite mass of several cubic kilometers or larger has formed by simple fractionation. There are several problems posed by

fractionation on such a scale that have not yet been fully resolved: one involves the small yield of siliceous liquid from basaltic liquid and the mechanics of its aggregation into large magma bodies [*Holmes*, 1936]. Another involves maintaining reservoirs of basaltic liquid in the crust of sufficient size to generate granitic batholiths 2 to 8 km thick and 5000–10,000 km^2 in area, such as the Pikes Peak batholith and the Wiborg granite massif of southern Finland and Russian Karelia. The intermediate to ultramafic residual material from such a large fractionation event would be of 25- to 100-km aggregate thickness. If such residua existed, have they all sunk back into the mantle? Lastly, isotopic studies of some granitic rocks long thought to be generated by simple fractionation indicate that they contain moderate to large fractions of wallrock material. A prominent example is the late-stage granophyre of the Skaergard intrusion, East Greenland [*Leeman and Dasch*, 1978].

Coupled Fractionation-Melting

The third major mode of origin of granite and rhyolite is a coupling or combination of crystal-liquid fractionation and melting of the enclosing crustal rocks (Table 1). As long ago as 1914, Daly speculated that superheated basaltic liquid might assimilate large fractions of crustal rocks (his 'abyssal assimilation'). In notable papers a few years later, *Bowen* [1922*b*, 1928] set forth the principles controlling reaction of magmas with inclusions. In particular, he pointed out that heats of crystallization of liquidus minerals—rather than superheat—would be the major energy source for the melting of siliceous to intermediate crustal inclusions in basaltic or andesitic liquids. Thus much of the heat originally supplied by a mantle reservoir in heating ultramafic mantle material to produce basalt is transferred by injection of that basaltic liquid into the crust and it becomes available for the melting of crustal rocks. Bowen, however, did not assign a major role to this mechanism for the production of granitic-rhyolitic liquids, as mentioned above. Holmes, however, did this in a notable but neglected paper of 1931, using as examples the largely bimodal gabbroic and dioritic-granitic Hebredean subvolcanic complexes of northwestern Scotland. *Wager et al.* [1965] revived Holmes' model for the shallow granites of the Western Red Hills complex, Skye. Strontium isotopic ratios indicate that these granites, indeed, were derived largely from Precambrian basement rocks [*Moorbath and Bell*, 1965].

The Hebredean granite bodies are roughly 10–100 km^3 in volume. Serious application of mantle-derived, basaltic heat sources to generation of larger batholiths include: (1) *Hargraves'* [1962] and *Ashwals'* [1978] discussion of anorthositic gabbro and the associated granite and syenite of the Adirondack massif; (2) *Presnall and Bateman's* [1973] and *Brown's* [1973] conclusion that andesitic or basaltic liquid generated at or near subduction zones migrated upward into the crust, causing melting of wallrocks and the extensive continental margin calc-alkaline magmatism of Sierra Nevadan type; and (3) *Hodge's* [1974] modelling of melting and other thermal relations around magma chambers. *Barker et al.* [1975] independently suggested that the widespread continental gabbro-anorthosite-syenite-potassic granite suites were formed by coupled fractionation-melting. *Smith and Shaw* [1975], *Duffield et al.* [1980], Bacon (this issue), and Hildreth (this issue) point out that basaltic liquid is a necessary heat source in the generation of continental rhyolites. The writer emphasizes that the plutonic suites of gabbro-anorthosite-syenite-granite type (e.g., the rapakivi massifs of southern Finland, and the Pikes Peak batholith) originally may have graded upward from deep anorthosite-gabbro complexes to syenite-granite complexes to rapakivitic batholiths to overlying subvolcanic-volcanic ring complexes (such as the Younger Granites and associated rhyolites and other rocks of Nigeria and nearby regions), and at the surface to largely bimodal basalt-rhyolite fields such as Yellowstone.

Taylor [1980] has considered the role of oxygen and strontium isotopes in coupled fractionation-melting. *DePaolo* [1981] has derived equations describing the behavior of trace elements and isotopes in such systems, and in this issue he considers the origin of the Sierra Nevada and Peninsular Ranges batholiths in this context.

Many aspects of coupled fractionation-melting need elucidation. Especially, do we have a complete range of interaction from an endmember in which the thermal source magma simply supplies the heat of partial melting but does not mix with or incorporate crustal material to situations in which the thermal source magma incorporates very high fractions of crustal melt?

FUTURE WORK

As seen in this issue, the currently active areas of research on granites and rhyolites are in the disciplines of geochemistry and petrology, and in volcanic processes. We need further studies on the magmatic source regions in the lower and intermediate crust. These would include modelling studies on thermal aspects of melting, such as that of *Yoder* [1980]; theoretical consideration of all possible source rocks, e.g., that of pelites by *Grant* [1973] and *Thompson and Algor* [1977]; study of geothermometers and geobarometers of xenoliths to give direct information on conditions of magma generation, like that of Wyborn et al. in this issue; geophysical studies that will give us physical information on regions where magmas are generated, such as that by the COCORP project of a magma body in the Rio Grande rift, New Mexico (see *Reilinger et al.* [1980] for references); and especially studies relating tectonism to the chemical style of magmatism.

Acknowledgments. I extend my thanks to many people for their guidance and cooperation with this special issue. Robert Coleman suggested JGR-Red as its vehicle, pointing out JGR's rare combination of worldwide distribution and modest cost. Allan Cox enthusiastically backed Coleman's suggestion. Editor Thomas Ahrens guided several aspects of the review process with care and good judgment and was helpful in many other ways. Ruth Ridenour gave exemplary editorial assistance and her expeditious handling of manuscripts and reviews made our present publication date possible. Lastly, the more than 50 earth scientists who reviewed the papers herein deserve our thanks for their effective commentary.

REFERENCES

Arth, J. G., and G. N. Hanson, Geochemistry and Origin of the early Precambrian crust of northeastern Minnesota, *Geochim. Cosmochim. Acta, 39*, 325–362, 1975.

Ashwal, L. D., Petrogenesis of massif-type anorthosites: Crystallization history and liquid line of descent of the Adirondack and Morin complexes, Ph.D. thesis, 136 pp., Princeton Univ., Princeton, N. J., 1978.

Baker, P. E., F. Buckley, and J. G. Holland, Petrology and geochemistry of Easter Island, *Contrib. Mineral. Petrol., 44*, 85–100, 1974.

Barker, F., D. R. Wones, W. N. Sharp, and G. A. Desborough, The Pikes Peak batholith, Colorado Front Range, and a model for the origin of the gabbro-anorthosite-syenite-potassic granite suite, *Precambrian Res., 2*, 97–160, 1975.

Bowen, N. L., The reaction principle in petrogenesis, *J. Geol., 30,* 177–198, 1922*a*.

Bowen, N. L., The behavior of inclusions in igneous magmas, *J. Geol., 30,* 513–570, 1922*b*.

Bowen, N. L., *The Evolution of the Igneous Rocks,* Princeton University Press, Princeton, N. J., 1928.

Bowen, N. L., The granite problem and the method of multiple prejudices, *Mem. Geol. Soc. Am., 28,* 79–90, 1948.

Brown, G. C., Evolution of granite magmas at destructive plate margins, *Nature Phys. Sci., 241,* 26–28, 1973.

Chappell, B. W., and A. J. R. White, Two contrasting granite types, *Pac. Geol., 8,* 173–174, 1974.

Cross, W. C., J. P. Iddings, L. V. Pirsson, and H. S. Washington, A quantitative chemico-mineralogical classification and nomenclature of igneous rocks, *J. Geol., 10,* 555–690, 1902.

Daly, R. A., *Igneous Rocks and Their Origin,* McGraw-Hill, New York, 1914.

Darwin, C. R., *Geological Observations on Coral Reefs, Volcanic Islands, and on South America,* Smith, Elder and Co., London, 1851.

DePaolo, D. J., Trace-element and isotopic effects of combined wallrock assimilation and fractional crystallization, *Earth Planet. Sci. Lett., 53,* 189–202, 1981.

Duffield, W. A., C. R. Bacon, and G. B. Dalrymple, Late Cenozoic volcanism, geochronology, and structure of the Coso Range, Inyo County, California, *J. Geophys. Res., 85,* 2381–2404, 1980.

Ewart, A., A review of the mineralogy and chemistry of Tertiary-Recent dacitic, latitic, rhyolitic, and related salic volcanic rocks, in *Trondhjemites, Dacites, and Related Rocks,* edited by F. Barker, pp. 13–121, Elsevier, Amsterdam, 1979.

Grant, J. A., Phase equilibria in high-grade metamorphism and partial melting of pelitic rocks, *Am. J. Sci., 273,* 289–317, 1973.

Grout, F. F., The use of calculations in petrology, *J. Geol., 34,* 549–581, 1926.

Hargraves, R. B., Petrology of the Allard Lake anorthosite suite, Quebec, in *Petrologic Studies: A Volume in Honor of A. F. Buddington,* edited by A. E. J. Engel, H. L. James, and B. F. Leonard, pp. 163–189, Geological Society of America, Boulder, Colo., 1962.

Hart, S. R., and C. J. Allegre, Trace-element constraints on magma genesis, in *Physics of Magmatic Processes,* edited by R. B. Hargraves, pp. 121–159, Princeton University Press, Princeton, N. J., 1980.

Hodge, D. S., Thermal model for origin of granitic batholiths, *Nature, 251,* 297–299, 1974.

Holmes, A., The problem of the association of acid and basic rocks in central complexes, *Geol. Mag., 68,* 241–254, 1931.

Holmes, A., The idea of contrasted differentiation, *Geol. Mag., 73,* 228–238, 1936.

Irvine, T. N., and W. R. B. Baragar, A guide to the chemical classification of the common igneous rocks, *Can. J. Earth Sci., 8,* 523–548, 1971.

Johannsen, A., *A Descriptive Petrography of the Igneous Rocks,* vol. 2, University of Chicago Press, Chicago, Ill., 1932.

Johannsen, A., *A Descriptive Petrography of the Igneous Rocks,* vol. 3, University of Chicago Press, Chicago, Ill., 1937.

Johannsen, A., *A Descriptive Petrography of the Igneous Rocks,* vol. 4, University of Chicago Press, Chicago, Ill., 1938.

Johannsen, A., *A Descriptive Petrography of the Igneous Rocks,* vol. 1, University of Chicago Press, Chicago, Ill., 1939.

Leeman, W. P., and E. J. Dasch, Strontium, lead and oxygen isotopic investigation of the Skaergard intrusion, East Greenland, *Earth Planet. Sci. Lett., 41,* 47–59, 1978.

Loewinson-Lessing, F., The fundamental problems of petrogenesis, or the origin of the igneous rocks, *Geol. Mag., 8,* 297–300, 1911.

Miyashiro, A., Volcanic rock series in island arcs and active continental margins, *Am. J. Sci., 274,* 321–355, 1974.

Moorbath, S., and J. D. Bell, Strontium isotope abundance studies and rubidium-strontium age determinations on Tertiary igneous rocks from the Isle of Skye, northwest Scotland, *J. Petrol., 6,* 37–66, 1965.

Morse, S. A., *Basalts and Phase Diagrams,* Springer-Verlag, Berlin, 1980.

Peacock, M. A., Classification of igneous rock series, *J. Geol., 39,* 65–67, 1931.

Peccerillo, A., and S. R. Taylor, Geochemistry of some calc-alkaline volcanic rocks from the Kastamonu area, northern Turkey, *Contrib. Mineral. Petrol., 58,* 63–81, 1976.

Presnall, D. C., and P. C. Bateman, Fusion relations in the system $NaAlSi_3O_8$-$CaAl_2Si_2O_8$-$KAlSi_3O_8$-SiO_2-H_2O and generation of granitic magmas of the Sierra Nevada batholith, *Geol. Soc. Am. Bull., 84,* 3181–3202, 1973.

Reilinger, R., J. Oliver, L. Brown, A. Sanford, and E. Balazs, New measurements of crustal doming over the Socorro magma body, New Mexico, *Geology, 8,* 291–295, 1980.

Sederholm, J. J., Om granit och gneis, *Bull. Comm. Geol. Finl., 23,* 1907.

Shand, S. J., *Eruptive Rocks,* John Wiley, New York, 1951.

Sigurdsson, H., Generation of Icelandic rhyolites by melting of plagiogranites in the oceanic layer, *Nature, 269,* 25–28, 1977.

Smith, R. L., and H. R. Shaw, Igneous-related geothermal systems, *Geol. Surv. Circ. U. S., 726,* 58–83, 1975.

Streckeisen, A., To each plutonic rock its proper name, *Earth Sci. Rev., 12,* 1–33, 1976.

Taylor, H. P., Jr., The effects of assimilation of country rocks by magmas on $^{18}O/^{16}O$ and $^{87}Sr/^{86}Sr$ systematics in igneous rocks, *Earth Planet. Sci. Lett., 47,* 243, 1980.

Thompson, A. B., and J. R. Algor, Model systems for anatexis of pelitic rocks, *Contrib. Mineral. Petrol., 63,* 247–269, 1977.

Tuttle, O. F., and N. L. Bowen, Origin of granite in the light of experimental studies in the system $NaAlSi_3O_8$-$KAlSi_3O_8$-SiO_2-H_2O, *Mem. Geol. Soc. Am., 74,* 1958.

Wager, L. R., E. A. Vincent, G. M. Brown, and J. D. Bell, Marscoite and related rocks of the Western Red Hills Complex, Isle of Skye, *Philos. Trans. R. Soc. London Ser. A, 257,* 273–307, 1965.

Wright, T. L., and R. T. Okamura, Cooling and crystallization of tholeiitic basalt, 1965 Makaopuhi lava lake, Hawaii, *Geol. Surv. Prof. Pap. U. S., 1004,* 1977.

Yoder, H. S., Jr., Heat and mass transfer in magma generation: A progress report of an experimental study, *Year Book Carnegie Inst. Washington, 79,* 263–267, 1980.

(Received March 12, 1981;
revised May 21, 1981;
accepted June 16, 1981.)

JOURNAL OF GEOPHYSICAL RESEARCH, VOL. 86, NO. B11, PAGES 10137-10152, NOVEMBER 10, 1981

A Summary of the Geology and Petrology of the Sierra La Primavera, Jalisco, Mexico

GAIL A. MAHOOD

Department of Geology, School of Earth Sciences, Stanford University, Stanford, California 94305

The Sierra La Primavera, near Guadalajara, Mexico, is a Late Pleistocene rhyolitic center consisting of lava flows and domes, ash flow tuff, air fall pumice, and caldera lake sediments. All eruptive units are high-silica rhyolites, but systematic compositional differences correlate with age and eruptive mode. The earliest lavas erupted approximately 145,000 years ago and were followed approximately 95,000 years ago by the eruption of about 20 km^3 of magma as ash flows that form the Tala Tuff. The Tala Tuff is zoned from a mildly peralkaline first-erupted portion enriched in Na, Rb, Cs, Cl, F, Zn, Y, Zr, Nb, Sb, HREE, Hf, Ta, Pb, Th, and U to a metaluminous last-erupted part enriched in K, LREE, Sc, and Ti; Al, Ca, Mg, Mn, Fe, and Eu are constant within analytical errors. Collapse of the roof zone of the magma chamber led to the formation of a shallow 11-km-diameter caldera in which lake sediments began to collect. The earliest postcaldera lava, the south-central dome, is nearly identical to the last-erupted portion of the Tala Tuff, whereas the slightly younger north-central dome is chemically transitional from the south-central dome to later, more mafic, ring domes. This sequence of ash flow tuff and domes represents the tapping of progressively deeper levels of a zoned magma chamber 95,000 ± 5,000 years ago. Sedimentation continued and a period of volcanic quiescence was marked by the deposition of some 30 m of fine-grained ashy sediments. Approximately 75,000 years ago a new group of ring domes erupted at the southern margin of the lake. These domes are lapped by only 10–20 m of sediments as uplift resulting from renewed insurgence of magma brought an end to the lake. This uplift culminated in the eruption, beginning approximately 60,000 years ago, of aphyric lavas along a southern arc. The youngest of these lavas erupted approximately 30,000 years ago. The lavas that erupted 75,000, 60,000, and 30,000 years ago became decreasingly peralkaline and progressively enriched only in Si, Rb, Cs, and possibly U with time. They represent successive eruption of the uppermost magma in the postcaldera magma chamber. Eruptive units of La Primavera are either aphyric or contain up to 15% phenocrysts of sodic sanidine ≥ quartz ≫ ferrohedenbergite > fayalite > ilmenite ± titanomagnetite. Major element compositions of sanidine, clinopyroxene, and fayalite phenocrysts vary only slightly between eruptive groups, but the concentrations of many trace elements change by factors of 5–10. This is reflected in phenocryst/glass partition coefficients that differ by factors of up to 20 between successively erupted units. Because the major element compositions of the phenocrysts and the pressure, temperature, and f_{O_2} of the magmas were essentially constant, the large variations in partitioning behavior are thought to result from small changes in bulk composition of the melt. Crystal settling and incremental partial melting are by themselves incapable of producing either the chemical gradients within the Tala Tuff magma chamber or the trends with time in the post-95,000-year lavas. Rather, diffusional processes in the silicate liquid are thought to have been the dominant differentiation mechanisms. The zonation in the Tala Tuff is attributed to transport of trace metals as volatile complexes within a thermal and gravitational gradient in a volatile-rich but water-undersaturated magma. The evolution of the postcaldera lavas with time is thought to involve the diffusive emigration of trace elements from a relatively dry magma as a decreasing proportion of network modifiers and/or a decreasing concentration of complexing ligands progressively reduced octahedral site availability in the silicate melt.

INTRODUCTION

One way to understand the differentiation processes operating in high-level magma chambers that solidify as granitic plutons is to study material erupted from such chambers. Ash flow tuffs are rapidly quenched voluminous samples of magma chambers; as such they have made possible the characterization of chemical and thermal gradients within the upper portions of silicic magma chambers just prior to eruption [*Lipman et al.*, 1966; *Smith and Bailey*, 1966; *Hildreth*, 1977, 1979; *Smith*, 1979; *Ritchie*, 1979; *Hildreth et al.*, 1980]. Complementary to studies of ash flow tuffs, which are inverted records of magma chambers at single points in time, is the information contained in a sequence of eruptive units, which record the chemical evolution of the upper portions of a silicic magma chamber through time. Making the reasonable assumption that a lava flow or ash flow taps the most differentiated uppermost magma in the system at a particular moment, a sequence of eruptive units provides progress reports on the differentiation mechanisms operating at depth. The main purpose of this study of the Sierra La Primavera, therefore, has been to trace the chemical evolution of a rhyolitic complex through time, interpreting it as the periodic sampling of an evolving magma chamber.

To determine the eruptive history, the Sierra La Primavera, located on the western outskirts of Guadalajara, Jalisco, Mexico (Figure 1), was mapped at a scale of 1:25,000. Eruptive units were classified into groups based on stratigraphic relations, and the eruptive sequence was calibrated with over 50 K-Ar dates performed at University of California, Berkeley [*Mahood*, 1980*a*]. This paper summarizes the geological and chemical evolution of the Primavera system; the geology of the Sierra La Primavera is described in more detail by *Mahood* [1980*a*, 1980*b*], whereas the petrology is discussed more fully by *Mahood* [1980*a*, 1981].

REGIONAL SETTING

The Sierra La Primavera lies at the intersection of the two major Cenozoic volcanic provinces of Mexico (Figure 1). Its mildly peralkaline rocks stand in marked chemical contrast to both the andesitic stratovolcanoes and basaltic cinder cones

Copyright © 1981 by the American Geophysical Union.

Paper number 1B0529.
0148-0227/81/001B-0529$01.00

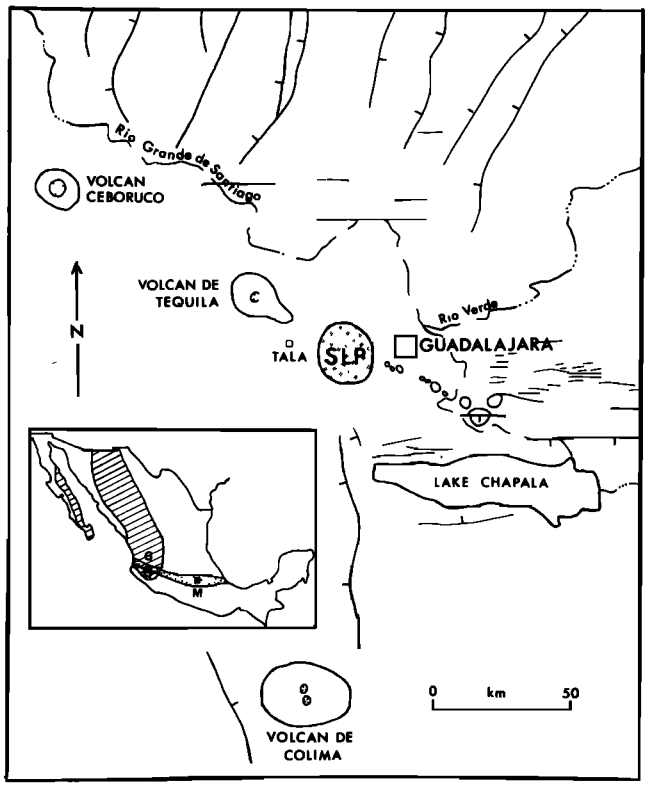

Fig. 1. Regional location map (modified from Mahood [1980*b*]). This map shows the location of the Sierra La Primavera (SLP) relative to the major andesitic stratovolcanoes of the western portion of the Pliocene-Recent Mexican Neovolcanic Belt (stippled), the Tertiary Cordilleran Province (diagonal ruling), regional faulting, and the cities of Guadalajara (G) and México (M). The Sierra La Primavera lies along a line parallel to the northwest trend of the western portion of the Mexican Neovolcanic Belt defined by Volcán Tequila and ten basaltic andesite cinder cones (small circles southeast of Guadalajara).

that make up the bulk of the Pliocene to Recent Mexican Neovolcanic Belt and to the largely metaluminous silicic lavas and ash flows that dominate the Tertiary Cordilleran Province. Normal faulting has broken the area into a series of grabens, one of the largest being occupied by Lake Chapala. Volcán Colima, south of La Primavera, sits within a large north–south graben and is on line with the east–west trend of the eastern portion of the Mexican Neovolcanic Belt. The intersection of extensional features near the Sierra La Primavera may have focused mafic volcanism in the area, leading to large-scale melting of crustal material to give rise to Primavera magmas.

Little is known of the prevolcanic basement that might be partially melted to give rise to the Primavera magmas. Despite the nearly 1000 m of relief in the nearby canyon of the Río Grande de Santiago, the oldest rocks exposed are Miocene ash flow tuffs [*Watkins et al.*, 1971]. Much of the area now occupied by the Sierra La Primavera appears to be immediately underlain by andesitic and basaltic lava flows, which are locally exposed in canyons within the Sierra and at its margins and are common as accidental debris in air fall pumice deposits.

All recognized faults in the Sierra La Primavera are related either to caldera collapse or to uplift thought to be a result of renewed insurgence of magma. All faults begin and end within the environs of the complex; none extend beyond the Sierra to offset older rocks. This suggests that, while the location of the Sierra La Primavera may be controlled by regional tectonics, faulting within the complex is a product of local hydrostatic adjustments to changes in the level of the underlying magma chamber. This lack of regional faults in the Sierra La Primavera is circumstantial evidence for an underlying magma chamber that cannot sustain brittle fracture.

SUMMARY OF THE GEOLOGIC HISTORY AND PETROLOGY

A brief history of the Sierra La Primavera follows and is summarized in Table 1. The earliest lavas erupted about 145,000–100,000 years ago. They were followed by eruption, approximately 95,000 years ago, of about 20 km^3 of magma as ash flows that formed the Tala Tuff. Collapse of the roof zone of the magma chamber upon eruption of the Tala Tuff produced an 11-km-diameter caldera that soon filled with water. Onset of lacustrine sedimentation was followed rapidly by eruption of two domes in the center of the lake (the south-central and north-central domes, which form the lower portions of Mesa El Nejahuete (I) and Cerro Alto (H), respectively, in Figure 2). The base of the south-central dome occurs at the same position within the sediments as the 'giant pumice horizon', an important stratigraphic marker, whereas the north-central dome overlies the giant pumice horizon. Ring domes representing some 5 km^3 of porphyritic magma then erupted along two concentric arcs: one along the northeast portion of the ring fracture and the other crossing the middle of the lake. A period of volcanic quiescence was marked by deposition of some 30 m of fine-grained ashy sediments. Approximately 75,000 years ago, activity resumed with the eruption of 3 km^3 of aphyric and porphyritic magma at the southern margin of the lake to form a younger group of ring domes. Ensuing uplift, thought to result from renewed insurgence of magma, brought an end to the lake. This uplift culminated in the eruption, beginning approximately 60,000 years ago, of 7 km^3 of aphyric lavas along a southern arc. The youngest of the southern arc lavas, Cerro El Colli (FF, Figure 2), erupted approximately 25,000–30,000 years ago.

All the eruptive units of the Sierra La Primavera are mildly peralkaline high-silica (>75% SiO_2 on an anhydrous basis) rhyolites. All of them are similar in gross composition, but there are systematic chemical differences that correlate with both age and eruptive mode. Variations in major element compositions at La Primavera are small; in contrast, variations in the minor and trace elements are striking. Representative analyses of major and minor elements by classical wet chemistry, and of minor and trace elements by instrumental neutron activation analysis (INAA) and X ray fluorescence are given in Table 2. Additional analyses can be found in works by *Mahood* [1980*a*, 1981]. In the following discussion, samples with variable degrees of posteruptive hydration have been compared on the basis of analyses recalculated free of water and normalized to 100%.

The proportion of phenocrysts in the porphyritic eruptive units ranges from less than 1% to 15% by volume. Sodic sanidine and quartz, the former generally more abundant, together comprise approximately 97–99% of the phenocrysts, the remainder being ferrohedenbergite, fayalite, and ilmenite, typically in the proportions 50:10:1. Titanomagnetite, zircon, and apatite occur in some units. Phenocryst assemblages of the various eruptive groups are summarized in Table 1, and representative analyses appear in Table 3. Sanidine, ferrohedenbergite, and ilmenite are unzoned and homogeneous. The compositions of the phenocrysts changed slightly with time,

TABLE 1. Summary of the Geologic History of the Sierra La Primavera

Event	Approximate Age Based on K-Ar Dates [*Mahood*, 1980*a*], years	Magma Volume, km^3	Total Phenocrysts, %	Phenocryst Assemblage
Eruption of precaldera lavas	144,000–100,000	2(?)	0 or 10–15	San ≥ Q ≫ Cpx ≫ Fa > Ilm > Mt
Eruption of the Tala Tuff		20	0–1	San ≥ Q
Caldera collapse				
Eruption of central domes and deposition of giant pumice horizon	95,000 ± 10,000			
Giant pumice horizon		0.15	1	San > Q ≫ Cpx ≫ Ilm
South central dome		0.8	1	San > Q ≫ Cpx > Fa ≫ Ilm
North central dome		0.7	10	San > Q ≫ Cpx > Fa ≫ Ilm
Eruption of older ring domes		5	10–15	San ≥ Q ≫ Cpx > Fa ≫ Ilm
Eruption of younger ring domes	75,000	3	0 or 10	San ≥ Q ≫ Cpx > Fa ≫ Ilm
Uplift				
Eruption of southern arc lavas	60,000 and 30,000	7	0	None

but within eruptive groups the phenocrysts are uniform in composition.

GEOLOGICAL AND CHEMICAL EVOLUTION OF THE SIERRA LA PRIMAVERA

Precaldera Lavas

About 145,000 years ago the first lavas of the Sierra La Primavera were erupted. These porphyritic and aphyric domes and flows presently crop out in two areas (Figures 2 and 3*a*), but there may well have been other lavas now covered by younger eruptive units. The precaldera lavas make up the compositionally most heterogeneous eruptive group. In the northern area, the porphyritic Río Salado dome (A, Figure 2) erupted first, followed by the aphyric Cañon de las Flores flow (B, Figure 2). Both units are clearly overlain by the porphyritic dome of Mesa El León (C, Figure 2) and by the Tala Tuff. These three units show no systematic chemical trends with time. Because the southern group of precaldera lavas has been blanketed by Tala Tuff, minor ash flows, air fall, and alluvium, neither the number of separate units nor their relative ages are known.

Tala Tuff

About 95,000 years ago, ash flows representing approximately 20 km^3 of magma erupted from the Sierra La Primavera and emptied into the surrounding basins, covering some 700 km^2 (Figure 4). These ash flows are collectively named the Tala Tuff for the village of Tala (Figure 1). The Tala Tuff consists of many small ash flows that are grouped into three easily recognized informal members:

1. The first member contains white aphyric pumice and makes up more than 90% of the volume of the tuff. It occurs as intracaldera ash flows within the Sierra La Primavera proper and as nonwelded, approximately 60-m-thick, outflow sheets filling the surrounding basins.

2. The second member of the Tala Tuff is about 10 m thick and is characterized by white aphyric pumice and grey pumice lapilli containing very sparse quartz and sanidine, as well as lapilli that represent the mixing of the two magmas. Despite their darker color, the grey pumice lapilli are the same composition as the white pumice lapilli in the overlying third member. The transition from the second member of the Tala Tuff to the underlying and overlying members is gradational but takes place within less than 1 m stratigraphically.

3. The third member of the Tala Tuff is 5–10 m thick and is characterized by white pumice lapilli, bearing less than 1% quartz and sanidine, set in a pink ashy matrix. In many places, the third member shows interlayering of ash flow and air fall layers, and the ash flow portions are laminated.

Compositional Zonation in the Tala Tuff

The Tala Tuff is mildly zoned; most major elements remain approximately constant through the erupted volume, and the most strongly zoned elements, Y and Sc, vary only by a little more than a factor of two. From the first-erupted through the last-erupted portion of the Tala Tuff, the molar ratio $Na_2O/(Na_2O + K_2O)$ drops from 0.6 to 0.55. Wet chemical analyses demonstrate that TiO_2 increases from 0.09 to 0.13 wt. %, while FeO* (total iron expressed as FeO), MnO, and MgO remain approximately constant at 1.70, 0.05, and 0.04 weight percent, respectively. Chlorine is strongly partitioned into water-rich vapor relative to a silicic liquid [*Burnham*, 1967]. Despite possible loss on eruption, Cl, as well as F, is enriched in the first-erupted portion of the Tala Tuff, which contains approximately 0.16% Cl and 0.12% F. Cl and F constitute about 0.11% and 0.09%, respectively, of the last-erupted portion of the Tala Tuff. Na, Rb, Cs, Sm, Gd, Tb, Tm, Yb, Lu, Y, Zr, Hf, Pb, Th, U, Nb, Ta, Sb, and Zn are all enriched in the first-erupted portion of the Tala Tuff, whereas K, Ca, La, Ce, Nd, Ti, and Sc are enriched in the last-erupted part. The Tala Tuff is zoned from a mildly peralkaline first-erupted portion (agpaitic index = 1.10, Zr ≃ 600 ppm) to a barely metaluminous last-erupted part (agpaitic index = 0.99, Zr ≃ 500 ppm). La Primavera is not unique in this regard. Some of the Tertiary caldera complexes of the western United States (e.g., the Black Mountain [*Christiansen and Noble*, 1965] and Silent Canyon [*Noble et al.*, 1968] calderas) produced ash flows zoned from peralkaline to subalkalic compositions. Many ring dike complexes in New England [*Billings*, 1956] and northern Nigeria [*Jacobsen*, 1977] show alternation of peralkaline and metaluminous granites in the same center.

Elemental abundances in the first-erupted portion of the Tala Tuff relative to those in the last-erupted portion are plotted in Figure 5, following *Hildreth* [1979]. This is equivalent to plotting the ratio of the abundance in the roof of the magma chamber to that in the deepest level tapped. As is true for the Bishop Tuff [*Hildreth*, 1979], light rare earth elements (LREE) are depleted and heavy rare earth elements (HREE) are enriched roofward. Sr and Ba (among the most strongly zoned elements in the Bishop Tuff) do not appear in Figure 5

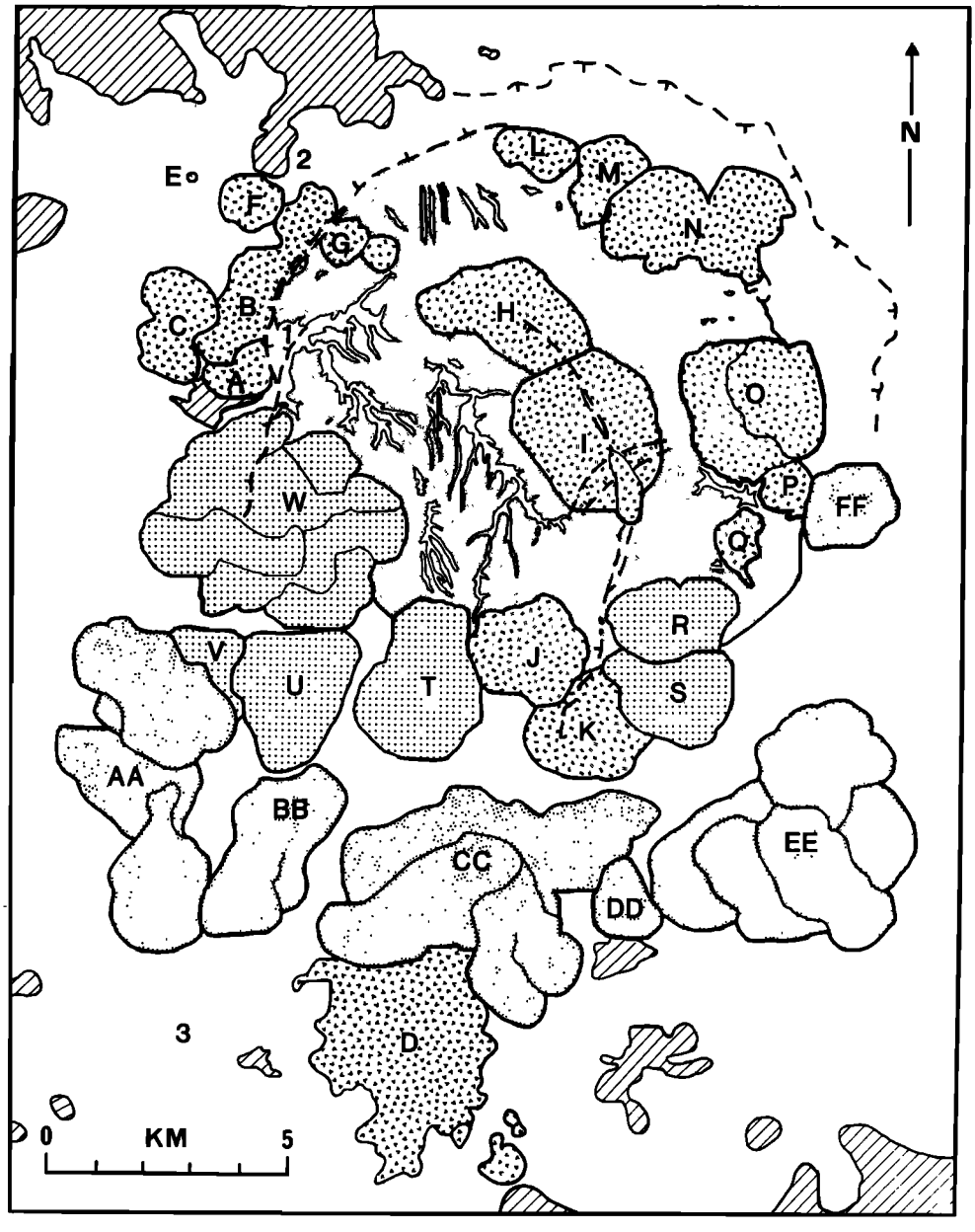

Fig. 2. Location map of the Sierra La Primavera (modified from *Mahood* [1980*b*]). The Sierra La Primavera is located on the western outskirts of Guadalajara, Jalisco, Mexico. Diagonal ruling: pre-Primavera volcanic rocks; V pattern: precaldera lavas; unpatterned: Tala Tuff (also includes minor ash flow tuffs, primary and reworked air fall deposits, and alluvium, all generally underlain by the Tala Tuff); light stipple: lake sediments; double-dash pattern: older ring domes; rectilinear dots: younger ring domes; heavy stipple: southern arc lavas. Faults are shown as heavy dashed lines. Letters refer to the names of eruptive centers, whereas numbers refer to cultural features, as follows: A: Río Salado dome; B: Cañon de Las Flores flow; C: Mesa El Léon dome; D: Arroyo Saucillo group; E: Mesa El Chiquihuitillo; F: Mesa El Burro dome; G: Cerro Chato dome; H: Cerro Alto composite dome; I: Mesa El Nejahuete composite dome; J: Cerro El Tule dome; K: El Madrón dome; L: Pinar de La Venta dome; M: Arroyo La Cuartilla dome; N: Mesa La Lobera dome; O: Cerro El Chapulín dome; P: Dos Coyotes dome; Q: Arroyo Las Pilas dome; R: Arroyo Ixtahuatonte dome; S: La Cuesta dome; T: Cerro El Culebreado dome; U: La Puerta dome; V: Arroyo Las Animas dome; W: Cerro El Pedernal center; AA: Cerro San Miguel center; BB: Llano Grande flow; CC: Cerros Las Planillas center; DD: Arroyo Colorado dome; EE: Cerro El Tajo center; FF: Cerro El Colli dome; 1: Río Caliente; 2: La Venta del Astillero; 3: Tierra Blanca.

because in all samples they are below detection levels (10 and 20 ppm, respectively). The antithetic behavior of Na_2O and K_2O in the Tala Tuff is common to a number of high-silica eruptive units, including the Bishop Tuff, the Bandelier Tuff [*Smith and Macdonald,* 1979], and several ash flows from the Yellowstone Plateau (W. Hildreth, personal communication, 1979).

Caldera Collapse

The second and third members of the Tala Tuff occur only in the central part of the Sierra La Primavera; they are not found as outflow sheets in the surrounding basins. This suggests that the estimated 150–500 m of collapse of the roof zone of the magma chamber began while the first member of the

TABLE 2. Representative Whole Rock Analyses

	Eruptive Group[1]								
	PCD	TT-E	TT-L	SCD	NCD	ORD	YRD	60	30
SiO_2	76.84	76.44	77.02	76.67	76.43	76.10	76.85	77.02	77.28
TiO_2	0.09	0.09	0.13	0.13	0.18	0.17	0.12	0.09	0.06
Al_2O_3	11.79	11.70	11.70	11.67	11.66	11.71	11.44	11.71	11.91
FeO*	1.55	1.70	1.72	1.76	1.79	2.02	1.72	1.42	1.18
MnO	0.04	0.05	0.05	0.05	0.05	0.07	0.05	0.04	0.04
MgO	0.04	0.04	0.05	0.05	0.05	0.05	0.04	0.03	0.02
CaO	0.21	0.18	0.26	0.27	0.20	0.27	0.20	0.23	0.30
Na_2O	4.25	4.70	3.88	4.42	4.60	4.62	4.54	4.69	4.51
K_2O	4.89	4.72	4.81	4.66	4.80	4.83	4.71	4.44	4.47
F	0.11	0.12	0.09	0.09	0.08	0.09	0.09	0.10	0.10
Cl	0.12	0.16	0.11	0.10	0.09	0.09	0.11	0.12	0.13
Agpaitic index	1.04	1.10	0.99	1.06	1.09	1.10	1.10	1.07	1.03
La	48	41	66	67	81	81	57	39	35
Ce	112	92	141	135	171	172	124	89	79
Nd	46	50	56	54	67	66	52	39	35
Sm	9.6	13.1	11.9	10.9	11.3	11.3	10.3	8.4	8.0
Eu	0.07	0.09	0.06	0.06	0.12	0.12	0.09	0.06	0.03
Tb	1.54	2.58	1.63	1.63	1.59	1.48	1.55	1.36	1.25
Yb	6.4	10.8	6.2	6.0	5.6	5.9	6.1	5.6	5.4
Lu	0.96	1.41	0.90	0.86	0.86	0.84	0.90	0.80	0.79
Rb	188	275	171	172	141	144	163	167	195
Cs	3.7	6.4	4.2	3.6	3.4	2.9	3.3	3.6	4.4
Th	18.4	27.3	18.9	19.1	18.1	17.6	18.2	16.6	19.6
U	7.0	9.5	6.2	7.0	6.6	5.1	5.8	5.7	6.5
Hf	13.6	20.0	13.2	13.3	15.3	15.2	14.7	11.3	8.9
Y	65	139	54	76	51	47	53	50	47
Zr	454	615	499	526	683	682	584	379	228
Nb	66	112	69	71	70	66	65	68	68
Ta	4.3	6.7	3.9	3.9	3.9	3.5	3.8	3.6	3.4
Sc	0.96	0.41	0.95	0.99	0.83	1.06	0.71	0.69	1.10
Zn	116	179	114	106	100	106	108	100	84

To facilitate comparison of variably hydrated samples, all analyses have been recalculated to 100%, free of water.

[1] PCD = precaldera dome, TT-E = early-erupted Tala Tuff, TT-L = late-erupted Tala Tuff, SCD = south-central dome, NCD = north-central dome, ORD = older (95,000-yr) ring domes, YRD = younger (75,000-yr) ring domes, 60 = 60,000-yr southern arc lavas, 30 = 30,000-yr-old youngest dome, Cerro El Colli.

Tala Tuff was still erupting, so that the two upper members were entirely ponded within the collapse basin. Topographic expression of a bounding ring fault is present only to the west of Río Caliente (1 in Figure 2), where the precaldera Río Salado and Cañon de las Flores lavas are truncated. The circular pattern defined by the vents for the northeastern arc of older ring domes and the younger ring domes indicates the location of the remainder of the master ring fault.

Caldera Lake Sedimentation

The caldera rapidly filled with water, and sediment began to be deposited on the surface of the Tala Tuff almost immediately, protecting it from all but minor fluvial erosion. These sediments consist dominantly of 15- to 50-cm-thick layers of planar-bedded and low-angle cross-bedded coarse ash and pumice lapilli that show repetitive normal grading with some erosion of the finely cross-bedded tops of the sequences. They seem to be saturated pumice turbidity flows. The source for most of this pumice appears to be erosion of small 'islands' of Tala Tuff within the shallow lake and reworking of immediately post-Tala air fall deposits, which are several meters thick outside the caldera. The thickness of this basal pumiceous section varies from 0 to 25 m due to pre-existing topography on the floor of the caldera, but everywhere the top is marked by a 30-cm-thick fine white ashy layer.

Then a rather spectacular sedimentation event occurred. A 3- to 13-m-thick horizon of giant pumice blocks set in a diatomaceous ashy matrix was deposited over the entire 110 km^2 of the lake. The blocks of fully inflated pumice range from 0.3 to more than 6 m across and are commonly columnar-jointed in a crudely radial pattern. The ashy matrix is finely laminated, and the laminae are deformed around the pumice blocks. The distribution of particle sizes is bimodal; pumice lapilli of intermediate size are rare. The unique character of this deposit made it an important stratigraphic marker bed within the lake bed sequence.

It is envisioned that the giant pumice blocks formed when phenocryst-poor lavas erupted into the middle of the shallow lake. The blocks floated over the surface of the lake and eventually saturating with water sank gently to the bottom of the lake, where fine wind-blown ash from the surrounding plains of the Tala Tuff and diatoms were accumulating as finely laminated sediments [*Mahood*, 1980*b*].

At the margins of the lake, the giant pumice horizon was deposited directly over the eroded Tala Tuff or on 'inselbergs' of pre-Tala rocks. Over most of the lake it was deposited on

TABLE 3. Representative Phenocryst Analyses

	Eruptive Group																					
	Sanidine					Ferrohedenbergite				Fayalite				Ilmenite				Titano-magnetite				
	PCD	TT-L	SCD	NCD	ORD	YRD	PCD	SCD	NCD	ORD	YRD	SCD	NCD	ORD	YRD	PCD	SCD	NCD	ORD	YRD	PCD	
SiO_2	66.0	66.6	66.7	67.0	66.5	66.2	47.5	47.3	47.6	48.1	48.1	29.5	29.4	29.9	30.2	0.01	0.02	0.05	0.16	0.10	0.03	
TiO_2							0.19	0.28	0.33	0.33	0.23	0.02	0.02	0.03	0.03	49.2	49.6	50.3	49.7	49.5	16.8	
Al_2O_3	19.5	19.3	19.4	19.4	19.3	19.0	0.25	0.29	0.24	0.22	0.22	0.02	0.04	0.02	0.02	0.01	0.04	0.06	0.01	0.01	0.26	
FeO*	0.20	0.19	0.21	0.19	0.21	0.22	30.3	31.0	30.3	30.1	30.0	64.8	64.7	64.5	65.7	48.4	47.9	47.1	46.8	47.6	76.5	
MnO							1.37	1.36	1.54	1.51	1.35	3.45	3.64	3.71	3.55	1.34	1.27	1.44	1.39	1.33	0.81	
MgO							0.34	0.28	0.71	0.62	0.40	0.19	0.28	0.33	0.19	0.04	0.04	0.06	0.06	0.04	0.03	
ZnO							18.9	18.5	18.5	18.5	18.7	0.13	0.28	0.10	0.12	0.10	0.09	0.03	0.05	0.08	0.33	
CaO	0.08	0.14	0.13	0.13	0.11	0.05	0.72	0.56	0.50	0.52	0.66	0.27	0.08	0.28	0.25	0.02	0.02	0.09	0.02	0.04	0.01	
Na_2O	6.17	6.68	6.67	6.98	6.68	6.26																
K_2O	7.94	7.21	7.29	6.97	7.16	7.63																

See footnote to Table 2 for Eruptive Group abbreviations.

top of the 30-cm-thick layer of fine white ash that caps the basal pumiceous sediments. The giant pumice horizon 'seals' faults in the Tala Tuff and the overlying pumiceous sediments, but is rarely cut by faults itself, showing that faulting related to caldera collapse had ceased by the time it was deposited.

Central Domes

A dome comprising the lower part of Mesa El Najahuete was emplaced at the stratigraphic level of the giant pumice horizon in the south-central portion of the lake (Figure 3*b*). Both the giant pumice horizon and this south-central dome have less than 1% phenocrysts, in contrast to later domes with approximately 10% phenocrysts that stratigraphically overlie the giant pumice horizon.

The chemical similarity of the last-erupted portion of the Tala Tuff to the south central dome and the presence of a 'co-ignimbrite lag-fall deposit' [*Wright and Walker,* 1977] near the dome suggest that the Tala Tuff may have erupted from a central vent near the present site of the south-central dome [*Mahood,* 1980*b*].

Shortly after emplacement of the south-central dome and deposition of the giant pumice horizon, a dome containing 10% phenocrysts erupted through the middle of the lake (Figure 3*b*). The base of this north-central dome overlies subaerial pumice breccias on top of the giant pumice horizon. The whole rock and phenocryst compositions of the giant pumice horizon are generally intermediate between those of the south- and north-central domes [*Mahood,* 1981].

The sedimentary section above the giant pumice horizon is quite variable. Typically the giant pumice horizon is overlain by less than 10 m of stratified pumice before the section becomes dominated by fine white ashy and diatomaceous beds. Locally, fine-grained deposits directly overlie the giant pumice horizon. The pumiceous lacustrine beds appear to be the product of air fall eruptions that preceded the emplacement of a group of ring domes.

Older Ring Domes

The older ring domes contain approximately 10% phenocrysts and represent some 5 km^3 of magma. They erupted along two concentric arcs: one along the ring fracture at the northeast margin of the lake, and the other through the middle of the lake (Figure 3c). The new magma erupted through the earlier central domes; thus Cerro Alto and Mesa El Nejahuete are composite domes, their lower and upper portions consisting of magmas of slightly different composition. The autobrecciated lower margins of older ring domes that erupted in the lake or at its margin are horizontal; the contacts generally occur within the lower portion of the fine-grained sediments, approximately 10 m above the giant pumice horizon. Locally (e.g., on the west flank of Mesa El Nejahuete) the intrusion of these domes deformed and uplifted the lake sediments, including the giant pumice horizon.

The cauldron block is cut by an arcuate system of normal faults that extends 9 km from Cerro Alto to just south of Cerro El Tule (Figure 2). This fault offsets Mesa El Nejahuete and seems to have provided structural control for the extrusion of a ridge of pumiceous porphyritic lava on its south flank, suggesting that faulting and eruption were closely related. This fault may represent a fracture developed in the roof zone of the underlying magma chamber on caldera collapse that was reactivated during eruption of the older ring

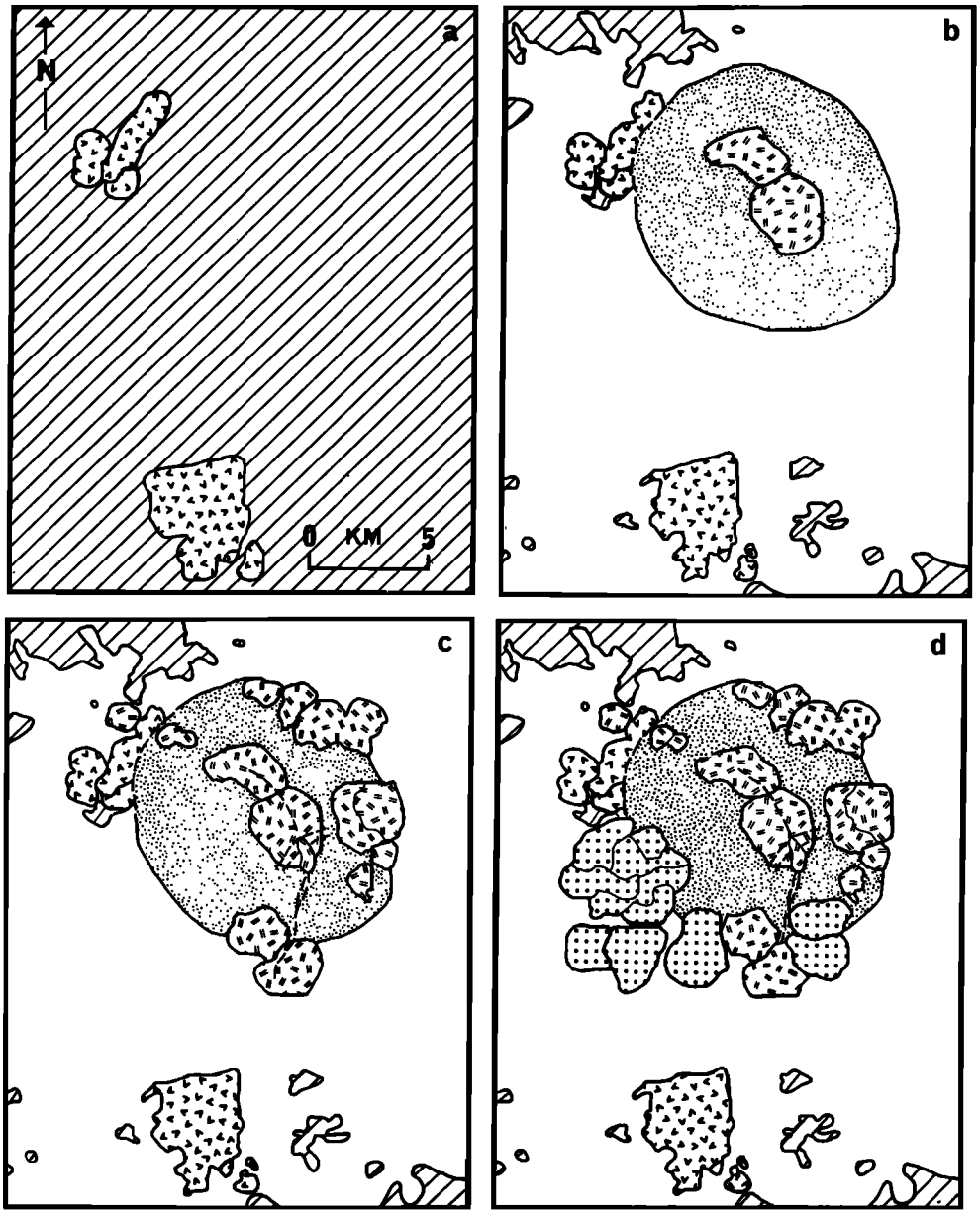

Fig. 3. Paleogeography of the Sierra La Primavera [from *Mahood,* 1980*b*]. Pre-Primavera volcanic rocks: diagonal ruling; precaldera lavas: V pattern; Tala Tuff: blank; lake sediments: light stipple; central domes and older ring domes: paired dashes; younger ring domes: rectilinear dots; faults: dashed lines. (*a*) 100,000 years ago, following eruption of the precaldera lavas. There may have been other lavas belonging to this period, now covered by younger eruptive units. (*b*) 95,000 years ago, following eruption of the Tala Tuff, caldera collapse, and the eruption of the central domes through the middle of the lake. (*c*) 90,000 years ago, following eruption of the older ring domes. These ring domes erupted along two concentric arcs: one along the ring fracture at the northeast margin of the lake, and the other through the middle of the lake. (*d*) 65,000 years ago, following eruption of the younger ring domes. Both aphyric and porphyritic lavas erupted along the ring fracture at the southern margin of the lake.

domes. The presence of the older ring domes Cerro Chato, Mesa El Burro, and Mesa El Chiquihuitillo (G, F, E, Figure 2) on the extension of the arcuate trend of the fault beyond the margin of the lake suggests that, at that time, the underlying magma chamber was somewhat larger than the collapse basin.

Tala Tuff Magma Chamber

The eruption of the Tala Tuff, caldera collapse, inception of lake sedimentation, deposition of the giant pumice horizon, and eruption of the two central domes followed by the older ring domes all occurred within a time span unresolvable by K-Ar dating, about 5,000–10,000 years [*Mahood,* 1980*a*, *b*]. The last-erupted portion of the Tala Tuff is compositionally nearly identical to the south-central dome, whereas the north-central dome and older ring domes are slightly more mafic in composition (Tables 2 and 3). This suggests continuity in compositional gradients from that part of the magma chamber that erupted explosively as the Tala Tuff to that which erupted as early postcaldera lavas. Similar relations have been documented in several large silicic systems, where the immediately post ash flow lavas are similar to or lie on slightly more mafic extensions of the chemical trends in the ash flows (e.g., Long Valley, California [*Bailey et al.,* 1976], the Valles cal-

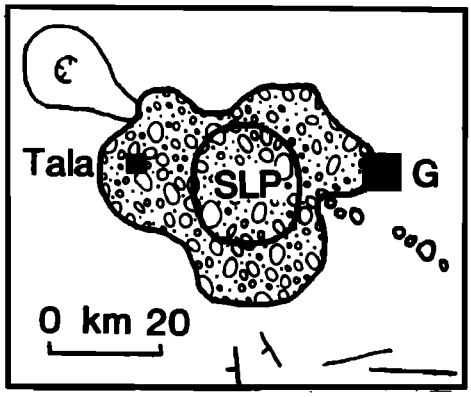

Fig. 4. Distribution of the Tala Tuff (modified from *Mahood* [1980*b*]). The Tala Tuff (pebble pattern) buried approximately 700 km^2.

dera, New Mexico [*Smith,* 1979], and Yellowstone [*Hildreth et al.,* 1980]). In all these examples, ring domes presumably represent the tapping of slightly deeper portions of the compositionally zoned magma chamber from which the ash flow erupted.

Most elements show unidirectional changes from the first-erupted portions of the Tala Tuff to the older ring domes (Figure 6). Certain elements, however, show a reversal in trend. Zr and Hf are most depleted in the last-erupted portion of the Tala Tuff and the south-central dome but increase again in the north-central and older ring domes. Likewise, Na_2O is most depleted in the last-erupted portion of the Tala Tuff but is significantly higher in the south-central dome. Whereas K_2O and Na_2O behave antithetically in the ash flow, they both increase in the central domes and older ring domes. Iron appears unzoned in the ash flow, but like Zr, Hf, and Na, it is more abundant in the north-central dome and older ring domes. The reversals in Na, Zr, and Hf parallel changes in the agpaitic index, which is 1.10 in the first-erupted portion of the Tala Tuff, falls to approximately 0.99 in the last erupted portion, and then rises to approximately 1.10 in the older ring domes.

The rapid evacuation of the Tala Tuff magma would lead to a rapid reorganization of the magma chamber, with magma from deeper levels becoming the most roofward. During this interval immediately following caldera collapse, the new roof zone magma may have been temporarily out of equilibrium with its surroundings. Additionally, a free vapor phase may have been present as a result of vesiculation during the caldera-producing eruption. During this period of re-establishment of magma chamber equilibrium, transient mechanisms may have produced the increase in Na, Fe, Zr, and Hf in the magma that erupted as the north-central dome and older ring domes. If so, the mechanisms must have operated on these elements alone or much more rapidly on them than on other elements. Alternatively these reversals may have been present within a continuously zoned magma chamber and reflect contrasting differentiation mechanisms and conditions in the volatile-enriched roof zone that erupted as the Tala Tuff and in the relatively drier, slightly hotter, deeper magma that erupted later as the older ring domes.

Younger Ring Domes

Caldera lake sedimentation continued after the emplacement of the older ring domes, with fine ashy and diatomaceous material dominating the section. The deposition of some 30 m of these fine-grained sediments indicates a period of volcanic quiescence. (The fine-grained nature of the lake sediments and the virtual absence of lithic debris derived from outside the caldera suggest that, prior to formation of the caldera, the whole region was elevated so that streams drained away from the future site of the Sierra La Primavera. This may represent an example of regional intumescence above a shallow silicic magma chamber, Stage 1 of the resurgent cauldron cycle [*Smith and Bailey,* 1968].) About 75,000 years ago, activity resumed with the eruption of a new group of ring domes at the southern margin of the lake (Figure 3d). Both aphyric and porphyritic lavas were erupted, totalling approximately 3 km^3 of magma. The younger K-Ar dates on these domes are corroborated by their position higher within the lake bed sequence [*Mahood,* 1980*b*]. The younger ring domes are lapped by only 10–20 m of sediment. Fine-grained sediments give way to fluvially reworked air fall pumice, and the uppermost part of the section consists of subaerially deposited tephra units.

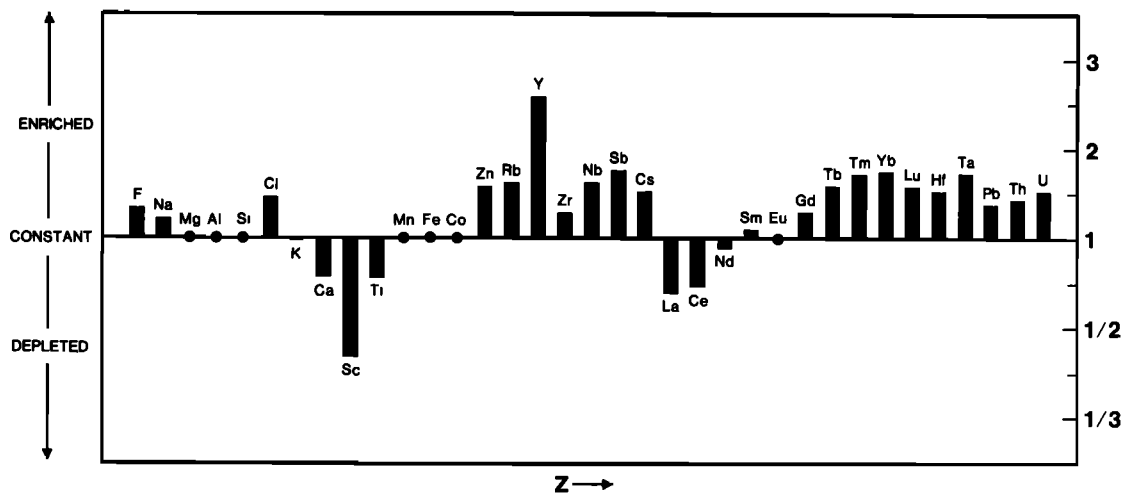

Fig. 5. Tala Tuff enrichment and depletion factors. The elemental abundances in the first-erupted portion of the Tala Tuff are ratioed to those in the last-erupted part. If an element plots above the line it is enriched roofward, below the line it is depleted roofward, in each case by the factor on the right.

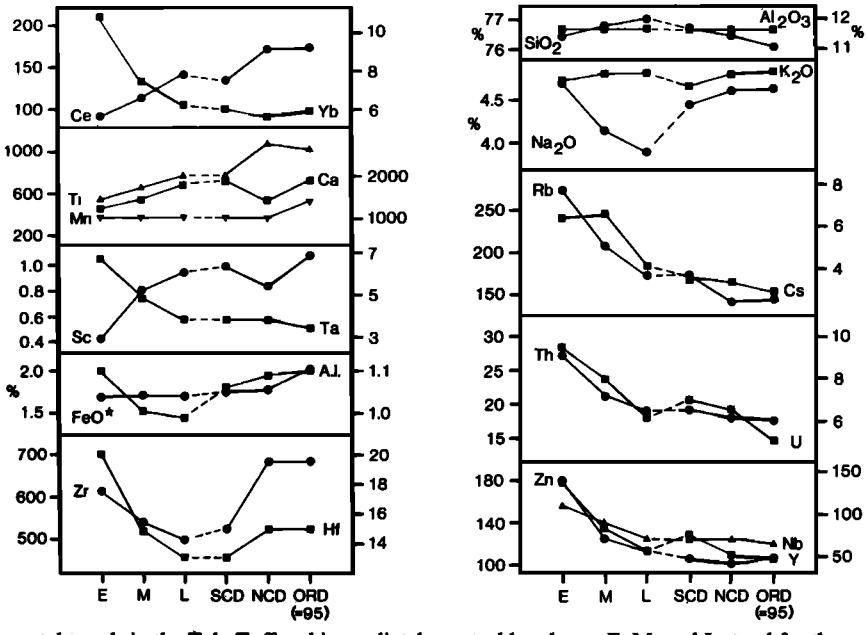

Fig. 6. Elemental trends in the Tala Tuff and immediately postcaldera lavas. E, M, and L stand for the early-, middle-, and late-erupted portions of the Tala Tuff, respectively, while SCD, NCD, and ORD refer to the south-central, north-central, and older (95,000-yr) ring domes, respectively. A.I. is the agpaitic index.

Uplift

Uplift that produced the topographic Sierra La Primavera brought an end to lacustrine sedimentation approximately 60,000 years ago. Much of the geomorphic expression of the caldera was destroyed because the hinge line for this uplift nearly coincided with the ring fracture of the caldera. The largest fault associated with this uplift parallels the caldera margin and can be traced for approximately 8 km from southwest of La Venta del Astillero (2 in Figure 2) to Cerro El Pedernal. The fault consists of two en echelon segments; the maximum displacement is found at Río Caliente (1 in Figure 2), where the Tala Tuff and overlying lacustrine deposits are cut by a 100-m scarp.

Deformation during uplift was concentrated at the margins of the lake. Radial dips of 10–20° on sediments at the margins of the former lake flatten to approximately 2° within a short distance towards its center. Uplift was assymetric to the caldera and was greatest at the southern margin of the lake; thus a gentle northerly component is superimposed on the radial dips of the lake sediments. Uplift of at least 250 m is indicated [*Mahood,* 1980*b*]. The notable scarcity of faults that cut sediments above the giant pumice horizon within the central portion of the former lake indicates that the uplift was piston-like; the former caldera block apparently rose as a single unit except at its margins.

Southern Arc Lavas

Uplift culminated in the eruption, beginning approximately 60,000 years ago, of 7 km^3 of magma as aphyric flows and domes. Contemporaneous with extrusion of these domes and flows were eruptions of air fall pumice, which caps the lake bed section, and a small ash flow that spread over approximately 2.5 km^2 near Tierra Blanca (3 in Figure 2). These tuffs have compositions relating them to the 60,000-yr-old southern arc lavas [*Mahood,* 1980*a*].

The lavas of the southern arc are generally younger toward the east. Cerro El Tajo and Cerro El Colli (EE, FF, Figure 2), the easternmost centers, give K-Ar dates of 25,000–30,000 years, which are in agreement with the youthful topographic expression of these units. Cerro El Colli is chemically distinct from the rest of the southern arc lavas, and its position in the compositional trend defined by the postcaldera domes indicates that it is the youngest eruptive unit in the Sierra La Primavera.

Post-95,000-Year Evolution of the Primavera Magma Chamber

After the eruption of the older (95,000-yr) ring domes, the lavas became progressively more silicic and less peralkaline (Table 2, Figure 7). Values for FeO*, TiO_2, MgO, and MnO in the older ring domes are approximately twice those in the most recently erupted unit, Cerro El Colli. There is some scatter in the alkali data due to mobility on posteruptive hydration, but Na_2O remained approximately constant while K_2O decreased from about 4.8 to 4.45% with time (Table 2). Cl concentrations appear to have increased slightly from 0.9 wt. % in the perlitic and pumiceous older ring domes to 0.13% in the youngest of the southern arc obsidians, although this may reflect better retention of Cl by obsidian samples. F remained approximately constant at about 0.10%. Rb, Cs, and possibly U are the only trace elements that increased monotonically with time in the lavas (Figure 7); nearly all other elements decreased (REE, Zr, Hf, K, Mg, Ti, Mn, Fe, and Zn) or remained approximately constant (Ta, Nb, Sb, Th, Pb, and Y). Sc, like Ca, is unsystematic in behavior, and Th, which remained approximately constant from the older ring domes to the 60,000-yr southern arc lavas, increased again in Cerro El Colli, the youngest dome.

In Figure 8, the elemental values for Cerro El Colli are shown in ratio to those in the older ring domes. This diagram is not strictly comparable to the enrichment factor diagram for the Tala Tuff (Figure 5) because it does not represent the chemical zonation present in the magma chamber at any one moment in time; rather, it is thought to illustrate the chemical

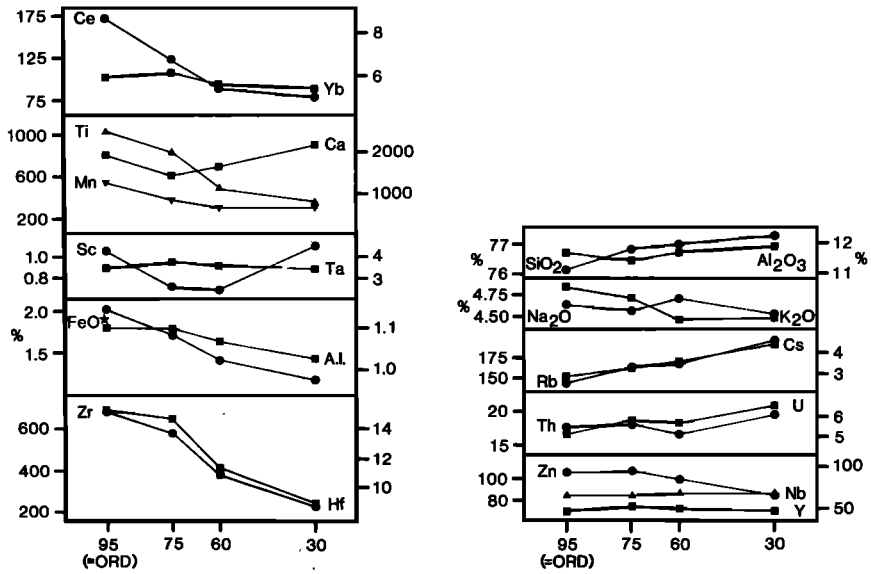

Fig. 7. Elemental trends in the post-95,000-yr lavas. This figure is similar to Figure 6. The 95: older ring domes (ORD of Figure 6); 75: younger ring domes; 60: 60,000-yr southern arc lavas; 30: the youngest southern arc lava, Cerro El Colli, erupted approximately 30,000 years ago.

evolution through time of the uppermost magma in the chamber. The difference between the two enrichment patterns is striking; with increasing differentiation, the ash flow magma was enriched in the HREE and many of the multivalent cations, whereas the post-95,000-yr lavas were enriched systematically only in Si, Rb, Cs, and possibly U. (Th plots above the no-enrichment line only because of its increase in Cerro El Colli.)

Intensive Parameters in Primavera Magmas

Temperature and Oxygen Fugacity

Neither the aphyric nature of many Primavera eruptive units nor the phenocryst assemblages in most others lend themselves to thermodynamic determination of crystal-liquid equilibration temperatures. Hence it remains uncertain whether the chemical evolution documented for the post-caldera lavas took place under a waxing, waning, or fluctuating thermal regime.

Microprobe analyses of titanomagnetite and ilmenite from the Río Salado dome (A, Figure 2) were recalculated using the method of *Carmichael* [1967], and the recast analyses were used to determine the temperature and oxygen fugacity using *Buddington and Lindsley*'s [1964] calibration of the Fe-Ti oxides. A temperature of 850°C and a log f_{O_2} of −13.8 were obtained, which are appropriate to a magma on the FMQ buffer. The small variations between eruptive units of the major element compositions of phenocrysts suggest only small differences in magma temperatures. This fact, coupled with the results of two geothermometers [*Mahood,* 1980*a*], leads to the conclusion that eruptive temperatures of porphyritic Primavera magmas probably varied by no more than 30°C.

Pressure

There is little direct evidence for the depth to the roof of the Primavera magma chamber. Formation of a caldera 11 km in diameter on eruption of only 20 km³ of magma as the Tala

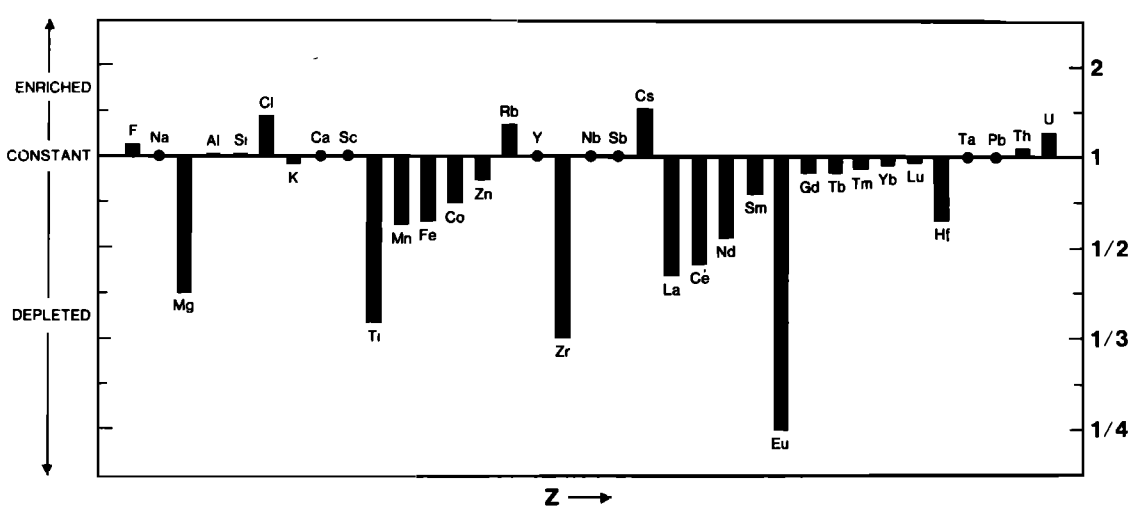

Fig. 8. Enrichment and depletion factors in the post-95,000-yr lavas. The elemental value in the youngest southern arc lava, Cerro El Colli, is ratioed to the average of the older ring domes. This figure is not directly analogous to Figure 5, as it does not represent the zonation present in the magma chamber at any one point in time; rather it presumably illustrates the evolution through time of the most roofward magma.

Tuff would seem to require a magma chamber with a fairly shallow roof. By analogy with eroded cauldrons and ring complexes of similar mineralogy and bulk composition, the roof of the Primavera magma chamber was probably between 2 and 6 km beneath the surface. Assuming that the phenocrysts precipitated within the upper portion of a high-level magma chamber, the small variation between eruptive groups of the major element compositions of the phenocrysts suggests that the depth to the roof of this magma chamber changed little after eruption of the Tala Tuff.

Evaluation of Differentiation Mechanisms

The homogeneity of phenocryst and whole rock compositions within each postcaldera eruptive group, along with the arcuate arrangement of vents, is strong evidence that these lavas erupted from a single unified magma chamber. Studies of large-volume zoned ash flow eruptions have shown that magma at the roof of the chamber is generally more differentiated and poorer in phenocrysts than at deeper levels. The trend in Primavera post-95,000-yr lavas is opposite to that expected on tapping successively deeper levels of a compositionally zoned magma chamber; the last lavas erupted are phenocryst-free and are the most siliceous. Thus it seems more likely that the Tala Tuff and all the postcaldera lavas erupted from a magma chamber that was evolving chemically with time. This is not to say that the geometry of the magma chamber did not change; indeed, the southern arc lavas may represent a southward expansion of the magma chamber. However, the magma chamber was (is) presumably large enough that magma in its roof zone did not immediately 'feel' the effects of new additions below, and thus changes in composition within the sequence of lavas reflect high-level differentiation mechanisms. Since there is no positive evidence of a unitary magma chamber during eruption of the precaldera lavas, they will not be considered further.

Crystal Fractionation

Most of the Tala Tuff and many of the Primavera lavas are aphyric. If crystal settling operated in these magmas, either all the phenocrysts settled out, or the magmas became superheated prior to eruption and the phenocrysts were resorbed. Phenocrysts show no evidence of having settled: they are euhedral, unzoned, and homogeneous. Repeated tapping of a cooling magma chamber that is crystallizing inward from its margins is equivalent geochemically to settling of the observed phenocryst phases; thus the chemical contraints on both of these differentiation mechanisms are similar.

The compositional zonation present in the magma chamber just prior to the eruption of the Tala Tuff was not the product of crystal fractionation alone for the following reasons:

1. Zn is enriched and Sc and Ti are depleted roofward, while Fe, Mg, and Mn are unzoned (Figure 5). These divergent trends are incompatible with the removal of mafic phenocrysts, which are strongly enriched relative to glass in these elements.

2. To produce the nearly two-fold roofward enrichment of elements such as Nb, Y, Ta, U, Rb, and Cs would require removal of at least half the magma as phenocrysts. But this would have profound effects on major elements such as Ca and Fe, effects that are not observed.

Separation of phenocrysts in their modal proportions does not account for the chemical trends in the post-95,000-yr lavas [*Mahood,* 1981]. Crystal fractionation models calculated using the computer program of *Wright and Doherty* [1970] require 1–30% fractionation. Sums of the least squares residuals are quite small (a necessary consequence of the slight compositional differences between parent and daughter magmas), but more than half the solutions require both the addition and subtraction of phases, a result that seems geologically improbable, especially in crystal-poor rhyolites.

The best computer solutions calculated on the basis of major elements were tested to see if they predicted correct trace element concentrations in the daughter magmas. Poor agreement was obtained between the predicted and measured concentrations of most trace elements in the daughter magmas [*Mahood,* 1981]. Most trace elements decrease or remain approximately constant with time in the postcaldera lavas (Figure 7), but the calculations predict increasing concentrations. This is a result of the large proportion of sanidine and quartz in the separating phases which, despite the strong enrichment of elements such as the LREE and Zn in the mafic phases, causes the bulk distribution coefficient D for these elements to be less than one. In all the calculated models the removal of phenocrysts does not produce the observed decrease in LREE with time. Also, despite the dominant role of sanidine in the calculated models and D_{Eu} for all cases being greater than one, the predicted decrease in Eu is always smaller than that observed.

Partial Melting

Incremental partial melting of a source region would not produce the trends observed in the post-95,000-yr lavas of La Primavera. The first partial melts would be enriched in Si, Rb, and Cs and depleted in Fe, Mg, and Ti relative to subsequent melt fractions. The reverse is observed in the post-95,000-yr lavas: they become increasingly siliceous and depleted in the mafic elements with time.

The chemical zonation in the Tala Tuff did not result from accretion of successive partial melt increments. Incremental partial melting does not readily explain the crossover in REE on the enrichment factor diagram (Figure 5) nor the divergent enrichment patterns of the first transition series elements [*Mahood,* 1980*a*; see also *Hildreth,* 1977].

Phenocryst/Glass Partitioning and Melt Structure

Crystal fractionation, whether during partial melting or due to crystal settling, cannot alone account for the compositional gradient in the Tala Tuff or the trends with time in the post-95,000-yr lavas. On the other hand, the progressive increase in the ratio of network-forming elements to network-modifying elements in the post-95,000-yr lavas suggests that trace-element evolution is associated with changing melt structure. (The term 'melt structure' is used here to signify the mutual spatial relationship between atoms in a silicate liquid. Since melts lack long-range order, a melt structural state is characterized by an average concentration of variously coordinated cations (e.g., a highly polymerized melt has, on the average, fewer octahedral 'sites' than a less polymerized melt). In this sense, at any given pressure, temperature, volatile content, and bulk composition, the melt structure is 'fixed' in a statistical sense.)

Crystal/liquid partition coefficients are thought to be functions of (1) temperature [*Häkli and Wright,* 1967; *Leeman and Lindstrom,* 1978], (2) f_{O_2} [*Drake,* 1975; *Sun et al.,* 1974], (3) pressure [*Mysen and Kushiro,* 1978], (4) composition of the

TABLE 4. Summary of Phenocryst/Glass Partition Coefficients

	Eruptive Group											
	Sanidine				Ferrohedenbergite				Fayalite			Ilmenite
	PCD	TT	ORD	YRD	PCD	SCD	ORD	YRD	SCD	ORD	YRD	ORD
La	0.06	0.037	0.057	0.11	23	2.9	3.5	24	1.08	2.0	23	1.31
Ce	0.033	0.031	0.043	0.095	20.9	3.5	4.0	21.6	0.93	1.78	20.4	1.19
Nd	0.01	0.02	0.04	0.09	16	5.3	5.9	17	0.77	1.5	14	0.96
Sm	0.019	0.020	0.029	0.946	14	6.2	6.2	13	0.496	1.060	8.4	0.684
Eu	2.3	2.3	2.0	2.2	12	5	6	10	0.1	0.4	5.8	0.4
Tb	0.012	0.016	0.023	0.022	6.9	5.0	4.0	6.1	0.31	0.54	2.8	0.36
Dy	0.01	0.02	0.02	0.02	6	4.5		4.8	1	1	3	0.4
Yb	0.005	0.014	0.016	0.018	6.4	5.0	4.5	5.5	0.92	0.98	1.96	0.55
Lu	0.008	0.010	0.015	0.014	8	6.9	6.1	7	1.3	1.3	2.2	0.72
Th	0.010	0.017	0.021	0.025	3.44	0.36	0.77	2.89	0.276	0.438	3.17	0.43
U	0.008	0.021	0.018	0.014	1.0	0.12	0.33	0.87	0.12	0.13	0.69	0.06
Hf	0.005	0.018	0.015	0.015	1.52	0.30	0.39	2.04	0.12	0.28	1.78	0.65
Ta	0.004	0.018	0.018	0.015	0.69	0.10	0.97	0.49	0.098	0.090	0.575	18.0
Sc	0.04	0.04	0.05	0.06	133	110	109	172	5.1	4.8	9.3	18
Ti	0.1	0.05	0.11	0.11	2.6	4	2.5	2.5	0.3	0.4	0.5	380
Mn	0.011	0.020	0.018	0.020	34	30		33	63	56	77	27
Fe	0.14	0.14	0.11	0.14	20	18	15	18	37	33	40	24
Zn	0.04	0.06	0.06	0.07	21	8.9	7.2	14.8	11.1	10.4	10.7	7.8
Rb	0.39	0.31	0.36	0.34								
Cs	0.012	0.023	0.009	0.028								

The calculated errors on the partition coefficients, the method of correcting for impurities in the mineral separates, and the INAA analyses of the separated glass and phenocrysts are given by *Mahood* [1980*a*]. Values are stated such that uncertainty is in the last digit. See footnote to Table 2 for the Eruptive Group abbreviations.

phenocryst phase [*Schnetzler and Philpotts,* 1970], and (5) bulk composition of the melt [*Watson,* 1977; *Takahashi,* 1978; *Hart and Davis,* 1978; *Mysen and Virgo,* 1980]. The temperature, oxygen fugacity, and pressure of the Primavera magmas are thought to have varied little between eruptive groups. Compositions of the mafic phenocrysts in the different groups are nearly identical, and the range of sanidine compositions is small. Thus variations in partition coefficients between the older and younger ring domes or between them and the Tala Tuff and its outgassed equivalent, the south-central dome, reflect changes in melt structure resulting from changes in bulk composition of the magma. A decrease in the concentration of the network modifiers, Fe, Mn, Mg, and Ca (and Na and K in peralkaline melts), or in dissolved H_2O or F would promote a higher proportion of bridging oxygen bonds and an increase in the polymerization of the melt [*Burnham,* 1975], with a corresponding increase in crystal-liquid partition coefficients.

With this in mind, seventeen mineral and glass separates from five representative Primavera samples were analyzed at Lawrence Berkeley Laboratory by INAA. The resulting analyses and partitioning patterns are discussed elsewhere [*Mahood,* 1980*a*; G. A. Mahood and W. Hildreth, manuscript in preparation, 1981]; the pertinent partition coefficients are summarized in Table 4. Despite only minor differences in the major element compositions of phenocrysts, the concentrations of many of the trace elements vary by factors of 5–10 among analyzed samples. This is reflected in crystal/glass partition coefficients that differ by as much as a factor of 20.

Phenocryst/Glass Partitioning in the Older and Younger Ring Domes

All the southern arc lavas are aphyric, so any discussion of the chemical evolution of the post-95,000-yr lavas as reflected in trace element partitioning is necessarily restricted to the older and younger ring domes. The behavior of trace element partition coefficients in the ring domes is systematic; the partition coefficients for all analyzed elements with the exception of Ta in ferrohedenbergite remain constant or increase from the 95,000- to the 75,000-yr dome. The single exception of Ta, however, might simply be an artifact of an improper correction for ilmenite inclusions in the clinopyroxenes.

The observed decrease in Fe, Mn, Mg, and K in the sequence of post-95,000-yr lavas would be expected to foster increasing polymerization of the melts and, as a result, increasing crystal/liquid partition coefficients. The changes in crystal/glass partition coefficients between the older and younger ring domes, however, seem remarkably large considering the small changes in major element composition. Such behavior suggests one or more of the following conclusions:

1. High-silica rhyolitic melts are so strongly polymerized that small changes in major element composition can greatly affect the number of sites in the liquid suitable for most trace elements. Small distortions of the silicate network may make already marginal sites even less energetically favored.

2. The increase in partition coefficients may reflect increasing melt polymerization and resultant decrease in trace metal sites caused chiefly by a decrease in the dissolved volatile content of the melt. Although the absolute difference in volatile content between the magmas of the older and younger ring domes could not have been large, at low water (or fluorine) concentrations, small variations can have great effects, as illustrated by the rapid drop in liquidus temperature on adding small amounts of water or fluorine to the anhydrous granitic system [*Naney and Swanson,* 1980; *Wyllie and Tuttle,* 1961].

3. If elements that are not easily accommodated by the silicate network are complexed by hydroxyl, fluoride, chloride, phosphate, sulfate, or carbonate ligands, any decrease in concentration of these complexing agents would increase the activity of the trace elements in the melt, favoring increased concentrations in the crystalline phases. Complexing could lead to discontinuities in crystal/liquid partitioning behavior; partition coefficients might remain low as long as the concen-

tration of the complexing ligands is sufficient to complex most of the trace metals, but once the concentration of complexing ligands falls below that threshold, the partition coefficients will rise. This mechanism might be most effective in relatively volatile-poor high-silica magmas where the total concentration of possible complexing ligands is of the same order as the sum of the trace metals. Other types of complexing may also be important in increasing the solubility of trace metals in melts. For example, *Watson* [1979] has suggested, on the basis of measurements demonstrating an increase in the solubility of Zr in silicate melts with increasing agpaicity, that Zr is associated with the alkalies as complexes.

Migration of Elements to Structurally More Favorable Melts

The combined effects of gradients in temperature, bulk composition, and volatile content should logically result in a magma chamber with a melt structural gradient. In the relatively dry post-95,000-yr system, the combined gradients could have been such that the roof was more polymerized than the more mafic, hotter, deeper levels. The progressive decrease in whole rock (and glass) abundances of most trace elements with time in the post-95,000-yr eruptive groups (each of which presumably represented the uppermost and most differentiated magma in the Primavera magma chamber at the moment of its eruption) may have been accomplished by migration of these elements out of the roofward magma into deeper, less polymerized levels of the magma chamber.

The two-liquid partitioning studies of *Watson* [1976] and *Ryerson and Hess* [1978] in immiscible mafic and silicic melts are examples of diffusion into a structurally more favorable melt. They found that Ti, Fe, Mn, Mg, Ca, P, Zr, Ta, Cr, REE, Sr, and Ba were partitioned into the less polymerized mafic melt and that Al, Na, K, and Cs were preferentially concentrated in the silicic melt. Aluminum apparently substitutes for silicon in tetrahedral coordination, which requires the coupled substitution of the alkalies to maintain local charge balance. The systematic enrichment of Primavera post-95,000-yr magmas in only Si, Rb, and Cs, while all other elements remain approximately constant or decrease in concentration, is analogous to the partitioning of all cations but aluminum and the alkalies into the less polymerized mafic melts in the two-liquid experiments. The observed decrease in total mole percent alkalies is consistent with the implications of the two-liquid data, because the measured decrease in magma viscosity with increasing peralkalinity [*Riebling,* 1966] indicates that alkalies in molecular excess of alumina are network modifiers and should, therefore, migrate to a less polymerized melt. At Primavera this less polymerized melt presumably lies at a slightly deeper level of the magma chamber.

Phenocryst/Glass Partitioning in the Ash Flow Magma and the Origin of Compositional Zoning in the Tala Tuff

If bulk composition had been the major control on partition coefficients in the Tala Tuff magma, the last-erupted portion of the Tala Tuff and its compositionally identical, outgassed equivalent, the south-central dome, could be expected to have partition coefficients similar to those of the younger ring dome, which, in turn, should be higher than those for the older ring dome. This is because the last-erupted Tala Tuff, the south-central dome, and the younger ring dome are similar in major element composition and all three are lower in Ti, Fe, Mn, and Mg than the older ring dome. On the contrary, for the elements and phases analyzed, partition coefficients for most trace elements in the Tala Tuff magma (Table 4) are significantly smaller than in the younger ring domes and, in fact, are smaller than or similar to those in the more mafic older ring dome.

Limited analytical data, thermodynamic calculations, and mineralogical evidence [*Smith and Bailey,* 1966; *Gibson,* 1970; *Noble and Parker,* 1974; *Sommer,* 1978; *Hildreth,* 1977, 1979; R. L. Smith, personal communication, 1979; this study] indicate that first-erupted portions of ash flow tuffs are enriched in H_2O, F, and Cl relative to the last-erupted portions, and, by inference, the roofward magmas are enriched in volatiles. An increase in the water and/or halogen content of a rhyolitic melt, like an increase in concentration of the cationic network modifiers, should depolymerize the magma [*Burnham,* 1975]. One expression of such depolymerization would be smaller phenocryst/glass partition coefficients, as indeed are found in the Tala Tuff and its outgassed equivalent, the south-central dome. The contrast in elemental enrichment patterns between the Tala Tuff and the post-95,000-yr lavas (Figures 5, 6, 7, and 8) suggests that mechanisms other than melt structural control produced the trace element gradients in the Tala Tuff magma. If melt structure had been the dominant control on trace element variations in the Tala Tuff, enrichment of those elements (Si, Al, and the alkalies) which have been shown experimentally to partition into the more strongly polymerized melt would be antithetic to those elements (Fe, Ti, REE, Zr, Ta, etc.) that partition into the less polymerized melts. The vertical trace element gradients in the Tala Tuff magma chamber are not in accord with such a model. Na and K behave antithetically, as do the HREE and LREE. Elements of the first transition series do not behave consistently: Sc and Ti are depleted and Zn is enriched roofward, whereas Fe is unzoned. These data suggest that melt structure did not exert as strong a control on trace element behavior in the ash flow magma as in the magmas of the ring domes, due to the depolymerizing effects of elevated volatile concentrations.

A number of elements that partition into less polymerized melts in the two-liquid experiments have opposite enrichment directions in different ash flow systems, despite the roofward depletion in all systems of the elements Ca, Mg, and Ti. Zr, Hf, Zn, and Fe are enriched roofward in moderately to strongly peralkaline systems (e.g., Fantale Tuff [*Gibson,* 1970]; Grouse Canyon member of the Belted Range Tuff [*Noble and Parker,* 1974]; Soldier Meadow Tuff [*Korringa,* 1973]), whereas these same elements are unzoned or depleted roofward in 'calc-alkalic' systems (e.g., Bishop Tuff [*Hildreth,* 1979]; Topopah Springs member of the Paintbrush Tuff [*Lipman et al.,* 1966]; Rainier Mesa member of the Timber Mountain Tuff [*Christiansen et al.,* 1977]). In mildly peralkaline or alkali-rhyolite systems (e.g., La Primavera; Bandelier Tuff (R. L. Smith, personal communication, 1979); Spearhead member of the Thirsty Canyon Tuff [*Noble and Parker,* 1974]) these elements are variously unzoned or slightly enriched roofward.

Such behavior seems inconsistent with melt structural control, and may be better explained by a mechanism in which trace elements migrate as volatile complexes in a thermal and gravitational gradient. As volatiles move roofward, they may preferentially complex with different trace metals; thus, systems with different volatile contents or ratios of H_2O, F, Cl, and CO_2 will have different elemental enrichment patterns. In this way the trace element enrichment pattern in the Tala

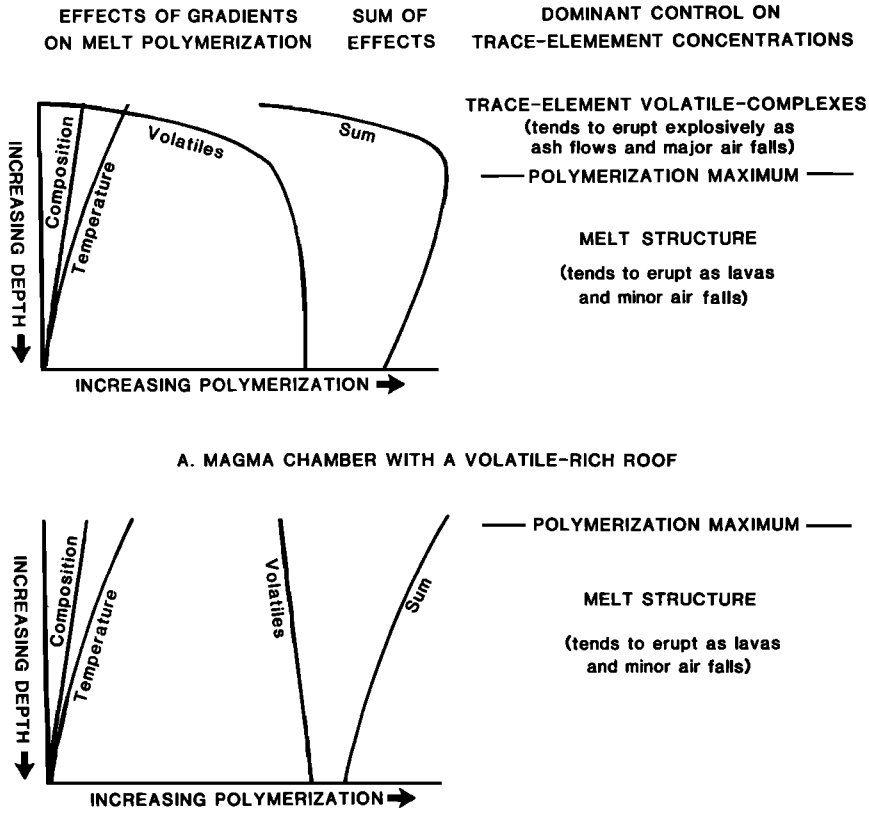

Fig. 9. Diagrammatic representation of melt polymerization gradients within silicic magma chambers. (*a*) Silicic magma chamber with a volatile-rich roof zone and maximum melt polymerization at an intermediate level. In the volatile-rich zone above the polymerization maximum, transport of trace metals as dissolved volatile complexes may be the dominant differentiation mechanism, while below the polymerization maximum, the distribution of trace metals may be determined by melt structure. (*b*) Silicic magma chamber lacking a volatile-rich roof zone. The roofward magma might be the most polymerized, so most trace metals would diffuse to deeper, hotter, more mafic levels of the chamber where the melt is less polymerized.

Tuff (and in other ash flow systems) may be the natural result of development of a volatile-enriched cap on a dominantly drier magma chamber. Roofward enrichment in trace metals may be linked to roofward enrichment in the volatiles required to produce an ash flow eruption.

Discussion and Conclusions

The structure of a silicate melt is determined by pressure, temperature, major element composition, and volatile content. Gradients in temperature and phenocryst and whole rock compositions preserved in ash flow tuffs are the main evidence for such gradients within silicic magma chambers and, inferentially, for the melt structural gradients that result from such zoning. The depolymerizing effect of a roofward increase in dissolved volatile content of a magma is counteracted by the roofward decrease in temperature and concentration of network-modifying cations. In different systems, the sum of these effects could result in maximum polymerization occurring at the roof, at deep levels, or at some intermediate position in a magma chamber, depending on the relative magnitudes of the individual gradients.

In chambers in which the roof zone is strongly enriched in water (or other volatiles), the melt may initially be increasingly polymerized with depth in the chamber, but as the water gradient flattens, increasing temperature and the more mafic composition of the magma with increasing depth in the chamber may overcome the roofward volatile gradient and reverse the polymerization gradient. The result could be a magma chamber with maximum melt polymerization at some intermediate level. In the volatile-rich zone above the polymerization maximum, transport of trace metals as dissolved volatile complexes may be the dominant differentiation mechanism, while below the polymerization maximum (which would roughly coincide with the leveling of the water gradient), the distribution of trace metals may be determined by melt structure. This concept is shown diagramatically in Figure 9*a*. If an eruption were to tap through the polymerization maximum, it would sample magmas that obtained their trace element abundance patterns through at least two different mechanisms; such an event might be manifested by discontinuities in elemental trends. Such a change in the dominant mechanism of differentiation might account for apparent reversals in the trends of Zr, Hf, Na, and the agpaitic index between the Tala Tuff and older ring domes (although a transient vapor phase produced on eruption may have been involved). Magma that erupted as the south-central dome may have occupied the boundary between the two differentiation regimes. The change in trace element trends coincides with

the end of the ash flow eruption, which is consistent with the eruption ceasing on exhaustion of the volatile-enriched magma.

In a silicic magma chamber that lacks a strongly volatile-enriched roof zone, the roofward magma might be the most polymerized, so most trace metals would diffuse to deeper, hotter, more mafic levels of the chamber where the melt is less polymerized (Figure 9*b*). Such a configuration might produce the trends observed in the post-95,000-yr lavas, each eruptive group representing successive samples of roof zone magma in a relatively dry system that became progressively more silicic and more polymerized with time.

The presence of gradients implies that the upper portion of the magma chamber that contains them is either static or, if convecting, consists of many convection cells with small vertical dimensions. In the latter case, migration of trace metals is facilitated, because diffusion is the rate-limiting step only at interfaces between cells of contrasting melt structure, and the chemical gradients across the interfaces are constantly replenished by convection [*Turner,* 1973, 1974; *McBirney and Noyes,* 1979; *Chen and Turner,* 1980; *Turner,* 1980].

The preceding discussion of the origin of the zonation in the Tala Tuff and the evolution of the postcaldera lavas with time has emphasized two contrasting modes of liquid state differentiation: one involves transport of trace metals as volatile complexes within a thermal and gravitational gradient in a volatile-rich magma undersaturated with respect to water; the second involves emigration of trace elements in response to changes in melt structure produced by minor decreases in the concentration of network modifiers, dissolved volatiles, and/or complexing ligands in a relatively 'dry' system. Both mechanisms could operate simultaneously and, at intermediate volatile concentrations, be of similar importance. Other differentiation mechanisms (e.g., crystal fractionation and contamination by assimilation of crustal material or by admixing of more mafic magmas from below) presumably influenced the compositions of magmas erupted at La Primavera, but their contribution has been largely obscured by the overprint of liquid state differentiation mechanisms which operated in the high-level magma chamber.

The composition of any magma is controlled by the relative efficiency of simultaneously operating differentiation mechanisms; for example, in highly polymerized high-silica rhyolites, melt structural effects may dominate, but in low-viscosity andesites and basalts, crystal fractionation may be more important. The relative efficiency of different mechanisms is controlled by physical properties of the melt (such as viscosity, density, and melt structure), the temperature gradient within the magma chamber, and the absolute abundances and relative proportions of volatile components. Because diffusive transport relies on limited convection to speed the process and the nature of convection is determined by density as well as temperature gradients, the chemical evolution and rheological evolution of a magma chamber are intertwined.

Acknowledgments. Discussions with E. W. Hildreth and I. S. E. Carmichael contributed to the petrological ideas presented in this paper, and the help of C. M. Gilbert in the field made the geological synthesis possible. The assistance of S. Anderson-Nosker, Z. deCserna, R. Drake, W. Duffield, A. Grunder, D. Kosco, and A. Razo at various stages in this study is greatly appreciated. I am grateful to R. L. Smith and R. Macdonald for arranging additional INAA and XRF analyses. Material support was provided by N. S. F. Grants EAR-74-12782 and EAR-78-03648 to Carmichael and EAR-76-21833 to G. Curtis, and by two University of California at Berkeley Graduate Division Grants-in-Aid and a N. S. F. Fellowship to the author. Early versions of this manuscript benefited from suggestions by Gilbert and Hildreth, and the final version from a review by J. Ratté.

REFERENCES

Bailey, R. A., B. Dalrymple, and M. A. Lanphere, Volcanism, structure, and geochronology of Long Valley caldera, Mono County, California, *J. Geophys. Res., 81,* 725–744, 1976.

Billings, M. P., The geology of New Hampshire, 2, Bedrock geology, report, N. H. State Planning Comm., Concord, N. H., 1956.

Buddington, A. F., and D. H. Lindsley, Iron-titanium oxide minerals and synthetic equivalents, *J. Petrol., 5,* 310–357, 1964.

Burnham, C. W., Hydrothermal fluids at the magmatic stage, in *Geochemistry of Hydrothermal Ore Deposits,* pp. 34–76, edited by H. L. Barnes, Holt, Rinehart, and Winston, New York, 1967.

Burnham, C. W., Thermodynamics of melting in experimental silicate-volatile systems, *Fortschr. Mineral., 52,* 101–118, 1975.

Carmichael, I. S. E., The iron-titanium oxides of salic volcanic rocks and their associated ferromagnesian silicates, *Contrib. Mineral. Petrol., 14,* 36–64, 1967.

Chen, C. F., and J. S. Turner, Crystallization in a double-diffusive system, *J. Geophys. Res., 85,* 2573–2593, 1980.

Christiansen, R. L., and D. C. Noble, Black Mountain volcanism of southern Nevada, *Spec. Pap. Geol. Soc. Am., 82,* 246, 1965.

Christiansen, R. L., P. W. Lipman, W. J. Carr, F. M. Byers, Jr., P. P. Orkild, and K. A. Sargent, Timber Mountain-Oasis Valley caldera complex of southern Nevada, *Geol. Soc. Am. Bull., 88,* 943–959, 1977.

Drake, M. F., The oxidation state of europium as an indicator of oxygen fugacity, *Geochim. Cosmochim. Acta, 39,* 55–64, 1975.

Gibson, I. L., A pantelleritic welded ash-flow tuff from the Ethiopian Rift Valley, *Contrib. Mineral. Petrol., 28,* 89–111, 1970.

Häkli, T. A., and T. L. Wright, The fractionation of nickel between olivine and augite as a geothermometer, *Geochim. Cosmochim. Acta, 31,* 877–884, 1967.

Hart, S. R., and K. Davis, Nickel partitioning between olivine and silicate melt, *Earth Planet. Sci. Lett., 40,* 203–219, 1978.

Hildreth, E. W., The magma chamber of the Bishop Tuff: Gradients in temperature, pressure, and composition, Ph.D. dissertation, Univ. of Calif., Berkeley, 1977.

Hildreth, W., The Bishop Tuff: Evidence for the origin of compositional zoning in silicic magma chambers, *Spec. Pap. Geol. Soc. Am., 180,* 43–75, 1979.

Hildreth, W., R. L. Christiansen, and J. R. O'Neil, Catastrophic isotopic modification of rhyolitic magma by creation of the Yellowstone caldera, *Geol. Soc. Am. Abstr. Programs, 12,* 111, 1980.

Jacobsen, R. R. E., Geology of the Liruei, Bante, and adjacent Younger Granite ring complexes, *Geol. Surv. Niger. Bull., 33,* 177 pp., 1977.

Korringa, M. K., Linear vent area of the Soldier Meadow Tuff, an ash-flow sheet in northwestern Nevada, *Geol. Soc. Am. Bull., 84,* 3849–3866, 1973.

Leeman, W. P., and D. J. Lindstrom, Partitioning of Ni^{2+} between basaltic and synthetic melts and olivines—An experimental study, *Geochim. Cosmochim. Acta, 42,* 801–816, 1978.

Lipman, P. W., R. L. Christiansen, and J. T. O'Connor, A compositionally zoned ash-flow sheet in southern Nevada, *Geol. Surv. Prof. Pap. U.S., 524-F,* 1–47, 1966.

Mahood, G. A., The geological and chemical evolution of a Late Pleistocene rhyolitic center: The Sierra La Primavera, Jalisco, México, Ph.D. dissertation, Univ. of Calif., Berkeley, 1980*a*.

Mahood, G. A., Geological evolution of a Pleistocene rhyolitic center: Sierra La Primavera, Jalisco, México, *J. Volcanol. Geotherm. Res., 8,* 199–230, 1980*b*.

Mahood, G. A., Chemical evolution of a Pleistocene rhyolitic center: Sierra La Primavera, Jalisco, México, *Contrib. Mineral. Petrol.,* in press, 1981.

McBirney, A. R., and R. M. Noyes, Crystallization and layering of the Skaergaard intrusion, *J. Petrol., 20,* 487–554, 1979.

Mysen, B. O., and I. Kushiro, The effect of pressure on the partitioning of nickel between olivine and aluminous silicate melt, *Year Book Carnegie Inst. Washington, 77,* 706–707, 1978.

Mysen, B. O., and D. Virgo, Trace element partitioning and melt structures: An experimental study at 1 atm pressure, *Geochim. Cosmochim. Acta, 44,* 1917–1930, 1980.

Naney, M. T., and S. E. Swanson, The effect of Fe and Mg on crystallization in granitic systems, *Am. Mineral., 65,* 639–653, 1980.

Noble, D. C., and D. F. Parker, Peralkaline silicic volcanic rocks of the western United States, *Bull. Volcanol., 38,* 803–827, 1974.

Noble, D. C., K. A. Sargent, H. H. Mehnert, E. B. Ekren, and F. M. Byers, Jr, Silent Canyon volcanic center, Nye County, Nevada, *Mem. Geol. Soc. Am., 110,* 65–76, 1968.

Riebling, E. F., Structure of sodium aluminosilicate melts containing at least 50 mole % SiO_2 at 1500°C, *J. Chem. Phys., 44,* 2857–2865, 1966.

Ritchie, J. L., Origin of divergent magmas at Crater Lake, Oregon, Ph.D. dissertation, Univ. of Oregon, Eugene, 1979.

Ryerson, F. J., and P. C. Hess, Implications of liquid-liquid distribution coefficients to mineral-liquid partitioning, *Geochim. Cosmochim. Acta, 42,* 921–932, 1978.

Schnetzler, C. C., and J. A. Philpotts, Partition coefficients of rare-earth elements between igneous matrix material and rock-forming mineral phenocrysts, 2, *Geochim. Cosmochim. Acta, 34,* 331–340, 1970.

Smith, R. L., Ash-flow magmatism, *Spec. Pap. Geol. Soc. Am., 180,* 5–27, 1979.

Smith, R. L., and R. A. Bailey, The Bandelier Tuff: A study of ash-flow eruption cycles from zoned magma chambers, *Bull. Volcanol., 29,* 83–104, 1966.

Smith, R. L., and R. A. Bailey, Resurgent cauldrons, *Mem. Geol. Soc. Am., 116,* 613–662, 1968.

Smith, R. L., and R. Macdonald, Rhyolitic volcanism and its relationship to granitic plutonism, *Geol. Soc. Am. Abstr. Programs, 11,* 520, 1979.

Sommer, M. A., II, Volatiles in silicate melt inclusions from the air-fall and ash-flow tuffs of the Bandelier Tuff, Jemez Mountains, New Mexico, *Geol. Soc. Am. Abstr. Programs, 10,* 495, 1978.

Sun, C. O., R. J. Williams, and S. S. Sun, Distribution coefficients of Eu and Sr for plagioclase-liquid and clinopyroxene-liquid equilibria in oceanic ridge basalt: An experimental study, *Geochim. Cosmochim. Acta, 38,* 1415–1433, 1974.

Takahashi, E., Partitioning of Ni^{2+}, Co^{2+}, Fe^{2+}, Mn^{2+}, and Mg^{2+} between olivine and silicate melts: Compositional dependence of partition coefficients, *Geochim. Cosmochim. Acta, 42,* 1829–1844, 1978.

Turner, J. S., *Buoyancy Effects in Fluids,* Cambridge University Press, London, 1973.

Turner, J. S., Double-diffusive phenomena, *Ann. Rev. Fluid Mech., 6,* 37–56, 1974.

Turner, J. S., A fluid dynamical model of differentiation and layering in magma chambers, *Nature, 285,* 213–215, 1980.

Watkins, N. D., B. M. Gunn, A. K. Baksi, D. York, and J. Ade-Hall, Paleomagnetism, geochemistry, and potassium-argon ages of the Rio Grande de Santiago volcanics, central Mexico, *Geol. Soc. Am. Bull., 82,* 1955–1968, 1971.

Watson, E. B., Two-liquid partition coefficients: Experimental data and geochemical implications, *Contrib. Mineral. Petrol., 61,* 35–48, 1976.

Watson, E. B., Partitioning of manganese between fosterite and silicate liquid, *Geochim. Cosmochim. Acta, 41,* 1363–1374, 1977.

Watson, E. B., Zircon saturation in felsic liquids: Experimental results and applications to trace element geochemistry, *Contrib. Mineral. Petrol., 70,* 407–420, 1979.

Wright, J. V., and G. P. L. Walker, The ignimbrite source problem: Significance of a co-ignimbrite lag-fall deposit, *Geology, 5,* 729–732, 1977.

Wright, T. L., and P. C. Doherty, A linear programming and least squares computer method for solving petrologic mixing problems, *Geol. Soc. Am. Bull., 81,* 1995–2008, 1970.

Wyllie, P. J., and D. F. Tuttle, Experimental investigations of silicate systems containing two volatile components, 2, The effects of NH_3 and HF, in addition to H_2O, on the melting temperatures of albite and granite, *Am. J. Sci., 259,* 128–143, 1961.

(Received December 8, 1980;
revised March 12, 1981;
accepted March 25, 1981.)

JOURNAL OF GEOPHYSICAL RESEARCH, VOL. 86, NO. B11, PAGES 10153–10192, NOVEMBER 10, 1981

Gradients in Silicic Magma Chambers: Implications for Lithospheric Magmatism

WES HILDRETH

U.S. Geological Survey, Menlo Park, California 94025

Every large eruption of nonbasaltic magma taps a magma reservoir that is thermally and compositionally zoned. Most small eruptions also tap parts of heterogeneous and evolving magmatic systems. Several kinds of compositionally zoned ash flow tuffs provide examples of preeruptive gradients in T and f_{O_2}, in chemical and isotopic composition, and in the variety, abundance, and composition of phenocrysts. Such gradients help to constrain the mechanisms of magmatic differentiation operating in each system. Roofward decreases in both T and phenocryst content suggest water concentration gradients in magma chambers. Wide compositional gaps are common features of large eruptions, proving the existence of such gaps in a variety of magmatic systems. Nearly all magmatic systems are 'fundamentally basaltic' in the sense that mantle-derived magmas supply heat and mass to crustal systems that evolve a variety of compositional ranges. Feedback between crustal melting and interception of basaltic intrusions focuses and amplifies magmatic anomalies, suppresses basaltic volcanism, produces and sustains crustal magma chambers, and sometimes culminates in large-scale diapirism. Degassing of basalt crystallizing in the roots of these systems provides a flux of He, CO_2, S, halogens, and other components, some of which may influence chemical transport in the overlying, more silicic zones. Basaltic magmas become andesitic by concurrent fractionation and assimilation of partial melts over a large depth range during protracted upward percolation in a plexus of crustal conduits. Zonation in the andesitic-dacitic compositional range develops subsequently within magma chambers, primarily by crystal fractionation. Some dacitic and rhyolitic liquids may separate from less-silicic parents by means of ascending boundary layers along the walls of convecting magma chambers. Many rhyolites, however, are direct partial melts of crustal rocks, and still others fractionate from crystal-rich intermediate parents. The zoning of rhyolitic magma is accomplished predominantly by liquid state thermodiffusion and volatile complexing; liquid structural gradients may be important, and thermal gradients across magma chamber boundary layers are critical. Intracontinental silicic batholiths form where extensional tectonism favors coalescence of crustal partial melts instead of hybridization with the intrusive basaltic magma. Cordilleran batholiths, however, result from prolonged diffuse injection of the crust by basalt that hybridizes, fractionates, and preheats the crust with pervasive mafic to intermediate forerunners, culminating in large-scale diapiric mobilization of partially molten zones from which granodioritic magmas separate. Much of the variability among magmatic systems probably reflects the depth variation of relative rates of transport of magma, heat, and volatile components, as controlled in turn by the orientation and relative magnitudes of principal stresses in the lithosphere, the thickness and composition of the affected crust, and variations in the rate and longevity of basaltic magma supply. Extension of the lithosphere may reduce the susceptibility of basaltic magmas to hybridization in the crust, but it can also enhance the role of mantle-derived volatiles in chemical transport.

Swallows are not the only summer birds.
Bowen [1945]

INTRODUCTION

Recent improvements in the quality and output of trace element and isotopic data have permitted wholesale reassessment of the processes and paths by which magmas originate and evolve. Sampling of igneous rocks from the lunar surface and the ocean floor has stimulated generation of more precise data and more quantitative methods of manipulating them; at the same time, however, such programs have tended to encourage terrestrial geologists, as well, to work on small suites of samples without much attention to their time-stratigraphic contexts. Elegant treatments of high-quality data sometime remain unconvincing because the studies deal with grab samples that are poorly understood in a time-volume-compositional context.

Lack of attention to such contexts has led to several widespread misconceptions:

1. Magmatic systems are conceived narrowly, without due attention to the time-space evolution of the broader (yet discrete) thermal anomaly that, in general, includes many lithospheric lithologies and many magma bodies.

2. A 'source' of magma is commonly thought of as a discrete place (or even by some as a specific lithology) rather than as a zone of crystal + melt ± vapor coexistence that has a characteristic lifetime in the range 10^6–10^7 years and a vertical extent of tens of kilometers.

3. Shallow magma bodies are often said to have 'risen' (with or without some residue) and to have been 'emplaced' (stopped), after which they are thought to solidify without interruption and to release fluids, sometimes differentiating to some degree in the process. Even treatments that consider interactions with the rock-water envelope during a pluton's protracted crystallization usually take this quasistatic viewpoint, which neglects the compositional and thermal effects of eruptive losses and of the long-continued input of relatively primitive magma into the root system deep beneath a high-level magma body. During the lifetime of even a modest volcano ($\sim 10^5$ years), let alone that of a large one ($\sim 10^6$ years) or that of an entire volcanic field ($\sim 10^7$ years), such open-system behavior may provide the fundamental controls over what ultimately solidifies as plutonic rock.

4. Often implicit in static perspectives is the assumption that intermediate and silicic magma bodies are more or less homogeneous. The eruptive evidence against this is overwhelming, heat flow and other geophysical arguments against it are often compelling [e.g., *Lachenbruch et al.*, 1976; *Eaton et al.*, 1975], and the degree of exposure in some granitoid plu-

This paper is not subject to U.S. copyright. Published in 1981 by the American Geophysical Union.

Paper number 1B0836.

tons is sufficient to reveal whatever evidence of the original magmatic zonation may have survived protracted fractionation during solidification.

These themes and the evidence and arguments to clarify them form much of what follows. The traditional views have permitted the wishful thought that (in its extreme development) detailed study of a few 'representative' samples from an igneous complex might reveal its high-level differentiation history, the interactive complexities of the magma ascent process, and even the compositional and intensive parameters at the 'source.' This paper summarizes the evidence that (perhaps excluding the melting relations of a few fairly primitive basalts) we have barely begun to unravel even the high-level history. I start by presenting the least equivocal evidence we have for the nature of high-level magma bodies, the voluminous pyroclastic eruptions that catch the thermal and differentiation processes in the act by abruptly quenching the zoned magma and pouring it all over the landscape.

COMPOSITIONAL GRADIENTS

The preeruptive gradients in magmatic composition that have been recognized in the products of large individual eruptions exhibit several different patterns (Figure 1). Distinctions between these patterns need to be clarified and emphasized because they show that the relative effectiveness of various processes that differentiate magmas is not everywhere the same. Nearly all compositionally graded (zoned) eruptions are pyroclastic, and most of those that exceed a few cubic kilometers in volume are deposited in part as pyroclastic flows. I know of no pyroclastic eruption greater than 1 km^3 that is compositionally homogeneous, and many that are an order of magnitude smaller exhibit marked zonation.

Sorting, welding, and postemplacement crystallization, as well as ease of erosion, create difficulties in working with ash flow tuffs. Upper nonwelded zones and distal nonwelded snouts can be stripped readily; this is especially troublesome because these often represent the least and most evolved ejecta respectively, of a given sheet. Hydration and alteration, either secular or during cooling, crystallization, and degassing, can affect concentrations of mobile elements in the tuff [*Lipman,* 1965; *Noble,* 1970; *Scott,* 1971; *Truesdell,* 1966]. A few tuff sheets contain few or no pumice lumps, so that bulk chemical data must be carefully evaluated for the effects of crystal-glass fractionation during eruption and outflow [*Hay,* 1959; *Walker,* 1972]. Despite these difficulties, however, careful work on the quenched products of large eruptions can provide partial reconstructions of magma bodies when they were still predominantly liquid and had not yet suffered the fractionations inherent in plutonic consolidation and hydrothermal exchange. Such reconstructions can be made by documenting changes in the compositions and species of phenocrysts [*Hildreth,* 1979; *Warshaw and Smith,* 1980]. In most fresh sheets, the compositional gradients can be defined by the glass phase alone [e.g., *Hildreth,* 1977, 1979; *Mahood,* 1979, 1980*a*; and Fig. 9 herein].

Eruptive sequences commonly, but not always, show an orderly progression from most evolved to least evolved magmatic ejecta. Several examples of reversed compositional sequences [*Ekren et al.,* 1980], or of concurrent ejection of various compositional levels of a chamber [*Hildreth and Grunder,* 1980], have been described. Such eruptions probably reveal more about the mechanics of the eruptive process than about gradients in magma chambers; they may also indicate that notions about the configuration of magma chambers, and of the isotherms and isopleths within them, are generally oversimplified.

The depth to which any erupting magma body is tapped, and the fraction of the magma present that is actually drained by a given eruption, must be influenced by volatile gradients in the magma, kinetics of volatile exsolution, viscosity distribution in the chamber, and the extent to which a foundering roof behaves as a chaotic breccia, a leaky piston, or a well-fit lid. Because the amount of magma erupted will generally be only some fraction of that present, a complete compositional gradient may only rarely be seen; thus, all enrichment factors (Figs. 7 and 14) are apparent minima. In fact, it seems likely that the most mafic magma in a chamber (let alone in the system as a whole) will actually be seen only in large eruptions from small chambers [cf. *Smith,* 1979]. Nevertheless, existing data are sufficient to identify the following styles of compositional gradation (zonation) present in magma chambers at times of major eruptions (Figure 1).

1. *High-silica rhyolites:* The term 'high-silica rhyolite' is here restricted to volcanic rocks that contain 75 to 77.4 wt.% SiO_2 when analyses are recalculated to 100% on an anhydrous basis. This range warrants separate treatment because of the extreme and distinctive compositional gradients (Figures 2, 7, 9, and Table 1) that usually characterize it. Fe, Mn, Ti, P, Ca, and Mg may show twofold changes over this narrow silica interval, whereas many trace element gradients are steeper still. The differentiation process that controls these patterns is thought to be fundamentally diffusive [*Hildreth,* 1976, 1977, 1979; *Shaw et al.,* 1976] and is discussed at length below. Diffusive differentiation is not limited to high-silica rhyolite, but in the range 75%–77.4% SiO_2 it characteristically becomes dominant. The 77.4% upper limit in SiO_2 is empirical; no unaltered rhyolite contains more than 77.4% SiO_2 when reasonable magmatic values are assumed for halogens and unanalyzed minor elements. Fayalite-bearing rhyolites (which typically contain ~1.5% FeO*) probably never exceed ~77.1% SiO_2 when fresh and nonhydrated.

Examples of ash flow sheets that illustrate this style of compositional gradient include the Bishop Tuff, California [*Hildreth,* 1979]; the Lava Creek and Huckleberry Ridge tuffs, Yellowstone [*Christiansen and Blank,* 1972]; the Fish Creek Mountains Tuff, Nevada [*McKee,* 1970]; the Akaishi welded tuff, central Honshu [*Masuda et al.,* 1976; *Okamoto et al.,* 1975]; the Joe Lott Tuff, Utah [*Cunningham and Steven,* 1979]; the Sunshine Peak Tuff, southwestern Colorado [*Steven and Lipman,* 1976]; and the tuff of Pine Grove, Utah [*Keith,* 1980]. The group includes both biotite rhyolite and fayalite rhyolite as well as units that apparently lack phenocrysts of ferromagnesian silicates. Several modestly peralkaline (comenditic) tuffs could be included here because they are also high-silica rhyolites, but instead they are treated below as a distinctive variant (perhaps arbitrarily).

2. *Rhyolites zoned to intermediate compositions:* Several well-documented ash flow sheets grade from initial ejecta of high-silica rhyolite similar to group 1 into less evolved compositions that variously range from low-silica rhyolite to andesite (Figure 1). In some cases a continuous range of compositions may be present, but for most such sheets both analytical data

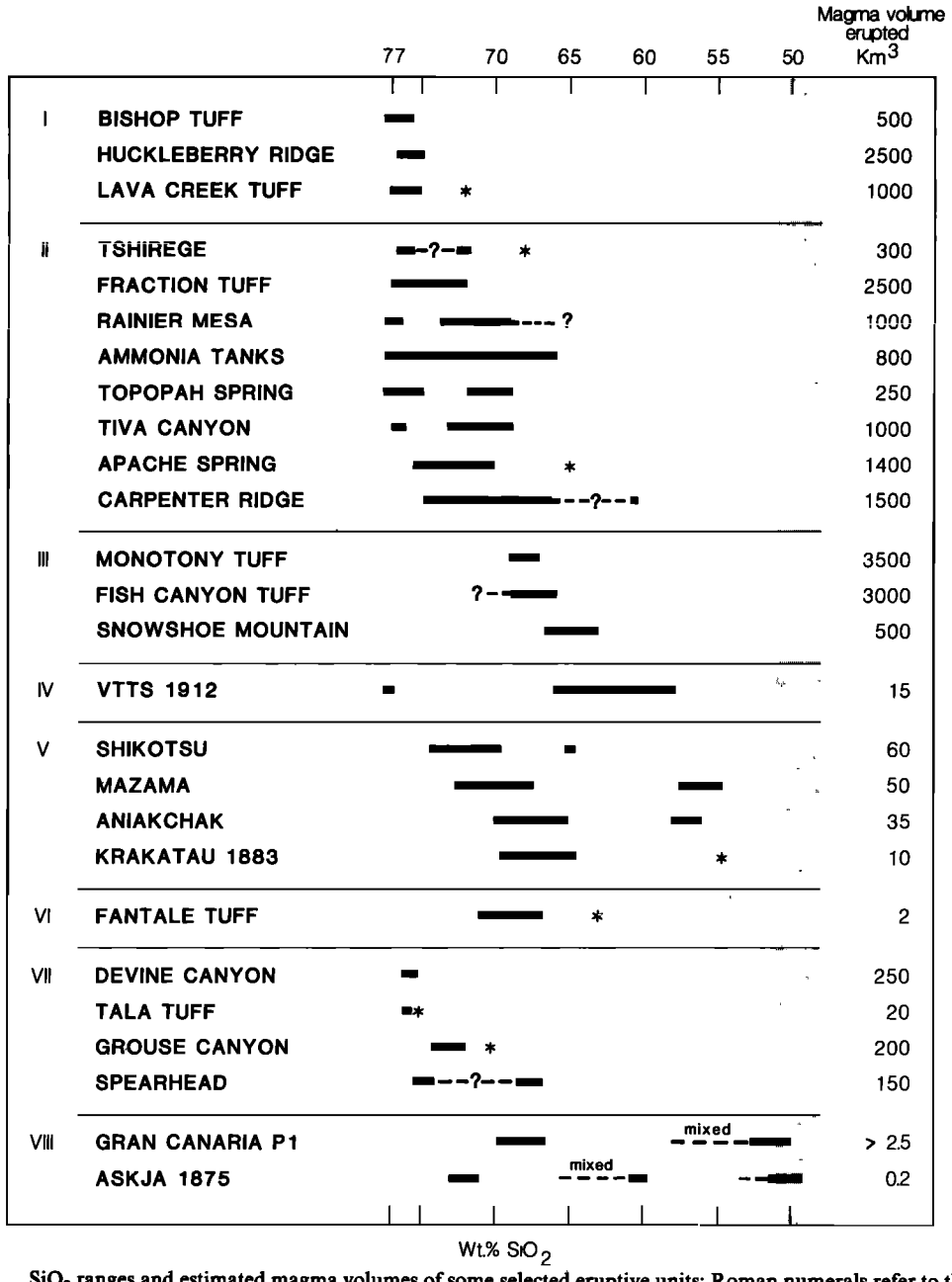

Fig. 1. SiO_2 ranges and estimated magma volumes of some selected eruptive units; Roman numerals refer to the informal groups discussed in the text. Solid bars represent data sufficient to assume continuous zonation; dashes and queries show where continuity is possible but uncertain. All gaps are thought to be real. Stars represent post-caldera lavas that erupted soon after the main unit and that appear to have tapped the same zoned magma reservoir. The three historic eruptions took place within 1 to 3 days; all the prehistoric units are thought to represent single eruptions or multipulse sequences limited to a few days duration. Volume estimates are recalculated to approximate magma volumes; in a few cases, the evidence is so fragmentary that estimates could be in error by as much as 50%. All compositional data here and elsewhere in this paper are recalculated to 100% on a water-free basis. Shaded region schematically indicates the basalt thought to be present in the roots of all magmatic systems (not necessarily of magma chambers; see Figures 12 and 15). Sources of data: Bishop Tuff, California (*Hildreth* [1979] and W. Hildreth, unpublished drill-core data, 1979); Huckleberry Ridge and Lava Creek Tuffs, Yellowstone (*Christiansen and Blank* [1972]; R. L. Christiansen, unpublished data, 1975); Tshirege Member of the Bandelier Tuff, New Mexico [*Smith*, 1979]; Fraction Tuff, Nevada [*Ekren et al.*, 1971]; Rainier Mesa and Ammonia Tanks members of the Timber Mountain Tuff and Topopah Spring and Tiva Canyon members of the Paintbrush Tuff, Nevada [*Byers et al.*, 1976; *Quinlivan and Byers*, 1977; *Christiansen et al.*, 1977]; 'Apache Spring Tuff,' New Mexico [*Rhodes*, 1976*a*, *b*]; Carpenter Ridge and Fish Canyon tuffs, Colorado [*Lipman*, 1975]; Snowshoe Mountain Tuff, Colorado [*Ratte and Steven*, 1967]; Monotony Tuff, Nevada [*Ekren et al.*, 1971]; VTTS = Valley of Ten Thousand Smokes, Katmai National Monument, Alaska, eruption of 1912 [*Hildreth*, 1980]; caldera-producing eruption of Shikotsu, Hokkaido [*Katsui et al.*, 1978]; climactic eruption of Mt. Mazama, Crater Lake, Oregon [*Williams*, 1942; *Ritchey*, 1980]; caldera-forming eruption of Aniakchak, Alaska [*Smith*, 1979]; 1883 eruption of Krakatau, Indonesia [*Westerveld*, 1952]; Fantale Tuff, Ethiopia [*Gibson*, 1970;, 1972, 1974]; Tuff of Devine Canyon, Oregon [*Greene*, 1973]; Tala Tuff, Jalisco, Mexico [*Mahood*, 1980*a*]; Grouse Canyon member of the Belted Range Tuff, Nevada [*Noble*, 1970]; Spearhead member of the Thirsty Canyon Tuff, Nevada [*Noble and Parker*, 1974]; Unit P1 on Gran Canaria [*Schmincke*, 1969*a*, *b*]; 1875 eruption of Askja, Iceland [*van Bemmelen and Rutten*, 1955; *Sparks et al.*, 1977; *Sigurdsson and Sparks*, 1981].

TABLE 1. Representative Chemical Data for Selected Units Mentioned in the Text

	Bishop Tuff		Lava Creek Tuff		VTTS (Katmai), 1912			Pantelleria		Devine Canyon Tuff		Rainier Mesa		Carpenter Ridge		Mazama Climax	
	Early	Late	Early	Late	Early	Middle	Late	Pantellerite	Trachyte	'Early'	'Late'	Early	Late	Early	Late	Early	Late
SiO_2	77.4	75.5	~77	~75.5	77.3	65.5	58.7	69.9	63.6	76.2	75.1	77.4	68.9	73	66.2	72	55
TiO_2	0.07	0.21	0.10	0.18	0.21	0.65	0.72	0.45	0.67	0.18	0.28	0.1	0.37	0.25	0.44	0.48	1.1
Al_2O_3	12.3	13.0	12.5	13.1	12.4	15.7	17.0	8.3	16.75	11.0	12.2	12.4	16.3	14.1	17.0	15	19
FeO*	0.7	1.1	1.1	1.8	1.2	5.0	6.8	7.8	4.5	2.9	2.6	0.6	1.9	1.35	3.3	2.4	6.7
MgO	0.01	0.25	0.01	0.11	0.09	1.9	3.7	0.07	0.8	~0.1	0.25	0.15	0.6	0.45	0.9	0.5	4.2
CaO	0.45	0.95	0.24	0.48	0.9	4.9	7.4	0.42	2.2	0.25	0.35	0.5	2.2	1.5	3.5	1.8	8.0
Na_2O	3.9	3.35	~3.8	~3.6	4.3	4.1	3.5	6.5	6.75	4.3	4.1	3.8	4.1	~3.9	3.7	5.0	4.2
K_2O	4.8	5.5	4.8	5.2	3.2	1.8	1.3	4.45	4.0	4.5	4.7	4.8	5.3	5.3	4.4	2.7	1.1
P_2O_5	0.01	0.06	~0.02	~0.03	0.02	0.13	0.13	0.13	0.21	0.04	0.06	0.01	0.13	~0.01	0.15	0.06	0.25
F	560	340	1600	650	500	400	300	3000	—	—	—	—	—	—	—	—	—
Cl	670	280	1100	500	1400	750	600	7600	300	—	—	—	—	—	—	—	—
Rb	190	95	300	150	75	30	20	210	65	170	85	—	—	—	—	58	23
Cs	7.2	1.9	7	3.3	3	1.5	1.1	3	—	5	1.2	—	—	—	—	3	1
Sr	4.8	110	<5	<5	40	250	330	5	185	<10	>30	~20	~700	~50	~500	300	1350
Ba	9.5	580	~70	~400	1020	600	395	~50	725	~30	~300	~50	~2000	~680	~4400	750	380
Ce	45	98	95	200	42	29	23	460	160	155	190	~150	~300	—	—	48	22
Eu	0.04	0.38	0.1	0.8	1.0	1.2	1.3	4.6	—	0.5	0.8	—	—	—	—	1.0	1.4
Yb	2.6	1.1	10	4.5	4.7	3.5	2.7	34	—	16	9	—	—	—	—	2.6	1.3
Y	25	12	65	~40	30	15	8	220	—	~150	~100	~50	~20	~30	<20	23	20
Zr	85	145	~200	~290	140	170	130	2200	595	~1300	~600	~70	~250	~220	~400	230	95
Hf	~3.6	~3.8	7	10	5.3	4.5	3.2	53	—	27	12	—	—	—	—	6.5	2
Ta	2.2	0.8	7	3.6	0.5	0.33	0.25	27	—	6.1	3	—	—	—	—	0.43	0.17
Th	22	12	37	25	5.6	3.2	2.9	55	9	15	8	—	—	—	—	5.3	1.4
U	6.5	2.6	12	6	2.6	1.4	1.2	17	1.4	5	3	—	—	—	—	2.2	0.6
Sc	3.0	1.8	1.2	2.3	7.8	18	27	1.5	—	0.2	1.7	<5	~5	~5	~8	6.5	12.5
Mn	270	175	~230	~340	375	950	1100	2150	1300	300	550	375	550	550	1100	440	760
Ni	1	3	<2	<2	9	15	19	<1	7	—	—	<3	<3	<4	<4	~1	~35
Cu	2	4.5	<2	<7	5	25	37	~2	21	—	—	~2	~7	~8	~13	—	—
Zn	38	40	50	80	30	55	65	450	135	225	120	—	—	—	—	40	60

Data are largely preliminary and incomplete, selected to illustrate the zonation in some important eruptive units. 'Early' and 'late' refer to eruptive sequences; that of the Devine Canyon Tuff is poorly known. For the Tala Tuff (Figures 1 and 2), see Mahood [this issue]. Dash indicates lack of data; ~ indicates approximate values for which better precision is needed. Sources of data: Bishop Tuff, California, *Hildreth* [1977, 1979]; Lava Creek Tuff, Yellowstone, *Hamilton* [1963], *Witkind* [1969], R. L. Christiansen and W. Hildreth (unpublished data, 1980); Valley-of-Ten-Thousand-Smokes (VTTS) eruption of 1912 at Katmai, W. Hildreth (unpublished data, 1979). Pantelleria, *Zies* [1960], *Chayes and Zies* [1964], *Nicholls and Carmichael* [1967], *Villari* [1974]; Tuff of Devine Canyon, Oregon, *Greene* [1973], W. Hildreth (unpublished INAA data, 1980); Rainier Mesa member of the Timber Mountain Tuff, Nevada, *Quinlivan and Byers* [1977]; Carpenter Ridge Tuff, Colorado, *Lipman* [1975]. Climactic eruptive sequence of Mt. Mazama, Oregon, *Williams* [1942], *Richey* [1980], and W. Hildreth (unpublished INAA data, 1977); phenocryst-rich 'late' Mazama samples are rather variable. Analytical methods are given in cited works; author's unpublished data are largely INAA, except XRF for major elements and Sr, Ba, Y, Zr, Cl, and Ni; F by specific ion electrode.

and field relations suggest that either a sharp compositional interface or a narrow transition zone had existed within the magma body prior to its eruption [e.g., *Quinlivan and Byers,* 1977; *Byers et al.,* 1976; *Christiansen et al.,* 1977; *Lipman et al.,* 1966]. As most such eruptions are hundreds to thousands of cubic kilometers in volume; usually progress from rhyolitic to less-silicic, more phenocryst-rich compositions; and result in subsidence of pistonlike cauldron blocks 10 to 30 km in diameter, it is reasonable to assume that single large chambers were tapped.

These strongly zoned sheets are an important link between groups 1 and 3. In the first place, they suggest that the magma of some strictly high-silica eruptions may also have been underlain by less-silicic magma that simply failed to erupt. Such an inference is indeed supported by well-documented eruptions on caldera floors of postcollapse lavas that are less silicic than any of the preceding caldera-forming ejecta; examples include the Yellowstone caldera [*Christiansen and Blank,* 1972; *Hildreth et al.,* 1980], the Valles caldera [*Smith,* 1979], and the Long Valley caldera [*Bailey et al.,* 1976]. Second, zoned sheets of this kind show that the voluminous intermediate magmas of the next eruptive class (3) sometimes develop rhyolitic upper levels.

3. *Monotonous intermediates:* These are mostly phenocryst-rich sheets of large volume but limited compositional range. Published data indicate ranges of generally <5% in SiO_2 content, generally within the 63%–71% SiO_2 interval. Examples include the Needles Range Formation [*Best et al.,* 1973], Monotony Tuff [*Ekren et al.,* 1971], and Loma Seca Tuff [*Hildreth et al.,* 1981], and the Fish Canyon, Treasure Mountain, and Snowshoe Mountain tuffs in the San Juan Mountains [*Lipman,* 1975; *Steven and Lipman,* 1976; *Ratté and Steven,* 1967]. No sheet of this type has yet been studied in sufficient petrologic detail to determine the relative importance of preeruptive gradients in the magma (or melt) and crystal-glass fractionation during emplacement of the tuff. Published data suggest that both factors have a role in determining the apparent compositional variations in these crystal-rich sheets, but only systematic work on pumice blocks or on phenocryst and matrix compositions will resolve the respective contributions.

These phenocryst-rich intermediate magmas appear to represent the 'dominant volume' [*Smith,* 1979] from which silicic upper layers sometimes develop within magma chambers. The existence of units like the Carpenter Ridge and Ammonia Tanks (Figure 1) shows that voluminous intermediate magmas do at times generate rhyolitic tops. The Wason Park and Mammoth Mountain tuffs of the San Juan Mountains [*Steven and Lipman,* 1976] also appear to have approached the kind of extensive zonation illustrated by the Carpenter Ridge Tuff (Table 1). Why some magmas should erupt voluminously without first producing a silicic cap remains poorly understood, but such processes may be related (as discussed below) to system dimensions, crustal thickness, crustal stress distribution, and the rate of input of basaltic magma into the roots of the system. Perhaps the small rhyolitic tuffs beneath and between the enormous sheets of the Needles Range Formation near the source areas in southwestern Utah [*Grant,* 1978; *Campbell,* 1978; *Best et al.,* 1979] indicate that many such systems start to generate rhyolitic upper boundary layers but that the process is aborted by premature venting of the dominant magma volume.

4. *Rhyolite plus zoned intermediate magma with a large compositional gap:* The best documented example is the 1912 eruption in the Valley of Ten Thousand Smokes, Alaska, where ejection of ~7 km^3 of very crystal-poor rhyolitic magma containing 77% SiO_2 was accompanied by a similar volume of crystal-rich intermediate magma that was zoned from 66% to 58% SiO_2 [Table 1; *Hildreth,* 1980; *Hildreth and Grunder,* 1980]. Compositions between 66.5% and 76.5% SiO_2 are not present; *Fenner*'s [1926, 1950] published data within this range represent mixed pumice, compositionally banded lava, and samples of bulk tephra that were mechanically fractionated and/or mixed during emplacement. The abundance of sharply banded pumice demonstrates commingling of magma from different levels during the eruptive process.

The mixed pumice supports neither the concept of an eruption-triggering arrival of new mafic magma nor the idea that the dacites are hybrid mixtures of andesite with rhyolite. That the zoned intermediate magma had coexisted with the rhyolite for a long time but was mixed with it only during the eruption itself is supported [*Hildreth,* 1980] by (1) the compositional complexity of the 1912 eruptive sequence, (2) the thermal continuity of the entire sequence (Figure 3), (3) the continuity in phenocrystic and bulk compositions of the crystal-rich andesitic and dacitic magmas, (4) the lack of any real transition from banding to blending in the pumice, and (5) the absence of mutual contamination of rhyolite and dacite by their contrasting suites of phenocrysts. The combined field, compositional, thermal, isotopic, and time constraints suggest that generation of the phenocryst-poor rhyolite took place either by partial remelting of young igneous rocks in the roof of an andesitic-dacitic chamber or by rapid extraction of rhyolitic liquid from dacitic magma in a manner so efficient that no dacitic phenocrysts were retained and no compositions in the 67%–76% SiO_2 range were produced.

This particular kind of zoned eruption provides an insight to processes governing the generation and occurrence of unzoned rhyolites of small volume that are occasionally erupted, both in predominantly intermediate volcanic fields and in basaltic fields that lack conspicuous intermediate extrusive rocks. Examples include the 1875 eruption of Askja [Figure 1, *Sigurdsson and Sparks,* 1981], the rhyolites of Umnak [*Byers,* 1961], the 1663 eruption of Usu [*Katsui et al.,* 1978], the rhyolites of Izu [*Kuno,* 1959], and, as I will argue below, many modest rhyolitic domes in the interior of continents as well as along their margins.

Important points here are (1) that 'bimodality' can mean rhyolite-basalt, rhyolite-intermediate, or even intermediate-basalt; (2) that some rhyolites are produced atop mafic systems but commonly lack compositional continuity with them; and (3) that the phenocryst-poor nature of many small-volume but long-lived rhyolitic systems indicates the sustained presence of subjacent mafic magma more as a heat source than as a parent [cf. *Bacon et al.,* this issue]. Much has been made recently of the suggestion that fortuitous injection of mafic magma into silicic chambers triggers eruptions; this process may indeed happen occasionally, but in general it looks to me like this is putting the cart before the horse.

5. *Zoned intermediate magmas—commonly with a compositional gap:* This is the commonest kind of large pyroclastic eruption from the intermediate volcanoes of the continental margins and mature island arcs. It is well illustrated (Figure 1) by the climactic ejecta of Shikotsu [*Katsui,* 1959, 1963; *Katsui et al.;* 1978], Mazama [*Williams,* 1942; *Ritchey,* 1980], and Aniakchak [*Smith,* 1979; *Miller and Smith,* 1977]. Zoning may

span any part of the range from rhyodacite to andesite; it can extend over as much as 15% SiO_2 (Figure 1) or can be rather restricted, as for example, in the 1929 eruption of Komagadake [58%–61.5% SiO_2, ~0.2 km^3 of magma; *Katsui et al.*, 1978; *Tsuya et al.*, 1930]. Larger eruptive volumes clearly tend to have wider zoning and extend to more silicic compositions, but the data base is still too small to be definitive. Small systems commonly show only modest zonation in the dacitic range, but they exhibit a much greater tendency for mafic magma from deeper levels to be commingled with the dacitic magma during eruptions. These tendencies are implicit in *Smith*'s [1979, Figure 12] model, wherein a capping zone of silicic magma in a small chamber can readily be drained to or penetrated by the subjacent mafic magma. Banded pumice is far more common than most geologists acknowledge, as it occurs in most large pyroclastic eruptions, and even in many small ones from volcanos of andesitic to rhyodacitic composition. Only rarely, however, does such mixing warrant the inference that the mafic component had newly intruded the silicic magma chamber. The thermal budgets, longevities, and compositional evolution of most such systems indicate that silicic magma chambers grade down into mafic root zones that are longer lived than the silicic volume itself (Figure 12).

A compositional interface between silicic and more mafic magma need not be breached in a large chamber if the silicic volume is thick enough or the eruptive drawdown small enough. Several dacitic ash flow sheets in this group are apparently zoned continuously through several percent in SiO_2 without any jump to a more mafic composition; however, older and younger more mafic lavas of associated volcanoes commonly suggest that more extensive zoning existed than was actually tapped by the major pyroclastic eruption. Examples include the climactic eruption of Mashu [*Katsui*, 1963], the 1883 eruption of Krakatau [*Westerveld*, 1952], and the sheets in Kyushu now designated Aso-4 [*Ono et al.*, 1977; *Lipman*, 1967] and Ata I and II [*Aramaki and Ui*, 1966*a*, *b*; *Ui*, 1971]. I reiterate here that the extent of zonation in the products of any eruption is limited by depth of drawdown and is necessarily a minimum for the chamber, and certaintly for the system as a whole.

6. *Strongly peralkaline silicic-to-intermediate magmas:* Compositionally zoned ejecta of pantellerite and low-silica comendite usually exhibit only a modest range of major-element zonation, generally within the interval 66%–71% SiO_2. Closely associated trachytes sometimes extend the range apparently coexisting in a given chamber to compositions a few percent less silicic. Examples include the Fantale Tuff of Ethiopia [Figure 1, *Gibson*, 1974] and some sheets on Gran Canaria [*Schmincke*, 1969*a*, *b*]. Despite additional piecemeal data from Pantelleria, Nevada, and elsewhere, however, the general lack of work on the internal variation of such sheets means that the following generalizations are tentative.

Eruptions of this kind rarely exceed a few cubic kilometers in volume, although the Gold Flat sheet in southern Nevada was ~20 km^3 [*Christiansen*, 1979]. Limited eruptive volumes and the common occurrence of succeeding eruptions of trachyte or basalt [e.g., *Noble and Christiansen*, 1974; *Schmincke*, 1969*a*, *b*] suggest that pantelleritic magma reservoirs are relatively small. If small volumes of silicic magma are intimately underlain by voluminous basaltic magma (with or without an intervening trachytic layer) or by an extensive and deep-reaching network of basaltic dikes, they may be subjected to extraordinarily steep thermal gradients and abnormally large fluxes of Cl and CO_2. Consequent thermogravitational [*Shaw et al.*, 1976; *Hildreth*, 1979] and volatile-complexing processes together may account for the enormous enrichments in Zn, Zr, Hf, Y, Nb, Ta, Mo, W, Fe, Na, Cl, and REE that characterize these magmas (Table 1). Magmas that might otherwise evolve toward true rhyolites probably have their SiO_2 and Al_2O_3 contents reduced to the levels of pantellerites, essentially by dilution with diffusively introduced Na, Fe, Zr, and halogens; such dilution would be over and above the concurrent effects of feldspar fractionation on Al, Ca, and alkali values.

The occurrence of pantellerite in areas of continental extension and along oceanic fracture zones is well established, as is its association with transitional to alkalic basalt and hawaiite. Only rarely are rocks that contain 54%–61% SiO_2, intermediate between basalt and trachyte, volumetrically significant, and the evidence from areas such as Gran Canaria [*Schmincke*, 1969*a*, *b*] and Tibesti [*Vincent*, 1963, 1970] strongly suggests that such intermediates are mostly hybrids. What appears to be essential in pantellerite genesis is not any elusive 'liquid line of descent' but a well-focused accumulation of intrusive basaltic magma, crystallizing at depth and releasing an extraordinarily halogen-rich but water-poor volatile flux into the overlying crust, either thickened oceanic or extending continental. The ubiquitous compositional gap and the strong enrichment of the select group of elements named above seems to demand a volatile focusing mechanism [*Bailey*, 1964, 1970; *Lloyd and Bailey*, 1975], probably in concert with fractionation and partial remelting of hot young basalt (gabbro) within the accumulating pile itself, as a means of producing the distinctive trachyte-pantellerite magma spectrum. If the extension rate were too great, however, the rate of upward magma transfer would overwhelm the effects of volatile ascent and shallow remelting, resulting in high eruption rates of relatively unenriched basalt. Variable rates and duration of processes influenced by the stress distribution in the lithosphere, rather than different source lithologies, seem more likely to account for the intimate associations of peralkaline and subalkaline silicic volcanic rocks (and of 'enriched' and 'depleted' basalt) recognized in numerous regions [*Noble et al.*, 1965, 1968; *Vincent*, 1970; *Cox et al.*, 1970; *Sigvaldason et al.*, 1976; *Macdonald*, 1974, for a summary].

7. *High-silica peralkaline magmas:* Compositionally zoned eruptions that begin with high-silica peralkaline magma represent at least two different, but apparently convergent, lines of magmatic evolution, one similar to group 1 and the other closer to group 4. In the first subgroup the pre-eruptive comenditic magma grades downward into subalkaline rhyolite, or even as far as a magma of intermediate (e.g., quartz-latitic) composition. In the second subgroup the less evolved compositions remain mildly peralkaline while zoning toward subjacent trachytic magma. In neither case does the zonation involve, or trend toward, pantellerite. The first subgroup is illustrated in Figure 1 by the Tala Tuff [*Mahood*, this issue], which zones from comendite to non-peralkaline rhyolite; the Spearhead Member of the Thirsty Canyon Tuff [*Noble and Parker*, 1974], which zones all the way to subalkaline quartz latite; and also the high-silica tuff of Devine Canyon [*Greene*, 1973]. The second subgroup is represented by the Grouse Canyon sheet and associated lavas [Figure 1; *Noble and Parker*, 1974] and probably by several sheets in Tibesti [*Vincent*, 1963] and northern Nevada [*Rytuba and Glanzman*, 1979].

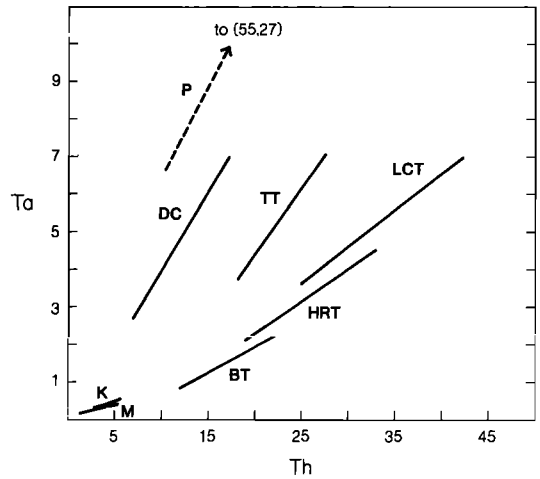

Fig. 2. Generalized plot of Ta and Th contents (in ppm) of several large eruptive units. Key to units, sources of data, and ranges in agpaitic index (AI) follow. AI increased roofward with both Ta and Th in all cases. For eruptive volumes and ranges in SiO_2, see Figure 1. M, climactic eruption of Mt. Mazama (Crater Lake, Oregon); W. Hildreth (unpublished data, 1977), *Ritchey* [1979], 0.37–0.83. K, 1912 eruption in the Valley of Ten Thousand Smokes, Alaska; *Hildreth* [1980] and W. Hildreth (unpublished data, 1977), 0.45–0.85. BT, Bishop Tuff, California; *Hildreth* [1977, 1979], 0.87–0.91. HRT, Huckleberry Ridge Tuff, Yellowstone; W. Hildreth and R. L. Christiansen (unpublished data, 1980), 0.82–0.93. LCT, Lava Creek Tuff, Yellowstone; same as HRT, 0.85–0.95. TT, Tala Tuff, Jalisco; *Mahood* [1980*a*], 0.98–1.09. DC, tuff of Devine Canyon, Oregon; *Greene* [1973], W. Hildreth (unpublished data, 1980), 0.96–1.08. Dashed line P, trend for silicic rocks of Pantelleria (which alone on this diagram does not represent a single eruption); *Villari* [1974], 1.25–1.85. All Ta and Th analyses by INAA. Note that absolute values and ranges of enrichment of both elements increase with alkalinity (AI) among the subalkaline sheets. The peralkaline sheets have steeper slopes and much higher Ta contents, suggesting more effective roofward volatile-complexing of Ta than of Th, probably with halogens. Together with Figure 7, this diagram may help to elucidate many trace- and minor-element patterns in silicic and intermediate igneous rocks.

Both lines are characterized by steep gradients in minor and trace elements that apparently indicate that liquid-state diffusive and/or volatile-complexing processes made significant contributions to their differentiation. In the only high-silica peralkaline sheet yet studied in detail, *Mahood* [1981*a*, and this issue] showed that SiO_2 may actually decrease slightly with increasing peralkalinity. Mahood proposed that this and other compositional variations reflect the sum of the effects of superimposed differentiation mechanisms that operate at different and fluctuating rates. Some comendites may simply be high-silica rhyolites that in the course of differentiating from less-silicic subalkaline magma were also affected by the introduction of excess Na and Fe related to volatile ascent from the deeper levels of extensional zones intruded by large volumes of basaltic magma that degas during crystallization.

Figure 2 illustrates some contrasts in the patterns of differentiation among several of the zoned magmas shown in Figure 1. Ta and Th were enriched roofward in all zoned eruptions that I know about, but the actual concentrations and, above all, their ranges show enormous differences from one magma to another. In Figure 2, the Mazama and Katmai ejecta, which are both calcic (Peacock index ~63), exhibit low values and ranges of both elements, in spite of having ranges in SiO_2 that approach 20 wt. % (Figure 1)! In contrast, the Bishop, Huckleberry Ridge, and Lava Creek tuffs are entirely rhyolitic, and though each sheet ranges through only ~2% in SiO_2, the Ta and Th ranges are large. Absolute concentrations, ranges, and the Ta/Th slopes all increase with alkalinity. The Tala Tuff and the tuff of Devine Canyon are both in part peralkaline, and though still more limited in SiO_2 range (Table 1; Figure 1), they have equally wide ranges and even steeper Ta/Th slopes than do the subalkaline rhyolitic sheets.

These effects are probably attributable to the enhanced role of halogens in the evolution of peralkaline magmas [*Bailey and Macdonald,* 1975; *Mahood,* this issue]. The most extreme magmas for which many data are now available is the suite from Pantelleria, which is the only data set in Figure 2 that represents more than a single eruption. Reconnaissance work [*Mahood and Hildreth,* 1980] leads us to anticipate, however, that individual eruptive units on the island may be zoned through much of the indicated range. The outstanding feature shown by the Pantelleria data is the extreme enrichment of Ta (and Nb, Mo, Zr, Hf, and Zn) relative to Th, behavior that we believe to be related to the very high Cl content of these magmas [*Zies,* 1960; *Carmichael,* 1962]. Enrichment of Th (and U, Be, Li, and Sn), on the other hand, may be more closely linked to roofward migration of F and/or H_2O.

8. *Rhyolite-basalt eruptions:* Eruptions in which silicic and basaltic magmas are ejected together from the same vent are relatively common in regions of thick oceanic crust or of extending continental crust [e.g., *Gibson and Walker,* 1963; *Schmincke,* 1969*a, b; Wilcox,* 1944; *Metz and Bacon,* 1980; *Sigurdsson and Sparks,* 1981]. Two moderately voluminous examples, from Askja and Gran Canaria, are given in Figure 1. Rhyolite-basalt eruptions do not generally occur in other crustal settings, on the one hand because thin mafic crust does not favor aggregation of enough basaltic magma to generate much rhyolitic magma by crustal melting and, on the other hand, because thick nonextending crust retards penetration by basalt and favors hybridism [*Eichelberger and Gooley,* 1977]. Because large silicic magma chambers are probably buffered by a thick root zone from direct penetration by basalt (Figure 12), the coeruption of rhyolite and basalt is only likely to occur around the periphery of such systems or in immature zones of crustal melting where silicic pods and dikes have not yet aggregated into 'chambers' larger than a few cubic kilometers in volume.

Several variants of this compositionally extreme 'zoned' eruptive type can be distinguished. High-silica rhyolite, together with basalt, is common on the continents; lower-silica rhyolite with basalt (and sparse intermediates) in Iceland; and sodic rhyodacite with basalt on Gran Canaria (Figure 1). *Chayes* [1977] convincingly and eloquently demonstrated the scarcity of intermediate compositions in the magmatic suites of many oceanic islands. Individual eruptive units that are themselves sharply bimodal confirm this observation and suggest that the scarce intermediate magmas are at least, in part, hybrids.

Rhyolite-basalt and trachyte-basalt eruptions are volumetrically minor but conceptually important, for they shed light on processes at work in the substructure of all systems, be they predominantly intermediate or predominantly bimodal. This matter is taken up again in the concluding part of the paper.

To summarize this discussion, I stress that groups 1 to 8 are in no way intended to be a classification of compositional gradients. Some of the groups grade into each other, and perhaps ultimately it will be shown that a multivariate field exists, within which all ranges of compositional zoning can be re-

lated. The most extreme and probably most fundamental kind of 'zoned' eruption is represented by group 8 of Figure 1, viz., rhyolite with basalt. To some degree, every zoned magma body must be unique; not surprisingly, therefore, some sheets fit poorly into the framework given. For instance, some very high temperature sheets (Figure 3) preserved along the margins of the Snake River Plain [*Coats,* 1964; *Ekren et al.,* 1978] may represent a class apart. Most sheets along the Taupo volcanic zone probably are readily referred to group 1 or 2, but the possibility of still other patterns there remains unevaluated because of insufficient information on their internal chemical variability. The data presented in Figure 1 are principally a framework for discussion, and the sheets selected as examples reflect little more than the availability of my own or published data. Other patterns of compositional zonation probably exist, so the discussion here is only a progress report.

The main points are: (1) No nonbasaltic eruption greater than ~1 km^3 is known to have been homogeneous—a generality that probably supports the assumption that all magma bodies worthy of the term 'chamber' are compositionally zoned (at least when capable of eruption). (2) A large pyroclastic eruption freezes time as a variable, minimizes eruptive rehomogenization, and reveals some of the instantaneous variability present in the upper part of a magmatic system. (3) Major-element zonation can be extensive in large chambers of intermediate to silicic composition regardless of the degree of alkalinity, but trace-element gradients are progressively steeper in more alkalic and in high-silica systems (Figure 2). (4) Crystal fractionation is but one of several processes working to establish compositional gradation in magma bodies; it is clearly only a second-order process in some high-silica and high-alkali systems [*Hildreth,* 1976, 1979; *Mahood,* 1981*a* and this issue; *Smith,* 1979]. (5) Large eruptions prove that compositional gaps are common within magmatic systems. The extreme case of the rhyolite-basalt eruption has been well known for years, as in Iceland [*Bunsen,* 1851], Yellowstone [*Wilcox,* 1944], and Gran Canaria [*Schmincke,* 1969*a, b*]. However, the magmatic interfaces represented by such gaps can occur at virtually any silica interval (Figure 1). (6) The most primitive magma present in a high-level chamber is seldom tapped, except by major eruptions of small systems. (7) It is argued below, but has been implicit above, that basalts are the initial magmas present in virtually every magmatic system in the lithosphere. Intermediate and silicic magmas are derivative, but only by long-lived and tortuous lithospheric paths, along which partial melting, crystal-vapor-liquid-fractionation, and hybridization of liquids are merely components in a complex transformation. (8) When we consider the full range of compositionally zoned magma chambers, a simple hierarchy that relates degree of petrologic evolution to system volume or age apparently does not exist. Rather, there is a complex interplay in each system between the fluxes of total mass, heat, and volatile components; the lithology and previous magmatic history of the affected lithosphere; and the depth variation of lithospheric stress states. These factors must exercise the principal controls upon the relative effectiveness of diking [*Shaw,* 1980] and diapirism [*Marsh,* 1978, 1979] on the upward propagation of melts, upon the transit time available for modification of such melts in the lithosphere, and upon their susceptibility to emplacement and crystallization at different levels. We will return to these themes as part of a broader view of crustal magmatism after first considering other kinds of gradients in magma chambers.

GRADIENTS IN TEMPERATURE AND OXYGEN FUGACITY

The view that magma bodies are isothermal is encountered less frequently than the assumption of compositional homogeneity. Nevertheless, arguments about magmas in the crust are commonly based on such notions as adiabatic ascent, instantaneous one-stage emplacement, and a solidification history that is rapid and uninterrupted. What may be approximately true for a basaltic dike is unrealistic for a major pluton. Fluctuations in the thermal regimes of many large continental magmatic centers are amply indicated by fluctuations in the crystallinity, volumes, and compositions of successive extrusive products and by eruptive lifetimes commonly in excess of 10^6 years.

Temperature

The thermal gradient in a large pluton at times of eruption can in part be reconstructed by application of mineral geothermometers based upon coexisting Fe-Ti oxides, coexisting feldspars, coexisting pyroxenes, $\Delta^{18}O$ (quartz-magnetite), etc., in the quenched ejecta. The titanomagnetite-ilmenite geothermometer of *Buddington and Lindsley* [1964] is by far the most sensitive and reproducible and is the one most in accord with both field and experimental measurements [*Hildreth,* 1977, 1979]. In Figure 3, I have summarized some of my results with this geothermometer for several voluminous eruptions. Aside from the units for which points are actually plotted, each data set consists of 20 to 80 samples. The diagram helps to illustrate several important points.

Most eruptive units exhibit a continuous thermal gradient. Two that appear not to do so (Cougar Point and Shikotsu) are represented by very few samples. I can't summarily dismiss the apparently wide thermal gap between the rhyolitic and quartz-latitic components of the Paintbrush and Timber Mountain tuffs [*Lipman,* 1971], but it should be noted that few suitably fresh samples were available and that the data certainly do not represent the full variability of these immense sheets. The apparent thermal gap seems physically unlikely.

In the Valley of Ten Thousand Smokes and Mazama sheets the thermal continuity spans well-documented bulk-compositional gaps of ~10% SiO_2 (Figure 1). This evidence weighs heavily in favor of the existence of interfaces of significant longevity between compositionally contrasting magmas rather than the fortuitous encounter of unrelated ones.

High-silica biotite rhyolites (here represented by the Bishop Tuff) exhibit temperatures in the range 700°–800°C. This range is supported in the Bishop Tuff by abundant $\Delta^{18}O_{Qz\text{-}Mt}$ data (W. Hildreth, unpublished data, 1978), and it is in good agreement with Fe-Ti-oxide results on biotite rhyolites from the Taupo volcanic zone [*Ewart et al.,* 1975] and from the Coso Range of California [*Bacon et al.,* this issue]. Biotite-bearing quartz latites (substantially different in bulk and mineral composition from the rhyolites), however, may attain much higher temperatures; I have obtained results as high as ~1060°C in the Holy Joe sheet in Arizona [*Krieger,* 1979].

The fayalite rhyolites from Yellowstone range from ~820° to more than 900°C, even though they contain 75%–77% SiO_2 and up to 17% phenocrysts (Table 1); experimental determinations of granitic liquidi indicate that such temperatures must reflect relatively low contents of magmatic H_2O [*Tuttle and Bowen,* 1958; *Wyllie,* 1977]. The high temperatures agree with estimates by *Mahood* [this issue] and by *Ewart et al.* [1975] for fayalite-bearing rhyolites from Mexico and New

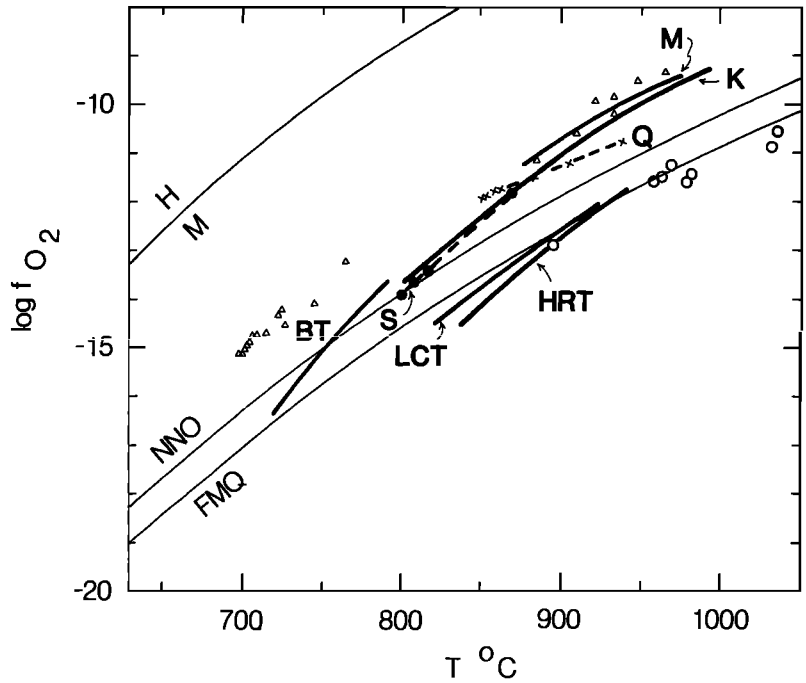

Fig. 3. Ranges of temperature and oxygen fugacity determined from microprobe analyses of coexisting Fe-Ti oxides in quenched glassy ejecta from several zoned eruptive units. All data were obtained by the author from homogeneous unaltered titanomagnetite-ilmenite microphenocryst pairs by using the same instrument, standards, and operating conditions, with the exception of the open triangles, which are the Paintbrush-Timber Mountain data of *Lipman* [1971]. All data were recalculated according to the procedures of *Carmichael* [1967]. Thick lines are the trends defined by 20 to 80 samples each from the following units: BT, Bishop Tuff [*Hildreth*, 1977]; K, 1912 eruption in the Valley of Ten Thousand Smokes [*Hildreth and Grunder*, 1980]; M, climactic eruption of Mt. Mazama (W. Hildreth, unpublished data, 1976); LCT and HRT Lava Creek Tuff and Huckleberry Ridge Tuff, Yellowstone (*Christiansen and Blank* [1972]; W. Hildreth and R. L. Christiansen, unpublished data, 1979). Large dots represent four samples thought to bracket most or all of the compositional range in the climactic eruption of Shikotsu (S), Hokkaido. Crosses are seven samples similarly spanning the compositional range and eruptive sequence in the 1932 eruption of Quizapu (Q), central Chile. Open circles are data from six conformable cooling units of the Cougar Point Tuff (~70 ± 2% SiO_2) near Jarbridge, Nevada [*Coats*, 1964]. Open triangles are samples from several different units of the Paintbrush and Timber Mountain tuffs, erupted at different times from the same caldera cluster; data of *Lipman* [1971] were recalculated for consistency with the other units shown here. Volumes and ranges in SiO_2 are given in Figure 1 for most units; preliminary data for Quizapu suggest ~7 km^3 of magma zoned from ~70 to ~56 wt.% SiO_2. HM, NNO, and FMQ are experimental oxygen-buffer curves, for reference only.

Zealand, respectively. Figure 3 shows that such rocks plot close to the FMQ buffer, in accord with their phenocryst contents of fayalite, titanomagnetite, and quartz.

The Valley of Ten Thousand Smokes, Mazama, Quizapu, and Shikotsu ejecta exhibit T-f_{O_2} patterns rather similar to each other; the differences are largely consistent with the respective ranges in bulk composition (Figure 1) and phenocryst contents (Table 2) of the ejecta. Of the four units, only the 1912 Valley of Ten Thousand Smokes sheets lacks hornblende phenocrysts, although these are exceedingly sparse or absent in the late-erupted andesitic components at Quizapu and Shikotsu. Plagioclase is present and sanidine absent throughout all four eruptive sequences. Of the pyroxenes, hypersthene is in each case predominant (or alone) at the silicic end, but augite is subequal or predominant at the andesitic end of the chemical-thermal spectra. The 940°–990°C values obtained for the Quizapu, Mazama, and Valley of Ten Thousand Smokes andesites are quite satisfactory in the light of experimental studies of similar bulk compositions [*Eggler*, 1972; *Eggler and Burnham*, 1973], especially in view of their phenocryst-rich nature (Table 2) and the moderate-to-high H_2O contents suggested by the explosive nature of all these eruptions. Confirmation of the temperature ranges shown in Figure 3 also comes from inclusions of coexisting glass and vapor within quartz phenocrysts in the rhyolitic component of the 1912 outburst in the Valley of Ten Thousand Smokes. *Clocchiatti* [1972, 1975] measured homogenization temperatures (assumed to be similar to entrapment temperatures) in the range 840°–860°C, in agreement with the upper end of the 800°–850°C range given by Fe-Ti oxides for the 1912 quartz-bearing ejecta.

The very high temperatures obtained for the K-rich rhyodacitic Cougar Point Tuff (70% ± 2% SiO_2 [*Coats*, 1964; *Weathers et al.*, 1973]) are consistent with the species and low contents of phenocrysts and with the secondary flowage behavior of these lavalike ash flow sheets. Some units have less than 2% phenocrysts, generally lack hydrous species, and contain pigeonite [*Coats*, 1964]. Coupled with a few temperatures >1000°C, these features suggest that the silicic magma body was closely underlain by the basaltic magma that subsequently flooded its source area in the Snake River Plain [*Bonnichsen et al.*, 1973; *Armstrong et al.*, 1975].

The data of Figure 3 demonstrate the reality of thermal gradients in magma chambers, but they provide only crude constraints on the magnitudes of those gradients because we don't know the preeruptive depth distribution of the ejected magma. Even if eruptive volumes were known accurately, little could be inferred about the geometry of parent chambers or

TABLE 2. Variations in Volume Percent and Species of Phenocrysts During Progressive Eruption of Voluminous Silicic Magmas

Unit	Phenocrysts		Phase Boundaries Crossed*		
	Range, %	Present at onset	Phase in	Phase out	Reference
Bishop Tuff	5–30	QSPBMIAlZAp	Op Cp Po	Al	1
Tala Tuff	0–2	none	Q S	—	2
Tshirege	5–35	QSFaCpMAlChZAp	Op I P Anor	Fa	3, 4
Fraction Tuff	22–38	QSPBMSpAlAp	Hb Z	—	5
Ammonia Tanks	4–52	QSPBMISpAlZAp Cp(?)	Cp(?) Hb	—	6–10
Rainier Mesa	5–35	QSPBMI Al(?)	Hb Cp Sp	—	ibid.
Tiva Canyon	2–25	QSPBHbMISp	Cp	Q	ibid.
Topopah Spring	1–21	QSPBMIAlZAp	Cp Hb Sp(?)	Q	ibid.
Lava Creek Tuff	1–17	QSPHbMIAlChZApPo	Cp Fa	Hb Al Ch(?)	11, 12, 13
Huckleberry Ridge	2–15	QSPCpMIAlChZApPo Fa(?)	Fa(?)	Al Ch	ibid.
Apache Spring	16–49	QSPBMISpZAp	Cp Hb	—	14
VTTS (Katmai) 1912	1–25	QPOpMIApPo	Cp Ol	Q	13, 15
Aso-4	5–25	POpMIAp	Hb Cp Ol	—	16,17
Mazama	5–50(−80)	POpHbMIApPo Cp(?)	Ol Cp(?)	—	13, 18, 19
Shikotsu	10–25	POpHbMIApPo	Cp	Hb(?)	20
Quizapu 1932	1–20	POpCpHbMIApPo	—	Hb	13, 21
Mammoth Mountain	5–50	SPBCpMIZApHb	—	S Hb	22, 23
Fantale Tuff	5–10	Anor, Cp, Aen	Fa	—	24
Ikeda	26–30	QPOpHbMI Ap(?)	Cp Ol	Hb	25
Whakamaru	7–37	PBOpMIZAp	Q Hb S	—	26

* Although some sequences are more complicated, most eruptions first tap lower-temperature roofward magma, so that 'phase-in' signifies that the phenocryst in question was not present at the top of the chamber but only appeared as the eruption proceeded to tap hotter magma.

Q, quartz; S. sanidine; P, plagioclase; B, biotite; M, titanomagnetite; I, ilmenite; Op, orthopyroxene, Cp, clinopyroxene; Hb, hornblende; Al, allanite; Ch, chevkinite; Z, zircon; Ap, apatite; Sp, sphene; Po, pyrrhotite; Fa, fayalite; Ol, olivine; Anor, anorthoclase; Aen, aenigmatite; (?), entry or loss of phase is probable but not certain.

Sources of data: (1) *Hildreth* [1977, 1979]; (2) *Mahood* [1980*a*, 1981*a*]; (3) *Smith and Bailey* [1966]; (4) *Warshaw and Smith* [1980]; (5) *Ekren et al.* [1971]; (6) *Byers et al.* [1976]; (7) *Quinlivan and Byers* [1977]; (8) *Lipman et al.* [1966]; (9) *Lipman* [1971]; (10) *Christiansen et al.* [1977]; (11) *Christiansen and Blank* [1972]; (12) R. L. Christiansen (unpublished data, 1975); (13) W. Hildreth (unpublished data, 1980); (14) *Rhodes* [1976*a*, *b*]; (15) *Hildreth and Grunder* [1980]; (16) *Lipman* [1967]; (17) *Ono et al.* [1977]; (18) *Williams* [1942]; (19) *Ritchey* [1979, 1980]; (20) *Katsui* [1959, 1963]; (21) *Larsson* [1936]; (22) *Ratté and Steven* [1967]; (23) *Steven and Lipman* [1976]; (24) *Gibson* [1970, 1972, 1974]; (25) *Ui* [1971]; (26) *Ewart* [1965]. Some of these studies were based only on thin sections and did not include mineral separations, so the behavior of minor phases may not always be correct. For further information on most of these units, see captions to Figures 1, 2, and 6.

the flow paths of escaping magmas. *Smith* [1979] summarized published data on volumes of large eruptions and areas of the associated calderas, showing that total apparent drawdown of magma bodies ranges from <0.1 to several kilometers. Smith reviewed some of the problems in making the volume estimates, but no less significant are uncertainties in assignment of subsidence area. Areas of calderas are rarely equivalent to areas of subsidence because they increase with time, owing to erosion and slumping of the walls [see *van Bemmelen and Rutten*, 1955, for the example of the 1875 Öskjuvatn (Knebel) caldera at Askja]. The area within the ring faults more accurately records the subsidence and thus provides a safe minimum estimate for the area of the magma chamber roof in strictly ring structure systems. However, many smaller systems may not undergo simple piston cylinder collapse as do the large ring structure calderas but may instead undergo both collapse and shallow cratering to produce flaring funnellike calderas (*Yokoyama* [1963]; *Aramaki*, [1969]; K. Ono and S. Aramaki, oral communication, 1979). Such geometric uncertainties probably lead most commonly to overestimates of magma chamber area and underestimates of drawdown; this may be particularly pertinent to the apparently high area/volume ratios of the Japanese caldera-forming units plotted by *Smith* [1979; Figure 2]. On the basis of these considerations and a volume and subsidence-area compilation similar to Smith's, as well as intracaldera accumulations of welded tuff commonly in excess of 1500 m, I would conclude that total eruptive drawdown in caldera-producing eruptions can be virtually anywhere in the range between 200 and 2500 m. No mineral geobarometers appear to be precise enough to provide any better resolution.

The thermal gradients represented by the 70°–200°C ranges for the eruptions plotted in Figure 3 thus remain very uncertain. No correlation is apparent between ΔT and either eruption volume or calculated drawdown. Furthermore, complex eruptive sequences like that of the 1912 Valley of Ten Thousand Smokes eruption demonstrate that less-viscous mafic magma sometimes surges from deeper levels to penetrate and fountain through the silicic capping magma that is venting concurrently. Orderly drawdown of progressively deeper hotter magma may be more typical of large chambers, atop which a cauldron block can remain coherent and behave as a subsiding piston. Even a major ring structure eruption, however, can be complicated by considerable departures from uniform drawdown, as illustrated by the composition-volume proportions in successively emplaced lobes of the Bishop Tuff [*Hildreth*, 1979].

Hence, as far as quantitatively defining the temperature-depth relations in magma chambers, eruptions tell us little more than that the lowest-temperature magma usually escapes first. Details of the temperature increase with depth in a chamber are likely to be unique and fluctuating. The surface area and configuration of a silicic magma chamber certainly affect the rates of heat removal above as well as the interception of hot mafic magma in a root zone below. The geometry of these interfaces and the thickness and aspect ratio (columnar, equant, or slablike) of a chamber must influence the distribution and behavior of stagnant and convecting zones within it (see Figure 12) as well as the thermal response time of such zones to new magma injections. In addition, crustal stress regimes can affect the thermal gradients in magma

chambers not only by controlling the rate of basaltic injection below but by influencing the cooling efficiency of hydrothermal systems in the roof rocks.

Oxygen Fugacity

In Figure 3, the fugacity of oxygen rises with temperature in all systems, and it apparently does not reflect the roofward increase in H_2O concentration that probably characterizes these explosive magma bodies. In a general way, Fe-Ti oxide pairs from calcic systems of the continental margins yield f_{O_2} values that are one to two log units more oxidizing than those of the more alkali-rich systems of the interior. The Bishop Tuff is intermediate in each of these respects: crustal setting, alkalinity, and relative range in f_{O_2}. The Paintbrush and Timber Mountain tuffs (Figure 3) do not conform to this generalization, even though *Lipman*'s [1971] data have been recalculated in accordance with *Carmichael*'s [1967] procedures, for the sake of consistency with the other systems shown. The Cougar Point and Yellowstone tuffs are poor in hydrous phenocrysts and belong to bimodal systems thought to be dominated by basalt. The Paintbrush and Timber Mountain suites, on the other hand, contain biotite and amphibole; some units have sphene (Table 2); and quartz-latitic intermediates are far more conspicuous than basalts. Their higher range in f_{O_2} is consistent with a greater contribution from relatively oxidized crustal rocks in the genesis of these southern Nevada magmas, whereas the suites that plot close to QFM may have been generated predominantly by interaction of basaltic magma with deep-crustal granulites.

Several of the data sets of Figure 3 have slopes steeper than the experimental oxygen-buffer curves. This effect is apparently too great to be simply a pressure shift with depth in the magma chamber, but the relative drop in f_{O_2} is, in each case, associated with a roofward increase in SiO_2, though not necessarily in the total alkali content of the magma. The rather sharp trend of the Bishop Tuff data across NNO is duplicated by that of the few biotite-bearing rhyolites in the Taupo volcanic zone [*Ewart et al.*, 1975]. Perhaps the roofward decreases in f_{O_2} (relative to the buffer curves) principally reflect a gradient in the structure of the silicate melt imposed by the gradients in temperature and composition.

Lauer [1977] showed that the following are all mutually interrelated variables: (1) temperature; (2) oxygen fugacity; (3) redox ratios of such ions as Eu^{2+}/Eu^{3+} and Fe^{2+}/Fe^{3+} in the melt; (4) the ratio of network-forming cations to oxygen; and (5) a complex parameter that expresses the effects of network-modifying cations upon the activity of free oxide ions (O^{2-}) in the melt. Of these, only T is in any sense externally imposed upon a magma chamber. Each of the compositional variables is intrinsic to the magma, and it seems reasonable that f_{O_2} is as well. The compositional controls on redox equilibria in silicate melts are complex and have been the subject of much recent experimental investigation [*Lauer*, 1977; *Lauer and Morris*, 1977; *Mysen et al.*, 1980*a*; *Sack et al.*, 1980]. The major-element gradients in all of these magmas would alone produce increased roofward polymerization and probably a roofward decrease in the activity of O^{2-} in the melt. However, the additional complication of volatile gradients of unknown magnitude and structural effect on the magmas renders interpretation of the f_{O_2} trends of Figure 3 very uncertain, in terms of melt composition.

External control of f_{O_2} by wall rocks or by a vapor phase is very unlikely in a large system, and internal imposition of f_{O_2} on a magma by its phenocryst assemblage seems equally unlikely, especially in phenocryst-poor magmas. Most of the units plotted in Figure 3 exhibited a change in phenocryst assemblage with depth in the chamber (Table 2) without any change in f_{O_2} trend. On the other hand, collapse of the Yellowstone caldera somehow produced in the immediate post-caldera lavas an increase in f_{O_2} of about one log unit relative to the trend of the caldera-forming Lava Creek Tuff [*Hildreth et al.*, 1980]; this increase can only have resulted from some abrupt change in bulk composition of the magma. Oxygen fugacity and phenocryst assemblage are probably both determined by the structural state of the melt, which is in turn controlled by the thermal and compositional gradients of the magma chamber. Perhaps a melt structural gradient also affects the distribution of Eu and other altervalent cations in zoned magmas (Figure 8), in part through its effect upon redox equilibria but also by means of a gradient in the availability of appropriate sites in the liquid (see Figure 14).

ISOTOPIC GRADIENTS

Few efforts have been made to characterize the isotopic gradients in magma chambers, in part because detailed chemical and stratigraphic knowledge is necessary to interpret them but also because of the widespread assumption that magma bodies should be isotopically homogeneous. Nevertheless, large age-corrected differences in $^{87}Sr/^{86}Sr$ ratio within voluminous ask flow sheets have been recognized [e.g., *Noble and Hedge*, 1970; *Stuckless and O'Neil*, 1973], and they clearly indicate isotopic zonation of the parent magma chambers. Successive eruptions from such chambers could be isotopically different. Figure 4 shows that for the Bishop Tuff such differences indeed reflect an isotopic gradient in the upper part of the chamber. The Sr data (W. Hildreth, unpublished data, 1978) represent analyses of sanidine separates that ranged in Sr content from ~20 to ~220 ppm, whereas corresponding whole-rock values ranged from ~10 to ~110 ppm. The data for the Bishop Tuff are plotted against the equilibration temperature of coexisting Fe-Ti oxides that serves both as an indicator of preeruptive relative proximity to the chamber boundary and as an eruption progress parameter [*Hildreth*, 1979]. Sr-isotopic gradients appear to be common, possibly ubiquitous, in the magmas that produce large caldera-forming eruptions in continental interiors, but more work needs to be done to define patterns of isotopic variability within units and to relate them to crustal age, thickness, and lithology and to volume and longevity of magmatic systems. At one extreme, the 15 km^3 of magma erupted at Novarupta in 1912 is isotopically uniform at 0.7036 [*Hildreth and Grunder*, 1980].

A magmatic gradient in the isotopic composition of oxygen has not been demonstrated previously in the products of a single eruption, although it is implicit in the observations of *Lipman and Friedman* [1975]. Figure 5, however, shows that the Yellowstone magma chamber was characterized by a modest gradient in $^{18}O/^{16}O$ at the time of the caldera-producing eruption of the 1000-km^3 Lava Creek Tuff [*Christiansen and Blank*, 1972; *Hildreth et al.*, 1980]. In the Long Valley magma chamber, at the time of eruption of the Bishop Tuff [*Hildreth*, 1979], however, any bulk $^{18}O/^{16}O$ gradient was too small to be resolved separately from the changes inherent in the temperature-dependent fractionations among coexisting phenocrysts (W. Hildreth, unpublished data, 1978). Whole-rock samples of pyroclastic rocks are generally unsuitable for measuring magmatic ^{18}O values because of oxygen-isotopic

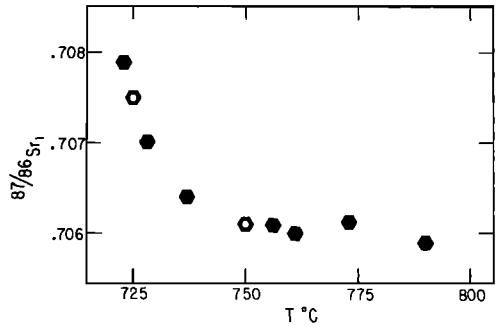

Fig. 4. Initial $^{87}Sr/^{86}Sr$ ratios of sanidine from the Bishop Tuff, plotted against Fe-Ti oxide equilibration temperatures of the same samples. Open symbols are data from *Noble and Hedge* [1970] with temperatures estimated (± 5°C) from the reported stratigraphic position. Closed symbols are author's unpublished data. Age corrections were made for 0.7 m.y. and amount to ~0.0003 in the roof-zone samples with lowest Sr; Rb/Sr in the sanidines ranges up to ~5. The magma that erupted with a ratio greater than 0.7061 exceeded 150 km^3 in volume.

fractionations that depend upon low-temperature crystallization of the groundmass in the presence of a vapor and upon secular hydration of volcanic glass.

The existence of isotopic gradients, coupled with changes in isotopic ratios from successive eruptions of the same chamber, demonstrates large-scale transport in the liquid phase within the time limitations of caldera-producing eruptive cycles. A major magma body with Rb/Sr > 3 and with a lifetime of ~10^6 years could develop internal differences in $^{87}Sr/^{86}Sr$ on the order of 0.0001 by in situ decay of ^{87}Rb [e.g., *McCarthy and Cawthorn,* 1980], but like the stable-isotope gradients, most of the Sr shift must result from other mechanisms. Whatever the relative contributions of variable source-rock inheritance, assimilation, equilibrium or nonequilibrium fractionation of crystals, isotope fractionation, gain or loss of a fluid phase, or isotopic exchange with roof rocks or stope blocks,

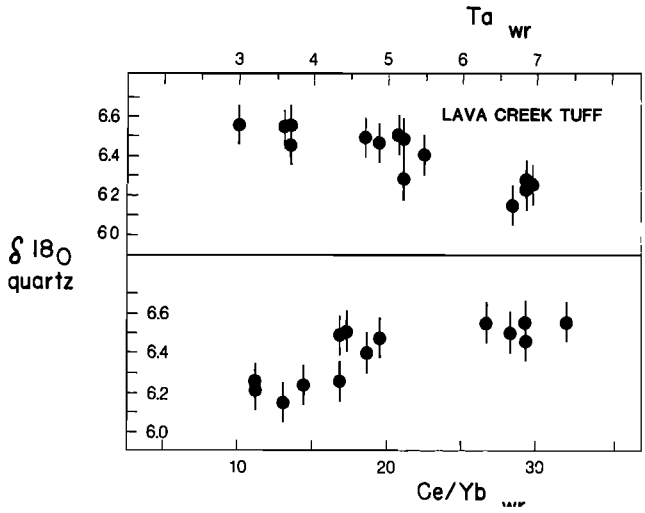

Fig. 5. Values of $\delta^{18}O_{smow}$ in quartz phenocrysts of the Lava Creek Tuff, plotted against whole-rock Ta contents and Ce/Yb ratios of the same samples. Both chemical parameters are good indicators of both eruption progress and compositional gradients in rhyolitic magma chambers (see Figures 7 and 9). Ta was highest and Ce/Yb lowest in the most evolved (roofward) magma. Hence, oxygen was isotopically lighter at the top of the magma chamber. All ^{18}O values were duplicated within 0.1 per mil or better; data from *Hildreth et al.* [1980] and W. Hildreth, unpublished data, 1980.

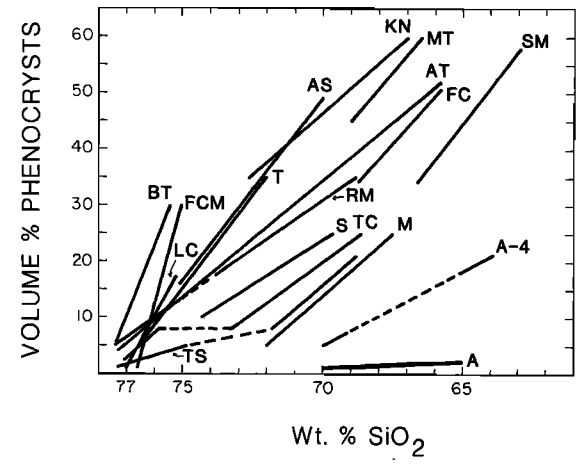

Fig. 6. Variation of phenocryst contents with bulk-rock SiO_2 for 17 selected eruptions. The quality and abundance of the data are very uneven, and the linear plots are simplified generalizations. The dashed lines indicate compositional gaps (cf. Figure 1). Abbreviations and sources of data: A, caldera-forming eruption of Aniakchak [*Miller and Smith,* 1977; *Smith,* 1979; andesitic part omitted, but see Figure 1]. FC, Fish Canyon Tuff [*Lipman,* 1975; *Steven and Lipman,* 1976]. FCM, Fish Creek Mountains Tuff [*McKee,* 1970]. KN, Kneeling Nun Tuff [*Elston et al.,* 1976]. MT, Monotony Tuff [*Ekren et al.,* 1971]. SM, Snowshoe Mountain Tuff [*Ratté and Steven,* 1967]. For the remaining units, see Table 2 for locations and data sources: AS, 'Apache Spring Tuff;' AT, Ammonia Tanks; A-4, Aso-4; BT, Bishop Tuff; LC, Lava Creek Tuff; M, climactic eruption of Mazama (andesitic part omitted, but see Figure 1); RM, Ranier Mesa; S, caldera-forming eruption of Shikotsu; T, Tshirege; TC, Tiva Canyon; TS, Topopah Spring. The Bishop, Tshirege, Mazama, Shikotsu, Aso-4, and Aniakchak data largely represent pumice lumps, but most of the remaining data are for welded tuff that may have suffered crystal-glass fractionation during emplacement. Phenocryst contents in excess of 40% should be regarded with appropriate caution. Silicic magma more than about half crystalline would commonly be too viscous to erupt [see *Shaw,* 1965, 1972, 1980; *Smith,* 1979].

the very existence of gradients implies a major role for diffusive transport.

These considerations indicate that it is dangerous to assume that the Sr- and O-isotopic variability of a granitic pluton, a volcano, or even a single eruptive unit is adequately represented by one or a few samples and that silicic magma may become isotopically distinct from some or all of the rocks that melted to produce it.

To date, isotopic gradients of Pb, Nd, S, and H within single eruptive units have not been reported, but, with very few exceptions [e.g., *Lipman et al.,* 1978], none have been looked for. Variation in the isotopic composition of Pb reported by *Lipman et al.* [1978] for lavas and tuffs from the same center, however, suggests the likelihood of finding such variability within a magma chamber and potentially within a single, large eruptive sheet. It should be no surprise if Pb, Nd, S, and H isotopic gradients were as common as those of Sr and O if the general model of lithospheric magmatism presented below is valid. Even Ar-isotopic gradients seem probable in large silicic magma chambers; they may complicate the dating of successive eruptions from such systems.

PHENOCRYST GRADIENTS AND PHASE BOUNDARIES

Table 2 gives the phenocryst contents of 20 eruptive units selected to illustrate some of the changes documented within the products of large eruptions. The data show that quartz and hydrous phases sometimes drop out of the assemblage as

an eruption taps successively deeper, higher-temperature parts of the magma. Conversely, Mg-rich olivine commonly joins the assemblage as an eruption taps downward from dacitic to andesitic magma; this olivine may sometimes be more appropriate to a basaltic liquid than to the immediate andesitic host [e.g., *Johnston,* 1978]. In certain alkalic rhyolites, as at Yellowstone (W. Hildreth, unpublished data, 1979), fayalite can be absent in the earliest ejecta, common throughout the dominant volume of an eruption, but give way to orthopyroxene at the deepest level tapped. Table 2 also shows that eight to twelve species of phenocrysts, typically euhedral, unzoned to poorly zoned, and in apparent mutual equilibrium, may coexist in the tops of silicic magma bodies, where fewer than 5% total crystals are present.

Figure 6 and Table 2 further show that total crystal contents of magma chambers usually increase markedly with depth. Because the first magma to escape is poorest in phenocrysts but must normally be closest to the main cooling surface (roof), the gradients in degree of crystallization suggest a progressive roofward depression of the liquidus by the upward enrichment of dissolved volatiles. In many voluminous magmas, neither accumulation of phenocrysts (as shown below) nor a gradient in liquidus temperature (due to the bulk-compositional gradient) is likely to account for the increase in crystallinity with depth in the erupting chamber. For example, during eruption of the Bishop Tuff, the total phenocryst content of the magma progressively changed from 5% to 30% (Figure 6), while the magma temperature increased by 70°C (Figure 3), but the bulk SiO_2 content decreased by only 2% (Figure 1), and that of the liquid by even less. The ubiquity of such relationships (Figure 6) underlines the fallacy in assuming that a magma body is always most crystal-rich at its cooling surface. Whether or not a pluton ultimately solidifies from its walls inward, it seems clear that crystallization is seldom a simple uninterrupted process. Not only does the degree of crystallinity usually decrease toward the cooling surfaces of chambers that produce large pyroclastic eruptions (Figure 6) but wide fluctuations in phenocryst content have been documented for lavas of similar composition that were sequentially erupted from certain large magma chambers [e.g., *Mahood,* this issue; *Bailey et al.* 1976]. Waxing and waning of phenocryst contents probably reflects the combined thermal effects of a variable rate of addition of mafic magma to the roots of the system and fluctuations in the cooling efficiency of superjacent hydrothermal regimes. The additional role of roofward enrichment of volatile components in depressing liquidi is addressed in following sections.

In some large eruptions the initially erupted magma is nearly or truly aphyric [e.g., *Mahood,* 1980*a*, 1981*a*]; in others a phenocryst-poor initial volume is followed by an abrupt transition to phenocryst-rich magma [e.g., *Noble,* 1970; *Byers et al.,* 1976; *Hildreth and Grunder,* 1980]. Such patterns suggest the existence of a volatile-rich boundary layer, tens to hundreds of meters thick, capping a dominant magmatic volume that is considerably richer in crystals. Eruptive sheets that show smooth changes in phenocryst content would seem to reflect smoother gradients in temperature and volatile distribution within the parent magma body.

Neither Table 2 nor Figure 6 reveal the progressive changes in the proportions and compositions of phenocrysts exhibited by virtually all these eruptive units. During the course of a large eruption, it is especially common for plagioclase to increase at the expense of quartz and sanidine, for the percentages of ferromagnesian silicates and oxides to increase strongly, and for the relative proportions of most species to change. The compositions of most or all phases normally change with depth in a chamber, consistent with the gradients in *T*, *P*, volatiles, and bulk composition [e.g., *Hildreth,* 1979]. In some major eruptive units these changes can be extreme; for example, in the climactic eruptive sequences at both the Yellowstone and Valles calderas the clinopyroxenes shift progressively from about $Ca_{40}Mg_7$ (Fe + Mn)$_{51-52}$ in the first magma erupted to Ca_{39} Mg_{35} (Fe + Mn)$_{23-25}$ at the deepest levels tapped (*Warshaw and Smith* [1980]; W. Hildreth unpublished data, 1980). In both magmas the ranges in composition of the feldspars, fayalite, and orthopyroxene were correspondingly extensive.

GRADIENTS IN VOLATILE COMPONENTS

Several lines of evidence suggest roofward increases in the concentrations of volatile components in silicic magma chambers.:

1. Preeruptive enrichment of volatile components toward the cooling surface appears to be the most plausible explanation of the direct relation between temperature and phenocryst content in the products of most major eruptions (Figure 6), especially for the high-silica sheets, where glass compositions generally change by no more than 1% in SiO_2 and bulk gradients in major-element composition are modest (Figure 1; Table 1). In a few sheets, sufficient work has been accomplished on glass and phenocryst compositions to exclude crystal accumulation as a complicating factor [*Hildreth,* 1977, 1979; *Smith,* 1979; *Mahood,* 1981*a*].

2. Roofward enrichments of F and Cl can be verified directly by measurement of the compositions of quenched ejecta and glass inclusions in their phenocrysts [*Smith,* 1979; *Hildreth,* 1979; *Johnston,* 1978].

3. For the Bishop Tuff, the existence of a preeruptive gradient in H_2O concentration could be demonstrated by calculating annite-sanidine-magnetite equilibria in a large number of samples in conjunction with T-f_{O_2} data from coexisting Fe-Ti oxides and the relation between f_{H_2O} and X_{H_2O} given by *Carmichael et al.* [1977]. Uncertainties in the free energy of formation of annite, activity-composition relations of the phases involved, and specific assumptions upon which the calculations were based have been treated in *Hildreth* [1977]. Whatever the uncertainties in the calculated water concentrations in the magma (2.8–4.9% by weight, increasing roofward), the existence of a gradient appears to be well established [see *Hildreth,* 1977, pp. 128–141].

4. The hydrous silicates, allanite and hornblende, are present in the early ejecta of some eruptions, but they disappear as deeper levels are tapped (Table 2), in spite of downward enrichment of Ca, Al, Fe, Mg, Ti, and LREE (Figure 7).

5. Large silicic eruptive sequences commonly exhibit progressive evolution from a towering Plinian column through voluminous pyroclastic flows to late pulsatory emplacement of smaller pyroclastic flows and finally to lava flows and domes. Although the kinetics of exsolution, magmatic viscosity gradients, and the behavior of the roof block complicate the interpretation of any such sequence, the prevalence of this pattern (over several orders of magnitude of eruptive volume) appears to demand a volatile-concentration gradient in each parent chamber.

Kennedy [1955] pointed out that dissolved magmatic water will tend to redistribute itself in a magma chamber so that its

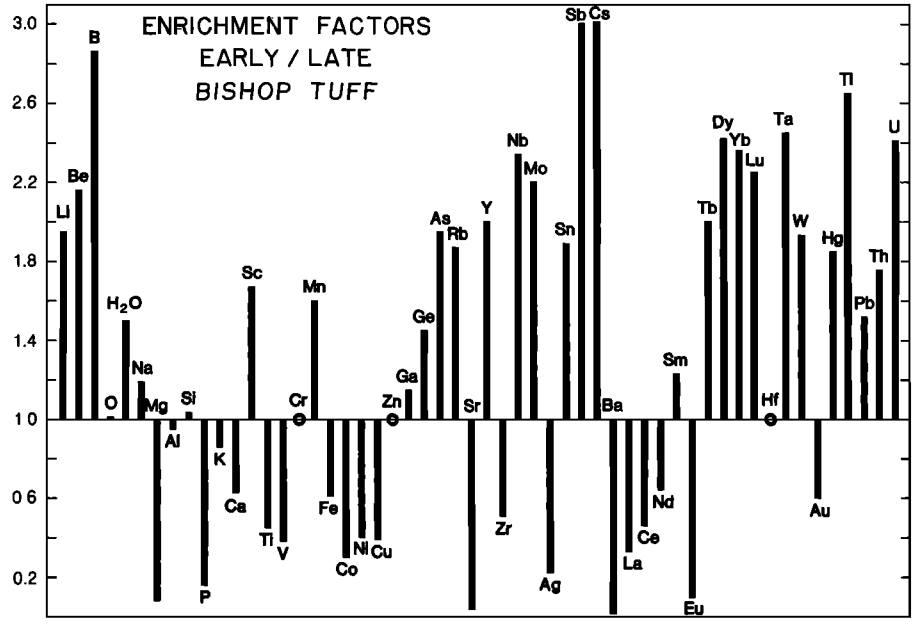

Fig. 7. Enrichment factors for 53 elements in the Bishop Tuff. Arranged by atomic number, the factors are simply concentrations in the earliest ejecta divided by those in ejecta at the end of the eruption. Because only an unknown fraction of the zoned chamber was tapped, the factors are a minimum measure of the zonation present at the time of eruption. F and Cl were both enriched roofward two- to threefold (Table 1), but the data at hand are too scattered (owing to syneruptive or subsequent losses) to present meaningful enrichment factors. The H_2O estimate is from *Hildreth* [1977]. Pt is <2 ppb, and Rh and Pd each <0.7 ppb throughout the Bishop Tuff. The nonenrichment of Zn has been demonstrated by both AAS and INAA. Most of the data are tabulated in *Hildreth* [1977, 1979]; some new data are unpublished.

chemical potential is everywhere equalized, thereby promoting enrichment of water toward the lower-*T* and -*P* roof zone. The arguments and data (Figures 3, 6, 7, and 12) presented here fully support that view. Because the deduced volatile gradients characterize magmas that represent a wide range in bulk composition and in species of phenocrysts (from fayalite rhyolites to pyroxene andesites), however, it seems unlikely that preeruptive saturation in H_2O is a common feature. Additionally, without the presence of an aqueous vapor phase, a halogen-bearing vapor is exceedingly unlikely, in view of the high solubilities of F and Cl in silicate melts [*Burnham, 1979a, b; Wyllie,* 1979] and the generally low-to-modest halogen contents of the quenched ejecta of voluminous eruptions. Hence, diffusive transport is thought to be the primary mechanism by which the volatile gradients are established [*Shaw,* 1974; *Hildreth,* 1979]. Ascent of bubbles in the aftermath of eruptive leaks cannot be excluded as a transient mechanism, nor can transport of H_2O and other components by CO_2-rich bubbles that would tend to rise through a CO_2-saturated silicic magma [*Holloway,* 1976] after release from crystallizing basalt emplaced into the root zone beneath the silicic part of a magmatic system (Figure 12). The relative importance of diffusive and vapor-phase transport will be taken up again below after discussion of the differentiation of silicic magmas in a broader context.

Liquid-State Differentiation of Rhyolitic Magma

Intensive study of the Bishop Tuff [*Hildreth,* 1976, 1977, 1979] led to the conclusion that the compositional zonation of high-silica rhyolitic magma bodies takes place in the silicate liquid itself, largely independent of the effects of crystal-liquid equilibria. This conclusion has been confirmed by new and ongoing work on several systems: the La Primavera complex, Jalisco [*Mahood,* 1979; this issue]; the Bandelier Tuff, New Mexico [*Smith,* 1979]; the Yellowstone system (*Hildreth et al.* [1980]; W. Hildreth, unpublished data, 1980); the rhyolites of the Coso Range [*Bacon et al.,* this issue]; rhyolites of western Utah [*Crecraft et al.,* this issue]; and even some high-silica plutonic rocks [*Ludington et al.,* 1979; *Miller and Mittlefehldt,* 1979]. The chemical patterns in all these systems are strikingly similar (but not identical) to those of the Bishop Tuff.

Figure 7 shows enrichment factors for 53 elements within the eruptive volume of the Bishop Tuff; additional and more precise analyses have improved the data base over previous presentations. Attention is directed to the following features: (1) Major-element gradients were modest. Ca, Ti and Fe increased about twofold during the course of the eruption, whereas the changes in Al, Si, Na, and K were considerably smaller. Silica content changed by less than 2.5 wt.% and alumina by less than 1 wt. %. (2) Several elements especially likely to form complex ions, Nb, Ta, As, Sb, Mo, W, Th, and U, were strongly enriched roofward. (3) Zr was concentrated downward, Y strongly upward, and Hf was about the same at all levels. (4) Relative to the deepest level tapped, Mg, P, Sr, Ba, and Eu were depleted in the roof zone by about an order of magnitude or more. (5) Na was enriched upward along with Li, Rb, Cs, Tl, and Pb, all being antithetic to K. (6) Among the metals of the first transition series, Sc and Mn were concentrated upward; Ti, V, Fe, Co, Ni, and Cu downward; and Cr and Zn remained about constant at all levels. All 10 elements, however, were partitioned strongly into ferromagnesian phenocrysts relative to the coexisting liquid. (7) Enrichment factors for the trivalent REE increased systematically from La to Dy, with a crossover (Figure 7) from downward to roofward enrichment between Nd and Sm. The falloff of Yb and Lu is real and appears to be characteristic of high-silica systems. (8) Eu deficiency (relative to other REE) characterized all bulk samples, glass, and every phenocryst

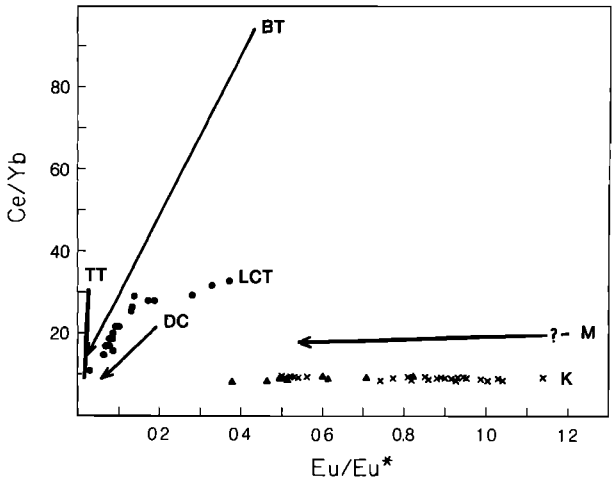

Fig. 8. Plot of Eu anomalies (Eu/Eu*) against the steepness of the REE pattern (Ce/Yb) for several zoned eruptions. The data contrast apparent Eu control by feldspar-liquid fractionation in eruptive units K and M with control by liquid-state diffusion in four rhyolitic units. K, the 1912 eruption in the Valley of Ten Thousand Smokes, Alaska; triangles for glasses, crosses for bulk pumice samples (W. Hildreth, unpublished data, 1977). M, main trend for the climactic eruption of Mt. Mazama (Crater Lake, Oregon), defined by 10 bulk samples and 10 glasses [*Ritchey*, 1979] and W. Hildreth, unpublished data, 1977). TT, Tala Tuff, Jalisco, including both bulk and glass samples [*Mahood*, 1980, and this volume]. BT, trend of the Bishop Tuff, California, defined by 43 whole-rock and 18 glass samples [*Hildreth*, 1977]. DC, tuff of Devine Canyon, Oregon [*Greene*, 1973]; REE data (W. Hildreth, unpublished data, 1980) are at present available for only four bulk samples, thought to embrace most of the compositional range. Dots are preliminary whole-rock data (W. Hildreth and R. L. Christiansen, unpublished data, 1980) for the Lava Creek Tuff, Yellowstone; the data show a transition from the diffusion-controlled mode of fractionation to feldspar control, in this case probably in part by feldspar-glass fractionation during the eruption. The other data shown are largely for pumice blocks and exhibit no such effects. Arrowheads give direction of SiO_2 enrichment. Query suggests that some high-Eu samples among the Mazama data may be crystal cumulates.

species except the feldspars. The magnitude of the negative Eu anomaly diminished greatly with increasing Ce/Yb (Figure 8) and with depth in the chamber for all these phases. Reflecting the extreme roof zone Eu depletion, the normally positive Eu anomaly in the feldspars disappeared in the lowest-temperature samples [*Hildreth*, 1977]. (9) H_2O concentration is thought to have increased roofward from <3 to >4 wt.% [*Hildreth*, 1977]. F and Cl were probably both enriched two- to threefold roofward in modest concentraions, but present data are scattered, owing to postmagmatic losses.

The compositional gradients can be defined by the glass phase alone, as illustrated by Figure 9. Mineral and glass analyses indicate that virtually all elements were predominantly resident in the liquid fraction, which constituted 75% to 95% of the magma at the time of eruption. Feldspars, zircon and ferromagnesian phenocrysts, respectively, could conceivably have accounted for 30%–50% of the Ba, Zr, and some first-transition-series metals at the deepest level tapped. Nevertheless, for all elements the bulk and liquid enrichment factors are similar.

The above patterns appear to be typical of compositional zonation in high-silica systems, but there are several variations on the theme: (1) Sc and Mn exhibit variable behavior from one system to another. The differences remain poorly understood and experimentally untested, but small amounts of pyroxene, oxide, or amphibole accumulation could reverse the roofward enrichment gradients of Sc and Mn (Figure 7). Their upward mobility in some systems may reflect straightforward thermodiffusion unperturbed by crystal settling, or it may be related to hydroxyl or carbonate complexing. Rarely is either Sc or Mn markedly enriched in a halogen-rich system. (2) Zn, Zr, Hf, and LREE are usually concentrated roofward in peralkaline, halogen-rich magmatic systems, in contrast to their behavior in many subalkaline magma chambers (as in Figure 7). The upward enrichment of Fe, Zn, Mo, W, Zr, Hf, Ta, Nb, Y, and all the trivalent REE is particularly strong in Cl-rich magmas. On the other hand, systems in which F is the dominant halogen exhibit more pronounced enrichment of Li, Na, Rb, Cs, Tl, Th, U, Sn, and Be, and their REE patterns usually have the crossover shown in Figure 7. Because both F and Cl are commonly enriched roofward in alkalic to peralkalic rhyolites, the two enrichment groups frequently overlap. Examples of Cl-dominant and F-dominant behavior are the silicic systems of Pantelleria [*Villari*, 1974] and of west-central Utah [*Christiansen et al.*, 1980], respectively. (3) In principle, enrichment factors should be greater in more alkalic systems (Figure 2), in more voluminous chambers where the repose time (Table 3) between major eruptive disturbances permits protracted chemical transport, and of course, in eruptive units characterized by greater drawdown. For individual elements and groups of elements (as above) both relative and absolute enrichments must be influenced by the magnitude of the thermal gradient; the concentrations of

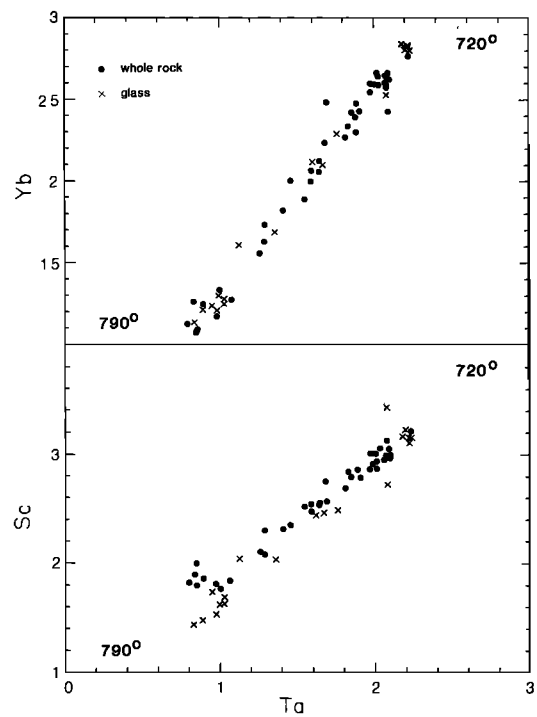

Fig. 9. Yb and Sc contents (in ppm) plotted against Ta contents in 43 bulk and 18 glass samples of the Bishop Tuff [*Hildreth*, 1977, 1979]. Fe-Ti-oxide quench temperatures are given for extremes of the eruptive sequence (see Figure 3). All three elements were enriched roofward, inconsistent with crystal fractionation. The near-identity of the whole-rock and glass ranges demonstrate that the compositional gradients were present in the liquid and were largely independent of phenocryst control. An exception may be the modest bulk enrichment of Sc relative to the glass at the deepest level tapped, possibly attributable to slight accumulation of pyroxene.

H_2O, F, Cl, CO_2, and possibly S; and the ratios and fluxes of these volatile components. Complications could be introduced by modest eruptive leaks that permitted transient exsolution of a roofward-concentrating vapor phase or by major injections of mafic magma that influenced either the convective regime or the CO_2 flux in the overlying silicic part of the system.

The unimportance of crystal settling. The Bishop Tuff is sufficiently extensive, glassy, and well preserved that detailed study permitted conclusive rejection of crystal fractionation as a significant mechanism in establishing its chemical variability [*Hildreth,* 1976, 1979]. Many of the lines of evidence summarized below are pertinent to other zoned rhyolitic systems, but it should not be concluded that crystal fractionation is never a recognizable component in the differentiation of rhyolites. In phenocryst-rich silicic magmas, such a component is to be expected, and certainly the separation of high-silica liquids from less-silicic progenitors is likely to reflect crystal-liquid fractionation.

Eruptive units of the Long Valley system during the 1.2-m.y. interval prior to the caldera-forming eruption of the Bishop Tuff were exclusively high-silica rhyolites that were both voluminous and virtually aphyric [*Bailey et al.,* 1976]. Liquid-state processes were apparently able to proceed in the crystal-poor upper part of a large magma chamber for a long time without the superimposed complication of crystal fractionation. When the hundreds of cubic kilometers of magma later erupted as the Bishop Tuff did begin to crystallize, the phenocryst compositions were controlled by the bulk compositional, isotopic, thermal, volatile, and resulting liquid-structural gradients already well established in the liquid itself. Either the time interval between phenocryst precipitation and subsequent eruption was short enough or the yield strength of the magma was great enough that the crystals were unable to fractionate sufficiently to disturb the simplicity of the precrystallization zonation.

Several lines of evidence indicate that the compositional zonation within the Long Valley magma chamber did not develop by settling of the observed, or any other, phenocrysts [*Hildreth,* 1979]:

1. Zircon, apatite, titanomagnetite, and ilmenite, each dense, unzoned, compositionally homogeneous within each sample, and early in the crystallization sequence, all display systematic compositional changes throughout the eruptive sequence. Within any given sample, crystals of each species are essentially identical in composition whether they occur as discrete grains or as inclusions sealed inside a variety of host crystals. Different grain sizes and host crystals require a range of potential settling velocities that would soon destroy their compositional uniformity at each level. This constraint can be tested for any zoned eruptive unit by means of systematic mineral separations and microprobe analysis tied to stratigraphic and bulk-chemical indices of the eruptive sequence.

2. Near the midpoint of the Bishop Tuff sequence, augite, hypersthene, and pyrrhotite made an abrupt co-appearance; they coexist in every sample that had an Fe-Ti-oxide temperature >737°C. A sharp interface, coinciding with the 737° isotherm in the chamber and common to three different phases having distinct sizes and densities, cannot long have been maintained if the crystals indeed had time and ability to settle, especially since the early-formed pyrrhotite occurs as inclusions in at least six other phases. The data compiled in Table 2 indicate that the crossing of phase boundaries is a common feature of voluminous eruptions. Because such boundaries apparently reflect isotherms and isopleths in magma chambers, careful work can place limits on the extent of crystal settling.

3. Allanite, invariably euhedral, unresorbed, and of similar composition everywhere, occurs in all geographic units of the Bishop Tuff and in every sample that had a temperature lower than ~763°C. Its distribution in the roof zone of the magma chamber thus appears to have been laterally homogeneous and its downward disappearance abrupt. The total absence of allanite beneath a sharp interface at the 763° isotherm signifies that, despite its high density (~4.0), allanite did not appreciably settle. In spite of its high content of LREE (>26 wt. % LRE oxides), allanite was confined to the roofward magma volume that was strongly depleted in LREE relative to deeper levels. Thus, allanite clearly did not influence REE fractionation. Its own roofward stabilization must have been controlled by temperature and/or volatile fugacities rather than by bulk composition, because concentration gradients of Ca, Al, Ti, Fe, and REE (Figure 7) were all antithetic to the observed allanite distribution. Similar relations characterized the preeruptive distribution of allanite in the Yellowstone magmas that erupted to form the Huckleberry Ridge and Lava Creek tuffs (see Table 2). If such relations are general in silicic magma chambers, precipitation of allanite must advance from a volatile-rich boundary layer into the main mass of a pluton only at a late stage in its solidification.

4. Settling of sanidine and plagioclase phenocrysts was also ruled out in the Bishop Tuff by their lack of zoning, their progressive compositional changes with position in the eruptive sequence, and by the fact that their Eu concentrations diminished roofward with that of the liquid. Early-erupted plagioclases lack any Eu anomaly whatsoever [*Hildreth,* 1977]. In addition, sanidines exhibit a systematic roofward increase in $(^{87}Sr/^{86}Sr)_i$ (Figure 4) that precludes significant settling or mixing. Not all voluminous eruptive units are likely to reveal such simple feldspar patterns; preliminary data suggest that the feldspar patterns of many rhyolitic units are similarly simple and systematic, but the feldspars of dacitic and quartz-latitic magmas commonly record a more complex history.

5. HREE, Y, Sc, and Mn were markedly enriched roofward (Figure 7 and 9; *Hildreth* [1979]) despite high concentrations in dense early-formed crystals (zircon, apatite, and pyroxenes). Antithetic (downward) enrichment of LREE, Zr, P, Ca, Mg, Ti, Fe, and Co rules out establishing such gradients by simple dilution (by settling quartz or feldspars) of deeper levels.

6. The lack of coherence between P and Y and between Zr and Hf (Figure 7) argues further against fractionation control by apatite or zircon. So do the insignificant mass fraction and Stokes Law settling rates of these tiny crystals.

7. With progressive eruption of the Bishop Tuff, Rb/Sr decreased about twentyfold, Mg/Fe and Eu/Eu* each increased about tenfold, and K/Rb and Zr/Hf both doubled [Figure 7; *Hildreth,* 1979]. Establishment of such gradients by crystal fractionation would require both the crystallization of unrealistic proportions of the magma and subtraction of phenocrysts incompatible with a high-silica rhyolite. Even if hornblende and andesine are added to the observed phenocrysts of the Bishop Tuff as potentially fractionating phases, mass-balance computations produce no combination capable of establishing even the major-element gradients let alone the trace-element patterns. The antithetic behavior of K and Na and of Fe and Mn are key obstacles, as are the extreme roof-

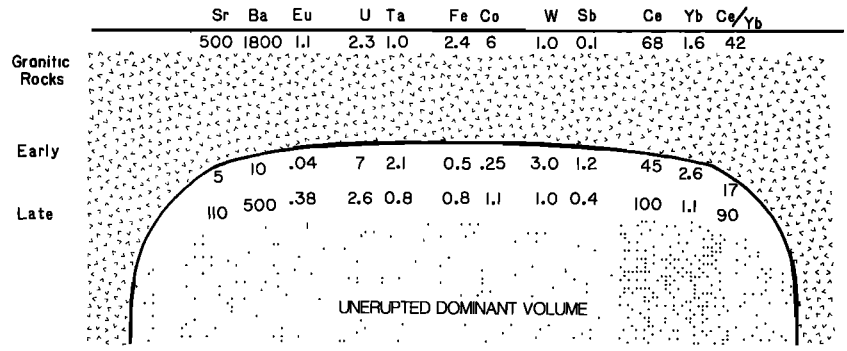

Fig. 10. Schematic portrayal of selected compositional contrasts between the zoned Bishop Tuff magma and some of its possible roof rocks. The values for the 'granitic rocks' are averages of analyses of Sierran plutonic rocks adjacent to Long Valley caldera [*Hildreth*, 1977; *Bateman et al.*, 1963]. Basement rocks cut by the caldera were ~70% Mesozoic granitoids and ~30% pregranitoid metasedimentary and metavolcanic rocks [*Rinehart and Ross*, 1957, 1964]. If the magma chamber were shallow, data for the exposed granitic rocks might approximate the composition of most of its roof rocks. If the actual roof rocks were more mafic and calcic, as seems likely, their contrast with the magma would be even greater. 'Early' and 'late' refer to the eruptive sequence of the Bishop Tuff, for which the compositional extremes are given. Many of the compositional gradients in the magma were antithetic to those expected to result from gross assimilation at the roof and walls. The many arguments that the magmatic gradients were not produced by partial melting of these (or any) roof rocks are given by *Hildreth* [1977, 1979] and are reviewed in the present text.

ward depletions of Mg, P, Sr, Ba, and Eu and enrichments of Cs and the highly charged cations.

If the phenocrysts did not settle within the erupted magma volume, neither could they have been the upper part of a postulated column of settling crystals continuously disappearing into an untapped magma reservoir below. The above and other lines of evidence are more fully discussed in *Hildreth* [1977, 1979]. In the light of accumulating evidence on other systems it now seems clear that the constraints against a significant role for crystal fractionation in the differentiation of the Bishop Tuff can be generalized to many other high-silica rhyolites.

Partial melting. Quantitative arguments that reject establishment of the compositional gradients in the Bishop Tuff magma by accretion of successive melt increments from a progressively depleted and/or heterogeneous source have already been elaborated [*Hildreth*, 1977, 1979]. Such arguments also apply to partial melting of roof and wall rocks. Although roof melting must take place to some extent, many of the observed gradients in the Bishop Tuff and other rhyolitic systems are antithetic to those expected if it were a major process (Figure 10).

The most compelling obstacles include the following:

1. Contents of Ba, Sr, and Eu were far too low in the topmost Bishop Tuff magma for that liquid to have been extracted as a partial melt of feldspar-bearing source rocks. Crystal/liquid partition coefficients of these (and other) elements were measured for most phenocryst species in several samples of the Bishop Tuff [*Hildreth*, 1977]. These data constrain the bulk distribution coefficient between virtually any postulated source (or roof) rock and the Bishop Tuff liquid to have been no larger than 3 for Ba, Sr, or Eu. Values would have been smaller for any less silicic and/or higher-temperature liquid predecessor. Accordingly, roof melting or incremental accretion of melt from a deep source could have produced the low-Ba-Sr-Eu roofward liquid and the succeeding gradients in these elements only if the source rock itself were predominantly a leucogranite with <50 ppm each of Ba and Sr and <0.5 ppm Eu. This is geologically unreasonable, not only for the Bishop Tuff that erupted through a Cordilleran batholithic basement but for the many comparable rhyolitic eruptions that begin with the ejection of magma strongly depleted in Ba, Sr, and Eu (Figures 8 and 11).

2. The antithetic enrichment trends of LREE and HREE cannot be modeled by partial melting of any realistic roof or

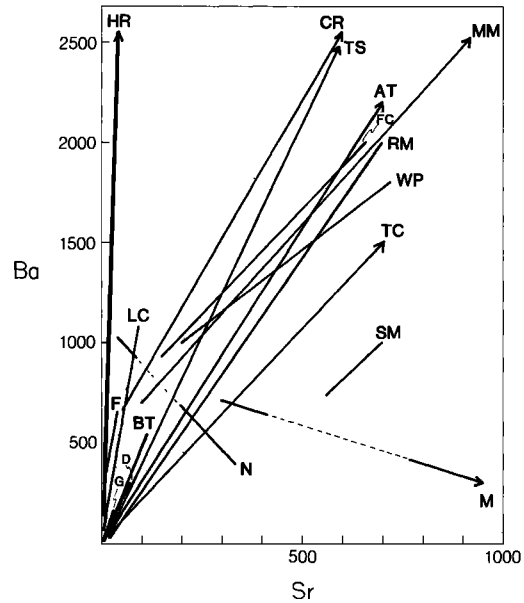

Fig. 11. Generalized plot of Ba vs. Sr contents (in ppm) of the ejecta from several large-zoned eruptions. All identifying symbols are at the low-SiO_2 end of the trend. Arrowheads indicate that the trends of reported data continue to compositions that were probably affected by crystal accumulation. Some values in excess of 1500 ppm Ba should be suspected of sanidine accumulation, but neither glass nor matrix data are available to verify this. Some lines are generalizations of limited data that do not require the continuity suggested. Dashed segments represent large compositional gaps in the Mazama and 1912 VTTS sequences (Figure 1). Symbols: AT, Ammonia Tanks; BT, Bishop Tuff; CR, Carpenter Ridge Tuff; D, Tuff of Devine Canyon; F, Fantale Tuff; FC, Fish Canyon Tuff; G, Grouse Canyon; HR, Huckleberry Ridge Tuff; LC, Lava Creek Tuff; M, climactic eruption of Mt. Mazama; MM, Mammoth Mountain Tuff; K, 1912 eruption at Novarupta; RM, Rainier Mesa; SM, Snowshoe Mountain Tuff; TC, Tiva Canyon; TS, Topopah Spring; WP, Wason Park. For locations and sources of data, see Figure 1 and/or Table 2, except for WP see *Lipman* [1975]. The Lava Creek Tuff trend includes immediately postcaldera lavas; for Ba-Sr limits of the tuff itself, see Table 1.

source rocks, irrespective of how one juggles the roles of allanite, sphene, apatite, zircon, and major phases during melting. Nevertheless, the REE-crossover pattern (Figure 7) has now been recognized in the products of several other ash flow eruptions, in granitic plutons, and in sequences of rhyolite domes.

3. The conflicting fractionation patterns among the elements of the first-transition series, Sc to Zn, cannot be explained by partial melting. Roofward enrichment of Sc and Mn (Figure 7), and in many systems, Zn, antithetic to gradients in the abundances of Ti, V, Fe, Co, Ni, and Cu, may be better explained by thermodiffusion and/or by volatile complexing. As all these elements are strongly concentrated into ferromagnesian phases relative to coexisting liquids ($D^{xtl/liq} \sim$ 10 to 100 in the Bishop Tuff) but are highly depleted in salic phases (generally $D^{xtl/liq} < 0.2$), control by crystal-liquid equilibria would require that they observe a common trend of enrichment or depletion in successive liquids. Hence, incremental accretion, roof melting, and, for that matter, crystallization at the roof and walls are inconsistent with the documented transition-metal gradients.

4. In the several zoned tuffs from which I have separated phenocrysts, the pumice has only trace contents (<1 ppm) of xenocrysts. If roof melting were a major process, one would anticipate that considerable amounts of refractory residue present in the magma would be erupted with it. Partially melted plutonic blocks ejected in large eruptions [e.g., *Ritchey,* 1979; *Eichelberger,* 1979] can usually be explained by short-term residence in the magma attendant to disruption of high-temperature roof rocks by the eruptive process itself. Systematic documentation of the xenocrysts contained by the pumice blocks of silicic eruptions would help to place limits on the extent of roof rock interaction with magmas. The scarcity of such material, particularly of exotic refractory oxide minerals and zircon, in pumiceous ejecta that I have studied leads me to think that assimilation of roof rocks above well-established magma chambers is not a continuous process. Perhaps high-contrast boundary layers normally insulate roof and wall rock from the magma, preventing much mechanical interaction except during eruption, diking, or rare insurgent events.

5. If roof melting were a general process that played a major role in zoning magma chambers, then most zoned eruptions would begin with high-silica minimum-melt magma. On the contrary, voluminous eruptions of exclusively high-temperature intermediate magma are fairly common, and sequences having high compositional contrast like the Askja and Katmai eruptions (Figure 1) are not so common.

6. Finally, if roof melting were important, $^{87}Sr/^{86}Sr$ ratios would be much higher than they are in the initial ejecta of many large eruptions. The Bishop Tuff had initial ratios that ranged from 0.7080 to 0.7059 (Figure 4), but it erupted through exposed basement rocks that had ratios of 0.711 to 0.715 [*Hurley et al.,* 1965; *Kistler and Peterman,* 1973]. The caldera-related magmas in the San Juan Mountains with initial ratios of 0.7050 to 0.7075 [*Lipman et al.,* 1978] and at Yellowstone, largely 0.708 to 0.712 [*Doe et al.,* this issue], passed through Precambrian crust in which Sr was far more radiogenic. In each area, geophysical evidence and the broad caldera geometry suggest a large shallow magma chamber. If chamber roofs were within several kilometers of the surface, as appears likely, the silicic magmas or their intermediate predecessors must have come into contact with highly radiogenic, comparatively Sr-rich, crystalline rocks of the upper crust without being strongly enriched in ^{87}Sr. Roof melting appears to be only a second-order effect that is usually overprinted by differentiation processes within the magma itself.

Subjacent mafic magma. Silicic-to-intermediate crustal magma chambers obstruct the passage of primitive melts from the mantle to the surface; growth of such chambers must in fact be a feedback response to this obstruction process. Many Cenozoic volcanic fields preserve evidence that records the failure of the basaltic magma, common enough around the periphery, to penetrate an active silicic focus. Particularly unequivocal and instructive examples are the fields at Yellowstone [*Christiansen and Blank,* 1972;], Long Valley [*Bailey et al.,* 1976], and the San Francisco Peaks [*Robinson,* 1913; *Moore and Wolfe,* 1976]. I do not suggest that basaltic magma directly intrudes the rhyolitic parts of magma chambers, except possibly in very small systems such as Askja (Figure 1). Rather, basalt lodges in what amounts to a lithospheric exchange column that ultimately produces the full range of intermediate and silicic magmas higher in the system by recurrent partial melting, mixing, and liquid, vapor, and crystal fractionation. The model is extensively discussed in a later section (Figures 12 and 15).

The observation that silicic foci intercept basalts has led some workers to the spurious idea that the zonation of crustal magma chambers is caused by direct mixing of rhyolitic and basaltic magmas. Direct encounters between rhyolitic and basaltic liquids certainly take place [e.g., *Bunsen,* 1851; *Wilcox,* 1944; *Sigurdsson and Sparks,* 1981], especially where pods or dikes of rhyolitic melt dominated by the basaltic flux appear more likely than a silicic body large enough to warrant the term 'chamber.' Commingling in such a system can produce a variety of disequilibrium textures and mineral assemblages in eruptive rocks [*Eichelberger,* 1978], and prolonged interaction at depth may lead to various intermediate hybrids [e.g., see *Schmincke,* 1969*a, b*], but basalt-rhyolite mixing certainly does not produce the compositional gradients characteristic of zoned silicic chambers. Gradients in Ba, LREE, Sc, Mn, and Zn would be opposite those in many zoned rhyolites (Figures 7 to 11), and the very low levels of V, Cr, Co, Ni, Cu, S, and Pt-group elements would surely be enhanced at deeper levels of the rhyolitic magmas.

It has previously been noted [*Hildreth,* 1979] that two-liquid partitioning data [*Watson,* 1976; *Ryerson and Hess,* 1978] appear to exclude equilibrium trace-element distribution between silicic and mafic melts (whether immiscibly separated or fortuitously conjoined) as a factor in producing the compositional gradients in rhyolites. The applicability of the isothermal partitioning data for Fe-rich synthetic liquids to natural systems can be questioned, but the very strong partitioning of Ta, Mn, and all REE into the more mafic melt and the relatively small preference of both Ba and Sr for the mafic liquid nevertheless seem to rule out any sort of immiscible relationship in the present context.

Although direct chemical impact of basalts upon the compositional zonation of silicic chambers can be ruled out as a generality, injection of basalt into a partially molten root zone that extends tens of kilometers downward beneath such chambers is nonetheless of fundamental importance. Not only might the flux of a volatile phase rich in CO_2, Cl, or S enhance the transport of mobile components, and the heat transfer influence the convective regime in high-level magma chambers, but basalt-fed root zones are probably the locus of generation of the voluminous andesitic-to-granodioritic magmas from

which many rhyolites ultimately separate. The concept of such root zones as long-lived lithospheric fractionation columns is further discussed below.

The thermogravitational effect and volatile complexing. Because crystal-liquid fractionation cannot account for the gradients present in rhyolitic magmas, I have reasoned previously that the chemical separations take place within the liquid phase itself, largely by diffusive processes but not excluding exchange with a transient vapor phase [*Hildreth,* 1976, 1977, 1979]. It was proposed by *Shaw et al.* [1976] that the thermogravitational effect [*Clusius and Dickel,* 1938; *Korsching and Wirtz,* 1939*a, b; Tyrrell,* 1961; *Schott,* 1973] plays a major transport role in establishing the chemical gradients within the zoned topmost parts of magma chambers. We argued that progressive growth of a high-silica roof zone is stabilized by a volatile-concentration gradient that may in part be generated by a water-rich boundary layer rising along the walls [*Shaw,* 1974; *Hildreth,* 1979, Figure 16]. The gravitational stability of the quasi-stagnant upper zone may be enhanced by other mechanisms of volatile transport, viz., by diffusive transfer from the convecting volume below, internal Soret diffusion, exchange with roof rocks, and, possibly, by the rise of CO_2-dominated vapor bubbles. Transport of trace metals, both by ionic thermodiffusion and as hydroxyl, halide, or carbonate complexes, is thus seen as part of a profound redistribution of components in those regions of the magma that have the strongest thermal gradients.

The steady state chemical distribution toward which a system might tend would be determined by its average composition, by the thermal and gravitational fields of the magma chamber itself, and by a feedback interaction between composition and site distribution in the structurally graded liquid (see Figures 13 and 14). Natural magmatic systems are unlikely to be closed, however, and the chemical evolution must be profoundly influenced by the fluctuating thermal evolution, by crystal-liquid fractionation, and recurrently, by injections of primitive magma into the root zone, with attendant augmentation of convective circulation and roofward volatile flux in the high-level chamber. The following discussion expands upon thermogravitational aspects of this model.

The Soret effect. Soret diffusion is the spontaneous growth of concentration gradients in solutions subjected to a gradient in temperature. First noted by *Ludwig* [1856] and investigated by *Soret* [1879, 1880], the effect is ubiquitous in gaseous and liquid solutions, including solutions of aqueous electrolytes, polymers, organic isomers, hydrocarbons, carbohydrate solutions, fatty acids, molten salts, and liquid metals [see *Grodzka and Facemire,* 1977, for a recent review]. Although few data have been obtained for liquids having diffusivities as small as those in magmas, very strong Soret gradients have been produced experimentally in liquid metals [*Ballay,* 1926; *Winter and Drickamer,* 1955; *Bhat and Swalin,* 1972; *Bhat et al.,* 1973] and their isotopes [*Lodding and Ott,* 1966], in molten salts [*Andreasson and Lunden,* 1970; *Schott and Costesèque,* 1978], and in silicate glass and olivine [*Schott and Costesèque,* 1978]. *Walker et al.* [1981], working with dry single-phase liquids of lunar and oceanic basaltic composition, have experimentally demonstrated Soret separations comparable in magnitude to the compositional changes produced by crystal fractionation over a 200°C cooling interval. At a temperature difference (ΔT) of ~250°C, liquids of intermediate composition have evolved by Soret diffusion alone in runs of only a few days duration. The main tendency has been for quasi-coherent separation of the Si-Al-Na-K network from potentially network-modifying species.

Isotopic fractionations have also been achieved in Soret experiments. Liquid metals of Li, K, Rb, and Ga have undergone isotopic separations of 1.5% to 4% in Soret cells at $\Delta T \sim 200°$ to 300°C within a few days [*Lodding and Ott,* 1966]. *Schott and Costesèque* [1978] have shown even larger fractionation of $^7Li/^6Li$ and $^{87}Rb/^{85}Rb$ in thermogravitationally circulating molten salts. In all cases, the light isotope diffusively concentrates toward the hot wall.

The steady state difference in concentration (ΔC) of any component demixing from an initially homogeneous concentration (C_0) is related to the temperature difference ΔT between the hot and cold walls of a container by

$$\Delta C/C_0 = \sigma \Delta T$$

where σ is called the Soret coefficient. For each component, this is defined (in $°C^{-1}$) by

$$\sigma = D'/D$$

TABLE 3. Recurrence Intervals and Eruptive Volumes of Some Multi-cyclic Centers

Caldera(s)	Recurrence Interval, m.y.	Magma Volumes Erupted, km^3	References
Yellowstone	0.7, 0.6, 0.45	2500, 280, 1000, 900	1, 2
Toledo-Valles	0.3	300, 300	3
Timber Mountain	~0.2	1200, 900	4, 5
Claim Canyon-Oasis Valley	~0.7	300, 1000	4, 5
Silent Canyon	<1.0	>60, 200	4, 6
Black Mountain	0.5 to 0.1 (each)	150, 150, 50, 20, 1	2
Platoro-Summitville	<0.7	>500, ~50, ~120	7, 8
La Garita-Bachelor	<1.1 (~0.5?)	>3000, ~1500	7, 8
San Luis	<0.3	<100, >500	8
Creede and predecessors	~0.3 (total)	<500, >100, >500	8
San Juan-Silverton	<1.0	>1000, <100	8
Aso (1, 2, 3, 4)	0.05 – 0.1	~25 (each sheet)	9
Aira (several sheets)	~0.005 – 0.01	~20, ~40 (largest)	10 – 13
Towada	~0.01	~20, 2	14, 15
Ceboruco	<0.001	~2, 1.4	16

(1) *Christiansen and Blank* [1972]; (2) *Christiansen* [1979]; (3) *Smith* [1979]; (4) *Byers et al.* [1976]; (5) *Christiansen et al.* [1977]; (6) *Noble et al.* [1968]; (7) *Lipman* [1975]; (8) *Steven and Lipman* [1976]; (9) *Ono et al.* [1977]; (10) *Ui* [1971]; (11) *Kigoshi et al.* [1972]; (12) *Yokoyama* [1974]; (13) *Aramaki and Ui* [1966*a, b*; 1976]; (14) *Chiba* [1966]; (15) *Aoki et al.* [1970]; (16) *Nelson* [1980].

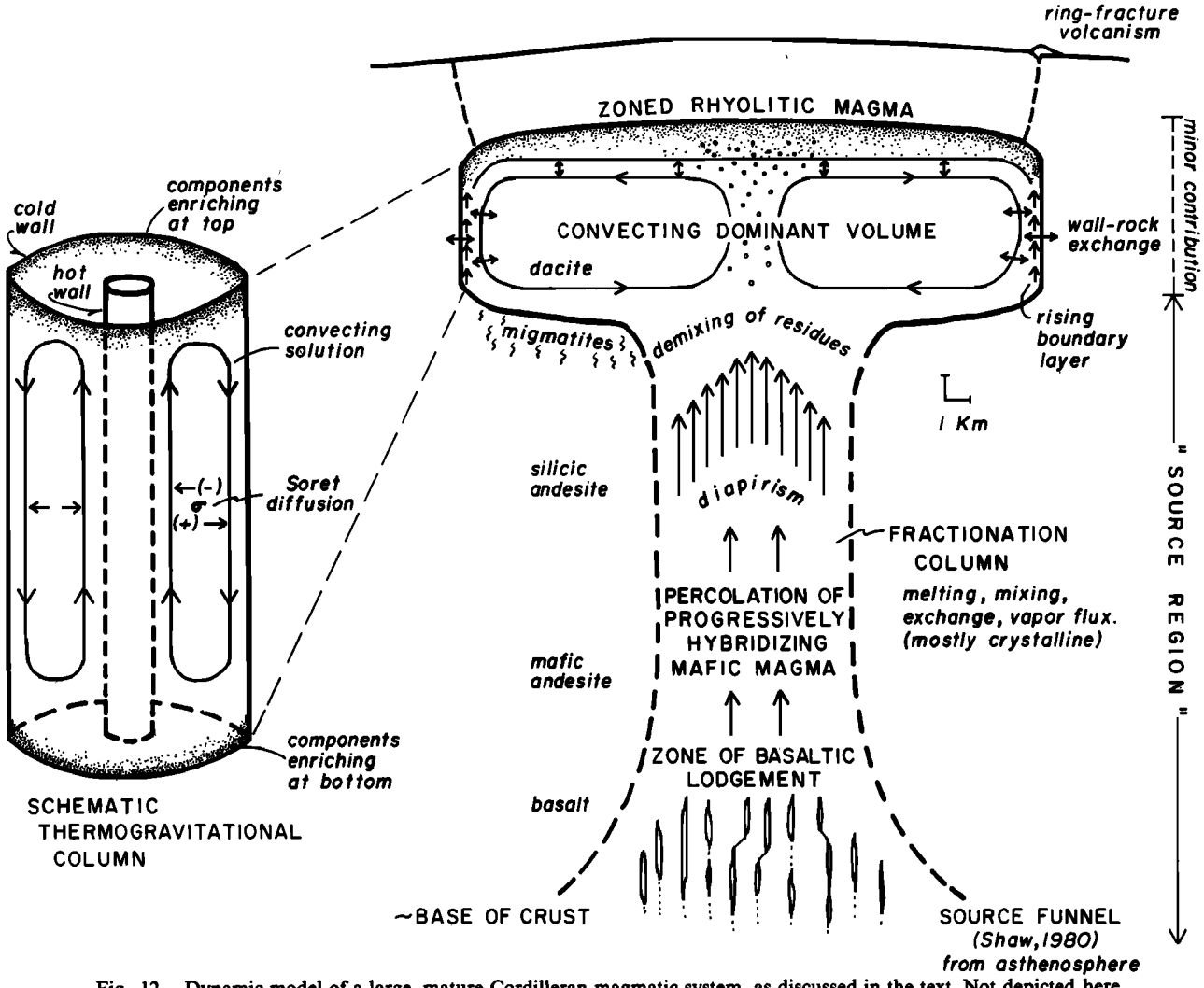

Fig. 12. Dynamic model of a large, mature Cordilleran magmatic system, as discussed in the text. Not depicted here are the earlier phases of intermediate-to-basaltic volcanism (Figure 15) that progressively heated the crust and culminated in large-scale crustal diapirism and upward segregation of liquid that produced the shallow silicic magma chamber. After becoming more than about half liquid, such a chamber must convect, thereby enhancing the fractionation role of Soret diffusion at convecting boundary layers (two-headed arrows), in partial analogy with the cascading principle of thermogravitational columns. Attention is directed to the rising boundary layer, which is thought to become enriched in species having positive Soret coefficients, particularly in volatile components and metals that form complexes with them. The quasi-stagnant roof-zone magma is stabilized by a volatile-concentration gradient; it progressively grows in volume at the expense of the better-mixed convecting magma, and it undergoes internal diffusive transport as well as continuous exchange with its surroundings. Bubbles depict the unknown contribution to the mass transport of CO_2-dominated vapor released by basaltic magma deep in the system. Stippling depicts enriched zones in the roof of a magma chamber and at both ends of a thermogravitational column, where experimental enrichments can be enormous (see text). The volumes and compositions of both mafic forerunners and intermediate to silicic plutons are thought to be determined by the basaltic flux from melting zones in the mantle and by the thickness, composition, and state of stress of the lithosphere [cf. *Shaw*, 1980]. These must be the first-order factors that control upward percolation rates of primitive magma, intrusion/extrusion ratios, and the depth distribution of mafic-magma emplacement in the lithosphere. These variables in turn must influence (1) the scale, degree, and rate of crustal heating and partial melting; (2) the degree to which the crustal response is dominated by diapirism or by extensional dike propagation; and (3) the integrated contact area and residence time available for reaction melting, hybridism, and vapor-crystal-liquid fractionation to modify the primitive magmas that intrude the crust. The complex and protracted interaction envisioned lasts longer than the eruptive history of any associated volcanic field, typically 10^6 to 10^7 years for a large system. The kind of silicic magma that might ultimately coalesce (or separate) into a large upper-crustal pluton would critically depend upon the thermal and stress-state history of the lithospheric 'fractionation column' beneath it. Upper-crustal influences should normally be small, but interaction with wall rocks of extreme (e.g., pelitic) composition could modify isotopic ratios, volatile fugacities, alkali/alumina ratios, and other compositional parameters in the upper parts of some systems. Note that the 'source' of the magma that ultimately forms any large high-level chamber consists of contributions from the mantle and from many levels of the crust, in unknown but variable proportions.

where D is its ordinary diffusivity in $cm^2\ s^{-1}$ and D' is its coefficient of liquid-state thermodiffusion in $cm^2\ s^{-1}\ °C^{-1}$. *Estèbe and Schott* [1971] and *Schott* [1973] showed experimentally that values of σ, hence potential degrees of enrichment, increase with both T and ΔT; differ strongly from one component to another; and can be either positive or negative in sign. If a component diffuses to the cold wall, the sign convention is usually that $\sigma > 0$. Measured values of σ are typically in

the range 10^{-1} to 10^{-3} °C^{-1} for a wide range of components and solutions [*Grodzka and Facemire,* 1977; *Schott and Costesèque,* 1978]. Hence, enormous enrichments are potentially attainable for $\Delta T \sim 100$°C (as in magmas; Figure 3) if remixing is suppressed and sufficient time is available.

Bowen [1921] suggested that ordinary chemical diffusivities in silicate magmas were too small to permit more than local effects by Soret diffusion. New information about diffusivities in magmas, the repose times of magma chambers (Table 3), and the thermogravitational effect in convecting liquid solutions demands a reopening of the whole question.

Thermogravitational fractionation. The ordinary diffusivity of H_2O itself in volatile-rich rhyolitic magma at 700° to 900°C lies between $10^{-6.5}$ and 10^{-8} cm^2 s^{-1} [*Shaw,* 1974]. *Watson* [1979] and *Jambon et al.* [1978] have recently shown that cation diffusivities in hydrous rhyolitic melts can be many orders of magnitude greater than the ranges summarized by *Hofmann* [1980] for dry melts. Even if chemical diffusivities (D) were as great as 10^{-7} cm^2 s^{-1}, characteristic transport distances (X) would be only $X = (Dt)^{1/2} \simeq 18$ m in 10^6 years, or ~5 m in 10^5 years, but ~2 cm in 1 year. Thus as *Shaw* [1974] pointed out, diffusive transport in static magma would not be an important mechanism of differentiation, but diffusion across convecting boundary layers could be exceedingly important in promoting chemical (and perhaps isotopic) separations. *Shaw* [1965, 1974] also showed that without a stabilizing volatile-concentration gradient, large silicic magma chambers less than about half crystallized must convect. It is toward the interfaces of the convecting central volume (Figure 12) with the cooler, more hydrous, magmas of the quasi-stagnant cap and the ascending boundary layers that the analogy with thermogravitational columns is directed.

In experimental and industrial thermogravitational columns, transverse Soret diffusion is combined with natural convective recycling of the liquid in the annular space between two concentric, usually vertical, cylinders (Figure 12). The intrinsic cascading promotes vertical concentration gradients, the components that diffuse toward the cold wall being preferentially swept toward the bottom. One of the many ways in which magma chambers are more complicated is that their walls may be neither smooth nor inert. The descending limb of the main thermal convection system might be displaced some unknown distance into the chamber, away from the wall. An ascending chemical boundary layer probably forms a lower-density counterflow (Figure 12) that rises slowly along the walls, abstracts volatiles and other diffusing components from the downgoing limb (and perhaps from the wall rocks as well), and helps to enrich the growing roof zone in such components [cf. *Shaw,* 1974, Figure 11; *Spera,* 1977]. Many granitoid plutons preserve multilayered vertical (or even overhanging) marginal zones that may indeed represent stagnant successors to such volatile-enriched boundary layers, which underwent protracted crystallization after convection ceased.

The theory of thermogravitational separation was presented by *Furry et al.* [1939], *de Groot* [1947], *Tyrrell* [1961], *Schott* [1973], and *Grodzka and Facemire* [1977]; aspects of design and phenomenology and various experimental results were summarized in the last three of these papers.

Vortices can produce remixing that counteracts the thermodiffusive demixing in such columns. Much effort has therefore been expended to design columns that eliminate nonlaminar flow, stabilize the low-density liquid at the top, and permit the optimal adjustment of vertical flow rate to the rate of transverse Soret diffusion for the species of interest [*Bott and Romero,* 1969; *Bott,* 1970; *Pinheiro and Bott,* 1976, 1977]. The high viscosity and presumably laminar convection in silicate magma chambers, the extended lifetimes of these naturally cascading systems, and the large stably graded reservoirs at the tops of zoned magma chambers all appear to be favorable for thermogravitational separations.

No experiments have yet been conducted using high-viscosity silicate melts in thermogravitational columns, but certain results with other liquids are sufficiently relevant to mention here, with the explicit caveat that simple extrapolation to magmas could be misleading. For example, large complex molecules commonly exhibit large thermogravitational separations that apparently depend on molecular size and shape as well as on mass [*Grodzka and Facemire,* 1977; *Gaeta and Cursio,* 1969]. In hydrocarbon mixtures, simple molecules tend to concentrate at the top of the column, whereas heavier or more compact polycyclic ones go to the cold wall and to the bottom of the column [*Tyrrell,* 1961, p. 248 ff.]. In many polymer solutions the degree of fractionation increases with the molecular weight of the polymer fractions [*Tyrrell,* 1961, pp. 223, 257 ff.], and really extreme separations take place between polymers and their low-molecular-weight solvents. If the solvent-solute distinction is largely arbitrary, can we find here an analogy to the roofward concentration of volatiles in highly polymerized silicate melts? Does the kind of extreme trace-element separation portrayed in Figure 7 develop most strongly in rhyolite because of the tendency for complexing with low-molecular-weight volatile components that are fractionated roofward in this highly polymerized solution? *Tyrrell* [1961] noted that one difficulty sometimes encountered in the industrial separation of polymer solutions by thermogravitational methods is a tendency for the low-molecular-weight fluid component to show a greater fractionation from the dissolved polymers than do the polymer species from each other.

Schott [1973] determined experimentally that for a given column design, the maximum separation attainable for a given component is an exponentially increasing function of both ΔT and σ; however, separation efficiency also depends upon column geometry, flow rate and path, and the viscosity, density, and bulk composition of the solution. In aqueous solutions the dependence on bulk composition is only modest, but temperature can be critical, since as much as a fivefold increase in the Soret coefficients of several aqueous electrolytes has been recorded between 20° and 100°C [*Schott,* 1973]. Potential enrichments increase greatly, therefore, with both T and ΔT, but at present only *Walker et al.* [1981] have generated any data bearing upon the signs, magnitudes, or temperature dependences of σ for components in a magma.

Column length (L) is important in a fixed temperature gradient because potential steady state enrichments increase exponentially with the total value of ΔT. For fixed ΔT, however, the transient enrichment factors (the values of ΔC between opposite ends of a column that are attained long before any approach to the steady state) are virtually independent of L [*Bott,* 1970; *Schott,* 1973] because the depletions and enrichments largely concentrate at the ends of the column and noticeably affect the central part only as the gradients encroach upon it from the extremities. It is tempting to think that some insight is provided into the variety of zoned magmas shown in Figure 1, particularly those in group II that show abrupt transitions from strongly zoned rhyolite to more homogeneous

quartz latite. The relaxation time to approach a steady state compositional gradient is, according to *Schott* [1973], an increasing function of L but decreases with ΔT. There appears, however, to be a root-time dependence of transient separations, ΔC being proportional to $t^{1/2}$ [*Bott*, 1970]. Although the time required to attain a steady state distribution should be roughly proportional to chamber volume, transient enrichments in magmatic boundary layers could become important in much shorter times.

Work by a group in Toulouse [*Dandurand et al.*, 1972; *Schott*, 1973; *Costesèque and Schott*, 1976; *Costesèque et al.*, 1977; *Schott and Costesèque*, 1978] has amply shown that large chemical and isotopic fractionations can be achieved in modest periods of time by using thermogravitational columns. Most of their work has been with aqueous solutions in porous media, but recent efforts have utilized higher-viscosity materials. Some of their results are recounted here because of the potential importance for magmatic as well as hydrothermal and phreatic processes.

1. In porous media, when 0.1 N aqueous halide solutions were held at an average temperature $\bar{T}$ = 30°C and ΔT = 20°C, pure Soret diffusion produced enrichment factors of 1.03, 1.79, and 3.20 for Na, K, and Ba, respectively, but in convecting columns the corresponding enrichments were 4, 23, and 270 in experiments of 1 to 2 months duration.

2. When $\bar{T}$ = 60°C and ΔT = 40°C, pure water attained steady state isotopic fractions of 1 to 3 per mil δD and $\delta^{18}O$ in a few days by the Soret effect alone, but thermogravitational circulation enhanced these fractionations to 162 per mil and 108 per mil, respectively.

3. In aqueous chloride solutions, isotopic enrichment of as much as 27 per mil in $^{41}K/^{39}K$ and 20 per mil in $^{87}Rb/^{85}Rb$ were achieved within 65–145 days in packed columns at $\bar{T}$ = 32°C and ΔT = 20°C.

4. An aqueous sodium silicate solution, having a viscosity of ~0.5 poise, underwent a fiftyfold enrichment toward the bottom of a nonpacked thermogravitational column at $\bar{T}$ = 25°C and ΔT = 23°C, in one month.

5. In mixtures of the molten salts, $AgNO_3$, $LiNO_3$, and $RbNO_3$ at $\bar{T}$ ~ 230°–420°C and ΔT = 20°–60°C, thermogravitational enrichments were said to range from twofold to more than tenfold. $^{7}Li/^{6}Li$ and $^{87}Rb/^{85}Rb$ fractionations in these experiments were estimated to be in the ranges 50–150 per mil and 30–90 per mil, respectively.

6. By processes thought to involve only solid state Soret diffusion, a 3-mm-thick disc of Pb-Ba-Al-silicate glass that was subjected to a gradient of $\Delta T \simeq$ 180°C at $\bar{T} \simeq$ 400°C for 24 days experienced Ba and Pb enrichments of 4.5% and 7.5%, respectively, on the cold side. A similar experiment at $\bar{T}$ = 615°C and ΔT = 360°C changed the Fe/Mg ratio of an Fo-rich olivine by ~2% in 16 days [*Schott and Costesèque* 1978]; Fe diffused toward the hot side, Mg toward the cold.

Winter and Drickamer [1955] reported enrichment factors by Soret diffusion alone of 0.1 to 4.1 in binary equimolar mixtures of molten Sn, Bi, Cd, Zn, Pb, Ga, and Hg. Other thermotransport studies of liquid metals and their isotopes include those by *Bhat et al.* [1973] on Be-Hg-Na, *Bhat and Swalin* [1972] on Ag-Au, and *Ott et al.* [1967] on In, Li, K, Rb, and Ga. In all instances, isotopic fractionations of a few percent and elemental separations of a few percent to several hundred percent were obtained at the steady state.

I have cited these various experimental results at length here in order to emphasize, for a geological readership, the large separations of elements and their isotopes that are readily achievable in the liquid state by thermogravitational and pure Soret processes. The isotopic fractionation of gases by thermodiffusion has, of course, been well known since the work of *Clusius and Dickel* [1938], and it is still used for concentrating rare-gas isotopes, such as ^{38}Ar, for spikes in geochronology [*Rutherford*, 1975].

Quantitative application of such results to magma chambers has been stymied by our ignorance of Soret coefficients in magmas, by uncertainty in the nature and identity of the ionic or molecular species that actually diffuse in silicate melts, and by poor knowledge of the effective thicknesses and transport rates of thermal and chemical boundary layers in magmas. The ongoing experiments of *Walker et al.* [1981] hold great promise of future breakthroughs in understanding both Soret separation and speciation; some modeling of boundary layer behavior has been presented by *Shaw* [1974] and *Carmichael et al.* [1977].

In view of the effectiveness of thermogravitational separations in the laboratory, it would be remarkable if thermodiffusion were not operative in long-lived magma chambers. Thermal gradients in such chambers are well documented (Figure 3), and convection is virtually required in large bodies of unzoned magma that contains less than ~50% phenocrysts [*Shaw*, 1965, 1969, 1974]. Proof that ordinary back-diffusion and nonlaminar flow are insufficient to rehomogenize the fractionated roof-zone reservoir is the eruptive zonation itself. The occurrences of low-^{18}O magmas [*Lipman and Friedman*, 1975; *Taylor*, 1974, 1977; *Hildreth et al.*, 1980], the gradients in $^{87}Sr/^{86}Sr$ ratio in silicic magma chambers [Fig. 4; *Noble and Hedge*, 1970], and the gradients in volatile and most other components in such chambers [Figures 2, 6, 7, 8, 9, and 14; *Kennedy*, 1955; *Hildreth*, 1979] provide compelling evidence for diffusive transport in the liquid phase within the time limitations of single caldera cycles (Table 3). The diffusion of H_2O and halogens down temperature gradients may be the first-order transport process in zoning the large chambers that produce explosive eruptions.

Where the thermal gradient is horizontal, as in most thermogravitational columns (and at the walls of magma chambers), the annular spacing between hot and cold walls (Figure 12) strongly affects both the steady state enrichment factors and the relaxation times needed to approach them [*Schott*, 1973; *Grodzka and Facemire*, 1977]. Although it is not clear what the magmatic analog of annular wall spacing might be, the contacts of boundary layers along the roof and walls with the convecting interior and with the country rocks are apparently the critical zones in considering flow rates, diffusion distances, and effective ΔT (Figure 12).

It seems reasonable to assume that Soret diffusion would be most effective in dikes, sills, and slablike chambers that have high ratios of surface area to volume. Many rhyolitic dome clusters of small volume have trace-element trends analogous to those of voluminous ash flow tuffs [*Evans and Nash*, 1975; *Crecraft et al.*, 1979, 1980, this issue; *Bacon et al.*, 1979, this issue]; perhaps the fractionation in such systems is better explained by Soret diffusion in relatively short-lived rhyolitic bodies of high aspect ratio and large ΔT than by rhyolitic caps atop large zoned magma chambers. Such a process has been suggested as a component of the differentiation in tabular aplitic and basaltic intrusions by *Barth* [1952], *Hamilton* [1965],

and *Wilshire* [1967]. The compositional effects of Soret diffusion, particularly of volatile species and of elements complexing with them, should be detectable in the liquid phase of any long-lived (or short-lived but tabular) magma body, especially at its margins, except where they are overwhelmed by the effects of crystal or vapor fractionation.

A free vapor phase? It is not known if any of the zoned magmas under discussion were H_2O saturated and whether they coexisted with an aqueous fluid (vapor) prior to eruption. Thus it appears impossible, at this time, to quantify the role that rising bubbles might play in establishing chemical gradients. Roofward decline in both crystallinity and temperature (Figures 3 and 6; Table 2) suggests roofward enrichment of water and halogens, but the data provide no certain evidence of saturation. The following points bear upon the question:

1. Many high-silica lava domes that erupted without significant pyroclastic accompaniment exhibit trace-element enrichment patterns like those in voluminous ash flow tuffs. This apparently indicates that volatile saturation is not necessary for such enrichment unless nearly aphyric rhyolitic magma can somehow lose most of its volatiles without the loss-impeding ascent or without inducing crystallization [see *Bacon et al.*, this issue].

2. Zoned rhyolites that are the initial products of many ash flow eruptions variously contain either one or two feldspars; one, two, or no pyroxenes; and either no hydrous phenocrysts or any combination of biotite, amphibole, allanite, or apatite, with no obvious consistency from one system to another. Some contain fayalite, and others are strictly aphyric. The phase assemblages do not indicate a consistent pattern that could require H_2O saturation at the roof.

3. The Fe-Ti oxide temperatures of various high-silica rhyolites that have rather similar major-element compositions and that form the initial products of several voluminous eruptions range over at least 100°C (possibly 150°C), indicating that at least the higher-temperature magmas (e.g., LCT and HRT in Figure 3) were undersaturated in water.

4. Biotite-bearing lava domes are sometimes spatially associated with caldera-forming pyroclastic units that lack hydrous phenocrysts (other than sparse allanite and apatite). Examples include the Valles caldera [*Smith et al.*, 1970] and the Henrys Fork caldera in Island Park near Yellowstone (R. L. Christiansen, unpublished data, 1975). Because major-element compositions of the associated ash flows and domes are similar, it appears that any general inference about relative H_2O saturation on the basis of either phenocryst assemblage or eruptive style is unwarranted.

5. In the early part of the eruption in the Bishop Tuff, biotite had suffered depletion in K and had undergone anomalous interlayer enrichment in H_2O, Rb, and Cs. This 'alteration' is thought to have taken place during or just before eruption because it did not modify the systematic gradient in cation proportions on the octahedral sites of all the biotites erupted [*Hildreth*, 1977, 1979]. Restriction of biotite with 'altered' interlayers to the earliest-erupted ejecta is consistent with the interpretation that H_2O saturation was attained in the uppermost few hundred meters of the chamber only at the time of eruption.

6. Summation deficiencies in microprobe analyses of glass inclusions within phenocrysts quenched at the onset of eruption of the Tshirege member of the Bandelier Tuff have been interpreted by *Sommer* [1977] as indicating high magmatic H_2O contents. Because these deficiencies scattered from 2.4 to 7.0 wt. % in inclusions from the same pumice fall, I remain skeptical that any meaningful conclusions can be drawn from such data. *Fenn and Luth* [1973] showed experimentally that crystallization kinetics permit inclusions of aqueous fluid to be trapped by crystals that grow in water-undersaturated melts. Other explosive rhyolitic units, having similar patterns of bulk zonation, including the Bishop Tuff, contain phenocrysts with virtually no fluid or glass inclusions. No general conclusion about fluid saturation seems warranted on the basis of inclusion data.

7. Different ash flow systems show characteristic enrichments in groups of elements associated (and thought to be transported) with F and Cl, e.g., Li, Be, Sn, and U with F, and Zr, Hf, Zn, Fe, Ta, and Nb with Cl. However, even for quenched glassy rocks containing as much as ~0.5 wt. % of each halogen, neither F nor Cl could have been close to saturation in the magma [*Burnham*, 1979*a*, *b*]. Hence, enrichment of trace-element suites that are apparently linked to roofward halogen transport need not be associated with a fluid phase and may instead be principally diffusive. Thermogravitational enrichment is similarly envisioned for H_2O.

8. *Holloway* [1976] pointed out that at crustal pressures the solubility of CO_2 is so low in silicic magma that a CO_2-dominated vapor could coexist with such a magma at virtually any stage in its evolution. In principle then, CO_2-rich bubbles could aid in the upward transport of H_2O, halogens, and associated trace metals in silicic magma chambers. If degassing of large volumes of basalt that intruded into the deep crust generated a high CO_2 flux, this might contribute to chemical zonation in overlying silicic systems (Figures 12 and 15). One indication that such a process is not a major contributor, however, is the experimental data of *Wendlandt and Harrison* [1979] and *Flynn and Burnham* [1978] on the partitioning of REE between vapor and silicate melt. These studies showed that at crustal pressures REE partitioning into aqueous vapor is very small. Though REE partitioning into CO_2-rich vapor from silicate melts is important, it is much stronger for LREE than for HREE, thus antithetic to the roofward enrichment pattern of REE in many nonperalkaline rhyolites (Figure 7). Upward flux of CO_2-rich bubbles might, therefore, contribute to total transport, but the effects appear to be overprinted in shallow silicic chambers by the liquid-state mechanisms discussed above.

9. The K/Na gradients in most zoned rhyolitic magmas (Figure 7) are antithetic to those predicted by *Orville*'s [1963] results on alkali partitioning between a vapor and coexisting feldspars in a thermal gradient. This implies either that such a vapor was not present or that it had little effect upon the alkali distribution in the magma.

On the whole, the weight of evidence is against preeruptive water and halogen saturation in explosive rhyolitic magmas, but the transient effects of CO_2-bearing vapor might be important to transport of some trace components.

The role of melt structure. The structure of silicate liquids is a lively and rapidly evolving field of study [e.g., *Hess*, 1980; *Mysen et al.*, 1980*a*, *b*]. Though particular melt structural groups may shift continuously, the proportions of monomers, dimers, chains, sheets, and network units are generally thought to be a reproducible function of pressure, temperature, and composition; so too, therefore, should be the average availability of any given kind of coordination site in the

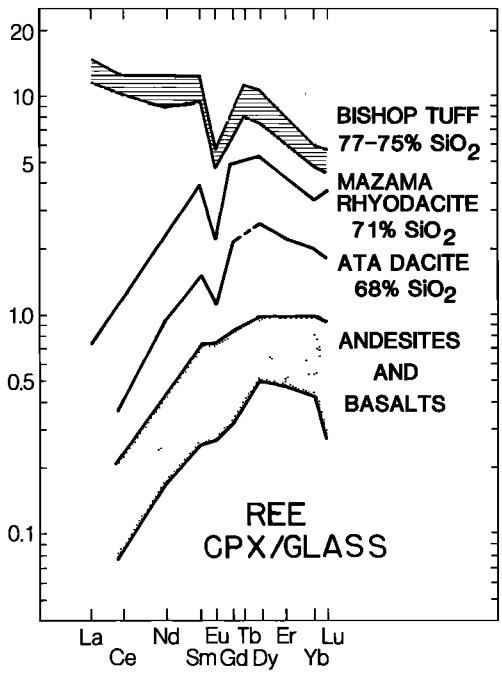

Fig. 13. Comparison of clinopyroxene/glass partition coefficients for REE in various igneous rocks, demonstrating the extreme changes with increasing SiO_2 content. The field for andesites and basalts is from *Arth* [1976]; the value for an Ata dacite is from [*Nagasawa and Schnetzler*, 1971]; unpublished data for rhyodacitic pumice from the climactic Mazama eruption are my own. The high values obtained for the Bishop Tuff [*Hildreth*, 1977] have also been found in the high-silica rhyolites of La Primavera [*Mahood*, this volume]. Similarly high values for partition coefficients have been found in high-silica rhyolites for several other phenocryst species and for many elements in addition to REE (G. A. Mahood and W. Hildreth, unpublished data, 1979).

melt. In a magma chamber large and mature enough to have established internal gradients in temperature and in volatile concentration, there must be a corresponding gradient in the degree of melt polymerization and, consequently, in the availability of octahedral (and other) sites in the liquid.

The influence of melt structure upon accommodation of trace elements by silicate liquids has been demonstrated experimentally by *Watson* [1976, 1977] and by *Ryerson and Hess* [1978, 1980]; its role in silicic magma chambers has been discussed by *Mahood* [1979, 1981*a*, and this issue] and by *Hildreth* [1979]. Melt structural influence is apparent in Figure 13, which gives an example of the enormous increases in the partitioning of trace cations into coexisting crystalline phases from progressively more polymerized liquids. Similar trends toward very high values of $D^{xtl/glass}$ in rhyolites are found for biotite, orthopyroxene, Fe-Ti oxides, fayalite, and feldspars, and such trends characterize many cations in addition to REE (G. A. Mahood and W. Hildreth, unpublished data, 1979). In comparisons like Figure 13 it is generally clear that the major-element composition of the liquid changes proportionally more than that of the phenocrystic phases, but the relative contributions of temperature, volatile content, and bulk composition as controls over the shift in partitioning are usually difficult to distinguish.

Mahood [1979, 1981*a*, and this issue] demonstrated, however, that high-silica rhyolites can show order-of-magnitude changes in crystal-liquid partitioning despite the virtual absence of any change in either temperature or (anhydrous) bulk composition. She suggested that such changes take place in response to shifts in magmatic volatile content and to subtle liquid structural changes in relatively volatile-poor magma. *Ryerson and Hess* [1980] similarly reported large (approximately fourfold) changes in two-liquid partitioning of REE caused by melt structural modifications that resulted from addition of a few percent P_2O_5 to silicate melts. Thus the importance of liquid structure to cation distribution is well established and appears to increase markedly in the most polymerized (rhyolitic) compositions.

Figure 14 portrays the elemental enrichment factors for the Bishop Tuff (as in Figure 7) divided into valence groups and plotted against the ionic radius that represents the oxygen coordination most likely to characterize each cation in the melt. The coordination numbers in the liquid are not necessarily well known, so more than one coordination radius is plotted for several elements; some arbitrary choices were made for cations more highly charged than 3^+. The valence-state ratios of Fe, Cr, V, and Eu in the melt are not well known, but this may matter little because the plotted values

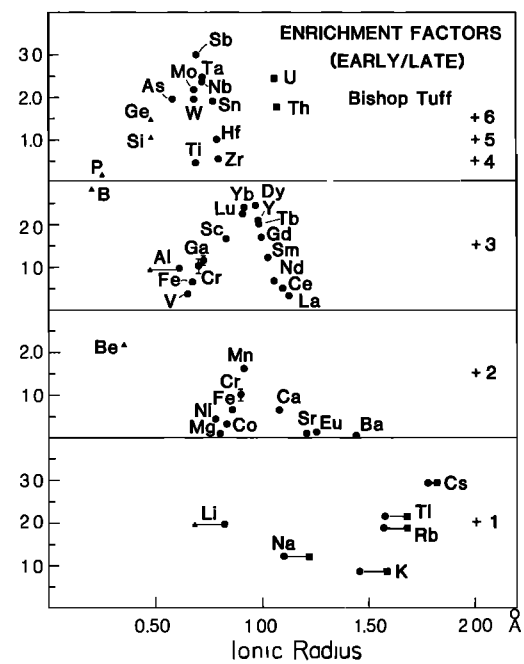

Fig. 14. Elemental enrichment factors in the erupted part of the Bishop Tuff magma chamber (as in Figure 7), plotted against ionic radius. Radii are from *Whittaker and Muntus* [1970]. Dots represent sixfold coordination with oxygen (or fluorine); triangles, fourfold; and squares, eightfold. High spin values are plotted for Cr, Mn, Fe, and Co. Error bars for Cr and Ga indicate the ranges in enrichment factor permitted by the analytical data at hand; analytical errors for other one-, two-, and three-valent elements are no larger than the plotted symbols. Cu, Zn, Ag, Hg, Pb, and Au are not plotted here (but see Figure 7) because of uncertain coordination, the likelihood of complex formation, and/or insufficient data. Eu and some transition metals probably existed in the magma in more than one valence (or coordination) state. Because the enrichment factors are simply ratios, the factor for, say, Fe^{2+} might not be very different from the value for Fe, even though some Fe^{3+} is sure to have been present. The systematic trends of divalent and trivalent cations about an octahedrally coordinated ionic radius of ~0.95 Å suggests that the structure of the silicate melt was important in controlling the enrichment patterns. Alternatively, the dominant volatile component (water) in the Bishop Tuff magma may have favored complexing with cations close to 0.95 Å in radius. The plot also suggests that the falloff in REE enrichment factors from Dy to Lu in Figure 7 is both real and significant.

are enrichment ratios, not concentrations. Some remarkable patterns are evident:

1. Both the divalent and trivalent groups were apparently distributed in the zoned magma chamber at the time of its eruption, in accord with the relative preference of each cation for a (presumably octahedral) melt structural site of radius ~0.95 Å. The concentrations of elements participating in this systematic behavior range from $<10^{-7}$ (Eu) to 10^{-2} (Fe). On the basis of relative fractionations of trivalent REE between pegmatitic melt and Cl-bearing aqueous vapor, *Flynn and Burnham* [1978] also deduced that REE cations occupy octahedral melt structural sites that have a preferred radius close to that of Yb^{3+} (as in Figure 14). As the lanthanide contraction promotes progressively stronger complexing from La to Lu, they pointed out that if vapor-phase complexing were more important than melt structure, the HREE would have been partitioned into the vapor more strongly than LREE, contrary to their experimental results. *Mahood* [1981*a*, and this issue] has similarly argued for liquid-site control of REE and other trace cation distribution on the basis of remarkable trends in both composition and partitioning during evolution of a series of closely related rhyolitic lava domes.

2. The monovalent cations do not reflect the same liquid-site control suggested for the 2^+ and 3^+ cations but show instead an enrichment minimum at K (Figure 14). This pattern appears to be common (if not ubiquitous) for the alkali metals in zoned rhyolites, but it shows no obvious systematic relationship of relative enrichment to field strength, electronegativity, or ionization potential. It could reflect the relative susceptibilities of the alkalies to roofward complexing with water or fluorine, but this is an unlikely explanation for the roofward absolute depletion of K. *Mahood* [1980*a*, 1981*a*] summarized the evidence against vapor loss through the roof, a process that would probably extract other alkalies (and U, Ta, Sn, etc.) as well as K from the topmost magma. Feldspar fractionation was quantitatively excluded as a major control on the various alkali gradients in the Bishop Tuff [*Hildreth*, 1977, 1979], but it cannot be summarily discarded as a contributing influence in rhyolitic systems where an insufficiency of data precludes quantitative treatment. Although probably critical in dacite-andesite zonation (Figure 8), feldspar control appears to be overwhelmed by liquid state redistribution of alkalies in rhyolites. If the alkalies diffuse as ions rather than as molecular complexes, their distribution might in part reflect different Soret coefficients, including a change of sign for K. Alternatively, the closer coupling of K with Al than with other alkalies may serve to charge balance and stabilize this (roofward-depleted) element in tetrahedral coordination within the melt.

3. Most elements that are more highly charged than 3^+ are strongly enriched roofward (Figure 14), and the thermogravitational transport of volatile complexes seems to be the most reasonable mechanism of enrichment. In systems richer in halogens than the Bishop Tuff these enrichments are correspondingly greater. Where Cl is abundant, Zr and Hf concentrate roofward (cf. Figure 7), parallel with enhanced enrichments of Zn, Nb, Ta, Mo, and W (see Table 1); where F is a more important ligand, enrichment of Sn, Li, Be, and U is more pronounced [cf. *Bacon et al.*, this issue; *Crecraft et al.*, this issue, *Christiansen et al.*, 1980]. Tetrahedrally coordinated Si, Al, Ti, P, Fe^{3+}, and Ge are part of the network structure in rhyolitic melts [*Mysen et al.*, 1980*a*; *Ryerson and Hess*, 1980], and it remains unclear how their contrasting distribution gradients are established in zoned magmas.

In summary, it seems likely that some kind of complex feedback takes place between composition and site availability in structurally and thermally zoned silicate liquids. In rhyolitic magmas, only H, O, Si, Al, Na, K, and sometimes Fe are 'major' elements; distribution of the other 76 must be influenced by the liquid structure imposed (in part) by the majors. In the composite mechanism suggested for differentiation of rhyolitic magmas (Figure 12), the thermal and gravitational fields of the magma chamber itself provide the potential gradients and driving force; the thermogravitational process is the transport system; volatile ligands the carriers; and liquid structural gradients at once the expression, host, and keeper of the order achieved.

In order to evaluate the validity of the suggested model, we need to know more about (1) Soret diffusion; (2) volatile complexing; (3) the relative importance of thermal, gravitational, and melt structural gradients in providing chemical potentials for transport; (4) which species diffuse as discrete ions and which as complex molecules; (5) the role (if any) of a free-vapor phase; (6) the relative importance of the buoyant boundary layer at the walls and that at the roof, as loci of diffusive exchange with the internal convecting domain(s) (Figure 12); (7) whether any tendency exists for the roofward graded zone to assume a multilayered double-diffusive configuration [*Turner*, 1973, 1974, 1980; *McBirney and Noyes*, 1979], which could greatly enhance internal thermogravitational transport; and (8) the extent of diffusive control on distribution of K, Ti, P, REE, and other trace components in basaltic and intermediate liquids where such effects may normally be masked by crystal-liquid fractionation.

In leaving rhyolites, I want to reemphasize that most of their compositional evolution takes place within high-level magma chambers; this means that trace-element modeling of their source materials (even if these were simply definable) is virtually impossible. Finally, as should be clear from the questions just listed, further advances in understanding igneous petrogenesis now require accumulation of experimental data that will permit the liquid and vapor-fractionation components of magmatic differentiation to be treated in as quantitative a way as we can already treat the crystal-fractionation component.

EXTRACTION OF RHYOLITIC MAGMA

The foregoing discussion has emphasized the internal differentiation of rhyolitic magma but not the origin of the rhyolitic liquid itself. Five different mechanisms for the generation of rhyolitic magmas are outlined below, two or more of which could act concurrently or successively within a given system.

1. *Crystallization-differentiation of less-silicic magma.* Some rhyolites, generally low-silica ones, were compositionally and physically continuous with associated dacites prior to eruption and may indeed have evolved from them, in part by crystal fractionation. Examples could include the strongly zoned Mazama and Carpenter Ridge eruptions (Figure 1) as well as plutons that zone from granodiorite to adamellite, such as the Tuolumne Intrusive Suite [*Bateman and Chappell*, 1979]. On the other hand the distinctive compositions and trifling volumes of silicic differentiates in ophiolitic gabbroid complexes [*Coleman*, 1977] and in layered gabbroid plutons such as the Skaergaard Intrusion [*Taylor and Forester*,

1979] provide the clearest evidence that quasi-closed-system crystallization-differentiation of mafic magma is not an important mechanism for the generation of voluminous rhyolites.

Studies of the progressive crystallization-differentiation of tholeiitic lava lakes in Hawaii, however, have shown that the final several percent residual liquid, though extraordinarily rich in K and Ti, is indeed high-silica rhyolite [*Wright and Okamura*, 1977]. If gash fracturing or other mechanisms were to permit extraction and coalescence of such liquids only late in the consolidation of basaltic magma bodies in the shallow crust, such processes might conceivably contribute to producing some of the bimodal volcanic associations in which rhyolite is a very subordinate member.

2. *Ascent of buoyant boundary layers.* Such ascent [*Shaw*, 1974; *Hildreth*, 1977, 1979; *McBirney*, 1980] along the walls of convecting chambers of intermediate magma may generate some roof-zone rhyolites as well as promote their subsequent internal differentiation (Figure 12). Examples may include any of the high-silica rhyolites that were presumably or demonstrably associated with subjacent intermediate magma, as in groups I, II, and IV of Figure 1. This process may also account for the generation of many dacitic magmas that subsequently fractionated to rhyolite, in part by mechanism 1. The most likely examples are dacites that exhibit compositional discontinuities with coeruptive or associated andesites, as in group V (Figure 1).

3. *Remelting of igneous forerunners.* Remelting of igneous forerunners, either intrusive or extrusive, within a thick volcanic pile could be promoted by increases in the rates of intrusion and/or storage of mafic magma. This mechanism might be especially important in parts of volcanic piles that had been rendered more susceptible to partial refusion by hydration and hydrothermal alteration. The low-^{18}O Icelandic rhyolites analyzed by *Muehlenbachs* [1973, 1974], notably the 1875 Askja ejecta (Figure 1), provide likely examples. If remelting were solely responsible for the silicic ejecta of Hekla, on the other hand, it is not clear why SiO_2 should increase with repose time between eruptions [*Thorarinsson*, 1967]; perhaps Hekla's cyclic differentiation is attributable to some combination of mechanisms 1 and 2, and 3.

Remelting may play some role in those arc systems where modest volumes of rhyolite are distinguished from an accompanying basalt-to-dacite suite by a wide compositional gap, as in the 1912 eruption at Katmai (Figure 1). Though probably complicated by the superimposed effects of volatile complexing and diffusion, remelting may also be an important process in generating the basalt-trachyte (± pantellerite) suite.

Most mafic and intermediate igneous and metaigneous rocks, however, are too calcic to permit direct production of typical rhyolitic liquids by partial melting alone [*Helz*, 1976]. In order to generate most true rhyolites by this mechanism or the following one, extraction of silicic partial melts probably has to be supplemented by fractionation of plagioclase (and/or another calcic phase).

Partial remelting might well be part of a multistage process wherein every successive pulse of basaltic injection results in partial refusion of progressively more evolved members of a complex, deep-seated assemblage. Successive intrusive events and attendant partial remelting probably alternate with repose intervals. During such intervals, partial or complete crystallization could produce a range of intermediate-to-silicic differentiates. In long-lived systems that have a moderate but fluctuating basaltic power supply, complex fractionation could thus take place within a plexus of dikes, pods, and irregular conduits, with or without large magma chambers ever developing. The eruptive products of such a system might evolve with time from mafic and intermediate to a predominantly bimodal suite that included silicic extracts from parts of the system that had been emplaced, fractionated, and even solidified long before.

Most of these remarks apply as well to the following mechanisms of rhyolitic extraction; the distinction here between partial melting of igneous forerunners and of older crustal rocks is only a conceptual convenience, and there can be little doubt that both are involved in the generation of silicic magma in long-lived crustal systems.

4. *Extraction of rhyolitic partial melts from older crustal rocks.* An extensional tectonic stress regime that favored the brittle failure of crustal rocks that were partially melted by intruding basalts could permit extraction of rhyolitic liquids in tabular bodies. At the same time it would suppress hybridization, entrainment of residues, and melting extensive enough to generate liquids much less silicic than rhyodacite. Propagation of dikes to the surface would produce clusters of silicic domes, whereas shallow aggregation could produce predominantly rhyolitic magma chambers of any size, even as large as at Yellowstone. In any case, most of these extensional magmatic systems are apparently bimodal, erupting little or no magma of intermediate composition. This is thought to be a leading mechanism for generation of continental rhyolites on all scales; it can be contrasted, in principle, with the following mechanism (see Figure 15).

5. *Separation of silicic liquid from partially molten diapirs.* Progressive upward segregation of the liquid fraction from partially molten crustal diapirs of grossly intermediate composition could provide the full spectrum of magmas usually represented in Cordilleran batholiths. The root cause of the diapirism is also thought to be basaltic injection of the crust, but compared to the extensional regime of mechanism 4, upward penetration of basalt is suppressed, and its lodgement is generally much deeper. An extended interval (typically $>10^6$ years) of crustal preheating is apparently required to produce sufficient partial melting for initiation of batholith-scale mobilization. The shallow expression of this preheating is an andesite-dacite volcanic field ('early intermediates') and the emplacement of modest stocks of gabbro and diorite ('mafic forerunners'). Ultimately, the injected crustal domain becomes buoyantly diapiric (Figure 15), and during its sluggish ascent, a range of granodioritic, adamellitic, and even alaskitic liquids progressively segregates from refractory residues. This is the modified 'restite model,' which is discussed further below.

Yoder [1973] proposed that rhyolite and basalt might be successively generated by thermally prograde but discontinuous partial melting of a given mantle domain without formation of intermediate liquids. The time-volume-compositional history of virtually every volcanic field weighs heavily against such a model. In each of the five mechanisms discussed above, rhyolite is necessarily a subordinate successor to intrusive mafic magmatism, not its predecessor. That any rhyolitic magma could wend its way to the surface from mantle depths without crystallization or severe hybridization is very unlikely. Finally, the necessity for any melt extracted from a peridotitic source to be in equilibrium with residual forsteritic olivine precludes derivation of rhyolite from the mantle.

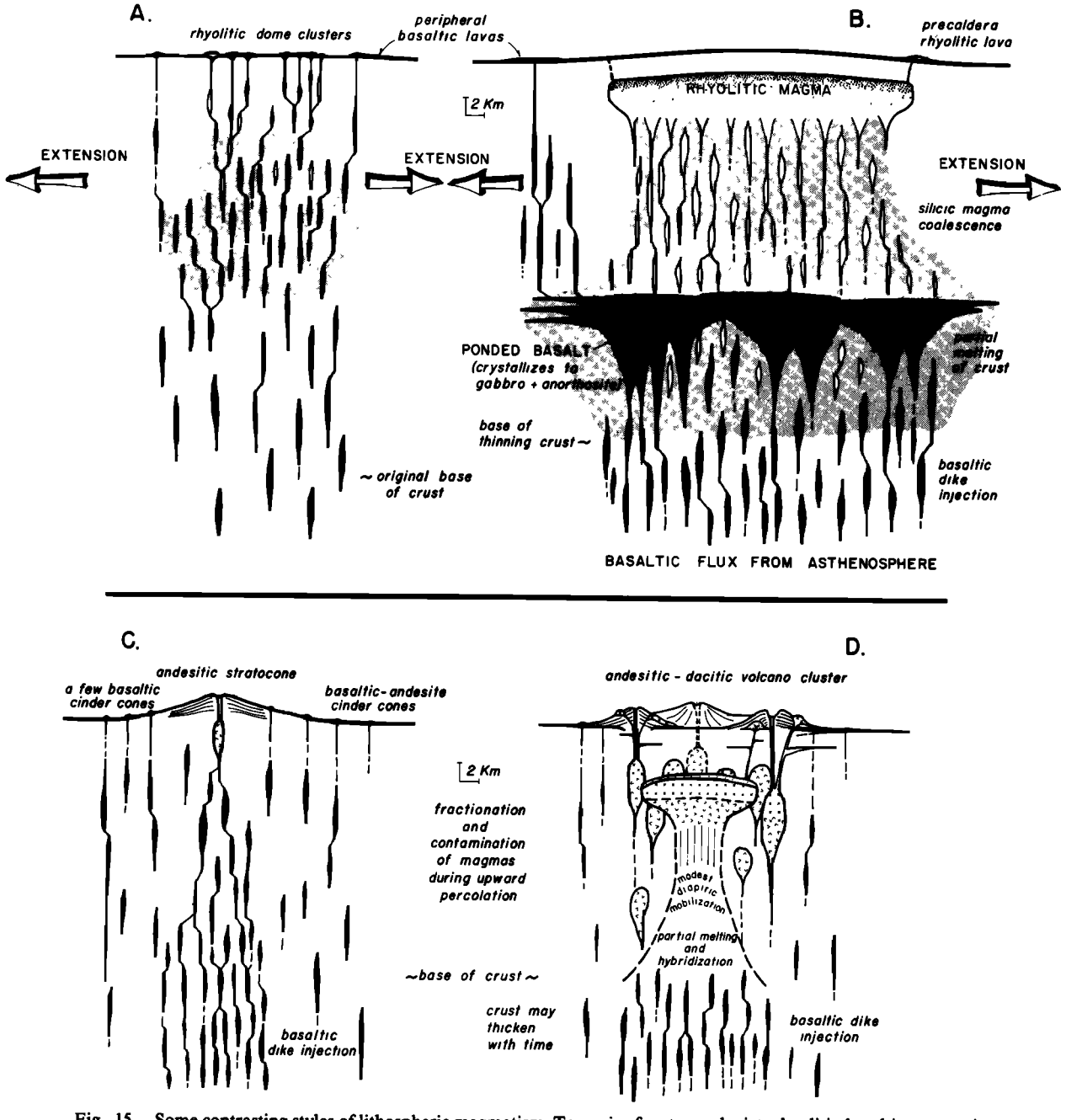

Fig. 15. Some contrasting styles of lithospheric magmatism. Top pair of cartoons depicts rhyolitic-basaltic magmatism under stress conditions favoring marked crustal extension: (A) modest power input; (B) large power input, advanced stage. Shaded regions indicate partial melting of crustal rocks sufficient to permit separation of rhyolitic magmas as gash veins and dikes. Lower pair of cartoons depicts two possible stages in development of volcanic systems where tectonic extension, if any, is subordinate and shallow: (C) early stage; (D) intermediate stage; for advanced stage see Figure 12. This model applies to island arc, continental margin arc, and continental interior systems that produce abundant intermediate magmas. All four sketches are idealized and refer to no particular systems. The models are independent of the mode or site of generation of basaltic magma, but basalt is thought to provide the power supply for virtually all other magmatism. The power spectrum, the percolation rate of magmas, and the volatile flux from the mantle, all in concert with the stress states, thermal history, and compositional structure of the lithosphere, must control the chemistry of the magma ultimately coalescing in shallow reservoirs.

The five mechanisms of rhyolite generation given above need by no means be mutually exclusive. In fact, the zoned silicic magmas discussed throughout this paper provide ample evidence that the coalescence of voluminous silicic magma chambers, whether principally by extensional mechanism 4 or diapiric mechanism 5, is commonly succeeded by high-level crystal fractionation and/or thermodiffusive boundary-layer fractionation. Partial remelting of intrusive forerunners is probably common to all systems that grow large, and rhyolitic residual liquids fractionated from bodies of more mafic magma crystallizing deeper in such systems may also contribute to the growth of overlying silicic chambers. A simple thermal and mechanical history is exceedingly unlikely for a long-lived magmatic system in a heterogeneous crust.

Crustal melting mechanisms for generation of silicic to intermediate magmas have sometimes been rejected on Sr-isotopic grounds, but in most cases such objections appear to be groundless. Relatively low $^{87}Sr/^{86}Sr$ ratios (~0.707) clearly exclude a major role for shallow radiogenic continental crust, but values in the range 0.704–0.706 are just what might be anticipated for deep- to mid-crustal granulites, amphibolites, and low-Rb/Sr tonalitic gneisses, with or without various admixtures of injected basalt. In regions of late Cenozoic magmatism, notably around the Pacific margins, rhyolite as nonradiogenic as 0.703 can be extracted by partial remelting of the volcanic pile itself or of its underlying intrusive equivalents.

A modified 'restite model.' The 'restite model,' whereby progressively more silicic (and potassic) magma is produced by separation of liquid from its refractory crystalline residue in ascending diapirs, has been widely advocated for Cordilleran batholiths [*Bateman et al.*, 1963; *Piwinskii*, 1968; *Piwinskii and Wyllie*, 1968, 1970; *White and Chappell*, 1977; *Compston and Chappell*, 1979]. Most discussions, however, have glossed over the problem of a heat source for such melting and mobilization. It is here postulated that melting temperatures are attained and sustained in the crust almost exclusively by intrusion and crystallization of mafic magma. I will argue below that this magma is basaltic, but if andesite were a primary magma, it too would suffice as a heat source for large-scale crustal mobilization. 'Ultrametamorphism,' the spontaneous initiation of crustal melting under normal geothermal gradients related only to conductive heat transfer and in situ heat production, is a very unlikely alternative, in view of (1) the relatively calcic and nonradioactive rock suites of the continental margins (see Figure 2); (2) inadequate geothermal gradients in mature continental crust, as reviewed by *Brown and Hennessy* [1978]; (3) the linear relationship between heat flow and near-surface heat production found in continental provinces little affected by mafic magmatism, a relationship requiring depletion of heat-producing elements with depth in the crust [*Sass and Lachenbruch*, 1979; *Lachenbruch and Sass*, 1977, 1978]; and (4) the ubiquitous mafic forerunners observed in most batholiths and volcanic fields.

Protracted intrusion of the crust by such forerunners may be the key process in initiating upward mobilization of large crustal diapirs. The objection that mafic forerunners are generally quite subordinate to felsic granitoids in exposed plutonic terranes is overruled by the very nature of the model (Figures 12 and 15); upward penetration of basalt will be progressively retarded by the crustal melting and diapirism it promotes. The diapirs must consist not only of partially molten crustal rocks but of a network of basaltic bodies intruding and hybridizing with them. Seen in this light, the modified restite model also resolves the debate over the origin of mafic inclusions in granitoids. The inclusions are, at the same time, remnants of injected basalt [*Eichelberger and Gooley*, 1977] and refractory residues of the source material [*White and Chappell*, 1977] because the mushy diapiric source from which the granodiorite-adamellite suite separates is itself a hybrid mixture of crustal and mantle contributions.

In other respects I accept the 'restite model' outlined by *White and Chappell* [1977] as one way of producing some of the diversity within and among Cordilleran plutons, but with the following qualifications:

1. The variability within high-level adamellites and granodiorites is often better attributed to fractionation between melt and phenocrysts than between melt and restite [e.g., *Bateman and Chappell*, 1979]. Much of this fractionation must take place after a magma body has become too crystal-rich to erupt (≳50% phenocrysts), but it is already well underway in most phenocryst-rich (restite-poor) dacitic-to-rhyodacitic-zoned eruptive units, as is implicit in Figures 6, 8, and 11.

2. Most high-silica rhyolites originate and differentiate by mechanisms other than separation of restite. Phenocryst-poor rhyolites containing 76%–77% SiO_2 are not necessarily granitic-minimum melts, as would be required if they had evolved simply by removal of restite. Fresh high-silica rhyolites from many provinces exhibit a wide range in K/Na and scatter widely to both sides of the line of minima on a normative Q-Ab-Or plot [*Tuttle and Bowen*, 1958; *Luth et al.*, 1964].

3. Linear trends on SiO_2-variation diagrams for individual plutons have been interpreted as restite-melt 'unmixing' lines [*White and Chappell*, 1977; *Chappell*, 1978]. Many zoned eruptions (Figure 1), however, span most or all of the SiO_2 range of such lines, but the zoned magmas contained little or no restite. Andesites commonly contain disequilibrium assemblages of crystals that could be restitic in part, but many dacites (that would solidify to granodiorite or tonalite) are poor in such material. Most porphyritic dacites and rhyodacites contain rhyolitic interstitial glass that evidently evolved in a magma virtually devoid of restite. A few voluminous zoned units of andesite-dacite are nearly aphyric (e.g., A in Figure 6). It seems clear that liquids of virtually any bulk composition can unmix from or entirely resorb their entrained residues; resorption can be easily visualized in terms of the intermittent nature of the postulated basaltic heat source. Therefore, reconstructing a 'source composition' at ~60% SiO_2 [*White and Chappell*, 1977] by means of supposed 'unmixing' lines is not likely to be meaningful since it ignores the thermal and mechanical history of the magma, the hybrid complexity of any reasonable 'source,' and especially the longevity of large igneous systems.

4. Source materials for the large granitoid plutons that have been interpreted in terms of the 'restite model' are not uniquely definable. The crust is known to be very heterogeneous, both vertically and horizontally, and the evidence given by mafic forerunners, synplutonic mafic dikes, and mafic clots and inclusions in granitoids [*Bateman et al.*, 1963; *Eichelberger and Gooley*, 1977] demands a mantle contribution as well. Compelling isotopic evidence for both mantle and crustal components in granitoid production are reviewed in a later section. The strongly peraluminous plutons that are common inboard of coastal batholiths [*White et al.*, 1976; *Miller and Bradfish*, 1980; *Strong and Dickson*, 1978], if not simply attributable to loss of an alkali-rich fluid phase, probably represent mid- to upper-crustal ingestion of metasedimentary rocks by otherwise normal igneous systems that penetrate the entire lithosphere (Figure 12). 'S-type' and other peraluminous plutons can be expected to grade down to 'I-type' roots.

5. The 'restite model' cannot be generalized to bimodal magmatic suites of extensional terranes. There is no evidence for the voluminous intermediate magma intrinsic to the model.

In summary, the separation of melt from restite is thought to be one viable mechanism for extracting dacitic to rhyodacitic liquids from less-silicic magmas, but the latter are hybrids of crustal and mantle components and are not derived from a uniform source. The silicic magma that progressively

concentrates toward the top of a large diapiric pluton probably grades down into restite-rich intermediate magma, and this, in turn, into a dike-rich root zone (Figures 12 and 15) where mantle-derived magmas partially melt, exchange with, hybridize with, and mobilize heterogeneous crustal rocks. Melt-restite separation may thus be viewed as but one stage in the protracted evolution of some large Cordilleran plutons. Silicic liquids so separated can generally be expected to show superimposed effects of subsequent differentiation by other processes.

PLUTONIC AND VOLCANIC ROCKS

No one familiar with the late Tertiary stocks exposed within active andesitic-dacitic arcs or with cratonic cauldrons and ring complexes any longer doubts the intimate relationship between eruptive and plutonic 'early intermediates' or between voluminous silicic volcanic rocks and granitoids. Some geologists, however, still question whether the great Cordilleran batholiths ever supported ash-flow fields on the scale of Taupo, northern Chile, or the Sierra Madre Occidental. Though I would not argue that all plutons erupt, there is considerable evidence that many of them did.

The fallacy that silicic magmas seldom erupt was laid to rest by *Smith*'s [1960] review of ash flows. 'Flood rhyolites' are at least as voluminous as continental flood basalts. Pyroclastic rocks erode rapidly, however, especially in icy Cordilleran mountain belts. This leads to severe underestimation of the volumes of silicic magma that actually erupted in such belts where resistant mafic and intermediate lavas are proportionately better preserved. Quaternary ash flow tuffs are abundant in Japan [*Aramaki*, 1957] and on the Alaska Peninsula [*Miller and Smith*, 1977]. More than 10% of the 1912 sheet at Katmai has already been stripped, and another major glaciation would remove all of it. In the southern Andes, long supposed to be devoid of ash flow tuffs, we have also found them to be common but eroding at high rates [*Drake*, 1976; *Hildreth et al.*, 1981].

Preservation of silicic pyroclastic rocks atop Mesozoic batholiths is poorer still, but many roof pendants in the Sierra Nevada contain remnants, and at least one major center, probably a caldera, has been identified there [*Fiske and Tobisch*, 1978]. Enormous volumes of volcanic detritus, much of it ash, in Mesozoic formations of the North American interior, such as the Chinle and Morrison formations and the Pierre Shale, suggest that explosive silicic volcanism was a conspicuous accompaniment to emplacement of the Cordilleran batholiths. Because, as shown above, all voluminous pyroclastic eruptions are zoned, the petrochemical relations between zoned eruptive units and their parent plutons warrants some discussion.

Is magmatic zonation preserved in plutonic rocks? If no further differentiation or open-system behavior took place within the unerupted magma after a zoned eruption, continuity between the volcanic and plutonic compositions might be preserved, but the compositional ranges would be different. However, reestablishment of compositional gradients has been widely documented in multicyclic systems (Table 3), which leads to the conclusion that magmatic differentiation can continue well after a pluton's last eruption [e.g., *Smith*, 1979, Figure 8]. This conclusion is sustained by petrochemical studies of plutonic rocks that apparently have acquired concentric zonation by progressive marginal crystallization [*Bateman et al.*, 1963; *Bateman and Nokleberg*, 1978; *Bateman and Chappell*, 1979; *Perfit et al.*, 1980]. It is hard to imagine the chamber geometry, temperature distribution, or eruption mechanics that could reconcile the consistent evidence for increases in temperature (Figure 3), mafic constituents (Figures 1 and 7), and phenocryst contents (Figure 6) during zoned eruptions with a mafic-to-felsic coreward zonation of the erupting chamber. This suggests that this type of marginal accretion does not take place in the volatile-rich tops of chambers that erupt. Instead, concentric zonation by inward solidification probably develops only late in a pluton's magmatic lifetime, perhaps after the mantle-derived thermal input has waned (cf. Figure 12).

A few plutonic suites have been described that appear to have preserved patterns of compositional zonation similar to those recorded in ash flow tuffs. Two small molybdenum-rich intrusions in southeastern Alaska, Quartz Hill and Divide Stock [*Hudson et al.*, 1979], have major- and trace-element concentrations similar to those of the Bishop Tuff. In both stocks the roofward enrichments over ~1 km of exposure are remarkably like those of Figure 7 for most elements. Compositional patterns like those in high-silica rhyolites have also been recognized in some of the Cape Granites of southern Africa [*Kolbe*, 1966], the Snowy Mountains leucogranites of southeastern Australia [*Kolbe and Taylor*, 1966], and in satellites of the Pikes Peak batholith [*Ludington et al.*, 1979]. *Aramaki et al.* [1977] reported a remarkable vertical zonation in the large Okueyama pluton of northeastern Kyushu; detailed study of this granitoid, which grades from ~66% SiO_2 to a high-silica aplitic cap, is the ongoing project of M. Takahashi. The Captains Bay pluton on Unalaska Island [*Perfit et al.*, 1980] is zoned from gabbro to granodiorite, has associated high-silica aplites and mafic forerunners, and shows many compositional similarities to the zoned ejecta of the 1912 eruption at Katmai [*Hildreth and Grunder*, 1980].

However, definitive matching of an ash flow sheet and related plutonic rocks will, in general, be very difficult because of posteruptive changes in composition of the unerupted magma and because of the compositional gradients themselves, especially those in isotopic and elemental ratios. The only convincing matches I know about are (1) *Keith*'s [1980] correlation of the Pine Grove stock, Utah, with its outflow sheet, where both contain garnet; and (2) eroded cauldrons where central stocks intrude related intracaldera welded tuff [e.g., *Marjaniemi*, 1970; *Aramaki et al.*, 1977]. Not only can 'comagmatic' volcanic and plutonic rocks represent different compositional levels of a system, but they represent very different points in its life history. In pre-Miocene rocks, important age differences become lost in the noise of geochronologic tools.

Do granitoids represent magmatic compositions? Attempts to establish specific correlations between ancient volcanic sequences and exposed plutons are hindered not only by alteration of the extrusive rocks, compositional gradients, posteruptive insurgences of primitive magma, and fractionation, convection, and remobilization of the crystal mush during protracted solidification but also by prolonged subsolidus reequilibration and alteration of the cooling granitoid.

Repeated cycles of roofward enrichment (Figures 7 and 10; Tables 1 and 3), coupled with eruptive losses and losses by emplacement of silicic dikes and enriched roof stocks, must leave a solidifying granitoid body considerably depleted in many elements relative to its 'initial' bulk magmatic composi-

tion. On the other hand, residual concentrations of such elements as Cu, Ag, and Au could be enhanced (Figure 7).

Waning of the thermal energy supplied to a magma chamber from the mantle through its root zone must lead at some point to collapse of the convective circulation critical to thermodiffusive fractionation in boundary layers (Figure 12). Such a transition could initiate inward solidification and perhaps even some degree of rehomogenization of the zoned magma by back-diffusion and local mixing. Such an interpretation may explain the compositional sequence during waning phases of eruptive activity at the Valles caldera [*Smith*, 1979, Figure 8].

Crystal-liquid fractionation, such as convective accretion of restite and phenocrysts to chamber walls or extraction of interstitial liquids from late mush by gash fracturing, could produce a granitoid composition for which a magmatic equivalent had never existed. Even the relatively orderly crystallization of the Tuolumne pluton [*Bateman and Chappell*, 1979] involved considerable feldspar accumulation, as shown by the erratic distribution of Ba, Sr, and alkalies.

Fluid losses during late stages of granitoid solidification must produce further depletion in alkalies, Be, B, Mn, U, and other mobile constituents. Late magmatic and subsolidus greisenization, muscovitization, and kaolinization enhance the Al/Na + K ratio, making the granitoid more corundum-normative than its parent magma. Formation of epidote, chlorite, sericite, and clays and protracted reequilibration of feldspars in the presence of a fluid phase inevitably entails bulk compositional changes [*Orville*, 1963]. Many Na_2O values reported for 'fresh' granitoids are too low to represent magmas. Because the muscovite and Or_{80-100} alkali feldspar so common in granitoids never erupt as phenocrysts, their presence in granitoids must reflect, in part, a late- to post-magmatic shift in bulk composition. The more volatile-rich the original magma, the more profound the shift induced by late fluid loss is likely to be. In addition, if subsolidus fluid circulation promoted isotopic exchange of the most abundant element, oxygen, in a cooling granitoid [*Taylor*, 1977], it could only be fortuitous if alkalies and other mobile elements were to retain their magmatic concentrations.

It is easy to lose sight of the time scales involved. Eye-catching textural features preserved during granitoid solidification (e.g., comb layers, truncation of mineral banding, or aggregations of megacrysts) may reflect transient events that lasted only days to a few years, but solidification of a large magma chamber may require a million years [e.g., *Bailey et al.*, 1976; *Smith*, 1979; *Lachenbruch et al.*, 1976], and hydrothermal stewing may last longer still. There is no lack of time for profound late- and post-magmatic changes in granitoid compositions. The pessimistic tone here is not meant to imply that little can be learned from the petrochemistry of granitoids but simply that caution is required in extrapolating such data to magmas. Most granitoids have suffered moderate to severe metamorphosis during and after solidification.

A FUNDAMENTALLY BASALTIC VIEW OF CRUSTAL MAGMATISM

Because virtually all large nonbasaltic eruptions tap magma that is zoned or otherwise inhomogeneous, it seems clear that few magma bodies, excluding some basalts, ascend from source to surface chemically unmodified. Small magma batches are even less likely to rise unmodified. Hence, nonbasaltic eruptive units that appear to be homogeneous probably represent small leaks from zoned systems and/or batches of zoned magma that rehomogenized during final ascent. Small volumes of rhyolitic magma produced by shallow crustal melting (Figure 15-A) may be the nearest thing to an exception, but andesites are not. In spite of the superficial monotony within many sequences of andesitic lavas, the macroscopic and microscopic heterogeneity of most andesites attests to complex ascent histories, which prove that andesites are not primary. It is argued here that the origin and evolution of intermediate and silicic magmas depend upon mantle-derived basalts, not as the starting point of any simple liquid line of descent but as the thermal basis of lithospheric magmatism.

Christiansen and Lipman [1972] proposed that the predominantly bimodal mafic-silicic volcanism associated with late Cenozoic extension in the western United States has been 'fundamentally basaltic.' I think that the evidence now warrants the more comprehensive proposal, in agreement with *Shaw* [1980], that almost all magmatism is fundamentally basaltic (Figures 1, 12, 15, and 16). The salient evidence includes the following:

1. Voluminous volcanic systems, whether their eruptive products are predominantly rhyolitic, intermediate, or basaltic, are characterized by a He flux that is clearly mantle-derived. Systems as different as Yellowstone, Lassen, Hakone, Usu, the Marianas arc, the Kurile-Kamchatka arc, the Red Sea, the Galapagos Rift, and midocean ridges have $^3He/^4He$ ratios that are 6–12 times the atmospheric value [*Craig et al.*, 1978; *Poreda et al.*, 1980; *Nagao et al.*, 1980]. In the largest systems, where basaltic injection of the lithosphere is probably greatest (Figures 12, 15, and 16), the highest $^3He/^4He$ ratios are found, viz., 15 to 23 times the atmospheric ratio at Yellowstone, Kilauea, and Iceland.

2. The flux of CO_2 from young volcanic centers and its range in $\delta^{13}C$ values imply a major contribution of mantle-derived carbon, irrespective of the magma compositions erupted [*Craig et al.*, 1980; *Barnes et al.*, 1978; *Irwin and Barnes*, 1980]. Values of $\delta^{34}S$ in most igneous rocks, and notably those for the andesitic-dacitic Cu-porphyry systems [*Gustafson*, 1979; *Ohmoto and Rye*, 1979], cluster tightly about the mantle (and chondritic) ratio. Such data suggest that magmatic fluxes of C and S are dominated by mantle sources, usually show little or no evidence for a contribution from crustal metasediments or subducted seafloor, and reflect the importance of basaltic magma crystallizing and degassing in the roots of a wide variety of volcanic systems.

3. Convincing evidence has been given by a number of authors that many andesites and dacites retain variable amounts of both crystals and glass derived from basaltic magmas that mingled with more silicic ones [*Anderson*, 1976; *Eichelberger and Gooley*, 1977; *Johnston*, 1978; *Eichelberger*, 1978]. *Arculus and Wills* [1980], on the other hand, showed that andesites commonly contain cumulate blocks, many of which contain interstitial glass, that they convincingly relate to the fractionation of such andesites from basaltic parents. There need be no contradiction because, at any stage, dikes of relatively primitive basalt could overtake and mix with dikes, pods, or larger reservoirs of evolved magma in the process of fractionating (see Figure 15). Either way, andesites appear to have basaltic predecessors.

4. One of the most compelling lines of evidence that basalt is essential to crustal magmatic systems is the apparent link between the size and maturity of an evolved system and the

degree to which basalt is capable of penetrating it. Basalt commonly erupts around the periphery of large rhyolitic systems but fails to erupt within the silicic focus; examples include the Long Valley, Valles, and Yellowstone calderas. Large andesitic-dacitic volcanos surrounded by fields of basaltic cinder cones are common, e.g., the San Francisco Peaks in Arizona [*Robinson*, 1913; *Moore et al.*, 1976] and Volcán Colima in Mexico [*Luhr and Carmichael*, 1980]. Smaller composite volcanos commonly experience central eruptions or rapid sequences of eruption that include both intermediates and basalt, e.g., Oshima-Ōshima [*Katsui et al.*, 1979] and Mount St. Helens [*Hopson*, 1971]. Many modest 'andesitic' volcanos are in reality largely basaltic, especially during their early phases of activity [*Katsui et al.*, 1978, 1979; *Gorshkov*, 1970; *López-Escobar et al.*, 1977; *Marsh*, 1980; *Myers et al.*, 1980]. Finally, there are the predominantly basaltic systems where small chambers, pods, or dikes of rhyolite are readily penetrated by and coerupted with basalts, e.g., Iceland [*Gibson and Walker*, 1963; *Sigurdsson and Sparks*, 1981], Coso [*Metz and Bacon*, 1980; *Bacon et al.*, this issue], and several areas outside the Yellowstone caldera [*Wilcox*, 1944]. An increasing degree of crustal melting and magma storage promotes accumulation of mantle-derived basalt, which in turn sustains and amplifies crustal melting. Long-lived feedback between intrusion of basalt and silicic-to-intermediate magmatism should produce a hierarchy of crustal systems that reflect principally the transport rate, vertical distribution, and residence time of basaltic magma within the lithosphere (Figures 12, 15, and 16.). The largest silicic systems clearly require continued intrusion of basaltic magma in order to support high heat flow, hydrothermal systems, and sporadic eruption of phenocryst-poor silicic magma for lifetimes up to a few million years [*Smith and Shaw*, 1975; *Lachenbruch et al.*, 1976].

5. Recent work demonstrating various correlations among ε_{Nd}, ε_{Sr}, $\delta^{18}O$, and/or Pb-isotopic ratios within intrusive and extrusive orogenic suites from many regions has added further compelling evidence for the ubiquity of a basaltic end member in such systems. These studies include those by *Taylor and Silver* [1978], *Carter et al.* [1978], *Harmon and Halliday* [1980], *De Paolo* [1980], *Allègre and Ben Othman* [1980], and *Tilton and Barreiro* [1980]. From andesites to rhyolites (or diorites to adamellites) and from one crustal province to another, major differences in the proportions of mantle and crustal isotopic contributions are indicated; but the cited studies generally agree upon a crust/mantle mass-provenance ratio in the range 0.5 to 4 for most nontholeiitic orogenic magmas.

6. Finally, basaltic magma occurs in nearly all magmatic provinces. In addition to volcanic associations, the frequency of pre- and syn-granitoid gabbros, net-veined plutonic rocks, and synplutonic mafic to hybrid dikes (injected while a host granitoid was partially liquid) attests to the role of basalt in the batholithic environment.

In some regions of thick continental crust, batholith-scale magmatism has apparently taken place without a significant amount of basaltic penetration to shallow levels (e.g., the Oligocene San Juan volcanic field of Colorado and parts of the Hercynian belt of Europe). For such occurrences I would nonetheless argue that basalt at depth was equally fundamental, but by the very nature of the crustal-melting-feedback mechanism, only hybrids and their fractionated descendants were able to reach the shallow crust. In the two examples just given, I would refer skeptics to the San Francisco Peaks of Arizona and the Jurassic ring complexes of Nigeria, respectively, for analogs in which somewhat more favorable stress fields permitted penetration of thick crust by at least a few of the basalts otherwise trapped in the roots of the system. An exception that proves the basaltic rule may be the Himalayan leucogranites, for which highly radiogenic Nd- and Sr-isotopic values indicate almost pure remelting of old continental crust, apparently related to the extraordinary thermal effects of continental collision [*Allègre and Ben Othman*, 1980].

The lithospheric fractionation column. The conceptual viewpoints summarized in Figures 12, 15, and 16 derive principally from consideration of the compositional and volumetric evolution in time and space of many magmatic systems, particularly those that experienced large zoned eruptions (Figure 1). The viewpoints have much in common with *Shaw*'s [1980] analysis of fracture mechanisms of magma ascent, *Smith*'s [1979] volume-composition hierarchy of ash flow systems, and the thermomechanical models of distributed lithospheric extension presented by *Lachenbruch and Sass* [1978]. Convergent but not identical views have recently been stated by *Michard-Vitrac et al.* [1980] and by Halliday [in *Leake et al.*, 1980].

Reduced to essentials, much of the variability of lithospheric magmatism probably reflects interaction of the following first-order factors: rates of basaltic magma production and transport in the asthenosphere, stress states in the lithosphere, and the thickness, age, and composition of the crust. These control characteristic rates and modes of magma ascent, the depth distribution and configuration of basaltic bodies emplaced in the lithosphere, and the relative proportions of magma crystallizing within the lithosphere and erupting at the surface. Such factors in turn influence the integrated contact areas and residence times of the basaltic magmas intruding the crust, the amount and rate of crustal melting, the extent of hybridization, and the degree to which the affected crust is thickened, extended, or diapirically mobilized.

Figure 15 depicts two extreme modes of lithospheric magmatism under stress conditions both favorable and unfavorable to tectonic extension of the lithosphere. In the extensional mode (Figure 15*a* and *b*), intermittent injection of basalt promotes crustal melting, but separation of silicic liquids is efficient enough that neither hybridization nor advanced melting can produce a predominance of intermediate magmas. Figure 15*a* depicts a modest basaltic power supply, distributed injection of basalt, and relatively easy escape of both rhyolitic and basaltic magmas along extensional fractures (which could include hydrofractures created by the magmas themselves). The melting process would be amplified to the extent that discontinuities in lithology, density, or rheology favored aggregation of basaltic liquid within or at the base of the crust; such amplification would be a natural feedback response to production of buoyant silicic magma by crustal melting. Such a possibility in conjunction with an enhanced basaltic power supply, is illustrated in Figure 15*b*, a cartoon that depicts incipient rifts or protorifts of continental lithosphere. Models that are, in part, similar have been adapted to particular rock suites by *Barker et al.* [1975] and *Emslie* [1978]. Advanced rifting, on the other hand, apparently involves ascent of asthenospheric ultramafic rocks [*Lachenbruch and Sass*, 1978], axial separation of older lithosphere, and a consequent predominance of basalt in the magma suite erupted; this is very different from the distributed extension depicted here and the variety of magma compositions resulting from basaltic injection of continental crust.

The more complex evolution of many Cordilleran and continental interior 'calc-alkaline' magmatic centers, from early mafic and intermediate forerunners to large batholiths (Figures 15*c* and *d* and 12), can be considered with reference to the magma transport model of *Shaw* [1980]. Geologic evidence at both plutonic and eruptive levels suggests that the predominant mechanism of large-scale magma transport evolves with time from diking toward eventual diapiric mobilization of large crustal domains. *Shaw* [1980] summarized evidence for the tensile strength of partially molten rock, discussed the sensitivity of effective-stress regimes and patterns of magma injection to variations in the 'pore-fluid pressure' of interstitial melts, and concluded that upward propagation of magma by extensional fracture takes place at any depth and over a wide range of melt fractions. As any crustal volume is progressively injected by basalt, its center is heated more than its periphery. Consequent increases in degree of crustal melting and pore pressure enhance the susceptibility of the central region to failure, thereby progressively focusing the injection process. Hybridization between basalt and local melts is similarly focused, leading to a focal zone in which magma lenses are both larger and more modified than in the periphery. A well-focused 'source funnel' [cf. *Shaw*, 1980] would support a persistent intermediate volcanic center. If the crustal stress field were appropriate [*Nakamura*, 1977; *Nakamura and Uyeda*, 1980], such a center could be surrounded by a halo of secondary centers and monogenetic cones formed by eruption of magmas that are typically more primitive, owing to their simpler ascent paths, than those in the focus.

If intrusion of the crust by basaltic magma is long-lasting, extensive partial melting of crustal rocks in response to crystallization of the basalt is inevitable. The resulting local weakening of the crust tends to focus and promote further intrusion and hybridization of basalt. Feedback between dike injection and partial melting can apparently lead eventually to local ascent of increasingly silicic hybrid magmas along paths that become better established with time; ultimately, if the affected crustal domain is voluminous enough, wholesale mobilization of the focal zone can take place on a batholithic scale (Figures 15*d* and 12]. Seen from this point of view, the preheating caused by dike injection is intrinsic to diapiric mobilization; largely liquid diapirs are exceedingly unlikely [cf. *Shaw*, 1980].

Early in this evolution, the 'source' of magmas that reach shallow levels is largely the mantle, but the crustal contribution to initially basaltic melt lenses increases upward, with time, and toward the focus. At the batholithic stage, magmas separating from restite clearly have 'sources' in the immediate crust, but that crust itself could consist of virtually any proportion of mantle-derived basalt injected during the protracted preheating that culminated in diapiric mobilization.

A lithospheric domain affected by long-lived magmatism is thus conceived as a gigantic 'fractionation column' (Figure 12), wherein a plexus of ascending mafic magma fractionates refractory components, exchanges mobile components with transient fluids, promotes partial melting of crustal rocks, and undergoes diffusive exchange and liquid mixing with a variety of crustal compositions. Such a polybaric and multicomponent model accounts better for the observable hierarchies of natural systems, their longevity, and their evolution in structure, size, and composition than do: (1) diapiric ascent of each magma batch directly from its 'source;' (2) 'selective assimilation' of specified trace elements or isotopes by magma batches undergoing simple ascent; (3) simple mixing of end-member magmas; or (4) reaction-assimilation at particular levels of the crust, also essentially a two-member mixing process (plus cumulates).

One implication of the present model is that the compositional and thermal structure of the crust changes with time and depends critically upon the extrusion/intrusion ratio of basaltic magma as well as its total flux from the asthenosphere. Consistent with this view of crustal transformation are the conclusions of *Michard-Vitrac et al.*, [1980] and *Taylor* [1980], who ruled out two-member assimilation-fractionation as a general explanation of correlations between pairs of isotopic systems in igneous suites and tentatively appealed instead to mixing of mantle and crustal components either prior to or during melting of a compositionally zoned crust.

There appear to be no difficulties with the thermal and mass budgets of the present model. *Burnham* [1979*b*] and *Taylor* [1980], for instance, calculated that the heat content (including latent heats of crystallization) of basalt crystallizing in contact with crustal rocks could generate anatectic melts equal to 10%–50% of the mass of the basalt itself. If crustal rocks had already been preheated to a temperature appropriate to the beginning of melting, subsequent injections of basalt might provide sufficient heat to produce a mass of rhyolitic melt equal to or even greater than that of the newly injected basalt [*DePaolo*, 1981]. The thermal energy provided to the crust by basaltic intrusion can be viewed in terms of three components: preheating to the melting range of silicic magma, maintenance of partial-fusion temperatures against conductive and convective heat losses, and additional heat to cause the crustal melting anomaly to grow. The actual proportion of crustal melt generated by a given mass of injected basalt would depend upon the crustal lithologies, the available mass of H_2O, the preintrusive geothermal gradient, and the efficiency of convective cooling above the melting anomaly. The growing scale of crustal mobilization and the progressive compositional modification intrinsic to the model presented in Figures 12 and 15 are consistent with these relations. Protracted intrusive heating of the focal region must lead to higher melt fractions, to partial remelting of intrusions emplaced earlier, and ultimately to large-scale diapirism. The eventual growth of large crustal magma chambers is a consequence of the annealing or stress relaxation related to such preheating; *Shaw* [1980] discussed such growth in terms of local diminution of the tectonic stress differences requisite to extensional failure within the preheated domains.

Two extreme scenarios have been outlined, one producing a suite of predominantly mafic and silicic magmas (Figure 15*a*, *b*) and the other potentially generating a full spectrum of compositions from basalt to rhyolite (Figure 15*c*, *d*). Only a few systems appear to approximate such end members; as systems evolve through time and depth, many probably experience elements of both models. In the first model, extension of the lithosphere favors upward transport of both crustal melts and asthenosphere-derived basalts; the lithosphere may or may not be thinned, depending on the relative amounts of stretching, diking, and melting vis-a-vis basaltic underplating and sill formation [cf. *Lachenbruch and Sass*, 1978]. In the second model a nonextending lithosphere is less accommodating, and magma transport is a fitful process of percolation slow enough that fractionation and hybridization in a plexus of lenticular conduits [cf. *Shaw*, 1980] lead to a predominance of intermediate magmas; the crust and lithosphere may be thick-

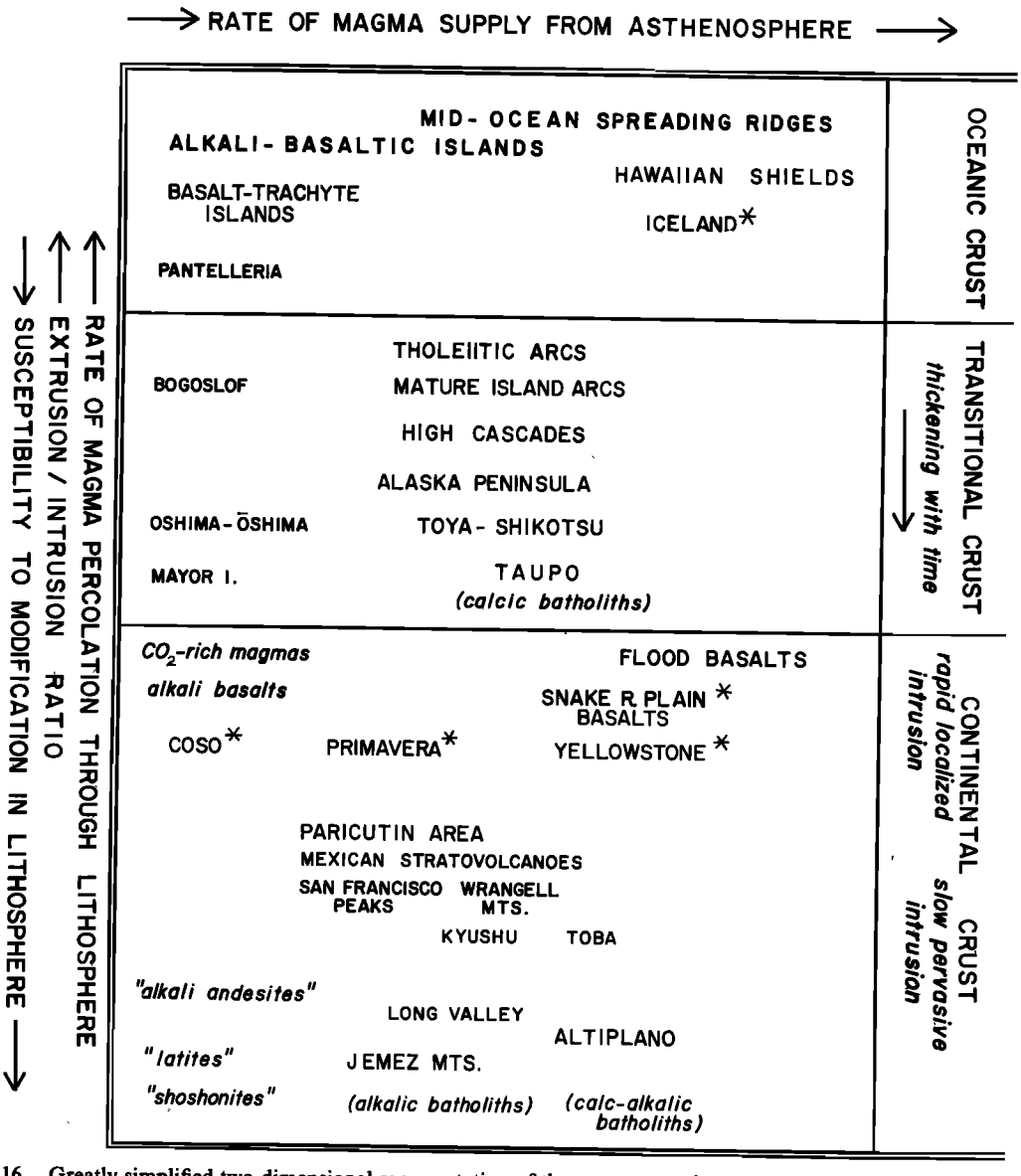

Fig. 16. Greatly simplified two-dimensional representation of the magma supply vs. percolation rate model of lithospheric magmatism discussed in the text. Note that 'magma supply' to the lithosphere and eruption rate are far from equivalent; they might differ by 1 to 3 orders of magnitude. See also Figures 12 and 15. Both axes are schematic and suggest only the relative magnitudes of supply and modification of primitive magma in the various systems represented. Important variables not depicted by the diagram include (1) the volatile flux, which can be critical to the differentiation of systems with low magma supply rates, and (2) the depth distribution of basaltic injection in the lithosphere. Stars indicate systems thought to be characterized by rapid transient injection of basalt at restricted crustal levels, resulting in generation and separation of rhyolite but few intermediates. In contrast, most continental and orogenic systems are thought to involve diffuse injection distributed throughout much of the lithosphere, with consequent hybridization and crustal mobilization leading to a predominance of intermediate magmas. Strict continuity between the three segments of the diagram is not implied, but the degree of potential modification of magmas obviously increases with crustal thickness, compositional contrast, and magma residence time. Although lithospheric extension can decrease the susceptibility of magmas to hybridization in the crust, it may, on the other hand, increase the likelihood of modification of magmas and their source volumes by mantle-derived volatiles.

ened significantly by the addition at depth of great volumes of basalt.

A more detailed analysis of the implications of particular stress regimes for particular styles of magmatic evolution is not presented here, but future effort along such lines appears to me as important for petrology as for tectonophysics. We need to know more about states of stress in the lithosphere and how they change with time and depth during the waxing and waning of a magmatic anomaly. We need to clarify how lateral and vertical changes in stress regime affect the transport, residence time, and composition of magmas. In particular we should ask how the orientations and relative magnitudes of principal stresses in the lithosphere affect the form, size, and rate of basaltic intrusion, the susceptibility of such basalt to interaction with lithospheric rocks, and the conditions favoring growth of magma chambers.

Figure 16 is a crude attempt to portray too many variables in two dimensions. In order to illustrate hierarchies of magma supply (not eruption) and degrees of magma modification, some gross generalizations have been made in ranking vol-

canic fields and provinces that are internally rather variable. Nonetheless, I think the heuristic value of the diagram outweighs the dangers of overinterpretation that its inherent oversimplicity invites. I present it here more as a way of regarding magmatism than as an expression of my present interpretive position on particular magmatic systems. With time, any evolving system should migrate within the diagram. Attention is directed to the following: (1) Extreme rates of crustal extension and mantle magma production culminate in flood basalts; toward the opposite extremes are small systems where the role of volatile components and crustal scavenging can be disproportionately large. (2) Most large silicic systems reflect intermediate rates of magma supply, and their growth and compositional evolution depend largely upon the rate and distribution of magma storage in thick or thickening crust (cf. Figure 15). (3) The three segments of the diagram are geologically significant and indicate that no volume-composition hierarchy of magmatic systems is independent of initial crustal condition.

The model summarized in Figures 12, 15, and 16 provides perspectives that may help to clarify several petrological puzzles: (1) The maturation of tholeiitic to 'calc-alkaline' arcs is a natural consequence of lengthening the 'fractionation column' by secular crustal intrusion. (2) The 'calc-alkaline' trend on an AFM diagram is a mixing line between basalt and crustal extracts that is extended by fractionation of the hybrids. (3) The shallow porphyries containing Cu and S anomalies, which are sometimes found in multipulse plutonic complexes of intermediate size and composition, are better understood as products of a complex distillation in a framework like Figure 15*d* than as primitive magma batches that ascended rapidly from their 'sources.' (4) Compositional and isotopic asymmetries across magmatic arcs [*Kuno*, 1959; *Kistler and Peterman*, 1973; *Armstrong et al.*, 1977; *Taylor and Silver*, 1978] may largely reflect inward changes in path length, percolation rate, magma-wallrock contrast, and the time-integrated degree of interaction between primitive magmas and the crust they traversed. Variations along arcs [*Brown et al.*, 1977; *Arculus and Johnson*, 1978; *Carr et al.*, 1979; *Hamilton*, 1979] can perhaps be explained in similar terms. The underthrusting of oceanic lithosphere need provide little more than perturbation of thermal gradients in the adjacent mantle. (5) Andesites that are not associated with concurrent subduction (e.g., Mt. Wrangell, Alaskan Mt. Edgecumbe, the San Francisco Peaks, Mt. Taylor, and many modest, late Cenozoic, alkalic intermediates in the western United States) are more plausibly explained by hybridization and fractionation of basalt than by appeal to imaginary relict 'slabs.' (6) The random intermingling of diorite, tonalite, and granodiorite with peraluminous granites in a single plutonic belt [*Harmon and Halliday*, 1980] can readily be explained if most 'S-type' and other peraluminous plutons grade down to 'I-type' roots. (7) Large ranges in mineralogy and composition among the plutonic or eruptive members of a given igneous complex [e.g., *Jacobson et al.*, 1958; *Smith*, 1979; *Bacon et al.*, this issue; *Mahood*, this issue] may simply reflect cycles of enrichment, rehomogenization, or crystallization that, in turn, reflect a fluctuating basaltic power supply.

Progress in understanding magmatism requires a broader, longer, and more dynamic view of magmatic systems. Major redistribution of components within shallow magma chambers is caused by liquid-state diffusion and by crystal-liquid and probably vapor-liquid fractionation. However, the magma chambers that evolve and the variety of magmas that produce them depend strongly upon the thermal, tectonic, and compositional history of the lithosphere below.

Acknowledgments. This work was initiated at Berkeley and has continued at the U. S. Geological Survey. It was provoked and in part supported by Ian Carmichael under NSF grant EAR-74-12782. Carmichael, Gail A. Mahood, H. R. Shaw, Charles R. Bacon, and Robert L. Smith substantially influenced the evolution of the ideas presented here. I was finally persuaded that andesites are not primary by David A. Johnston on a sunny summer day at Augustine, a volcano nearly, but not quite, devoid of basalt. Collaboration with Robert L. Christiansen, Roy A. Bailey, Robert E. Drake, Bacon, Johnston, Shaw, and Mahood has been its own reward. James R. O'Neil made me welcome in his laboratory, and Ronald W. Kistler and Allen C. Robinson graciously provided Sr-isotopic analyses. For stalwart support under sometimes outrageous conditions, I am grateful to successive Katmai companions Larry Jager, Anita L. Grunder, and Judy Fierstein. For meticulous technical support, I am indebted to Fierstein, Anne Gartner, and Dorothy Johnson. Thoughtful reviews by Bacon, Carmichael, Mahood, Shaw, and Rosalind Tuthill Helz improved the manuscript in both form and substance.

Any paper relying in part on interpretation of others' data owes many debts (and possibly apologies). In the present context, I am particularly grateful to Peter W. Lipman, Thomas A. Steven, Shigeo Aramaki, Bart Ekren, Hans Schmincke, and Yoshio Katsui for their impressive records of productivity and publication.

REFERENCES

Allègre, C. J., and D. Ben Othman, Nd-Sr isotopic relationship in granitoid rocks and continental crust development: A chemical approach to orogenesis, *Nature, 286,* 335–342, 1980.

Anderson, A. T., Magma mixing: Petrological process and volcanological tool, *J. Volcanol. Geotherm. Res., 1,* 3–33, 1976.

Andreasson, D., and A. Lunden, Isotope effect of thermal diffusion in some pure molten salts, *Z. Naturforsch., 25a,* 793–794, 1970.

Aoki, K., T. Sato, T. Takeuchi, and T. Tatsumi, Kuroko deposits and Towada and Hakkoda volcanoes, *Guideb. 3,* 53 pp., Int. Assoc. Genesis Ore Deposits, Tokyo, 1970.

Aramaki, S., the 1783 activity of Asama Volcano, Part II, *Jpn. J. Geol. Geogr., 28,* 11–33, 1957.

Aramaki, S., Some problems of the theory of caldera formation, *Kazan (Bull. Volcanol. Soc. Jpn.), 14,* 55–76, 1969.

Aramaki, S., and T. Ui, Aira and Ata pyroclastic flows and related caldera depressions in southern Kyushu, Japan, *Bull. Volcanol., 29,* 29–48, 1966*a*.

Aramaki, S., and T. Ui, Ata pyroclastic flows and the Ata Caldera in southern Kyushu, Japan, *Chishitsugaku Zasshi (J. Geol. Soc. Jpn.), 72,* 337–349, 1966*b*.

Aramaki, S., and T. Ui, Pyroclastic deposits in southern Kyushu—A correlation by the Ca-Mg-Fe ratios of the phenocrystic minerals, *Tokyo Daigaku Jishin Kenkyusho Iho (Bull. Earthquake Res. Inst. Tokyo Univ.), 51,* 151–182, 1976.

Aramaki, S., M. Takahashi, and T. Nozawa, Kumano acidic rocks and Okueyama complex; two examples of the granitic rocks in the outer zone of southwestern Japan, in *Plutonism in Relation to Volcanism and Metamorphism, Proceedings of the 7th Circum-Pacific Plutonism Project Meeting,* edited by N. Yamada, pp. 127–147, International Geological Correlation Program (UNESCO), Toyama, Japan, 1977.

Arculus, R. J., and R. W. Johnson, Criticism of generalized models for the magmatic evolution of arc-trench systems, *Earth Planet. Sci. Lett., 39,* 118–126, 1978.

Arculus, R. J., and K. J. A. Wills, The petrology of plutonic blocks and inclusions from the Lesser Antilles arc, *J. Petrol., 21,* 743–799, 1980.

Armstrong, R. L., W. P. Leeman, and H. E. Malde, K-Ar dating, Quaternary and Neogene volcanic rocks of the Snake River Plain, Idaho, *Am. J. Sci., 275,* 225–251, 1975.

Armstrong, R. L., W. H. Taubeneck, and P. O. Haes, Rb-Sr and K-Ar geochronology of Mesozoic granitic rocks and their Sr-isotopic composition, Oregon, Washington, and Idaho, *Geol. Soc. Am. Bull., 88,* 397–411, 1977.

Arth, J. G., Behavior of trace elements during magmatic processes—A summary of theoretical models and their applications, *J. Res. U. S. Geol. Surv., 4,* 41–47, 1976.

Bacon, C. R., R. Macdonald, and J. Metz, Petrogenesis of the Quater-

nary high-silica rhyolites of the Coso Range geothermal area, California, *Geol. Soc. Am., Abstr. Programs, 11,* 382, 1979.
Bacon, C. R., R. Macdonald, R. L. Smith, and P. A. Baedecker, Pleistocene high-silica rhyolites of the Coso volcanic field, Inyo County, California, *J. Geophys. Res.*, this issue, 1981.
Bailey, D. K., Crustal warping—A possible tectonic control of alkaline magmatism, *J. Geophys. Res., 69,* 1103–1111, 1964.
Bailey, D. K., Volatile flux, heat focussing, and the generation of magma, *Geol. J. Spec. Issue 2,* 177–186, 1970.
Bailey, D. K., and R. Macdonald, Fluorine and chlorine in peralkaline liquids and the need for magma generation in an open system, *Mineral. Mag., 40,* 405–414, 1975.
Bailey, R. A., G. B. Dalrymple, and M. A. Lanphere, Volcanism, structure, and geochronology of Long Valley caldera, Mono County, California, *J. Geophys. Res., 81,* 725–744, 1976.
Ballay, M., Le phénomène de Ludwig-Soret dans les aillages, *C. R. Hebd. Seances Acad. Sci., 183,* 603–604, 1926.
Barker, F., D. R. Wones, W. N. Sharp, and G. A. Desborough, The Pikes Peak batholith, Colorado Front Range, and a model for the origin of the gabbro-anorthosite-syenite-potassic granite suite, *Precambrian Res., 2,* 97–160, 1975.
Barnes, I., W. P. Irwin, and D. E. White, Global distribution of carbon dioxide discharges and major zones of seismicity, *Water-Resour. Invest. (U.S. Geol. Surv.), Open-File Rep. 78-39,* 12 pp., 1978.
Barth, T. F. W., The differentiation of a composite aplite from the Pribilof Islands, Alaska, *Am. J. Sci., Bowen Vol.,* 27–36, 1952.
Bateman, P. C., and B. W. Chappell, Crystallization, fractionation, and solidification of the Tuolumne Intrusive Series, Yosemite National Park, California, *Geol. Soc. Am. Bull., 90,* 465–482, 1979.
Bateman, P. C., L. D. Clark, N. K. Huber, J. G. Moore, and C. D. Rinehart, The Sierra Nevada batholith—A synthesis of recent work across the central part, *U. S. Geol. Surv. Prof. Pap. 414-D,* 46 pp., 1963.
Bateman, P. C., and W. J. Nokleberg, Solidification of the Mount Givens granodiorite, Sierra Nevada, California, *J. Geol., 86,* 563–579, 1978.
Best, M. G., R. T. Shuey, C. F. Caskey, and S. K. Grant, Stratigraphic relations of members of the Needles Range Formation at type localities in southwestern Utah, *Geol. Soc. Am. Bull., 84,* 3269–3278, 1973.
Best, M. G., S. K. Grant, and R. D. Holmes, Geologic map of the Miners Cabin Wash and Buckhorn Spring quadrangles, Beaver County, Utah, *U.S. Geol. Surv. Open-File Rep. 79-1612,* 13 pp., 1979.
Bhat, B. N., and R. A. Swalin, Thermotransport of silver in liquid gold, *Acta Metall., 20,* 1387–1396, 1972.
Bhat, B. N., S. P. Murarka, and R. A. Swalin, Thermotransport of beryllium and mercury in liquid sodium, *Scr. Metall., 7,* 523–528, 1973.
Bonnichsen, B., W. B. Travers, and M. Weathers, Regional doming and rhyolitic volcanism, Snake River Plain, Idaho, *Eos Trans. AGU, 54,* 512, 1973.
Bott, T. R., Separation by liquid thermal diffusion in a concentric cylinder column with one cylinder rotating, in *Chemeca 70,* pp. 35–48, Butterworths, Melbourne, 1970.
Bott, T. R., and J. J. B. Romero, Effect of variable annulus width on separation by liquid thermal diffusion in a concentric cylinder column, *Trans. Inst. Chem. Eng., 47,* 166–172, 1969.
Bowen, N. L., Diffusion in silicate melts, *J. Geol., 29,* 295–317, 1921.
Bowen, N. L., Phase equilibria bearing on the origin and differentiation of alkaline rocks, *Am. J. Sci., Daly Vol., 243-A,* 75–89, 1945.
Brown, G. C., and J. Hennessy, The initiation and thermal diversity of granite magmatism, *Phil. Trans. R. Soc. London (A), 288,* 631–643, 1978.
Brown, G. M., J. G. Holland, H. Sigurdsson, J. F. Tomblin, and R. J. Arculus, Geochemistry of the Lesser Antilles volcanic arc, *Geochim. Cosmochim. Acta, 41,* 785–801, 1977.
Buddington, A. F., and D. H. Lindsley, Iron-titanium oxide minerals and synthetic equivalents, *J. Petrol., 5,* 310–357, 1964.
Bunsen, R., Über die Prozesse der volkanischen Gesteinbildungen Islands, *Ann. Phys. Chem., 83,* 197–272, 1851.
Burnham, C. W., The importance of volatile constituents, in *The Evolution of the Igneous Rocks,* edited by H. S. Yoder, Jr., pp. 439–482, Princeton University Press, Princeton, N. J., 1979*a*.
Burnham, C. W., Magmas and hydrothermal fluids, in *Geochemistry of Hydrothermal Ore Deposits, 2nd ed.,* edited by H. L. Barnes, chap. 3, John Wiley, N. Y., 1979*b*.
Byers, F. M., Jr., Petrology of three volcanic suites, Umnak and Bogoslof islands, Aleutian Islands, Alaska, *Geol. Soc. Am. Bull., 72,* 93–128, 1961.
Byers, F. M., Jr., W. J. Carr, P. P. Orkild, W. D. Quinlivan, and K. A. Sargent, Volcanic suites and related cauldrons of Timber Mountain-Oasis Valley caldera complex, southern Nevada, *U. S. Geol. Surv. Prof. Pap. 919,* 70 pp., 1976.
Campbell, D. R., Stratigraphy of pre-Needles Range Formation ash-flow tuffs in the northern Needle Range and southern Wah Wah Mountains, Beaver County, Utah, *Brigham Young Univ. Geol. Stud., 25,* 31–46, 1978.
Carmichael, I. S. E., Pantelleri[illegible] liquids and their phenocrysts, *Mineral. Mag., 33,* 86–113, 1962.
Carmichael, I. S. E., The iron-titanium oxides of salic volcanic rocks and their associated ferromagnesian silicates, *Contrib. Mineral. Petrol., 13,* 36–64, 1967.
Carmichael, I. S. E., J. Nicholls, F. J. Spera, B. J. Wood, and S. A. Nelson, High-temperature properties of silicate liquids: Applications to the equilibration and ascent of basic magma, *Philos. Trans. R. Soc. London (A), 286,* 373–431, 1977.
Carr, M. J., W. I. Rose, and D. G. Mayfield, Potassium content of lavas and depth to the seismic zone in Central America, *J. Volcanol. Geotherm. Res., 5,* 387–401, 1979.
Carter, S. R., N. M. Evensen, P. J. Hamilton, and R. K. O'Nions, Neodymium and strontium evidence for crustal contamination of continental volcanics, *Science, 202,* 743–747, 1978.
Chappell, B. W., Granitoids from the Moonbi district, New England batholith, eastern Australia, *J. Geol. Soc. Aust., 25,* 267–283, 1978.
Chayes, F., The oceanic basalt-trachyte relation in general and in the Canary Islands, *Am. Mineral., 62,* 666–671, 1977.
Chayes, F., and E. G. Zies, Notes on some Mediterranean comendite and pantellerite specimens, *Year Book Carnegie Inst. Washington, 63,* 186–190, 1964.
Chiba, M., Genesis of magma producing pumice flow and fall deposits of Towada caldera, Japan, *Bull. Volcanol., 29,* 545–558, 1966.
Christiansen, E. H., J. V. Bikun, and D. M. Burt, Petrology and geochemistry of topaz rhyolites, western U.S.A., in Uranium Mineralization in Fluorine-Enriched Volcanic Rocks, edited by D. M. Burt and M. F. Sheridan, *Rep. GJBX-225,* pp. 38–122, U.S. Dep. of Energy, Washington, D. C., 1980.
Christiansen, R. L., Cooling units and composite sheets in relation to caldera structure, *Geol. Soc. Am. Spec. Pap. 180,* 29–42, 1979.
Christiansen, R. L., and H. R. Blank, Jr., Volcanic stratigraphy of the Quaternary rhyolite plateau in Yellowstone National Park, *U. S. Geol. Surv. Prof. Pap. 729-B,* 18 pp., 1972.
Christiansen, R. L., and P. W. Lipman, Cenozoic volcanism and plate-tectonic evolution of the western United States—Part II, Late Cenozoic, *Phil. Trans. R. Soc. London (A), 271,* 249–284, 1972.
Christiansen, R. L., P. W. Lipman, W. J. Carr, F. M. Byers, Jr., P. P. Orkild, and K. A. Sargent, Timber Mountain-Oasis Valley caldera complex of southern Nevada, *Geol. Soc. Am. Bull., 88,* 943–959, 1977.
Clocchiatti, R., Les cristaux de quartz des ponces de la Vallée des Dix Mille Fumées (Katmai, Alaska), *C. R. Hebd. Seances Acad. Sci., Ser. D., 274,* 3037–3040, 1972.
Clocchiatti, R., Les inclusions vitreuses des cristaux de quartz, *Mem. Hors-Ser. Soc. Geol. Fr., Mém. 122,* 1975.
Clusius, K., and G. Dickel, Neues verfahren zur Gasentmischung und Isotopentrennung, *Die Naturwissenschaften, 26,* 546, 1938.
Coats, R. R., Geology of the Jarbridge quadrangle, Nevada-Idaho, *U. S. Geol. Surv. Bull. 1141-M,* 24 pp., 1964.
Coleman, R. G., *Ophiolites,* 229 pp., Springer-Verlag, Berlin, 1977.
Compston, W., and B. W. Chappell, Sr-isotope evolution of granitoid source rocks, in *The Earth, Its Origin, Structure, and Evolution,* edited by M. W. McElhinny, pp. 377–426, Academic, New York, 1979.
Costesèque, P., and J. Schott, Fractionnement isotopique et thermodiffusion en milieu poreux pour quelques éléments importants en géochimie, *C. R. Hebd. Seances Acad. Sci., Ser. D., 282,* 1913–1916, 1976.
Costesèque, P., J.-P. Fortuné, and J. Schott, On the importance of thermal diffusion in the formation of brines in geothermal systems, paper presented at 2nd International Symposium on Water-Rock Interaction, Strasbourg, Aug. 17–25, 1977.
Cox, K. G., I. G. Gass, and D. I. Mallick, The peralkaline volcanic suite of Aden and Little Aden, South Arabia, *J. Petrol., 11,* 433–461, 1970.

Craig, H., J. E. Lupton, J. A. Welhan, and R. Poreda, Helium isotope ratios in Yellowstone and Lassen Park volcanic gases, *Geophys. Res. Lett., 5,* 897–900, 1978.

Craig, H., J. A. Welhan, K. Kim, R. Poreda, and J. E. Lupton, Geochemical studies of the 21°N EPR hydrothermal fluids, *Eos Trans. AGU, 61,* 992, 1980.

Crecraft, H. R., W. P. Nash, and S. H. Evans, Jr., Chemical evolution and development of compositional gradients in a silicic magma, *Geol. Soc. Am., Abstr. Programs, 11,* 406, 1979.

Crecraft, H. R., W. P. Nash, and S. H. Evans, Jr., Petrology, geochronology, and chemical evolution of the Twin Peaks rhyolite domes, Utah, *Top. Rep. DOE/ID/12079-4,* 200 pp., U. S. Dep. of Energy, Washington, D. C., 1980.

Crecraft, H. R., W. P. Nash, and S. H. Evans, Jr., Late Cenozoic volcanism at Twin Peaks, Utah; Part I: Geology and petrology, *J. Geophys. Res.,* this issue, 1981.

Cunningham, C. G., and T. A. Steven, Mount Belknap and Red Hills calderas and associated rocks, Marysvale volcanic field, west-central Utah, *U. S. Geol. Surv. Bull. 1468,* 34 pp., 1979.

Dandurand, J. L., J.-P. Fortuné, R. Perami, J. Schott, and F. Tollon, On the importance of mechanical action and thermal gradient in the formation of metal-bearing deposits, *Mineral. Deposita, 7,* 339–350, 1972.

de Groot, S. R. *L'Effet Soret,* North Holland, Amsterdam, 1947.

De Paolo, D. J., Sources of continental crust: Neodymium isotope evidence from the Sierra Nevada and Peninsular Ranges, *Science, 209,* 684–687, 1980.

Doe, B. R., W. R. Leeman, R. L. Christiansen, and C. E. Hedge, Lead and strontium isotopes and related trace elements as genetic tracers applied to the Quaternary rhyolite-basalt association of the Yellowstone Plateau volcanic field, U. S. A., *J. Geophys. Res.,* this issue, 1981.

Drake, R. E., Chronology of Cenozoic igneous and tectonic events in the central Chilean Andes—Latitudes 35°30′ to 36° S, *J. Volcanol. Geotherm. Res., 1,* 265–284, 1976.

Eaton, G. P., R. L. Christiansen, H. M. Iyer, A. M. Pitt, D. R. Mabey, H. R. Blank, Jr., I. Zietz, and M. E. Gettings, Magma beneath Yellowstone Park, *Science, 188,* 787–796, 1975.

Eggler, D. H., Water-saturated and undersaturated melting relations of Paricutin andesite and an estimate of water content in the natural magma, *Contrib. Mineral. Petrol., 34,* 261–271, 1972.

Eggler, D. H., and C. W. Burnham, Crystallization and fractionation trends in the system Andesite-H_2O-CO_2-O_2 at pressures to 10 kb., *Geol. Soc. Am. Bull., 84,* 2517–2532, 1973.

Eichelberger, J. C., Andesitic volcanism and crustal evolution, *Nature, 275,* 21–27, 1978.

Eichelberger, J. C., Lithic fragments in the Bandelier Tuff, Jemez Mountains, New Mexico, *J. Volcanol. Geotherm. Res., 5,* 115–134, 1979.

Eichelberger, J. C., and R. Gooley, Evolution of silicic magma chambers and their relationship to silicic volcanism, in *The Earth's Crust, Geophys. Monogr. Ser.,* vol. 20, edited by J. G. Heacock, pp. 57–77, AGU, Washington, D. C., 1977.

Ekren, E. B., R. E. Anderson, C. L. Rogers, and D. C. Noble, Geology of the northern Nellis A.F.B. Bombing and Gunnery Range, Nye County, Nevada, *U. S. Geol. Surv. Prof. Pap. 651,* 91 pp., 1971.

Ekren, E. B., F. M. Byers, Jr., R. F. Hardyman, R. F. Marvin, and M. L. Silberman, Stratigraphy, preliminary petrology, and some structural features of Tertiary volcanic rocks in the Gabbs Valley and Gillis Ranges, Mineral County, Nevada, *U. S. Geol. Surv. Bull. 1464,* 54 pp., 1980.

Ekren, E. B., D. H. McIntyre, and E. H. Bennett, Preliminary geologic map of the west half of Owyhee County, Idaho, *U. S. Geol. Surv. Open-File Rep. 78-341,* 1978.

Elston, W. E., R. C. Rhodes, P. J. Coney, and E. G. Deal, Progress report on the Mogollon Plateau volcanic field, southwestern New Mexico, 3, Surface expression of a pluton, *Spec. Publ. 5,* pp. 3–28, N. Mex. Geol. Soc., Albequerque, N. Mex., 1976.

Emslie, R. F., Anorthosite massifs, rapakivi granites, and late Proterozoic rifting of North America, *Precambrian Res., 7,* 61–98, 1978.

Estèbe, J., and J. Schott, Nouvelle méthode de détermination des coefficients de Soret, *C. R. Hebd. Seances Acad. Sci., Ser. D., 272,* 905–908, 1971.

Evans, S. H., Jr., and W. P. Nash, Low-temperature rhyolites from the Roosevelt geothermal area, Utah, *Geol. Soc. Am. Abstr. Programs, 7,* 1070, 1975.

Ewart, A., Mineralogy and petrogenesis of the Whakamaru ignimbrite in the Maraetai area of the Taupo volcanic zone, New Zealand, *N. Z. J. Geol. Geophys., 8,* 611–677, 1965.

Ewart, A., W. Hildreth, and I. S. E. Carmichael, Quaternary acid magma in New Zealand, *Contrib. Mineral. Petrol., 51,* 1–27, 1975.

Fenn, P. M., and W. C. Luth, Hazards in the interpretation of primary fluid inclusions in magmatic minerals, *Geol. Soc. Am. Abstr. Programs, 5,* 617, 1973.

Fenner, C. N., The Katmai magmatic province, *J. Geol., 34,* 673–772, 1926.

Fenner, C. N., The chemical kinetics of the Katmai eruption, *Am. J. Sci., 248,* 593–627, and 697–725, 1950.

Fiske, R. S. and O. T. Tobisch, Paleogeographic significance of volcanic rocks of the Ritter Range pendant, central Sierra Nevada, California, in *Mesozoic Paleogeography of the Western United States,* edited by D. G. Howell and K. A. McDougall, pp. 209–222, Society of Economic Paleontology and Mineralogy, Los Angeles, Calif., 1978.

Flynn, R. T., and C. W. Burnham, An experimental determination of rare-earth partition coefficients between a chloride-containing vapor phase and silicate melts, *Geochim. Cosmochim. Acta, 42,* 685–701, 1978.

Furry, W. H., R. C. Jones, and L. Onsager, On the theory of isotope separation by thermal diffusion, *Phys. Rev., 55,* 1083–1095, 1939.

Gaèta, F. S., and N. M. Cursio, Thermogravitational effect in macromolecular solutions, *J. Polymer Sci. 7,* 1697–1716, 1969.

Gibson, I. L., A pantelleritic welded ash-flow tuff from the Ethiopian rift valley, *Contrib. Mineral. Petrol., 28,* 89–111, 1970.

Gibson, I. L., The chemistry and petrogenesis of a suite of pantellerites from the Ethiopian rift, *J. Petrol., 13,* 31–44, 1972.

Gibson, I. L., A review of the geology, petrology, and geochemistry of the volcano Fantale, *Bull. Volcanol., 38,* 791–802, 1974.

Gibson, I. L., and G. P. L. Walker, Some composite rhyolite/basalt lavas and related composite dykes in eastern Iceland, *Proc. Geol. Assoc., 74,* 301–318, 1963.

Gorshkov, G. S., *Volcanism and the Upper Mantle,* 385 pp., Plenum, New York, 1970.

Grant, S. K., Stratigraphic relations of the Escalante Desert Formation near Lund, Utah, *Brigham Young Univ. Geol. Stud., 25,* 27–30, 1978.

Greene, R. C., Petrology of the welded tuff of Devine Canyon, southeastern Oregon, *U. S. Geol. Surv. Prof. Pap. 797,* 26 pp., 1973.

Grodzka, P. G., and B. Facemire, Clusius-Dickel separation: A new look at an old technique, *Separ. Sci., 12,* 103–169, 1977.

Gustafson, L. B., Porphyry copper deposits and calc-alkaline volcanism, in *The Earth, Its Origin, Structure, and Evolution,* edited by M. W. McElhinny, pp. 427–468, Academic, New York, 1979.

Hamilton, W., Petrology of rhyolite and basalt, northwestern Yellowstone Plateau, *U. S. Geol. Surv. Prof. Pap. 475-C,* 78–81, 1963.

Hamilton, W., Diabase sheets of the Taylor Glacier region, Victoria Land, Antarctica, *U. S. Geol. Surv. Prof. Pap. 456-B,* 71 pp., 1965.

Hamilton, W., Tectonics of the Indonesian region, *U. S. Geol. Surv. Prof. Pap. 1078,* 345 pp., 1979.

Harmon, R. S., and A. N. Halliday, Oxygen and strontium isotope relationships in the British late Caledonian granites, *Nature, 283,* 21–25, 1980.

Hay, R. L., Formation of the crystal-rich glowing avalanche deposits of St. Vincent, B.W.I., *J. Geol., 67,* 540–562, 1959.

Helz, R. T., Phase relations of basalts in their melting ranges at P_{H2O} = 5 kb., Part II, Melt compositions, *J. Petrol., 17,* 139–193, 1976.

Hess, P. C., Polymerization model for silicate melts, in *Physics of Magmatic Processes,* edited by R. B. Hargraves, pp. 3–48, Princeton University Press, Princeton, N. J., 1980.

Hildreth, W., The Bishop Tuff: Compositional zonation in a silicic magma chamber without crystal settling, *Geol. Soc. Am. Abstr. Programs, 8,* 918, 1976.

Hildreth, E. W., The magma chamber of the Bishop Tuff: Gradients in temperature, pressure, and composition, Ph.D. thesis, 328 pp., Univ. Calif., Berkeley, 1977.

Hildreth, W., The Bishop Tuff: Evidence for the origin of compositional zonation in silicic magma chambers, *Geol. Soc. Am. Spec. Pap. 180,* 43–75, 1979.

Hildreth, W., Novarupta 1912: Petrology of the ejecta, *Eos Trans. AGU, 61,* 66, 1980.

Hildreth, W., and A. L. Grunder, The Valley-of-Ten-Thousand-Smokes Tuff, II, Compositional and isotopic variability of the ejecta, *Geol. Soc. Am. Abstr. Programs, 12,* 111, 1980.

Hildreth, W., R. L. Christiansen, and J. R. O'Neil, Catastrophic iso-

topic modification of rhyolitic magma by creation of the Yellowstone caldera, *Geol. Soc. Am. Abstr. Programs, 12,* 111, 1980.
Hildreth, W., R. E. Drake, and W. D. Sharp, Voluminous late-Pleistocene ash-flow and caldera complex in the Andes of central Chile, *Geol. Soc. Am. Abstr. Programs, 13,* 61, 1981.
Hofmann, A. W., Diffusion in natural silicate melts: A critical review, in *Physics of Magmatic Processes,* edited by R. B. Hargraves, pp. 385–417, Princeton University Press, Princeton, N. J., 1980.
Holloway, J. R., Fluids in the evolution of granitic magmas: Consequences of finite CO_2 solubility, *Geol. Soc. Am. Bull., 87,* 1513–1518, 1976.
Hopson, C. A., Eruptive sequence at Mount St. Helens, Washington, *Geol. Soc. Am. Abstr. Programs, 3,* 138, 1971.
Hudson, T., J. G. Smith, and R. L. Elliott, Petrology, composition, and age of intrusive rocks associated with the Quartz Hill molybdenite deposit, southeastern Alaska, *Can. J. Earth Sci., 16,* 1805–1822, 1979.
Hurley, P. M., P. C. Bateman, H. W. Fairbairn, and W. H. Pinson, Jr., Investigation of initial Sr^{87}/Sr^{86} ratios in the Sierra Nevada plutonic province, *Geol. Soc. Am. Bull., 76,* 165–174, 1965.
Irwin, W. P., and I. Barnes, Tectonic relations of carbon dioxide discharges and earthquakes, *J. Geophys. Res., 85,* 3115–3121, 1980.
Jacobson, R. R. E., W. N. MacLeod, and R. Black, Ring complexes in the Younger Granite Province of Northern Nigeria, *Geol. Soc. London Mem. 1,* 72 pp., 1958.
Jambon, A., J.-P. Carron, and F. Delbove, Données préliminaires sur la diffusion dan les magmas hydratés: le césium dans une liquide granitique à 3 kb, *C. R. Hebd. Seances Acad. Sci., Ser. D., 287,* 403–406, 1978.
Johnston, D. A., Volatiles, magma mixing, and the mechanism of eruption of Augustine volcano, Alaska, Ph.D. thesis, 177 pp., Univ. of Wash., Seattle, 1978.
Katsui, Y., On the Shikotsu pumice-fall deposit, *Kazan (Bull. Volcanol. Soc. Jpn.), 2nd Ser., 4,* 33–48, 1959.
Katsui, Y., Evolution and magmatic history of some Krakatoan calderas in Hokkaido, Japan, *J. Fac. Sci. Hokkaido Univ., Ser. 4, 11,* 631–650, 1963.
Katsui, Y., Y. Ōba, S. Ando, S. Nishimura, Y. Masuda, H. Kurasawa, and H. Fujimaki, Petrochemistry of the Quaternary volcanic rocks of Hokkaido, North Japan, *J. Fac. Sci. Hokkaido Univ., Ser. 4, 18,* 449–484, 1978.
Katsui, Y., M. Yamamoto, S. Nemoto, and K. Niida, Genesis of calc-alkalic andesites from Oshima-Ōshima and Ichinomegata volcanoes, North Japan, *J. Fac. Sci. Hokkaido Univ., Ser. 4, 19,* 157–168, 1979.
Keith, J. D., Miocene porphyry intrusions, volcanism, and mineralization, southwestern Utah and eastern Nevada, M.S. thesis, Univ. Wis., Madison, 1980.
Kennedy, G. C., Some aspects of the role of water in rock melts, *Geol. Soc. Am. Spec. Pap. 62,* 489–504, 1955.
Kigoshi, K., T. Fukuoka, and S. Yokoyama, ^{14}C age of Tsumaya pyroclastic flow, Aira caldera, southern Kyushu, Japan, *Kazan (Bull. Volcanol. Soc. Jpn.), 17,* 1–8, 1972.
Kistler, R. W., and Z. E. Peterman, Variation in Sr, Rb, K, Na, and initial Sr^{87}/Sr^{86} in Mesozoic granitic rocks and intruded wall rocks in California, *Geol. Soc. Am. Bull., 84,* 3489–3512, 1973.
Kolbe, P., Geochemical investigations of the Cape Granite, southwestern Cape Province, South Africa, *Trans. Geol. Soc. S. Afr., 69,* 161–199, 1966.
Kolbe, P., and S. R. Taylor, Geochemical investigation of the granitic rocks of the Snowy Mountains area, New South Wales, *J. Geol. Soc. Aust., 13,* 1–25, 1966.
Korsching, H., and K. Wirtz, Trennung von flussigkeitsgemischen mittels kombinierten thermodiffusion und thermosiphonwirkung, *Die Naturwissenschaften, 27,* 110, 1939*a*.
Korsching, H., and K. Wirtz, Zur trennung von flussigkeitsgemischen im clusiusschen trennrohr (Trennung der zinkisotope), *Die Naturwissenschaften, 27,* 367–368, 1939*b*.
Krieger, M. H., Ash-flow tuffs of the Galiuro Volcanics in the northern Galiuro Mountains, Pinal County, Arizona, *U. S. Geol. Surv. Prof. Pap. 1104,* 32 pp. 1979.
Kuno, H., Origin of Cenozoic petrographic provinces of Japan and surrounding areas, *Bull. Volcanol., 20,* 37–76, 1959.
Lachenbruch, A. H., and J. H. Sass, Heat flow in the United States and the thermal regime of the crust, in *The Earth's Crust, Geophys. Monogr. 20,* edited by J. G. Heacock, pp. 626–275, AGU, Washington, D. C., 1977.
Lachenbruch, A. H., and J. H. Sass, Models of an extending lithosphere and heat flow in the Basin and Range province, in Cenozoic Tectonics and Regional Geophysics of the Western Cordillera, edited by R. B. Smith and G. P. Eaton, *Mem. Geol. Soc. Am., 152,* 209–250, 1978.
Lachenbruch, A. H., J. H. Sass, R. J. Munroe, and T. H. Moses, Jr., Geothermal setting and simple heat conduction models for the Long Valley caldera, *J. Geophys. Res., 81,* 769–784, 1976.
Larsson, W., Vulkanische asche vom ausbruch des chilenischen vulkans Quizapu (1932) in Argentine gesammelt, *Bull. Geol. Inst. Upsala, 26,* 27–52, 1936.
Lauer, H. V., Jr., Effect of glass composition on major element redox equilibria: $Fe^{2+}Fe^{3+}$, *Phys. Chem. Glasses, 18,* 49–52, 1977.
Lauer, H. V., Jr., and R. V. Morris, Redox equilibria of multivalent ions in silicate glasses, *J. Am. Ceram. Soc., 60,* 443–451, 1977.
Leake, B. E., G. C. Brown, and A. N. Halliday, The origin of granite magmas: A discussion, *J. Geol. Soc. London, 137,* 93–97, 1980.
Lipman, P. W., Chemical comparison of glassy and crystalline volcanic rocks, *U. S. Geol. Surv. Bull. 1201-D,* 24 pp., 1965.
Lipman, P. W., Mineral and chemical variations within an ash-flow sheet from Aso caldera, southwestern Japan: *Contrib. Mineral. Petrol., 16,* 300–327, 1967.
Lipman, P. W., Iron-titanium oxide phenocrysts in compositionally zoned ash-flow sheets from southern Nevada, *J. Geol., 79,* 438–456, 1971.
Lipman, P. W., Evolution of the Platoro caldera complex and related volcanic rocks, southeastern San Juan Mountains, Colorado, *U. S. Geol. Surv. Prof. Pap. 852,* 128 pp., 1975.
Lipman, P. W., and I. Friedman, Interaction of meteoric water with magma: An oxygen-isotope study of ash-flow sheets from southern Nevada, *Geol. Soc. Am. Bull., 86,* 695–702, 1975.
Lipman, P. W., R. L. Christiansen, and J. T. O'Connor, A compositionally zoned ash-flow sheet in southern Nevada, *U. S. Geol. Survey Prof. Pap. 524-F,* 47 pp. 1966.
Lipman, P. W., B. R. Doe, C. E. Hedge, and T. A. Steven, Petrologic evolution of the San Juan volcanic field, southwestern Colorado: Pb and Sr isotope evidence, *Geol. Soc. Am. Bull., 89,* 59–82, 1978.
Lloyd, F. E., and D. K. Bailey, Light element metasomatism of the continental mantle: The evidence and the consequences, *Phys. Chem. Earth, 9,* 389–416, 1975.
Lodding, A., and A. Ott, Isotope thermotransport in liquid potassium, rubidium, and gallium, *Z. Naturforsch., 21a,* 1344–1347, 1966.
López-Escobar, L., F. A. Frey, and M. Vergara, Andesites and high-alumina basalts from the central-south Chile High Andes: Geochemical evidence bearing on their petrogenesis, *Contrib. Mineral. Petrol., 63,* 199–228, 1977.
Ludwig, C., Diffusion zwischen ungleich erwarmten Orten gleich zusammengesetzter Lösungen, *Sitzungber. Akad. Wiss. Wien, Math. Naturwiss. Kl. Abt. 20,* 539, 1856.
Ludington, S., W. N. Sharp, D. McKowan, and F. Barker, The Redskin granite—A Proterozoic example of thermogravitational diffusion?, *Geol. Soc. Am. Abstr. Programs, 11,* 469, 1979.
Luhr, J. F., and I. S. E. Carmichael, The Colima volcanic complex, Mexico, I, *Contrib. Mineral. Petrol., 71,* 343–372, 1980.
Luth, W. C., R. H. Jahns, and O. F. Tuttle, The granite system at pressures of 4 to 10 kilobars, *J. Geophys. Res., 69,* 759–773, 1964.
Macdonald, R., Tectonic setting and magma associations, *Bull. Volcanol., 38,* 575–593, 1974.
Mahood, G. A., Contrasting trace element behavior in rhyolitic ash flows and lavas, Sierra La Primavera, Mexico, *Geol. Soc. Am., Abstr. Programs, 11,* 471, 1979.
Mahood, G. A., The geological and chemical evolution of a late Pleistocene rhyolitic center: The Sierra La Primavera, Jalisco, Mexico, Ph.D. thesis, 245 pp., Univ. Calif., Berkeley, 1980*a*.
Mahood, G. A., Geological evolution of a Pleistocene rhyolitic center—Sierra La Primavera, Jalisco, Mexico, *J. Volcanol. Geotherm. Res., 8,* 199–230, 1980*b*.
Mahood, G. A., Chemical evolution of a Pleistocene rhyolitic center—Sierra La Primavera, Jalisco, Mexico, *Contrib. Mineral. Petrol.,* in press, 1981*a*.
Mahood, G. A., A summary of the geology and petrology of the Sierra La Primavera, Jalisco, Mexico, *J. Geophys. Res.,* this issue, 1981*b*.
Mahood, G. A., and W. Hildreth, Pantelleria, A new interpretation, *Eos Trans. AGU, 61,* 1141, 1980.
Marjaniemi, D. K., Geologic history of an ash-flow sequence and its source area in the Basin and Range province of southeastern Arizona, Ph.D. thesis, 176 pp., Univ. Ariz., Tucson, 1970.

Marsh, B. D., On the cooling of ascending andesitic magma, *Phil. Trans. R. Soc. London (A), 288,* 611–625, 1978.
Marsh, B. D., Island arc development: Some observations, experiments, and speculations, *J. Geol., 87,* 687–713, 1979.
Marsh, B. D., Geology and petrology of northern Atka, Aleutian Islands, Alaska, *Geol. Soc. Am. Abstr. Programs, 12,* 476, 1980.
Masuda, Y., S. Nohda, and K. Okamoto, Major and trace element geochemistry of the Nohi rhyolitic volcanic rocks, central Japan, *Chishitsugaku Zasshi (J. Geol. Soc. Jpn.), 82,* 595–601, 1976.
McBirney, A. R., Mixing and unmixing of magmas, *Jour. Volcanol. Geotherm. Res., 7,* 357–371, 1980.
McBirney, A. R., and R. M. Noyes, Crystallization and layering of the Skaergaard intrusion, *J. Petrol., 20,* 487–554, 1979.
McCarthy, T. S., and R. G. Cawthorn, Changes in initial $^{87}Sr/^{86}Sr$ ratio during protracted fractionation in igneous complexes, *J. Petrol., 21,* 245–264, 1980.
McKee, E. H., Fish Creek Mountains Tuff and volcanic center, Lander County, Nevada, *U. S. Geol. Surv. Prof. Pap. 681,* 17 pp., 1970.
Metz, J., and C. R. Bacon, Quenched blobs of mafic magma in high-silica rhyolite of the Coso volcanic field, California, *Geol. Soc. Am. Abstr. Programs, 12,* 120, 1980.
Michard-Vitrac, A., F. Albarede, C. Dupuis, and H. P. Taylor, Jr., The genesis of Variscan (Hercynian) plutonic rocks: Inferences from Sr, Pb, and O studies on the Maladeta Igneous Complex, central Pyrenees (Spain), *Contrib. Mineral. Petrol., 72,* 57–72, 1980.
Miller, C. F., and L. J. Bradfish, An inner Cordilleran belt of muscovite-bearing plutons, *Geology, 8,* 412–416, 1980.
Miller, C. F., and D. W. Mittlefehldt, Rare-earth-element depletion accompanying differentiation of felsic plutonic rocks, *Geol. Soc. Am. Abstr. Programs, 11,* 479–480, 1979.
Miller, T. P., and R. L. Smith, Spectacular mobility of ash flows around Aniakchak and Fisher calderas, Alaska, *Geology, 5,* 173–176, 1977.
Moore, R. B., and E. W. Wolfe, Geologic map of the eastern San Francisco volcanic field, Arizona, *U. S. Geol. Surv. Misc. Invest. Map I-953,* 1976.
Moore, R. B., E. W. Wolfe, and G. E. Ulrich, Volcanic rocks of the eastern and northern parts of the San Francisco volcanic field, Arizona, *J. Res. U. S. Geol. Surv., 4,* 549–560, 1976.
Muehlenbachs, K., The oxygen isotope geochemistry of siliceous volcanic rocks from Iceland, *Year Book Carnegie Inst. Washington, 72,* 593–597, 1973.
Muehlenbachs, K., A. T. Anderson, Jr., and G. E. Sigvaldason, Low-O^{18} basalts from Iceland, *Geochim. Cosmochim. Acta, 38,* 577–588, 1974.
Myers, J. D., A. K. Sinha, and B. D. Marsh, The Edgecumbe volcanic field: A model for basalt-crust interaction, *Geol. Soc. Am. Abstr. Programs, 12,* 489, 1980.
Mysen, B. O., F. Seifert, and D. Virgo, Structure and redox equilibria of iron-bearing silicate melts, *Am. Mineral., 65,* 867–884, 1980*a*.
Mysen, B. O., D. Virgo, W. J. Harrison, and C. M. Scarfe, Solubility mechanisms of H_2O in silicate melts at high pressures and temperatures: a Raman spectroscopic study, *Am. Mineral., 65,* 900–914, 1980*b*.
Nagao, K., N. Takaoka, S. Matsuo, Y. Mizutani, and O. Matsubayashi, Change in rare gas composition of the fumarolic gases from the Showa-shinzan volcano, *Geochem. J., 14,* 139–143, 1980.
Nagasawa, H., and C. C. Schnetzler, Partitioning of rare-earth, alkali, and alkaline-earth elements between phenocrysts and acidic igneous magma, *Geochim. Cosmochim. Acta, 35,* 953–968, 1971.
Nakamura, K., Volcanoes as possible indicators of tectonic stress orientation—Principle and proposal, *J. Volcanol. Geotherm. Res., 2,* 1–16, 1977.
Nakamura, K., and S. Uyeda, Stress gradient in arc-back-arc regions and plate subduction, *J. Geophys. Res., 85,* 6419–6428, 1980.
Nelson, S. A., Geology and petrology of Volcán Ceboruco, Nayarit, Mexico, *Geol. Soc. Am. Bull., 91,* 2290–2431, 1980.
Nicholls, J., and I. S. E. Carmichael, Peralkaline acid liquids: A petrological study. *Contrib. Mineral. Petrol., 20,* 268–294, 1969.
Noble, D. C., Loss of sodium from crystallized comendite welded tuffs of the Miocene Grouse Canyon member of the Belted Range Ruff, Nevada, *Geol. Soc. Am. Bull., 81,* 2677–2688, 1970.
Noble, D. C., and R. L. Christiansen, Black Mountain volcanic center, *Rep. 19,* pp. 27–34, Nev. Bur. Mines Geol., Reno, 1974.
Noble, D. C., and C. E. Hedge, Sr^{87}/Sr^{86} variations within individual ash-flow sheets, *U. S. Geol. Surv. Prof. Pap. 650-C,* 133–139, 1970.
Noble, D. C., and D. F. Parker, Peralkaline silicic volcanic rocks of western United States, *Bull. Volcanol., 38,* 803–827, 1974.
Noble, D. C., R. W. Kistler, R. L. Christiansen, P. W. Lipman, and F. G. Poole, Close association in space and time of alkalic, calc-alkalic, and calcic volcansim in southern Nevada, *Geol. Soc. Am. Spec. Pap. 82,* 143, 1965.
Noble, D. C., K. A. Sargent, H. H. Mehnert, E. B. Ekren, and F. M. Byers, Jr., Silent Canyon Volcanic center, Nye County, Nevada, *Geol. Soc. Am. Mem., 110.* 65–75, 1968.
Ohmoto, H., and R. O. Rye, Isotopes of sulfur and carbon, in *Geochemistry of Hydrothermal Ore Deposits, 2nd. Ed.,* edited by H. L. Barnes, pp. 509–567, John Wiley, New York, 1979.
Okamoto, K., S. Nohda, Y. Masuda, and T. Matsumoto, Significance of Cs/Rb ratios in volcanic rocks as exemplified by the Nohi Rhyolite complex, central Japan, *Geochem. J., 9,* 201–210, 1975.
Ono, K., Y. Matsumoto, M. Miyahisa, Y. Teraoka, and N. Kambe, Geology of the Taketa district, *Geol. Surv. Jpn., Quad. Ser., Kagoshima. 15,* 23, 145 pp., 1977.
Orville, P. M., Alkali ion exchange between vapor and feldspar phases, *Am. J. Sci., 261,* 201–237, 1963.
Ott, A., L. Löwenberg, and A. Lodding, Isotope thermotransport in liquid indium metal, *Z. Naturforsch., 22a,* 2112–2113, 1967.
Perfit, M. R., H. Brueckner, J. R. Lawrence, and R. W. Kay, Trace element and isotopic variations in a zoned pluton and associated volcanic rocks, Unalaska Island, Alaska: A model for fractionation in the Aleutian calcalkaline suite, *Contrib. Mineral. Petrol., 73,* 69–87, 1980.
Pinheiro, J. de D. R. S., and T. R. Bott, A method of improving liquid thermal diffusion separations, *Separ. Sci., 11,* 193–199, 1976.
Pinheiro, J. de D. R. S., and T. R. Bott, Separation by thermal diffusion in a rotary column, *Separ. Sci., 12,* 485–497, 1977.
Piwinskii, A. J., Experimental studies of igneous rock series: Central Sierra Nevada batholith, California, *J. Geol., 76,* 548–570, 1968.
Piwinskii, A. J., and P. J. Wyllie, Experimental studies of igneous rock series: A zoned pluton in the Wallowa batholith, Oregon, *J. Geol., 76,* 205–234, 1968.
Piwinskii, A. J., and P. J. Wyllie, Experimental studies of igneous rock series: 'Felsic-body suite' from the Needle Point pluton, Wallowa batholith, Oregon, *J. Geol., 78,* 52–76, 1970.
Poreda, R., H. Craig, and J.-G. Schilling, $^3He/^4He$ variations along the Reykjanes Ridge, *Eos Trans. AGU, 61,* 1158, 1980.
Quinlivan, W. D., and F. M. Byers, Jr., Chemical data and variation diagrams of igneous rocks from the Timber Mountain-Oasis Valley caldera complex, southern Nevada, *U. S. Geol. Surv. Open-File Rep. 77-724,* 9 pp., 1977.
Ratté, J. C., and T. A. Steven, Ash flows and related volcanic rocks associated with the Creede caldera, San Juan Mountains, Colorado, *U. S. Geol. Surv. Prof. Pap. 524-H,* 58 pp., 1967.
Rhodes, R. C., Volcanic geology of the Mogollon Range and adjacent areas, Catron and Grant Counties, New Mexico, *Spec. Publ. N. Mex. Geol. Soc., 5,* 42–50, 1976*a*.
Rhodes, R. C., Petrologic framework of the Mogollon Plateau volcanic ring complex, New Mexico—Surface expression of a major batholith, *Spec. Publ. N. Mex. Geol. Soc., 5,* 103–112, 1976*b*.
Rinehart, C. D., and D. C. Ross, Geology of the Casa Diablo Mountain quadrangle, California, *U. S. Geol. Surv. Map GQ-99,* 1957.
Rinehart, C. D., and D. C. Ross, 1964, Geology and mineral deposits of the Mount Morrison quadrangle, Sierra Nevada, California, *U. S. Geol. Surv. Prof. Pap. 385,* 106 pp., 1964.
Ritchey, J. L., Origin of divergent magmas at Crater Lake, Oregon, Ph.D. thesis, 209 pp., Univ. Oregon, Eugene, 1979.
Ritchey, J. L., Divergent magmas at Crater Lake, Oregon: Products of fractional crystallization and vertical zoning in a shallow, water-undersaturated chamber, *J. Volcanol. Geotherm. Res., 7,* 373–386, 1980.
Robinson, H. H., The San Francisco volcanic field, Arizona, *U. S. Geol. Surv. Prof. Pap. 76,* 213 pp., 1913.
Rutherford, W. M., Separation of isotopes in the thermal diffusion column, *Separ. Purif. Methods, 4,* 305–350, 1975.
Ryerson, F. J., and P. C. Hess, Implications of liquid-liquid distribution coefficients to mineral-liquid partitioning, *Geochim. Cosmochim. Acta, 42,* 921–932, 1978.
Ryerson, F. J., and P. C. Hess, The role of P_2O_5 in silicate melts, *Geochim. Cosmochim. Acta, 44,* 611–624, 1980.
Rytuba, J. J., and R. K. Glanzman, Relation of mercury, uranium,

and lithium deposits to the McDermitt caldera complex, Nevada-Oregon, *Rep. 33,* pp. 109–117, Nev. Bur. Mines, Reno, 1979.

Sack, R. O., I. S. E. Carmichael, M. Rivers, and M. S. Ghiorso, Ferric-ferrous equilibria in natural silicate liquids at 1 bar, *Contrib. Mineral. Petrol., 75,* 369–376, 1980.

Sass, J. H., and A. H. Lachenbruch, Thermal regime of the Australian continental crust, in *The Earth, Its Origin, Structure, and Evolution,* edited by M. W. McElhinny, pp. 301–351, Academic, New York, 1979.

Schmincke, H.-U., Petrologie der phonolithischen bis rhyolithischen vulkanite auf Gran Canaria, Kanarische Inseln, Habilitationsschrift, Ruprecht-Karl-Universität zu Heidelberg, 136 pp., 1969*a*.

Schmincke, H.-U., Ignimbrite sequence on Gran Canaria, *Volcanology, 33,* 1199–1219, 1969*b*.

Schott, J., Contribution à l'étude de la thermodiffusion dans des milieux poreux—Application aux possibilités de concentrations naturelles, Ph.D. thesis, 573, 198 pp., Univ. Paul Sabatier de Toulouse, Toulouse, France, 1973.

Schott, J., and P. Costesèque, Effet thermogravitationnel et concentrations sélectives dans les magmas, Hautes Températures et Sciences de la Terre, Table Ronde du CNRS, 11 pp., Toulouse, France, 1978.

Scott, R. B., Alkali exchange during devitrification and hydration of glasses in ignimbrite cooling units, *J. Geol., 79,* 100–110, 1971.

Shaw, H. R., Comments on viscosity, crystal settling, and convection in granitic magmas, *Am. J. Sci., 263,* 120–152, 1965.

Shaw, H. R., Rheology of basalt in the melting range, *J. Petrol., 10,* 510–535, 1969.

Shaw, H. R., Viscosities of magmatic silicate liquids: An empirical method of prediction, *Am. J. Sci., 272,* 870–893, 1972.

Shaw, H. R., Diffusion of H_2O in granitic liquids, Geochemical Transport and Kinetics, edited by A. W. Hofmann et al., *Publ. 634,* pp. 139–170, Carnegie Inst. Wash., Washington, D. C., 1974.

Shaw, H. R., The fracture mechanisms of magma transport from the mantle to the surface, in *Physics of Magmatic Processes,* edited by R. B. Hargraves, pp. 201–264, Princeton University Press, Princeton, N. J., 1980.

Shaw, H. R., R. L. Smith, and W. Hildreth, Thermogravitational mechanisms for chemical variations in zoned magma chambers, *Geol. Soc. Am. Abstr. Programs, 8,* 1102, 1976.

Sigurdsson, H., and R. S. J. Sparks, Petrology of rhyolitic and mixed magma ejecta from the 1875 eruption of Askja, Iceland, *J. Petrol., 22,* 41–81, 1981.

Sigvaldason, G. E., S. Steinthorsson, N. Oskarsson, and P. Imsland, The simultaneous production of basalts, enriched and depleted in large lithophilic trace ions (LIL), within the same fissure swarms in Iceland, *Bull. Soc. Geol. Fr., 18,* 863–867, 1976.

Smith, R. L., Ash flows, *Geol. Soc. Am. Bull., 71,* 795–842, 1960.

Smith, R. L., Ash-flow magmatism, *Geol. Soc. Am. Spec. Pap. 180,* 5–27, 1979.

Smith, R. L., and R. A. Bailey, The Bandelier Tuff A study of ash-flow eruption cycles from zoned magma chambers, *Bull. Volcanol., 29,* 83–104, 1966.

Smith, R. L., and H. R. Shaw, Igneous-related geothermal systems, Assessment of Geothermal Resources of the United States, edited by D. E. White and D. L. Williams, *Circ. 726,* pp. 58–83, U. S. Geol. Surv., Washington, D. C., 1975.

Smith, R. L., R. A. Bailey, and C. S. Ross, Geologic map of the Jemez Mountains, New Mexico, *U.S. Geol. Surv. Misc. Invest. Map I-571,* 1970.

Sommer, M. A., Volatiles H_2O, CO_2, and CO in silicate melt inclusions in quartz phenocrysts from the rhyolitic Bandelier air-fall and ash-flow tuff, New Mexico, *J. Geol., 85,* 423–432, 1977.

Soret, C., Une dissolution saline primitivement homogène dont deux parties sont portées a des températures différentes, *Arch. Sci. Phys. Natur., 7,* 48–61, 1879.

Soret, C., Influence de la température sur la distribution des sels dans leurs solutions, *C. R. Hebd. Seances Acad. Sci., 91,* 289–291, 1880.

Sparks, S. R. J., H. Sigurdsson, and L. Wilson, Magma mixing: A mechanism for triggering acid explosive eruptions, *Nature, 267,* 315–318, 1977.

Spera, F. J., Aspects of the thermodynamic and transport behavior of basic magmas, Ph.D. thesis, 178 pp., Univ. Calif., Berkeley, 1977.

Steven, T. A., and P. W. Lipman, Calderas of the San Juan volcanic field, southwestern Colorado, *U. S. Geol. Surv. Prof. Pap. 958,* 35 pp., 1976.

Strong, D. F., and W. L. Dickson, Geochemistry of Paleozoic granitoid plutons from contrasting tectonic zones of northeast Newfoundland, *Can. J. Earth Sci., 15,* 145–156, 1978.

Stuckless, J. S., and J. R. O'Neil, Petrogenesis of the Superstition-Superior volcanic area as inferred from strontium- and oxygen-isotopic studies, *Geol. Soc. Am. Bull., 84,* 1987–1998, 1973.

Taylor, H. P., Jr., Oxygen and hydrogen isotope evidence for large-scale circulation and interaction between ground waters and igneous intrusions, with particular reference to the San Juan volcanic field, Colorado, in Geochemical Transport and Kinetics, edited by A. W. Hoffmann et al., *Carnegie Inst. Washington Publ. 634,* 299–324, Washington, D. C., 1974.

Taylor, H. P., Jr., Water/rock interactions and the origin of H_2O in granitic batholiths, *J. Geol. Soc. London, 133,* 509–558, 1977.

Taylor, H. P., Jr., The effects of assimilation of country rocks by magmas on $^{18}O/^{16}O$ and $^{87}Sr/^{86}Sr$ systematics in igneous rocks, *Earth Planet. Sci. Lett., 47,* 243–254, 1980.

Taylor, H. P., Jr., and R. W. Forester, An oxygen and hydrogen isotope study of the Skaergaard Intrusion and its country rocks: A description of a 55-m.y. old fossil hydrothermal system, *J. Petrol., 20,* 355–419, 1979.

Taylor, H. P., Jr., and L. T. Silver, Oxygen-isotope relationships in plutonic igneous rocks of the Peninsular Ranges batholith, southern and Baja California, *U. S. Geol. Surv. Open-File Rep. 78-701,* 423–426, 1978.

Thorarinsson, S., *The Eruption of Hekla 1947–1948, 1,* 183 pp., H. F. Leiftur, Reykjavik, 1967.

Tilton, G. R., and B. A. Barreiro, Origin of lead in Andean calc-alkaline lavas, southern Peru, *Science, 210,* 1245–1247, 1980.

Truesdell, A. H., Ion-exchange constants of natural glasses by the electrode method, *Am. Mineral., 51,* 110–122, 1966.

Tsuya, H., S. Tsuboi, F. Kishinouye, R. Takahasi, C. Tsuboi, K. Nakata, and N. Miyabe, The eruption of Komagatake, Hokkaido, in 1929, *Tokyo Daigaku Jishin Kenkyusho Iho (Bull. Earthquake Res. Inst. Tokyo Univ.), 8,* 237–270, 1930.

Turner, J. S., *Buoyancy Effects in Fluids,* 367 pp., Cambridge Univ. Press, London, 1973.

Turner, J. S., Double-diffusive phenomena, *Annu. Rev. Fluid Mech., 6,* 37–56, 1974.

Turner, J. S., A fluid-dynamical model of differentiation and layering in magma chambers, *Nature, 285,* 213–215, 1980.

Tuttle, O. F., and N. L. Bowen, Origin of granite in the light of experimental studies in the system $NaAlSi_3O_8 - KAlSi_3O_8 - SiO_2 - H_2O$, *Geol. Soc. Am. Mem. 74,* 153 pp., 1958.

Tyrrell, H. J. V., *Diffusion and Heat Flow in Liquids,* 319 pp., Butterworths, London, 1961.

Ui, T., Genesis of magma and structure of magma chamber of several pyroclastic flows in Japan, *J. Fac. Sci. Univ. Tokyo. Sec. 2, 18,* 53–127, 1971.

van Bemmelen, R. W., and M. G. Rutten, *Table Mountains of Northern Iceland,* 217 pp., E. J. Brill, Leiden, 1955.

Villari, L., The island of Pantelleria, *Bull. Volcanol., 38,* 689–724, 1974.

Vincent, P. M., Les volcans tertiaires et quaternaires du Tibesti occidental et central (Sahara du Tchad), *Bur. Rech. Geol. Minieres, Mem. 23,* 297 pp., 1963.

Vincent, P. M., The evolution of the Tibesti volcanic province, eastern Sahara, in *African Magmatism and Tectonics,* edited by T. N. Clifford and I. G. Gass, pp. 301–319, Hafner, Darien, Conn., 1970.

Walker, G. P. L., Crystal concentration in ignimbrites, *Contrib. Mineral. Petrol., 36,* 135–146, 1972.

Walker, D., C. E. Lesher, and J. F. Hays, Soret separation of lunar liquid, *Lunar Planet. Sci. Abstr., 12,* 1130–1132, 1981.

Warshaw, C. M., and R. L. Smith, Ferromagnesian silicates in the Bandelier Tuff, *Geol. Soc. Am. Abstr. Programs, 12,* 545, 1980.

Watson, E. B., Two-liquid partition coefficients: Experimental data and geochemical implications, *Contrib. Mineral. Petrol.,* 56, 119–134, 1976.

Watson, E. B., Partitioning of manganese between forsterite and silicate liquid, *Geochim. Cosmochim. Acta, 41,* 1363–1374, 1977.

Watson, E. B., Diffusion of cesium ions in H_2O-saturated granitic melt, *Science, 205,* 1259–1260, 1979.

Weathers, M. S., B. Bonnichsen, and W. B. Travers, Low-silica rhyolites from the Snake River Plain, Idaho, *Eos Trans. AGU, 54,* 512, 1973.

Wendlandt, R. F., and W. J. Harrison, Rare-earth partitioning be-

tween immiscible carbonate and silicate liquids and CO_2 vapor: Results and implications for the formation of light-rare-earth-enriched rocks, *Contrib. Mineral. Petrol., 69,* 409–419, 1979.
Westerveld, J., Quaternary volcanism on Sumatra, *Geol. Soc. Am. Bull., 63,* 561–594, 1952.
White, A. J. R., and B. W. Chappell, Ultrametamorphism and granitoid genesis, *Tectonophysics, 43,* 7–22, 1977.
White, A. J. R., I. S. Williams, and B. W. Chappell, The Jindabyne thrust and its tectonic, physiographic, and petrogenetic significance, *J. Geol. Soc. Aust., 23,* 105–112, 1976.
Whittaker, E. J. W., and R. Muntus, Ionic radii for use in geochemistry, *Geochim. Cosmochim. Acta, 34,* 945–956, 1970.
Wilcox, R. E., The rhyolite-basalt complex on Gardiner River, Yellowstone Park, Wyoming, *Geol. Soc. Am. Bull., 55,* 1047–1080, 1944.
Williams, H., The Geology of Crater Lake National Park, Oregon, with a reconnaissance of the Cascade Range southward to Mount Shasta, *Carnegie Inst. Washington Publ. 540,* 162 pp., 1942.
Wilshire, H. G., The Prospect alkaline diabase-picrite intrusion, New South Wales, Australia, *J. Petrol., 8,* 97–163, 1967.
Winter, F. R., and H. G. Drickamer, Thermal diffusion in liquid metals, *J. Phys. Chem., 59,* 1229–1230, 1955.
Witkind, I. J., Geology of the Tepee Creek quadrangle, Montana-Wyoming, *U. S. Geol. Survey Prof. Pap. 609,* 101 p., 1969.
Wright, T. L., and R. T. Okamura, Cooling and crystallization of tholeiitic basalt, 1965 Makaopuhi Lava Lake, Hawaii, *U. S. Geol. Surv. Prof. Pap. 1004,* 78 pp., 1977.
Wyllie, P. J., Crustal anatexis: An experimental review, *Tectonophysics, 43,* 41–71, 1977.
Wyllie, P. J., Magmas and volatile components, *Am. Mineral., 64,* 469–500, 1979.
Yoder, H. S., Jr., Contemporaneous basaltic and rhyolitic magmas, *Am. Mineral., 58,* 153–171, 1973.
Yokoyama, I., Structure of caldera and gravity anomaly, *Bull. Volcanol. 26,* 67–72, 1963.
Yokoyama, S., Mode of movement and emplacement of Ito pyroclastic flow from Aira caldera, Japan, *Tokyo Kyoiku Daigaku Chishisugaku Kobutsugaku Kyoshitsu Kenkyu Hokoku, C, 12,* 17–62, 1974.
Zies, E. G., Chemical analysis of two pantellerites, *J. Petrol., 1,* 304–308, 1960.

(Received January 20, 1981;
revised May 11, 1981;
accepted May 14, 1981.)

JOURNAL OF GEOPHYSICAL RESEARCH, VOL. 86, NO. B11, PAGES 10193–10199, NOVEMBER 10, 1981

Partitioning of Rare Earths and Other Trace Elements Between Sanidine and Coexisting Volcanic Glass

WILLIAM P. LEEMAN

Geology Department, Rice University, Houston, Texas 77001

DAVID W. PHELPS

Lockheed, Houston, Texas 77058

Major and trace element contents have been measured for sanidine-glass pairs separated from eight high-SiO_2 rhyolite lavas from the Yellowstone volcanic field. Sanidine/glass partition coefficients for most elements based on these data are uniform to within the cumulative analytical errors. This uniformity reflects similarities in major element compositions and inferred physical conditions for the analyzed samples, which are considered representative of most Yellowstone rhyolites. Of particular note are very high partition coefficients for Ba (~22), Sr (~28), and Eu (~9), relative to the sparse data for other rhyolites available in the literature. With the exception of Na, K, and Pb, which have sanidine/glass partition coefficients of approximately unity, all other elements determined are strongly fractionated into the melt phase relative to sanidine. These data may be used in modeling crystallization of sanidine from Yellowstone or other rhyolites or anatexis of crustal rocks containing sanidine (or K-feldspar sensu lato), but only with due caution. In particular, the wide range in reported partition coefficients for those elements (Sr, Ba, Eu) strongly incorporated in sanidine suggests that compositional and physical characteristics exert significant influence on these values. Accordingly, applicable partition coefficients are poorly known for these elements in most systems. Care must be taken to select appropriate values or to measure these partition coefficients directly in specific suites of rocks. Difficulties with direct experimental studies in silicic magmas seemingly preclude systemization of element partitioning at present.

INTRODUCTION

As part of a study of rhyolites from the Snake River Plain-Yellowstone province, glass and sanidine separates from seven rhyolite flows have been analyzed by instrumental neutron activation analysis. These data provide a set of sanidine/glass (= liquid) partition coefficients that may be used in detailed petrogenetic modeling studies for high-silica rhyolite magmas. Very few such data have been published previously; these data generally represent a limited number of samples from any given area and apply to liquid compositions of a less siliceous character [*Schnetzler and Philpotts,*, 1970; *Nagasawa*, 1971, 1973; *Ewart et al.*, 1977].

K-feldspar/liquid partition coefficients are essential to evaluate partial melting processes of 'granitic' crustal rocks, crystal/liquid fractionation processes in rhyolitic magmas, etc., because K-feldspar is a major phase in these silicic systems. It is difficult to obtain such data via direct experimental studies owing to the well-known sluggishness of reactions in silicic melts. Thus, an empirical approach, utilizing glassy volcanic rocks, provides a practical method of acquiring partition coefficient data. Some problems associated with this method are evident. One must demonstrate or assume that the analyzed coexisting phases are homogeneous (or nearly so), and that they represent an equilibrium assemblage. The effects of impurities in the analyzed phases also must be considered. In utilizing the results, one must consider possible variances in partition coefficients as a function of temperature and liquid or solid composition. These latter effects must await further study before they can be fully characterized.

Copyright © 1981 by the American Geophysical Union.

Paper number 1B0528.
0148-0227/81/001B-0528$01.00

SAMPLES STUDIED

The samples utilized in this study are representative of rhyolite flows from the Yellowstone Plateau volcanic complex [*Christiansen and Blank*, 1972; *Christiansen*, 1981]. K-Ar age determinations [J. D. Obradovich, personal communication, 1975; *Friedman et al.*, 1974] indicate that most of the flows (Central Plateau Member) postdate collapse of the Yellowstone caldera associated with eruption of the Lava Creek Tuff (0.6 m.y. ago); one sample predates that event (1.15 m.y. old). The bias in sampling toward young eruptive materials is dictated by the difficulty to obtain fresh glass from many of the older flows. All of our samples appear to be fresh. All are dominantly glassy and contain less than about 10% phenocrysts of quartz and sanidine. Minor phenocryst and microphenocryst phases include ferroaugite, magnetite, rare fayalitic olivine, and ilmenite and trace accessory zircon, allanite and chevkinite [cf., *Christiansen*, 1981].

Glasses from these samples have been analyzed for major element composition by electron microprobe. All are high silica rhyolites containing about 77% SiO_2 on an anhydrous basis (see Table 1). These glasses have very low contents of CaO and MgO and are suitably represented by the system $KAlSi_3O_8$-$NaAlSi_3O_8$-SiO_2. In this system, normative components calculated for the glasses plot near the ternary minimum appropriate for 0.5 kb P_{H_2O}. Direct analysis of fresh glasses indicates that they contain less than 0.5% H_2O^+ (I. Friedman, personal communication, 1976). The absence of hydrous phenocryst phases in the flows studied indicates that the corresponding magmas probably were not water-saturated. Fe-Ti oxide geothermometry (W. Hildreth, personal communication, 1980) for many of these flows indicates relatively high and uniform liquidus temperatures (ca. 850°–900°C.)

TABLE 1. Electron Microprobe Analyses of Yellowstone Glasses

	YG70-13	YG70-10	0CB66-09*	YG72-5	72-0-75	6YC-143*	6YC-148*	0YC-601
SiO_2	77.3	78.1	77.2	77.7	77.4	76.9	77.5	77.9
TiO_2	0.14	0.11	0.07	0.10	0.13	0.09	0.10	0.08
Al_2O_3	11.1	11.3	11.9	11.4	11.7	11.9	11.9	11.1
FeO	1.49	1.46	1.32	1.37	1.13	1.47	0.98	0.78
MnO	0.04	0.05	...	0.01	0.03	...	...	0.03
MgO	0.02	0.02	0.01	0.02	0.01	0.05	0.03	0.02
CaO	0.45	0.45	0.44	0.41	0.33	0.49	0.43	0.39
Na_2O	3.26	3.18	3.73	3.27	3.03	3.58	3.52	2.97
K_2O	5.16	5.24	5.38	5.17	5.73	5.47	5.55	5.74
P_2O_5	...	...	0.02	0.02	...	0.01	0.02	...
Total	98.96	99.91	100.07	99.47	99.49	99.96	100.03	99.01
n†	15	16	10	13	17	10	10	13

* Analyses made at University of Oregon (WPL); all others at NASA-JSC (DWP).
† Number of point analyses averaged.

The sanidine phenocrysts likewise have been analyzed via electron microprobe. They exhibit little zoning and typically vary in composition by about 2% Or or less in any given sample. The range in composition for all samples is about Or_{50}-Or_{55} (Table 2). In the samples analyzed, there is little textural evidence of exsolution, resorption, reverse (or other) zoning, etc., that would suggest significant disequilibria between sanidine and coexisting magma.

For the purposes of this study it will be assumed that the glasses represent quenched liquids that were in equilibrium with the sanidines with respect to the minor and trace elements determined. In support of this assumption, we note that coexisting sanidine and glass from two of the flows have indistinguishable Pb isotopic compositions [*Leeman*, 1979].

Experimental Details

Sanidine and glass phases were separated by conventional heavy liquid and magnetic separation techniques, then further purified by hand-picking under a microscope. The analyzed separates approach 100% purity for glass and exceed 95% purity for sanidine. In the samples studied the only significant impurity is quartz, which could not be entirely removed from all of the sanidine separates. The quartz impurity only mildly dilutes the concentrations of the elements determined.

Splits of these materials (0.1–0.5 g) were irradiated in Triga reactors at Oregon State and Texas A & M Universities (about 10^{13} neutrons/cm^2-s). Gamma ray spectra were obtained by using high-resolution Ge(Li) detectors and counting facilities at University of Oregon or NASA-Johnson Spacecraft Center [cf., *Gordon et al.*, 1968; *Jacobs et al.*, 1977]. With each irradiated batch of samples, several USGS standard rocks were included to monitor accuracy and precision. Typical two-sigma counting errors (reported as coefficient of variation) are indicated in Table 3; these values are considered representative of actual analytical uncertainties based on comparisons between observed and recommended concentrations determined for the standards.

Experimental Results

Analyses of eight sanidines are given in Table 3, and the corresponding sanidine/glass partition coefficients (weight basis) are given in Table 4. Sanidines from all samples display a range in absolute REE contents of less than a factor of 2 for most elements (Figure 1). In contrast, Ba contents display a

TABLE 2. Analyses of Sanidines From Yellowstone Rhyolites

Unit (age, m.y.)	Sample	N*	Or, percent†	Ab, percent	An, percent
Grants Pass flow (0.07)	YG 70-13	9	51.8 ± 0.8	46.1 ± 0.7	2.1 ± 0.2
Summit Lake flow (0.11)	YG 70-10	9	50.3 ± 0.5	47.0 ± 0.6	2.7 ± 0.2
Bechler River flow (0.12)	72-0-75	6	52.0 ± 0.5	45.5 ± 0.4	2.5 ± 0.1
West Yellowstone flow (0.12)	0CB66-09	10	50.0 ± 1.4	47.4 ± 0.9	2.6 ± 0.5
	YG 72-5	6	50.6 ± 0.7	46.9 ± 0.5	2.5 ± 0.2
Nez Perce flow (0.15)					
Firehole River	72-0-76	5	54.4 ± 1.3	42.6 ± 0.9	3.0 ± 0.5
	0CB66-12	9	54.5 ± 1.4	42.9 ± 0.8	2.6 ± 0.4
	6YC-143	10	54.5 ± 1.1	43.0 ± 0.6	2.5 ± 0.5
Gibbon Canyon	72-0-72	6	55.3 ± 0.3	42.3 ± 0.3	2.4 ± 0.2
Dry Creek flow (0.15)	0CB66-14A	7	55.1 ± 0.5	42.5 ± 0.4	2.4 ± 0.1
	6YC-148	10	54.9 ± 2.5	42.5 ± 2.0	2.7 ± 0.4
	0CB66-13	9	54.4 ± 0.9	43.0 ± 1.1	2.6 ± 0.2
Mary Lake flow (0.16)	YG 72-7	6	54.7 ± 0.6	42.7 ± 0.5	2.6 ± 0.2
Cougar Creek flow (0.39)	6YC-138	9	66.9 ± 0.6	31.6 ± 0.6	1.5 ± 0.1
Wapiti Lake flow (1.15)	0YC-601	9	58.6 ± 0.3	39.4 ± 0.5	2.0 ± 0.1
Mesa Falls Tuff (1.2)‡	0CB66-04	8	59.0 ± 0.7	39.4 ± 0.6	1.6 ± 0.2
	6YC-141	10	59.3 ± 1.1	39.1 ± 0.6	1.7 ± 0.4
Huckleberry Ridge Tuff (1.9)					
Member B	0CB66-01	9	54.0 ± 0.9	43.8 ± 0.9	2.2 ± 0.3
Member A	0CB66-03	9	53.4 ± 1.6	44.3 ± 1.0	2.3 ± 0.3

* Number of individual grains analyzed (each grain represented by 3 or more spot analyses).
† Mole percent; uncertainty = 1 standard deviation of mean. This statistic is given to indicate degree of homogeneity of the feldspar populations.
‡ Also see *Basu and Vitaliano* [1976] for more detailed characterization of sanidines from this unit.

TABLE 3. Analyses of Sanidines From Yellowstone Rhyolites

	YG70-13	YG70-10	0CB66-09*	YG72-5	72-0-75	6YC-143*	6YC-148*	0YC-601
FeO, percent	0.25	0.31	0.17	0.22	0.31	0.15	0.15	0.22
Na_2O, percent	5.15	4.35	5.18	5.21	5.16	4.53	4.67	4.44
Ba	1480	8410	5200	4180	3210	5750	5690	2800
Rb	85	83	80	84	82	88	91	120
Th	0.75	0.60	0.6	0.45	0.57	0.5	0.8	0.68
Hf	0.28	0.33	...	0.35	0.32	0.3	0.3	0.33
Ta	0.06	0.10	...	0.05	0.04	...	...	0.12
La	11.0	9.5	10.8	11.4	10.9	12.7	11.9	11.1
Ce	12.6	9.7	11.1	11.0	11.2	11.1	11.0	9.9
Nd	4.4	...	...	4.1	3.1	...	...	3.6
Sm	0.54	0.31	0.37	0.30	0.39	0.38	0.32	0.27
Eu	3.17	5.64	5.18	4.55	4.32	5.12	5.24	2.11
Tb	0.047	0.055	...	0.032	0.037	...	...	0.031
Yb	0.104	0.11	...	...	0.106	...	0.13	0.106
Lu	0.016	0.013	...	0.011	0.016	...	...	0.013
Sc	0.04	0.05	0.04	0.05	0.05	0.07	0.06	0.06
Cs	0.08	0.12	...	0.05	0.10	...	...	0.11
Zr	90	130	100	145	140	110	120	70

Note: Typical analytical uncertainties (2 sigma counting statistics, given as coefficient of variation) are as follows: 1–5%: (Na_2O, La, Sm, Eu, Sc); 5–10%: (FeO, Rb, Th, Hf, Ce, Yb, Lu); 10–20%: (Ba, Nd, Tb, Cs, Zr, Ta).

* Samples analyzed at University of Oregon; all others analyzed at Johnson Space Center.

large range (1500–8400 ppm). Considering the overall similarity in major element compositions of glasses and sanidines and the small range in Fe-Ti oxide equilibration temperatures noted earlier, it seems likely that the observed ranges in trace element contents in sanidines reflect corresponding compositional variations in the magmas from which they crystallized. Apparently, significant trace element inhomogeneities exist even within individual lava flows (e.g., samples OCB66-09

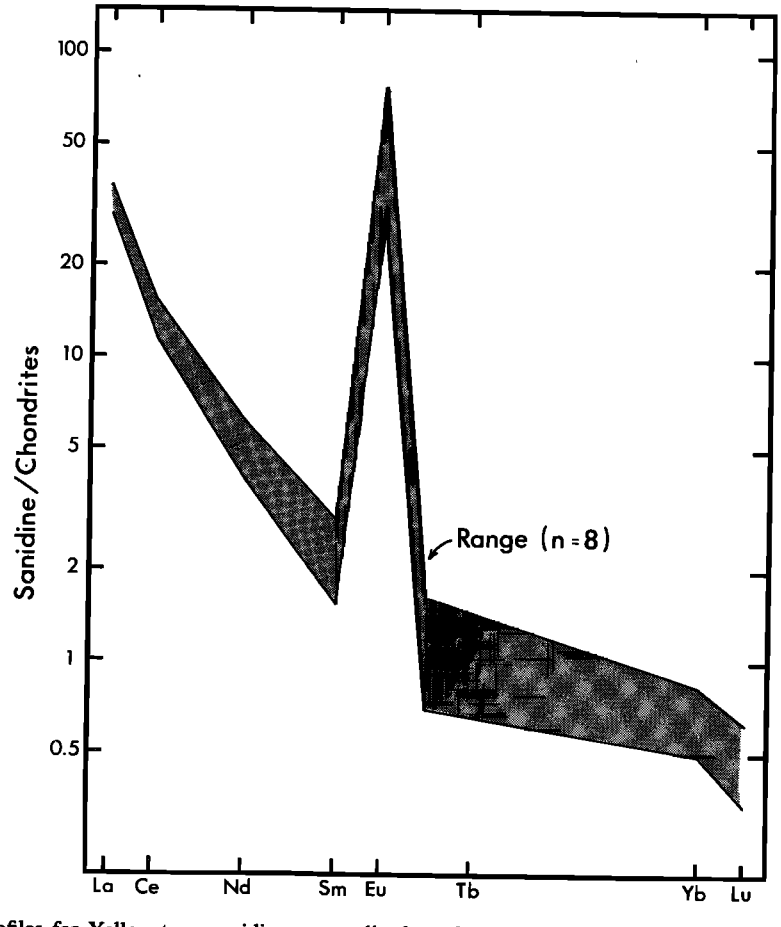

Fig. 1. REE profiles for Yellowstone sanidines normalized to chondritic values (Leedey × 1.2; cf. *Sun and Hanson* [1976]).

TABLE 4. Sanidine/Glass Partition Coefficients

Sample	YG70-13	YG70-10	OCB66-09	YG72-5	72-O-75	7YC-143	6YC-148	OYC-601
Age (m.y.)	0.07	0.11	0.12	0.12	0.12	0.15	0.15	1.15
Fe	0.17	0.20	0.13	0.14	0.20	0.11	0.16	0.16
Na	1.36	1.15	1.38	1.41	1.47	1.26	1.33	1.35
K	1.34	...	...	1.16	1.10	...	...	1.35
Ba	13	(44)	26	22	20	27	26	21
Rb	0.37	0.42	0.38	0.40	0.33	0.43	0.43	0.40
Th	0.026	0.023	0.022	0.016	0.021	0.018	0.028	0.019
Hf	0.023	0.032	...	0.032	0.033	0.040	0.036	0.042
Ta	0.010	0.021	...	0.010	0.009	...	...	0.024
La	0.13	0.10	0.12	0.125	0.120	0.15	0.15	0.135
Ce	0.074	0.054	0.061	0.061	0.065	0.073	0.071	0.063
Nd	0.064	...	...	0.053	0.044	...	...	0.056
Sm	0.034	0.021	0.026	0.019	0.027	0.028	0.029	0.023
Eu	8.57	9.56	8.49	9.48	9.19	9.19	8.83	9.17
Tb	0.019	0.024	...	0.013	0.016	...	...	0.016
Yb	0.012	0.015	...	...	0.014	0.021	...	0.015
Lu	0.013	0.012	...	0.009	0.015	...	...	0.013
Sc	0.031	0.033	0.025	0.031	0.029	0.032	0.025	0.029
Cs	0.020	0.036	...	0.013	0.026	...	...	0.024
Zr	0.22	0.45	0.29	0.41	0.44	0.38	0.41	0.26

and YG72-5 from the West Yellowstone flow). Despite the existence of such inhomogeneities and the overall range in trace element contents for the seven analyzed flows, the sanidine/liquid partition coefficients display a restricted range of values (usually within the combined counting statistics) for each element (Figure 2). Other sources of variance (e.g., zoning of trace element contents and minor occult inclusions within the feldspars or glasses) cannot be precluded, but overall uniformity of the partition coefficients suggests that these are probably negligible compared to our present analytical uncertainties.

Trace element partition coefficients for Yellowstone sani-

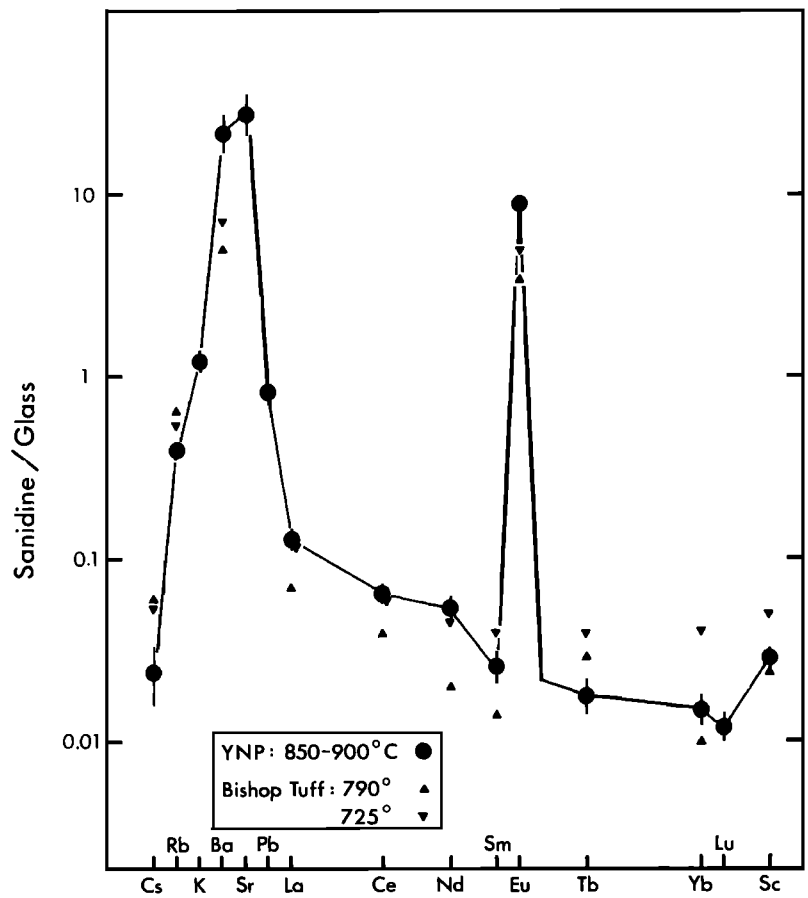

Fig. 2. REE and other trace element partition coefficients for Yellowstone sanidines (solid circle) and for high (solid triangle) and low (solid inverted triangle) temperature phases of the Bishop Tuff (see Table 5). Also included are values of D_{Sr} (W. Leeman et al., manuscript in preparation, 1981) and D_{Pb} [Leeman, 1979] for Yellowstone sanidines. Spacing of REE along abcissa is based on ionic radii; other elements (Cs to Pb) are arbitrarily spaced at equal intervals.

dines are contrasted with most of the available results for other siliceous magma types in Table 5 and Figure 2. It is important to note that this data base includes calcalkalic rhyodacites, trachytes, and so-called anorogenic rhyolites (of which Yellowstone and the Bishop Tuff are examples) that differ in silica content, degree of peralkalinity, and probably in liquidus temperature, oxygen fugacity, etc. Considering these differences one might expect the observed wide ranges in partition coefficients for such elements as Ba (20 fold), trivalent REE (2 fold), Sr (8 fold), Eu (9 fold), etc. Partition coefficients for many other elements display more restricted ranges (e.g., Fe, K, Th, Sc). We also note that sanidine/liquid partition coefficients for Sr (28 ± 7) are considerably higher for Yellowstone rhyolites (W. P. Leeman et al., manuscript in preparation, 1981) compared with the values shown in Table 5. The sparse available data are not adequate to unravel the effects of varying P, T, or composition on trace element partitioning. Consequently, in practice partitioning data must be acquired for specific magma suites to evaluate meaningfully any trace element fractionation trends extant in those suites. Clearly, no single set of 'best values' can be selected to represent sanidine/liquid partition coefficients for rhyolitic magmas (sensu lato), although those reported here are likely representative for rhyolites from Yellowstone and the closely associated Snake River Plain.

The problems in estimating trace element partition coefficients for silicic magmas are further emphasized in experimental studies. Hydrothermal experiments (1–8 kbar), using simplified 'rhyolitic' compositions illustrate that melt composition apparently has great influence on partitioning of elements such as Ba and Sr between alkali feldspars and liquid [*Pierozynski*, 1977; *Long*, 1978]. Also for small ranges in melt composition, decreasing temperature results in elevated partition coefficients for these elements. In these two experimental studies, wide ranges in D_{Sr} (1.2–38) and D_{Ba} (6–14) have been reported. Both Pierozynski and Long attribute these observations to composition-related changes in the structures of highly polymerized silicic melts. It is not clear whether or not natural silicic magmas, which contain higher contents of so-called network modifying cations (Fe, Ca, etc.) or volatiles (H_2O, CO_2, F, etc.), generally will behave in a similar fashion to the simplified rhyolite melts. The data in Table 5 suggest that they exhibit similar effects to some extent [also see *Mahood*, 1979].

A further difficulty in evaluating empirical or experimentally determined partition coefficients is the uncertain effect of high-low phase transitions in alkali feldspar structure on the incorporation of certain trace elements within this phase [*De Pieri and Quareni*, 1978]. Such transitions may affect the liquidus solubility or subsolidus mobility of certain trace elements in the feldspar structures.

Use of so-called Onuma diagrams [cf., *Philpotts*, 1978] have helped to systematize element partitioning data for natural magmatic samples. In such diagrams, variations of partition coefficient data as a function of ionic radii commonly define smooth profiles that, among other applications, can be used to test the consistency of partition coefficients for homovalent cations. Figure 3 shows an Onuma diagram for Yellowstone sanidines (averaged data from Table 5 are shown). Because cation sites are in fact irregular and characterized by deviations from ideal symmetrical coordination in sanidines, we have plotted a range in ionic radii corresponding to seven- to eight-fold coordination, using the estimates of *Whittaker and Muntus* [1970]. In Figure 3 it is seen that our data define regular profiles for monovalent (Cs, Rb, K, Na), divalent (Ca, Sr, Ba, Eu?), and trivalent (La to Lu) cations. Based on comparisons with data for other minerals [cf., *Philpotts*, 1978], these variations may be considered necessary, though not sufficient, indications that our data are in accordance with crystal-chemical controls on element partitioning. For unclear reasons, data for other elements (e.g., Th, Zr, Sc, Pb, Fe) do not define any systematic trends in Figure 3. However, there is some uncertainty concerning valence states, ionic radii, and nature of bonding for some of these elements as well as the degree to which their incorporation in sanidine is controlled by crystal structure. *Hildreth*'s [1977; not plotted in Fig. 3] data displays essentially the same features as ours. Until further studies are available, it will be difficult to assess unambiguously the mechanisms affecting trace element partitioning between sanidines and silicate melts.

TABLE 5. Comparative Estimates of Sanidine/Liquid Partition Coefficients

Reference*	This study	1	2	3	4
Fe	0.16 ± 0.03	0.15	0.15	...	...
Na	1.34 ± 0.10	...	...	...	...
K	1.24 ± 0.13	...	...	1.49	...
Ba†	22 ± 5	7.	5.	6.12	3.2
Rb	0.40 ± 0.03	0.55	0.65	0.34	...
Th	0.022 ± 0.004	0.03	0.015	...	...
Hf	0.034 ± 0.006	0.06	0.025	...	...
Ta	0.015 ± 0.007	0.04	0.03	...	...
La	0.129 ± 0.017	0.12	0.07	...	...
Ce	0.065 ± 0.007	0.06	0.04	0.044	0.16
Nd	0.054 ± 0.008	0.05	0.02	0.025	0.15
Sm	0.026 ± 0.005	0.04	0.014	0.018	0.15
Eu	9.06 ± 0.40	4.8	3.5	1.13	2.2
Gd	...	...	...	0.011	...
Tb	0.018 ± 0.004	0.04	0.03	...	...
Dy	...	...	...	0.006	...
Er	...	...	...	0.006	0.15
Yb	0.015 ± 0.003	0.04	0.01	0.012	0.15
Lu	0.012 ± 0.002	...	...	0.006	0.15
Sc	0.029 ± 0.003	0.05	0.025	...	...
Cs	0.024 ± 0.008	0.05	0.06	...	...
Zr	0.36 ± 0.09	...	...	...	...
Sr†	...	3.8‡	...	3.87	3.1

* Sources of data: This study, mean and standard deviation from Table 4. (1) Average low T (725°C) phase, Bishop Tuff [*Hildreth*, 1977]. (2) Average high T (790°C) phase, Bishop Tuff [*Hildreth*, 1977]. (3) Tabulation of data from *Arth* [1976], rhyolites and rhyodacites. (4) Average for trachytes 6 and 10 [*Nagasawa*, 1973].

† Additional values of D_{Sr} (1.2–2.8) and D_{Ba} (1.2–9.0) for trachytes and phonolites [*Berlin and Henderson*, 1969] and values of D_{Sr} (7.6) and D_{Ba} (20) calculated for an anorogenic rhyolite [*Ewart et al.*, 1977].

‡ Single sample of Bishop Tuff (T phase unknown) [*Nagasawa*, 1971].

CONCLUSIONS

The available data for sanidine/liquid trace element partitioning indicate a wide range of values that probably reflect differences in melt composition (hence structure), temperature, and other intensive parameters including volatile component activities. At present it seems desirable to determine partition coefficients for individual magmatic suites rather than utilize values selected from Table 5 without due consideration of magma compositions. The internal consistency of the data presented herein suggests that our partition coefficients are applicable to most Yellowstone rhyolites, especially considering their relatively narrow compositional range, but we caution against their uncritical use.

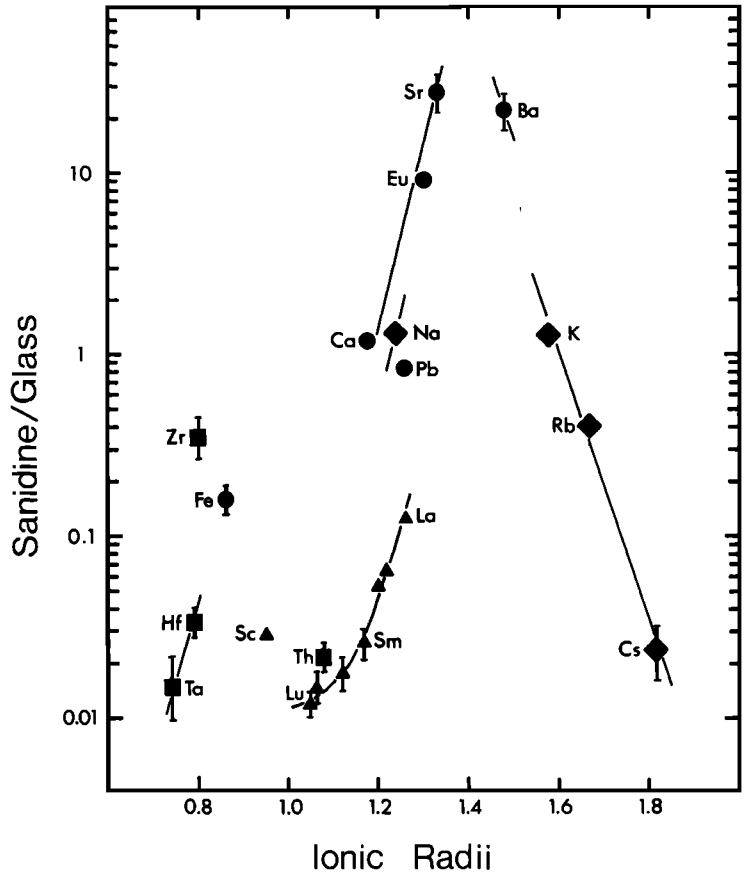

Fig. 3. Onuma diagram showing partition coefficient values as a function of ionic radii [*Whittaker and Muntus*, 1970]. The ionic radii portrayed represent the average for seven-and eight-fold coordination for monovalent and divalent cations, eight-fold coordination for trivalent cations, and six-fold coordination for tetravalent cations. Eu and Fe values are plotted arbitrarily at ionic radii for the divalent cations; although these elements undoubtedly occur in both divalent and trivalent states, they are believed to be dominantly divalent at the redox conditions pertinent to the rhyolite magmas (W. Hildreth, personal communication, 1980).

Applications of such data [e.g., *Condie and Hunter*, 1976; *McCarthy and Hasty*, 1976; *Hanson*, 1978] to calculations of crystal fractionation or partial melting processes are not straightforward, considering probable variation in partition coefficients with melt composition and temperature. In particular, empirical partition coefficients based on alkali feldspars in volcanic rocks are not necessarily representative for modeling crustal anatexis, in which case differences in the composition and structure of alkali feldspars (orthoclase, microcline, etc.) may result in significantly different trace element partitioning. Data in Table 5 may be used to establish first-order constraints on compositions of anatectic melts, but such models may have large uncertainties, particularly for elements such as Eu, Ba, and Sr, which are characterized by large partition coefficients. For elements having low partition coefficients (<0.1), the data in Table 5 will probably yield more meaningful constraints insofar as alkali feldspar is concerned. Effectively, all such elements (e.g., Th, Ta, Hf, trivalent REE, Sc, Cs, and Zr) will strongly partition into the melt phase (relative to alkali feldspar) despite a two- or three-fold uncertainty in the partition coefficient.

A final word of caution is needed concerning the role of minor phases such as zircon, apatite, allanite, chevkinite, etc. As emphasized by *Hanson* [1978], the presence of even minor amounts of such phases in crustal rocks and as accessory phenocrysts in many high-silica magmas may effectively dominate the partitioning of certain trace elements (e.g., U, Th, Zr, Hf, REE) between condensed phases and coexisting magma.

Acknowledgments. We would like to thank John Obradovich and Bruce Doe for providing the samples used in this study. Without their generosity this study probably would not have materialized. We also thank G. G. Goles and D. A. Blanchard for providing access to their laboratory facilities to carry out this work. Portions of this work have been supported by NSF grants EAR79-19998 and EAR80-18580.

REFERENCES

Arth, J. G., Behavior of trace elements during magmatic processes—A summary of theoretical models and their applications, *J. Res. U.S. Geol. Survey, 4*, 41–47, 1976.

Basu, A., and C. J. Vitaliano, Sanidine from the Mesa Falls Tuff, Ashton, Idaho, *Am. Mineral., 61*, 405–408, 1976.

Berlin, R., and C. M. B. Henderson, The distribution of Sr and Ba between the alkali feldspar, plagioclase and groundmass phases of porphyritic trachytes and phonolites, *Geochim. Cosmochim. Acta, 33*, 247–255, 1969.

Christiansen, R. L., Quaternary and Pliocene volcanism of the Yellowstone rhyolite plateau region of Wyoming, Idaho, and Montana, *U.S. Geol. Surv. Prof. Pap. 729*, in press, 1981.

Christiansen, R. L., and H. R. Blank, Jr., Volcanic stratigraphy of the Quaternary rhyolite plateau in Yellowstone National Park, *U.S.*

Geol. Surv. Prof. Pap. 729-B, 1972.
Condie, K. C., and D. R. Hunter, Trace element geochemistry of Archean granitic rocks from the Barberton region, South Africa, *Earth Planet. Sci. Lett., 29,* 389–400, 1976.
De Pieri, R., and S. Quareni, Partition coefficients of alkali and alkaline earth elements between alkali feldspar phenocrysts and their lava matrix, *Min. Mag., 42,* 63–67, 1978.
Ewart, A., V. M. Oversby, and A. Mateen, Petrology and isotope geochemistry of Tertiary lavas from the northern flank of the Tweed volcano, southeastern Queensland, *J. Petrol., 17,* 73–113, 1977.
Friedman, I., P. W. Lipman, J. D. Obradovich, J. D. Gleason, and R. L. Christiansen, Meteoric water in magmas, *Science, 184,* 1069–1072, 1974.
Gordon, G. E., K. Randle, G. G. Goles, J. B. Corliss, M. H. Beeson, and S. S. Oxley, Instrumental activation analysis of standard rocks with high-resolution γ-ray detectors, *Geochim. Cosmochim. Acta, 32,* 369–396, 1968.
Hanson, G. N., The application of trace elements to the petrogenesis of igneous rocks of granitic composition, *Earth Planet. Sci. Lett., 38,* 26–43, 1978.
Hildreth, E. W., The magma chamber of the Bishop Tuff: gradients in temperature, pressure, and composition, Ph.D., dissertation, Univ. of Calif., Berkeley, 1977.
Jacobs, J. W., R. L. Korotev, D. P. Blanchard, and L. A. Haskin, A well-tested procedure for instrumental neutron activation analysis of silicate rocks and minerals, *J. Radioanal. Chem., 40,* 93–114, 1977.
Leeman, W. P., Partitioning of Pb between volcanic glass and coexisting sanidine and plagioclase feldspars, *Geochim. Cosmochim. Acta, 43,* 171–175, 1979.
Long, P. E., Experimental determination of partition coefficients for Rb, Sr, and Ba between alkali feldspar and silicatè liquid, *Geochim. Cosmochim. Acta, 42,* 833–846, 1978.
Mahood, G., Constrasting trace element behavior in rhyolitic ash flows and lavas, Sierra La Primavera, Mexico, *Geol. Soc. Am. Abst. Programs, 11,* 471, 1979.
McCarthy, T. S., and R. A. Hasty, Trace element distribution patterns and their relationship to the crystallization of granitic melts, *Geochim. Cosmochim. Acta, 40,* 1351–1358, 1976.
Nagasawa, H., Partitioning of Eu and Sr between coexisting plagioclase and K-feldspar, *Earth Planet. Sci. Lett., 13,* 139–144, 1971.
Nagasawa, H., Rare earth distribution in alkali rocks from Oki-Dogo Island, Japan, *Contrib. Mineral. Petrol., 39,* 301–308, 1973.
Philpotts, J. A., The law of constant rejection, *Geochim. Cosmochim. Acta, 42,* 909–920, 1978.
Pierozynski, W. J., The effects of varying bulk composition on the partitioning of Sr, Ba, and Rb between alkali feldspar and coexisting silicate liquid (abstract), in *Papers Presented to the International Conference on Experimental Trace Element Geochemistry,* Publisher, Location, 1977.
Schnetzler, C. C., and J. A. Philpotts, Partition coefficients of rare-earth elements between igneous matrix material and rock-forming mineral phenocrysts, *Geochim. Cosmochim. Acta, 34,* 331–340, 1970.
Sun, S.-S., and G. N. Hanson, Rare earth evidence for differentiation of McMurdo volcanics, Ross Island, Antarctica, *Contrib. Mineral. Petrol., 54,* 139–151, 1976.
Whittaker, E. J. W., and T. Muntus, Ionic radii for use in geochemistry, *Geochim. Cosmochim. Acta, 34,* 945–956, 1970.

(Received December 19, 1980;
revised March 2, 1981;
accepted March 26, 1981.)

JOURNAL OF GEOPHYSICAL RESEARCH, VOL. 86, NO. B11, PAGES 10200–10222, NOVEMBER 10, 1981

Volcanic Ash Beds: Recorders of Upper Cenozoic Silicic Pyroclastic Volcanism in the Western United States

GLEN A. IZETT

U.S. Geological Survey, Reston, Virginia 22092

Stratigraphic relationships and tephrochronologic information for volcanic ash beds (4.0–0.1 m.y.) of the Western Interior allow the recognition of at least 68 different ash falls. The average reoccurrence rate, based on the succession of the isotopically dated ash beds, is near one eruption every 57,000 years. The ash beds were grouped into two chemical types, rhyolitic and dacitic; the main property that distinguishes dacitic from rhyolitic ashes is the larger Ca and Mg and smaller K content in dacitic ashes. Dacitic volcanic ashes were defined to have more than 0.55 wt % Ca. Rhyolitic ashes were subdivided further into two types, W- and G-type, based on the presence of biotite in the W-type and its absence in G-type. W-type rhyolitic ashes are chalky white, have less than 0.55 wt % Fe, have colorless glass shards of pumiceous habit. G-type rhyolitic ashes are light to medium gray, have from 0.55 to 2.0 wt % Fe in the glass shards, lack biotite, have colorless, platy, bubble wall, and bubble junction glass shards. Dacitic ashes are light gray to grayish brown, have more than 0.55 wt % Fe and Ca, and have a complex mixture of colorless to light brown shards, including pumiceous, fibrous, chunky, and bubble wall and bubble junction types. W-type rhyolitic ashes possibly formed from magmas that were cooler (695° to 830°C) and thus more viscous than the hotter (870° to 1000°C) magma progenitors of G-type ashes based on Fe-Ti oxide mineral compositions. Primary microphenocrysts in the ash beds comprise assemblages of the following: quartz, sanidine, plagioclase, biotite, amphibole, clinopyroxene, orthopyroxene, fayalite, zircon, apatite, allanite, chevkinite, sphene, magnetite, and ilmentite. Fayalite and chevkinite only have been found in G-type; biotite and sphene only have been found in W-type. Rhyolitic ashes are highly evolved and contain 74–79 wt % SiO_2; dacitic ashes vary from 67–77 wt % SiO_2. Al ranges from 10.5 to 14.5 wt % Al_2O_3, Mg ranges from 0.06 to 1.0 wt % MgO, and Fe (as Fe_3O_4) ranges from 0.50 to 4.1 wt %. Dacitic ash beds have the most (0.80–3.8 wt % as Fe_3O_4) and rhyolitic ashes have the least (0.50–1.9 wt % as Fe_3O_4). Ca varies from an unusually low amount (0.25 wt % CaO) in a few rhyolitic ashes to as much as 2.2% in some dacitic ashes. Rhyolitic glasses show larger Eu deficiencies compared to dacitic glasses on rare-earth element diagrams. W-type rhyolitic glasses have moderately large La to Sm ratios and have La contents from about 30 to 100 times chondrite values; G-type rhyolitic glasses also have moderately large La to Sm ratios and contain somewhat more La than do the W-type rhyolitic ashes, generally from 100 to 300 times chondrites amounts.

INTRODUCTION

The nature of silicic, Cenozoic pyroclastic volcanism in the western United States has been intensively studied during the last 10 to 15 years. Large areas of silicic volcanic rocks that have been studied include the San Juan Mountains of Colorado [*Ratté and Steven,* 1967; *Lipman et al.,* 1973; *Lipman,* 1975; *Steven and Lipman,* 1976], the Basin and Range province [*Noble,* 1968; *Noble et al.,* 1968; *Byers et al.,* 1976; *Christiansen et al.,* 1976; *Ekren et al.,* 1971], the Jemez Mountains of New Mexico [*Smith and Bailey,* 1966; *Smith et al.,* 1970; *Smith,* 1979], the Yellowstone National Park area [*Christiansen and Blank,* 1972; *Christiansen,* 1979], east-central California [*Bailey et al.,* 1976; *Hildreth,* 1977]. Some of the smaller areas of silicic volcanic rocks include areas in eastern and northern California [*Duffield et al.,* 1980; *Hearn et al.,* 1976; *Heiken,* 1978; *Donnelly et al.,* 1981] and numerous areas in the Cascade volcanic field of Washington and Oregon. These volcanic fields were chosen for study because they have large areas of geologically young and relatively unaltered glassy rocks ideal for petrologic studies. A multidisciplinary approach was used in many of these studies, and cooperation among volcanologists, geochronologists, geophysicists, and geochemists led to the gathering of important basic data such as (1) determining the spatial distribution and age of the various rock units, (2) determining the variation in chemical composition and mineralogy of erupted materials with time, and (3) delineation of crustal structure. The above information provides constraints for speculative models concerning (1) the understanding of the mechanics of pyroclastic eruptions and their associated caldera collapses, (2) the estimation of the degree of chemical zonation within magma chambers, (3) the evaluation of rival petrologic models for the evolution of silicic rocks sequences, (4) the speculation of source materials and regions of silicic magma, (5) the estimation of the physical conditions (temperature, pressure, viscosity, and chemical gradients) in magma chambers just prior to eruption of silicic composition tephra, and (6) the relationship between volcanism and metallization.

Large volumes of silicic volcanic ash were produced in Pliocene and Pleistocene time from some of the aforementioned volcanic centers during intense, plinian-style eruptions, and this ash was carried far downwind and deposited as ash blankets covering, in some instances, large areas [*Eaton,* 1964; *Wilcox,* 1965; *Izett et al.,* 1970; *Izett and Wilcox,* 1981]. (Volcanic ash rather than tuff is used in this report for all fine-grained, wind-transported pyroclastic materials, although some of the materials are semiconsolidated and more accurately should be termed tuff. Tephra is used in this report for all air-transported pyroclastic material near volcanic vent areas.) In some places, these ashes were preserved by being deposited in favorable sedimentary environments including lacustrine, fluvial, and paludal; following erosional incision of these deposits, the ash beds can be mapped, sampled, and studied. By sampling volcanic ash beds of many different Cenozoic ages on a regional scale, a rather complete composite record of the volcanic activity for the western United States can be acquired. Study of the chemical composition, mineral-

This paper is not subject to U.S. copyright. Published in 1981 by the American Geophysical Union.

Paper number 1B0835.

ogy, pertrographic features, and isotopic age of samples of these glass-rich ashes provides another approach to gain information concerning volcanic processes that prevailed in distant source areas at the time the ashes were erupted.

Aside from the value ash beds have for understanding volcanic processes, they also are useful for other reasons. In the last 10 years there has been an increased interest, by many workers in a variety of earth science disciplines, for tephrochronological information gathered with the goal of establishing volcanic ash beds as time-stratigraphic markers that are useful for correlation and dating of associated upper Cenozoic sedimentary deposits.

When tephrochronological data are combined with other geological information, such as stratigraphic position, faunal age, paleomagnetic direction, and isotopic age, the result is a multipronged analytical device with a combined resolving power that is far greater than that of any single geologic technique. Correct identification and dating of an ash bed can provide critical information to help resolve problems such as (1) the determination of the time and rate of fault movements and other types of crustal deformation, (2) the determination of the rate of deposition of sediments, (3) the evaluation of geologic hazards such as volcanic and earthquake, (4) the calibration of paleomagnetic and faunal chronologies, (5) the calibration of new isotopic dating methods such as uranium trend, (6) the identification of tephra provenance, and (7) the frequency of large, ash-forming eruptions in the geologic record.

In the past, many tephrochronological studies were unsuccessfully attempted by using only one analytical technique for the chemical, mineralogical, or petrographical characterization of an ash bed. The need for using a broad approach, employing many analytical techniques, is obvious in view of the large number of ash beds and the possibility of duplication of properties. No single rapid scan chemical, mineralogical, petrographical, isotopic, or paleomagnetic method of characterizing ash beds will result in establishing correlations with a high probability of success.

PURPOSE OF THE REPORT

The purpose of this report is to bring together pertinent tephrochronological information relative to upper Cenozoic silicic volcanic ash beds of the western United States and to summarize this information on a chart (Plate 1, folded in pocket). Plate 1 comprises a composite stratigraphic summary of the known and inferred sequences of ash beds that range from 4.0 to 0.1 m.y. and that are found in Pliocene sedimentary rocks and Quaternary deposits. Ash beds younger than 0.1 m.y. were not compiled on Plate 1 because of a lack of detailed chemical and mineralogical data for many of the ash beds and because of the writers unfamiliarity with their stratigraphic relationships. Ash beds older than 4.0 m.y. have been compiled by the writer but were not added to Plate 1 because of a lack of detailed chemical and mineralogical data for some of the ash beds. As more tephrochronological information is gathered, additions and changes in this first version of Plate 1 will undoubtedly be needed.

FREQUENCY OF ASH-FORMING ERUPTIONS

A minimum of 68 silicic ash-forming eruptions occurred between 4.0 and 0.1 m.y. in the western United States (Plate 1). Several times as many more eruptions undoubtedly took place, but either the ashes produced during the eruptions were (1) too thin for ash beds to be preserved and identified in sedimentary deposits far downwind from their source areas or (2) so sparse that the ashes have not been found yet because they were deposited in such narrow sectors away from their vent areas. Although far from complete, this composite, ash bed record suggests that plutonism and accompanying cataclysmic, ash-forming eruptions took place at the minimum average rate of about one eruption every 57,000 years.

This minimum average rate is, in some ways, not too meaningful because it fails to encompass the wide range in magnitude and the episodic nature of ash-forming volcanic eruptions. Almost certainly, small-magnitude eruptions have occurred in the past and will occur in the future, much more frequently than will large-magnitude eruptions. It seems likely that a logarithmic relationship may exist between the frequencies and magnitudes of pyroclastic eruptions, but insufficient information is available to define the relationship mathematically. More realistic eruption rates can be estimated by relating the magnitudes of ash-forming eruptions to frequency of eruptions. The magnitude (M) of an ash-forming eruption is here arbitrarily defined as the volume of tephra (in cubic kilometers) in the source region (including air fall, surge, and ash flow deposits) divided by 100 (only to reduce the size of the number). *Sapper* [1927] defined a scale ranging from magnitude 1 to 8 that could be used to compare volcanic eruptions based on the volume of material ejected in which magnitude 1 was assigned to eruptions greater than 1 km^3 and magnitude 8 to those less than 10^3 m^3. *Tsuya* [1955, p. 381] related the intensity of volcanic eruptions to the volume of solid ejecta. An eruption of intensity 10 would produce more than 100 km^3 of ejecta, and a eruption of intensity zero would produce only fumarolic activity, according to Tsuya. *Smith* [1979, Figure 1] used a logarithmic scale to define the volume of tephra in source areas in order to compare the relative sizes of eruptions, but he excluded the volume of ash carried downwind in his volume estimates. Of course, any scheme devised to quantify eruptions by using volumes of tephra erupted must be rather crude owing to problems such as determining thicknesses of pyroclastic material in downdropped caldera blocks, estimating densities of nonwelded and welded parts of ash flows, and estimating the volume of ash carried downwind.

Bailey et al. [1976, p. 730] calculated the volume of the Bishop Tuff in the source area of eastern California to be 500 km^3 (uncompacted volume). Using magnitude as herein defined, the eruption of the Bishop Tuff would be magnitude 5. Perhaps another 500 km^3 of ash from the early, plinian phase of the Bishop eruption formed the Bishop ash bed (Plate 1, bed 13). By combining the Bishop Tuff and Bishop ash volumes and by reducing the uncompacted volume by appropriate factors for porosity, *Bailey et al.* [1976, p. 731] estimated the volume of magma ejected during the eruption of the Bishop Tuff to be 600 km^3. Ash bed 36 of Plate 1 formed during the gigantic pyroclastic eruptive event that formed the Huckleberry Ridge Tuff in the Yellowstone National Park area about 2.01 m.y. ago. *Christiansen* [1979, p. 36] estimated that the volume of pyroclastic ejecta formed in the source area during the formation of the Huckleberry Ridge Tuff was 2000 km^3. Possibly as much as 2000 km^3 more ash was carried far downwind from the source area during the eruption, as judged by the distribution and thicknesses of the Huckleberry Ridge ash [*Izett and Wilcox*, 1981]. Using magnitude as herein defined, the eruption of the Huckleberry Ridge Tuff would be

magnitude 20. Table 1 shows the magnitudes of a few of the ash beds of Plate 1 and, in addition, shows the magnitudes of some other well-known ash-forming eruptions of the past.

The magnitudes of ash-forming eruptions are further grouped, for purposes of discussion only, into four classes: small (0–0.05 *M*), medium (0.06–0.5 *M*), large (0.51–5.0 *M*), and gigantic (>5.00 *M*). If, as suggested, many small-magnitude eruptions rarely have preserved ash bed counterparts at appreciable distances from their source areas, then the average frequency of 57,000 years calculated from data on Plate 1 may be underestimated by several orders of magnitude. For example, *Mullineaux* [1974, p. 1] described 22 tephra beds in postglacial deposits (last 10,000 years) near Mount Rainier in the Cascade volcanic field of Washington. These near-source tephra beds probably formed during small-magnitude eruptions. The recorded, time-stratigraphic data for eruptions in the Mount Rainier area suggest an average frequency of about one ash-forming eruption every 500 years. Mullineaux, however, further pointed out that 11 of the 22 tephra beds had their source at Mount Rainier volcano and the remainder had their source elsewhere in the Cascade volcanic field. Of the 11 eruptions that occurred at Mount Rainier volcano, eight happened in a period of 2500 years, or at a calculated frequency of one eruption every 300 years. Only three eruptions took place in the remaining 7500 years, or an average frequency of one eruption in 2500 years. As suggested by the data given and from the record of historic eruptions, such as the recent eruptions of ash at Mount St. Helens volcano [*Sarna-Wojcicki et al.*, 1981], the frequency of small-magnitude eruptions can vary widely from a few months to several thousands of years. Some of the beds of Plate 1 that probably formed during small-magnitude eruptions include ash beds 48, 25, 24, 21, 20, 17, 16, 14, 2, and 1.

Medium-magnitude, ash-forming eruptions are probably less frequent than are small-magnitude, ash-forming eruptions, as suggested, and they probably generated several of the ash beds shown on Plate 1. Their expected frequency may be something near one eruption every 100,000 years. An example of a medium-magnitude, ash-forming eruption is the one near Glass Mountain, California, that formed the tuff of Taylor Canyon [*Krauskopf and Bateman*, 1977] and its downwind equivalent (bed 37 on Plate 1) about 2.10 m.y. ago.

The frequency of large-magnitude pyroclastic eruptions, such as the ones that formed the Otowi (Guaje Pumice Bed, bed 27) and Tshirege (Tsankawi Pumice Bed, bed 18) Members of the Bandelier Tuff of northeastern New Mexico, is almost certainly far less than the frequency of small- and medium-magnitude eruptions. Based on the isotopic ages of ashes (beds 27 and 18 on Plate 1) formed during the large-magnitude eruptions of the Jemez Mountains area of New Mexico (see Smith [1979, p. 16] for volume estimates), their expected frequency may be something near one eruption in several hundred thousand years.

The frequency of gigantic ash-forming eruptions (>5 *M*) that formed the Huckleberry Ridge (20 *M*) and Lava Creek Tuffs (10 *M*) in Yellowstone National Park [*Christiansen*, 1979, p. 36] and their downwind equivalents, ash beds 36 and 11 (see Plate 1) is almost certainly far less than that of medium- and large-magnitude eruptions. The isotopic ages shown on Plate 1 suggest that gigantic ash-forming eruptions are infrequent and occur only about once in 1–2 m.y., on the average, in areas undergoing major episodes of plutonism and related ash flow magmatism.

The overall rate of ash-forming eruptions for the age span 4.0-0.1 m.y. can be compared to the rate of ash-forming eruptions at other times in the upper Mesozoic and Cenozoic in western North America. Ash and tuff beds (and their altered counterparts, bentonite beds) are widespread and common in sedimentary rocks of these ages. For example, 71 bentonite beds were counted in a roadcut exposure of 73 m of Lower Cretaceous (Albian Stage) marine rocks of the Mowry Shale near Casper, Wyoming [*Heathman*, 1939, pp. 16–17]. The Mowry is not unusual in its content of large numbers of bentonite beds. Hundreds of bentonites also occur in other Lower and Upper Cretaceous marine shale formations of the Western Interior [*Knechtel and Patterson*, 1956]. *Mapel and Pillmore* [1963, p. N54] recorded 16 bentonite beds (one bed 2 m thick) in the lower 23 m of the Mitten Black Shale Member of the Pierre Shale near Newcastle, Wyoming. The age span for the Mowry in eastern Wyoming is about 3.0 m.y. as determined by K-Ar dating of minerals in bentonite beds [*Obradovich and Cobban*, 1975, 1977, p. 1117]. Thus, the calculated average eruption rate for part of the Albian Stage of the Early Cretaceous is one eruption about every 40,000 years. The eruptions that formed the ash beds, now bentonite beds, in the Mowry (97–94 m.y. ago) and other Cretaceous marine rocks

TABLE 1. Eruption Magnitudes of a Few of the Ash Beds of Plate 1 and Some Other Well-Known Catastrophic Ash-Forming Eruptions of the Past

Eruption Unit or Ash Bed*	Date	Location	Magnitude, volume $km^3 \times 10^{-2}$	Reference
Huckleberry Ridge (36)	2.01 m.y. ago	Wyoming	20	*Christiansen* [1979]
Toba	75,000 years B.P.	Sumatra	20	*van Bemmelen* [1932]
Lava Creek B (11)	0.61 m.y. ago	Wyoming	10	*Christiansen* [1979]
Bishop (13)	0.74 m.y. ago	California	5	*Bailey et al.* [1976]
Upper Bandelier (18)	1.15 m.y. ago	New Mexico	3	*Smith* [1979]
Lower Bandelier (27)	1.47 m.y. ago	New Mexico	3	*Smith* [1979]
Mesa Falls (22)	1.27 m.y. ago	Idaho	2.8	*Christiansen* [1979]
Tambora	1815 A.D.	Tambora	1–3	*Lamb* [1970, p. 512]
Taupo ignimbrite	1,820 years B.P.	New Zealand	0.7	*Froggatt et al.* [1981, p. 109]
Mazama	6,500 years B.P.	Oregon	0.3	*Williams and Goles* [1968]
Santorini	1500 B.C.	Thera	0.3	*Watkins et al.* [1978]
Katmai	1912 A.D.	Alaska	0.2	*Curtis* [1968, p. 207]
Krakatoa	1883 A.D.	Java	0.06–0.18	*Lamb* [1970, p. 519]
Vesuvius	79 A.D.	Italy	0.026	*Lirer et al.* [1973]
Mount St. Helens	May 18, 1980	Washington	0.01	*Sarna-Wojcicki et al.* [1981]

* Number in parentheses refers to Plate 1.

of the Western Interior probably had their origin in the prolonged plutonic and related volcanic episodes that formed the Cretaceous batholiths of California and Idaho.

Desborough et al. [1973, p. 42] studied 23 different, thick biotite-bearing tuffs in the lacustrine rocks of the middle Eocene Green River Formation in the Uinta Basin of Utah. That part of the Green River Formation that contains the biotite-bearing tuffs studied by Desborough et al. spans about 5 m.y., as suggested by K-Ar age determinations made by *Mauger* [1977]. These data suggest an average rate of about one eruption every 200,000 years for the middle Eocene. However, J. R. Dyni of the U.S. Geological Survey has identified many more tuffs in equivalent middle and upper Eocene rocks near Indian Canyon in the Uinta Basin, Utah. J. R. Dyni (written communication, 1980) counted 165 tuffs thicker than 0.5 cm in a 953-m-thick shale sequence that ranges from about 46–40 m.y., as estimated from the geochronologic work of *Mauger* [1977]. These data suggest an average rate of one eruption every 35,000 years in the middle and late Eocene. A minimum of 37 ash beds were recorded by the late T. Galusha in the continental sedimentary rocks of the Miocene Skull Ridge Member of the Tesuque Formation of the Santa Fe Group of *Galusha and Blick* [1971, Figure 17] during an age span of about 3 m.y. [*Izett and Naeser,* 1981]. This information suggests an average minimum rate of about one eruption every 80,000 years for the middle Miocene. A minimum of 40 tuffs were counted by the author in the Miocene continental rocks of the Troublesome Formation in Middle Park, Colorado. The age span, based on fission-track zircon ages [*Izett and Barclay,* 1973], of that part of the Troublesome Formation in which these tuffs were deposited is about 7 m.y. Accordingly, one eruption in every 175,000 years is recorded by the Miocene rocks of the Troublesome.

The calculated eruption frequencies for rocks deposited in continental fluvial environments must vary widely and be much less than the calculated frequencies for rocks deposited in marine or lucustrine environments such as the Mowry and Green River formations. The wide variation and less frequent, calculated eruption rates for ashes in continental fluvial environments most probably result from the smaller chance for ash bed preservation in high-energy regimes.

ASH BED CLASSIFICATION

Most highly siliceous volcanic ash beds of the western United States, including those listed on Plate 1, can be grouped into two somewhat intergradational chemical types, rhyolitic and dacitic ashes. (The definitions used for rhyolite and dacite in this paper are somewhat different than the definitions recently used by *Ewart* [1979, p. 15] for salic volcanic rocks. Ewart defined dacite as a volcanic rock that contains 63–69 wt % SiO_2 and rhyolite as a volcanic rock that contains more than 69 wt % SiO_2. As used in the present report, dacite can be nearly as highly siliceous as rhyolite except dacite has more calcium and less potassium than rhyolite.)

These two different ash bed types can be distinguished based on the chemical composition of their glass shards. The main property that distinguishes dacitic from rhyolitic ashes is the greater Ca and Mg and smaller K content in glass shards of dacitic ashes compared to rhyolitic ashes. Dacitic volcanic ashes are here arbitrarily defined to have more than 0.55 wt % Ca. Rhyolitic ashes were subdivided further into two types, W- and G-type rhyolites, based on the presence of biotite in the W-type and its absence in G-type rhyolitic ashes. Chemical analyses of the glass shards of the ash beds of Plate 1 and hundreds of other vitric Tertiary ashes and tuffs show that nearly all W-type rhyolitic ashes have Fe and Ca contents less than 0.55 wt %. A plot of the Ca and Fe content of the glass shards of many of the volcanic ash beds listed on Plate 1 is shown on Figure 1. Ca and Fe were chosen because they are elements that have fairly large weight percent variation in comparison with other major rock-forming elements. Additional characteristics of the three ash bed types, W-type rhyolitic, G-type rhyolitic, and dacitic are given in the discussion that follows.

W-type rhyolitic ashes (1) are chalky white megascopically, (2) have less than 0.55 wt % Fe and less than 0.55 wt % Ca in the glass shards, (3) always have phenocrystic biotite and lack fayalite, (4) characteristically have a large percentage of microscopically colorless glass shards of pumiceous habit whose indices of refraction generally range from 1.494 to 1.497, (5) have a low percentage of glass shards that contain microlites, (6) generally have microphenocrysts of quartz, sanidine (soda poor), plagioclase (oligoclase), clinopyroxene, hornblende, magnetite, ilmenite, apatite, and allanite (mineral species that occur in a few rhyolitic ash beds include orthopyroxene and sphene), (7) generally have SiO_2 contents of the glass shards (corrected volatile-free) from 76 to 79 wt %, and (8) have glass shards with narrow compositional ranges for the major rock-forming elements.

G-type rhyolitic ashes (1) are light to medium gray megascopically, (2) have from 0.55 to 2.0 wt % Fe and less than 0.55 wt % Ca in the glass shards (some upper Cenozoic, G-type rhyolitic ashes, but none shown on Plate 1, have as much as 2.5 wt % Fe in glass shards), (3) lack phenocrystic biotite, (4) mainly have colorless (microscopically), platy bubble wall and bubble junction glass shards whose indices of refraction range from 1.497 to 1.520, (5) generally lack glass shards that contain microlites, (6) have a microphenocryst asemblage that generally includes sanidine (soda rich), sodic plagioclase (oligoclase), clinopyroxene and hornblende (Fe-rich varieties in some instances), fayalite, magnetite, ilmenite, apatite, allanite, and chevkinite, (7) generally have SiO_2 contents of the glass shards (corrected volatile-free) from 72 to 79 wt %, and (8) have glass shards with narrow compositional ranges for the major rock-forming elements.

Dacitic ashes (1) are white to light gray or light grayish brown megascopically, (2) have more than 0.55 wt % Fe and Ca in the glass shards, (3) may have a complex mixture of shard shapes, including pumiceous, fibrous, chunky, and bubble wall and bubble junction types, (4) have indices of refraction of glass shards that range widely from 1.496 to 1.530, (5) commonly contain appreciable numbers of light brown glass shards compared to the numbers of colorless glass shards, (6) commonly contain glass shards charged with ferromagnesian mineral and feldspar microlites, (7) frequently lack microphenocrystic quartz, sanidine, and biotite but have a microphenocryst suite that may contain plagioclase (typically andesine), clinopyroxene, orthopyroxene, amphibole (hornblende and cummingtonite), magnetite, ilmenite, and apatite, (8) generally have SiO_2 contents of glass shards that are less than the SiO_2 contents in W- and G-type rhyolitic ashes and that range from 67 to 77 wt %, and (9) for a particular ash bed, have glass shards that have wide compositional ranges for the major rock-forming elements.

In summary, the chief chemical property that distinguishes

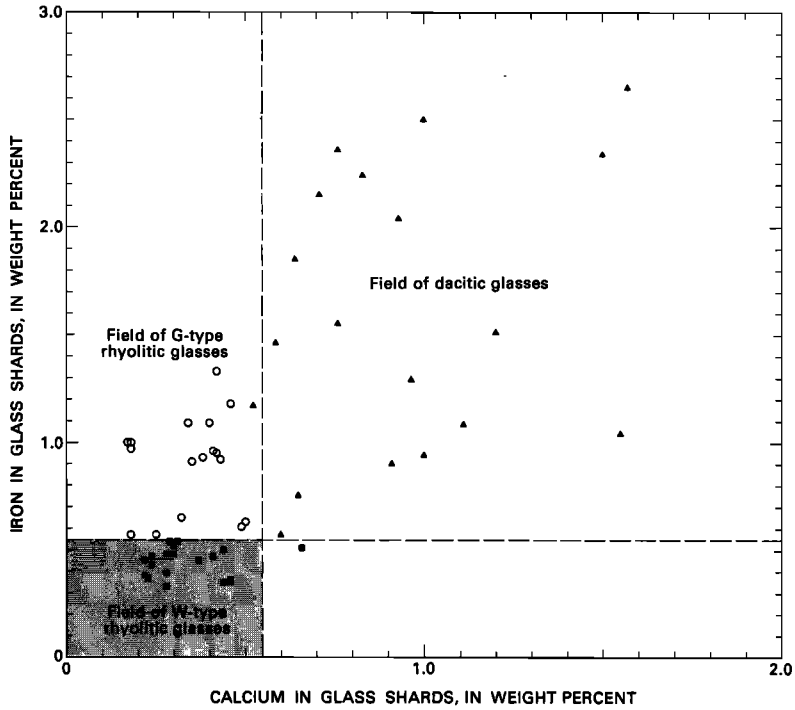

Fig. 1. Diagram showing the iron and calcium content of some of the ash beds of Plate 1. Circle, G-type rhyolitic glasses; square, W-type rhyolitic glasses; triangle, dacitic glasses. Field of biotite-bearing rhyolitic glasses shaded.

the rhyolitic ash beds from the dacitic ash beds of Plate 1 is the greater Ca content in the glass shards of the dacitic ashes. Of nearly equal importance is the lower K and higher Mg content of the glass shards of dacitic ashes compared with rhyolitic ashes. In addition, dacitic volcanic ashes frequently lack quartz and sanidine microphenocrysts.

The most important characteristic of W-type (as compared to G-type) rhyolitic ash beds is their ubiquitous content of biotite. Of secondary importance is the general lack of fayalite in W-type rhyolitic ashes and the characteristically lower Fe content of the glass shards (less than 0.55 wt % Fe) of W-type compared with G-type ashes.

The geologic setting in which most W- and G-type rhyolitic magma systems, including the Long Valley, Yellowstone National Park, and Jemez Mountains, were generated is in areas underlain by continental crust undergoing extensional tectonics. The geologic setting in which most dacitic ash beds were generated is chiefly in areas near active continental-oceanic plate convergence such as the Cascade Mountains region of the Pacific Northwest.

SHARD SHAPE

As mentioned before, one of the characteristic properties of most W-type rhyolitic ashes is their pumiceous shard shape that contrasts markedly with the platy, bubble wall and bubble junction shard shape of many, but not all, G-type rhyolitic ashes. One possible explanation for this difference in shard shape may be that W-type rhyolitic ashes formed from magmas that were more viscous than were the magma progenitors of G-type rhyolitic ashes. The dominant factors that govern the viscosity of a magma, and perhaps the shard morphology of ashes formed during a pyroclastic eruption of that magma, include temperature, chemical composition, and volatile content (H_2O and halogens). For magmas of very similar major element composition, such as progenitors of W- and G-type rhyolitic ashes, temperature may have a first-order effect on controlling the viscosity. Inferred quench temperatures calculated for the parent magmas of several G- and W-type rhyolitic ashes listed on Plate 1 and of certain other upper Cenozoic rhyolitic ashes are given on Table 2, as are their dominant shard habits and Fe contents. Temperatures were calculated using electron microprobe analyses of coexisting, unaltered, glass-mantled titanomagnetite and ilmenite microphenocrysts. The method of *Carmichael* [1967] was applied to recast the electron microprobe data and the regression curve of *Powell and Powell* [1977] was used to infer temperature.

Table 2 shows that most W-type rhyolitic ashes, which have pumiceous shard shapes, seemingly were formed at temperatures between 695°C and 830°C. In contrast, most G-type rhyolitic ashes, which mainly have bubble wall and bubble junction shard shapes, seemingly were formed at higher temperatures between 870°C and 1000°C. Small, but consistent, compositional differences between W- and G-type rhyolitic magmas may have had a second-order effect on controlling the viscosity and subsequent shard shape. W- and G-type rhyolitic ashes have similar major element compositions, but the Fe content of the two ash types are consistently different (see Plate 1 and Table 3). Metallic elements such as Fe have a marked effect on breaking the polymerized Si-O tetrahedra in a silicate melt [*Mason*, 1966, p. 119], and thus, rhyolitic magmas that had a low Fe content (W-type) may have been slightly more viscous than rhyolitic magmas that had a higher Fe content (G-type).

An example of how small differences in the Fe content of rhyolitic magmas may perhaps influence which shard morphologies form during pyroclastic eruptions is provided by the Mesa Falls (bed 22) and Lava Creek B (bed 11) ash beds of Plate 1 and Table 2. These ash beds formed during eruptions in the Yellowstone National Park area at 1.27 and 0.61 m.y. (Plate 1), and they have a remarkably similar major element

TABLE 2. Inferred Temperatures of Equilibration and Compositions of Coexisting Titanomagnetite and Ilmenite Microphenocrysts From Certain Upper Cenozoic Rhyolitic Ash Beds Listing the Iron Content of Glass Shards and Shard Morphology

Shard Shape	Location	Ash Bed Name or Age	Magnetite, wt %					Ilmenite, wt %							Temperature,† °C	Fe in Glass Shards, wt %
			Fe	Ti	Mg	Mn	Al	Fe	Ti	Mg	Mn	Al	Usp	Hm		
			W-Type Rhyolitic Glasses													
P	Long Canyon, Calif.*	Long Canyon	65.7	2.7	0.09	2.9	0.4	29.9	28.3	0.2	8.8	0.0	13.1	9.0	695‡	0.36
P	Cowan Mine, Calif.	Taylor Canyon-P	64.0	2.6	0.2	1.6	0.4	32.8	25.8	0.6	3.9	0.1	12.9	12.0	690	0.36
P	Ranch Canyon, Utah	Ranch Canyon	66.7	2.4	0.1	2.1	0.6	34.8	26.1	0.4	5.5	0.4	11.5	15.8	710	0.39
P	Middle Park, Colo.	Miocene	64.3	5.6	0.3	0.5	0.7	35.9	26.0	0.6	2.8	0.1	26.5	14.0	825	0.43
P	Middle Park, Colo.	Miocene	65.2	4.9	0.4	1.1	0.5	37.1	27.8	0.5	1.3	0.4	23.2	10.4	740	0.50
P	Browns Park, Colo.	Miocene	64.5	4.5	0.2	0.9	0.6	35.6	28.4	0.5	2.1	0.1	21.7	8.3	710	0.52
P	western U.S.	Bishop	63.8	5.2	0.2	0.7	0.7	34.5	27.4	0.4	1.4	0.1	25.2	7.3	720	0.52
P	Espanola Basin, N.M.	Miocene	62.6	5.6	0.1	0.9	0.6	36.5	28.4	0.5	1.5	1.2	27.3	8.4	775	0.54
B,P	Chimney Rock, Neb.	Oligocene	63.6	3.9	0.5	1.3	0.5	38.5	23.8	0.8	1.7	0.1	19.0	20.6	830	0.57
			G-Type Rhyolitic Glasses													
B	Hemphill County, Tex.	Miocene	61.5	8	0.8	0.4	0.7	36.7	27.3	0.7	0.6	0.8	40.9	10.3	870	0.88
P	western U.S.	Mesa Falls	57.1	10.6	0.1	0.4	0.6	35.9	27.5	0.2	0.5	0.1	52.0	7.1	880	0.95
B	western U.S.	Lava Creek B	56.7	10.8	0.1	0.4	0.6	35.2	27.1	0.2	0.5	0.1	53.1	6.9	880	1.09
B	western U.S.	Huckleberry Ridge	56.3	11.5	0.1	0.4	0.6	35.0	27.5	0.2	0.5	0.1	56.3	5.8	870	1.18
B	Middle Park, Colo	Miocene	51.8	13.3	0.4	0.3	0.8	35.1	27.9	0.6	0.5	0.2	66.3	6.9	980	1.45
B	Browns Park, Colo.	Miocene	50.4	13.8	0.9	0.2	0.5	35.3	28.1	0.6	0.3	0.2	69.2	6.3	985	1.50
B	Sioux County, Neb.	Miocene	51.7	14.5	0.1	0.4	0.6	35.2	28.3	0.6	0.3	0.2	72.0	5.9	1000	2.32

* Analytical data from source area rock (rhyolite of Long Canyon) [from *Bacon and Duffied*, 1981].

†Microprobe anaytical data recast using the method of *Carmichael* [1966]. Temperatures of equilibrated magnetite and ilmenite microphenocrysts of the ashes calculated using the method of *Powell and Powell* [1977] based on the data of *Buddington and Lindsley* [1964]. Temperatures rounded to nearest 5°C.

‡ Temperature calculated by *Bacon and Duffied* [1981].

composition, with the exception of their Fe content of glass shards (Table 3). Lava Creek B ash beds have consistently more Fe (0.14 wt %) in their glass shards compared with the Fe content of glass shards of Mesa Falls ash beds. Moreover, the compositions and inferred quench temperatures of unaltered, glass-mantled titanomagnetite and ilmenite microphenocrysts of these ash beds are also nearly identical (Table 2). However, the shard shapes of the two ash beds are strikingly different. The glass shards of Lava Creek B ash (bed 11 on Plate 1) are chiefly large radius, bubble wall and bubble junction types, whereas the glass shards of Mesa Falls ash beds (bed 22 on Plate 1) are mainly pumiceous types. Figure 2 illustrates the typical shard habits of the Mesa Falls and Lava Creek B ash beds, and in addition, the pumiceous, low-Fe-content shards of the Bishop ash bed.

The combined effect of higher magmatic temperature and greater Fe content (see Table 2) of G-type magmas (if it is assumed that the volatile and SiO_2 contents are nearly equal in the two magma types) may have exerted an important influence on the way in which the magmas vesiculated to produce, on the one hand, bubble wall and bubble junction shards of G-type rhyolitic ashes and, on the other hand, pumiceous shards of W-type rhyolitic ashes.

The foregoing remarks concerning the physical and chemical conditions in magma chambers that may influence glass shard morphologies formed during pyrolclastic eruptions are

TABLE 3. Chemical Composition of the Glass Shards of the Mesa Falls and Lava Creek B Volcanic Ash Beds

	Mesa Falls Ash*	Lava Creek B Ash†
SiO_2	72.96 ± 0.17	72.97 ± 0.31
Al_2O_3	11.88 ± 0.14	11.77 ± 0.10
Fe_2O_3	0.49 ± 0.03	0.57 ± 0.05
FeO	0.79 ± 0.03 (total iron as Fe 0.95)	0.89 ± 0.04 (total iron as Fe 1.09)
MgO	0.06 ± 0.006	0.08 ± 0.04
CaO	0.59 ± 0.01	0.56 ± 0.07
Na_2O	2.46 ± 0.24	3.01 ± 0.26
K_2O	6.10 ± 0.39	5.38 ± 0.39
H_2O^+	3.79 ± 0.19	3.77 ± 0.21
H_2O^-	0.22 ± 0.06	0.16 ± 0.06
TiO_2	0.11 ± 0.006	0.12 ± 0.01
P_2O_5	0.005 ± 0.006	0.03 ± 0.02
MnO	0.03 ± 0.001	0.04 ± 0.001
CO_2	0.01 ± 0.06	0.02 ± 0.02
Cl	0.13 ± 0.005	0.13 ± 0.03
F	0.17 ± 0.01	0.14 ± 0.04

Analyses by E. L. Brandt, E. E. Engleman, P. Montaldo, C. L. Parker, and D. F. Powers of the U.S. Geological Survey; ± is one standard deviation about the mean; analytical data in weight percent.

* Mean of four standard gravimetric analyses of the Mesa Falls ash (bed 22 on Plate 1) from scattered localities in the western United States.

† Mean of 12 standard gravimetric analyses of the Lava Creek B ash (bed 11 on Plate 1) from scattered localities in the western United States.

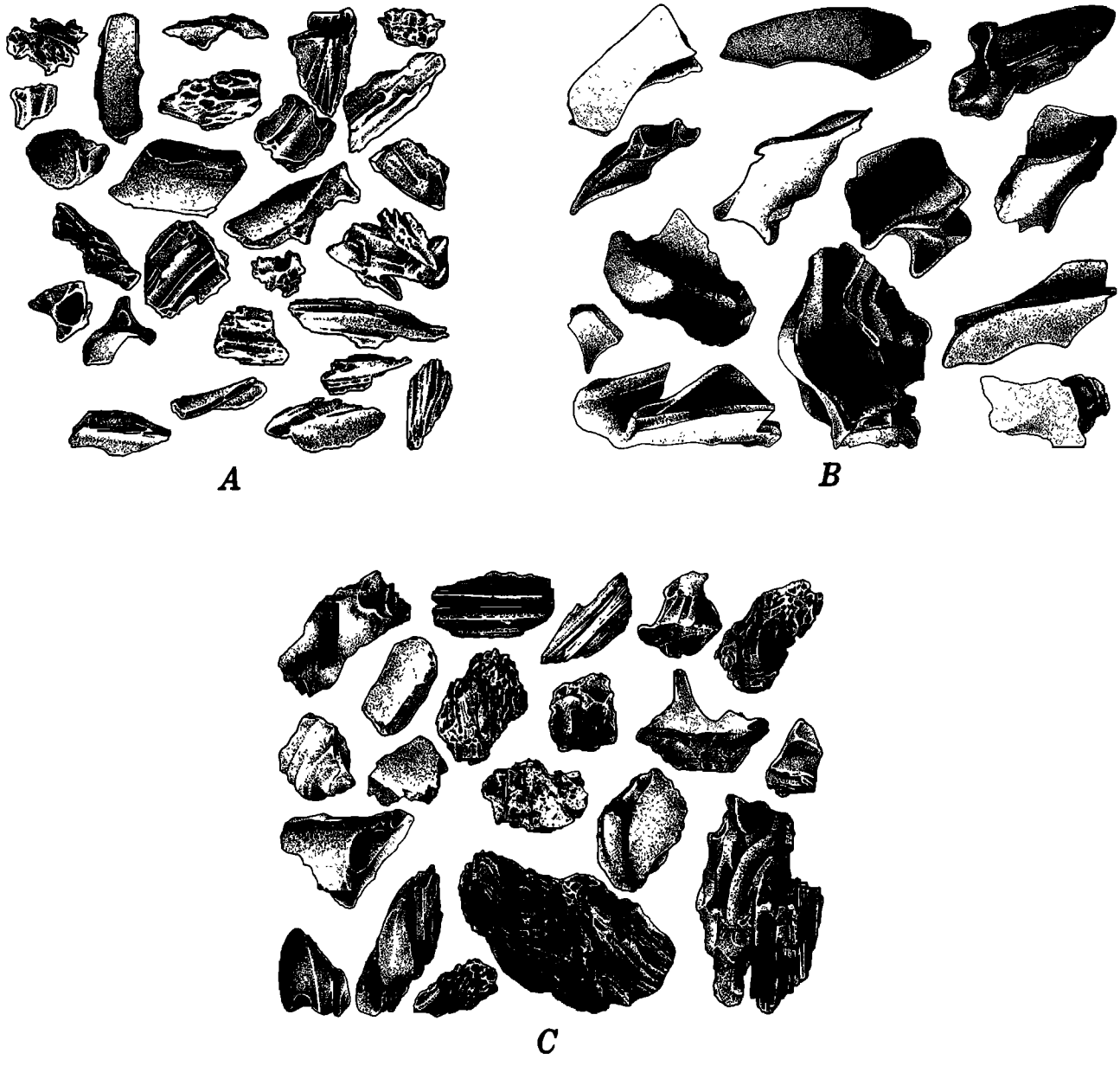

Fig. 2. Drawings made from photomicrographs showing typical shard morphology for Mesa Falls, Lava Creek B, and Bishop ash beds. (*a*) Mesa Falls ash from Nebraska showing its typical chunky, pumiceous shards. (*b*) Lava Creek B ash from Utah showing its typical bubble wall and bubble junction shards. (*c*) Bishop ash from Wyoming showing its typical pumiceous shards. Drawings made by A. L. Isom of the U.S. Geological Survey. Magnification about 100 ×.

undoubtedly oversimplified. Other factors, such as as vent shape and depth of vesiculation, may also affect the type of shard morphology formed. Furthermore, the volatile content of magmas just prior to their eruption and vesiculation is difficult to ascertain, but its influence on viscosity of magmas is pronounced [*Shaw*, 1965, p. 121].

To determine the amount of volatiles in magmas, *Anderson* [1976] measured the concentration of major and minor elements in glass inclusions in phenocrysts in some mafic and intermediate composition volcanic rocks using the electron microprobe. As shown by Anderson, the amount of major and minor elements in some glass inclusions totals only about about 95 wt %. The assumptions, which seem valid, are that the glass inclusions are tiny samples of magma trapped by crystals during growth and that the difference between the sum of the major and minor elements and 100% is an indication of the amount of volatiles that were present in the magma. The writer made electron microprobe analyses of glass inclusions in quartz, sanidine, and plagioclase microphenocrysts separated from tephra from the Yellowstone National Park area (bed 11, Plate 1), the Jemez Mountains area of New Mexico (beds 24 and 27, Plate 1), and the Long Valley area of California (beds 13, 37, and 38, Plate 1). The analyses suggest that the volatile contents of their magmas was about 5 wt % (G. A. Izett, unpublished data, 1981). In each instance, the major element composition (Si, Al, Mg, Ca, and Fe) of the glass inclusions in quartz and felpspars exactly mimic the composition of the host hydrated glass of the tephra. In contrast, electron microprobe analyses of glass inclusions in quartz and feldspar separated from several rhyolite obsidian flows from Yellowstone National Park suggest that the volatile content of their magmas may have been considerably less, no more than 1–2 wt % (G. A. Izett, unpublished data, 1981). Another line of evidence suggesting that glass inclusions con-

tain appreciable amounts of volatiles is the observation that the index of refraction of glass inclusions in quartz and feldspar microphenocrysts of the rhyolite tephras of Plate 1 are significantly greater than would be expected for nonhydrated glasses of their compositions (G. A. Izett, unpublished data, 1981).

MINERALOGY OF ASH BEDS

Primary crystals in volcanic ash beds generally can be distinguished from detrital minerals incorporated in ashes during deposition by the presence of glass coatings, crusts, or mantles on the primary microphenocrysts and the absence of glass coatings on detrital minerals. During study of volcanic ashes, application of the glass-mantle criteria [see *Wilcox,* 1965, p. 813] must be strictly invoked to insure that the primary mineral assemblage of volcanic ashes, which is used to characterize a certain ash, is correctly compiled.

The primary minerals of volcanic ash beds are generally small euhedral crystals and broken crystals that grew just prior to the time of vesiculation and quenching of a magma. The amount of crystals in pumice blocks found in volcanic source areas is small, generally from 5 to 15%. In contrast, the amount of primary crystals in ash beds far downwind from their source areas is typically far less than 1%.

The primary microphenocrysts found in volcanic ash beds, and in particular, the volcanic ash beds on Plate 1, comprise assemblages of the following minerals: quartz, sanidine, sodic-plagioclase, biotite, amphibole, clinopyroxene, orthopyroxene, fayalite, zircon, apatite, allanite, chevkinite, sphene, magnetite, and ilmenite. Study of hundreds of samples of volcanic ash beds of Oligocene to Holocene age from the Western Interior by the author shows that they also may contain the above listed minerals, but in a few ash beds, perrierite and monazite. Most ash beds contain only one compositional type of each of the above listed minerals. An exception to this observation is that certain ashes derived from some Cascade volcanoes contain two kinds of amphibole, common hornblende and cumingtonite.

Some primary minerals of those listed above, seemingly are restricted to one of the three ash bed types. Fayalite and chevkinite have been found only in G-type rhyolitic ash beds. Biotite, sphene, monazite, and perrierite have only been found in W-type rhyolitic ash beds. High-temperature beta quartz and sanidine nearly always constitute the chief microphenocrysts of W- and G-type rhyolitic ashes, but they rarely are found in dacitic ash beds. Zircon typically occurs in many rhyolitic ash beds but is not nearly as common in dacitic ash beds. Although small amounts of allanite and apatite are present in some G-type rhyolitic ash beds, they are pervasive members of the accessory mineral suite of most W-type rhyolitic ash beds. Apatite typically occurs in dacitic ash beds.

Noteworthy is the observation that glass-mantled primary microphenocrysts of garnet, anorthoclase, and sodic-amphibole and sodic-clinopyroxene have not been in volcanic ash beds of the western United States, although these minerals are reported to occur in some ash flow tuffs. Garnet, for example, is reported to occur in some tuffs [*Wood,* 1974, p. 768], but in the authors experience, garnet either occurs as a vapor phase crystallization mineral or a xenocryst but not as a primary, glass-mantled microphenocryst.

The chemical composition, with respect to major elements, of crystals of many rhyolitic volcanic ash beds are generally uniform from crystal to crystal and within individual crystals. Electron microprobe analyses of feldspar, ferromagnesian, iron-titanium oxide, and accessory minerals of the Bishop Tuff [*Hildreth,* 1977] show that individual crystals are not compositionally zoned. In a similar manner, electron microprobe analyes of primary crystals in ashes derived from the Yellowstone National Park area (G. A. Izett, unpublished data, 1981) and from the Jemez Mountains area [*Izett et al.,* 1972] also are not compositionally zoned with respect to major elements. However, study of the nonopaque crystals of volcanic ash beds using a petrographic microscope and the focal masking technique [*Wilcox,* 1962] to measure their refractive indices suggests that some individual crystals may have very small compositional variations not detectable by the electron microprobe.

Whether primary crystals of volcanic ashes are uniform with respect to trace elements is, in general, difficult to ascertain. However, trace amounts of uranium can be detected and the uranium distribution determined by recording the damage traces of ^{235}U fissions in muscovite detectors placed over crystal surfaces [see *Naeser,* 1969]. Primary, glass-mantled zircon microphenocryts in the Huckleberry Ridge Tuff and Huckleberry Ridge ash (bed 36 on Plate 1) contain a bimodal assemblage of glass-mantled zircons, both pink and colorless. Using the above technique, uranium distribution maps of zircon crystals (Figure 3) show that pink zircons of this tuff and ash bed contain several orders of magnitude more uranium than do colorless zircon crystals. In some instances, the boundary between the areas of high- and low-uranium concentration within a zircon crystal are sharp, linear, and outline a uranium-rich core (Figure 3*b*). Perhaps the zircon crystals that have uranium-rich cores are (1) xenocrysts derived from much older country rocks and incorporated in the Huckleberry Ridge magma or (2) crystals that grew early in the magmatic history of the Huckleberry Ridge in an enrironment conducive to formation of uranium-rich zircon.

Primary zircon crystals from some W-type rhyolitic ash beds, for example, the lower part of the Bishop Tuff and all Bishop ashes (bed 13 on Plate 1), have zircons with uniform uranium concentrations. In contrast, zircon microphenocrysts from the upper part of the Bishop Tuff (orthopyroxene and clinopyroxene-bearing unit) include colorless and pink varieties. Many pink zircon crystals from the cores of large pumice blocks from the upper pyroxene-bearing unit of the Bishop Tuff have uranium-rich cores and markedly more uranium than do colorless zircon crystals.

Before turning to the discussion of the chemical composition of the ash beds, the question of why biotite seemingly is found only in low-Fe content rhyolitic volcanic ash beds (herein called W-type) might be speculated upon. One possible explanation may be that biotite is only stable in rhyolitic magmas at temperatures of less than about 850°C, as suggested by the data of Table 2 and by data of *Wall and Clemens* [1979]. However, other factors than temperature doubtlessly also have an affect on the stability of biotite in rhyolitic magmas including pressure, oxygen fugacity, and composition of the magma including its content of H_2O and halogens.

CHEMICAL COMPOSITION OF ASH BEDS

In the past four decades, chemical composition has been used extensively to fingerprint or characterize volcanic ash beds for correlation, including studies by *Swineford and Frye* [1946], *Powers et al.* [1958], *Powers and Malde* [1961], *Jack and Carmichael* [1968], *Theisen et al.* [1968], *Smith and Westgate* [1969], *Borchardt* [1970], *Izett et al.* [1970], *Borchardt and*

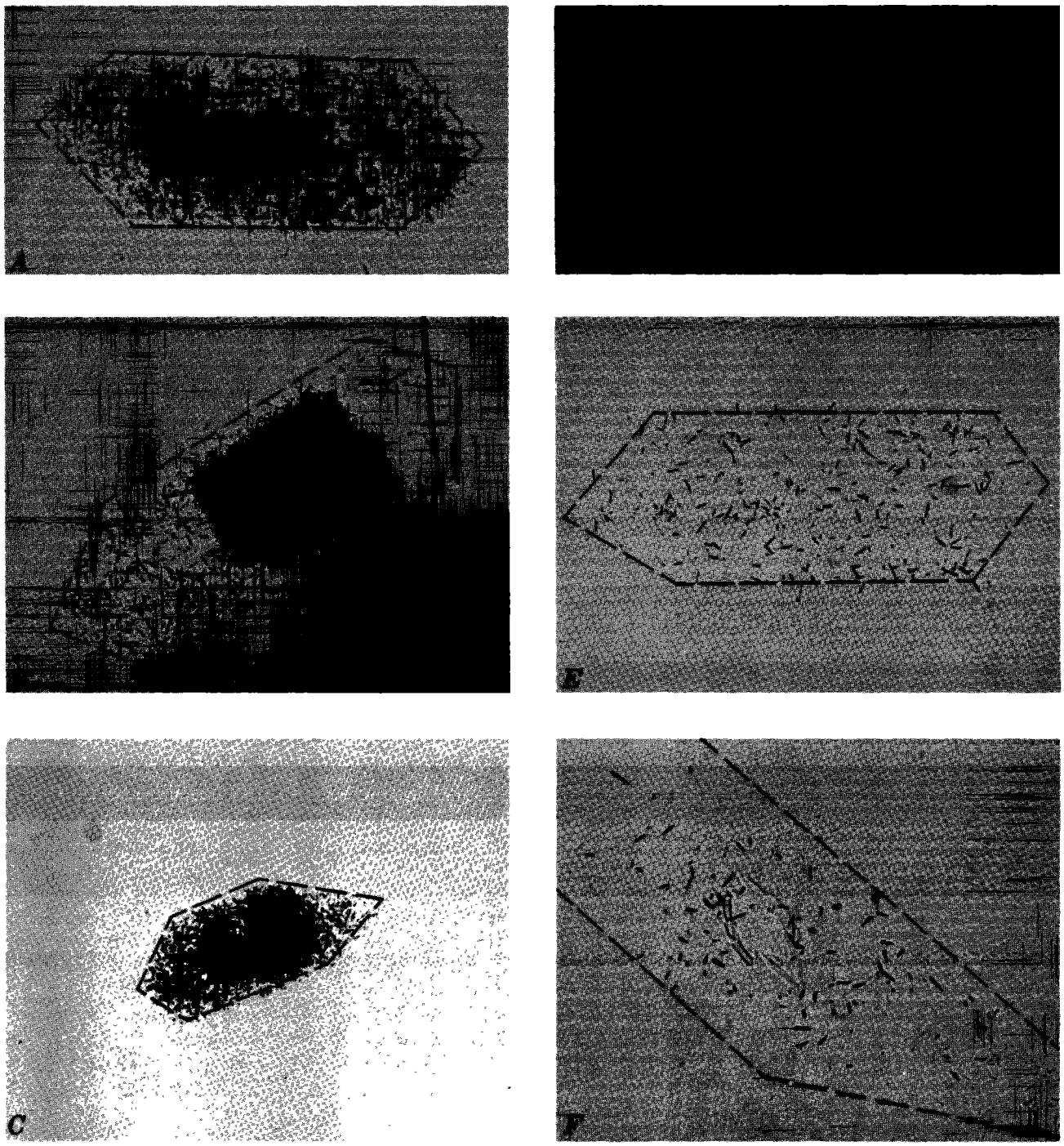

Fig. 3. Photomicrographs of fission tracks in muscovite detectors placed over pink and colorless glass-mantled zircon crystals from a Huckleberry Ridge ash bed from Kansas (bed 36, Plate 1). Uranium-rich cores of pink zircons clearly shown by induced fission track density. Approximate outline of polished surfaces of zircon crystals that were below muscovite detectors shown by dashed lines. Pink and colorless zircon crystals received the same neutron fluence (1.0×10^{15} cm^2) and had adjacent positions in the reactor package during irradiation. (*a*)–(*c*) Pink zircon crystals. (*d*)–(*f*) Colorless zircon crystals. Zircon crystals about 100 μm long.

Harward [1971], *Borchardt et al.* [1972], *Izett et al.* [1972], *Sarna-Wojcicki* [1976], *Nash and Smith* [1977], *Sarna-Wojcicki et al.* [1979], *Scheidegger et al.* [1980], and *Sarna-Wojcicki et al.* [1980].

Partial chemical analyses of the glass shards for most of the ash beds are shown on Plate 1. Considerably more chemical data for the ash beds are available, but only a condensed array of chemical data is presented here. Differences and similarities in chemical composition among some of the ash beds are pointed out on Plate 1.

The composition of the glass shards of the volcanic ash beds listed on Plate 1 are highly silicic in that their Si content ranges from about 67 to 79 wt % SiO_2 (calculated volatile-free). Most of the rhyolitic ashes are highly evolved types that contain from about 74 to 79 wt % SiO_2, calculated volatile-free. The dacitic ashes on Plate 1 vary from about 67 to as much as 77 wt % SiO_2; the Al content ranges from about 10.5 to 14.5 wt % Al_2O_3. In general, the G-type rhyolitic ashes have the lowest Al content, and the dacitic ashes have the highest content of Al. The Mg content is low in the rhyolitic ashes (as

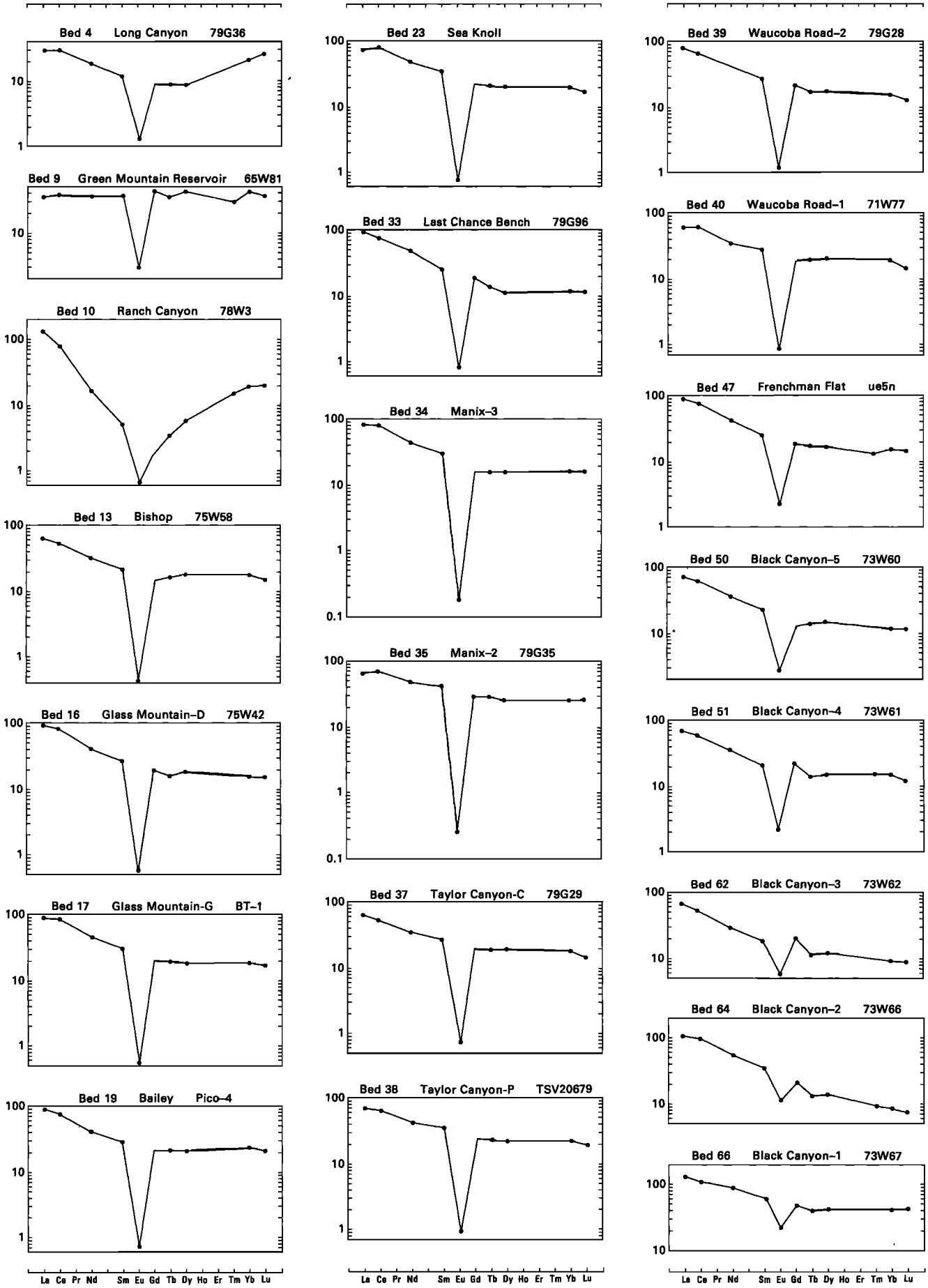

Fig. 4. Rare-earth element diagrams for W-type rhyolitic glasses of ash beds shown on Plate 1 for which analytical data are available. Amounts of rare-earth elements were normalized to amounts of these elements in chondritic meteorites; they were plotted on a logarithmic scale against rare-earth element numbers increasing from left to right. Explanation for Figures 4, 5, and 6 is shown on Figure 5.

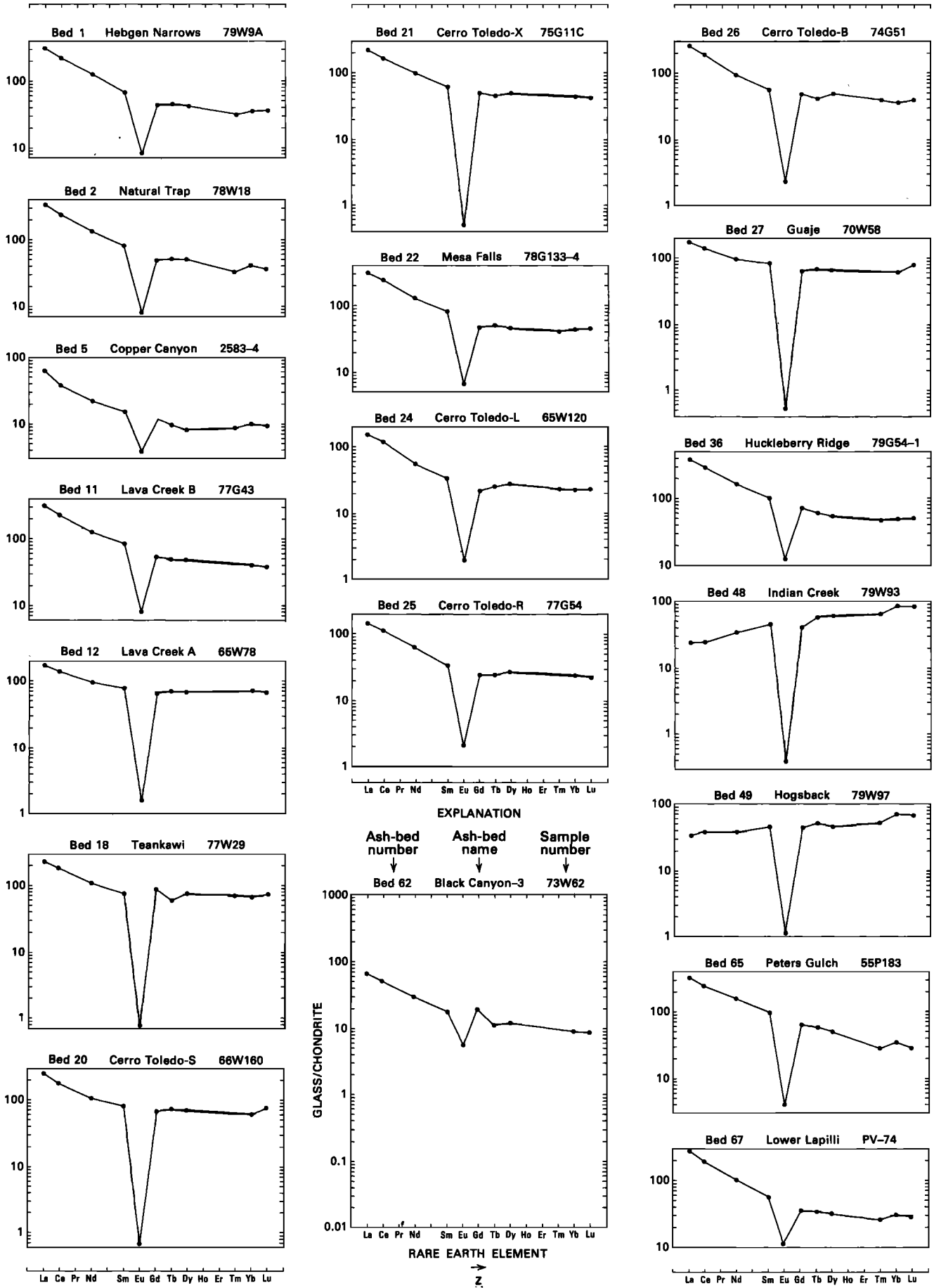

Fig. 5. Rare-earth element diagrams for G-type rhyolitic glasses of ash beds shown on Plate 1 for which analytical data are available. Amounts of rare-earth elements were normalized to amounts of these elements in chondritic meteorites and plotted on a logarithmic scale against rare-earth element numbers increasing from left to right.

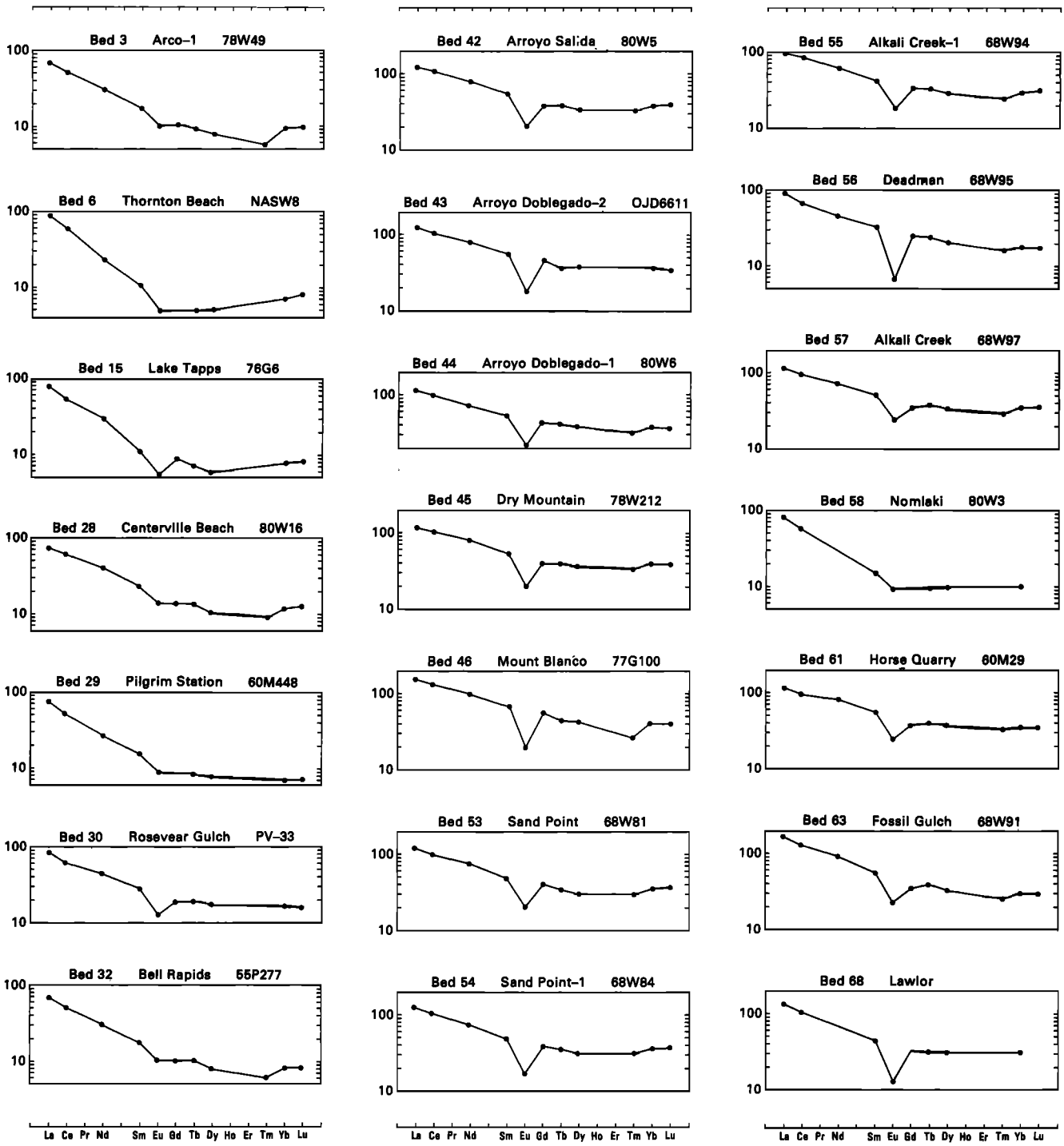

Fig. 6. Rare-earth element diagrams for dacitic glasses of ash beds shown on Plate 1 for which analytical data are available. Amounts of rare-earth elements were normalized to amounts of these elements in chondritic meteorites and plotted on a logarithmic scale against rare-earth element numbers incresing from left to right.

little as 0.06 wt % MgO) and is considerably higher in dacitic ashes (1.0 wt % MgO). Dacitic ashes have the highest Fe content in the glass shards (expressed as Fe_3O_4) ranging from about 0.80 to 3.8 wt %; rhyolitic ashes have the lowest amounts of Fe expressed as Fe_3O_4 (0.5–1.9 wt %). Ca ranges from an unusually low amount (0.25 wt % CaO) in ashes derived from the Jemez Mountains area (especially beds in beds 27 and 18) to as much as 2.2 wt % CaO in dacitic ashes derived from the Cascade volcanic province.

All the glass shards of the ashes listed on Plate 1 are hydrated (as are all other ash beds of the upper Cenozoic) and some contain as much as 4.5 wt % H_2O. The original amounts of Na and K in the glass shards of the ashes, as they were erupted, cannot be accurately determined because of cation exchange between ground water and the glasses during hydration [*Lipman*, 1965]. In general, Na is lost and K is gained, and this diagentetic change probably accounts for much of the differences in Na and K content (Table 3) of the Mesa Falls (bed 22 of Plate 1) and Lava Creek B ashes (bed 11 of Plate 1).

W-type rhyolitic ashes were probably peraluminous to met-

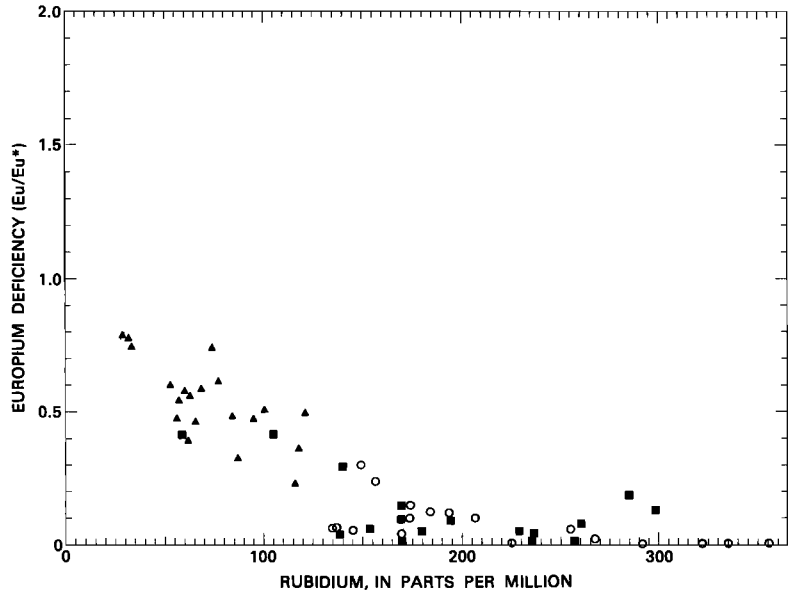

Fig. 7. Diagram showing a plot of the amount of rubidium (in ppm) against the europium deficiency (Eu/Eu*) estimated from rare-earth element diagrams for the ash beds shown on Plate 1 for which data are available. Eu* is the europium concentration estimated by projection of the rare-earth element line between samarium and gadolinium, as if no europium anomaly were present. Circle, G-type rhyolitic glasses; square, W-type rhyolitic glasses; triangle, dacitic glasses.

aluminous when erupted, and G-type rhyolitic ashes were probably subaluminous to peralkaline. However, the original content of the alkali elements K and Na, relative to Al, in the glass shards of the ashes as erupted, cannot be determined as suggested above.

Rare-earth element (REE) plots for the glasses of those ash beds and tuffs listed on Plate 1, for which analytical data are now available, were drawn. Plots of W- and G-type rhyolitic and dacitic glasses are grouped on Figures 4, 5, and 6. The localities of the ash beds on these diagrams are described in the section of this report listing the principal occurrences of each ash bed.

Only one REE plot for each ash bed is shown on Figures 4, 5, and 6, and it was chosen, in most instances, for the ash bed at its principal geographic locality. REE plots of ashes of the same fall, but at different localities, are nearly identical. Moreover, REE diagrams for volcanic ash beds generated from the same volcanic source region, such as the Yellowstone National Park area, are also much alike (compare REE diagrams from ash beds 36, 22, 12, 11, 2, 1). In a similar way, REE diagrams of ash beds suspected to have been generated in the Long Valley-Glass Mountain area, California (ash beds 62, 51, 50, 47, 40, 39, 38, 37, 35, 34, 33, 23, 19, 17, 16, and 13), over a considerable time span are much alike. These two groups of ash beds provide insight into the changes that took place in the mineralogical-chemical evolution of their source area magma systems in the Yellowstone National Park and Long Valley-Glass Mountain areas.

As shown on Figures 4, 5, and 6, nearly all of the W- and G-type rhyolitic glasses have fairly large Eu deficiencies compared with adjacent rare-earth elements. In contrast, dacitic glasses have much smaller Eu deficiencies. Ashes (dacitic type) thought to originate during small-magnitude eruptions in the Cascade volcanic province, in a continental-oceanic plate collision setting, have low Rb concentration and small Eu deficiencies. Ashes thought to originate from large-magnitude eruptions in areas underlain by continental crust such as in the Jemez Mountains area, New Mexico (such as ash beds 27 and 18), have large Eu deficiencies. In the main, dacitic ashes have significantly less Rb as well as other large-ion lithophile elements such as U, Th, and Cs, than do rhyolitic ashes. A plot of the magnitude of the Eu deficiencies of the glass shards of the ashes (Figure 7) against one of these (Rb) large-ion lithophile elements shows that a rough correlation exists.

Nearly all, except ash bed 9, W-type rhyolitic glasses have moderately large La to Sm ratios and have La contents from about 30 to 100 times the amounts of chondrites. Most of the G-type rhyolitic glasses, except bed 48, also have moderately large La to Sm ratios and contain somewhat more La than do the W-type rhyolitic glasses, generally from 100 to 300 times chondrite amounts. The REE patterns for ash beds 48 and 49 (Figure 5) are unusual in that they have less La than Sm. The pattern for the heavy rare-earth elements is nearly flat for most of the analyzed glasses except glasses of ash beds 65, 64, 10, and 4.

Special mention should be made about the REE pattern for the glass of ash bed 10, which has an unusual V shape. This is the only ash bed listed on Plate 1 that contains microphenocrysts of sphene, and possibly the unusual V-shaped REE pattern results from the early crystallization of sphene from the magma progenitor of ash bed 10 and sphene's preference, in some instances, for middle Z-number REE. REE contents of the glass shards of ash beds 68, 58, 34, 23, 19, 17, and 6 used to compile REE patterns shown on Figures 4 and 6 were obtained from analytical data of *Sarna-Wojcicki et al.* [1980].

APPENDIX: EXPLANATORY NOTES FOR PLATE

Paleomagnetic Reversal Sequence

The paleomagnetic reversal sequence shown on Plate 1 follows that published by *Mankinen and Dalrymple* [1979]. To calculate ages for their accompanying time scale, they used

atomic abundances and decay constants recommended by the International Union of Geological Sciences [*Steiger and Jäger,* 1977]. The measured paleomagnetic polarity (DRM) of most of the ash beds shown on Plate 1 were, in most instances, determined by either the writer, J. G. Honey, or J. J. Dickson, all of the U.S. Geological Survey. J. W. Hillhouse (oral communication, 1978) of the U.S. Geological Survey determined the paleomagnetic direction of ash bed 6 of Plate 1.

Boundary Between the Pliocene and Pleistocene

The boundary between the Pliocene and Pleistocene used on Plate 1 is 1.8 m.y., as suggested by isotopic age studies done in the continuous marine Pliocene and Pleistocene sequence in the stratotype area of southern Italy, near the Vrica section about 4 km south of Crotone, Calabria. The Vrica section has been proposed as a Pliocene and Pleistocene boundary stratotype [*Selli et al.,* 1977]. *Selli et al.* [1977], p. 195] reported a fission track age of 2.07 ± 0.33 m.y. (corrected for fission track annealing) measured on glass shards from an ash bed, m marker bed, at the inferred Pliocene and Pleistocene boundary at the Vrica section. The m bed is near the stratigraphic level at which fossils are found that suggest climatic deterioration (cooling) in the Mediterranean Sea and accordingly marks the beginning of Pleistocene time. In addition, *Selli et al.* [1977, p. 194], reported a K-Ar age of 2.2 ± 0.2 m.y. measured on glass shards that were separated from the m ash bed at the Pliocene and Pleistocene boundary at the Vrica section. They also reported a K-Ar glass age of 2.0 ± 0.1 m.y. measured on glass separated from a sample of a large pumice block (found by quarry workers in the southern part of the city of Crotone) at a level thought to correlate with the marker horizon at the Vrica section (G. Bigazzi and G. Pasini, oral communication, 1979). The m marker bed also was dated by *Boellstorff* [1978], who reported a fission track age of 2.5 ± 0.1 m.y. measured on glass (uncorrected for fission track annealing).

The ash dated by G. Bigazzi and reported by *Selli et al.* [1977] is not the m marker bed but an ash that lies 300 m stratigraphically below the m bed (C. W. Naeser and G. Bigazzi, written communication, 1980). The index of refraction of glass shards, trace element composition of glass shards, and the mineralogy of a split of the sample dated by G. Bigazzi [from *Selli et al.,* 1977] do not match samples of the m marker bed collected by the author, C. W. Naeser, and J. D. Obradovich. These properties, however, do match the properties of the ash that lies about 300 m below the m bed in the Vrica area. Seemingly, samples of the m ash bed and the ash bed that occurs 300 m below were inadvertently switched in the field at the time the samples were collected or later in the laboratory.

Until precise K-Ar ages are determined on minerals rather than on glass of the ashes at the Vrica section (work in progress by C. W. Naeser, J. D. Obradovich, and G. A. Izett), the precise age of the Pliocene and Pleistocene boundary at Vrica remains uncertain. Preliminary K-Ar (mineral) and fission track (zircon) ages from the m marker bed and the ash bed that occurs about 300 m below the m marker bed indicate that the Pliocene and Pleistocene boundary of *Seli et al.* [1977], at the Vrica section near Crotone, Italy, is somewhat younger than 2.1 m.y. and is arbitrarily placed on Plate 1 at 1.8 m.y.

Range Zones of Certain Large Fossil Mammals

The range zones of certain fossil mammals commonly found in nonmarine sedimentary rocks of the Western Interior (shown on Plate 1) include the elephant, *Mammuthus* (Irvingtonian and Rancholabrean); the mastodon, *Stegomastodon* (Blancan); the zebra, *Equus (Dolichohippus)* (Blancan); and the horse *Equus (Equus)* (Irvingtonian and Rancholabrean). These range zones are based on reported occurrences of the above fossils in Pliocene and Pleistocene deposits of the Western Interior and from unpublished data from fossil mammal collections made near the Blancan and Irvingtonian transition in Kansas and Texas by the writer and J. G. Honey.

Ash Bed Name

The informal naming of volcanic ash beds is a long-accepted practice in American geology as evidenced by the use of such names as the 'Pearlette ash' [*Cragin,* 1896, p. 54]. Since that time, many other ash beds and bentonite beds (altered volcanic ash beds) have been named in either an informal or, in some instances, a formal sense. Some examples of formally named ash beds are (1) the Pearlette Ash Member of the Sappa Formation [*Flint,* 1955, pp. 41–54], (2) the Pearlette ash lentil of the Atwater Member of the Crooked Creek Formation [*Hibbard,* 1958, pp. 55–57], and (3) the Pedro Bentonite Bed (Ardmore Bentonite Bed of current usage) of the Mitten Black Shale Member of the Pierre Shale [*Mapel and Pillmore,* 1963]. Either formal or informal usage is acceptable as outlined in the Code of Stratigraphic Nomenclature, Article 8 (a,b) [*American Commission on Stratigraphic Nomenclature,* 1970]. However, the informal naming of ash beds can led to a complex nomenclature if scattered volcanic ash deposits, which are remnants of a single, formerly extensive ash blanket generated during a brief, intense volcanic eruption, are each given a different name. Thus, an unnecessarily complex nomenclature could result in considerable confusion for those not acquainted with the latest nomenclature changes and additions. Another practice used, which should be discouraged, is the proposal of a new name for an ash bed using evidence only from isotopic age data and ignoring other tephrochronologic data. Because a bed of volcanic ash has a slightly different isotopic age than other ash beds with which it certainly correlates, based on abundant mineralogical and chemical data, is a poor reason to assign it a new ash bed name.

The nomenclature system used for naming many of the previously unnamed ash beds listed on Plate 1, and the one currently used by many tephrochronologists, is to name an ash bed informally for its source area rock unit, if known, or to name it informally for its principal geographic occurrence if the source area and rock unit are not known. In a few instances, ash bed names used on Plate 1 were named previously by geologists (1) for a person (T. L. Bailey) by *Yeats and McLaughlin* [1970] (Bailey ash, bed 19) and (2) for a petrographic feature by *Malde* [1972] (upper lapilli, bed 60 and lower lapilli, bed 67, for their coarse-grained, pumiceous shard habit).

All ash beds that clearly correlate with a previously named ash bed should be assigned the same name. An example of this practice is the naming of the Peters Gulch ash bed (65 of Plate 1) for its occurrence at Peters Gulch near Hagerman, Idaho [*Powers and Malde,* 1961]. If more occurrences of the Peters Gulch ash bed are found, they also should be called the Peters Gulch ash.

If enough tephrochronologic data are available to correlate an ash bed, with a high probability, with its source area rock unit, the ash bed is given the source area rock unit name in or-

der to avoid duplication of names and to establish its genetic relation with a source area rock unit. An example of this practice was the informal naming of the Bishop ash bed (bed 13 on Plate 1) of the western United States [*Izett et al.*, 1970] for its source area rock unit, the Bishop Tuff of eastern California. In some instances, an ash bed was informally named and correlated to a formally named source area rock unit of bed rank. An example [*Izett et al.*, 1972] of this situation was the informal naming of the Guaje ash bed (bed 27 on Plate 1) of the southern Great Plains for its source area rock unit, the Guaje Pumice Bed of the Otowi Member of the the Bandelier Tuff of north-central New Mexico.

Applying the above nomenclatural principles, several new names for ash beds are introduced on Plate 1 and are named for either geographic localities or for source area rock units. In particular, new names for the Pearlette ash beds type B, type S, and type O of *Izett et al.* [1970] and of *Naeser et al.* [1973] are here used, based on the high probability of their correlation with formally named pyroclastic source area rock units in the Yellowstone National Park area of Wyoming and Idaho. The Pearlette type B ash was named the Huckleberry Ridge ash bed (bed 36 on Plate 1) by *Izett and Wilcox* [1981] for its equivalent source area rock unit, the Huckleberry Ridge Tuff of *Christiansen and Blank* [1972, pp. 3–4]. The Pearlette type S ash bed was named the Mesa Falls ash bed (bed 22 on Plate 1) by *Izett and Wilcox* [1981] for its equivalent source area rock unit, the Mesa Falls Tuff of *Christiansen and Blank* [1972, pp. 5–6]. The Pearlette type O ash bed was named [*Izett and Wilcox*, 1981] the Lava Creek B ash bed (bed 11 on Plate 1) for its equivalent source area rock unit, the Lava Creek Tuff, member B of *Christiansen and Blank* [1974*a*]. A newly adopted unit of the Pearlette family of ash beds was named the Lava Creek A ash bed (bed 12 on Plate 1) by *Izett and Wilcox* [1981], and it was named for its equivalent source area rock unit, the Lava Creek Tuff, member A of *Christiansen and Blank* [1974*a*]. Lava Creek A ash bed underlies Lava Creek B ash bed in Wyoming, and recognition of Lava Creek A ash bed is based on significant mineralogical and chemical differences between the two units. These differences include (1) much greater proportion of hornblende and allanite in Lava Creek A ash than in Lava Creek B, (2) lack of clinopyroxene and ilmenite in Lava Creek A and its presence in Lava Creek B ashes, (3) the pumiceous shard habit of Lava Creek A as compared to the platy, bubble wall shard habit of Lava Creek B, and (4) significantly less iron and more uranium in the glass shards of Lava Creek A compared with Lava Creek B ashes. The nomenclature changes made by *Izett and Wilcox* [1981] for Pearlette family ash beds were based on a large amount of mineralogical and chemical data that relate downwind ash beds to their source area tephra units [*Izett et al.*, 1970, 1972; *Naeser et al.*, 1973; G. A. Izett, unpublished data, 1980].

Stratigraphic Relationships

The stratigraphic relationships among the various ash beds are shown on Plate 1. Information concerning localities at which the superposition of several ash beds can be demonstrated is given in that part of the appendix that describes the principal occurences of the ash beds.

Source Area Rock Unit and Source Area

The source area, rock unit name and the source area of the ash beds are listed on Plate 1 for those beds that have sufficient chemical and mineralogical information available to establish reasonably their correlations with their suspected source area pyroclastic equivalents. In addition, the source areas of some of the other ash beds on Plate 1 are inferred using their chemical and mineralogical similarities with ash beds of known source areas.

Numerous volcanic ash beds have been found in sedimentary deposits far downwind from the three largest rhyolite volcanic centers of the western United States, including the Yellowstone National Park area of Idaho and Wyoming, the Long Valley-Glass Mountain area north of Bishop, California, and the Jemez Mountain area of north-central New Mexico [*Izett et al.*, 1970, 1972, 1978*b*]. These ash beds can be correlated with plinian, air fall pumice deposits that underlie the largest caldera-forming pyroclastic flows in the aforementioned source areas. In addition, ash beds are currently being found and correlated with small-volume rhyolitic, pyroclastic units that were generated prior to or following the emplacement of the enormous pyroclastic flows in the three large rhyolite volcanic centers. However, downwind volcanic ash beds have not been certainly identified from some of the volcanic fields of the western United States that generated small-volume silicic pyroclastic flows and related plinian pumice falls such as the Clear Lake volcanic field of northern California [*Hearn et al.*, 1976], the Coso volcanic field of east-central California [*Duffield et al.*, 1980], the Mount Taylor volcanic field of New Mexico [*Lipman and Mehnert*, 1979, p. B3], and the San Francisco Peaks volcanic field of Arizona [*Sheridan and Updike*, 1975]. Downwind volcanic ash beds from these and other small-volume, silicic volcanic centers will almost certainly be found in the future.

Isotopic Age

Published isotopic ages and their source references for some ash beds and tuffs are shown on Plate 1, as are several previously unreported isotopic ages. Potassium-argon age data for previously unreported ages on Plate 1 are given on Table 4, and previously unreported fission track (FT) age data are given on Table 5. Potassium-argon ages of glass shards have been determined for some of the ash beds and tuffs, but they are not listed because of their unreliability [*Curtis*, 1966; *Izett et al.*, 1978*a*; *Naeser et al.*, 1980]. Fission track ages measured on glass shards of volcanic ash beds have been used by others to date upper Cenozoic beds but are not used for age control on Plate 1. Fission track ages of glass shards from upper Cenozoic ash and tuff beds are generally younger than the zircon fission track ages from the same beds; the tendency for fission track glass ages to be younger than zircon crystals from the same beds results from the well-established fact of track fading or annealing in the glass shards of the beds during geologic time [*Lakatos and Miller*, 1972; *Storzer and Poupeau*, 1973; *Naeser et al.* 1980]. Most of the K-Ar ages on Plate 1 were calculated using isotope concentrations and decay constants recommended by the International Union of Geological Sciences [*Steiger and Jäger*, 1977]. Fission track ages were calculated using a decay constant (λ_f) for the spontaneous decay of ^{238}U of $7.03 \times 10^{-17} yr^{-1}$.

In a few instances the isotopic age of an ash bed is apparently not exactly compatible with the plotted positions (based on stratigraphic or other field evidence) of adjacent ash beds on Plate 1 (for example, ash bed 6). However, considering the analytical uncertainty associated with the isotopic ages, the conflicts are not important.

TABLE 4. K-Ar Ages of Certain Ash Beds and Tephra Units of Plate 1 for Which Analytical Data Previously Have Not Been Reported

Ash Bed Number From Plate 1	Lab Number	K_2O, wt %	Sample Weight, grams	Radiogenic ^{40}Ar, mol/g	Radiogenic ^{40}Ar, %	Age × 10^6, years	Sample Number and Mineral	Sample Location
10	DKA 3809	10.64	7.561	8.477×10^{-12}	72.4	0.55 ± 0.01	78G175 sanidine	pumice lapilli from pumice pits at the Pumice Hole Mine in the NW1/4NE1/4 section 2, T 28 S, R 9 W, Adamsville 15-min quadrangle, Beaver County, Utah; collector G. A. Izett
16	DKA 3811	10.30	8.633	1.576×10^{-11}	91.4	1.06 ± 0.01	78G12 sanidine	pumice blocks from pumice pit in the NE1/4NE1/4 section 23, T 2 S, R 31 E, Glass Mountain 15-min quadrangle, Mono County, Calif.; collectors G. A. Izett, J. G. Honey, and G. T. Cebula
37	DKA 3808	9.43	2.755	2.859×10^{-11}	82.6	2.10 ± 0.02	79G10 sanidine	pumice lapilli from the uppermost unit of air fall tephra at the Cowan Mine in the NW1/4NE1/4 section 23, T 2 S, R 31 E, Glass Mountain 15-min quadrangle, Mono County, Calif.; collectors G. A. Izett J. G. Honey, and G. T. Cebula

Argon isotope analyses by G. A. Izett, J. D. Obradovich, and H. H. Mehnert; potassium determined by flame photometry by V. Merritt; decay constants used $^{40}K/K_{total} = 1.167 \times 10^{-4}$; $\lambda_\epsilon + \lambda_{\epsilon'} = 0.581 \times 10^{-10}$ yr^{-1}; $\lambda_\beta = 4.962 \times 10^{-10}$ yr^{-1}; ± is one sigma.

Principal Occurrences and Remarks Concerning Ash Beds Listed on Plate 1

The initial number is the ash bed number followed by the ash bed name. The principal occurrence of each ash bed is described first (T = township, R = range); the number of known localities is shown in parentheses following the discussion of each bed.

1. *Hebgen Narrows.* In sediments below till of Bull Lake age in the SW1/4SW1/4 section 11, T 12 S, R 5 E at Hebgen Narrows in the Tepee Creek 15-min quadrangle, Wyoming (collected by K. L. Pierce); another locality of this ash is in the Main Canyon Formation of *Bright* [1967, p. 2] at Main Canyon Dugway in the SE1/4 section 7, T 12 S, R 41 E, Thatcher 7 1/2-min quadrangle, Franklin County, Idaho. Ash from these and several other localities recently has been studied and found to be remarkably similar in chemical composition to the Pearlette family of ashes. However, small differences in the chemical composition of the glass shards of the two young Yellowstone Park-derived ash beds (Hebgen Narrows, bed 1 and Natural Trap, bed 2) allow them to be separated from the Pearlette family of ashes. It should be emphasized that the stratigraphic relationship between the two young Yellowstone Park-derived ashes has not been determined as yet, although the Hebgen Narrows ash is arbitrarily shown to be younger than the Natural Trap ash. These ahses (Hebgen Narrows and Natural Trap) were surely derived from pyroclastic eruptions in Yellowstone National Park in late Pleistocene time. Possible source area rock units for these ash beds (beds 1 and 2) are either the tuff of Bluff Point of *Christiansen*[1974] in the West Thumb 15-min quadrangle or the tuff of Cold Mountain Creek of *Christiansen and Blank* [1974*b*] in the Old Faithful 15-min quadrangle, Yellowstone National Park, Wyoming (3).

2. *Natural Trap.* In Pleistocene deposits in Natural Trap Cave in the SE1/4 section 28, T 58 N, R 94 W, Natural

TABLE 5. Fission-Track Ages of Zircon Microphenocrysts of Ash Beds Listed on Plate 1 for Which Analytical Data Previously Have Not Been Reported

Ash Bed Number of Plate 1	Lab Number	Sample	Ps × 10^5, t/cm^2	Pi × 10^6, t/cm^2	F × 10^{15}, n/cm^2	Age × 10^6, years
14	DF 928	Ar-SP	15.9 (257)	14.40 (1167)	0.122	0.80 ± 0.10
15	DF 2733	—	1.17 (15)	7.86 (504)	0.946	0.84 ± 0.42
28	—	OJD-67-4	1.31 (20)	5.38 (411)	1.02	1.48 ± 0.56
41	—	OJD-67-17	3.64 (32)	9.55 (420)	0.958	2.20 ± 0.3
46	—	79W211	2.95 (60)	7.39 (1598)	0.976	2.32 ± 0.15
64	DF 652	73W66	8.20 (88)	15.4 (1650)	1.11	3.53 ± 0.68
65	DF 3050	60M59	19.3 (219)	9.13 (1034)	0.296	3.75 ± 0.36

Analysts for ash beds: 15, N. D. Briggs; 14, 28, and 41, C. W. Naeser; 46, J. J. Dickson; 64 and 65, G. A. Izett; number of tracks counted in parentheses; t, track; Ps, spontaneous track density; Pi, induced track density; F, neutron fluence; n, neutron; dashes indicate no sample or lab number assigned; ± is 2 sigma; $\lambda_f = 7.03 \times 10^{-17}$ yr^{-1}.

Trap Cave 7 1/2-min quadrangle, Big Horn County, Wyoming; see *Martin and Gilbert* [1978] for a list of fossil mammals found in the cave deposits. Other localities, where ash or tephra of similar composition and age occur, are (1) at Ash Hill at the Gay Mines, Idaho (K. L. Pierce, written communication, 1979), (2) from a trench in section 35, T 5 N, R 26 E in the Arco North 7 1/2-minute quadrangle, Butte County, Idaho, and (3) the lower of two tephra beds K-Ar dated (sanidine) at about 0.15 m.y. by J. D. Obradovich in lake silt along the shore of Yellowstone Lake at Rock Point in the Frank Island 15-min quadrangle, Yellowstone National Park, Wyoming [*Richmond,* 1974, stratigraphic sections 20, 21, 22, 23, and 24]. Ash from another locality in Wyoming that may also be a correlative with the ash in Natural Trap Cave is in brown silt stratigraphically below till of Bull Lake (?) age in a roadcut along U.S. Highway 14 in Tensleep Canyon in the NE1/4 section 26, T 48 N, R 87 W in the Old Maid Gulch 7 1/2-min quadrangle, Washakie County, Wyoming; a second ash occurs stratigraphically 3 m below the ash in Tensleep Canyon. Possible source area rock units for this ash bed and bed 1 are either the tuff or Bluff Point of *Christiansen* [1974] in the West Thumb 15-min quadrangle or the tuff of Cold Mountain Creek of *Christiansen and Blank* [1974*b*] in the Old Faithful 15-min quadrangle, Yellowstone National Park, Wyoming (5).

3. *Arco-1.* In Pleistocene deposits in trench across the Arco fault near the center of section 35, T 5 N, R 26 E, in the Arco North 7 1/2-min quadrangle, Butte County, Idaho; separated by 25 cm of silt from overlying ash bed that correlates with ash bed 2 (described above); sample collected by K. L. Pierce (1).

4. *Long Canyon.* In the upper part of Pleistocene lake deposits of ancient Lake Manix in the SE1/4SW1/4 section 10, T 10 N, R 4 E, Newberry 15-min quadrangle, San Bernardino County, California; this ash bed was incorrectly correlated with the ash of Green Mountain Reservoir (bed 9 on Plate 1) by *Izett et al.* [1970, p. 126]; named for its source area tephra, the rhyolite of Long Canyon of *Bacon and Duffield* [1981], Kern Plateau, California (1).

5. *Copper Canyon.* In Pleistocene deposits about 1.6 km north of Copper Canyon on the west side of Walker Lake in the NE1/4 section 6, T 10 N, R 29 E, Mt. Grant 15-min quadrangle, Mineral County, Nevada (R. C. Buckham, written communication, 1980); position in stratigraphic column of Plate 1 is uncertain (1).

6. *Thornton Beach.* In the Merced Formation in the SE1/4 section 3, T 3 S, R 6 W, in sea cliff exposures at Thornton State Park, San Francisco South 7 1/2-min quadrangle, San Francisco, California [*Hall,* 1965, p. 155]; this ash bed has been informally called the Maidu (middle Pleistocene volcano in the Lassen, California area) and has been extensively studied by A. M. Sarna-Wojcicki; he has identified this ash bed at other localities in California and Nevada; the fission track age (zircon) of this ash bed at two localities near San Francisco, California, was determined by C. W. Naeser (Plate 1, this report) and by *Meyer et al.* [1980] at about 0.45 m.y. N. D. Briggs (written communication, 1981) recently dated glass shards of the ash bed at Thornton Beach, California at 0.54 ± 0.11 m.y., using the fission track method. Fission track glass ages usually yield minimum ages owing to track fading or annealing [*Naeser et al.,* 1980]. An ash bed in the Raft(?) Formation in the NW1/4 section 1, T 10 S, R 28 E, in Lanes Gulch, in the Yale 15-min quadrangle, Cassia County, Idaho (K. L. Pierce, written communication, 1979), probably is also the Thornton Beach ash bed. Another locality of this ash (identified by A. M. Sarna-Wojcicki, oral communication, 1980) was called the Mexican Dam ash bed by *Davis* [1977, p. 29]; according to *Davis* [1977], the Mexican Dam ash stratigraphically overlies the Dibekulewe ash (bed 7 on Plate 1) (6).

7. *Dibekulewe.* South Curry Street, Carson City, Nevada; chemical and other data from *Davis* [1977]; named by *Davis* [1977] for the Woho Indian term for a cove in the hills near Stewart, Nevada (1).

8. *Rye Patch Dam.* In Pleistocene deposits near Rye Patch Dam in the NE1/4 section 18, T 30 N, R 33 E, Oreana 15-min quadrangle, Pershing County, Nevada; chemical and other data from *Davis* [1977]; stratigraphic position uncertain; named by *Davis* [1977] (1).

9. *Green Mountain Reservoir.* In Pleistocene sediments at Green Mountain Reservoir in the SE1/4 section 18, T 2 S, R 79 W, Mount Powell 15-min quadrangle, Summit County, Colorado; overlies a Lava Creek B ash bed [*Izett et al.,* 1970] (2).

10. *Ranch Canyon.* In Pleistocene deposits in a borrow pit along the south side of I-70 near Cove Fort Junction in the SW1/4 section 31, T 5 S, R 6 W, Cove Fort 15-min quadrangle, Millard County, Utah; about 10 m above a Bishop ash bed; several other localities of this tephra bed are known in the Beaver Valley area, Utah; named for its source area tephra, the tuff of Ranch Canyon, Mineral Mountains, Utah (4).

11. *Lava Creek B.* In the Harpole Mesa Formation along Onion Creek, in the SE1/4SE1/4 section 26, T 24 S, R 24 E, Polar Mesa 15-min quadrangle, Grand County, Utah [*Izett et al.,* 1970; *Naeser et al.,* 1973]. Many other localities of this ash are known in the western United States and are spread from California to central Iowa and from southern Canada to southern Texas; formerly called Pearlette type O ash bed; overlies Lava Creek A ash beds in the Mexican Ridge and Black Mountain 7 1/2-min quadrangles, Wyoming (see description of ash bed 12 for locations); overlies a Bishop ash (bed 13 on Plate 1) at several localities [*Izett et al.,* 1970]; overlies a Huckleberry Ridge ash (bed 36 of Plate 1) in the Irish Flats NE 7 1/2-min quadrangle, Kansas; named for its source area tephra, the Lava Creek Tuff, member B in Yellowstone National Park (125).

12. *Lava Creek A.* In Pleistocene deposits in the SE1/4 SW1/4 section 4, T 3 N, R 4 E, Mexican Pass 7 1/2-min quadrangle, Fremont County, Wyoming; directly overlain by a Lava Creek B ash bed; a second locality of this ash occurs at the mouth of Shell Canyon in the NE1/4SW1/4 section 17, T 53 N, R 90 W, Black Mountain 7 1/2-min quadrangle, Big Horn County, Wyoming; named for its suspected source area tephra, the Lava Creek Tuff, member A in Yellowstone National Park (2).

13. *Bishop.* In Pleistocene deposits near Cove Fort Junction (principal locality same locality as ash bed 10); see *Izett et al.* [1970] for other localities of this bed; overlies beds 16 and 19 according to *Sarna-Wojcicki et al.* [1980]; named for its source area tephra, the Bishop Tuff of eastern California (30).

14. *Flagstaff.* In pumice pits north of Flagstaff, Arizona,

in the S1/2 section 28, T 25 N, R 8 E, SP Mountain 15-min quadrangle, Coconino County, Arizona (1).

15. *Lake Tapps.* In Pleistocene deposits at the type area of the Salmon Springs Drift, Puget Sound lowlands, Washington; see *Crandell et al.* [1952] and *Easterbrook and Briggs* [1979]; assigned the name Lake Tapps tephra by *Easterbrook et al.* [1981] (1).

16. *Glass Mountain-D.* In Pleistocene sediments below the Bishop Tuff in roadcut adjacent to Owens River in the E1/2 section 21, T 6 S, R 32 E, Bishop 15-min quadrangle, Inyo County, California; a second locality of this ash is in the Pico Formation near Ventura, California; chemical data from *Sarna-Wojcicki et al.* [1980, p. 29, samples 17 and 18]; overlies ash bed 17 [*Sarna-Wojcicki et al.,* 1980]; named for its suspected source area tephra, the rhyolite of Glass Mountain, near Bishop, California (2).

17. *Glass Mountain-G.* In Pleistocene sediments below Glass Mountain-D ash bed (bed 16 on Plate 1) at Chalk Bluffs north of Bishop, California; informally called the gray ash by *Sarna-Wojcicki et al.* [1980, p. 31, sample 19] for locality information and chemical data; here named for its suspected source area tephra, the rhyolite of Glass Mountain, near Bishop, California (2).

18. *Tsankawi.* In Pleistocene sediments in a roadcut along U.S. Highway 64 about 0.98 km southwest of the junction with New Mexico State Highway 96 in the Taos Southwest 7 1/2-min quadrangle, Taos County, New Mexico (G. R. Scott, written communication, 1977); several other localities of this ash bed are known in New Mexico; source area tephra of this ash overlies source area tephra of ash 21 in the Jemez Mountains, New Mexico [see *Izett et al., 1978b,* 1981]; named for its source area tephra, the Tsankawi Pumice Bed of the Tshirege Member of the Bandelier Tuff, Jemez Mountains, New Mexico (2).

19. *Bailey.* In the Pico Formation near Ventura, California; other ash bed chemical data from *Sarna-Wojcicki et al.* [1980]; overlies ash beds 23 and 36 according to *Sarna-Wojcicki et al.* [1980]; named by *Yeats and McLaughlin* [1970] (4).

20. *Cerro Toledo-S.* In Pleistocene channel deposits at the north edge of the New Mexico Institute of Mining and Technology, Socorro, New Mexico; tentatively assigned to the Cerro Toledo-S bed; overlies source area tephra of bed 24 in the source area [*Izett et al.,* 1981]; named for its source area tephra, the Cerro Toledo Rhyolite, Jemez Mountain area, New Mexico (1).

21. *Cerro Toledo-X.* In the Tule Formation (Pleistocene) along Rock Creek in the Cope Creek 7 1/2-min quadrangle Briscoe County, Texas, about 35 m stratigraphically below a Lava Creek B ash; a second locality of this ash is in NE1/4 section 18 block 49 above windmill 3555 ft along Rita Blanca Creek in the Channing NW 7 1/2-min quadrangle west of Channing, Texas; named for its source area tephra, the Cerro Toledo Rhyolite, Jemez Mountains, New Mexico [see *Izett et al.,* 1981] (2).

22. *Mesa Falls.* In Pleistocene sediments at the type locality of the Sappa Formation in the SW1/4NW1/4 section 12, T 2 N, R 20 W, Stamford 7 1/2-min quadrangle Harlan County, Nebraska; other localities of this ash bed given by *Izett et al.* [1970]; formerly called Pearlette type S ash bed; named for its source area tephra, the Mesa Falls Tuff, Yellowstone National Park (4).

23. *South Mountain.* In the Pico Formation (Pliocene and Pleistocene) at a locality informally called the Sea Knoll locality west of South Mountain, California, described by *Sarna-Wojcicki et al.* [1980, p. 36, sample 27]; see also *Sarna-Wojcicki et al.* [1980, p. 36, sample 27]; see also *Sarna-Wojcicki et al.* [1980] for stratigraphic relationship with other ash beds of the Ventura, California area (1).

24. *Cerro Toledo-L.* In abandoned pumice pits in the SE1/4NE1/4 section 24, T 16 N, R 8 E, Turquoise Hill 7 1/2-min quadrangle, Santa Fe County, New Mexico; tentatively assigned to the Cerro Toledo-L ash bed; overlies source area tephra of ash bed 25 in the source area [*Izett et al.,* 1981]; named for its source area tephra, the Cerro Toledo Rhyolite, Jemez Mountains, New Mexico (3).

25. *Cerro Toledo-R.* No downwind localities of this tephra unit identified as yet; nearly identical in chemical composition to bed 24; overlies source area tephra of bed 27 in the source area [*Izett et al.,* 1981]; named for source area tephra, the Cerro Toledo Rhyolite, Jemez Mountains, New Mexico (0).

26. *Cerro Toledo-B.* In the Pliocene and Pleistocene Crooked Creek Formation of *Hibbard* [1958] in the SW1/4 SE1/4 section 16, T 33 S, R 28 W in the Irish Flats NE 7 1/2-min quadrangle Meade County, Kansas; about 10 m above a Huckleberry Ridge ash [*Izett et al.,* 1981]; named for its suspected source area tephra, the Cerro Toledo Rhyolite, Jemez Mountains, New Mexico (2).

27. *Guaje.* In Pleistocene deposits near Mount Blanco, Texas; see *Izett et al.* [1972] for locality information and stratigraphic relationship with ash bed 46; several other localities of this ash bed are known from New Mexico and Texas [*Izett et al.,* 1981]; named for its source area tephra, the Guaje Pumice Bed of the Otowi Member of the Bandelier Tuff, Jemez Mountains, New Mexico (8).

28. *Centerville Beach.* In the upper member (Pleistocene) of the Rio Dell Formation in the SE1/4NW1/4 section 13, T 2 N, R 3 W, at Centerville Beach, Humbolt County, California; see *Ogle* [1953, pp. 31 and 44, sample 80-381] for other information (1).

29. *Pilgrim Station.* In the Bruneau Formation (Pleistocene) west of Pilgrim Station along the Oregon Trail, near the center section 21, T 6 S, R 11 E, Pasadena Valley 15-min quadrangle, Elmore County, Idaho; measured section 71 of H. E. Malde (written communication, 1980); inferred to overlie ash bed 30 (H. E. Malde, oral communication, 1980) (1).

30. *Rosevear Gulch.* In the Bruneau Formation (Pleistocene) in the section 22, T 6 S, R 10 E, Glenns Ferry(?) 15-min quadrangle, Elmore County, Idaho; another locality of this ash is at measured section 62 of H. E. Malde [written communication, 1980); overlies as bed 31 (H. E. Malde, oral communication, 1980) (2).

31. *Indian Butte.* In the Tuana Gravel (Pleistocene) in the SE1/4 section 5, T 8 S, R 12 E, at Indian Butte, Indian Butte 7 1/2-min quadrangle, Owyhee County, Idaho; locality of H. E. Malde (written communication, 1980) (1).

32. *Bell Rapids.* In the Tuana Gravel (Pleistocene) in Peters Gulch, in the NE1/4NW1/4SE1/4 section 32, T 7 S, R 13 E, near Bell Rapids (submerged) along the Snake River in the Hagerman 7 1/2-min quadrangle, Twin Falls County, Idaho; stratigraphic position relative to bed 31 uncertain (1).

33. *Last Chance Bench.* In Pliocene sediments along

Last Chance Bench in the SW1/4 section 1, T 29 S, R 8 W, in the Beaver 15-min quadrangle, Beaver County, Utah; overlies ash bed 36 (about 20 m) as determined by M. N. Machette of the U.S. Geological Survey (written communication, 1980) (3).

34. *Manix-3.* In Pliocene sediments of ancient Lake Manix in the SE1/4 section 10, T 10 N, R 4 E, San Bernardino County, California; chemical data and stratigraphic relationship with ash bed 35 from *Sarna-Wojcicki et al.* [1980] (1).

35. *Manix-2.* In Pliocene sediments of ancient Lake Manix, San Bernardino County, California; same locality as ash bed 34; chemical data and stratigraphic relationship with ash bed 36 from *Sarna-Wojcicki et al.* [1980] (3).

36. *Huckleberry Ridge.* In the Crooked Creek Formation (Pliocene and Pleistocene) at the type locality of the Borchers fauna in the NW1/4NE1/4 section 21, T 33 S, R 28 W, Irish Flats NE 7 1/2-min quadrangle, Meade County, Kansas; see *Naeser et al.* [1973]; about 25 other localities of this ash known in the western United States including localities in eastern California (Lake Tecopa), southwest Utah (Beaver Valley and Black Rock Desert), southwest Idaho (Gem and Gentile Valley), near Snyder, Texas, in western Texas in the Camp Rice Formation of *Strain* [1969], near Finlay, Texas, in central Kansas at the site of the Kentuck assemblage of *Hibbard* [1952, p. 6], and in the St. David Formation of *Johnson et al.* [1975] at California Wash near Benson, Arizona; the Huckleberry Ridge ash bed previously called the type B Pearlette ash; overlies ash beds 37 and 48 in the Beaver, Utah area (G. A. Izett, unpublished data, 1980); named for its source area tephra, the Huckleberry Ridge Tuff, Yellowstone National Park, Wyoming (25).

37. *Taylor Canyon-C.* In Pliocene deposits along Waucoba Road in exploration pits in NE1/4NE1/4 section 2, T 9 S, R 34 E, Waucoba Mountain 15-min quadrangle, Inyo County, California; uppermost of three superposed ash beds exposed in this excavation; overlies beds 39 and 40; other localities of this ash bed are 33 m below the Huckleberry Ridge ash in the Beaver 15-min quadrangle, Utah; named for its source area tephra, the rhyolite of Taylor Canyon, Glass Mountain area, California (6).

38. *Taylor Canyon-P.* In Pliocene deposits in section 4, T 17 S, R 51 E, Specter Range 15-min quadrangle, Nye County, Nevada; source area tephra of this ash bed underlies source area tephra of bed 37; another locality of this ash bed is the uppermost of six superposed ash beds separated by sediments at Black Canyon southeast of Bishop, California; named for its source area tephra, the rhyolite of Taylor Canyon, Glass Mountain area, California (2).

39. *Waucoba Road-2.* In exploration pit in Pliocene deposits along Waucoba Road; same locality as principal locality of bed 37; middle of three ash beds (2).

40. Waucoba Road-1. In exploration pit in Pliocene deposits along Waucoba Road; same locality as ash bed 39; lowest of three beds in exploration pit (1).

41. *Avenal.* In the lowermost part of the Tulare Formation in the S1/2NE1/4 section 28, T 21 S, R 17 E, in the Avenal 7 1/2-min quadrangle Kettleman Hills, Kings County, California; might be an equivalent of beds 42, 43, or 44; samples and locality information supplied by J. D. Obradovich (written communication, 1980) (1).

42. *Arroyo Salida.* In the lowermost part of the Tulare Formation in Arroyo Salida in the NW1/4 section 17, T 23 S, R 19 E, Los Viejos 7 1/2-min quadrangle, Kettleman Hills, Kings County, California; locality information supplied by J. D. Obradovich (written communication, 1980); see *Woodring et al.* [1940, p. 19, unit 6a] (1).

43. *Arroyo Doblegado-2.* In the lowermost part of the Tulare Formation in Arroyo Doblegado in the NE1/4NE1/4 section 16, T 22 S, R 18 E, La Cima 7 1/2-min quadrangle, Kettleman Hills, Kings County, California; uppermost of two superposed ash bed separated by a few meters of sediments; locality information supplied by J. D. Obradovich (written communication, 1980); see *Woodring et al.* [1940] (1).

44. *Arroyo Doblegado-1.* In the lowermost part of the Tulare Formation in Arroyo Doblegado; stratigraphically underlies bed 43; same locality as bed 43 (1).

45. *Dry Mountain.* In Pliocene deposits in the SE1/4 SW1/4SE1/4 section 27, T 8 S, R 28 E, Dry Mountain 7 1/2-min quadrangle, Graham County, Arizona; about 15 m stratigraphically above an ash bed possibly correlative with bed 46; locality information from R. H. Tedford (written communication, 1978) (1).

46. *Mount Blanco.* In the Blanco Formation (Pliocene) near Mount Blanco, Texas; see *Izett et al.* [1972] for locality information; a second locality of this ash bed occurs in a trench in Lubbock, Texas; a third possible locality of this ash, fission track zircon dated at about 2.3 m.y. by J. J. Dickson of the U.S. Geological Survey, occurs in Pliocene deposits in the NE1/4SE1/4 section 27, T 8 S, R 28 E, Dry Mountain 7 1/2-min quadrangle, Graham County, Arizona, at the 111 Ranch fossil locality; several other ash beds occur in the 111 Ranch area (R. H. Tedford, written communication 1978) (3).

47. *Frenchman Flat.* In Pliocene sediments at 195 m depth in drill hole Ue5n at Frenchman Flat, at the Nevada Test Site, Nye County, Nevada; an ash bed found in a drill hole in the Searles Valley area, California [*Sarna-Wojcicki et al.*, 1980; sample 49] is probably the equivalent of the Frenchman Flat ash bed; another locality of this ash is in the SE1/4 section 15 T 14 S, R 49 E, Lathrop Wells 15-min quadrangle, Nye County, Nevada (3).

48. *Indian Creek.* In Pliocene sediments along Indian Creek in the NE1/4SW1/4 section 31, T 28 S, R 7 W, in the Beaver 15-min quadrangle, Beaver County, Utah; about 30 m below ash bed 36 of Plate 1 (1).

49. *Hogsback.* In Pliocene sediments along The Hogsback in the NW1/4SW1/4 section 30, T 28 S, R 7 W, Beaver 15-min quadrangle, Beaver County, Utah; possibly a few meters stratigraphically below bed 48 collected by M. N. Machette (1).

50. *Black Canyon-5.* In Pliocene sediments at Black Canyon, southeast of Bishop, California, in section 4, T 8 S, R 34 E, Bishop 15-min quadrangle, Inyo County, California; second ash from the top of the ash bed sequence; overlies bed 51 (1).

51. *Black Canyon-4.* In Pliocene sediments at Black Canyon, southeast of Bishop, California (same locality as ash bed 50); third ash from the top of the ash bed sequence; overlies ash bed 62 at Black Canyon, California (R. E. Wilcox, written communication, 1974) (1).

52. *Post Ranch.* In the St. David Formation at Post Ranch south of Benson, Arizona; in the NE1/4 section 28, T 17 S, R 20 E, Benson 15-min quadrangle; see *Tahirkheli and Naeser* [1975] for other information (1).

53. *Sand Point.* In the Pliocene Glenns Ferry Formation

at Sand Point in the SE1/4SW1/4 section 1, T 6 S, R 8 E, Glenns Ferry 15-min quadrangle, Owyhee County, Idaho; see *Malde* [1972] for localities and stratigraphic relationship with ash bed 54; an ash correlated with the Sand Point ash bed by *Malde* [1972, Plate 1, measured section 56] is not the Sand Point ash based on chemical analyses of the ash; ash bed named by *Malde* [1972] (3).

54. *Sand Point-1.* In the Pliocene Glenns Ferry Formation; same locality as bed 53; stratigraphically underlies (6 m) bed 53; another thin ash bed underlies this ash at locality 53. (1).

55. *Alkali Creek.* In the Glenns Ferry Formation; in the east fork of Alkali Creek in the SW1/4SW1/4 section 14, T 5 S, R 9 E, Glenns Ferry 15-min quadrangle, Elmore County, Idaho; recollected by R. E. Wilcox; see *Malde* [1972] for localities and stratigraphic relationship with ash bed 56; named by *Malde* [1972] (2).

56. *Deadman.* In the Glenns Ferry Formation, Snake River Plain, Idaho; measured section 44 of *Malde* [1972, Plate 1]; underlies ash bed 55; see *Malde* [1972] for localities and stratigraphic relationship with bed 57; named by *Malde* [1972] (3).

57. *Alkali Creek-1.* In the Glenns Ferry Formation, Snake River Plain, Idaho; same locality as bed 55; collected by R. E. Wilcox; see *Malde* [1972] for stratigraphic relationship with bed 58; overlies an ash bed correlative of bed 58 (the Narrows ash bed of *Powers and Malde* [1961]) (1).

58. *Nomlaki.* In the Tehama Formation (Pliocene) in the northern Sacramento Valley, California; see *Sarna-Wojcicki et al.* [1979] for localities and chemical data; A. M. Sarna-Wojcicki (oral communication, 1980) correlated an ash in the Fernando Formation (Repetto Formation of former usage) at Malaga Cove, Palos Verdes Hills, California, dated by the fission track method at 3.4 ± 0.3 m.y. [*Obradovich et al.,* 1978] with the Nomlaki Tuff Member of the northern Sacramento Valley, California; this correlation is confirmed by the author based on chemical analyses of an ash collected by J. C. Ingle (Ingle's sample 18) and J. D. Obradovich and the author; *Ingle* [1967, p. 252] reported three superposed ash beds in the Fernando Formation at Malaga Cove, California; the Narrows ash bed of *Powers and Malde* [1961] and *Malde* [1972, Plate 1, measured section 52] is also an equivalent of the Nomlaki ash bed (5).

59. *Putah.* In the Tehama Formation in northern California; see *Sarna-Wojcicki et al.* [1979] for localities (2).

60. *Upper Lapilli.* In the Glenns Ferry Formation, Snake River Plain, Idaho; section 31, T 5 S, R 9 E, in roadcut along U.S. Highway 30, in the Glenns Ferry 15-min quadrangle, Idaho; see *Malde* [1972] for localities and stratigraphic relationship with ash bed 61; named by *Malde* [1972]; chemical composition of this ash bed (standard gravimetric analyses) is nearly identical to ash bed 67 (3).

61. *Horse Quarry.* In the Glenns Ferry Formation, Snake River Plain, Idaho; see *Malde* [1972, Plate 1, measured sections F and P] for localities and stratigraphic relationship with ash bed 63; named by *Malde* [1972] (1).

62. *Black Canyon-3.* In Pliocene sediments at Black Canyon southeast of Bishop, California; same locality as ash bed 50; fourth ash bed from the top of the ash bed sequence; overlies ash bed 64 (R. E. Wilcox, written communication, 1974) (1).

63. *Fossil Gulch.* In the Pliocene Glenns Ferry Formation, Snake River Plain Idaho; see *Malde* [1972, Plate 1] for localities and stratigraphic relationship with ash bed 65; named by *Malde* [1972] (3).

64. Black Canyon-2. In Pliocene sediments at Black Canyon southeast of Bishop, California; same locality as ash bed 50; fifth ash bed from the top of the ash bed sequence; overlies ash bed 66 at Black Canyon, California (R. E. Wilcox, written communication, 1974) (1).

65. *Peters Gulch.* In the Glenns Ferry Formation in the NW1/4 section 33, T 7 S, R 13 E, Hagerman 7 1/2-min quadrangle, Twin Falls County, Idaho; see *Malde* [1972] for other localities; stratigraphic relationship with ash bed 67 given by *Malde* [1972]; named by *Powers and Malde* [1961] (4).

66. Black Canyon-6. In Pliocene sediments at Black Canyon southeast of Bishop, California; same locality as bed 50; lowermost ash in the sequence of six ash beds at Black Canyon (1).

67. *Lower Lapilli.* In the Glenns Ferry Formation, Snake River Plain, Idaho; see *Malde* [1972, Plate 1, measured sections 24, 25, and 30]; named by *Malde* [1972] (3).

68. *Lawlor.* Tassajara Formation, northern California; chemical data from *Sarna-Wojcicki et al.* [1979]; underlies ash bed 46 according to *Sarna-Wojcicki et al.* 1979] (6).

Acknowledgments. The writer thanks his colleagues R. E. Anderson, R. C. Bucknam, W. J. Carr, H. E. Malde, M. N. Machette, J. D. Obradovich, K. L. Pierce, H. A. Powers, G. R. Scott, R. A. Sheppard, and R. E. Wilcox, who have contributed ash samples from their collections in addition to pertinent stratigraphic information. Discussions with the aforementioned and other U.S. Geological Survey geologists have been helpful in preparing this paper. Unpublished isotopic ages were kindly made available to the writer by N. D. Briggs, J. J. Dickson, H. H. Mehnert, C. W. Naeser, and J. D. Obradovich. Mineral separations used for some of the isotopic age determinations were made by G. T. Cebula, J. W. Groen, J. J. Dickson, and J. G. Honey. Special thanks are given to R. E. Wilcox and A. M. Sarna-Wojcicki for making available unpublished data and for valuable discussions concerning field relations of volcanic ash beds they have studied. Analyses of the ash beds of Plate 1 for Fe, Hf, Mn, Rb, Ta, and U were made by instrumental neutron activation methods by D. M. McKown, H. T. Millard, Jr., and R. J. Knight of the U.S. Geological Survey. Analyses for Ca and Zn (by atomic absorption photospectrometric methods) and for Ti (by colorimetric methods) were made by V. M. Merritt and G. T. Burrow of the U.S. Geological Survey. Thoughtful reviews of this report were made by A. M. Sarna-Wojcicki and F. C. Dodge, and the writer appreciates their efforts.

REFERENCES

American Commission on Stratigraphic Nomenclature, Code of stratigraphic nomenclarue, 32 pp., Am. Assoc. Pet. Geol., Tulsa, Okla., 1970.

Anderson, A. T., Magma mixing: Petrological process and volcanological tool, *J. Volcanol. Geotherm. Res., 1,* 3–33, 1976.

Bacon, C. R., and W. A. Duffield, Late Cenozoic rhyolites from the Kern Plateau, southern Sierra Nevada, California, *Am. J. Sci., 281,* 1–34, 1981.

Bailey, R. A., G. B. Dalrymple, and M. A. Lanphere, Volcanism, structure, and geochronology of Long Valley caldera, Mono County, California, *J. Geophys. Res., 81,* 725–744, 1976.

Boellstorff, J. D., North American Pleistocene stages reconsidered in light of probable Pliocene-Pleistocene continental glaciation, *Science, 202*(4365), 305–307, 1978.

Borchardt, G. A., Neutron activation analysis for correlating volcanic ash soils, Ph. D. dissertation, 219 pp., Oreg. State Univ., Corvallis, 1970.

Borchardt, G. A., and M. E. Harward, Trace element correlation of volcanic ash soils, *Soil Sci. Soc. Am. Proc. 35*(4), 626–631, 1971.

Borchardt, G. A., P. J. Aruscavage, and H. T. Millard, Jr., Correlation of the Bishop ash, a Pleistocene marker bed, using instrumental neutron activation analyses, *J. Sediment. Petrol., 42,* 301–306, 1972.

Bright, R. C., Late-Pleistocene stratigraphy in Thatcher basin, southeastern Idaho, *Tebiwa, 10,* 1–7, 1967.

Buddington, A. F., and D. H. Lindsley, Iron-titanium oxide minerals and synthetic equivalents, *J. Petrol., 5,* 310–357, 1964.

Byers, F. M., Jr., W. J. Carr, P. P. Orkild, W. D. Quinlivan, and K. A. Sargent, Volcanic suites and related cauldrons of Timber Mountain-Oasis Valley caldera complex southern Nevada, *U.S. Geol. Surv. Prof. Pap., 919,* 70 pp., 1976.

Carmichael, I. S. E., The iron-titanium oxides of salic volcanic rocks and their associated ferromagnesian silicates, *Contrib. Mineral. Petrol., 14,* 36–64, 1967.

Christiansen, R. L., Geologic map of the West Thumb quadrangle, Yellowstone National Park, Wyoming, *Geol. Quad. Map GQ-1191,* scale 1:62,500, U.S. Geol. Surv., Reston, Va., 1974.

Christiansen, R. L., Cooling units and composite sheets in relation to caldera structure in Ash-Flow Tuffs, edited by C. E. Chapin and W. E. Elston, *Spec. Pap. Geol. Soc. Am., 180,* 29–42, 1979.

Christiansen, R. L., and H. R. Blank, Jr., Volcanic stratigraphy of the Quaternary rhyolite plateau in Yellowstone National Park, *U.S. Geol. Surv. Prof. Pap., 729-B,* 18 pp., 1972.

Christiansen, R. L., and H. R. Blank, Jr., Geologic map of the Madison Junction quadrangle, Yellowstone National Park, Wyoming, *Geol. Quad. Map GQ-1190,* scale 1:62,500, U.S. Geol. Surv., Reston, Va., 1974*a*.

Christiansen, R. L., and H. R. Blank, Jr., Geologic map of the Old Faithful quadrangle, Yellowstone National Park, Wyoming, *Geol. Quad. Map GQ-1189,* scale 1:62,500, U.S. Geol. Surv., Reston, Va., 1974*b*.

Christiansen, R. L., P. W. Lipman, W. J. Carr, F. M. Byers, Jr., P. P. Orkild, and K. A. Sargent, Timber Mountain-Oasis Valley caldera complex of southern Nevada, *Geol. Soc. Am. Bull., 88,* 943–959, 1976.

Cragin, F. W., Preliminary notice of three late Neocene terranes of Kansas, *Studies 6,* pp. 53–54, Colo. Coll., Colorado Springs, 1896.

Crandell, D. R., D. R. Mullineaux, and H. H. Waldron, Pleistocene sequence in southeastern part of the Puget Sound Lowland, Washington, *Am. J. Sci., 256,* 384–397, 1952.

Curtis, G. H., The problem of contamination in obtaining accurate dates of young geologic rocks, in *Potassium Argon Dating,* compiled by O. A. Schaeffer and J. Zahringer, pp. 151–162, Springer-Verlag, New York, 1966.

Curtis, G. H., The stratigraphy of the ejecta from the 1912 eruption of Mount Katmai and Novarupta, Alaska, in *Studies in Volcanology—A Memoir in Honor of Howel Williams,* edited by R. R. Coats, R. L. Hay, and C. A. Anderson, *Mem. Geol. Soc. Am., 116,* 153–210, 1968.

Davis, J. O., Quaternary tephrochronology of the Lake Lahontan area, Nevada and California, Ph. D. dissertation, 150 pp., Univ. of Idaho, Moscow, 1977.

Desborough, G. A., J. K. Pitman, and J. R. Donnell, Microprobe analysis of biotites—A method of correlating tuff beds in the Green River Formation, Colorado and Utah, *J. Res. U.S. Geol. Surv., 1,* 39–44, 1973.

Doell, R. R., G. B. Dalrymple, R. L. Smith, and R. A. Bailey, Paleomagnetism, potassium-argon ages, and geology of rhyolites and associated rocks of the Valles caldera, New Mexico, in *Studies in Volcanology—A Memoir in Honor of Howel Williams,* edited by R. R. Coats, R. L. Hay, and C. A. Anderson, *Mem. Geol. Soc. Am., 116,* 211–248, 1968.

Donnelly, J. H., B. C. Hearn, G. H. Curtis, and R. E. Drake, Geochronology and evolution of the Clear Lake volcanics, *U.S. Geol. Surv. Prof. Pap., 1141,* in press, 1981.

Duffield, W. A., C. R. Bacon, and G. B. Dalrymple, Late Cenozoic volcanism, geochronology, and structure of the Coso Range, Inyo County, California, *J. Geophys. Res., 85,* 2381–2404, 1980.

Easterbrook, D. J., and N. D. Briggs, Age of the Auburn reversal and the Salmon Springs and Vashon galciations in Washington, *Geol. Soc. Am. Abstr. Programs, 11,* 76–77, 1979.

Easterbrook, D. J., N. D. Briggs, J. A. Westgate, and M. P. Gorton, Age of the Salmon Springs glaciation in Washington, *Geology, 9,* 87–93, 1981.

Eaton, G. P., Windborne volcanic ash—A possible index to polar wandering, *J. Geol., 72,* 1–35, 1964.

Ekren, E. B., R. E. Anderson, C. L. Rogers, and D. C. Noble, Geology of northern Nellis Air Force Base Bombing and Gunnery Range, Nye County, Nevada, *U.S. Geol. Surv. Prof. Pap., 651,* 91 pp., 1971.

Evernden J. F., D. E. Savage, G. H. Curtis, and G. T. James, Potassium-argon dates and the Cenozoic mammalian chronology of North America, *Am. J. Sci., 262,* 145–198, 1964.

Ewart, A., A review of the mineralogy and chemistry of Tertiary-Recent dacitic, latitic, rhyolitic, and related salic volcanic rocks, in *Trondhjemites, Dacites, and Related Rocks,* edited by F. Barker, pp. 13–121, Elsevier, Amsterdam, 1979.

Flint, R. F., Pleistocene geology of eastern South Dakota, *U.S. Geol. Surv. Prof. Pap., 262,* 173 pp., 1955.

Froggatt, P. C., C. J. N. Wilson, and G. P. L. Walker, Orientation of logs in the Taupo Ignimbrite as an indicator of flow direction and vent position, *Geology, 9,* 109–111, 1981.

Galusha, T., and J. C. Blick, Stratigraphy of the Santa Fe Group, New Mexico, *Bull. Am. Mus. Nat. Hist., 144,* 127 pp., 1971.

Gilbert, C. M., M. N. Christensen, Y. Al-Rawi, and K. R. Lajoie, Structural and volcanic history of Mono Basin, California-Nevada, in *Studies in Volcanology—A Memoir in Honor of Howel Williams,* edited by R. R. Coats, R. L. Hay, and C. A. Anderson, *Mem. Geol. Soc. Am., 116,* 275–329, 1968.

Gilbert, N. J., Chronology of post-Tuscan volcanism in the Manton area, M. S. thesis, 72 pp., Univ. of Calif., Berkeley, 1969.

Hall, N. T., Late Cenozoic stratigraphy between Mussel Rock and Fleishhacker Zoo, San Francisco Peninsula, in *Guidebook for Field Conference 1, Northern Great Basin and California, International Association for Quaternary Research, 7th Congress, U.S.A.,* pp. 151–158, Nebraska Academy of Science, Lincoln, 1965.

Hearn, B. C., J. M. Donnelly, and F. E. Goff, Preliminary geologic map and cross-section of the Clear Lake volcanic field, Lake County, California, *U.S. Geol. Surv. Open File Rep., 76-751,* 1976.

Heathman, J. H., Bentonite in Wyoming, *Bull. 28,* 20 pp., Wyo. Geol. Soc. Am., Laramie, 1939.

Heiken, G., Plinian-type eruptions in the Medicine Lake Highland, California, and the nature of the underlying magma, *J. Volcanol. Geotherm. Res., 4,* 375–402, 1978.

Hibbard, C. W., Vertebrate fossils from late Cenozoic deposits of central Kansas, *Paleontol. Contrib. Univ. Kans., 2,* 1–14, 1952.

Hibbard, C. W., New stratigraphic names for early Pleistocene deposits in southwestern Kansas, *Am. J. Sci., 256,* 54–59, 1958.

Hildreth, E. W., The magma chamber of the Bishop Tuff—Gradients in temperature, pressure, and composition, Ph. D. dissertation, 328 pp., Univ. of Calif., Berkeley, 1977.

Ingle, J. C., Foraminiferal biofacies variation and the Miocene-Pliocene boundary in southern California, *Bull. Am. Paleontol., 52,* 217–394, 1967.

Izett, G. A., and C. S. V. Barclay, Geologic map of the Kremmling quadrangle, Grand County, Colorado, *Geol. Quad. Map GQ-1115,* scale 1:62,500, U.S. Geolo. Surv., Reston, VA., 1973.

Izett, G. A., and C. W. Naeser, Age of the Bishop Tuff of eastern California as determined by the fission-track method, *Geology, 4,* 587–590, 1976.

Izett, G. A., and C. W. Naeser, Fission-track ages of tuffs in Miocene sedimentary rocks of the Espanola basin, Santa Fe County, New Mexico, *U.S. Geol. Surv. Open File Rep., 80-161,* 1981.

Izett, G. A., and R. E. Wilcox, Map showing localities and inferred distributions of the Huckleberry Ridge, Mesa Falls, and Lava Creek ash beds (Pearlette family ash beds) of Pliocene and Pleistocene age in the western United States and southern Canada, *Misc. Invest. Map MI-1325,* scale 1:4,000,000, U.S. Geol. Surv., Reston, Va., in press, 1981.

Izett, G. A., R. E. Wilcox, H. A. Powers, and G. A. Desborough, The Bishop ash bed, a Pleistocene marker bed in the western United States, *Quat. Res., 1,* 121–132, 1970.

Izett, G. A., R. E. Wilcox, and G. A. Borchardt, Correlation of a volcanic ash bed in Pleistocene deposits near Mount Blanco, Texas, with the Guaje pumice bed of the Jemez Mountains, New Mexico, *Quat. Res., 2,* 554–578, 1972.

Izett, G. A., C. W. Naeser, and J. D. Obradovich, Fission track age of zircons from an ash bed in the Pico Formation (Pliocene and Pleistocene) near Ventura, California, *Geol. Soc. Am. Abstr. Programs 6,* 197, 1974.

Izett, G. A., C. W. Naeser, and J. D. Obradovich, Ages of natural glasses by the fission-track and K-Ar methods, *U.S. Geol. Surv. Open File Rep., 78-701,* 189–192, 1978*a*.

Izett, G. A., J. D. Obradovich, C. W. Naeser, and G. T. Cebula, K-Ar

and fission-track zircon ages of Cerro Toledo Rhyolite tephra units in the Jemez Mountains, north-central New Mexico, *U.S. Geol. Surv. Open File Rep., 78-931,* 1978*b*.

Izett, G. A., J. D. Obradovich, C. W. Naeser, and G. T. Cebula, Potassium-argon and fission-track zircon ages of Cerro Toledo Rhyolite tephra in the Jemez Mountains, New Mexico, *U.S. Geol. Surv. Prof. Pap., 1199-D,* 37–43, 1981.

Jack, R. N., and I. S. E. Carmichael, The chemical 'fingerprinting' of acid volcanic rocks, *Spec. Rep. Calif. Div. Mines Geol., 100,* 17–32, 1968.

Johnson, N. M., N. D. Opdyke, and E. H. Lindsay, Magnetic polarity stratigraphy of Pliocene-Pleistocene terrestrial deposits and vertebrate faunas, San Pedro Valley, Arizona, *Geol. Soc. Am. Bull., 86,* 5–12, 1975.

Knechtel, M. M., and S. M. Patterson, Bentonite deposits in marine Cretaceous formation, Hardin district, Montana and Wyoming, *U.S. Geol. Surv. Bull., 1023,* 116 pp., 1956.

Krauskopf, K. B., and P. C. Bateman, Geologic map of the Glass Mountain quadrangle, Mono County, California, and Mineral County, Nevada, *Geol. Quad. Map GQ-1099,* scale 1:62,500, U.S. Geol. Surv., Reston, Va., 1977.

Lakatos, S. and D. S. Miller, Evidence for the effect of water content on fission-track annealing in volcanic glass, *Earth Planet. Sci. Lett., 14,* 128–130, 1972.

Lamb, H. H., Volcanic dust in the atmosphere; with a chronology and assessment of its meteorological significance, *Philos. Trans. R. Soc. London, 266,* 425–533, 1970.

Lipman, P. W., Chemical comparison of glassy and crystalline volcanic rocks, *U.S. Geol. Surv. Bull., 1201-D,* 24 pp., 1965.

Lipman, P. W., Evolution of the Platoro caldera complex and related volcanic rocks, southwestern San Juan Mountains, Colorado, *U.S. Geol. Surv. Prof. Pap., 852,* 128 pp., 1975.

Lipman, P. W., and H. H. Mehnert, Potassium-argon ages from the Mount Taylor volcanic field, New Mexico, *U.S. Geol. Surv. Prof. Pap., 1124-B,* B1–B8, 1979.

Lipman, P. W., T. A. Steven, R. G. Luedke, and W. S. Burbank, Revised volcanic history of the San Juan, Uncompahgre, Silverton, and Lake City calderas in the western San Juan Mountains, Colorado, *J. Res. U.S. Geol. Surv., 1,* 627–642, 1973.

Lipman, P. W., P. D. Rowley, H. H. Mehnert, S. H. Evans, W. P. Nash, and F. H. Brown, Pleistocene rhyolite of the Mineral Mountains, Utah—Geothermal and archeological significance, *J. Res. U.S. Geol. Surv., 6,* 133–147, 1978.

Lirer, L., T. Pescatore, B. Booth, and G. P. L. Walker, Two plinian pumice-fall deposits from Somma-Vesuvius, Italy, *Geol. Soc. Am. Bull., 84,* 759–772, 1973.

Malde, H. E., Stratigraphy of the Glenns Ferry Formation from Hammett to Hagerman, Idaho, *U.S. Geol. Surv. Bull., 1331-D,* 19 pp., 1972.

Mankinen, E. A., and G. B. Dalrymple, Revised geomagnetic polarity time scale for the interval 0–5 m.y. B.P., *J. Geophys. Res., 84,* 615–626, 1979.

Mapel, W. J., and C. L. Pillmore, Geology of the Newcastle area, Weston County, Wyoming, *U.S. Geol. Surv. Bull., 1141-N,* N1–N85, 1963.

Martin, L. D., and Gilbert, B. M., Excavations at Natural Trap Cave, Lincoln, *Trans. Neb Acad. Sci., 6,* 107–115, 1978.

Marvin, R. F., and S. W. Dobson, Radiometric ages; Compilation B, U.S. Geological Survey, *Isochron/West, 26,* 3–32, 1979.

Mason, B., *Principles of Geochemistry,* 3rd ed. 329 pp., John Wiley, New York, 1966.

Mauger, R. L., K-Ar ages of biotites from tuffs in Eocene rocks of the Green River, Washakie, and Uinta Basins, Utah, Wyoming, and Colorado, *Contrib. Geol., 15,* 14–72, 1977.

Meyer, C. E., M. J. Woodard, A. M. Sarna-Wojcicki, and C. W. Naeser, Zircon fission-track age of 0.45 million years on ash in the type section of the Merced Formation, west-central California, U.S. Geol. Surv. Open File Rep., 80-1071, 6 pp., 1980.

Mullineaux, D. R., Pumice and other pyroclastic deposits in Mount Rainier National Park, Washington, *U.S. Geol. Surv. Bull., 1326,* 83 pp., 1974.

Naeser, C. W., Etching fission tracks in zircons, *Science, 165,* 388, 1969.

Naeser, C. W., G. A. Izett, and R. E. Wilcox, Zircon fission-track ages of Pearlette family ash beds in Meade County, Kansas, *Geology, 1,* 187–189, 1973.

Naeser, C. W., G. A. Izett, and J. D. Obradovich, Fission-track and K-Ar ages of natural glasses, *U.S. Geol. Surv. Bull., 1489,* 31 pp., 1980.

Nash, W. P., and R. P. Smith, Pleisocene volcanic ash deposits in Utah, *Utah Geol., 4,* 35–42, 1977.

Noble, D. C., Gold Flat Member of the Thirsty Canyon Tuff—A pantellerite ash-flow sheet in southern Nevada, *U.S. Geol. Surv. Prof. Pap., 525-B,* B85–B90, 1968.

Noble, D. C., K. A. Sargent, H. H. Mehnert, E. B. Ekren, and F. M. Byers, Jr., Silent Canyon volcanic center, Nye County, Nevada, in *Nevada Test Site,* edited by E. B. Eckel, *Mem. Geol. Soc. Am., 110,* 65–75, 1968.

Obradovich, J. D., and W. A. Cobban, A time-scale for the Late Cretaceous of the western interior of North America, *Spec. Pap. Geol. Assoc. Can., 13,* 31–54, 1975.

Obradovich, J. D., and W. A. Cobban, Speculations on the age span of the Albian Stage (Early Cretaceous), *Geol. Soc. Am. Abstr. Programs, 9,* 1117–1118, 1977.

Obradovich, J. D., C. W. Naeser, and G. A. Izett, Geochronology of late Neogene marine strata in California, in *Correlation of Tropical Through High Latitutde Marine Neogene Deposits of the Pacific Basin* (abstracts and programs), pp. 40–43, International Geological Correlation Progress Project 114, Stanfrod, Calif., 1978.

Ogle, B. A.. Geology of the Eel River Valley area, Humbolt County, California, *Bull. Calif. Div. Mines Geol., 164,* 128 pp., 1953.

Powell, R., and M. Powell, Geothermometry and oxygen barometry using coexisting iron-titanium oxides—A reappraisal, *Mineral. Mag., 41,* 257–263, 1977.

Powers, H. A., and H. E. Malde, Volcanic ash beds as stratigraphic markers in basin deposits near Hagerman and Glenns Ferry, Idaho, *U.S. Geol. Surv. Prof. Pap., 424-B,* 167–170, 1961.

Powers, H. A., E. J. Young, and P. R. Barnett, Possible extension into Idaho, Nevada, and Utah of the Pearlette ash of Meade County, Kansas (abstract), *Geol. Soc. Am. Bull., 69,* 1631, 1958.

Ratté, J. C., and T. A. Steven, Ash flows and related volcanic rocks associated with the Creede caldera, San Juan Mountains, Colorado, *U.S. Geol. Surv. Prof. Pap., 525-H,* 58 pp., 1967.

Richmond, G. M., Surficial geologic map of the Frank Island quadrangle, Yellowstone National Park, Wyoming, *Misc. Invest. Map I-642,* scale 1:62,500, U.S. Geol. Surv., Reston, Va., 1974.

Sapper, K. T., *Vulkankunde,* 424 pp., Verlag Engelhorns, Stuttgart, 1927.

Sarna-Wojcicki, A. M., Correlation of late Cenozoic tuffs in the Central Coast Ranges of California by means of trace- and minor-element chemistry, *U.S. Geol. Surv. Prof. Pap., 972,* 30 pp., 1976.

Sarna-Wojcicki, A. M., H. W. Bowman, and P. C. Russell, Chemical correlation of some late Cenozoic tuffs of northern and central California by neutron activation analysis of glass and comparison with X-ray fluorescence analysis, *U.S. Geol. Surv. Prof. Pap., 1147,* 15 pp., 1979.

Sarna-Wojcicki, A. M., H. W. Bowman, C. E. Meyer, P. C. Russell, F. Asaro, H. Michael, J. J. Rowe, and P. A. Baedecker, Chemical analyses, correlations, and ages of late Cenozoic tephra units of east-central and southern California, *U.S. Geol. Surv. Open File Rep., 80-231,* 1980.

Sarna-Wojcicki, A. M., S. Shipley, R. B. Waitt, Jr., D. Dzurisin, and S. H. Wood, Areal distribution, thickness, mass, volume, and grain size of air-fall ash from the six major eruptions of 1980, *U.S. Geol. Surv. Prof. Pap., 1250,* in press, 1981.

Scheidegger, K. F., J. B. Corliss, P. A. Jezek, and D. Ninkovich, Compositions of deep-sea ash layers derived from North Pacific volcanic arcs—Variations in time and space, *J. Volcanol. Geotherm. Res., 7,* 107–137, 1980.

Selli, R., C. A. Accorsi, M. M. Bandini, M. D. Bertolani, G. Bigazzi, F. P. Bonadonna, A. M. Borsetti, F. Cati, M. L. Colalongo, S. D'Onofrio, W. Landini, E. Menesini, R. Mezzetti, G. Pasini, C. Savelli, and R. Tampieri, The Vrica section (Calabria, Italy)—A potential Neogene/Quaternary boundary stratotype, *Gi. Geol. 42*(1), 181–204, 1977.

Shaw, H. R., Comments on viscosity, crystal settling, and convection in granitic magmas, *Am. J. Sci., 263,* 120–152, 1965.

Sheridan, M. F., and Updike, R. G., Sugarloaf Mountain tephra—A Pleistocene rhyolitic deposit of base-surge origin in Northern Arizona, *Geol. Soc. Am. Bull., 86*(4), 571–581, 1975.

Smith, D. G. W., and J. A. Westgate, An electron probe technique for characterising pyroclastic deposits, *Earth Planet. Sci. Lett., 5,* 313–319, 1969.

Smith, R. L., Ash-flow magmatism, in *Ash-Flow Tuffs,* edited by C. E.

Chapin and W. E. Elston, *Spec. Pap. Geol. Soc. Am., 180,* 1–27, 1979.

Smith, R. L., and R. A. Bailey, The Bandelier Tuff—A study of ash-flow eruption cycles from zoned magma chambers, *Bull. Volcanol., 29,* 83–104, 1966.

Smith, R. L., R. A. Bailey, and C. S. Ross, Geologic map of the Jemez Mountains, New Mexico, *Misc. Invest. Map I-571,* scale 1:125,000, U.S. Geol. Surv., Reston, Va., 1970.

Steiger, R. H., and E. Jäger, Subcommission on Geochronology—Convention on the use of decay constants in geo- and cosmochronology, *Earth Planet. Sci. Lett., 36,* 359–362, 1977.

Steven, T. A., and P. W. Lipman, Calderas of the San Juan volcanic field, southwestern Colorado, *U.S. Geol. Surv. Prof. Pap., 958,* 35 pp., 1976.

Storzer, D., and G. Poupeau, Ages-plateaux de mineraux et verres par la methode des traces de fission, C. R. *Hebd. Séances Acad. Sci. Ser. D., 276,* 137–139, 1973.

Strain, W. S., Late Cenozoic strata of the El Paso-Juarez area, N. Mex. *Field Conf. Guideb. N.M. Geol. Soc., 20,* 155–177, 1969.

Swineford, A., and J. C. Frye, Petrographic comparison of Pliocene and Pleistocene volcanic ash, *Bull. Kans. State Geol. Surv., 64,* 1–32, 1946.

Tahirkheli, R. A. K., and C. W. Naeser, Zircon fission track age of Post Ranch ash bed near Benson, Arizona, *J. Ariz. Acad. Sci., 10,* 111–113, 1975.

Theisen, A. A., G. A. Borchardt, M. E. Harward, and R. A. Schmidt, Neutron activation for distinguishing Cascade Range pyroclastics, *Science, 161,* 1009–1011, 1968.

Tsuya, H., Geological and petrological studies of volcano, Fuji, 5, On the 1707 eruption of volcano Fuji, *Bull. Earthquake Res. Inst. Tokyo Univ., 33,* 341–383, 1955.

van Bemmelen, R. W., *The Geology of Indonesia,* vol. 1A, 732 pp., Government Printing Office, The Hague, 1932.

Wall, V. J., and J. D. Clemens, Experimental studies on peraluminous (S-Type) granitic magmas, *Geol. Soc. Am. Abstr. Programs, 11,* 534, 1979.

Watkins, N. D., R. S. J. Sparks, H. Sigurdsson, T. C. Huang, A. Federman, and S. Carey, Volume and extent of the Minoan tephra from Santorini volcano: New evidence from deep-sea sediment cores, *Nature, 271,* 122–126, 1978.

Wilcox, R. E., Cherkasov's 'focal screening' for determination of refractive index by the immersion method, in *Proceedings of the International Microscopy Symposium, 1960,* pp. 160–165, McCrone Associates, Chicago, 1962.

Wilcox, R. E., Volcanic ash chronology, in *The Quaternary of the United States,* edited by H. E. Wright, Jr., and D. C. Frey, pp. 807–816, Princeton University Press, Princeton, N. J., 1965.

Williams, H., and G. Goles, Volume of the Mazama ash-fall and the origin of Crater Lake caldera, in *Andesite Conference Guidebook, edited by H. M. Dole, Bull. Oreg. Dep. Geol. Mineral. Ind., 62,* 37–41, 1968.

Wood, C. P., Petrogenesis of garnet-bearing rhyolites from Canterbury, New Zealand, *N. Z. J. Geol. Geophys. 17,* 759–785, 1974.

Woodring, W. P., R. Stewart, and R. W. Richards, Geology of the Kettleman Hills oil field, California; stratigraphy, paleontology, and structure, *U.S. Geol. Surv. Prof. Pap., 195,* 170 pp., 1490.

Yeats, R. S., and W. A. McLaulghlin, Potassium-argon mineral age of an ash bed in the Pico Formation, Ventura basin, Calif., *Spec. Pap. Geol. Soc.* Am., *124,* 173–206, 1970.

(Received November 17, 1980;
revised May 5, 1981;
accepted May 15, 1981.)

JOURNAL OF GEOPHYSICAL RESEARCH, VOL. 86, NO. B11, PAGES 10223–10241, NOVEMBER 10, 1981

Pleistocene High-Silica Rhyolites of the Coso Volcanic Field, Inyo County, California

CHARLES R. BACON

U.S. Geological Survey, Menlo Park, California 94025

RAY MACDONALD

Department of Environmental Sciences, University of Lancaster, England LA1 4YQ

ROBERT L. SMITH AND PHILIP A. BAEDECKER

U.S. Geological Survey, Reston, Virginia 22092

The high-silica rhyolite domes and lava flows of the bimodal Pleistocene part of the Coso volcanic field provide an example of the early stages of evolution of a silicic magmatic system of substantial size and longevity. The rhyolites are sparsely porphyritic to virtually aphyric, containing qz + pl + san + bi + hb + mt ± allanite ± opx ± cpx ± fa ± il ± ap ± zircon phenocrysts. Major and trace element compositions of all 38 rhyolite extrusions are consistent with derivation from somewhat less silicic parental material by liquid state differentiation processes in compositionally and thermally zoned magmatic systems. Seven chemically homogeneous eruptive groups emplaced approximately 1.0, 0.6, 0.24, 0.17, 0.16(?), 0.09, and 0.06 m.y. ago can be distinguished on the basis of trace element and K-Ar data. The oldest two groups are volumetrically minor and geochemically distinct from the younger groups, all five of which appear to have evolved from the same magmatic system. Erupted volume–time relations suggest that small amounts of magma were bled from the top of a silicic reservoir at a nearly constant long-term rate over the last 0.24 m.y. The interval of repose between eruptions appears to be proportional to the volume of the preceding eruptive group. This relationship suggests that eruptions take place when some parameter which increases at a constant rate reaches a critical value; this parameter may be extensional strain accumulated in roof rocks. Extension of the lithosphere favors intrusion of basalt into the crust, attendant partial melting, and maintenance of a long-lived silicic magmatic system. Consideration of the mass of magma that must have been intruded into the crust in order to explain the anomalously high heat flow near the center of the rhyolite field and comparison of age, volume, mineralogic, and compositional characteristics of the rhyolites with those of caldera-forming systems suggest that the Coso silicic system may contain a few hundred cubic kilometers of magma. The Coso magmatic system may eventually have the potential for producing voluminous pyroclastic eruptions if the safety valve provided by rapid crustal extension becomes inadequate to (1) defuse the system through episodic removal of volatile-rich magma from its top and (2) prohibit migration of the reservoir to a shallow crustal level.

INTRODUCTION

Much progress has been made in understanding the genesis of silicic magmas through detailed study of the products of voluminous pyroclastic eruptions. Relatively little is known, however, of the early stages of development of magmatic systems that eventually erupt in large volume and form calderas because of the difficulty of recognizing such systems in their infancy, because of limits of resolution of dating techniques and because much of the evidence is buried or lost in systems that have evolved to the caldera stage. The Quaternary part of the Coso volcanic field of California appears to provide an example of the early stage of development of a silicic system that is well suited for petrologic and geochronologic study.

The Coso volcanic field is located at the margin of the Basin and Range province, immediately east of the Sierra Nevada, approximately 60 km north of the Garlock fault (Figure 1). The Coso region is characterized by block faulting [*Duffield et al.*, 1980; *Roquemore*, 1980] and intense seismicity [*Weaver and Hill*, 1978/79; *Walter and Weaver*, 1980] that indicate considerable late Cenozoic extension in an approximately west-northwest–east-southeast direction. Volcanism began about 6 m.y. ago on the northeastern flank of the Coso Range [*Bacon et al.*, 1981]; the most voluminous volcanic rocks were erupted between 4 and 2.5 m.y. ago within the range and local basaltic volcanism occurred ~2.0 and ~1.8 m.y. ago [*Duffield et al.*, 1980]. The pre-Pleistocene volcanic rocks span the compositional range from basalt to rhyolite. Pleistocene volcanism took place in the southwestern Coso Range and was strikingly bimodal in character [*Babcock and Wise*, 1973; *Bacon et al.*, 1980]. Nearly aphyric, high-silica (~77 percent SiO_2) rhyolite domes and flows were accompanied by basaltic lava flows erupted from vents marginal to the rhyolite field. The silicic rocks appear to range in age from 1.04 to 0.06 m.y. They are highly differentiated and similar in composition to metaluminous high-silica rhyolite domes elsewhere and to the first-erupted products of some voluminous zoned pyroclastic eruptions. The silicic magma reservoir has contributed a substantial flux of heat to the overlying rocks which support an active hydrothermal system [*Duffield et al.*, 1980; *Combs*, 1980; *Fournier et al.*, 1980].

In this paper we describe the field relations of the rhyolites, their ages, mineralogy, and major and trace element composition. This information is employed to develop a model for the petrogenetic and eruptive history of the Pleistocene Coso silicic system that is consistent with all existing geologic and geophysical observations.

This paper is not subject to U.S. copyright. Published in 1981 by the American Geophysical Union.

Paper number 1B0907.

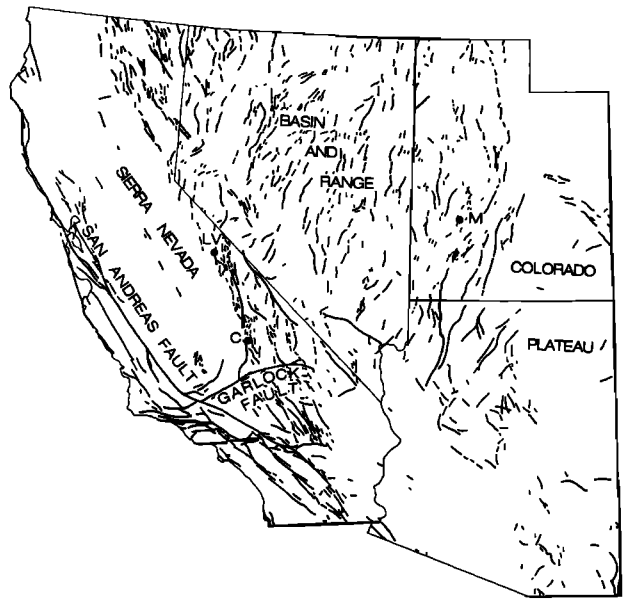

Fig. 1. Location map showing late Cenozoic faults in California, Nevada, Arizona, and Utah [modified after *Howard et al.*, 1978] and Coso Range (C), Long Valley (LV), and Mineral Range (M) Pleistocene silicic volcanic centers.

FIELD RELATIONS

All of the Pleistocene rhyolite extrusions in the Coso volcanic field were emplaced as steep-sided domes and short, thick lava flows. Individual extrusions range in volume from 0.0003 to 0.3 km^3; the total volume of domes and flows is about 1.6 km^3. At least 0.3 km^3 of pyroclastic material is associated with the rhyolite extrusions. Each silicic eruption apparently began with excavation of a crater by phreatomagmatic explosions as magma heated shallow groundwater. Deposits from this phase of eruption commonly contain accretionary lapilli and abundant lithic fragments and show evidence of deposition by high-energy transport or 'surge' mechanisms. These grade upward into pumice fall, lapilli-rich deposits that thicken toward vents to form partial to complete tephra rings. Pumice clasts typically are finely vesicular, blocky prisms. All gradations of lava extrusion exist, from no visible outcrops in craters through low domes surrounded by tephra rings to steep-sided, high domes and broad, thick flows that completely cover any preexisting rings of fragmental material.

Surfaces of the younger, virtually uneroded domes and flows consist of jumbled blocks of hydrated, vesicular glass. In eroded areas and roadcuts, dense obsidian is visible under this pumiceous carapace. Deeper within the domes and flows obsidian becomes spherulitic and ultimately gives way to completely crystalline felsite.

The relative ages of many domes remain uncertain, but some can be determined from superposition. Determination of relative age through study of tephra layers is hampered by scarcity of suitable outcrops and by the homogeneous chemical and mineralogic composition of coeval eruptive products from multiple vents, described in a later section. In several instances, field evidence indicates unambiguous relative ages of basalts and rhyolites, but most of the temporal information presented in this paper was obtained by K-Ar dating [*Lanphere et al.*, 1975; *Duffield et al.*, 1980; G. B. Dalrymple and C. R. Bacon, unpublished data, 1980].

ANALYTICAL METHODS

Because of the extreme elemental enrichments and depletions known to exist in high-silica rhyolites, special precautions were taken to minimize contamination during sample preparation. All samples were carefully broken and examined for foreign material and then ground in an agate mortar. Only glassy rocks were prepared for analysis.

Silica was determined by the spectrophotometric technique of *Shapiro* [1974], Al_2O_3, total Fe as Fe_2O_3, CaO, MgO, MnO, Li, Be, and Sn by atomic absorption spectrometry, Na_2O and K_2O by flame photometry, TiO_2 and P_2O_5 colorimetrically, FeO by a modified version of *Wilson*'s [1955] method, H_2O gravimetrically, and F by specific ion electrode. Special emission spectrographic techniques were developed for the determination of Sr and Ba. X ray fluorescence spectrometry was employed in analysis for Rb, Y, Zr, Nb, and Pb, using a Philips 1212 automatic spectrometer and holding sample powder on mylar film. The abundances of Sc, Co, Zn, Sb, Cs, La, Ce, Nd, Sm, Eu, Tb, Tm, Yb, Lu, Hf, Ta, Th, and U and an independent determination of Fe were obtained through instrumental neutron activation analysis. Precision, based on repeated analysis of U.S.G.S. standards G-2 and GSP-1 and (or) Bandelier sample RJM-22, is given in Table 1 for each element.

Whole rock analyses were supplemented by electron microprobe analyses of glass in order to provide independent determinations of 'major' elements and to study the effects of elemental mobility due to the process of hydration of glass.

RESULTS

Chemical Composition

A striking geochemical feature of the rhyolites is their major element homogeneity (Table 1). Silica varies no more than 0.6 percent absolute from 77.0 percent (anhydrous) in all of the glassy rocks from the 38 domes and flows; even this small variation may be due in large part to analytical imprecision. Alumina varies within a similar range around 12.5 percent. In the 15 nonhydrated obsidians, Na_2O and K_2O range from 4.25 to 4.58 and 4.15 to 4.61, respectively. It is noteworthy that these alkali metals vary inversely with one another. Other 'major' element abundances are typical of metaluminous high-silica rhyolites. These chemical features characterize the Pleistocene rhyolites of the Coso Range as highly evolved magmas.

The rhyolites of the Coso Range are similar to many other crystal-poor, high-silica, metaluminous rhyolites, such as those at Mono Craters and Glass Mountain, California [*Carmichael*, 1967; *Jack and Carmichael*, 1968; *Noble et al.*, 1972; *Bailey et al.*, 1976] and the more differentiated portions of the products of continental caldera-forming eruptions, notably the Bishop Tuff [*Hildreth*, 1979, this issue]. Moderate to extreme enrichments, relative to less silicic rhyolites in F, Cl, H_2O and elements such as Li, Be, Na, Rb, Y, Nb, Sn, Sb, Cs, Sm, HREE, Ta, Pb, Th, and U are characteristic of such magmas, as are depletions in Mg, P, K, Ca, Ti, Co, Sr, Ba, La, Ce, Nd, and Eu. The Coso rhyolites show these attributes to varying degrees, but all 38 domes and flows fit this pattern. Compositions generally fall between those of Long Valley rhyolites [*Hildreth*, 1979] and the generally more alkalic Valles magmas [*Smith*, 1979]. Abundances of Li, Be, and Sn in the most evolved Coso rhyolite are actually somewhat higher than the maximum concentrations observed in the earliest

TABLE 1*a*. Whole Rock Chemical Analyses

	Sample/Groups*										
	38†/1	28/2	2/3	11/3	13‡/3	10‡/3	10B/3	14‡/3	12/3	15‡/3	19‡/3
					Wet Chemical Analyses, %						
SiO_2	73.8	74.5	74.3	75.0	76.9	76.9		76.6	74.7	76.2	76.9
Al_2O_3	12.3	12.62	12.18	12.21	12.41	12.77		12.41	12.29	12.57	12.39
Fe_2O_3	0.74	0.69	0.51	0.45	0.50	0.43		0.40	0.47	0.40	0.64
FeO		0.31	0.48	0.53	0.54	0.56		0.58	0.55	0.53	0.39
MgO	0.03	0.05	0.12	<0.01	<0.01	<0.01		<0.01	0.01	<0.02	0.02
CaO	0.44	0.40	0.55	0.34	0.35	0.39		0.35	0.51	0.39	0.35
Na_2O	3.45	4.15	4.05	4.32	4.45	4.58		4.52	4.38	4.31	4.55
K_2O	5.05	4.60	4.76	4.25	4.40	4.19		4.15	4.25	4.50	4.18
H_2O^+	4.72	2.15	1.96	2.44	0.19	0.21		0.29	2.68	0.22	0.08
H_2O^-		0.05	0.18	0.22	0.10	0.08		0.09	0.24	0.08	0.16
TiO_2	0.08	0.05	0.09	0.06	0.06	0.06		0.07	0.07	0.06	0.06
P_2O_5	0.02	<0.01	0.01	0.01	<0.01	<0.01		0.03	<0.01	0.01	0.02
MnO	0.11	0.032	0.020	0.019	0.018	0.019		0.019	0.019	0.017	0.020
F	0.140	0.245	0.180	0.177	0.186	0.189	0.183	0.186	0.186	0.174	0.184
Less O	0.06	0.10	0.08	0.07	0.08	0.08		0.08	0.08	0.07	0.08
Total	100.82	99.76	99.31	99.96	100.03	100.30		99.62	100.28	99.39	99.86
$SiO_{2(n)}$§	76.9	76.4	76.5	77.1	77.1	76.9		77.2	76.8	76.9	77.2
Li, ppm	27	110				180	75	120			
Be, ppm	13	15				11	11				
Sn, ppm	11	16				11	8.3				
					X Ray Fluorescence Analyses, ppm						
Rb	485	425	315	315	330	325		315	305	335	320
Y		74	69	74		72		76	74	70	75
Zr	100	100	100	100	105	105		100	100	100	100
Nb	100	90	75	72	75	71		77	80	80	78
Pb	57	37	26	30	34	38		31	35	39	33
					Emission Spectrographic Analyses, ppm						
Sr	2.0	9.8			2.8	3.2		3.7	2.4		2.2
Ba	<2	23			8	5.4		6.0	7		6
					Instrumental Neutron Activation Analyses, ppm						
Sc	3.33	0.50	0.96	0.96	0.99	0.99	0.97	0.97	0.97	0.95	1.00
Fe, %	0.47	0.75	0.72	0.71	0.75	0.74	0.74	0.74	0.74	0.73	0.74
Co	<0.2	0.3	0.1	0.1	0.1	0.1	0.1	0.1	0.1	0.2	0.1
Zn	50	66	55	53	55	59	53	53	59	57	57
Sb	4.1	1.8	1.1	0.9	0.9	0.9	0.9	1.2	1.2	1.0	1.0
Cs	23.2	13.2	6.8	6.8	7.0	7.1	7.0	6.9	7.0	7.2	7.2
La	13‖	26	16	16	16	16	18	16	17	16	17
Ce	18‖	48	38	39	40	39	42	38	39	37	40
Nd	13‖	22	24	22	25	21	21	23	27	25	23
Sm	5.4‖	5.9‖	6.4	6.5	6.9	6.8	8.2	7.0	7.0	6.6‖	7.0
Eu	0.03	0.08	<0.03	<0.03	0.02	0.02	<0.03	<0.03	<0.03	<0.03	0.04
Tb	1.61	1.41	1.56	1.49	1.67	1.60	1.53	1.57	1.67	1.63	1.58
Tm		1.24	0.99	0.96	1.03	1.05	1.06	1.10	1.11	1.10	1.11
Yb	8.5	8.7	7.1	7.1	7.5	7.4	7.4	7.2	7.7	7.3	7.4
Lu	1.17	1.17	0.94	0.94	0.99	1.07	0.97	0.99	0.99	0.97	0.98
Hf	6.5	6.8	5.8	5.8	6.0	6.1	5.9	5.7	6.0	5.9	5.9
Ta	15.0	12.2	6.64	6.76	7.00	6.66	6.96	6.97	7.08	7.54	7.00
Th	35.9	41.8	33.2	33.4	34.3	34.3	35.3	34.7	35.2	34.7	34.8
U	22.8	13.9	12.1	12.2	12.3	12.5		13.4	14.0	15.4	11.2
					Crystal Content						
Phenocrysts, wt %	2	15	0.1	0.1	0.01	0.01		0.01	0.01	1	1

*Samples assigned to groups on basis of similarity in composition (see text and Figure 6).
†X-ray fluorescence analysis. Loss on fusion reported as H_2O^+.
‡Obsidian. All other samples are hydrated glassy rhyolite. See Figure 7 for sample localities.
§SiO_2 content calculated H_2O-free with analysis normalized to total 100.00
‖Correction for fission product interference exceeds 20% of reported value.
¶Estimated precision based on repeated analysis of standard rhyolite and granitic materials, reported as one standard deviation in percent of amount present.

emplaced part of the Otowi Member of the Bandelier Tuff (R. L. Smith, unpublished data, 1980), the most evolved erupted magma of the Valles silicic system. The least differentiated Pleistocene rhyolites of the Coso Range are similar in composition to the initial air fall component of the Bishop Tuff [*Hildreth*, 1979], though substantially richer in Na, HREE, and Ta and poorer in Sc and Sb.

In any treatment of the geochemistry of glassy silicic volcanic rocks other than obsidians, the effects of the hydration process must be evaluated. Microprobe analyses of pairs of

TABLE 1*b*. Whole-Rock Chemical Analyses

	Sample/Group*										
	22/3	37/3	23/3	33/3	5‡/4	32/4	3/4	16‡/5	39/5	20‡/5	20B/5
					Wet Chemical Analyses, %						
SiO_2	74.4	74.6	75.5	75.1	76.9	74.5	75.2	76.2		76.4	
Al_2O_3	12.28	11.86	12.20	12.77	12.68	12.15	12.28	12.56		12.56	
Fe_2O_3	0.42	0.49	0.38	0.64	0.40	0.67	0.53	0.56		0.35	
FeO	0.49	0.47	0.45	0.40	0.44	0.32	0.45	0.44		0.60	
MgO	0.05	0.13	0.01	0.02	<0.01	0.06	0.02	0.02		0.02	
CaO	0.69	0.54	0.37	0.31	0.32	0.54	0.31	0.43		0.44	
Na_2O	4.18	3.89	4.12	4.45	4.58	4.20	4.42	4.07		4.32	
K_2O	4.44	4.87	4.53	4.20	4.30	4.39	4.25	4.87		4.58	
H_2O^+	2.05	2.67	1.72	2.41	0.14	2.49	2.50	0.51		0.28	
H_2O^-	0.15	0.29	0.13	0.21	0.08	0.12	0.04	0.04		0.09	
TiO_2	0.05	0.07	0.04	0.06	0.05	0.06	0.05	0.09		0.09	
P_2O_5	<0.01	0.03	<0.01	<0.01	<0.01	0.01	<0.01	<0.01		<0.01	
MnO	0.017	0.020	0.017	0.020	0.020	0.021	0.020	0.019		0.016	
F	0.166	0.205	0.205	0.199	0.252	0.237	0.237	0.114		0.144	
Less O	0.07	0.09	0.09	0.08	0.11	0.10	0.10	0.05		0.06	
Total	99.32	100.05	99.59	100.71	100.05	99.67	100.21	99.87		99.83	
$SiO_{2(n)}$§	76.6	76.9	77.3	76.6	77.1	76.8	77.0	76.7		76.8	
Li, ppm					150	86				89	
Be, ppm					13	12				8.9	
Sn, ppm					13	11				9.6	
					X Ray Fluorescence Analyses, ppm						
Rb	325	320	340	330	370	350	360	270	235	270	
Y	69	73	73	74		81					
Zr	105	95	95	100	100	110	110	115	120	110	
Nb	75	72	74	73	88	79	79			57	
Pb	32	36	33	38	36	33	35	21	24	31	
					Emission Spectrographic Analyses, ppm						
Sr					1.4					6.8	
Ba					<2					32	
					Instrumental Neutron Activation Analyses, %						
Sc, ppm	0.96	0.99	0.99	1.00	0.87	1.21	1.25	0.76	0.73	0.80	0.76
Fe	0.72	0.74	0.73	0.76	0.68	0.68	0.70	0.75	0.73	0.81	0.76
Co	0.1	0.1	0.1	0.2	0.1	0.2	0.1	0.2	0.2	0.2	0.3
Zn	57	57	59	57	53	58	60	43	44	44	45
Sb	0.9	1.1	1.0	0.9	1.3	1.0	1.3	0.9	1.2	1.0	1.1
Cs	6.8	7.2	6.9	7.1	9.2	7.9	8.5	6.7	5.9	6.5	6.2
La	17	19	19	19	13	15	16	30	28	32	29
Ce	39	39	38	40	32	32	32	56	57	61	59
Nd	24	22	22	25	22	20	21	33	25	27	25
Sm	6.8	7.2	7.2	7.5	6.9‖	7.5	8.1	5.9‖	5.7	6.2	5.9
Eu	0.01	0.02	<0.03	<0.03	<0.03	<0.03	<0.03	0.11	0.08	0.09	0.08
Tb	1.56	1.61	1.57	1.67	1.83	1.72	1.82	1.28	1.20	1.20	1.24
Tm	1.05	1.04	1.07	1.13	1.32	1.17	1.19	0.92	0.65	0.80	0.70
Yb	7.5	7.5	7.3	7.6	9.0	8.0	8.4	5.9	5.8	6.1	6.0
Lu	0.97	0.98	1.00	0.99	1.20	1.05	1.10	0.80	0.78	0.82	0.80
Hf	5.9	6.0	5.9	6.1	6.2	6.5	6.7	5.1	5.0	5.3	5.1
Ta	6.76	7.42	7.34	7.21	8.99	8.10	8.76	6.33	5.42	5.52	5.42
Th	34.3	35.3	34.6	36.0	42.1	35.6	38.0	32.5	29.4	31.6	30.4
U	10.8	12.3	11.9	11.8	16.7	12.9	14.6	14.8	9.8	9.3	9.8
					Crystal Content						
Phenocrysts, wt %	1	1	1	1	2	0.01	0.01	<0.001		0.001	

See footnotes to Table 1*a* for notes.

obsidian and hydrated glass from the same Coso localities show consistent slight depletion in Na_2O and suggest an increase in K_2O. Whole rock analyses (Table 1) suggest depletion of Na_2O and an increase in Fe_2O_3/FeO ratio due to hydration when obsidians ($H_2O^+ \leq 0.5\%$) are compared with hydrated pumiceous glasses (H_2O^+ generally $> 2\%$). These effects apparently are typical of the hydration process [*Noble*, 1967]. Addition of CaO and MgO to hydrated samples is apparent in the whole rock data but was not detected with the microprobe. Small amounts of secondary calcite and dolomite have been recovered in mineral separates of the hydrated samples; these appear to have originated by precipitation from groundwater in cracks and vesicles and probably account for the higher whole rock CaO and MgO in the hydrated pumiceous samples.

Zielinski et al. [1977] reported losses of Li, gains of Sr and Ba, and variable F in perlites relative to coexisting obsidians. Few hydrated Coso samples were analyzed for these elements, but a loss of Li owing to hydration is apparent and possibly a slight gain of Sr, as might be expected from the Na_2O, CaO,

TABLE 1c. Whole Rock Chemical Analyses

	Sample/Group*										
	34/5	35/5	36/6	24‡/6	25‡/6	4‡/7	31/7	30/7	29/7	6‡/7	7/7
Wet Chemical Analyses, %											
SiO_2	75.3	75.2	74.8	76.5	76.7	77.0	75.3	74.6	75.3	76.6	74.8
Al_2O_3	11.89	11.88	12.22	12.57	12.45	12.06	12.24	12.12	12.12	12.42	11.92
Fe_2O_3	0.55	0.73	0.53	0.31	0.40	0.38	0.50	0.53	0.46	0.69	0.44
FeO	0.50	0.28	0.57	0.65	0.63	0.57	0.43	0.40	0.44	0.30	0.47
MgO	0.03	0.09	0.03	0.02	0.02	0.02	0.03	0.07	0.02	<0.01	0.03
CaO	0.39	0.65	0.31	0.42	0.41	0.31	0.34	0.86	0.33	0.36	0.39
Na_2O	3.99	4.00	4.00	4.32	4.34	4.44	4.02	4.04	4.18	4.36	4.24
K_2O	4.66	4.67	4.60	4.58	4.61	4.41	4.59	4.36	4.41	4.24	4.35
H_2O^+	2.08	2.01	2.40	0.37	0.19	0.23	2.39	1.74	2.17	0.38	2.37
H_2O^-	0.15	0.21	0.12	0.05	0.01	0.02	0.16	0.37	0.14	0.11	0.26
TiO_2	0.07	0.07	0.08	0.07	0.09	0.06	0.06	0.05	0.05	0.08	0.07
P_2O_5	0.02	0.03	0.01	<0.01	<0.01	<0.01	0.02	0.02	<0.01	<0.01	0.01
MnO	0.020	0.021	0.020	0.018	0.016	0.021	0.021	0.022	0.023	0.021	0.021
F	0.144	0.132	0.120	0.118	0.124	0.129	0.126	0.159	0.128	0.134	0.128
Less O	0.06	0.06	0.05	0.05	0.05	0.05	0.05	0.07	0.05	0.06	0.05
Total	99.73	99.91	99.76	99.95	99.94	99.60	100.18	99.27	99.72	99.63	99.45
$SiO_{2(n)}$§	77.3	77.0	77.0	76.9	76.9	77.5	77.2	76.8	77.3	77.3	77.3
Li, ppm					76				76		
Be, ppm					6.5				7.7		
Sn, ppm					6.7				8.5		
X Ray Fluorescence Analyses, ppm											
Rb	275	265	210	195	210	250	250	245	245	235	250
Y	63	60	53	47	47	59	59	57	55	55	58
Zr	115	105	125	140	135	95	95	85	85	90	90
Nb	52	53	50	52	49	53	50	48	50	47	48
Pb	27	35	25	23	26	36	29	30	34	28	32
Emission Spectrographic Analyses, ppm											
Sr			6.5		10.2						
Ba			35		55						
Instrumental Neutron Activation Analyses, ppm											
Sc	0.79	0.77	0.83	0.90	0.85	0.50	0.49	0.49	0.48	0.51	0.50
Fe, %	0.78	0.77	0.83	0.88	0.84	0.68	0.68	0.66	0.67	0.71	0.68
Co	0.2	0.2	0.2	0.3	0.2	0.1	0.1	0.1	0.1	0.1	0.1
Zn	44	48	43	49	45	44	44	41	42	44	44
Sb	1.0	1.1	0.7	0.8	0.6	0.9	0.9	0.9	0.9	0.9	1.0
Cs	6.7	6.7	4.4	4.5	4.4	5.8	5.7	5.8	5.9	6.0	5.8
La	32	31	41	44	41	17	17	17	17	17	17
Ce	59	58	69	78	74	36	36	36	35	37	37
Nd	28	26	32	34	31	21	22	23	23	25	19
Sm	6.7	6.5	6.6	6.7	6.6	4.8‖	4.8‖	4.6‖	4.7‖	4.9‖	4.9‖
Eu	0.10	0.09	0.14	0.13	0.15	0.07	0.07	0.07	0.06	0.06	0.06
Tb	1.25	1.24	1.08	1.12	1.06	1.06	1.11	1.09	1.02	1.06	1.09
Tm	0.96	0.94	0.67	0.64	0.72	0.75	0.91	0.80	0.79	0.81	0.77
Yb	6.3	6.2	4.9	5.2	4.9	5.5	5.3	5.4	5.4	5.6	5.6
Lu	0.83	0.82	0.64	0.67	0.62	0.72	0.74	0.78	0.72	0.77	0.74
Hf	5.4	5.3	5.3	5.6	5.1	4.9	4.8	4.8	4.9	5.0	4.9
Ta	5.97	5.91	4.29	4.29	4.02	5.16	5.26	5.24	5.12	5.43	5.50
Th	32.4	32.1	25.5	26.3	25.3	28.4	27.9	27.8	28.0	29.2	28.4
U	10.9	11.0	8.2	8.1	7.8	12.1	12.2	12.2	12.1	12.9	12.4
Crystal Content											
Phenocrysts, wt %	0.001	<0.001		0.01	0.01	1	1	1	1	1	1

See footnotes to Table 1a for notes.

and MgO results. Other trace elements do not appear to be significantly affected by the degree of hydration experienced by the Coso rhyolites, with the possible exception of F in sample 38, the oldest, and only greenish, perlite analyzed.

Correlations between abundances of pairs of elements in the Coso rhyolites are impressive, the degree of scatter depending largely on analytical precision. The majority of elements fall into two groups: (1) Li, Be, F, Na, Sc, Mn, Zn, Rb, Y, Nb, Sn, Sb, Cs, Sm, HREE, Ta, Pb, Th, U and (2) Mg, K, Ca, Ti, Co, Fe, Sr, Zr, Ba, La, Ce, Nd, Eu. Elements within each group generally show positive correlations with each other, but negative correlations with elements of the other group (Figures 2, 3, and 4). The type of behavior exhibited by most elements matches that in the Long Valley [*Hildreth*, 1979, this issue] and Valles [*Smith*, 1979] systems (see also Figure 11). It has been possible to reconstruct the chemical stratification of the roof zones of the silicic magma chambers of both of these systems prior to eruption of major ash flow tuffs; certain elements were concentrated upward toward the roof and others downward in the chamber. Some elements ex-

TABLE 1*d*. Whole Rock Chemical Analyses

	Sample/Group*										
	27‡/7	9/7	8/7	17‡/7	18‡/7	26‡/7	26B/7	26C/7	21/7	1/7	σ^1, %
						Wet Chemical Analyses, %					
SiO_2	77.0	74.4	74.3	76.8	77.5	76.4			75.8	74.6	0.5
Al_2O_3	12.54	12.09	12.38	12.41	12.57	12.43			12.16	12.47	2
Fe_2O_3	0.43	0.75	0.44	0.28	0.26	0.32			0.34	0.50	2
FeO	0.50	0.29	0.40	0.55	0.54	0.50			0.46	0.43	5
MgO	0.03	0.07	<0.01	0.03	0.02	<0.02			0.06	<0.01	3
CaO	0.38	0.59	0.45	0.42	0.41	0.37			0.50	0.44	4
Na_2O	4.32	4.03	4.15	4.40	4.25	4.44			4.12	4.10	2
K_2O	4.37	4.27	4.30	4.38	4.56	4.36			4.30	4.46	1
H_2O^+	0.27	2.54	2.60	0.22	0.17	0.31			2.30	2.05	10
H_2O^-	0.09	0.18	0.17	0.10	0.07	0.10			0.19	0.11	10
TiO_2	0.04	0.05	0.08	0.07	0.06	0.05			0.05	0.09	4
P_2O_5	<0.01	0.01	0.01	<0.01	<0.01	<0.01			<0.01	0.03	20
MnO	0.023	0.021	0.023	0.018	0.020	0.019			0.019	0.023	5
F	0.124	0.195	0.126	0.130	0.124	0.122	0.110	0.126	0.138	0.134	4
Less O	0.05	0.08	0.05	0.05	0.05	0.05			0.06	0.06	
Total	100.06	99.41	99.38	99.76	100.50	99.37			100.38	99.37	
$SiO_{2(n)}$§	77.3	77.0	76.9	77.3	77.3	77.2			77.5	76.8	
Li, ppm						92		57			5
Be, ppm						7.9		8.0			5
Sn, ppm						8.3		8.5			15
						X Ray Fluorescence Analyses, ppm					
Rb	230	225	235	240	245	255			245	245	5
Y	62		63	57		60			58	62	10
Zr	95	90	85	90	95	90			95	90	5
Nb	50	49	47	51	55	52			50	55	5
Pb	29	25	30	30	32	27			27	31	10
						Emission Spectrographic Analyses, ppm					
Sr						4.8		5.3			15
Ba						12.8		13.0			10
						Instrumental Neutron Activation Analyses, ppm					
Sc	0.55	0.49	0.51	0.53	0.52	0.53	0.52	0.51	0.50	0.52	4
Fe, %	0.70	0.67	0.69	0.72	0.71	0.71	0.71	0.69	0.68	0.68	3
Co	0.1	0.1	0.1	0.1	0.1	0.1	0.2	0.1	0.1	0.2	30
Zn	45	42	44	46	45	43	44	45	42	44	4
Sb	1.0	0.8	1.0	1.0	0.8	0.9	0.9	0.8	0.9	1.0	15
Cs	6.2	5.8	6.0	6.3	6.1	6.2	6.0	6.1	5.9	6.3	3
La	17	18	18	19	17	19	19	18	19	19	6
Ce	37	36	37	38	36	38	39	37	37	37	5
Nd	23	18	26	27	20	24	23	23	20	20	11
Sm	4.9‖	4.8‖	4.9‖	5.0‖	5.0‖	5.0‖	5.0‖	5.0‖	5.2	5.7	8
Eu	0.08	0.07	0.06	0.08	0.07	0.07	0.08	0.08	0.07	0.07	17
Tb	1.20	1.05	1.10	1.11	1.11	1.12	1.13	1.21	1.08	1.15	4
Tm	0.76	0.78	0.83	0.82	0.86	0.86	0.60	0.90	0.71	0.86	13
Yb	5.5	5.4	5.4	5.7	5.2	5.3	5.3	5.4	5.4	5.7	5
Lu	0.75	0.73	0.80	0.77	0.73	0.75	0.73	0.74	0.71	0.76	3
Hf	4.9	4.7	4.8	5.1	5.0	5.1	4.8	4.9	4.7	4.9	3
Ta	5.48	5.45	5.48	5.81	5.83	5.76	5.51	5.84	5.21	5.79	5
Th	29.0	28.2	28.6	29.9	29.8	29.8	28.7	29.4	27.8	30.1	4
U	12.8	13.1	13.1	13.6	14.4	14.3	14.0	13.6	9.7	11.3	12
						Crystal Content					
Phenocrysts, wt %	1	0.001	0.001	0.001	0.01	0.01			0.001	1	

See footnotes to Table 1*a* for notes.

hibit variable behavior between silicic systems, apparently depending largely on the relative abundances of H_2O, F, and Cl (see summary by *Hildreth* [this issue]). By analogy with chemical stratigraphy reconstructed for the Long Valley magma chamber, elements of group 1 are termed 'upward-concentrating' and those of group 2 'downward-concentrating' in the Coso silicic magmatic system.

The REE show a particularly diagnostic pattern that appears to be typical of high-silica metaluminous rhyolites and some aplites [*Hon and Noyes*, 1977] and high-level silicic plutons [*Taylor et al.*, 1968; *Dodge*, 1979; *Ludington et al.*, 1979; *Miller and Mittlefehldt*, 1979]. Chondrite-normalized REE patterns (Figure 5) are relatively flat; rocks rich in HREE are relatively depleted in REE lighter than Sm. Negative Eu anomalies are very large and Eu abundances are commonly less than chondritic. Figure 5 shows, for rhyolites of several different ages, the same qualitative type of REE variation displayed by the range of compositions of the zoned Bishop Tuff [*Hildreth*,

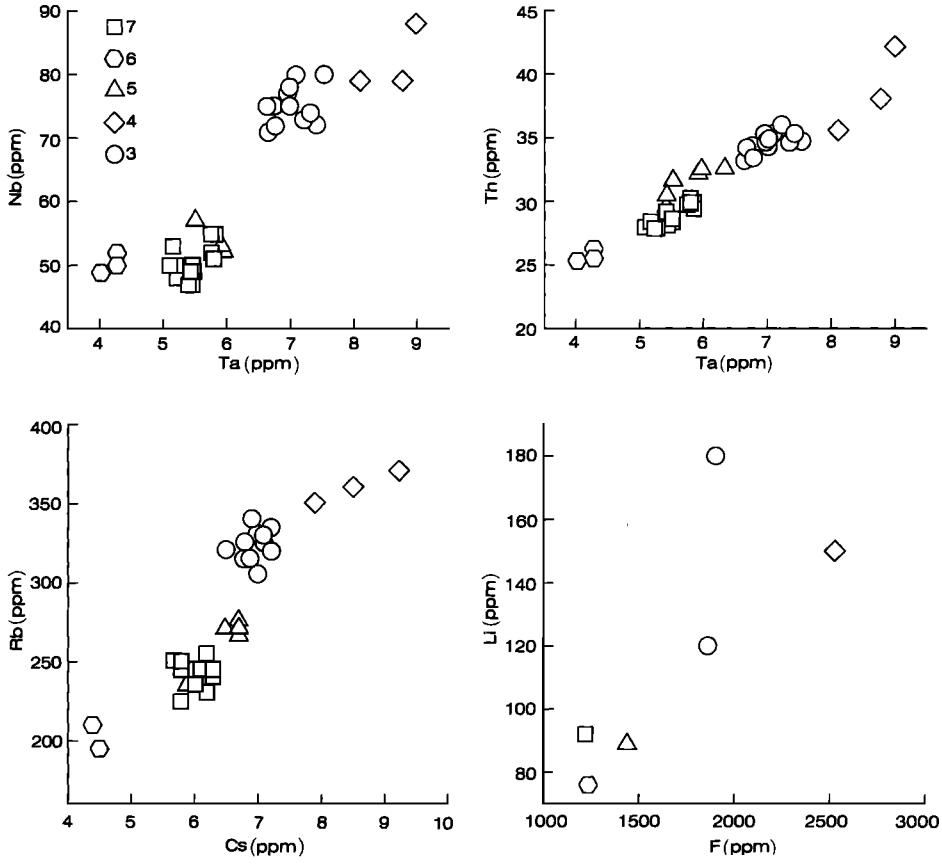

Fig. 2. Correlation of abundances in rhyolites (excluding samples 28 and 38) of some elements concentrated upward in highly differentiated metaluminous silicic magmatic systems. The highest value for Li (180 ppm) has been reproduced but probably is not representative of magmatic Li content; this sample consists of glass from spherulitic obsidian. Symbols correspond to eruptive groups 3 through 7 discussed in section on groups of chemically similar coeval domes.

1979, Figure 13], all of which existed within the Long Valley magma chamber at the same time. *Hildreth* [1979, this issue] has shown that REE variation in the Bishop Tuff cannot be explained by conventional petrogenetic models and was most probably generated by liquid state differentiation processes.

Groups of Chemically Similar Coeval Domes

It is possible to divide the 38 rhyolite extrusions into at least 7 groups on the basis of trace element composition. Within each group the variation of all analytical data is generally within the estimated precision, whereas between groups the difference in abundance of several elements is much greater than that attributable to analytical error. Surface morphology of domes and flows, field relations, and K-Ar and obsidian hydration rind dating [*Duffield et al.*, 1980] suggest that each chemical group of rhyolites consists of virtually coeval extrusions that were emplaced during periods that were very short relative to the overall life span of the rhyolite field.

In order to quantify the chemical grouping, data for 25 elements in the 38 samples were subjected to cluster analysis using methods previously applied to correlation of volcanic ash deposits [*Sarna-Wojcicki*, 1976; *Smith and Nash*, 1976]. A similarity matrix was computed between the samples and the two samples with the highest similarity were combined into a pair group. The similarity matrix was then recomputed with the pair group treated as a single sample; pair and larger groups in subsequent iterations were weighted according to the number of original analyzed samples they contained. The degree of similarity between samples is expressed as the distance function, plotted on a log scale in the dendrogram in Figure 6. Most samples are clearly grouped; samples 3, 5, and 32 are shown as group 4, but the variation of a few elements among them is significant. Group 4 was not further divided because age data exist for only one of the three domes (dome 5) and because significant intragroup differences are limited to a few elements (Sc, Zn, Nb, Cs, Ta, Th, U). Figure 6 indicates that compositional differences between groups 1 and 2 and between them and the rest of the rhyolites are relatively large.

Two observations can be made on the basis of the chemical data, as illustrated by cluster analysis, that are fundamental to interpretation of the Coso silicic system. First, samples from the same group are chemically indistinguishable regardless of phenocryst content, which ranges from ~2% (except dome 28 with 15%) to ~0.001% (Table 1). Second, even the most geographically widespread groups of domes, which in the extreme case of the youngest group spans the entire ~18 km long dimension of the rhyolite field, are homogeneous within the precision of the data (with the possible exception of group 4). Furthermore, an obsidian (26) and two hydrated pumiceous glass samples (26B, 26C) from widely spaced localities on Sugarloaf Mountain are indistinguishable in trace element content as determined by INAA and show that this relatively voluminous flow is compositionally homogeneous. We shall argue on the basis of the compositions of the rhyolites and longevity of volcanic activity that the magma reservoir(s) that

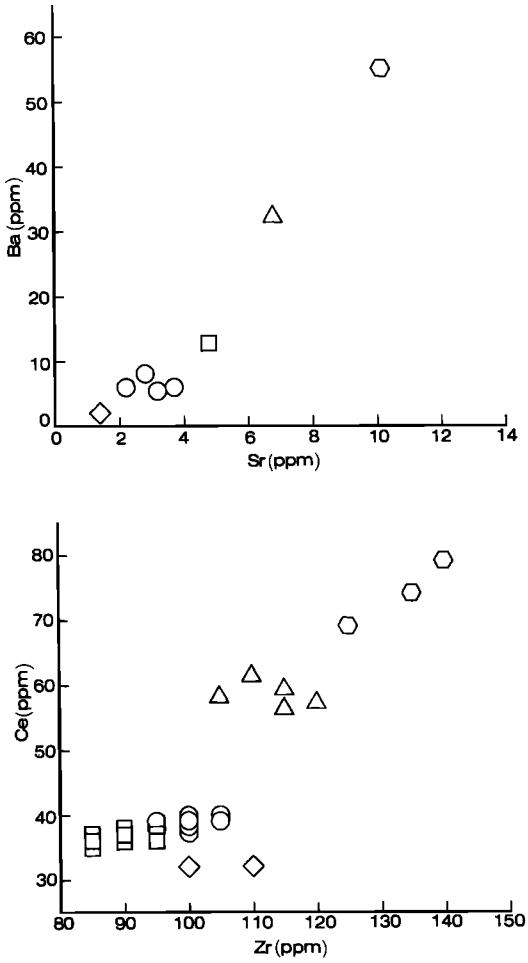

Fig. 3. Correlation of abundances in rhyolites of some elements concentrated downward in highly differentiated metaluminous silicic magmatic systems. Symbols as in Figure 1.

fed each group of domes was compositionally zoned. The erupted rhyolites represent samples of magma withdrawn at different times from the differentiated top of such a reservoir. In order to preserve the uniformity of composition within each group, the magmatic system must have been of substantial size, despite the comparatively small erupted volume of rhyolite.

Ages of Lava Domes and Flows

Accurate dating of eruptive episodes is essential to interpretation of the chemical data. The Pleistocene rhyolites of the Coso Range are well suited for K-Ar dating, because many domes contain recoverable sanidine and obsidian is exposed on several domes and flows. A few K-Ar obsidian ages are inconsistent with field relations, obsidian hydration rind measurements [*Friedman and Obradovich*, 1981], and the chemical data of Table 1, possibly owing to excess ^{40}Ar [*Duffield et al.*, 1980]. Weighted mean K-Ar ages calculated from the data of *Lanphere et al.* [1975], *Duffield et al.* [1980], and G. B. Dalrymple and C. R. Bacon (unpublished data, 1980) provide control for six of the seven groups of domes (Table 2); individual determinations are weighted by the inverse of the variance and the uncertainty is taken to be the square root of the sum of the variances, divided by the number of ages.

A single group (5) composed of four domes and an extensive lava flow could not be dated by K-Ar with acceptable precision. On the basis of relative degree of erosion of the group 4 and 5 domes, those of group 4 are thought to be somewhat older, as the K-Ar data suggest. We have tentatively assigned an age of 0.16 ± 0.03 m.y. to group 5 on the basis of maximum obsidian hydration rind thicknesses from lava flow 20 and dome 5 (group 4) [*Friedman and Obradovich*, 1981, Table 3] and because group 5 appears to be closer in age to group 4 than to group 6. We have no further control on the age of group 5 other than stratigraphic relations, which indicate that it is older than group 7 and younger than group 3 (Figure 7). Results of K-Ar dating of group 5 obsidians are inconclusive [*Lanphere et al.*, 1975; C. R. Bacon and G. B. Dalrymple, unpublished data, 1980], but suggest that the estimated 0.16 m.y. is probably a maximum age.

The three domes of group 4 may not be coeval. Chemical similarity between them is not as pronounced as within other groups of rhyolites. Because the dated dome (5) is far more voluminous than the other two, relations between erupted volume and time, discussed in a later section, are not seriously affected by the inference that all three domes are effectively the same age.

The age and chemical grouping of rhyolites has been used to reconstruct the sequential growth of the rhyolite field shown in Figure 7. Each episode of rhyolitic volcanism has either or both of (1) an associated episode of basaltic volcanism external to the area of rhyolite eruption within at most a few tens of thousands of years and/or (2) spheroidal, vesicular mafic inclusions. Only in the 0.587-m.y.-old dome (group 2) have inclusions been found in the central area of the rhyolite field. They are also known to be present in the northwestern and southern clusters of group 3 domes and are rare in the group 6 flows. The inclusions are believed to represent blobs of mafic magma that were incorporated into the high-silica rhyolite prior to eruption and quenched owing to the lower temper-

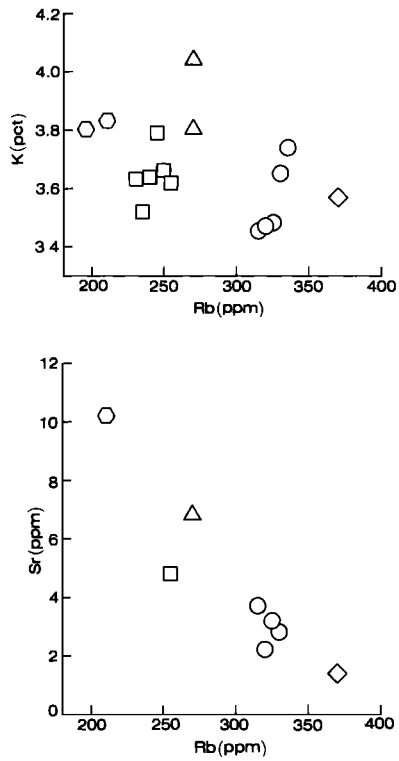

Fig. 4. K versus Rb and Rb versus Sr for obsidians. Symbols as in Figure 1.

ature of the host [*Metz and Bacon*, 1980]. Both rhyolitic and basaltic magmas were present throughout the development of the rhyolite field. Basaltic magma was apparently unable to reach the surface in the central part of the field in at least the last ~0.24 m.y. because of the presence of relatively low density silicic magma within the crust.

Distribution of Vents

Bacon et al. [1980] have presented a model for emplacement of the Pleistocene rhyolites of the Coso Range on the basis of *Nakamura*'s [1977] analysis of the relations between preferred orientation of dikes and the horizontal components of the regional stress field. Because all groups of rhyolite domes and flows, except the oldest dome, vented either near the center of the field or virtually throughout its length in crudely linear arrays, *Bacon et al.* [1980] suggested that the magma reservoir(s) may have underlain the central part of the field, with outlying domes fed by dikes. Dikes may have initially emanated in a radial pattern from a centrally located reservoir where local stresses related to the reservoir may have dominated. However, once beyond the influence of the reservoir-related stress field, dikes would be expected to propagate parallel to the azimuth of maximum horizontal compressive stress (perpendicular to the minimum compressive stress axis). Mapping of faults [*Duffield and Bacon*, 1980; *Roquemore*, 1980] and earthquake focal mechanisms [*Walter and Weaver*, 1980] suggest that the late Cenozoic and present regional stress fields are very similar and that the maximum horizontal compressive stress axis is oriented north-northeast and minimum horizontal compressive stress axis west-northwest.

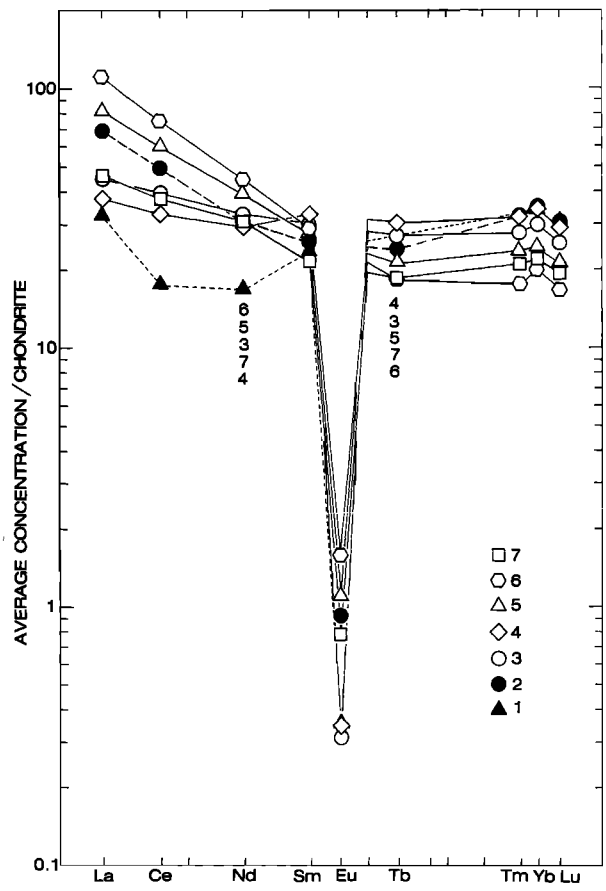

Fig. 5. Average REE abundances for groups of rhyolites normalized to values for the Leedy chondrite [*Masuda et al.*, 1973]. Symbols as in Figure 1.

Thus coeval rhyolite domes—or basalt vents—would be expected to define roughly north-northeast arrays, as commonly observed (Figure 7). The west-northwest alignments of vents both similar (e.g. 17 and 18) and different in age (e.g. 17, 18, and 19; 4, 5, and 38; general area of concentration of basalt vents), both rhyolite and basalt, probably reflect the importance of preexisting fractures in shallow crustal rocks to vent location; this is the dominant trend of old structures in the granitic and metamorphic basement rocks. Other alignments of domes, particularly coeval domes of very small volume (e.g. 29, 30, and 31), must indicate the intersection of dikes at shallow depth with either old fractures or late Cenozoic conjugate northwest-trending right lateral or east-northeast-trending left lateral strike-slip faults. This model is consistent with the ages of rhyolite domes and with geophysical studies [*Plouff and Isherwood*, 1980; *Reasenberg et al.*, 1980; *Walter and Weaver*, 1980; *Young and Ward*, 1980] which have not detected a silicic magma body of substantial area at depths less than ~8 km, but which do not rule out the presence of a body of magma up to ~10 km in diameter at this or greater depth.

Temporal Variation in Composition

The age and chemical information suggest that all but two domes are no older than ~0.24 m.y. The small volume of the two oldest domes and lengthy intervals between their emplacement and the start of the more voluminous rhyolitic volcanism argue for at least three separate periods of magmatic evolution. The comparatively short intervals between eruptions of the younger groups of domes and flows, however, and their nearly aphyric nature suggests that they constitute leaks from the top of a single evolving system.

Average compositions of the rhyolites of groups 3 through 7 are given in Table 3. These average abundances and data for the two older domes for selected elements are plotted against age in Figure 8. Each plot contrasts an upward-concentrating element with a downward-concentrating element. Many more plots could be shown, but the general patterns would be similar. The relative sense of variation between the younger rhyolites, groups 3 through 7, shown schematically in Figure 9, is remarkably consistent.

For all but the youngest (7) of the five groups, the patterns shown in Figure 9 are mirror images. Upward-concentrating elements have abundances in the order group 4 > 3 > 5 > 6. The only exceptions appear to be Sc, Sm, and probably, Zn and Hf, which in group 6 are intermediate in concentration between those of groups 3 and 5. All of the downward-concentrating elements occur in the reverse order of abundance: group 4 < 3 < 5 < 6. Though variation with time is not regular, the sense and relative magnitude of change are consistent, within analytical precision, for virtually all elements for which data exist.

The rhyolites of group 7 are very similar to those of the other groups, but the systematics of elemental abundances, as depicted in Figure 9, suggest some significant differences. Downward-concentrating elements are depleted to levels between those of groups 4 and 5, whereas upward-concentrating elements show relatively less change and are enriched only to levels between those of groups 5 and 6. Furthermore, the upward-concentrating elements U and, especially, Mn are greatly enriched, while the downward-concentrating elements La, Ce, Nd, and, particularly, Zr are depleted more than other

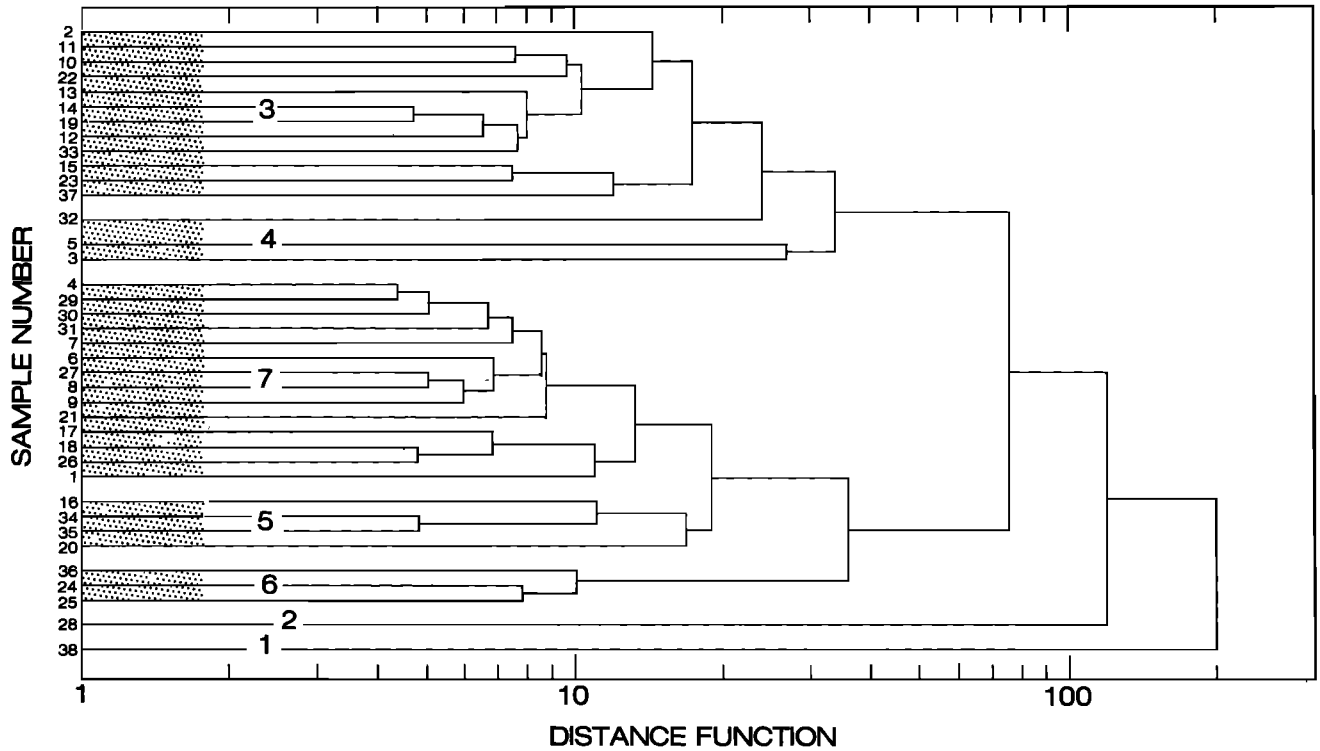

Fig. 6. Dendrogram linking statistically similar analyses on the basis of the distance function calculated from data for 25 elements using cluster analysis. Degree of difference between samples is proportional to horizontal distance from left margin to connecting vertical line (note log scale). Patterned areas indicate groups (numbered). Samples 3, 5, and 32 shown as group 4 partly on the basis of subjective evaluation of age and chemical data. Sample numbers at left.

such elements. Enrichment in U and depletion in LREE in group 7 rhyolites relative to groups 3 through 6 are shown clearly by plots of U versus Th and Ce versus Yb in Figure 10. In both plots groups 3 through 6 are linearly related; group 7 lies off the trend. By analogy with other silicic systems, in which concentration of certain elements can be correlated with F, Cl, or inferred H_2O abundances [e.g., *Hildreth,* this issue], the change in degree of enrichment of upward-concentrating and depletion in downward-concentrating elements shown by the group 7 rhyolites may reflect increased influence of H_2O, relative to halogens, in the liquid state differentiation process (discussed in a later section). Sc, Zn, Sm, and Hf, which are enriched to a greater degree in group 6 than other upward-concentrating elements, commonly show variable behavior from one silicic system to another [*Hildreth,* this issue]. Subtle changes in proportions of volatile components may also have been responsible for the aberrant enrichment of these elements in the group 6 rhyolites.

Many pairs of upward- and downward-concentrating elements in the group 1 and 2 domes do not fit the mirror image pattern of relative enrichment and depletion shown by the younger rhyolites (Figure 8). In general the older dome appears to be the more evolved. Neither dome falls on the linear trends of Figure 10, nor do they differ from one another in a consistent sense. Moreover, the two oldest domes do not fit extensions of the nearly linear covariance of Nb with Ta and Th with Ta (Figure 2 and Table 1) shown by all other Coso rhyolites. This may reflect differences in source. The oldest dome lies farthest from the trend, perhaps because it is geographically separated from the probable site of magma reservoirs for the other domes [*Bacon et al.*, 1980]. The second oldest dome was emplaced near what was to become the center of the rhyolite field, but is roughly 0.35 m.y. older than the group 3 rhyolites. The above-cited differences in composition (see also Figure 6) and comparatively great differences in age of the two oldest domes, both relative to each other and to the rest of the rhyolites, suggest that these domes represent magmatic systems, or thermal events independent of the system that evolved later. This conclusion is supported by Pb isotopic data, which are consistent with Pb being from slightly different sources for each of the oldest domes but a uniform source for all of the others (C. R. Bacon, H. Kurasawa, and M. H. Delevaux, unpublished data, 1980). Independent thermal events are also implied for the two oldest domes by the timing

TABLE 2. Volumes and Weighted Mean Ages of Groups of Rhyolite Domes and Lava Flows

	Group						
	1	2	3	4	5	6	7
Volume, km^3	0.01 ± 0.005	0.04 ± 0.02	0.27 ± 0.03	0.12 ± 0.01	0.305 ± 0.060	0.17 ± 0.03	0.66 ± 0.07
Age, m.y.	1.04[1] ± 0.02	0.587[1] ± 0.018	0.235[2] ± 0.025	0.170[2] ± 0.011	0.16[3] ± 0.03	0.089[2] ± 0.010	0.063[2] ± 0.009

[1] K-Ar sanidine age reported by *Duffield et al.* [1980].
[2] Weighted mean of K-Ar ages reported by *Duffield et al.* [1980] and G. B. Dalrymple and C. R. Bacon (unpublished data, 1980).
[3] Obsidian hydration age calculated from hydration rind thickness measurements [*Friedman and Obradovich,* 1981] and K-Ar age of group 4.

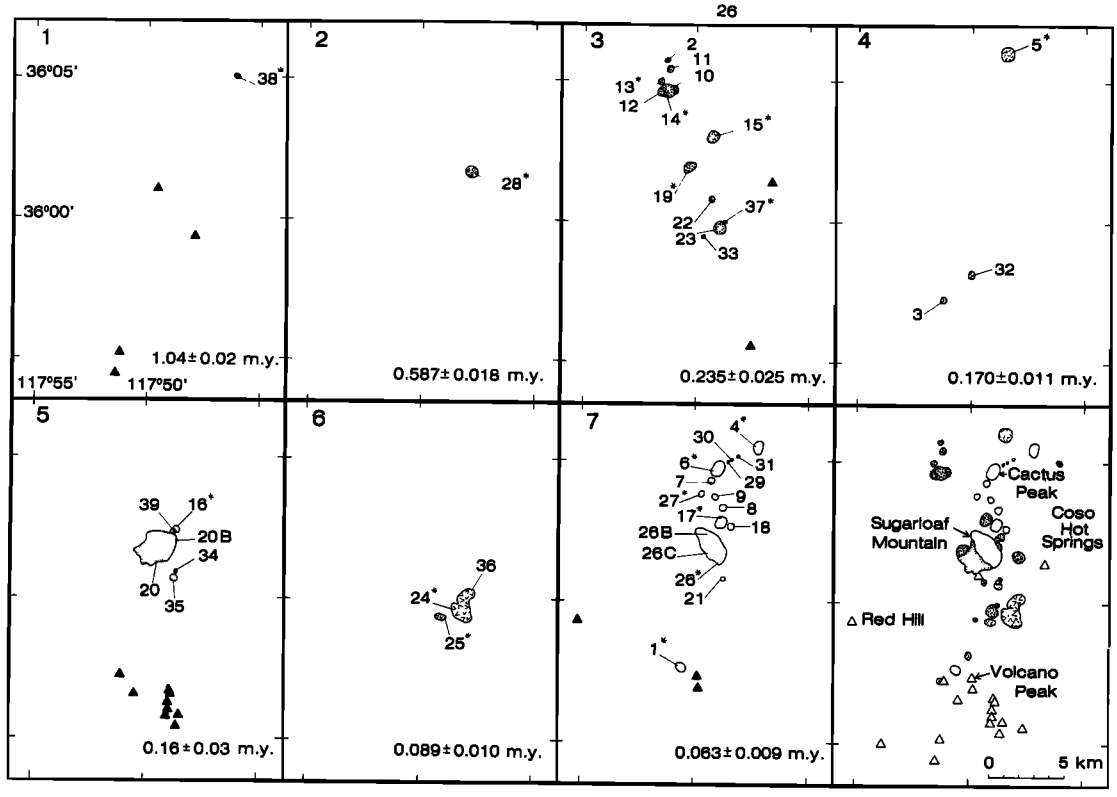

Fig. 7. Maps of rhyolite domes (some reconstructed) and lava flows and basalt vents of the Pleistocene part of the Coso volcanic field [modified after *Duffield and Bacon*, 1980]. Maps 1–7 show coeval groups of rhyolite extrusions with sample localities and approximately coeval basaltic vents (triangles). Map at lower right is a composite of 1–7.

of corresponding basaltic volcanism, discussed in a later section.

Mineralogy

We believe that one of the most significant observations that can be made concerning the Pleistocene rhyolites of the Coso Range is that they contain very few phenocrysts, a common but by no means universal feature of high-silica rhyolites. Crystal contents range from at most 2% to probably less than 0.001%, except for the 0.587-m.y.-old dome (group 2), which contains about 15% crystals. Phenocrysts of salic minerals are typically about 1 mm in size; mafic phenocrysts other than hornblende are generally much smaller and might more accurately be termed microphenocrysts. Large samples of all rhyolites were crushed and crystals concentrated for study by electron microprobe. The detailed results of this work will be the subject of another report.

All of the rhyolites possess a common assemblage of phenocrysts of quartz, sodic oligoclase, sanidine, biotite, hornblende, and titanomagnetite. The abundances of each of these phases in all but the 0.587-m.y.-old dome range from about 0.5% to zero among the individual members of any group of domes, but at least one of each group contains all phases in substantial quantity. In any group of rhyolites the feldspar and magnetite phenocrysts in visibly porphyritic samples, all of which come from domes rather than flows, generally do not vary in composition. A few crystals of similar composition can commonly be found in the nearly aphyric samples.

Zircon and apatite microphenocrysts are ubiquitous in the rhyolites of groups 3–6, mostly as minute inclusions in mafic phases. Ilmenite is present in all but group 4, commonly as inclusions in mafic silicates. Allanite phenocrysts occur in some samples from groups 3, 6, and 7; these show evidence of resorption in the group 6 flows. Fayalitic olivine is present as euhedral phenocrysts in group 5 rocks, and as resorbed (?) phenocrysts in groups 2, 6, and 7. Euhedral Fe-rich orthopyroxene occurs in groups 3, 6, and 7, with resorbed (?) examples in groups 2 and 5. Fe-rich clinopyroxene is euhedral in groups 3, 6, and 7, and resorbed (?) in 2, 4, and 5. Tiny blebs of pyrrhotite occur as inclusions in mafic phenocrysts and as very rare droplets in glass of groups 3, 5, 6, and 7.

In most samples the compositions of the mafic silicates and ilmenite inclusions vary significantly, but are appropriate for crystals precipitated from highly differentiated rhyolitic magmas. A second population of resorbed mafic minerals, including very rare Cr-rich spinel, and some plagioclase and olivine of basaltic origin can be found in almost all samples. These xenocrysts are most obvious in the nearly aphyric rocks, but whether this is because of their relative or absolute abundance is not known. Rare feldspar xenocrysts probably derived from granitic rocks are present in a few samples.

Except for the feldspars in the relatively crystal-rich domes, intergrown coexisting mafic minerals, and some pairs of Fe-Ti oxides, equilibration of homogeneous populations of phenocrysts cannot be demonstrated for the rhyolites. The phenocrysts apparently record some aspects of the thermal and compositional histories of the magmas that have disturbed any preexisting equilibrium assemblages, including contact with basaltic magma, with accompanying superheating of the rhyolitic magma and dissolution of phenocrysts.

Another petrogenetic constraint provided by phenocryst

TABLE 3. Average Compositions of Groups of Rhyolite Domes and Lava Flows

	Group				
	3	4	5	6	7
	Percentages				
SiO_2*	76.9	77.0	77.0	76.9	77.2
Al_2O_3*	12.59	12.60	12.41	12.56	12.51
Fe	0.74	0.69	0.78	0.85	0.69
MgO†	0.01	<0.01	0.02	0.02	0.02
CaO†	0.37	0.32	0.44	0.42	0.38
Na_2O†	4.48	4.58	4.32	4.33	4.39
K_2O†	4.28	4.30	4.58	4.60	4.39
TiO_2	0.06	0.05	0.08	0.08	0.06
MnO†	0.019	0.020	0.018	0.017	0.020
F†	0.184	0.252	0.129	0.121	0.127
	Parts per Million				
Li†	120	150	89	76	92
Be	11	12.5	8.9	6.5	7.9
Sc	0.98	1.11	0.78	0.86	0.51
Co	0.1	0.1	0.2	0.2	0.1
Zn	57	57	45	46	44
Rb	323	360	270	205	243
Sr†	2.9	1.4	6.8	9.0	4.7
Y	73	81	62	49	58
Zr†	102	100	113	138	92
Nb	75	82	54	50	50
Sn†	11	13	9.6	6.7	8.3
Sb	1.0	1.2	1.0	0.7	0.9
Cs	7.0	8.5	6.6	4.4	6.0
Ba†	6.5	<2	32	48	13
La	17	14	31	42	18
Ce	39	32	58	73	37
Nd	24	21	28	32	22
Sm	6.9	7.5	6.3	6.6	4.9
Eu	0.02	<0.03	0.10	0.14	0.07
Tb	1.59	1.79	1.24	1.08	1.10
Tm	1.06	1.22	0.91	0.68	0.81
Yb	7.4	8.5	6.1	5.0	5.5
Lu	0.98	1.12	0.81	0.64	0.75
Hf	5.9	6.4	5.3	5.3	5.1
Ta	7.0	8.6	5.9	4.2	5.5
Pb	34	35	29	25	30
Th	34.6	38.6	32.2	25.7	28.8
U	12.5	14.7	11.5	8.0	12.6

*Analyses normalized to total 100% anhydrous.
† Average of obsidian data only.

mineralogy is that of H_2O fugacity and concentration. The rhyolitic magmas were precipitating biotite and hornblende prior to eruption. Though difficult to quantify, the fugacity of H_2O must have been relatively high in the high-silica part of the magma reservoir in order to stabilize biotite and hornblende, which themselves are not particularly halogen rich (C. R. Bacon, unpublished data, 1980). Despite this observation the Coso rhyolite magma was erupted mainly as domes and flows, preceded by relatively low volumes of pyroclastic material, a situation that contrasts with voluminous, caldera-forming pyroclastic eruptions, whose products commonly also contain hydrous ferromagnesian silicates. The Coso rhyolite magma apparently ascended relatively slowly or from rather great depths so that H_2O was lost from the magma in the subsurface. This concept of relatively great depth to the top of the magma reservoir(s) is in harmony with the results of the previously mentioned geophysical studies.

Pre-eruption magmatic temperatures were probably within 50° of 780°C on the basis of Fe-Ti oxide and coexisting feldspar geothermometry (C. R. Bacon, unpublished data, 1980) and by comparison with ash flow tuffs that apparently underwent little or no thermal disturbance immediately prior to their eruption [*Hildreth*, 1979]. Low crystal contents and pre-eruption temperatures coupled with highly differentiated compositions imply substantial magmatic H_2O contents. The presence of quartz and both feldspars as phenocrysts in most samples and their apparent existence prior to heating events in others suggest that the rhyolite magmas were in a condition of low thermodynamic variance, despite the wide range in minor and trace element abundances. A possible controlling factor might be a buffering of magmatic temperature and to some extent, major element composition, by interaction with and partial melting of country rocks, the absolute temperature depending on the availability and thus fugacity of H_2O and probably F and Cl.

DISCUSSION

Petrogenetic Processes

The petrogenesis of the Pleistocene rhyolites of the Coso Range cannot be modeled by any simple conventional scheme. The differentiation processes that produced the observed major element compositions and extreme enrichments and depletions in many trace elements are evidently the same as those that brought about the vertical compositional zonations in the magma chambers of the Bandelier Tuff [*Smith and Bailey*, 1966; *Smith*, 1979], Bishop Tuff [*Hildreth*, 1979, this issue], and many other voluminous silicic pyroclastic fall and flow deposits [*Hildreth*, this issue]. The most extensive published data exist for the Bishop Tuff, and *Hildreth*'s [1979] comprehensive study provides the basis for interpretation of the differentiation of the Coso silicic magma.

Hildreth [1979; this issue, Figure 7] used a plot of enrichment factors against atomic number to portray the sense and degree of compositional zonation in the erupted part of the magma chamber of the Bishop Tuff. In the Biship Tuff and other dominantly pyroclastic eruptive sequences of very brief duration, such as a single ash flow cooling unit, enrichment factors are defined by the concentration of an element in the earliest erupted pumice divided by that element's concentration in the last material ejected, presumed to be from the deepest level tapped by the eruption. Enrichment factors thus defined obviously depend upon the level to which magma was withdrawn from the reservoir. No compositional zonation has been detected within the individual groups of rhyolites of the Coso Range, each of which is thought to represent the most differentiated eruptable magma at the time of its emplacement. Thus we compare eruptive groups of different ages in order to document the sense of elemental concentration. Groups 4 and 5 appear to be closely spaced in time, the more evolved rhyolites (4) being slightly older. Enrichment factors have been calculated by dividing concentrations in the most evolved rhyolite of group 4 (rhyolite 5) by average concentrations in group 5. It is possible, but cannot be proven, that group 5 magma was present at a lower level in the reservoir at the time of emplacement of group 4, but this is not essential to the argument for differentiation by liquid state processes. Similar patterns, but of course different enrichment factors, are obtained regardless of which of groups 3, 4, 5, and 7 is normalized to a less differentiated group (recall that group 6 is the least differentiated; see Figures 5, 8, and 9).

The Coso enrichment factors are compared with those for the Bishop Tuff [*Hildreth*, this issue, Figure 7] in Figure 11. The sense of all enrichments and depletions (with the exceptions

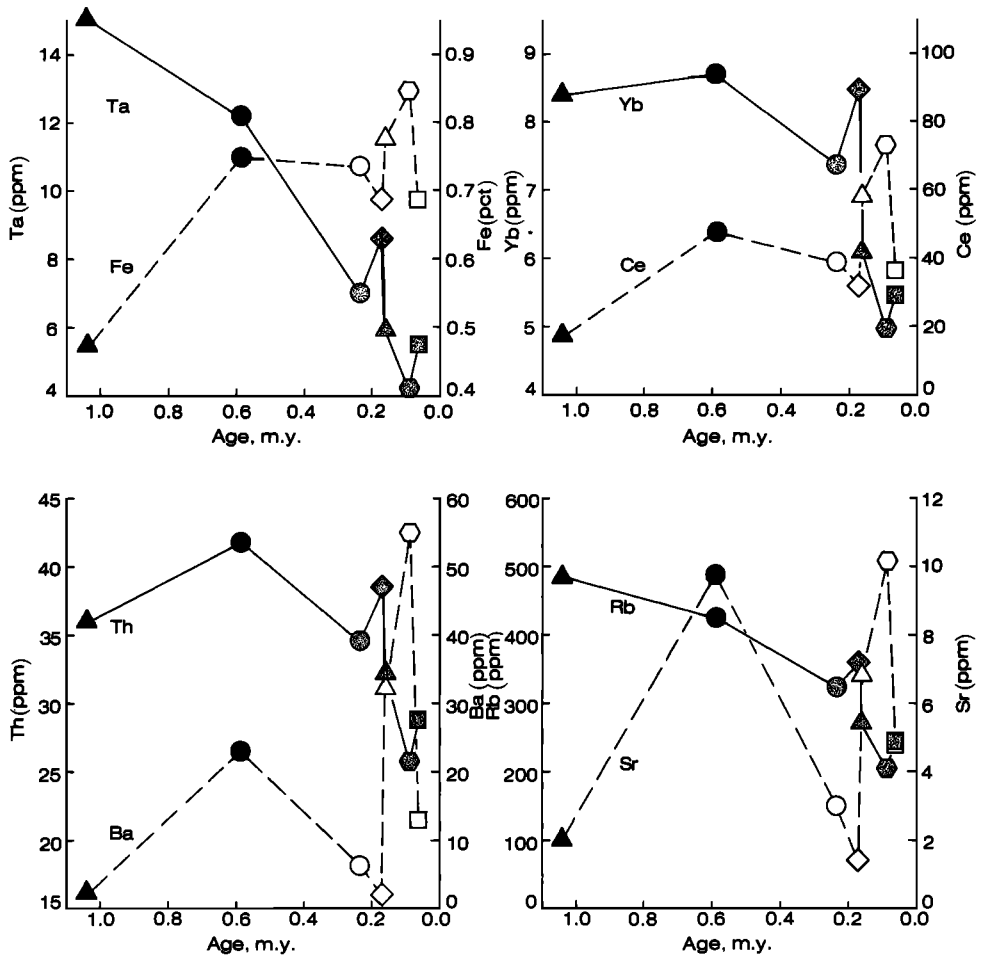

Fig. 8. Average compositions of all groups of rhyolites versus age. Concentrations of elements that are concentrated upward in metaluminous silicic magma chambers connected with solid lines, with reference to left-hand scales; downward-concentrated elements connected with dashed lines, with reference to right-hand scales. Symbols as in Figure 1.

of Zn and Hf, whose abundances do not vary detectably in the Bishop Tuff) and the relative magnitudes of many are virtually identical for all elements for which high-precision data exist for both systems. The absolute magnitudes are not strictly comparable because the Coso enrichment factors employ only ~77% SiO_2 rhyolites whereas the last-erupted Bishop Tuff pumice contained 75.5% SiO_2 and was much less differentiated than any of the rhyolites of the Coso Range. Recall that the least evolved Coso rhyolite is roughly comparable in composition to the most evolved pumice of the Bishop Tuff.

It may be inferred from Figure 11 that the same processes that created the compositional zonation near the top of the magma chamber of the Bishop Tuff were responsible for the differentiation of the rhyolites of the Coso Range. *Hildreth* [1979, this issue] has shown that no plausible scheme involving crystal settling, assimilation, basaltic contamination, liquid immiscibility, or progressive partial melting can create the extreme elemental enrichments and depletions and the type of compositional variation observed within the Bishop Tuff. Similar calculations indicate that differentiation of the Coso rhyolites, too, cannot be explained by any of these processes; some other process dominates chemical differentiation in at least the upper reaches of very silicic magmatic systems. *Shaw et al.* [1976], *Hildreth* [1979, this issue], and *Smith* [1979] proposed a possible process which they called 'convection-driven thermogravitational diffusion' and set forth the following general model (discussed at length by *Hildreth* [this issue]). Intrusion of basaltic magma into the crust leads to and maintains partial melting of crustal rocks, creating a body of silicic magma. Crystal-liquid equilibrium processes may be effective agents of differentiation within this part of the system if the magma's silica content is less than ~74%. This silicic magma is likely to convect in a system of substantial dimensions, driven by continued addition of heat from below by intrusion of basalt [*Smith and Shaw*, 1975]. Because gradients in temperature and, probably, volatile content are present near the interface between magma and wall and roof rocks, a gravitationally stable zone of volatile-rich magma forms at the top of the system; the upward decrease in temperature due to conductive or hydrothermal convective cooling of the roof is offset by an upward increase in H_2O and other volatile constituents. The liquidus temperature is lowered owing to the high volatile content, and the magma chamber tends to show a decrease in phenocrysts upward toward its roof. *Hildreth* [this issue] has suggested that in some systems compositional contrasts may be extreme and a convecting zone of intermediate magma, separating mafic magma below from highly silicic magma near the roof, may be absent or very thin. It is in the roof region of the magma reservoir that the great enrichments and depletions in minor elements develop, apparently in response to the combined effects of the thermal gradient and of H_2O, F, and Cl

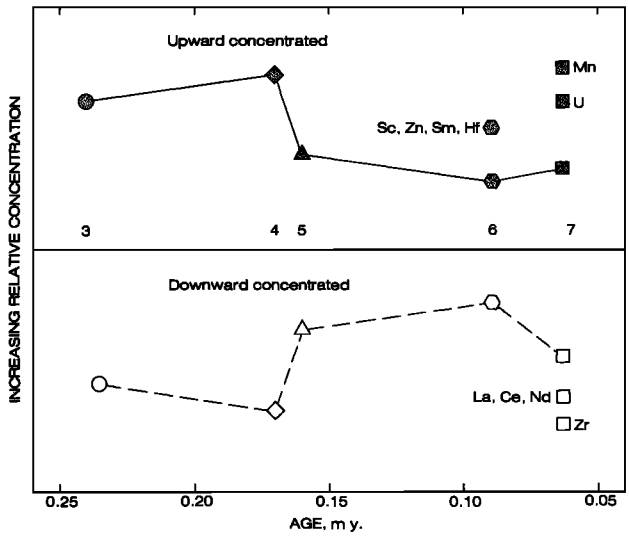

Fig. 9. Generalized relative behavior of average compositions of rhyolites of groups 3–7. The solid lines connect points representing relative abundances of upward-concentrated elements; the dashed lines connect downward-concentrated elements. Exceptions to relative order of abundance are indicated by points off of the trend and are identified with element symbols. Symbols as in Figure 1.

concentration on the availability of suitable sites, formation of ionic complexes, and degree of polymerization of the melt. Material is probably supplied to the gravitationally stable zone by upward convection of a volatile-rich boundary layer, as described by *Shaw* [1974*a*,*b*], which may 'peel off' at the level of gravitational stability according to its density. The stable zone of vertical compositional gradients may in fact be a stack of convection cells of very large aspect ratio, that is, of great areal relative to vertical dimensions. Effective diffusion distances might thus be greatly decreased, and diffusion rates increased relative to those of ions in static, anhydrous silicic magma.

At any rate, though the process of differentiation of very silicic magmas is still poorly understood, the gradients in temperature and composition have been well documented. The Pleistocene rhyolites of the Coso Range are all examples of magmas leaked from the top of such a system. Evidence for the basaltic heat source is present in the form of the roughly coeval basaltic volcanism, which was peripheral to the rhyolite field at any given time, and the mafic inclusions. The occurrence of mafic inclusions in some rhyolites away from the central part of the field suggests that a significant volume of intermediate magma may not have been present in the Coso system.

The ultimate source of the silicic magma cannot be elucidated by chemical and mineralogic studies alone because of the masking of earlier history by differentiation processes. By comparison with data for Sierran batholithic rocks [*Doe and Delevaux*, 1973; *Chen*, 1977] the isotopic composition of Pb suggests a mid- to upper crustal source for Pb in the rhyolites ($^{206}Pb/^{204}Pb$ = 19.29), clearly distinct from the source of the basalts ($^{206}Pb/^{204}Pb$ = 19.15); Pb in the mafic inclusions in the rhyolites appears to be a mixture of Pb from these two reservoirs (C. R. Bacon et al., unpublished data, 1980). Because of the Pb-enriched composition of high-silica magmas, it is unlikely that the mid- to upper crustal component of the Pb comes from roof rocks alone. On the other hand, Sr is so depleted in the Coso rhyolites that even minor contamination by roof rocks, which are likely to be rich in Sr, would greatly affect its isotopic composition. Available Sr data for the rhyolites (initial $^{87}Sr/^{86}Sr$ = 0.7055) suggest midcrustal initial values that are somewhat less radiogenic than present-day upper crustal Sr [*Kistler and Peterman*, 1978] and substantially more radiogenic than the initial $^{87}Sr/^{86}Sr$ ratio (0.7044) of relatively primitive basalt erupted 1.08 ± 0.06 m.y. ago near the center of what was to become the rhyolite field (C. R. Bacon and R. W. Kistler, unpublished data, 1979).

Volume-Time Relations

The Coso rhyolite field provides an excellent opportunity to examine erupted volume as a function of time because of the youth of the domes, the systematics of trace element variation, and the precision of K-Ar dating of sanidine and obsidian in the ~0.05 to 1 m.y. interval. Furthermore, because the major element composition and mode of emplacement are similar for all the rhyolites, it is reasonable to assume that the calculated volume of material emplaced as domes and lava flows will be proportional to the total volume of eruption, including tephra, with approximately the same proportionality constant for each group of rhyolite extrusions. We use the volume of domes and flows in the following discussion because it can be determined with precision and therefore relative volumes of groups of rhyolites can be compared with some confidence; the volume of tephra is comparatively minor and has been partly accounted for by internal void space between near-surface blocks that is included in calculated volumes of domes and flows. Volume data are presented in Table 2 in the form of the sum of volumes of reconstructed domes and flows calculated from the geologic map of *Duffield and Bacon* [1981] for each group of rhyolites.

The variation of erupted volume with time is shown in Figure 12. Volumetric relations alone suggest that the two oldest domes represent separate silicic magmatic systems, whereas all of the younger rhyolites may be products of a single system as implied by their trace element systematics and their nearly identical Pb-isotopic compositions. The oldest two domes will not be considered further in our discussion of volume-time relations.

Figure 12 suggests a form of behavior that has far-reaching consequences for the eruptive mechanism and for the origin of the Coso silicic magmatic system itself. Inspection of the points for groups 3–7 suggests a systematic relation between the interval of repose between emplacement of eruptive groups and the volume of the preceding eruptive group. No systematic relation is apparent between repose time and the

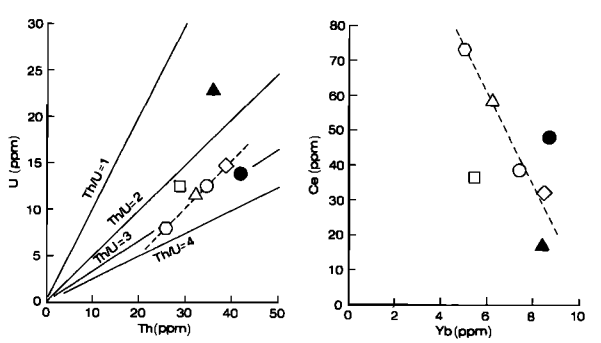

Fig. 10. Average U versus Th and Ce versus Yb in groups of rhyolites. Dashed lines are best fit to groups 3, 4, 5, and 6. Symbols as in Figure 1.

volume of the ensuing eruptive group. These relations are more clearly illustrated by a plot of cumulative erupted volume against time (Figure 13, solid symbols). Points generated by projecting individual cumulative volumes to the times of successive eruptive episodes (open symbols) have been fitted with a line by least squares, taking uncertainties into account [*York*, 1969]. The slope of this line gives a long-term rate of increase in cumulative erupted volume with time of 5.4 ± 0.6 km³/m.y. The intercept on the volume axis at zero time (present) is 1.20 ± 0.09 km³. The fit of the line is surprisingly good, and the intercept on the age axis is within the uncertainty of the weighted mean K-Ar age of group 3. Because the time of the next eruption can be anticipated from knowledge of the volume of the previous eruption and the eruption rate, the relation depicted in Figure 13 is called time predictable.

The significance of Figure 13 becomes apparent by analogy with relations between cumulative slip on faults and recurrence interval of earthquakes. *Bufe et al.* [1977] have shown that the recurrence interval of frequent earthquakes of $M < 4$ along a segment of the right lateral strike slip Calaveras fault zone in central California is linearly dependent on the coseismic slip accompanying the preceding earthquake. In addition, *Shimazaki and Nakata* [1980] have shown that a time predictable model fits three different sites of plate convergence around the Japan arcs, where large earthquakes have been separated by periods of time whose lengths are proportional to the amount of coseismic uplift associated with the preceding earthquake. Similarity between Figure 13 and those relating slip on faults to time [*Bufe et al.*, 1977, Figure 2; *Shimazaki and Nakata*, 1980, Figure 4] suggests that (1) eruptions take place when some parameter reaches a critical value and that (2) this value is approached at a constant rate. Magma apparently leaves the system by forming dikes when the magmatic pressure exceeds the sum of the ambient minimum horizontal compressive stress and the tensile strength of the roof rocks [*Bacon et al.*, 1980; *Shaw*, 1980]. Either magmatic pressure increases or, alternatively, the minimum horizontal compressive stress decreases as extensional strain accumulates in roof rocks, at a constant rate.

Figure 13 implies that the long-term rate of leakage from the Coso system is constant if the volume of material erupted as domes and flows is proportional to the volume bled from the reservoir. In a static lithosphere a constant leak rate might imply a constant rate of buildup of volatile pressure or some other factor related to magmatic pressure. However, in a crust that has been shown, through studies of faulting [*Duffield et al.*, 1980; *Roquemore*, 1980] and seismicity [*Weaver and Hill*, 1978/79; *Walter and Weaver*, 1980], to be undergoing extension, the controlling variable may be tectonic stress. That is, the magmatic system may have erupted in a passive way in response to extension of the crust. In fact, the Coso volcanic field is located within the zone of the Great Basin that is recognized as undergoing the highest rate of extensional strain [*Greensfelder et al.*, 1980]. Silicic volcanic centers, such as those at Long Valley and in the Coso Range, may develop where the extension rate is higher still [*Lachenbruch et al.*, 1976]. This extensional deformation is apparently elastic in the upper crust but becomes increasingly plastic at lower crustal and upper mantle depths.

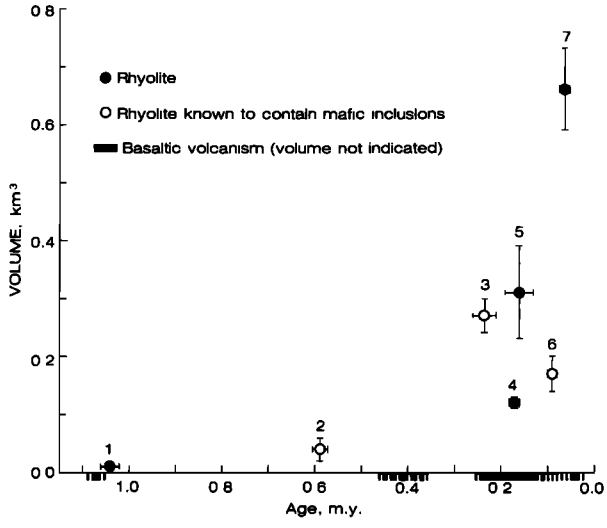

Fig. 12. Volumes of groups of rhyolite domes and lava flows vs. age. Episodes of basaltic volcanism [*Duffield et al.*, 1980] and rhyolites known to contain mafic inclusions [*Metz and Bacon*, 1980] are noted. Uncertainties are from Table 2 for rhyolites and from *Duffield et al.* [1980] for ages of basalts.

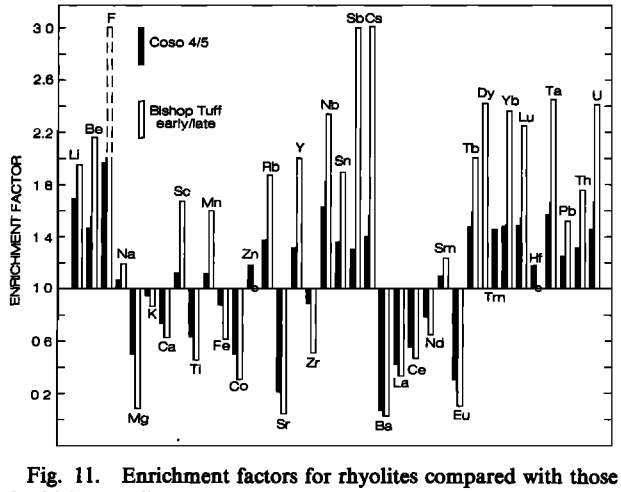

Fig. 11. Enrichment factors for rhyolites compared with those of the Bishop Tuff [*Hildreth*, this issue, Figure 7]. Coso enrichment factors based on composition of sample 5 of rhyolite eruptive group 4 divided by average composition of group 5 rhyolites.

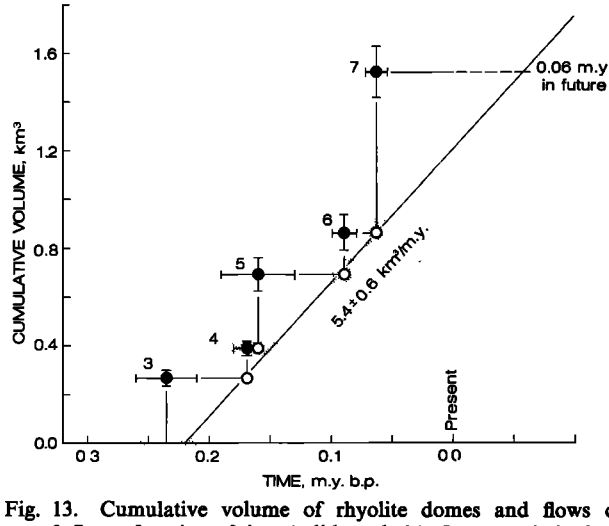

Fig. 13. Cumulative volume of rhyolite domes and flows of groups 3–7 as a function of time (solid symbols). Open symbols show volumes of groups projected to times of emplacement of succeeding groups. Pattern indicates uncertainty for open symbols. Long-term rate of eruption is given by slope of line fitted to data shown by open symbols.

In light of the tectonic setting of the Coso Range we suggest the following explanation for the time predictable eruptive behavior, but recognize that alternative models may apply. If the long-term extension rate is constant in the Coso region, extensional strain must accumulate in roof rocks at a constant rate. In the uppermost crust much of this strain may be relieved by faulting. However, in areas such as the Pleistocene part of the Coso volcanic field, a sizeable component of this strain may be relieved by the emplacement of dikes oriented perpendicular to the minimum principal stress. If the cumulative width of silicic dikes is proportional to the cumulative volume of erupted rhyolite, it follows that during the emplacement of a group of domes or flows a certain amount of extensional strain is relieved that is proportional to the volume erupted. At a steady rate of extension the time necessary for accumulation of strain in roof rocks to the point where dikes may again form is thus a linear function of the volume of magma bled from the system in the previous eruptive episode, a fixed proportion of which reaches the surface. The similarity between Figure 13 and the plots of cumulative coseismic slip versus time may be no coincidence, because the principal control on rhyolite eruption may have been the elastic behavior of rocks subjected to tectonic stress. The time predictable model for groups 3–7 (Figure 13) suggests that if eruption continues in a lava dome or flow mode, with no change in the depth to the roof of the magma reservoir, and the regional extension rate remains constant, the next eruption may take place in about 60,000 years.

Chemical Evolution

The constant rate of leakage implied by Figure 13 suggests that tectonic extension has acted as a safety valve allowing highly differentiated magma to be bled from the top of the system and prohibiting the reservoir to advance to a level sufficiently shallow for a voluminous pyroclastic eruption to take place [*Bacon et al.*, 1980]. No simple relation between rhyolite composition and time has been found. The variation in chemistry shown in Figure 9 suggests that the evolution of the system toward more differentiated compositions exceeded tectonically induced bleeding from group 3 to 4 and that group 5 may have tapped slightly less evolved, possibly hotter (aphyric, extensive lava flow) magma left at the top of the system after eruption of group 4. During the approximately 70,000 years after emplacement of group 5, some event(s), perhaps a subtle change in the proportions of H_2O, F, and Cl, produced slight increases in Sc, Zn, Sm, and Hf superimposed on an overall tendency toward less evolved composition in the rhyolite flows of group 6. The location of all of the group 6 vents somewhat south of the center of the rhyolite field suggests that this magma might have been drawn from a deeper level in the system than groups 5 and 7 or may reflect proximity to the margin of the magma reservoir.

The volume of magma erupted during the emplacement of group 7 was more than twice as great as that of any of the other groups and may indicate an increase in the size of the silicic reservoir. The chemical differences cited earlier, e.g., a rapid increase in the apparent rate of chemical evolution (Figure 9) off the chemical trends established by groups 3–6 (Figure 10), suggest that whatever controls the rates of enrichment and depletion of some elements changed significantly during the period between emplacement of groups 6 and 7. Because the youngest rhyolites show no indication of significant crystallization, because basalt was erupted near the margin of the rhyolite field after group 7, and because the crust continues to extend, it is likely that the silicic reservoir still exists.

RESERVOIR VOLUME

The impressive homogeneity of each group of rhyolites, and especially group 7, suggests that the material erupted was in fact a very small fraction of a much larger volume of magma, representing only one horizon at the top of a vertically compositionally zoned system. Geophysical constraints, most of which are in fact detection limits, suggest that a magma body would be less than ~10 km in diameter, with its top at ~8 km or greater depth [see *Bacon et al.*, 1980, for summary]. In addition, the heat lost due to extrusion of rhyolite is very small compared to the total current heat flux from the area of the rhyolite field [*Combs*, 1980], indicating the presence of a large heat source beneath the central portion of the rhyolite field. The midcrustal low velocity region detected by *Reasenberg et al.* [1980] from a study of teleseismic *P* wave delays, the surface projection of which coincides with the heat flow high, may approximately outline the silicic magmatic system and the mafic dikes thought to underlie it.

Models of Basin and Range heat flow [*Lachenbruch*, 1978/79; *Lachenbruch and Sass*, 1978] and heat flow in the Long Valley [*Lachenbruch et al.*, 1976] and Coso [*Combs*, 1980] areas indicate that intrusion of basalt into, and sometimes through, the crust goes hand in hand with lithospheric extension, commonly gives rise to rhyolitic volcanism, and apparently provides the thermal energy necessary to build and sustain silicic systems that may last for many hundreds of thousands of years [*Christiansen and Lipman*, 1972; *Smith and Shaw*, 1975]. Influx of basalt and eruption of silicic magma in an open system must be typical of such long-lived magmatic systems [*Smith*, 1979; *Hildreth*, this issue]. A long period of preheating of the crust is apparently necessary before large volumes of silicic magma can be generated. Immediately north and east of the Pleistocene part of the Coso volcanic field are at least 31 km^3 of volcanic rocks ranging in age from about 4 to 2.5 m.y. and spanning the compositional range of basalt to high-silica rhyolite [*Duffield et al.*, 1980]. The most voluminous Pliocene silicic products (porphyritic rhyodacite) vented within a few km of the Pleistocene rhyolite field. Furthermore, at least four basaltic vents dated at approximately 2 m.y. occur on the southwest flank of the Pleistocene rhyolite field [*Duffield et al.*, 1980]. These volcanic events and the emplacement of groups 1 and 2 and associated basalts indicate that a considerable amount of heat must have been added to the crust in the general vicinity of the rhyolite field long before the extrusion of the first high-silica rhyolite of groups 3 through 7. Heat flow in the region surrounding the rhyolite field averages ~80 mW/m^2 [*Combs*, 1980] and may reflect a component of thermal energy added to the crust by basaltic magma intruded during the Pliocene episode of volcanic activity, setting the stage for creation of a long-lived silicic magmatic system. The current silicic system must be at least as old as the group 3 rhyolites; if group 2 represents the beginnings of the modern system, it could be as old as 0.6 m.y.

Heat flow in the vicinity of the central part of the rhyolite field averages ~250 mW/m^2 in excess of typical regional values over an area of ~150 km^2 [*Combs*, 1980]. Heat is apparently transferred from roof rocks above the silicic reservoir to the surface by convection in a hot water geothermal system [*Fournier et al.*, 1980]. Approximately this rate of convective heat loss may have been occurring for as long as ~0.3 m.y.,

because siliceous hot spring sinter immediately east of the rhyolite field is overlain by an unaltered basalt flow dated at 0.234 ± 0.022 m.y. [*Duffield et al.*, 1980]. Calculated closed system solidification times for plutons are sufficiently short [*Smith and Shaw*, 1975] that, given the measured hydrothermal convective heat loss from the Coso rhyolite field, the eruption of nearly aphyric magma over a period of at least 0.18 m.y. would not be expected unless heat has been continually added to the magmatic system by intrusion of basalt. Following the reasoning of *Lachenbruch and Sass* [1978], the amount of basalt that would need to be intruded into the crust and cool to temperatures appropriate for partial melting of crustal rocks in order to explain the above heat loss would be at least ~170 km^3. The amount of silicic magma generated in response to intrusion of this basalt could be as much as twice the volume of basalt but would be expected to be less than this value by a degree dependent upon the initial temperature of crustal source rocks and the efficiency of heat loss to wall and roof rocks.

Large continental silicic magmatic systems are thought to possess magma chambers at least 10 times as voluminous as the amounts of magma ejected in caldera-forming ash flow eruptions [*Smith and Shaw*, 1975; *Smith*, 1979]. Moreover, the size of such systems appears to be crudely proportional to their age such that the average rate of growth of silicic magma chambers, obtained from the recurrence intervals and eruption volumes of multicycle caldera-forming systems, may be about 10^{-3} km^3/yr. If the Pleistocene rhyolites of the Coso Range represent a silicic system growing at this rate following 2 to 4 million years of local 'preheating,' the volume of silicic magma presently in the system may be a few hundred cubic kilometers. A reservoir of this size would be within the limits permitted by geophysical data [*Bacon et al.*, 1980] and the above interpretation of the local heat flow anomaly.

The estimated volume of silicic magma presently in the Coso system is clearly speculative, but we maintain that such a figure is reasonable. However, despite the impressive suggested volume, a voluminous pyroclastic eruption seems unlikely so long as continuing tectonic extension inhibits the migration of the reservoir to shallow crustal depth. As noted earlier, the depth to the top of the system may be too great for volatile supersaturation and rapid growth of bubbles to take place explosively upon release of confining pressure during a 'bleeding' event. Rather the mode of emplacement in which magma escapes from the reservoir by forming dikes in response to extensional tectonism apparently allows H_2O to be largely lost during ascent, thus defusing eruptions. There is no evidence for leakage from radial or ring dikes, as apparently takes place above large shallow magma chambers where bouyant rise of the magma body dominates the upper crustal stress regime, as in Stage 1 of the resurgent cauldron cycle of *Smith and Bailey* [1968].

Silicic magmatic systems of somewhat greater areal extent than that of the Coso Range with well-documented precaldera high-silica rhyolitic domes and lava flows include the approximately 12-km-diameter mildly peralkaline Primavera complex of Mexico [*Mahood*, this issue] and the considerably larger metaluminous Long Valley system [*Bailey et al.*, 1976]. Single or small groups of approximately coeval high-silica rhyolite domes are fairly common in the western U. S., marking sites of silicic systems that, for reasons of inadequate prolonged thermal flux, failed to grow to sufficient proportions to produce caldera-forming eruptions. Perhaps something near the maximum size and longevity for such a system may be indicated by the Quaternary rhyolites of the Mineral Range of Utah [*Lipman et al.*, 1978[in which two nearly aphyric lava flows and several porphyritic domes vented over a distance of about 12 km along the axis of a granitic horst during at least two eruptive episodes ~0.8 m.y. and ~0.5 m.y. ago, respectively. Voluminous pyroclastic eruptions did not result from the Pleistocene silicic reservoir(s) of the Mineral Range. The Coso silicic system, to date, appears to be intermediate in size between that of the Mineral Range and those epicratonic systems which have ultimately produced voluminous high-silica pyroclastic eruptions and formed calderas.

CONCLUSION

The Pleistocene part of the Coso volcanic field appears to represent the early stages of development of a silicic magmatic system of substantial size and longevity. Magmatism has occurred in response to prolonged and comparatively rapid lithospheric extension near the western margin of the Basin and Range province. Basaltic magma provides the source of heat to partially melt intermediate to silicic rocks at midcrustal levels, giving rise to silicic magma. Continued influx of basalt is necessary to maintain the silicic system for the observed period of eruptive activity and to account for the local anomalously high heat flow. The erupted high-silica rhyolites apparently represent only a small, highly differentiated fraction of the total volume of silicic magma at any given time. Differentiation processes suggested by the composition of the erupted rhyolites operated in the liquid state, probably by the thermogravitational diffusion mechanism described by *Hildreth* [this issue]. Eruption of high-silica rhyolitic magma was episodic; seven eruptive groups are represented by one or more domes or lava flows. The degree of chemical evolution of the different groups of rhyolites did not vary in a simple progressive way but, rather, this irregular variation underscores the long-lived open system behavior implied by repetitive bimodal volcanism.

All but two of the domes were emplaced during the last ~0.24 m.y., the last eruptive group being the most voluminous. Relations of volume of eruptive groups and cumulative volume to time suggest that the system has erupted at a virtually constant long-term rate that may reflect the influence of an approximately constant crustal extension rate acting as a safety valve, allowing highly differentiated magma to be bled from the top of the reservoir. The last four eruptive groups were each emplaced at times predictable from the volume of the preceding eruption. If this pattern continues, the next eruption can be expected to occur about 60,000 years from now.

Evaluation of heat flow data and comparison of cumulative volume-time systematics for the rhyolites with well-studied systems that produced voluminous pyroclastic eruptions suggests that the Coso silicic system may have a volume on the order of a few hundred cubic kilometers. Geophysical studies, however, suggest that any silicic magma reservoir now present may be at least ~8 km deep and no more than ~10 km in diameter. These observations, coupled with the nearly aphyric but biotite- and hornblende-bearing character of the highly differentiated rhyolites, suggest that comparatively slow ascent of initially volatile-rich magma in dikes from relatively great depth allows a large proportion of the initial H_2O to be lost before magma nears the surface. Rapid crustal extension and tectonically induced bleeding of the system has inhibited

upward advance of the silicic magma reservoir to depths sufficiently shallow for a voluminous pyroclastic eruption to occur. However, petrologic, volumetric, and geochronologic data argue for the continued existence and probable growth of a silicic magmatic system which provides thermal energy for the observed anomalously high heat flow [*Combs*, 1980] and hot water geothermal system [*Duffield et al.*, 1980].

Acknowledgments. We wish to thank Brent Dalrymple for his patience and willingness to make repeated determinations of K-Ar ages of the Coso rhyolites. Keith Waterhouse of the University of Lancaster determined major element abundances in the rhyolites. E. Y. Campbell, P. J. Aruscavage, J. S. Kane, and A. K. Neuville provided the wet chemical and R. E. Mays the emission spectrographic trace element data in Table 1. We are indebted to W. A. Duffield, Wes Hildreth, A. H. Lachenbruch, H. R. Shaw, David Gottfried, Jenny Metz and many other colleagues for stimulating discussion and assistance throughout this study. We also thank Hildreth, Duffield, R. L. Christiansen, M. F. Sheridan, R. F. Heming, and A. M. Kudo for helpful reviews of earlier drafts of the manuscript.

REFERENCES

Babcock, J. W., and W. S. Wise, Petrology of contemporaneous basalt and rhyolite in the Coso Mountains, California, *Geol. Soc. Am. Abstr. Programs, 5*(6), 1973.

Bacon, C. R., W. A. Duffield, and K. Nakamura, Distribution of Quaternary rhyolite domes of the Coso Range, California: Implications for extent of the geothermal anomaly, *J. Geophys. Res., 85,* 2425–2433, 1980.

Bacon, C. R., D. M. Giovannetti, W. A. Duffield, G. B. Dalrymple, and R. E. Drake, Age of the Coso Formation, Inyo County, California, *U. S. Geol. Surv. Bull.*, in press, 1981.

Bailey, R. A., G. B. Dalrymple, and M. A. Lanphere, Volcanism, structure, and geochronology of Long Valley Caldera, Mono County, California, *J. Geophys. Res., 81,* 725–744, 1976.

Bufe, C. G., P. W. Harsh, and R. O. Burford, Steady-state seismic slip—A precise recurrence model, *Geophy. Res. Lett., 4,* 91–94, 1977.

Carmichael, I. S. E., The iron-titanium oxides of salic volcanic rocks and their associated ferromagnesian silicates, *Contrib. Mineral. Petrol., 14,* 36–64, 1967.

Chen, J. H., Uranium-lead isotopic ages from the southern Sierra Nevada and adjacent areas, California, Ph. D. thesis, Univ. of Calif., Santa Barbara, 1977.

Christiansen, R. L., and P. W. Lipman, Cenozoic volcanism and plate-tectonic evolution of the Western United States, 2, Late Cenozoic, *Philos. Trans. R. Soc. London, Ser. A, 271,* 249–284, 1972.

Combs, J., Heat flow in the Coso geothermal area, Inyo County, California, *J. Geophys. Res., 85,* 2411–2424, 1980.

Dodge, F. C. W., The Uyaijah ring structure, Kingdom of Saudi Arabia, *U.S. Geol. Surv. Prof. Pap., 774-E,* 1979.

Doe, B. R., and M. H. Delevaux, Variations in lead-isotopic compositions in Mesozoic granitic rocks of California: a preliminary investigation, *Geol. Soc. Am. Bull., 84,* 3513–3526, 1973.

Duffield, W. A., and C. R. Bacon, Geologic map of the Coso volcanic field and adjacent areas, Inyo County, California, scale 1 : 50,000, miscellaneous geological investigation map, *I-1200,* U.S. Geol. Surv., Menlo Park, Calif., 1981.

Duffield, W. A., C. R. Bacon, and G. B. Dalrymple, Late Cenozoic volcanism, geochronology, and structure of the Coso Range, Inyo County, California, *J. Geophys. Res., 85,* 2381–2404, 1980.

Fournier, R. O., J. M. Thompson, and C. F. Austin, Interpretation of chemical analyses of waters collected from two geothermal wells at Coso, California, *J. Geophys. Res., 85,* 2405–2410, 1980.

Friedman, I., and J. Obradovich, Obsidian hydration dating of volcanic events, *Quat. Res.*, in press, 1981.

Greensfelder, R. W., F. C. Kintzer, and M. R. Somerville, Seismotectonic regionalization of the Great Basin, and comparison of moment rates computed from Holocene strain and historic seismicity, *Geol. Soc. Am. Bull., 91,* 2039–2111, 1980.

Hildreth, W., The Bishop Tuff: Evidence for the origin of compositional zonation in silicic magma chambers, *Geol. Soc. Am. Spec. Pap., 180,* 43–75, 1979.

Hildreth, W., Gradients in silicic magma chambers: Implications for lithospheric magmatism, *J. Geophys. Res., 86,* this issue.

Hon, R., and H. J. Noyes, REE and other trace elements during fractionation of granitic aplites of Sierra Nevada batholith, CA, and Katahdin pluton, ME, *Geol. Soc. Am. Abstr. Programs, 7,* 1023–1024, 1977.

Howard, K. A., et al., Preliminary map of young faults in the United States as a guide to possible fault activity, scale 1 : 5,000,000, miscellaneous field studies map, *MF-916,* U.S. Geol. Surv., Reston, Va., 1978.

Jack, R. N., and I. S. E. Carmichael, The chemical fingerprinting of acid volcanic rocks, *Spec. Rep. Calif. Div. Mines Geol., 100,* 17–32, 1968.

Kistler, R. W., and Z. E. Peterman, Reconstruction of crustal blocks of California on the basis of initial strontium isotopic compositions of Mesozoic granitic rocks, *U.S. Geol. Surv. Prof. Pap., 1071,* 1978.

Lachenbruch, A. H., Heat flow in the Basin and Range province and thermal effects of tectonic extension, *Pure Appl. Geophys., 117,* 34–50, 1978/1979.

Lachenbruch, A. H., and J. H. Sass, Models of an extending lithosphere and heat flow in the Basin and Range province, *Geol. Soc. Am. Mem., 152,* 209–350, 1978.

Lachenbruch, A. H., J. H. Sass, R. J. Munroe, and T. H. Moses, Jr., Geothermal setting and simple heat conduction models for the Long Valley caldera, *J. Geophys. Res., 81,* 769–784, 1976.

Lanphere, M. A., G. B. Dalrymple, and R. L. Smith, K-Ar ages of Pleistocene rhyolitic volcanism in the Coso Mountains, California, *Geology, 3,* 339–341, 1975.

Lipman, P. W., P. D. Rowley, M. H. Mehnert, S. H. Evans, Jr., W. P. Nash, and F. H. Brown, Pleistocene rhyolite of the Mineral Mountains, Utah—Geothermal and archeological significance, *J. Res. U. S. Geol. Surv., 6,* 133–147, 1978.

Ludington, S., W. N. Sharp, D. McKowan, and F. Barker, The Redskin granite—A proterozoic example of thermogravitational diffusion. *Geol. Soc. Am. Abstr. Programs, 11,* 469, 1979.

Mahood, G. A., A summary of the geology and petrology of the Sierra la Primavera, Jalisco, Mexico, *J. Geophys. Res., 86,* this issue.

Masuda, A., N. Nakamura, and T. Tanaka, Fine structures of mutually normalized rare-earth patterns of chondrites, *Geochim. Cosmochim. Acta, 37,* 239–248, 1973.

Metz, J., and C. R. Bacon, Quenched blobs of mafic magma in high-silica rhyolite of the Coso volcanic field, California, *Geol. Soc. Am. Abstr. Programs, 12*(3), 120, 1980.

Miller, C. F., and D. W. Mittlefehldt, Rare earth depletion accompanying differentiation of felsic plutonic rocks, *Geol. Soc. Am. Abstr. Programs, 11*(7), 479–480, 1979.

Nakamura, K., Volcanoes as possible indicators of tectonic stress orientation, *J. Volcanol. Geotherm. Res., 2,* 1–16, 1977.

Noble, D. C., Sodium, potassium, and ferrous iron contents of some secondarily hydrated natural silicic glasses, *Am. Mineral., 52,* 280–286, 1967.

Noble, D. C., M. K. Korringa, C. E. Hedge, and G. O. Riddle, Highly differentiated subalkaline rhyolite from Glass Mountain, Mono County, California, *Geol. Soc. Am. Bull, 83,* 1179–1184, 1972.

Plouff, D., and W. F. Isherwood, Aeromagnetic and gravity surveys in the Coso Range, California, *J. Geophys. Res., 85,* 2491–2501, 1980.

Reasenberg, P., W. Ellsworth, and A. Walter, Teleseismic evidence for a low-velocity body under the Coso geothermal area, *J. Geophys. Res., 85,* 2471–2483, 1980.

Roquemore, G., Structure, tectonics, and stress field of the Coso Range, Inyo County, California, *J. Geophys. Res., 85,* 2434–2440, 1980.

Sarna-Wojcicki, A., Correlation of Late Cenozoic tuffs in the central Coast Ranges of California by means of trace- and minor-element chemistry, *U.S. Geol. Surv. Prof. Pap., 972,* 1976.

Shapiro, L., Spectrophotometric determination of silica at high concentrations using fluoride as a depolymerizer, *J. Res. U.S. Geol. Surv., 2,* 357–360, 1974.

Shaw, H. R., Diffusion of H_2O in granitic liquids, 1, Experimental data, *Carnegie Inst. Washington Publ.,* 634, 139–1xx, 1974*a*.

Shaw, H. R., Diffusion of H_2O in granitic liquids, 2, Mass transfer in magma chambers, *Carnegie Inst. Washington Publ., 634,* 1xx–170, 1974*b*.

Shaw, H. R., The fracture mechanisms of magma transport from the mantle to the surface, in *Physics of Magmatic Processes,* pp. 201–

264, edited by R. B. Hargraves, Princeton University Press, Princeton, N. J., 1980.

Shaw, H. R., R. L. Smith, and W. Hildreth, Thermogravitational mechanisms for chemical variations in zoned magma chambers, *Geol. Soc. Am. Abstr. Programs, 8*(6), 1102, 1976.

Shimazaki, K., and T. Nakata, Time-predictable recurrence model for large earthquakes, *Geophys. Res. Lett., 7,* 279–282, 1980.

Smith, R. L., Ash-flow magmatism, *Geol. Soc. Am. Spec. Pap., 180,* 5–27, 1979.

Smith, R. L., and R. A. Bailey, The Bandelier Tuff: A study of ash-flow eruption cycles from zoned magma chambers, *Bull. Volcanol., 29,* 83–104, 1966.

Smith, R. L., and R. A. Bailey, Resurgent cauldrons, *Geol. Soc. Am. Mem., 116,* 613–662, 1968.

Smith, R. P., and W. P. Nash, Chemical correlation of volcanic ash deposits in the Salt Lake Group, Utah, Idaho and Nevada, *J. Sediment. Petrol., 46,* 930–939, 1976.

Smith, R. L., and H. R. Shaw, Igneous-related geothermal systems, *U.S. Geol. Surv. Circ., 726,* 58–83, 1975.

Taylor, S. R., A. Ewart, and A. C. Capp, Leucogranites and rhyolites: Trace element evidence for fractional crystallization and partial melting, *Lithos, 1,* 179–186, 1968.

Walter, A. W., and C. S. Weaver, Seismicity of the Coso Range, California, *J. Geophys. Res., 85,* 2441–2458, 1980.

Weaver, C. S., and D. P. Hill, Earthquake swarms and local crustal spreading along major strike-slip faults in California, *Pure Appl. Geophys., 117,* 51–64, 1978/1979.

Wilson, A. D., A new method for the determination of ferrous iron in rocks and minerals, *Bull. Geol. Surv. G. B., 9,* 56–58, 1955.

York, D., Least squares fitting of a straight line with correlated errors, *Earth Planet. Sci. Lett., 5,* 320–324, 1969.

Young, C. -Y., and R. M. Ward, Three-dimensional Q^{-1} model of the Coso Hot Springs Known Geothermal Resource Area, *J. Geophys. Res., 85,* 2459–2470, 1980.

Zielinski, R. A., P. W. Lipman, and H. T. Millard, Jr., Minor-element abundances in obsidian, perlite, and felsite of calc-alkalic rhyolites, *Am. Mineral., 62,* 426–437, 1977.

(Received December 19, 1980;
revised May 14, 1981;
accepted May 19, 1981.)

JOURNAL OF GEOPHYSICAL RESEARCH, VOL. 86, NO. B11, PAGES 10242–10256, NOVEMBER 10, 1981

The Mineralogy and Chemistry of the Anorogenic Tertiary Silicic Volcanics of S.E. Queensland and N.E. New South Wales, Australia

A. EWART

Department of Geology & Mineralogy, University of Queensland, St. Lucia, Brisbane, Queensland 4067

The Late Oligocene-Early Miocene volcanism of this region is chemically strongly bimodal; the mafic lavas (volumetrically dominant) comprise basalts, hawaiites, and tholeiitic andesites, while the silicic eruptives are mainly comendites, potassic trachytes, and potassic, high-silica rhyolites. The comendites and rhyolites have distinctive trace element abundance patterns, notably the extreme depletions of Sr, Ba, Mg, Mn, P, Cr, V, and Eu, and the variable enrichment of such elements as Rb, Zr, Pb, Nb, Zn, U, and Th. The trachytes exhibit these characteristics to lesser degrees. The comendites are distinguished from the rhyolites by their overall relative enrichment of the more highly charged cations (e.g., LREE, Nb, Y, and especially Zr) and Zn. The phenocryst mineralogy of the trachytes and rhyolites comprises various combinations of the following phases: sodic plagioclase (albite-andesine), calcic anorthoclase, sanidine, quartz, ferroaugite-ferrohedenbergite, ferrohypersthene, fayalitic olivine, ilmenite, titanomagnetite, and rarely biotite (near annite) and Fe-hastingsitic amphibole. Accessories include apatite, zircon, chevkinite (ferrohedenbergite-bearing rhyolites only), and allanite (amphibole and botite rhyolites only). The comendites generally contain Ca-poor anorthoclase-sanidine, quartz, fluorarfvedsonite, aegirine and aegirine-augite (Zr-bearing), aenigmatite, and ± ilmenite. Coexisting Fe-Ti oxides are absent in the comendites and relatively uncommon in the rhyolites and trachytes. Where present, they indicate equilibration temperatures of 885°–980°C and fo_2 between QFM and WM buffers. The magmas are thus interpreted to have been strongly water undersaturated during phenocryst equilibration, which is also consistent with the general paucity of pyroclastics, the rarity of hydrous mineral phases, and the extreme Fe-enriched ferromagnesian phenocryst compositions. The chemical and mineralogical data are interpreted to indicate the operation of extreme fractionation processes controlling the development of the silicic magmas, and the comendites, trachytes, and certain trachyte-rhyolite series are considered to have evolved from a mafic parentage. The available oxygen, Sr, and Pb isotopic data, however, point to some modification of the magnas through crustal equilibration processes. The remaining high-silica rhyolites are considered to most likely represent crustal partial melts but are again modified by extensive fractionation.

INTRODUCTION

The region in question forms part of the broad belt of Cainozoic volcanism, some 3000 km long, that extends along the eastern and southeastern coastal region of Australia. *Wellman and McDougall* [1974] have shown that volcanic activity commenced about 70 Ma ago and has continued through the Cainozoic at a nearly constant rate. More than 50 volcanic provinces are recognized throughout the whole coastal region. Although basalts, hawaiites and tholeiitic andesites are the dominant lavas, some of the provinces contain minor associated silicic volcanism, namely trachytes, rhyolites, and/or comendites. In certain areas, especially southern Queensland, isolated outcrops of trachytes and comendites are found with apparently no associated mafic extrusives.

Consideration of the overall distribution of chemistry of the erupted magmas in S.E. Queensland reveals that the volcanism is very strongly bimodal [*Ewart et al.*, 1980]. Where both mafic and silicic eruptives occur within a given center, estimates suggest that the relative volumes are at least 7:1 in favor of the mafic eruptives.

The following is a brief outline of the volcanism found within some of the more prominent volcanic centers to which particular references are made in this paper and which indicate the diversity found among the various provinces. A locality map, showing the extent of the S.E. Queensland-N.E. New South Wales volcanic regions, is provided in Figure 1.

Tweed Shield Volcano. This constitutes the eroded remnants of a former shield volcano some 100 km in diameter. The generalized volcanic succession comprises a lower mafic sequence followed by several distinct rhyolite units (two of which are considered in this paper, namely the Binna Burra and Springbrook rhyolites) that are overlain by a younger mafic sequence; a separate comenditic dyke phase also occurs. Volcanism is dated from 20.5–22.3 Ma [*Ewart et al.*, 1977].

Focal Peak Shield Volcano. This again constitutes the eroded remnants of a shield volcano situated within a complex ring structure some 14 km in diameter, the periphery of which is marked by rhyolite intrusions and extrusions (the Mt. Gillies Rhyolites). The massive Mt. Barney granophyre plug also outcrops within this ring structure. The generalized volcanic succession comprises an older mafic sequence followed by the Mt. Gillies Rhyolites. Reported ages range between 23 and 25.6 Ma [*Ross*, 1977].

Glass Houses and Maleny Centers. The Glass House Mountains constitute a spectacular group of eroded domes and plugs composed mainly of comendites but with subordinate trachytes. A few kilometers to the north of these plugs is the isolated mafic Maleny eruptive center, which may be related to the Glass House extrusions. This is supported by K-Ar dates of 25.2 and 25.4 Ma for a young Maleny flow and a comendite, respectively. Extending NNE along the S.E. Queensland coast are several quite isolated silicic extrusive centers, namely, the Mt. Coolum comendite and the Fraser Island trachytes.

Mt. Alford Ring Complex. This represents an eroded plug of microdiorite and subordinate granophyre intruded by a core of tholeiitic andesite; the complex is cut by a semicircular zone of rhyolitic and trachytic ring dykes (25.2 Ma) and a second nonarcuate set of cross-cutting rhyolite, comendite, and basalt dykes [*Stevens*, 1962].

Copyright © 1981 by the American Geophysical Union.

Paper number 1B0531.
0148-0227/81/001B-0531$01.00

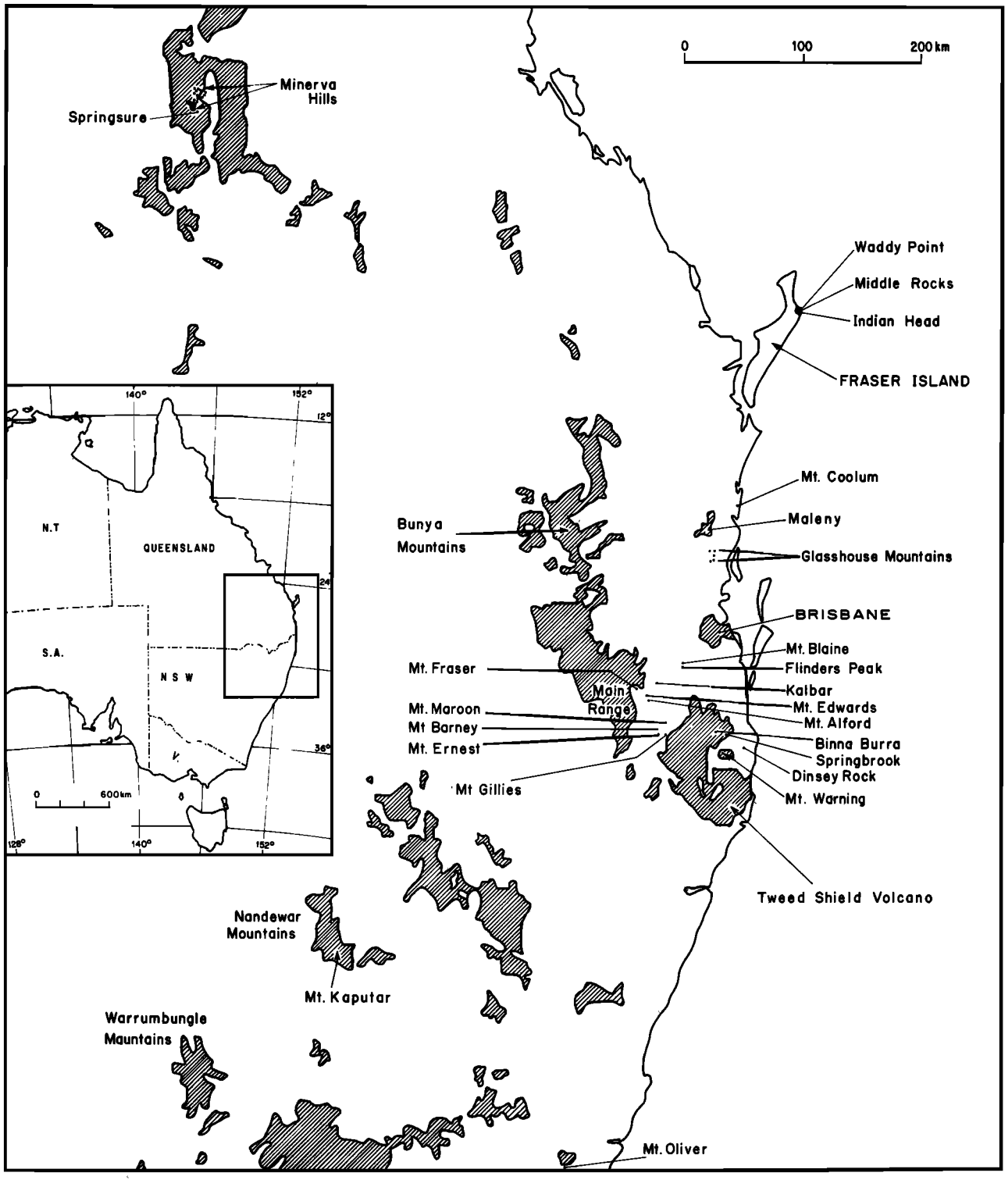

Fig. 1. Map of S.E. Queensland and N.E. New South Wales showing the distribution of the Tertiary volcanic centers.

Minerva Hills. The volcanic sequence from this rather complex center has been broadly divided into a basal series of mafic lavas (some 70 m thick) that are overlain by a younger series of intercalated mafic lavas and trachytic pyroclastics. K-Ar dates of approximately 33–34 Ma and 24–28.5 Ma are obtained from the two series, respectively. The pyroclastics are closely associated with a concentration of numerous plugs, domes, thick flows, sills, and dykes of mainly trachyte with subordinate rhyolite. These are the Minerva Hills volcanics [*Veevers et al.*, 1964].

CHEMISTRY

It is emphasized that within the volcanic provinces being considered there is a strong bimodality of magma compositions with respect to their SiO_2 distributions [*Ewart et al.*, 1980]. This paper is concerned with the silicic compositions,

i.e., those that are greater than 59% SiO_2. In addition, some mineralogical comparisons are made with associated, although rare, microsyenites that occur in certain of the volcanic centers. Averaged major and trace element data and mineralogical data, are summarized in Table 1. The trachyte data are based on sequential averages with increasing SiO_2 contents of the respective samples.

For purposes of this paper the distinction between trachytes and rhyolites is taken as 73% SiO_2. The peralkaline types are readily distinguished by their distinctive sodic mineralogy. Very rare lavas occur that are described as dacites; these are readily distinguished from trachytes by the absence of both phenocrystal alkali feldspar and quartz. In this paper, four distinct types of rhyolites are recognized on the basis of both occurrence and mineralogical criteria (Table 1).

Major Elements

A. Metaluminous and peraluminous rhyolites and trachytes. The majority of the trachytes and rhyolites analyzed are chemically very close to the metaluminous/peraluminous boundary, and it is believed that the magmas were metaluminous prior to the processes of cooling and devitrification. No evidence, however, of the occurrence of systematic selective alkali leaching within the various extrusives has been found. The silicic extrusives of Minerva Hills and the hypersthene-bearing rhyolites are noteworthy in that they consistently show peraluminous chemistry.

The trachytes and rhyolites are all relatively potassic and exhibit progressively depleted Ti, Fe, Mg, Mn, Ca, and P abundances with increasing SiO_2, culminating in very strong depletions of these elements in the rhyolites (the hypersthene rhyolites exhibiting least depletion). Figure 2 indicates that the normative compositions of the rhyolites (excepting the Minerva type) closely approach the quartz-saturated two-feldspar boundary curve (Figure 2*a*) and the 'minimum' (piercing point) in the projection of the $[Ab\text{-}Or\text{-}Q]_{97}An_3$ system (Figure 2*b*) [*James and Hamilton,* 1969], although plotting within the sanidine fields. These can be classed as high-silica, potassic rhyolites. The plots of the trachytes within the quartz-feldspar system (Figure 2*b*) show that they lie in a zone close to, and essentially parallel to, the projection of the two-feldspar boundary curve as defined by *James and Hamilton* [1969] for those compositions low in normative An (see also Figure 2*a*). The Minerva Hills extrusives seem to be unique within the region in that they show a complete continuity of major element chemistry from trachyte to rhyolite in the one volcanic center; it is thus noteworthy that the Minerva rhyolites are lower in normative *Q* (Figure 2*b*) and generally exhibit a more trachytic chemistry compared to the other rhyolites of the region (Table 1).

B. Peralkaline extrusives. These are characterized by normative ac, and less commonly normative ns. The majority of the extrusives are highly silicic and can be classified as comendites (Table 1), although peralkaline trachytes sporadically occur. The comendites exhibit highly depleted Mg, Mn, Ca, and P abundances, with Na and Fe^{3+} significantly enriched compared to the nonperalkaline rhyolites. Their normative compositions, when plotted in the quartz-feldspar system (Figure 2*b*), project in a zone lying between the thermal valley in the ternary system [*Tuttle and Bowen,* 1958] and the projection of the two-feldspar boundary curve in the $[Ab\text{-}Or\text{-}Q]_{97}An_3$ system; a systematic shift of Ab/Or ratios therefore occurs with increasing normative *Q*.

Trace Elements

Three distinct patterns of trace element behavior are recognizable within the silicic eruptives of this province:

1. Those behaving as incompatible elements, which thus show a progressive and regular enrichment through the trachyte to rhyolite compositional spectrum: Rb, Th, and to a lesser extent Pb are the most notable examples in this province. For example, there is an almost logarithmic relationship between Rb versus K/Rb [*Ewart et al.,* 1976], which suggests that Rb is effectively excluded from fractionating phenocryst phases (except biotite, which is, however, a very rare phase in the extrusives of the region). This is confirmed by analyses of phenocryst phases from the silicic eruptives. Thus, measured Rb partition coefficients for alkali feldspars range between 0.31 and 0.65 (averaging 0.46) and are <0.1 for all other phases (except biotite). Th partition coefficients are also low, except for certain accessories (zircon, allanite, and chevkinite), while Pb partition coefficients are uniformly higher for the feldspars (0.5 to 1.7).

2. Those elements exhibiting very strong depletion through the compositional spectrum from trachyte to rhyolite, most notably Ba, Sr, V, Ni, and Cr, and also including Mg, Mn, Ca, and P. Extreme Eu depletion also occurs [*Ewart et al.,* 1976]. Such depletions are illustrated by the plot of Rb versus Ba (Figure 3). The behavior of these elements can, in principle, be explained by fractionation of feldspars and Fe-Mg silicates.

3. The highly charged cations, notably Zr, Ce, Y, and Nb. Although these elements normally exhibit enrichment during crystal fractionation within the S.E. Queensland silicic magmas, they also exhibit a mutally 'decoupled' behavior, resulting in poor correlations (Figure 4). This behavior can probably be attributed mainly to the crystallization and fractionation of minor microphenocryst phases such as zircon, chevkinite, allanite, and possibly apatite, in the nonperalkaline lavas, and to sodic pyroxenes and sodic amphiboles in the peralkaline types.

The averaged data for the rhyolites (presented in Table 1) illustrates the above patterns of behavior, and their overall element abundance patterns would seem to be readily interpreted as indicating strong crystal fractionation control (see, however, *Hildreth* [1979] and later discussion). Nevertheless, it is apparent that each rhyolite type has its own distinctive trace element patterns, indicating an independent line of evolution. The Minerva Hills trachytes and rhyolites exhibit a complete continuity of trace element abundances, in conformity with their major element chemistry, and the rhyolites are notably enriched in Zr and Nb compared to the other rhyolite types within the region.

The comendites have certain trace element characteristics (Table 1) that tend to distinguish them from the nonperalkaline rhyolites, most notably the strong enrichments of the highly charged cations (e.g., Zr, Nb, LREE, Y) and Zn. Nevertheless, Table 1 and Figure 4 show that the nonperalkaline trachytes and rhyolites may also exhibit enriched concentrations of certain of these elements, overlapping the abundances found in the comendites. The factor that seems to most characterize the comendites is the relative enrichment of the whole spectrum of the highly charged cations, which is not found in the nonperalkaline lavas. The enrichment of Zr in the comendites is particularly characteristic [see also *Nicholls and Carmichael,* 1969] and is readily explicable by the experi-

TABLE 1. Averaged Major Element, Trace Element, and Mineralogical Data for the S.E. Queensland Trachytes (Based on Sequential Averages), Rhyolites, and Comendites

	Trachytes†			Minerva Hills Trachytes		Rhyolites, >73%				
SiO_2 Range	<66%	66%–69%	69%–73%	66%–69	69%–73%	Hypersthene-Bearing Type	Ferrohedenbergite-Fayalite Type	Binna Burra Type	Minerva Hills Type	Average Comendite >69%
SiO_2	63.15	67.92	69.79	67.79	71.19	76.57	76.02	76.72	73.80	74.28
TiO_2	0.49	0.50	0.45	0.25	0.16	0.26	0.17	0.07	0.14	0.21
Al_2O_3	16.57	15.25	15.67	16.33	15.75	12.23	12.30	12.57	15.06	12.17
Fe_2O_3	2.97	2.41	1.17	3.95	1.54	0.68	0.72	0.77	0.90	2.37
FeO	3.15	1.88	1.45	0.03	0.25	0.94	1.16	0.46	0.04	0.97
MnO	0.13	0.09	0.04	0.08	0.03	0.02	0.03	0.01	0.004	0.04
MgO	0.42	0.24	0.41	0.08	0.06	0.18	0.15	0.03	0.05	0.04
CaO	1.95	1.21	1.05	0.58	0.43	0.60	0.68	0.44	0.21	0.13
Na_2O	5.61	5.03	4.66	5.11	4.90	3.27	3.42	3.60	4.79	5.10
K_2O	5.41	5.37	5.21	5.75	5.65	5.20	5.32	5.31	4.99	4.67
P_2O_5	0.15	0.10	0.10	0.05	0.02	0.05	0.02	0.01	0.02	0.01
Trace Elements, ppm										
Rb	104	115	134	128	165	228	165	471	173	258
Ba	788	835	869	226	64	206	96	11	30	22
Sr	112	80	164	27	12	41	11	1	6	2
Pb	14	15	16	13	14	20	22	44	15	30
Zn	129	169	137	161	174	51	145	147	114	240
Zr	742	724	549	966	612	195	387	137	562	1228
Th	9	10	12	17	22	20	20	44	20	33
Nb	68	53	45	144	198	12	35	58	188	147
Ce	124	155	114	280	156	76	168	60	99	141
Y	50	61	56	79	86	34	74	95	77	120
Cr	0.5	1	1	0.5	1	2	1	<0.5	0.5	<0.5
V	0.5	2	2	<0.5	<0.5	4	2	1	<0.5	1
Phenocryst Mineralogy, modal, vol %										
Plagioclase	—	1.8	3.8	—	0.1	2.8	—	0.2	<0.1	—
Alkali feldspar	8.8	10.7	9.7	5.1	4.3	2.1	11.9	1.2	6.8	3.4
Quartz	—	—	3.3	—	0.3	0.6	3.5	0.7	—	0.5
Clinopyroxene	0.5	0.7	0.2	0.3	0.1	—	0.7	—	<0.1	0.06
Orthopyroxene	—	—	—	—	—	0.6	—	—	—	—
Olivine	0.3	0.4	0.1	0.1	<0.1	—	0.2	—	<0.1	—
Amphibole	—	—	—	—	<0.1	—	—	—	<0.1	0.1
Biotite	—	—	0.1	—	—	—	—	<0.1	—	—
Fe-Ti oxides	0.3	0.2	0.1	0.2	0.1	0.1	0.1	0.1	0.1	0.04
Total phenocrysts	9.9	13.8	17.3	5.7	4.9	6.2	16.4	2.2	6.9	4.1
n*	6	9	5	3	19	3	18	10	8	14

Major elements recalculated on anhydrous basis.
* Number of samples within each data grouping.
† Excluding Minerva Hills.

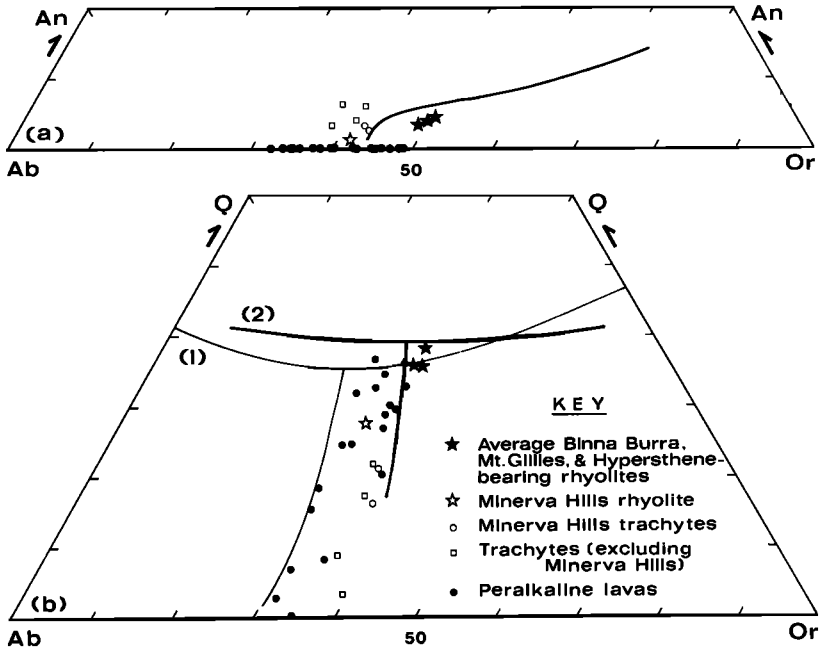

Fig. 2. Normative (CIPW) quartz and feldspar compositions of trachytes, rhyolites, and peralkaline lavas plotted in the quartz-feldspar and feldspar ternary systems. Heavy solid curve in plot (*a*) represents quartz-saturated two-feldspar boundary curve, and in plot (*b*) (curve 2) represents the quartz-feldspar and two-feldspar boundary curves for composition $(Ab\text{-}Or\text{-}Q)_{97}An_3$ (at 1-kbar water vapor pressure), both after *James and Hamilton* [1969]. Curve labeled (1) in plot (*b*) is after *Tuttle and Bowen* [1958] (also for 1 kbar).

mental work of *Watson* [1979], which shows that zircon crystallization is inhibited in peralkaline liquids, supporting the petrographic observations of the absence of zircon in the comendites. This may also explain the enrichment of Y and Th in these peralkaline magmas.

The comendites also exhibit enrichments of Rb and Pb (and probably also such elements as Ga, Be, and U, for which only limited data are available; see *Ewart et al.* [1976]). In contrast, extreme depletions are observed for Ba, Sr, Eu, Ni, Cr, V, Mg, Mn, Ca, and P.

MINERALOGY

Introduction

The following characteristic phenocryst assemblages are observed:

Rhyolites. (a) Sodic plagioclase + sanidine + quartz + Fe-biotite + allanite ± ilmenite ± titanomagnetite. (b) Sanidine + quartz + fayalite + ferrohedenbergite + chevkinite + ilmenite ± titanomagnetite. (c) Sodic plagioclase + quartz + sanidine + ferrohypersthene + ilmenite.

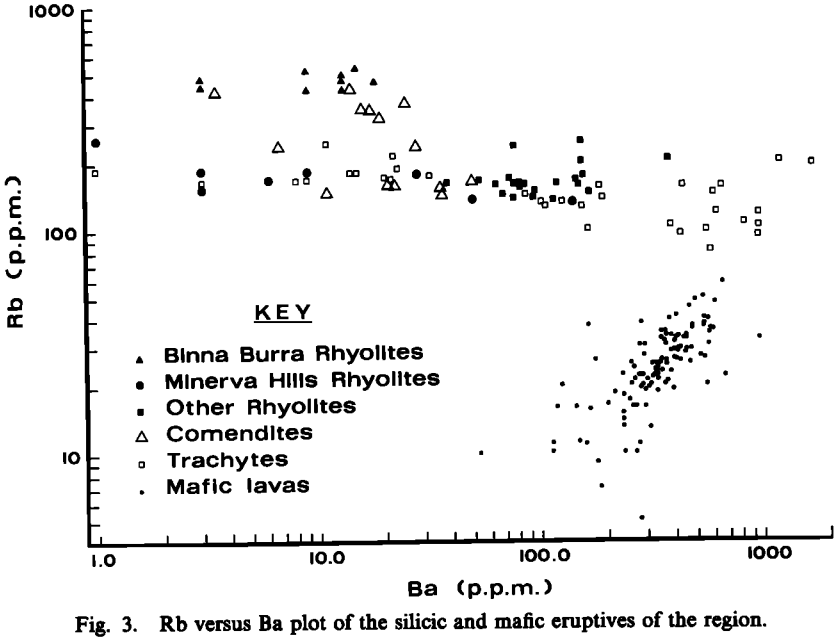

Fig. 3. Rb versus Ba plot of the silicic and mafic eruptives of the region.

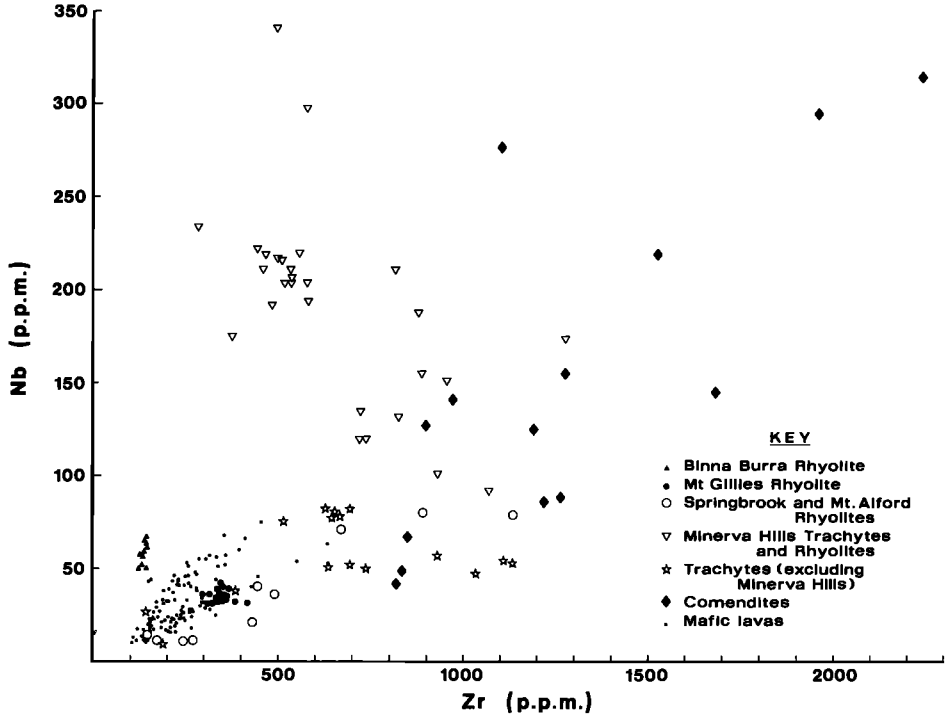

Fig. 4. Zr versus Nb plot of the silicic and mafic eruptives of the region.

Nonperalkaline trachytes. (a) Sanidine + sodic plagioclase + Fe-olivine + ferroaugite + titanomagnetite ± ilmenite. (b) Sanidine-anorthoclase + ferroaugite ± Fe-olivine + titanomagnetite ± ilmenite. (c) Sanidine + hastingsitic amphibole + allanite + ilmenite + titanomagnetitie ± fayalite ± ferrohedenbergite.

Dacites. Plagioclase + augite + ferropigeonite + ilmenite.

Comendites. (a) Phenocrysts: Ca-poor anorthoclase-sanidine ± quartz ± ferrohedenbergite (zoned to aegirine-augite) ± ilmenite. (b) Groundmass: Ca-poor anorthoclase-sanidine + quartz ± aegirine + fluorarfvedsonite ± aenigmatite ± ilmenite.

The silicic magmas from this province were erupted with relatively low phenocryst contents (<10%), although some variation is found, as illustrated in Figure 5 (see also Table 1). No systematic overall differences are apparent between the trachytes, rhyolites, and comendites in their volume percent phenocrysts.

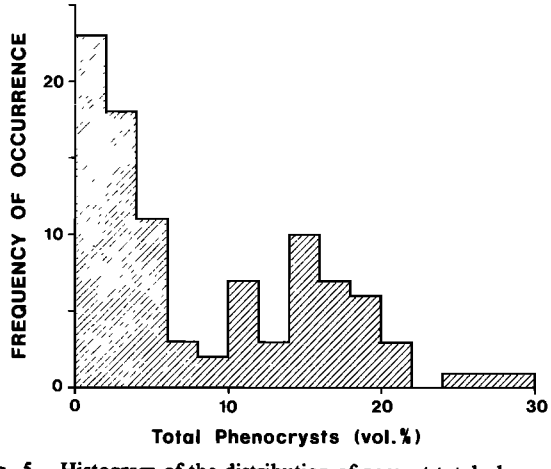

Fig. 5. Histogram of the distribution of percent total phenocrysts in the silicic eruptives (including peralkaline and nonperalkaline types).

Feldspar Phenocrysts

A. Nonperalkaline eruptives. Individual specimens may contain coexisting plagioclase + sanidine, calcic anorthoclase + sanidine, sanidine, calcic anorthoclase zoned to sanidine, or rarely, plagioclase + anorthoclase + sanidine. Compositional relations are thus complex. Extensive chemical zoning occurs in both plagioclase and the alkali feldspars, usually amounting to at least 20 mol. %; the plagioclases and sanidines are zoned to more sodic rims, while the calcic anorthoclase phenocrysts are commonly zoned toward sanidine rims (varying from Or_{25-50}). In certain of the lavas, cores of sodic plagioclase are enclosed by sharply defined zones of sanidine.

Composite plots of the feldspar compositions (microprobe analyses) occurring within the microsyenites, trachytes, and rhyolites are presented in Figure 6. The trachytic feldspar phenocrysts exhibit extensive ternary solid solution, which decreases somewhat in the most siliceous trachytes. Calcic anorthoclase is characteristic of the less siliceous trachytes, whereas the more siliceous trachytes contain a much wider spectrum of compositions, which extend from andesine through to sanidine (Or_{65}). The rhyolitic feldspars are equally variable. The Minerva Hill type is dominated by anorthoclase-sanidine, with rare occurrences of a primary but unusually sodic plagioclase (averaging $An_{6.5}Or_{8.7}$). The Mt. Gillies rhyolites contain almost exclusively sanidine, which occasionally contains cores of corroded plagioclase. The Binna Burra and the hypersthene rhyolites contain coexisting plagioclase and sanidine, the latter rhyolite type having generally more calcic plagioclases.

B. Peralkaline eruptives. Composite plots of the feldspars (Figure 7) in these magmas reveal that Ca-poor anorthoclase-sanidine is the only type found, although considerable compo-

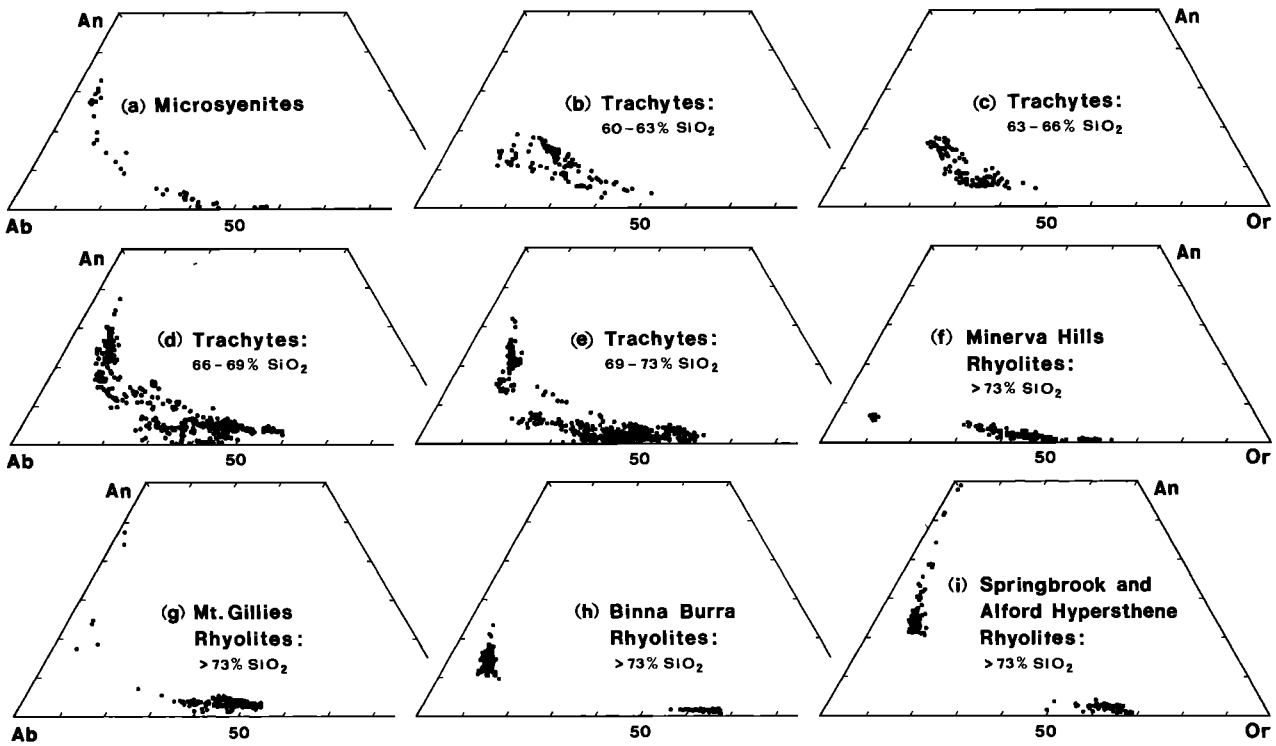

Fig. 6. Composite plots of phenocryst feldspar compositions (mol. %), based on microprobe data, occurring within the microsyenites, trachytes (sequentially subdivided according to total rock silica contents), and rhyolite types.

sitional variation is apparent, that can be broadly correlated with the whole rock normative Ab/Or ratios (Figure 2*b*). Thus the feldspars in the siliceous comendites tend to be more potassic (Or_{37-45}) than those occurring in the less siliceous peralkaline magmas (Or_{22-45}).

Pyroxenes and Olivines

Four distinct pyroxene occurrences are recognized, as follows: (a) phenocrysts of ferroaugite-ferrohedenbergite (± fayalitic olivine); (b) phenocryst ferrohypersthene; (c) phenocryst ferropigeonite (± ferrohypersthene); and (d) ferrohedenbergite-aegirine solid solution series occurring as groundmass phases within the peralkaline extrusives.

In addition, magnesian orthopyroxene, augite, and olivine phases are found in a dacite flow (hybrid), and very rarely in the hypersthene rhyolites, and are clearly xenocrystal.

Figure 8 illustrates the pyroxene compositions found within the trachytes, the pyroxene-bearing rhyolites, and a hybrid dacite. It is clear that these anorogenic silicic magmas are characterized by the development of extreme Fe-enrichment in their phenocryst pyroxenes and olivines, with ferroaugite-ferrohedenbergite being the dominant pyroxene in the nonperalkaline magmas (Table 2). Ferrohypersthene (extending to Fs_{75}) occurs as the characteristic ferromagnesian phenocryst phase in the Springbrook rhyolite and also within isolated rhyolites from the Mt. Alford and Mt. Gillies groups (Table 3). Ferropigeonite occurs as a distinctive phenocryst phase in a unique hybrid dacite flow and very rarely in samples of the Mt. Gillies ferrohedenbergite-fayalite rhyolites. The conditions of precipitation of ferropigeonite are unknown, as it does not occur with coexisting Fe-Ti oxides in these Queensland lavas.

Na-enrichment in the pyroxenes. The extent of Na-enrichment in the pyroxenes from the peralkaline magmas, nonperalkaline magmas, and intrusive microsyenites is compared in Figure 9. It is clear that Na-enrichment is relatively minor in the nonperalkaline magmas, whereas the peralkaline magmas are characterized by complete solid solutions between pure aegirine and ferrohedenbergite, nearly always as groundmass phases. It is therefore evident that Na-enrichment in these pyroxenes occurs only after extreme Fe-enrichment has been attained. A notable feature of the chemistry of the sodic pyroxenes is their relatively high ZrO_2 (Table 4), which is, however, very variable even within the one sample.

Possible factors leading to Na-enrichment in pyroxenes during fractional crystallization can be approached by considering the following two exchange reactions:

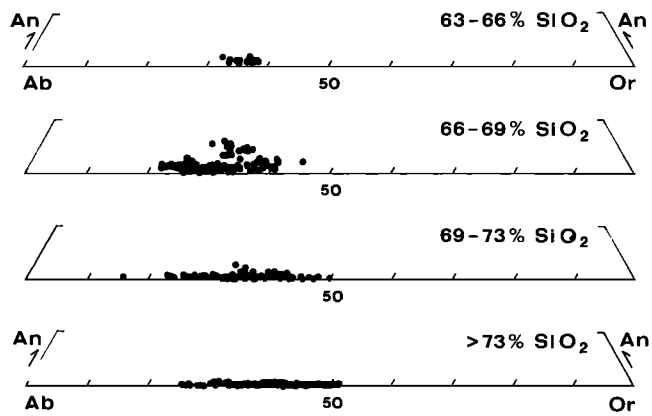

Fig. 7. Composite plots of phenocryst feldspar compositions (mol. %), based on microprobe data, occurring within the peralkaline extrusives (subdivided according to total rock silica contents).

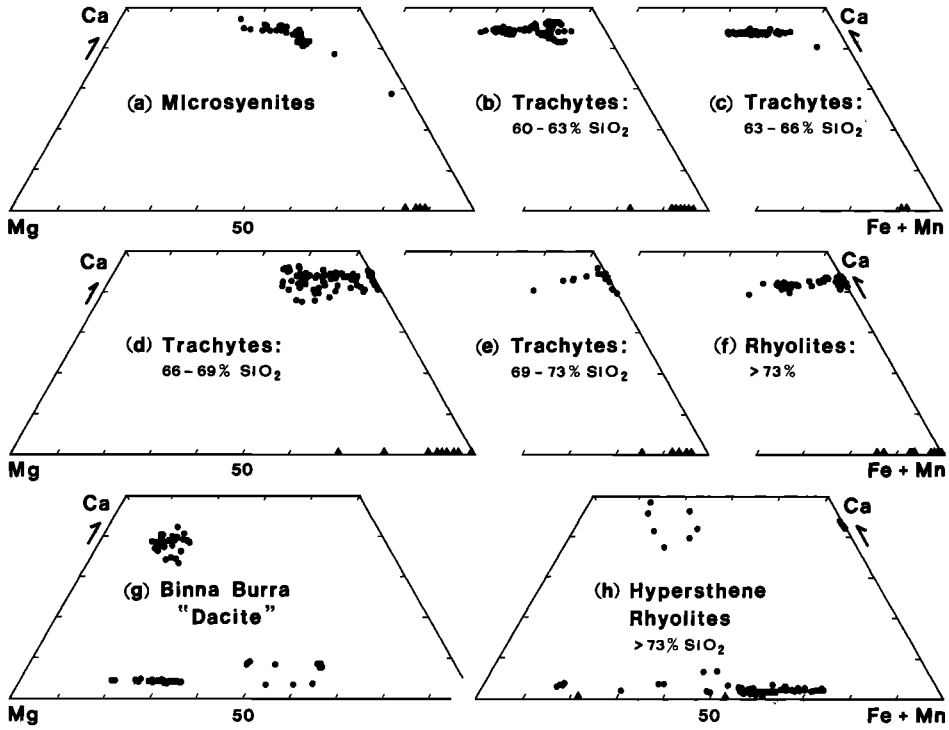

Fig. 8. Composite plots of phenocryst pyroxenes (solid dots) and olivines (solid triangles), based on microprobe data, occurring within the microsyenites, trachytes, and various rhyolite types. Trachyte data subdivided according to total rock silica contents. Atomic percent.

$$NaAlSi_3O_8 + \tfrac{1}{4}O_2 + \tfrac{1}{2}Fe_2SiO_4 = \tfrac{1}{2}Al_2O_3 + NaFeSi_2O_6 + 1\tfrac{1}{2}SiO_2$$

albite gas fayalite liquid acmite (pyroxene S.S.) quartz

$$NaAlSi_3O_8 + \tfrac{1}{2}Fe_2O_3 = \tfrac{1}{2}Al_2O_3 + NaFeSi_2O_6 + SiO_2$$

albite hematite (ilmenite S.S.) liquid acmite (pyroxene S.S.) quartz

These reactions can be applied in principle to the nonperalkaline rhyolites of the region (containing alkali feldspar, calcic pyroxenes, ilmenite, quartz, and fayalite), to the microsyenites, and also to the syenites of the Mt. Warning complex [*Ewart et al.*, 1976]; these microsyenites and syenites show late-stage Na-enrichment of the constituent calcic pyroxenes in the presence of quartz, alkali feldspar, ilmenite, and fayalite.

The first reaction suggests that $a_{NaFeSi_2O_6}^{pyroxene}$ is likely to be sensitive to changes of $a_{Al_2O_3}^{liquid}$ and fO_2 (and also $a_{SiO_2}^{liquid}$). This is illustrated in Figure 10*a* (modified from *Ewart et al.*[1976],) assuming $a_{SiO_2}^{quartz} = a_{Fe_2SiO_4}^{olivine} = 1$, and $a_{NaAlSi_3O_8}^{feldspar} = 0.75$, with the calculations repeated for the three stated oxygen buffers. The results suggest that for a given $a_{Al_2O_3}^{liquid}$ and T, increasing fO_2 favors increasing $a_{NaFeSi_2O_6}^{pyroxene}$, whereas if crystallization follows a constant fO_2 buffer, then decreasing $a_{Al_2O_3}^{liquid}$ favors increasing $a_{NaFeSi_2O_6}^{pyroxene}$.

TABLE 2. Selected Averaged Microprobe Analyses of Phenocrystal Ferroaugites and Ferrohedenbergites From Rhyolites and Trachytes

	1	2	3	4	5	6	7	8
SiO_2	50.12	49.37	49.25	48.97	47.30	48.19	47.54	48.28
TiO_2	0.58	0.49	0.54	0.29	0.38	0.43	0.30	0.32
Al_2O_3	1.13	1.15	0.85	0.49	0.63	0.90	0.83	0.24
Fe_2O_3*	1.33	1.17	1.46	0.57	0.25	—	2.50	0.92
FeO*	19.27	20.37	22.13	25.50	30.93	30.25	28.17	30.12
MnO	0.69	0.71	0.81	0.66	0.78	0.75	1.11	0.81
MgO	6.90	5.87	4.84	4.12	0.21	0.20	0.03	0.03
CaO	20.26	19.91	19.99	18.63	18.46	19.43	19.35	18.04
Na_2O	0.48	0.52	0.47	0.29	0.25	0.38	0.64	0.84
Σ	100.75	99.56	100.35	99.61	99.19	100.53	100.47	99.60

1, 3—Fraser Island trachytes (samples 36367 and 38986); 2—Glass Houses trachyte (sample 38669)†; 4, 5—Mt. Gillies rhyolites (33030, 9570); 6—Mt. Flinders trachyte (38702); 7—Minerva Hills trachyte (38739c); 8—Mt. Alford rhyolite (38710c).

* Calculated on basis of O = 6; cations = 4.

† Sample numbers listed in Tables 2–8 refer to collections in Department of Geology, University of Queensland.

TABLE 3. Selected Averaged Microprobe Analyses of Phenocrystal Orthopyroxenes (1–3) and Ferropigeonite (4) From Rhyolites

	1	2	3	4
SiO_2	48.30	48.12	49.39	49.95
TiO_2	0.23	0.19	0.53	0.55
Al_2O_3	0.94	0.36	0.89	0.74
Fe_2O_3*	2.46	0.38	—	2.11
FeO*	34.18	40.64	35.28	26.87
MnO	0.69	0.80	0.75	0.72
MgO	12.08	8.37	12.57	15.50
CaO	0.71	0.91	0.54	3.03
Na_2O	0.14	0.14	0.04	0.24
Σ	99.73	99.81	99.99	99.71

1—Springbrook rhyolite (sample 31052); 2—Mt. Alford rhyolite (38990); 3, 4—Mt. Gillies rhyolites (samples 33033, 33037).
* Calculated on basis of O = 6; cations = 4.

Figure 10*b* illustrates the relationship between $a_{Al_2O_3}^{liquid}$ and $a_{NaFeSi_2O_6}^{pyroxene}$ as calculated from the second reaction and utilizing estimates of $a_{Al_2O_3}^{liquid}$ for the comendites and the Mt. Gillies metaluminous rhyolites from the reactions and data listed in *Ewart et al.* [1976]. It is further assumed that $a_{Fe_2O_3}^{ilmenite} = 0.03$, with the activities of the other components as above. The relatively higher $a_{NaFeSi_2O_6}^{pyroxene}$ calculated for the comenditic pyroxenes is thus consistent with observation, although it should be noted that reaction (2) is not strictly applicable to those comendites not containing ilmenite.

In summary, the reactions considered suggest that the progressive development of decreasing $a_{Al_2O_3}^{liquid}$ during the petrogenesis of certain groups of the southern Queensland silicic magmas will result in pyroxene Na-enrichment; this presumably must represent an advanced stage of fractionation of these magmas. The stage at which Na-enrichment actually occurs, however, is likely to be controlled by additional parameters such as fo_2 and $a_{SiO_2}^{liquid}$ (i.e., is dependent on the mineral assemblages present). In these Queensland silicic magmas it will be subsequently shown that crystallization occured at an fo_2 below the QFM buffer, which is evidently consistent with the development of pyroxene Na-enrichment only in extreme Fe-enriched pyroxene compositions.

Olivines. Compositions range from approximately Fa_{70} to pure fayalite, most analyzed compositions being between Fa_{90} and Fa_{100}. Olivines occur throughout the trachyte-rhyolite compositional range only as phenocryst phases, but are very rare in comendites.

Amphiboles and Biotites

Three distinct occurrences of amphibole (Figure 11 and Table 5) can be recognized as follows, using the nomenclature of *Ernst* [1968]: (a) pure Fe-hastingsite, occurring as phenocrysts only in certain of the Minerva Hills trachytes. This amphibole shows little chemical variation. A typical formula is $(Ca_{1.77}Na_{0.73}K_{0.34})$ $(Fe_{4.56}Mn_{0.10}Ti_{0.34}Al_{0.10})$ $(Al_{1.63}Si_{6.37})$ $(OH_{1.71}F_{0.29})$; (b) fluorarfvedsonite, characteristic as a groundmass phase within the peralkaline extrusives. They are strongly Mg depleted and contain significant ZrO_2; (c) intermediate Na-Ca amphiboles, classified as ferrorichterites, oc-

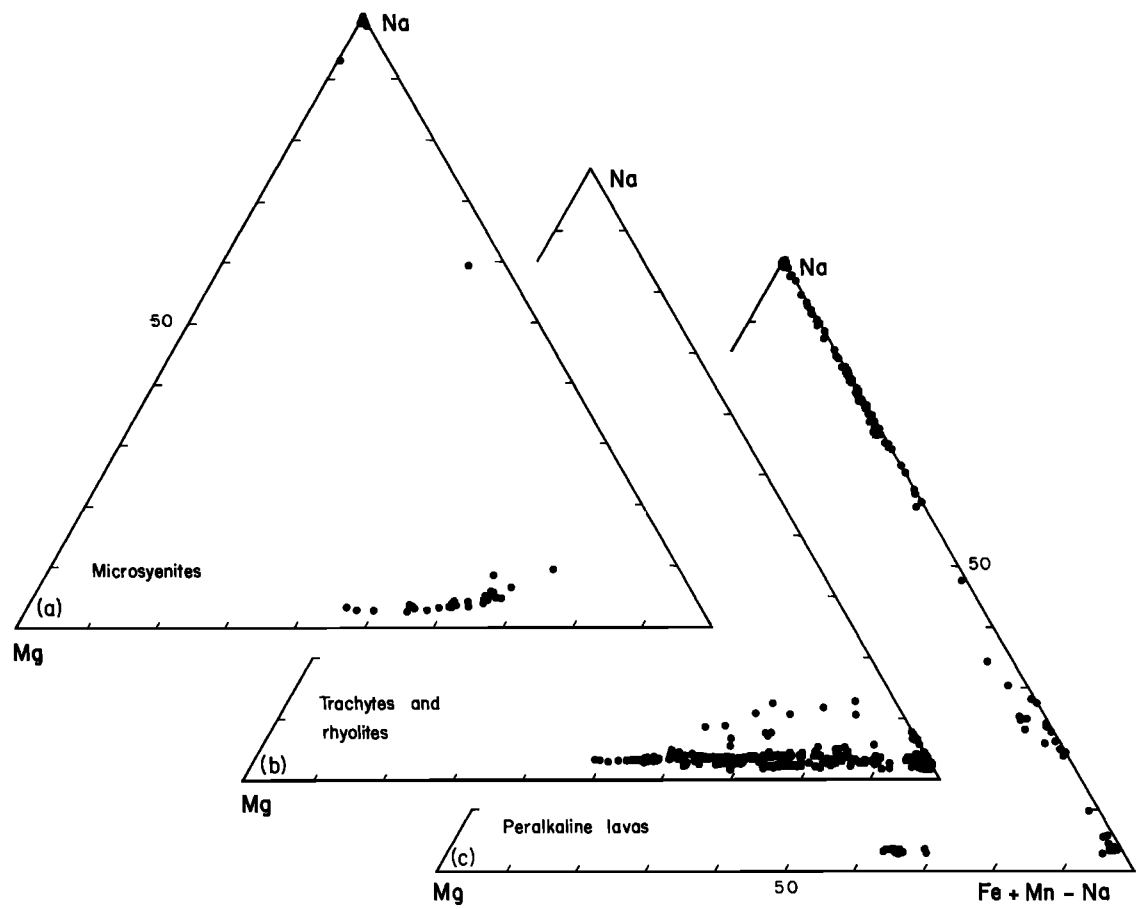

Fig. 9. Composite plots, based on microprobe data, comparing the levels of Na enrichment within the pyroxenes occurring within the microsyenites, trachytes and rhyolites, and peralkaline extrusivs. Atomic percent.

TABLE 4. Selected Averaged Microprobe Analyses of Groundmass Sodic Pyroxenes From Peralkaline Trachytes and Comendites

	1	2	3	4	5	6	7
SiO_2	51.59	50.80	52.04	52.80	51.58	48.64	51.76
TiO_2	1.43	0.81	3.58	1.16	0.45	0.21	1.18
ZrO_2	2.92	2.85	0.56	0.77	2.43	0.49	0.18
Al_2O_3	0.23	0.17	0.22	0.47	1.01	0.68	0.34
Fe_2O_3*	22.43	18.50	25.87	29.01	24.28	8.52	29.79
FeO*	6.45	11.04	3.87	1.72	5.79	20.03	1.89
MnO	0.36	0.63	0.35	0.15	0.26	1.01	0.55
MgO	—	0.01	—	—	0.03	0.54	0.06
CaO	2.61	5.35	0.43	0.93	2.61	16.54	1.54
Na_2O	11.69	9.56	13.08	13.20	11.59	3.31	12.55
Σ	99.71	99.72	99.99	100.22	100.02	99.96	99.85

1, 2—Glass House Mountains comendite and trachyte (38672, 38605); 3—Binna Burra comendite (15779); 4—Mt. Alford comendite (538); 5, 6—Warrumbungle Mountains trachyte (38993), aegirine and aegirine augite; 7—Nandewar Mountains trachyte (39000).

* Calculated on basis of O = 6; cations = 4.

curring as interstitial phases within the intrusive microsyenites. These amphiboles are more magnesian than the above-described amphiboles, in conformity with the associated more magnesian pyroxenes in the microsyenites.

Biotite is a very rare phenocryst phase in the silicic magmas, occurring in certain rhyolites (Figure 12; Table 5). The compositions are again very Fe-rich and approach annite. F is present, but has probably been reduced by posteruption hydroxyl exchange. Coexisting Fe-Ti oxides are absent in these biotite-bearing rhyolites.

Fe-Ti Oxides

Nonperalkaline eruptives. Within the lower SiO_2 trachytes (<66%), titanomagnetite (ulvöspinel 40–75 mol. %) is the sole oxide phase (including phenocrysts and groundmass). Coexisting, discrete phenocryst titanomagnetite and ilmenite do occur in some, but by no means all, of the more siliceous trachytes; only in the vitreous or extremely fine-grained lavas are the oxides homogeneous. These spinel phases are characterized chemically (Table 6) by very low Mg, V, and Cr levels, and variable Mn.

Within the rhyolites, there is an almost complete absence of a phenocryst spinel phase; the only oxide phase is normally an almost stoichiometric phenocryst ilmenite (Table 7). One exception is found in a single Binna Burra rhyolite flow that contains trace quantities of almost pure ulvöspinel (Usp. 95–99 mol. %; see *Ewart et al.* [1977]).

Peralkaline eruptives. Fe-Ti oxides are commonly absent,

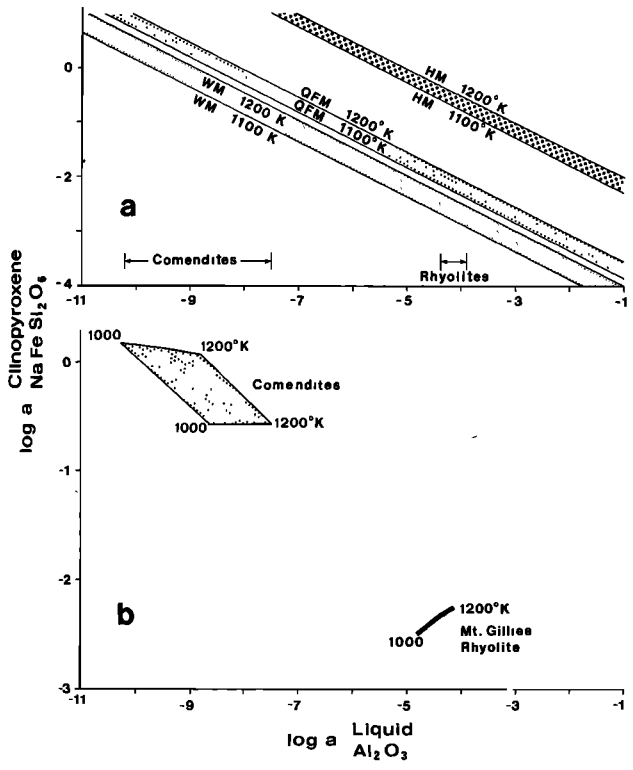

Fig. 10. Schematic plots illustrating the calculated relationships between $a_{NaFeSi_2O_6}^{clinopyroxene}$ and $a_{Al_2O_3}^{liquid}$, utilizing reactions (l) (Figure 10*a*) and (s) (Figure 10*b*) given in the text. In Figure 10*a* the data are plotted for the three fo_2 buffers, each calculated at 1 bar for two temperatures (1100° and 1200°K). Based on thermodynamic data from *Stull and Prophet* [1971], *Nicholls and Carmichael* [1969], *Marsh* [1975], and *Robie et al.* [1978]. Estimates of $a_{Al_2O_3}^{liquid}$ for the rhyolitic and comenditic magmas is based on reactions given in *Ewart et al.* [1976]. See text for further details.

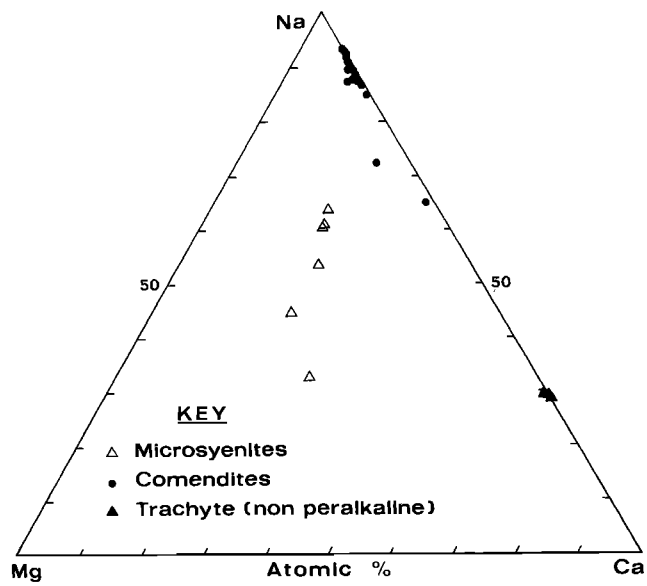

Fig. 11. Plot of amphibole compositions, in terms of Mg, Na, and Ca (atomic %), from microsyenites, trachytes, and comendites. Microprobe data.

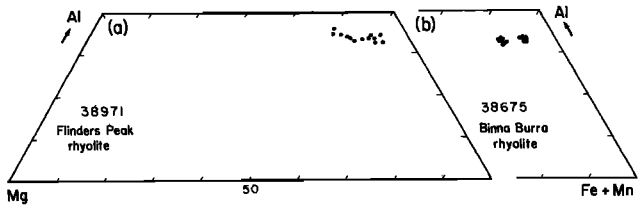

Fig. 12. Compositions of phenocryst biotites, expressed in terms of Al, Mg, and Fe + Mn (atomic %), from two rhyolites. Microprobe data.

but where present they are most frequently represented by ilmenite in the comendites, or less commonly a titanomagnetite in the peralkaline trachytes. In two comendites, disequilibrium-coexisting Fe-Ti oxide phases have been observed. The oxides in the peralkaline magmas are highly depleted in Mg but may contain significant Zn concentrations (Table 7).

$T°C - fo_2$ data. Only relatively few estimates have been made on account of the paucity of suitable coexisting Fe-Ti oxide phases. Available data (using the *Buddington and Lindsley* [1964] geothermometer) are plotted in Figure 13, no data being available for the peralkaline magmas. Equilibration temperatures, for which specific estimates have been determined, lie between 885° and 980°C, with a single microsyenite giving 840°C. All data plot between the QFM and WM buffer curves. It has been previously argued [*Ewart et al.*, 1976] that the presence within the rhyolites of almost stoichiometric ilmenite without a coexisting spinel phase indicates their equilibration at an fo_2 close to the WM buffer, and analogy was drawn with the Skaergaard intrusion [Lindsley et al. 1969]. Thus, these Queensland silicic magmas are interpreted to be relatively reduced, which is consistent with the occurrence of very Fe-enriched ferromagnesian phenocryst silicate assemblages.

Trace Microphenocryst Phases

Chevkinite. This rare-earth titanosilicate is restricted to the ferrohedenbergite-fayalite rhyolites in which it occurs as nonmetamict, euhedral, deep-brown, prismatic microphenocrysts; it may occur as discrete crystals or as inclusions within pyroxene. Modal abundances are estimated to be ≤0.001%. Identification as chevkinite has been confirmed by X ray diffraction, as discussed by *Izett and Wilcox* [1968]. These authors also describe the occurrence of chevkinite in various Cenozoic ash deposits in the western United States. Partial microprobe analyses are presented in Table 8 of two chevkinites occurring in Mt. Gillies and Mt. Alford rhyolite samples. The most notable feature is the huge enrichment in LREE together with significant concentrations of Th, Zr, Nb, and Zn. The compositions are generally similar to those summarized by *Vlasov* [1966].

Allanite. This rare-earth calcium aluminosilicate occurs as discrete, nonmetamict, euhedral, stubby prismatic to equant microphenocrysts. It is found only in those relatively rare rhyolites and trachytes of the region containing Fe-biotite or hastingsitic amphibole. Three of these amphibole-allanite-bearing trachytes give Fe-Ti oxide equilibration temperatures of 920°–980°C, which are significantly higher than the upper limit of 763°C reported for allanite occurrence in the Bishop Tuff by *Hildreth* [1979]. Partial microprobe analyses of selected allanites are presented in Table 8 and are closely comparable to those presented by *Hildreth* [1979]. They exhibit extreme LREE enrichment, with significant Th contents.

Zircon. Euhedral prismatic microphenocrysts of zircon are ubiquitous in the nonperalkaline trachytes and rhyolites but, as previously discussed, are conspicuously absent from the peralkaline lavas. Microprobe analyses of selected zircons (Table 8) indicate HREE enrichment (based on Y data), significant Fe, and Zr/Hf ratios that most commonly range between 41 and 48 but decrease to 26 in zircon from the Binna Burra rhyolite. These Zr/Hf ratios correlate with the available data for the whole rocks, which range from 34 to 45 for most rhyolites, 44 to 50 for the comendites, but decrease to 24 in the most highly fractionated Binna Burra rhyolite.

PETROGENESIS

The anorogenic volcanic suite described is strongly bimodal. *Ewart et al.* [1980] have discussed the possible development of the mafic magmas, concluding that although originally mantle derived, these have undergone lower-crust fractionation within the region of the crust-mantle boundary.

TABLE 5. Selected Averaged Microprobe Analyses of Biotites (1, 2), Calcic Amphiboles (3–5), and Groundmass Arfvedsonites (6–11)

	1	2	3	4	5	6	7	8	9	10	11
SiO_2	34.63	34.13	38.43	38.58	49.32	49.25	49.45	49.30	49.15	48.34	48.41
TiO_2	5.64	4.77	2.65	2.76	2.27	0.58	0.60	0.85	1.08	0.90	1.28
ZrO_2	—	—	—	—	—	1.33	0.78	0.56	0.32	0.77	0.55
Al_2O_3	12.59	12.68	8.39	8.94	0.63	0.66	0.47	0.53	0.38	0.47	0.73
FeO*	29.98	32.69	33.33	33.00	28.61	34.00	34.15	34.27	34.05	33.28	33.25
MnO	0.22	0.17	0.68	0.65	0.55	1.19	0.81	1.16	0.68	1.68	0.89
MgO	2.90	2.01	—	0.05	3.65	0.05	0.06	0.09	—	0.15	0.66
CaO	—	—	9.69	10.02	4.68	2.38	1.55	2.00	1.18	1.81	3.76
Na_2O	0.45	0.46	2.16	2.27	6.21	7.59	7.90	7.86	8.14	7.97	6.70
K_2O	8.51	8.55	1.48	1.63	1.27	1.35	1.38	1.26	1.35	1.17	1.27
F	0.30	0.77	0.49	0.53	n.d.	2.17	2.32	2.44	2.62	2.78	n.d.
Σ†	95.09	95.91	97.09	98.21	97.19	99.64	98.49	99.29	97.85	98.15	97.50

1—Flinders Peak rhyolite (sample 38971), phenocrysts; 2—Binna Burra rhyolite (38675), phenocrysts; 3, 4—Hastingsite, Minerva Hills trachytes (samples 38739a and b), phenocrysts; 5—Ferrorichterite, microsyenite (38979), interstitial phase; 6, 7, 8—Glass Houses comendites (samples 38672, 38606, 38605); 9—Binna Burra comendite (15779); 10—Warrumbungle Mountains peralkaline trachyte (38994); 11—Nandewar Mountains peralkaline trachyte (39000).

* Total Fe as FeO.

† Less 0 for F; n.d., no data.

TABLE 6. Selected Averaged Microprobe Analyses of Titanomagnetite Phenocryst Phases Occurring in Trachytes and Rhyolites

	1	2	3	4	5	6	7
SiO_2	0.09	0.09	0.13	0.27	0.07	0.21	0.07
TiO_2	19.24	20.91	21.13	21.44	22.95	22.60	22.11
Al_2O_3	0.58	0.07	0.16	0.94	0.98	1.28	0.72
V_2O_3	—	—	—	—	0.04	—	0.17
Cr_2O_3	0.01	0.01	—	—	0.02	0.04	0.05
Fe_2O_3*	31.32	28.31	27.03	24.31	23.96	22.34	25.23
FeO*	48.12	48.10	49.69	50.01	51.77	50.91	50.94
MnO	0.66	0.63	0.86	0.72	0.62	1.13	0.45
MgO	0.12	—	0.02	0.04	0.12	—	0.14
CaO	—	—	—	—	—	0.06	—
ZnO	0.37	2.13	n.d.	—	0.38	n.d.	0.30
NiO	—	—	—	—	—	—	—
Σ	100.51	100.26	99.02	97.74	100.91	98.57	100.18
Mol.% Usp	54.6	59.7	61.0	62.8	64.3	65.2	62.5

1, 2—Glass Houses trachytes (38669, 38668); 3—Fraser Island trachyte (38986); 4, 5—Flinders Peak trachytes (38702, 28678); 6—Minerva Hills trachyte (38739a); 7—Mt. Gillies rhyolite (33030).
* Calculated on ulvospinel basis; n.d., no data.

A number of possible paths of evolution may thus be appropriate for the silicic magmas. These include: (a) fractional crystallization from parental basalts; (b) as previously, but with subsequent modification by crustal assimilation/equilibration either during or after fractionation; (c) crustal melting with or without subsequent crystal fractionation. The problem is complicated by the presence of peralkaline and nonperalkaline eruptives in the region, often occurring within the same eruptive center.

The following lines of evidence are relevant to these alternatives:

(a) Within those eruptive centers containing silicic and mafic lavas, the silicic eruptives are always subordinate in volume by at least a 1:7 proportion.

(b) Trace element abundance patterns provide convincing evidence for fractional crystallization control of the rhyolite and comendite chemistries especially. Examples are the extreme depletions of Sr, Ba, V, Mg, P, Cr, and Eu together with the variable enrichment of Rb, U, Th, Nb, Y, and Zn, etc. The trachytes exhibit these trace element patterns to lesser degrees, favoring an interpretation that they represent erupted magmas at progressively less advanced stages of the fractionation processes. Nevertheless, discontinuities in the trace element abundances do occur between the silicic and the exposed mafic lavas.

(c) Normative compositions of the trachytes and rhyolites plot close to the two-feldspar boundary curve and the quartz-feldspar 'minima' in the $(Ab\text{-}Or\text{-}Q)_{97}An_3$ phase system, which again is consistent with crystal-liquid fractionation.

(d) The continuity of phenocryst compositions through the trachyte-rhyolite compositions, especially notable within the pyroxenes and olivines that extend to the pure Fe end-members. An analogy can be drawn here, for example, with the late stages of fractionation of the Skaergaard intrusion [*Brown and Vincent*, 1963].

(e) Fe-Ti oxide equilibration temperatures of the trachytes and rhyolites range from 885° to 980°C. Application of the olivine-clinopyroxene geothermometer [*Powell and Powell*, 1974] suggests temperatures (1 bar) of 890°–1100°C, averaging 976°C for the trachytes and 942°C for the rhyolites. These increase to 920–1130°C if 5 kbar is assumed. Finally, *Ewart et al.* [1976] estimated equilibration temperatures of approximately 900°–1000°C for the Springbrook hypersthene rhyolites, based on calculations of the ilmenite-orthopyroxene exchange reaction. Although varying in their likely reliability, all three temperature estimates are consistent in indicating rel-

TABLE 7. Selected Averaged Microprobe Analyses of Ilmenite Phenocryst Phases Occurring in Trachytes, Rhyolites, and Comendites

	1	2	3	4	5	6	7	8	9	10
SiO_2	—	—	—	—	0.12	—	—	—	—	—
TiO_2	50.23	50.47	48.69	48.24	51.18	51.54	51.44	50.96	50.52	51.57
Al_2O_3	0.02	0.06	0.03	0.08	—	0.06	0.09	0.04	0.04	0.03
V_2O_3	—	—	—	—	—	0.02	0.27	—	—	—
Cr_2O_3	—	—	0.05	—	—	0.01	0.04	—	—	—
Fe_2O_3*	5.00	4.62	6.61	6.09	2.20	0.83	2.39	2.59	3.53	1.38
FeO*	43.86	44.17	42.11	31.29	45.19	45.19	43.24	44.95	43.24	44.39
MnO	1.14	0.73	1.59	11.90	0.96	0.73	0.48	0.72	1.06	1.14
MgO	—	0.22	—	—	—	0.17	1.39	0.01	—	—
ZnO	0.17	0.09	n.d.	n.d.	n.d.	0.13	0.06	0.15	1.27	0.94
NiO	—	—	—	—	—	—	—	—	—	—
Σ	100.42	100.36	99.08	97.60	99.65	98.68	99.40	99.42	99.65	99.45
Mol.%R_2O_3	4.8	4.5	6.5	6.1	2.1	0.9	2.7	2.5	3.4	1.4

1—Glass Houses trachyte (38668); 2—Flinders Peak trachyte (38678); 3, 4—Minerva Hills trachytes (38739a; 38739b, single grain); 5—Mt. Alford rhyolite (38710c); 6—Binna Burra rhyolite (38675); 7—Springbrook rhyolite (38679); 8—Mt. Gillies rhyolite (9570); 9—Glass Houses comendite (38606); 10—Binna Burra comendite (15779).
* Calculated on R_2O_3 basis; n.d., no data.

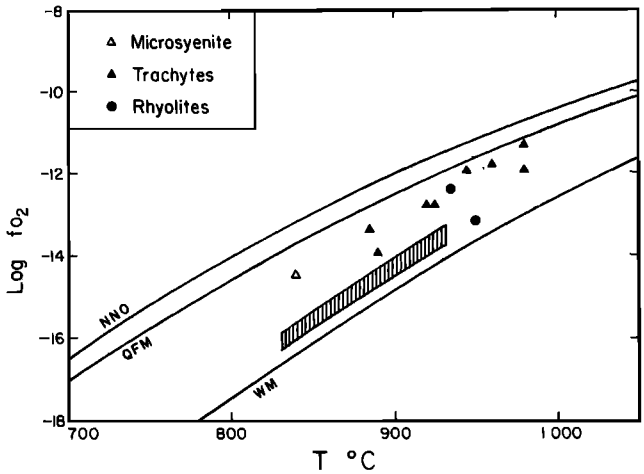

Fig. 13. T(°C)-fo_2 data deduced from coexisting Fe-Ti oxides [*Buddington and Lindsley*, 1964], from a microsyenite, trachytes, and rhyolites. The hatched area is the possible region of equlibration of a single Binna Burra rhyolite sample, in which the Fe-Ti oxides do not give a unique solution [*Ewart et al.*, 1977]. Three buffer curves are plotted (1 bar), representing quartz-fayalite-magnetite, nickel-nickel oxide, and wüstite- magnetite [after *Eugster and Wones*, 1962; *Hewitt*, 1978].

atively high temperatures of phenocryst equilibration, further implying that the magmas were strongly water undersaturated during phenocryst equilibration. This is again consistent with the general paucity of pyroclastics, the paucity of hydrous phenocryst phases, the relatively reducing fo_2 buffer conditions estimated to have existed during phenocryst equilibration, and the occurrence of extremely Fe-enriched phenocryst compositions.

Application of least squares linear mixing calculations [*Bryan et al.*, 1969] have been undertaken to test possible combinations of parental magmas plus mineral compositions and assemblages that can in principle account for the production of specific silicic magma compositions by crystal fractionation. Theoretically, it has been found feasible to derive the comendites, trachytes, and rhyolites from various silica-saturated and undersaturated hawaiite magma compositions from the region [e.g., *Ross*, 1977; *Ewart et al.*, 1977]. The mineral assemblages normally required are plagioclase + olivine + aluminous augite + apatite ± titanomagnetite ± ilmenite ± alkali feldspar. Calculated weight fractions of derivative rhyolitic or comenditic liquids range between 0.05 and 0.18, with plagioclase being the most important subtracted mineral phase (amounting to between 0.4 and 0.5 weight fraction), except where alkali feldspar is also involved. Little difference is noted in these calculations as to the proportions or types of minerals that can produce the peralkaline or nonperalkaline derivatives, with the notable exception of those solutions involving alkali feldspar. This mineral phase always comprises a proportionately higher weight fraction in the feasible solutions involving the peralkaline derivatives. Trace element data do not, however, fully support these least squares mixing calculations. For example, considering the Binna Burra rhyolites, which exhibit the most extreme trace element fractionation abundance patterns in the region, it is possible to readily account for the almost complete Sr depletion (caused by the high weight fractions of feldspar required in the calculated solutions), but it is not possible using the same (or even similar) least squares solutions, to simulate the complementary level of Ba depletion nor the observed high levels of Rb or Pb concentrations. Similar results are obtained for the more fractionated comendites, although the calculations do reproduce the high Zr concentrations. Clearly, therefore, the least squares mixing calculations are not wholly duplicating the inferred crystal fractionation processes, and the trace element data may be indicating the occurrence of additional fractionation phenomena, such as liquid-state differentiation, as advocated to account for similar trace element behavior in the Bishop Tuff [*Hildreth*, 1979]. This is, perhaps, emphasized further by the observed Eu depletion in the Binna Burra rhyolites, which

TABLE 8. Selected Averaged Microprobe Analyses of Microphenocrystal Zircon (1–5), Chevkinite (6–7), and Allanite (8–10), Occurring in Trachytes and Rhyolites

	1	2	3	4	5	6	7	8	9	10
SiO_2	32.44	32.59	31.61	32.38	32.44	19.28	18.41	30.40	30.25	30.54
TiO_2	0.16	0.05	0.05	0.12	0.05	19.58	18.63	2.95	1.72	2.41
ThO_2	0.19	0.07	0.11	0.25	0.17	1.04	0.43	0.36	0.84	0.37
ZrO_2	65.5	65.4	65.9	64.2	65.4	0.80	0.44	—	—	0.05
HfO_2	1.33	1.19	1.41	2.19	1.24	n.d.	n.d.	n.d.	n.d.	n.d.
Al_2O_3	—	—	—	—	—	0.68	0.14	11.47	12.88	12.25
La_2O_3	—	0.02	—	0.01	—	12.6	14.3	8.0	5.9	7.5
Ce_2O_3	0.07	0.03	0.02	0.03	—	20.8	22.2	12.2	11.7	12.2
Nd_2O_3	0.03	0.03	0.03	0.04	—	8.2	7.6	4.0	4.9	4.2
Y_2O_3	0.15	0.33	0.50	0.40	0.41	0.56	0.43	0.19	0.55	0.19
Nb_2O_5	—	—	—	—	—	0.73	0.94	0.05	—	0.04
FeO*	0.30	0.26	0.15	0.45	0.64	9.87	11.04	17.35	16.27	16.63
MnO	—	—	—	—	—	0.10	0.15	0.42	0.23	0.21
MgO	—	—	—	—	—	—	—	—	0.19	0.19
CaO	—	—	—	—	—	3.50	2.64	9.37	9.45	10.18
Na_2O	—	—	—	—	—	—	0.03	0.09	0.13	0.13
F	—	—	—	—	—	0.34	0.28	0.25	0.20	0.23
Σ	100.17	99.97	99.78	100.07	100.35	98.08	97.66	97.10	95.21	97.32
Zr/Hf	42.9	48.0	40.6	25.6	46.1	—	—	—	—	—

1, 2—Mt. Gillies rhyolites (33033, 33030); 3—Mt. Alford hypersthene rhyolite (38990); 4—Binna Burra rhyolite (38675); 5—Springbrook rhyolite (31052); 6—Mt. Gillies rhyolite (33033); 7—Mt. Alford fayalite rhyolite (38710c); 8—Minerva Hills trachyte (38739c); 9—Binna Burra rhyolite (38675); 10—Finders Peak rhyolite (38971).

* Total Fe as FeO; n.d., not determined.

based on REE analyses of coexisting feldspars and total rock, is calculated to require at least 95% feldspar fractionation [*Ewart et al.* 1977].

Although the above discussion has dealt with possible fractionation processes in the development of the silicic magmas, the previous data presented cannot be readily used to evaluate crustal contributions caused by equilibration or even fusion processes. The following is a summary tabulation of available isotopic data for the various Queensland magma types [*Ewart et al.*, 1977; and unpublished data, 1981]:

	$\delta O^{18}‰$ (Feldspars)	$(^{87}Sr/^{86}Sr)_0$	$^{206}Pb/^{204}Pb$
Hawaiites, tholeiitic andesites	5.6–7.0	0.7036–0.7046	17.78–18.70
Trachytes	4.9–8.7	0.7043–0.7059	17.78–18.65
Rhyolites	6.9–10.4	0.7071–0.7086	18.40–18,68
Peralkaline lavas	6.2–10.9	0.7048–0.709	17.78–18.57

It is clear that considerable isotopic variability exists within each magma type, but a general increase in $\delta^{18}O$ and initial Sr ratios occurs with increasing silica. Although these isotope data remain to be fully interpreted, the shift of oxygen and Sr compositions certainly suggest the incorporation of some upper crustal components into the magmas either during or after their development [e.g., *Taylor*, 1980]. Moreover, the relatively unradiogenic Pb compositions occurring within certain of the lavas suggests that a moderately old and relatively U-depleted crustal component may also have been at least partially involved.

With respect to the rhyolites, it is still uncertain whether they represent original crustal melts, or are essentially fractionated from parental mafic magma. A possible approach is provided by the Zr experimental results of *Watson* [1979, p. 417], who notes that in magmas whose origins involve crustal partial fusion, their Zr abundances should be buffered at a relatively low and constant level by residual zircon. Thus the relatively lower abundances of Zr in the Binna Burra rhyolites, the hypersthene rhyolites, and to a lesser extent, the Mt. Gillies rhyolites (Table 1), may be indicative of such an origin.

SUMMARY

The following are the currently suggested interpretations of the origins and development of the various silicic extrusive units recognized in the S.E. Queensland-N.E. New South Wales region:

(a) The peralkaline magmas are considered to develop primarily by fractionation, through trachytic derivatives, from parental basaltic or hawaiitic magmas (presumably silica saturated). Isotopic data suggest some crustal equilibration, but to preserve the peralkaline chemistry, little introduction of Al_2O_3 could have occurred (which might be consistent, for example, with a mafic lower crustal wallrock).

(b) The trachytes, including the Minerva Hills trachyte-rhyolite series, are likewise interpreted as derived by fractional crystallization from a parental mafic magma. Isotopic data again indicate a degree of crustal interaction.

(c) The remaining high-silica rhyolites of the region are interpreted to represent local melts generated by partial fusion of relatively dehydrated crustal materials but subsequently modified by fractionation processes of varying intensity.

Viscosity Considerations. Emphasis has been given to the fact that the trace element abundance patterns of the silicic magmas have been controlled by fractionation processes, which are presumed to be dominated by crystal-liquid equilibrium; viscosity considerations, however, suggest some potential difficulties. Using the data of *Shaw* [1972], the viscosities of the average Binna Burra rhyolite and comendite (Table 1) are extrapolated to be approximately 10^{10} and $10^{8.7}$ poises at 900°C, respectively, assuming anhydrous compositions. If 0.5% water is assumed to be present, these values drop to approximately $10^{9.1}$ and $10^{8.3}$, respectively. These viscosities are high, and it seems doubtful as to whether any mechanism of fractionation involving crystal settling could occur (simple calculations indicating, for example, settling rates <1 cm yr^{-1}). One alternative mechanism might be the mechanical segregation of phenocrysts and liquid during flowage through vertical feeder dykes (flowage differentiation; *Komar* [1972, 1976]) caused by the phenomena of grain dispersive pressure, which appears to be favored by increasing fluid viscosity, providing the dyke width is sufficiently small [*Barrière*, 1976]. In principle, this process would seem to allow a more unconstrained degree of crystal-liquid separation than possible in conventional, closed-system crystal settling. Further possibilities, as previously noted, include liquid-state differentiation [*Hildreth*, 1979]. Such additional processes seem to be required by the extreme fractionation exhibited by the trace element abundance patterns within certain groups of the silicic magmas.

Acknowledgments. Most of the analytical work undertaken during this project has been supported by grants from the Australian Research Grants Committee, including support to use the microprobe facility at the University of Melbourne. The generous hospitality of the Department of Geology at the University of Melbourne is gratefully acknowledged. Thanks are also due to A. S. Bagley (University of Queensland) for continued support with X ray analytical work. Thoughtful reviews of the manuscript were provided by W. P. Nash and W. P. Leeman.

REFERENCES

Barrière, M., Flowage differentiation: Limitation of the 'Bagnold Effect' to the narrow intrusions, *Contrib. Mineral. Petrol., 55,* 139–145, 1976

Brown, G. M., and E. A. Vincent, Pyroxenes from the late stages of fractionation of the Skaergaard Intrusion, East Greenland, *J. Petrol., 4,* 175–197, 1963.

Bryan, W. B., L. W. Finger, and F. Chayes, Estimating proportions in petrographic mixing equations by least squares approximations, *Science, 163,* 926–927, 1969.

Buddington, A. F., and D. H. Lindsley, Iron-titanium oxide minerals and synthetic equivalents, *J. Petrol., 5,* 310–357, 1964

Ernst, W. G. Amphiboles, in *Experimental Mineralogy, 1,* Minerals, Rocks, and Inorganic Materials, pp. 1–125, Springer-Verlag, New York, 1968.

Eugster, H. P., and D. R. Wones, Stability relations of the ferruginous biotite, annite, *J. Petrol., 3,* 82–125, 1962.

Ewart, A., A. Mateen, and J. A. Ross, Review of mineralogy and chemistry of Tertiary central volcanic complexes in southeast Queensland and northeast New South Wales, in *Volcanism in Australasia,* edited by R. W. Johnson, pp. 21–39, Elsevier, New York, 1976.

Ewart, A., V. M. Oversby, and A Mateen, Petrology and isotope geochemistry of Tertiary lavas from the northern flank of the Tweed volcano, southeastern Queensland, *J. Petrol., 18,* 73–113, 1977.

Ewart, A., K. Baxter, and J. A. Ross, The petrology and petrogenesis of the Tertiary anorogenic mafic lavas of southern and central Queensland, Australia—Possible implications for crustal thickening, *Contrib. Mineral. Petrol., 75,* 129–152, 1980.

Hewitt, D. A., A redetermination of the fayalite-magnetite-quartz equilibrium between 650°C and 850°C, *Am. J. Sci., 278,* 715–724, 1978.

Hildreth, W., The Bishop Tuff: Evidence for the origin of compositional zonation in silicic magma chambers, *Geol. Soc. Am. Spec. Pap. 180,* 43–75, 1979.

Izett, G. A., and R. E. Wilcox, Perrierite, chevkinite, and allanite in upper Cenozoic ash beds in the western United States, *Am. Mineral., 53,* 1558–1567, 1968.

James, R. S., and D. L. Hamilton, Phase relations in the system $NaAlSi_3O_8$-$KAlSi_3O_8$-$CaAl_2Si_2O_8$-SiO_2 at 1 kilobar water vapour pressure, *Contrib. Mineral. Petrol., 21,* 111–141, 1969.

Komar, P. D., Mechanical interactions of phenocrysts and flow differentiation of igneous dikes and sills, *Geol. Soc. Am. Bull., 83,* 973–988, 1972.

Komar, P. D., Phenocryst interactions and the velocity profile of magma flowing through dikes or sills. *Geol. Soc. Am. Bull., 87,* 1336–1342, 1976.

Lindsley, D. H., G. M. Brown, and I. D. Muir, Conditions of the ferrowollastonite-ferrohedenbergite inversion in the Skaergaard intrusion, East Greenland, in Pyroxenes and Amphiboles: Crystal Chemistry and Phase Petrology, *Mineral. Soc. Am. Spec. Publ., 2,* 193–201, 1969.

Marsh, J. S., Aenigmatite stability in silica-undersaturated rocks, *Contrib. Mineral. Petrol., 50,* 135–144, 1975.

Nicholls, J., and I. S. E. Carmichael, Peralkaline acid liquids: A petrological study, *Contrib. Mineral. Petrol., 20,* 268–294, 1969.

Powell, M., and R. Powell, An olivine-clinopyroxene geothermometer, *Contrib. Mineral. Petrol., 48,* 249–263, 1974.

Robie, R. A., B. S. Hemingway, and J. R. Fisher, Thermodynamic properties of minerals and related substances at 298.15 K and 1 bar (10^5 Pascals) pressure and at higher temperatures, *U.S. Geol. Surv. Bull., 1452,*1–456, 1978.

Ross, J. A., The Tertiary Focal Peak shield volcano, south-east Queensland—A geological study of its eastern flank, Ph.D. thesis, Univ. of Queensland, Brisbane, Australia, 1977.

Shaw, H. R., Viscosities of magmatic silicate liquids: An empirical method of prediction, *Am. J. Sci., 272,* 870–893, 1972.

Stevens, N. C., The petrology of the Mt. Alford ring-complex, S. E. Queensland, *Geol. Mag., 99,* 501–515, 1962.

Stull, P. R., and H. Prophet, JANAF thermochemical tables (2nd ed), *Nat. Stand. Ref. Data Ser., Nat. Bur. Stand. (U.S.), 37,* p. 1141, 1971.

Taylor, H. P., The effects of assimilation of country rocks by magmas on $^{18}O/^{16}O$ and $^{87}Sr/^{86}Sr$ systematics in igneous rocks, *Earth Planet. Sci. Lett., 47,* 243–254, 1980.

Tuttle, O. F. and N. L. Bowen, Origin of granite in the light of experimental studies in the system $NaAlSi_3O_8$-$KAlSi_3O_8$-SiO_2-H_2O, *Geol. Soc. Am. Mem., 74,* 1–153, 1958.

Veevers, J. J., R. G. Mollan, F. Olgers, and A. G. Kirkegaard, The geology of the Emerald 1:250,000 sheet area, Queensland, *Rep. 68,* Bur. Miner. Resour. (Australia), 1964.

Vlasov, K. A. (Ed.), Mineralogy of rare earths, *Geochemistry and Mineralogy of Rare Elements and Genetic Types of Their Deposits,* vol. 2, Academy of Sciences of the USSR, translated from Russian by Z. Lerman, Israel Program for Scientific Translations, Jerusalem, 1966.

Watson, E. B., Zircon saturation in felsic liquids: Experimental results and applications to trace element geochemistry, *Contrib. Mineral. Petrol., 70,* 407–419, 1979.

Wellman, P., and I. McDougall, Cainozoic igneous activity in eastern Australia, *Tectonophysics, 23,* 49–65, 1974.

(Received October 20, 1980;
revised March 19, 1981;
accepted March 25, 1981.)

JOURNAL OF GEOPHYSICAL RESEARCH, VOL. 86, NO. B11, PAGES 10273–10286, NOVEMBER 10, 1981

Petrogenesis of Oceanic Andesites

SVEN MAALØE

Department of Geology, University of Bergen, 5014 Bergen, Norway

TOM SVANE PETERSEN

Geological Survey of Denmark, 2400 Copenhagen, Denmark

The andesites and cogenetic rocks of the intraoceanic island arc systems vary in silica content from 49–50% SiO_2 to about 76% SiO_2. The most primitive compositions, having contents of about 50% SiO_2, are the basaltic andesites, which are primary compositions generated by partial melting of the uppermost section of the subducted oceanic crust. The oceanic andesites cannot have assimilated material from the continental crusts, but their petrogenesis bears on the origin of the continental crust. The fractionation of andesitic magmas occurs at relatively low pressures, within the stability range of plagioclase. Basaltic andesites fractionate mainly orthopyroxene + plagioclase, while andesites fractionate clinopyroxene + orthopyroxene + plagioclase. The petrogenesis of the continental andesites is more complex, as the primary andesites contain sedimentary material from the continental crusts.

INTRODUCTION

The geophysical and geomorphological features of the intraoceanic island arcs and the continental margins around the Pacific ocean suggest that there must be a well-defined relationship between the subduction zones and the andesitic volcanism [*Kuno,* 1950; *Benioff,* 1954; *Coats,* 1962; *Green and Ringwood,* 1968; *Sykes et al.,* 1969; *Ringwood,* 1974; *Uyeda,* 1977]. There has been less agreement on the detailed processes that determine the generation of andesites: both partial melting of the oceanic crust and its sediments and partial melting of the mantle overlying the subducted crust have been considered sources for the andesitic magmas [*Wyllie,* 1979]. In addition there is some evidence which indicates that the magmas forming the large batholiths have been generated by anatexis of the lower crust [*Sederholm,* 1967; *Presnall and Bateman,* 1973]. The evaluation of the source for the andesitic magmas has been especially confused for the last few years by the $^{87}Sr/^{86}Sr$ data, which apparently excluded subducted oceanic crust as the source material for the andesites. However, recent investigations of the ε_{Nd} values of andesites and related rock types have shown that the source for the intraoceanic island arc andesites must be subducted oceanic crust contaminated by radiogenic strontium from sea water [*DePaolo and Wasserburg,* 1977; *DePaolo and Johnson,* 1979; *Allégre and Othman,* 1980]. The origin of the andesitic magmas by partial melting of mantle material contaminated with water is not acceptable in terms of the isotope data and appears highly unlikely from phase relations and from the low water content of andesitic magmas.

It is now clearly evident from the ε_{Nd} data that some and perhaps the majority of andesitic and rhyolitic magmas erupted within continental regions have undergone contamination by material from the continental crust [*Allégre and Othman,* 1980], and we must therefore distinguish between andesites in the same manner as for granites. The old and persistent granite controversy between magmatists and transformists [*Bowen,* 1948; *Read,* 1957], now finally appears to have found its solution, since the ε_{Nd} data provide the fundamental evidence about the source rocks for the andesites and granites. The andesites which have been generated within the intraoceanic island arc systems have a fundamental significance for the petrogenesis of andesites because contamination by continental crust is excluded here. These andesites are a primitive type, and they will be called oceanic andesites in order to distinguish them from the more or less contaminated continental andesites. It is these oceanic andesites which mainly must have added granitic material to the continental crusts during the history of the Earth, and their origin has fundamental implications for the origin of the continents [*Barker et al.,* 1981].

This paper deals mainly with the petrogenesis of the oceanic andesites. The major element variations are important because they can be related to results obtained from phase equilibrium studies. The major element trends for the oceanic andesites will therefore be considered first and then will be compared with the continental trends. Next, the evidence from REE and isotope data and phase relations will be dealt with. Finally, the dynamic aspects of the partial melting and accumulation processes will be evaluated.

MAJOR ELEMENT TRENDS

The andesitic trends are here represented in Harker diagrams, which have the SiO_2 content as an independent parameter. The analyses were recalculated to 100%, omitting water, after which first- and second-order regression analyses were peformed using computer methods. It is evident from the point distributions in the Harker diagrams that most of the trends are curved (Figures 1–6), and the regression constants for the second-order regression are therefore most relevant and are listed in Table 1. The regression constants for oceanic and continental analyses and analyses of rocks from batholiths are listed in Table 1, while other constants can be obtained on request. The andesitic trends are sometimes represented in more complicated diagrams, which have the differentiation index or other indexes as abcissa, but it can be shown that the simple Harker diagram provides the most accurate representation of the analyses, and there are no quantitative advantages in using such indexes. For the quantitative analysis of trend control the Harker diagram is far superior [*Maaløe,* 1981].

Copyright © 1981 by the American Geophysical Union.

Paper number 1B0906.
0148-0227/81/001B-0906$01.00

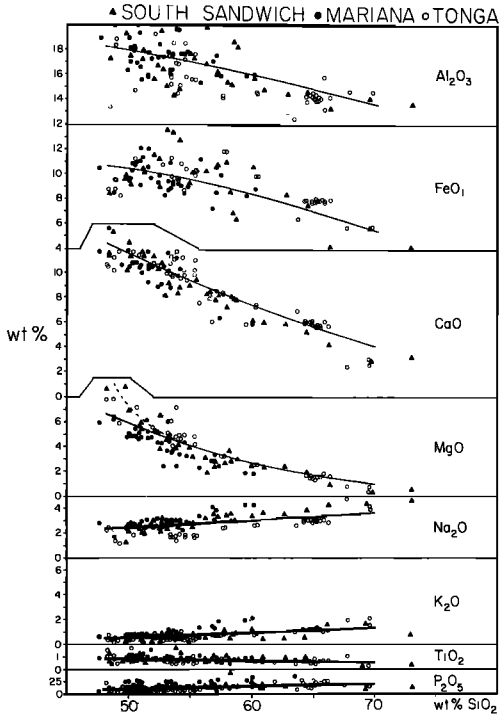

Fig. 1. The analyses and the trend from the intraoceanic island arcs. There is a possibility that the trend for MgO is steeper at low SiO_2 values than indicated by the trend obtained from regression (dashed curve), but a marked change in trend slope is not evident from other oxides.

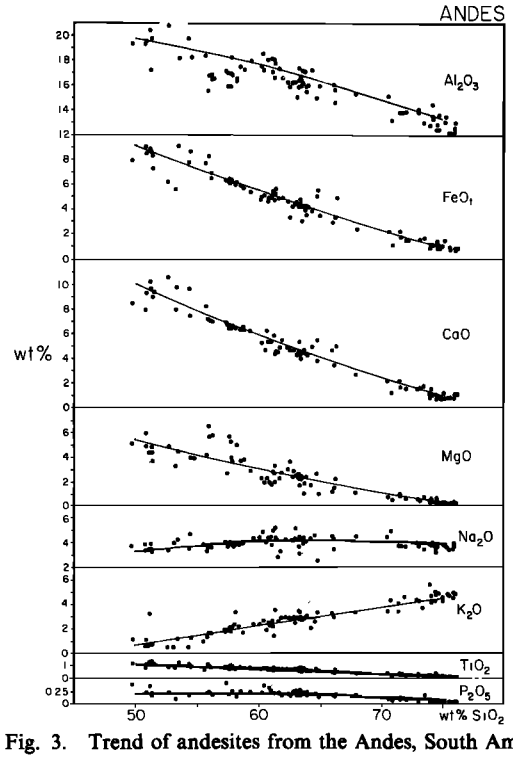

Fig. 3. Trend of andesites from the Andes, South America.

The Harker diagrams have been criticized from a statistical point of view by *Chayes* [1962, 1964]; however, the criticism is not entirely justified. Chayes showed that the correlation coefficients estimated for percentages are too high, because the percentages have a constant sum of 100%. It is true that the closure constraint induces some correlation, but as Chayes demonstrated, the induced correlation is small. The effect of the induced correlation on the confidence limits are more important for practical applications, and it was shown by *Maaløe* [1981] that the effect of the induced correlation is equivalent to an increase in the confidence limits of about 30% for the type of data considered here. The confidence limits given in Table 1 are for linear regression, as these values can not be estimated for curved regression, and have been corrected according to the procedure given by Maaløe.

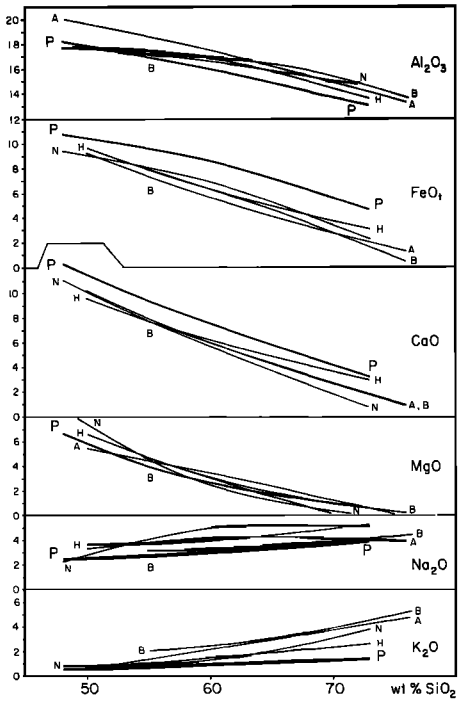

Fig. 2. Comparison between the trends for oceanic andesites (P), and continental andesites (A: Andes, H: Mt. Hood, N: Newberry, B: batholiths (Sierra Nevada and Coast Range)). The distribution of analyses for each of these trends is shown in Figures 1, 3, 4, 5, and 6.

The regression analysis will not only define the trends but will also allow the calculation of representative rock compositions. It should be noted here that the andesitic trends are curved, and that average estimates will therefore result in compositions which not are representative. It is only by linear trends that averages can have some relevance. Representative compositions for andesites with 50, 55, 60, 65, and 75% SiO_2 are listed in Table 2.

There is no general consensus on the nomenclature for the andesitic series [*Irvine and Baragar,* 1971]. Many different types of criteria are used. It is evident from the trends shown here and by other investigators that the trends for the major elements are relatively well defined, and it is therefore both relevant and most convenient to use the SiO_2 content as parameter for the classification. The more recent classifications based on the SiO_2 contents are shown in Table 3. The most primitive basaltic andesites contain 48–50% SiO_2 and there is no obvious difference between what is classified as basalts and basaltic andesite by *Bryan et al.* [1972], *Wise* [1969], and *Baker* [1978], so it is considered appropriate to call all the andesites with 48–54% SiO_2 basaltic andesites. On the other hand there is some evidence in the trends that that there might be a break in the trends at about 53–55% SiO_2, so that a natural division between basaltic andesites and andesites could be at 54% SiO_2. The nomenclature shown in the right

column of Table 3 is considered a reasonable compromise and will be used here.

The trend for the andesites from the intraoceanic island arcs, which are called oceanic andesites here, was estimated on the basis of analyses from the Mariana, Tonga, and South Sandwich islands. The trends for continental andesites were estimated for two volcanoes of the Cascades, the Mt. Hood and Newberry volcanoes, and for a compilation of analyses from the Andes in South America. A trend for the batholiths was estimated from the analyses of rocks from the Coast Range batholiths and the Sierra Nevada batholith.

The trend for the oceanic andesites was estimated from a compilation of analyses from the Mariana, Tonga, and South Sandwich Islands, the number of analyses being 35, 73, and 43 [*Tanadata,* 1940; *Smith,* 1957; *Melson et al.,* 1970; *Bryan et al.,* 1972; *Ewart and Bryan,* 1972; *Ewart et al.,* 1973; *Larsson et al.,* 1974; *Dixon and Batiza,* 1979; *Stern,* 1979]. The distribution of the analyses are very similar for all three arc systems, and they are plotted together in Figure 1. The scatter of analyses is larger for the oceanic andesites than for the continental ones and is especially large for Al_2O_3 and FeO_t. The use of second-order regression implies that the trend curves are parabolas, and it is therefore not given that the trend curves entirely represent true trend curves. For the oceanic andesites the estimated curves appear reasonable for all oxides except MgO. The distribution of analyses for low SiO_2 values suggests that the slope of the trend curve for MgO may be steeper and more negative than the calculated trend curve at low SiO_2 contents, but similar changes in slope are not obvious from the other curves.

The various trends are compared with the trend for oceanic andesites in Figure 2. Apparently the oceanic andesites contain more FeO and CaO and less K_2O and Na_2O than the continental andesites, while the percentages for the other oxides are similar. It might also be noted that there is no tendency for a convergence towards a common primitive composition at about 50% SiO_2, even though the differences in compositions are small.

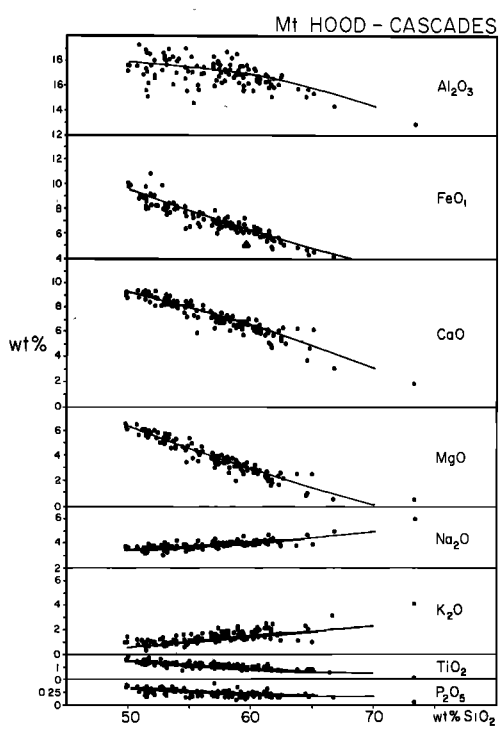

Fig. 4. Trend for the Mt. Hood volcano, High Cascades, Oregon.

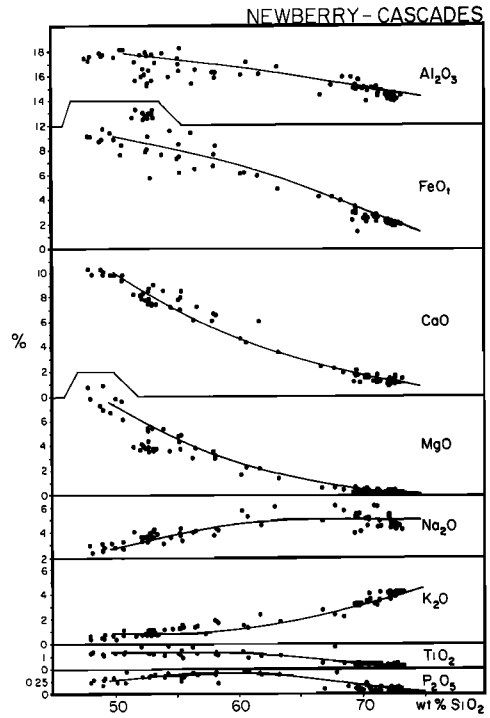

Fig. 5. Trend of lavas from the Newberry volcano, High Cascades, Oregon.

The trend for the andesites from the Andes, was estimated from 88 analyses reported by *Zeil and Pichler* [1968], *Francis et al.* [1974], *Thorpe et al.* [1976], *Dostal et al.* [1977], and *Lopez-Escobar et al.* [1977]. The trend is fairly well defined and

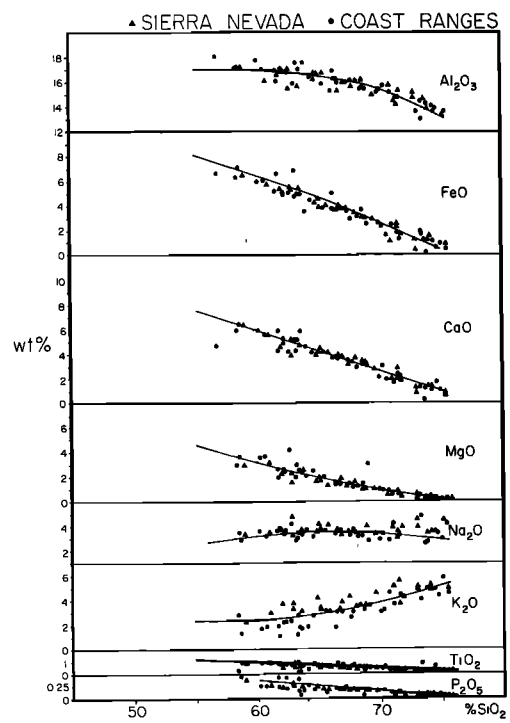

Fig. 6. The trend for the Sierra Nevada and Coast Range batholiths. The analyses nearly coincide, and the trends have been calculated from both sets of analyses. These trends do not appear much different from the trends of continental andesites (Figures 4 and 5).

TABLE 1. Regression Constants and Confidence Limits for a Confidence Level of 99%

	Oceanic Andesites				Continental Andesites				Batholiths			
	a	*b*	*c*	CL	*a*	*b*	*c*	CL	*a*	*b*	*c*	CL
SiO_2	0	1.0000	0	0	0	1.0000	0	0	0	1.0000	0	0
Al_2O_3	$2.0944 \times 10^{+1}$	4.4935×10^{-2}	-2.1138×10^{-3}	0.91	8.7229	4.3584×10^{-1}	-4.9357×10^{-3}	0.50	-1.0855×10	1.0040	-8.9515×10^{3}	1.08
Fe_2O_3	3.5750	7.6950×10^{-2}	-9.8755×10^{-3}	0.18	4.3780	-5.7735×10^{-2}	3.6275×10^{-5}	0.11	3.7227	-3.1177×10^{-2}	-2.2187×10^{-4}	0.13
FeO	1.8230	3.9235×10^{-1}	-5.0358×10^{-3}	0.89	2.2239×10	-2.9445×10^{-1}	1.8496×10^{-4}	0.56	1.8981×10	-1.5897×10^{-1}	-1.1313×10^{-3}	0.74
MgO	4.0062×10	−1.0022	6.3206×10^{-3}	0.69	4.2453×10	−1.0269	6.1770×10^{-3}	0.50	3.4031×10	-7.6825×10^{-1}	4.2226×10^{-3}	0.92
CaO	3.7056×10	-6.1717×10^{-1}	2.0970×10^{-3}	0.76	2.8586×10	-3.8380×10^{-1}	1.8394×10^{-4}	0.57	2.4766×10	-2.9802×10^{-1}	-2.6532×10^{-4}	0.96
Na_2O	-8.5972×10^{-1}	7.1359×10^{-2}	-1.0768×10^{-4}	0.42	1.4039×10	5.4303×10^{-1}	-3.9938×10^{-3}	0.26	−5.9578	$2.6536 \text{ m } 10^{-1}$	-1.8489×10^{-3}	0.35
K_2O	−1.0039	2.3121×10^{-2}	1.4275×10^{-4}	0.19	1.8750	-1.4180×10^{-1}	2.3217×10^{-3}	0.36	2.8404×10	-9.1125×10^{-1}	8.0045×10^{-4}	0.17
MnO	6.0246×10^{-1}	-9.9217×10^{-3}	3.9741×10^{-5}	0.01	3.9247	-1.1204×10^{-1}	8.0817×10^{-4}	0.01	2.3194	-6.0365×10^{-2}	4.0388×10^{-4}	0.01
TiO_2	6.0520×10^{-1}	2.0184×10^{-2}	-3.1654×10^{-4}	0.18	3.4292	-3.4557×10^{-2}	-1.1845×10^{-4}	0.12	-5.0990×10^{-1}	7.1354×10^{-2}	-8.2929×10^{-4}	0.15
P_2O_5	-6.3893×10^{-1}	2.4040×10^{-2}	-1.7734×10^{-4}	0.10	3.6924×10^{-1}	2.7154×10^{-2}	2.8813×10^{-4}	0.10	6.2051	-1.5370×10^{-1}	9.6080×10^{-4}	0.10

Oxide % = $a + b(SiO_2) + c(SiO_2)^2$, where SiO_2 is in weight percent. CL is the confidence limit.

extends from 50 to more than 76% SiO_2. Apparently there is a maximum in the Na_2O content at about 65% SiO_2 (Figure 3).

Two trends from the Cascades have been estimated here using the analyses from Mt. Hood [*Higgins*, 1973] and Newberry [*Wise*, 1969], the total number of analyses being 161. The two trends show some minor but noticeable differences (Figures 4 and 5). The decrease in CaO and MgO for low SiO_2 contents is more pronounced for Newberry than for Mt. Hood, and there is evidence for a maximum in the Na_2O curve of Newberry, while the Na_2O content for Mt. Hood is steadily increasing.

The trend for granitic batholiths was estimated from the analyses reported by *Bateman et al.* [1963] and *Ross* [1972, 1969] for the Coast Range batholiths and the Sierra Nevada batholith, the total number of analyses being 76. The analyses form a well-defined trend from 58 to 78% SiO_2, which does not differ much from the trends of continental andesites except that basaltic andesites apparently are absent from the batholiths (Figure 6).

The present compilation of the trends for different andesites and related rocks shows that the total range of silica contents is from 48% to more than 76% SiO_2. All rock types of the andesitic series are present both in continental and oceanic areas; even the highly differentiated rhyolitic compositions are more rare in the intraoceanic island arcs [*Baker*, 1978]. Furthermore, it is evident that oceanic andesites differ from the continental ones in their major element compositions. There is overlap between the analyses, but the differences in compositions are so large that the two types of rocks differ significantly in composition, and it is most likely that their origins are different.

The major element characteristics for the andesitic series have now been estimated, and the next problem will be an estimate of the origin of the trends. The basaltic andesites with about 50% SiO_2 might either be primitive compositions or primary compositions formed directly by partial melting. It will not be possible, from the major element evidence alone, to estimate the nature of the basaltic andesites. The required additional evidence is therefore considered below, before the significance of the major element trends is evaluated.

Isotope Data

The Nd and Sr isotope data obtained during the last few years have provided fundamental evidence about the source material for the oceanic andesites [*DePaolo and Wasserburg*, 1977; *Hawkesworth et al.*, 1977]. The results for the Nd isotopes are represented by the ε_{Nd} values or the Δ_{Nd} values which are identical and defined by the following equation:

$$\varepsilon_{Nd} = \left(\frac{(^{143}Nd/^{144}Nd)_{sample,today} - (^{143}Nd/^{144}Nd)_{planet}}{(^{143}Nd/^{144}Nd)_{planet}} \right) \cdot 10^4$$

where the value of $(^{143}Nd/^{144}Nd)_{planet}$ is the average value of the ratio for the Earth and generally assumed to be 0.51264 [*Allègre and Othman*, 1980]. The abyssal tholeiites have ε_{Nd} values within the range from +5 to +12 (Figure 7), and the mantle which have formed these abysal tholeiites must have an identical range of ε_{Nd} values. The ε_{Nd} values for the oceanic andesites have been estimated by *DePaolo and Wasserburg* [1977], *Hawkesworth et al.* [1977], and *DePaolo and Johnson* [1979], the range being from +7.5 to +9.5 (Figure 7). The ε_{Nd} values for the primitive andesites are thus clearly within the range for abyssal tholeiites. The value for seawater was estimated by *DePaolo and Wasserburg* [1977] as −9.2, but despite

TABLE 2. Oceanic and Continental Andesitic, Compositions Obtained From Regression

	Oceanic Andesites						Continental Andesites					
	1	2	3	4	5	6	1	2	3	4	5	6
SiO_2	50.00	55.00	60.00	65.00	70.00	75.00	50.00	55.00	60.00	65.00	70.00	75.00
Al_2O_3	17.91	17.02	16.03	14.90	13.76	12.42	18.18	17.76	17.10	16.20	15.05	13.65
Fe_2O_3	1.73	1.60	1.41	1.19	0.91	0.57	1.58	1.31	1.04	0.78	0.51	0.25
FeO	8.85	8.17	7.24	6.05	4.61	2.92	7.98	6.61	5.24	3.88	2.54	1.20
MgO	5.76	4.06	2.69	1.63	0.88	0.45	6.55	4.66	3.08	1.81	0.84	0.18
CaO	11.44	9.45	7.57	5.80	4.12	2.56	9.86	8.03	6.22	4.42	2.62	0.84
Na_2O	2.44	2.74	3.03	3.32	3.61	3.89	3.13	3.75	4.17	4.38	4.40	4.24
K_2O	0.51	0.70	0.90	1.10	1.31	1.53	0.59	1.10	1.73	2.47	3.33	4.30
MnO	0.21	0.18	0.15	0.13	0.10	0.05	0.34	0.21	0.11	0.06	0.04	0.04
TiO_2	0.82	0.76	0.68	0.58	0.47	0.34	1.41	1.17	0.93	0.68	0.43	0.17
P_2O_5	0.12	0.15	0.17	0.17	0.17	0.17	0.27	0.25	0.22	0.18	0.12	0.05
Sum	99.79	99.83	99.87	99.87	99.94	99.90	99.89	99.89	99.84	99.86	99.88	99.92
						Norm						
Q		7.68	15.97	23.93	31.48	38.82		3.32	9.86	16.67	23.65	31.14
Or	3.01	4.14	5.32	6.50	7.74	9.04	3.49	6.50	10.22	14.60	19.68	25.41
Ab	20.65	23.19	25.64	28.09	30.55	32.92	26.49	31.73	35.29	37.06	37.23	35.88
An	36.41	32.08	27.48	22.51	17.47	11.59	33.82	28.38	22.83	17.25	11.48	3.84
Di	16.17	11.53	7.55	4.39	1.60		10.92	8.08	5.45	2.92	0.62	
Hy	16.44	17.11	14.18	11.23	8.49	5.54	11.40	17.15	12.41	8.52	5.39	2.24
Ol	2.77						8.19					
Mt	2.51	2.32	2.04	1.73	1.32	0.83	2.29	1.90	1.51	1.13	0.74	0.36
Il	1.56	1.44	1.29	1.10	0.89	0.65	2.68	2.22	1.77	1.29	0.82	0.32
Ap	0.28	0.35	0.39	0.39	0.39	0.39	0.63	0.58	0.51	0.42	0.28	0.12

the large difference in ε_{Nd} between sea water and abyssal tholeiite there is apparently no significant contamination of the abyssal basalts, a relationship which probably is related to the small concentration of Nd in sea water [*DePaolo and Johnson,* 1979]. The coincidence of ε_{Nd} values for the abyssal tholeiites and oceanic andesites shows that these andesites have provenance either to the abyssal crust or the suboceanic mantle situated above the subduction zone.

The Sr isotope data are here represented by the familiar $^{87}Sr/^{86}Sr$ ratio, as there is no general consensus on the $(^{87}Sr/^{86}Sr)_{planet}$ ratio which enters the ε_{Sr} value, which is defined in the same manner as the ε_{Nd} value (Figure 7). The $^{87}Sr/^{86}Sr$ ratio for abyssal tholeiites varies from 0.7022 to 0.7035, the average being 0.7029 [*Hofmann and Hart,* 1978]. The ratios for the oceanic andesites are not much higher, the range being from 0.7031 to 0.7035, but the difference is significant. These ratios are quite similar to those of oceanic island basalts, which are believed to have originated by plume activity (Figure 7) [*Hofmann and Hart,* 1978]. Several investigators therefore concluded, before the ε_{Nd} values became available, that andesites must stem from the mantle and not from the subducted oceanic crust. It might, however, be noted that the mantle above the subduction zone is former suboceanic mantle which has been formed at the midocean ridges, and its isotope data must therefore be the same as those of the abyssal crust. It is therefore not obvious how a mantle origin can explain the Sr isotope data for the oceanic andesites.

Recent investigations have shown that the upper part of the oceanic crust exchanges Sr with the sea water, whereby the $^{87}Sr/^{86}Sr$ ratio in the oceanic crust increases (Figure 7) [*DePaolo and Wasserburg,* 1977; *Mottl and Holland,* 1978; *Humphries and Thompson,* 1978]. The range of Sr ratios for the oceanic crust thus indicates that they may have originated from the subducted oceanic crust rather than the mantle. The hydrothermal alteration and contamination of the oceanic crust will only occur where the seawater has access to the crust, and it will therefore only be the pillow lava section that undergoes contamination by the sea water. Thus the combined evidence from the Nd and Sr isotope data shows that the oceanic andesites might originate by partial melting of the uppermost part of the oceanic crust, a result which is consistent with the dynamic features of the magma generation considered below.

The continental andesites and rhyolites have ε_{Nd} values within the range −15 to +5 and relatively high $^{87}Sr/^{86}Sr$ ratios (Figure 7). Similarly, the Pb isotope systematics for Central Andean andesites show that material of crustal origin must constitute part of the andesitic magmas [*Barreiro and Tilton,* 1980]. There are essentially two possibilities for an explanation of these isotope data. The crustal material may enter the primary magmas in the form of subducted sediments, or the primary andesites may become contaminated with crustal material when they reach the crust during their ascent from the Benioff zone. Variations in the $^{18}O/^{16}O$ and $^{87}Sr/^{86}Sr$ ratios result from independent processes. It was shown by *Thorpe and Francis* [1981] that these two ratios are positively correlated for the andesites of the Andes. This correlation and the obtained $\delta^{18}O$ values show that it must be the sedimental materials which enter the primary andesitic magmas. The pri-

TABLE 3. Nomenclature for Andesite Based on the SiO_2 Contents

	Bryan et. al., [1972]	*Baker* [1978]	*Wise* [1969]	This Paper
Basalt	48–52	50–54	48–54	
Basaltic andesite	52–55	54–57	54–58	48–54
Andesite	55–63	57–63	58–62	54–63
Dacite	63–68	63–70	62–66	63–69
Rhyolite	68–80	70–80	66–80	70–80

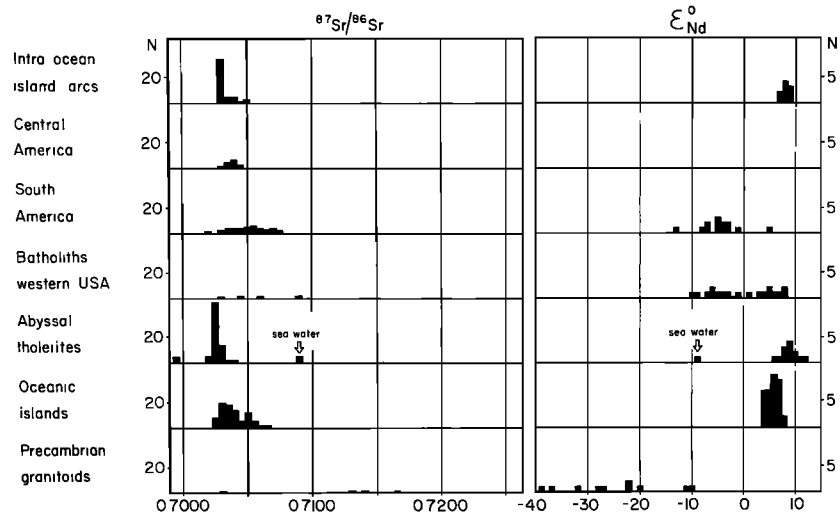

Fig. 7. Isotope data for andesites from different regions and abyssal theoleiites. *N* is the number of analyses. The data have been compiled from *Gledhill and Baker* [1973], *McNutt et al.* [1975], *DePaolo and Wasserburg* [1976, 1977], *Hawkesworth et al.* [1977], *Hofman and Hart* [1978], *DePaolo and Johnson* [1979], *DePaolo* [1980], and *Allegre and Othman* [1980].

mary continental andesites are thus derived from a mixture of sedimental and basaltic material. This difference in the source material for the two types of andesites is in agreement with the major element trends which show that the basaltic andesites of oceanic and continental provenance differ. In the case that there was a common primary magma for the two series, one would expect a convergence of the trends for low SiO_2 contents, but no such convergence is observed.

The oceanic andesites and rhyolites are thus generated from subducted abyssal tholeiite, while the continental andesites are formed by partial melting of a mixture of sediments and tholeiite. Since the source material for the continental andesites must be considered to be rather ill-defined, the evaluation of the partial melting process in the Benioff zone must be based on the oceanic andesites, because their source material is known.

Rare Earth Abundances

The REE abundances for oceanic basaltic andesites with about 50% SiO_2 display a chondritic pattern, the rock/chondrite ratio curves are nearly horizontal, with a slight tendency for either positive or negative slopes. The ratio for La varies from 10 to 30, with a concentration at about 20 [*Hawkesworth et al.*, 1977; *DePaolo and Johnson*, 1979; *Dixon and Batiza*, 1979]. The rock/chondrite ratio for abyssal tholeiites also displays some variation; the ratio for La varies from 3 to 20, and is typically about 20 [*Kay and Hubbard*, 1978]. The overlap between the ratios for La for the two rock types is too large for an approximate estimate of the degree of partial melting required for the formation of basaltic andesite from abyssal tholeiite, but the ratios show that the degree of melting must be large and probably of the order of 50%. Furthermore, it is evident that the amount of fractionation that can have occurred during the ascent of the basaltic andesites must have been either small or negligible. An alternative model considering the REE evidence alone is the generation of andesite by total melting of the oceanic crust followed by 50% fractionation during ascent, but this model appears unlikely from the dynamic features of the partial melting process.

The REE relationships between andesite and tholeiite were investigated by *Gill* [1974], who compared the REE abundances of andesite with the calculated abundances based on partial melting of eclogite. The calculated abundances only approximated the natural abundances, and it was consequently considered that partial melting of eclogitic abyssal crust cannot account for the generation of andesites. However, the La ratios of the andesites considered were quite high, about 30, and the SiO_2 content about 55%, so it is unlikely that the andesites considered are primary.

The variation in the distribution coefficients $D = c_s/c_l$ for the REE is very different for clinopyroxene and garnet. Even the D values for both minerals display some variation; the systematic differences are so large that a qualitative estimate can be made of the relative proportions of the two minerals in the residuum formed by partial melting of the oceanic crust. The D values for the heavy REE are much larger for garnet than for clinopyroxene, while the D values for the light REE are smaller for garnet than for clinopyroxene. The variation in D from La to Lu is quite small for clinopyroxene as D increases from 0.1 to 0.5 [*Irving*, 1978]. These variations show either that the residuum must contain much more clinopyroxene than garnet or that garnet is absent from the residuum when the melt attains the composition of basaltic andesite.

Phase Relations

The primitive andesitic magmas have been considered to be generated by the partial melting of the subducted crust [*Coats*, 1962; *Ringwood and Green*, 1966] and by partial melting of the mantle above the subducted crust which has been considered to take up water from the subducted oceanic crust [*Kushiro et al.*, 1968; *Mysen and Boettcher*, 1975]. Both models have been discussed extensively in the literature [cf. *Wyllie*, 1979], and additional variants have been proposed [*Nicolls and Ringwood*, 1972; *Nicholls*, 1974]. The most conspicuous difference between the different models is the role which is lent to the fluid phase, which is believed to consist mainly of water. If the fluid phase is mostly water and there is enough water to saturate the melt, then the liquids formed by partial melting of lherzolitic materials will be either quartz or hypsthene normative [*Kushiro et al.* 1972; *Mysen and Boettcher*, 1975]. The

principal phase relations can be illustrated by the ternary system diopside-forsterite-silica, where the invariant reaction point *L*, *S*(olivine, diopside, enstatite) moves from the olivine-diopside-enstatite field into the enstatite-diopside-quartz field by the transition from dry to water-saturated conditions. It is not only the composition of the invariant point that changes. The reaction relationships also change: while enstatite has a reaction relationship with the liquid at dry conditions, olivine has a reaction relationship at water excess conditions [*Eggler,* 1972]. Thus liquids generated at dry conditions will have a tholeiitic affinity, while the liquids generated at water excess conditions will be quartz normative and more or less similar to andesitic compositions. The solubility of water in andesitic and basaltic melts is quite high at 30 kbar, about 25% [*Wyllie,* 1979], and the amount of water required for excess conditions is therefore high. If the source material only contains 1% H_2O, the first melt will be water-saturated up to 4% melting and of andesitic affinity, but by larger degrees of partial melting, say 10%, the liquids will attain tholeiitic affinity.

Since olivine has a reaction relationship with the liquid at water-saturated conditions, the andesitic magmas should, at water excess conditions, be in equilibrium with clinopyroxene and enstatite near the liquidus, while olivine should be absent. However, a water-saturated andesitic magma contains only garnet and kyanite on the liquidus at high pressures [*Stern et al.,* 1975], while olivine, enstatite, and clinopyroxene are absent. Hence it is clear that andesitic magmas cannot be generated by partial melting of lherzolitic mantle material at water excess conditions.

The melts formed by partial melting of peridotite at water excess conditions were investigated by *Mysen and Boettcher* [1975], and liquids with a relatively high SiO_2 content were obtained, which were considered of andestic affinity. The CaO contents of the liquids are, however, far too high, and the MgO and FeO contents too low for these liquids to be andesites; they do not plot within the andesitic fields defined by Figure 2.

The implications of water-saturated conditions may be considered further. If the andesites were generated at water excess conditions at high pressures, they should remain saturated at any given lower pressure because they can only release water, either by decompression or by crystallization [*Yoder,* 1965]. The actual water content is therefore crucial in this context. It was shown by *Eggler* [1972] from experimental studies of a Paricutin andesite that the andesitic magma must have contained 2.2 ±0.5% H_2O, and *Anderson* [1975] showed that glass trapped in inclusions in olivine phenocrysts of andesites contain 3–5% H_2O. The later estimate is an absolute maximum estimate, as the growth of olivine will increase the concentration of water around the crystal. Furthermore, it was shown from an experimental study by *Maaløe and Wyllie* [1975] that granitic magma crystallizes with less than 1.7% H_2O. All three estimates are consistent and show that the magmas within the andesitic or granitic magma series have crystallized at strictly water-undersaturated conditions and that their primary magmas cannot have formed at water excess conditions.

The basaltic rocks of the ocean floor are transformed into eclogite at pressures above 20 kbar [*Cohen et al.,* 1967], and the eclogitic mineralogy is preserved both at dry and water excess conditions [*Stern et al.,* 1975; *Green,* 1972]. A melt generated by partial melting of eclogite should therefore be in equilibrium with both garnet and clinopyroxene when it is reequilibrated at the same pressure as it was generated. At water excess conditions the andesitic melts contain garnet and kyanite on the liquidus, while the liquidus assemblage is garnet and clinopyroxene for water contents less than 1–2% H_2O [*Wyllie,* 1979]. These phase relations consequently show that andesitic magmas can be generated from the subducted oceanic crust and that the water content should be fairly small, about 1%, in agreement with the observed water contents.

MAJOR ELEMENTS

The major element trend for the oceanic andesites may now be considered in the light of the above results, which have shown that the primary andesitic magmas must have been generated by partial melting of the subducted oceanic crust and that the degree of partial melting must be relatively high.

The seismic focii of the topmost part of the Benioff zone define a plane which is situated at depths between 70 and 150 km beneath the andesitic volcanoes, the typical depth being 100 km [*Isacks and Barazangi,* 1977; *Condie,* 1976], which is equivalent to a pressure of 30 kbar. The basaltic crust has an eclogitic mineralogy at this pressure [*Cohen et al.,* 1967], and the melt generated by partial melting of the crust will be in equilibrium with garnet and clinopyroxene. The compositions of these two minerals in basaltic and andesitic melts have been estimated by *Green and Ringwood* [1968] at pressures up to 36 kbar at dry conditions. The compositional fields defined by the two minerals at high pressures are shown in Figure 8.

If an andesitic magma has been generated by partial melting of abyssal tholeiite, some compositional constraints should be fulfilled, as will be explained on the basis of the diagram inserted into the MgO diagram of Figure 8. Consider that basaltic andesite with 50% SiO_2 is a primary magma generated in equilibrium with garnet and clinopyroxene. If this is the case, then the composition of abyssal tholeiite, the source material, should be situated inside the triangle formed by clinopyroxene, garnet, and basaltic andesite. This relationship should not only hold for one but for all oxides and other chemical constituents. The triangles are shown in Figure 8 for the most important oxides, and it is evident that the constraint is fulfilled for these oxides. The major element composition of basaltic andesite is thus consistent with an origin by partial melting of eclogite with the composition of abyssal tholeiite. The ratio between the line segment *pq* will define the degree of partial melting as $L/S = p/q$, where *L* and *S* are the amount of liquid and solid, respectively. It is evident from the triangles defined by the different oxides that the ratio p/q attains values near 1.0, so that the degree of partial melting must be about 50% for the basaltic andesite with 50% SiO_2. Furthermore, the ratio *r/s* will define the proportions of clinopyroxen and garnet in the residuum as (clinopyroxene)/(garnet) = *r/s*. This ratio varies for the different oxides but is about 5, so that the amount of garnet in the residuum is about 20%.

The major elements allow an alternative phase assemblage for the residuum, which also is possible from the REE results. A line can be drawn between the compositions between basaltic andesite with about 50% SiO_2, abyssal tholeiite, and clinopyroxene. The residuum might therefore consist of clinopyroxene alone. It is not possible from the major element compositions to distinguish between a residuum consisting of garnet and pyroxene and one consisting of pyroxene alone, but as both garnet and clinopyroxene are in the liquidus at pressure between 20 and 40kbar for a tholeiite with 7.6% MgO, which is similar to the average composition of abyssal

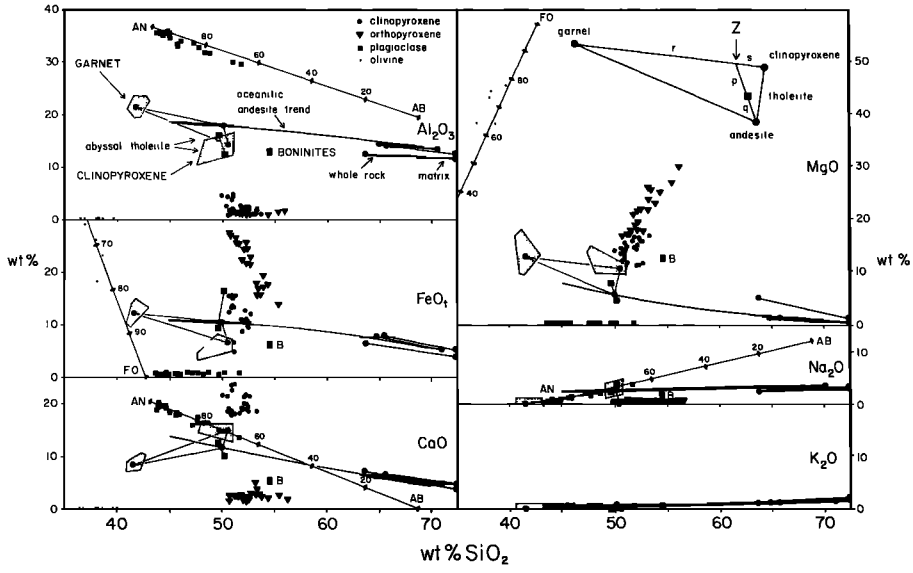

Fig. 8. The trend for oceanic andesites compared with the compositions of phenocrysts, abyssal tholeiites, and experimentally equilibrated mineral compositions. The areas labeled 'Garnet' and 'Clinopyroxene' show the compositional ranges of these minerals at high pressures. Boninite has been considered a primary composition for the andesites [*Dietrich et al.*, 1978; *Cameron et al.*, 1979], but it is apparent from the diagrams that it is not possible to fractionate from the average composition 'B' to basaltic andesite. The signatures for the phenocryst compositions are shown in the upper right corner of the Al_2O_3 diagram.

tholeiite, it is most likely that the residuum consists of both minerals. This is in agreement with the phase relations of andesite with less than about 1% H_2O, as both garnet and clinopyroxene are in the liquidus at pressures above 20 kbar [*Wyllie*, 1979].

The major element trend and the mineral compositions shown in Figure 8 also afford some evidence about the possible range of primary compositions. The line joining clinopyroxene and primary andesite should be situated to the right of abyssal tholeiite if garnet and clinopyroxene both form the residuum. By inspection of the diagrams for the different oxides the lowest possible SiO_2 content for primary andesite is obtained as 48% SiO_2, which is in agreement with the observed range of SiO_2 contents (Figures 1–6). The highest possible SiO_2 content for the primary andesites is more difficult to estimate. If the composition of primary andesite is moved toward high SiO_2 contents, then the r/s ratio will decrease and the amount of garnet in the residuum will increase, which is inconsistent with the REE data. It is most likely that the SiO_2 contents of primary andesites are less than 55% SiO_2, but available data do not specify any particular range. Evidently, the major element results considered above rest on somewhat arbitrarily chosen compositions, but the major features will not be changed if other relevant compositions are chosen.

FRACTIONAL CRYSTALLIZATION

Primary basaltic andesites are apparently generated at depths between 80 and 150 km, since the upper boundary of the Benioff zone is situated at these depths. Primary andesitic magma can therefore undergo various types of fractionation during its ascent. The fractionation may occur mainly at high pressures, and the fractionate will then be eclogitic. The fractionation can also occur at low pressures, and the fractionate will then be more or less similar to the phenocryst assemblages. Possibly, the fractionation can be polybaric, in which case the mineralogical constitution of the fractionate changes continuously during the ascent. These three possibilities are related to the dynamics of the ascent of the magma. Fractionation mainly at either high or low pressures will imply a fast ascent rate, while polybaric fractionation might imply a diapiric type of ascent or slow ascent through dykes. It is not considered possible from the available data to provide compelling evidence for any one of these three models, but the evidence suggests that the trend of the oceanic andesites is controlled mainly by low pressure fractionation.

Some andesites may undergo high pressure fractionation, while others ascend directly to the surface. However, whatever the extent of the high pressure fractionation might be, it will always be possible for the andesitis magmas to fractionate towards dacite or rhyolite at low pressures, as all these compositions are situated on the silica-rich side of both the high-pressure and low-pressure thermal divides given by the planes garnet-clinopyroxene-orthopyroxene and olivine-plagioclase-diopside, respectively [*Maaløe and Petersen*, 1976; *Yoder and Tilley*, 1962; *O'Hara*, 1968].

Primary basaltic andesites are generated in equilibrium with garnet and clinopyroxene, and these two minerals will therefore be in the liquidus of basaltic andesites at high pressures. The ascending andesitic magmas will therefore be able to fractionate eclogite as soon as it leaves its depth of generation. As far as major elements are concerned, an eclogitic fractionate will only be possible if the tangent to the trend curves intersects or joins between garnet and clinopyroxene. This will be possible for all oxides except MgO. The MgO content is apparently too high for this intersection to occur (Figure 8). However, the distribution of MgO analyses for oceanic andesites near 50% SiO_2 might suggest that the trend curve obtained by regression is not entirely representative (Figure 1). If the trend curve bends more in this part of the trend, an eclogitic fractionate will be possible. It will be evident from Figure 8 that the amount of garnet in the fractionate should be relatively large, about 50%, and the rock/chondrite for the light REE should therefore increase rapidly if the fractionation is from basaltic andesite to andesite, but this is contrary

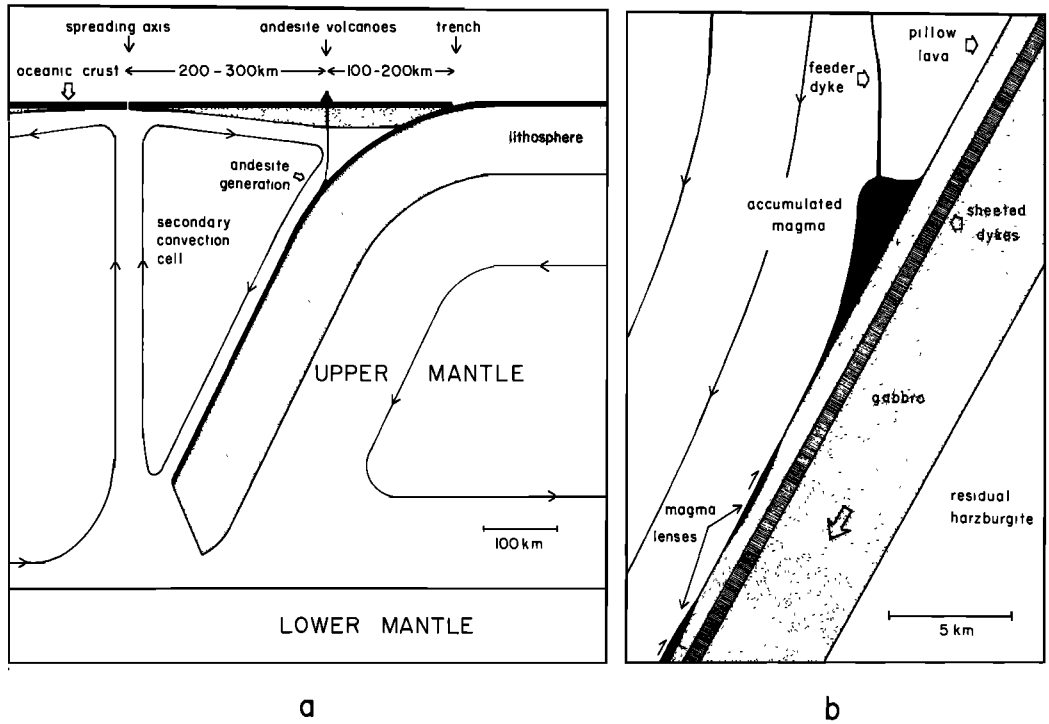

Fig. 9. The percentages of phenocrysts in basaltic andesites, andesites, and dacites. The percentatge of plagioclase is highly variable, while the percentages of olivine and clinopyroxene are decreasing with increasing SiO_2 contents.

to what is observed [*Ewart at al.*, 1973; *Dixon and Batiza,* 1979; *DePaolo and Johnson,* 1979]. Both major element data and REE abundances thus appear to exclude eclogite fractionation as the control of the andesitic trend.

The other extreme possibility is fractionation mainly at low pressures. Because a rather high concentration of phenocrysts is a characteristic feature of the andesitic lavas, it will be reasonable first to consider the significance of the phenocryst assemblages.

Basaltic andesites may be aphyric or contain up to 50% phenocrysts of plagioclase, olivine, and clinopyroxene and minor amounts of orthopyroxene. Andesites and dacites mainly contain phenocrysts of plagioclase, clinopyroxene, and orthopyroxene and subordinate amounts of magnetite. Hydrous minerals are notoriously rare in oceanic andesites, brown amphibole having been observed in andesite, while biotite is absent. The absolute amounts of phenocrysts in oceanic andesites have been plotted in Figure 9 as a function of SiO_2 content, and the relative proportions of phenocrysts are shown in Figure 10*a*. The data have been compiled from *Ewart et al.* [1973], *Dixon and Batiza* [1979], *Baker* [1978], and *Stern* [1979]. It is evident that the content of phenocrysts is highly variable for a given SiO_2 content. The maximal mode for plagioclase appear to be 35% by volume. Both clinopyroxene and olivine display decreasing modes with increasing SiO_2 content, while orthopyroxene show evidence for a maximum near 60–65% SiO_2. Even though a high content of phenocrysts is typical for many andesites, it should be noted that both basaltic andesites and andesite can be aphyric, so that these compositions represent liquid compositions [*Baker,* 1978].

The plagioclase phenocrysts display evidence for fast growth: they contain marginal inclusions of glass and are oscillatory zoned and resorbed. For the South Sandwich island andesites there is no systematic relationship between rock composition and anorthite content of plagioclase phenocrysts. It is most likely that such phenocrysts formed from the enclosing lava by fast crystallization. The high content of plagioclase could be due to a higher rate of accumulation for olivine and augite than for plagioclase, but the cumulus gabbro xenoliths observed by *Stern* [1979] have phenocryst proportions which are similar to those of the lavas (Figure 10).

If the basaltic andesites represent magmas fractionated at low pressures, their phenocryst assemblages should have a rather constant composition and concentrate around a point in a diagram, as in Figure 10*a*. However, no such concentration is apparent, so the basaltic andesites have not undergone fractionation at low pressures. Both the aphyric state of some basaltic andesites and the high proportion of plagioclase suggests that the basaltic andesites can be primary compositions, as suggested above.

Reported compositions of phenocrysts in andesitic lavas are

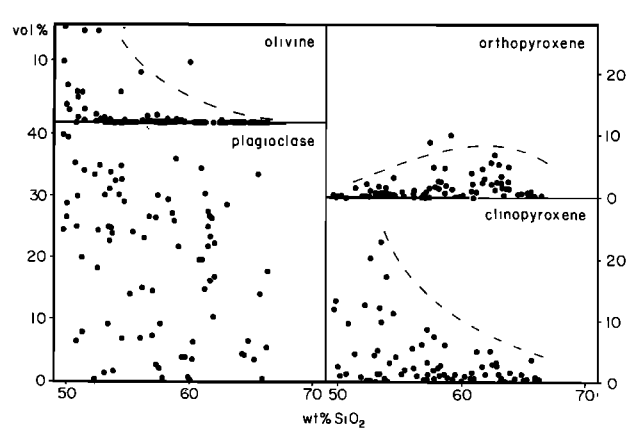

Fig. 10. (*a*) The relative proportions of phenocrysts in andesites and cumulates. (*b*) Part of the quarternary system anorthite-forsterite-silica-diopside at 1 bar [*Presnall et al.*, 1978]. Single arrows indicate cotectic curves, while double arrows indicate reaction curves.

TABLE 4. The Mineralogical Constituents of the Fractionates Estimated From Least Squares Methods

	SiO_2 Content		
	50–55%	55–60%	60–70%
Plagioclase	60%	60%	65%
Orthopyroxene	40%	30%	15%
Clinopyroxene		10%	15%
Magnetite			5%
Anorthite in plagioclase	90%An	80%An	60%An
Amount of liquid left*	50%	30%	20%

* Initial amount was 100%.

shown in Figure 8. The compositions shown cover the whole range from basaltic andesite to dacite [*Ewart et al.* 1973; *Stern,* 1979; *Bryan et al.,* 1972; *Flood et al.,* 1977]. The composition of a given fractionate should be situated on the extrapolated line that joins the initial and derivative compositions. As the curvature of the trend is small, the trend curve itself might be used instead of the line as a first approximation. Let us first consider the fractionation of basaltic andesite with 50% SiO_2 to andesite with 60% SiO_2. According to the Al_2O_3 diagram in Figure 8, the fractionate should consist of about 50% plagioclase and 50% of some combination of olivine, clinopyroxene, and orthopyroxene. Considering the MgO diagram, it is evident that the fractionate must consist mainly of plagioclase and clinopyroxene if plagioclase constitute 50% of the fractionate. From the CaO diagram it is now evident that this fractionate is not possible, as both plagioclase and clinopyroxene are situated on the same side of the trend curve. The typical phenocryst assemblage consisting of plagioclase and clinopyroxene cannot account for the trend. Several least squares tests with variable mineral compositions yielded the same result. Various combinations of plagioclase, orthopyroxene, clinopyroxene, olivine, and magnetite can be tested using least squares methods, but it will be more appropriate first to consider the possible phase assemblages indicated by phase relations.

The phase relations for the quaternary system anorthite-diopside-forsterite-silica is shown in Figure 10 [*Presnall et al.,* 1978]. This system will demonstrate the fundamental low-pressure phase relations for the andesitic magmas. The point *p* with the phase assemblage *L*, *S*(ol, en, di, pl) is a reaction point, and the curve from *c* to *p* is a reaction curve where olivine reacts with the liquid-forming enstatite. The phenocryst assemblages suggest that the basaltic andesites initially have plagioclase in the liquidus, while the fractionation towards rhyolite shows that the fractionating magmas end up in a point like *e*. It will therefore be appropriate to test the binary phase assemblages, olivine + plagioclase, clinopyroxene + plagioclase, and orthopyroxene + plagioclase, as the fractionation of these assemblages will move to liquid toward the curve *p–e*. Of these three combinations, the two first can be excluded due to evidence from the oxide digrams in Figure 8, while the latter appears possible. The combination plagioclase + orthopyroxene and combinations of plagioclase + orthopyroxene + clinopyroxene was tested in several least squares runs using different compositions of the minerals based on their phenocryst compositions, and the estimated fractionates are shown in Table 4. It is emphasized here that the detailed results are very dependent on the compositions of the minerals, and the figures given in Table 4 should therefore be considered approximate.

It is evident from the percentages of melt given in Table 4 that the largest amount of fractionation takes place between basaltic andesite and andesite, where the liquid loses 50% of its mass, while fractionation from basaltic andesite to rhyolite implies a loss of 80% of the initial liquid.

The obtained results suggest that basaltic andesite fractionate plagioclase + orthopyroxene, whereby andesite is generated. The andesite fractionates plagioclase + orthopyroxene + clinopyroxene towards dacite, and magnetite is then added to the fractionate, whereafter the liquid moves towards rhyolite. The latest part of the trend from dacite to rhyolite has been demonstrated by paired analyses of the whole rock and matrix compositions by *Ewart et al.* [1973]; the tie lines for the compositions are parallel and in some cases coincident with the trend (Figure 8). The relatively high contents of plagioclase in the fractionates suggested by the least squares results will imply that the andesites with more than 50–55% SiO_2 should show negative Eu anomalies. The REE abundances from Tonga, Mariana, and the South Sandwich islands show that the andesites display negative anomalies, while no anomalies are evident for the most primitive basaltic andesites [*Ewart et al.* 1973; *Hawkesworth et al.,* 1977; *Dixon and Batiza,* 1979].

VOLUME RELATIONSHIPS

It was shown by *Francis and Rundle* [1976] that the volume of the andesitic magmas produced in the Andes is very small compared to the volume of oceanic crust subducted. The implication of this result is not immediately obvious, but it must have important bearings on the dynamic processes which control the andesite genesis.

Consider a unit section being 1 km wide in the direction of the trenches or the line of volcanoes. The volume of andesitic magma erupted in the central Andes was estimated as 5×10^{-6} km^3/yr km by *Francis and Rundle* [1976]. The oceanic crust is about 6.5 km thick, so for a subduction rate of 5 cm/yr the volume subducted for the unit section is given as 3.25×10^{-4} km^3/yr km. The andesitic magma constitutes 1.5% of the subducted crust for this subduction rate.

Similar relationships hold for the intraoceanic island arcs. The best determination on the eruption rate is obtained from the South Sandwich Islands. A sample of the lowermost exposed part of Bristol island in this arc system is 4×10^6 years old. The island itself is about 11×11 km in area, and its volume above sea level is about 60 km^3 [*Baker,* 1978]. The average diameter of the island is 11 km, so that the volume produced along a unit section is 5.45 km^3. With these figures the andesites constitute 0.25% of the subducted crust, with the subduction rate 8.5 cm/yr [*Saunders and Tarney,* 1979]. As the island indicates a maximal production rate, it is given that the proportion of andesite erupted must be an order of magnitude or more lower than 0.25%.

The small percentages of andesite erupted compared to the amount of crust subducted are surprising, as the REE results show that the degree of partial melting must be about 50%. The small percentage may be due to the consolidation of andestitic material at depths, or may be related to a small generation rate of andesitic magma.

The REE abundances of the basaltic andesites show that if any fractionation of the ascending magmas takes place, the amount of fractionation must be small, and it is unlikely that any essential amounts of material are left behind. Andesitic magmas might intrude the oceanic crust beneath the volcanoes and form batholiths, but the geophysical evidence does

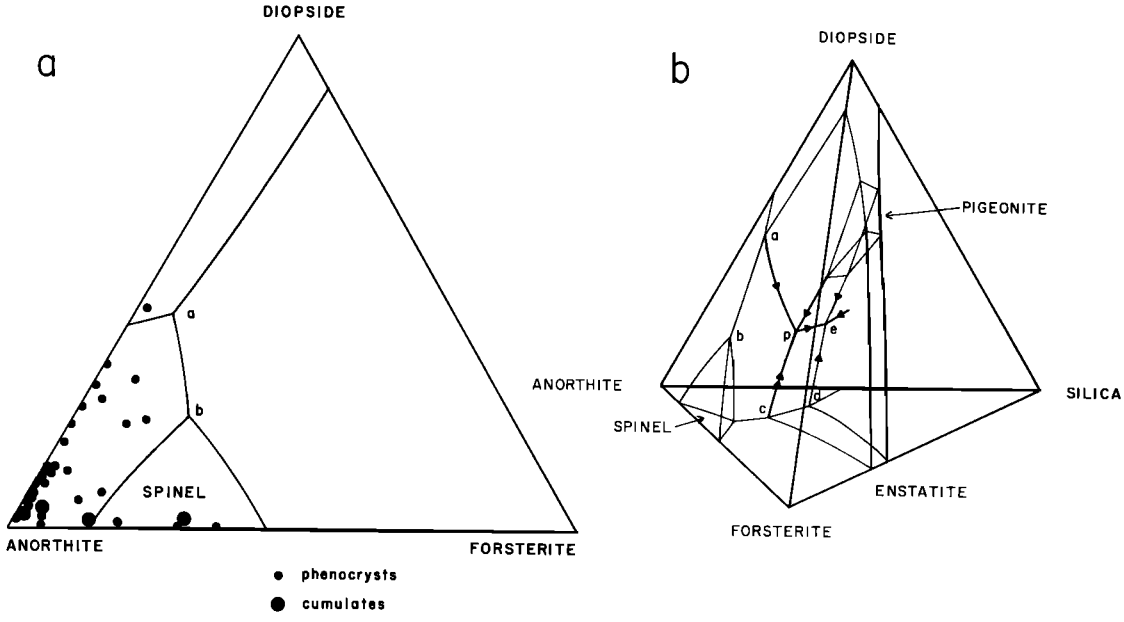

Fig. 11. Petrogenetic model for the generation of oceanic andesites. (*a*) The subductiing lithosphere and the secondary convection cell. The cell transfers mantle material at high temperatures toward the subducted crust, which begins to melt. (*b*) The melt formed at the surface of the subducted crust forms lenses of magma that accumulate in a major magma chamber [cf. *Marsh,* 1976].

not lend support to this possibility. The *P* wave structure of the crust beneath the Kermandec arc system does not indicate the presence of granodioritic layer [*Karig,* 1970]. Similary, the positive gravity anomalies at the center line of the arcs suggest a thickening of the oceanic crust, rather than the presence of bodies of low density [*Hatherton,* 1974]. It is thus considered that the small volume of andesite erupted must be due to a small generation rate of primary andesitic magma.

Dynamic Control of Magma Generation

The descending oceanic crust will receive heat from the mantle situated above it, and its temperature will increase with depth as the temperature of the mantle increases with depth. As new cold oceanic crust descends continuously, the mantle near the crust will undergo steady cooling and its temperature will decrease. So it is unlikely that the mantle will be able to heat the crust to temperatures above its melting point [*Oxburgh and Turcotte,* 1970]. A heat source is needed, Oxburgh and Turcotte suggested that the surface of the subducted crust is heated by friction between the crust and the mantle. It is rather unlikely that friction can produce any large quantities of heat, as the presence of magma will decrease the friction. Hyalomylonites have been observed, but their widths are generally less than a meter, and the generation of melt require extreme velocities for the fault movements [*Wallace,* 1976].

The heat source for the andesite generation is most certainly the secondary convection cell which cause the back arc spreading observed by the intraoceanic island arcs [*Karig,* 1974]. The upper mantle beneath the back-arc spreading axis is highly attenuated, and the attenuation zone extends to the Benioff zone under the volcanoes [*Ewart et al.,* 1973]. The ascending limb of the secondary cell will first generate the new oceanic crust behind the arc systems and will thereafter move towards the Benioff zone and heat the oceanic crust (Figure 11) [*Gill,* 1976; *Tarney et al.,* 1977]. The descending oceanic crust will therefore at some depth come into contact with hot mantle material and be heated. It might be noted here that the convection velocity of the secondary cell should be equal to or higher than the descending velocity of the oceanic crust if the cell supplies heat to the oceanic crust. At some stage the upper surface of the oceanic crust will begin to melt. The solidus temperature increases with increasing depth, and the amount of melt generated will therefore increase until a maximum is reached at a certain depth, whereafter the melt generated begins to solidify. The accumulation of andesitic magma will therefore be confined to a certain depth interval.

The latent heat of silicates is about 100 cal/g, and the specific heat is about 0.25 cal/g [*Yoder,* 1976]. The generation of melt will thus require a large influx of heat from the mantle, and the melting zone will act as a heat sink. The temperature in the oceanic crust below the melting zone will not increase in temperature as long as melting goes on, and the partial melting will be confined to a relatively narrow zone near the crust mantle contact. The rate of descent of the mantle and the oceanic crust must be different, and the upper part of the subducted oceanic crust will therefore be sheared. The liquid is squeezed out to form lensoid bodies of different sizes near the contact plane [Figure 11*b*]. As the melting of the subducted crust takes place along the contact plane for a certain distance, perhaps 10–20 km, it is considered that a series of lensoid bodies is formed.

The liquidus for an andesite with 1% H_2O is 1400°C at 30 kbar, and as the liquidus for a tholeiitic basalt is about 1500 °C at the same conditions, the liquidus for a basaltic andesite must be about 1450 °C [*Wyllie,* 1979]. The temperature of the mantle inducing the partial melting must be somewhat higher and is probably at least 1500 °C. The solidus temperature of lherzolitic materials at 30 kbar is 1500 ± 50 °C [*Yoder,* 1976], and the temperature of the mantle must be near its solidus temperature. It is unlikely that the mantle will surrender any essential amounts of melt as the amount of melt within the crust is much larger than the amount of melt in the lherzolite at these temperatures.

The following features constrain the dynamic models for the genesis of primary andesite, and will form the basis for the model suggested here.

1. Both the convecting mantle in the secondary cell and the subducted oceanic crust are moving downwards, and the melt generated in the crust will also be moved downwards.

2. The eruption from depths of about 100 km require that the magma be accumulated in magma chambers with a volume of about 30 km^3 before the eruption occur [*Maaløe,* 1981].

3. The andesite volcanoes are situated at a constant vertical distance above the Benioff zone, and the source region for the volcanoes must remain at a constant position and depth.

4. The partial melting occurs within a depth interval; the degree of partial melting will first increase with increasing depth and then decrease.

The pressure in the lensoid bodies of magma will increase when they are brought towards greater depths. This applies to the upper part of the melting zone, above the level of maximum degree of partial melting; below this maximum the liquid will solidify by increasing pressure, and the pressure of the liquid will consequently decrease. At some stage the pressure of the magma in the lenses may become so large that the liquid is able to fracture the enclosing rock; thereafter it will move up towards the next lens situated at a higher level (Figure 11*b*). Since a series of lenses is formed near the contact plane, it is thought that the magma will move from one lens to the next until it is finally stored in a major magma chamber situated in the upper part of the melting zone. The depth of this chamber will be determined by the rheological properties of the rocks and is difficult to determine. In the upper part of the melting zone there will probably be a transition from ductile to elastic rocks, and the position of the chamber may be related to such a transition. The major chamber is situated at a constant depth despite the fact that the mantle and subducted crust surrounding it are moving downwards. It must therefore move upwards in relation to the surrounding rocks with the same velocity as their rate of descent. The upward movement may be due to two factors. The influx of magma from the lenses situated below will increase the pressure of the magma in the chamber, and it can therefore move upwards along the contact plane, which is a plane of weakness (Figure 11*b*). The buoyancy of the magma may also be important [*Marsh,* 1978]. Using the equation for diapiric ascent by *Whitehead and Luther* [1975, equation (12)] and assuming that the viscosity of the mantle is 10^{20} poise, that of the magma is 100 poise, and the difference in density between the mantle and the magma is 0.5 g/cm^3, the ascent rate of a diapir with a radius of 3 km is calculated as 5 cm/yr. The volume of this chamber is 113 km^3, and therefore it is of the required size for eruption to occur. As the magma is accumulated from a planar surface region, there is no reason to assume that the major chamber is spherical, but the calculations show that buoyancy may be important for the behavior of the major magma chamber.

As the lenses of magma are brought downwards, it is likely that at least part of the generated magma solidifies and never reaches the major chamber. A reason for the very modest eruption rates may therefore be the descending movement of the whole system. However, the isotope data show that it is only the hydrothermally contaminated basaltic section that forms andesitic magmas, and the thickness of the zone undergoing partial melting is therefore less than about 3 km.

PETROGENESIS OF ANDESITES

On the basis of the features described above, the following model for the petrogenesis of andesites is considered appropriate:

1. The basaltic section of the abyssal crust is contaminated with radiogenic Sr, while its ε_{Nd} remains unchanged.

2. The oceanic crust is subducted, while the veneer of sediment is accreted in the trenches.

3. The subducted crust is heated by the secondary convection cell and is dehydrated or nearly dehydrated before the melting starts [*Huang and Wyllie,* 1973].

4. Partial melting of the crust begins at depths of about 100 km or slightly less. Accumulation of magma occurs at depths larger than 100 km, and a major magma chamber, which is the source for the andesite volcanoes, is formed at depths of about 100 km or more. It is not yet known if the source region for the volcanoes is situated vertically beneath the volcanoes.

5. Melting occurs in a zone which is less that 3 km thick, and the magma forms lenses from near the contact plane to the mantle above the subducted crust. Magma in the major chamber is accumulated from these minor lensoid bodies, which are spread over the contact plane. The distances between the volcanoes in the intraoceanic island arcs vary from about 50 to 100 km, and the source region for the major chambers is apparently quite large.

6. The andesitic volcanoes of the intraoceanic island arcs erupt at intervals of about 50–100 years. The mantle above the source region is hot, and the primary andesitic magmas, with the composition of basaltic andesite, are not fractionated during their ascend. The fractionation towards rhyolite occurs at relatively low pressures of less than 10 kbar, where plagioclase is stable.

7. In the oceanic regions the basaltic andesites tend to erupt at the surface [*Baker,* 1978], and basalts fractionated of rhyolitic composition are relatively uncommon. In the continental regions the primary andesitic magmas undergo contamination with sedimentary material whereby intermediate grandioritic magmas are formed. The ε_{Nd} values for continental basaltic andesites are not yet known, but it will be interesting to see if they are positive or negative.

Acknowledgments. The authors express their gratitude to H. Furnes for his advice during the preparation of this paper.

REFERENCES

Allégre, C. J., and D. B. Othman, Nd-Sr isotopic relationships in granitoid rocks and continental crust development: a chemical approach to orogenesis, *Nature, 286,* 335–342, 1980.

Anderson, A. T., Some basaltic and andesitic gases, *Rev. Geophys. Space Phys., 13,* 37–55, 1975.

Baker, P. E., The South Sandwich islands, 3, Petrology of the volcanic rocks, *Sci. Rep. 93,* 34 pp., Brit. Antarctic Surv., London, 1978.

Barker, F., J. G. Arth, and T. Hudson, Tonalites in crustal evolution, *Phil. Trans. R. Soc. Lond. A,* in press, 1981.

Barreiro, B., and G. R. Tilton, U-Th-Pb studies on quaternary volcanics and precambrian basement rocks from southern Peru, *Geol. Soc. Am. Ann. Meet. Abstr. 80,* 1980.

Bateman, P. C., L. D. Clark, N. K. Harker, J. G. Moore, and C. D. Rinehardt, The Sierra Nevada Batholith, A synthesis of recent work across the central part, *U.S. Geol. Surv. Prof. Pap., 414D,* 1963.

Benioff, H., Orogenesis and deep crustal structures—Additional evidence from seismology, *Geol. Soc. Am. Bull., 65,* 385–400, 1954.

Bowen, N. L., The granite problem and the method of multiple prejudices, *Geol. Soc. Am. Mem. 28,* 79–90, 1948.

Bryan, W. B., G. D. Stice, and A. Ewart, Geology, petrography, and geochemistry of the volcanic islands of Tonga, *J. Geophys. Res., 77,* 1566–1585, 1972.

Cameron, W. E., E. G. Nisbet, and V. J. Dietrich, Boninites, komatiites and ophiolitic basalts, *Nature, 280,* 550–553, 1979.

Chayes, F., Numerical correlation and petrographic variation, *J. Geol., 70,* 440–452, 1962.

Chayes, F., Variance-covariance relations in some published Harker diagrams of volcanic suites, *J. Petrol., 5,* 219–237, 1964.

Coats, R. R., Magma type and crustal structure in the Aleutian arc, in *The Crust of the Pacific Basin, Geophys. Monogr. Ser.,* vol. 6, edited by G. A. Macdonald and H. Kuno, pp. 92–109, AGU, Washington, D. C., 1962.

Cohen, L. H., K. Ito, and G. C. Kennedy, Melting and phase relations in anhydrous basalt to 40 kilobars, *Am. J. Sci., 265,* 475–537, 1967.

Condie, K. C., *Plate Tectonics and Crustal Evolution,* Pergamon, New York, 1976.

DePaolo, D. J., Sources of continental crust: Neodymium isotope evidence from the Sierra Nevada and Peninsular Ranges, *Science, 209,* 684–687, 1980.

DePaolo, D. J., and R. W. Johnson, Magma genesis in the New Britain island arc: Constraints from Nd and Sr isotopes and trace element patterns, *Contrib. Mineral. Petrol., 70,* 367–379, 1979.

DePaolo, D. J., and G. J. Wasserburg, Nd isotope variations and petrogenetic models, *Geophys. Res. Lett.,* 3, 249–252, 1976.

DePaolo, D. J., and G. J. Wasserburg, The sources of island arcs as indicated by Nd and Sr isotopic studies, *Geophys. Res. Lett., 4,* 465–468, 1977.

Dietrich, V., R. Emmermann, R. Oberhänsli, and H. Puchelt, Geochemistry of basaltic and gabbroic rocks from the west Mariana basin and the Mariana trench, *Earth Planet. Sci. Lett., 39,* 127–144, 1978.

Dixon, T. H., and R. Batiza, Petrology and chemistry of recent lavas in the northern Marianas: Implications for the origin of island arc basalts, *Contrib. Mineral. Petrol, 70,* 167–181, 1979.

Dostal, J., M. Zentilli, J. C. Caellis, and A. H. Clark, Geochemistry and origin of oceanic rocks of the Andes (26°–28°S), *Contrib. Mineral. Petrol., 63,* 113–128, 1977.

Eggler, D. H., Water saturated and undersaturated melting relations in a Paracutin andesite and an estimate of water content in a natural magma, *Contrib. Mineral. Petrol., 34,* 261–271, 1972.

Eggler, D. H., Effect of CO_2 on the melting of periodotite, *Yearbook Carnegie Inst. Wash., 73,* 215–224, 1974.

Ewart, A., and W. B. Bryan, Petrography and geochemistry of the igneous rocks from Eua, Tonga Islands, *Geol. Soc. Am. Bull., 83,* 3281–3298, 1972.

Ewart, A., W. B. Bryan, and J. B. Gill, Mineralogy and geochemistry of the younger volcanic islands of Tonga, S. W. Pacific, *J. Petrol., 14,* 429–465, 1973.

Flood, R. H., R. M., Vernon, S. E. Shaw, and B. W. Chappell, Origin of pyroxene-plagioclase aggregates in a rhyodacite, *Contrib. Mineral. Petrol., 60,* 299–309, 1977.

Francis, P. W., and C. C. Rundle, Rates of production of the main magma types in the Central Andes, *Geol. Soc. Am. Bull., 87,* 474–480, 1976.

Francis, P. W., M. J. Roobot, G. P. L. Walker, P. R. Cobbold, and M. Coward, The San Pedro and San Pablo volcanoes of northern Chile, *Geol. Rundsch.,* 357–388, 1974.

Gill, J. B., Role of undertrust oceanic crust in the genesis of a Fijian calc-alkaline suite, *Contrib. Mineral. Petrol., 43,* 29–45, 1974.

Gill, J. B., Composition and age of the Lau basin and ridge volcanic rocks: Implications for evolution of intra oceanic arc basin and remnant arc, *Geol. Soc. Am. Bull., 87,* 1384–1395, 1976.

Gledhill, A., and P. E. Baker, Strontium isotope ratios in volcanic rocks from the South Sandwich islands, *Earth Planet. Sci. Lett., 19,* 369–372, 1973.

Green, T. H., Crystallization of calc-alkaline andesites under controlled high pressure hydrous conditions, *Contrib. Mineral. Petrol., 34,* 150–166, 1972.

Green, T. H., and A. E. Ringwood, Genesis of the calcalkaline igneous rock suite, *Contrib. Mineral. Petrol., 18,* 105–162, 1968.

Hatherton, T., Active continental margins and Island arcs, in *The Geology of Continental Margins,* pp. 93–103, edited by C. A. Burk, and C. L., Drake, Springer-Verlag, Berlin, 1974.

Hawkesworth, C. J., R. K. O'Nions, R. J. Pankhurst, P. J. Hamilton, and N. M. Evensen, A geochemical study of island arc and back-arc tholeiites from the Scotia sea, *Earth Planet. Sci. Lett., 36,* 253–262, 1977.

Higgins, M. W., Petrology of Newberry volcano, central Oregon, *Geol. Soc. Am. Bull., 84,* 455–488, 1973.

Hofmann, A. W., and S. R. Hart, An accessment of local and regional isotopic equilibrium in the mantle, *Earth Planet. Sci. Lett., 38,* 44–62, 1978.

Huang, W., and P. J. Wyllie, Melting relations of muscovite-granite to 35 kbar as a model for fusion of metamorphosed subducted oceanic sediments, *Contrib. Mineral. Petrol., 42,* 1–14, 1973.

Humphries, S. E., and G. Thompson, Trace element mobility during hydrothermal alteration of oceanic basalts, *Geochim. Cosmochim. Acta, 42,* 127–136, 1978.

Irvine, T. N., and W. R. A. Baragar, A guide to the chemical classification of the common volcanic rocks, *Can. J. Earth Sci., 8,* 523–548, 1971.

Irving, A. J., A review of experimental studies of crystal/liquid trace element partitioning., *Geochim. Cosmochim. Acta, 42,* 743–770, 1978.

Isacks, B. L., and M. Barazangi, Geometry of Benioff zones: Lateral segmentation and downward bending of the subducted lithosphere, in *Island Arcs, Deep Sea Trenches and Back-Arc Basins, Maurice Ewing Ser.,* vol. 1, edited by M. Talwani and W. C. Pitman, pp. 99–114, AGU, Washington D. C., 1977.

Karig, D. E., Ridges and basins of the Tonga-Kermandec island arc system, *J. Geophys. Res., 75,* 239–254, 1970.

Karig, D. E., Evolution of arc systems in the western Pacific, *Ann. Rev. Earth Planet. Sci., 2,* 51–75, 1974.

Kay, R. W., and N. J. Hubbard, Trace elements in ocean ridge basalts, *Earth Planet. Sci. Lett., 38,* 95–118, 1978.

Kuno, H., Petrology of Hakone volcano and the adjacent areas, Japan, *Geol. Soc. Am Bull., 61,* 957–1020, 1950.

Kushiro, I., H. S. Yoder, and M. Nishihawa, Effect of water on the melting of enstatite, *Bull. Geol. Soc. Am., 79* 1685–1692, 1968.

Larsson, E. E., R. L. Reyneolds, R. Merrill, S. Levi, M. Ozima, Y. Aoki, H. Kinoshita, S. Zassku, N. Kawai, T. Nakajima, and K. Hirooka, Major element petrochemistry of some extrusive rocks from the volcanically active Mariana islands, *Bull. Volcanol., 38,* 361–377, 1974.

Lopez-Escobar, L., F. A. Frey, and M. Vergara, Andesites and high alumina basalts from the central south Chile high Andes: Geochemical evidence bearing on their petrogenesis, *Contrib. Mineral. Petrol., 63,* 199–228, 1977.

Maaløe, S., Quantitative analysis of trends controlled by fractional crystallization, *Bull. Geol. Soc. Den.,* in press, 1981.

Maaløe, S., and T. S. Petersen, Phase relations governing the derivation of alkaline basaltic magmas from primary magmas at high pressure, *Lithos, 9,* 243–252, 1976.

Maaløe, S., and P. J. Wyllie, Water content of a granite magma deduced from the sequence of crystallization determined experimentally with water-undersaturated conditions, *Contrib. Mineral. Petrol., 52,* 175–191, 1975.

Marsh, B. D., Mechanics of Benioff zone magmatism, *Geophys. Monogr. 19,* 337–350, 1976.

Marsh, B. D., On the cooling of ascending andesite magma, *Phil. Trans. R. Soc. Lond. A, 288,* 611–625, 1978.

McNutt, R. H., J. H. Crocket, A. H. Clark, J. C. Caelles, E. Farrar, and S. J. Haynes, Initial $^{87}Sr/^{86}Sr$ ratios of plutonic and volcanic rocks of the central Andes, between latitudes 26° and 29° South, *Earth Planet. Sci. Lett., 27,* 305–313, 1975.

Melson, W. G., E. Jarosewich, and C. A. Lundquist, Volcanic eruption at Metis shoal, Tonga, 1967–1968: Description and petrology, *Smithson. Contrib. Earth Sci., 4,* 1970.

Mottl, M. J., and H. D. Holland, Chemical exchange during hydrothermal alteration of basalt by seawater, 1, Experimental results for major and minor components of seawater, *Geochim. Cosmochim. Acta, 42,* 1103–1115, 1978.

Mysen, B. O., and A. L. Boettcher, Melting of a hydrous mantle: II. Geochemistry of crystals and liquids formed by anatexis of mantle periodtite at high pressures and high temperatures as a function of controlled activities of water, hydrogen, and carbon dioxide, *J. Petrol., 16,* 549–593, 1975.

Nicolls, I. A., Liquids in equilibrium with peridotitic mineral assemblages at high water pressures, *Contrib. Mineral. Petrol., 45,* 289–316, 1974.

Nicolls, I. A., and A. E. Ringwood, Production of silica saturated tho-

leiitic magmas in island arcs, *Earth Planet. Sci. Lett., 17,* 243–246, 1972.

O'Hara, M. J., The bearing of phase equilibria studies in synthetic and natural systems on the origin and evolution of basic and ultrabasic rocks, *Earth Planet. Sci. Rev., 4,* 69–133, 1968.

Oxburgh, E. R., and D. L. Turcotte, Thermal structure of island arcs, *Geol. Soc. Am. Bull., 81,* 1665–1688, 1970.

Presnall, D. C., and P. C. Bateman, Fusion relations in the system $NaAlSi_3O_8$-$CaAl_2Si_2O_8$-$KAlSi_3O_8$-SiO_2-H_2O and generation of granitic magma in the Sierra Nevada batholith, *Geol. Soc. Am. Bull., 84,* 3181–3202, 1973.

Presnall, D. C., S. A. Dixon, J. R. Dixon, T. H. O'Donnell, N. L. Brenner, R. L. Schrock, and D. W. Dycas, Liquidus phase relations on the join diopside-forsterite-anorthite from 1 bar to 20 kbar: Their bearing on the generation and crystallization of basaltic magma, *Contrib. Mineral. Petrol., 66,* 203–220, 1978.

Read, H. H., *The Granite Controversy,* Thomas Murby, London, 1957.

Ross, D. C., Descriptive petrography of three large granitic bodies in the Ingo mountains, California, *U. S. Geol. Surv. Prof. Pap., 601,* 1969.

Ross, D. C., Petrographic and chemical reconnaiscance study of some granitic and gneissic rocks near the San Andreas fault from Bodega to Cajon Pass, California. *U.S. Geol. Surv. Prof. Pap., 698,* 1972.

Ringwood, A. E., The petrological evolution of island arc systems, *J. Geol. Soc. London, 130,* 183–204, 1974.

Ringwood, A. E., and D. H. Green, An experimental investigation of the gabbro-eclogite transformation and some geological implications, *Tectonophysics, 3,* 383–427, 1966.

Saunders, A. D., and J. Tarney, The geochemistry of basalts from a back arc spreading center in the east Scotia sea, *Geochim. Cosmochim. Acta, 43,* 555–572, 1979.

Sederholm, J. J., *Selected Works: Granite and Migmatites,* Oliver and Boyd, Edinburgh, 1967.

Smith, R. G., Geology of Saipan, Mariana Islands. Petrology of the volcanic rocks, *U. S. Geol. Surv. Prof. Pap., 280-B,* 127–174, 1957.

Stern, R. J., On the origin of andesite in the northern Mariana island arc: Implications from Agrigan, *Contrib. Mineral. Petrol., 68,* 207–219, 1979.

Stern, C. R., W. L., Huang, and P. J. Wyllie, Basalt-andesite-rhyolite-H_2O: crystallization intervals with excess H_2O, and H_2O undersaturated liquidus surfaces to 35 kilobars, with implications for magma genesis, *Earth Planet. Sci. Lett., 28,* 189–196, 1975.

Sykes, L. R., B. L. Isacks, and J. Oliver, Spatial distribution of deep and shallow earthquakes, of small magnitudes in the Fiji-Tonga region, *Bull. Seismol. Soc., Am. 59,* 1093–1113, 1969.

Tanadata, H., Volcanoes in the Mariana islands in the Japanese mandated south seas. *Bull. Volcanol., 5,* 199–226, 1940.

Tarney, J., A. D. Saunders, S. D. Weaver, Geochemistry of volcanic rocks from the island arcs and marginal basins of the Scotia arc region, in *Island Arcs, Deep Sea Trenches, and Back-Arc Basins, Maurice Ewing Ser., vol.* 1, edited by M. Talwani, and W. C. Pitman, pp. 367–378., AGU, Washington, D. C., 1977.

Thorpe, R. S., P. J. Potts, and P. W. Francis, Rare earth data and petrogenesis of andesite from the northern Chilean Andes, *Contrib. Mineral. Petrol., 54,* 65–78, 1976.

Uyeda, S., Some basic problems in the trench-arc-back arc system, in *Island Arcs, Deep Sea Trenches, and Back-Arc Basins,* Maurice Ewing Ser., vol. 1, edited by M. Talwani, and W. C. Pitman, pp. 1–14, AGU, Washington, D. C., 1977.

Wallace, R. C., Partial fusion along the alpine fault zone, New Zealand, *Geol. Soc. Am. Bull., 87,* 1225–1228, 1976.

Whitehead, J. A., and D. S. Luther, Dynamics of laboratory diapir and plume models, *J. Geophys. Res., 80,* 705–717, 1975.

Wise, W. S., Geology and petrology of the Mt. Hood area: A study of high Cascade volcanism, *Geol. Soc. Am. Bull., 80,* 969–1006, 1969.

Wyllie, P. J., Magmas and volatile components, *Am. Mineral., 64,* 469–500, 1979.

Yoder, H. S., Diopside-anorthite-H_2O at five and ten kilobars and its bearing on explosive volcanism, *Yearbook Carnegie Inst. Wash., 64,* 82–89, 1965.

Yoder, H. S., *Generation of Basaltic Magma,* National Academy of Science, Washington, D.C., 1976.

Yoder, H. S., and C. E. Tilley, Origin of basalt magmas: An experimental study of natural and synthetic systems, *J. Petrol., 3,* 342–532, 1962.

Zeil, W, and H. Pichler, Die känozoische rhyolith-formation im mittleren Absnitt der Anden, *Geol. Rundsch., 57,* 48–81, 1968.

(Received November 3, 1980;
revised May 14, 1981;
accepted May 19, 1981.)

JOURNAL OF GEOPHYSICAL RESEARCH, VOL. 86, NO. B11, PAGES 10287-10302, NOVEMBER 10, 1981

GRAVITY AND THERMAL MODELS FOR THE TWIN PEAKS SILICIC VOLCANIC CENTER, SOUTHWESTERN UTAH

Daniel L. Carrier[1] and David S. Chapman

Department of Geology and Geophysics, The University of Utah
Salt Lake City, Utah 84112

Abstract. Gravity, heat flow, and surface geology observations have been used as constraints for a thermal model of a late Tertiary silicic volcanic center at Twin Peaks, Utah. Silicic volcanism began in the area with the extrusion of the Coyote Hills rhyolite 2.74 ± 0.1 m.y. ago, followed by the Cudahy Mine obsidian, felsite, and volcanoclastics, and finally by a complex sequence of domes and flows that lasted until 2.3 ± 0.1 m.y. ago. Basalt sequences span the time 2.5 to 0.9 m.y. Terrain-corrected Bouguer gravity anomalies at Twin Peaks are shaped by three features of varying characteristic dimensions: (1) a major north-northeast trending -30 mGal gravity trough roughly 40 km wide caused by a thick sequence of Cenozoic sediments in the Black Rock Desert Valley, (2) a local roughly circular -7 mGal gravity low, 26 km across, probably related to an intrusive body in the basement, and (3) a series of narrow positive anomalies up to +10 mGal produced by the major Twin Peaks volcanic domes. The intrusive bodies have been modeled as three-dimensional vertical cylinders; the total volume of intrusive material is estimated to be about 500 km^3. Simple thermal models, assuming conductive heat transfer and using geometrical constraints from the gravity results, predict that a negligible thermal anomaly should exist 1 m.y. after emplacement of the intrusion. This prediction is consistent with an average heat flow of 96 $mW\ m^{-2}$ for the area, not significantly different from eastern Basin and Range values elsewhere. Magmatic longevity of this system, 2.7 to 2.3 m.y. for silicic volcanism or 2.5 to 0.9 m.y. for basaltic volcanism, does not seem to prolong the cooling of this system substantially beyond that predicted by conductive cooling.

Introduction

'The principal basis for estimating thermal energy in igneous-related geothermal systems is the evidence for the existence of high-level silicic magma chambers, their volumes, and the ages of the latest eruptions from them.' [Smith and Shaw, 1978] A simplified rationale for evaluating geothermal systems associated with young igneous rocks based on this premise is shown in Figure 1 [Smith and Shaw, 1975, 1978]. The models assume cooling of a fixed volume by conduction in surrounding rock from a specified initial temperature. Solid lines on Figure 1 indicate the age-volume interplay which divides active from extinct systems. Principal uncertainties in this theoretical scheme concern the effects of hydrothermal circulation in and around magma bodies which would accelerate postsolidification cooling, and magmatic longevity which would have an opposite effect (see Smith and Shaw [1978], for discussion). The most important uncertainty in evaluating actual systems is the volume estimate.

In the context of the cooling of igneous-related geothermal systems we have investigated the Twin Peaks silicic volcanic system of south-central Utah. The system, although believed to be extinct (see Figure 1) is of particular interest because the period of magmatic activity preceding final cooling (magmatic longevity) is comparable to its cooling time. By combining volume estimates from gravity measurements with new dates for the system [Evans et al., 1980] we are able to evaluate the age-volume and theoretical cooling characteristics of the system in the sense of Figure 1. We have also made five new heat flow determinations in and around Twin Peaks, and these results serve as a limiting constraint to test the applicability of the cooling models. The petrologic and geochemical evolution of the Twin Peaks system is described in an accompanying paper [Crecraft et al., this issue].

Geologic Setting

The Twin Peaks, Utah, silicic volcanic center, is located in the Black Rock Desert Valley, near the eastern margin of the Basin and Range Province (Figure 2). This broad valley is bounded by early Paleozoic and late Precambrian rocks in the Beaver and Cricket mountains to the west, Paleozoic and Mesozoic rocks in the Pavant Range to the east, and early Paleozoic rocks in the northern Mineral Mountains to the south. Precambrian rocks in the region surrounding Twin Peaks are composed of gneisses and schists similar to those of the Farmington complex [Nielson et al., 1978] and quartzites in the Beaver Mountains [Woodward, 1976]. Late Precambrian quartzites in the Beaver Mountains are transitional into the Prospect Mountain quartzites of the Lower Cambrian. Overlying Paleozoic rocks are dominated by limestones in the west and dolomites in the east. Mesozoic rocks near Twin Peaks are exposed only in the Pavant Range and include the Triassic Moenkopi Formation through the Jurassic Navajo sandstone in the western range and the Cretaceous Price River Conglomerates and North Horn Formation in the eastern range. Cenozoic sedimentation in the Black Rock Desert Valley is dominated by the deposition of a thick sequence of freshwater and alluvial sediments and is discussed by MacDonald [1976].

Volcanic activity began to the southeast of

[1]Now at Union Geothermal Division Santa Rosa, California 95401.

Copyright 1981 by the American Geophysical Union.

Paper number 1B1477.
0148-0227/81/001B-1477$01.00

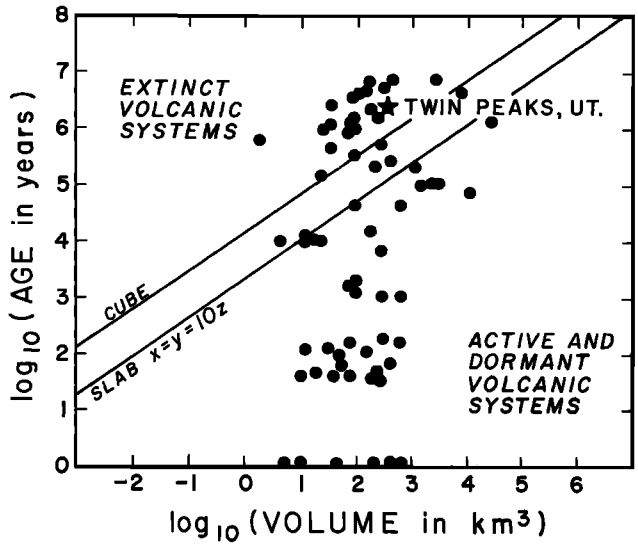

Fig. 1. Age-volume estimates and cooling models (lines) for young igneous systems of the western United States [after Smith and Shaw, 1978, Figure 3]. Systems which plot above the lines are predicted to be approaching ambient temperatures at emplacement depth. Most of the systems younger than 10,000 years are associated with Aleutian, Cascade or Hawaiian volcanoes. The Twin Peaks silicic volcanic system described in this study is identified by the star.

Twin Peaks in the vicinity of the Tushar Mountains during the Oligocene [Hintze, 1973] and southwest of Twin Peaks in the Mineral Mountains in mid-Miocene. There is no direct suggestion that this early activity extended into the Twin Peaks area. Volcanic activity in the Twin peaks area proper (Figure 3) began with the extrusion of the Coyote Hills rhyodacite dated by K/Ar methods at 2.7 ± 0.1 m.y. [Evans et al., 1980]. A period of quiescence that followed lasted nearly 0.3 m.y., being interrupted by the extrusion of a complex sequence of domes and flows (see Figure 3) that lasted until 2.3 ± 0.1 m.y. Preliminary geochemistry and petrology results show a trend of increasing silica concentration with time, each extrusive event representing successive tappings of a single evolving magma chamber [Crecraft et al., 1980, this issue]. Chemically, the Coyote Hills rhyolite contains the least amount of silica and is the least evolved rhyolite in the area. The Cudahy Mine rhyolite is the most evolved rhyolite exposed at the surface, although an even more evolved rhyolite was found in a drill hole core sample.

Local basaltic volcanism began with the extrusion of the Black Point basalt 2.0 m.y. ago [Clark, 1977]. Four other basic flows were mapped by Clark [1977]. They are the Black Rock basalt, extruded at 0.97 m.y. ago, and three younger flows belonging to the Burnt Mountain Field (Figure 3). Lacustrine sediments and basalts are domed to the southeast of South Twin peak (Figure 3); the cause of the doming is unknown but may be caused by late-stage rhyolitic material emplaced in the area.

Gravity

Density, Lithology, and Seismic Control

The volume of an intrusive can only be determined by gravity methods if the density of the intrusive differs from that of the country rock. To determine the sensitivity of gravity methods in the Twin Peaks region, we first made a density analysis of representative rocks from the area. Results of water saturated densities for samples from 122 localities are given in Table 1. Samples were initially separated into regional and local groupings and further classified by lithology, the latter description coinciding with mapped units on the Utah state geologic map [Stokes, 1963].

Measured densities of the regional limestones, quartzites, and dolomites are tightly distributed about their means. With the exception of shale and quartzite, the average densities of these rock types are distinguishable from one another with 99% confidence, using a one-sided Student t-test of significance [Daniel, 1977]. Densities of the local rocks exhibit a greater range than those of regional rocks, with the density of surface lacustrine sediments showing the greatest scatter. There is little overlap between densities of local and regional units, and significantly, the density of the dome rhyolite is distinguishable from the density of regional rocks with a high confidence limit.

Lithological and structural control for pre-Tertiary regional rocks is based on the work of Hintze [1973], Woodward [1973], and Stokes [1963]. For purposes of gravity modeling, rocks in the Cricket and Beaver mountains were divided into two dominant rock types (Table 2) to which average densities were assigned based on lithology. A third group of rocks is composed of gneiss and schists, which are exposed in the Mineral Range about 30 km south of the Twin Peaks area [Hintze, 1973; Nielson et al., 1978]. These rocks, likened to the Farmington complex [Nielson et al., 1978], are assigned a density of 2.81 g/cm^3 from seismic velocities [Gertson, 1979; Woollard, 1962]. An average density of 2.71 g/cm^3 was assigned to the general basement rocks, based upon the lithology of pre-Mesozoic rocks in the Pavant Range [Hintze, 1973]. Cenozoic sediments in the Twin Peaks area are divided into two layers. The upper layer composed of late Tertiary-Quaternary lacustrine sediments, was assigned a density of 2.30 g/cm^3 while the second layer, composed of Tertiary lacustrine and land sediments and volcanics [MacDonald, 1976], was assigned a density of 2.40 g/cm^3. Both the layering and the density contrasts are consistent with seismic refraction results and gravity modeling in the adjacent Milford Valley graben [Gertson, 1979].

Structural control for the western part of the Black Rock Desert Valley was obtained from two seismic reflection lines [MacDonald, 1976] located 15 km (line 20, Figure 2) and 25 km north of the Twin Peaks area, respectively. Time was converted to depth for line 20 in Figure 6 using seismic velocities in Table 2.

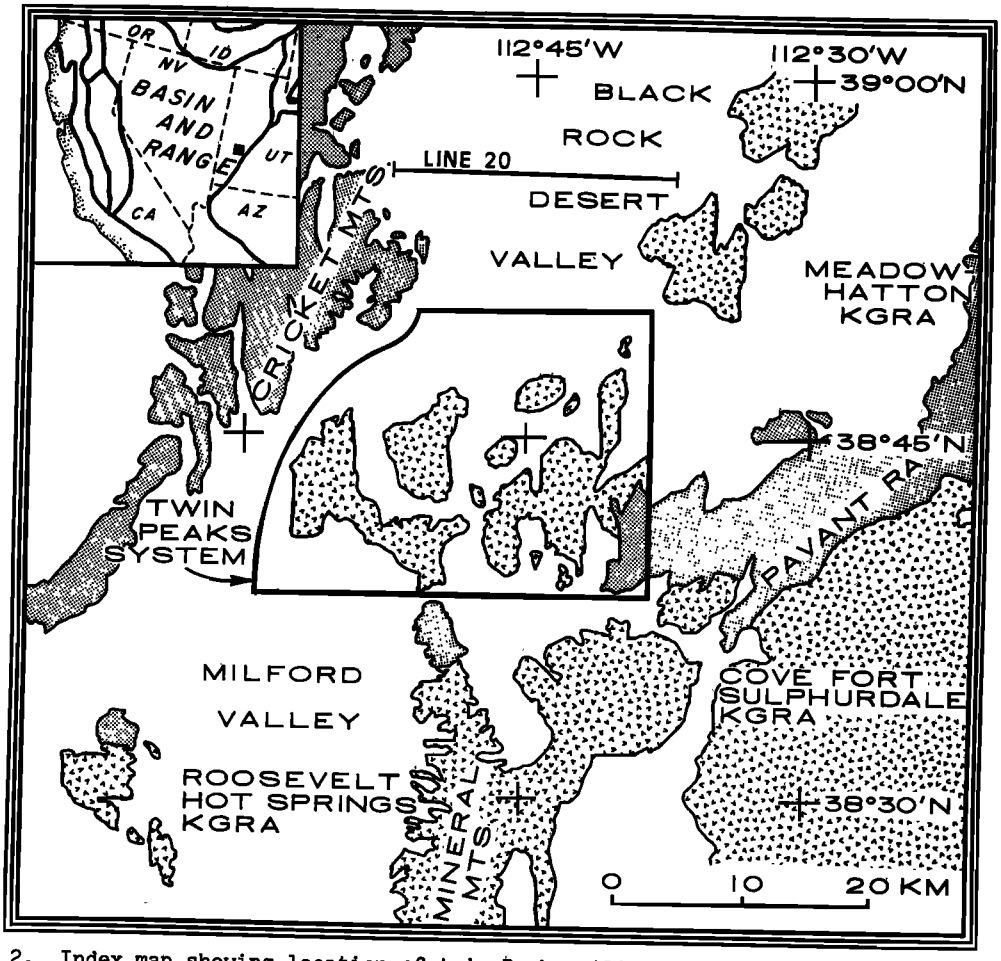

Fig. 2. Index map showing location of twin Peaks silicic volcanic center (irregular solid outline) in west central Utah and its relation to three known geothermal resource areas (KGRA's). Stipled pattern represents Tertiary igneous rocks. Line 20 identifies a seismic reflection profile discussed in the text. All following geologic and gravity maps (Figures 3, 4, 6, and 7) are bounded by the solid outline in this figure and include North Twin Peak (NTP) and South Twin Peak (STP) for orientation.

Gravity Data Acquisition and Reduction

Gravity data used in this study include 349 previously obtained gravity stations [Isherwood, 1967; Brumbaugh, 1978; Case, 1977; Carter, 1978; Serpa, 1980] supplemented by an additional 285 gravity stations collected during the summers of 1977 and 1978. Principal facts for the new gravity stations are recorded in Appendix D of Carrier [1979].

Gravity readings were reduced to a minimum elevation datum of 1371.6 m (4500 ft), with a density of 2.45 g/cm^3 and further to sea level with the normal 2.67 g/cm^3 density. The density of 2.45 g/cm^3 is based on measured densities of rocks representative of local surface geology. Several attempts were made to estimate surface density utilizing the density profile method [Nettleton, 1942]; however, the influence of subsurface structure on measured gravity was such that it negated the effectiveness of the technique.

Terrain corrections were made using U.S. Coast and Geodetic Survey terrain correction charts [Swick, 1942] through zone E and a computer technique from E to a radial distance of 20 km from each station. The average terrain correction using a density of 2.45 g/cm^3 was 0.47 mGal with a range of 0.08 to 4.85 mGal. Terrain corrections for stations taken in the survey generally did not exceed 2.5 mGal. We estimate the uncertainty in our gravity values, including reading, location, elevation, and topographic correction uncertainties to be about 1 mGal.

Terrain Corrected Bouguer Anomaly Map

A terrain-corrected Bouguer anomaly gravity map with a contour interval of 2 mGal is shown in Figure 4. The western portion of the map is dominated by a strong east-west gravity gradient across gravity contours that trend roughly north-south and are continuous for an additional 80 km to the north [Cook et al., 1975]. Gravity decreases from -164 mGal on the eastern outcrop of the Cricket Mountains to -200 mGal in the vicinity of North and South Twin Peaks and

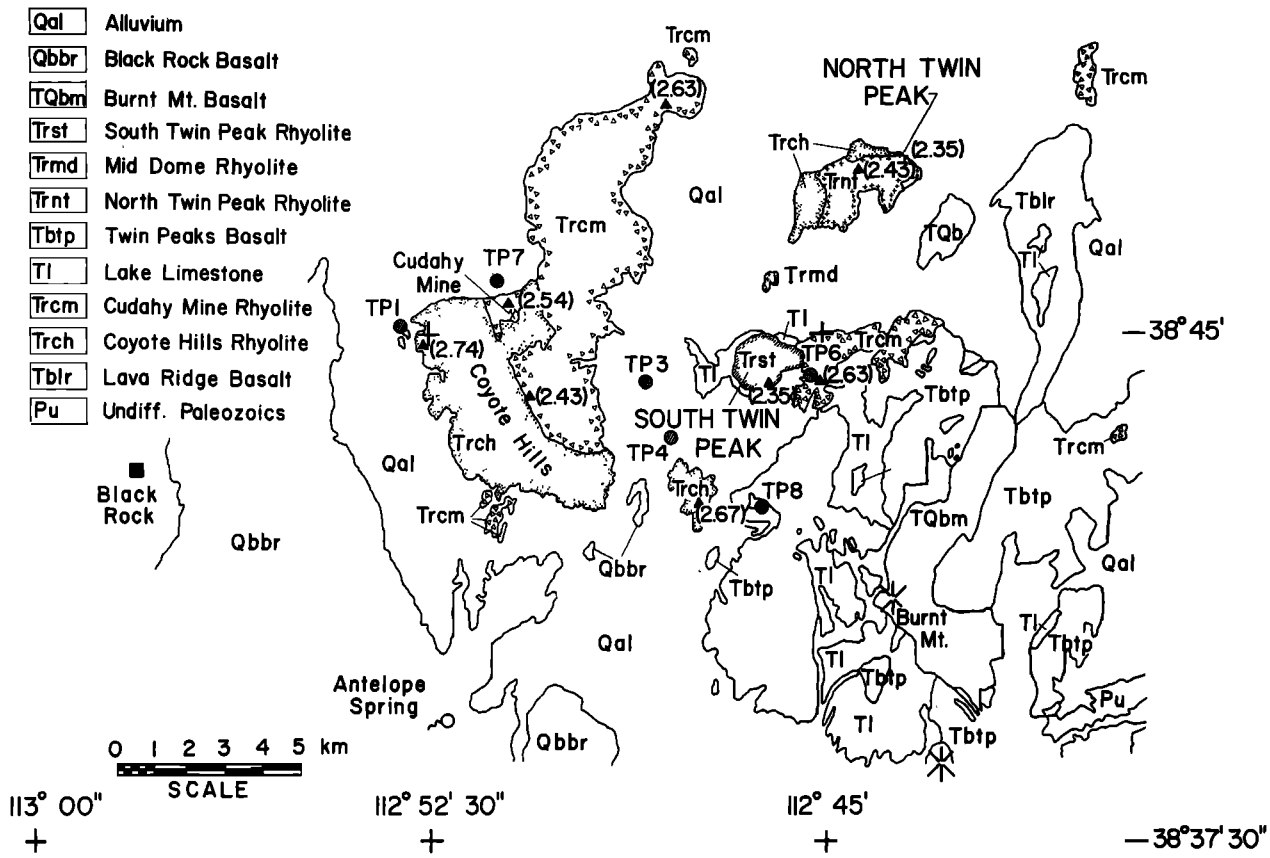

Fig. 3. Geological map of the Twin Peaks magma system within the boundary shown in Figure 2. North Twin Peak and South Twin Peak are two prominent rhyolite domes, hence the name for the igneous system. Rhyolites are marked with patterns. Solid triangles indicate sample locations for K/Ar dating; ages in m.y. B.P. are in parentheses. Heat flow drill hole locations are indicated by TP1 through TP8.

recovers to -190 mGal approaching the Pavant Range to the east. This north-northeast trending gravity trough is the major feature of the gravity field and is undoubtably caused by the low-density sediments of the Black Rock Desert Valley. Other obvious features in the gravity field are a pronounced gravity low in the southwest corner of the map (Figure 4) associated with the Milford Valley graben [Carter, 1978], positive gravity spurs to the southwest of the Cricket Mountains and in the northern Mineral Mountains due to buried ridges of high density Paleozoic formations, and local positive anomalies associated with North and South Twin Peaks domes. The gravity field is thus seen to be a superposition of effects from both Basin and Range horst-graben structure and from the volcanic field, the subsurface configuration of which is our prime interest. In the following section we attempt to separate these two effects.

TABLE 1. Measured Densities for Rocks of the Twin Peaks Area

Rock Type	N	Average, g/cm^3	Standard Deviation, g/cm^3
Regional			
Shale	7	2.63	0.07
Quartzite	29	2.63	0.03
Limestone	31	2.72	0.05
Dolomite	16	2.83	0.04
Local			
Lacustrine sediments	15	2.30	0.15
Rhyolite			
Dome	6	2.46	0.03
Flow	7	2.29	0.04
Basalt	11	2.66	0.07

TABLE 2. Compilation of Densities and Seismic Velocities for Characteristic Rocks in the Twin Peaks Area and Vicinities

Symbol	Rock Types	Area of Surface Exposure	Thickness, km	Average Density g/cm^3	Density Constrast g/cm^3	Seismic Velocities km/s	Sources*
TQls	LACUSTRINE SEDIMENTS	Twin Peaks	undetermined	2.30	-0.41	1.8	b
Tls	LACUSTRINE and LAND SED and volcanics	Eastern Cricket	undetermined	2.40	-0.31	4.0	b, d, f
C-Ols	LIMESTONE, shale, and quartzite	Cricket Mountains	1.7±.3	2.70	-0.01	6.5	a, c
PC-Cq	QUARTZITE, shale, limestone and slate	Cricket and Beaver Mountains	4.0±.5	2.66	-0.05	6.1	a, c, e
PCgs	GNEISS and SCHIST	Mineral Range	undetermined	2.81	0.10	6.7	a, b, c
Pb	BASEMENT	Pavant Range	undetermined	2.71	0	undetermined	a

Dominant rock types are capitalized. Symbol identifies unit in Figure 5. Density contrast is in comparison to Precambrian-Paleozoic basement rock.
*Sources: a, Hintze 1973 ; b, Gertson 1979 ; c, Woollard 1962 ; d, MacDonald 1976 ; e, Woodward 1973 ; f, Hintze 1959 .

Regional Gravity Anomalies

We assume that the general shape of the terrain-corrected Bouguer anomaly gravity map in Figure 4 is controlled by two major features: (1) part of a major regional north-northeastern trending gravity trough roughly 80 km long and 40 km wide [Cook et al., 1975], resulting from a thick section of Cenozoic sediments, and (2) a local roughly circular gravity low up to 30 km in diameter, related to the outcrop of silicic material over an area 15 km wide and its deeper source. Superposition of the broad lows associated with the valley and the volcanism, both having characteristic wavelengths of the same order, makes separation by analytical techniques difficult. The Twin Peaks region is also located on the flank of a strong gravity gradient toward the Colorado Plateau [Cook et al., 1975], but as this gradient affects at most the extreme south east corner of our gravity map (Figure 4), it is not modeled in connection with the volcanic system.

To determine and eventually separate the gravity effect of the valley fill alone, a regional east-west gravity profile was compiled north of the volcanic system along latitude $39^{\circ}00'$N using the published data of Cook et al. [1975] augmented by detailed data of Case [1977] and Serpa [1980]. An orthogonal polynomial fit to the regional data, shown as a solid line in Figure 5a, has less than 1 mGal rms misfit to the data and likely represents the gravity expression of the Black Rock Desert Valley undisturbed by the igneous activity.

It is instructive to demonstrate that the regional gravity trough we have described is indeed consistent with a Cenozoic sediment-filled valley whose structure is known from seismic reflection results [MacDonald, 1976]. Figure 5b shows a two-dimensional gravity model for this trough using the rock thicknesses and densities given in Table 1. The ambiguities inherent in gravity modeling are reduced by recognizing the further geological constraints placed on the model by the Cricket Mountains and the structural constraints placed on the model by the seismic reflection profile in Figure 5c. The model shows rocks composing the Cricket Mountains descending beneath the Cenozoic sediments with a dip between 4° and 11° depending on position, and terminating at a depth of 3 km below the surface into a basement detachment plane that is rising with a dip of about 8°. The late Tertiary-Quaternary sediments reach a maximum thickness of 1.2 km and then thin to 0.4 km at the eastern margin of the profile. The maximum thickness for Cenozoic sediments in the model is 3 km, in good agreement with the thickness estimated from the seismic reflection profile in Figure 5c.

Residual Gravity Anomaly

A residual gravity anomaly pattern for the Twin Peaks region was determined by removing a two-dimensional gravity trough from the terrain-corrected Bouguer anomaly gravity field. The two-dimensional trough was constructed by projecting the profile shown in Figure 5a into the Twin Peaks area with a strike of $N15^{\circ}E$, a direction consistent with the trend of gravity contours and with the strike of Cambrian rocks mapped in the Cricket Mountains. The resulting residual gravity pattern for the Twin Peaks area (Figure 6) has the appearance of a broad circular gravity depression with an amplitude of 7 mGal and an east-west diameter of 26 km inside the 0 mGal contour. Near the center of the gravity depression, a positive residual anomaly, with a total relief of about 10 mGal and a width of 5 km at the -2 mGal contour, rises abruptly over North Twin Peak. A smaller positive anomaly, with a total relief of about 6 mGal occurs over South Twin Peak. East of the two domes the gravity decreases again to -4 mGal and then rises to 0 mGal at the edge of the map.

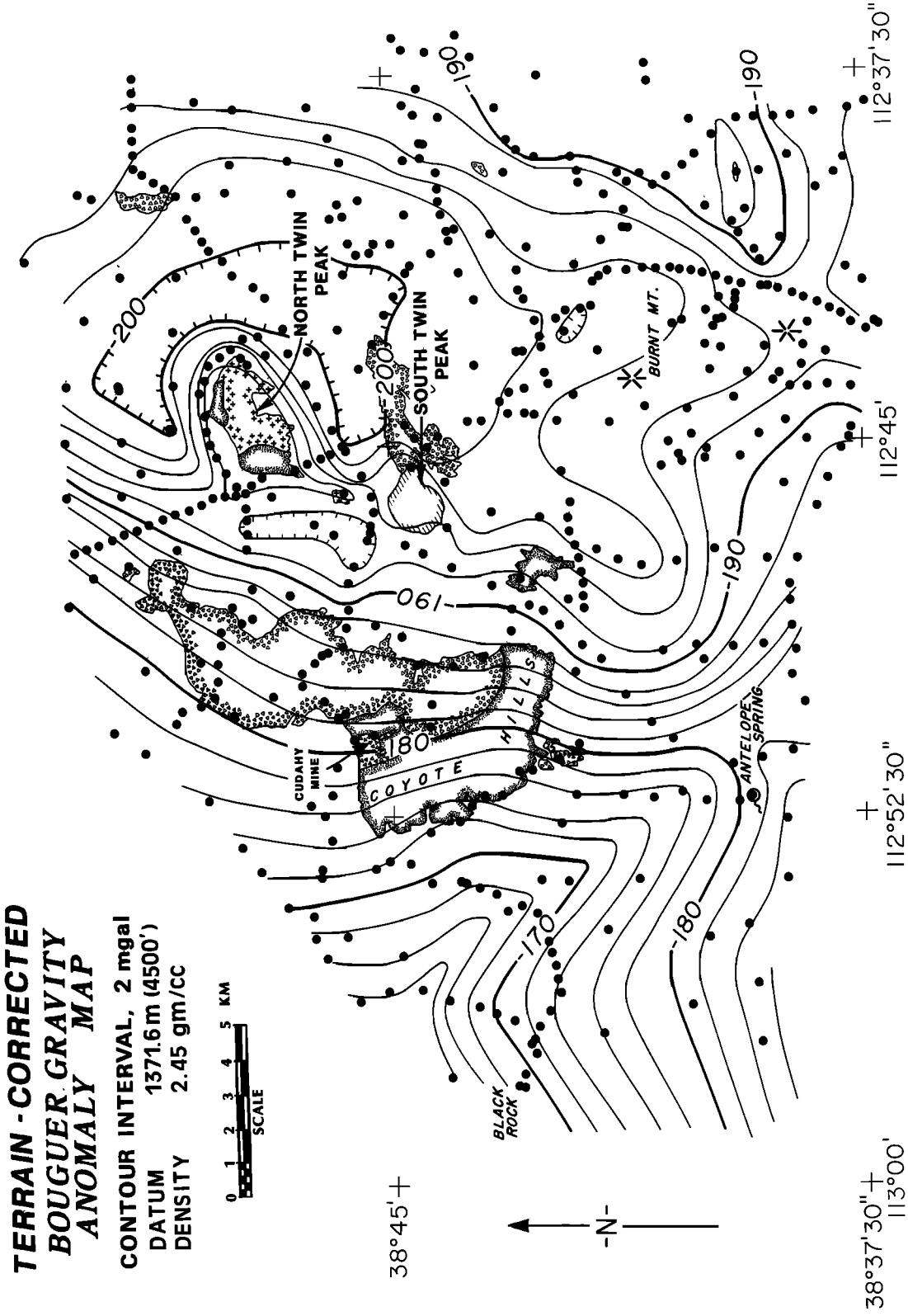

Fig. 4. Terrain corrected bouguer anomaly map of the Twin Peaks magma system within the boundary shown in Figure 2. Contour interval is 2 mGal. Solid dots indicate gravity stations. Rhyolite outcrop from Figure 3 is repeated here for orientation.

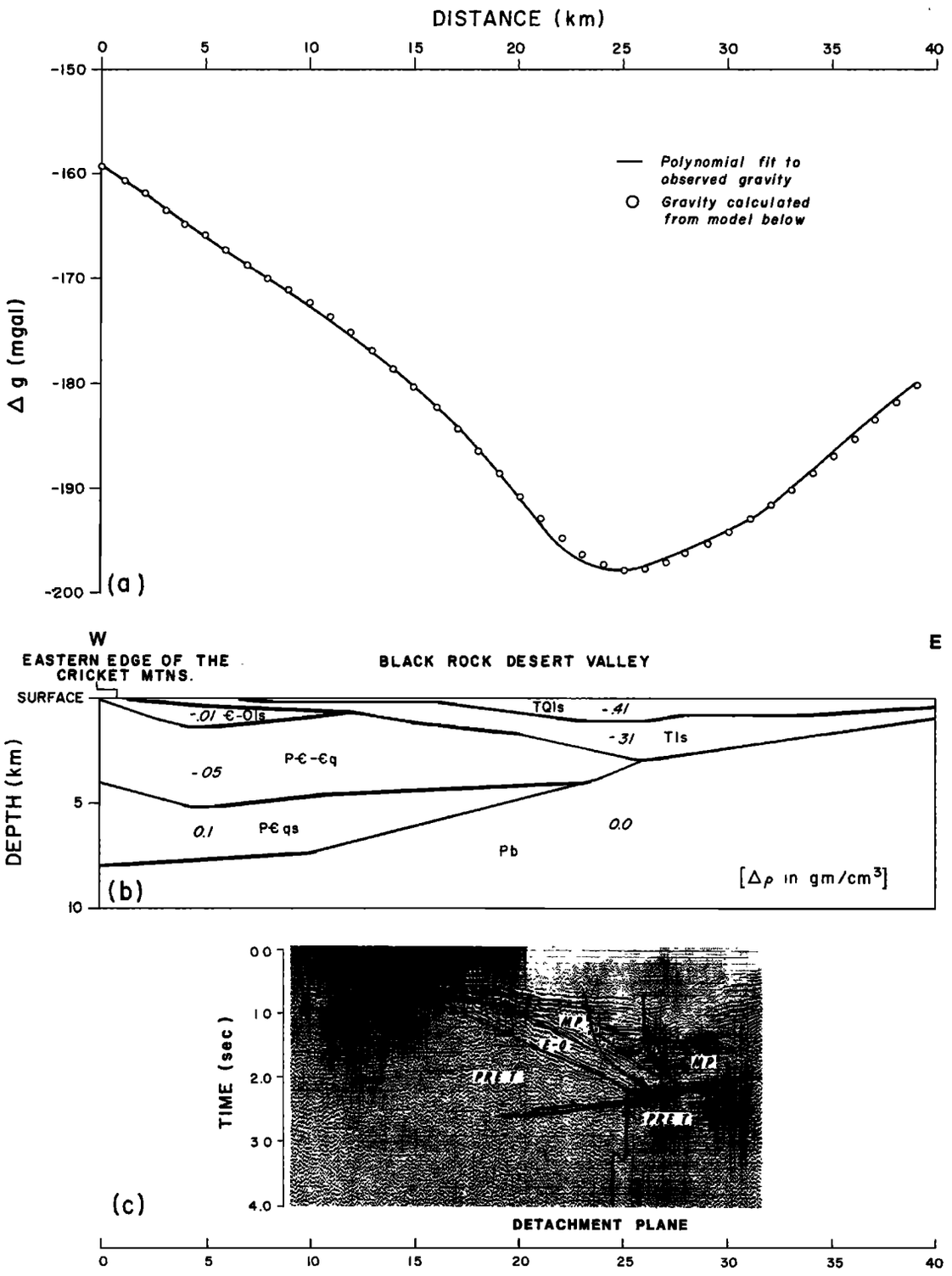

Fig. 5. Gravity and structure model for the Black Rock Desert Valley north of the volcanic system. (a) Regional gravity due to valley structure deduced from observations (solid line) and gravity calculated from the two-dimensional geologic model in Figure 5b below (open circles). (b) Two-dimensional interpretive geologic model of the Black Rock Desert generated to fit regional gravity model in Figure 5a. Lithologic symbols, unit thicknesses and densities are given in Table 2. Structural control used in the geologic model was obtained from Hintze [1959] and MacDonald [1976]. (c) Seismic reflection line 20 published by MacDonald [1976] and located in Figure 2. The dominant reflector in this section is described as a detachment plane along which pre-Tertiary rocks moved east.

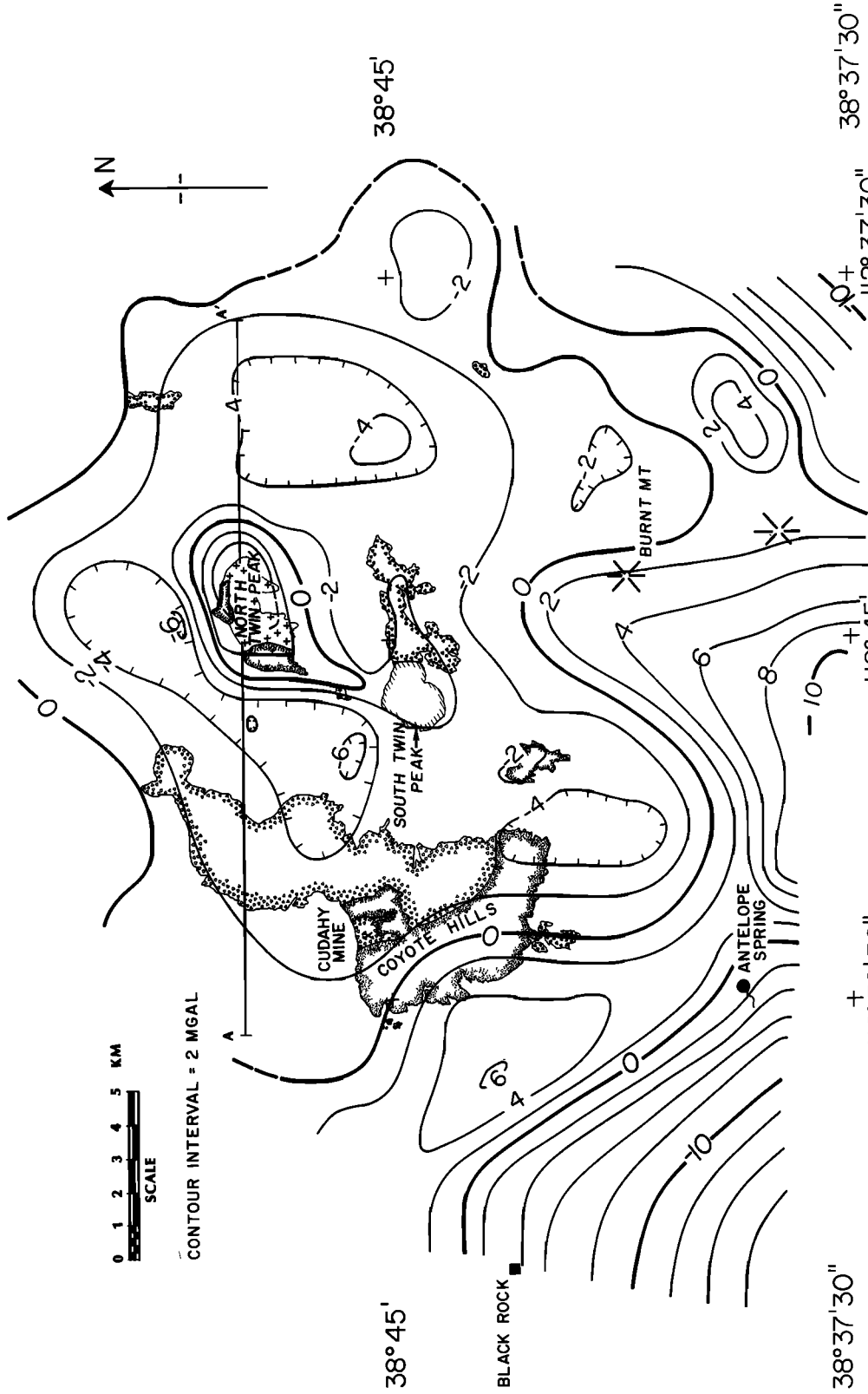

Fig. 6. Residual Bouguer anomaly map of the Twin Peaks magma system after effects of the Black Rock Desert valley have been removed from Figure 4. Contour interval is 2 mGal. Rhyolite outcrop is shown by patterns identical to Figure 3 for purposes of orientation.

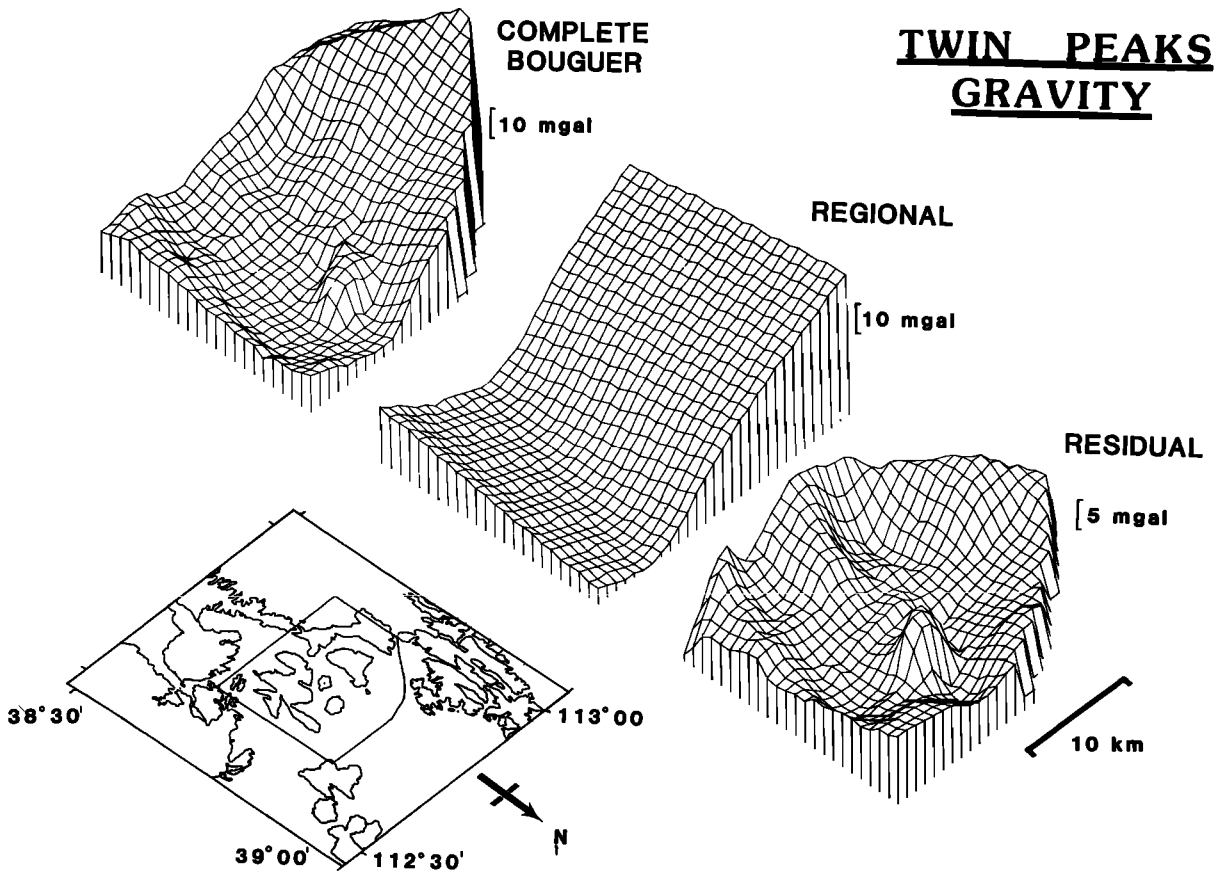

Fig. 7. Isometric representation, looking from northeast, of three gravity surfaces for the Twin Peaks area. Index geologic map from Figure 2 is repeated at bottom left in the new map projection for orientation. Isometric gravity surfaces cover the truncated rectangle shown in the inset. The complete Bouguer anomaly surface (Figure 4 rotated) is at upper left; projected regional anomaly discussed in text accounts for the Basin and Range valley structure; residual Bouguer anomaly (Figure 6 rotated) can be related to the Twin Peaks igneous system.

Relative positive gravity features outside the area of rhyolite exposures include a +4 mGal residual over the Paleozoic rock outcrop in the southeastern part of the map and a broad +6 mGal residual southwest of the Coyote Hills rhyolite in the vicinity of the gravity spur in Figure 4. A negative gravity feature is produced by the Milford Valley graben which reaches -16 mGal at the southwestern edge of the map. Similarly, in the southeast, the negative gravity associated with the Beaver Valley graben reaches -10 mGal at the map edge.

The positive gravity anomaly over the domed sediments and basalts southwest of Burnt Mountain in the residual map is without closure. Outside the domed area the gravity high broadens out to the west where it swings to the south around the northwestern part of the Mineral Range [see also Brumbaugh, 1978], suggesting that the positive gravity feature is due either to a late-stage intrusion of rhyolitic material that caused the doming of the Tertiary rocks and was stranded beneath the surface or to pre-Tertiary basement rising in the south and west in the vicinity of the Mineral Mountains.

A summary of the complete Bouguer, the regional Bouguer and residual Bouguer gravity maps, is shown in isometric representation in Figure 7. For orientation purpose, the generalized geological outcrop pattern of Figure 3 is shown in the inset with the same projection. It is clear from Figure 7 that the regional trough dominates the complete Bouguer gravity field, but with the removal of this valley-fill trough effect, a residual anomaly is produced which is correlatable spatially with the volcanics outcrop pattern. It is the residual gravity anomaly that we now address and model as being composed of two parts: a broad gravity depression, which we hypothesize is caused by an intrusive granitic body emplaced within the high density Paleozoic and Precambrian basement rock, and sharp positive anomalies associated with the rhyolitic domes similar in density to the intrusive but which are more dense than the surrounding shallow Tertiary valley fill.

Models for the Residual Anomaly

The broad residual gravity depression and the positive anomaly over North Twin Peak are very roughly circular. Departure from a more circular pattern can be attributed to encroaching shallow basement southwest of Coyote Hills and stranded rhyolite beneath domed sediments or a rising basement southeast of South Twin Peak. We have

therefore modeled the residual gravity field by a series of three-dimensional vertical cylinders [Telford et al., 1976, p. 63].

Data for modeling the deep intrusion are taken from several profiles crossing the center of the residual gravity low in Figure 6 (see also Figure 4). These data were superimposed to produce an effectively radially averaged anomaly shown in Figure 8. Gravity data from the center of the low have been excluded so that the strongly positive anomalies of the Twin Peaks domes do not influence the modeling of the negative anomaly.

The critical parameters to be considered in modeling with vertical cylinders are the radius, burial depth, density contrast, and thickness of the body. The outcrop pattern of the rhyolite (Figure 3) suggests a radius of 6-7 km for the parental intrusion. The body is most likely of granitic composition having a density between 2.5 and 2.8 g/cm^3 [Telford et al., 1976]. In this particular case a gravity low from a granitic body will be produced only if the intrusive is below 3 km, the depth of the Tertiary basement interface, and if the intrusive has a density less than 2.71 g/cm^3, the average density of the basement rocks in the region (Table 2).

Cross sections of two three-dimensional vertical cylinders that produced reasonable fits to the residual gravity negative anomaly from the radially averaged profiles are shown in Figure

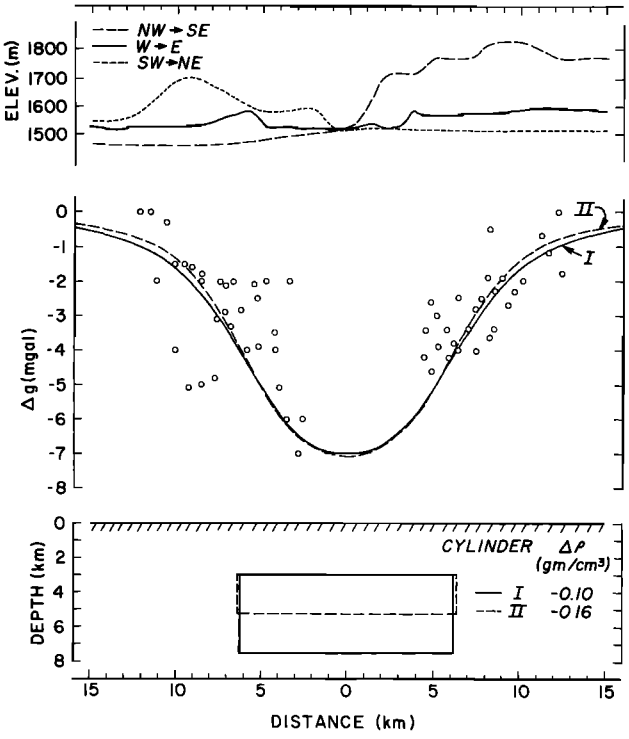

Fig. 8. Topography profiles and composite residual gravity values (open circles) along three profiles crossing through the center of the Twin Peaks gravity low and calculated gravity (solid lines) for three-dimensional circular cylinders shown in cross section. Scatter in the observed gravity is caused by lack of perfect radial symmetry in the residual gravity field. Data in the center of the profile is ommitted here but is shown and modeled in Figure 9.

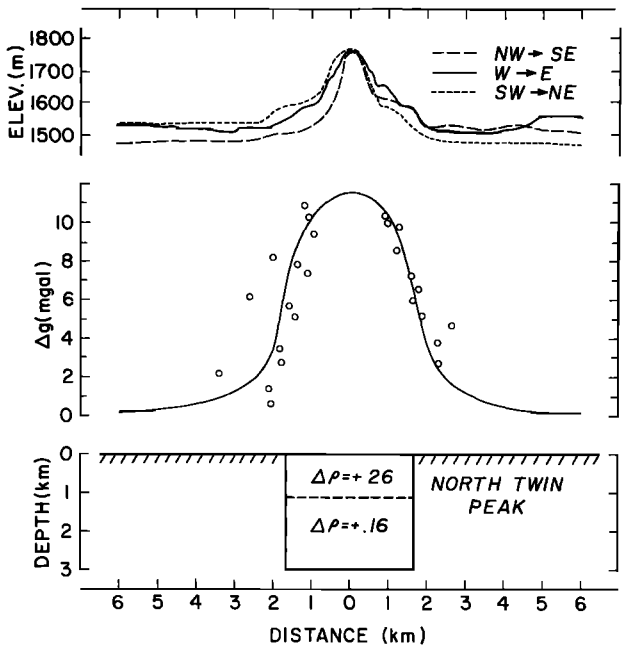

Fig. 9. Topography along three profiles crossing North Twin Peak and composite residual gravity around North Twin Peak with the effect of cylinder I of Figure 8 removed. Open circles represent residual gravity along six radial profiles centered on North Twin Peak. Solid line is calculated gravity for the three dimensional circular cylinder shown in cross section.

8. Cylinder I has a radius of 6.25 km, a thickness of 3.5 km (volume 430 km^3), and a density contrast of -0.10 g/cm^3 (an actual density of 2.61 g/cm^3); cylinder II has a slightly greater radius of 6.4 km, a lesser thickness of 2.25 km (volume 290 km^3) and a greater density contrast of -0.16 g/cm^3 (an actual density of 2.55 g/cm^3) than cylinder I. Both cylinders were buried below 3 km.

A model for the positive gravity anomalies associated with the rhyolite domes was derived in a similar manner, although the data spacing in this case combined with uncertainties arising from topographic effects provide less of a constraint compared to the broad gravity low. The residual positive gravity anomaly for North Twin Peak after the effect of cylinder I of Figure 8 has been removed is shown in Figure 9. Data were taken along six radial profiles centered on North Twin Peak. Three-dimensional vertical cylinders were again used to model this anomaly, but in this case, composite cylinders were introduced in order to accommodate the density structure indicated by the layering of the Tertiary valley fill (see Figure 5). A satisfactory fit to the data (Figure 9) is produced by a vertical cylinder of radius 1.67 km extending from the surface to a depth of 3 km, the top of the parental intrusive. The density contrasts of +0.26 g/cm^3 from 0 to 1.1 km depth and +0.16 g/cm from 1.1 to 3.0 km, when compared to sediment densities (Table 2), implies a rhyolite density at depth of 2.56 g/cm3, about 4% higher than that measured on surface samples (Table 1). Models for South Twin Peak (described

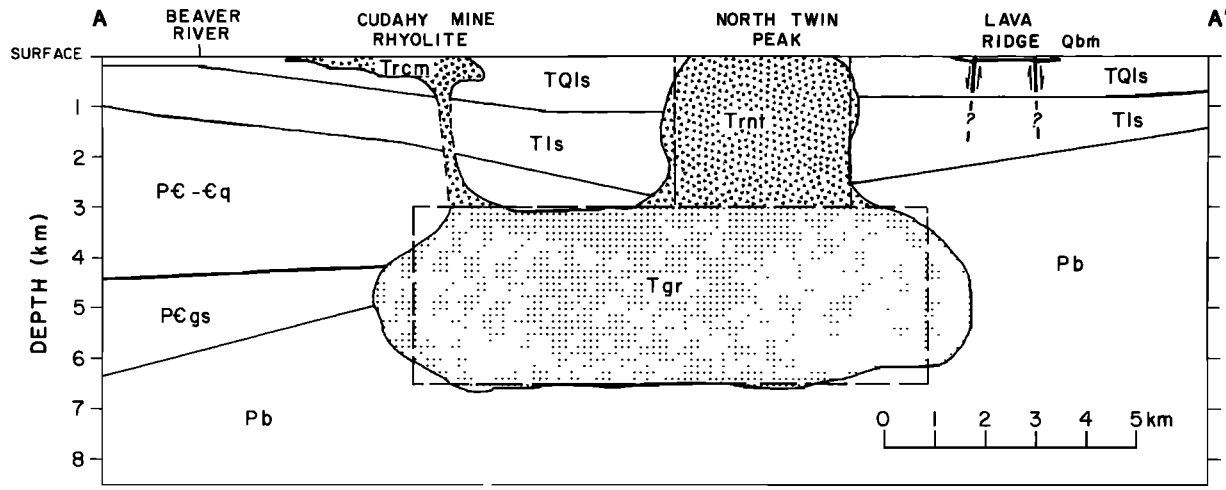

SEDIMENTARY ROCKS		IGNEOUS ROCKS	
TQls	Lacustrine Sediments and Volcanics	Qbm	Burnt Mtn Basaltic Andesite
Tls	Lacustrine Sediments	Trnt	North Twin Peak Rhyolite
P€-€q	Quartzite - Shale - Slate	Trcm	Cudahy Mine Rhyolite
P€gs	Gneiss and Schist	Tgr	Twin Peaks Granite (?)
Pb	Undifferentiated Paleozoic and Precambrian Rocks		

Fig. 10. East west cross section along profile AA' of Figure 6 interpreted from gravity models in Figures 9 and 10.

in detail by Carrier [1979]) are similar, although there are less data to provide constraints. Results from the gravity models in Figures 8 and 9 are summarized in an idealized east-west geological cross section through the center of North Twin Peak, shown in Figure 10.

Included in the cross section are Cudahy Mine rhyolite and Lava Ridge of Burnt Mountain and Twin Peaks basaltic andesites, both of which have not been modeled in detail. The Cudahy Mine rhyolite is constrained at the surface by outcrop. Subsurface shape and extent of the Cudahy Mine rhyolite in Figure 13 is arbitrary; however, it is not unlike rhyolite sections in other localities [see, e.g., Smith et al., 1961; Williams and McBirney, 1968]. The faulting in the east has been suggested by Clark [1977], but the lack of an obvious gravity expression suggests that it is minor.

Haugh [1978] has suggested, primarily from the circular geometry of rhyolite outcrop, that the Twin Peaks system has undergone a caldera collapse. The ambiguities inherent in modeling rock bodies from gravity data do not preclude that the broad gravity low may be due in part to caldera subsidence rather than entirely a granitic intrusion. The amount of subsidence that could have occurred may be estimated from the eruptive material, which is composed almost exclusively of flow and dome material since voluminous ash flow deposits, characteristic of many silicic calderas, are absent. Eruptive material at the surface is estimated to be 3.5 km^3 by Haugh [1978]. For a caldera with a radius of 6.25 km, this could result in a subsidence of only 28 m, the gravity expression of which would probably not be separable from the intrusive model we have proposed.

Further support for our intrusive model may be drawn from magnetic data for the area (D. Mabey, written communication, 1980). The local magnetic field consists of two highs associated with the moderately magnetized North and South Twin Peaks domes superimposed upon a more extensive magnetic high, possibly caused by a buried intrusive.

Heat Flow

Heat flow determinations were made at six sites in the vicinity of the Twin Peaks magma system. These data were acquired to detect any residual heat that may remain from the emplacement of the intrusion and the subsequent volcanic activity, thereby assisting in evaluating the area's geothermal potential and providing constraints for cooling models. The heat flow sites are distributed over roughly 100 km^2 centered on the rhyolite domes (Figure 3). Drill hole depths range from 48 to 152 m. Three drill holes, TP3, 6, and 8 were released by Chevron Resources for the study, while holes TP1, 4, and 7 were obtained independently.

Thermal data for each hole are summarized in Table 3; details are given in Appendix C of Carrier [1979]. Thermal gradients were determined from temperature-depth data using a linear least squares fit to the data over the interval indicated in Table 3. The temperature-depth profiles for each hole (Figure 11) show little disturbance below 40 m, suggesting that heat transfer in these holes is predominately by conduction. Thermal conductivities were measured

TABLE 3. Summary of Heat Flow Data in the Twin Peaks Area

Site	Latitude (North)	Longitude (West)	Elevation, m	Depth Range, m	Gradient, °C/km	Conductivity, W/m K	Heat Flow, mW/m^2
TP1	38°45.13'	112°53.00'	1563	15-48.5	53.4±3.9	1.78±.15	95±11
TP3	38°44.33'	112°48.31'	1607	43-152	45.0±1.7	2.18±.07	98±5
TP4	38°43.47'	112°47.87'	1575	30-58	86.9±10.5	1.63±.16	142±22
TP6	38°44.43'	112°45.25'	1665	43-151	42.7±1.9	2.02±.03	86±4
TP7	38°45.87'	112°51.18'	1536	30-90	49.9±10.8	2.09±.21	104±25
TP8	38°42.48'	112°46.18'	1646	27-130	55.5±4.1	1.17±.07	95±8

on saturated drill chips and solid discs of core for four holes using a divided bar apparatus [Roy et al., 1968] and the methods of Sass et al. [1971]. Samples were not available for TP4 and TP7. Instead, conductivities were estimated for these holes from surface lithology and an average conductivity for rhyolite in TP6 (for TP7) and basalt in TP8 (for TP4). The vertical component of the heat flow was then calculated by taking the product of the harmonic mean thermal conductivity and the thermal gradient for each hole.

Measured heat flow at Twin Peaks ranges from 86 to 142 mW m^{-2} with an average and standard deviation of 103 and 20 mW m^{-2}, respectively. The one anomalous heat flow value of 142 mW m^{-2} is for TP4 where the thermal conductivity is poorly constrained. Excluding the value of 142 mW m^{-2} from the rest of the data set results in an average and standard deviation in the heat flow of 96 and 6 mW m^{-2}. This is very near the mean for eastern Basin and Range heat flow of 90 mW m^{-2} [Chapman et al., 1979] and certainly within the range considered to be characteristic. Heat flow observations therefore suggest that there is no noticeable present day thermal anomaly associated with the silicic volcanism in the Twin Peaks area.

Thermal Model

A model for the anomalous heat flow, Δq, at the surface above a cooling intrusion was constructed using the following constraints: (1) the body is emplaced instantaneously at a time t = 0, (2) the magma stagnates after emplacement, and (3) heat loss is by conduction. Anomalous surface heat flow produced by a cooling vertical prism appropriate to the Twin Peaks intrusion (model I, Figure 8) is shown in Figure 12. Parameters used to constrain the thermal model were determined by gravity modeling, geochemistry, and surface geology, and are summarized in Table 4. The intrusion is modeled as a body 3.5 km thick, 11 km wide, emplaced to a depth of 3 km with an initial temperature of 850°C (W. P. Nash, personal communication, 1978) in an area with an average background thermal

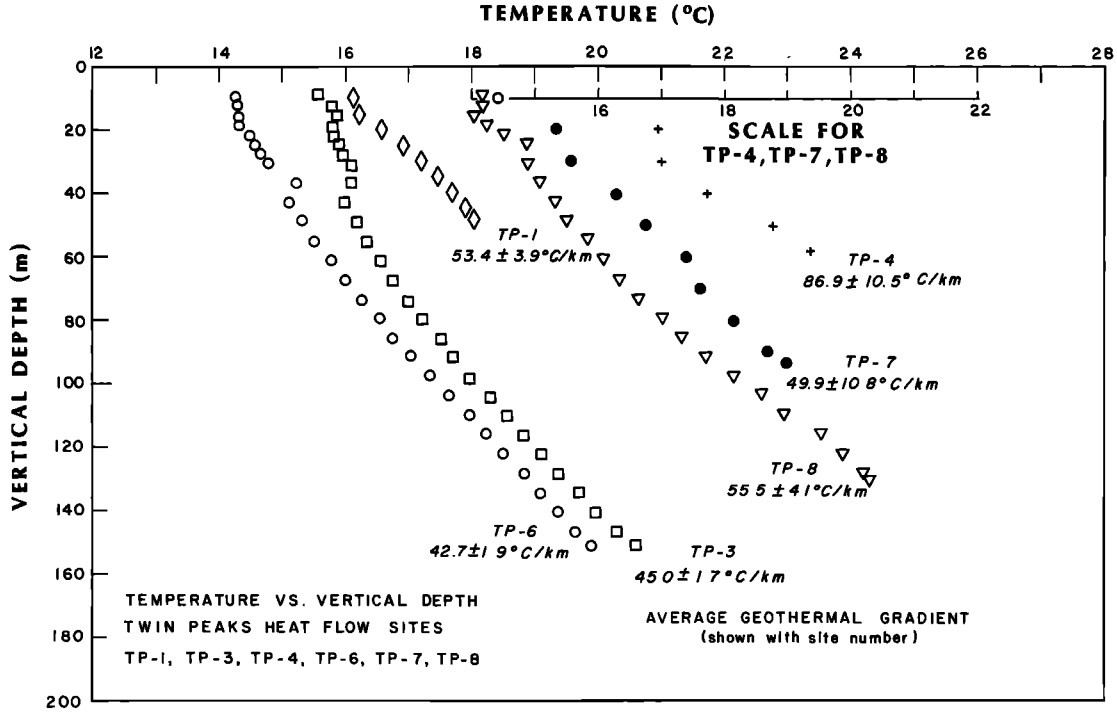

Fig. 11. Temperature-depth profiles for six drill holes in the Twin Peaks area. Scale for TP 4, 7, and 8 is offset by 4°C to avoid overlap. Borehole locations are shown on Figure 3.

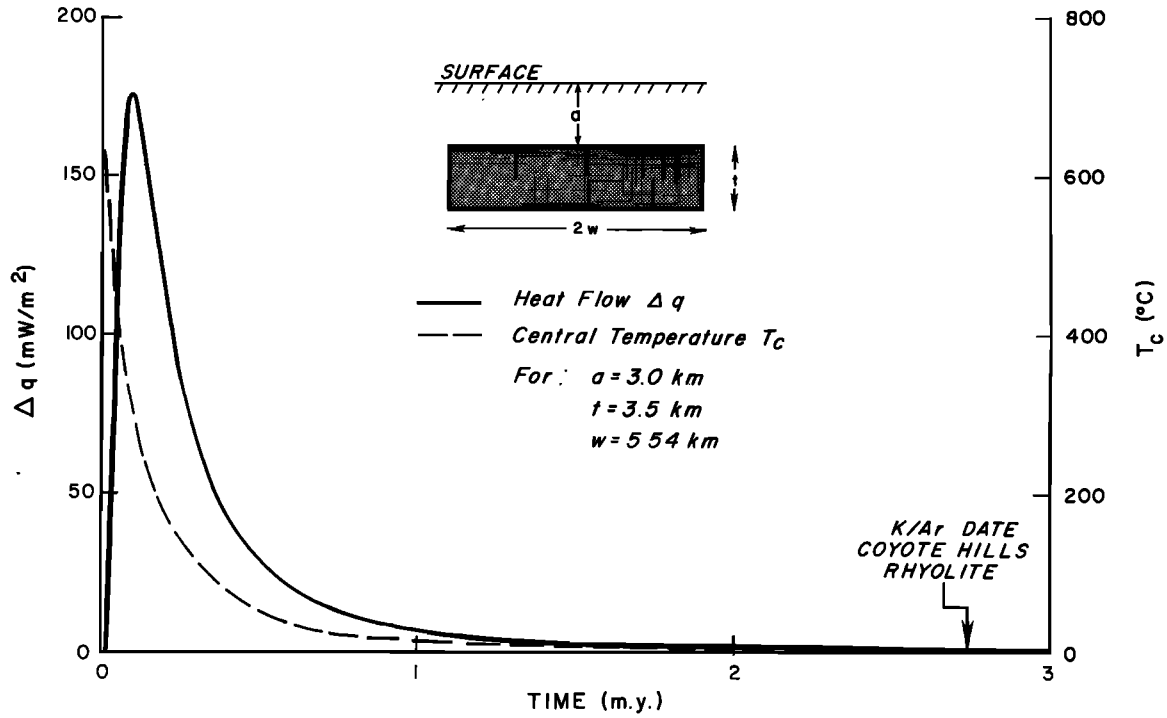

Fig. 12. Anomalous surface heat flow (solid line) and central temperature (dashed line) for the cooling of an instantaneously emplaced igneous body. The cross section area thickness, and depth of this body match that of cylinder I shown in Figure 8. Details are given in Table 3 and in text.

gradient of 45°C/km. This body has identical cross section area to the cylindrical model I of Figure 8. Time of emplacement of the intrusion and of extrusion of the Coyote Hills rhyolite are considered to be indistinguishable. The intrusion modeled would produce an anomalous surface heat flow that reached a maximum of 175 mW m^{-2}, 9 x 10^4 years after the time of emplacement; the anomalous surface heat flow would decay to one half the maximum value 0.25 m.y. after emplacement, and would be indistinguishable from background after 1.0 m.y. After 2.74 m.y., the time since the extrusion of the Coyote Hills rhyolite, the intrusion should contribute less than 1 mW m^{-2} to the heat flow in the Twin Peaks area, consistent with the lack of an observable thermal anomaly.

The cooling curve for the center of the intrusion is also shown in Figure 12. The center of the intrusion cools down from an anomalous 636°C at emplacement to less than one half of this value 0.1 m.y. later. The central temperature decreased to one tenth the original value, 0.45 m.y., after emplacement. Finally,

TABLE 4. Parameters for Thermal Models

Parameter	Symbol	Granitic Intrusive	North Twin Peak	Principal Source
Thermal diffusivity	α	32 km^2/m.y.	32 km^2/m.y.	average for crustal rocks
Temperature of emplacement	Ti	850°C	700°C	geochemistry
Initial temperature at center of body above country rocks	T_o	636°C	632°C	calculated
Background thermal gradient	dT/dz	45°C/km	45°C/km	thermal measurements
Thermal conductivity Tertiary sediments	K	2 W/m K	2 W/m K	thermal measurements
Thickness of body	Δ	3.5 km	3 km	gravity models
Width of the body square prism	w	11 km	3.1 km	gravity models surface geology
Depth to top of body	a	3 km	0.01 km*	gravity models surface geology
Age of body	-	2.74±0.1 m.y.	2.3±0.1 m.y.	geochronology (K/Ar dates)

*Body is required to be emplaced below surface.

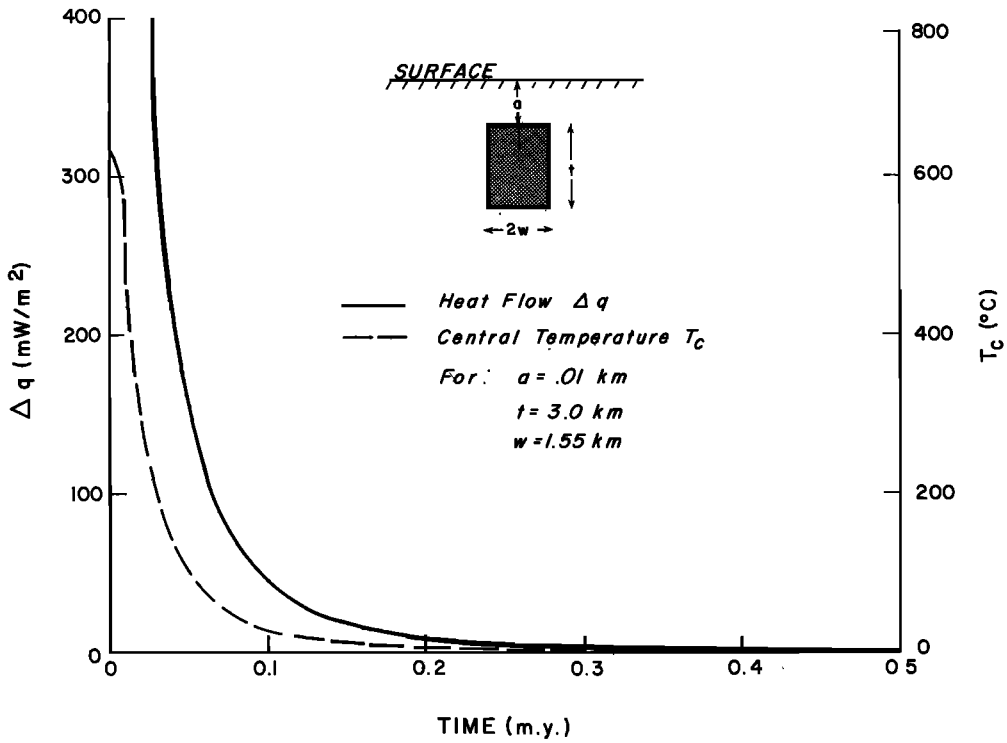

Fig. 13. Anomalous surface heat flow (solid line) and central temperature (dashed line) for the cooling of an instantaneously emplaced igneous body. The cross section area, thickness and depth of this body matches that of the cylinder shown in Figure 9. Details are given in Table 3 and in text.

2.74 m.y. after the extrusion of the Coyote Hills rhyolite, only 2°C of the anomalous temperature at the center should remain.

Anomalous surface heat flow produced by the extrusion of the North Twin Peak dome has also been calculated and is shown in Figure 13. The cooling of the dome is modeled using constraints again determined by the gravity model, geochemistry, and surface geology (listed in Table 4). The body was placed at a depth of 10 m to avoid computation difficulties. The body has a width of 3.1 km, a thickness of 3 km, and was emplaced at a temperature of 700°C (W. P. Nash, personal communication, 1978), into an area with a background thermal gradient of 45°C/km. As this body is smaller and shallower than the parental igneous body, cooling will advance at a faster pace, and negligble heat will be left after only 0.2 m.y.

Our thermal model of the cooling intrusive assumes that heat transfer is by conduction and allows for no hydrothermal circulation of groundwater in the overlying Tertiary sediments. Hydrothermal circulation exterior to the magma has little effect on the magma solidification time but may decrease the postsolidification cooling time by a factor of 5. This depends on the permeability of the host rock, presumably high in this case, the availability of fluids, possibly low, and the chemical sealing of fluid paths, which is unknown. Prolongation of cooling over that predicted in Figures 12 and 13 on the other hand would be expected if multiple intrusions had effectively preheated a large volume prior to final cooling. Two pulses of silicic volcanism are present at Twin Peaks [Evans et al., 1980; Crecraft et al., this issue]. The first sequence includes Coyote Hills rhyolite and the Cudahy Mine obsidians, felsite, and volcanoclastics and spans the period 2.7 to 2.5 m.y. ago. A second sequence includes the North and South Twin Peak rhyolite domes and spans the period 2.5 to 2.3 m.y. Each sequence is characterized by systematic progression from less silicic to more silicic rocks [Crecraft et al., 1980, this issue]. Basaltic volcanism in the same region extends from about 2.5 m.y. to 0.9. m.y. ago. Magmatic longevity is thus comparable to the cooling time for this volcanic center.

Our observation that heat flow at Twin Peaks is close to background Basin and Range values suggests that magmatic longevity, if important, does not extend cooling times by a factor of 3 or more, otherwise, we should have seen a thermal anomaly. A more sensitive test of the magmatic longevity versus hydrothermal cooling efficiency would have been provided had the parental igneous body been much larger or younger or both.

Conclusions

Gravity, heat flow, and surface geology have been integrated in study of an area of late Tertiary silicic volcanism at Twin Peaks, Utah. Volcanism began in the area with the extrusion of the Coyote Hills rhyodacite 2.74 ± 1 m.y. ago. A period of quiescence followed lasting nearly 0.3 m.y., interrupted by the extrusion of a complex sequence of domes and flows that lasted until 2.3 ± 0.1 m.y. ago.

Terrain corrected Bouguer gravity at Twin

Peaks is shaped by three features of varying characteristic dimension: (1) a major N-NE trending -30 mGal gravity trough roughly 40 km wide and extending 80 km to the north, caused by a thick sequence of Cenozoic sediments in the Black Rock Desert Valley, (2) a local, roughly circular, -7 mGal gravity low related to an intrusive body in the basement that produces an anomaly nearly 26 km broad, and (3) a series of very narrow positive anomalies up to + 10 mGal produced by the major Twin Peak volcanic domes. The intrusive can be approximated by a three-dimensional vertical cylinder with a roof at a depth of 3 km and a radius of 6.25-6.4 km and a thickness of 2.25-3.5 km. Similarly, the North and South Twin Peak domes can be approximated by vertical cylinders that extend to a depth of 3 km. The North Twin Peak model has a radius of 1.67-1.75 km. Our best estimate of the total volume of silicic material at and below the surface is about 480 km^3.

Simple thermal models, assuming conductive heat transfer, predict that a maximum anomalous heat flow would have occurred within 0.1 m.y. and that negligible heat flow or central temperature anomalies should exist after 1 m.y. Aided by convection, the anomaly would have been greater and would have occurred sooner. Model predictions of a negligible residual heat flow anomaly 2.74 ± 0.1 m.y. after emplacement of the intrusion is consistent with the present day local heat flow of 96 mW m^{-2} which is indistinguishable from background Basin and Range heat flow in Utah. These geological and geophysical observations and models provide a consistent description of the Twin Peaks silicic volcanic center, its structure, and its thermal evolution.

Acknowledgments. K. L. Cook suggested undertaking gravity studies at Twin Peaks, assisted us in the aquisition of data and made a careful critique of an early version of this paper. Matthew Mabey made some of the thermal conductivity measurements and produced the isometric plots of the gravity field; his father Don Mabey provided a constructive criticism of this paper. Chevron Resources Company kindly permitted the release of both gravity and thermal gradient data. This work was partially supported under the U.S. Geological Survey Geothermal Research Program by grant 14-08-0001-G-544.

REFERENCES

Brumbaugh, W. D., Gravity survey of the Cove Fort-Sulphurdale KGRA and the North Mineral Mountains area, Millard and Beaver counties, Utah, M.S. thesis, 130 pp., Univ. of Utah, Salt Lake City, 1978.

Carrier, D. L., Gravity and heat flow studies at Twin Peaks, an area of late Tertiary silicic volcanism in Millard County, Utah, M. S. thesis, 120 pp., Univ. of Utah, Salt Lake City, 1979.

Carter, J. A., Regional gravity and aeromagnetic surveys of the Mineral Mountains and vicinity, Millard and Beaver counties, Utah, M.S. thesis, 128 pp., Univ. of Utah, Salt Lake City, 1978.

Case, R. W., A regional gravity survey of the Sevier Lake area, Millard County, Utah, M.S. thesis, 95 pp., Univ. of Utah, Salt Lake City, 1977.

Chapman, D. S., D. D. Blackwell, W. T. Parry, W. R. Sill, S. H. Ward, and J. A. Whelan, Regional heat flow and geochemical studies in southwest Utah, vol. 2, final report, contract 14-08-001-G-341, 119 pp., U.S. Geol. Surv., Reston, Va., 1979.

Clark, E. E., Late Cenozoic volcanic and tectonic activity along the eastern margin of the Great Basin in the proximity of Cove Fort, Utah, Brigham Young Univ. Geol. Stud., 24 (1), 87-114, 1977.

Cook, K. L., J. R. Montgomery, J. T. Smith, and E. F. Gray, Simple Bouguer gravity anomaly map of Utah, map 37, Utah Geol. and Miner. Surv., Salt Lake City, Utah, 1975.

Crecraft, H. R., W. P. Nash, and S. H. Evans, Jr., Chemical and thermal evolution of the Twin Peaks magma system, west central Utah, Trans. 4, pp. 117-120, Geotherm. Resour. Counc., Davis, California, 1980.

Crecraft, H. R., W. P. Nash, and S. H. Evans, Jr., Late Cenozoic volcanism at Twin Peaks, Utah, 1, Geology and petrology, J. Geophys. Res., this issue.

Daniel, W. W., Introductory Statistics With Applications, 473 pp., Houghton Mifflin, Boston, Mass., 1977.

Evans, S. H., Jr., H. R. Crecraft, and W. P. Nash, K/Ar ages of silicic volcanism in the Twin Peaks/Cove Creek Dome area, southwestern Utah, Isochron/West, 28, 21-24, 1980.

Gertson, R. C., Interpretation of a seismic refraction profile across the Roosevelt Hot Springs, Utah and vicinity, M.S. thesis, 109 pp., Univ. of Utah, Salt Lake City, 1979.

Haugh, G. R., Late Cenozoic, cauldron-related silicic volcanism in the Twin Peaks area, Millard County, Utah, Brigham Young Univ. Geol. Stud., 25, 67-82, 1978.

Hintze, L. F., Geology of the Cricket Mountains, Millard County, Utah, map, Brigham Young Univ., Provo, Utah, 1959.

Hintze, L. F., Geologic history of Utah, Brigham Young Univ. Geol. Stud., 20, (3), 181 pp., 1973.

Isherwood, W. F., Regional gravity survey of parts of Millard, Juab, and Sevier counties, Utah, M.S. thesis, 31 pp., Univ. of Utah, Salt Lake City, 1967.

MacDonald, R. E., Tertiary tectonics and sedimentary rocks along the transition, Basin and Range Province to Plateau and Thrust Belt Province Utah, in Symposium on Geology of the Cordilleran Hingeline, edited by J. G. Hill, pp. 281-317, Rocky Mountain Association of Geologists, Denver, Colorado, 1976.

Nettleton, L. L., Gravity and magnetic calculations, Geophysics, 7, 293-310, 1942.

Nielson, D. L., B. S. Sibbett, D. B. McKinney, J. B. Hulen, J. N. Moore, and S. M. Samberg, Geology of Roosevelt Hot Springs KGRA, Beaver County, Utah, technical report, Grant EG-78-C-07-1701, 120 pp., Dep. of Energy, Div. Geothermal Energy, Washington, D.C., 1978.

Roy, R. F., E. R. Decker, D. D. Blackwell, and F. Birch, Heat flow in the United States, J. Geophys. Res., 73, 5207-5221, 1968.

Sass, J. H., A. H. Lachenbruch, and R. J. Munroe, Thermal conductivity of rocks from measurements

on fragments and its application to heat flow determinations, J. Geophys. Res., 76, 3391-3401, 1971.

Serpa, L. F., Detailed gravity and aeromagnetic surveys in the Black Rock Desert area, Utah, M.S. thesis, 207 pp., Univ. of Utah, Salt Lake City, 1980.

Smith, R. L., R. A. Bailey, and C. S. Ross, Structure evolution of the Valles caldera, New Mexico, and its bearing on the emplacement of ring dikes, U.S. Geol. Surv. Prof. Pap., 424D, D145-D149, 1961.

Smith, R. L., and H. R. Shaw, Igneous-related geothermal systems, Assessment of Geothermal Resources of the United States--1975, edited by D. E. White and D. L. Williams, Circ. U.S. Geol. Surv., 726, 58-83, 1975.

Smith, R. L., and H. R. Shaw, Igneous-related geothermal systems, Assessment of Geothermal Resources of the United States--1978, edited by L. J. P Muffler, Circ. U.S. Geol. Surv., 790, 12-17, 1978.

Stokes, W. L., Geologic map of southwestern Utah, Coll. of Mines and Miner. Ind., Univ. of Utah, Salt Lake City, 1963.

Swick, C. H., Pendulum gravity measurements and isostatic reductions, Spec. Publ. 232., U.S. Coast and Geod. Surv., Washington, D. C., 1942.

Telford, W. M., L. P. Geldart, R. E. Sheriff, and D. A. Keys, Applied Geophysics, 860 pp., Cambridge University Press, New York, 1976.

Williams, H., and A. R. McBirney, Geologic and geophysical features of calderas, I, research grant NGR-38-033-012, 87 pp., NASA, Houston, Texas, 1968.

Woodward, L. E., Upper Precambrian and lower Cambrian rocks of the Milford area, Utah, Geology of the Milford Area, edited by L. F. Hintze and J. A. Whelan, Utah Geol. Assoc. Publ., 3, 5-8, 1973.

Woodward, L. E., Stratigraphy of younger precambrian rocks along Cordilleran Hingeline, Utah and Southern Idaho, in Symposium on Geology of the Cordilleran Hingeline, edited by J. G. Hill., pp. 83-90, Rocky Mountain Association of Geologists, Denver, Colorado, 1976.

Woollard, G. P., The relation of gravity anomalies to surface elevation, crustal structure, and geology, Tech. Rep. AF 23(601)-3455, 69-9, Dep. of Geol., Univ. of Wis., Madison, Wisconsin, 1962.

(Received December 1, 1980;
revised August 17, 1981;
accepted September 21, 1981.)

JOURNAL OF GEOPHYSICAL RESEARCH, VOL. 86, NO. B11, PAGES 10287-10302, NOVEMBER 10, 1981

GRAVITY AND THERMAL MODELS FOR THE TWIN PEAKS SILICIC VOLCANIC CENTER, SOUTHWESTERN UTAH

Daniel L. Carrier[1] and David S. Chapman

Department of Geology and Geophysics, The University of Utah
Salt Lake City, Utah 84112

Abstract. Gravity, heat flow, and surface geology observations have been used as constraints for a thermal model of a late Tertiary silicic volcanic center at Twin Peaks, Utah. Silicic volcanism began in the area with the extrusion of the Coyote Hills rhyolite 2.74 ± 0.1 m.y. ago, followed by the Cudahy Mine obsidian, felsite, and volcanoclastics, and finally by a complex sequence of domes and flows that lasted until 2.3 ± 0.1 m.y. ago. Basalt sequences span the time 2.5 to 0.9 m.y. Terrain-corrected Bouguer gravity anomalies at Twin Peaks are shaped by three features of varying characteristic dimensions: (1) a major north-northeast trending -30 mGal gravity trough roughly 40 km wide caused by a thick sequence of Cenozoic sediments in the Black Rock Desert Valley, (2) a local roughly circular -7 mGal gravity low, 26 km across, probably related to an intrusive body in the basement, and (3) a series of narrow positive anomalies up to +10 mGal produced by the major Twin Peaks volcanic domes. The intrusive bodies have been modeled as three-dimensional vertical cylinders; the total volume of intrusive material is estimated to be about 500 km^3. Simple thermal models, assuming conductive heat transfer and using geometrical constraints from the gravity results, predict that a negligible thermal anomaly should exist 1 m.y. after emplacement of the intrusion. This prediction is consistent with an average heat flow of 96 $mW\ m^{-2}$ for the area, not significantly different from eastern Basin and Range values elsewhere. Magmatic longevity of this system, 2.7 to 2.3 m.y. for silicic volcanism or 2.5 to 0.9 m.y. for basaltic volcanism, does not seem to prolong the cooling of this system substantially beyond that predicted by conductive cooling.

Introduction

'The principal basis for estimating thermal energy in igneous-related geothermal systems is the evidence for the existence of high-level silicic magma chambers, their volumes, and the ages of the latest eruptions from them.' [Smith and Shaw, 1978] A simplified rationale for evaluating geothermal systems associated with young igneous rocks based on this premise is shown in Figure 1 [Smith and Shaw, 1975, 1978]. The models assume cooling of a fixed volume by conduction in surrounding rock from a specified initial temperature. Solid lines on Figure 1 indicate the age-volume interplay which divides active from extinct systems. Principal uncertainties in this theoretical scheme concern the effects of hydrothermal circulation in and around magma bodies which would accelerate postsolidification cooling, and magmatic longevity which would have an opposite effect (see Smith and Shaw [1978], for discussion). The most important uncertainty in evaluating actual systems is the volume estimate.

In the context of the cooling of igneous-related geothermal systems we have investigated the Twin Peaks silicic volcanic system of south-central Utah. The system, although believed to be extinct (see Figure 1) is of particular interest because the period of magmatic activity preceding final cooling (magmatic longevity) is comparable to its cooling time. By combining volume estimates from gravity measurements with new dates for the system [Evans et al., 1980] we are able to evaluate the age-volume and theoretical cooling characteristics of the system in the sense of Figure 1. We have also made five new heat flow determinations in and around Twin Peaks, and these results serve as a limiting constraint to test the applicability of the cooling models. The petrologic and geochemical evolution of the Twin Peaks system is described in an accompanying paper [Crecraft et al., this issue].

Geologic Setting

The Twin Peaks, Utah, silicic volcanic center, is located in the Black Rock Desert Valley, near the eastern margin of the Basin and Range Province (Figure 2). This broad valley is bounded by early Paleozoic and late Precambrian rocks in the Beaver and Cricket mountains to the west, Paleozoic and Mesozoic rocks in the Pavant Range to the east, and early Paleozoic rocks in the northern Mineral Mountains to the south. Precambrian rocks in the region surrounding Twin Peaks are composed of gneisses and schists similar to those of the Farmington complex [Nielson et al., 1978] and quartzites in the Beaver Mountains [Woodward, 1976]. Late Precambrian quartzites in the Beaver Mountains are transitional into the Prospect Mountain quartzites of the Lower Cambrian. Overlying Paleozoic rocks are dominated by limestones in the west and dolomites in the east. Mesozoic rocks near Twin Peaks are exposed only in the Pavant Range and include the Triassic Moenkopi Formation through the Jurassic Navajo sandstone in the western range and the Cretaceous Price River Conglomerates and North Horn Formation in the eastern range. Cenozoic sedimentation in the Black Rock Desert Valley is dominated by the deposition of a thick sequence of freshwater and alluvial sediments and is discussed by MacDonald [1976].

Volcanic activity began to the southeast of

[1]Now at Union Geothermal Division Santa Rosa, California 95401.

Copyright 1981 by the American Geophysical Union.

Paper number 1B1477.
0148-0227/81/001B-1477$01.00

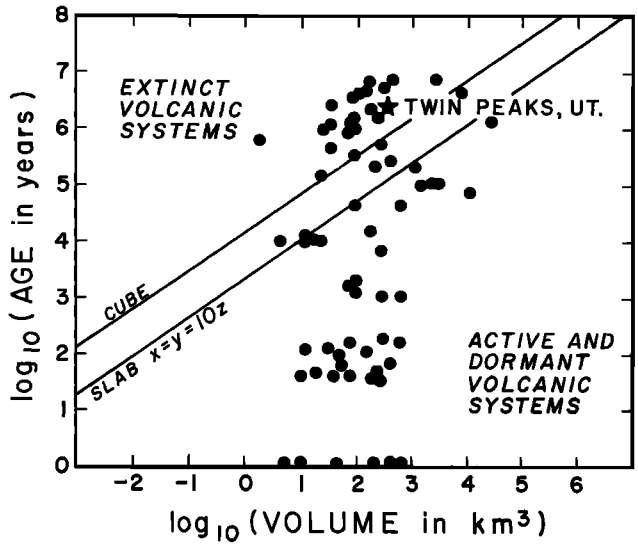

Fig. 1. Age-volume estimates and cooling models (lines) for young igneous systems of the western United States [after Smith and Shaw, 1978, Figure 3]. Systems which plot above the lines are predicted to be approaching ambient temperatures at emplacement depth. Most of the systems younger than 10,000 years are associated with Aleutian, Cascade or Hawaiian volcanoes. The Twin Peaks silicic volcanic system described in this study is identified by the star.

Twin Peaks in the vicinity of the Tushar Mountains during the Oligocene [Hintze, 1973] and southwest of Twin Peaks in the Mineral Mountains in mid-Miocene. There is no direct suggestion that this early activity extended into the Twin Peaks area. Volcanic activity in the Twin peaks area proper (Figure 3) began with the extrusion of the Coyote Hills rhyodacite dated by K/Ar methods at 2.7 ± 0.1 m.y. [Evans et al., 1980]. A period of quiescence that followed lasted nearly 0.3 m.y., being interrupted by the extrusion of a complex sequence of domes and flows (see Figure 3) that lasted until 2.3 ± 0.1 m.y. Preliminary geochemistry and petrology results show a trend of increasing silica concentration with time, each extrusive event representing successive tappings of a single evolving magma chamber [Crecraft et al., 1980, this issue]. Chemically, the Coyote Hills rhyolite contains the least amount of silica and is the least evolved rhyolite in the area. The Cudahy Mine rhyolite is the most evolved rhyolite exposed at the surface, although an even more evolved rhyolite was found in a drill hole core sample.

Local basaltic volcanism began with the extrusion of the Black Point basalt 2.0 m.y. ago [Clark, 1977]. Four other basic flows were mapped by Clark [1977]. They are the Black Rock basalt, extruded at 0.97 m.y. ago, and three younger flows belonging to the Burnt Mountain Field (Figure 3). Lacustrine sediments and basalts are domed to the southeast of South Twin peak (Figure 3); the cause of the doming is unknown but may be caused by late-stage rhyolitic material emplaced in the area.

Gravity

Density, Lithology, and Seismic Control

The volume of an intrusive can only be determined by gravity methods if the density of the intrusive differs from that of the country rock. To determine the sensitivity of gravity methods in the Twin Peaks region, we first made a density analysis of representative rocks from the area. Results of water saturated densities for samples from 122 localities are given in Table 1. Samples were initially separated into regional and local groupings and further classified by lithology, the latter description coinciding with mapped units on the Utah state geologic map [Stokes, 1963].

Measured densities of the regional limestones, quartzites, and dolomites are tightly distributed about their means. With the exception of shale and quartzite, the average densities of these rock types are distinguishable from one another with 99% confidence, using a one-sided Student t-test of significance [Daniel, 1977]. Densities of the local rocks exhibit a greater range than those of regional rocks, with the density of surface lacustrine sediments showing the greatest scatter. There is little overlap between densities of local and regional units, and significantly, the density of the dome rhyolite is distinguishable from the density of regional rocks with a high confidence limit.

Lithological and structural control for pre-Tertiary regional rocks is based on the work of Hintze [1973], Woodward [1973], and Stokes [1963]. For purposes of gravity modeling, rocks in the Cricket and Beaver mountains were divided into two dominant rock types (Table 2) to which average densities were assigned based on lithology. A third group of rocks is composed of gneiss and schists, which are exposed in the Mineral Range about 30 km south of the Twin Peaks area [Hintze, 1973; Nielson et al., 1978]. These rocks, likened to the Farmington complex [Nielson et al., 1978], are assigned a density of 2.81 g/cm^3 from seismic velocities [Gertson, 1979; Woollard, 1962]. An average density of 2.71 g/cm^3 was assigned to the general basement rocks, based upon the lithology of pre-Mesozoic rocks in the Pavant Range [Hintze, 1973]. Cenozoic sediments in the Twin Peaks area are divided into two layers. The upper layer composed of late Tertiary-Quaternary lacustrine sediments, was assigned a density of 2.30 g/cm^3 while the second layer, composed of Tertiary lacustrine and land sediments and volcanics [MacDonald, 1976], was assigned a density of 2.40 g/cm^3. Both the layering and the density contrasts are consistent with seismic refraction results and gravity modeling in the adjacent Milford Valley graben [Gertson, 1979].

Structural control for the western part of the Black Rock Desert Valley was obtained from two seismic reflection lines [MacDonald, 1976] located 15 km (line 20, Figure 2) and 25 km north of the Twin Peaks area, respectively. Time was converted to depth for line 20 in Figure 6 using seismic velocities in Table 2.

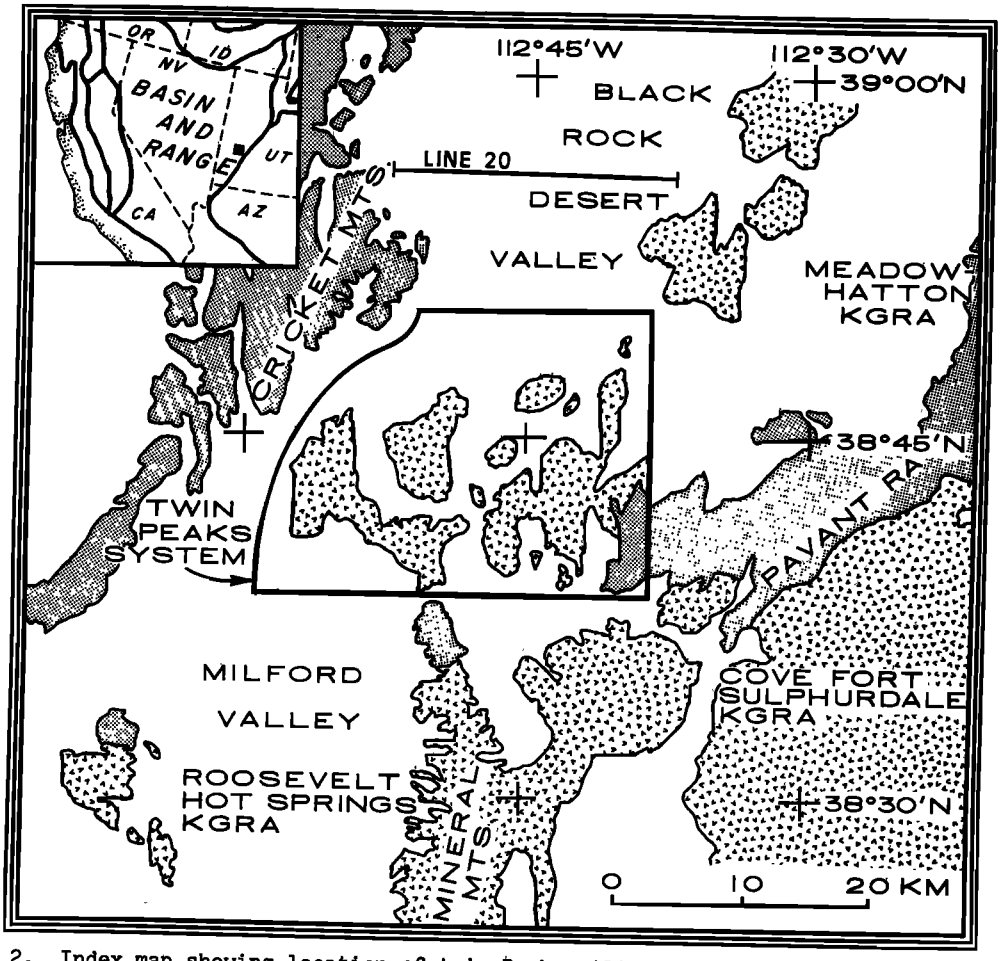

Fig. 2. Index map showing location of twin Peaks silicic volcanic center (irregular solid outline) in west central Utah and its relation to three known geothermal resource areas (KGRA's). Stipled pattern represents Tertiary igneous rocks. Line 20 identifies a seismic reflection profile discussed in the text. All following geologic and gravity maps (Figures 3, 4, 6, and 7) are bounded by the solid outline in this figure and include North Twin Peak (NTP) and South Twin Peak (STP) for orientation.

Gravity Data Acquisition and Reduction

Gravity data used in this study include 349 previously obtained gravity stations [Isherwood, 1967; Brumbaugh, 1978; Case, 1977; Carter, 1978; Serpa, 1980] supplemented by an additional 285 gravity stations collected during the summers of 1977 and 1978. Principal facts for the new gravity stations are recorded in Appendix D of Carrier [1979].

Gravity readings were reduced to a minimum elevation datum of 1371.6 m (4500 ft), with a density of 2.45 g/cm^3 and further to sea level with the normal 2.67 g/cm^3 density. The density of 2.45 g/cm^3 is based on measured densities of rocks representative of local surface geology. Several attempts were made to estimate surface density utilizing the density profile method [Nettleton, 1942]; however, the influence of subsurface structure on measured gravity was such that it negated the effectiveness of the technique.

Terrain corrections were made using U.S. Coast and Geodetic Survey terrain correction charts [Swick, 1942] through zone E and a computer technique from E to a radial distance of 20 km from each station. The average terrain correction using a density of 2.45 g/cm^3 was 0.47 mGal with a range of 0.08 to 4.85 mGal. Terrain corrections for stations taken in the survey generally did not exceed 2.5 mGal. We estimate the uncertainty in our gravity values, including reading, location, elevation, and topographic correction uncertainties to be about 1 mGal.

Terrain Corrected Bouguer Anomaly Map

A terrain-corrected Bouguer anomaly gravity map with a contour interval of 2 mGal is shown in Figure 4. The western portion of the map is dominated by a strong east-west gravity gradient across gravity contours that trend roughly north-south and are continuous for an additional 80 km to the north [Cook et al., 1975]. Gravity decreases from -164 mGal on the eastern outcrop of the Cricket Mountains to -200 mGal in the vicinity of North and South Twin Peaks and

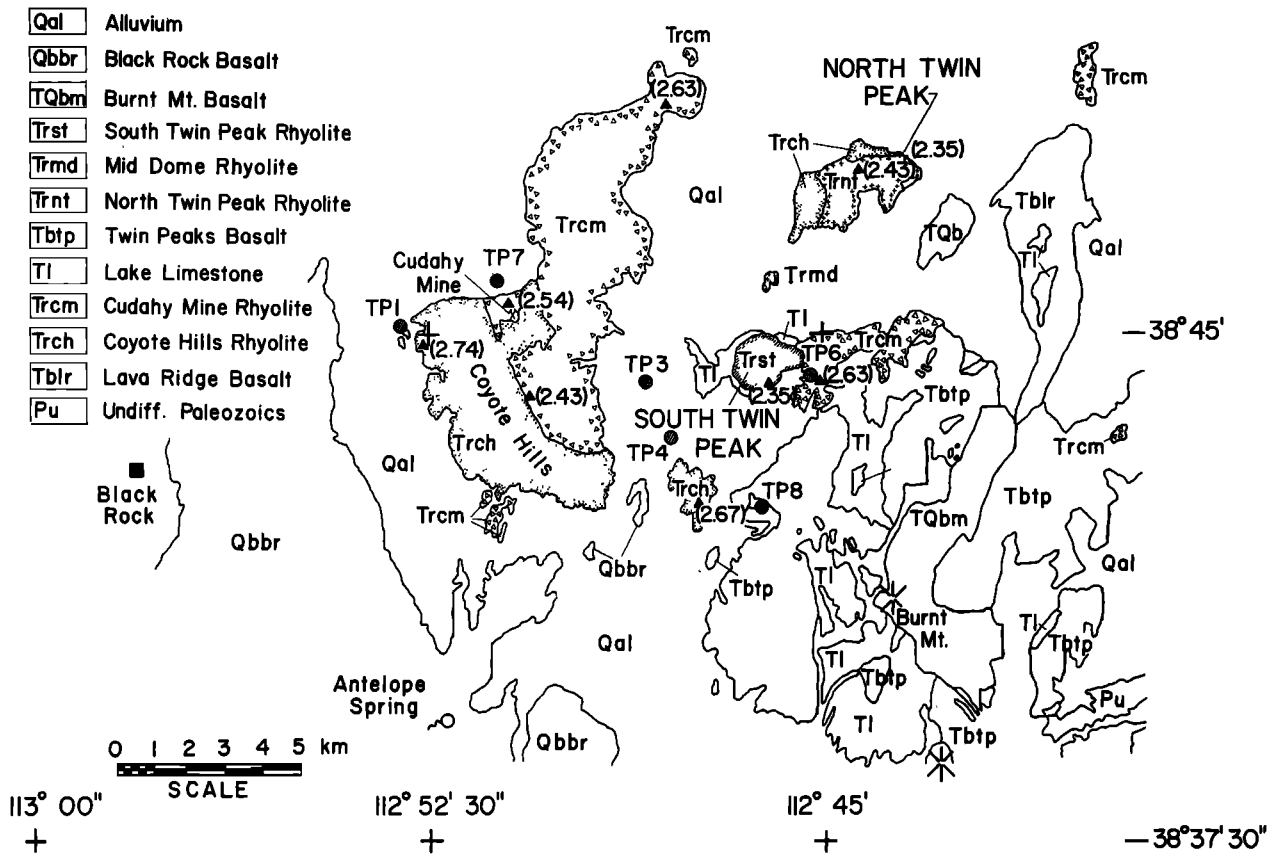

Fig. 3. Geological map of the Twin Peaks magma system within the boundary shown in Figure 2. North Twin Peak and South Twin Peak are two prominent rhyolite domes, hence the name for the igneous system. Rhyolites are marked with patterns. Solid triangles indicate sample locations for K/Ar dating; ages in m.y. B.P. are in parentheses. Heat flow drill hole locations are indicated by TP1 through TP8.

recovers to -190 mGal approaching the Pavant Range to the east. This north-northeast trending gravity trough is the major feature of the gravity field and is undoubtably caused by the low-density sediments of the Black Rock Desert Valley. Other obvious features in the gravity field are a pronounced gravity low in the southwest corner of the map (Figure 4) associated with the Milford Valley graben [Carter, 1978], positive gravity spurs to the southwest of the Cricket Mountains and in the northern Mineral Mountains due to buried ridges of high density Paleozoic formations, and local positive anomalies associated with North and South Twin Peaks domes. The gravity field is thus seen to be a superposition of effects from both Basin and Range horst-graben structure and from the volcanic field, the subsurface configuration of which is our prime interest. In the following section we attempt to separate these two effects.

TABLE 1. Measured Densities for Rocks of the Twin Peaks Area

Rock Type	N	Average, g/cm^3	Standard Deviation, g/cm^3
Regional			
Shale	7	2.63	0.07
Quartzite	29	2.63	0.03
Limestone	31	2.72	0.05
Dolomite	16	2.83	0.04
Local			
Lacustrine sediments	15	2.30	0.15
Rhyolite			
Dome	6	2.46	0.03
Flow	7	2.29	0.04
Basalt	11	2.66	0.07

TABLE 2. Compilation of Densities and Seismic Velocities for Characteristic Rocks in the Twin Peaks Area and Vicinities

Symbol	Rock Types	Area of Surface Exposure	Thickness, km	Average Density g/cm^3	Density Constrast g/cm^3	Seismic Velocities km/s	Sources*
TQls	LACUSTRINE SEDIMENTS	Twin Peaks	undetermined	2.30	-0.41	1.8	b
Tls	LACUSTRINE and LAND SED and volcanics	Eastern Cricket	undetermined	2.40	-0.31	4.0	b, d, f
C-Ols	LIMESTONE, shale, and quartzite	Cricket Mountains	1.7±.3	2.70	-0.01	6.5	a, c
PC-Cq	QUARTZITE, shale, limestone and slate	Cricket and Beaver Mountains	4.0±.5	2.66	-0.05	6.1	a, c, e
PCgs	GNEISS and SCHIST	Mineral Range	undetermined	2.81	0.10	6.7	a, b, c
Pb	BASEMENT	Pavant Range	undetermined	2.71	0	undetermined	a

Dominant rock types are capitalized. Symbol identifies unit in Figure 5. Density contrast is in comparison to Precambrian-Paleozoic basement rock.
*Sources: a, Hintze 1973 ; b, Gertson 1979 ; c, Woollard 1962 ; d, MacDonald 1976 ; e, Woodward 1973 ; f, Hintze 1959 .

Regional Gravity Anomalies

We assume that the general shape of the terrain-corrected Bouguer anomaly gravity map in Figure 4 is controlled by two major features: (1) part of a major regional north-northeastern trending gravity trough roughly 80 km long and 40 km wide [Cook et al., 1975], resulting from a thick section of Cenozoic sediments, and (2) a local roughly circular gravity low up to 30 km in diameter, related to the outcrop of silicic material over an area 15 km wide and its deeper source. Superposition of the broad lows associated with the valley and the volcanism, both having characteristic wavelengths of the same order, makes separation by analytical techniques difficult. The Twin Peaks region is also located on the flank of a strong gravity gradient toward the Colorado Plateau [Cook et al., 1975], but as this gradient affects at most the extreme south east corner of our gravity map (Figure 4), it is not modeled in connection with the volcanic system.

To determine and eventually separate the gravity effect of the valley fill alone, a regional east-west gravity profile was compiled north of the volcanic system along latitude $39^{\circ}00'$N using the published data of Cook et al. [1975] augmented by detailed data of Case [1977] and Serpa [1980]. An orthogonal polynomial fit to the regional data, shown as a solid line in Figure 5a, has less than 1 mGal rms misfit to the data and likely represents the gravity expression of the Black Rock Desert Valley undisturbed by the igneous activity.

It is instructive to demonstrate that the regional gravity trough we have described is indeed consistent with a Cenozoic sediment-filled valley whose structure is known from seismic reflection results [MacDonald, 1976]. Figure 5b shows a two-dimensional gravity model for this trough using the rock thicknesses and densities given in Table 1. The ambiguities inherent in gravity modeling are reduced by recognizing the further geological constraints placed on the model by the Cricket Mountains and the structural constraints placed on the model by the seismic reflection profile in Figure 5c. The model shows rocks composing the Cricket Mountains descending beneath the Cenozoic sediments with a dip between 4° and 11° depending on position, and terminating at a depth of 3 km below the surface into a basement detachment plane that is rising with a dip of about 8°. The late Tertiary-Quaternary sediments reach a maximum thickness of 1.2 km and then thin to 0.4 km at the eastern margin of the profile. The maximum thickness for Cenozoic sediments in the model is 3 km, in good agreement with the thickness estimated from the seismic reflection profile in Figure 5c.

Residual Gravity Anomaly

A residual gravity anomaly pattern for the Twin Peaks region was determined by removing a two-dimensional gravity trough from the terrain-corrected Bouguer anomaly gravity field. The two-dimensional trough was constructed by projecting the profile shown in Figure 5a into the Twin Peaks area with a strike of $N15^{\circ}E$, a direction consistent with the trend of gravity contours and with the strike of Cambrian rocks mapped in the Cricket Mountains. The resulting residual gravity pattern for the Twin Peaks area (Figure 6) has the appearance of a broad circular gravity depression with an amplitude of 7 mGal and an east-west diameter of 26 km inside the 0 mGal contour. Near the center of the gravity depression, a positive residual anomaly, with a total relief of about 10 mGal and a width of 5 km at the -2 mGal contour, rises abruptly over North Twin Peak. A smaller positive anomaly, with a total relief of about 6 mGal occurs over South Twin Peak. East of the two domes the gravity decreases again to -4 mGal and then rises to 0 mGal at the edge of the map.

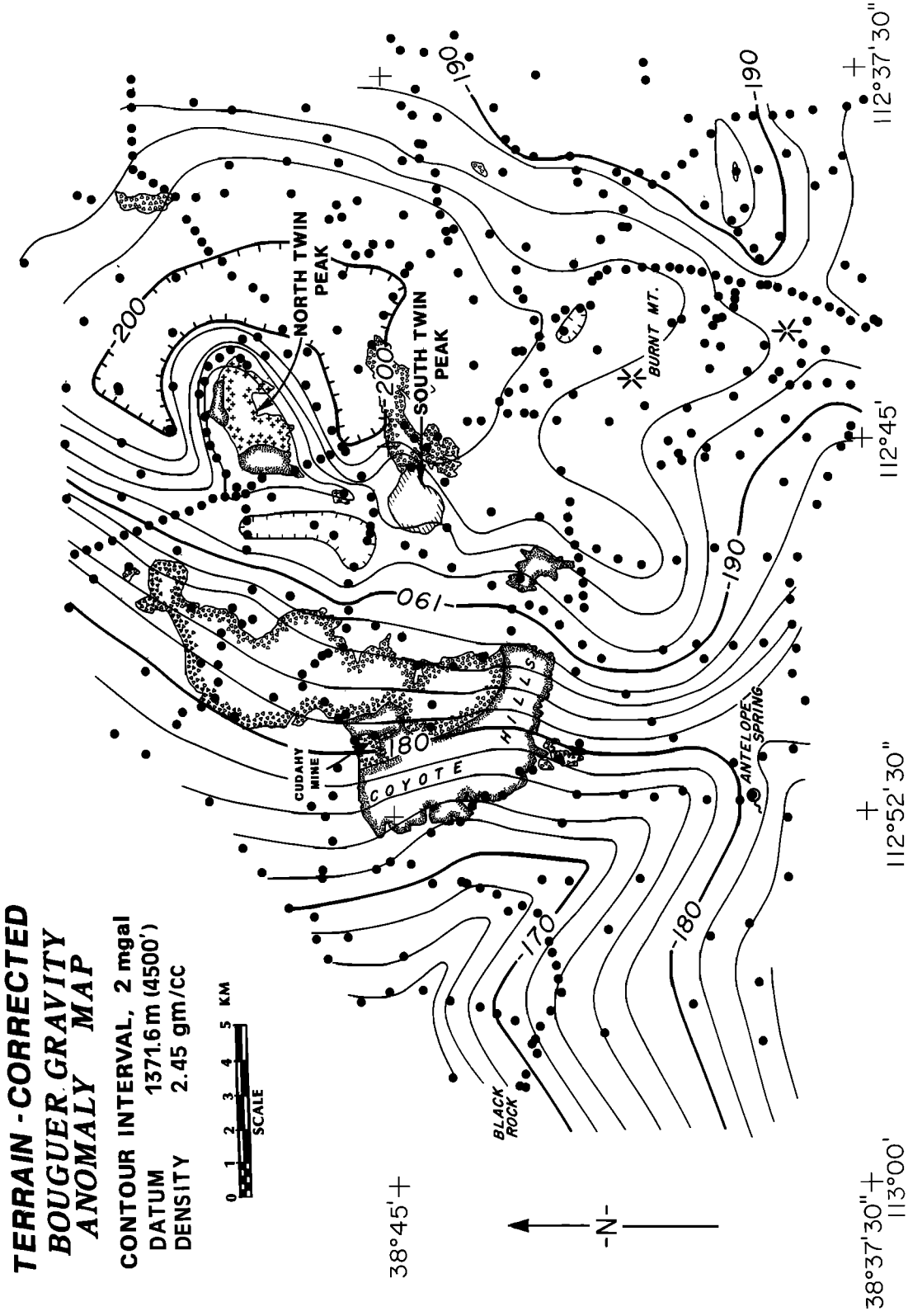

Fig. 4. Terrain corrected bouguer anomaly map of the Twin Peaks magma system within the boundary shown in Figure 2. Contour interval is 2 mGal. Solid dots indicate gravity stations. Rhyolite outcrop from Figure 3 is repeated here for orientation.

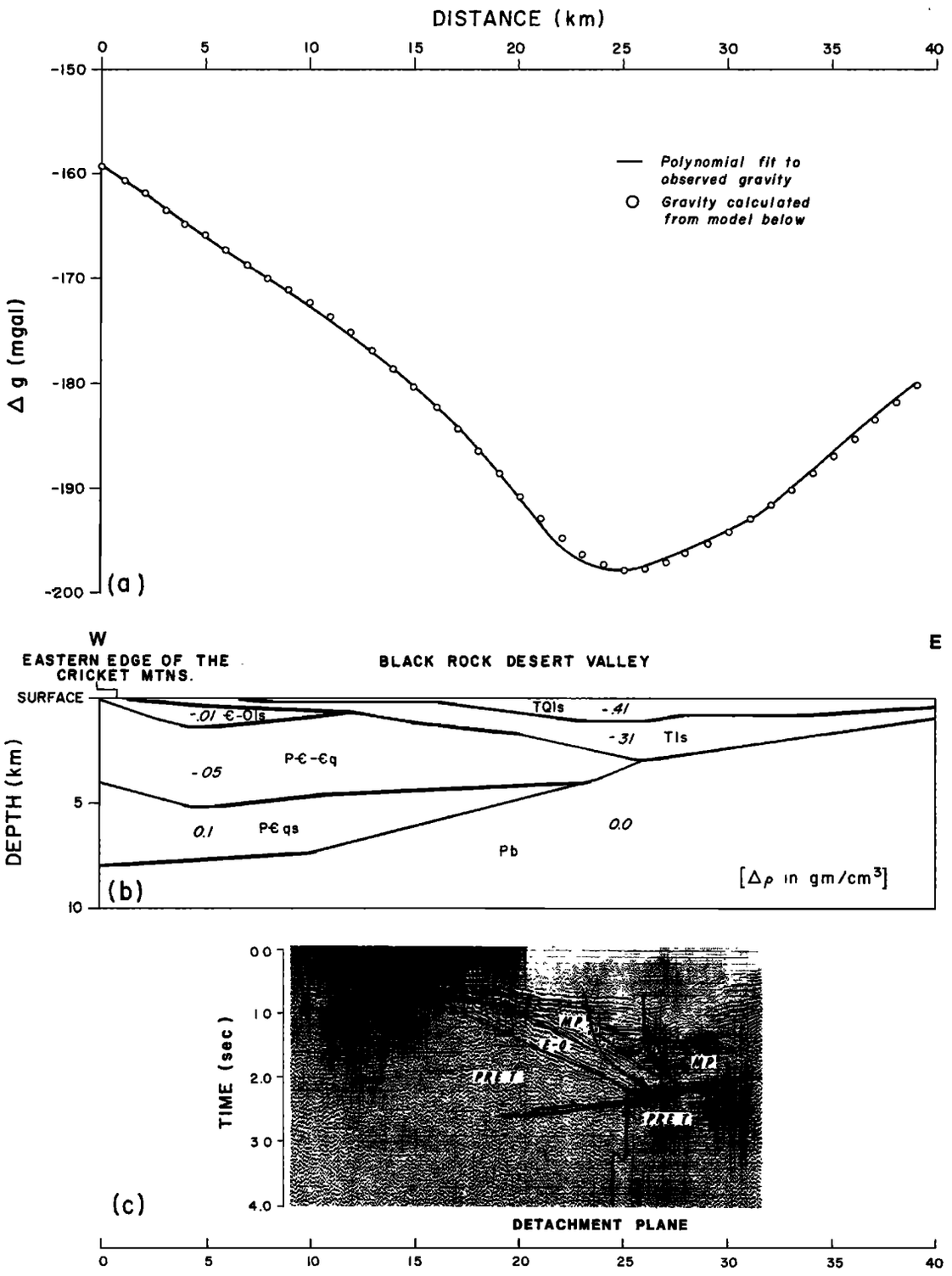

Fig. 5. Gravity and structure model for the Black Rock Desert Valley north of the volcanic system. (a) Regional gravity due to valley structure deduced from observations (solid line) and gravity calculated from the two-dimensional geologic model in Figure 5b below (open circles). (b) Two-dimensional interpretive geologic model of the Black Rock Desert generated to fit regional gravity model in Figure 5a. Lithologic symbols, unit thicknesses and densities are given in Table 2. Structural control used in the geologic model was obtained from Hintze [1959] and MacDonald [1976]. (c) Seismic reflection line 20 published by MacDonald [1976] and located in Figure 2. The dominant reflector in this section is described as a detachment plane along which pre-Tertiary rocks moved east.

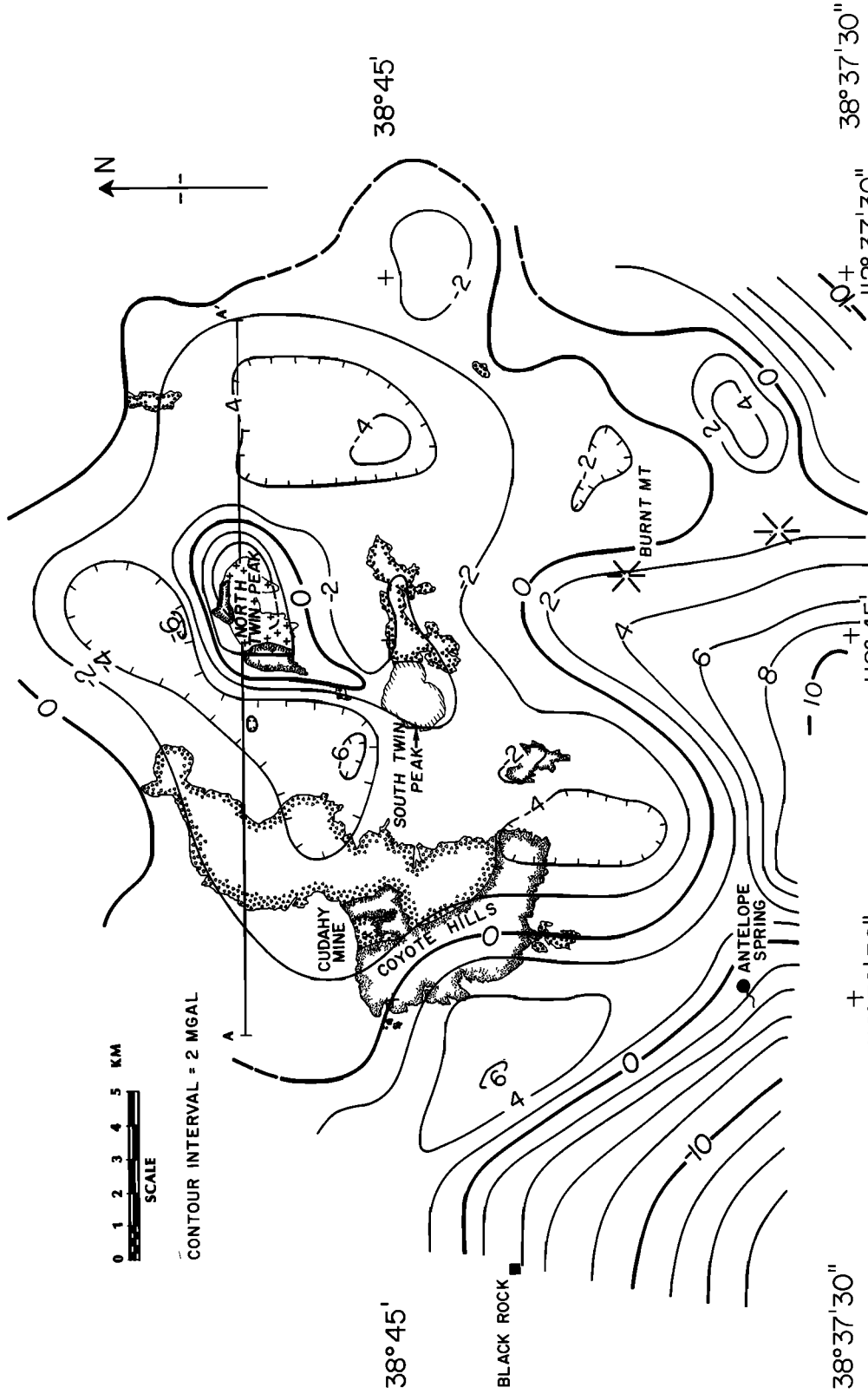

Fig. 6. Residual Bouguer anomaly map of the Twin Peaks magma system after effects of the Black Rock Desert valley have been removed from Figure 4. Contour interval is 2 mGal. Rhyolite outcrop is shown by patterns identical to Figure 3 for purposes of orientation.

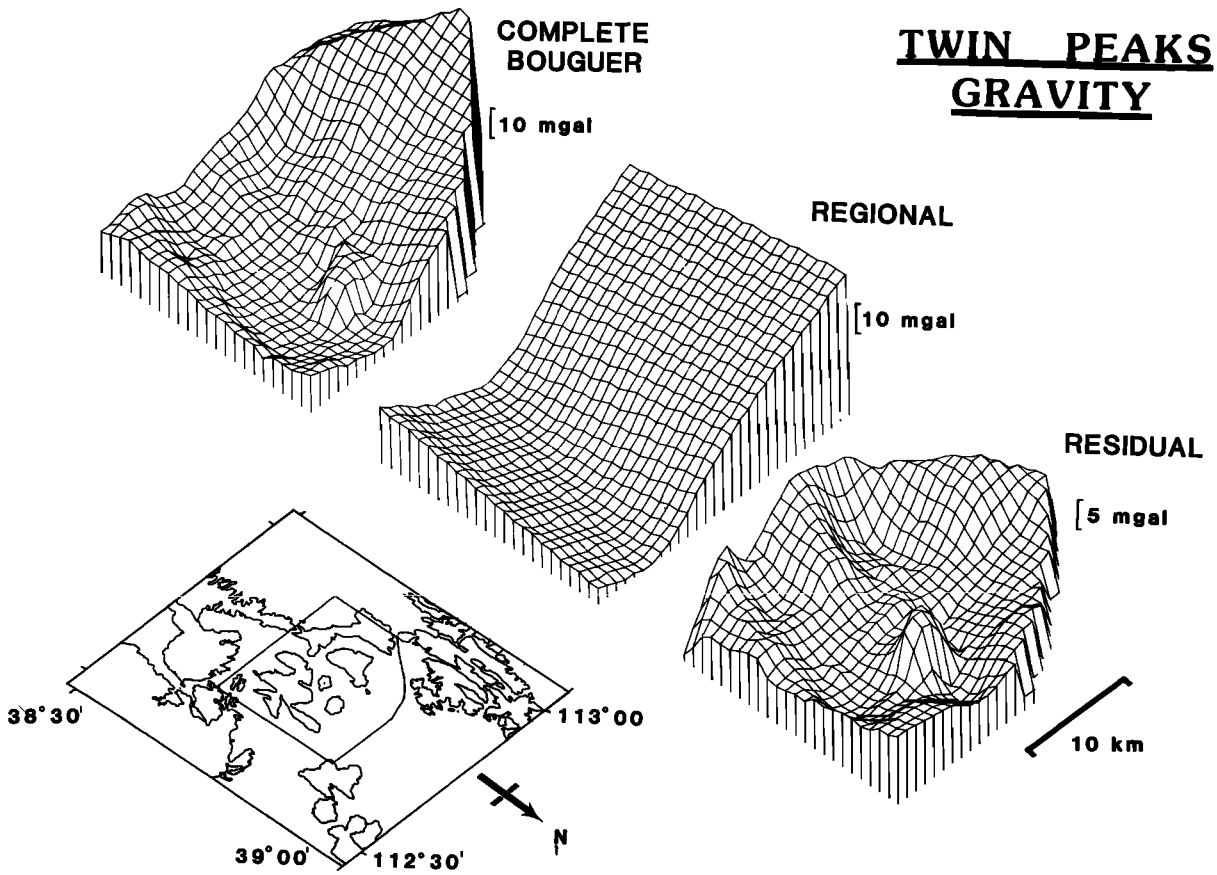

Fig. 7. Isometric representation, looking from northeast, of three gravity surfaces for the Twin Peaks area. Index geologic map from Figure 2 is repeated at bottom left in the new map projection for orientation. Isometric gravity surfaces cover the truncated rectangle shown in the inset. The complete Bouguer anomaly surface (Figure 4 rotated) is at upper left; projected regional anomaly discussed in text accounts for the Basin and Range valley structure; residual Bouguer anomaly (Figure 6 rotated) can be related to the Twin Peaks igneous system.

Relative positive gravity features outside the area of rhyolite exposures include a +4 mGal residual over the Paleozoic rock outcrop in the southeastern part of the map and a broad +6 mGal residual southwest of the Coyote Hills rhyolite in the vicinity of the gravity spur in Figure 4. A negative gravity feature is produced by the Milford Valley graben which reaches -16 mGal at the southwestern edge of the map. Similarly, in the southeast, the negative gravity associated with the Beaver Valley graben reaches -10 mGal at the map edge.

The positive gravity anomaly over the domed sediments and basalts southwest of Burnt Mountain in the residual map is without closure. Outside the domed area the gravity high broadens out to the west where it swings to the south around the northwestern part of the Mineral Range [see also Brumbaugh, 1978], suggesting that the positive gravity feature is due either to a late-stage intrusion of rhyolitic material that caused the doming of the Tertiary rocks and was stranded beneath the surface or to pre-Tertiary basement rising in the south and west in the vicinity of the Mineral Mountains.

A summary of the complete Bouguer, the regional Bouguer and residual Bouguer gravity maps, is shown in isometric representation in Figure 7. For orientation purpose, the generalized geological outcrop pattern of Figure 3 is shown in the inset with the same projection. It is clear from Figure 7 that the regional trough dominates the complete Bouguer gravity field, but with the removal of this valley-fill trough effect, a residual anomaly is produced which is correlatable spatially with the volcanics outcrop pattern. It is the residual gravity anomaly that we now address and model as being composed of two parts: a broad gravity depression, which we hypothesize is caused by an intrusive granitic body emplaced within the high density Paleozoic and Precambrian basement rock, and sharp positive anomalies associated with the rhyolitic domes similar in density to the intrusive but which are more dense than the surrounding shallow Tertiary valley fill.

Models for the Residual Anomaly

The broad residual gravity depression and the positive anomaly over North Twin Peak are very roughly circular. Departure from a more circular pattern can be attributed to encroaching shallow basement southwest of Coyote Hills and stranded rhyolite beneath domed sediments or a rising basement southeast of South Twin Peak. We have

therefore modeled the residual gravity field by a series of three-dimensional vertical cylinders [Telford et al., 1976, p. 63].

Data for modeling the deep intrusion are taken from several profiles crossing the center of the residual gravity low in Figure 6 (see also Figure 4). These data were superimposed to produce an effectively radially averaged anomaly shown in Figure 8. Gravity data from the center of the low have been excluded so that the strongly positive anomalies of the Twin Peaks domes do not influence the modeling of the negative anomaly.

The critical parameters to be considered in modeling with vertical cylinders are the radius, burial depth, density contrast, and thickness of the body. The outcrop pattern of the rhyolite (Figure 3) suggests a radius of 6-7 km for the parental intrusion. The body is most likely of granitic composition having a density between 2.5 and 2.8 g/cm^3 [Telford et al., 1976]. In this particular case a gravity low from a granitic body will be produced only if the intrusive is below 3 km, the depth of the Tertiary basement interface, and if the intrusive has a density less than 2.71 g/cm^3, the average density of the basement rocks in the region (Table 2).

Cross sections of two three-dimensional vertical cylinders that produced reasonable fits to the residual gravity negative anomaly from the radially averaged profiles are shown in Figure

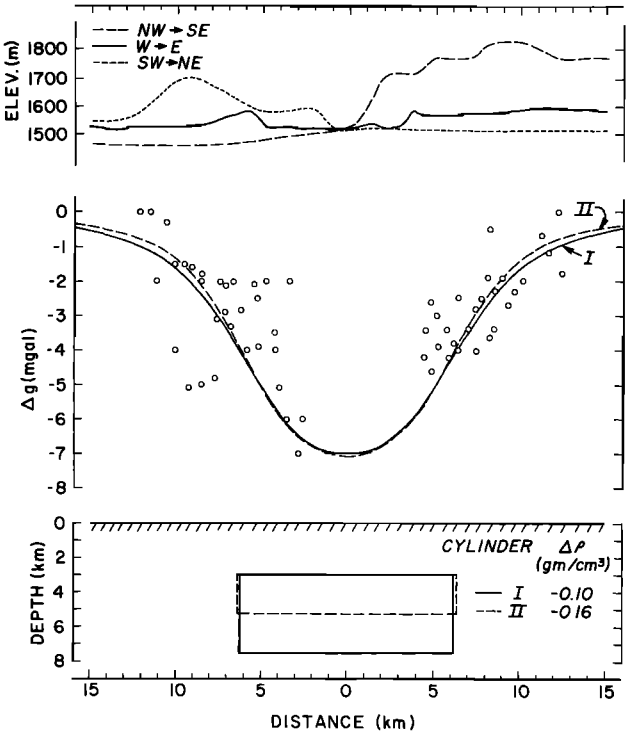

Fig. 8. Topography profiles and composite residual gravity values (open circles) along three profiles crossing through the center of the Twin Peaks gravity low and calculated gravity (solid lines) for three-dimensional circular cylinders shown in cross section. Scatter in the observed gravity is caused by lack of perfect radial symmetry in the residual gravity field. Data in the center of the profile is ommitted here but is shown and modeled in Figure 9.

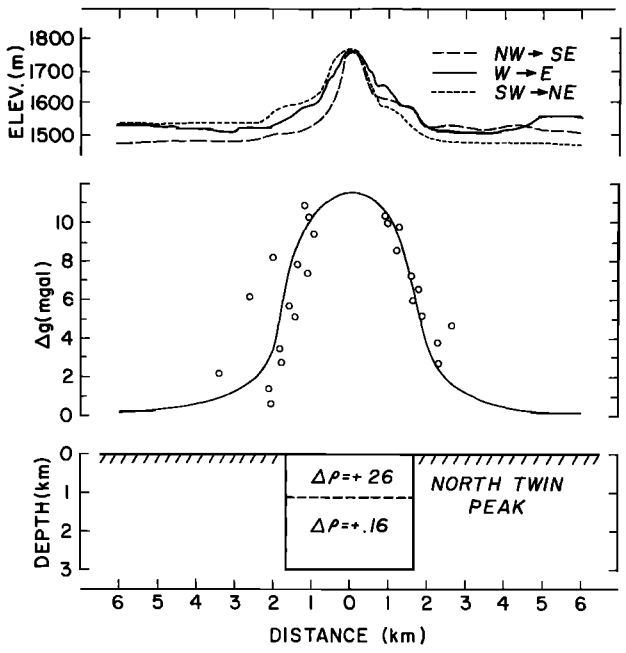

Fig. 9. Topography along three profiles crossing North Twin Peak and composite residual gravity around North Twin Peak with the effect of cylinder I of Figure 8 removed. Open circles represent residual gravity along six radial profiles centered on North Twin Peak. Solid line is calculated gravity for the three dimensional circular cylinder shown in cross section.

8. Cylinder I has a radius of 6.25 km, a thickness of 3.5 km (volume 430 km^3), and a density contrast of -0.10 g/cm^3 (an actual density of 2.61 g/cm^3); cylinder II has a slightly greater radius of 6.4 km, a lesser thickness of 2.25 km (volume 290 km^3) and a greater density contrast of -0.16 g/cm^3 (an actual density of 2.55 g/cm^3) than cylinder I. Both cylinders were buried below 3 km.

A model for the positive gravity anomalies associated with the rhyolite domes was derived in a similar manner, although the data spacing in this case combined with uncertainties arising from topographic effects provide less of a constraint compared to the broad gravity low. The residual positive gravity anomaly for North Twin Peak after the effect of cylinder I of Figure 8 has been removed is shown in Figure 9. Data were taken along six radial profiles centered on North Twin Peak. Three-dimensional vertical cylinders were again used to model this anomaly, but in this case, composite cylinders were introduced in order to accommodate the density structure indicated by the layering of the Tertiary valley fill (see Figure 5). A satisfactory fit to the data (Figure 9) is produced by a vertical cylinder of radius 1.67 km extending from the surface to a depth of 3 km, the top of the parental intrusive. The density contrasts of +0.26 g/cm^3 from 0 to 1.1 km depth and +0.16 g/cm from 1.1 to 3.0 km, when compared to sediment densities (Table 2), implies a rhyolite density at depth of 2.56 g/cm3, about 4% higher than that measured on surface samples (Table 1). Models for South Twin Peak (described

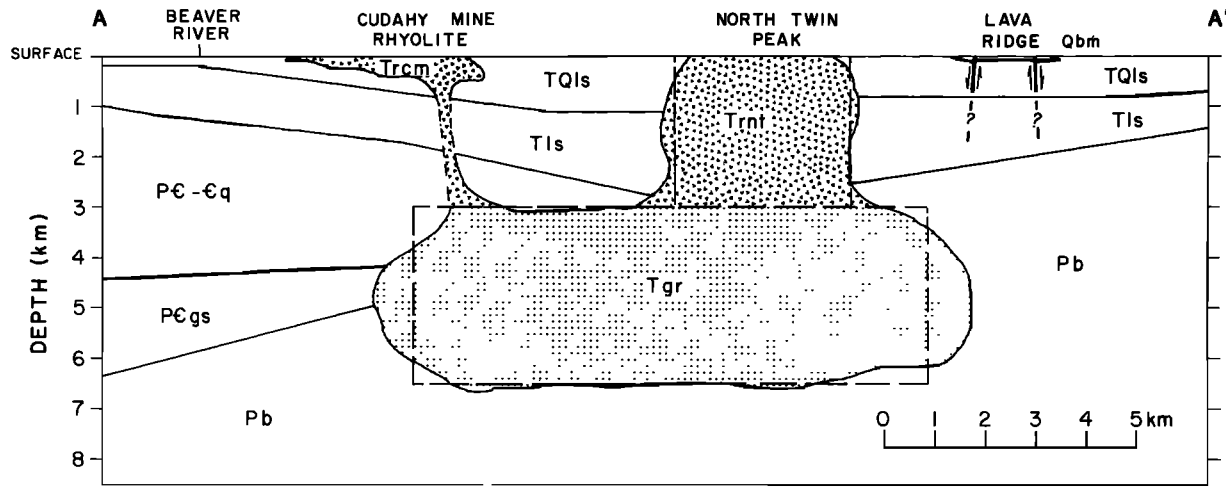

SEDIMENTARY ROCKS		IGNEOUS ROCKS	
TQls	Lacustrine Sediments and Volcanics	Qbm	Burnt Mtn Basaltic Andesite
Tls	Lacustrine Sediments	Trnt	North Twin Peak Rhyolite
P€-€q	Quartzite - Shale - Slate	Trcm	Cudahy Mine Rhyolite
P€gs	Gneiss and Schist	Tgr	Twin Peaks Granite (?)
Pb	Undifferentiated Paleozoic and Precambrian Rocks		

Fig. 10. East west cross section along profile AA' of Figure 6 interpreted from gravity models in Figures 9 and 10.

in detail by Carrier [1979]) are similar, although there are less data to provide constraints. Results from the gravity models in Figures 8 and 9 are summarized in an idealized east-west geological cross section through the center of North Twin Peak, shown in Figure 10.

Included in the cross section are Cudahy Mine rhyolite and Lava Ridge of Burnt Mountain and Twin Peaks basaltic andesites, both of which have not been modeled in detail. The Cudahy Mine rhyolite is constrained at the surface by outcrop. Subsurface shape and extent of the Cudahy Mine rhyolite in Figure 13 is arbitrary; however, it is not unlike rhyolite sections in other localities [see, e.g., Smith et al., 1961; Williams and McBirney, 1968]. The faulting in the east has been suggested by Clark [1977], but the lack of an obvious gravity expression suggests that it is minor.

Haugh [1978] has suggested, primarily from the circular geometry of rhyolite outcrop, that the Twin Peaks system has undergone a caldera collapse. The ambiguities inherent in modeling rock bodies from gravity data do not preclude that the broad gravity low may be due in part to caldera subsidence rather than entirely a granitic intrusion. The amount of subsidence that could have occurred may be estimated from the eruptive material, which is composed almost exclusively of flow and dome material since voluminous ash flow deposits, characteristic of many silicic calderas, are absent. Eruptive material at the surface is estimated to be 3.5 km^3 by Haugh [1978]. For a caldera with a radius of 6.25 km, this could result in a subsidence of only 28 m, the gravity expression of which would probably not be separable from the intrusive model we have proposed.

Further support for our intrusive model may be drawn from magnetic data for the area (D. Mabey, written communication, 1980). The local magnetic field consists of two highs associated with the moderately magnetized North and South Twin Peaks domes superimposed upon a more extensive magnetic high, possibly caused by a buried intrusive.

Heat Flow

Heat flow determinations were made at six sites in the vicinity of the Twin Peaks magma system. These data were acquired to detect any residual heat that may remain from the emplacement of the intrusion and the subsequent volcanic activity, thereby assisting in evaluating the area's geothermal potential and providing constraints for cooling models. The heat flow sites are distributed over roughly 100 km^2 centered on the rhyolite domes (Figure 3). Drill hole depths range from 48 to 152 m. Three drill holes, TP3, 6, and 8 were released by Chevron Resources for the study, while holes TP1, 4, and 7 were obtained independently.

Thermal data for each hole are summarized in Table 3; details are given in Appendix C of Carrier [1979]. Thermal gradients were determined from temperature-depth data using a linear least squares fit to the data over the interval indicated in Table 3. The temperature-depth profiles for each hole (Figure 11) show little disturbance below 40 m, suggesting that heat transfer in these holes is predominately by conduction. Thermal conductivities were measured

TABLE 3. Summary of Heat Flow Data in the Twin Peaks Area

Site	Latitude (North)	Longitude (West)	Elevation, m	Depth Range, m	Gradient, °C/km	Conductivity, W/m K	Heat Flow, mW/m^2
TP1	38°45.13'	112°53.00'	1563	15-48.5	53.4±3.9	1.78±.15	95±11
TP3	38°44.33'	112°48.31'	1607	43-152	45.0±1.7	2.18±.07	98±5
TP4	38°43.47'	112°47.87'	1575	30-58	86.9±10.5	1.63±.16	142±22
TP6	38°44.43'	112°45.25'	1665	43-151	42.7±1.9	2.02±.03	86±4
TP7	38°45.87'	112°51.18'	1536	30-90	49.9±10.8	2.09±.21	104±25
TP8	38°42.48'	112°46.18'	1646	27-130	55.5±4.1	1.17±.07	95±8

on saturated drill chips and solid discs of core for four holes using a divided bar apparatus [Roy et al., 1968] and the methods of Sass et al. [1971]. Samples were not available for TP4 and TP7. Instead, conductivities were estimated for these holes from surface lithology and an average conductivity for rhyolite in TP6 (for TP7) and basalt in TP8 (for TP4). The vertical component of the heat flow was then calculated by taking the product of the harmonic mean thermal conductivity and the thermal gradient for each hole.

Measured heat flow at Twin Peaks ranges from 86 to 142 mW m^{-2} with an average and standard deviation of 103 and 20 mW m^{-2}, respectively. The one anomalous heat flow value of 142 mW m^{-2} is for TP4 where the thermal conductivity is poorly constrained. Excluding the value of 142 mW m^{-2} from the rest of the data set results in an average and standard deviation in the heat flow of 96 and 6 mW m^{-2}. This is very near the mean for eastern Basin and Range heat flow of 90 mW m^{-2} [Chapman et al., 1979] and certainly within the range considered to be characteristic. Heat flow observations therefore suggest that there is no noticeable present day thermal anomaly associated with the silicic volcanism in the Twin Peaks area.

Thermal Model

A model for the anomalous heat flow, Δq, at the surface above a cooling intrusion was constructed using the following constraints: (1) the body is emplaced instantaneously at a time t = 0, (2) the magma stagnates after emplacement, and (3) heat loss is by conduction. Anomalous surface heat flow produced by a cooling vertical prism appropriate to the Twin Peaks intrusion (model I, Figure 8) is shown in Figure 12. Parameters used to constrain the thermal model were determined by gravity modeling, geochemistry, and surface geology, and are summarized in Table 4. The intrusion is modeled as a body 3.5 km thick, 11 km wide, emplaced to a depth of 3 km with an initial temperature of 850°C (W. P. Nash, personal communication, 1978) in an area with an average background thermal

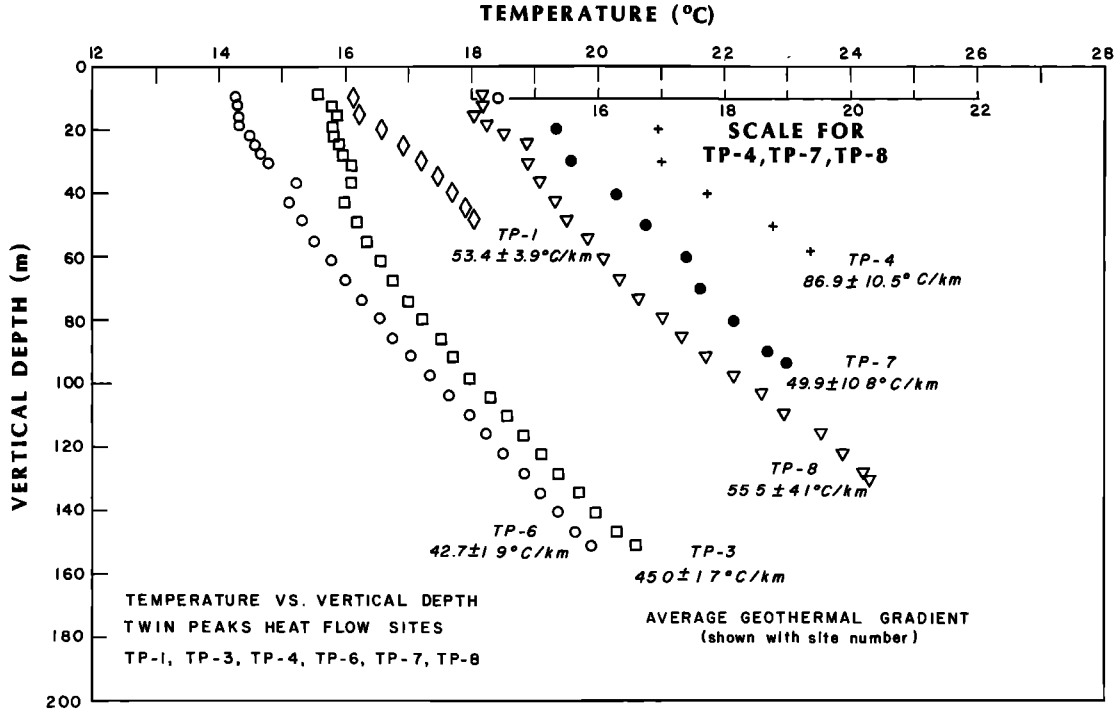

Fig. 11. Temperature-depth profiles for six drill holes in the Twin Peaks area. Scale for TP 4, 7, and 8 is offset by 4°C to avoid overlap. Borehole locations are shown on Figure 3.

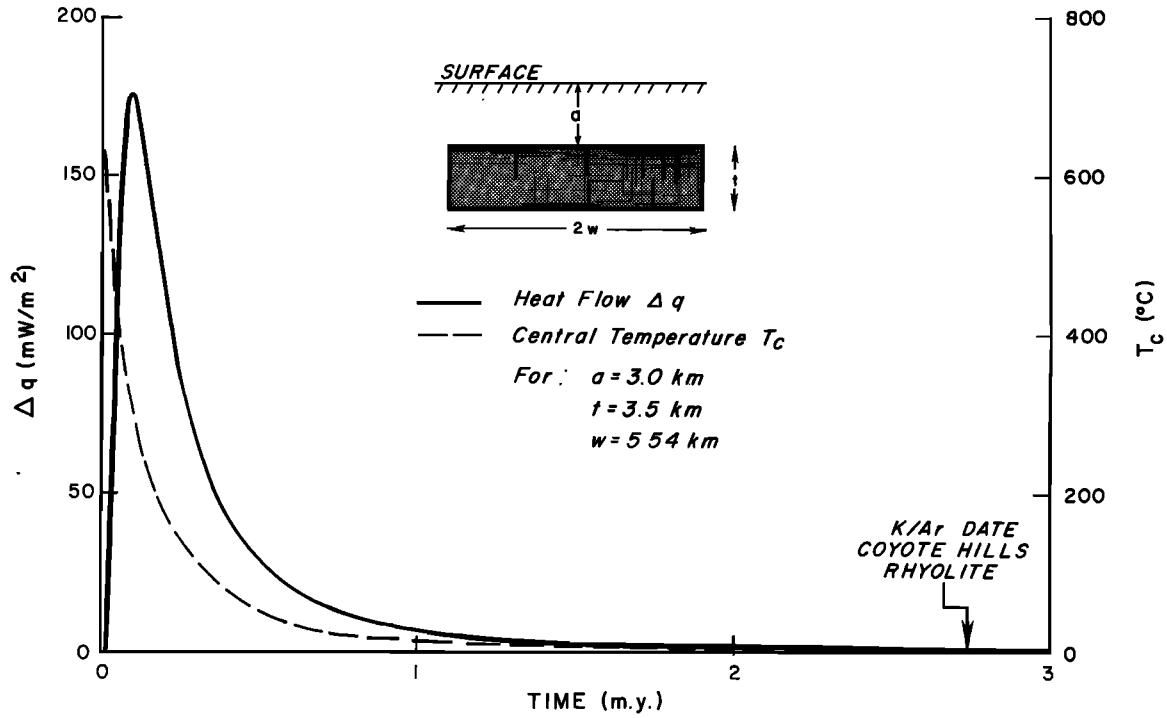

Fig. 12. Anomalous surface heat flow (solid line) and central temperature (dashed line) for the cooling of an instantaneously emplaced igneous body. The cross section area thickness, and depth of this body match that of cylinder I shown in Figure 8. Details are given in Table 3 and in text.

gradient of 45°C/km. This body has identical cross section area to the cylindrical model I of Figure 8. Time of emplacement of the intrusion and of extrusion of the Coyote Hills rhyolite are considered to be indistinguishable. The intrusion modeled would produce an anomalous surface heat flow that reached a maximum of 175 mW m^{-2}, 9 x 10^4 years after the time of emplacement; the anomalous surface heat flow would decay to one half the maximum value 0.25 m.y. after emplacement, and would be indistinguishable from background after 1.0 m.y. After 2.74 m.y., the time since the extrusion of the Coyote Hills rhyolite, the intrusion should contribute less than 1 mW m^{-2} to the heat flow in the Twin Peaks area, consistent with the lack of an observable thermal anomaly.

The cooling curve for the center of the intrusion is also shown in Figure 12. The center of the intrusion cools down from an anomalous 636°C at emplacement to less than one half of this value 0.1 m.y. later. The central temperature decreased to one tenth the original value, 0.45 m.y., after emplacement. Finally,

TABLE 4. Parameters for Thermal Models

Parameter	Symbol	Granitic Intrusive	North Twin Peak	Principal Source
Thermal diffusivity	α	32 km^2/m.y.	32 km^2/m.y.	average for crustal rocks
Temperature of emplacement	Ti	850°C	700°C	geochemistry
Initial temperature at center of body above country rocks	T_o	636°C	632°C	calculated
Background thermal gradient	dT/dz	45°C/km	45°C/km	thermal measurements
Thermal conductivity Tertiary sediments	K	2 W/m K	2 W/m K	thermal measurements
Thickness of body	Δ	3.5 km	3 km	gravity models
Width of the body square prism	w	11 km	3.1 km	gravity models surface geology
Depth to top of body	a	3 km	0.01 km*	gravity models surface geology
Age of body	-	2.74±0.1 m.y.	2.3±0.1 m.y.	geochronology (K/Ar dates)

*Body is required to be emplaced below surface.

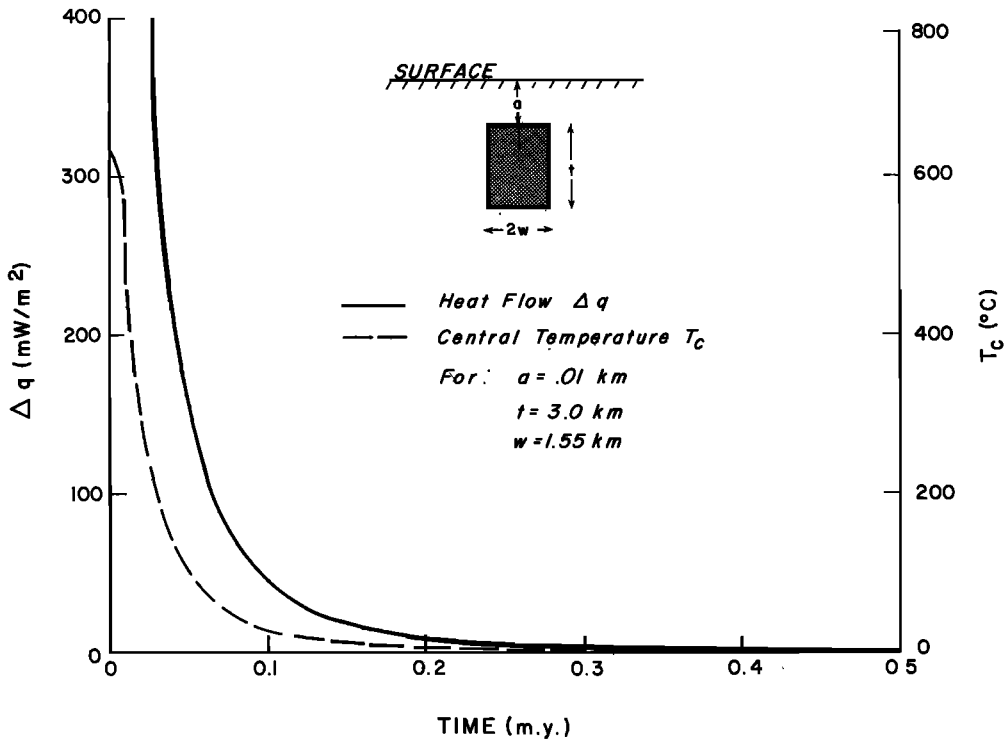

Fig. 13. Anomalous surface heat flow (solid line) and central temperature (dashed line) for the cooling of an instantaneously emplaced igneous body. The cross section area, thickness and depth of this body matches that of the cylinder shown in Figure 9. Details are given in Table 3 and in text.

2.74 m.y. after the extrusion of the Coyote Hills rhyolite, only 2°C of the anomalous temperature at the center should remain.

Anomalous surface heat flow produced by the extrusion of the North Twin Peak dome has also been calculated and is shown in Figure 13. The cooling of the dome is modeled using constraints again determined by the gravity model, geochemistry, and surface geology (listed in Table 4). The body was placed at a depth of 10 m to avoid computation difficulties. The body has a width of 3.1 km, a thickness of 3 km, and was emplaced at a temperature of 700°C (W. P. Nash, personal communication, 1978), into an area with a background thermal gradient of 45°C/km. As this body is smaller and shallower than the parental igneous body, cooling will advance at a faster pace, and negligble heat will be left after only 0.2 m.y.

Our thermal model of the cooling intrusive assumes that heat transfer is by conduction and allows for no hydrothermal circulation of groundwater in the overlying Tertiary sediments. Hydrothermal circulation exterior to the magma has little effect on the magma solidification time but may decrease the postsolidification cooling time by a factor of 5. This depends on the permeability of the host rock, presumably high in this case, the availability of fluids, possibly low, and the chemical sealing of fluid paths, which is unknown. Prolongation of cooling over that predicted in Figures 12 and 13 on the other hand would be expected if multiple intrusions had effectively preheated a large volume prior to final cooling. Two pulses of silicic volcanism are present at Twin Peaks [Evans et al., 1980; Crecraft et al., this issue]. The first sequence includes Coyote Hills rhyolite and the Cudahy Mine obsidians, felsite, and volcanoclastics and spans the period 2.7 to 2.5 m.y. ago. A second sequence includes the North and South Twin Peak rhyolite domes and spans the period 2.5 to 2.3 m.y. Each sequence is characterized by systematic progression from less silicic to more silicic rocks [Crecraft et al., 1980, this issue]. Basaltic volcanism in the same region extends from about 2.5 m.y. to 0.9. m.y. ago. Magmatic longevity is thus comparable to the cooling time for this volcanic center.

Our observation that heat flow at Twin Peaks is close to background Basin and Range values suggests that magmatic longevity, if important, does not extend cooling times by a factor of 3 or more, otherwise, we should have seen a thermal anomaly. A more sensitive test of the magmatic longevity versus hydrothermal cooling efficiency would have been provided had the parental igneous body been much larger or younger or both.

Conclusions

Gravity, heat flow, and surface geology have been integrated in study of an area of late Tertiary silicic volcanism at Twin Peaks, Utah. Volcanism began in the area with the extrusion of the Coyote Hills rhyodacite 2.74 ± 1 m.y. ago. A period of quiescence followed lasting nearly 0.3 m.y., interrupted by the extrusion of a complex sequence of domes and flows that lasted until 2.3 ± 0.1 m.y. ago.

Terrain corrected Bouguer gravity at Twin

Peaks is shaped by three features of varying characteristic dimension: (1) a major N-NE trending -30 mGal gravity trough roughly 40 km wide and extending 80 km to the north, caused by a thick sequence of Cenozoic sediments in the Black Rock Desert Valley, (2) a local, roughly circular, -7 mGal gravity low related to an intrusive body in the basement that produces an anomaly nearly 26 km broad, and (3) a series of very narrow positive anomalies up to + 10 mGal produced by the major Twin Peak volcanic domes. The intrusive can be approximated by a three-dimensional vertical cylinder with a roof at a depth of 3 km and a radius of 6.25-6.4 km and a thickness of 2.25-3.5 km. Similarly, the North and South Twin Peak domes can be approximated by vertical cylinders that extend to a depth of 3 km. The North Twin Peak model has a radius of 1.67-1.75 km. Our best estimate of the total volume of silicic material at and below the surface is about 480 km^3.

Simple thermal models, assuming conductive heat transfer, predict that a maximum anomalous heat flow would have occurred within 0.1 m.y. and that negligible heat flow or central temperature anomalies should exist after 1 m.y. Aided by convection, the anomaly would have been greater and would have occurred sooner. Model predictions of a negligible residual heat flow anomaly 2.74 ± 0.1 m.y. after emplacement of the intrusion is consistent with the present day local heat flow of 96 mW m^{-2} which is indistinguishable from background Basin and Range heat flow in Utah. These geological and geophysical observations and models provide a consistent description of the Twin Peaks silicic volcanic center, its structure, and its thermal evolution.

Acknowledgments. K. L. Cook suggested undertaking gravity studies at Twin Peaks, assisted us in the aquisition of data and made a careful critique of an early version of this paper. Matthew Mabey made some of the thermal conductivity measurements and produced the isometric plots of the gravity field; his father Don Mabey provided a constructive criticism of this paper. Chevron Resources Company kindly permitted the release of both gravity and thermal gradient data. This work was partially supported under the U.S. Geological Survey Geothermal Research Program by grant 14-08-0001-G-544.

REFERENCES

Brumbaugh, W. D., Gravity survey of the Cove Fort-Sulphurdale KGRA and the North Mineral Mountains area, Millard and Beaver counties, Utah, M.S. thesis, 130 pp., Univ. of Utah, Salt Lake City, 1978.

Carrier, D. L., Gravity and heat flow studies at Twin Peaks, an area of late Tertiary silicic volcanism in Millard County, Utah, M. S. thesis, 120 pp., Univ. of Utah, Salt Lake City, 1979.

Carter, J. A., Regional gravity and aeromagnetic surveys of the Mineral Mountains and vicinity, Millard and Beaver counties, Utah, M.S. thesis, 128 pp., Univ. of Utah, Salt Lake City, 1978.

Case, R. W., A regional gravity survey of the Sevier Lake area, Millard County, Utah, M.S. thesis, 95 pp., Univ. of Utah, Salt Lake City, 1977.

Chapman, D. S., D. D. Blackwell, W. T. Parry, W. R. Sill, S. H. Ward, and J. A. Whelan, Regional heat flow and geochemical studies in southwest Utah, vol. 2, final report, contract 14-08-001-G-341, 119 pp., U.S. Geol. Surv., Reston, Va., 1979.

Clark, E. E., Late Cenozoic volcanic and tectonic activity along the eastern margin of the Great Basin in the proximity of Cove Fort, Utah, Brigham Young Univ. Geol. Stud., 24 (1), 87-114, 1977.

Cook, K. L., J. R. Montgomery, J. T. Smith, and E. F. Gray, Simple Bouguer gravity anomaly map of Utah, map 37, Utah Geol. and Miner. Surv., Salt Lake City, Utah, 1975.

Crecraft, H. R., W. P. Nash, and S. H. Evans, Jr., Chemical and thermal evolution of the Twin Peaks magma system, west central Utah, Trans. 4, pp. 117-120, Geotherm. Resour. Counc., Davis, California, 1980.

Crecraft, H. R., W. P. Nash, and S. H. Evans, Jr., Late Cenozoic volcanism at Twin Peaks, Utah, 1, Geology and petrology, J. Geophys. Res., this issue.

Daniel, W. W., Introductory Statistics With Applications, 473 pp., Houghton Mifflin, Boston, Mass., 1977.

Evans, S. H., Jr., H. R. Crecraft, and W. P. Nash, K/Ar ages of silicic volcanism in the Twin Peaks/Cove Creek Dome area, southwestern Utah, Isochron/West, 28, 21-24, 1980.

Gertson, R. C., Interpretation of a seismic refraction profile across the Roosevelt Hot Springs, Utah and vicinity, M.S. thesis, 109 pp., Univ. of Utah, Salt Lake City, 1979.

Haugh, G. R., Late Cenozoic, cauldron-related silicic volcanism in the Twin Peaks area, Millard County, Utah, Brigham Young Univ. Geol. Stud., 25, 67-82, 1978.

Hintze, L. F., Geology of the Cricket Mountains, Millard County, Utah, map, Brigham Young Univ., Provo, Utah, 1959.

Hintze, L. F., Geologic history of Utah, Brigham Young Univ. Geol. Stud., 20, (3), 181 pp., 1973.

Isherwood, W. F., Regional gravity survey of parts of Millard, Juab, and Sevier counties, Utah, M.S. thesis, 31 pp., Univ. of Utah, Salt Lake City, 1967.

MacDonald, R. E., Tertiary tectonics and sedimentary rocks along the transition, Basin and Range Province to Plateau and Thrust Belt Province Utah, in Symposium on Geology of the Cordilleran Hingeline, edited by J. G. Hill, pp. 281-317, Rocky Mountain Association of Geologists, Denver, Colorado, 1976.

Nettleton, L. L., Gravity and magnetic calculations, Geophysics, 7, 293-310, 1942.

Nielson, D. L., B. S. Sibbett, D. B. McKinney, J. B. Hulen, J. N. Moore, and S. M. Samberg, Geology of Roosevelt Hot Springs KGRA, Beaver County, Utah, technical report, Grant EG-78-C-07-1701, 120 pp., Dep. of Energy, Div. Geothermal Energy, Washington, D.C., 1978.

Roy, R. F., E. R. Decker, D. D. Blackwell, and F. Birch, Heat flow in the United States, J. Geophys. Res., 73, 5207-5221, 1968.

Sass, J. H., A. H. Lachenbruch, and R. J. Munroe, Thermal conductivity of rocks from measurements

on fragments and its application to heat flow determinations, J. Geophys. Res., 76, 3391-3401, 1971.

Serpa, L. F., Detailed gravity and aeromagnetic surveys in the Black Rock Desert area, Utah, M.S. thesis, 207 pp., Univ. of Utah, Salt Lake City, 1980.

Smith, R. L., R. A. Bailey, and C. S. Ross, Structure evolution of the Valles caldera, New Mexico, and its bearing on the emplacement of ring dikes, U.S. Geol. Surv. Prof. Pap., 424D, D145-D149, 1961.

Smith, R. L., and H. R. Shaw, Igneous-related geothermal systems, Assessment of Geothermal Resources of the United States--1975, edited by D. E. White and D. L. Williams, Circ. U.S. Geol. Surv., 726, 58-83, 1975.

Smith, R. L., and H. R. Shaw, Igneous-related geothermal systems, Assessment of Geothermal Resources of the United States--1978, edited by L. J. P Muffler, Circ. U.S. Geol. Surv., 790, 12-17, 1978.

Stokes, W. L., Geologic map of southwestern Utah, Coll. of Mines and Miner. Ind., Univ. of Utah, Salt Lake City, 1963.

Swick, C. H., Pendulum gravity measurements and isostatic reductions, Spec. Publ. 232., U.S. Coast and Geod. Surv., Washington, D. C., 1942.

Telford, W. M., L. P. Geldart, R. E. Sheriff, and D. A. Keys, Applied Geophysics, 860 pp., Cambridge University Press, New York, 1976.

Williams, H., and A. R. McBirney, Geologic and geophysical features of calderas, I, research grant NGR-38-033-012, 87 pp., NASA, Houston, Texas, 1968.

Woodward, L. E., Upper Precambrian and lower Cambrian rocks of the Milford area, Utah, Geology of the Milford Area, edited by L. F. Hintze and J. A. Whelan, Utah Geol. Assoc. Publ., 3, 5-8, 1973.

Woodward, L. E., Stratigraphy of younger precambrian rocks along Cordilleran Hingeline, Utah and Southern Idaho, in Symposium on Geology of the Cordilleran Hingeline, edited by J. G. Hill., pp. 83-90, Rocky Mountain Association of Geologists, Denver, Colorado, 1976.

Woollard, G. P., The relation of gravity anomalies to surface elevation, crustal structure, and geology, Tech. Rep. AF 23(601)-3455, 69-9, Dep. of Geol., Univ. of Wis., Madison, Wisconsin, 1962.

(Received December 1, 1980;
revised August 17, 1981;
accepted September 21, 1981.)

JOURNAL OF GEOPHYSICAL RESEARCH, VOL. 86, NO. B11, PAGES 10303-10320, NOVEMBER 10, 1981

LATE CENOZOIC VOLCANISM AT TWIN PEAKS, UTAH: GEOLOGY AND PETROLOGY

H. R. Crecraft, W. P. Nash, and S. H. Evans, Jr.

Department of Geology and Geophysics, University of Utah
Salt Lake City, Utah 84112

Abstract. Bimodal volcanism that formed in the Twin Peaks volcanic complex, west-central Utah, spanned a period from 2.7 to <1 m.y., and produced approximately 12 km^3 of erupted material. Two sequences of differentiation can be discerned in the silicic lavas; both are characterized by increases in SiO_2 from 71% to 76% and decreases in temperature from 875°C to 775°C. The first sequence erupted from 2.7 to 2.5 m.y., produced >10 km^3 of aphyric lavas and pyroclastic deposits and resulted in a local subsidence of approximately 100 m. Tuffaceous lake deposits followed by voluminous olivine tholeiites subsequently filled the depression. Eruption of the second sequence of silicic rocks spanned a short time at 2.4 m.y. and produced a total volume of 0.7 km^3 of strongly porphyritic felsites. At least two subsequent episodes of basaltic volcanism followed. Chemical variations displayed by the early differentiation sequence of silicic rocks are characterized by increases in volatiles, SiO_2, Na_2O, heavy rare-earths, Rb, and highly charged cations and decreases in all other major components, light rare-earths, Sr, and Ba. These variations in time closely resemble spatial variations in compositionally zoned ash flow sheets and are incompatible with crystal fractionation. The early differentiation sequence resulted in the development of a highly evolved, compositionally stratified roof zone, from which the ash and aphyric lavas were tapped. Conductive cooling models for the silicic magma chamber require thermal input into the system, probably by underplating a large volume of basalt, during the early eruptive sequence to sustain it beyond 50,000 years after initial emplacement. Chemical variations displayed by the second eruptive sequence exhibit an increase in K and decrease in Na and are consistent with crystal fractionation as the dominant control. Crystal fractionation and a short eruptive history indicate rapid cooling and a cessation of thermal input for the second sequence.

Introduction and Geological Setting

Late Cenozoic volcanism in the Basin and Range province of the western United States is dominantly basaltic in nature [Christiansen and Lipman, 1972]. Commonly associated with this type of volcanism are bimodal basalt-rhyolite volcanic suites. These generally consist of high-silica rhyolite and tholeiitic or alkalic basalt, with few or no volcanics of intermediate compositions. Young silicic volcanics in the western interior of the United States are generally found in this association, and they have become the subject of especial interest because of their association with geothermal resources [Smith and Shaw, 1978].

The Twin Peaks volcanic field lies along the eastern edge of the Basin and Range province at the southern edge of the Black Rock desert in west-central Utah. The field is situated in an area of active late Cenozoic extension and consists of a bimodal association of mafic lavas ranging from basaltic andesite to tholeiite and low- to high-silica rhyolites. Episodic bimodal basalt-rhyolite volcanism and associated Basin and Range faulting began in this region about 20 m.y. ago, and have continued into the Holocene [Rowley et al., 1979; Nash et al., 1978]. This region is still active seismically [Smith and Sbar, 1973; Olson, 1976] and has a high heat flow of 96 mW/m^2 [Carrier and Chapman, this issue].

The bimodal basalt-rhyolite association is well exhibited in the Twin Peaks volcanic field (Figure 1). Silicic volcanism spanned the period 2.7 to 2.4 m.y. [Evans et al., 1980] and produced predominately high-silica rhyolite (76%) obsidian lavas, volcaniclastics, and felsite lava flows, with subordinate low- to intermediate-silica (70-75%) rhyodacite and rhyolite lava flows. We estimate the total volume of silicic material exposed and in the subsurface to be at least 12 km^3. Silicic volcanics comprise North Twin Peak, Coyote Hills, and South Twin Peak and define a semicircular pattern around the perimeter of the field. Basalt flows occur primarily in the southern portion of the Twin Peaks field. The mafic lavas consist predominantly of olivine tholeiite and basaltic andesite and range from 49 to 55% in silica content.

Geologic History

The oldest dated volcanic event in the Twin Peaks area is the eruption of the Coyote Hills rhyodacite at about 2.7 m.y. [Evans et al., 1980]. This unit occurs in the southern portion of the Coyote Hills and in the north and southwest portions of the North Twin Peak (Figure 1) and has an exposed volume of 1 km^3.

The next series of silicic eruptions formed a number of coalescing domes, flows, and volcaniclastics consisting of high-silica obsidian and felsite of the Cudahy Mine unit. Whole rock ages on obsidian range from 2.63±0.10 to 2.43±0.12 m.y. [Evans et al., 1980]. However, a rapid sequence of eruptions within a short time interval is suggested by pervasive chemical homogeneity. This unit has an exposed volume of 2 km^3; it comprises the bulk of Coyote Hills and also occurs just east of South Twin Peak and in a small exposure northeast of North Twin Peak. In addition, a tuffaceous member at least 80 m thick was encountered in a drill hole 10 km south of South Twin Peak, and a small vent is also exposed

Copyright 1981 by the American Geophysical Union.

Paper number 1B0212.
0148-0227/81/001B-0212$01.00

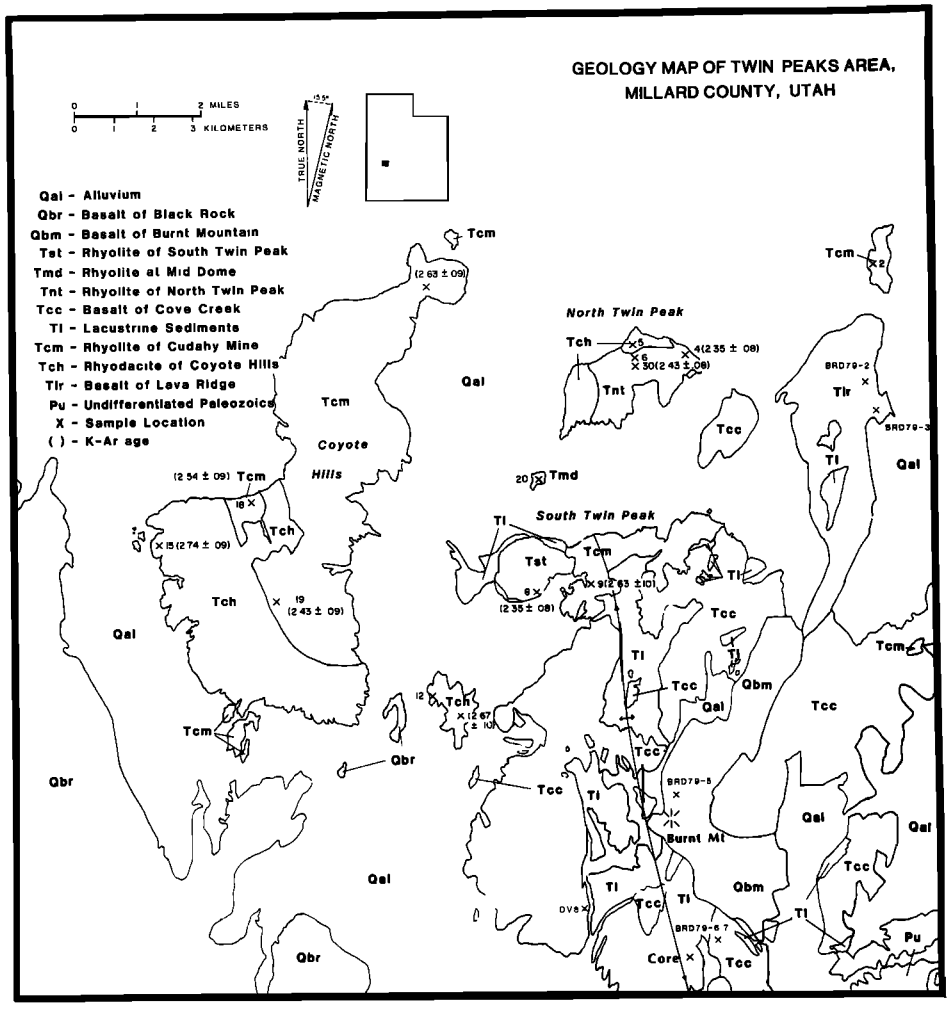

Fig. 1. Generalized geologic map of the Twin Peaks Volcanic Field, Utah.

through a window in overlying basalt, 10 km east of South Twin Peak. These encounters suggest that an additional 8 km^3 or more is buried by younger basalts.

We infer that the eruption of the Cudahy Mine unit resulted in local subsidence as revealed by the timing and distribution of the lacustrine sequence and by the volume equivalency of the lacustrine sediments and the volcanic products of the first eruptive episode. The lowermost exposed sediments are fluvial pebble conglomerates which grade rapidly upward into shoreline deposits and then 90 m of limestones of a deeper water facies. Volcanic detritus consists of crystals of orthopyroxene, hornblende, biotite, sodic plagioclase, alkali feldspar, and quartz as well as lithic fragments of felsite, obsidian, and pumice derived from the Coyote Hills and Cudahy Mine volcanic units. Upper portions of the lacustrine sequence lie uncomformably on rhyolite domes and pyroclastic deposits of the Cudahy Mine unit. Although lacustrine deposits of late Tertiary age are common along the eastern margin of the Basin and Range province, indurated limestone is confined to the Twin Peaks area, and there is no indication that the limestone facies is contemporaneous with other lake deposits of unknown age in the surrounding region.

The Twin Peaks lacustrine sequence postdates the initiation of silicic volcanism at 2.7 m.y. and is capped by a major basaltic episode at 2.5 m.y. This interval corresponds to the period of major silicic eruptive activity in which an estimated 10 km^3 of material was erupted. Assuming a magma chamber approximately 12 km in diameter, 10 km^3 corresponds to a uniform drawdown of approximately 88 m which is nearly equivalent to the maximum measured thickness of the lacustrine sequence of 90 m. This amount of subsidence is below the resolution limit for gravity modeling, and none was detected at Twin Peaks [Carrier and Chapman, this issue]. There is also a lack of structural evidence for subsidence, and we conclude that any subsidence-related structural features are covered by basalts or are buried by Quaternary alluvium.

Deposition of lacustrine limestones on top of the Lava Ridge basalt (Figure 1) indicates that basaltic volcanism predated these sediments and probably the eruption of the Cudahy Mine unit. Toward the end of and following deposition of the lacustrine limestones, a series of basalts flowed into the lake. These Cove Creek basalts are intercalated with limestones and water-laid silicic tuffs in the upper portions of the lacustrine unit, and they subsequently covered

TABLE 1. New K/Ar Dates From Twin Peaks, Utah

Sample	Unit	Material Dated	Weight, g	%K	Ar^{40}_{rad} ($\times 10^{11}$) mol/g	Ar^{40}_{atm} %	Age, m.y.
CC 79-4	Black Rock basalt	whole rock	5.03275	1.058	0.242	80.2	1.32±0.09
DV 79-8L	Cove Creek basalt	whole rock	5.15022	0.847	0.372	93.2	2.53±0.52
DV 79-8U	Cove Creek basalt	whole rock	5.02432	0.822	0.374	89.8	2.62±0.35

Constants used: $\lambda_\beta = 4.962 \times 10^{-10}$/yr; $\lambda_\varepsilon = 0.581 \times 10^{-10}$/yr; and $K^{40}/K_{Tot.} = 1.167 \times 10^{-4}$ mol/mol.

the entire sequence. Dates of 2.53±0.52 and 2.62±0.35 (Table 1) for the Cove Creek basalts are consistent with these stratigraphic relations.

A second sequence of silicic eruptions began with the eruption of the rhyolite of North Twin Peak, dated at 2.43±0.08 and 2.35±0.08 m.y., followed in turn by eruptions of the rhyolite at the Mid Dome, at 2.51±0.08 m.y., and the rhyolite of South Twin Peak, the youngest silicic volcanic in the area, at 2.35±0.08 m.y. [Evans et al., 1980]. Sanidine in rhyolite at the Mid Dome rhyolite exhibits incipient alteration which may have affected its calculated age. These rhyolites define a second trend of increasing silica content. These later silicic eruptions spanned a relatively short time and produced a much smaller exposed volume of only 0.7 km^3. Possibly associated with the emplacement of these later domes was the development of a doubly plunging anticline which extends from the east side of South Twin Peak southward for 12 km. The absence of a gravity anomaly along the anticline [Carrier and Chapman, this issue] indicates that the uplift is not the result of the emplacement of a large mafic body. The anticline produced a maximum 400 m of uplift of the lacustrine sequence, which is exposed in its core, together with the overlying Cove Creek basalts. Younger flows of the Burnt Mountain basalts were erupted from cinder cones along the axis of the anticline and flowed down its eroded eastern flanks. These flows have not been dated but clearly postdate the development of the anticline. The youngest dated event in the Twin Peaks volcanic field was the eruption of the Black Rock basalt, dated at 0.97±0.25 [Condie and Barsky, 1972] and 1.32±0.09 m.y. (Table 1).

Petrography

Modal analyses of silicic volcanic rocks are given in Table 2, and sample locations are indicated in Figure 1. Additional modal analyses are given by Haugh [1978]. Petrographic descriptions of basalt units are given by Clark [1977] and are not presented here.

The rhyodacite of the Coyote Hills (samples 12, 15) contains 71% SiO_2 and is the least silicic felsic rock at Twin Peaks. Zoned plagioclase phenocrysts, 1-2 mm in length, are dominant in this unit and comprise 6-12% by volume. Microphenocrysts of sanidine, generally less than 0.5 mm in diameter, comprise only 1-2% of the rock. Quartz phenocrysts are extremely rare. Mafic minerals are augite and hypersthene, and are generally 0.2 to 0.8 mm long. These commonly occur in cumulophyric aggregates with oxides and commonly with plagioclase. The groundmass comprises 87% of the rhyodacite and consists predominantly of plagioclase, quartz, sanidine, oxides, and zircon.

The rhyolite of the Cudahy Mine contains 76% SiO_2 and consists of obsidian and felsite lava flows and volcaniclastic material. The obsidian (samples 9, 18, and 19) contains traces of quartz, sanidine, plagioclase, biotite, hornblende, augite, orthopyroxene, fayalite, magnetite, and ilmentite phenocrysts set in a glassy matrix comprising >99% by volume. Chemically similar felsite contains sanidine, plagioclase, quartz, and biotite in a devitrified matrix which exhibits relict flow layering and contains spherulites and lithophysae with vapor phase quartz and sanidine. A core sample was obtained from the base of a drill hole which penetrated 80 m into a nonwelded ash flow tuff, 10 km south of South Twin Peak. This tuff is a highly siliceous member of the Cudahy Mine unit. Additional petrographic descriptions of the volcaniclastic members of this unit are given by Haugh [1978].

The North Twin Peak rhyolite dome exhibits pronounced chemical and mineralogical variation and may actually consist of two or more discrete flow units. Samples 4 and 6 exhibit extremes in mineralogical variation of the 12 samples taken and represent, respectively, the most and least silicic phases of this unit. Plagioclase is generally strongly zoned (Figure 7) and occurs in individual grains as much as 5 mm long, and in composite aggregates, some of which may be xenolithic. Large sanidine crystals as much as 3 cm long have resorbed edges and in places contain plagioclase inclusions. Sanidine graphically intergrown with quartz is also present. Quartz

TABLE 2. Modal Compositions (Volume Percent) and Index of Rhyolite Samples

	Samples							
	4	6	8	12	15	19	20	30
Quartz	10.4	4.2	7.0	0.0	0.0	tr	9.7	7.0
Sanidine	5.2	3.5	7.1	2.0	1.0	tr	11.5	4.2
Plagioclase	13.5	16.0	4.1	6.4	11.8	tr	11.0	12.7
Biotite	2.0	0.4	0.4	0.0	0.0	tr	1.1	0.5
Hornblende	0.0	0.0	0.0	0.0	0.0	tr	0.0	0.0
Clinopyroxene	0.0	1.8	0.0	1.0	0.9	tr	0.0	0.9
Orthopyroxene	0.0	0.0	0.0	.3	0.6	tr	0.0	0.0
Fayalite	0.0	0.0	0.0	0.0	0.0	tr	0.0	0.0
Oxides	0.5	0.2	0.6	0.7	0.7	tr	0.2	1.0
Groundmass	68.4	73.9	80.8	89.6	85.0	>99	66.5	73.7

Sample	Unit	Rock Type
2	Cudahy Mine	rhyolite/felsite
4	North Twin Peak	rhyolite/felsite
5	Coyote Hills	rhyodacite/felsite
6	North Twin Peak	rhyolite/felsite
8	South Twin Peak	rhyolite/felsite
9	Cudahy Mine	rhyolite/obsidian
12	Coyote Hills	rhyodacite/felsite
15	Coyote Hills	rhyodacite/felsite
18	Cudahy Mine	rhyolite/obsidian
19	Cudahy Mine	rhyolite/obsidian
20	Mid Dome	rhyolite/felsite
30	North Twin Peak	rhyolite/felsite
C	Cudahy Mine	rhyolite/ash flow tuff

occurs as rounded grains 3 to 8 mm in diameter. Biotite is generally rimmed with oxides and is commonly associated with sphene. Clinopyroxene and sparse orthopyroxene occur only in the less silicic phases where they form phenocrysts generally 0.1 to 0.2 mm long but locally as long as 1 mm. The pyroxene phenocrysts are commonly surrounded by reaction rims or in places are entirely replaced by amphibole. Coarse-grained groundmass comprises about 70% of the unit by volume; it is composed of quartz and feldspar grains commonly 0.1 mm or longer, with accessory oxides, apatite, sphene, and zircon.

The rhyolite of the Mid Dome (sample 20) comprises a small exposure located between North and South Twin Peaks. Petrographically, it is similar to the more silicic portions of the rhyolite of North Twin Peak.

The rhyolite of South Twin Peak (sample 8) contains about 76% SiO_2. Its phenocryst content ranges from less than 3% by volume along the northern margin of the South Twin Peak to 20% higher up the northern slope and along the southwestern margin. Quartz forms rounded grains up to 4 mm long. Plagioclase occurs as individual grains, generally 1 mm in diameter or less, and in cumulophyric aggregates similar to those in the rhyolite of North Twin Peak. Sanidine forms large grains up to 5 mm long, and biotite is the only mafic mineral.

The groundmass consists of fine-grained (0.01 to 0.05 mm) quartz, sanidine, plagioclase, oxides, and accessory zircon. Hematite in the groundmass gives this unit a characteristic red hue in hand specimen.

Whole Rock Chemistry

Major element analyses of the rhyolite units were performed by wet chemical methods described by Carmichael et al. [1968] except for F, which was analyzed by specific ion electrode, and alkalis, which were analyzed by flame photometry following a lithium metaborate fusion [Shapiro, 1975]. X ray fluorescence (XRF) was used for all basalt analyses. Major element analyses and CIPW norms are given in Table 3 for rhyolites and in Table 5 for basalts. Additional major element XRF analyses for basalts are given by Clark [1977]. Trace elements were analyzed by XRF, atomic absorption (AA), and instrumental neutron activation analysis (INAA) [Perlman and Asaro, 1969]. Sulfur was determined with a Leeco Sulfur analyzer. Trace element analyses are listed in Table 4 for rhyolites and in Table 6 for basalts.

Silicic Lavas

When plotted against order of eruption, most major elements show two sequential assemblages with generally parallel trends. The rhyodacite and rhyolite of the Coyote Hills and Cudahy Mine

TABLE 3. Whole Rock Major Element Analyses and CIPW Norms of Twin Peaks Rhyolites

	Sample												
	2	4	5	6	8	9	12	15	18	19	20	30	C
SiO_2	75.26	73.83	71.58	71.91	76.18	75.24	71.62	70.92	75.67	75.86	74.99	72.73	76.59
TiO_2	0.06	0.30	0.30	0.41	0.08	0.09	0.41	0.47	0.12	0.11	0.26	0.40	0.04
Al_2O_3	13.05	13.04	12.73	13.53	12.30	12.88	13.30	13.47	12.94	12.86	12.97	12.93	12.11
Fe_2O_3	0.89	0.77	2.10	1.35	0.81	0.29	1.31	1.17	0.22	0.21	1.06	1.62	0.62
FeO	0.08	1.19	0.48	0.93	0.40	0.62	1.26	1.53	0.65	0.66	0.24	1.10	0.18
MnO	0.06	0.02	0.03	0.03	0.01	0.05	0.05	0.05	0.04	0.05	0.00	0.08	0.03
MgO	0.08	0.34	0.44	0.50	0.16	0.07	0.50	0.53	0.08	0.07	0.20	0.65	0.07
CaO	0.72	1.30	2.00	1.50	0.89	0.72	1.80	2.09	0.72	0.74	1.20	1.35	0.35
Na_2O	3.96	3.70	3.25	3.96	3.20	3.67	3.48	3.50	3.99	3.93	2.95	2.95	4.02
K_2O	5.26	4.72	4.38	4.97	5.18	5.31	5.24	5.19	4.90	4.96	4.93	5.55	4.41
P_2O_5	0.08	0.09	0.10	0.14	0.02	0.01	0.11	0.12	0.02	0.02	0.05	0.13	0.02
H_2O+	0.09	0.49	0.63	0.17	0.11	0.03	0.08	0.55	0.30	0.35	0.35	-	0.34
H_2O-	0.02	0.04	0.03	0.02	0.01	0.05	0.01	0.01	0.04	0.04	0.06	-	0.06
F	0.16	0.21	0.10	0.05	0.14	0.76	0.15	0.15	0.22	0.20	0.14	0.14	0.42
CO_2	0.00	0.02	0.95	0.00	0.05	0.01	0.24	0.44	0.00	0.00	0.16	0.01	0.00
Sum	99.77	100.06	100.10	99.47	99.54	99.80	99.56	100.19	99.90	100.06	99.56	99.64	99.38
-O=F	0.07	0.09	0.04	0.02	0.06	0.32	0.06	0.06	0.09	0.08	0.06	0.06	0.18
Total	99.70	99.97	100.06	99.45	99.48	99.48	99.50	100.13	99.81	99.98	99.50	99.58	99.08
Q	31.15	31.31	30.14	26.70	36.20	33.07	27.84	26.80	32.36	32.57	37.04	31.21	36.22
c	0.14	0.22	0.49	0.00	0.33	1.10	0.00	0.00	0.38	0.26	1.41	0.31	0.72
or	31.08	27.89	31.79	29.37	30.61	31.38	30.96	30.67	28.96	29.31	29.13	32.80	26.06
ab	33.51	31.31	27.50	33.51	27.08	31.05	29.45	29.62	33.76	33.25	24.96	24.96	34.02
an	1.90	4.43	2.93	4.47	3.00	0.00	5.20	5.72	1.90	2.08	3.73	4.80	0.00
di-wo	0.00	0.00	0.00	0.88	0.00	0.00	0.34	0.17	0.00	0.00	0.00	0.00	0.00
di-en	0.00	0.00	0.00	0.76	0.00	0.00	0.21	0.09	0.00	0.00	0.00	0.00	0.00
di-fs	0.00	0.00	0.00	0.00	0.00	0.00	0.11	0.08	0.00	0.00	0.00	0.00	0.00
hy-en	0.20	0.85	1.10	0.48	0.40	0.17	1.03	1.23	0.20	0.17	0.50	1.62	0.17
hy-fs	0.00	1.09	0.00	0.00	0.00	0.84	0.54	1.08	0.89	0.95	0.00	0.17	0.00
mt	0.28	1.12	0.78	1.91	1.09	0.42	1.90	1.70	0.32	0.30	0.02	2.35	0.56
il	0.11	0.57	0.57	0.78	0.15	0.17	0.78	0.89	0.23	0.21	0.49	0.76	0.08
hm	0.70	0.00	1.57	0.03	0.06	0.00	0.00	0.00	0.00	0.00	1.05	0.00	0.23
ap	0.19	0.21	0.24	0.33	0.05	0.02	0.26	0.28	0.02	0.05	0.12	0.31	0.05
fr	0.32	0.42	0.20	0.09	0.29	0.98	0.30	0.30	0.45	0.41	0.28	0.28	0.45
cc	0.00	0.05	2.16	0.00	0.11	0.00	0.55	1.00	0.00	0.00	0.36	0.02	0.00

TABLE 4. Trace Element Analyses of Silicic Volcanics

	Sample												
	2	4	5	6	8	9	12	15	18	19	20	C	s
La	16.8	69.7	89.0	69.1	33.2	11.6	87.9	85.9	12.1	14.0	57.9	8.4	2
Ce	45.5	150.	183.	133.	74.8	34.5	186.	181.	34.2	38.1	122.	26.0	1
Nd	24.	61.	74.3	51.5	33.98	19.5	75.6	73.6	20.1	21.3	45.6	18.2	4
Sm	5.99	8.12	11.0	7.22	5.58	5.51	11.2	10.8	5.55	5.57	6.21	7.24	1
Eu	0.28	1.21	1.52	1.33	0.53	0.21	1.70	1.75	0.22	0.22	0.80	0.03	3
Tb	1.13	0.88	1.26	0.81	0.72	1.07	1.31	1.26	1.05	1.08	0.64	1.89	5
Dy	7.98	5.93	8.44	5.38	4.91	8.10	8.70	7.80	8.08	7.55	4.47	14.8	2
Yb	6.97	4.31	5.26	3.81	4.27	7.47	5.51	4.98	7.55	7.15	3.57	13.3	1
Lu	1.02	0.64	0.74	0.59	0.61	1.12	0.77	0.72	1.12	1.05	0.51	1.76	3
Sc	1.87	4.51	5.44	5.79	1.46	1.89	6.81	6.83	1.92	1.86	2.37	1.74	1
Th	28.2	18.2	15.4	16.7	21.5	28.4	15.4	15.1	28.5	27.8	23.1	36.1	1
U	6.69	2.41	1.52	1.69	3.73	5.98	2.36	2.29	7.07	6.65	2.71	7.68	2
Cs	3.39	2.05	1.80	0.56	1.90	5.11	1.18	1.09	5.34	4.94	1.59	11.9	3
Hf	4.94	6.76	8.46	9.64	4.44	5.06	9.62	8.93	4.89	5.03	5.55	6.81	1
Rb	275.	116.	138.	95.	192.	290.	132.	1.30	284.	275.	152.	480.	3
Ba	16.	761.	1400.	1270.	69.	n.d.	1510.	1520.	n.d.	n.d.	338.	n.d.	2
Cr	n.d.	2.7	n.d.	3.6	n.d.	n.d.	3.7	n.d.	n.d.	1.4	2.0	3.1	26
Sb	0.23	0.20	0.12	0.08	0.20	0.20	0.18	n.d.	0.14	0.21	0.12	0.82	25
Mo	n.d.	n.d.	1.5	n.d.	7.9	3.4	2.8	3.3	3.2	4.3	4.5	n.d.	25
Ta	2.98	1.38	1.37	1.26	1.84	2.57	1.57	1.30	2.62	2.47	1.60	5.50	1
Mn	394.	110.	211.	177.	52.	423.	408.	390.	426.	407.	87.4	494.	1
Nb[1]	34.	19.	25.	18.	13.	38.	26.	28.	41.	34.	19.	66.	5
Zr[1]	95.	198.	275.	270.	95.	87.	319.	321.	89.	91.	145.	81.	5
Y[1]	42.	25.	33.	25.	29.	43.	32.	30.	43.	40.	22.	82.	5
Sr[1]	21.	190.	143.	240.	48.	10.	170.	197.	9.	10.	141.	4.	5
Pb[1]	36.	12.	17.	9.	31.	42.	24.	24.	43.	45.	26.	44.	5
Zn[1]	36.	15.	39.	9.	9.	42.	42.	43.	36.	35.	9.	39.	5
Li[2]	36.	29.	20.	19.	37.	74.	25.	22.	-	68.	24.	105.	3
Be[2]	3.5	2.1	2.1	2.0	2.6	4.5	1.1	2.5	5.2	7.0	2.6	8.7	5
Cu[2]	-	-	-	-	-	-	-	8.0	-	5.4	5.6	7.1	4
S	5.	47.	36.	5.	10.	16.	36.	19.	2.	n.d.	271.	23.	10

All analyses by INAA except (1) by XRF and (2) by AA; S by Leeco Sulfur Analysis. n.d. = not detected; dash = not determined; s = average relative standard deviation in percent.

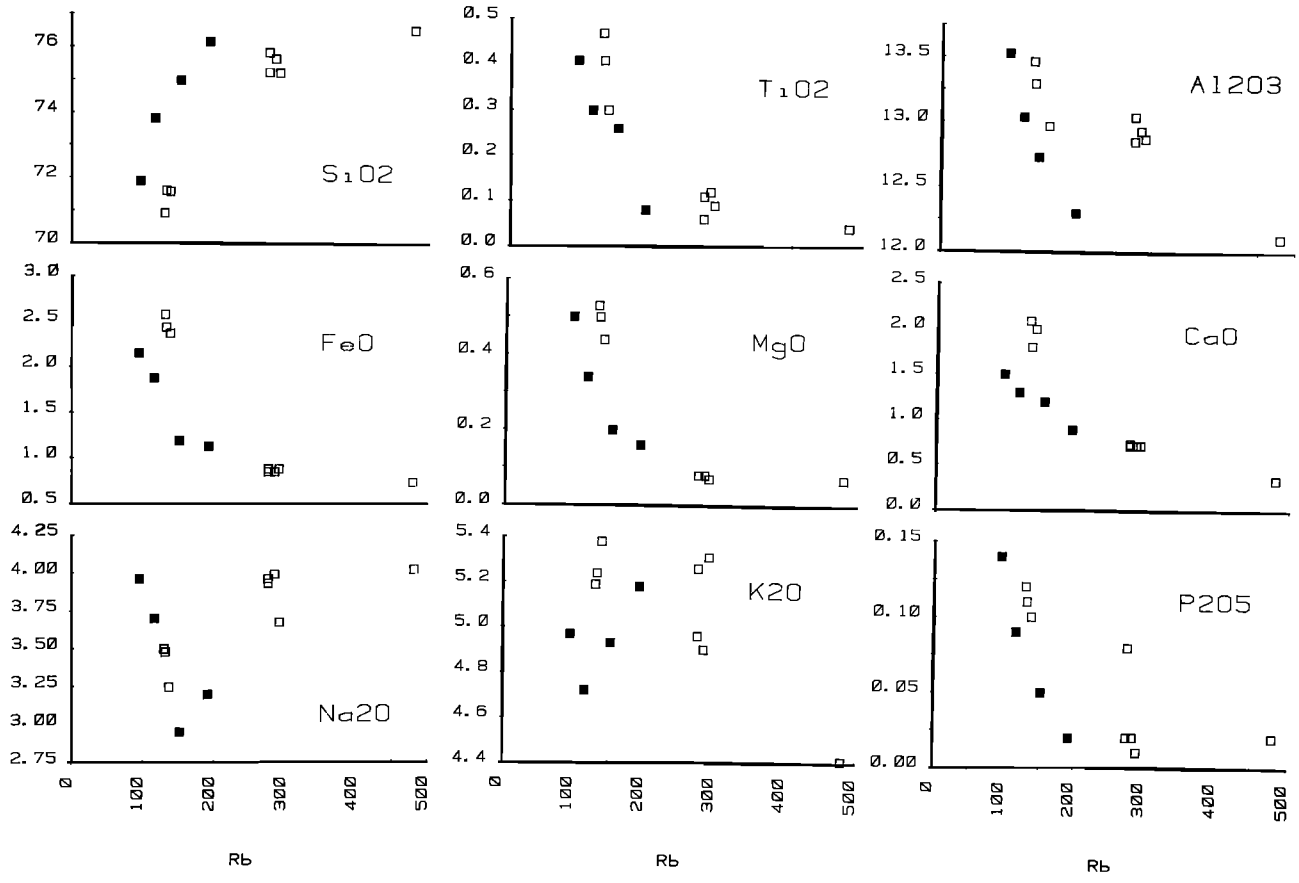

Fig. 2. Major element concentrations of silicic lavas versus rubidium. Open squares signify the early sequence; solid squares signify the late sequence. The two paths are generally parallel, but differences for the alkalis indicate contrasting mechanisms for these.

comprise the early trend, and the rhyolite from North Twin Peak, Mid Dome, and South Twin Peak comprise the later trend. These two trends are apparent for the major elements in Figure 2, where they are plotted against rubidium. Rubidium has been selected because (1) analytical precision is good, and (2) it is enriched in residual liquids by either crystal fractionation or liquid-state differentiation, as described by Hildreth [1979]. Rubidium content therefore indicates a relative degree of evolution of a silicic magma. The two sequences of differentiated rocks are distinguished by the open squares (trend I) and the closed squares (trend II). For all the major elements except the alkalis, and to a lesser extent Al_2O_3, the two trends are nearly parallel to each other. These particular elements are apparently controlled to some extent by contrasting mechanisms in each sequence.

Whole rock analyses are plotted in Figure 3 for the system $NaAlSi_3O_8$-$KAlSi_3O_8$-$CaAl_2Si_2O_8$-SiO_2. Also shown are the piercing points for this system at 1 kbar water pressure with 3% and 5% anorthite [James and Hamilton, 1969] and at 1 and 5 kbar water pressure and no anorthite [Tuttle and Bowen, 1958]. One kilobar would be the approximate total pressure near the top of a magma chamber at the 3 km depth estimated by Carrier and Chapman [this issue] using gravity modeling, and is an upper limit for water pressure. The path traced by the earlier sequence of differentiation moves away from the Or apex and crosses the Ab-Or thermal trough with decrease in temperature. The path is similar to that observed by Hildreth [1977] for the Bishop Tuff and is not consistent with the path of a salic liquid controlled by feldspar fractionation. The observed chemical trend is believed to be due to the same liquid state differentiation process postulated by Shaw et al. [1976], Hildreth [1977, 1979], and Smith [1979]. The samples from the younger eruptive sequence (6, 4, 20, 8), in contrast, plot along a path that is at a high angle to the earlier sequence and is more consistent with the path of a salic liquid containing between 3 and 4% anorthite, which is controlled by feldspar-liquid equilibria. The arrows in Figure 3 indicate the direction the liquid would move with crystallization of the sanidine and plagioclase contained in each sample; the net chemical vector would lie somewhere between the individual feldspar conjugation lines for each sample, depending upon the ratio of the phases precipitating.

Trace elements are plotted against Rb in Figure 4. Sr, La, Zr, and Eu decrease with increasing Rb, whereas Ta, U, Li, Lu, Pb, and Nb generally increase. Many of the trace element variations can be resolved into the two differen-

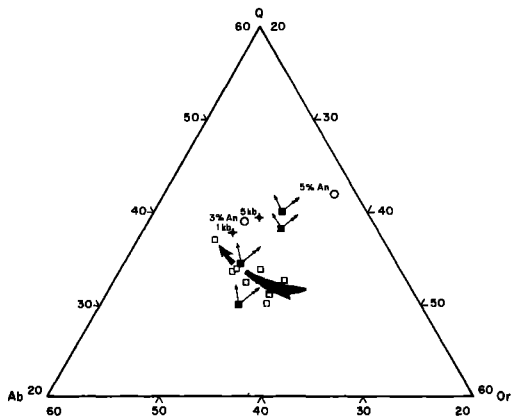

Fig. 3. Twin Peaks rhyolite in terms of normative quartz, albite, and orthoclase. Open squares represent early sequence; solid squares represent the late sequence. Heavy arrow indicates direction of increasing evolution in the early sequence. Vectors indicate the directions the liquid of the second sequence would proceed with fractionation of plagioclase (double arrow) and sanidine (single arrow). crosses indicate minima at .05 and 1 kbar water pressure [Tuttle and Bowen, 1958], and circles indicate piercing points for 3% and 5% anorthite at 1 kbar water pressure [James and Hamilton, 1969].

tiation trends and are distinguished by open squares for the early trend and closed squares for the late trend. The paths for most trace elements are again generally parallel. Specific differences, e.g., Lu, Mn, and Nb, do exist, however, and attest to the operation of contrasting differentiation mechanisms.

The rare-earth elements (REE) for representative samples are plotted in Figure 5. The more highly evolved rocks show a characteristic flattening (and even reversal for sample C) of the slope and an increase in the europium anomaly.

The overall pattern of chemical changes for all elements is best illustrated by enrichment factors for the two sequences (Figure 6). For each sequence the concentration of each element in the late erupted rhyolite is divided by its concentration in the early erupted rhyolite. The chemical changes over time for the early sequence closely approximate the chemical changes upward in the chemically zoned Bishop Tuff magma [Hildreth, 1979]. These changes are in part characterized by increases in volatiles, Si, Na, and heavy REE (HREE), and decreases in K and light REE (LREE). This similarity suggests that the chemical changes developed in time in the early sequence are related to the development of a chemically zoned magma, similar to the Bishop Tuff magma [Hildreth, 1979]. In contrast,

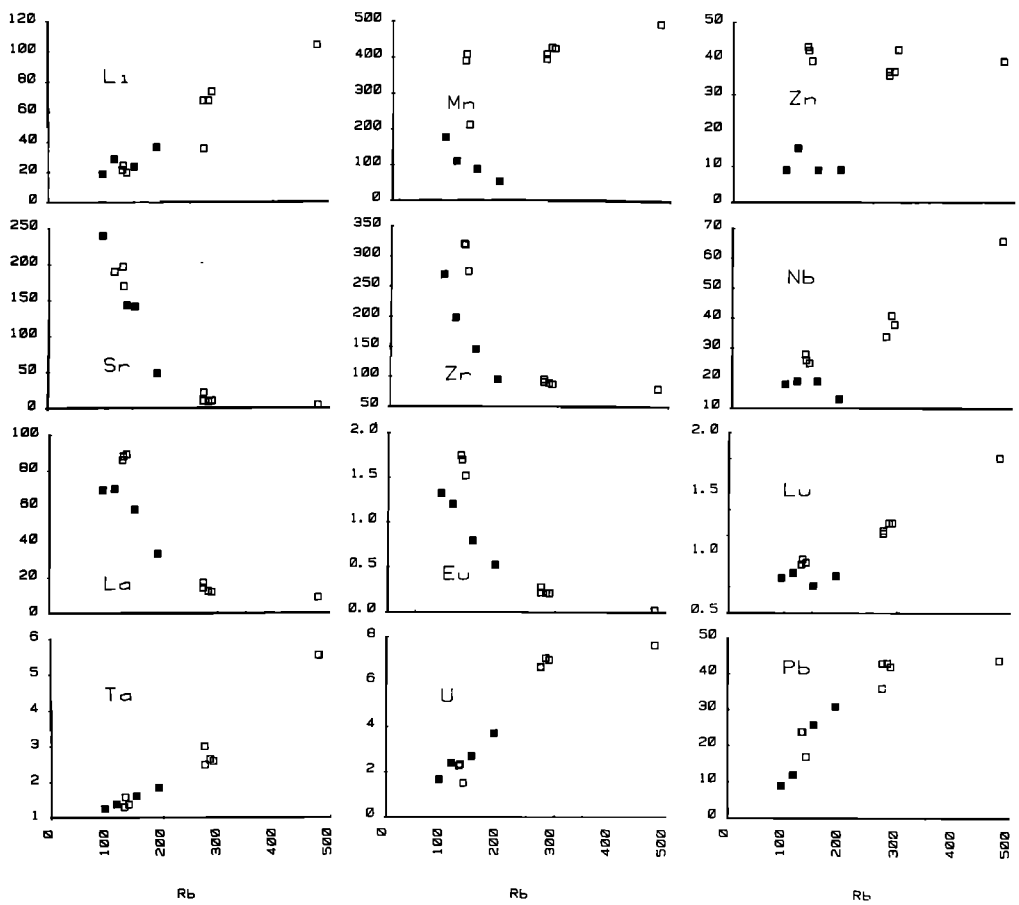

Fig. 4. Concentrations of selected trace elements of rhyolites versus rubidium. Open squares are for the early sequence and solid squares are for the late sequence.

chemical changes displayed by the later sequence exhibit a decrease in Na and an increase in K and decreases in almost all REE, changes which are characteristic of crystal fractionation, although the trace element variations require the involvement of other mechanisms as well.

Mafic Lavas

X ray fluorescence analyses for basalts in the Twin Peaks Field are presented in Table 5 (major elements) and Table 6 (trace elements). The Lava Ridge flow (BRD79-2,3) consists of olivine normative basaltic andesite. This flow occurs in the northeast part of the field (Figure 1). Samples BRD79-6, BRD79-7, DV8L, and DV8U are all assigned to the extensive Cove Creek flows. These consist of olivine tholeiites, although insignificant normative quartz occurs in BRD79-7. These are in general less silicic and less alkalic than the Lava Ridge flow. The young Burnt Mountain basalt (BRD79-5) consists of olivine normative basaltic andesite.

Mineral Chemistry

Major Elements

Feldspar compositions in terms of mole percent albite, orthoclase, and anorthite are given in Figure 7. Oscillatory zoning in both feldspars is most prominant in rhyodacite and low-silica rhyolites. Zoned sanidine in the rhyolite of North Twin Peak ranges from Ab_{40} to Ab_{55}. In felsites from both the Cudahy Mine unit and South Twin Peak, sanidine is moderately zoned from Ab_{23} to Ab_{33}, and in Cudahy Mine obsidian, it is homogeneous at Ab_{25}. For the entire Twin Peaks suite, average sanidine analyses range from Ab_{48} in the rhyolite of North Twin Peak to Ab_{25} in obsidian. The celsian component decreases from 4.9% in the Coyote Hills sanidine to nearly zero in sanidine from the highly silicic rocks. Compositionally zoned plagioclase in the Coyote Hills and North Twin Peak rhyolites ranges from An_{60} to An_{30}. Plagioclase becomes more homogeneous and more albitic in the more silicic

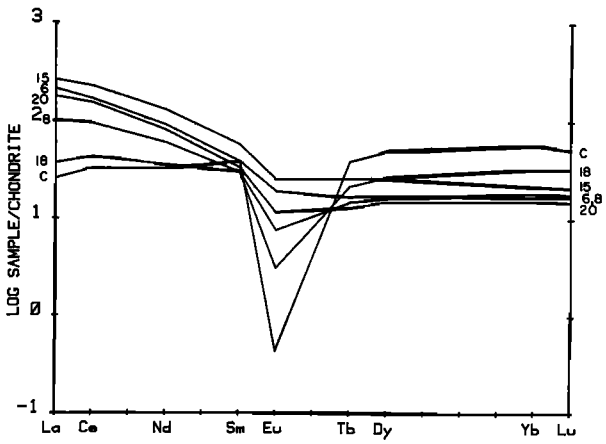

Fig. 5. Chondrite normalized [Evensen et al., 1978] whole rock rare-earth concentrations for representative rhyolites. More evolved lavas have flatter slopes and more pronounced europium anomalies.

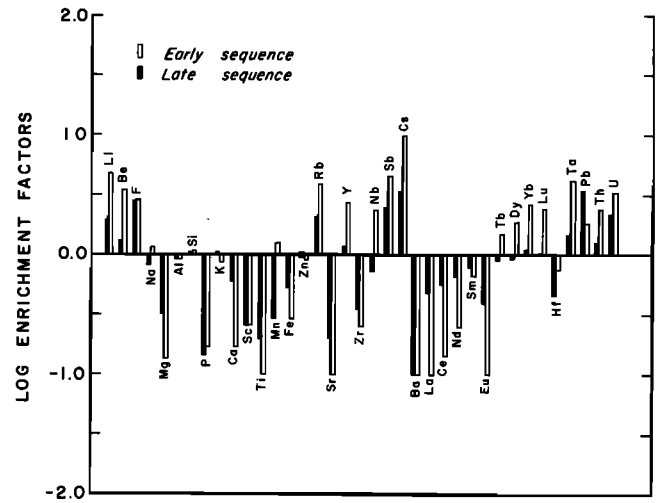

Fig. 6. Enrichment factors for the early (open bars) and late (solid bars) sequences. For each element, concentrations in the late erupted rhyolite are divided by concentrations in the early erupted rhyolite of each sequence.

rocks. In Cudahy Mine obsidian, individual grains are homogeneous, although variations between grains are evident. The average composition of plagioclase ranges from An_{35} in North Twin Peak and Coyote Hills rhyolites to An_{23} in Cudahy Mine obsidians.

Average microprobe analyses of biotite are given in Table 7. Biotite shows the greatest degree of inhomogeneity of all the phenocrysts, which is most pronounced in the rhyolite of North Twin Peak. Variability occurs within grains, is unsystematic, and does not resemble zoning. Fe exhibits the greatest degree of inhomogeneity with a relative standard deviation of 11%. F, Ti, Mg, and Al also exhibit significant variability with relative standard deviations of 4.8%, 3.6%, 3.5%, and 3.0%, respectively, in the North Twin Peak biotite. Biotite from the Mid Dome and South Twin Peak are considerably more uniform, with a relative standard deviation of 3.7% for Fe in the South Twin Peak biotite. Biotite from the Cudahy Mine obsidian is homogeneous. The North Twin Peak biotite exhibits late stage oxidation, with biotite reacting to form sphene and Fe-Ti oxides. Chemical variability of the North Twin Peak biotite is presumed to be due to this late stage oxidation. Despite this variability, however, systematic chemical changes are evident. Atomic Fe/(Fe + Mg) ratios increase with increasing whole rock silica content from 0.33 in North Twin Peak to 0.62 in South Twin Peak and Cudahy Mine biotites, and the fraction of F in the hydroxyl site shows a concommitant decrease from 0.69 to 0.14.

Major element analyses for pyroxenes are listed in Table 7, and compositions in terms of mole percent end members are plotted in Figure 7. The two distinct groupings for orthopyroxene from North Twin Peak (sample 6) are due to the scarcity of orthopyroxene; only three phenocrysts were analyzed, and they probably represent a continuous range rather than two discrete populations. Only one phenocryst of each

TABLE 5. Major Element and Normative Compositions of Basalts

	BRD79-2	BRD79-3	BRD79-5	BRD79-6	BRD79-7	DV8L	DV8U
SiO_2	50.7	53.6	51.2	51.3	49.4	49.9	49.4
TiO_2	1.26	1.20	1.26	1.39	1.99	1.63	1.57
Al_2O_3	15.9	16.5	16.0	17.0	14.1	16.0	16.1
Fe_2O_3(T)	9.37	8.89	9.69	9.64	12.24	11.27	11.07
MnO	0.14	0.14	0.16	0.16	0.19	0.18	0.17
MgO	5.70	5.76	6.30	6.40	5.89	5.77	5.86
CaO	9.02	8.04	9.27	10.01	9.92	9.85	9.77
Na_2O	3.13	3.37	3.12	3.00	2.83	2.88	2.87
K_2O	1.25	1.93	1.26	1.00	0.83	0.98	0.93
P_2O_5	0.39	0.35	0.40	0.34	0.53	0.54	0.54
Loss*	1.86	0.03	1.18	0.00	0.63	0.26	0.28
Total	98.7	99.8	99.8	100.2	98.4	99.3	98.6
Q	0.00	0.00	0.00	0.00	0.02	0.00	0.00
or	7.39	11.40	7.45	5.91	4.90	5.38	5.50
ab	26.49	28.52	26.40	25.38	23.95	24.37	24.28
an	25.70	24.06	25.93	30.02	23.43	28.02	28.30
di-wo	6.89	7.28	5.65	7.27	9.32	7.23	6.95
di-en	3.75	4.05	3.15	4.10	4.63	3.70	3.60
di-fs	2.90	2.95	2.28	2.87	4.50	3.36	3.16
hy-en	9.40	8.67	10.61	8.98	9.54	9.21	8.46
hy-fs	7.28	6.32	7.70	6.29	9.28	8.36	7.45
fo	0.73	2.09	0.41	2.00	0.00	1.02	1.78
fa	0.62	1.68	0.33	1.55	0.00	1.02	1.72
mt	1.57	1.62	1.49	1.62	2.06	1.88	1.86
il	2.39	2.39	2.28	2.64	3.78	3.10	2.98
ap	0.92	0.95	0.83	0.81	1.26	1.28	1.28

*Loss on ignition.

pyroxene from Cudahy Mine obsidian was analyzed. Because of the uniformity of minerals analyzed in this unit, however, these analyses probably closely represent the average pyroxene compositions. Both orthopyroxene and augite from the North Twin Peak show greater compositional variability and are richer in Mg compared with those from the Coyote Hills. Compositional variability occurs primarily between grains rather than within them. Pyroxenes from the Cudahy Mine unit are the most Mg-rich, despite a cooler temperature of crystallization.

Microprobe analyses for titanomagnetite and ilmenite are given in Table 8. End-member mole fraction compositions [Carmichael, 1967] and temperature and oxygen fugacities [Buddington and Lindsley, 1964] are also listed and discussed later. Unoxidized Fe-Ti oxides are homogeneous within and between grains. However, oxidation of both oxides was common in most of the rocks, particularly in the rhyolites of North Twin Peak, where late stage oxidation was also indicated by the chemical inhomogeneity of the biotite.

In addition to the minerals discussed above, single grains of fayalite and hornblende were found in obsidian from the Cudahy Mine unit. Microprobe analyses of these are given in Table 7. The fayalite is very iron-rich and contain substantially more MnO (1.81%) than MgO (0.23%). The amphibole is a Fe-rich hastingsite with Cl content comparable to biotites from the Twin Peaks area but with substantially less F.

TABLE 6. X Ray Fluorescence Trace Element Analyses of Basalts

	BD79-2	BD79-3	BD79-5	BD79-6	BD79-7	DV8L	DV8U
Nb	15	14	12	13	14	12	11
Zr	152	225	154	125	159	136	134
Y	27	28	26	29	34	30	30
Sr	725	696	711	462	425	401	419
Rb	20	35	19	12	15	17	19
Th	9	11	9	0	4	1	8
Pb	6	14	8	7	11	2	4

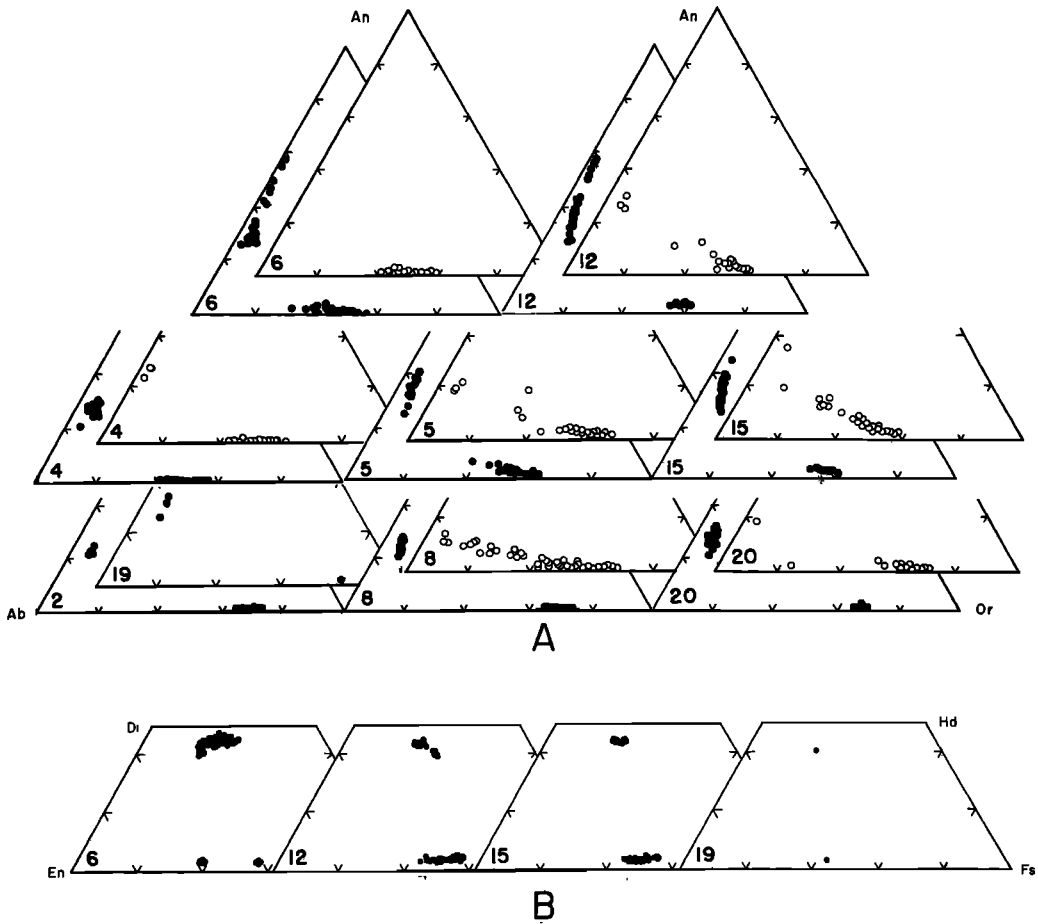

Fig. 7. (a) Microprobe analyses of feldspars, in mole percent albite, orthoclase and anorthite. (b) Microprobe analyses of pyroxenes in terms of mole percent enstatite, ferrosilite, diopside, and hedenbergite. Solid circles = phenocrysts; open circles = groundmass.

Trace Elements

Mineral separates from rhyolites at Twin Peaks were analyzed by INAA, and feldspar and biotite were also analyzed by XRF. Details of these analyses appear elsewhere (H. R. Crecraft and W. P. Nash, manuscript in preparation, 1981). Reference to the summary of partition coefficients in Table 9 illustrates that the following phases may concentrate selected elements relative to the liquid as follows: sanidine (Rb, Sr, Ba, Pb, and Eu), plagioclase (Sr and Eu), biotite (all elements analyzed except Sr, and usually Pb, Th, U), orthopyroxene (Sc, Mn, Nd, Sm, Tb, Dy, Yb, and Lu), clinopyroxene (Sc, Mn, REE), magnetite (Sc, Mn, Zn, Hf, Ta, REE), ilmenite (Sc, Mn, Zn, Hf, Ta, Th, U, REE), and quartz (none).

Summary of Chemical Data

A detailed interpretation of the chemical data, including the partition coefficient data, is discussed elsewhere (H. R. Crecraft and W. P. Nash, manuscript in preparation, 1981). However, some conclusions may be immediately drawn.

1. Crystal fractionation can not by itself account for the chemical changes developed over time, particularly for the early sequence where it was already seen that the increase in Na and decrease in K are inconsistent with feldspar fractionation. Trace element data impose much more severe constraints on crystal fractionation. Mn is strongly concentrated into ferromagnesians and oxides, and hence its enrichment during the early sequence severely constrains the degree of fractionation of these minerals. However, this is clearly inconsistent with the pronounced decreases in Fe, Mg, and Ti. The enrichment of Li, Rb, Sb, Cs, and Ta 5 to 10 times during the early sequence requires crystallization of at least 80% to 90% of the magma, and similar amounts are required by the pronounced depletions of Sr, Ba, and Eu. The enrichment of HREE and strong depletion of LREE are also incompatible with crystal fractionation. Chemical changes over the late sequence are much more moderate and can be more closely modeled by crystal fractionation, but inconsistencies are still apparent, particulary for the REE. These conclusions, based on chemical data, are supported by the short time interval for the late sequence, the crystal-rich volcanics, and the cessation of silicic volcanism following the South Twin Peak eruption, all of which indicate that crystallization of the magma chamber was much more

TABLE 7. Microprobe Analyses of Silicates

	Biotite					Augite				Orthopyroxene				Fayalite	Hornblende
	4	6	8	19	20	6	12	15	19	6	12	15	19	19	19
SiO_2	38.7	39.5	36.4	36.2	37.4	52.2	51.8	51.8	50.8	51.3	51.7	51.7	50.7	28.9	42.6
TiO_2	4.54	4.62	4.28	4.19	4.46	0.32	0.29	0.29	0.23	0.26	0.19	0.16	0.19	0.02	1.73
Al_2O_3	12.1	11.6	12.1	12.1	12.6	0.70	1.38	1.28	1.42	0.48	0.85	0.79	0.82	0.25	8.40
FeO	13.7	13.4	24.6	24.4	19.7	13.5	14.9	14.3	13.0	29.9	27.2	27.1	26.1	68.4	21.6
MnO	0.09	0.05	0.44	0.37	0.66	0.37	0.62	0.63	0.52	1.43	1.16	1.15	0.86	1.81	0.60
MgO	15.5	15.8	8.84	8.53	11.6	11.9	12.1	12.0	12.8	15.4	17.9	17.8	18.2	0.23	7.96
CaO	0.27	0.03	0.16	0.02	0.09	20.2	19.3	19.8	19.2	1.26	1.16	1.39	1.32	0.03	10.46
BaO	0.18	0.26	0.22	0.03	0.24	–	–	–	–	–	–	–	–	–	0.00
K_2O	9.92	9.98	9.60	9.13	9.61–	–	–	–	–	–	–	–	–	–	1.34
Na_2O	0.67	0.70	0.45	0.53	0.52	0.55	0.56	0.54	0.33	0.02	0.12	0.09	0.06	0.00	1.83
F	5.07	5.86	2.46	1.12	4.47	–	–	–	–	–	–	–	–	–	0.70
Cl	0.12	0.06	0.17	0.19	0.17	–	–	–	–	–	–	–	–	–	0.16
H_2O*	1.59	1.25	2.65	3.23	1.79	–	–	–	–	–	–	–	–	–	1.54
$-O = F,Cl$	2.16	2.16	1.08	0.51	1.92	–	–	–	–	–	–	–	–	–	0.33
Total	100.3	101.0	101.3	99.5	101.4	99.7	101.0	100.6	98.3	101.1	100.3	100.2	98.3	99.7	98.6

Dashes indicate value not determined.

* H_2O calculated on basis of filled hydroxyl sites.

TABLE 8. Microprobe Analysis of Iron Titanium Oxides

	6	8		12		15		19		20	
	I	M	I	M	I	M	I	M	I	M	I
SiO_2	0.00	0.07	0.07	0.16	0.05	0.18	0.07	0.00	0.00	0.04	0.06
TiO_2	48.0	10.3	48.3	16.3	48.8	16.5	48.7	10.7	48.2	15.7	48.6
Al_2O_3	0.01	0.99	0.04	1.12	0.03	1.27	0.04	1.12	0.03	1.29	0.05
FeO(T)	50.0	81.9	50.8	78.2	50.0	77.5	50.1	82.8	50.0	78.5	49.3
MnO	1.19	0.26	0.73	0.78	1.20	0.76	1.06	0.95	1.94	0.75	1.05
MgO	0.39	0.08	0.17	0.17	0.23	0.29	0.34	0.26	0.61	0.25	0.64
CaO	0.02	0.01	0.05	0.05	0.05	0.06	0.00	0.00	0.00	0.03	0.04
Cr_2O_3	0.01	0.01	0.00	0.02	0.00	0.03	0.01	0.00	0.00	0.02	0.01
V_2O_3	0.06	0.09	0.03	0.20	0.05	0.19	0.04	0.18	0.01	0.21	0.04
ZnO	0.09	0.08	0.11	0.25	0.05	0.25	0.06	0.11	0.04	0.22	0.08
Sum	99.7	93.8	100.3	97.2	100.5	97.0	100.4	96.1	100.8	97.1	99.9
%FeO	41.1	40.1	42.3	45.5	42.2	45.5	42.1	40.0	43.5	44.8	41.4
$\%Fe_2O_3$	9.82	46.5	9.52	36.3	8.72	35.6	8.87	47.5	7.20	37.5	8.80
Recalculated total	100.7	98.5	101.3	100.8	101.4	100.6	101.3	100.8	101.5	100.8	100.7
Mole % USP	-	30.3	-	46.2	-	46.9	-	28.4	-	44.2	-
Mole % R_2O_3	9.36	-	9.05	-	8.29	-	8.42	-	10.14	-	8.40
T°C	-	775		875		880		780		865	
$-\log fO_2$	-	14.4		12.9		12.8		14.1		13.1	

I, ilmenite and M, magnetite.

TABLE 9. Summary of Crystal-Liquid Distribution Coefficients

	Sanidine	Plagioclase	Quartz	Biotite	Orthopyroxene	Augite	Magnetite	Ilmenite
Rb	0.98-1.3	0.05-0.19	0.002-0.015	2.0-3.0	n.d.	n.d.	n.d.	n.d.
Cs	0.09-0.32	0.04-0.16	0.019-0.042	1.8-3.4	0.58	n.d.	n.d.	n.d.
Sr	2.7-3.5	3.5-10.5	-	0.13-0.31	-	-	-	-
Ba	3.4-7.5	0.37-1.2	0.009-0.055	3.0-18.	n.d.	n.d.	n.d.	n.d.
Sc	0.01-0.03	0.01-0.06	0.009-0.011	4.1-18.	11.	25.-31.	4.6-8.0	2.3.
Mn	n.d.	0.003-0.5	0.004-0.032	11.9-110.	25.	14.-17.	13.-16.	49.
Zn	n.d.	0.44-1.9	-	10.7-50.	-	-	48.-64	75.
Y	n.d.	0.04-0.18	-	0.99-1.3	-	-	-	-
Zr	0.01-0.05	0.03-0.34	-	0.65-1.7	-	-	-	-
Nb	n.d.	n.d.	-	3.1-8.8	-	-	-	-
Hf	0.01-0.05	0.05-0.24	0.018-0.033	0.36-18.	0.19	0.5-0.9	0.9-2.8	3.0
Ta	0.001-0.02	0.02-0.05	0.006-0.009	1.0-2.0	0.16	0.09-0.46	5.6-13.	20.
Pb	0.82-2.8	0.38-1.5	-	0.07-1.1	-	-	-	-
Th	0.01-0.02	0.03-0.07	0.006-0.02	0.24-1.2	0.13	0.09-0.22	0.09-0.3	7.3
U	0.03-0.05	0.03-0.12	0.014-0.04	0.59-1.2	0.14	n.d.	0.2-0.8	3.1
La	0.05-0.07	0.29-0.39	0.012-0.015	0.67-14.7	0.70	0.68-1.5	0.74-1.7	0.23
Ce	0.02-0.05	0.19-0.29	0.005-0.017	0.77-10.1	0.83	1.1-2.5	.99-2.4	6.8
Nd	00.2-0.03	0.12-0.24	0.001-0.023	0.80-5.4	1.2	2.0-4.5	1.3-3.0	6.3
Sm	0.01-0.03	0.10-0.19	0.007-0.017	0.87-4.0	1.4	3.2-6.9	1.7-3.5	5.5
Eu	2.1-3.3	2.3-3.5	0.18-0.033	0.35-3.3	0.55	2.2-2.6	0.25-1.2	1.0
Tb	0.01-0.04	0.08-0.15	0.007-0.025	0.10-3.6	1.7	4.0-10.3	1.7-3.5	4.8
Dy	<0.004-0.07	0.06-0.15	0.009-0.016	0.62-3.2	1.6	3.9-9.8	1.5-3.3	3.6
Yb	0.02-0.03	0.05-0.10	0.012-0.024	0.49-2.9	2.0	3.2-9.5	0.89-1.6	3.1
Lu	0.02-0.03	0.05-0.12	0.002-0.024	0.49-3.1	2.0	3.0-8.8	0.84-1.2	2.1

Dashes = not determined and n.d. = not detected in phenocryst.

significant during the late sequence than during the early sequence.

2. Partition coefficients in the high-silica rhyolite at Twin Peaks are comparable to values in the high-silica rhyolite of the Bishop Tuff [Hildreth, 1979]. In the low-silica rhyolite and rhyodacite, values are intermediate to values for high-silica rhyolites and dacites [Arth, 1976]. Partition coefficients generally exhibit systematic changes with changes in liquid composition. The equilibrium partitioning of a trace element between a crystal and liquid phase is proportional to the ratio of activity coefficients for that element in each phase. Thus, systematic changes in crystal-liquid partitioning indicate systematic changes in the activity coefficients. As a possible application of this, the REE partitioning for orthopyroxenes in the rhyodacite of the Coyote Hills and in the Bishop Tuff may be compared. Since the temperatures of the two magmas were different, trends, rather than absolute values, are significant (assuming that temperature differences affect all REE similarly). In the Bishop Tuff, the partition coefficients decrease systematically from LREE to HREE, whereas in the rhyodacite of the Coyote Hills, they increase. Since the major element compositions of (and presumably activity coefficients in) the orthopyroxene from the two localities are very similar, this reverse in partitioning trends should reflect a reverse in the trend of activity coefficients in the two liquids. Thus, in the high-silica Bishop Tuff magma, LREE have high activity coefficients relative to the HREE (thereby driving LREE into the pyroxene), as compared to the Coyote Hills magma. This would imply that for an equilibrium distribution of REE between the high-silica Bishop Tuff and the Coyote Hills magmas, the former would be enriched in HREE and depleted in LREE relative to the latter. This is the relationship observed at Twin Peaks and in zoned ash flows.

3. The changes in the activity coefficients with liquid composition are probably related either to changes in the liquid structure due to changes in the concentrations of network modifying cations, or to dissolved volatile complexes [Mahood, 1980; Hildreth, 1979]. Mysen and Virgo [1980] have recently determined experimentally a dependence of REE and Ni partitioning between a crystal of constant composition and temperature and liquids of variable composition. Their results indicate that crystal-liquid partitioning (and hence activity coefficients in the liquid) for both light and heavy REE and Ni decreases in liquids with higher ratios of nonbridging oxygens to tetrahedral cations. These results indicate that in dry zoned magmas, these trace elements would all be concentrated into the less silicic liquid. This demonstrates the effect of liquid structure on trace element gradients, but it also suggests a need for some other mechanism, such as volatile complexing, to effect a differential distribution of REE as is apparent at Twin Peaks and in zoned ash flow tuffs.

Intensive Parameters

Temperatures and oxygen fugacities have been determined from the analyzed magnetite-ilmentite oxide pairs (Table 8) using the curves of Buddington and Lindsley [1964]. In addition to the chemical similarities, the two sequences of silicic volcanic rocks at Twin Peaks also exhibit parallel changes in Fe-Ti oxide temperatures. Temperatures obtained for Coyote Hills rhyodacites are 880° and 875°C. This represents the approximate initial temperature of emplacement of the Twin Peaks magma. The Cudahy Mine obsidian was considerably cooler and had a temperature of 780°C. Rhyolite from the Mid Dome, although it was erupted approximately 300,000 years after rhyolite from the Coyote Hills, was nearly as hot and had a temperature of 865°C. Rapid cooling following the eruption of the Mid Dome rhyolite is indicated by a temperature of 775° for rhyolite from South Twin Peak, which followed the rhyolite at Mid Dome closely in time.

Oxygen fugacities decrease with decreasing temperature from $10^{-12.8}$ in the Coyote Hills to $10^{-14.4}$ in rhyolite from South Twin Peak. The temperature-oxygen fugacity data plot slightly above the fayalite-magnetite-quartz buffer curve. The deviation is greater for biotite-bearing rhyolites than for pyroxene rhyolites and is consistent with other pyroxene and biotite-bearing rhyolites [Carmichael, 1967].

Water fugacities for the South Twin Peak, Mid Dome, and Cudahy Mine magmas were calculated using the reaction:

$$KFe_3AlSi_3O_{10}(OH)_2 + 1/2\ O_2 =$$

annite

$$KAlSi_3O_8 + Fe_3O_4 + H_2O$$

sanidine magnetite fluid

This reaction yields the relation [Hildreth, 1977]

$$\ln f_{H_2O} = \ln a^{bi}_{ann} + 1/2 \ln fO_2 - \ln a^{mt}_{Fe_3O_4} - \ln a^{san}_{KAlSi_3O_8} + \frac{19,973}{T} + 5.66 + \frac{0.00903}{T}(P-1)$$

The activity of Fe_3O_4 is assumed to equal its mole fraction in magnetite, and for annite, multisite ideal ionic mixing is assumed. Sanidine activity was determined using data of Waldbaum and Thompson [1969]. Calculated water fugacities are 162 bars for Mid Dome rhyolite, 550 bars for South Twin Peak rhyolite, and 760 bars for Cudahy Mine obsidian. Calculated water contents [Nicholls, 1977; Burnham and Davis, 1974] indicate 1.3% water in the Mid Dome magma, 3.0% in the South Twin Peak magma, and 3.5% water in the Cudahy Mine magma.

Although the uncertainties in these calculations are large [see Hildreth, 1977], the results are reasonable and indicate that very significant water enrichment occurred over both sequences of differentiation. Crystal fractionation may be responsible for the water enrichment in the second sequence. Enrichment during the early sequence is due to the development of an upward concentration of water in the zoned and highly differentiated Cudahy Mine magma, accompanied by the upward enrichments of other volatile components, as observed in major zoned

magma systems [Hildreth, 1979; Smith, 1979]. Upward water enrichment is of fundamental significance to the development and stabilization of the highly differentiated and chemically stratified roof zone from which the Cudahy Mine extrusives were erupted.

Discussion

The Bimodal Basalt-Rhyolite Association

The Twin Peaks volcanic field consists of bimodal basalt-rhyolite lavas. The lack of intermediate composition volcanics so evident at Twin Peaks is characteristic of bimodal suites in general and suggests separate but related sources for the two magma types. A currently favored model holds that in an area of high heat flow and crustal extension, such as in the Basin and Range province, injection of mantle-derived basalts into the lower crust causes partial melting of the more silicic components. When a sufficiently large volume of silicic melt accumulates, buoyancy causes it to ascend into the upper crust. Ascent of material through the crust helps accommodate extensional strain and would be facilitated in an extensional stress field. It may therefore be significant that bimodal volcanism in the Black Rock Desert region, including the Twin Peaks volcanic field, occupies a north-south trending zone of normal faulting which is perpendicular to the direction of Basin and Range extension.

The path through which a large volume of silicic magma ascended would certainly be one of least resistance for subsequent basalt dikes, so that basalt flows would be expected to be localized in areas of silicic volcanism. Correspondingly, previous extensional fracturing and basalt injection through the crust could provide a less resistant path for the ascent of silicic magma as well. It has not been determined whether the Lava Ridge basalt predated or postdated the Coyote Hills rhyolite which marked the inception of rhyolitic volcanism, or even if it is cogenetic with the other basalts. The bulk of basaltic volcanism, however, followed the emplacement of the Coyote Hills magma into the shallow crust.

The model presented above is appealing for at least two reasons. First, it accounts for the close spatial and temporal association of compositionally distinct magmas. In addition, it provides a ready means of thermally sustaining the silicic magma body. The first sequence of differentiated rocks at Twin Peaks was erupted over a span of approximately 200,000 years which is considerably longer than the 50,000 years estimated for the solidification of the Twin Peaks magma chamber by a simple conductive cooling model [Carrier and Chapman, this issue]. The chemical coherence indicates that the entire silicic volcanic suite was erupted from a single evolving magma (H. R. Crecraft and W. P. Nash, manuscript in preparation, 1981). Thus, without the addition of large quantities of heat to the system, it is difficult to account for the temperature of the Mid Dome magma which was nearly as high as the Coyote Hills magma, erupted about 300,000 years earlier. At Long Valley and at the Coso Range, California, chemically similar high-silica volcanic rocks were erupted from zoned magma chambers of contrasting sizes [Hildreth, 1979; Bacon et al., 1979; Duffield et al., 1980]. In each of these, as at Twin Peaks, thermal modeling requires additional heat input to sustain the magmas for lengths of time spanned by volcanism and required for the development of chemical zonation. Basaltic volcanism is spatially and temporally associated with the silicic volcanism of these areas and has been postulated as the sources of additional heat [Hildreth, 1979; Lachenbruch et al., 1976; Bacon et al., 1980].

Chemical Evolution of Silicic Magmas

Two significant features characterize the behavior of silicic magmas in the upper crust. First, magmas evolve with time to change their chemical and mineralogical composition. Smith [1979] has documented in detail the temporal variation in niobium content in the eruptive products of the Jemez Mountains, and the systematic temporal evolution of a variety of elements is established for the Twin Peaks magma system. Second, silicic magma chambers become chemically zoned as revealed in ash flow deposits from large-volume eruptions [Smith and Bailey, 1966; Smith, 1979; Hildreth, 1979; Lipman et al., 1966]. Given sufficient time, a chemically stratified roof zone is produced which is characterized by upward increases in volatiles, Si, Na, HREE, Rb, and highly charged cations, and decreases in all other major elements, LREE, Ba, and Sr. Because traditional crystal-liquid mechanisms of magmatic differentiation fail to account for this chemical behavior, it has been attributed to differentiation in the liquid state and has been termed thermo-gravitational diffusion and liquid-state differentiation [Smith, 1979; Hildreth, 1979].

Changes in the liquid structure due primarily to the water gradient may induce the trace element gradients which are characteristic of liquid-state differentiation [Hildreth, 1979]. The time span required to develop a highly differentiated and stratified roof zone is typically of the order of hundreds of thousands of years and increases with increasing magma volumes [Smith, 1979], and it greatly exceeds predicted cooling times. A sustained heat input is evident at Twin Peaks, Coso, Vallez, and Long Valley, where liquid-state differentation effects are apparent. It seems likely that a sustained heat input is a necessary condition in order to provide sufficient time for liquid-state differentiation to produce the highly evolved, volatile charged roof zones from which zoned ash flows erupt.

Conclusions

Silicic volcanism at Twin Peaks produced two sequences of rhyolites, each characterized by increases in silica and volatiles over time. The first sequence spanned 200,000 years and culminated in the eruption of >10 km^3 of rhyolite lavas and volcaniclastics. Thermal input into the magma during this interval, probably by underplating of basalt, provided sufficient time for liquid-state differentiation to produce the

highly evolved roof zone from which the silicic volcanic rocks were erupted. Following this eruption, thermal input into the magma diminished, perhaps due to the extensive eruption of basalt lavas onto the surface rather than underplating the silicic magma. The second sequence of differentiated rhyolites records the additional effects of crystal fractionation in a rapidly crystallizing magma which produced only 0.7 km^3 of extrusive volcanic material.

Acknowledgments. This study of the evolution of rhyolite magma has been made all the more enjoyable by stimulating discussion with R. L. Smith and Charles Bacon. Thomas Steven and David Phelps provided constructive reviews of the manuscript. Neutron activation analyses were performed by F. Asaro and H. Michel at the Lawrence Berkeley Laboratory, and R. L. Holmes assisted in the wet chemical whole rock analyses. Funding for this study was provided by Department of Energy grant DE-AC07-80ID12079 and U.S. Geological Survey grant 14-08-0001-G-343. Support for the electron microprobe laboratory was provided in part by the Institutional Fund of the University of Utah.

References

Arth, J. G., Behavior of trace elements during magmatic processes—A summary of theoretical models and their applications, J. Res. U.S. Geol. Surv., 4, 41-47, 1976.

Bacon, C. R., R. MacDonald, and J. Metz, Petrogenesis of the Quaternary rhyolites of the Coso Range geothermal area, California, Geol. Soc. Am. Abstr. Programs, 11, 382, 1979.

Bacon, C. R., W. A. Duffield, and K. Nakamurma, Distribution of Quaternary rhyolite domes of the Coso Range, California: Implications for the extent of the geothermal anomaly, J. Geophys. Res., 85, 2425-2433, 1980.

Buddington, A. F., and D. H. Lindsley, Iron-titanium oxide minerals and synthetic equivalents, J. Petrol., 5, 310-357, 1964.

Burnham, C. W., and N. F. Davis, The role of H_2O in silicate melts, II, Thermodynamics and phase relations in the system $NaAlSi_3O_8$-H_2O to 10 kilobars, 700°-1100°C, Am. J. Sci., 274, 902-940, 1974.

Carmichael, I. S. E., The iron-titanium oxides of silicate rocks and their associated ferromagnesian silicates, Contrib. Mineral. Petrol., 14, 36-64, 1967.

Carmichael, I. S. E., J. Hampel, and R. N. Jack, Analytical data on the USGS standard rocks, Chem. Geol., 3, 59-64, 1968.

Carrier, D. L., and D. S. Chapman, Gravity and thermal models for the Twin Peaks silicic volcanic center, southwestern Utah, J. Geophys. Res., this issue.

Christiansen, R. L., and P. W. Lipman, Cenozoic volcanism and plate-tectonic evolution of the Western United States, II, Late Cenozoic, Philos. Trans. R. Soc. London, Ser. A., 271, 249-284, 1972.

Clark, E. E., Late Cenozoic volcanic and tectonic activity along the eastern margin of the Great Basin in the proximity of Cove Fort, Utah, Brigham Young Univ. Geol. Stud., 24, 87-114, 1977.

Condie, K. C., and C. K. Barsky, Origin of the Quaternary basalts from the Black Rock Desert region, Utah, Geol. Soc. Am. Bull., 83, 333-352, 1972.

Duffield, W. A., C. R. Bacon, and G. B. Dalrymple, Late Cenozoic volcanism, geochronology, and structure of the Coso Range, Inyo County, California, J. Geophys. Res., 85, 2381-2404, 1980.

Evans, S. H., Jr., H. R. Crecraft, and W. P. Nash, K/Ar ages of silicic volcanism in the Twin Peaks/Cove Creek dome area, Isochron/West, 28, 21-24, 1980.

Evensen, N. M., P. J. Hamilton, and R. K. O'Nions, Rare earth abundances in chondritic meteorites, Geochim. Cosmochim. Acta, 42, 1199-1212, 1978.

Haugh, G. R., Late Cenozoic, cauldron-related silicic volcanism in the Twin Peaks area, Millard County, Utah, Brigham Young Univ. Geol. Stud., 25(3), 67-82, 1978.

Hildreth, E. W., The magma chamber of the Bishop Tuff: Gradients in temperature, pressure, and composition, Ph.D. thesis, 328 pp., Univ. of Calif., Berkeley, 1977.

Hildreth, E. W., The Bishop Tuff: Evidence for the origin of compositional zonation in silicic magma chambers, in Ash Flow Tuffs, Spec. Pap. Geol. Soc. Am., 180, 43-76, 1979.

James, R. S., and D. C. Hamilton, Phase relations in the system $NaAlSi_3O_8$-$KAlSi_3O_8$-$CaAl_2Si_2O_8$-SiO_2-H_2O at 1 kilobar water vapor pressure, Contrib. Mineral. Petrol., 21, 111-141, 1969.

Lachenbruch, A. H., J. H. Sass, P. I. Munroe, and T. H. Moses, Jr., Geothermal setting and simple heat conduction models for the Long Valley caldera, J. Geophys. Res., 81, 769-784, 1976.

Lipman, P. W., R. L. Christiansen, and J. T. O'Connor, A compositionally zoned ash-flow sheet in southern Nevada, U.S. Geol. Surv. Prof. Pap., 524-F, F1-F47, 1966.

Mahood, G. A., The geological and chemical evolution of a Late Pleistocene rhyolitic center: Sierra La Primavera, Mexico, Ph.D. thesis, 245 pp., Univ. of Calif., Berkeley, 1980.

Mysen, B. O., and D. Virgo, Trace element partitioning and melt structure and experimental study at 1 atm pressure, Geochim. Cosmochim. Acta, 44, 1917-1930, 1980.

Nash, W. P., C. Turley, and J. Petersen, Volcanism and the regional assessment of geothermal potential in West-Central Utah, Trans. Geotherm. Res. Counc., 2, 475-477, 1978.

Nicholls, J., The calculation of the displacement of mineral equilibria by the solution of H_2O in silicate melts, in Short Course in the Application of Thermodynamics to Petrology and Ore Deposits, edited by H. J. Greenwood, pp. 160-184, Mineralogical Association of Canada, 1977.

Olson, T. L., Earthquake surveys of the Roosevelt Hot Springs and the Cove Fort area, Utah, M.S. thesis, 80 pp., Univ. of Utah, Salt Lake City, 1976.

Perlman, I., and F. Asaro, Pottery analyses by neutron activation, Archeometry, 11, 21-52, 1969.

Rowley, P. D., T. A. Steven, J. J. Anderson, and C. G. Cunningham, Cenozoic stratigraphic and structural framework of southwestern Utah, U.S. Geol. Surv. Prof. Pap., 1149, 22 pp., 1979.

Shapiro, L., Rapid analysis of silicate, carbonate, and phosphate rocks - revised edition, U.S. Geol. Surv. Bull., 1401, 76 pp., 1975.

Shaw, H. R., R. L. Smith, and E. W. Hildreth, Thermogravitational mechanisms for chemical variations in zoned magma chambers, Geol. Soc. Am. Abstr. Programs, 8(6), 1102, 1976.

Smith, R. B., M. L. Sbar, Contemporary tectonics and seismicity of the Intermountain West, Earthquake Notes, 44(1-2), 39-40, 1973.

Smith, R. L., Ash flow magmatism, in Ash Flow Tuffs, Spec. Pap. Geol. Soc. Am., 180, 5-28, 1979.

Smith, R. L., and R. A. Bailey, The Bandalier Tuff: A study of ash flow eruption cycles from zoned magma chambers, Bull. Volcanol., 29, 83-103, 1966.

Smith, R. L., and H. R. Shaw, Igneous related geothermal systems, in Assessment of Geothermal Resources of the United States, Circ. U.S. Geol. Surv., 790, 12-17, 1978.

Tuttle, O. F., and N. L. Bowen, Origin of granite in the light of experimental studies in the system $NaAlSi_3O_8$-$KAlSi_3O_8$-SiO_2-H_2O, Mem. Geol. Soc. Am., 74, 153 pp., 1958.

Waldbaum, D. R., and J. B. Thompson, Jr., Mixing properties of sanidine crystalline solutions, IV, Phase diagrams from equations of state, Am. Mineral., 54, 1274-1298, 1969.

(Received November 21, 1980;
revised January 26, 1981;
accepted January 30, 1981.)

JOURNAL OF GEOPHYSICAL RESEARCH, VOL. 86, NO. B11, PAGES 10321-10334, NOVEMBER 10, 1981

GEOCHEMISTRY AND PETROLOGY OF MID-TERTIARY ASH FLOW TUFFS FROM THE SIERRA EL VIRULENTO AREA, EASTERN CHIHUAHUA, MEXICO

Elizabeth J. Moll[1]

University of California, Santa Cruz, CA 95064

Abstract. The Sierra el Virulento, located in the Mexican Basin and Range province of eastern Chihuahua, is composed of over 700 m of siliceous high-K calc-alkalic ash flow tuff ranging in age from 33.7 ± 0.3 to 29.5 ± 0.5 m.y. At least 70% of phenocrysts in the tuffs are zoned feldspar crystals that have andesine cores and anorthoclase rims. Subordinate phenocrysts include clinopyroxene, biotite, ilmenite, magnetite, sanidine, hornblende, quartz, and orthopyroxene. Pyroxenes are Mg-rich and have a restricted range of Mg-Fe ratios. Fe-Ti oxide minerals equilibrated at high temperatures (880°-1055°C) and oxygen fugacities (-log fO_2 = 8.3-11.0). The tuffs are strongly enriched in light rare earth elements (LREE) and have moderate negative Eu anomalies. Initial $^{87}Sr/^{86}Sr$ ratios range from 0.7043 to 0.7065 and show a rough correlation with SiO_2, Sr, and Rb/Sr. The Sr-isotopic compositions suggest that the rocks formed from an isotopically heterogeneous source material and were modified by later crustal contamination. Dacite tuffs may have originated by either fractional crystallization of more mafic magmas or by partial melting of crustal material. The series dacite to rhyolite seems to have evolved by a combination of low-pressure fractionation in shallow magma chambers and crustal interaction. If variations from dacite to rhyolite are the result of crystal fractionation, the mineralogy and major-element data suggest that anorthoclase was the dominant fractionating phase.

Introduction

The Sierra el Virulento lies in the Basin and Range province of eastern Chihuahua, Mexico, about 160 km east of the city of Chihuahua (Figure 1). The Sierra is composed of flat-lying mid-Tertiary ash flow tuffs that were erupted as part of widespread Tertiary igneous activity in western North America. Many workers agree that this widespread igneous activity was related to subduction along the west coast of North America in Tertiary time. Lipman [1980] recently summarized work on the calc-alkalic rocks in the western United States and K. Cameron et al. [1980] described the mid-Tertiary volcanic rocks in northern Mexico. In northern Mexico, K. Cameron et al. [1980] have recognized moderate-K and high-K facies of calc-alkalic volcanism. The moderate-K facies is found in the Sierra Madre Occidental along the west coast of Mexico; the high-K facies lies farther inland in the Basin and Range province of Chihuahua. This paper describes the stratigraphy, mineralogy, chemistry, and petrogenesis of the rocks from the Sierra el Virulento--an area chosen for detailed investigation because it contains rocks typical of the high-K facies and because the ash flow tuffs in the area are thick and laterally continuous. The study is significant because it describes an area where previous work was very limited. Campbell [1977] studied the mid-Tertiary calc-alkalic rocks in the La Perla area (Figure 1), and Van Allen [1978] described the geology and origin of the La Perla iron ore deposit.

Description and Age of Units

Five formations, formed chiefly of siliceous ash flow tuff, were distinguished in the Sierra el Virulento area. The detailed descriptions of these units given by Moll [1979] are summarized here.

The El Ranchito Formation, the lowest stratigraphic unit in the map area (Figure 2), consists chiefly of siliceous, densely-welded ash flow tuff overlain by a thin, mildly alkalic basalt flow. The ash flow tuff is divided into two lithologically distinct members. The lower member is a gray rhyolite ash flow tuff which is at least 500 m thick (Figure 2). Sanidine from this member has been dated at 33.7 ± 0.3 m.y. by K-Ar methods [K. Cameron et al., 1980]. The member is characterized by phenocrysts of zoned andesine to oligoclase chatoyant sanidine, embayed quartz, and subordinate altered biotite and Fe-Ti oxide minerals. The upper member is less than 10 m thick and composed of dark-red devitrified dacite and rhyolite tuff. This member has about 30% phenocrysts including feldspar that is zoned from andesine cores to anorthoclase rims, quartz, and subordinate clinopyroxene, biotite, and Fe-Ti oxide minerals. Both ash flow tuff members are discontinuously overlain by a dark-gray, mildly alkalic basalt flow member that is usually less than 1 m thick. The basalt is composed of about 10% phenocrysts of weakly zoned labradorite, pale-green clinopyroxene, olivine, opaque minerals, and rare orthopyroxene in a groundmass of dark-brown glass, opaque dust, plagioclase microlites, and patches of secondary calcite.

The Rancho Virulento Tuff, immediately above the El Ranchito Formation, is the thickest and most extensive stratigraphic unit in the Sierra el Virulento (Figure 2). It is a single cooling unit as much as 360 m thick that covers at least 85 km^2 in the Sierra el Virulento area and can be traced at least 10 km to the north. A K-Ar age on biotite from the Rancho Virulento Tuff is 30.5 ± 0.2 m.y. [K. Cameron et al., 1980] or about 3 m.y. younger than the El Ranchito Formation. The contact between the two formations has local relief of as much as 200 m. The Rancho Virulento Tuff consists of a 2- to 3-m-thick, black basal vitrophyre overlain by a thick pink devitrified, densely to partially welded zone. The tuff contains about 35-40% phenocrysts, including feldspar consisting of andesine zoned to anorthoclase, sanidine, biotite, green

[1]Present address: U.S. Geological Survey, 345 Middlefield Road, Menlo Park, Calif. 94025

Copyright 1981 by the American Geophysical Union.

Paper number 1B0905.
0148-0227/81/001B-0905$01.00

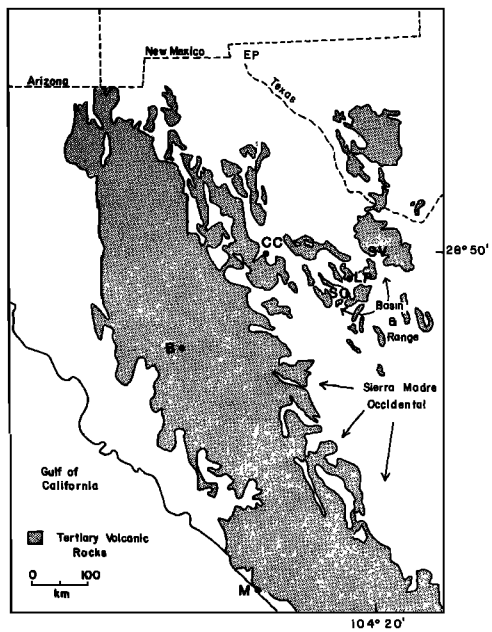

Fig. 1. Map showing the distribution of Tertiary volcanic rocks in Mexico and the southwest United States. The area described in this paper is the Sierra el Virulento. Abbreviations: B, Batopilas; CC, Chihuahua City; EP, El Paso; LP, La Perla; M, Mazatlan; SC, Sierra los Cajones; SV, Sierra el Virulento.

clinopyroxene, ilmenite, magnetite, and rare orthopyroxene.

Overlying the Rancho Virulento Tuff is the Agua de Mayo Tuff which has a total thickness of approximately 150 m and, along with the Rancho Virulento Tuff, forms the steep, prominent columnar-jointed cliffs and ridges that characterize the Sierra el Virulento. Biotite from the Agua de Mayo Tuff gives a K-Ar age of 29.5 ± 0.5 m.y. [K. Cameron et al., 1980]. The Agua de Mayo and Rancho Virulento Tuffs are very similar except for the following minor differences in mineralogy: (1) sanidine is absent or very rare in the Agua de Mayo Tuff; (2) orthopyroxene is more common in the Agua de Mayo Tuff; and (3) the Agua de Mayo Tuff has a more variable phenocryst content than the Rancho Virulento Tuff. Parts of the Agua de Mayo Tuff have 20% fine-grained (1-2 mm) phenocrysts; other parts, similar to the Rancho Virulento Tuff, contain 30-40% coarse-grained (3-4 mm) phenocrysts. Because fine-grained crystal-poor samples are not restricted to the base of the ash flow, the variation in crystal size is thought to be the result of innumerable separate ash flows, perhaps from a heterogeneous magma chamber, rather than the result of sorting during eruption and emplacement.

The Las Yeguas Formation overlies the Agua de Mayo Tuff (Figure 2). Outcrops of this formation and the overlying Cerro los Picachos Tuff are restricted to erosional remnants that crop out on the highest ridge in the area. The Las Yeguas Formation is divided into three members which are designated from bottom to top, K, L, and M. The K member is thin (less than 60 cm) and discontinuous and is interpreted to consist of large airfall blocks and bombs. It is mineralogically similar to the Rancho Virulento and Agua de Mayo Tuffs. The L member is no more than 3 m thick and consists of well-bedded (5 to 10 cm thick) very coarse to fine-grained ash, pumice, and crystals. This member displays local cross-bedding and reverse-grading similar to that described by Sheridan and Updike [1975] in base-surge deposits. The M member consists of about 60 m of homogeneous, white, nonwelded ash. It is more silicic and contains more quartz and sanidine than the Rancho Virulento or Agua de Mayo Tuffs. Mafic minerals include biotite, possible pyroxene pseudomorphs, and Fe-Ti oxide minerals.

The Cerro los Picachos Tuff, the stratigraphically highest formation in the Sierra el Virulento (Figure 2), gives a hornblende K-Ar age

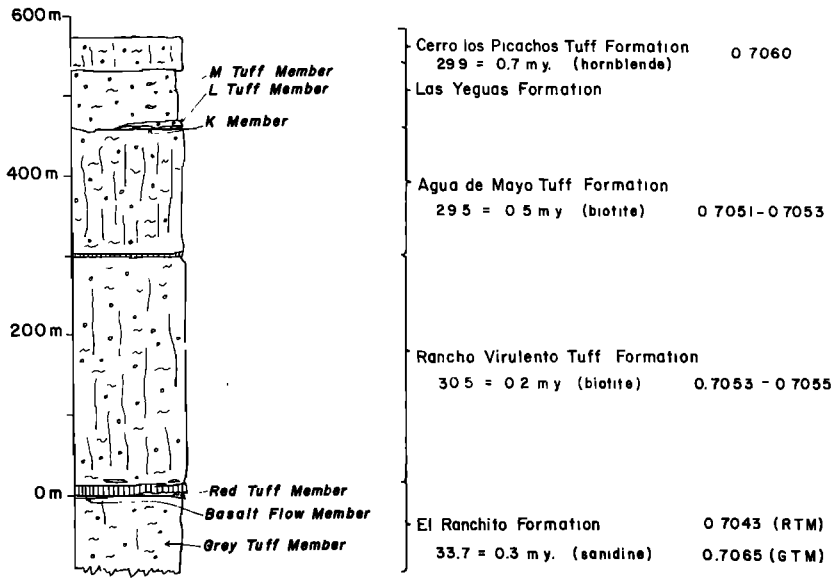

Fig. 2. Generalized stratigraphic section, K-Ar ages and initial $^{87}Sr/^{86}Sr$ for the volcanic formations in the Sierra el Virulento. K-Ar ages are reported by Cameron et al. [1980].

of 29.9 ± 0.7 m.y. [K. Cameron et al., 1980]. It is a densely welded rhyolite ash flow tuff which is distinguished from the Rancho Virulento and Agua de Mayo Tuffs by the presence of a brown basal vitrophyre. It also differs mineralogically from the underlying formations because it contains 2-3% greenish-brown hornblende, lacks biotite, and has more sanidine (26% of the total phenocrysts).

Mineral Chemistry

Feldspars generally comprise more than 70% of the phenocrysts in the Sierra el Virulento volcanic rocks. Feldspar compositions reflect the high-K contents of the rocks and are characterized by extensive ternary solid-solution (Table 1; Figure 3). The typical phenocryst is a zoned crystal with a plagioclase core (An 45) and an anorthoclase rim. In addition, all the rocks, except the Agua de Mayo Tuff and the Red Tuff Member of the El Ranchito Formation, contain sanidine phenocrysts which are generally more potassic than Or 45.

Mg-rich pyroxenes, either clinopyroxene, orthopyroxene, or both, are present in all the volcanic rocks in the Sierra el Virulento (Table

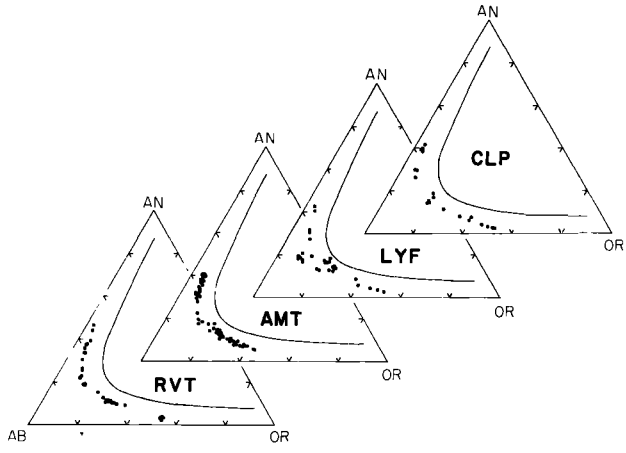

Fig. 3. Composition of feldspar phenocrysts in the Sierra el Virulento volcanic rocks. Each dot represents a single spot analysis. Abbreviations: RVT, Rancho Virulento Tuff; AMT, Agua de Mayo Tuff; LYF, Las Yeguas Formation; CLP, Cerro los Picachos Tuff.

TABLE 1. Representative Electron Microprobe Analysis of Feldspars

	Cerro los Picachos Tuff				Las Yeguas Formation			Agua de Mayo Tuff			
	EC11				K--Member--EC52			EC5		EC45	
	3637.6	3637.0	3637.3	3632.3	3641.0	3643.0	3645.0	3602.5	3606.3	3673.0	3675.0
CaO	0.56	7.60	5.25	2.87	8.53	2.47	6.10	3.53	1.18	2.40	5.40
K_2O	8.52	0.69	1.22	3.10	0.60	4.42	1.34	2.40	7.09	4.48	1.41
Na_2O	5.41	6.89	7.76	7.93	6.33	7.31	7.20	8.14	5.90	7.16	7.50
SiO_2*	65.30	58.98	61.03	64.14	57.41	64.69	60.04	63.85	64.04	63.91	60.55
Al_2O_3*	19.15	25.89	23.62	21.62	26.58	21.28	24.38	22.21	19.55	20.98	23.67
Total	98.94	100.04	98.88	99.66	99.45	100.17	99.06	100.04	97.76	98.83	98.53
An	2	37	26	14	42	12	30	17	6	12	27
OR	50	4	7	18	3	26	7	14	42	26	8
AB	46	58	66	67	53	61	61	67	50	61	64

	Rancho Virulento Tuff			El Ranchito Formation					
	EC40			Basalt - EC28	Red Tuff - EC24			Grey Tuff - EC42	
	3623.1	3625.0	3630.1	3616.0	3665.0	3667.0	3670.6	3653.0	3655.4
CaO	0.57	3.70	8.88	12.03	9.02	2.36	3.65	7.49	4.62
K_2O	8.88	2.24	0.57	0.41	0.51	4.36	2.23	0.67	1.16
Na_2O	5.20	8.07	6.19	4.39	5.96	7.20	8.04	7.00	8.32
SiO_2*	65.50	63.42	57.22	52.91	56.01	63.60	63.08	59.33	62.68
Al_2O_3*	19.22	22.42	26.94	29.55	26.78	20.85	22.26	25.86	23.32
Total	99.37	99.85	99.80	99.29	98.28	98.37	99.26	100.36	100.10
AN	2	18	44	60	45	11	18	37	22
OR	52	13	3	2	3	26	13	3	6
AB	44	68	52	37	51	61	68	59	70

* Calculated assuming stoichiometry

TABLE 2. Representative Electron Microprobe Analysis of Pyroxene Phenocrysts

	CLP	AMT	AMT	RVT	RVT	RT	B
	EC11	EC5	EC45	EC40	EC40	EC24	EC28
	142328	143406	143455	143427	143419	143446	143411
SiO_2	53.32	51.67	53.80	52.86	53.49	52.88	49.37
Al_2O_3	0.12	0.80	1.24	0.61	0.51	0.51	4.06
TiO_2	0.09	0.36	0.40	0.20	0.20	0.17	1.34
Fe_2O_3*	0.19	1.98	1.09	1.79	0.0	1.52	3.94
FeO*	20.17	7.80	15.97	7.40	21.60	8.23	7.62
MnO	2.63	1.05	1.01	1.15	2.23	1.09	0.32
MgO	22.26	14.52	25.36	14.55	21.57	14.34	14.50
CaO	1.08	20.63	1.66	20.86	1.16	20.91	19.14
Na_2O	0.01	0.51	0.05	0.44	0.0	0.41	0.42
K_2O	0.09	0.08	0.05	0.06	0.07	0.0	0.0
Total	99.97	99.41	100.63	99.92	100.83	100.05	100.70

*Proportions of FeO and Fe_2O_3 calculated after Papike et al., [1974].
CLP, Cerro los Picachos Tuff; AMT, Agua de Mayo Tuff; RVT, Rancho Virulento Tuff; RT, Red Tuff Member (El Ranchito Formation); B, Basalt Flow Member (El Ranchito Formation).

2; Figure 4). The pyroxenes are unzoned and have a restricted range of Mg-Fe ratios; orthopyroxene shows slightly more variation than the clinopyroxene (Mg/Mg + Fe = 0.64 - 0.73 for opx versus 0.71 - 0.77 for cpx). Although the Rancho Virulento and Agua de Mayo Tuffs have approximately the same whole-rock composition, tie-line orientations between coexisting orthopyroxene and clinopyroxene compositions for the two tuffs are not parallel (Figure 4), suggesting pyroxene disequilibrium for at least one of the tuffs. Orthopyroxene in the Agua de Mayo Tuff shows no petrographic evidence for disequilibrium; however, orthopyroxene is rare in the Rancho Virulento Tuff and is often rimmed by clinopyroxene.

The high magnesium contents seem unusual for such siliceous rocks (68-72% SiO_2), but Mg-rich pyroxene phenocrysts that have a limited range of Fe-Mg ratios have been reported in rocks ranging from basalt to rhyolite from numerous calc-alkaline terranes including the Cascades [Smith and Carmichael, 1968], Raubal Caldera, Papua, New Guinea [Heming and Carmichael, 1973], the Mogollon-Datil [Foder, 1971], New Britain [Lowder, 1970], and Central North Island, New Zealand [Ewart and Taylor, 1969]. The high Mg-Fe ratios of the rocks are probably due to crystallization at high oxygen fugacities.

Amphibole occurs only in the youngest unit, the Cerro los Picachos Tuff. The amphibole is edenite [Leake, 1978], a calcic amphibole with a

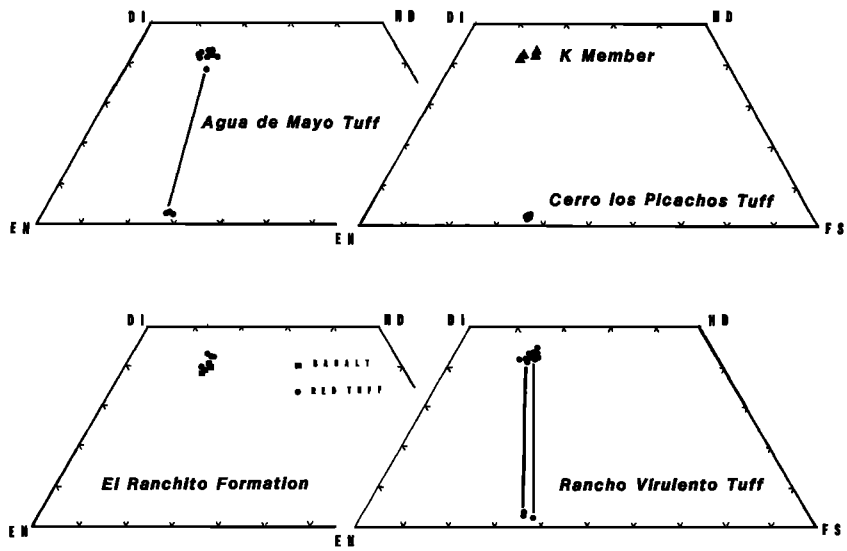

Fig. 4. Composition of pyroxenes from the Sierra el Virulento plotted on the pyroxene quadrilateral: Agua de Mayo (EC5, MC45, AM1); K-Member of the Las Yeguas Formation (EC52); Cerro los Picachos Tuff (EC11, EC48); El Ranchito Formation (EC28, EC24), and Rancho Virulento Tuff (EC40, M267). Tie lines connect coexisting pyroxenes in the same rock.

TABLE 3. Representative Electron Microprobe Analyses of Amphibole and Biotite Phenocrysts

	Amphibole		Biotite
	CLP	CLP	RVT
	EC11	EC48	EC40
	143102	143105	143204
SiO_2	47.04	48.84	39.86
Al_2O_3	6.02	5.84	12.11
TiO_2	1.56	1.46	4.72
FeO	11.72	10.88	11.82
MnO	0.66	0.68	0.25
MgO	15.83	16.50	17.33
CaO	10.99	10.61	0.04
Na_2O	2.14	2.17	0.77
K_2O	0.60	0.84	8.99
Total	96.56	97.82	95.89

CLP, Cerro los Picachos Tuff; RVT, Rancho Virulento Tuff.

moderate Al content and a moderately high Mg/(Mg + Fe) ratio (Table 3). In general, the Sierra el Virulento amphiboles are similar to those from other siliceous calc-alkalic terranes, including New Britain [Lowder, 1970]; Lassen [Carmichael, 1967], New Zealand [Ewart and Taylor, 1969], and the Cascades [Smith and Carmichael, 1968].

Biotite is a common phenocryst phase and occurs in every ash flow except the Cerro los Picachos Tuff. In general, the biotite is Ti-rich and Al-poor (Table 3). Sierra el Virulento biotites are also Mg-rich with Mg/(Mg + Fe) about 0.72. The composition of the biotites is similar to those found in siliceous rocks from Inyo Craters, Tererite, Lassen [Carmichael, 1967], and New Britain [Lowder, 1970].

Magnetite and ilmenite occur as phenocrysts or inclusions in mafic minerals in all the units. Temperatures and oxygen fugacities from coexisting ilmenite and magnetite from the Sierra el Virulento are listed in Table 4. Temperatures and oxygen fugacities are 870° to 960°C and -10.0 to -10.9 log units fO_2 for the Rancho Virulento Tuff, 935° to 1055°C and -8.3 to -10.0 log units fO_2 for the Agua de Mayo Tuff, and 880° to 885°C and -11.0 log units fO_2 for the Cerro los Picachos Tuff. Both temperatures and oxygen fugacities are high and do not plot within the range of Buddington and Lindsley's [1964] original curves. Carmichael's [1967] extrapolation of Buddington and Lindsley's 1964 curves was used to determine temperatures and oxygen fugacities for the Sierra el Virulento rocks.

Fe-Ti oxide data document a variation in temperatures and oxygen fugacities within two of the ash flow cooling units. Temperatures vary 90°C between two samples of the Rancho Virulento Tuff and 120°C between three samples of the Agua de Mayo Tuff. Hildreth [1979] showed that Fe-Ti oxide temperatures within the Bishop Tuff varied 70°C and increased with eruptive progress. It is not possible to test for an increase in temperature with eruptive progress in the Sierra el Virulento ash flows because the only fresh Fe-Ti oxides are in vitrophyric samples from bases of the ash flow sheets. Because the analyzed samples are mineralogically fresh glassy rocks, the Fe-Ti oxide temperatures are considered quench temperatures and the range in temperatures and oxygen fugacities is interpreted to represent inhomogeneities in the magma chamber.

Whole-Rock Geochemistry

Chemical trends in the southeastern Chihuahua volcanic suite show smooth, continuous variation in major element concentrations with silica in the range 65 to 76% (Table 5; Figure 5). CaO,

TABLE 4. Temperatures and Oxygen Fugacities From Fe-Ti Oxide Data

	Cerro los Picachos Tuff		Agua de Mayo Tuff			Rancho Virulento Tuff	
	EC11		EC5	EC29	EC45	EC40	M131
% ulvöspinel	20.5	20.0	22.4	31.6	23.1	30.5	16.9
% ilmenite	77.6	76.7	70.5	70.6	72.8	78.5	74.3
Temperature, °C	885	880	980	1055	935	960	870
-log fO_2	11.0	11.0	9.0	8.3	10.0	10.0	10.9

Carmichael's [1967] extrapolation of Buddington and Lindsley's [1964] Fe-Ti oxide temperature-oxygen fugacity curves was used to determine temperatures and oxygen fugacities for the Sierra el Virulento rocks.

TABLE 5. Representative Chemical Analyses

	Cerro los Picachos Tuff		Las Yeguas Formation K-member	Agua de Mayo Tuff			Rancho Virulento Tuff		El Ranchito Formation			
									Grey Tuff		Red Tuff	Basalt Flow
	EC11	EC12	EC52	EC5	EC45	EC6	EC40	EC41	M278	EC24	EC42	EC28
SiO_2, wt. %	74.66	74.83	69.19	69.90	68.57	69.17	69.89	70.15	66.44	71.07	75.77	54.16
TiO_2	0.28	0.26	0.66	0.59	0.61	0.60	0.54	0.54	0.73	0.50	0.21	2.38
Al_2O_3	13.49	13.22	15.15	15.30	15.66	15.43	15.29	15.09	16.52	14.27	12.67	15.42
Fe_2O_3*	1.48	1.42	2.19	2.16	2.17	2.11	2.11	2.06	2.25	2.02	1.60	3.90
FeO*	0.0	0.0	0.79	0.36	0.69	0.56	0.55	0.68	2.05	0.57	0.0	6.50
MnO	0.06	0.04	0.08	0.09	0.09	0.08	0.07	0.05	0.11	0.07	0.03	0.16
MgO	0.36	0.23	0.53	0.60	0.66	0.43	0.63	0.45	0.35	0.39	0.17	3.02
CaO	0.81	0.59	1.99	1.14	1.69	1.13	1.63	1.12	1.66	1.49	0.57	7.19
Na_2O	3.92	3.87	4.69	5.21	4.99	4.76	4.40	4.30	4.32	4.36	3.66	3.70
K_2O	4.89	5.47	4.51	4.51	4.69	5.57	4.75	5.43	5.38	5.09	5.27	2.56
P_2O_5	0.05	0.06	0.21	0.14	0.18	0.16	0.16	0.14	0.20	0.15	0.06	1.00
LOI	2.91	1.08	1.43	4.64	3.28	0.92	3.70	1.48	1.20	1.05	0.96	1.84
Total	100.05	100.31	99.78	100.03	99.79	99.99	99.30	100.19	99.88	100.17	99.95	100.64
Y	46.	47.	43.	52.	48.	50.	44.	44.	43.	43.	41.	44.
Sr	72.	61.	288.	102.	214.	172.	207.	186.	245.	176.	80.	572.
Rb	219.	226.	106.	227.	166.	167.	184.	175.	122.	166.	202.	60.
Th	25.	26.	11.	16.	17.	18.	19.	17.	9.	18.	22.	1.
Zr	251.	234.	657.	n.d.	584.	n.d.	430.	430.	n.d.	443.	200.	n.d.
Nb	57.	59.	46.	n.d.	51.	n.d.	49.	53.	n.d.	51.	30.	n.d.
Sample type**	V	D	D	V	V	D	V	D	D	D	D	D

*Fe_2O_3 calculated to be no greater than TiO_2 + 1.5% [Irvine and Baragar, 1971].

**Sample types: V, vitrophyre; D, partially devitrified; L, lava flow.

Oxides recalculated to 100% anhydrous. Samples were analyzed by X ray fluorescence at University of California, Santa Cruz. Methods of analysis are described by Moll [1979]. In this report rhyolite has 70% SiO_2 or more, dacite has 63-70% SiO_2, and basalt has less than 54% SiO_2. LOI, loss on ignition. Totals are before recalculation to anhydrous. n.d., not determined.

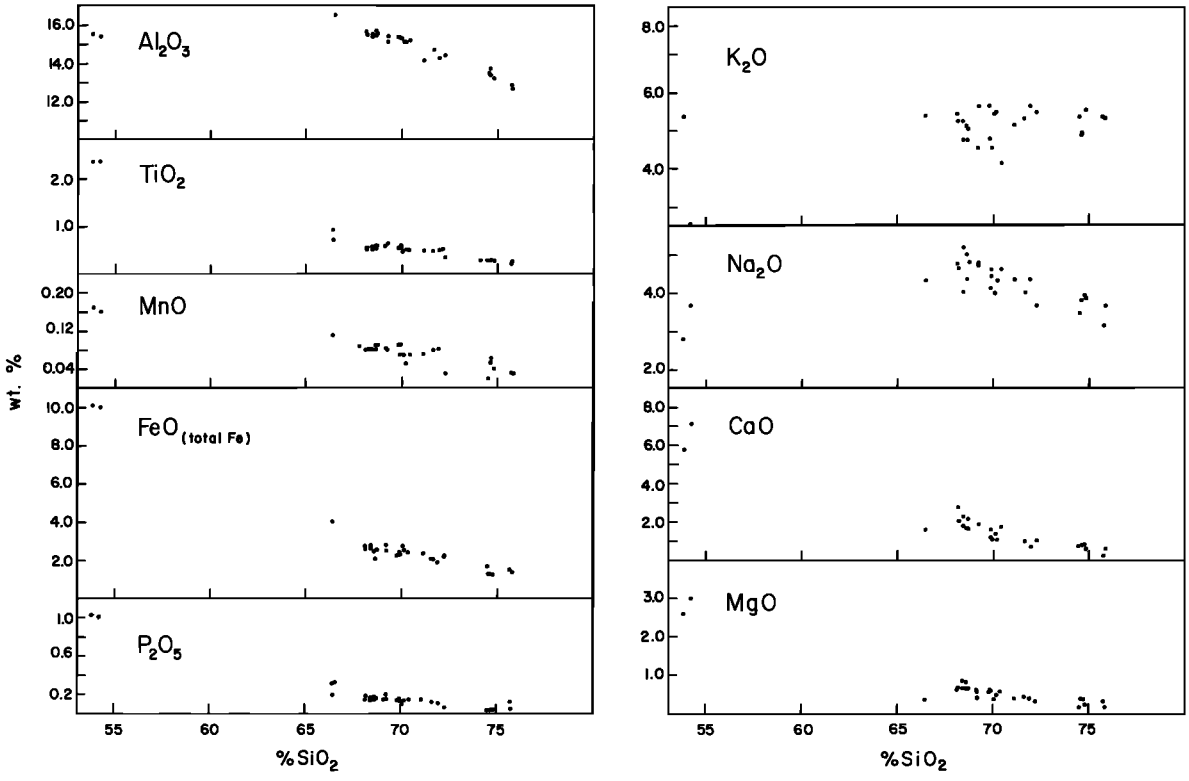

Fig. 5. Variation of the major element oxides with silica. Total Fe is plotted as FeO*. Analyses reported in Table 5 and Moll [1979]. Chemical data are recalculated to 100% anhydrous before plotting.

TiO_2, MgO, FeO*, and P_2O_5 all decrease with increasing silica. The K_2O and Na_2O concentrations are high and show considerable scatter, possibly due in part to post-depositional alteration. Na_2O appears to decrease and K_2O remains fairly constant with increasing SiO_2. The mildly alkalic basalt at the top of the El Ranchito Formation is the only rock with an SiO_2 content less than 65%. However, other mafic and intermediate rocks are present elsewhere in eastern Chihuahua. Campbell [1977] reports major-element chemistry for a calc-alkalic andesite (60% SiO_2) from the La Perla area (Figure 1), and there are calc-alkalic basaltic andesites in the Sierra los Cajones (Figure 1) [Barry and Gordon, 1979]. However, basalt and andesite are much less common than rhyolite and dacite in most of eastern Chihuahua. Although no direct stratigraphic correlation can be made between ash flow sheets from the La Perla area and the Sierra el Virulento, chemical analyses from La Perla [K. Cameron et al., 1980; Campbell, 1977] plot along the same trend on major element-silica variation diagrams as the eastern Chihuahua analyses reported herein.

Trace-element variation diagrams are shown in Figure 6. Sr decreases with increasing SiO_2. Moderate Y contents (between 30 and 50 ppm) remain constant from 68 to 75% SiO_2, a trend consistent with constant HREE contents for three tuffs from 68 to 75% SiO_2 (Figure 7). Rb and Th are both high, as expected in rocks with high alkali contents, and increase with SiO_2. Nb shows no clear trend. Zr concentrations are high, 650 ppm at 68% SiO_2, but decrease to 200 ppm at 75% SiO_2.

Rb/Sr ratios of the siliceous rocks increase from 0.5 at 68% SiO_2 to 3.0 at 75% SiO_2. K/Rb decreases from 375 to 200 with increasing SiO_2 over the range 68 to 75% SiO_2.

Siliceous ash flow tuffs, which are the most common rock type in the Sierra el Virulento, often vary significantly in chemical composition. These variations can be the result of several processes, including original magma inhomogeneities within the magma chamber [Lipman et al., 1966; Hildreth, 1979], sorting of crystals, ash, and pumice during ash flow emplacement [Sparks et al., 1973], or post-emplacement alteration [Lipman, 1965; Lipman et al., 1969; Noble, 1967; Scott, 1971]. The effects of sorting and secondary alteration apparently are minor in the Sierra el Virulento and do not affect classification or general compositional trends of the suite. They are considered in more detail in Moll [1979]. Primary chemical variations within single cooling units are more significant. Rb varies from 90 to 200 ppm and Th from 9 to 19 ppm between Rancho Virulento Tuff vitrophyres from various sample localities. The Bishop Tuff has a similar range in Rb content [Hildreth, 1979], and it seems probable that at least some of the Rb and Th variation must be inherited from original inhomogeneities within the magma chamber. Primary chemical variations also are found in the El Ranchito Formation: SiO_2 varies from 66 to 74% for three analyses of the Red Tuff Member and from 70 to 76% for four analyses of the Grey Tuff

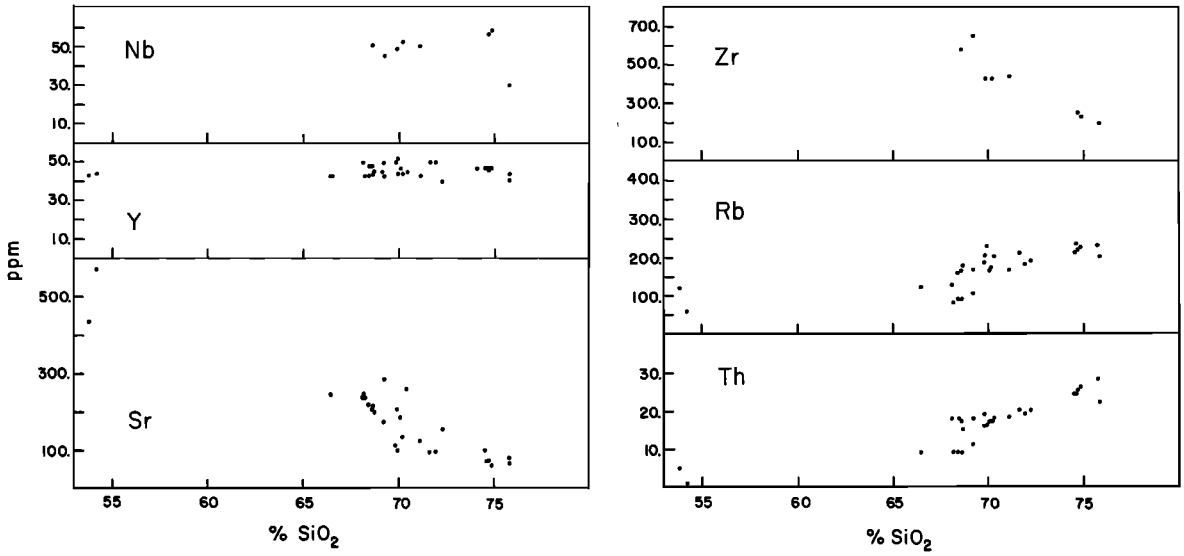

Figure 6. Variation of selected trace elements with silica.

Member. These variations are too large to be attributed solely to post-magmatic processes and must represent actual differences in magma composition between separate flows of individual cooling units.

Classification

The Sierra el Virulento rocks are part of the Chihuahua calc-alkalic suite described by K. Cameron et al. [1980]. The calc-alkalic suite is divided into two facies: a moderate-K facies found in the Sierra Madre Occidental [M. Cameron et al., 1980] and a high-K facies located in eastern Chihuahua. Except for K-contents the two facies have strikingly similar mineralogy and chemistry. The high-K facies, which includes rocks from the Sierra el Virulento, Sierra los Cajones, and La Perla area (Figure 1) are calc-alkalic (index = 59) according to Peacock's 1931 classification [K. Cameron et al., 1980]. Because of their high-K-contents Sierra el Virulento rocks plot in the alkalic field of Miyashiro's [1978] total alkalis versus silica diagram. On Irvine and Baragar's [1971] Q-Ol-Ne ternary diagram, the Sierra el Virulento rocks plot in the subalkalic field, and on an Al_2O_3 versus normative plagioclase diagram, the rocks plot in the calc-alkalic field. The basalt has TiO_2 values that are higher (2.2%) and Al values that are lower (15.5%) than those found in typical calc-alkalic basalts [Lopez-Escobar et al., 1977]. The basalt is interpreted to be a local alkalic flow with no genetic relationship to the overwhelmingly predominant calc-alkalic siliceous rocks.

Rare Earth Elements

Chondrite-normalized rare earth elements (REE) patterns for three tuffs from the Sierra el Virulento are shown in Figure 7, and REE concentrations are given in Table 6. All three tuffs are strongly LREE enriched having LREE values about 200 and HREE values about 20 to 25 times chondrites. LREE enrichment is common in many calc-alkalic suites, but the total REE content for the Sierra el Virulento rocks is slightly higher than that in most calc-alkalic rocks [Taylor and Hallberg, 1977; Noble et al., 1976; Lopez-Escobar et al., 1977; Dostal et al., 1977; Thorpe et al., 1976; Zielinski and Lipman, 1976] but similar to some of the fayalite-free Pikes Peak granites [Barker et al., 1976]. Concentrations of REE in the dacites and rhyolite are similar, except that the rhyolite has a larger negative Eu anomaly.

Sr Isotopes

Initial Sr-isotope ratios for five of the tuffs range from 0.7043 to 0.7065, and four values for the Rancho Virulento and Agua de Mayo

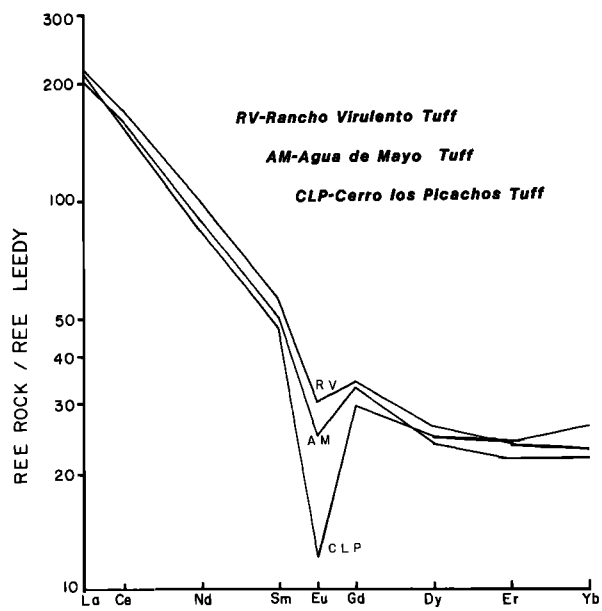

Figure 7. REE patterns for three tuffs from the Sierra el Virulento. Rancho Virulento Tuff (EC40), Agua de Mayo Tuff (EC45), and Cerro los Picachos Tuff (EC11).

TABLE 6. REE Data for Whole-Rock Samples

	Rancho Virulento Tuff EC40		Cerro los Picachos Tuff EC11		Agua de Mayo Tuff EC45	
	ppm	Normalized	ppm	Normalized	ppm	Normalized
La	62.4	201.	66.5	211.	68.2	216.
Ce	131.	161.	125.85	155.	138.7	170.6
Nd	53.2	89.1	47.9	80.3	59.3	99.3
Sm	9.66	50.3	8.99	46.8	10.8	56.3
Eu	1.81	25.1	0.878	12.16	2.19	30.4
Gd	8.54	33.	7.65	29.54	8.86	34.2
Dy	7.76	23.4	8.025	24.7	8.50	26.2
Er	4.59	21.5	5.07	23.8	4.97	23.4
Yb	4.55	21.9	5.43	26.1	4.77	22.9

Normalized to Leedy chondrite/1.2 [Masuda et al., 1973]. Analyses by K. L. Cameron in G. N. Hanson's laboratory at the State University of New York, Stony Brook, by the isotope-dilution, mass-spectrometric technique.

Tuffs cluster at 0.7053 ± 0.0002 (Table 7). These values are higher than typically found for island-arc rocks, but are within the range of values found for the calc-alkalic rocks from continental arcs [Peterman and Hedge, 1972]. The data are scattered, but there are rough positive correlations between initial ratios and whole-rock SiO_2, and Rb/Sr, and negative correlation with Sr contents (Figure 8).

Interpretation of the Isotopic Data

The range of initial $^{87}Sr/^{86}Sr$ is indicative of either an isotopically heterogeneous source region or crustal contamination of an originally homogeneous magma. Several lines of evidence argue for crustal contamination of the Sierra el Virulento rocks. First, there is a rough correlation between initial $^{87}Sr/^{86}Sr$ and whole-rock SiO_2, Sr, and Rb/Sr. Second, Sr contents of the rocks are low--between 70 and 220 ppm; therefore, a small amount of Sr-rich contaminant would significantly alter their $^{87}Sr/^{86}Sr$ isotopic composition. Third, many ash flow tuffs, from which all the analyzed samples were collected, are isotopically and chemically zoned with the most silicic and radiogenic material at the base of the ash flow sheet [Noble and Hedge, 1969; Hildreth, 1979]. Such zonations probably result from assimilation [Noble and Hedge, 1969] of radiogenic crustal material near the tops of volatile-rich magma chambers.

To test the contamination hypothesis, the equations of Ewart and Stipp [1968] were used to calculate the amount of crustal contaminant needed to change the initial $^{87}Sr/^{86}Sr$ ratios over the observed range. The largest uncertainty in these calculations arises from a lack of knowledge of the nature of the crust in the Sierra el Virulento area. Hawley [1969] stated that Cretaceous carbonate rocks are the predominant bedrock lithology in the eastern Chihuahua Basin and Range. In addition, a wide variety of Precambrian rocks that give radiometric ages of about 1100 m.y. crop out north of the study area in the Franklin Mountains north of El Paso and in the Van Horn area of West Texas [King, 1976]. It is not known if these Precambrian rocks underlie the Sierra el Virulento area, but, for the purposes of the calculation, I will assume the upper

TABLE 7. Sr-Isotope Compositions of Tuffs From the Sierra el Virulento

Sample No.	SiO_2 (wt. %) (Volatile Free)	Rb,* ppm	Sr,* ppm	Age, m.y. (Approx.)	$^{87}Sr/^{86}Sr$ Measured	$^{87}Sr/^{86}Sr$ Initial	1
EC11(CLP)	74.6	219	72	30	0.7097	0.7060	0.0002
EC5 (AM)	69.9	227	102	30	0.7080	0.7053	0.0002
EC45(AM)	68.6	166	214	30	0.7060	0.7051	0.0002
EC40(RV)	69.9	184	207	30	0.7066	0.7055	0.0002
M131(RV)	68.4	158	218	30	0.7062	0.7053	0.0002
EC24(ERF-red)	71.1	166	176	33	0.7055	0.7043	0.0002
EC42(ERF-grey)	75.8	202	80	33	0.7096	0.7065	0.0002

*Rb and Sr concentrations by X ray fluorescence.

One determination Eimer and Amend standard 0.7080_5 ± 0.0003 (accepted value 0.7080). Three determinations NBS987 standard, 0.7102, 0.7100, 0.7102; average = 0.7101_5. $^{88}Sr/^{86}Sr$ normalized to a value of 0.1194. Analyses made by K. L. Cameron, at the State University of New York, Stony Brook. Abbreviations: CLP, Cerro los Picachos Tuff; AM, Agua de Mayo Tuff; RV, Rancho Virulento Tuff; ERF-red, El Ranchito Formation, Red Tuff; ERF-grey, El Ranchito Formation, Grey Tuff.

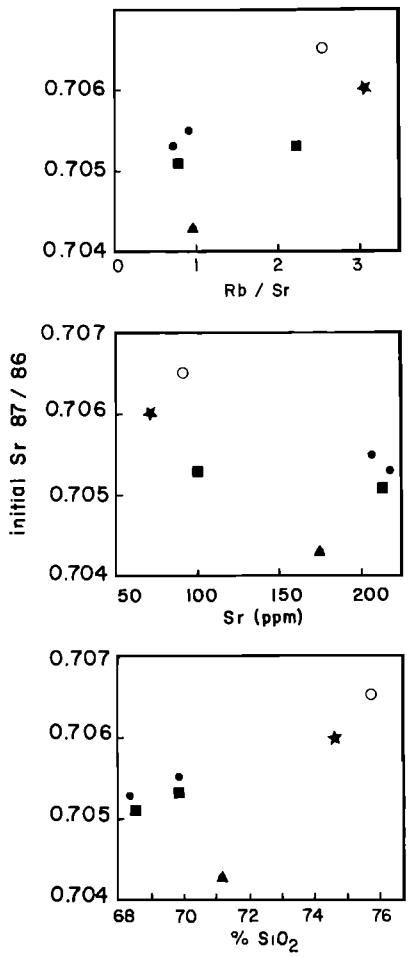

Fig. 8. Variation of initial $^{87}Sr/^{86}Sr$ with SiO_2, Sr, and Rb/Sr. Symbols: star, Cerro los Picachos Tuff; squares, Agua de Mayo Tuff; circles, Rancho Virulento Tuff; solid triangle, Red Tuff Member; and open triangle, Grey Tuff Member, El Ranchito Formation.

crustal contaminant is either a carbonate with a Sr-isotope ratio of 0.7080 and a Sr content of about 600 ppm or a Precambrian rock with a Sr-isotope ratio of 0.7160 and Sr content of about 375 ppm. The composition of the Agua de Mayo Tuff was used for the parent magma (Sr-isotope 0.7053), and the composition of the Cerro los Picachos Tuff (Sr-isotope 0.7060) was assumed to be the daughter magma. The calculations show that the addition of about 5.6% carbonate or 2% Precambrian crust--a relatively small amount--raises the Sr-isotope composition from 0.7053 to 0.7060. This relatively small amount of contaminant reasonably accounts for the variation between the Agua de Mayo Tuff and the Cerro los Picachos Tuff. To change the Sr-isotope composition from the lowest to the highest ratio (0.7043 to 0.7065) would require the addition of either 30% carbonate rock or 10% Precambrian crust. The addition of 30% carbonate rock would greatly influence the composition of the magma. For example, Ca would be increased by 15% and Sr increased by 180 ppm. This is not supported by the major- or trace-element data. However, the addition of only 10% Precambrian crust reasonably accounts for the observed variation. The main objection to this crustal contamination hypothesis is that it is not known if highly radiogenic crustal material actually underlies the Sierra el Virulento area. Furthermore, if contamination of an isotopically homogeneous parent magma were responsible for all the observed variations, the sample with the lowest Sr content should have the highest $^{87}Sr/^{86}Sr$ ratio. However, four samples from the Rancho Virulento and Agua de Mayo Tuffs with Sr contents ranging from 102 to 218 ppm have identical $^{87}Sr/^{86}Sr$ ratios within the analytical uncertainty (Table 7). Finally, there is more scatter in the $^{87}Sr/^{86}Sr$ versus SiO_2, Rb/Sr, and Sr plots than expected if crustal contamination of isotopically homogeneous parent magmas were responsible for all the observed variations.

An alternative to the contamination hypothesis is that the range in Sr-isotopic composition is the result of an isotopically heterogeneous source area. However, a heterogeneous source area fails to account for the correlation between SiO_2 and Sr with initial $^{87}Sr/^{86}Sr$. The most likely hypothesis appears to be one where some of the Sr-isotopic variation originated in an isotopically heterogeneous source area, but the variation was later increased by crustal contamination.

Petrogenesis and Evolution of Magmas

Overall similarities in mineralogy and major- and trace-element chemistry suggest that the Sierra el Virulento volcanic rocks may be genetically related. The two most probable hypotheses to account for compositional variations within the suite are fractional crystallization of a common or similar parent magmas or different amounts of partial melting of a common source. It is difficult to test definitively the models for the following reasons: first, the suite has a very limited range in silica content; second, source areas for the tuffs have not been located and it is uncertain that they are part of the same magma system; third, little is known about the upper or lower crust in the Sierra el Virulento area; and fourth, at least trace-element contents within cooling units appear to be inhomogeneous. By careful sampling, Hildreth [1979] documented elemental zonations in the Bishop Tuff that could not be attributed to fractional crystallization or to progressive partial melting. He suggested that convection-driven thermogravitational diffusion produced zonations in the ash flow magma chamber. It is not possible to test definitely for thermogravitational diffusion given the altered state of the Sierra Virulento rocks. The shape of the REE patterns argues against thermogravitational diffusion in Sierra el Virulento magmas [Ludington, this issue], but the range in trace element concentrations, crystallization temperatures, and oxygen fugacities within a single cooling unit suggest that the magma chamber was inhomogeneous.

The simplest crystal fractionation model involves fractionating the dacites to produce the rhyolites. To test such a relationship, a least squares mixing model [Wright and Doherty, 1970] was used to calculate the proportions of minerals that must be subtracted from a parent magma of known composition in order to produce a daughter

TABLE 8. Least Squares Calculations [Wright and Doherty, 1970] for Fractionating Anorthoclase, Sanidine, Hornblende, Magnetite, Ilmenite, Orthopyroxene and Apatite From a Dacite Magma to Produce a Rhyolite Magma

Least Squares Calculations

	Observed	Calculated	Variable	Weight %
SiO_2	68.57	68.52	rhyolite (EC11)	59.27%
Al_2O_3	15.66	15.63	anorthoclase	32.50
Fe_2O_3	2.86	2.83	sanidine	3.56
MgO	0.66	0.63	hornblende	1.95
CaO	1.69	1.65	magnetite	1.50
Na_2O	4.99	4.94	ilmenite	0.67
K_2O	4.69	4.64	orthophroxene	0.27
TiO_2	0.61	0.58	apatite	0.31
P_2O_5	0.18	0.16		
MnO	0.09	0.09		

Composition of Variables

	Rhyolite (EC11)	Anorthoclase	Sanidine	Hornblende	Magnetite	Ilmenite	Orthopyroxene	Apatite
SiO_2	74.66%	64.28%	65.01%	47.12%	0.12%	0.08	53.79%	---
Al_2O_3	13.49	21.01	19.03	5.62	1.12	0.17	0.17	--
Fe_2O_3*	1.48	---	---	11.28	87.91	53.15	20.44	0.32
MgO	0.36	---	---	16.15	1.17	2.37	22.29	0.05
CaO	0.81	2.34	0.53	10.84	---	---	1.04	55.08
Na_2O	3.92	7.32	5.32	2.05	---	---	0.01	0.04
K_2O	4.89	4.37	8.59	0.56	---	---	0.08	0.01
TiO_2	0.28	---	---	1.42	7.11	41.11	0.15	---
P_2O_5	0.05	---	---	---	---	---	---	42.40
MnO	0.06	---	---	0.72	1.28	1.54	2.65	---

*Total Fe as Fe_2O_3.

$R^2 = 0.01$. R^2 is the sum of the residues squared. A good fit is achieved when R^2 is less than or equal to 0.01.

magma of known composition. An Agua de Mayo Tuff sample (EC45; 69% SiO_2) was used for the parent magma, and a Cerro los Picachos Tuff sample (EC11; 75% SiO_2) was used for the daughter magma (Table 8). Microprobe analyses of phenocrysts from both tuffs were used for the compositions of the fractionating minerals. The calculations show that the fractionation of anorthoclase, sanidine, hornblende, magnetite, ilmenite, and trace amounts of apatite and orthopyroxene from the Agua de Mayo Tuff will produce a melt having a major-element composition similar to that of the Cerro los Picachos Tuff (Table 8). In addition, the relative proportions of fractionated minerals are approximately the same as the actual phenocryst proportions in the rocks [Moll, 1979].

To test further if the Cerro los Picachos rhyolite was produced by crystal fractionation of the Agua de Mayo dacite, a hypothetical daughter REE curve is calculated using the minerals from the major-element calculations as the fractionating minerals and the Agua de Mayo Tuff REE concentrations for the parent magma. The calculations show that fractionation of the minerals from the major-element calculations will increase the REE content of the magma for all elements except Eu (Figure 9). These calculations indicate that Cerro los Picachos Tuff was not generated by simple crystal fractionation of the Agua de Mayo magma because the two units have similar REE contents (Figure 7). Nevertheless, the calculated daughter REE curve and the actual Cerro los Picachos curve have very similar shapes. This suggests that the Cerro los Picachos magma may have been derived from a melt with a REE pattern similar to that of the Agua de Mayo Tuff, but with lower concentrations of REE.

Although the Cerro los Picachos rhyolite was not formed by simple crystal fractionation of the Agua de Mayo dacite, the overall similarities in mineralogy and major- and trace-element geochemistry of the Sierra el Virulento siliceous rocks suggest that the suite may have been derived by a common process such as fractional crystallization of similar parent magmas. The following constraints can be placed on such a crystal fractionation model:

1. The decrease in Eu and Sr and the increase in Rb/Sr that accompanies the increased SiO_2 indicate that feldspars were fractionated. In addition, the decrease in K/Rb with increased SiO_2 is evidence that at least some of the fractionating feldspar was potassium feldspar. This is also supported by the K_2O and Na_2O data which do not increase with increasing silica (Figure 6). The most likely candidate is the zoned plagioclase-anorthoclase crystals that are the dominant phenocrysts in rocks of the Sierra el Virulento.

2. Zr and P_2O_5 decrease with increasing

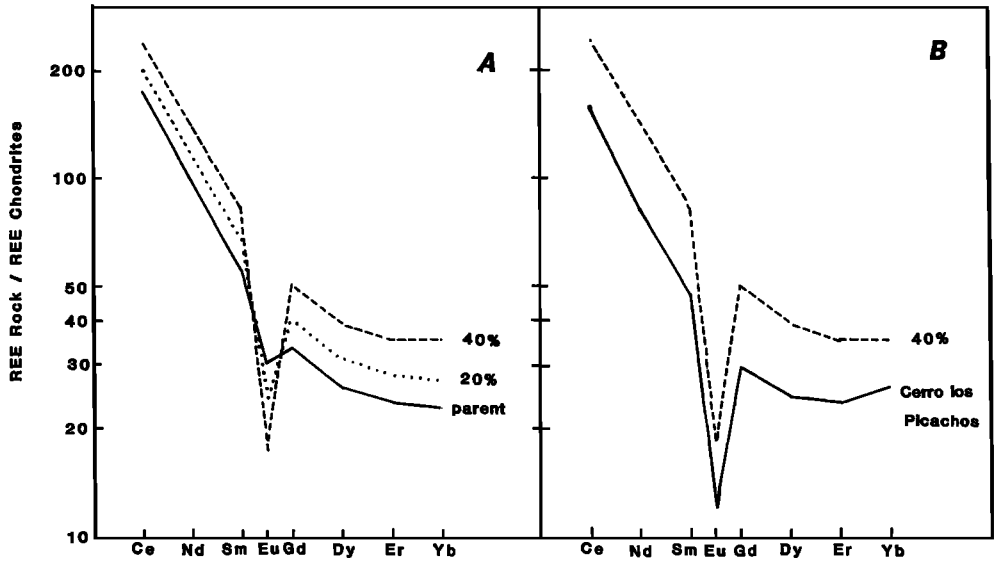

Fig. 9. (a) Diagram comparing REE patterns of parent (Agua de Mayo Tuff) and hypothetical daughter magmas at 20% and 40% fractionation. Fractionating minerals are those in Table 5. The curves are calculated using the Rayleigh fractionation equation [Hanson, 1978]. Distribution coefficients for siliceous magmas are from Schnetzler and Philpotts [1970], Nagasawa and Schnetzler [1971], Arth and Barker [1976], and Zielinski and Lipman [1976]. (b) Comparison of REE patterns for hypothetical daughter magma at 40% fractionation and Cerro los Picachos Tuff. The two curves have very similar shapes, although REE concentrations are lower in the Cerro los Picachos Tuff.

silica (Figures 5 and 6). Both zircon and apatite are visible in thin section in most of the siliceous rocks, and the decrease in Zr and P_2O_5 with increasing SiO_2 indicates separation of zircon and apatite from the liquid.

3. If fractional crystallization was the dominant process, it took place in the crust (less than 15 kbar) where plagioclase, pyroxene, and hornblende are stable, rather than high pressures where minerals such as garnet are stable.

4. In order to be consistent with the Sr-isotopic data, there cannot be one uncontaminated liquid line of ascent for the entire Sierra el Virulento suite. If the parent magma underwent extensive crystal fractionation at shallow crustal levels, the contamination hypothesis easily accounts for the observed Sr-isotope variation. Lipman et al. [1978] found that Oligocene ash flow tuffs from the San Juan volcanic field that had differentiated in low-pressure magma chambers showed evidence for contamination by upper crustal material. However, an origin by fractional crystallization and the presence of an isotopically heterogeneous source area are not mutually exclusive. A possible model that would combine both would be generation of several separate parent magmas from a heterogeneous source area with later fractionation as they rose to the surface. The fractionated magmas could later be contaminated to increase the range of Sr-isotopic composition or be erupted with the original $^{87}Sr/^{86}Sr$ of their parent magmas.

An alternative to the crystal fractionation scheme is generation of the suite by direct partial melting of a common source. The obvious advantage of a partial melting model is that it easily accounts for the siliceous composition of the rocks without necessitating large volumes of mafic or intermediate parent magmas. Because almost nothing is known about the crust in the Sierra el Virulento area, this model cannot be rigorously tested. However, the initial $^{87}Sr/^{86}Sr$ ratios are probably too low (0.7043-0.7065) for the suite to be generated by upper crustal melting because the rocks are less radiogenic than most upper crustal material. Direct partial melting of the mantle is also unlikely because of the siliceous composition of the rocks. The lower crust probably has the most suitable chemical and isotopic composition for generation of the Sierra el Virulento magmas. Sierra el Virulento dacites (68% SiO_2) average 150 ppm Rb; rhyolites (70% SiO_2) average about 175 ppm Rb; and high-silica rhyolites (75% SiO_2) average about 225 ppm Rb. If the lower crust has a Rb content of 15 ppm [Hurley, 1968], and Rb behaves as an incompatible element, 10, 8, and 6% melting would be required to produce the dacites, rhyolites and high-silica rhyolites, respectively.

A few limits on the mineralogy of the source region can be made from the REE data. The REE data show that the source must either be LREE enriched or contain enough hornblende, pyroxene, or garnet to produce an LREE-enriched magma. In addition, the generative process must contain enough plagioclase to produce a slight negative Eu anomaly. Garnet probably was not present because the REE patterns for the rhyolites and dacites have approximately the same Ce/Yb ratios (Figure 7).

Summary and Conclusions

In conclusion, the mode of origin of the dacites remains uncertain. They may have been generated by fractionation of more mafic parent

magmas or by partial melting of crustal material. The series dacite to rhyolite appears to have evolved by a combination of low-pressure fractionation in shallow magma chambers and crustal interaction.

The trace-element and Sr-isotopic data are consistent with the following possible model for the origin of the dacites and rhyolites:

1. Dacite parent magmas with initial $^{87}Sr/^{86}Sr$ ratios of 0.7043 to 0.7053 were generated either by partial melting of the lower crust or by fractionation of more mafic mantle derived magmas.

2. The dacite parent magmas rose towards the surface and fractionated in low-pressure magma chambers. Anorthoclase was the overwhelmingly dominant mineral involved in the crystal fractionation process at silica contents greater than 65%. The major-element data suggest that ilmenite, magnetite, biotite, pyroxene, hornblende, apatite, and zircon were fractionated in addition to anorthoclase.

3. During low-pressure fractionation, the $^{87}Sr/^{86}Sr$ ratios of some of the volatile-rich magmas increased to at least 0.7065 by contamination of crustal material.

Acknowledgments. This project was undertaken as part of a Master's thesis at the University of California, Santa Cruz. I wish to thank Ken and Maryellen Cameron for suggesting the problem and for their advice and criticism throughout the course of the study. I am grateful to W. C. Bagby for voluntarily assisting me in the field. I thank C. R. Bacon and E. W. Hildreth for help in obtaining the Fe-Ti oxide data, and G. N. Hanson for access to the isotope lab at the State University of New York, Stony Brook. E. W. Hildreth and W. W. Patton, Jr., offered helpful comment on an earlier draft; F. Barker and G. A. Izett reviewed the manuscript. The work was supported by National Science Foundation grant EAR 77-09006.

References

Arth, J. G., and F. Barker, Rare-earth partitioning between hornblende and dacitic liquid and implications for the genesis of trondhjemitic-tonalitic magmas, Geology, 4, 534-536, 1976.

Barker, F., C. E. Hedge, and H. T. Millard, Jr., Pikes Peak Batholith: Geochemistry of some minor elements and isotopes, and implications for magma genesis, Prof. Contrib. Colo. Sch. Mines, 8, 44-56, 1976.

Barry, J. H., and R. W. Gordon, Geology of the Sierra los Cajones area, Chihuahua, Mexico, B.S. thesis, Univ. of Calif., Santa Cruz,1979.

Buddington, A. F., and D. H. Lindsley, Iron-titanium oxide minerals and synthetic equivalents, J. Petrol., 5, 310-357, 1964.

Cameron, K. L., M. Cameron, W. C. Bagby, E. J. Moll, and R. E. Drake, Petrologic characteristics of mid-Tertiary volcanic suites, Chihuahua, Mexico, Geology, 8, 87-91, 1980.

Cameron, M., W. C. Bagby, and K. L. Cameron, Petrogenesis of voluminous mid-Tertiary ignimbrites of the Sierra Madre Occidental, Chihuahua, Mexico, Contrib. Mineral. Petrol., 74, 271-284, 1980.

Campbell, A. R., Volcanic rocks of the La Perla area, Chihuahua, Mexico, M.S. thesis, Univ. of Tex., Austin, 1977.

Carmichael, I. S. E., The iron-titanium oxides of salic volcanic rock and their associated ferromagnesian silicates, Contrib. Mineral. Petrol., 14, 36-64, 1967.

Dostal, J., M. Zentilli, J. C. Caelles, and A. H. Clark, Geochemistry and origin of volcanic rocks of the Andes (26°-28°S), Contrib. Mineral. Petrol., 63, 113-128, 1977.

Ewart, A., and S. R. Taylor, Trace element geochemistry of the rhyolitic volcanic rocks, central North Island, New Zealand; phenocryst data, Contrib. Mineral. Petrol., 22, 127-146, 1969.

Ewart, A., and J. J. Stipp, Petrogenesis of the volcanic rocks of the central North Island, New Zealand, as indicated by a study of Sr 87/86 ratios, and Sr, Eb, K, U and Th abundances, Geochim. Cosmochim. Acta, 32, 699-736, 1968.

Foder, R. V., Fe content in pyroxenes from calc-alkalic volcanic suites, New Mexico, U.S.A., Earth Planet. Sci. Lett., 11, 385-390, 1971.

Hanson, G. N., The application of trace elements to the petrogenesis of igneous rocks of granitic composition, Earth Planet. Sci. Lett., 38, 26-43, 1978.

Hawley, J. W., Notes on the geomorphology and late Cenozoic geology of northwestern Chihuahua, in New Mexico Geological Society Guidebook of the Border Region, Twentieth Field Conference, pp. 131-142, New Mexico Geological Society, Socorro, 1969.

Heming, R. F., and I. S. E. Carmichael, High-temperature pumice flows from the Rabaul Caldera, Papua, New Guinea, Contrib. Mineral. Petrol., 38, 1-20, 1973.

Hildreth, W., The Bishop Tuff: Evidence for the origin of compositional zonation in silicic magma chambers, Geol. Soc. Am. Spec. Pap. 180, 43-75, 1979.

Hurley, P. M., Absolute abundance and distribution of Rb, K, and Sr in the earth, Geochim. Cosmochim. Acta, 32, 273, 1968.

Irvine, T. N., and W. R. A. Baragar, A guide to the chemical classification of the common volcanic rocks, Can. J. Earth Sci., 8, 523-548, 1971.

King, P. B., Precambrian geology of the United States; an explanatory text to accompany the geologic map of the United States, Geol. Surv. Prof. Pap. U.S., 902, 69-72, 1976.

Leake, B. E., Nomenclature of amphiboles, Am. Mineral., 63, 1023-1052, 1978.

Lipman, P. W., Chemical comparison of glassy and crystalline volcanic rocks, Geol. Surv. Bull. U.S., 1201-D, 29-39, 1965.

Lipman, P. W., Cenozoic volcanism in the western United States: Implications for continental tectonics, in Studies in Geophysics: Continental Tectonics, National Academy of Sciences, Washington, D.C., 1980.

Lipman, P. W., R. L. Christiansen, and J. T. O'Conner, A compositionally zoned ash-flow sheet in southern Nevada, Geol. Surv. Prof. Pap. U.S., 524-F, 1966.

Lipman, P. W., R. L. Christiansen, and R. E. Van Alstine, Retention of alkalis by calc-alkalic rhyolites during crystallization and

hydration, Am. Mineral., 54, 286-291, 1969.
Lipman, P. W., B. R. Doe, C. E. Hedge, and T. A. Steven, Petrologic evolution of the San Juan volcanic field, southwestern Colorado; Pb and Sr isotope evidence, Geol. Soc. Am. Bull., 89, 59-82, 1978.
Lopez-Escobar, L., F. A. Frey, and M. Vergara, Andesites and high-alumina basalts from the central-south Chile high Andes; Geochemical evidence bearing on their petrogenesis, Contrib. Mineral. Petrol., 63, 199-228, 1977.
Lowder, G. G., The volcanos and caldera of Talassa, New Britain; mineralogy, Contrib. Mineral. Petrol., 26, 324-340, 1970.
Ludington, S., The Redskin Granite--evidence for thermogravitational diffusion in a Precambrian granite batholith, J. Geophys. Res., this issue.
Masuda, A., N. Nakamura, and T. Tanaka, Fine structures of mutually normalized rare-earth patterns of chondrites, Geochim. Cosmochim. Acta, 37, 239-248, 1973.
Miyashiro, A., Nature of alkalic volcanic rock series, Contrib. Mineral. Petrol., 66, 91-104, 1978.
Moll, E. J., Geology and geochemistry of the Sierra el Virulento area, southeastern Chihuahua, Mexico, M.S. thesis, 151 pp., Univ. of Calif., Santa Cruz, 1979.
Nagasawa, H., and C. C. Schnetzler, Partitioning of rare-earth, alkali and alkaline earth elements between phenocrysts and acidic igneous magma, Geochim. Cosmochim. Acta, 35, 953-968, 1971.
Noble, D. C., Sodium, potassium, and ferrous iron contents of some secondarily hydrated natural silicic glasses, Am. Mineral., 52, 280-286, 1967.
Noble, D. C., and C. E. Hedge, Sr 87/86 variations within individual ash-flow sheets, Geol. Surv. Prof. Pap. U.S., 650-C, C133-C139, 1969.
Noble, D. C., M. J. Korringa, S. E. Church, H. R. Bowman, M. L. Silberman, and C. E. Heropoulos, Elemental and isotopic geochemistry of non-hydrated quartz latite glasses from the Eureka Valley Tuff, east-central California, Geol. Soc. Am. Bull., 87, 754-762, 1976.
Papike, J. J., K. L. Cameron, and K. Baldwin, Amphiboles and pyroxenes; characterization of other than quadrilateral components and estimates of ferric iron from microprobe data (abstract), Geol. Soc. Am. Abstr. Programs, 6, 1053-1054, 1974.
Peterman, Z. E., and C. Hedge, Strontium, in Handbook of Geochemistry, II/4, edited by K. H. Wedepohl, Springer-Verlag, Berlin-Heidelberg, 1972.
Schnetzler, C. C., and J. A. Philpotts, Partition coefficients of rare-earth elements between igneous matrix material and rock-forming mineral phenocrysts, II, Geochim. Cosmochim. Acta, 34, 331-340, 1970.
Scott, R. B., Alkali exchange during devitrification and hydration of glasses in ignimbrite cooling units, J. Geology, 79, 100-110, 1971.
Sheridan, M. F., and R. G. Updike, Sugarloaf Mountain Tephra; a Pleistocene rhyolite deposit of base-surge origin in northern Arizona, Geol. Soc. Am. Bull., 86, 571-581, 1975.
Smith, A. L., and I. S. E. Carmichael, Quaternary lavas from the southern Cascades, western U.S.A., Contrib. Mineral. Petrol., 19, 385-390, 1968.
Sparks, R. S. J., S. Self, and G. P. L. Walker, Products of ignimbrite eruptions, Geology, 1, 115-118, 1973.
Taylor, S. R., and J. A. Hallberg, Rare-earth elements in the Marda calc-alkaline suite; an Archaean geochemical analogue of Andean-type volcanism, Geochim. Cosmochim. Acta, 41, 1125-1129, 1977.
Thorpe, R. S., P. J. Potts, and P. W. Francis, Rare earth data and petrogenesis of andesites from the North Chilean Andes, Contrib. Mineral. Petrol., 54, 65-78, 1976.
Van Allen, B. R., Hydrothermal iron ore and related alteration in volcanic rock of La Perla, Chihuahua, Mexico, M.S. thesis, 131 pp., Univ. of Tex., Austin, 1978.
Wright, T. L., and P. C. Doherty, A linear programming and least squares computer method for solving petrologic mixing problems, Geol. Soc. Am. Bull., 81, 1995-2008, 1970.
Zielinski, R. A., and P. W. Lipman, Trace-element variations at Summer Coon volcano, San Juan Mountains, Colorado, and the origin of the continental-interior andesites, Geol. Soc. Am. Bull., 87, 1477-1485, 1976.

(Received October 27, 1980;
revised May 13, 1981;
accepted May 20, 1981.)

JOURNAL OF GEOPHYSICAL RESEARCH, VOL. 86, NO. B11, PAGES 10335–10348, NOVEMBER 10, 1981

Three S-Type Volcanic Suites From the Lachlan Fold Belt, Southeast Australia

D. WYBORN

Bureau of Mineral Resources, Canberra, A.C.T., Australia

B. W. CHAPPELL AND R. M. JOHNSTON

Geology Department, Australian National University, Canberra, A.C.T., Australia

The concept that granitoids of the Lachlan Fold Belt in southeast Australia, are derived from either igneous or sedimentary source rocks (I- or S-type), can be extended to volcanic rocks of the same age. Three suites of late Silurian S-type volcanics are described, two of which can be matched quite closely with plutonic equivalents. A large part of the Paleozoic continental margin volcanic activity in southeast Australia consisted of the magmatic recycling of old metasedimentary crust, probably of late Proterozoic age. The three volcanic suites are moderately to strongly peraluminous, with the corresponding presence of Al-rich minerals. Variation within the volcanic suites is ascribed chiefly to progressive removal of restite, or source material residual from partial melting. The most mafic suite, the Hawkins Suite, contains plagioclase, cordierite, orthopyroxene, biotite and quartz as restite components, with less abundant almandine. These rocks are chemically equivalent to mafic biotite-rich and cordierite-bearing granitoids from parts of the Berridale and Murrumbidgee Batholiths. Garnet is absent from the Goobarragandra Suite volcanics, which are a little more felsic and close in compositon to granitoids of the Young and Maragle Batholiths. The S-type character of the Laidlaw Suite is less pronounced although a sedimentary source seems to be established. Such a source would be less mature than those for the other two volcanic suites. The Laidlaw Suite resembles, but cannot be closely identified with, felsic S-type granitoids of the Murrumbidgee and Berridale Batholiths. Low-grade regional metamorphism in most of the volcanic rocks has resulted in much mineralogical alteration and mobility of alkali and alkaline earth elements. Despite this alteration, unaltered rocks are present in all three suites. Compositional data for the phenocryst phases within the unaltered rocks has allowed estimation of some intensive parameters. Hawkins Suite volcanics were extruded directly from their source region and preserve phenocryst equilibria established at 5–6 kbar at 800°C. The Laidlaw and Goobarragandra Suites reequilibrated at lower pressures than their source before extrusion. The Laidlaw Suite reequilibrated at estimated temperatures of 725°–730°C, fO_2 of $10^{-15.5}$ to 10^{-14} bars, and $f(H_2O)$ of 2 to 2.5 kbar. Differing mineral compositions in the three suites are related to differing source rock compositons and oxygen fugacities. Relative biotite and orthopyroxene mg is possibly pressure dependent.

INTRODUCTION

Felsic volcanics in the Palaeozoic Lachlan Fold Belt of southeast Australia dominate over mafic types. Felsic granitoids dominate the Paleozoic intrusive rocks as well and these have been divided into S- and I-types based on whether their source rocks are of sedimentary or igneous composition [*Chappell and White*, 1974]. The recognition of source rock types becomes clear when restite unmixing models, first developed by *Chappell* [1966] and refined by *White and Chappell* [1977], are applied to explain the variation in any cogenetic group of granitoids (a suite). Lachlan Fold Belt I-type granitoids have been divided into several separate suites which have geographical sense and geochemically reflect variation in source rock compositions across the Fold Belt [*Griffen et al.*, 1978; *Compston and Chappell*, 1979; *Beams*, 1980]. The S-type granitoids can also be divided into suites (B. W. Chappell, unpublished data, 1980) based on variations in source rocks, but the differences are not as pronounced as with the I-type suites.

Owen and Wyborn [1979] first showed that, like the granitoids, some of the felsic volcanics of the Lachlan Fold Belt can be subdivided into S- and I-types, and *Johnston* [1979] detected chemical differences between S-type units north of Canberra. The distribution of S- and I-type granitoids and volcanics is shown in Figure 1. Granitoids occupy about 35% of the well exposed part of the Lachlan Fold Belt, of which 60% are S-type. Felsic volcanics occupy about 13%, of which 50% are S-type. Nearly all these rocks are of Silurian to early Devonian age. They represent the period of greatest Phanerozoic magmatic and tectonic development of the Lachlan Fold Belt. The purpose of this paper is to show that the S-type volcanics of the Canberra area (Figure 1) can be divided into three separate suites derived from different sources, to account for the differences in the sources and to relate the three suites to possible cogenetic granitoids.

DISTRIBUTION AND STRATIGRAPHY

S-type volcanics of the Canberra area can be divided into three groups based on their distribution and stratigraphic position and it is on this basis that we shall examine their mineralogical and chemical features. The Long Plain Fault divides two eastern volcanic groups, here designated as the Hawkins and Laidlaw Suites, from a western group, the Goobarragandra Suite (Figure 2).

The Goobarragandra Suite consists of massive porphyritic dacites and rare rhyolites deposited as subaerial ignimbrites and lavas, and ranges in age from late Wenlockian to Ludlovian (Late Silurian) [*Owen and Wyborn*, 1979]. Interbedded epiclastic rocks are rare. The volcanics are intruded by S-type plutons of the Young Batholith which together with S-type plutons of the Maragle Batholith to the south form the Ma-

Copyright © 1981 by the American Geophysical Union.

Paper number 1B0779.
0148-0227/81/001B-0779$01.00

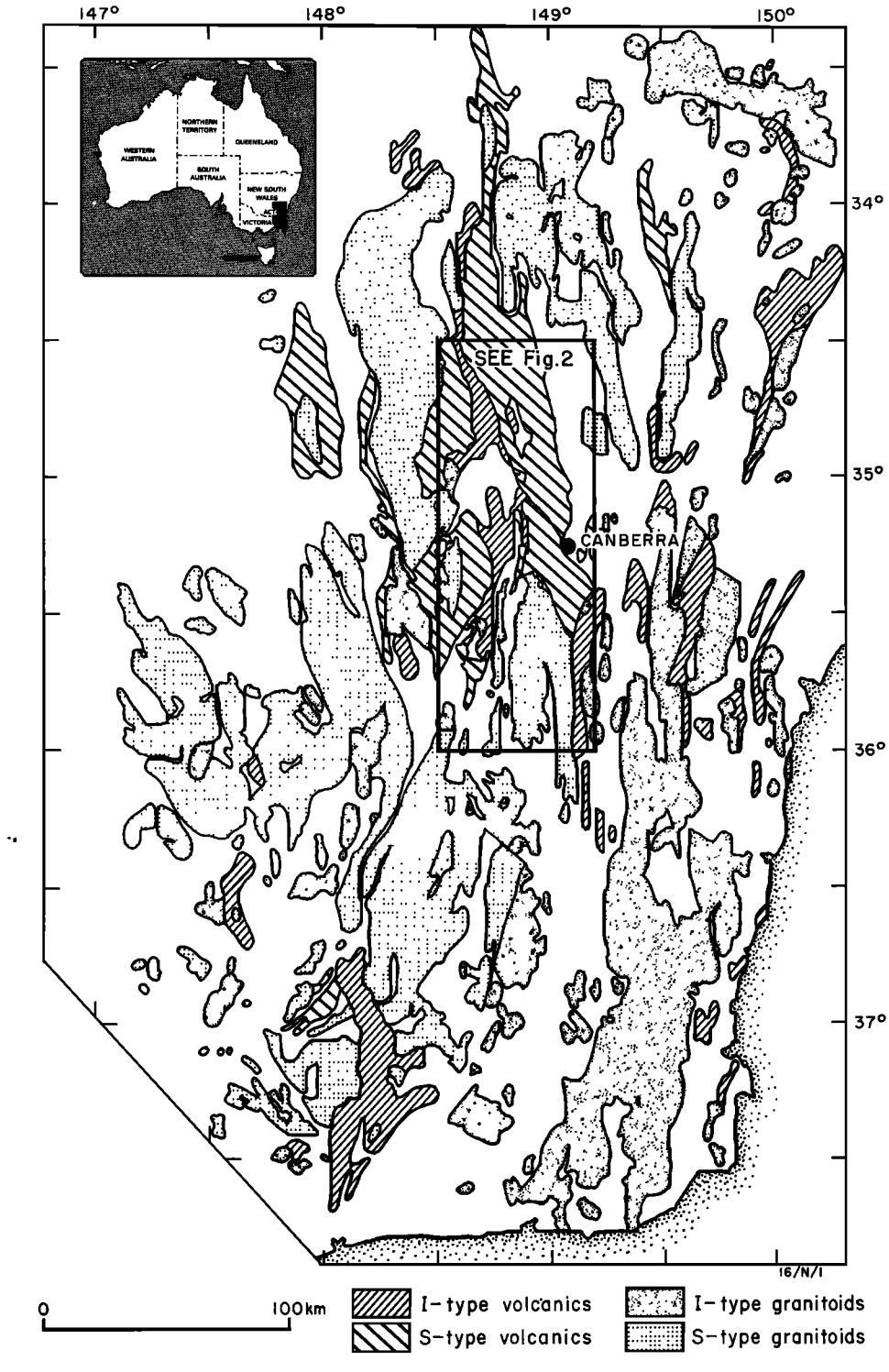

Fig. 1. Distribution of S- and I-type granitoids and volcanics from the better exposed part of the Lachlan fold Belt.

ragle-Young association (B. W. Chappell, unpublished data, 1980).

Where relations can be established the late Wenlockian Hawkins Suite is separated from the early Ludlovian Laidlaw Suite by a disconformity or a narrow belt of sediments containing early Ludlovian fossils [*Link and Druce*, 1972]. In the immediate vicinity of Canberra an internal stratigraphy is recognizeable in the Hawkins Suite. Older ignimbrites and lavas are overlain by a distinct unit, the Mount Painter Volcanics [*Henderson*, 1980], composed of abundant crystals (70–80%), pumice fragments and lithic fragments. Similar rocks occur in the Hawkins Suite away from Canberra, but their stratigraphic position is unclear. The Mount Painter Volcanics may represent an extreme example of crystal concentration in an explosive ignimbrite eruption in the manner envisaged by *Walker* [1972] and *Sparks and Walker* [1977]. Total thickness of the Hawkins Suite just north of Canberra is about 2000 m, of which the top 600 m is Mount Painter Volcanics.

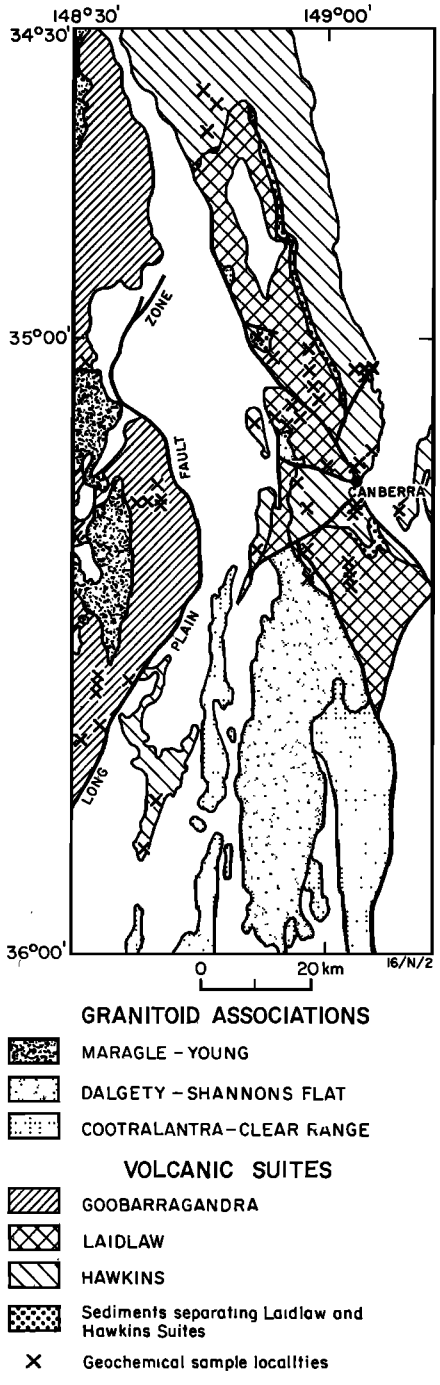

Fig. 2. Distribution of the three S-type volcanic suites and three S-type granitoid associations in the Canberra region.

Most of the Laidlaw Suite consists of a massive dark grey ignimbrite up to 1000 m thick, extending over a strike length of 80 km and probably representing an extensive single cooling unit. To the south, smaller ignimbrite flows, lavas and interbedded sediments underlie the main cooling unit but are still regarded as part of the Laidlaw Suite. There is a systematic change in composition upwards through the main cooling unit from mafic-poor, sanidine-rich rhyolites at the base to mafic-rich, sanidine-poor rhyodacites at the top. This suggests that a large stratified magma chamber was tapped.

Like the volcanics east of the Long Plain Fault, the S-type granitoids can be divided into two associations (B. W. Chappell, unpublished data, 1980): the Cootralantra–Clear Range association and the Dalgety–Shannons Flat association (Figure 2). Although published isotopic dates on these granitoids indicate very similar ages in the range 410–420 m.y. [*Roddick and Compston*, 1976; *Williams et al.*, 1976], field relations show that, in the Berridale Batholith, the Dalgety Granodiorite is younger than the Cootralantra Granodiorite [*White et al.*, 1976], and in the Murrumbidgee Batholith and Shannons Flat Adamellite is younger than the Clear Range Granodiorite [*Owen and Wyborn*, 1979]. Thus the Dalgety–Shannons Flat association is slightly younger than the Cootralantra–Clear Range association. The Dalgety and Cootralantra Granodiorites are immediately south of the area shown in Figure 2. Figure 3 is a summary of the stratigraphy of Figure 2.

MINERALOGY

The phenocryst mineralogy of the three suites is shown in Table 1.

Hawkins Suite

The dominant rock-type of the Hawkins Suite, discounting later metamorphic effects (see below), is a highly porphyritic dacite with about 60% phenocrysts. Quartz and plagioclase phenocrysts up to about 5mm across each occupy about 20% of the rock. Biotite (10%) occurs as flakes averaging 2 × 0.5 mm, is strongly pleochroic from pale brown to dark red-brown, and contains inclusions of apatite, and zircons with pleochroic haloes. Biotite from lava flows is invariably rimmed or totally replaced by an exceedingly fine-grained, almost isotropic intergrowth of K-feldspar, orthopyroxene, cordierite and ilmenite, probably as a result of dehydration of the magma on eruption. Cordierite and orthopyroxene (5% each) occur as euhedral phenocrysts 1 to 2 mm in diameter, but cordierite can be up to 5 mm across and occur as anhedral ovoids. Inclusions of biotite, quartz, zircon, and plagioclase are common in the ovoidal cordierites. Most euhedral cordierites are free of includions but some contain a core area with abundant sillimanite needles up to 0.1 mm long oriented in a schistose alignment. Hercynite octahedra up to 0.03 mm across commonly accompany the sillimanite inclusions. The inclusion-rich cordierite cores are surrounded by euhedral inclusion-free overgrowths. Orthopyroxene is pleochroic from pale green to pale pink. Ilmenite, with minor associated magnetite, apatite, zircon and monazite are accessory phases. Red almandine garnets are a common accessory phase occurring as widely scattered grains up to 10 mm across. Sillimanite needles in a schistose alignment are present in the cores of some garnets. The garnets are large and rounded and surrounded by a symplectite intergrowth of dominant cordierite and lesser orthopyroxene similar to those commonly present in pelitic granulites [e.g., *Van Reenen and Du Toit*, 1978; *Lonker*, 1980]. Small angular garnet fragments probably broken from larger grains during ignimbritic eruption occur in the crystal-rich ignimbrites of the Mount Painter Volcanics.

Xenoliths are common in the Hawkins Suite. Several types are present. Gneissic xenoliths up to 20 cm across consist of garnet + cordierite + sillimanite + biotite + quartz + plagioclase. Lumps of resite quartz [*White et al.*, 1976] up to 10 cm have been observed and are made up of irregular composite crystals similar to vein quartz. A common xenolith is a granophyric type in which plagioclase, biotite and orthopyroxene are set in a matrix of poikilitic quartz. Rare granular micro-

TABLE 1. Mineralogy of Most Common Rock Types

	Hawkins Suite	Laidlaw Suite	Goobarragandra Suite
Rock types in suite	Highly porphyritic dacite lava and ignimbrite, rare rhyolite.	Porphyritic rhyodacite ignimbrite, lesser rhyodacite lava and rhyolite.	Porphyritic dacite lava and ignimbrite, rare rhyolite.
Felsic phenocrysts	Quartz 20%, plagioclase 20%	Plagioclase 25%, quartz 20%, sanidine 5%	Plagioclase 20%, quartz 10–15%
Mafic phenocrysts	Biotite 10%, cordierite 5%, orthopyroxene 5%, garnet, ilmenite, magnetite	Biotite 10%, orthopyroxene 5%, ilmenite, magnetite, allanite	Biotite 5%, cordierite, orthopyroxene, ilmenite

xenoliths up to 10 mm across contain cordierite + garnet + biotite + orthopyroxene + plagioclase. There is no evidence of biotite/orthopyroxene incompatibility in either the granular microxenoliths or the phenocryst assemblage except at a very late stage when biotite phenocrysts become unstable.

Less abundant rock types in the Hawkins Suite include phenocryst-poor (and often quartz phenocryst-free) dacites and sanidine-bearing rhyolites.

Goobarragandra Suite

Unmetamorphosed samples of the Goobarragandra Suite are rare, so their original mineralogy is not as clear as that of the Hawkins Suite. Dacites are again the dominant rock type but phenocryst content (40%) is lower than in the Hawkins Suite and plagioclase phenocrysts (20%) are more abundant than quartz (10–15%). Dominant biotite and lesser cordierite and orthopyroxene make up the minor (compared to Hawkins Suite) mafic phenocryst content. Ilmenite, apatite and zircon are accessories. Garnet and magnetite have not been observed. K-feldspar phenocryst-bearing rhyolites are rare.

Laidlaw Suite

Rocks from the main cooling unit of the Laidlaw Suite are crystal-rich (65%) ignimbrites ranging in composition from sanidine-rich (10%) rhyolite at the base to sanidine-poor (2%) rhyodacite at the top. The most common rock type is a rhyodacite with about 25% plagioclase phenocrysts about 3 mm across, 20% quartz phenocrysts up to 5 mm across, 3–5% sanidine, 10% biotite, 5% orthopyroxene, 1% opaques (ilmenite and magnetite roughly equal) and accessory allanite, apatite and zircon. The biotite is pleochroic from pale straw yellow to brown. Unlike biotite in the Hawkins suite those from the Laidlaw Suite show no sign of late dehydration and remain unaltered around the rims, but some orthopyroxene crystals are rimmed by greenish biotite and quartz intergrowth perhaps as a deuteric effect. Orthopyroxene pleochroism is not as strong as that in the Hawkins Suite. The accessory allanite occurs at the rate of about 1 or 2 crystals per thin-section forming euhedral zoned prisms up to 2 × 1 mm. Cordierite and garnet are absent from the Laidlaw Suite.

Rocks from the ignimbrites and lavas underlying the main cooling unit contain the same phenocryst mineralogy but they occur in an area of higher metamorphism and are quite altered.

Mineral Compositions and Intensive Parameters

Several relatively fresh samples from each suite were studied with an energy dispersive electron microprobe. Data reduction was by the method of *Reed and Ware* [1975].

Only one sample from the Goobarragandra Suite contains unaltered biotite, cordierite, and orthopyroxene so the mineral compositions established for this sample may not be representative of the whole suite. For the other two suites, samples from widely scattered localities were quite consistent so we are confident that the compositions reported here are a good representation of the original mineral compositions of the whole suite. Examples of typical compositions for the three suites are shown in Tables 2–4. Where there is a range in composition due to zoning or variation from crystal to crystal this range is given in the structural formula and the number of separate analyses is also given. Table 5 is a summary of the main chemical features of minerals in each suite.

Hawkins Suite

Biotite phenocrysts from the Hawkins Suite are of fairly uniform composition with mg (100 Mg/Mg + Fe) averaging 55. TiO_2 is consistently high, up to 6.5% in one analysis, and there is a small amount of octahedral Al present. Biotites from gneissic xenoliths have a greater range of mg and TiO_2. They also contain much greater proportions of octahedral Al—up

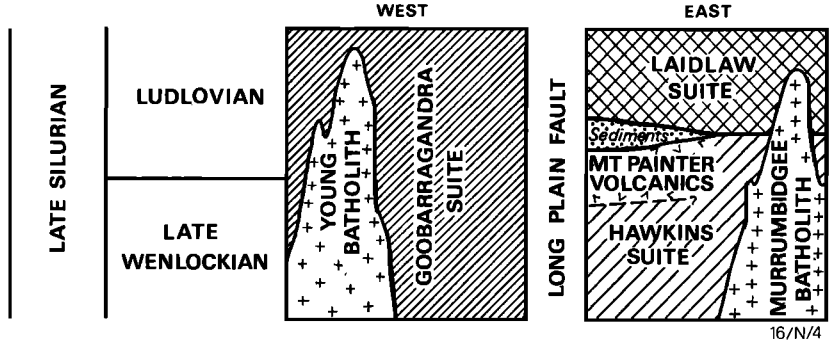

Fig. 3. Stratigraphic column summarizing relationships of units shown in Figure 2.

TABLE 2. Hawkins Suite Mineral Compositions

	Biotite	Orthopyroxene	Cordierite	Garnet
SiO_2	36.66	49.82	48.84	37.44
TiO_2	5.70	0.12	...	...
Al_2O_3	14.85	2.14	33.36	21.37
FeO	17.68	32.26	8.18	31.18
MnO	...	0.56	...	1.54
MgO	12.20	15.92	8.62	5.97
CaO	...	0.09	...	1.34
Na_2O	0.55	...	...	...
K_2O	8.98	...	...	...
Total	96.62	100.91	99.00	98.84
Si	5.465	1.930	4.985	2.988
Al^{iv}	2.536	0.070	1.015	0.012
Al^{vi}	0.075 (0–0.127)	0.028 (0.005–0.060)	2.998	1.998
Ti	0.639 (0.582–0.743)	0.004 (0–0.008)	...	...
Fe	2.204	1.045	0.698	2.081
Mn	...	0.019	...	0.104 (0.034–0.2)
Mg	2.711	0.920	1.312	0.710
Ca	...	0.004 (0.002–0.015)	...	0.114 (0.087–0.1)
Na	0.158	...	...	...
K	1.708	...	...	...
Total	15.496	4.020	11.008	8.007
O	22	6	18	12
mg	55.2 (51.5–58.1)	46.8 (44.8–49.7)	65.3 (61.1–67.7)	25.4 (21.8–30.8)
No. of analyses	18	36	50	46

to 1 atom per formula unit compared to about 0.05 atom for the biotite phenocrysts. This supports the conclusion that the biotites in the gneissic xenoliths were not in equilibrium with the melt. However the consistent compositions of the biotite phenocrysts and those from granular xenoliths point to equilibrium with the melt at some stage.

Most orthopyroxene phenocrysts have a fairly uniform composition with mg about 47 and Al_2O_3 contents of about 2%. Rarely phenocrysts have strongly zoned cores with mg up to 80, but rim compositions are still near 47. The compositions in the range given in Table 1 are all regarded as being rim compositions and in equilibrium with the melt. Cores with higher mg probably represent relict metamorphic crystals. Orthopyroxenes in symplectite reaction rims with cordierite

TABLE 3. Goobarragandra Suite Mineral Compositions

	Biotite	Orthopyroxene	Cordierite
SiO_2	34.85	49.64	46.95
TiO_2	4.86	0.19	...
Al_2O_3	15.24	2.08	32.96
FeO	21.85	31.54	8.23
MnO	...	0.69	...
MgO	9.34	15.73	8.04
CaO	...	0.13	...
Na_2O	0.28	...	...
K_2O	9.14	...	...
Total	95.56	100.00	96.18
Si	5.401	1.937	4.919
Al^{iv}	2.599	0.063	1.081
Al^{vi}	0.181 (0.109–0.463)	0.033 (0–0.037)	2.990
Ti	0.566 (0.499–0.601)	0.006 (0–0.013)	...
Fe	2.794	1.029	0.721
Mn	...	0.023	...
Mg	2.155	0.915	1.256
Ca	...	0.006 (0.005–0.010)	...
Na	0.085	...	...
K	1.806	...	...
Total	15.587	4.012	10.967
O	22	6	18
mg	43.5 (37.9–45.8)	47.1 (43.5–49.0)	63.5 (61.9–65.8)
No. of analyses	20	17	5

TABLE 4. Laidlaw Suite Mineral Compositions

	Biotite	Orthopyroxene
SiO_2	37.24	51.72
TiO_2	4.17	...
Al_2O_3	13.93	0.78
FeO	19.05	27.24
MnO	...	0.80
MgO	11.83	18.60
CaO	...	0.86
Na_2O	0.37	...
K_2O	8.58	...
Total	95.17	100.00
Si	5.607	1.978
Al^{iv}	2.393	0.022
Al^{vi}	0.078 (0–0.150)	0.013 (0–0.027)
Ti	0.472 (0.412–0.547)	... (0–0.004)
Fe	2.399	0.871
Mn	...	0.026
Mg	2.654	1.060
Ca	...	0.035 (0.027–0.044)
Na	0.108	...
K	1.647	...
Total	15.358	4.005
O	22	6
mg	52.5 (50.5–55.2)	54.9 (51.2–62.0)
No. of analyses	19	22

around garnets have mg similar to the orthopyroxene phenocrysts but contain more Al_2O_3 (4.44%, average of 9 analyses) and up to 0.5% Cr_2O_3. In contrast, Cr_2O_3 cannot be detected in the cordierites in the symplectite (detection limit 0.08% Cr_2O_3). Thus any uvarovite molecule in the original garnet has been strongly partitioned into the orthopyroxene. The high Al_2O_3 content of the orthopyroxenes rimming garnet relative to the orthopyroxene phenocrysts clearly show there is compositional dependence of Al_2O_3 solubility in orthopyroxene.

Cordierite phenocrysts have mg averaging about 65. Reverse zoning is present in some crystals, with cores as low as mg 61.1 and rims of mg 67.5. MnO is low, mostly below detection limit (0.09%), but some analyses with low mg have up to 0.2% MnO. Cordierites in reaction rims around garnets are very consistent, with mg averaging 63.2 (16 analyses) and range from 62.1 to 65.1. They are thus slightly more iron-rich compared to average cordierite phenocryst rim compositions.

Garnet mg ranges from 30.8 (cores) to 21.8 (rims). Spessartine contents are mostly about 3–4% but range from 1 to 9%, the higher values being at rims. Grossularite content shows no trend from core to rim and ranges from 2 to 4%.

Overall there is general consistency within all ferromagnesian phases, with $mg^{garnet} < mg^{opx} < mg^{biotite} < mg^{cord}$. The same sequence of mg has been reported elsewhere [*Grant*, 1973, 1978; *Lonker*, 1980] in equilibrium conditions in metamorphic rocks, and in experimental studies [*Hoffer and Grant*, 1980].

Plagioclase phenocrysts from the Hawkins Suite are mostly zoned from An_{65} to An_{50}. Rim compositions are consistently around An_{51} though some grains contain narrow rims of An_{20-25}. Plagioclase of composition An_{51} is considered to be the composition closest to equilibrium with other phenocryst phases. The narrow oligoclase rims probably formed at low temperatures during groundmass crystallization.

Both magnetite and ilmenite are present in the Hawkins Suite, ilmenite dominating. The ilmenite contains 2–2.5% MnO and 4 to 6% hematite solid solution, and is probably primary. However, as the magnetite is titanium-poor (less than 1% TiO_2) it must have equilibrated at low temperatures. Application of the magnetite-ilmenite geothermometer and oxybarometer [*Buddington and Lindsley*, 1964] would thus be inappropriate.

Silicate minerals from the Hawkins Suite are ideal for the application of several currently available geothermometers and geobarometers. *P* and *T* can be estimated from the garnet-cordierite-hypersthene-quartz equilibria of *Hensen and Green* [1973], from the *Ferry and Spear* [1978] calibration of Fe-Mg exchange between garnet and biotite, and from the equations given by *Powell* [1978] for the reaction

TABLE 5. Phenocryst Compositions

	Hawkins Suite	Goobarragandra Suite	Laidlaw Suite
Biotite			
mg	51–58	38–48	50–55
TiO_2, %	5.2–6.5	4.3–5.2	3.6–4.8
Al^{iv} atoms/formula unit	0–0.13	0.11–0.46	0–0.15
Orthopyroxene			
mg	45–50	44–49	51–62
Al_2O_3, %	0.5–4.5	1–3	0.1–1.5
CaO, %	0.05–0.3	0.1–0.2	0.7–1.0
Cordierite			
mg	61–68	62–66	...
Garnet			
mg	22–31	...	...
MnO, %	0.5–3.8		
CaO, %	1.0–2.1		
Plagioclase	An 65–50, rare narrow An 20–25 rims	An 50–20, broad rims	An 70–35
Sanidine	...	...	Or 70–76
Ilmenite			
MnO, %	2–2.5	2–2.5	4–5.6
Fe_2O_3, %	4–6	4–6	8–10
Magnetite			
TiO_2, %	<1	...	7–8

TABLE 6. Pressure and Temperature Estimates for the Hawkins Suite

Mineral Assemblage	Compositional Data: mg^{Gt}	mg^{Cd}	$K_D = \frac{(XMg/XFe)Cd}{(XMg/XFe)Gt}$	P, kbar	T, °C	Method of Calculation
Granular xenolith of cordierite-garnet-biotite-orthopyroxene-plagioclase	23.7	62.7	5.41	5.4	790	*Hensen and Green* [1973]
	25.3	63.2	5.06	5.5	810	
	24.3	63.8	5.52	5.5	800	
Cordierite-orthopyroxene around garnet	24.4	66.0	6.02	5.6	750	
	25.1	63.2	5.16	5.5	810	

Mineral Assemblage	Compositional Data: X_{Mg}^{Gt}	X_{Fe}^{Gt}	X_{Ca}^{Gt}	X_{Mn}^{Gt}	X_{Mg}^{Opx}	X_{Fe}^{Opx}	$K_D = \frac{(XMg/XFe)Opx}{(XMg/XFe)Gt}$	T, °C	Method of Calculation
Cordierite-orthopyroxene around garnet	0.234	0.698	0.036	0.033	0.436	0.510	2.55	956	*Dahl* [1980]

Mineral Assemblage	Compositional Data: X_{Mg}^{Gt}	X_{Fe}^{Gt}	X_{Mg}^{Biot}	X_{Fe}^{Biot}	$K_D = \frac{(XMg/XFe)Biot}{(XMg/XFe)Gt}$	T, °C at 2.07 kbar	T, °C at 5.5 kbar	Method of Calculation
Granular xenolith of cordierite-garnet-biotite-orthopyroxene-plagioclase	0.253	0.662	0.498	0.363	3.56	755	771	*Ferry and Spear* [1978]
	0.234	0.687	0.486	0.385	3.70	736	752	
	0.222	0.688	0.454	0.427	3.30	794	811	
Biotite and garnet—Table 2	0.236	0.692	0.482	0.392	3.61	748	764	
Biotite inclusion in garnet	0.294	0.663	0.415	0.417	2.25	1051	1071	

Mineral Assemblage	Compositional Data: X_{Ca}^{Plag}	X_{Ca}^{Gt}	T, °C at 5.5 kbar	Method of Calculation
Gneissic plagioclase-cordierite-garnet-biotite-sillimanite-quartz xenolith	0.5023	0.0444	664	*Powell* [1978]
	0.5163	0.0381	732	
	0.5064	0.0512	619	
	0.5439	0.0392	742	
Granular xenolith of cordierite-garnet-biotite-orthopyroxene-plagioclase	0.4660	0.0456	629	

For garnet $Xi = i/(Mg + Fe + Mn + Ca)$; for orthopyroxene $Xi = i/(Mg + Fe + Ca + Mn + Al^{vi})$; for biotite $Xi = i/(Mg + Fe + Mn + Ti + Al^{vi})$.

$$\text{Ca-plagioclase} = \text{grossularite} + \text{sillimanite} + \text{quartz}$$

A temperature-dependent equation for the Fe-Mg exchange between garnet and orthopyroxene given by *Dahl* [1980] has also been employed. Mineral compositions, K_D values and calculated P and T using the appropriate cation exchange equilibria data are shown in Table 6.

The *Hensen and Green* [1973] calibration for the reaction garnet +quartz = cordierite + orthopyroxene gives consistent results for different samples, of $P \doteq 5.5$ kbar and $T \doteq 800$°C. Garnet-cordierite exchange equilibria have recently received a great deal of attention, mainly involving the effect of water in cordierite on the reaction

$$\text{garnet} + \text{sillimanite} + \text{quartz} + H_2O = \text{cordierite}$$

High water activities can increase the stability of cordierite by 2 kbar relative to anhydrous cordierite [*Newton and Wood,* 1979; *Lonker,* 1981]. Hensen and Green's calibration of the sillimanite-bearing reaction commonly gives conflicting results with other geobarometers and other calibrations of the garnet-cordierite geobarometer [*Ellis,* 1980], but their calibration of the orthopyroxene-bearing reaction gives good agreement [*Ellis,* 1980]. We are therefore confident of the pressure estimate given by the cordierite-garnet pairs, particularly as any water involved in the exchange equilibria would be strongly partitioned into the melt fraction rather than into cordierite. Since both granular xenoliths and garnet reaction rims from several different samples give essentially the same result it is likely that they were both in equilibrium with the melt near its source and the Hawkins Suite was produced by partial melting at about 5 to 6 kbar.

Temperature estimates using cordierite-garnet pairs and biotite-garnet pairs [*Ferry and Spear,* 1978] at 5.5 kbar are in reasonable agreement at 750°–800°C. Plagioclase-garnet pairs [*Powell,* 1978] give slightly lower temperatures, but a single determination (average of 6 analyses) for a garnet-orthopyroxene pair [*Dahl,* 1980] from a garnet reaction rim gives a temperature of 950°C.

The overall consistency of phenocryst compositions including euhedral inclusion free overgrowths on inclusion bearing cordierites, euhedral rims on orthopyroxenes with high mg cores and cordierite-orthopyroxene rims around garnets imply equilibration with the melt. Yet the garnets, inclusion bearing cordierite cores and high mg orthopyroxene cores are most likely relict metamorphic minerals. Thus there is a continuum of crystal growth from a metamorphic environment into an anatectic environment. Apart from the relict metamorphic cores, the cordierite and orthopyroxene are then best regarded as products of incongruent melting reactions such as those outlined by *Grant* [1973]. Quartz, plagioclase, and biotite were

probably in excess during melting so all phenocrysts present in the Hawkins Suite are strictly restite phases rather than products of crystallization from the melt.

Goobarragandra Suite

Biotite, orthopyroxene and cordierite phenocryst analyses are given in Table 3. Only one sample contained fresh biotite, orthopyroxene and cordierite and two others contained fresh biotite. Relative to biotites from the Hawkins Suite the Goobarragandra biotites have more octahedral Al, less Ti, and lower mg. The orthopyroxenes and cordierites are virtually indistinguishable from those in the Hawkins Suite. Plagioclase phenocrysts are strongly zoned, with cores of An_{50} and rims of An_{20}. Unlike plagioclase phenocrysts from the Hawkins Suite, broad oligoclase rims are present on all crystals. Ilmenite is virtually indistinguishable from those in the Hawkins Suite, containing 2–2.5% MnO and 4–6% hematite solid solution.

No quantitative estimates of intensive parameters can be made at present for the Goobarragandra Suite, but comparison with the Hawkins Suite may help in a qualitative manner. The main differences between phenocryst content are that in the Goobarragandra Suite (1) garnet and magnetite are absent; (2) biotites have more octahedral aluminum, less TiO_2, and lower mg; and (3) plagioclase is more sodic and rimmed by oligoclase. The absence of magnetite, less TiO_2 in biotite and lower mg all indicate lower fO_2 than the Hawkins Suite, considering the similar titanium, iron and magnesium contents of the total rocks (see geochemistry below). Under less oxidizing conditions lower Fe^{3+} activity would stabilize ilmenite rather than magnetite, thus leaving less available Ti to enter biotite. It would also result in higher activity of Fe^{2+}, thus reducing biotite mg. A comparable decrease in orthopyroxene and cordierite mg has not been observed in the single sample analyzed. More data might change this conclusion. The lack of equilibration with an Fe-rich phase such as garnet should also tend to decrease mg for biotite, orthopyroxene and cordierite.

Unlike the Hawkins Suite, the equilibrium conditions in high grade metamorphic terrains [*Grant,* 1973, 1978; *Lonker,* 1980] and the experimental study of *Hoffer and Grant* [1980] $mg^{biotite}$ is less than $mg^{orthopyroxene}$ for the Goobarragandra Suite. For the Mg-Fe exchange reaction

$$\text{phlogopite} + \text{orthoferrosillite} = \text{annite} + \text{enstatite}$$

ΔV equals +0.068 cal/bar (data from *Robie et al.* [1967]). Thus low pressures would favor the right hand side of the reaction. It is therefore possible that the phenocrysts have equilibrated in a magma chamber at low pressures, and at temperatures well above those in the *Hoffer and Grant* [1980] experiments (550°–650°C, results: $mg^{biotite} = mg^{orthopyroxene}$). If the magma spent some time in a high level chamber it would allow mafic restite phases to settle out, and some crystallization to take place. This is consistent with the more felsic character of the Goobarragandra Suite relative to the Hawkins Suite and the presence of broad oligoclase rims on the plagioclase phenocrysts.

The absence of garnet in the Goobarragandra Suite may be a compositional effect, but it is more likely that any garnets originally present have been removed by settling out as a result of their high density. Rare garnet is present in plutons of the Maragle-Young S-type granitoid association.

Laidlaw Suite

Typical biotite and orthopyroxene analyses are shown in Table 4. Compared to Hawkins and Goobarragandra Suite analyses, the Laidlaw Suite biotites have (1) low Al, mainly in the tetrahedral site compared to Hawkins biotites, but in both tetrahedral and octahedral sites compared to Goobarragandra biotites—as a consequence of their low tetrahedral Al they are high in Si; (2) TiO_2 comparable to Goobarragandra biotites; and (3) high mg. The Laidlaw orthopyroxenes have low Al_2O_3 (0.1–1.5%) and TiO_2, and high SiO_2, mg and CaO.

Plagioclase phenocrysts in the Laidlaw Suite are zoned from An_{70} to An_{35}; sanidine phenocrysts are relatively uniform Or_{70-76} (20 analyses); ilmenite is high in MnO (4–5.6%) and hematite (8–10%)—(10 analyses). Unlike magnetites from the Hawkins Suite most magnetites from the Laidlaw Suite have not reequilibrated to low temperatures as they contain 7–8% TiO_2. The presence of phenocrysts of quartz, plagioclase and alkali feldspar in the Laidlaw Suite indicates that the magma was in univariant equilibrium in the quaternary system $NaAlSi_3O_8$-$KAlSi_3O_8$-$CaAl_2Si_2O_8$–SiO_2 [*James and Hamilton,* 1969] before extrusion. The absence of alkali feldspar phenocrysts in the Hawkins and Goobarragandra Suites (except in rare rhyolites) indicates they had not cooled down to the univariant assemblage before extrusion and were in equilibrium on the divariant plagioclase-quartz surface. The low K_2O in the Laidlaw Suite relative to the Goobarragandra and especially the Hawkins Suite (see geochemistry below) indicates that alkali feldspar is unlikely to be a residual phase in the source region. Thus the Laidlaw Suite must have cooled down to the univariant, equilibrium curve from some higher temperature before extrusion. This is in keeping with the compositional zoning of the main cooling unit which suggests that it was erupted from a stratified (? high level) magma chamber. The relative amounts of Fe and Mg in biotites and orthopyroxenes ($mg^{biotite}$ slightly less than or equal to $mg^{orthopyroxene}$ (see Table 4) could also indicate equilibration at fairly low pressures.

Ilmenite-magnetite pairs from the Laidlaw Suite give temperatures ranging from 714° to 742°C and corresponding fO_2 of $10^{-15.5}$ to $10^{-14.1}$ bars according to the equations of *Powell and Powell* [1977] based on the experimental data of *Buddington and Lindsley* [1964]. This corresponds to quite oxidizing conditions for an S-type magma, above the NNO buffer and within the stability field of sphene + magnetite + quartz given by *Wones* [1981]. Allanite, rather than sphene, is present in the Laidlaw Suite because of the aluminous nature of S-type magmas.

The biotite + magnetite + K-feldspar assemblage of the Laidlaw Suite corresponds to the equilibrium:

$$\text{annite} + O_2 = \text{K-feldspar} + \text{magnetite} + H_2O$$

[*Wones and Eugster,* 1965]. Since we have estimates of T and fO_2, and microprobe data giving a^{annite} in biotite, and $a^{Fe_2TiO_4}$ in magnetite the equation given by *Wones* [1972] can be used to estimate $f(H_2O)$ in the Laidlaw Suite:

$$\log f(H_2O) = 7409/T + 4.25 + \tfrac{1}{2}\log fO_2 + 3\log x - \log a^{KAlSi_3O_8} - \log a^{Fe_2TiO_4}$$

Here T is in °K, x is the fraction of Fe^{2+} in octahedral sites in biotite, and a is activity. Assuming that all iron in the biotite is

Fe^{2+} gives a maximum value for $f(H_2O)$. The average composition of 19 microprobe analyses for biotite and 20 analyses for alkali feldspar are used in the calculation combined with the magnetite compositions and temperature and fO_2 values determined for each magnetite-ilmenite pair (5 magnetite analyses). The resulting $f(H_2O)$ ranges from 3.8 kbar at 742°C, $fO_2 = 10^{-14.1}$ to 1.2 kbar at 714°C, $fO_2 = 10^{-15.5}$.

An independent estimate of temperature, determined by the *Stormer* [1975] two-feldspar geothermometer, using plagioclase rim compositions (An_{35}) and sanidine compositions (Or_{70-75}) yields temperatures of 700°–750°C at 5 kbar total pressure and 670°–750° at 2 kbar total pressure. *James and Hamilton* [1969] have given the position of the univariant quartz-plagioclase-orthoclase curve at $f(H_2O) = 1$ kbar. For compositions of $Ab_{21}:Or_{34}:Q_{20}:An_5$ the curve is at 745° ± 5°–10°C. This is close to the equilibrium composition of the Laidlaw Suite in terms of feldspar compositions. At higher water pressures the univariant curve will be at lower temperatures [*Tuttle and Bowen,* 1958; *Winkler et al.,* 1975] yet water pressure is proportional to temperature for the biotite–magnetite–K-feldspar equilibria of *Wones* [1972]. Thus, together, the two sets of equilibria constrain the temperature and water pressure. Perhaps the best estimate then, is a median value of the range given by the *Wones* [1972] equilibria, viz., 2–2.5 kbar water pressure and 725°–730°C. Total pressure cannot be estimated, so the depth of the magma chamber is unknown.

The high fO_2 of the Laidlaw Suite relative to the Hawkins and Goobarragandra Suites helps explain the high MnO content of Laidlaw ilmenites [*Czamanske and Mihalik,* 1972] and the high mg of Laidlaw biotites and orthopyroxenes. The lack of equilibration with high-Mg cordierite would also increase mg for biotite and orhopyroxene in the Laidlaw Suite.

Summary of Intensive Parameters

The available evidence indicates that the Hawkins Suite was extruded directly from its source area with little chance of upper crustal equilibration of phenocryst phases. The source area was at 5–6 kbar total pressure and temperatures of about 800°C. The Goobarrangandra and Laidlaw Suites equilibrated in high-level magma chambers before extrusion. In the case of the Laidlaw Suite water pressures were about 2–2.5 kbar in this magma chamber.

The Laidlaw Suite was crystallizing on the quartz-plagioclase-alkali feldspar univariant curve before extrusion but the Hawkins and Goobarragandra Suites were crystallizing on the divariant quartz-plagioclase surface.

Magma temperatures were estimated at about 800°C for the Hawkins Suite and 725°C for the Laidlaw Suite, and they were probably about 700°–750°C for the Goobarragandra Suite.

Oxygen fugacities were highest in the Laidlaw Suite (10^{-14}–$10^{-15.5}$ bars) and lowest in the Goobarrangandra Suite.

METAMORPHIC ALTERATION

All three volcanic suites have in part been subjected to low-grade regional metamorphism which in many rocks has had a pronounced effect on mineralogy and chemistry. Alteration patterns are also present in related high-level porphyritic intrusions and rare cross-cutting dolerite dykes, so they cannot be ascribed to diagenetic effects on the volcanic pile soon after eruption.

The main effect of this metamorphism, apart from groundmass recrystallization, has been the widespread albitization of plagioclase. Metamorphic minerals such as prehnite, pumpellyite, epidote and calcite are commonly present in the groundmass of the volcanics as a result of albitization but in most cases these minerals are not abundant so there has probably been a net loss of Ca from homogeneous rock along joints and fractures. Epidote veins are common in all suites. Plagioclase phenocrysts are perfectly pseudomorphed by albite, albite twinning is poorly developed and commonly diffuse, and in many crystals concentric bands of sericitic alteration mimic primary growth zones in the original plagioclase. In the Laidlaw Suite and in rhyolites from the other suites metamorphism has resulted in the unmixing of sanidine phenocrysts into coarse patch perthites.

Apart from garnet in the Hawkins Suite, which remains unaltered, all primary mafic minerals in the volcanics have been completely altered at or before the stage of plagioclase phenocryst albitization. Biotite has altered to an intergrowth of chlorite, ilmenite and sphene oriented parallel to cleavage traces in the original biotite. Epidote, nontronite and sericite are commonly also present in the biotite alteration assemblage. Orthopyroxene alters to a coarse patchy intergrowth of chlorite. In most cases it also contains pale brownish quartz dusted with chlorite inclusions and a small amount of opaque minerals. In the Hawkins and Goobarragandra Suites, cordierite phenocrysts are perfectly pseudomorphed by chlorite or sericite. When both alteration products are present sericite occupies the core and is surrounded by a chlorite rim. The chlorite alteration has a fine-grained serpentine-like mesh structure. Both orthopyroxene and cordierite also rarely contain epidote, pumpellyite or carbonates as alteration products, the mafic minerals apparently being favorable sites for fixing of otherwise mobile calcium ions. Given the different alteration patterns of cordierite and orthopyroxene and their different crystal shape, only rarely can their original character be confused. In some rocks where chlorite is the only alteration product of both orthopyroxene and cordierite, the coarser texture and often anomalous interference colours of the more Fe-rich chlorite after orthopyroxene are diagnostic. In the Hawkins Suite, when orthopyroxene and cordierite reaction rims occur around garnets their symplectite intergrowth texture is still preserved by the pseudomorphing of two different chlorites in different orientations.

The overall effect of the metamorphism has resulted in very little textural change; original phenocryst mineralogy can still be determined despite quite pronounced mineralogical changes. The mineralogical evidence indicates that K, Na, Ca, Al, and Si have been mobile during metamorphism but Al and Si have probably not moved far. Mg, Fe, and Ti appear to have remained fixed. The preservation of cordierite-orthopyroxene intergrowth textures by different chlorite types points to the immobility of Mg and Fe.

GEOCHEMISTRY

Analytical Techniques

All major elements except Na (flame photometry), Fe^{2+} (titration), H_2O and CO_2, and all trace elements, were determined by X ray spectrometry using the methods described by *Norrish and Chappell* [1977].

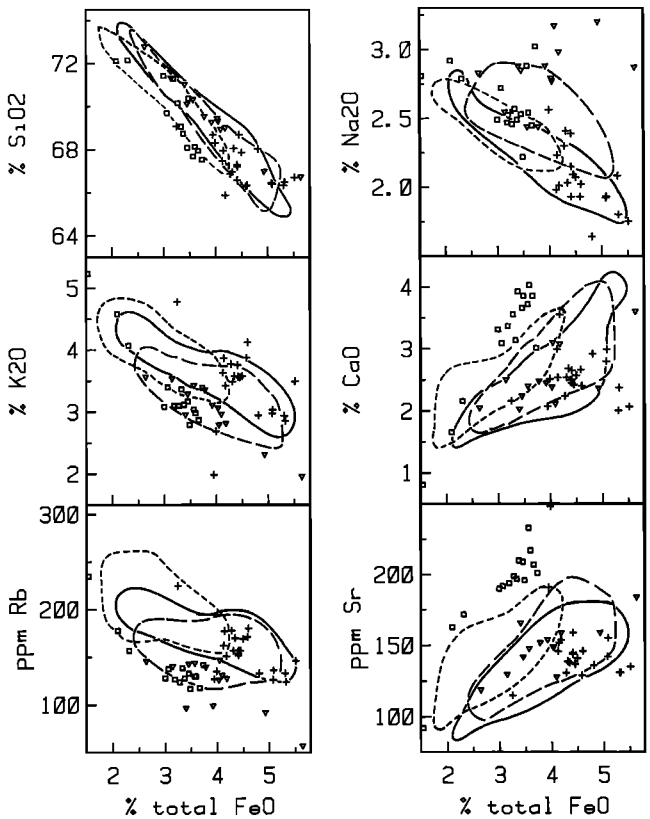

Fig. 4. Element variations for samples from the three volcanic suites: Crosses-Hawkins Suite, Triangles-Goobarragandra Suite, Squares-Laidlaw Suite. Also shown are fields for the three granitoid associations based on 228 analyses. Field outlined by solid line—Cootralantra–Clear Range association; long dashed line—Maragle-Young association; short dashed line—Dalgety–Shannons Flat association.

Characteristics of the Three Granitoid Associations

In Figures 4 and 5 the fields of the three granitoid associations shown in Figure 2 are outlined separately. The fields are compiled from an unpublished data set of 228 samples analyzed by B. W. Chappell. They show that the main differences between the Cootralantra–Clear Range association and the Maragle-Young association is the higher Na and lower K and Rb in the latter. Ca and Sr show slight differences but there is much overlap. The Dalgety–Shannons Flat association contains more Ca, Sr and V, and lower Si and Al/(Ca + Na + K) and the more mafic samples (from the Dalgety Granodiorite) have high Mg/Ni while the more felsic samples (from the Shannons Flat Adamellite) contain more Ce and Ba. The Shannons Flat Adamellite is also richer in Al, Nb, La, Th and U but these elements are not shown in Figures 4 and 5. There is no significant difference between the three associations for TiO_2, $FeO_{(total)}$, MnO, MgO, P_2O_5, K/Rb, Pb, Zr, Y, Cr, Sc, Cu, Zn and Ga. The main differences between the associations occur in the elements in feldspars.

Volcanic Geochemistry

In view of the important role alkali and alkaline earth elements play in distinguishing the grantoid associations, and their relatively high mobility during metamorphism of the volcanics, careful petrographic screening of volcanic samples was made before selection for geochemical analysis. In all over 500 samples were examined and from these 51 were selected for analysis. The criterion used for selection was the presence of unalbitized plagioclase phenocrysts which were relatively free of sericitic alteration. Twenty-three samples came from the Hawkins Suite, 13 from the Goobarragandra Suite and 15 from the Laidlaw Suite. Their locations are shown in Figure 2. Means and standard deviations for the samples from the three suites are presented in Table 7. Also shown are the averages of the three granitoid associations.

From the means it can be seen that the Hawkins Suite is more mafic then the other two suites. At a normalized $FeO_{(total)}$ level, (1) the Hawkins Suite is richer in K and Rb, (2) the Goobarragandra Suite is richer in Na, and (3) the Laidlaw Suite is richer in Ca, Ba, Sr, La, and Ce.

The means and standard deviations do not give a true picture of the differences between the suites as there is often extreme skewness in the data set so that one or two very high or low values bias the means and result in a large standard deviation. To demonstrate the differences more closely element values for all samples are plotted in Figures 4 and 5. Elements are mainly plotted against $FeO_{(total)}$ because (1) there is nearly a four-fold difference between the most Fe-poor and Fe-rich samples, whereas SiO_2, the component most commonly used in such plots, shows relatively little variation; (2) plots of S-type granitoids give higher correlation coefficients with $FeO_{(total)}$ than SiO_2, S-types being by nature fairly uniformly rich in SiO_2; (3) there is textural evidence that $FeO_{(total)}$ is quite immobile during the metamorphism of the volcanics.

Figures 4 and 5 show that, in addition to the differences given above, the Laidlaw Suite is lower in Si and has higher Mg/Ni ratios. On a K_2O versus Na_2O plot the three suites plot in fields with very little overlap, the Hawkins Suite at low

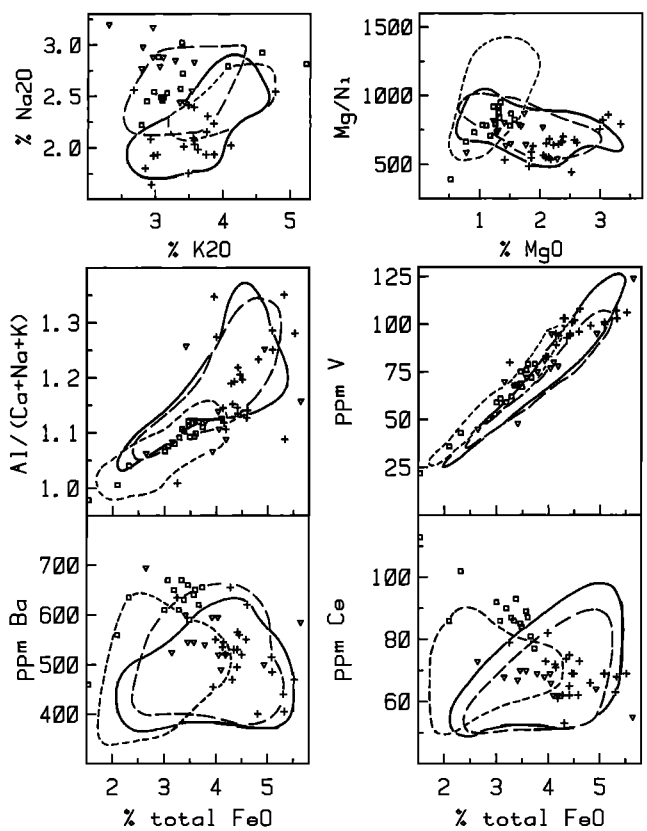

Fig. 5. Element variations as for Figure 4.

TABLE 7. Average Composition of the Three Volcanic Suites and Three Granitoid Associations

	Hawkins Suite (23 Samples)		Cootrantra–Clear Range Association (129 Samples)	Goobarragandra Suite (13 Samples)		Maragle-Young Association (41 Samples)	Laidlaw Suite (15 Samples)		Dalgety–Shannons Flat Association (58 Samples)
	$\bar{x}$	S	$\bar{x}$	$\bar{x}$	S	$\bar{x}$	$\bar{x}$	S	$\bar{x}$
Major oxides, %									
SiO_2	67.31	0.93	68.74	69.60	1.58	68.59	69.94	2.01	70.69
TiO_2	0.60	0.03	0.56	0.55	0.11	0.60	0.43	0.11	0.41
Al_2O_3	14.05	0.59	14.32	13.60	0.24	14.40	14.34	0.67	13.96
Fe_2O_3	1.43	0.29	0.73	0.94	0.23	0.80	1.35	0.24	0.79
FeO	3.30	0.57	3.41	3.07	0.60	3.36	1.89	0.45	2.26
MnO	0.06	0.02	0.07	0.05	0.01	0.07	0.04	0.01	0.06
MgO	2.36	0.46	2.03	1.54	0.37	1.91	1.19	0.28	1.20
CaO	2.57	0.36	2.59	2.52	0.45	2.71	3.14	0.89	2.61
Na_2O	2.10	0.40	2.17	2.82	0.23	2.39	2.62	0.21	2.46
K_2O	3.35	0.68	3.53	3.01	0.45	3.26	3.42	0.66	4.02
P_2O_5	0.14	0.01	0.13	0.13	0.02	0.14	0.10	0.02	0.10
Total	97.27		98.28	97.83		98.23	98.46		98.56
Trace elements, ppm									
Ba	510	75	450	560	55	480	620	50	490
Rb	152	29	173	122	27	161	142	29	201
Sr	147	26	134	149	16	147	191	31	144
Pb	38.5	19.5	26.5	31.0	4.5	26.0	50.0	47.0	27.0
Th	18.6	1.2	17.4	17.4	2.0	17.6	19.8	2.8	20.6
U	3.2	0.6	3.1	3.2	0.4	3.0	3.0	0.8	4.0
Zr	182	11	162	191	12	178	170	30	150
Nb	10.5	1.0	10.5	9.0	0.5	10.5	9.5	1.0	10.5
Y	31	6	31	32	3	32	27	2	36
La	29	3	29	28	2	30	39	5	31
Ce	68	6	65	66	5	70	89	8	70
Sc	16	3	15	12	2	14	12	2	14
V	97	7	76	78	19	75	62	16	58
Cr	62	14	53	22	13	40	n.d.*	...	23
Mn	480	150	490	440	90	505	315	50	440
Ni	22.0	3.5	18.0	13.0	4.5	18	9.0	1.5	8.5
Cu	15.5	11.5	13.0	11.0	4.5	13.5	7.5	2.0	5.0
Zn	78	18	64	60	14	66	61	38	44
Ga	17.4	0.6	16.0	16.2	0.4	16.8	16.4	1.4	15.4

* Not determined.

Na_2O values, the Laidlaw at intermediate values, and the Goobarragandra at high values. The Goobarragandra Suite plots between the other two suites for K_2O, Rb, CaO, Sr, Ba and Mg/Ni, but there is considerable overlap. Elements not plotted in Figures 4 and 5 (TiO_2, MnO, MgO, P_2O_5, Pb, Th, U, Zr, Nb, V, Cu, Zn, Sc, and Ga) show no differences between the suites. The Laidlaw Suite is high in Al_2O_3 and La and low in Ni and Y relative to the other two suites. The higher values for light rare earth elements and lower values for yttrium in the Laidlaw Suite imply more fractionated rare earth elements, which is surprising considering that garnet was a residual phase in the Hawkins Suite and probably also in the Goobarragandra Suite.

In Figure 5 all three volcanic suites have a positive correlation of Al/(Ca + Na + K) with $FeO_{(total)}$. Applying restite unmixing principles this means that the sources for the three suites are more alumnious than the melt derived from that source. Hence all three volcanic suites are S-type. This is obvious for the Goobarragandra and Hawkins Suite in view of their phenocryst mineralogy but it is not obvious for the Laidlaw Suite as its high calcium masks its peraluminous character. The ACF digram in Figure 6 displays these characteristics very well. Hawkins Suite samples mainly plot in the biotite + cordierite + plagioclase field, Goobarragandra Suite samples plot in the biotite + plagioclase and biotite + cordierite + plagioclase fields, whereas Laidlaw Suite samples plot mainly in the biotite + plagioclase field much closer to the plagioclase end of the plagioclase-biotite join. The one Laidlaw sample well into the biotite + cordierite + plagioclase field is a rather altered rhyolite from the base of the main cooling unit. This sample was included in the analyzed samples because it was the most felsic sample collected for petrographic examination.

Volcanic Versus Granitoid Comparison

Based on geographical distribution and age relations one would expect

Goobarragandra Suite = Maragle-Young association

Hawkins Suite = Cootralantra–Clear Range association

Laidlaw Suite = Dalgety–Shannons Flat association

Those elements which show no significant differences between the three granitoid associations are almost the same as the list given for the volcanics in the preceding subsection above. Ti, $Fe_{(total)}$, Mn, Mg, P, Pb, Zr, Cu, Zn, Sc and Ga show no significant differences for all three granitoid associations and all three volcanic suites. The high Na and low K and Rb of the Goobarragandra Suite relative to the Hawkins Suite corresponds exactly with the high Na and low K and Rb of the Maragle-Young association relative to the Cootra-

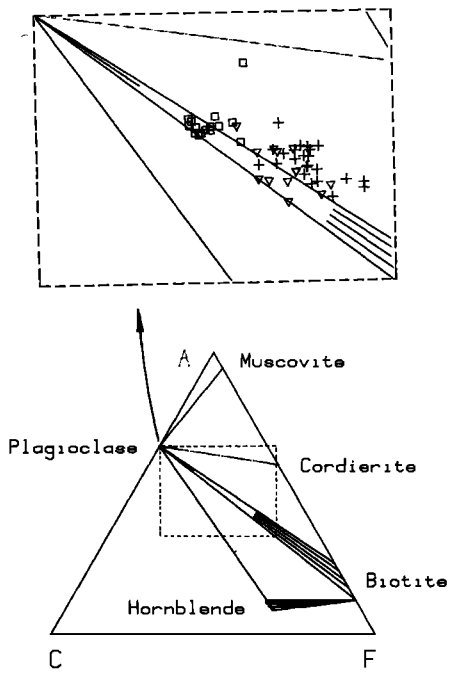

Fig. 6. ACF diagram of analysed volcanic samples. Symbols as for Figure 4.

lantra–Clear Range association. Likewise the slightly higher Ca and Sr in the Maragle-Young association relative to the Cootralantra–Clear Range association is also found in the Goobarragandra Suite relative to the Hawkins Suite. Allowing for the slightly more scattered trends for the volcanics due to alteration, in particular the high Na in some of the Goobarragandra Suite samples, there is virtually perfect correlation of the Goobarragandra Suite with the Maragle-Young association and the Hawkins Suite with the Cootralantra–Clear Range association, and in view of their geographic relationships we are very confident that they each form comagmatic volcanoplutonic associations.

The Laidlaw Suite is more of a problem. It shows some similarities to the Dalgety–Shannons Flat association in that both are high in Ca and Sr and low in Si relative to the other suites at normalized $FeO_{(total)}$ levels. It is similar to the Shannons Flat Adamellite in being rich in Al, Ba, La and Ce and similar to the Dalgety Granodiorite in being high in Mg/Ni relative to the other suites. It plots in the same field as the Dalgety–Shannons Flat association on a V versus $Fe_{(total)}$ plot, but the granitoid association fields are quite tight (Figure 5) and the volcanic suites cannot be resolved on this diagram. The slightly higher vanadium contents of the Dalgety–Shannons Flat association correlate with the presence of magnetite in these granitoids [*Whalen,* 1981], and they are relatively oxidized. The Laidlaw Suite shares these characteristics. Despite these similarities the volcanics do not precisely correspond to the granitoids as they do in the Hawkins and Goobarragandra Suites. Relative to the Dalgety–Shannons Flat association the Laidlaw Suite has higher Ca, Sr, Ba, Ce and La and lower K, Rb and Y. SiO_2 is also rather low (Figure 4). The low K and Rb are probably in part due to the removal of groundmass material as volcanic dust during eruption [*Sparks and Walker,* 1977], as all samples analyzed are crystal-rich ignimbrites. This argument is strengthened by the fact that Rb has been depleted relative to K. The higher Ca, Sr, Ba and light rare earths and lower SiO_2 and Y are more likely to be related to differences in the source rocks.

Discussion

There is almost perfect matching of the chemistry of the Hawkins Suite with the Cootralantra–Clear Range granitoid association and the Goobarragandra Suite with the Maragle-Young granitoid association. They can therefore be each grouped together as volcanoplutonic associations. The only detectable differences between these two associations are the much higher Na, slightly higher Ca and Sr and lower K and Rb for the western Goobarragandra-Maragle-Young association. No other elements show any differences between the two associations. The differences can be attributed to more plagioclase of a more sodic type and less K-feldspar in the source for the western association. Alternatively, postgranitoid metamorphism of the western suite might possibly have enriched both the western granitoids and volcanics in Na and removed K and Rb. If this was the case then the only difference between the sources for the two associations would be more plagioclase in the western source. As the Goobarragandra Suite is the most highly altered of the three suites studied here, and prehnite-pumpellyite alteration has been reported in plutons of the Young Batholith [*Owen and Wyborn,* 1979] the latter alternative is preferred.

The Hawkins Suite has a classic S-type character as defined by *Chappell and White* [1974], being low in Na and high in Al/(Ca + Na + K). The higher plagioclase in the source, lower Al/(Ca + Na + K), and slightly less aluminous nature as indicated on the ACF diagram (Figure 6) for the Goobarragandra Suite indicate that chemical weathering of the source sediments was not as complete as for the source sediments for the Hawkins Suite. The sources for the Dalgety–Shannons Flat granitoid association and the even more extreme Laidlaw Suite show even less evidence of surface processes effecting them. The Laidlaw Suite must have been derived from immature feldspathic sediments. Despite this immaturity the source can still be recognised as being sedimentary and not igneous.

CONCLUSIONS

The Hawkins, Goobarragandra and Laidlaw volcanic suites were all derived by partial melting of metasedimentary rocks in the crust. Each suite is distinct in mineralogy and geochemistry, being derived from very mature, mature and immature sediments respectively. The first two suites compositionally match associated S-type granitoids, but granitoids of the Dalgety–Shannons Flat association, though derived from relatively immature sediments, cannot be matched with the third (Laidlaw) suite. The main differences between the suites are in the elements present in feldspars. S-type suites derived from immature sediments are richer in Ca, Na and Sr and have lower K, Rb and Al/(Ca + Na + K) than S-type suites derived from mature sediments.

The Hawkins Suite has a phenocryst mineralogy of quartz + plagioclase + biotite + orthopyroxene + cordierite + garnet + ilmenite + magnetite. It was derived from metasediments at 5–6 kbar and 800°C and extruded before these minerals could undergo low-pressure equilibration. Although these minerals are called phenocrysts they are regarded as restite phases and were never actually incorporated into the melt. Quartz, plagioclase and biotite were in excess in the source rocks dur-

ing partial melting. Orthopyroxene and cordierite were both relict metamorphic minerals and products of incongruent melting reactions. Garnet was relict metamorphic. Biotite and orthopyroxene were compatible mineral phases over a divariant field at the conditions of melting.

The Goobarragandra Suite has a phenocryst mineralogy of quartz + plagioclase + biotite + orthopyroxene + cordierite + ilmenite. It was probably derived under similar conditions to the Hawkins Suite, but reequilibrated at low pressure before extrusion. During this reequilibration plagioclase (An_{20-25}) and quartz crystallized from the magma.

The Laidlaw Suite has the phenocryst mineral assemblage quartz + plagioclase + sanidine + biotite + orthopyroxene + allanite + magnetite + ilmenite. Being slightly younger than the Hawkins Suite and occurring in the same area it must have been derived during the same crustal melting event from sediments beneath the Hawkins Suite and therefore it pressures greater than 5–6 kbar. The minerals reequilibrated to lower pressures and temperatures before extrusion, and during this reequilibration quartz, plagioclase (An_{35}) and sanidine (Or_{70-75}) crystallized from the melt. Sanidine was not a restite phase and quartz also might not have been. Conditions during reequilibration were $T = 725°–730°C$, $fO_2 = 10^{-15.5}$–10^{-14} bars, $f(H_2O) \doteq 2$–2.5 kbar. It is unlikely that before reequilibration the magma became saturated in water and lost a fluid phase as then the anhydrous mineral orthopyroxene would be unlikely to be a phenocryst phase. Thus the magma must have been quite undersaturated in water at its source ($P(H_2O) \doteq 2$ kbar, $P_{total} \geq 6$ kbar).

Oxygen fugacities were highest in the Laidlaw Suite and lowest in the Goobarrangandra Suite. Mafic silicate mg, biotite TiO_2 and ilmenite MnO were sensitive to these differing oxygen fugacities. The high mg for biotite and orthopyroxene in the Laidlaw Suite can also be attributed to a lack of equilibration with cordierite. Low Al in biotites and low Al and high Ca in orthopyroxenes from the Laidlaw Suite could depend on source rock composition. Variations in $mg^{biotite}$ and $mg^{orthopyroxene}$ ranging from $mg^{biotite} > mg^{opx}$ in the Hawkins Suite, through $mg^{biotite} \leq mg^{opx}$ in the Laidlaw Suite to $mg^{biotite} < mg^{opx}$ in the Goobarrangandra Suite may be pressure dependent at roughly equal temperatures.

Acknowledgments. The authors would like to thank D. R. Wones, M. Owen, and L. A. I. Wyborn for useful discussions; Z. Wasik, R. Freeman, and E. Webber for assistance in geochemical analyses; and N. G. Ware for assistance with electron probe analyses. The manuscript benefited considerably from comments by P. L. Williams and an anonymous reviewer. This paper is published with permission of the Director, Bureau of Mineral Resources.

REFERENCES

Beams, S. D., Magmatic evolution of the Southeast Lachlan Fold Belt, Australia, Ph. D. thesis, Aust. Nat. Univ., Canberra, 1980.

Buddington, A. F., and D. H. Lindsley, Iron-titanium oxide minerals and synthetic equivalents, *J. Petrol., 5,* 310–357, 1964.

Chappell, B. W., Petrogenesis of the granites at Moonbi NSW, Ph.D. thesis, Aust. Nat. Univ., Canberra, 1966.

Chappel, B. W., and A. J. R., White, Two contrasting granite types, *Pac. Geol., 8,* 173–174, 1974.

Compston, W., and B. W. Chappell, Sr-isotope evolution of granitoid source rocks, in *The Earth, Its Origin, Structure and Evolution,* edited by M. W. McElhinny, Academic, New York, 1979.

Czamanske, G. K., and P. Mihalik, Oxidation during magmatic differentiation, Finnmarka Complex, Oslo area, Norway, 1, The opaque oxides, *J. Petrol., 13,* 493–509, 1972.

Dahl, P. S., The *P-T-X* dependence of Fe^{2+}-Mg distributions between coexisting garnet and pyroxene, with applications to geothermometry, *Geol. Soc. Am. Abstracts Programs, 12,* 409–410, 1980.

Ellis, D. J., Osumilite-sapphirine-quartz granulites from Enderby Land, Antarctica: *P-T* conditions of metamorphism, implications for garnet-cordierite equilibria and the evolution of the deep crust, *Contrib. Mineral. Petrol., 74,* 201–210, 1980.

Ferry, J. M., and F. S. Spear, Experimental calibration of the partitioning of Fe and Mg between biotite and garnet, *Contrib. Mineral. Petrol., 66,* 113–117, 1978.

Grant, J. A., Phase equilibria in high grade metamorphism and partial melting of pelitic rocks, *Am. J. Sci., 273,* 289–317, 1973.

Grant, J. A., Orthoamphibole and orthopyroxene relations in high grade metamorphism, *Geol. Soc. Am. Abstracts Programs, 10,* 411, 1978.

Griffen, T. J., A. J. R. White, and B. W. Chappell, The Moruya Batholith and a comparison of the chemistry of Moruya and Jindabyne Suites, *J. Geol. Soc. Aust., 25,* 235–247, 1978.

Henderson, G. A. M., Geology of Canberra, Queanbeyan and environs, geological sheet, scale 1:50,000, Bur. of Miner. Resour., Canberra, Australia, 1980.

Hensen, B. J., and D. H. Green, Experimental study of the stability of cordierite and garnet in pelitic compositions at high pressures and temperatures, III, Synthesis of experimental data and geological applications, *Contrib. Mineral. Petrol., 38,* 151–166, 1973.

Hoffer, E., and J. A. Grant, Experimental investigation of the formation of cordierite-orthopyroxene parageneses in pelitic rocks, *Contrib. Mineral. Petrol., 73,* 15–22, 1980.

James, R. S., and D. L. Hamilton, Phase relations in the system $NaAlSi_3O_8$-$KAlSi_3O_8$– $CaAl_2Si_2O_8$–SiO_2 at 1 kilobar water vapour pressure, *Contrib. Mineral Petrol., 21,* 111–141, 1969.

Johnston, R. M., The geology of the Yass-Binalong area, B.S. thesis, Aust. Nat. Univ., Canberra, 1979.

Link, A. G., and E. C. Druce, Ludlovian and Gedinnian conodont stratigraphy of the Yass Basin, New South Wales, *Bull. Bur. Miner. Resour., 134,* 1972.

Lonker, S. W., Conditions of metamorphism in high-grade pelitic gneisses from the Frontenac Axis, Ontario, Canada, *Can. J. Earth Sci., 17,* 1666–1684, 1980.

Lonker, S. W., The *P-T-X* relations of the cordierite-garnet-sillimanite equilibrium, *Am. J. Sci.,* in press, 1981.

Newton, R. C., and B. J Wood, Thermodynamics of water in cordierite and some petrologic consequences of cordierite as a hydrous phase, *Contrib. Mineral. Petrol., 68,* 391–405, 1979.

Norrish, K., and B. W. Chappell, X-ray fluorescence spectrometry, in *Physicial Methods in Determinative Mineralogy,* edited by J. Zussman, pp. 201–272, Academic, New York, 1977.

Owen, M., and D. Wyborn, Geology and geochemistry of Tantangara and Brindabella 1:100,000 sheet areas, New South Wales and Australian Capital Territory, *Bull. Bur. Miner. Resour., 204,* 1979.

Powell, R., *Equilibrium Thermodynamics in Petrology—An Introduction,* Harper and Row, New York, 1978.

Powell, R., and M. Powell, Geothermometry and oxygen barometry using coexisting iron-titanium oxides: A reappraisal, Mineral. Mag., 41, 257–263, 1977.

Reed, S. J. B., and N. G. Ware, Quantitative electron microprobe analysis of silicates using energy-dispersive X-ray spectrometry, *J. Petrol., 16,* 499–579, 1975.

Robie, R. A., P. M. Bethke, and K. M. Beardsley, Selected X-ray crystallographic data, molar volumes, and densities of minerals and related substances, *Geol. Surv. U.S. Bull., 1248,* 1967.

Roddick, J. C., and W. Compston, Radiometric evidence for the age of emplacement and cooling of the Murrumbidgee Batholith, *J. Geol. Soc. Aust., 23,* 223–233, 1976.

Sparks, R. S. J., and G. P. L. Walker, The significance of vitric-enriched air-fall ashes associated with crystal-enriched ignimbrites, *J. Volcanol. Geotherm. Res., 2,* 329–341, 1977.

Stormer, J. C., Jr., A practical two feldspar geothermometer, *Am Mineral., 60,* 667–674, 1975.

Tuttle, O. F., and N. L. Bowen, Origin of granite in the light of experimental studies in the system $NaAlSi_3O_8$-$KAlSi_3O_8$-SiO_2-H_2O, *Geol. Soc. Am. Mem., 74,* 1958.

Van Reenen, D. D., and M. C. Du Toit. The reaction garnet + quartz = cordierite + hypersthene, in granulites of the Limpopo Metamorphic Complex in Northern Transvaal, in *Mineralization in Metamorphic Terrains, Spec. Publ. 4,* edited by W. J. Verwoerd, pp. 149–177, Geological Society of South Africa, Johannesburg, 1978.

Walker, G. P. L., Crystal concentration in ignimbrites, *Contrib. Mineral. Petrol., 36,* 135–146, 1972.
Whalen, J. B., Opaque mineralogy and mafic mineral chemistry of I- and S-type granitoids of the Lachlan Mobile Zone, southeast Australia, *J. Geol. Soc. Aust.,* in press, 1981.
White, A. J. R., and B. W. Chappell, Ultrametamorphism and granitoid genesis, *Tectonophysics, 43,* 7–22, 1977.
White, A. J. R., I. S. Williams, and B. W. Chappell, Berridale, New South Wales, geological sheet, scale 1:100,000, Geol. Surv. of New South Wales, Sydney, 1976.
Williams, I. S., W. Compston, B. W. Chappell, and T. Shirahase, Rb-Sr age determinations on micas from a geologically controlled, composite batholith, *J. Geol. Soc. Aust., 22,* 497–505, 1976.
Winkler, H. G. F., M. Boese, and T. Marcopoulos, Low temperature granitic melts, *N. Jb. Miner. Mh., 6,* 245–268, 1975.
Wones, D. R., Stability of biotite—A reply, *Am. Mineral., 57,* 316–317, 1972.
Wones, D. R., A re-examination of the significance of sphene-magnetite-quartz assemblages in granitic rocks, *Am. Mineral.,* in press, 1981.
Wones, D. R., and H. P. Eugster, Stability of biotite: Experimental theory and application, *Am. Mineral., 50,* 1228–1272, 1965.

(Received February 13, 1981;
revised April 20, 1981;
accepted May 8, 1981.)

JOURNAL OF GEOPHYSICAL RESEARCH, VOL. 86, NO. B11, PAGES 10349-10364, NOVEMBER 10, 1981

CALDERAS IN THE PRECAMBRIAN TERRANE OF THE ST. FRANCOIS MOUNTAINS, SOUTHEASTERN MISSOURI

J. Ronald Sides

Department of Geology, University of Texas at Arlington, Arlington, Texas 76019

M. E. Bickford, R. D. Shuster, and R. L. Nusbaum

Department of Geology, University of Kansas, Lawrence, Kansas 66045

Abstract. Precambrian igneous rocks in the St. Francois Mountains of southeastern Missouri consist of silicic volcanic rocks, mostly ash flow tuff, which crop out mostly in the western and southwestern part of the region, and epizonal granitic plutons which are mostly exposed in the northeastern part of the area. These relations suggest that the exposures in the northeast are of a somewhat deeper part of the crust and that rocks there are now exposed because of west-southwesterly tilting and beveling by erosion. In the eastern St. Francois Mountains the occurrence of a thick rhyolitic ash flow tuff, Grassy Mountain ignimbrite, and its distribution relative to a large, high-silica pluton, Butler Hill granite, suggest that the ash flow is the principal eruptive material of a caldera, the Butler Hill caldera, and that Butler Hill granite is the frozen magma chamber that was originally beneath it. Structural relations indicate that Butler Hill granite was emplaced into the volcanic rocks of the caldera during resurgent doming. Four small low-silica plutons, Silvermine, Stono, Knoblick, and Slabtown granites, are distributed peripherally to the Butler Hill granite and are interpreted as ring plutons emplaced along the ring fracture of the caldera or along arcuate intracaldera faults, after resurgent doming and emplacement of Butler Hill granite. More than 3 km of silicic volcanic rocks occupy a basinal structure in the western St. Francois Mountains. These rocks lie with angular unconformity upon up-domed older rocks of the Butler Hill caldera along an arcuate zone of megabreccia and disturbed structure on the western margin of the older caldra. This feature is interpreted as the topographic wall of a second caldera which lies to the west. The occurrence of the thick Taum Sauk rhyolite stratigraphically about 3 km higher than the rocks involved in the megabreccias may indicate that there was yet another caldera formed in this western part of the St. Francois Mountains.

Introduction

Regional Setting

The St. Francois Mountains are located about 160 km south of St. Louis in southeastern Missouri. A location map is included on Plate 1 a geologic map of the area. This hilly region, located at the structural apex of the Ozark Uplift, exposes a well-preserved terrane of Precambrian silicic volcanic rocks and associated granitic plutons. The volcanic rocks are mostly rhyolitic in composition, although quartz latite, trachyte, and minor andesite are also present [Tolman and Robertson, 1969; E. B. Kisvarsanyi, 1979; Pratt et al. 1979]. Diagnostic volcanic features such as crushed pumice fragments, shard structures, and eutaxitic texture are well-preserved despite the age of these rocks which were mostly formed 1485 m.y. ago [Bickford and Mose, 1975]. Intrusive rocks are mostly granite and can be seen to intrude earlier volcanic rocks wherever contacts are exposed. Minor volumes of mafic rocks, occurring as small gabbroic sills and diabasic dikes, intrude all other crystalline rocks and are thus the products of the most recent Precambrian igneous event [Amos and Desborough, 1970].

Hills in the St. Francois Mountains rise as much as 250 m above valleys and are composed of igneous rocks, whereas valleys are filled with Upper Cambrian sedimentary rocks. Where the nonconformable contact between sedimentary rocks and Precambrian igneous rocks is exposed at lower elevations, it is typically with the Upper Cambrian Lamotte sandstone, but at higher elevations the somewhat younger Bonnterre formation or younger formations rest upon the Precambrian. These relations indicate that there was a period of erosion, during which considerable relief was developed, prior to the deposition of the Lamotte sandstone in Late Cambrian time. The present landscape is largely an exhumed pre-Late Cambrian terrain.

In the St. Francois Mountains some 900 km^2 of Precambrian rocks are exposed. This exposure is by far the largest in the central part of the continent, and forms an important 'window' on a much larger subsurface terrane of rocks of similar age and petrography that extends from northern Ohio to the Texas Panhandle [Lidiak et al., 1966; Muehlberger et al., 1966; Bickford and Lewis, 1979; Van Schmus and Bickford, 1981; R. E. Denison et al., manuscript in preparation, 1981; Bickford et al., 1981].

Previous Work

Although Schoolcraft [1819] published the first study of the St. Francois Mountains and Haworth [1894] described the igneous rocks, the first complete geologic map of the region was that of Tolman and Robertson [1969]. Important contributions were made by R. E. Anderson [1963, 1970], who mapped the region around Taum Sauk Mountain (Plate 1) and recognized that the thick accumulation of volcanic rocks there was mostly ash flow tuff. Berry [1970, 1976] extended R. E. Anderson's mapping and established a consistent stratigraphy for parts of the western St. Fran-

Copyright 1981 by the American Geophysical Union.

Paper number 1B0892.
0148-0227/81/001B-0892$01.00

cois Mountains. J. E. Anderson et al. [1969] mapped arcuate faults in the western St. Francois Mountains and proposed that they were the bounding faults of a caldera that they called the Taum Sauk caldera. Important contributions to the geology of the eastern St. Francois Mountains have been made by Sides [1978], Shuster [1978], Scully [1978], and Nusbaum [1980].

The ages of rocks in this area were determined by Bickford and Mose [1975] on the basis of measurement of the Rb-Sr system in whole-rock samples and of the U-Pb system in separated zircons; all samples studied yielded zircon U-Pb ages of 1485 m.y. (recalculated to the decay constants recommended by Steiger and Jäger [1977]) except the Munger granite porphyry which occurs in the western St. Francois Mountains and yielded an age of 1380 ± 12 m.y. Rb-Sr ages determined in this study were all significantly lower, an effect attributed by the authors to loss of radiogenic Sr from the rock samples. A detailed geochemical study of samples from the St. Francois Mountains was made by E. B. Kisvarsanyi [1961, 1972], and G. Kisvarsanyi [1966] has studied the geochemistry of these rocks with respect to iron mineralization. Numerous thesis studies in the St. Francois Mountains have also contributed to our present understanding of this region. These are summarized by Bickford and Mose [1975] and will not be listed here.

Sources of Data and Goals of This Paper

The geologic map that accompanies this paper (Plate 1) is based upon mapping by the authors and other students at the University of Kansas as follows: Lake Killarney quadrangle, Sides [1978]; Iron Mountain Lake quadrangle, Nusbaum [1980]; Wachita Mountain and northern portion of Rhodes Mountain quadrangles, M. E. Bickford and J. R. Sides (previously unpublished); portions of Graniteville and Ironton quadrangles, Berry [1970]. Additionally, we have drawn upon the excellent mapping of R. E. Anderson [1970] in parts of the Taum Sauk area and the regional maps of Tolman and Robertson [1969]. The sources of data for the geologic map (Plate 1) are also shown graphically as an inset with the legend of the map.

The purpose of this paper is to present the results of our field and petrographic studies and some descriptive aspects of our chemical studies and to interpret these features in terms of the great body of data on the origin of collapse calderas and their associated pyroclastic deposits that has accumulated since 1960 [Smith, 1960a, b; Ross and Smith, 1961; Smith and Bailey, 1966; Ratté and Steven, 1967; Lipman et al., 1966; Lipman, 1976; Steven and Lipman, 1976; Bailey et al., 1976; and numerous others]. In two other papers in this volume [Bickford et al., this issue; Cullers et al., this issue] we present the results of an extensive study of the major and trace element chemistry of rocks from the St. Francois Mountains with an interpretation of the origin of the parental magmas and their evolution to form the suite of plutonic and volcanic rocks that are now observed.

Volcanic Stratigraphy

The determination of stratigraphic relationships in any volcanic terrane is difficult because of the variable lateral extent and thickness of the deposits and because deposits may be introduced from multiple sources. In the Precambrian terrane of the St. Francois Mountains these difficulties are compounded by limited exposures and varying degrees of silicification and alteration. Most of the stratigraphy presented here is the result of the studies of R. E. Anderson [1970] and Berry [1970, 1976], who established stratigraphic relationships in the western St. Francois Mountains. Stratigraphy in the eastern part of this region has been established mainly through the studies of Sides [1978] and Nusbaum [1980]. The stratigraphic sequence of volcanic rocks in the mapped portions of the St. Francois Mountains is given in Table 1. It is beyond the scope and purpose of this paper to give detailed petrographic descriptions of all of the volcanic units that we have studied in the St. Francois Mountains; these descriptions are available in the referenced publications, most of which are theses. Modal data for selected samples and chemical data for samples analyzed for major elements are given in another paper in this volume [Bickford et al., this issue] and will not be presented here, although important mineralogical and chemical aspects of these rocks will be mentioned where appropriate. What follows are brief descriptions of the major volcanic units.

Lake Killarney Formation

This unit is the oldest known rock mass exposed in the St. Francois Mountains. It is at least 390 m thick and consists of at least two ash flow sheets, one or two rhyolitic lava flows, and minor intercalated volcaniclastic sedimentary rock units. Most of the Lake Killarney formation is porphyritic dark-maroon ash flow tuff with phenocrysts of quartz and pink perthite. Locally, the rock has abundant crushed pumice fragments, and rarely it displays autobreccia and lithophysae. Microscopically, the matrix consists of a granular aggregate of quartz and feldspar; quartz phenocrysts are embayed, euhedral crystals or fragments, and feldspar phenocrysts are euhedral to fragmental and perthitic. Plagioclase as small crystals and lithic fragments both occur rarely.

The formation has a persistent unit, the Anderson Mountain member, in its uppermost part that consists of coarse fragmental tuff, coarse breccia, or both. The fragmental tuff consists of a fine-grained matrix of quartz and feldspar with larger crystal fragments of quartz and perthite. The breccia consists of rounded to angular clasts of silicic volcanic rocks in a fine quartzo-feldspathic matrix; clasts range from a few millimeters to as large as 30 cm in diameter, but the approximate mean diameter is 5 to 10 cm. Clasts make up from 25 to 75% of the rock. In one outcrop the Anderson Mountain member exhibits crude bedding, but in most other exposures it is apparently unsorted and unstratified.

Grassy Mountain Ignimbrite

This unit is a thick and very uniform ash flow tuff that occurs in the eastern St. Francois Mountains (Plate 1). On Kelley Mountain, in the

TABLE 1. Stratigraphy and Volcanic Rocks in the St. Francois Mountains

Proposed Stratigraphy	Description	Thickness, m
Cope Hollow formation[1]	rhyolitic ash flow, volcaniclastic sedimentary rock unit, basaltic flow	42
Johnson Shut-Ins rhyolite[1]	rhyolitic ash flow tuff and intercalcated volcaniclastic sedimentary rocks	55
Proffit Mountain formation[1]	rhyolitic ash flow tuff with minor air fall tuff and volcaniclastic sedimentary rocks	138
Taum Sauk rhyolite[1]	rhyolitic ash flow tuff	>1000
Royal Gorge rhyolite[1]	rhyolite lava flow	0-700
Bell Mountain rhyolite[1]	rhyolitic air fall tuff	25
Wildcat Mountain rhyolite[1]	rhyolitic ash flow tuff	90
Lindsey Mountain rhyolite[1]	rhyolitic ash flow tuff	500-700
Ironton rhyolite[1]	rhyolitic ash flow tuff	340
Buck Mountain Shut-Ins formation[1]	andesitic lava flow	80-1000
Pond Ridge rhyolite[1]	rhyolitic ash flow tuff	130
Cedar Bluff rhyolite[1]	rhyolitic ash flow tuff	580
Shepherd Mountain rhyolite[1]	rhyolitic ash flow tuff	600
Unit 690[2]	dacitic lava flow	>610
Ironton Hollow rhyolite[4]	rhyolitic lava flow	>130
Wolf Mountain ignimbrite[3]	rhyolitic ash flow tuff	160
Tribby breccia[3]	rhyolitic ash flow breccia	200
Iron Mountain Lake felsite[3]	rhyolitic ash flow tuff	300
	Angular Unconformity	
Grassy Mountain ignimbrite[4]	rhyolitic ash flow tuff	~1000
Lake Killarney formation[4]	rhyolitic ash flows, breccias, and intercalated volcaniclastic sedimentary rocks	>390

Sources: 1. Berry [1976]. 2. Berry [1970]. 3. Nusbaum [1980]. 4. Sides [1978].

southeastern part of the Lake Killarney quadrangle, Grassy Mountain ignimbrite is at least 1000 m thick. The rock is very distinctive. consisting of abundant phenocrysts of quartz and salmon-colored perthite in a dark-maroon to black matrix. Crushed pumice fragments are generally quite rare, although they are locally abundant.

Microscopically, the matrix is a granular aggregate of quartz and feldspar which rarely preserves the structure of flattened shards. Quartz phenocrysts are 1 to 2.5 mm in diameter and commonly show hexagonal outlines that are deeply embayed. Perthite phenocrysts occur both as fragments and as euhedral crystals 1 to 5 mm in diameter. A blue-green amphibole is common as rounded aggregates or tiny needles in the matrix, particularly in the upper 200 m of the unit. Lithic fragments are rare and include older ash flow tuff, granophyre, and basalt or diabase.

Besides its thickness and distinctive mineralogy and texture, two features of Grassy Mountain ignimbrite are important. First, is its uniformity through great thickness. Shuster [1978] examined two thick sections of Grassy Mountain for petrographic and chemical variations and found none. One of these sections, located in the long road cut at Stout's Creek Shut-Ins on Missouri Highway 72 about 7.4 km east of Arcadia (Plate 1) is continuously exposed through 240 m of Grassy Mountain with almost vertically dipping compaction foliation. No physical or textural breaks are evident in this section. A second important feature of Grassy Mountain ignimbrite is that its matrix is everywhere granular and does not show the well-developed eutaxitic texture that characterizes many of the thinner ash flow tuff units higher in the section, such as the Lindsey Mountain, Russell Mountain, and Wildcat Mountain rhyolites. The lack of penetrative deformation and scarcity of even low-grade metamorphic minerals, such as chlorite and epidote in Grassy Mountain ignimbrite, suggest that the granular matrix is a primary feature caused by devitrification of an originally glassy matrix that was facilitated by retention of heat, and possibly volatiles, in this thick unit.

Sequence Iron Mountain Lake Felsite Through Ironton Hollow Rhyolite

This sequence of volcanic rock units lies with apparent angular unconformity upon tilted and deformed rocks of Grassy Mountain ignimbrite and Lake Killarney formation along a zone extending from near Iron Mountain south to Ironton (Plate 1). The sequence is apparently generally concordant and dips to the southwest at 12° to 20°.

Iron Mountain Lake felsite is a homogeneous welded ash flow tuff breccia. Its matrix is uniformly black because of extensive replacment by iron oxides, but its eutaxitic texture and abundant flattened pumice fragments clearly indicate its ash flow origin. Lithic fragments are quite abundant, consist of rhyolitic ash flow tuff, altered basaltic rocks, and graphic granite, and are generally about 2 cm in diameter. Phenocrysts, which consist of epidotized plagioclase, quartz, and chloritized hornblende, are not abundant.

Tribby breccia is a thin (about 200 m thick) ash flow breccia that has intercalated volcan-

iclastic sedimentary units. The rock consists of quartz and plagioclase phenocrysts in a generally granular quartz-feldspar matrix. Flattened pumice fragments with a length-to-thickness ratio of about 4 to 1 are present, indicating that the unit was emplaced as an ash flow. Lithic fragments include rhyolitic ash flow tuff that megascopically resembles Grassy Mountain ignimbrite and mafic fragments that are basalt with trachytic or diabasic textures. Tribby breccia may be observed in contact with steeply tilted Grassy Mountain ignimbrite. At such contacts, Grassy Mountain is oxidized for several meters and microscopically appears to be somewhat recrystallized.

Ironton Hollow rhyolite is a series of rhyolitic lava flows, locally autobrecciated; the unit also includes a breccia which may be a lahar. Most of Ironton Hollow rhyolite can be described as a dark-maroon porphyritic rock consisting of quartz and plagioclase phenocrysts in a matrix of fine granular quartz and feldspar. Flow lineation and flow banding are commonly observed on weathered surfaces, as are angular autoclasts. Lithophysae are also abundant locally. The volcaniclastic sedimentary hematite at Pilot Knob [Tolman and Robertson, 1969; Sides, 1978] lies within or just above Ironton Hollow rhyolite. Elsewhere a thin, crystal-rich ash flow tuff which Nusbaum [1980] called Wolf Mountain ignimbrite overlies Tribby breccia, and at still other localities 'Unit 690' of Berry [1970] overlies Tribby breccia. Thus the stratigraphic level mostly occupied by Ironton Hollow rhyolite is clearly complex and most or all of the units described here are probably discontinuous laterally.

Sequence 'Unit 690' Through Russell Mountain Rhyolite

The sequence of lava and ash flow to be described here includes the lower units described by Berry [1970, 1976]. Rocks of this sequence dip to the southwest at about 15° and are probably conformable with the sequence of rocks just described, Iron Mountain Lake felsite through Ironton Hollow rhyolite. The contact between Ironton Hollow rhyolite or Tribby breccia and Unit 690 is not exposed and is evidently buried beneath lower Paleozoic sedimentary rocks or recent alluvium in the region between Middlebrook and Pilot Knob (Plate 1).

The petrography of the rocks in this sequence has been described by Berry [1970, 1976] and by Berry and Bickford [1972], who concluded that variations in mineralogy of these rocks indicated derivation from a single differentiating magma chamber. Details of petrography will not be given here, but the sequence varies upward from dacite with only plagioclase phenocrysts ('Unit 690') to rhyolitic ash flow tuff containing phenocrysts of quartz, alkalic feldspar, and minor plagioclase (Russell Mountain rhyolite). It is of interest that the Buck Mountain Shut-Ins formation, which occurs near the middle of this sequence, is one of the very rare andesites that occur in the St. Francois Mountains. Berry and Bickford [1972] suggested that this flow might have been the result of magma withdrawal from the bottom of a proposed differentiating chamber, but it is also possible that it was erupted from a separate source.

Sequence Wildcat Mountain Rhyolite Through Royal Gorge Rhyolite

Wildcat Mountain rhyolite [Berry, 1976] is a distinctive unit that is 90 m thick. It is a deep maroon rhyolitic ash flow tuff that is characterized by abundant small (about 2 to 3 cm in average diameter and a few millimeters in thickness) flattened pumice fragments. Phenocrysts include euhedral to anhedral perthite, strongly corroded quartz, and rare magnetite or ilmenite crystals, all set in a matrix that varies from microeutaxitic to granular. In some samples the outlines of shards can be seen in plane light, although devitrification has destroyed the original glassy shards.

Bell Mountain rhyolite is one of the most distinctive units in the whole region and has served as a major stratigraphic marker. The unit is mostly bedded air fall tuff that is about 25 m thick and contains a conspicuous zone of lithophysae that is 2 to 5 m thick. The tuff may be crossbedded and consists of deformed shards and fine-grained pyroclastic material which display spherulitic intergrowths. Lapilli up to 20 mm in diameter are common but not abundant, making up 2 to 3% of the rock.

The lithophysal zone is quite resistant to weathering and is normally the best exposed part of this unit. The lithophysae range in size from a few millimeters to nearly 25 cm and consist of an outer shell of modified tuff with an interior filled with coarsely crystalline alkalic feldspar, quartz, fluorite, and magnetite or hematite.

Royal Gorge rhyolite is a rhyolitic lava flow consisting of a fine-grained maroon matrix of devitrified glass with about 5% of quartz and alkalic feldspar phenocrysts. The characteristic feature of this flow, which ranges in thickness from a few meters to more than 700 m, is distinctive flow banding in its upper part. According to Berry [1970] the lower part of the flow is massive and is always present above the Bell Mountain rhyolite, whereas the flow-banded upper part is restricted to exposures on Russell Mountain and Taum Sauk Mountain. The flow banding consists of layers of recrystallized pumiceous material that is light pink in contrast to the maroon of the matrix. Bickford and Mose [1975] determined a U-Pb age of 1495 $\pm$ 6 m.y. from zircons separated from Royal Gorge rhyolite.

Taum Sauk rhyolite

Taum Sauk rhyolite is a widespread unit that occurs on Taum Sauk Mountain in the southwestern part of the mapped area (Plate 1) and to the west and southwest of there. The unit is between 850 and 1200 m thick according to Berry [1970, 1976] and R. E. Anderson [1970]. Mineralogically and chemically (see data of Bickford et al. [this issue]), Taum Sauk rhyolite is essentially identical with the Grassy Mountain ignimbrite. A minor, though significant, chemical difference is that the Taum Sauk rhyolite has greater weight percent K_2O (5.70 $\pm$ 0.59) than Grassy Mountain (4.51 $\pm$ 0.15) and less Na_2O (Taum Sauk = 2.54 $\pm$

0.69; Grassy Mountain = 3.66 ± 0.17). Other than these minor differences, rocks of these two units are quite similar, consisting of a black to maroon, fine-grained granular matrix of quartz and alkalic feldspar in which are abundant phenocrysts of corroded quartz and salmon-colored perthitic alkali feldspar. Both units have minor blue-green amphibole as tiny needles or granules in the matrix, particularly in the upper parts. Crushed pumice fragments are generally more abundant in the Taum Sauk than in Grassy Mountain.

Sequence Proffit Mountain Formation Through Cope Hollow Formation

This sequence includes the Proffit Mountain formation, the Johnson Shut-Ins rhyolite, and the Cope Hollow formation. These rocks are stratigraphically the highest known in the St. Francois Mountains. According to Berry [1976] the Proffit Mountain formation is about 139 m thick and includes at least two ash flow tuff sheets interrupted by a thin air fall tuff. Berry includes in the Proffit Mountain formation 22 m of volcaniclastic sedimentary rocks above the highest ash flow tuff, but Blades and Bickford [1976] called these rocks the 'Lower Swimming Hole Section.' The Johnson Shut-Ins rhyolite is about 55 m thick and consists of a lower rhyolitic ash flow tuff, a thin middle volcaniclastic sedimentary unit, and an upper rhyolitic ash flow tuff. These rocks have been described in considerable detail by Blades and Bickford [1976] and by Blades-Zeller [1980]. The highest unit in this sequence, the Cope Hollow formation is at least 50 m thick and consists of a lower, cross-bedded volcaniclastic rock, perhaps an air fall tuff or base surge deposit (9 m); a thin (5 m) rhyolitic ash flow tuff; a unit that is about 28 m thick and consists of an air fall tuff within which is interbedded a vesicular basalt flow of unknown thickness and extent; and a rhyolitic ash flow tuff of unknown total thickness.

Plutonic Rocks

Petrography and Chemistry

Exposed plutonic rocks in the St. Francois Mountains are granite except for the minor volumes of gabbro and diabase that occur as small sills and dikes [Amos and Desborough, 1970]. All of the granitic rocks have petrographic features suggesting emplacement under relatively low PH_2O and thus shallow crustal levels. These features include strongly perthitic alkalic feldspars, which are abundant in all of the plutons, and fine-grained to granophyric texture and miarolitic cavities, which occur in some of them. It is convenient to divide the granites, on the basis of their occurrence and major element chemical composition, into high silica granites (SiO_2 > 74 wt %; K_2O/Na_2O > 1.1; sum of wt % (CaO + MgO) < 0.9), low silica granites (SiO_2 = 66 to 70 wt %; K_2O/Na_2 < 1.0; sum of wt % (CaO + MgO) > 1.60), and granite porphyries of the Taum Sauk area (SiO_2 = 67 to 72 wt %; K_2O/Na_2O > 1.3; sum of wt % (CaO + MgO) = 0.70 to 1.50). Modal data and major element chemical data can be found in the paper by Bickford et al. [1981; this issue].

High Silica Granites

The major plutons in this group are the Butler Hill-Breadtray granite, the Brown Mountain rhyolite porphyry, and the Graniteville granite [Tolman and Robertson, 1969]. The Butler Hill and Breadtray granites were mapped as separate bodies by Tolman and Robertson, who described a gradational contact between them. For reasons summarized below, we believe that the Breadtray granite is the granophyric roof facies of the Butler Hill granite.

The Butler Hill granite pluton is a large, approximately circular mass that intrudes Grassy Mountain ignimbrite and Lake Killarney formation on the west, south, and east, and is overlain nonconformably on the north and northeast by lower Paleozoic rocks, most commonly the Lamotte sandstone (Upper Cambrian). Exposures in the northeastern part of the body are of a medium-to coarse-grained granite that has well-developed hypidiomorphic-granular texture and is composed of perthite, quartz, biotite, and plagioclase (about An_{14}); alkali amphibole is rare, and muscovite occurs in some samples. In many samples there are clearly two generations of quartz: one is early, euhedral, and sometimes partially resorbed, whereas the other is late and anhedral and molded around earlier feldspar crystals. Fluorite, apatite, and zircon are common accessory minerals. In the most extreme northeastern exposures, Butler Hill granite has well-developed rapakivi texture, with mantled alkali feldspar ovoids as large as 3 cm in diameter [Lowell and Sides, 1973]. This texture is rare in exposures more than 2 km southwest of the most northeasterly ones.

The grain size of the granite decreases gradually to the southwest, and its typically gray color changes to pink. Biotite decreases in abundance, but most samples contain a few shreds of chlorite. Feldspars are increasingly clouded and turbid to the southwest. In the extreme southwestern exposures, the rock is very fine-grained and distinctly granophyric in texture. These rocks, which are the typical Breadtray granite of Tolman and Robertson [1969], were designated the Breadtray facies of the Butler Hill granite by Sides [1980]. They consist of euhedral (but commonly partially resorbed) quartz phenocrysts, euhedral perthitic alkalic feldspar phenocrysts, and rare plagioclase phenocrysts, all in a matrix of granophyrically intergrown quartz and alkalic feldspar. Fluorite is a common accessory mineral in these rocks, also occurring in miarolitic cavities.

Nusbaum [1980] has shown that within the Breadtray facies, rocks with the most complete development of granophyric texture occur at the tops of hills, whereas rocks exposed at lower elevations have less well-developed granophyric textures to fine-grained granular textures. Miarolitic cavities are rather common within strongly granophyric rocks. These relationships suggest that the Breadtray facies was developed in the upper part of the magma body, presumably by loss of volatiles and pressure quenching of the melt. Thus, as will be discussed more fully in the next section of this paper, the gradational change of texture in the Butler Hill granite from northeast to southwest may reflect original

vertical changes in a body that has been tilted to the southwest after crystallization and then beveled by erosion. The chemical composition of the Butler Hill granite and its Breadtray facies show that the Breadtray is somewhat enriched in SiO_2 and K_2O, and depleted in Na_2O, Fe_2O_3, TiO_2, CaO, and MgO relative to the more typical Butler Hill. These chemical variations have been discussed by Sides [1978, 1980] and are compatible with vertical differentiation.

Brown Mountain rhyolite porphyry is a body of extremely fine-grained granite that is exposed to the south of the main mass of the Breadtray facies of the Butler Hill granite (Plate 1). The Brown Mountain is granophyric, at least in part, and consists of quartz and perthite phenocrysts in a reddish matrix of fine-grained quartz and feldspar. Mafic minerals are exceedingly rare to absent. Modal and chemical data are not available for this body, but from its mineralogy it appears to be similar to the granophyric rocks of the Breadtray facies.

Graniteville granite is exposed near the village of Graniteville in the west-central part of the St. Francois Mountains (Plate 1). Drill hole data indicate that it underlies much of the Bellview Valley to the west (not shown in Plate 1), where it is covered by Paleozoic sedimentary rocks [E. B. Kisvarsanyi, 1980]. Although there are only limited exposures of this body, it is evidently one of the major plutons of the terrane. Graniteville granite is similar to the Butler Hill granite in its major element chemistry and petrographic characteristics. Typical samples of Graniteville granite consist of plagioclase (An_{10}), microcline perthite, quartz, minor biotite (usually partially to completely chloritized), and primary muscovite. The most abundant accessory mineral is fluorite, which occurs as a late-crystallizing mineral in interstices along with chlorite and sometimes epidote; magnetite, apatite, and zircon also occur. Quartz commonly occurs as euhedral to subhedral crystals and was evidently the first phase to crystallize, followed by plagioclase, then alkalic feldspar (now perthite), and finally a late generation of quartz, biotite, muscovite, and fluorite. The occurence of microcline perthite in the Graniteville granite is the only real petrographic difference between it and the Butler Hill granite, in which perthite does not show microcline twinning.

Low Silica Granites

The plutons in this group include Knoblick, Silvermine, Slabtown, and Stono granites [Tolman and Robertson, 1969]. These bodies are notable in that they contain numerous xenoliths, whereas the high-silica granites rarely contain xenoliths. The xenoliths in the low-silica granites are commonly less than 4 cm in diameter and are conspicuously more mafic than the granites. Most of the xenoliths that we have studied petrographically are composed of plagioclase, perthite, quartz, biotite, and abundant elongate hornblende crystals; the texture suggests recrystallized igneous rocks. In most of these plutons, xenoliths are uniformly distributed, but in the Silvermine granite at least two xenolith swarms are exposed over areas of about 400 m^2. In these areas, xenoliths are larger (up to 30 cm in diameter) and much more abundant than elsewhere in the low-silica granites.

Exposures of the Silvermine granite are the most extensive of any of the low-silica plutons, extending about 4 km north-south and 8 km east-west (Plate 1); the actual shape of the pluton is not known because it is nonconformably overlain by the Lamotte sandstone (Upper Cambrian) to the northeast. The contacts of the Silvermine granite with country rocks are well exposed in many places; their linear trace across topography indicates that they dip steeply. Alteration of intruded rocks includes recrystallization, silicification, and pyritization, commonly extending as much as 100 m away from the contact. Locally, brecciation of country rocks is extensive, and there are numerous inclusions of them in the granite.

There are two principal textural types of the Silvermine granite, a medium-grained variant which is the most abundant in outcrop, and a fine-grained prophyritic type which caps cliffs along the St. Francis River (Plate 1) and is apparently a roof facies [Scully, 1978]. The medium-grained variety (average grain size = 1.5 mm) has a well-developed hypidiomorphic granular texture and is essentially composed of quartz, perthite, plagioclase (An_{14}), hornblende, and chlorite (after biotite). Sphene, magnetite, apatite, and zircon are accessory minerals, and chlorite and epidote are common alteration products. Plagioclase and hornblende crystallized early. Plagioclase is zoned and commonly embayed by perthite or quartz, minerals which show coarse graphic intergrowths in most samples. The fine-grained porphyritic variety is mineralogically similar to the medium-grained type except that hornblende is rare, occurring only in samples near the gradational boundary with the medium-grained rocks. Both plagioclase (An_{14}) and perthite occur as phenocrysts in a generally fine-grained matrix, and some samples show graphic intergrowths of quartz and alkalic feldspar. Scully [1978] has shown that the chemical composition of the fine-grained porphyritic variety is such that it could have been derived from the medium-grained variety by fractional crystallization of plagioclase, hornblende, biotie, and sphene. This model is further discussed by Bickford et al. [this issue].

We have not studied the Knoblick granite in as great detail as Silvermine granite. It is texturally and mineralogically similar to the medium-grained variety of Silvermine granite except that it is somewhat finer-grained (average grain size = 1.0 mm) and sphene is not as abundant; hand specimens of the two rocks cannot be distinguished. The chemical composition of Knoblick granite also shows that it is extremely similar to Silvermine granite [Davis, 1969; E. B. Kisvarsanyi, 1972; Bickford et al., 1981]. The contacts of Knoblick granite with the Lake Killarney formation are well-exposed (Plate 1), and inclusions of the intruded rock are common in the granite near contacts. It is of interest that a granitic dike can be traced from the main body of the granite through the Lake Killarney formation and into Grassy Mountain ignimbrite for about 1 km. The dike rock is porphyritic, with plagioclase phenocrysts in a fine-grained matrix,

GEOLOGIC MAP OF THE PRECAMBRIAN ROCKS OF THE CENTRAL ST. FRANCOIS MOUNTAINS, MISSOURI

TO ACCOMPANY "CALDERAS IN THE PRECAMBRIAN ST. FRANCOIS MOUNTAINS, SOUTHEASTERN MISSOURI"
BY J. R. SIDES, M. E. BICKFORD, R. D. SHUSTER, AND R. L. NUSBAUM

Plate 1. Geologic map of portions of the St. Francois Mountains, southeastern Missouri. Copies of this map at 1:62,500 may be obtained from the authors on request.

but mineralogically it is clearly the same as Knoblick granite. The radial orientation of this dike with respect to Knoblick granite suggests fracturing of country rock during emplacement in a shallow crustal environment. Slabtown granite is exposed in several relatively small outcrops in the southeastern part of the mapped area (Plate 1). In outcrop the rock appears quite fine-grained; in thin section the rock is distinctly granophyric, with phenocrysts of plagioclase (An_{14}) up to 1.5 mm in diameter in a matrix composed mostly of graphically to granophyrically intergrown quartz and perthite. Other essential minerals are hornblende and minor biotite. Both plagioclase and the mafic minerals are extensively altered, plagioclase to epidote and clay minerals and the mafic minerals to chlorite. Chlorite is so abundant that some samples show no primary biotite at all. Accessory minerals include magnetite, apatite, zircon, sphene, and allanite. Plagioclase and hornblende were evidently the first minerals to crystallize. Plagioclase is embayed where it is in contact with quartz and perthite.

Stono Granite is a fine-grained grey to brown rock that occurs as a small pluton located about halfway between the towns of Iron Mountain and Doe Run (Plate 1). The rock consists essentially of plagioclase (An_{14}), quartz, perthite, and hornblende. Plagioclase is euhedral to subhedral and extensively altered to kaolinite and epidote; it was evidently the first mineral to crystallize, probably along with hornblende which is also euhedral to subhedral. The presence of abundant chlorite suggests that the rock originally had significant amounts of biotite as a second mafic phase. Accessory minerals include ilmenite, associated with leucoxene, and apatite. Both plagioclase and perthite occur as phenocrysts set in a matrix that may be either graphic, with intergrowths of quartz and perthite, or granular, in which quartz occurs as an anhedral interstitial phase. The mafic inclusions mentioned earlier are particularly abundant in Stono granite, but in contrast to the hornblende-rich nature of the inclusions in Silvermine and Knoblick granites, they are usually granular, fine-grained, and composed of plagioclase, quartz, perthite, chlorite, and diseminated iron oxides.

Granite Porphyries of the Taum Sauk Area

These small intrusive bodies include the Munger granite porphyry and the Carver Creek granite porphyry of Tolman and Robertson [1969]. Both bodies have textural and other petrographic features suggestive of emplacement as hypabyssal intrusives.

The Munger granite porphyry is a fine-grained porphyritic rock. Quartz, microcline-perthite, and plagioclase make up the phenocrysts, which typically have diameters of about 3.5 mm (feldspars) to about 1.5 mm (quartz). The matrix averages about 0.2 mm in grain diameter and is composed of quartz, microcline-perthite, plagioclase, and chloritized biotite. Phenocrysts are mostly subhedral, whereas the matrix is allotriomorphic granular. Commonly, euhedral plagioclase phenocrysts are enclosed by phenocrystic perthite. Accessory minerals include apatite, magnetite, sphene, zircon, and a little fluorite. The Munger granite prophyry is extensively altered. Feldspars, particularly plagioclase, are altered to kaolinite, sericite, and epidote. Biotite and possibly small amounts of hornblende are extensively altered to chlorite; no unaltered hornblende was observed in thin section. Calcite was also observed as a fairly abundant alteration mineral.

The Carver Creek granite porphyry has been briefly described by Tolman and Robertson [1969], who state that it is fine-grained with a 'green and purple mottled groundmass' containing clusters of mafic minerals and large pink K-feldspar phenocrysts. They also described the groundmass as microgranitic and indicate that the accessory minerals include zircon, epidote, fluorite, apatite, and a little leucoxene. We have not studied the Carver Creek granite porphyry petrographically, but from the above description we believe that it is quite similar to Munger granite porphyry. The two granite bodies are very similar in major and trace element chemical compositions (see analytical data of Bickford et al.[1981] and Cullers and others [this issue].)

Age and Contact Relationships Among Plutonic and Volcanic Rocks

Everywhere that contacts are observed it is clear that the plutonic rocks are younger than, and intrude, the volcanic rocks of the St. Francois Mountains. BIckford and Mose [1975] indicated a U-Pb age of 1495 $\pm$ 6 m.y. for zircons from the Royal Gorge rhyolite, whereas most of the plutonic rocks they dated yielded ages of about 1485 m.y. Thus, the Royal Gorge is essentially the same age as the plutons, and it is clear that at least this volcanic unit was not erupted significantly earlier than crystalization of the granites. The available age data, field relationships, and chemical similarities between the volcanic rocks and the plutons [see Bickford et al., 1981, this issue] reinforce the suggestion made by earlier workers that the volcanic rocks are esentially comagmatic with the plutons and their eruption preceded emplacement of the plutons by a relatively short period of time.

Regional Distribution of Rock Types

An obvious feature of the distribution of rock types in the St. Francois Mountains is that plutonic rocks are mostly exposed in the northeastern part of the terrane, whereas the western and southwestern region is mostly underlain by volcanic rocks. We interpret this distribution as indicating that the rocks exposed are part of a more-or-less tabular complex of volcanic and associated plutonic rocks that have been tilted to the west-southwest and subsequently beveled by erosion [Bickford et al., 1977; Sides, 1977, 1980]. This conclusion is supported by the following observations (Plate 1):

1. The contact of the major pluton, the Butler Hill granite, with volcanic rocks appears to dip gently to the southwest in many places in the region between Ironton and Doe Run [Tolman and Robertson, 1969].

2. The only occurrence of coarse-grained granitic rocks occurs in the most northeasterly

exposures of the Butler Hill granite. The pluton is progressively finer-grained and more oxidized to the southwest. If these were originally vertical changes, the observed distribution would indicate southwesterly tilting and erosion. Sides [1980] has shown that chemical variations in the Butler Hill from northeast to southwest are consistent with differentiation in response to fractional crystallization, a mechanism which would be expected to produce vertical variations in composition, and has shown that the direction of tilting is about S68°W.

3. Grassy Mountain ignimbrite that is exposed in the eastern St. Francois Mountains has a notably more granular groundmass than that exposed farther to the west. This is consistent with the suggestion that the eastern rocks were originally deeper in the volcanic pile and were nearer to major magma bodies. The granular matrix in these rocks may have resulted from retention of heat following eruption of originally finer-grained, perhaps glassy material.

4. Allingham [1960] has shown that aeromagnetic anomalies across the contracts of the plutonic and volcanic rocks are best explained if the contact dips to the southwest.

The inferred southwesterly tilt is not critical to the identification of collapse calderas in the St. Francois Mountains. However, if the calderas exist, the inferred southwesterly tilt is consistent with a deeper level of exposure of the more easterly one (the Butler Hill caldera) than the more westerly one (the Taum Sauk caldera or calderas).

Critical to the interpretations to be made here is the occurrence of two thick ash flow tuff units, the Grassy Mountain ignimbrite in the eastern St. Francois Mountains and the Taum Sauk rhyolite in the west. Each of these rock units is about 1 km thick. Although structural and stratigraphic relationships indicate that Taum Sauk rhyolite is stratigraphically well above the Grassy Mountain and thus younger, the two rocks are petrographically similar. If one considers only the exposed portion of these ash flows, Grassy Mountain has a volume of at least 32 km^3 and Taum Sauk has a volume of at least 59 km^3; it is likely that both originally were rock volumes considerably in excess of 100 km^3. The eruption of such large volumes of magma must have resulted in the formation of collapse calderas.

The low-silica plutons (Silvermine granite, Stono granite, Knoblick granite, and Slabtown granite) are situated around the margins of the larger, high-silica Butler Hill granite (Plate 1). Although both Stono granite and Silvermine granite are in contact with Butler Hill granite, the contacts are not exposed well enough for intrusive relations to be determined. Silvermine granite, as noted earlier, intrudes Brown Mountain rhyolite prophyry, which we have interpreted to be a part of the Butler Hill because of their compositional similarity. We believe that the available data suggest that the low-silica plutons were emplaced later than the Butler Hill granite.

Finally, we call attention to the occurrence of a large mass of Grassy Mountain ignimbrite in the eastern part of the mapped area (Plate 1). At the northern end of this mass, Grassy Mountain apparently overlies Lake Killarney formation in normal stratigraphic position, and Lake Killarney is intruded by Knoblick granite. The map pattern suggests that Lake Killarney formation, which underlies Grassy Mountain ignimbrite, was dragged up as Knoblick granite was emplaced and is now exposed following erosion of an essentially domal structure. The large mass, or block, of Grassy Mountain is intruded by Butler Hill granite all along its western margin; this contact is quite well-exposed, and there is no question about the cross-cutting relation. Similarly, the block of Grassy Mountain is intruded on its eastern margin by Slabtown granite. The occurrence of this block of volcanic rocks in the eastern part of the St. Francois Mountains suggests that it has been downdropped in some way, since the general west-southwest tilt of the region should otherwise have caused it to be removed by erosion.

Structural Evidence for Calderas

Eastern St. Francois Mountains

We infer the existence of the Butler Hill caldera, a caldera in the eastern St. Francois Mountains, on the basis of six principal lines of evidence. These are (1) the great thickness, uniformity, and broad distribution of Grassy Mountain ignimbrite, (2) the occurrence of a large mass of Grassy Mountain ignimbrite and Lake Killarney formation on the eastern side of the Butler Hill granite pluton, (3) the orientation of flow direction indicators that show that the source of Grassy Mountain ignimbrite was in the region now occupied by Butler Hill granite [Sides, 1981], (4) the chemical similarity of Butler Hill granite and Grassy Mountain ignimbrite, (5) the presence of a zone along the western margin of the Butler Hill granite and the southwestern margin of the Brown Mountain rhyolite porphyry in which Lake Killarney formation and Grassy Mountain ignimbrite dip steeply away from the contacts, and (6) the distribution of the smaller, low-silica granite plutons peripherally around the Butler Hill. Specifically, these lines of evidence are as follows:

1. Grassy Mountain ignimbrite is very thick (at least 1 km thick on Kelley Mountain) and remarkably uniform. Shuster [1978] demonstrated that there are no chemical or mineralogical breaks in Grassy Mountain that might, if present, indicate the presence of multiple eruptive units. We believe that the eruption of such a large volume of magma (at least 32 km^3 and probably 100 km^3) must have formed a caldera. Grassy Mountain ignimbrite is therefore probably a major collapse ash flow tuff and its occurrence around the margins of Butler Hill granite suggests that the granite was emplaced at about the locus of the caldera. It is possible that the lithic-rich Lake Killarney formation is the product of an earlier phase of the caldera-forming eruptive event.

2. Grassy Mountain ignimbrite and Lake Killarney formation occur mainly on the western margin of the Butler Hill granite. Especially significant is exposure of these units in the eastern St. Francois Mountains (Plate 1) where Lake Killarney formation is intruded by the Knob Lick granite and Grassy Mountain ignimbrite is

intruded by Butler Hill granite. We suggest that these units were downfaulted into their present location during the collapse event. It is noteworthy in this regard that Grassy Mountain ignimbrite in these eastern outcrops has a groundmass that is significantly more granular than that exposed elsewhere. We suggest that this is because these rocks were near the base of a thick, caldera-filling sequence that was near the subjacent magmas and retained heat longer than other parts of the Grassy Mountain.

3. Sides [1981] has measured the orientation of phenocrysts in Grassy Mountain ignimbrite as indicators of flow direction. He found that flow directions are consistently radially away from the location of the Butler Hill granite, indicating that Grassy Mountain ignimbrite originated in that area.

4. As indicated by the chemical data given by Bickford, et al. [this issue], Butler Hill granite and Grassy Mountain ignimbrite are very similar in major element chemical composition. We suggest that Butler Hill granite is the frozen magma thay lay beneath the caldera and was not erupted.

5. In the area southwest of Roselle, Lake Killarney formation and Grassy Mountain ignimbrite dip away from the intrusive Brown Mountain rhyolite porphyry. This zone can be followed to the north-northwest where these units, particularly Grassy Mountain ignimbrite, are rotated to very high dips, locally vertical or overturned. We interpret this structure to be the result of resurgent doming of the Butler Hill caldera, probably at the time Butler Hill granite and Brown Mountain rhyolite porphyry were emplaced. We suspect that similar structure exists in the large block of Grassy Mountain along the eastern side of the Butler Hill granite, but we have been unable to find structural indicators (i.e., compaction foliation) in these rocks.

6. Finally, we note the occurrence of small, low-silica plutons around the periphery of Butler Hill granite. We suggest that these are ring plutons, perhaps the roots of former ring domes such as those in the Valles caldera [Smith et al., 1970] and the Long Valley caldera [Bailey et al., 1976]. In another paper in this volume [Bickford et al., this issue] we argue, on chemical and mineralogical grounds, that these low-silica plutons represent the parental magmas from which Butler Hill granite and Grassy Mountain ignimbrite were formed by fractional crystallization. The ring plutons, then, represent late-stage intrusions of deep-seated magmas from below the caldera. In this connection we note that all of the low-silica granites have abundant mafic inclusions, whereas the Butler Hill granite is virtually devoid of such inclusions except in its extreme northeastern exposure (its lowest exposed part).

We infer that the present exposures are of deeply eroded portions of the former Butler Hill caldera, a conclusion consistent with the regional tilting model. Thus, only those volcanic rocks that were relatively deep in the former caldera are still preserved. Moreover, direct evidence of the caldera, such as a preserved topographic wall, ring fractures, caldera-wall breccias, etc. has been removed. Consequently, we cannot precisely locate the caldera boundary, and the inferred locations of the caldera boundary and intracaldera arcuate faults that are shown on the geological map (Plate 1) require some discussion.

We have drawn an inferred caldera boundary (the outer ring on the map) so as to include most of the mapped Grassy Mountain ignimbrite but particularly thick sections of it such as the section on Kelley Mountain to the south of Roselle, since these may represent caldera fill deposits. In many major calderas, such as those in the San Juan Volcanic Field [e.g., Steven and Lipman, 1976], pyroclastic eruptive material has ponded within calderas and thus attained great thickness. The unusual thickness of Grassy Mountain ignimbrite on Kelley Mountain (possibly 1.5 km as inferred from its map distribution; Plate 1) suggests that the caldera boundary may be south of that region. However, it is also possible that Grassy Mountain ignimbrite is unusually thick there because outflow from a caldera located somewhat to the north filled a paleovalley or other topographic depression. To the east, in the vicinity of Fredericktown, we have drawn the boundary through the easternmost exposures of Slabtown granite. Since the whole eastern side of the proposed caldera is overlain nonconformably by Lamotte sandstone and younger sedimentary rocks, this interpretation may be in error.

Within the proposed caldera boundary, we have drawn a proposed intracaldera arcuate fault to pass through the major masses of the low-silica plutons on the assumption that the emplacement of these around the main mass of the Butler Hill granite was guided by some such feature. It is conceivable that the actual margin of the caldera is marked by the locations of the low-silica granite plutons; however, this model leaves thick sections of Grassy Mountain ignimbrite outside of the caldera.

Finally, we note that the Butler Hill caldera appears to be truncated on its western margin by a somewhat younger structure. We believe that this structure, described below, is the margin of a caldera to the west.

Central and Western St. Francois Mountains

One of the most significant structural features that we have found in the St. Francois Mountains was first noted in the region about 2 km east and northeast of Ironton (Plate 1). Here Ironton Hollow rhyolite, dipping gently 15° to 20° to the southwest, is in contact with Grassy Mountain ignimbrite in which compaction foliation stands nearly vertically. This feature was interpreted by Sides [1978] as an angular unconformity, primarily because of the lack of brecciation, slickensides, or other evidence for a fault. Later mapping to the north in the Iron Mountain Lake quadrangle (Plate 1) by Nusbaum [1980] showed that this feature is continuous over a distance of about 6 km and is concave westward. Nusbaum also observed an unconformable contact bewteen Tribby breccia, which dips easterly at low angles, and steeply dipping, oxidized Grassy Mountain ignimbrite in the area 2 to 3 km east of Iron Mountain, confirming that the feature is an angular unconformity, at least at that location. Along this unconformity from a

point about 3 km east of Arcadia to just east of Iron Mountain, units of Iron Mountain Lake felsite, Tribby breccia, and Ironton Hollow rhyolite, mostly dipping 10° to 20° to the west-southwest, rest in apparent angular unconformity upon steeply dipping rocks of Grassy Mountain ignimbrite and Lake Killarney formation.

Nusbaum also found that large (up to 45 x 10^3 m^2) blocks of Grassy Mountain ignimbrite, many showing petrographic evidence of mechanical disruption, are completely isolated within the younger volcanic rocks. The blocks of Grassy Mountain show widely variable dip and strike of compaction foliation. Moreover, rocks of the Grassy Mountain ignimbrite and Lake Killarney formation along the east side of the angular unconformity also show highly variable dip and strike; dips are uniformly high angle. Wolf Mountain ignimbrite, a crystal-rich ash flow tuff, occurs only along the angular unconformity.

Nusbaum mapped an arcuate fault within units of Tribby breccia and Iron Mountain Lake felsite. Along this fault, which is concave westward like the angular unconformity, apparent fault blocks of Lake Killarney formation and a body of granite porphyry occur. Relative displacement along this fault has not been determined.

This zone of chaotic breccia, arcuate faults, and angular unconformity, which can be traced from just northeast of Iron Mountain more than 6 km to the south, is strongly suggestive of a caldera boundary. The contact relations of Iron Mountain felsite, Tribby breccia, and Ironton Hollow rhyolite indicate that they were deposited upon and against steeply tilted blocks of older volcanic rocks (Lake Killarney formation and Grassy Mountain ignimbrite). The presence of chaotically oriented blocks of these older volcanic rocks within the younger units strongly suggests that the angular unconformity was formed against the topographic wall of a caldera and that the blocks had slumped down from it to become incorporated in newly formed volcanic material. Just to the west of this unconformity there is an arcuate fault that has been intruded by two small bodies of granite porphyry. This structure is concave westward and appears to be related to further subsidence following emplacement of Iron Mountain Lake felsite, Tribby breccia, and Ironton Hollow rhyolite. The collapse caldera represented by this feature evidently formed later than the Butler Hill caldera and truncates its western margin.

There has been considerable discussion over the existence of a second caldera in the western St. Francois Mountains. The geologic map (Plate 1) shows that a large basinal, or synclinal, structure, involving almost exclusively volcanic rocks, lies in the southwestern part of the mapped area. R. E. Anderson [1962, 1970] mapped and studied rocks in this area (the Taum Sauk Mountain area) and proposed that the volcanic rocks occupy a structural depression or sag in the roof of an underlying batholith. J. E. Anderson et al. [1969] concluded that the structural sag was a caldera, the Taum Sauk caldera, mainly on the basis of three lines of evidence: (1) the occurrence of arcuate faults in the western St. Francois Mountains (Plate 1), (2) Rb-Sr age determination data which suggested that rocks within the caldera were 100 m.y. younger than surrounding rocks, and (3) the proximity of Munger granite prophyry to the arcuate faults. These authors interpreted the arcuate faults as ring faults and Munger granite porphyry exposures as ring dikes. Berry [1970] proposed that the Taum Sauk rhyolite (then called tuff of Taum Sauk Mountain) was the major collapse ash flow tuff of the caldera and suggested that the pattern of faulting in the Taum Sauk area is similar to those of the resurgent domes of the Valles caldera, Creede caldera, Timber Mountain caldera, and the Toba cauldron of Samosir Island [Smith and Bailey, 1968]. If this is the case, the structure must have been greatly modified following resurgent doming, since the overall structure is basinal and not domal.

Bickford and Mose [1975] have subsequently shown that the age data cited by J. E. Anderson et al. [1969] were in error. Their measurements of the U-Pb system in zircons showed that the Taum Sauk rhyolite is 1495 m.y. old and is thus not younger than other rocks in the St. Francois Mountains. Further, zircons from the Munger granite porphyry yielded an age of about 1380 m.y. Thus, this body, and probably also the Carver Creek granite porphyry, were intruded about 100 m.y. after the eruption of Taum Sauk rhyolite and are probably not related to the formation of a caldera.

The arcuate faults mapped in the western St. Francois Mountains [R. E. Anderson, 1970] show only small displacements and their extensions by J. E. Anderson et al. [1969] are through valleys mostly covered by Paleozoic rocks and alluvium. R. E. Anderson [1970], noting the small displacement on the faults, concluded that the depression was not a caldera. He proposed that the Taum Sauk rhyolite had been erupted upon a preexisting southwesterly sloping surface, citing the orientation of rheoignimbritic flow folds as evidence that the unit flowed in a southwesterly direction. Anderson also noted that the tuff of Johnson Shut-Ins (includes the Proffit Mountain formation, Johnson Shut-Ins rhyolite, and Cope Hollow formation of this paper), the youngest volcanic rocks mapped, are apparently conformable with the underlying Taum Sauk rhyolite, suggesting that the depression or sag formed after the eruption of these youngest rocks.

Anderson's arguments regarding the orientation of flow folds in Taum Sauk rhyolite are compelling and of interest. However, we note that his map shows axial directions of flow folds indicating flowage in a northwesterly or southeasterly direction in a region on the southeastern margin of the Taum Sauk depression, and axial directions indicating flowage in either a northerly or southerly direction in a region on the northwestern side of the proposed depression. These directions might indicate flowage radially into (or out of) the depressed area and thus be consistent with the formation of a caldera at the time of eruption of Taum Sauk rhyolite. The apparent conformity of the tuff of Johnson Shut-Ins upon Taum Sauk rhyolite does not seem inconsistent with a caldera, since the dip of these units and those of Taum Sauk rhyolite may well have been modified after the deposition of the tuff of Johnson Shut-Ins.

We believe that the basinal structure in the Taum Sauk area is consistent with magma with-

drawal and the formation of a caldera at the time of the eruption of the voluminous Taum Sauk rhyolite. The whole structure could conceivably be related to one caldera-forming event, as envisioned by J. E. Anderson et al., [1969], but that would require that the eruption of the thick Taum Sauk rhyolite be approximately coincident with collapse along the region now marked by the zone of chaotic breccias and the angular unconformity. This would require that Iron Mountain felsite, Tribby breccia, and Ironton Hollow rhyolite be approximately correlative with Taum Sauk rhyolite, perhaps as essentially equivalent pyroclastic units ponded against the wall of a caldera formed mostly by collapse following the eruption of Taum Sauk rhyolite. However, Iron Mountain felsite, Tribby breccia, and Ironton Hollow rhyolite are units that may dip conformably beneath a thick stack of volcanic flows and ash flows of which Taum Sauk rhyolite is an upper member. In this case the volcanic rocks adjacent to the caldera wall would be separated from Taum Sauk rhyolite by more than 3 km of volcanic rocks unless there is a major fault hidden somewhere in the vicinity of Pilot Knob and Ironton. The question of whether one or two calderas occur in the western St. Francois Mountains is unresolved, but we currently prefer a 'two-caldera' model on the basis of the structural and stratigraphic data in hand.

Summary of Igneous and Structural Events

The igneous and structural events discussed here are summarized in Figure 1, a series of diagrammatic cross sections drawn across the mapped area of Plate 1 from approximately northeast of Knob Lick to the extreme southwest corner of the map. The sections show our interpretation of the formation of the caldera, as described below:

1. A body of magma whose composition is approximated by that of the medium-grained part of the Silvermine granite was emplaced into the shallow crust at a depth of about 8 km or less [Sides, 1980]. This magma began to crystallize, and a compositional zonation was introduced through fractional crystallization. This process is discussed in detail in the paper by Bickford et al. [this issue]. Following differentiation, the upper part of the magma was high in silica and was of the compostion of the Grassy Mountain ignimbrite and the Butler Hill granite. These relationships are shown in Figure 1a.

2. As indicated in Figure 1b, the crust above the eastern part of the magma body fractured on steep, arcuate faults. Large volumes of magma were erupted from vents along these fractures, and a central block subsided, forming the Butler Hill caldera. In the interpretation shown here, the earliest material erupted was lithic-rich and accumulated to form the Lake Killarney formation, the Anderson Mountain member of which probably represents slumped material from the caldera wall. However, it is also possible that Lake Killarney formation is precaldera material. Subsequent voluminous eruption caused subsidence and the emplacement of Grassy Mountain ignimbrite as caldera-filling ash flow tuff. It seems likely that a thinner outflow facies was developed, as shown in the figure, but this material has not been identified in the field. The precaldera

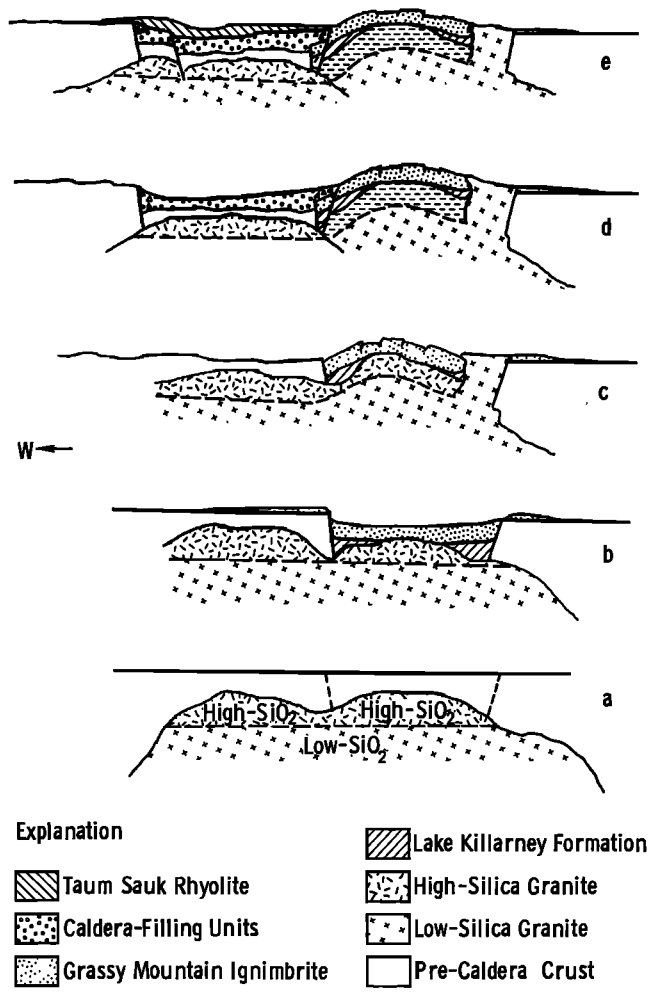

Fig. 1. Sequential cross sections showing inferred development of calderas in the St. Francois Mountains. See text for detailed explanation.

crust is not exposed in the field unless it is the Lake Killarney formation, and we have not attempted to show what happened to the subsided block; presumably it sank into or was intruded by magma.

3. The Butler Hill caldera was resurgently domed with intrusion of silica-rich magma from the upper part of the magma chamber to form the Butler Hill granite. The compositional zonation now observed in the Butler Hill may have formed after intrusion into Lake Killarney formation and Grassy Mountain ignimbrite, or it may have been developed in the upper part of the magma chamber prior to intrusion. Magma from the deeper, silica-poor parts of the magma chamber was then intruded along arcuate fractures developed around, and probably within, the caldera to form ring intrusives. This magma may have reached the surface to form ring domes, as noted in many younger calderas. At least one body, the Silvermine granite, differentiated vertically after emplacement to form a silica-rich cap (see detailed discussion by Bickford et al. [this issue].) These relationships are shown in Figure 1c.

4. Following the resurgent doming of the

Butler Hill caldera, a new caldera formed to the west in what is now the Taum Sauk area. As shown in Figure 1d, the eastern ring fault of this caldera cut across the western margin of the Butler Hill caldera, truncating its western margin. The fault shown bounding the western side of this caldera is speculative. This caldera continued to subside with the eruption of a thick sequence of volcanic rocks.

5. Extrusion of the thick Taum Sauk rhyolite occurred with the probable formation of another caldera somewhere in the Taum Sauk area. In Figure 1e we have speculatively shown the formation of a trap door caldera, with a bounding fault only on its western side and the Taum Sauk rhyolite lapping onto the older sequence of volcanics unconformably. As stated earlier in this paper, the caldera boundary mapped in the Iron Mountain-Ironton area may not be the margin of the caldera formed by the extrusion of Taum Sauk rhyolite because of the possible stratigraphic separation of the Taum Sauk from the breccias associated with the older caldera wall. In the absence of a mapped fault that could form the eastern margin of the younger caldera associated with extrusion of Taum Sauk rhyolite and the presence of arcuate faults that cut pre-Taum Sauk volcanic rocks on the western margin of the Taum Sauk area, we have shown the trap door structure indicated in Figure 1e. Continued subsidence of this caldera may have formed the basinal structure in the Taum Sauk area that is shown on the geologic map (Plate 1).

6. The Munger granite prophyry and the Carver Creek granite were intruded at a time evidently much later than the formation of the Taum Sauk rhyolite. As noted earlier, the Munger has yielded a zircon U-Pb age of 1380 m.y. [Bickford and Mose, 1975], whereas there is reason to believe that the Taum Sauk is about 100 m.y. older than this. The Munger and the Carver Creek may, however, have been intruded along an arcuate ring fracture within the trap door structure shown in Figure 1e.

7. The final igneous event was evidently the emplacement of basaltic magma in the form of diabasic dikes and gabbroic sills. The age or ages of these mafic rocks is not known; they could be older than the Munger granite porphyry and the Carver Creek granite. However, the fact that the mafic rocks ubiquitously cut older silicic rocks throughout the St. Francois Mountains suggests that their emplacement was the last igneous event.

8. The present level of exposures has evidently been formed by extensive pre-Late Cambrian erosion, and is now being exhumed. The southwesterly tilting postulated to account for the distribution of Precambrian rocks must have occurred prior to the development of the pre-Late Cambrian erosion surface and its burial by Upper Cambrian and younger sedimentary rocks, for hills of Precambrian rocks unconformably buried by sedimentary rocks occur in the eastern St. Francois Mountains as well as in the west.

Acknowledgments. This work was supported by NSF grants GA 11128, GA 35837, and EAR76-03769 and by a grant from the General Research Fund of the University of Kansas. The senior author was supported during field work by funds from the Missouri Department of Natural Resources, Division of Geological Survey, which also provided maps and other materials and advice to us. Much of this work was submitted to the Graduate Faculty of the University of Kansas in the form of graduate theses. JRS's work was a doctoral dissertation, whereas RDS and RLN submitted their studies as Masters theses.

References

Allingham, J. W., Interpretation of aeromagmatic anomalies in southeast Missouri, Short Papers in the Geological Sciences, U.S. Geol. Surv. Prof. Pap., 400-B, B216-219, 1960.

Amos, D. H., and G. A. Desborough, Mafic intrusive rocks of Precambrian age in southeast Missouri, Rep. Invest. Mo. Geol. Surv., 47, 23 pp., 1970.

Anderson, J. E., M. E. Bickford, A. L. Odom, and A. W. Berry, Jr., Some age relations and structural features of the Precambrian volcanic terrane, St. Francois Mountains, southeastern Missouri, Geol. Soc. Am. Bull., 80, 1815-1818, 1969.

Anderson, R. E., Pyroclastic flows of the Missouri Precambrian (abstract), Spec. Pap. Geol. Soc. Am., 73, 105, 1963.

Anderson, R. E., Ash-flow tuffs of Precambrian age in southeast Missouri, Rep. Invest. Mo. Geol. Surv., 46, 50 pp., 1970.

Bailey, R. A., G. B. Dalrymple, and M. A. Lanphere, Volcanism, structure, and geochronology of Long Valley caldera, Mono County, California, J. Geophys. Res., 81, 725-744, 1976.

Berry, A. W., Jr., Proposed stratigraphic column for Precambrian volcanic rocks, western St. Francois Mountains, Missouri, in Studies in Precambrian Geology of Missouri, edited by E. B. Kisvarsanyi, Rep. Invest. Mo. Geol. Surv., 61, 81-90, 1976.

Berry, A. W., Jr., and M. E. Bickford, Precambrian volcanics associated with the Taum Sauk caldera, St. Francois Mountains, Missouri, U.S.A., Bull. Volcanol., 36, 308-318, 1972.

Bickford, M. E., and Lewis, R. D., U-Pb geochronology of exposed basement rocks in Oklahoma, Geol. Soc. Am. Bull., 90, 540-544, 1979.

Bickford, M. E., and D. G. Mose, Geochronology of Precambrian rocks in the St. Francois Mountains, southeast Missouri, Geol. Soc. Am. Spec. Pap. 165, 48 pp., 1975.

Bickford, M. E., G. R., Lowell, J. R. Sides, and R. L. Nusbaum, Inferred structural configuration of the St. Francois Mountains Batholith, southeastern Missouri, Geol. Soc. Am. Abst. Programs, 9, 574-575, 1977.

Bickford, M. E., K. L. Harrower, W. J. Hoppe, B. K. Nelson, R. L. Nusbaum, and J. J. Thomas, Rb-Sr and U-Pb geochronology and distribution of rock types in the Precambrian basement of Missouri and Kansas, Geol. Soc. Am. Bull., Pt. I, 9, 323-341, 1981.

Bickford, M. E., K. L. Harrower, W. J. Hoppe, B. K. Nelson, R. L. Nusbaum, and J. J. Thomas, Supplementary data for: Rb-Sr and U-Pb geochronology and distribution of rock types in the Precambrian basement of Missouri and Kansas, Geol Soc. Am. Bull., Pt. II, 92, 963-996 (microfiche), 1981.

Bickford, M. E., J. R. Sides, and R. L. Cullers, Chemical evolution of magmas in the Proterozoic terrane of the St. Francois Mountains, southeastern Missouri, 1, Field, Petrographic, and major element data, J. Geophys. Res., this issue.

Blades-Zeller, E. L., Rhyolitic ash-flow tuff and intercalated volcaniclastic sedimentary rocks at Johnson Shut-ins, Reynolds County, Missouri, M.S. thesis, 45 pp., Univ. of Kansas, Lawrence, 1980.

Blades, E. L., and M. E. Bickford, Rhyolitic ash-flow tuffs and intercalated volcaniclastic tuffaceous sedimentary rocks at Johnson Shut-ins, Reynolds County, Missouri, in Studies in Precambrian Geology of Missouri, edited by E. B. Kisvarsanyi, Rep. Invest. Mo. Geol. Surv., 61 91-104, 1976.

Cullers, R. L., R. J. Koch, and M. E. Bickford, Chemical evolution of magmas in the Proterozic terrane of the St. Francois Mountains, southeastern Missouri, 2, Trace element data, J. Geophys. Res., this issue.

Davis, J. W., Petrogenesis and structure of the Knoblick Granite, M.S. thesis, St. Louis Univ., St. Louis, Mo., 1969.

Haworth, E., The crystalline rocks of Missouri, Mo. Geol. Surv., 8, 81-222, 1894.

Kisvarsanyi, E. B., Spectroscopic distribution of the trace elements in the Precambrian granitic rocks of southeastern Missouri, in Guidebook to the Geology of the St. Francois Mountain Area, Rep. Invest. Mo. Geol. Surv., 26, 95-105, 1961.

Kisvarsanyi, E. B., Petrochemistry of a Precambrian igneous province, St. Francois Mountains, Missouri, Rep. Invest. Mo. Geol. Surv., 51, 103 pp., 1972.

Kisvarsanyi, E. B., Geologic map of the Precambrian basement of Missouri, Missouri Department of Natural Resources, Division of Geological Survey, Contrib. Precambrian Geol., No. 7, Rolla, 1979.

Kisvarsanyi, E. B., Granitic ring complexes and Precambrian hot-spot activity in the St. Francois terrane, midcontinent region, United States, Geology, 8, 43-47, 1980.

Kisvarsanyi, G., Geochemical and petrological study of Precambrian iron metallogenic province of southeast Missouri, Ph.D. dissertation, Univ. of Mo., Rolla, 1966.

Lidiak, E. G., R. F. Marvin, H. H. Thomas, and M. N. Bass, Geochronology of the midcontinent region, United States, 4, Eastern area, J. Geophys. Res., 71, 5427-5438, 1966.

Lipman, P. W., Caldera-collapse breccias in the western San Juan Mountains, Colorado, Geol. Soc. Am. Bull., 87, 1397-1410, 1976.

Lipman, P. W., R. L. Christiansen, and J. T. O'Connor, A compositionally zoned ash-flow sheet in southern Nevada, U.S. Geol. Surv., Prof. Pap., 524-F, 1966.

Lowell, G. R., and J. R. Sides, The occurrence and origin of rapakivi granite in the St. Francois Mountain batholith of southeast Missouri, Geol. Soc. Am. Abst. Programs, 5, 332-333, 1973.

Muehlberger, W. R., C. E. Hedge, R. E. Denison, and R. F. Marvin, Geochronology of the midcontinent region, United States, 3, Southern area, J. Geophys. Res., 71, 5409-5426, 1966.

Nusbaum, R. L., A Precambrian collapse caldera boundary in the St. Francois Mountains, southeast Missouri, M.S. thesis, 77 pp., Univ. of Kansas, Lawrence, 1980.

Pratt, W. P., R. E. Anderson, A. W. Berry, Jr., M. E. Bickford, E. B. Kisvarsanyi, and J. R. Sides, Geologic map of exposed Precambrian rocks, Rolla 1° x 2° quadrangle, Missouri, U. S. Geol. Surv. Misc. Invest. Ser. 1-1161, 1:125,000 scale, 1979.

Ratté, J. C., and T. A. Steven, Ash-flows and related volcanic rocks associated with the Creede Caldera, San Juan Mountains, Colorado, U.S. Geol. Surv. Prof. Pap., 524-H, 58 pp., 1967.

Ross, C. S., and R. L. Smith, Ash-flow tuffs: Their origin, geologic relations, and identification, U.S. Geol. Surv. Prof. Pap., 366, 81 pp., 1961.

Schoolcraft, H. R., A View of Lead Mines of Missouri (Including Some Observations on the Mineralogy, Geology, Geography, Antiquities, Soil, Climate, Population, and Production of Missouri and Arkansas and Other Sections of Western Country), 229 pp., Charles Wiley, New York, 1819.

Scully, E. M., Silvermine granite: A differentiated ring pluton of the St. Francois Mountains batholith, southeastern Missouri, M.S. thesis, 45 pp., Univ. of Kansas, Lawrence, 1978.

Shuster, R. D., Chemistry and petrography of caldera-related ash-flows, St. Francois Mountains, Missouri: Grassy Mountain Ignimbrite and Taum Sauk Rhyolite, M.S. thesis, 45 pp., Univ. of Kansas, Lawrence, 1978.

Sides, J. R., Trend-surface analysis of chemical data across the St. Francois Mountains Batholith, southeastern Missouri: A test of regional tilting, Geol. Soc. Am. Abstr. Programs, 9, 651, 1977.

Sides, J. R., A study of the emplacement of a shallow granite batholith: The St. Francois Mountains, Missouri, Ph.D. thesis, 124 pp., Univ. of Kansas, Lawrence, 1978.

Sides, J. R., Emplacement of the Butler Hill Granite, a shallow pluton within the St. Francois Mountains batholith, southeastern Missouri, Geol. Soc. Am. Bull., Pt. I, 91, 535-540, 1980.

Sides, J. R., Geology the Ketcherside Mountain area, southeastern Missouri, and the source of Grassy Mountain Ignimbrite, Geol. Soc. Am. Bull., Pt I, in press, 1981.

Smith, R. L., Ash flows, Geol. Soc. Am. Bull., 71, 795-842, 1960a.

Smith, R. L., Zones and zonal variations in welded ash-flows, U.S. Geol. Surv. Prof. Pap., 354-F, 149-159, 1960b.

Smith, R. L., and R. A. Bailey, The Bandelier Tuff, a study of ash-flow eruption cycles from zoned magma chamber, Bull. Volcanol., 29, 83-104, 1966.

Smith, R. L., and R. A. Bailey, Resurgent cauldrons, in Studies in Volcanology (Williams Volume), Mem. Geol. Soc. Am. 116, 613-662, 1968.

Smith, R. L., R. A. Bailey, and C. S. Ross, Geologic map of the Jemez Mountains, New Mexico, Misc. Geol. Invest. Map I-571, U.S. Geol. Surv. Reston, Va., 1970.

Steiger, R. H., and E. Jäger, Subcommission on

Geochronology: Convention on the use of decay constants in geo- and cosmochronology, Earth Planet. Sci. Lett., 36, 359-362, 1977.

Steven, T. A., and P. W. Lipman, Calderas of the San Juan volcanic field, southwestern Colorado, U.S. Geol Surv. Prof. Pap., 958, 35 pp., 1976.

Tolman, C., and F. Robertson, Exposed Precambrian rocks in southeast Missouri, Rep. Invest. Mo. Geol Surv. 44, 68 pp., 1969.

Van Schmus, W. R., and M. E. Bickford, Proterozoic chronology and evolution of the midcontinent region, North America, in Precambrian Plate Tectonics, edited by A. Kroner, Elsevier, New York, 781 pp., 1981.

(Received December 22, 1980;
revised May 18, 1981;
accepted May 19, 1981.)

JOURNAL OF GEOPHYSICAL RESEARCH, VOL. 86, NO. B11, PAGES 10365-10386, NOVEMBER 10, 1981

CHEMICAL EVOLUTION OF MAGMAS IN THE PROTEROZOIC TERRANE OF THE ST. FRANCOIS MOUNTAINS, SOUTHEASTERN MISSOURI 1. FIELD, PETROGRAPHIC, AND MAJOR ELEMENT DATA

M. E. Bickford

Department of Geology, University of Kansas, Lawrence, Kansas 66045

J. R. Sides

Department of Geology, University of Texas at Arlington, Arlington, Texas 76019

R. L. Cullers

Department of Geology, Kansas State University, Manhattan, Kansas 66506

Abstract. Major element chemical data for plutonic and volcanic rocks of the eastern St. Francois Mountains indicates that ring plutons of the Butler Hill caldera are low-silica granites and chemically distinct from the high-silica Butler Hill granite and Grassy Mountain ignimbrite. Additionally, the ring plutons (Silvermine, Stono, Knoblick, and Slabtown granites) are characterized by abundant mafic inclusions, whereas these are almost completely absent in Butler Hill granite. Silvermine granite is mostly of a medium-grained variety, but cliffs along the St. Francis River expose gradations upward to a high-silica, fine-grained 'cap rock'. Least squares mixing calculations indicate that the cap rock could have formed by the fractional crystallization of plagioclase, hornblende, biotite, magnetite, and sphene, all of which are liquidus phases in the medium-grained Silvermine granite. The chemical similarity of the fine-grained cap rock to Butler Hill granite and Grassy Mountain ignimbrite suggested that Silvermine granite might be a sample of the parental magma from which the high-silica-rocks were derived. Least squares mixing calculations indicate that Butler Hill granite magma could have been derived from the composition of the average medium-grained Silvermine by fractional crystallization of the same liquidus phases indicated above. The major element composition of Grassy Mountain ignimbrite can be derived from the average Butler Hill granite magma by fractional crystallization of plagioclase, alkalic feldspar, quartz, biotite, and magnetite, all of which are liquidus phases in Butler Hill granite. Textural and chemical variations in Butler Hill granite from northeast to southwest suggest that the body was internally differentiated and that the present distribution of rock types is due to tilting and erosion. The internal zonation of Butler Hill granite can be accounted for by fractional crystallization of plagioclase, alkalic feldspar, quartz, biotite, sphene, and magnetite. The chemical data and calculations indicate that the primary magma emplaced at the beginning of igneous activity was of Silvermine type. The magma crystallized fractionally so that the magma chamber became compositionally zoned, with high-silica magma in the upper part. The top-most part of this material was erupted to form Grassy Mountain ignimbrite during formation of the Butler Hill caldera. Subsequently, more of the high-silica magma was emplaced into the volcanic material in the caldera during resurgent doming. After formation and resurgent doming of the Butler Hill caldera, some of the parental magma from deeper in the chamber leaked upward into the ring fracture or into arcuate faults within the caldera, forming the ring plutons. The abundant mafic inclusions in the ring plutons may be earlier crystallized magma carried upward during intrusion. One of the ring plutons, Silvermine granite, apparently formed a sill-like intrusion and underwent in situ differentiation.

A body of foliated granodiorite exposed as a giant inclusion in granite at Hawn State Park, east of the principal exposures of the St. Francois Mountains, has the mineralogy, major element chemistry, and trace element chemistry to be a sample of the cumulate resulting from the processes in the magma chamber.

Copyright 1981 by the American Geophysical Union.

Introduction

The St. Francois Mountains are located about 160 km south of St. Louis in southeastern Missouri (Figure 1). This hilly region, which has local relief of up to 250 m, is the structural apex of the Ozark Uplift and exposes a well-preserved middle Proterozoic volcanic-shallow plutonic terrane. The principal rock types are silicic volcanic rocks, mostly rhyolitic ash flow tuff, and epizonal granitic plutons of similar composition; andesitic to trachytic flows are rare. Diabasic dikes and small gabbroic sills, which make up a small part of the total volume of igneous material, were the last igneous rocks emplaced [Amos and Desborough, 1970].

The St. Francois Mountains expose about 900 km^2 of a much larger terrane of rock similar in age and petrography. The larger terrane (Figure 1) extends at least from northern Ohio to the Texas Panhandle, a distance of about 2000 km, and is about 500 km wide [Muehlberger et al., 1966; Lidiak et al., 1966; Van Schmus and Bickford, 1981; R. E. Denison et al, manuscript in preparation, 1981]. The thickness of this terrane is unknown, but if it were only 1 km thick, the total volume represented would be 10^6 km^3, a sizeable portion of the North American continental crust. Age data for the larger terrane are scanty in its eastern part, where minerals and whole rocks dated by the Rb-Sr

Paper number 1B0893.
0148-0227/81/001B-0893$01.00

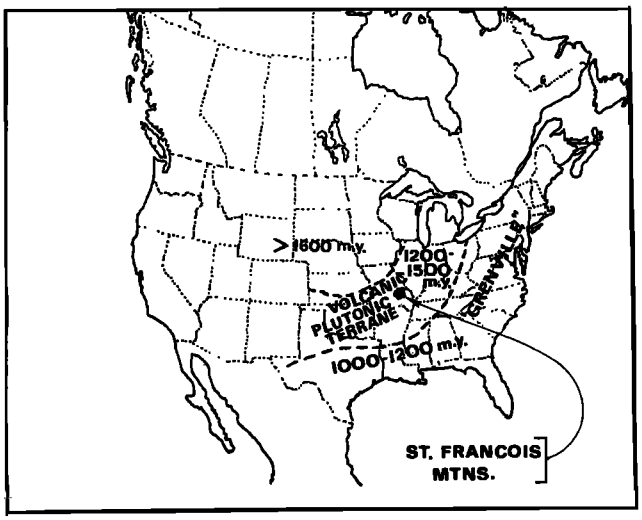

Fig. 1. Sketch map showing location of St. Francois Mountains within volcanic-plutonic terrane.

method yield ages ranging from 1200 to 1500 m.y. [Lidiak et al, 1966; R. E. Denison et al, manuscript in preparation, 1981]. Bickford and Mose [1975] have reported ages of 1485 m.y. for rocks in the St. Francois Mountains on the basis of U-Pb measurement on zircons (recalculated to the decay constants of Steiger and Jäger [1977] from the original data), and Bickford et al., [1981] have reported similar ages from zircons separated from basement rocks in Missouri and Kansas. In southern Kansas, basement rocks that are petrographically similar to those in the St. Francois Mountains yielded zircon U-Pb ages of 1380-1360 m.y. and Bickford and Lewis [1979] reported ages of 1380-1400 m.y. for shallow granite in northeastern Oklahoma and mesozonal granite and gneiss from the eastern Arbuckle Mountains in southeastern Oklahoma.

Previous Studies

Although the St. Francois Mountains have been studied since 1819 [Schoolcraft, 1819], the first complete geologic map was not published until 1969 [Tolman and Robertson, 1969]. R. E. Anderson [1970] published an excellent study of the Taum Sauk area in the western St. Francois Mountains [see Sides et al., this issue, Plate 1]. Anderson's study, which was based upon his doctoral dissertation [R. E. Anderson, 1962], was the first in which the ash flow origin of most of the rhyolitic rocks was recognized. In a later study, Berry [1970, 1976] extended the mapping of Anderson into the northeastern part of the Taum Sauk region and established a fairly detailed stratigraphy of volcanic units. Anderson recognized a thick accumulation of volcanic rocks in the Taum Sauk area and proposed that it occupies a volcanic depression. Later, J. E. Anderson et al., [1969] proposed that this structure was a caldera and named it the Taum Sauk caldera. Extensive field and petrographic study in the St. Francois Mountains beginning in 1973 has led to the recognition of a second, more deeply eroded caldera (the Butler Hill caldera) in the eastern St. Francois Mountains and has indicated that at least two calderas exist in the Taum Sauk area [Sides et al., this issue].

Petrochemical studies of rocks from the St. Francois Mountains have been published by E. B. Kisvarsanyi [1961, 1972] and by G. Kisvarsanyi [1966]. The paper of E. B. Kisvarsanyi [1972] was a particularly valuable presentation of chemical data from a large number of rock analyses with an interpretation of the chemical evolution of the suite.

Goals of this Paper

We have studied the St. Francois Mountains terrane because it is one of very few well-preserved Precambrian volcanic terranes and because it is the only well-exposed part of a buried terrane that makes up a major part of the continent. Our sampling is based upon extensive field work, begun in 1973, and our interpretation has been guided by structural and stratigraphic data gained during field work and synthesis. The purpose of this paper, and part 2 which follows it [Cullers et al., this issue, hereinafter referred to as part 2] is to present the results of an extensive chemical and petrographic study aimed at understanding the origin of the magmas that formed the exposed rocks and the process or processes by which primary magmas may have been modified to yield the observed suite of rocks. This paper will summarize the field and petrographic data, present the major element chemical data, and propose a model for the chemical evolution of the exposed rock types. Part 2 will present trace element data, including analyses of the rare earth elements (REE), and show how those data are consistent with and support the model proposed.

Geological Relations and Petrography

Field and Structural Relations

In the following discussion, the reader is referred to the geologic map of portions of the St. Francois Mountains presented as Plate 1 in the paper by Sides et al. [this issue]. The exposed portion of the Precambrian terrane of the St. Francois Mountains is dominated by rocks associated with at least two calderas. The existence of these calderas, the Butler Hill caldera in the eastern St. Francois Mountains and one or more calderas in the Taum Sauk area to the west, is based upon structural, stratigraphic, and petrologic considerations presented by Sides et al. [this issue]. In summary the evidence is as follows:

1. The Butler Hill caldera is inferred from the presence of a very thick, uniform rhyolitic ash flow tuff, Grassy Mountain ignimbrite, which is distributed around a large, roughly circular granite pluton, Butler Hill granite. Butler Hill granite grades from medium to coarse-grained in its northeastern exposures to fine-grained and granophyric in its western and southwestern outcrops, a variation interpreted by Bickford et al. [1977], Sides [1980], and Sides et al. [this issue] to indicate original vertical variations followed by west-southwesterly tilting and erosion. The western contact of Butler Hill granite is with volcanic rocks of the Lake Killarney

TABLE 1. Average Modes of Plutonic Rocks

	Rock Unit									
	m/g Silvermine Granite[a]	f/g Silvermine Granite[a]	Knoblick Granite[b]	Slabtown Granite	Stono Granite[c]	Butler Hill Granite Type 1	Butler Hill Granite Type 2	Butler Hill Granite Type 3	Graniteville Granite	Hawn Park Granodiorite[d]
Number of samples	8	9	6	2	1	5	4	2	2	
Quartz	25.7±3.4	34.4±3.2	24.4	23.6±7.8	24.4	32.0±6.6	33.7±3.5	38.4±3.9	40.4±4.8	15
Perthite	24.7±4.9	29.7±5.1	43.1	32.2±7.8	61.4	36.6±11.2	33.9±4.4	50.9±10.5	30.4±2.8	10
Plagioclase	42.5±5.1	32.7±4.3	25.8	36.2±6.9	4.6	27.9±10.3	31.2±2.3	10.2±14.4	26.9±3.3	60
Biotite/Chlorite	3.7±1.9	2.3±1.0	1.5	3.7±1.6	---	2.8±0.9	1.8±1.2	tr	0.7±0.1	
Hornblende	2.3±1.6	0.2±0.5	4.6	---	5.7	tr	---	---	---	15
Muscovite	---	---	---	---	---	tr	---	---	tr	---
Sphene	0.6±0.6	0.1±0.3	tr	---	---	tr	---	---	---	tr
Opaque	0.7±0.4	0.9±0.5	0.1	1.0±0.5	3.2	0.3±0.2	0.4±0.2	---	tr	tr
Accessories	0.3±0.1	0.5±0.3	tr	2.8±2.0	tr	tr	0.2±0.9	tr	tr	tr
Total	100.5	100.8	99.5	99.5	99.3	99.6	101.2	99.5	98.4	100
Average composition of zoned plagioclase (An)	av. 14±4	av. 14±4	ND	av. 14±4	ND	av. 14±4	av. 14±4	av. 14±4	av. 10±4	ND
Composition of alkalic feldspar										
Or	74.9	63.4	68.8	ND	ND	74.6	64.2	60.2	85.7	ND
Ab	21.6	32.5	27.3	ND	ND	23.7	34.5	38.2	14.0	ND
An	3.5	4.1	3.9	ND	ND	1.7	1.3	1.6	0.3	ND

[a]Scully [1978].
[b]R. L. Nusbaum (unpublished data, 1977).
[c]Nusbaum [1980].
[d]Lowell [1976].

formation and the overlying Grassy Mountain ignimbrite. Along and to the west of this contact, compaction foliation in these volcanic rock units dips away from the pluton at high angles, suggesting that Butler Hill granite was emplaced during resurgent doming. Four low-silica granite plutons, Stono, Knoblick, Slabtown, and Silvermine granites, occur around the margins of the Butler Hill granite along its contacts with volcanic rocks, suggesting that these smaller plutons were emplaced as ring intrusives.

2. To the west of the Butler Hill caldera in the Taum Sauk area is an accumulation of more than 3 km of volcanic rocks. These rocks range in composition from andesite through dacite to rhyolite, but high-silica rhyolite greatly predominates. The sequence rests with apparent angular unconformity upon steeply dipping rocks of the Lake Killarney formation and Grassy Mountain ignimbrite along a boundary that can be traced from near Iron Mountain southward to the vicinity of Arcadia. In the area just south of Iron Mountain, this boundary is concave westward and is marked by a zone of chaotic megabreccia in which large, diversely oriented blocks of older rocks (Lake Killarney formation and Grassy Mountain ignimbrite) are enclosed in the lowest units of the sequence of rocks above the angular unconformity. Sides et al. [this issue] believe this boundary to be the eastern topographic wall of a caldera. An extensive arcuate fault just west of the zone of chaotic megabreccia may be the ring fracture of this caldera.

Other evidence for a caldera in the Taum Sauk area is the presence of the Taum Sauk rhyolite, a high-silica rhyolitic ash flow tuff that is greater than 1 km thick. The eruption of a voluminous ash flow tuff like the Taum Sauk rhyolite, whose exposed volume is at least 59 km^3 and whose probable volume is greater than 100 km^3, must have formed a caldera. However, it is not clear that it was the same caldera whose topographic wall is exposed to the east near Iron Mountain, for Taum Sauk rhyolite may be separated from the volcanic units there by about 3 km of volcanic rocks [Sides et al., this issue].

Plutonic Rocks

The plutonic rocks to be described here include those associated with the Butler Hill caldera (low-silica 'ring plutons' and high-silica Butler Hill granite); the Graniteville granite, a high-silica pluton that intrudes lower units of the thick volcanic sequence in the Taum Sauk area; and hypabyssal, medium-silica intrusives of the Taum Sauk area. Table 1 gives average modes (or modes of typical samples) and the compositions of plagioclase and alkalic feldspar from most of the rocks.

The compositions of the alkalic feldspars were determined by chemical analysis of bulk perthite separated from the rocks (Appendix A). Plagioclase in these rocks is commonly somewhat altered and, in most rocks, is complexly zoned. Consequently, it was difficult to determine the composition of the plagioclase. Extinction angle measurements made with a universal stage and the optically negative character of most of the plagioclase indicate that at least parts of the

TABLE 2. Average Modes of Volcanic Rocks

	Rock Unit				
	Lake Killarney Formation[a]		Ironton Hollow Rhyolite[a]	Grassy Mountain Ignimbrite[b]	Taum Sauk Rhyolite[c]
	Lower Member	Anderson Mt. Member			
Number of samples	15	3	8	24	12
Phenocrysts					
Quartz	3.3 ±1.3	1.5 ±0.7	0.9 ±0.6	8.9 ±1.8	8.4 ±2.0
Perthite	4.6 ±1.2	1.6 ±0.7	tr	13.5 ±2.5	11.6 ±5.6
Plagioclase	tr	tr	1.0 ±0.5	---	---
Matrix	87.3 ±9.1	94.1 ±1.0	96.7 ±2.9	73.3 ±5.3	76.9 ±6.6
Pumice	4.2 ±9.1	---	---	1.6 ±3.0	ND
Lithics	tr	1.5 ±2.6	tr		ND
Amphibole	---	---	---	tr	ND
Hematite	tr	tr	tr	0.9 ±0.7	ND
Fluorite	---	---	---	0.1 ±0.3	ND
Epidote	tr	tr	tr	tr	ND
Chlorite	tr	tr	tr	1.7 ±0.9	ND
Calcite	tr	0.9 ±1.1	tr		ND
Total	99.4	99.6	98.6	100	96.9

[a]Data from Sides [1978]
[b]Data from Shuster [1978].
[c]Data from Berry [1970].

crystals are as calcic as An_{30-32}, but mass balance calculations, made on the basis of modal data, the compositions of mineral phases other than plagioclase, and the bulk chemical composition of the rock samples, indicate that that the bulk composition of plagioclase in most of these rocks is about An_{14}. The plagioclase compositions indicated in the following descriptions and used in the later section on modeling of fractional crystallization were determined by mass balance calculations. The field occurrence of these rocks and regional variations in texture and composition are described by Sides et al. [this issue].

Low-Silica 'Ring Plutons'

Silvermine granite. Silvermine granite has been described previously by Scully [1978]. The pluton displays two principal textural types, a medium-grained variant which is the most abundant in outcrop and a fine-grained porphyritic type which caps cliffs along the St. Francis River and is apparently a roof facies. The medium-grained variety (average grain size = 1.5 mm.) has well-developed hypidiomorphic granular texture and is composed essentially of quartz, zoned plagioclase (average about An_{14}), perthite, hornblende, and chlorite (after biotite). Sphene, magnetite, apatite, and zircon are accessory minerals, and chlorite and epidote are common alteration products. Plagioclase and hornblende were early crystallizing phases; hornblende is commonly euhedral. Plagioclase is commonly embayed by perthite or quartz, minerals which show coarse graphic intergrowths in most samples.

The fine-grained porphyritic variety is mineralogically similar except that hornblende and sphene are rare, occurring only near the gradational boundary with the medium-grained rock. Both plagioclase (average about An_{14}) and perthite occur as phenocrysts in a generally fine-grained matrix of quartz and perthite; in some samples, quartz and perthite are graphically intergrown in the matrix.

Knoblick granite. This rock has been described by Davis [1969] and by R. L. Nusbaum (unpublished data, 1977). It is texturally and mineralogically quite similar to Silvermine granite except that it is somewhat finer-grained (average grain size = 1.0 mm.) and sphene is not as abundant (Table 1).

Mafic inclusions in Silvermine and Knoblick granites. Mafic inclusions varying in size from less than 1 cm in diameter to greater than 5 cm are common in both Silvermine and Knoblick granites. The inclusions appear to be somewhat more abundant in Knoblick granite, but this may not be a real distinction between the two bodies, for much less of Knoblick granite than Silvermine is exposed, and the distribution of mafic inclusions is not uniform in either body. At least two areas, each 400 m^2 or greater, in which mafic inclusions make up approximately half of the exposed rock were observed in the Silvermine granite.

All of the mafic inclusions that we have studied petrographically are composed of quartz, plagioclase, hornblende, biotite, minor perthite, opaques, and minor accessory minerals. Plagioclase crystals are zoned, and hornblende is quite abundant and commonly elongate and embayed. The texture and mineral assemblages suggest that the inclusions are of preexisting igneous rocks. Those that we have analyzed for major elements (Table 3) are chemically quartz diorites.

Slabtown granite. This rock is composed essentially of plagioclase (average about An_{14}), perthite, quartz, hornblende, and minor biotite. Accessory minerals include magnetite, apatite, zircon, sphene, and allanite. The rock is typically porphyritic, with phenocrysts of plagioclase up to 1.5 mm in diameter in a granophyrically intergrown matrix of quartz and perthite. Plagioclase and hornblende were evidently the first minerals to crystallize; plagioclase is commonly embayed where it is in contact with quartz and perthite. Alteration is extensive, with clay minerals and epidote developed from plagioclase and chlorite formed from the mafic minerals, particularly biotite.

Stono granite. This rock is composed ess-

entially of plagioclase (average about An_{14}), quartz, perthite, and hornblende. Plagioclase is euhedral to subhedral and extensively altered to kaolinite and epidote. The presence of abundant chlorite suggests that the rock originally had significant amounts of biotite as a second mafic phase. Accessory minerals include ilmenite, associated with leucoxene, and apatite. Both plagioclase and perthite occur as phenocrysts set in a matrix that may be either graphic, with intergrowths of quartz and perthite, or granular, in which quartz occurs as a anhedral interstitial phase. The mafic inclusions mentioned above are particularly abundant in Stono granite, but in contrast to the hornblende-rich nature of the inclusions in Silvermine and Knoblick granites, inclusions in Stono granite are composed of fine-grained granular aggregates of plagioclase, quartz, perthite, chlorite, and disseminated iron oxides.

High-Silica Granites

Butler Hill granite. As indicated earlier in this paper and described in detail by Sides et al. [this issue], Butler Hill granite grades from a medium to coarse-grained rock in its northeasterly exposures to a fine-grained, typically granophyric, reddish rock in its southwesterly and westerly exposures. In the northeast, the rock is essentially composed of quartz, perthite, zoned plagioclase (average about An_{14}), and biotite; an alkali amphibole is rarely observed, and muscovite occurs in some samples. Fluorite, apatite, zircon, and rarely sphene are accessory minerals. Textures are typically hypidiomorphic granular with average grain size of about 3.0 mm. In many samples there are clearly two generations of quartz: one is early, euhedral, and sometimes partly resorbed, whereas the other is late, anhedral, and molded around earlier feldspar crystals. In the extreme northeast, Butler Hill granite has well-developed rapakivi texture, with mantled alkali feldspar ovoids as large as 3 cm in diameter [Lowell and Sides, 1973].

To the southwest the granite gradually is finer-grained and redder in color. Biotite decreases in abundance, but most samples contain some chlorite. Feldspars are increasingly turbid. In extreme southwestern and western exposures, the rock is very fine-grained and distinctively granophyric in texture, consisting of euhedral (but commonly partly resorbed) quartz phenocrysts, euhedral perthite phenocrysts, and rare plagioclase phenocrysts, all in a matrix of granophyrically intergrown quartz and alkalic feldspar. Fluorite is a common accessory mineral in these rocks, occurring both interstitially and in miarolitic cavities. In Table 1, modes are given for the northeastern part of the body (Butler Hill type 1), the middle part (Butler Hill type 2) and the western and southwestern parts (Butler Hill type 3).

Brown Mountain rhyolite porphyry [Tolman and Robertson, 1969] is a mass of extremely fine-grained granite that occurs somewhat to the south of the main mass of the fine-grained portion of Butler Hill granite. It is granophyric, at least in part, and consists of quartz and perthite phenocrysts in a reddish matrix of fine-grained quartz and feldspar. Mafic minerals are exceedingly rare to absent. We believe that this body is related to the main part of the Butler Hill granite.

Graniteville granite. Typical samples of Graniteville granite are medium to coarse-grained (average grain size = 3.0 mm) and consist of plagioclase (average about An_{10}), microcline-perthite, quartz, minor biotite (usually partly to completely chloritized), and primary muscovite. The most abundant accessory mineral is fluorite, which occurs as a late-crystallizing mineral in interstices along with chlorite and sometimes epidote. Magnetite, apatite, and zircon also occur. Quartz commonly occurs as euhedral to subhedral crystals and was evidently the first phase to crystallize. Quartz was followed by plagioclase, then alkalic feldspar (now perthite), and finally a late generation of quartz, biotite, muscovite, and fluorite.

Hypabyssal intrusives of the Taum Sauk area. The Munger granite porphyry and the Carver Creek granite porphyry [Tolman and Robertson, 1969] have been described by Sides et al. [this issue]. Although we report major element chemical compositions in Table 3, these bodies are not discussed further in this paper; the trace element composition and origin of these bodies is discussed in part 2.

Gneissoid granodiorite of Hawn Park. A large mass of gneissoid granodiorite occurs in exposures along Pickle Creek in Hawn State Park, Ste. Genevieve County, Missouri. This locality is about 20 km northeast of Knoblick, Missouri [Sides et al., this issue, Plate 1] and is not shown on the geologic map. In this occurrence, which has been described by Lowell [1976], the granodiorite is apparently enclosed by a granite that is similar in field appearance to Butler Hill granite.

As described by Lowell, the granodiorite is foliated and has abundant mafic schlieren. Its texture is decussate-granoblastic and it is composed of abundant plagioclase, with quartz, hornblende, biotite, and mesoperthite as other essential minerals. Apatite, zircon, sphene, and opaques are typical accessory minerals. An original interpretation of this rock by Lowell, and by the senior author, was that it was a large xenolith of older continental crust that was incorporated in magmas of the St. Francois Mountains igneous suite, but a U-Pb zircon age of 1480 m.y. [Bickford and Mose, 1975] precludes this interpretation. The significance of this rock will be discussed later.

Volcanic rocks

The volcanic rocks to be described here include only those for which we have determined major element chemical compositions: Lake Killarney formation, Grassy Mountain ignimbrite, Ironton Hollow rhyolite, and Taum Sauk rhyolite. For descriptions of other volcanic rocks in the St. Francois Mountains, the reader is referred to Sides et al. [this issue], Blades and Bickford [1976], Sides [1976], and to the theses by Berry [1970], Sides [1978], and Nusbaum [1980]. Table 2 gives average modes and the compositions of plagioclase and alkalic feldspars.

Lake Killarney formation. This volcanic unit is probably the oldest rock mass exposed in the

TABLE 3. Average Major Element Compositions and Rb, Sr, and Ba Abundances for Plutonic and Volcanic Rocks

	Number of Samples	SiO_2[a]	Al_2O_3[a]	Fe_2O_3[a]	CaO[a]	K_2O[a]	Na_2O[a]	MgO[a]	MnO[a,c]	TiO_2[a]	LOI[a]	Total[a]	Rb[b]	Sr[b]	Ba[b]
Ring Plutons															
Silvermine granite															
medium-grained	5	68.62	14.50	3.31	1.79	3.86	4.03	0.93	0.08(2)	0.44	1.68	99.24	119	198	940
	±1σ	0.44	0.21	0.19	0.33	0.27	0.88	0.17	0.01	0.03	0.99		19	45	44
fine-grained	9	74.24	12.83	1.58	0.55	4.44	3.71	0.29	0.02(1)	0.24	1.18	99.08	164	96	731
	±1σ	0.97	0.37	0.25	0.14	1.24	0.85	0.09	---	0.04	0.48		57	35	229
Knoblick granite	4	66.40	14.95	4.08	2.68	3.17	4.48	0.99	0.07(2)	0.47	0.92	98.21	104	262	862
	±1σ	0.81	0.99	0.39	0.40	0.07	0.07	0.17	---	0.04	0.21		4	28	29
Stono granite	1	67.93	12.44	4.94	1.49	3.87	4.44	0.84	0.10	0.63	0.92	97.6	139	86	566
	--	--	--	--	--	--	--	--	---	--	--	--	--	--	--
Slabtown granite	2	70.44	12.97	3.52	1.23	3.60	4.70	0.40	0.13	0.45	0.96	98.4	91	121	1034
	±1σ	0.70	0.25	0.08	0.07	0.02	0.01	0.06	---	0.02	0.02		9	13	147
High-Silica Plutons															
Butler Hill granite															
Group 1, lowest	17	75.17	12.60	1.62	0.75	4.61	3.55	0.21	0.04(15)	0.19	1.81	100.55	231	83	463
	±1σ	1.77	0.30	0.53	0.30	0.21	0.19	0.09	0.02	0.05	0.65		21	32	108
Group 2, middle	17	76.28	12.25	1.30	0.37	4.92	3.48	0.12	0.04(6)	0.16	1.22	100.14	246	46	349
	±1σ	0.95	0.68	0.19	0.14	0.25	0.23	0.04	0.02	0.01	0.50		34	19	103
Group 3, highest	10	75.94	12.13	1.00	0.24	4.97	3.14	0.09	0.03(3)	0.15	1.38	99.07	174	26	328
	±1σ	0.73	0.73	0.22	0.21	0.31	0.70	0.05	0.02	0.03	0.33		61	12	135
All samples	44	75.77	12.36	1.35	0.49	4.80	3.44	0.15	0.04(24)	0.17	1.48	100.05	224	56	389
	±1σ	1.36	0.59	0.43	0.31	0.28	0.38	0.08	0.02	0.04	0.59		46	33	126
Graniteville granite	4	75.36	12.39	1.25	0.65	4.59	4.07	0.04	0.002(3)	0.11	1.53	99.99	346	19	139
	±1σ	1.93	0.31	0.18	0.15	0.17	0.14	0.01		0.03	0.74		41	5	45
Taum Sauk Area															
Munger granite	8	71.56	13.21	3.23	0.55	5.85	3.34	0.16	0.07(5)	ND	0.01	97.98	213	66	1515
	±1σ	0.91	0.26	0.27	0.25	0.20	0.08	0.03	0.01		0.004		72	30	53
Carver Creek granite	1	69.69	13.05	4.69	1.12	4.87	3.81	0.34	0.09	0.47	1.17	99.31	157	89	963
		--	--	--	--	--	--	--		--	--	--	--	--	--
Inclusions															
Knoblick granite	6	56.55	15.23	8.64	4.71	2.06	4.21	3.06	0.20(3)	0.82	1.28	96.76	93	282	569
	±1σ	1.90	0.26	1.42	0.81	0.51	0.62	0.68	0.04	0.17	0.41		24	20	116
Butler Hill granite	1	61.75	15.22	6.68	2.25	1.04	6.77	1.21	ND	0.44	1.56	96.92	168	47	103
		--	--	--	--	--	--	--		--	--	--	--	--	--

					Possible Cumulate										
Hawn Park gneissoid	2	56.27	18.67	7.71	4.94	2.12	4.38	1.66	0.14	1.08	0.62	97.59	51	455	1409
granodiorite	±1σ	0.22	0.22	0.18	0.05	0.04	0.08	0.08	0.08	0.01	0.13		1	1	187
						Volcanic Rocks									
Grassy Mountain	15	76.34	11.40	2.18	0.25	4.58	3.67	0.05	0.06	0.18	2.15	100.86	163	12	200
ignimbrite	±1σ	0.75	1.38	0.12	0.14	0.19	0.17	0.02	0.01	0.02	1.44		14	4	96
Lake Killarney	2	76.67	11.12	2.47	0.26	6.01	2.75	0.04	0.02	0.17	0.54	100.05	ND	ND	ND
Formation	±1σ	0.34	0.04	0.04	0.04	0.25	0.06	--	0.01	0.04	0.16				
Ironton Hollow	3	74.52	12.48	0.46	0.46	6.43	2.85	0.07	0.02	0.11	1.00	98.4	ND	ND	ND
rhyolite	±1σ	1.34	0.78	--	0.35	0.66	0.48	0.03	0.01	0.01	0.32				
Taum Sauk rhyolite	6	75.06	11.48	2.51	0.22	5.70	2.54	0.05	ND	0.21	3.39	101.16	229	35	271
	±1σ	2.40	0.56	0.36	0.11	0.54	0.69	0.02		0.08	1.68		46	7	72

[a]Percent by weight.
[b]Parts per million by weight.
[c]Number of samples analyzed for MnO in parenthesis following weight percent.

St. Francois Mountains. It is at least 390 m thick and lies beneath the Grassy Mountain ignimbrite within the Butler Hill caldera; it is possible that it is part of the caldera fill and was formed at about the same time as Grassy Mountain ignimbrite. The unit consists of at least two ash flow tuff sheets, one or two rhyolite lava flows, and minor intercalated volcaniclastic sedimentary rock units. Most of the Lake Killarney is a porphyritic, dark-maroon ash flow tuff with phenocrysts of quartz and pink perthite. Locally, it has abundant crushed pumice fragments, and rarely it displays autobreccia and lithophysae. Microscopically, the matrix consists of a granular aggregate of quartz and feldspar; quartz phenocrysts are embayed euhedral crystals or fragments, and feldspar phenocrysts are euhedral to fragmental and perthitic. Plagioclase, as small crystals, and lithic fragments, both occur rarely.

The formation has a persistent unit, the Anderson Mountain member [Sides, 1978], in its uppermost part that consists of coarse fragmental tuff, coarse breccia, or both. The fragmental tuff consists of a fine-grained matrix of quartz and feldspar with larger crystal fragments of quartz and perthite. The breccia consists of rounded to angular clasts of silicic volcanic rocks in a fine, quartzofeldspathic matrix; clasts range from a few millimeters to as large as 30 cm in diameter, but the approximate mean diameter is 5 to 10 cm. Clasts make up from 25 to 75% of the rock.

Grassy Mountain ignimbrite. This unit is a thick and very uniform ash flow tuff that occurs around the Butler Hill granite. Sides et al. [this issue] have interpreted it as the major intracaldera ash flow of the Butler Hill caldera. The rock is distinctive, consisting of abundant phenocrysts of quartz and salmon-pink perthite in a dark-maroon to black matrix. Crushed pumice fragments are rare, but they are locally abundant and extremely flattened with length to breadth ratios of 20 or more.

Microscopically, the matrix is a granular aggregate of quartz and feldspar which rarely preserves the structure of flattened shards. Quartz phenocrysts are 1 to 2.5 mm in diameter and commonly show hexagonal outlines that are deeply embayed. Perthite phenocrysts occur both as fragments and as euhedral crystals 1 to 5 mm in diameter. A blue-green amphibole is common as rounded aggregates or tiny needles in the matrix, particularly in the upper 200 m of the unit. Lithic fragments are rare and include older ash flow tuff, granophyre, and basalt or diabase. As noted by Sides et al. [this issue] an important feature of Grassy Mountain ignimbrite is its great thickness (at least 1 km) and its uniform texture and composition. Flow direction indicators demonstrate that Grassy Mountain ignimbrite originated within the area now occupied by Butler Hill granite [Sides, 1981].

Ironton Hollow rhyolite. Ironton Hollow rhyolite has been described by Sides [1978] and by Sides et al. [this issue]. It is mentioned here because we will present some major element chemical data from it in Table 3. Otherwise, however, it is not described further and will not be described here.

Taum Sauk rhyolite. Taum Sauk rhyolite, as

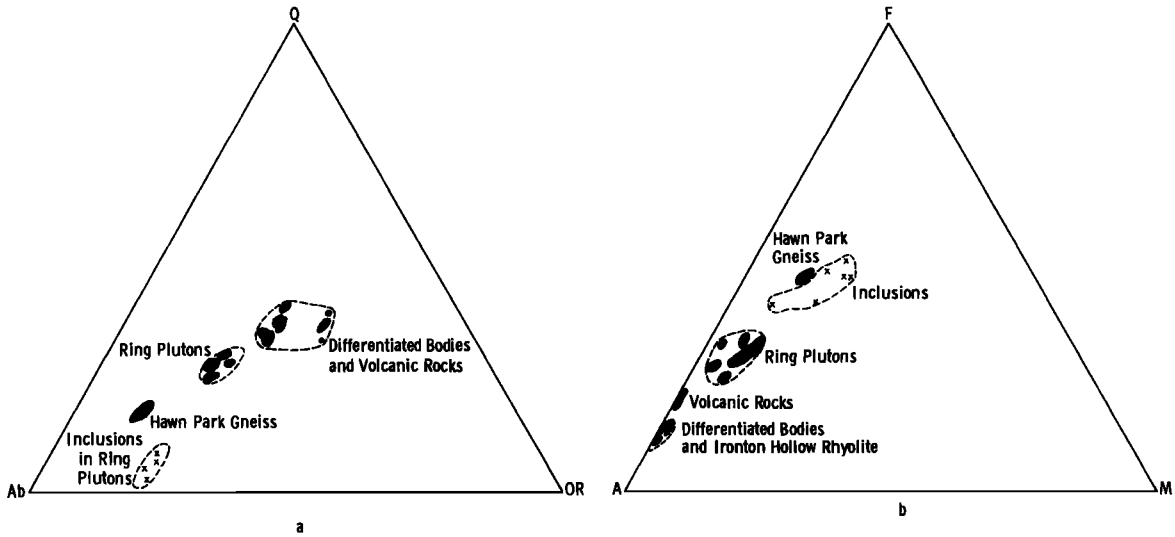

Fig. 2. Chemographic representations of major element trends in igneous rocks of St. Francois Mountains. (a) Quartz-Albite-Orthoclase plot. (b) A-F-M plot.

mentioned earlier, is a thick rhyolitic ash flow tuff that occurs in the Taum Sauk area in the western St. Francois Mountains. Mineralogially and texturally it is very similar to Grassy Mountain ignimbrite; it is described in detail by Sides et al. [this issue]. Major element data and abundances of Rb, Sr, and Ba are given in Table 3, but this unit will not be discussed in detail in this paper. Consequently, it will not be further described here.

Major Element Chemical Compositions

We have analyzed 119 samples of igneous rocks from the St. Francois Mountains for nine major elements (Si, Al, Na, Mg, K, Ca, Fe, Ti, and Mn) and three trace elements (Ba, Rb, and Sr); analysis of some of these samples for other trace elements, including REE, is reported in part 2 of this paper [Cullers et al., this issue]. All elements except Na, Mg, and Mn were analyzed by X ray fluorescence spectrometry, whereas Na was determined by flame photometry, Mg by atomic absorption spectrophotometry, and Mn by neutron activation., Fe was determined only as total Fe and was calculated as Fe_2O_3.

Complete analytical data are given in Appendix A. Sampling localities are shown on the map in Appendix B (Figure B1). Analytical methods, including the results of analyses of U.S. Geological Survey (USGS) standard rocks and a discussion of precision and accuracy, are presented in Appendix C.

In this paper, we will focus mostly upon the major element compositions of these igneous rocks. The trace element data given here will be discussed along with additional trace element data in part 2 of this paper.

Table 3 gives the average major element compositions of the rock units we have studied. Notice that the ring plutons of the Butler Hill caldera (Knoblick, Slabtown, Stono, and medium-grained Silvermine granites) and the hypabyssal intrusives of the Taum Sauk area (Munger and Carver Creek granites) are generally low-silica (66-71.5 wt % SiO_2) whereas the Butler Hill and Graniteville granites are high-silica (74.5-76.7 wt % SiO_2). Silvermine granite shows a major increase in SiO_2 and K_2O between its medium-grained, lower, and most abundant part (68.6 wt % SiO_2 and 3.86 wt % K_2O) and its fine-grained 'cap' (74.2 wt % SiO_2 and 4.44 wt % K_2O), with concomitant decreases in Al_2O_3, MgO, CaO, Fe_2O_3, and TiO_2; Na_2O remains essentially constant. Butler Hill granite shows regular decreases in Al_2O_3, Na_2O, CaO, MgO, Fe_2O_3, and TiO_2 and an increase in K_2O from its northeastern (lowest) exposures (Butler Hill type 1) to its western and southwestern (highest) exposures (Butler Hill type 3). SiO_2 increases from Butler Hill type 1 to the middle part of the body (Butler Hill type 2) but remains essentially constant between Butler Hill type 2 and Butler Hill type 3. The volcanic rocks analyzed (Grassy Mountain ignimbrite, Lake Killarney formation, Ironton Hollow ryolite, and Taum Sauk rhyolite) are all high-silica rocks and chemically similar to Butler Hill and Graniteville granites.

Particularly noteworthy are the compositions of inclusions from the Knoblick granite (but typical of those from Silvermine granite as well) and the composition of the gneissoid granodiorite of Hawn Park. These rocks are the most mafic materials we have studied in the St. Francois Mountains.

The analytical data are shown plotted on standard AFM and Q-Ab-Or triangular diagrams in Figures 2a and 2b. In these diagrams, Q, Ab, and Or are the normative minerals quartz, albite, and orthoclase, respectively, as calculated from the chemical data and A is the sum of the wt % Na_2O + K_2O, F = total Fe calculated as wt % FeO, and M = wt % MgO.

The chemical trends on these diagrams suggest that the rocks studied are serially related by either processes operating in the magmas or progressive partial melting. As shown in part 2 of this paper, trace element distributions in these rocks preclude their derivation by progressive partial melting. Because Silvermine granite

is demonstrably vertically differentiated in its field exposures and because petrographic considerations suggested that the vertical chemical changes observed could be accounted for by fractional crystallization, we tested the hypothesis through least squares modeling [Wright and Doherty, 1970]. Further, because the composition of the fine-grained 'cap rock' of the Silvermine granite closely approaches the composition of Butler Hill granite, Graniteville granite, and the volcanic rocks Grassy Mountain ignimbrite and Lake Killarney formation, we tested the additional hypothesis that the low-silica magmas that formed the ring plutons were parental melts from which the more silica-rich magmas were formed by simple fractional crystallization. In the following section we shall present arguments based upon variations in major element composition, but it will be seen that some of our decisions were affected by constraints placed upon the process by variations in trace element abundances. Modeling of the trace element data to test the fractional crystallization process developed here, and to address the question of the source region of the primary magmas, will be presented in part 2 of this paper.

Chemical Evolution of Magmas

Silvermine Granite as Representative Parental Magma

Above it was suggested that the ring plutons of the Butler Hill caldera might be good candidates for samples of parental magma. In the computations and arguments that follow, we have chosen the average composition of one of them, medium-grained Silvermine Granite, as the composition of the 'starting' or parental magma. Our reasons for this choice are summarized below:

1. The ring plutons of the Butler Hill caldera are the lowest in SiO_2 of any granitic intrusive rocks in the St. Francois Mountains, and they are spacially and structurally related to the large Butler Hill granite pluton and the voluminous Grassy Mountain ignmibrite. Moreover, the ubiquitous mafic inclusions in rocks of the ring plutons, which are essentially absent in Butler Hill granite and rare in Grassy Mountain ignimbrite, suggest that the ring plutons might be intruded from deeper magma sources. The high-silica rocks may lack significant inclusions because they are high-level differentiates of the low-silica magmas, and xenolithic material was removed along with more dense crystals.

2. We excluded the hypabyssal intrusives of the Taum Sauk area (Munger granite porphyry and Carver Creek granite) from consideration because of their distance from the major plutons, because of their somewhat higher SiO_2 concentration (Table 3), and because of the considerable uncertainty that they are coeval with other rocks of the region. Bickford and Mose [1975] reported that zircons from the Munger granite porphyry yielded a U-Pb age of 1380 ± 12 m.y., about 100 m.y. younger than any of the other rocks dated.

3. The Taum Sauyk rhyolite, which occurs in the western St. Francois Mountains, is probably the same age as the rocks of the Butler Hill caldera, for Bickford and Mose obtained an age of 1495 ± 6 m.y. from the Royal Gorge rhyolite, which, according to Berry [1970], is a basal lava flow of the Taum Sauk. We have, nevertheless, excluded Taum Sauk rhyolite from our considerations because of its distance from the Butler Hill caldera and because of uncertainty about its source and associations.

4. We chose medium-grained Silvermine granite as most representative of the ring pluton magmas because it is the largest of the ring plutons and because we could demonstrate the composition of its differentiate unequivocally from field, petrographic, and chemical data. Knoblick granite, although petrographically almost indistinguishable from Silvermine granite, is choked with small mafic inclusions; this probably accounts for its lower SiO_2 concentration. Stono granite is a small body and quite altered. Slabtown granite is somewhat higher in SiO_2 than Silvermine.

5. Finally, we note that other authors have interpreted late, lower-silica magmas typically erupted into the ring fractures of calderas after major collapse, as samples of the deeper parts of differentiated magma chambers. For example,

TABLE 4. Average Medium-Grained Silvermine Granite to Intermediate Silvermine (BSF 255)

m/g Silvermine Starting Magma Oxide	Weight Percent	Computed Liquid wt%	Intermediate Silvermine Granite (BSF 255), wt%	Residual
SiO_2	70.39	74.29	73.92	0.22
TiO_2	0.45	0.15	0.30	-0.12
Al_2O_3	14.87	14.23	13.73	0.38
Fe_2O_3	3.40	2.09	2.07	0.01
MgO	0.95	0.11	0.41	-0.24
CaO	1.84	1.05	0.78	0.21
Na_2O	4.13	3.38	4.10	-0.58
K_2O	3.96	4.71	4.69	0.01

The weight mode mineral phases removed are plagioclase (An_{14}), 12.72; biotite, 2.21; hornblende, 4.08; sphene, 0.44; and magnetite, 0.64 for a total of 20.10.

TABLE 5. Intermediate Silvermine (BSF 255) to Fine-Grained 'Cap Rock' (BSF 233)

Intermediate Silvermine Starting Magma Oxide	Weight Percent	Computed Liquid wt%	f/g Silvermine Cap Rock (BSF 233), wt%	Residual
SiO_2	73.92	75.98	75.83	0.13
TiO_2	0.30	0.21	0.25	-0.04
Al_2O_3	13.73	12.99	12.91	0.07
Fe_2O_3	2.07	1.61	1.55	0.05
MgO	0.41	0.09	0.20	-0.09
CaO	0.78	0.66	0.65	0.01
Na_2O	4.10	3.87	3.97	-0.09
K_2O	4.69	4.60	4.64	-0.04

The weight mode mineral phases removed are plagioclase (An_{14}), 5.90; biotite, 2.91; and alkali feldspar, 3.04 for a total of 11.85.

TABLE 6. Compositions of Minerals Removed in Silvermine Granite Crystallization

Mineral	SiO_2	Al_2O_3	Fe_2O_3	MgO	CaO	Na_2O	K_2O	TiO_2
Plag (An_{14})	64.99	21.97	---	---	2.96	10.08	---	---
Biotite	38.82	14.10	22.47	11.24	0.51	0.61	8.17	4.09
Hornblende	45.25	10.06	14.51	15.10	12.06	1.00	0.51	1.51
Sphene	30.65	---	---	---	28.60	---	---	40.75
Magnetite	---	---	99.99	---	---	---	---	---
Alkalic Feldspar	65.18	18.90	---	---	0.36	2.48	13.08	---

Bailey and others (1976) have described the late stage emplacement of coarsely porphyritic hornblende-biotite rhyodacite, containing 70-64 percent SiO_2, along the rim of the Long Valley caldera of eastern California, and suggest that it was derived from deeper parts of the magma chamber.

Differentiation of Medium-Grained Silvermine Granite to Form Its Cap Rock

Scully [1978] studied the Silvermine granite and its differentiated 'cap rock', concluding that the mineralogical and chemical changes observed could be accounted for by fractional removal of plagioclase (average about An_{14}), hornblende, biotite, and sphene, all of which are apparently liquidus phases. We have modeled fractional crystallization of this body in two stages, being constrained by the requirement that significant degrees of crystallization and removal of an alkalic feldspar were required to account for trace element variation [see Cullers et al., this issue]. We have proceeded as follows:

1. We modeled fractional crystallization of medium-grained Silvermine granite as a starting magma, removing plagioclase (An_{14}), biotite, amphibole, sphene, and magnetite and using the composition of an intermediate composition rock (our sample BSF 255, see Appendix A for analytical data) as the liquid end-member. BSF 255 occurs in a zone of porphyritic rock below the fine-grained 'cap rock' but above the typical medium-grained Silvermine granite. The results of this calculation are given below in Table 4. Notice that the residuals from this calculation are small and that the phases removed adequately account for the changes in composition except for Na_2O which deviates by about 21%. About 20% crystallization by weight is required.

2. Next we modeled fractional crystallization of the intermediate composition rock (BSF 255), using the composition of a sample of the most silica-rich 'cap rock' (BSF 233, see Appendix A for analytical data) as the liquid end-member. We found that this process could be modeled best removing only plagioclase (An_{14}), biotite, and an alkalic feldspar. The results of this calculation are given in Table 5; the residuals are quite small. The process requires the crystallization of an additional 12% of the remaining magma by weight.

The results of these two calculations show that a magma of the composition of the medium-grained Silvermine granite could yield a melt of the composition of the fine-grained 'cap rock' by simple fractional crystallization, initially involving removal of plagioclase (An_{14}), biotite, hornblende, sphene, and magnetite until almost 20% of the magma had crystallized and then crystallization of about 12% of the remaining melt with the fractional removal of plagioclase (An_{14}), an alkalic feldspar, and biotite. The phases involved are all liquidus phases in these rocks. The plagioclase composition used is based

TABLE 7. BSF 255 to Average Butler Hill Granite

Int. Silvermine (BSF 255) Starting Magma		Computed Liquid, wt%	Average Butler Hill Granite, wt%	Residual
Oxide	Weight Percent			
SiO_2	73.92	76.91	76.92	-0.01
TiO_2	0.30	0.17	0.17	0.00
Al_2O_3	13.73	12.52	12.54	-0.02
Fe_2O_3	2.07	1.46	1.37	0.07
MgO	0.41	-0.02	0.15	-0.14
CaO	0.78	0.53	0.49	0.03
Na_2O	4.10	3.54	3.49	0.04
K_2O	4.69	4.90	4.87	0.03

The weight mode mineral phases removed are plagioclase (An_{14}), 10.65; biotite, 3.81; and alkali feldspar, 2.28 for a total of 16.74.

TABLE 8. Internal Differentiation of Butler Hill Granite

Average Butler Hill Granite Starting Magma		Computed Liquid, wt%	Average Composition of Western Part of Butler Hill, wt%	Residual
Oxide	Weight Percent			
SiO_2	76.92	77.76	77.76	0.00
TiO_2	0.17	0.15	0.15	0.00
Al_2O_3	12.54	12.42	12.42	0.00
Fe_2O_3	1.37	1.02	1.02	0.00
MgO	0.15	0.09	0.09	0.00
CaO	0.49	0.25	0.25	0.00
Na_2O	3.49	3.22	3.22	0.00
K_2O	4.87	5.09	5.09	0.00

The weight mode mineral phases removed are plagioclase (An_{14}), 9.61; alkali feldspar, 16.68; quartz, 14.46; biotite, 0.87; sphene, 0.12; magnetite, 0.59 for a total of 42.33.

TABLE 9. Average Grassy Mountain From Average Butler Hill Granite

Average Butler Hill Granite Starting Magma		Computed Liquid wt%	Average Grassy Mountain Ignimbrite wt%	Residual
Oxide	Weight Percent			
SiO_2	76.92	77.99	77.39	0.23
TiO_2	0.17	0.21	0.18	0.01
Al_2O_3	12.54	11.93	11.56	0.14
Fe_2O_3	1.37	2.32	2.21	0.04
MgO	0.15	-0.27	0.05	-0.12
CaO	0.49	0.22	0.25	-0.01
Na_2O	3.49	3.17	3.72	-0.20
K_2O	4.87	4.43	4.64	-0.08

The weight mode mineral phases removed are plagioclase (An_{14}), 12.08; alkali feldspar, 27.12; quartz, 21.15; and biotite, 2.24; for a total of 62.59.

TABLE 11. Average Medium-Grained Silvermine Granite to Graniteville Granite

Average m/g Silvermine Granite Starting Magma		Computed Liquid wt%	Average Graniteville Granite, wt%	Residual
Oxide	Weight Percent			
SiO_2	70.39	77.19	76.54	0.37
TiO_2	0.45	-0.17	0.11	-0.19
Al_2O_3	14.87	13.37	12.58	0.53
Fe_2O_3	3.40	1.30	1.27	0.02
MgO	0.95	-0.49	0.04	-0.37
CaO	1.84	1.12	0.66	0.32
Na_2O	4.13	2.92	4.13	-0.84
K_2O	3.96	4.75	4.66	0.06

The weight mode mineral phases removed are plagioclase (An_{14}), 19.18; biotite, 8.02; hornblende, 2.60; sphene, 0.49; and magnetite, 0.32 for a total of 30.61.

upon mass balance calculations for the medium-grained Silvermine granite and the fine-grained 'cap'. The alkalic feldspar composition used is the composition of bulk perthite separated from the medium-grained granite and analyzed for Ca, Al, Na, K, and Si by standard methods (Appendix C). The compositions of the other phases were approximated from analyses published for similar rocks. Table 6 gives the chemical compositions used for phases removed in these calculations.

Differentiation of Medium-Grained Silvermine Granite to Form Butler Hill Granite

In order to test the hypothesis that a magma of the composition of the medium-grained Silvermine granite could yield the magma that formed the Butler Hill granite by simple fractional crystallization, we modeled this process using medium-grained Silvermine granite as a starting magma, removing plagioclase (An_{14}), biotite, hornblende, sphene, and magnetite and using the average of all of our analyses of Butler Hill granite as the end-member. The compositions of the phases removed are the same as those in the previous calculation and are given in Table 6.

Removal of these phases from a magma of the composition of medium-grained Silvermine yields a computed liquid that approximates the bulk composition of the Butler Hill granite in terms of major elements except for Na_2O, which deviates by about 34%; about 32% crystallization is required. As will be shown in part 2 of this paper, it is difficult to account for some of the variations in trace element composition with this model, specifically the observed increases in Rb and the decrease in Ba, both of which suggest removal of an alkalic feldspar.

With these constraints in mind, we modeled the derivation of Butler Hill granite from an intermediate differentiate of Silvermine granite, such

TABLE 10. Average Butler Hill Granite to Lake Killarnev Formation

Average Butler Hill Granite Starting Magma		Computed Liquid wt%	Average Lake Killarney, wt%	Residual
Oxide	Weight Percent			
SiO_2	76.92	77.72	77.06	0.26
TiO_2	0.17	0.25	0.17	0.03
Al_2O_3	12.54	11.53	11.18	0.13
Fe_2O_3	1.37	2.52	2.48	0.02
MgO	0.15	-0.13	0.04	-0.06
CaO	0.49	-0.12	0.26	-0.14
Na_2O	3.49	2.39	2.76	-0.14
K_2O	4.87	5.83	6.04	-0.08

The weight mode mineral phases removed are plagioclase (An_{14}), 16.70; alkali feldspar, 22.21; quartz, 20.83; and biotite, 1.77 for a total of 61.51.

TABLE 12. Average Butler Hill Granite to Graniteville Granite

Average Butler Hill Granite Starting Magma		Computed Liquid wt%	Average Graniteville Granite wt%	Residual
Oxide	Weight Percent			
SiO_2	76.92	77.14	76.54	0.34
TiO_2	0.17	0.11	0.11	0.00
Al_2O_3	12.54	12.89	12.58	0.17
Fe_2O_3	1.37	1.39	1.27	0.07
MgO	0.15	-0.25	0.04	-0.16
CaO	0.49	0.48	0.66	-0.10
Na_2O	3.49	3.75	4.13	-0.21
K_2O	4.87	4.49	4.66	-0.10

The weight mode mineral phases removed are plagioclase (An_{14}), 5.91; alkalic feldspar, 18.86; quartz, 15.82; and biotite, 2.59 for a total of 43.18

as our sample BSF 255, on the hypothesis that fractional crystallization proceeded in steps in the larger magma chamber just as it apparently did in the Silvermine pluton. The results of this calculation are given in Table 7 and show that the average composition of Butler Hill granite can be closely derived by fractional removal of plagioclase (An_{14}), an alkalic feldspar, and biotite. This process requires about 17% crystallization in addition to 20% fractional crystallization of plagioclase, biotite, hornblende, sphene, and magnetite to derive a liquid of the composition of BSF 255 from average medium-grained Silvermine magma.

The Internal Differentiation of the Butler Hill Granite

As noted earlier, there is a significant variation in major element abundance between the most northeasterly, and presumably lowest, exposures of the Butler Hill granite and the rocks exposed in the western and southwestern parts of the pluton. These chemical changes accompany textural variations that suggest that the body originally underwent vertical differentiation and was subsequently tilted to the west-southwest and eroded.

We tested the hypothesis that the observed chemical changes occurred because of fractional crystallization by using the bulk composition of Butler Hill granite, based upon the average of all of our analyses of this rock, as a starting magma, the composition of rocks in the western and southwestern parts of the pluton as the liquid end-member, and removing plagioclase (An_{14}), alkalic feldspar, quartz, biotite, sphene, and magnetite. The composition of the alkalic feldspar removed was determined from an analysis of separated bulk perthite from a sample of the medium to coarse-grained Butler Hill granite from the northeastern part of the pluton (BSF 177; Appendix A). The composition of biotite and sphene are as given in Table 6. As noted earlier, petrographic study of the Butler Hill granite indicates that quartz was an early liquidus phase, as was an alkali feldspar; thus, removal of these minerals during fractional crystallization is consistent with the nature of the rocks.

The results of this calculation are given in Table 8. It will be seen that removal of these phases yields a calculated liquid that, to two decimal places, perfectly matches the average composition of the differentiated uppper part of the Butler Hill granite. The process requires 42.33% crystallization by weight, including removal of 9.61% of a plagioclase whose composition is An_{14}.

Derivation of Grassy Mountain Ignimbrite and Lake Killarney Formation From Butler Hill Granite Magma

Sides et al. [this issue] propose that Butler Hill granite represents the frozen magma chamber that was beneath the caldera that erupted Grassy Mountain ignimbrite and perhaps Lake Killarney formation as well. We tested this hypothesis by modeling the composition of both Grassy Mountain ignimbrite and Lake Killarney formation from average Butler Hill granite magma.

For this calculation we used the average composition of Butler Hill granite as a starting magma, the average composition of Grassy Mountain ignimbrite as the liquid end-member, and removed plagioclase (An_{14}), an alkali feldspar whose composition was determined by analysis of bulk perthite separated from a sample of medium to coarse-grained Butler Hill granite from the northeastern part of the pluton, quartz, and biotite. As noted earlier, all of these minerals are liquidus phases in Butler Hill granite. The results of this calculation are given in Table 9. It can be seen that the calculated liquid approximates the major element composition of Grassy Mountain closely and that 62.59% crystallization is required. However, as shown in part 2 of this paper and discussed below, limited trace element data from Grassy Mountain ignimbrite are not consistent with its derivation from Butler Hill granite magma by fractional crystallization involving feldspars.

We also modeled the composition of Lake Killarney formation using average Butler Hill granite as the starting magma and removing the same phases as above. The result of this computation is given in Table 10 and shows that the Lake Killarney magma could have been derived from Butler Hill type magma by fractional crystallization of plagioclase, alkali feldspar, quartz, and biotite in amounts totalling 61.51 wt%. Removal of about 4% more plagioclase and correspondingly less alkali feldspar and quartz is required to yield this high-K_2O liquid than the more normal Grassy Mountain.

The role of the Lake Killarney formation in the igneous processes leading to formation of the Butler Hill caldera is not as clear as that of Grassy Mountain ignimbrite and the plutonic rocks. The Lake Killarney formation is quite diverse lithologically, and our samples may not represent its chemical composition very well. Moreover, its unusually high K_2O/Na_2O ratio (Table 3 and Appendix A) suggests posteruptive alkali mobility.

Derivation of Graniteville Granite From Medium-grained Silvermine Granite or Butler Hill Granite

As will be seen in part 2 of this paper, Graniteville granite appears to be the most highly evolved granite body of any we have studied in terms of its trace element abundances and in the magnitude of its negative Eu anomaly. Consequently, we wanted to see whether it could be derived from either the proposed parental magma, medium-grained Silvermine type, or perhaps from average Butler Hill granite magma, by fractional crystallization. The results of these calculations are given in Tables 11 and 12. It can be seen from these results the Graniteville granite could be derived directly from a Silvermine-type magma by removal of liquidus phases totaling 30.61 wt%. However, the residuals are relatively large, and such a small degree of crystallization cannot account for the trace element data, particularly the depletion in Ba and Sr. The calculation using average Butler

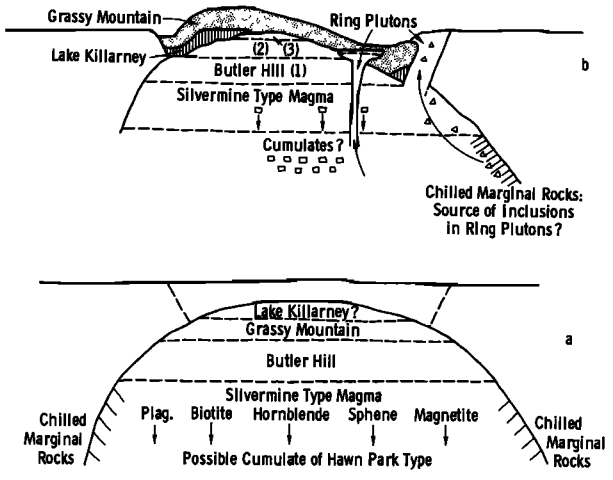

Fig. 3. Diagramatic representation of evolution of magmas in Butler Hill caldera. (a) Emplacement of magma body of medium-grained Silvermine composition and differentiation of a high-silica upper portion by crystal fractionation. (b) Formation of Butler Hill caldera, including eruption of Lake Killarney formation and Grassy Mountain ignimbrite, emplacement of Butler Hill granite during resurgent doming, and emplacement of low-silica ring plutons.

Hill magma as a staring material yields a computed liquid that is much closer to the composition of Graniteville granite with removal of 43.18% liquidus phases, including an alkalic feldspar. Trace element data presented in part 2 of this paper are also most consistent with derivation of Graniteville granite magma from Butler Hill.

As noted earlier and also by Sides et al. [this issue] Graniteville granite intrudes volcanic rocks on the western side of the angular unconformity that separates the Butler Hill caldera from the calderas of the western St. Francois Mountains. Graniteville granite is, therefore, at least somewhat younger than the plutonic and volcanic rocks associated with the Butler Hill caldera, and there is no structural reason suggesting that it should be related to the magmatic system of the Butler Hill caldera. It may be that Graniteville granite was derived by fractional crystallization from a separate, but similar, magmatic system located to the west of the Butler Hill caldera.

Discussion

Evolution of Magmas

The analytical data and the computations presented here suggest that the following is the most reasonable interpretation of the evolution of magmas in the Butler Hill caldera. The relationships to be discussed below are summarized diagrammatically in Figures 3a and 3b.

The most primitive magmas appear to be those that crystallized to form the ring plutons (Silvermine granite, Knoblick granite, Stono granite, and Slabtown granite). They have the lowest SiO_2 content and the highest CaO, MgO, TiO_2, MnO, and Fe_2O_3; their chemistry is reflected in modal hornblende and sphene and relatively abundant plagioclase, in contrast to Butler Hill granite, Graniteville granite, and the Grassy Mountain ignimbrite. As will be shown in part 2 of this paper, the trace element abundances in the ring plutons are also consistent with their being the most primitive rocks exposed. We believe that igneous activity in the St. Francois Mountains began with the emplacement of significant volumes of magma of approximately the composition of the average medium-grained Silvermine granite (Table 3). In the Butler Hill caldera area, a magma body about 25 km in diameter was emplaced at relatively shallow depths (8 km or less; [Sides, 1978]).

The upper part of this magma body began crystallizing hornblende, biotite, sphene, magnetite, and plagioclase (about An_{14}) as early liquidus phases, and these settled in the chamber gravitationally. The result was the formation of a differentiated liquid of approximately the composition of the average Butler Hill granite (Table 3) which occupied the upper part of the chamber. This process, which is modeled in Table 7, required crystallization of about 37% of the liquid.

As the temperature fell, alkalic feldspar, plagioclase, quartz, sphene, and magnetite continued to crystallize fractionally in the upper part. As indicated by the calculations in Tables 8, 9, and 10, this process led to compositional zoning of the upper part of the chamber such that the upper part had the composition of Grassy Mountain ignimbrite. It is also possible, though less certain, that the uppermost part of the chamber had the composition of Lake Killarney formation (Figure 3a). Magma below this upper zone may also have been zoned in the manner now exhibited by the Butler Hill granite during this period, or this zonation may have formed somewhat later.

As shown diagramatically in Figure 3b, the crust above the magma chamber fractured with the eruption of large volumes of Grassy Mountain ignimbrite and the formation of the Butler Hill caldera. On the basis of its abundant lithic fragments and stratigraphic position, it is also possible that Lake Killarney formation was the earliest part of this eruptive cycle. Following emplacement of Grassy Mountain ignimbrite and the formation of the caldera, the structure was resurgently domed, presumably attendant upon the intrusion of the remaining compositionally zoned upper part of the magma chamber into the structure to form the Butler Hill granite. As noted above, the compositional zoning of the Butler Hill granite may have been formed after eruption of Grassy Mountain or even after intrusion of the Butler Hill magma into the caldera fill during resurgent doming.

As discussed in part 2 of this paper, the limited trace element data for Grassy Mountain ignimbrite, especially the magnitude of the negative Eu anomaly, is inconsistent with derivation of Grassy Mountain magma from Butler Hill magma by a process involving the separation of feldspar. The two samples of Grassy Mountain ignimbrite which were analyzed for trace elements came from masses of this unit separated by several kilometers; one sample is from near the base

of the unit, whereas the other is from near the top. When detailed trace element data are available for Grassy Mountain ignimbrite, they may be consistent with the simple model given here. Alternatively, such data may show that Grassy Mountain was not derived from Butler Hill magma or was derived by a mechanism more complex than simple fractional crystallization.

After emplacement of Butler Hill granite and resurgent doming of the caldera, essentially undifferentiated magma from deeper in the chamber moved upward and was emplaced along arcuate fractures in the caldera to form the ring plutons. At least one of these, Silvermine granite, underwent vertical differentiation through fractional crystallization after emplacement. This process initially involved removal of plagioclase (about An_{14}), hornblende, biotite, sphene, and magnetite, as indicated in Table 4, and then proceeded by fractional removal of plagioclase, biotite, and an alkalic feldspar only, as indicated by the calculations in Table 5.

It may be that the abundant inclusions that are found in all of the ring plutons are earlier crystallized parts of the primary magmas, perhaps from the walls of the primary magma chamber (Figure 3b). The abundance of hornblende and plagioclase in these inclusions and their bulk major element chemical compsition (Table 3) suggest that they could be such material. If so, they could have been detached and carried upward during intrusion of magma from the deeper parts of the chamber. The trace element compositions of the inclusion, as will be shown in part 2 of this paper, preclude the possibility that the inclusions are either cumulates from the primary magma or residual material from partial melting of source rocks.

The best candidate for a major sample of the cumulate resulting from crystallization of early phases is the gneissoid granodiorite of Hawn Park [Lowell, 1976]. This rock occurs as a giant inclusion in a granite that is similar to Butler Hill granite in an exposure along Pickle Creek in Hawn State Park, a locality about 20 km northeast of Knoblick and not shown on the geologic map [Sides et al., this issue, Plate 1]. The gneissoid granodiorite is foliated and consists of abundant plagioclase, with hornblende, biotite, quartz, and perthite (Table 1). The rock contains only about 56% SiO_2 (Table 3) and has greater abundances of Fe_2O_3, MgO, CaO, MnO, and TiO_2 than any other rock we have studied. We will show in part 2 of this paper that trace element abundances (e.g., a positive Eu anomaly) support the idea that the gneissoid granodiorite might be a sample of the cumulate material from differentiation of parental magmas of Silvermine type.

We have considered the possibility that compositional variations in rocks associated with the Butler Hill caldera could be the result of either progressive partial melting or a magmatic process such as the thermo-gravitational diffusion proposed by Hildreth [1979] to account for upward chemical changes in the magma that erupted the Bishop Tuff of northeastern California. As noted earlier, the trace element data presented in part 2 of this paper preclude progressive partial melting as a mechanism.

Thermo-gravitational diffusion of the type proposed for the Bishop Tuff magma apparently did not operate, at least in the larger magmatic system considered here. Hildreth [1979] suggests upward (i.e., in the magma chamber) increases in Na/K and Mn coupled with depletion of Ba, Sr, P, and Mg levels below 100 ppm are indicative that thermo-gravitational diffusion became a dominant process in a magma chamber. We note that in the rocks discussed here Na/K and Mn in fact decrease as SiO_2 increases, and of Ba, Sr, P, and Mg, only Sr is depleted below 100 ppm in the high-silica rocks (Butler Hill granite, Graniteville granite, Grassy Mountain ignimbrite, and Taum Sauk rhyolite).

It is entirely possible that a mechanism such as that described by Hildreth was dominant in the upper part of the magma chamber that erupted Grassy Mountain ignimbrite, a rock not unlike Bishop Tuff in many aspects. We have not yet made the kind of detailed study of Grassy Mountain ignimbrite that would be necessary to identify the effects of such a process, if indeed the record is still preserved in these Precambrian rocks.

Comparison With Wolf River Batholith, Wisconsin

The igneous rocks of the St. Francois Mountains are chemically similar to some of the plutons of the coeval Wolf River batholith of central Wisconsin [Van Schmus et al., 1975; Anderson and Cullers, 1978]. The rocks of the Wolf River batholith range in composition from anorthosite, through monzonite and adamellite to granite, a much greater compositional spread than is observed in the St. Francois Mountains. Anderson and Cullers [1978] believe that much of the batholith represents a sequence of older rapakivi granite to younger adamellite formed by progressive partial melting of a tonalitic, granodioritic, or andesitic source. High-silica granites (Belongia coarse and Belongia fine granites), however, have chemical characteristics suggesting that they were derived from the more volumninous Wolf River granite by fractional crystallization involving removal of K-feldspar, plagioclase, biotite, hornblende, ilmentite, and possibly some quartz. Trace element considerations require that about 55% crystallization of these phases plus additional removal of accessory minerals occur to yield the Belongia coarse granite from the Wolf River granite magma and that about 70% crystallization of the same phases occur to yield the Belongia fine granite.

The major element compositions of Belongia coarse and Belongia fine granites compare closely with the compositions of average Butler Hill granite and its fine-grained differentiate (Butler Hill type 3), but the parental Wolf River granite is more silica-rich than medium-grained Silvermine granite (73.3% volatile-free versus 70.39% volatile-free). Anderson and Cullers state that there are 'low-silica' portions of the Wolf River granite (these are about 68% silica on a volatile-free basis) and suggest that they are cumulates. It seems likely that the Wolf River batholith represents a deeper level of exposure than the present outcrops in the St. Francois Mountains.

TABLE A1. Analytical Data

	SiO_2	TiO_2	Al_2O_3	Fe_2O_3	MgO	MnO	CaO	Na_2O	K_2O	LOI	Total	Ba	Sr	Rb
Ring Plutons														
Silvermine granite														
Medium-grained type														
268	67.88	0.45	14.81	3.15	0.79	0.08	2.12	4.93	3.38	1.19	98.70	873	210	106
222	68.71	0.43	14.33	3.16	0.81	0.08	1.69	4.33	3.98	1.52	98.96	963	149	98
223[a]	68.87	0.45	14.49	3.55	1.22	ND	1.64	2.65	4.02	1.19	98.08	919	197	147
58[a]	68.64	0.48	14.58	3.39	0.95	ND	2.14	3.73	3.94	1.07	98.92	956	268	122
Intermediate type														
255	70.96	0.29	13.18	1.99	0.39	0.04	0.75	3.94	4.50	1.51	97.51	1054	153	156
Fine-grained type														
52[a]	72.94	0.28	12.96	1.65	0.31	ND	0.62	3.53	4.61	1.56	98.46	1010	121	173
53[a]	74.55	0.28	13.11	1.68	0.39	ND	0.51	3.98	4.65	1.40	100.55	867	84	172
54[a]	74.76	0.27	13.19	1.62	0.29	ND	0.28	2.70	5.37	1.32	99.80	806	50	263
61[a]	72.70	0.28	13.25	1.81	0.42	ND	0.75	3.70	4.62	1.17	98.70	991	105	154
72[a]	75.49	0.22	12.52	1.64	0.36	ND	0.52	5.71	1.21	1.32	98.99	415	158	47
77[a]	74.42	0.19	12.56	1.38	0.21	ND	0.50	3.20	5.27	1.01	98.74	520	72	154
227[a]	75.25	0.18	12.17	1.04	0.15	ND	0.42	3.12	4.86	1.03	98.22	422	55	191
232[a]	73.59	0.26	13.02	1.85	0.30	ND	0.67	3.52	4.78	1.23	99.22	832	123	185
233	74.42	0.24	12.67	1.52	0.20	0.02	0.64	3.90	4.55	1.62	99.74	712	95	141
Slabtown granite														
258	69.95	0.44	12.80	3.46	0.36	0.12	1.28	4.62	3.73	1.10	97.74	1138	131	98
259	70.94	0.47	13.15	3.58	0.45	0.13	1.18	4.79	3.47	0.83	98.86	930	112	85
Stono granite														
N6976	67.97	0.63	12.44	4.94	0.84	0.10	1.49	4.44	3.87	0.95	97.53	566	86	139
Knoblick granite														
27	65.57	0.52	16.41	4.61	1.21	0.09	3.20	4.49	3.18	0.93	102.12	836	293	101
33	67.51	0.44	14.40	3.68	0.79	0.07	2.24	4.57	3.25	0.98	97.86	887	227	110
35	66.37	0.47	14.73	4.09	1.00	0.07	2.68	4.46	3.09	1.14	98.03	888	275	104
41	66.22	0.44	14.25	3.93	0.95	0.08	2.60	4.41	3.15	0.64	96.60	839	255	103
High-Silica Plutons														
Butler Hill granite														
Type 1														
277	72.88	0.25	12.78	2.12	0.31	0.04	1.02	3.33	4.77	2.82	100.27	483	85	259
12-5-9	76.05	0.24	12.86	1.90	0.24	0.04	0.74	3.79	4.65	0.88	101.36	472	75	232
42	73.10	0.22	12.46	2.05	0.30	0.06	0.83	3.21	4.30	1.28	97.75	423	90	202
5-5-9	73.34	0.24	12.67	2.05	0.26	0.07	1.40	3.75	4.30	1.14	99.15	594	147	201
155	74.21	0.24	13.14	2.12	0.26	0.04	0.95	3.52	4.78	2.17	101.39	403	71	241
51	72.71	0.29	13.03	2.68	0.40	0.09	1.23	3.87	4.19	1.52	99.92	704	141	208
SSF 76	74.45	0.17	12.25	1.67	0.14	0.04	0.71	3.44	4.62	1.52	98.98	423	68	251
SSF 75	74.76	0.16	12.54	1.54	0.19	0.05	0.56	3.59	4.58	2.64	100.55	441	57	231
179	74.28	0.23	12.69	1.75	0.29	0.05	0.93	3.57	4.36	2.30	100.38	699	122	190
123	75.61	0.16	12.11	1.56	0.17	0.02	0.70	3.68	4.67	2.08	100.73	307	56	259
119	74.04	0.16	12.55	1.27	0.18	0.03	0.70	3.30	4.66	1.41	98.27	392	65	228
280	76.76	0.17	12.65	1.48	0.18	0.05	0.44	3.53	4.75	2.46	102.41	433	53	257
5-5-7	76.99	0.15	12.10	1.52	0.13	0.02	0.43	3.64	4.74	0.85	100.56	483	132	241
177	78.66	0.10	12.84	0.63	0.20	0.04	0.80	3.28	4.86	1.82	103.20	414	63	248
283	76.66	0.17	12.72	1.29	0.17	0.05	0.39	3.67	4.74	2.75	102.56	442	61	226
5-5-17	77.55	0.17	12.45	0.58	0.04	0.01	0.20	3.60	4.88	1.08	100.54	413	65	224
188	75.79	0.15	12.28	1.33	0.14	0.03	0.66	3.57	4.57	1.98	100.49	350	66	236

TABLE A1. (continued)

	SiO_2	TiO_2	Al_2O_3	Fe_2O_3	MgO	MnO	CaO	Na_2O	K_2O	LOI	Total	Ba	Sr	Rb
High-Silica Plutons (continued)														
Type 2														
SSF-92	77.61	0.13	11.94	0.92	0.05	0.01	0.21	3.52	5.14	1.55	101.08	125	15	242
286	77.05	0.18	12.30	1.39	0.14	0.04	0.56	3.29	4.96	2.46	102.34	372	51	236
5-5-19	77.54	0.16	12.40	1.32	0.19	0.02	0.29	3.58	4.80	0.91	101.19	444	59	220
287	77.09	0.17	12.45	1.41	0.30	0.03	0.46	3.48	4.90	1.27	101.36	353	61	244
5-5-5	76.01	0.15	12.12	1.40	0.12	0.03	0.38	3.64	5.01	0.98	99.82	435	60	248
290	77.57	0.16	12.39	1.36	0.12	0.02	0.39	3.41	5.01	1.16	101.57	367	60	261
12-5-3	75.97	0.16	11.99	1.39	0.13	0.07	0.39	3.90	4.69	0.87	99.49	420	60	216
207	76.32	0.16	12.05	1.44	0.18	0.02	0.46	3.70	4.84	2.21	101.36	356	45	239
SSF 88	75.57	0.16	12.21	1.46	0.15	0.04	0.55	3.45	4.75	1.31	99.61	391	55	199
SSF 11	74.78	0.16	12.08	1.23	0.12	0.05	0.45	3.50	4.89	1.28	98.49	387	53	250
284	76.90	0.17	12.65	1.47	0.16	0.04	0.51	3.61	4.26	0.51	100.23	471	68	194
SSF 22	75.33	0.14	12.31	1.22	0.11	0.04	0.47	3.28	5.21	1.44	99.52	405	44	244
5-5-3	76.60	0.15	11.90	1.47	0.12	0.04	0.42	3.78	4.90	0.96	100.30	383	62	237
5-5-13	74.63	0.20	12.87	1.96	0.23	0.05	0.85	3.72	4.70	0.82	99.99	ND	ND	ND
12-5-5	75.09	0.14	12.27	1.37	0.11	0.04	0.11	3.34	4.98	1.28	98.70	429	48	258
N 3475	76.29	0.15	11.34	0.92	0.06	0.01	0.26	3.10	5.20	0.67	98.00	206	11	266
N 3775	74.70	0.18	14.52	0.95	0.06	0.01	0.11	3.05	5.26	1.03	99.87	221	15	278
N 6275	76.29	0.14	11.37	1.33	0.05	0.01	0.21	2.66	2.75	0.79	95.58	175	17	343
Type 3														
N 5775	74.85	0.16	12.05	1.38	0.12	0.03	0.47	3.43	4.91	1.32	98.68	464	37	249
N 575	77.27	0.13	11.32	1.04	0.09	0.02	0.45	3.57	4.97	1.51	100.36	108	19	246
N 4175	75.32	0.11	12.14	1.09	0.14	0.06	0.18	2.57	4.59	1.87	98.05	438	44	217
N 1475	76.61	0.15	12.89	1.18	0.05	0.01	0.07	1.76	5.47	1.17	99.36	275	16	167
N 6276 B	75.42	0.13	11.45	0.73	0.06	0.01	0.20	3.32	5.01	1.35	97.67	158	17	111
N 7175	76.47	0.14	11.51	1.05	0.04	0.01	0.04	3.48	2.32	1.15	96.20	376	21	140
N 5276	76.12	0.16	11.58	0.67	0.06	0.01	0.17	5.36	1.09	0.90	96.17	235	22	54
N 5475	76.20	0.15	12.02	1.03	0.07	0.03	0.17	3.31	5.06	1.14	99.15	291	22	163
N 3575	75.73	0.22	13.42	0.77	0.19	0.02	0.66	4.08	4.51	1.95	101.53	505	49	198
N 2775	75.37	0.13	12.95	1.02	0.05	0.01	0.04	3.11	5.21	1.44	99.33	430	14	191
Graniteville granite														
242	72.99	0.16	12.20	1.48	0.03	0.002	0.49	4.03	4.57	1.63	97.57	123	17	400
243	76.71	0.09	12.78	1.11	0.05	0.001	0.57	4.20	4.80	0.65	100.96	148	14	351
244	77.14	0.09	12.50	1.31	0.05	0.002	0.69	4.15	4.38	1.40	101.71	88	18	333
246	74.61	0.10	12.08	1.12	0.05	0.002	0.84	3.89	4.62	2.45	99.76	196	26	301
Plutons of Taum Sauk Area														
Munger granite[b]														
RK-1	71.30	ND	13.30	2.91	0.13	0.06	0.39	3.27	5.78	0.01	97.15	1460	50	170
RK-2	71.50	ND	13.04	3.25	0.12	0.08	0.63	3.39	5.81	0.01	97.93	1460	115	195
RK-3	70.10	ND	13.01	3.20	0.12	0.08	0.69	3.35	6.14	0.01	96.70	1490	36	300
RK-4	72.10	ND	13.57	2.78	0.18	ND	0.41	3.23	5.52	0.005	97.80	1610	58	130
RK-5	71.10	ND	13.08	3.34	0.13	ND	0.97	3.44	6.02	0.01	98.09	1525	50	320
RK-6	70.90	ND	12.81	3.58	0.15	0.09	0.74	3.30	5.66	0.002	97.23	1550	90	146
RK-7	72.40	ND	13.49	3.43	0.18	0.07	0.30	3.45	5.92	0.003	99.17	ND	ND	182
RK-8	73.00	ND	13.38	3.35	0.17	0.06	0.25	3.31	5.94	0.01	99.47	1510	ND	261
Carver Creek granite														
CC	69.69	0.47	13.05	4.69	0.34	0.09	1.12	3.81	4.87	1.17	99.22	963	89	157
KSU[b]	70.00	ND	13.16	4.71	0.33	0.09	1.09	3.89	4.79	0.88	98.94	1140	82	157

TABLE A1. (continued)

	SiO_2	TiO_2	Al_2O_3	Fe_2O_3	MgO	MnO	CaO	Na_2O	K_2O	LOI	Total	Ba	Sr	Rb
Inclusions														
In Knoblick granite														
28A	55.29	1.15	15.34	10.57	3.33	0.25	4.34	4.70	1.81	0.79	97.32	562	285	75
28B	56.33	0.80	14.93	9.30	3.44	0.18	5.03	4.60	1.94	0.96	97.33	517	267	81
28C	55.52	0.70	15.23	8.76	3.49	0.17	5.63	4.27	1.78	1.57	96.94	431	307	118
28D	57.90	0.77	15.49	7.20	2.60	0.14	4.13	3.99	3.09	1.38	96.56	593	317	129
30A	54.57	0.79	14.92	9.23	3.62	0.22	5.54	4.62	1.87	1.10	96.27	535	261	76
30B	59.65	0.68	15.47	6.79	1.89	0.14	3.62	3.06	1.88	1.90	94.94	778	255	81
In Butler Hill granite														
279	61.75	0.44	15.22	6.68	1.21	0.14	2.25	6.77	1.04	1.56	96.92	103	47	168
Possible Cumulate														
Hawn Park gneissoid granodiorite														
MB-73-1J	56.11	1.02	18.51	7.58	1.60	0.13	4.91	4.43	2.08	0.53	96.73	1541	455	52
MB-73-1I	56.42	1.14	18.82	7.83	1.72	0.15	4.97	4.32	2.15	0.71	98.08	1277	456	51
Volcanic Rocks														
Lake Killarney formation														
7-5-38[c]	76.91	0.15	11.09	2.50	0.04	0.01	0.17	2.79	5.84	0.43	99.92	ND	ND	ND
12-5-21[c]	76.43	0.20	11.15	2.44	0.04	0.03	0.35	2.71	6.19	0.66	100.17	ND	ND	ND
Grassy Mountain ignimbrite														
6-4-13[c]	75.90	0.16	11.07	2.16	0.04	ND	0.16	3.87	4.63	0.49	98.48	ND	ND	ND
6-4-19[c]	77.51	0.15	11.07	2.10	0.04	0.06	0.12	3.75	4.88	0.56	100.18	ND	ND	ND
6-5-8[c]	75.70	0.18	11.13	2.14	0.06	0.07	0.26	3.65	4.60	1.12	98.83	ND	ND	ND
12-5-24[c]	76.52	0.18	11.11	2.28	0.06	ND	0.20	3.43	4.94	0.71	99.42	ND	ND	ND
772[d]	76.90	0.19	12.48	2.02	0.08	ND	0.05	3.66	4.41	2.66[e]	102.45	227	13	147
774[d]	76.00	0.19	11.78	1.99	0.02	ND	0.07	3.53	4.36	2.95[e]	100.88	229	10	149
776[d]	76.68	0.19	11.49	2.23	0.07	ND	0.23	3.45	4.52	3.48[e]	102.34	390	15	163
779[d]	76.40	0.19	11.49	2.27	0.04	ND	0.21	3.42	4.45	3.88[e]	102.35	298	12	159
7712[d]	78.18	0.20	11.69	2.42	0.03	ND	0.42	3.81	4.27	5.60[e]	106.62	229	12	139
7717[d]	75.50	0.22	11.46	2.30	0.07	ND	0.53	3.84	4.50	2.71[e]	101.13	249	18	157
7730[d]	75.86	0.18	11.46	2.08	0.06	ND	0.41	3.56	4.49	2.05[e]	100.15	145	15	181
7731[d]	75.77	0.17	11.36	2.13	0.04	ND	0.37	3.59	4.82	0.99	99.24	123	12	176
7736[d]	75.54	0.18	11.19	2.03	0.05	ND	0.30	3.73	4.52	1.49	99.03	151	16	169
7741[d]	76.61	0.18	11.17	2.28	0.10	ND	0.13	3.74	4.61	2.24[e]	101.06	60	4	177
7744[d]	76.09	0.18	11.09	2.24	0.05	ND	0.28	3.97	4.67	1.25	99.82	95	11	179
Ironton Hollow rhyolite														
6-5-19[c]	73.61	0.11	12.21	1.63	0.04	ND	0.75	2.93	5.67	0.69	97.64	ND	ND	ND
6-5-21[c]	76.06	0.11	11.88	1.87	0.09	0.03	0.55	2.34	6.83	1.33	101.05	ND	ND	ND
12-5-33[c]	73.90	0.12	13.36	1.56	0.09	0.02	0.07	3.29	6.78	0.98	100.14	ND	ND	ND
Taum Sauk rhyolite														
TSR-1	75.90	0.20	11.36	2.35	0.04	ND	0.28	3.04	5.01	4.31[e]	102.49	305	45	184
TSR-3	76.60	0.20	11.53	2.36	0.05	ND	0.27	3.05	5.39	2.76[e]	102.21	321	34	204

TABLE A1. (continued)

	SiO_2	TiO_2	Al_2O_3	Fe_2O_3	MgO	MnO	CaO	Na_2O	K_2O	LOI	Total	Ba	Sr	Rb
TSR-5	78.28	0.17	10.74	2.40	0.04	ND	0.04	1.28	6.60	3.65[e]	103.20	263	34	318
810-3	74.29	0.15	11.23	2.42	0.04	ND	0.30	2.23	5.95	2.31[e]	98.92	318	26	221
810-6	73.76	0.17	11.56	2.28	0.03	ND	0.31	2.92	5.24	1.75	98.02	149	31	223
810-12	71.56	0.38	12.49	3.24	0.09	ND	0.15	2.71	6.01	2.84[e]	99.47	1749	41	226
Alkali Feldspar Separates[f]														
Silvermine (m/g)														
268	65.18		18.90				0.36	2.48	13.08					
222	65.53		19.08				0.43	3.77	11.18					
Knoblick granite														
41	65.34		19.01				0.41	3.15	12.08					
Butler Hill														
Type 1														
177	65.90		18.84				0.14	3.95	11.17					
277	65.44		18.76				0.18	2.70	12.92					
Type 3														
N 5775	66.01		18.92				0.18	4.37	10.53					
MO-7	66.06		18.89				0.14	4.43	10.48					
Graniteville granite														
242	65.21		18.53				0.03	1.57	14.66					
Munger granite														
MO-10	65.59		19.01				0.36	3.68	11.36					
Grassy Mountain														
MO-9	66.12		18.88				0.13	4.54	10.34					

Major elements in weight percent; Ba, Sr, Rb in ppm by weight.

[a]Analyses from Scully [1978].

[b]Analyses from Koch [1978].

[c]Analyses from Sides [1978].

[d]Analyses from Shuster [1978].

[e]Excessive LOI due to improper drying of samples prior to analysis.

[f]Calculated from analysis of separated feldspars, assuming CaO in stoichiometric An, Na_2O in stoichiometric Ab, and K_2O in stoichiometric Or.

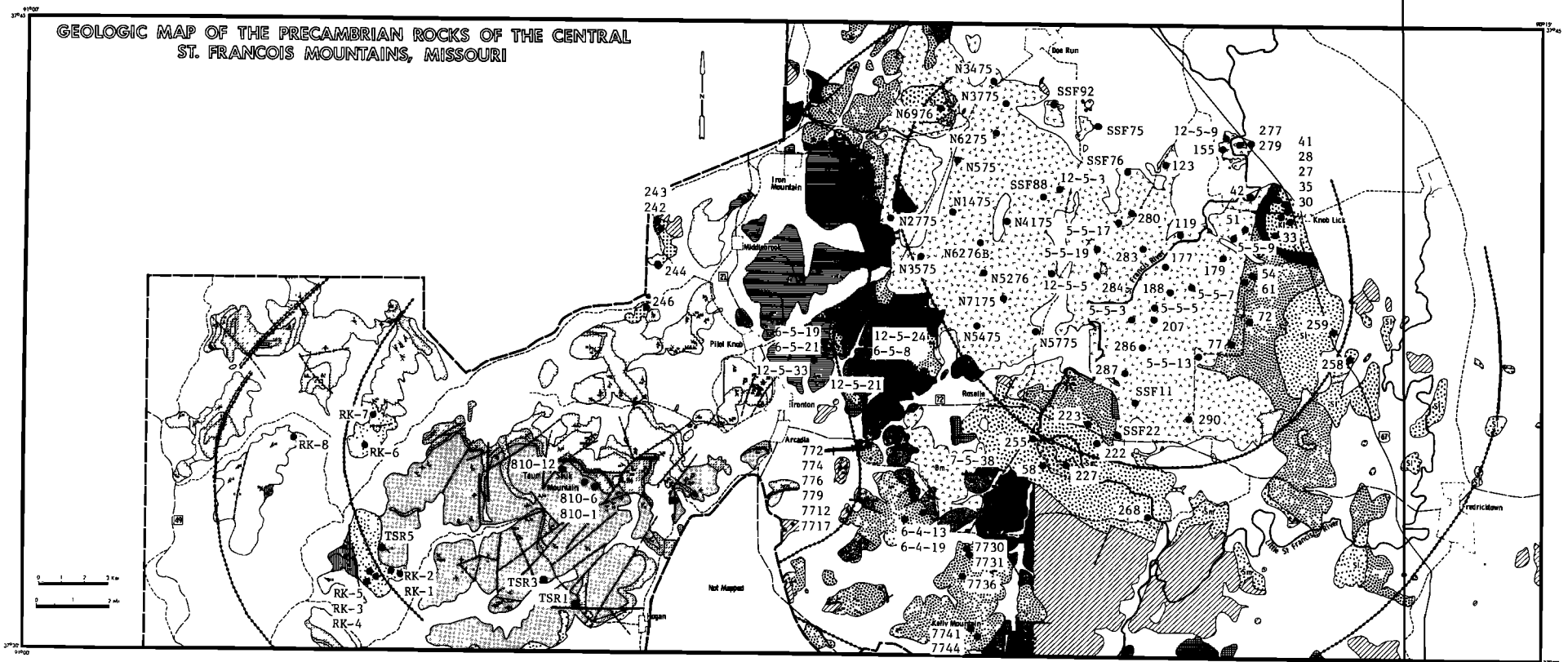

Fig. B1. Location of analyzed samples. Sample numbers without letter disignation are all BSF samples except 810-1, 6, 12 and samples in format such as 6-5-19. This is a reduced version of the geologic map that accompanies the paper by Sides et al. [this issue, Plate 1]. Please refer to that map for descriptive legend.

10383

Appendix C: Analytical Methods and Results of Analyses of Standard Rocks

The analyses for major elements reported here were done at the University of Kansas by X ray fluorescence emission spectrometry (Si, Al, Fe, Ca, K, and Ti), by atomic absorption spectrophotometry (Mg), and by flame photometry (Na). Additionally, Rb, Sr, and Ba were determined by X ray spectrometry. Other trace elements including Mn and duplicate analyses for Na and Fe, were done at Kansas State University by neutron activation analysis [Cullers et al., this issue].

The samples were ground in a small jaw crusher with tungsten carbide plates and then in a tungsten carbide ball mill. About 100 mg was dried and fuzed with spectroflux (a mixture composed of lithium tetraborate, lithium carbonate, and lanthanum oxide; Johnson Matthey Chemicals Limited) and cast into a glass disc according to the technique of Norrish and Hutton [1969] as modified by Harvey et al. [1973]. The discs were introduced into a General Electric XRD-6 X ray spectrometer for analysis. Another 100 mg was dissolved in HF in an enclosed teflon vessel, converted to chloride form with HCl, and aliquoted for Na and Mg analysis. Na was run directly on a Zeiss PMQ-II flame photometer, using a ratioing technique against a standard solution. The Mg aliquot was run by ratioing against a standard solution on a Perkin-Elmer model 360 atomic absorption spectrophotometer after first removing Fe as the hydroxide. Some of the remaining powdered sample was pressed into a powder pellet and analyzed for Rb, Sr, and Ba by X ray fluorescence methods.

Calibration curves for the XRF analyses were made from the USGS standard rocks G-2, GSP-1, AGV-1, DTS-1, and BCR-1, and the standard K-feldspar NBS 70a. Calibration curves for the flame photometer and atomic absorption analyses were made from dilutions of standard Na and Mg solutions.

Table C1 gives the results of analyses of USGS standard rocks and of an intralaboratory standard. We take the standard deviation of each oxide reported from the multiple analyses of the intralaboratory standard rock to be a measure of analytical precision, whereas the results for the USGS standard rocks are a measure of analytical accuracy.

TABLE C1. Major Element Analytical Data for USGS Standard Rocks And Replicate Analyses of an Intralaboratory Standard

	USGS Standard Rocks						Intralaboratory Standard
Oxides	G-2[a]	G-2[b] (5)	AVG-1[a]	AVG-1[b] (5)	GSP-1[a]	GSP-1[b] (3)	MO-23[c]
SiO_2	69.19	69.22 ±0.73	58.99	59.92 ±0.63	67.27	67.38 ±0.47	72.45 ±0.64
Al_2O_3	15.34	15.69 ±0.15	17.01	17.80 ±0.94	15.11	15.29 ±0.16	12.88 ±0.33
Fe_2O_3	2.76	2.52 ±0.02	6.80	6.53 ±0.14	4.33	4.08 ±0.03	2.65 ±0.12
CaO	1.98	1.95 ±0.03	4.98	5.03 ±0.11	2.03	2.01 ±0.05	1.06 ±0.02
K_2O	4.51	4.47 ±0.04	2.89	2.95 ±0.06	5.48	5.44 ±0.08	4.27 ±0.17
TiO_2	0.53	0.51 ±0.004	1.08	1.09 ±0.03	0.69	0.68 ±0.02	0.27 ±0.02
Na_2O	4.15	4.14(3) ±0.16	4.33	4.31(4) ±0.08	2.88	2.85 ±0.03	3.97(13) ±0.19
MgO	0.78	0.74(4) ±0.003	1.49	1.49 ±0.05	0.95	0.98 ±0.06	0.33(7) ±0.01
MnO	0.03	0.03(1) ----	0.09	0.07(3) ±0.05	0.04	0.04(2) ----	ND
Ignition loss	0.56	0.65(2) ±0.17	1.34	1.39(3) ±0.22	0.79	0.67(2) ±0.01	1.58 ±0.54
Total	99.76	99.92	99.00	100.60	99.57	99.42	99.46

[a] Indicates averages from Flanagan [1969].

[b] Indicates KU analyses.

[c] MO-23: 12 replicate analyses of intralaboratory granite standard from scratch.

Errors given are standard deviations; number of analyses of each rock is given in parantheses after the rock identification; numbers in parentheses after oxide values indicate number of determinations of that oxide if different from number of total analyses.

Acknowledgements. This work was supported by NSF grant EAR 76-03769. JRS received support from the Missouri Department of Natural Resources, Division of Geological Survey for some of his field work. Some of the analytical work was done by JRS as part of his doctoral dissertation at the University of Kansas. Special thanks go to Paul L. Hulen, who did much of the analytical work, and to Eugene I. Smith, University of Nevada, Las Vegas, who wrote the least squares program used in modeling fractional crystallization.

References

Amos, D. H., and G. A. Desborough, Mafic intrusive rocks of Precambrian age in southeast Missouri, Rep. Invest. Mo. Geol. Surv., 47 , 23 pp. 1970.

Anderson, J. E., M. E. Bickford, A. L. Odom, and A. W. Berry, Jr., Some age relations and structural features of the Precambrian volcanic terrane, St. Francois Mountains, southeastern Missouri, Geol. Soc. Am. Bull., 80, 1815-1818, 1969.

Anderson, J. L., and R. L. Cullers, Geochemistry and evolution of the Wolf River Batholith, a late Precambrian rapakivi massif in north Wisconsin, U.S.A., Precambrian Res., 7, 287-324, 1978.

Anderson, R. E., Igneous petrology of the Taum Sauk area, Missouri, Ph.D. dissertation, Wash. Univ., St. Louis, Mo., 1962.

Anderson, R. E., Ash-flow tuffs of Precambrian age in southeast Missouri, Rep. Invest. Mo. Geol. Surv., 46, 50 pp., 1970.

Bailey, R. A., G. B. Dalrymple, and M. A. Lanphere, Volcanism, structure and geochronology of Long Valley caldera, Mono County, California, J. Geophys. Res., 81, 725-744, 1976.

Berry, A. W., Precambrian volcanic rocks associated with the Taum Sauk caldera, St. Francois Mountains, Missouri, Ph.D. thesis, 147 pp., Univ. of Kansas, Lawrence, 1970.

Berry A. W., Jr., Proposed stratigraphic column for Precambrian volcanic rocks, western St. Francois Mountains, Missouri, in Studies in Precambrian Geology of Missouri, edited by E. B. Kisvarsanyi, Rep. Invest. Mo. Geol. Surv., 61, 81-90, 1976.

Bickford, M. E., and D. G. Mose, Geochronology of Precambrian rocks in the St. Francois Mountains, southeast Missouri, Spec. Pap. Geol. Soc. Am., 165, 48 pp., 1975.

Bickford, M. E., G. R. Lowell, J. R. Sides, and R. L. Nusbaum, Inferred structural configuration of the St. Francois Mountains batholith, southeastern Missouri, Geol. Soc. Am. Abstr. Programs, 9, 574-575, 1977.

Bickford, M. E., and R. D. Lewis, U-Pb geochronology of exposed basement rocks in Oklahoma, Geol. Soc. Am. Bull., 90, 540-544, 1979.

Bickford, M. E., K. L. Harrower, W. J. Hoppe, B. K. Nelson, R. L. Nusbaum, and J. J. Thomas, Rb-Sr and U-Pb geochronology and distribution of rock types in the Precambrian basement of Missouri and Kansas, Geol. Soc. Am. Bull., Pt. I, 92, 323-341, 1981.

Bickford, M. E., K. L. Harrower, W. J. Hoppe, B. K. Nelson, R. L. Nusbaum, and J. J. Thomas, Supplementary data for: Rb-Sr and U-Pb geochronology and distribution of rock types in the Precambrian basement of Missouri and Kansas, Geol. Soc. Am. Bull., Pt. II, 92, 963-996 (microfiche), 1981.

Blades, E. L., and M. E. Bickford, Rhyolitic ash-flow tuffs and intercalated volcaniclastic tuffaceous sedimentary rocks at Johnson Shutins, Reynolds County, Missouri, in Studies in Precambrian Geology of Missouri, edited by E. B. Kisvarsanyi, Rep. Invest. Mo. Geol. Surv., 61, 91-104, 1976.

Cullers, R. L., R. Koch, and M. E. Bickford, Chemical evolution of magmas in the Proterozoic terrane of the St. Francois Mountains, southeastern Missouri, 2, Trace element data, J. Geophys. Res., this issue.

Davis, J. W., Petrogenesis and structure of the Knoblick granite, M.S. thesis, St. Louis Univ., St. Louis, Mo., 1969.

Flanagan, F. J., U.S. Geological Survey Standards, II, First compilation of data for the new U.S.G.S. rocks, Geochim. Cosmochim. Acta, 33, 81-120, 1969.

Harvey, P. K., D. M. Taylor, R. D. Hendry, and F. Bancroft, An accurate fusion method for the analysis of rocks and chemcially related materials by X ray fluorescence spectrometry, X Ray Spectrom., 2, 33-44, 1973.

Hildreth, E. W., The Bishop tuff: Evidence for the origin of compositional zonation in silicic magma chambers, in Ash-Flow Tuffs, edited by C. E. Chapin and W. E. Elston, Geol. Soc. Am., Spec. Pap. 180, 43-75, 1979.

Koch, Richard J., Petrogenesis of the Precambrian Bevos and Musco groups, St. Francois Mountains Igneous Complex, Missouri, M.S. thesis, Kansas State Univ., Manhattan, 114 pp., 1978.

Kisvarsanyi, E. B., Spectroscopic distribution of the trace elements in the Precambrian granitic rocks of southeastern Missouri, in Guidebook to the Geology of the St. Francois Mountain Area, Rep. Invest. Mo. Geol. Surv., 26, 95-105, 1961.

Kisvarsanyi, E. B., Petrochemistry of a Precambrian igneous province, St. Francois Mountains, Missouri, Rep. Invest. Mo. Geol. Surv., 51, 103 pp., 1972.

Kisvarsanyi, G., Geochemical and petrological study of Precambrian iron metallogenic province of southeast Missouri, Ph.D. dissertation, Univ. of Mo., Rolla, 1966.

Lidiak, E. G., R. F. Marvin, H. H. Thomas, an M. N. Bass, Geochronology of the midcontinen region, United States, 4, Eastern area, J. Geophys. Res., 71, 5427-5438, 1966.

Lowell, G. R., Petrography of Precambrian rocks in the Hawn State Park area, Ste. Genevieve County, Missouri, in Studies in Precambrian Geology of Missouri, edited by E. B. Kisvarsanyi, Rep. Invest. Mo. Geol. Surv., 61, 140-148, 1976.

Lowell, G. R., and J. R. Sides, The occurrence and origin of rapakivi granite in the St. Francois Mountains Batholith of southeast Missouri, Geol. Soc. Am. Abstr. Programs, 5, 332-333, 1973.

Muehlberger, W. R., C. E. Hedge, R. E. Denison, and R. G. Marvin, Geochronology of the midcontinent region, United States, 3, Southern area, J. Geophys. Res., 71, 5409-5426, 1966.

Norrish, K., and J. T. Hutton, An accurate X-ray

spectorgraphic method for the analysis of a wide range of geological samples, Geochim. Cosmochim. Acta, 33, 431-454, 1969.

Nusbaum, R. L., A Precambrian collapse caldera boundary in the St. Francois Mountains, southeast Missouri, M.S. thesis, 77 pp., University of Kansas, Lawrence, 1980.

Schoolcraft, H. R., A view of Lead Mines of Missouri (Including Some Observations on the Mineralogy, Geology, Geography, Antiquities, Soil, Climate, Population, and Production of Missouri and Arkansas and Other Sections of Western Country), 229 pp., Charles Wiley, New York, 1819.

Scully, E. M., Silvermine granite: A differentiated ring pluton of the St. Francois Mountains batholith, southeastern Missouri, M.S. thesis, 45 pp., Univ. of Kansas, Lawrence, 1978.

Shuster, R. D., Chemistry and petrography of caldera-related ash-flows, St. Francois Mountains, Missouri: Grassy Mountain ignimbrite and Taum Sauk rhyolite, M.S. thesis, 45 pp., Univ. of Kansas, Lawrence, 1978.

Sides, J. R., Stratigraphy of volcanic rocks in the Lake Killarney quadrangle, Iron and Madison Counties, Missouri, in Studies in Precambrian geology of Missouri, edited by E. B. Kisvarsanyi, Rep. Invest. Mo. Geol. Surv., 61, 105-113, 1976.

Sides, J. R., A study of the emplacement of a shallow granite batholith: The St. Francois Mountains, Missouri, Ph.D. thesis, 124 pp., Univ. of Kansas, Lawrence, 1978.

Sides, J. R., Emplacement of the Butler Hill granite, a shallow pluton within the St. Francois Mountains batholith, southeastern Missouri, Geol. Soc. Am. Bull., Pt. I, 91, 535-540, 1980.

Sides, J. R., Geology of the Ketcherside Mountain area, southeastern Missouri, and the source of Grassy Mountain Ignimbrite, Geol. Soc. Am. Bull., Pt. I, in press, 1981.

Sides, J. R., M. E. Bickford, R. D. Shuster, and R. L. Nusbaum, Calderas in the Precambrian terrane of the St. Francois Mountains, southeastern Missouri, J. Geophys. Res., this issue.

Steiger, R. H., and E. Jäger, Subcommission on geochronology: Convention on the use of decay constants in geo- and cosmochronology, Earth Planet. Sci. Lett., 36, 359-362, 1977.

Tolman, C., and F. Robertson, Exposed Precambrian rocks in southeast Missouri, Rep. Invest. Mo. Geol. Surv., 44, 68 pp., 1969.

Van Schmus, W. R., L. G. Medaris, Jr., and P. O. Banks, Geology and age of the Wolf River batholith, Wisconsin, Geol. Soc. Am. Bull., 86, 907-914, 1975.

Van Schmus, W. R., and M. E. Bickford, Proterozoic chronology and evolution of the midcontinent region, North America, in Precambrian Plate Tectonics, edited by A. Kroner, Elsevier, New York, 781 pp., 1981.

Wright, T. L. and P. C. Doherty, A linear programming and least squares computer method for solving petrologic mixing problems, Geol. Soc. Am. Bull., 81, 1995-2007, 1970.

(Received December 22, 1980;
revised May 11, 1981;
accepted May 19, 1981.)

JOURNAL OF GEOPHYSICAL RESEARCH, VOL. 86, NO. B11, PAGES 10388–10401, NOVEMBER 10, 1981

Chemical Evolution of Magmas in the Proterozoic Terrane of the St. Francois Mountains, Southeastern Missouri 2. Trace Element Data

R. L. CULLERS AND R. J. KOCH

Department of Geology, Kansas State University, Manhattan, Kansas 66506

M. E. BICKFORD

Department of Geology, University of Kansas, Lawrence, Kansas 66045

The St. Francois Mountains igneous complex of Proterozoic age consists of hypabyssal, granite plutons intruded into the overlying rhyolites of similar age. Melting and crystallization models of these rocks suggested by the field, petrographic, and major element contents are further refined using Rb, Ba, Sr, REE (rare-earth element), Th, Sc, and Co contents. There are two groups of relatively undifferentiated plutons associated with the Butler Hill caldera and Taum Sauk area that could have formed by partial melting of lower crustal rocks. The plutons associated with the Butler Hill caldera (Knoblick and Silvermine granites) could have formed by about 30% aggregate melting of a quartz diorite, graywacke, or subgraywacke. The plutons associated with the Taum Sauk area could have formed by about 30% equilibrium melting of a subarkose or arkose. More silicic rocks of the Butler Hill caldera could have formed by fractional crystallization. The Silvermine granite is internally zoned. Crystallization of plagioclase/biotite/hornblende/magnetite/apatite/zircon/sphene in a ratio of 0.70/0.10/0.15/0.04/0.005/0.003/0.007 from the least differentiated portion of the Silvermine granite could have formed intermediate portions of the Silvermine. Further crystallization of the Silvermine requires more biotite (Ba begins to decrease) and less hornblende, zircon, and sphene (HREE increase) to precipitate and form the most differentiated portions. Also fractional crystallization of undifferentiated Silvermine-type magmas could have produced the sequence of Butler Hill-Breadtray-Graniteville granites as residual liquids, respectively. The early crystallizing mineral assemblage is dominated by plagioclase and biotite, while the late crystallizing mineral assemblage is dominated by quartz, K-feldspar, and lesser plagioclase. The Gneissoid granodiorite in the Hawn Park area has the mineral assemblage and composition of a cumulate derived from the Silvermine granite-type differentiation sequence. The associated volcanic rocks could not have formed from melts of exactly the same composition of any of the associated intrusive rocks. Rather, the volcanic rocks formed from melts of slightly different chemistry.

INTRODUCTION

Trace element models applied to the evolution of granitic rocks, including 1.4–1.8 b.y. old granitics in the midcontinent of the United States, suggest that they may be formed in a variety of ways [*Cullers and Graf,* 1981; *J. L. Anderson et al.,* 1980; *J. L. Anderson and R. Cullers,* 1978; *Condie,* 1978]. For example, *Condie* [1978] argues that granitic plutons of 1.4–1.8 b.y. age from New Mexico formed by partial melting of siliceous granulite with plagioclase, K-feldspar, quartz, magnetite, biotite, and amphibole as residual phases or by fractional crystallization of feldspars, biotite, amphibole, magnetite, or other minor accessory minerals. The composition of low-silica granitic melts of the 1.4–1.5 b.y. old Wolf River batholith of Wisconsin are consistent with their melting from a source with the mineralogy of a quartz diorite [*J. L. Anderson and R. Cullers,* 1978]. Minor portions of more silicic granites in the Wolf River batholith formed as residual liquids or cumulates by fractional crystallization of predominantly two feldspars, quartz, and lesser biotite and hornblende.

Field, petrographic, and major element data were used by *Bickford et al.* [this issue] to determine the petrogenesis of the granitic rocks of the 1.4–1.5 b.y. old St. Francois Mountains igneous complex. The trace element data (Rb, Ba, Sr, REE, Th, Co, and Sc) are found to be consistent with previous melting and fractional crystallization models for the chemical evolution of the melts. The trace elements further constrain the evolution of the system.

Copyright © 1981 by the American Geophysical Union.

ANALYTICAL TECHNIQUES

The REE were analyzed by radiochemical neutron activation [after *Denechaud et al.,* 1970] or with Co, Th, and Sc by instrumental neutron activation [after *Gordon et al.,* 1968; *Jacobs et al.,* 1977]. Analyses of standard rocks using these techniques are reported by *Cullers et al.* [1974, 1979].

Ba, Rb, and Sr contents are reported by *Bickford et al.* [this issue]. Only a few samples that represent the range of composition of each pluton were analyzed for the REE, Co, Th, and Sc (see the appendix).

RESULTS

Introduction

The summary of the igneous rocks studied, including an interpretation of origin, are included in Table 1. The range of SiO_2 and trace element contents in each unit are summarized in Table 2. Variation diagrams of selected trace elements are included in Figure 1, and the range of REE contents and patterns is shown in Figure 2.

In the discussion that follows, it will be shown that the trace element data are consistent with the interpretation that there are two groups of primary magmas, one in the Butler Hill caldera area and the other in the Taum Sauk area. As suggested by *Bickford et al.* [this issue], the generally larger volumes of

Paper number 1B0902.
0148-0227/81/001B-0902$01.00

TABLE 1. Summary of Igneous Rocks Studied in the St. Francois Mountains, Missouri

Rock Units	Interpreted Origin
Butler Hill caldera	
Low-silica ring plutons	primary magmas from partial melting of graywacke or quartz diorite
Medium-grained Silvermine granite	
Knoblick granite	
Slabtown granite	
Stono granite	
High-silica granite	evolved magmas
Butler Hill granites (includes Breadtray facies)	
Volcanic rocks	evolved magmas
Lake Killarney formation	
Grassy Mountain ignimbrite	
Ironton Hollow rhyolite (Pilot Knob)	
Taum Sauk area	
Hypabyssal intrusives	primary magmas from partial melting of arkose
Munger granite porphyry	
Carver Creek granite porphyry	
Buford Mountain granite porphyry	
High-silica granite	evolved magma
Graniteville granite	
Volcanic rocks	evolved magma
Taum Sauk rhyolite	
Hawn Park area	
Gneissoid granodiorite	cumulate

magma formed in association with the Butler Hill caldera underwent progressive fractional crystallization to form cumulates and liquids during the differentiation process. The following summary is organized accordingly.

Plutonic Rocks of the Butler Hill Caldera

Plutons associated with the Butler Hill caldera have a wide range of trace element contents that, like the major elements [*Bickford et al.*, this issue], vary in a systematic way. In the order Gneissoid granodiorite of the Hawn Park area, Knoblick granite, Silvermine and Slabtown granites, Stono granite, Butler Hill granite, the Breadtray facies of the Butler Hill granite, and Graniteville granite, there is a gradual increase in Si, K (early only), Rb, ΣREE (slight; Eu excluded), Th, Rb/Sr, and Ba/Sr, and a decrease in Al (early stages), total Fe (early), Ca (early), Mg, Mn, Ti, Ba, Sr, Eu, Sc, K/Rb, Eu/Sm, and Ba/Rb. The few Co data are highly variable, but Co appears to be more or less constant on the average from the Gneissoid granodiorite of the Hawn Park area to the Stono granite. The Co content appears to increase on the average in the Butler Hill-Breadtray-Graniteville sequence, although there is significant overlap among all units.

Several important points concerning the variation diagrams should be emphasized. First, there is a gradual and overlapping change in chemistry from the composition of the Knoblick granite to the Graniteville granite. Also, the Gneissoid granodiorite of the Hawn Park area falls along chemical trends of the other units associated with the Butler Hill cal-

TABLE 2. Ranges of SiO_2 and Trace Elements in the St. Francois Mountains Batholith

	Presumed Primary Melts		Presumed Differentiates Associated With the Butler Hill Caldera			
Element	Low-Silica Plutons, Butler Hill Caldera–Knoblick and Normal Silvermine Granites	Low-Silica Plutons Taum Sauk Area–Munger, Carver Creek, Buford Granites	Presumed Cumulate–Gneissoid of the Hawn Park Area	Slabtown–Stono Granites	Butler Hill–Breadtray Facies of the Butler Hill Granite	Graniteville Granite
SiO_2	65.5–67.9	69.7–73.0	56.1–56.4	68–70.9	72.4–78.6	73–77.1
Rb	101–110	130–320	51–52	85–139	54–343	301–400
Sr	210–293	36–115	455	86–131	11–147	14–26
Ba	712–1054	963–1955	1280–1440	566–1140	108–704	88–196
La	28–30	31.4–60.3	31.8	39.0–44.9	7.6–85.2	54.5–59.2
Ce	53–61	51.4–120	69.3	75.1–98.1	72–140	98–124
Sm	4.9–6.1	5.8–14.2	8.7	9.3–11.1	3.0–12.7	10.8–15.6
Eu	1.30–1.44	1.47–2.78	3.7	1.56–2.5	0.10–0.96	0.14–0.27
Tb	1.22–1.26	1.12–2.30	1.74	1.3–1.84	0.75–2.1	2.1–3.5
Yb	3.40–4.9	3.7–9.2	4.3	6.5–6.8	5.9–9.6	14.3–16.8
Lu	0.48–0.63	0.66–1.55	0.61	0.70–1.15	0.92–1.48	2.7–3.3
Th	6.8–7.2	7.0–14.2	3.3	7.6–10.2	15.2–31	40–40.5
Co	15.4–19.3	5.8–36	17.1	20.4–21.8	16.5–70.3	25.4–42.5
Sc	8.3–10.5	4.8–9.0	19.0	12.8–18.6	2.7–4.7	1.8–2.5
Eu/Sm	0.24–0.27	0.13–0.26	0.27	0.17–0.23	0.017–0.084	0.007–0.021
$(La/Lu)_{c.n.}$	5.0–6.1	3.6–6.7	6.1	4.0–6.2	0.67–6.8	1.9–2.1

* SiO_2 in wt %; rest in ppm.

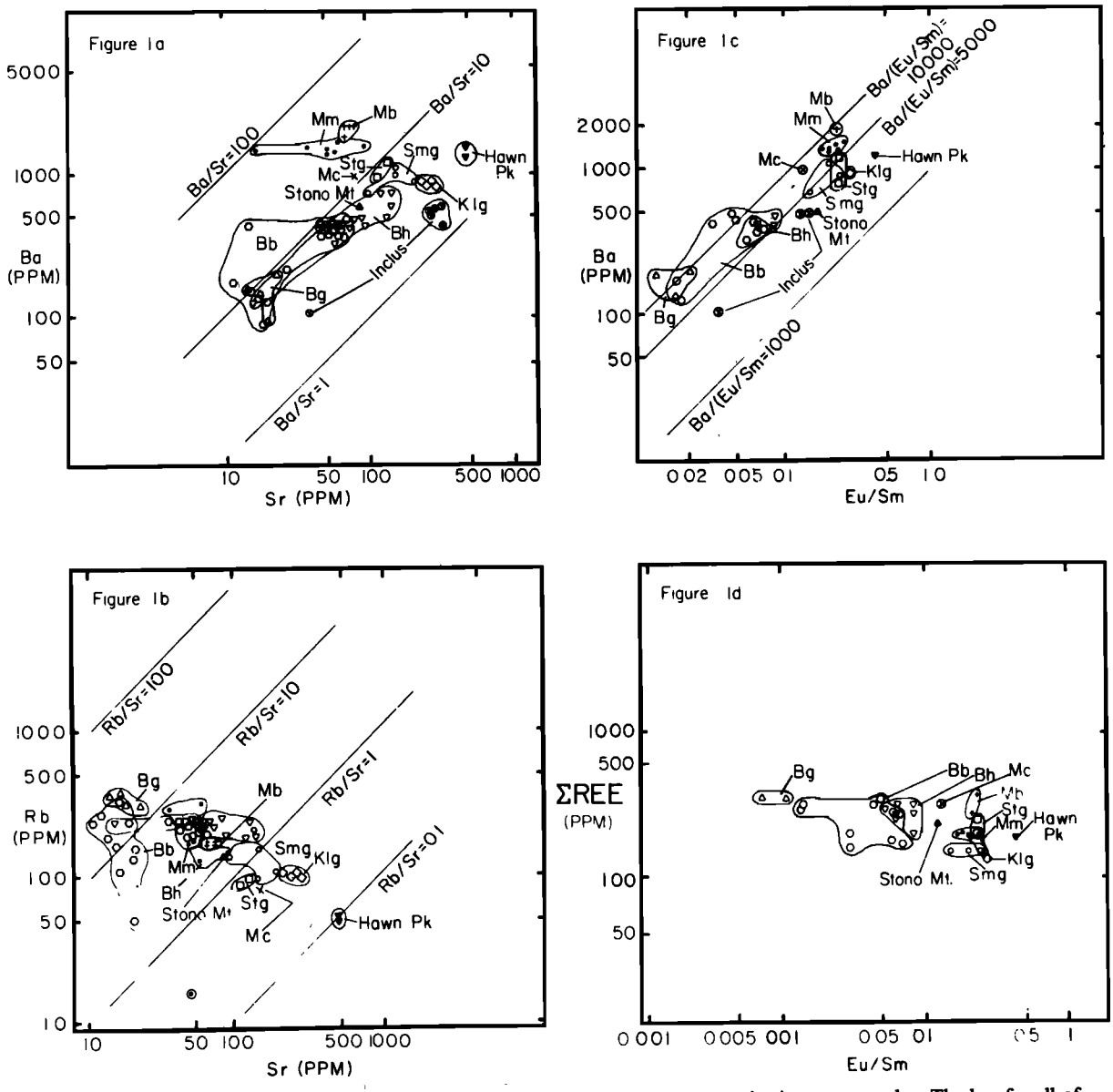

Fig. 1. Ba versus Sr contents of the plutonic rocks of the St. Francois Mountains igneous complex. The key for all of Figure 1 is as follows: solid inverted triangles, Gneissoid granodiorite of the Hawn Park area (Hawn Pk); open diamonds, Knoblick granite (klg); open circles, Silvermine granite (Smg); open squares, Slabtown granite (Stg); Solid triangles, Stono granite (Stono Mt.); open inverted triangles, Butler Hill granite (Bh); open hexagons, Breadtray facies of the Butler Hill granite (Bb); open triangles, Graniteville granite (Bg); solid circles, Munger granite-porphyry (Mm); crosses, Carver Creek granite porphyry (Mc); pluses, Buford granite (Mb); circled crosses, inclusions (Inclus). (*b*) Rb versus Sr contents of the plutonic rocks. (*c*) Ba versus Eu/Sm ratios of the plutonic rocks. (*d*) $\sum$ REE versus Eu/Sm ratios of the plutonic rocks.

dera. The Gneissoid granodiorite does not overlap with the other units and exhibits extreme chemistry compared to the other units associated with this caldera. Finally, some portions of the Breadtray facies of Butler Hill granite have significantly divergent trends in K, Rb, and Ce relative to La from the main Butler Hill-Breadtray-Graniteville sequence. These aspects of chemistry are discussed below.

Hypabyssal Intrusives of the Taum Sauk Area

The granitic rocks of the Taum Sauk area include the Carver Creek granite porphyry, the Munger granite porphyry, and the Buford Mountain granite porphyry [*Tolman and Robertson,* 1969; *R. E. Anderson,* 1970; *Berry,* 1970, 1976; *Sides et al.,* this issue; *Bickford et al.,* this issue]. Buford Mountain granite porphyry, a body occurring in the northern part of the Graniteville, Missouri 7½-min quadrangle, is not shown on the map of *Sides et al.* [this issue] and is not discussed by *Bickford et al.* [this issue], but trace element data are presented here.

These shallow granitic bodies are grossly similar in chemistry to the relatively undifferentiated granitic rocks of the Butler Hill caldera, the Knoblick and Silvermine granites. The Fe, Mn, Ti, Co, and Sc contents and K/Rb, Ba/Rb, and La/Lu ratios have enough overlap between undifferentiated plutons of the two areas that they may be considered the same.

There are some differences between the undifferentiated portions of the Butler Hill caldera and the Taum Sauk area. Most notable differences are the much smaller Ca, Mg, Na, and Sr, and much larger K, Rb, Ba, Rb/Sr, Ba/Sr of the Taum Sauk area compared to the undifferentiated plutons of the Butler Hill caldera. Other more subtle differences between

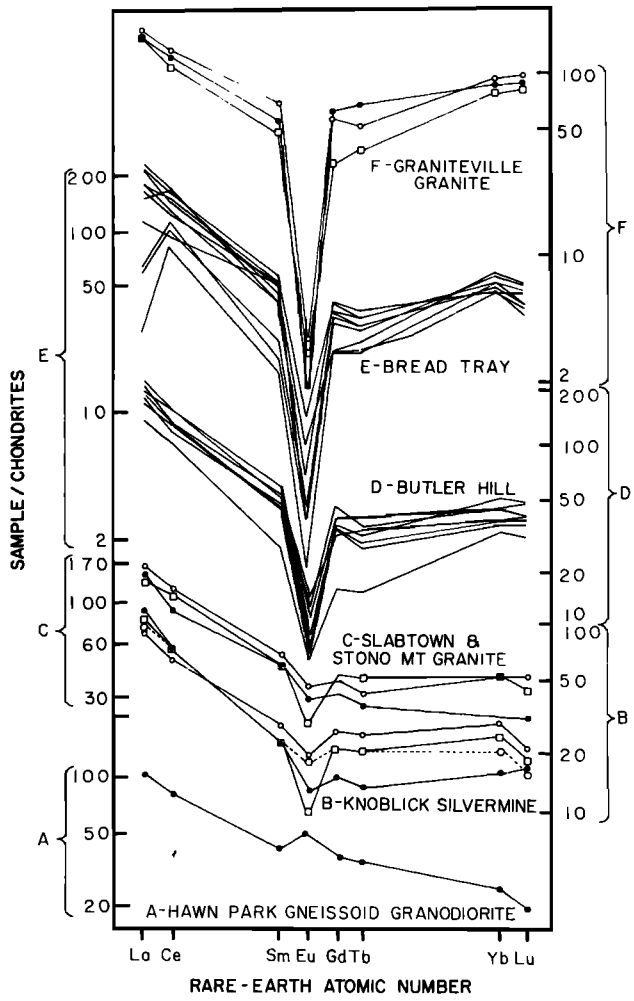

Fig. 2a. REE contents normalized to chondrites [after *Haskin et al.*, 1968] for the rocks associated with the presumed Butler Hill caldera. The Graniteville granite has been included here because of its possible formation by fractional crystallization from liquids similar in composition to less differentiated melts in this sequence. A, Gneissoid granodiorite of the Hawn Park area (1 sample); B, Knoblick (solid lines) and Silvermine (dashed lines) granites (4 samples); C, Slabtown and Stono granites (3 samples); D, Butler Hill granite (7 samples); E, Breadtray facies of the Butler Hill granite (12 samples); and F, Graniteville granite (3 samples).

the two areas include somewhat higher Si, REE, and Th, and somewhat lower Al and Eu/Sm in the Taum Sauk area plutons compared to undifferentiated Butler Hill plutons.

Volcanic Rocks

The volcanic rocks of the complex (Grassy Mountain ignimbrite, Lake Killarney formation, Ironton Hollow rhyolite, Taum Sauk rhyolite) have very similar major element contents to one another [*Bickford et al.*, this issue]. The major element abundances of the volcanic rocks are most similar to the high-silica plutons associated with the Butler Hill caldera (Butler Hill granite, Breadtray facies of the Butler Hill granite) and to the Graniteville granite. However, the Fe content of the volcanic rocks is significantly higher than these high-silica plutons.

So few volcanic rocks have been analyzed for trace elements (Table A1) that only the most general comments and conclusions are warranted. The trace element contents of the volcanic rocks vary significantly from one another. Ironton Hollow rhyolite is the least differentiated of the volcanic rocks. Its Ba content is much higher, and its REE content and negative Eu anomaly size are much lower than the high-silica rocks of the Butler Hill caldera. At the other extreme, the Lake Killarney formation is the most differentiated of the volcanic rocks, containing the largest negative Eu anomalies and fairly high REE contents. The trace element contents of the Lake Killarney formation are more similar to the Butler Hill granite (and its Breadtray facies) than any of the other volcanic rocks.

Inclusions

Some of the inclusions that are incorporated into the granites that represent the main rock types were anlayzed to see if they could be possible sources that would yield the presumed primary magmas of the complex. Inclusions 279 from the Butler Hill granite and 28b from the Knoblick granite have very similar trace element contents. Sample 30a from the Knoblick granite differs from the other two in that it contains higher Rb and HREE, and lower Sr, Ba, LREE, Eu/Sm, Th, Co, and Sc (Figure 3). These inclusions exhibit large, negative Eu anomalies.

DISCUSSION

Introduction

In part 1 of this paper [*Bickford et al.*, this issue], field relations, major element contents, and petrography have been used to define the primary magmas associated with the Butler Hill caldera (Knoblick and medium-grained Silvermine granites). In the Taum Sauk area the Munger, Carver Creek, and Buford Mountain granite porphyries have major and trace element characteristics that suggest that they are also primary magmas. Also defined are differentiates of the Butler Hill caldera produced by fractional crystallization either as cumulates (Gneissoid granodiorite of the Hawn Park area) or as residual liquids (portions of the Silvermine granite, and the Stono, Slabtown, Butler Hill granite, Breadtray facies of the Butler Hill granite, and Graniteville granites in that order). The trace elements, Rb, Sr, Ba, REE, Th, Co, and Sc may be used further to limit possible comagmatic models. Less importance is put on the Th, Co, and Sc values because of the limited data available. Below we give a discussion of trace element modeling techniques used, a model for crustal fusion for the origin of the low silica melts of the St. Francois Mountains, and a

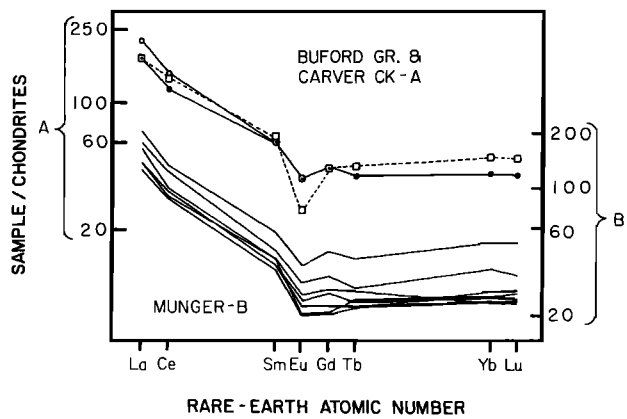

Fig. 2b. REE contents normalized to chondrites for rocks associated with the presumed Taum Sauk area. A, Buford (solid lines) and Carver Creek (dashed lined) granite-porphyrys and B, Munger granite (8 samples).

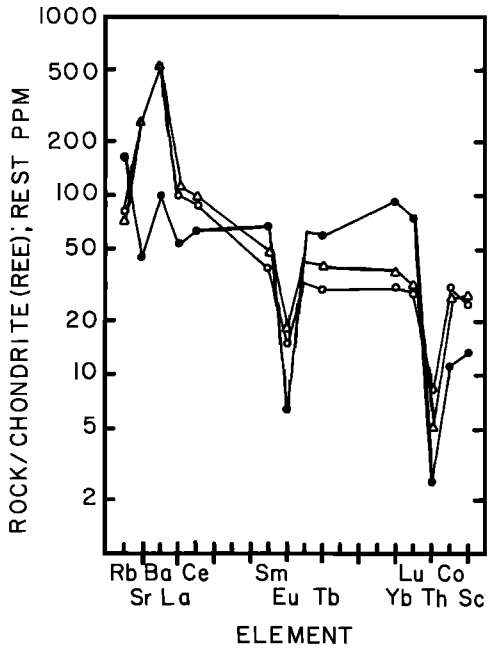

Fig. 3. Rb, Sr, Ba, REE, Th, Co, and Sc contents in the inclusions found in the plutonic rocks (REE normalized to chondrites; rest of the elements are ppm). Solid circle, sample 279; open circle, 28b; and open triangle, 30a.

fractional crystallization model to account for trace element distributions in the high-silica magmas.

Trace Element Modeling

The distribution of a trace element between a liquid and coexisting mineral may be quantitatively summarized as a D.C. (distribution coefficient), defined as the equilibrium concentration of the trace element between mineral and melt. The distribution of an element between a mineral-melt pair may vary with temperature, pressure, and disequilibrium effects so conclusions based on D.C. may be considered semiquantitative. The D.C. used for this study are those for silicic rocks as summarized by *Arth and Hanson* [1975] and by *J. L. Anderson and R. Cullers* [1978] with the few D.C. for Th, Co, and Sc further added (Table A2). Mineral-silicic melt pairs that may be potentially important for petrogenesis during partial melting or fractional crystallization are given in Table 3.

Quantitative models for prediction of the trace element content of a melt by fusion of a mineral assemblage with an assumed trace element content have been developed assuming modal or nonmodal fusion [*Gast,* 1968; *Shaw,* 1970] or by assuming that some phases are consumed during progressive melting [*Hertogen and Gijbels,* 1976]. The aggregate or equilibrium fusion models are used in this study. The main assumptions include the choice of D.C., proportion of mineral fusion, percent fusion, mineralogy and composition of the source, degree of equilibrium fusion, and oxygen fugacity for elements with more than one common oxidation state (Eu). Also the D.C. of many metamorphic minerals (sillimanite, cordierite) relative to silicate melts are not known for any elements, and some elements such as Th, Sc, and Co have rather limited D.C. available in silicic systems. In spite of these limitations, possible sources may be limited to a relative few. Because of the many assumptions that need to be made in the melting models, a number of specific examples will be given at first in our discussion of the melting models so that the reader will better see the uniqueness of these models. It will be especially important to see which rock types in the source may be rejected on the basis of the trace element data.

Semiquantitative models for fractional crystallization may be used with greater confidence than for partial melting [*Haskin et al.,* 1970; *Greenland,* 1970; *McCarthy and Hasty,* 1976], since the trace element content of the presumed parent and progressive magma (liquid plus cumulate minerals) may be measured and related to the mineral contents of the samples [e.g., *J. L. Anderson and R. Cullers,* 1978]. Other limitations such as arbitrary choice of D.C. still apply. However, it is difficult to assess petrographically the relation of cumulate phases relative to melt in intrusive silicic rocks.

Finally, element concentrations may be altered by metasomatic processes for which mineral-melt equilibria do not apply. This may have occurred for the alkali elements in some portions of the Breadtray facies of the Butler Hill granite since the alkalies fall off smooth trends in variation diagrams (Figure 1). Certainly, Rb-Sr ages have been reset relative to U-Pb Zircon ages in the St. Francois Mountains [*Bickford and Mose,* 1975]. Also oxygen isotope studies support a later metasomatic event in the igneous system [*Wenner and Taylor,* 1976]. Nevertheless, most samples fall on smooth trends in trace element variation diagrams, and many plutons have fairly constant trace element contents over wide areas. Thus, we believe that in most but not all areas metasomatic effects have been minimal in producing changes in element contents.

Crustal Fusion Model for Low-Silica Magma of the St. Francois Mountains and Comparison With the Wolf River Batholith, Wisconsin

Introduction. The low silica plutons of the St. Francois Mountains batholith have a gross similarity in composition to

TABLE 3. Phases Into Which the Elements Concentrate When These Minerals Coexist With a Silicic Liquid

	Elements Concentrated in the Mineral	Elements Concentrated in the Silicic Liquid
Quartz	none	Rb, Sr, Ba, REE, Th, Co, Sc
Alkali feldspar	Sr, Ba, Eu	Rb, REE (except Eu), Th, Co, Sc
Plagioclase	Sr, Eu	Rb, Ba, REE (except Eu), Th, Co, Sc
Biotite	Rb, Ba, Co, Sc	Sr, REE, Th
Hornblende	intermediate and HREE, Co, Sc	Rb, Sr, Ba, LREE, Th(?)
Clinopyroxene	intermediate and HREE, Co, Sc	Rb, Sr, Ba, LREE, Th
Allanite	REE, especially LREE	
Garnet	HREE, Co, Sc	Rb, Sr, Ba, LREE
Apatite	REE, Th(?)	Co, Sc
Zircon	REE, especially LREE, Th(?)	
Sphene	REE, especially LREE, Th(?)	

undifferentiated portions of the Wolf River batholith, Wisconsin [*J. L. Anderson and R. Cullers,* 1978]. These authors believed that the undifferentiated portions of the Wolf River batholith were primary melts from 20% fusion of an intermediate and heterogeneous source mineralogically similar to a quartz diorite (plagioclase, 40–65%; biotite, 10–15%; apatite, 0.1–0.2%; possibly hornblende, 0–5%; pyroxene, 0–20%). Metabasalts, amphibolites, mantle rocks, and many felsic crustal rocks were excluded as potential sources for the Wolf River primary melts. As argued previously [*Bickford et al.,* this issue], the low-silica portions of the St. Francois Mountains batholith may be primary melts. These low-silica portions may have formed by melting of a source similar to that of the Wolf River batholith, but there are some differences between the two areas.

Low-silica granites of the Butler Hill caldera. The low-silica granites associated with the Butler Hill caldera are higher in Al (slightly), Ca, Mg, Na, and Sr contents and lower in K, Rb, and REE contents compared to the presumed primary melts of the Wolf River batholith. The Eu/Sm and Ba/Rb ratios are higher and the Rb/Sr, Ba/Sr, and La/Lu ratios are lower in the low-silica granites of the Butler Hill caldera compared to those of the Wolf River batholith.

The major element differences suggest that more plagioclase and a more Mg-rich phase and less K-feldspar, muscovite, or biotite melted into the liquid to form the low-silica granites associated with the Butler Hill caldera compared to the undifferentiated plutons of the Wolf River batholith. The increased amount of plagioclase melting could increase the amount of Al, Ca, and Na in the melt. Increased melting of a Mg-rich mafic mineral could increase the amount of Mg in the melt. Lesser melting of a K-rich mineral might decrease the K content of the melt.

The trace element differences between the undifferentiated plutons of the Butler Hill caldera and the Wolf River batholith give some insight as to the differences in the residual minerals left behind after melting. These differences are consistent with the differences in the melting minerals between the two areas suggested by the major elements. The higher Sr content and Eu/Sm ratios and the lower Ba/Sr ratios of undifferentiated melts of the Butler Hill caldera compared to the Wolf River batholith suggests that less feldspar was present in the residuum of the Butler Hill melts compared to those of the Wolf River batholith. More biotite or muscovite are necessary in the residuum of primary melts produced in the Butler Hill caldera compared to the Wolf River batholith to explain the lower Rb content and Rb/Sr ratios of the melts of the Butler Hill caldera. Also a phase that concentrates the REE (hornblende, clinopyroxene, apatite, zircon, allanite, etc.) is also necessary in the residuum of the melts produced in the Butler Hill caldera in order to decrease the REE contents of the melt. These data imply that a greater degree of melting may have formed the primary melts of the Butler Hill caldera compared to the Wolf River melts. Alternately, the source may have had a somewhat different element content. Accordingly, the quantitative models that follow reflect these differences. A number of examples are given to illustrate modeling of trace elements to produce melts of the Butler Hill caldera since it is important for the reader to understand how various assumptions affect the predictions. Only the best fit models will be discussed after these first examples.

Quantitative modeling of the presumed primary melts of the Butler Hill caldera. First of all, a quartz diorite source (Table A3) the same as that used to produce primary melts of the Wolf River batholith is assumed to melt (Figure 4*a*). The predicted trace element contents in this model are too high for the REE and Th, too low for Sr, Eu/Sm, and Co, and about right only for Rb, Ba, and Sc.

A different mineral assemblage or an increased degree of melting than used in the model of Figure 4*a* is necessary to produce agreement between the predicted trace element contents and those observed. Increasing the degree of melting will produce better agreement in REE and Th contents but does not produce agreement for all elements. Reducing the amount of plagioclase, K-feldspar, biotite, and adding hornblende and a small amount of allanite in the model of Figure 4*a* gives good agreement for all elements but Co and perhaps Sc (Figure 4*b*). Such a source remains within the ranges of tonalite composition. Co is quite variable in all units and only two analyses of Co are included for the Knoblick and Silvermine granites. Also the D.C. for these two elements for mineral-silicate melt pairs are only poorly known, so we believe this model is acceptable for the formation of undifferentiated portions of the Butler Hill caldera.

The presumed source being melted in the above models is in the range of tonalite compositions. Precambrian graywackes and subgraywackes have wider ranges in compositions (Table A3) than tonalites. Predicted element contents of melts derived from the melting of these graywackes and subgraywackes are also consistent with the measured element contents of the undifferentiated rocks of the Butler Hill caldera (Figure 4*c*). Thus, these sedimentary rocks or their metamorphic equivalents are permissable sources. A limitation of this model is not knowing precisely the relation of trace element content to the quite variable mineralogy of graywackes and subgraywackes.

Finally, an alternate source is considered in which hornblende or clinopyroxene are decreased and the minor accessory minerals, allanite, garnet, and apatite are added to the previous tonalite source (Figure 4*d*). Melting of such a tonalite source produces the trace element content observed in the undifferentiated rocks of the Butler Hill caldera.

Thus, melting of metamorphosed quartz diorites, graywackes, or subgraywackes could produce the composition of primary melts associated with the Butler Hill caldera. As in the Wolf River batholith [*J. L. Anderson and R. Cullers,* 1978], possible sources excluded for the primary magmas of the Butler Hill caldera are mantle rocks, metabasalt, amphibolite, and many felsic crustal rocks.

Crustal fusion models for the low-silica portions of the Taum Sauk area. The presumed primary melts of the Taum Sauk area, the Munger, Carver Creek, and Buford Mountain granite porphyries are higher in Si, K, Rb, Ba, REE contents and lower in Al, Ca, Na, Mg, and Sr contents compared to presumed primary melts of the Butler Hill caldera. The primary melts of the Taum Sauk area are also higher in Rb/Sr and Ba/Sr ratios and lower in Ca/(Ca + Na) and Eu/Sm ratios compared to primary melts of the Butler Hill caldera.

The major element differences between the two areas suggest that more quartz, K-feldspar, or mica and less plagiocalse and Mg-rich mafic minerals melted into the liquid to form the presumed primary melts of the Taum Sauk area compared to those of the Butler Hill caldera. The greater amount of quartz melting could produce the more silica-rich melts in the Taum Sauk area compared to the Butler Hill caldera. More K-feldspar or mica melting could produce the higher K contents of

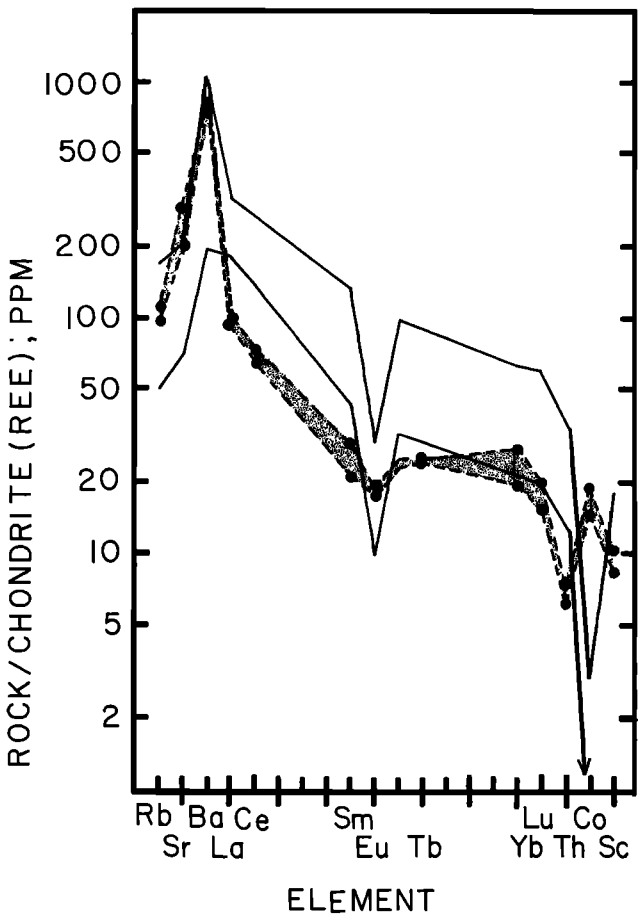

Fig. 4*a*. A range of compositions (Table A3) of quartz diorite with quartz/K-feldspar/plagioclase/biotite in a ratio of 20/5/55/20 is assumed to undergo 30% aggregate melting to produce the presumed primary melts of the Butler Hill caldera. The minerals melt in the ratio of quartz/K-feldspar/plagioclase/biotite = 0.22/0.22/0.50/0.04 so all the K-feldspar melts at 20%. This yields a predicted melt with the approximate amount of quartz, K-feldspar, and plagioclase in the low-silica plutons but poor agreement in trace element contents between the range of predicted melts (solid lines) and range of observed rocks (shaded and dashed lines).

the primary melts of the Butler Hill caldera compared to the Taum Sauk area. Finally, the lower Ca, Al, and Na content and the lower Mg content of the primary melts of the Taum Sauk area compared to those of the Butler Hill caldera could be explained by less plagioclase and Mg-rich mafic minerals melting in the former compared to the latter case.

The trace element differences between the presumed primary melts of the Butler Hill caldera and the Taum Sauk area suggest differences in mineral assemblages of the source between the two areas and perhaps a lesser degree of melting of the source to produce melts in the Taum Saux area. This different source for the Taum Sauk area requires more residual plagioclase to explain the lower Sr content and Eu/Sm ratios and higher Ba/Sr and Rb/Sr ratios of melts of the Taum Sauk area compared to melts of the Butler Hill caldera. The melts of the Taum Sauk area should contain little or no residual mica or K-feldspar so the melts have high Rb and Ba contents and Rb/Sr and Ba/Sr ratios. Presumably, these phases melt completely to produce the high K content of the melts. Finally, some minerals that concentrate the REE-like hornblende or clinopyroxene need to be present as residual minerals when the primary melts of the Taum Sauk area are produced. Also a lesser degree of melting or a high Rb or Ba source could help explain the relatively high concentrations of these elements in primary melts in the Taum Sauk area compared to those of the Butler Hill caldera.

Quantitative modeling of presumed primary melts of the Taum Saux area. To better meet the qualitative criteria above, equilibrium melting is assumed so that the melt maintains contact with the solid over the entire course of melting rather than being continuously extracted and added together as in the previous models of aggregate melting. The best fit residual mineral assemblage needed to be in equilibrium with the initial melt is most similar to a metaarkose or metasubarkose (Figure 5) rather than a metagraywacke or quartz diorite required for the Butler Hill caldera. The source needs to contain about 25% quartz, 45–60% plagioclase, 15% K-feldspar (completely melts), and less than 4% residual biotite, hornblende, or clinopyroxene. In addition, arkoses contain somewhat higher Ba contents than the previous source rocks as required in this model (Table A3). Other trace elements in arkoses appear to have a similar range in content as the range of graywackes or shales. Arkoses may not be very abundant, but the volume of these primary melts associated with the

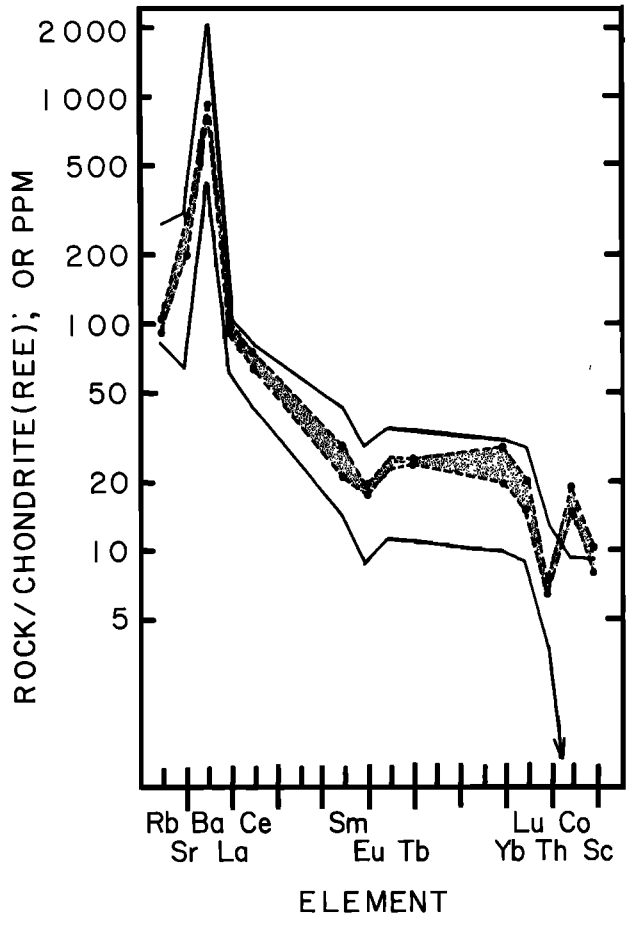

Fig. 4*b*. A range of quartz diorite compositions with quartz/plagioclase/biotite/hornblende/clinopyroxene/allanite in a ratio of 0.2/0.4/0.1/0.2/0.0005 is assumed to undero 30% aggregate melting. The minerals melt in the ratio of quartz/plagioclase/biotite/hornblende/clinopyroxene/allanite = 0.25/0.5/0.05/0.1/0.1/0. This yields a melt with the approximate amounts of quartz and plagioclase as in the low-silica plutons, but it is too K-poor unless a K-rich phase like muscovite breaks down to provide the K. All trace elements except Co and perhaps Sc give good agreement between the range of predicted melts (solid lines) and range of observed melts (dashed lines).

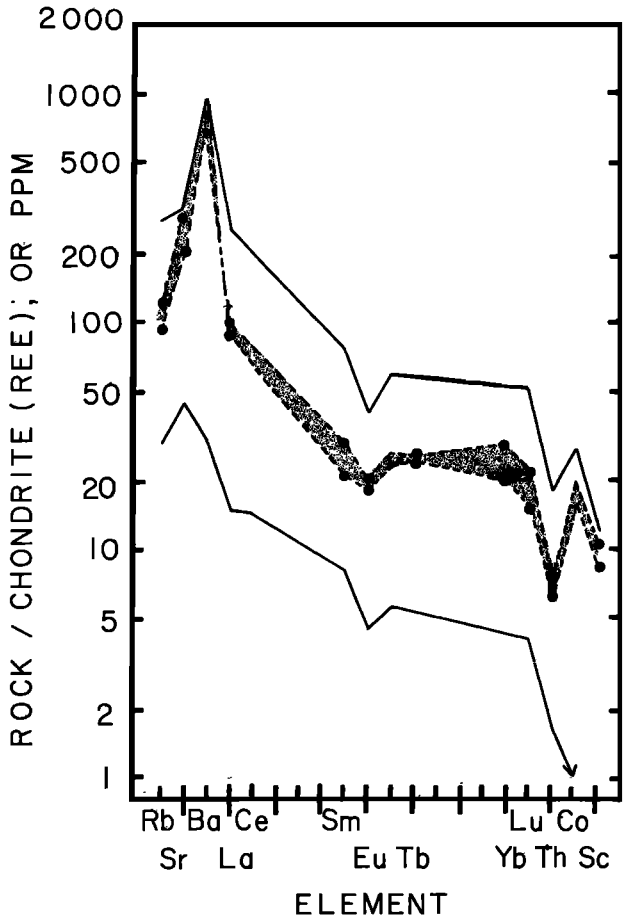

Fig. 4c. A range of graywacke-subgraywacke compositions with the ratio of minerals the same as in Figure 4b is assumed to undergo 30% aggregate melting. This yields a range of trace elements in predicted melts (solid line) that overlaps with the observed range of the rocks in the low-silica plutons of the Butler Hill caldera (shaded and dashed lines).

Taum Sauk area are not very large so the volume of arkoses in the Precambrian may not be a problem.

The size of the negative Eu anomaly predicted in the upper range of REE contents in Figure 5 is a bit too large compared to the size of the anomaly in the samples, since the arkosic source used to calculate the upper limit initially has a negative anomaly. However, most Precambrian arkoses have no Eu anomaly or a slight positive anomaly. Such samples may melt to produce liquids with negative Eu anomalies that are similar to those of the Carver Creek or Munger granites. Alternately, the oxygen fugacity could have been large during melting of arkose with an initial negative Eu anomaly causing much of the Eu^{2+} to be oxidized to Eu^{3+}. This could reduce the size of the negative Eu anomaly in the melt.

Small inclusions. The small inclusions are simple quartz and feldspar-rich rocks. They could not be either cumulate material from any of the melts of this batholith or a source rock for any of the presumed primary melts of the batholith. For example, they contain large, negative Eu anomalies (Figure 3). Melting of such inclusions would produce even larger, negative Eu anomalies in the melt, and the presumed primary melts contain very small, negative Eu anomalies. Similarly, the inclusions could not be cumulate material from the enclosing melt since, for example, such cumulate material would be expected to have positive, Eu anomalies from significant feldspar accumulation.

Such inclusions are quite abundant in some of the presumed primary melts, so they could possibly have contaminated these melts. The lack of any significant reaction relations between the inclusions and the primary melts and the similar trace element contents of the inclusions and the primary melts suggest that the inclusions have not contaminated these primary melts to any great extent. In part 1 of this paper, Bickford et al. state that the inclusions may have been derived from early chilled parts of the primary magmas. The possibly large xenolith of the Gneissoid granodiorite of the Hawn Park area will be discussed in the next section on the fractional crystallization models of the more evolved magmas since this large body does have the mineralogy and composition of a cumulate from one of the primary melts.

Fractional Crystallization Models for the Formation of Higher-Silica Plutons of the Butler Hill Caldera

Introduction. Petrographic, field, and major element trends are consistent with the formation of higher silica gran-

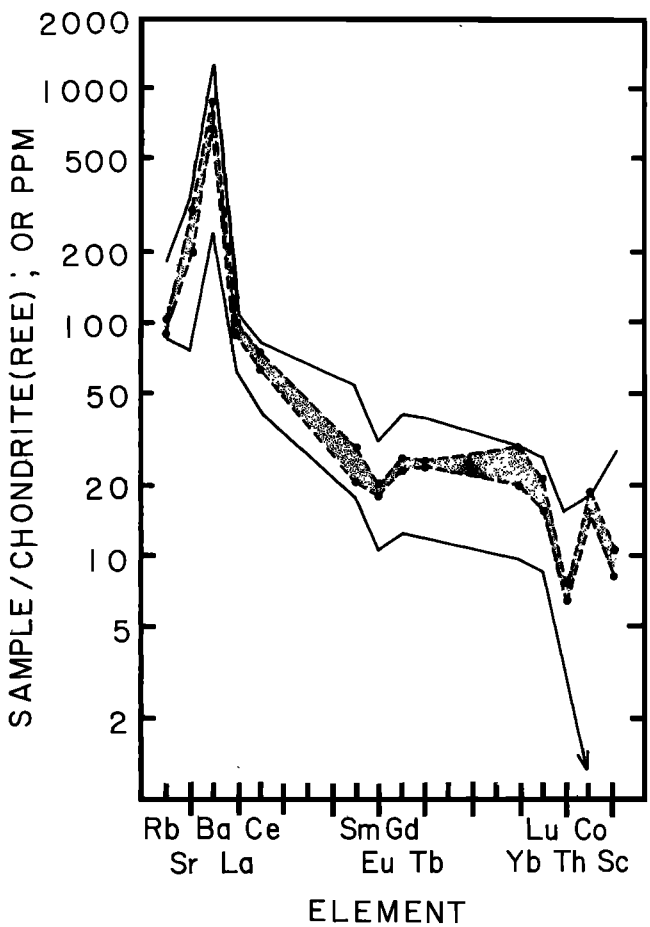

Fig. 4d. A range of tonalite compositions with quartz/plagioclase/biotite/muscovite/allanite/garnet/apatite in a ratio of 0.35/0.43/0.10/0.10/0.0005/0.015/0.005 is assumed to undergo 30% aggregate melting. The minerals melt in the ratio quartz/plagioclase/biotite/muscovite/allanite/garnet/apatite = 0.30/0.55/0.05/0.10/0/0/0. Some Ca, Mg, and Fe-rich phase such as hornblende may be presumed to be present initially as long as it melts completely to give the relatively large Ca, Mg, and Fe contents of the low-silica melts. This yields a melt with the approximate major element contents as the primary melts of the Butler Hill caldera. Trace element predictions (solid line) give good agreement with that observed.

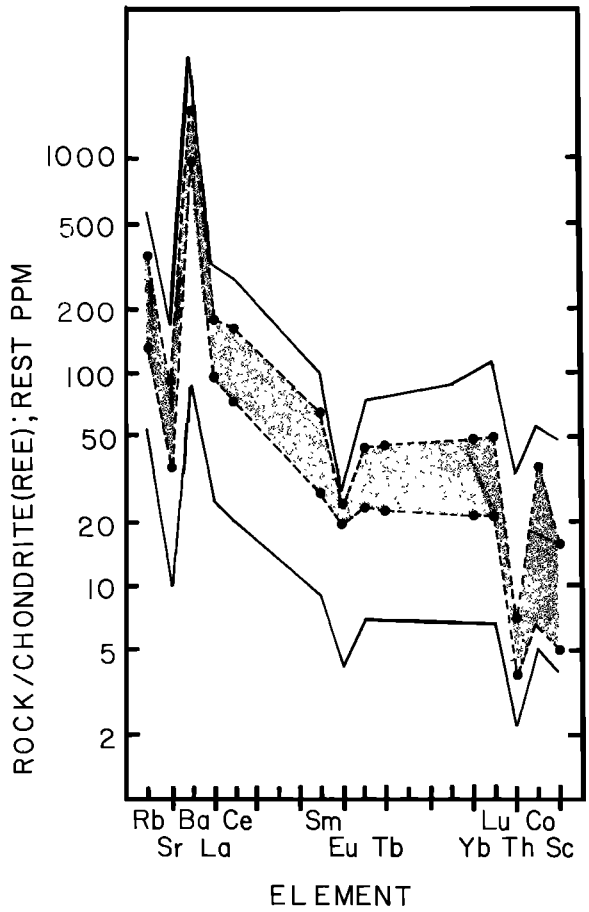

Fig. 5. A range of subarkose or arkose compositions with quartz/K-feldspar/plogioclase/biotite/apatite = 0.25/0.16/0.56/0.03/0.005 is assumed to undergo 30% equilibrium melting to produce presumed primary melts (Munger and Carver Creek granites) of the Taum Sauk area. The minerals melt in the ratio quartz/K-feldspar/plagioclase/biotite/apatite = 0.20/0.50/0/0.5/0. This produces a predicted melt with the approximate major and trace element content (solid lines) observed in the presumed primary melts (shaded and dashed lines).

ites associated with the Butler Hill caldera by a process of fractional crystallization of feldspar, biotite, and other minor phases [*Bickford et al.*, this issue]. The trace element trends are also consistent with this hypothesis and not with derivation by partial melting. For example, progressive melting of a feldspar-rich residue would not produce much change in the Ba, Sr, or Eu content of the liquid since these phases concentrate in the feldspar [*Hanson*, 1978], yet these elements change dramatically from the lower-silica granites to the higher-silica granites. The most notable trends caused by crystallizing phases are increasing Si, K, Rb, REE, Th, Rb/Sr, and Ba/Sr and decreasing Na, Fe, Ca, Mg, Ti, Mn, Sr, Ba, Sc, Eu/Sm, K/Rb, and Ba/Rb in residual liquids. Ba may be constant or increase initially, but it decreases when biotite or K-feldspar crystallization becomes important. As discussed in detail in Part 1 of this paper, the crystallization of the Silvermine granite appears to be a trend in miniature that reflects the crystallization trends of the larger plutons in the Butler Hill caldera, so it will be discussed first.

Fractional crystallization of the Silvermine granite. The Silvermine granite is zoned petrographically and chemically [*Scully*, 1978]. The lower, medium-grained portion is assumed to be a primary liquid for rocks in the Butler Hill caldera [*Bickford et al.*, this issue; *Scully*, 1978]. The medium-grained portion grades up into a porphyritic, fine-grained portion. The change of element concentrations are the same as trends summarized above and suggest that the upper portion is a differentiate of the lower portion (Figure 6).

The elemental and mineralogic trends in the Silvermine granite (Figure 7*a*) suggest initially about 20% of the original parent liquid similar in composition to sample BSF 268 (Appendix A of *Bickford et al.* [this issue] and Table A1 of this paper) crystallized plagioclase/biotite/hornblende/magnetite/apatite/zircon/sphene in the ratio 0.70/0.10/0.15/0.04/0.005/0.003/0.007 to form the presumed differentiate BSF 255 [*Bickford et al.*, this issue]. The fit between predicted liquid composition and observed composition is fairly good although the predicted contents of elements with low D.C. do not increase quite enough.

This model assumes complete separation of minerals and liquid, and this may not be geologically reasonable for intrusive rocks. A model in which there is incomplete separation of cumulate minerals and liquid can explain the trace element distributions, but it is not clear if such a model is consistent with the major elements. A limitation of the major element models is the uncertain composition of phases like hornblende or biotite. The trace element changes from the presumed primary melt such as BSF 268 to an intermediate melt such as BSF 255 could also be explained by about 40% crystallization of the same minerals as in the previous model but assuming the derivative rock contains about 15% of the cumulate minerals. This would give a better fit for trace elements with low D.C., since such elements would increase in the liquid even more than in the previous model during differentiation. The presence of cumulate minerals would not change the concentration of such elements in the whole rocks very much. Trace elements with large D.C. would decrease drastically in the liquid with 40% crystallization, but the incorporation of the cumulate phases with high concentrations of these elements still allows a good fit between predicted and observed trace element contents in the magma. The former model is preferred because it is not clear if the major elements fit the latter model. Further discussion will only consider rocks as residual liquids or cumulates with no intermediate mixes of liquid with cumulate.

Further crystallization within the Silvermine granite from intermediate rocks such as BSF 255 to silica-rich rocks such as BSF 233 requires more biotite crystallization to decrease Ba

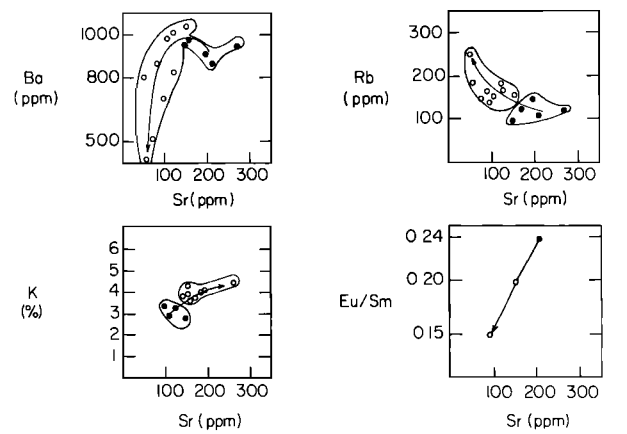

Fig. 6. Trace element and K variations in the Silvermine granite [*Scully*, 1978]. Solid circles, medium-grained Silvermine granite; open circles, prophyritic fine-grained Silvermine granite.

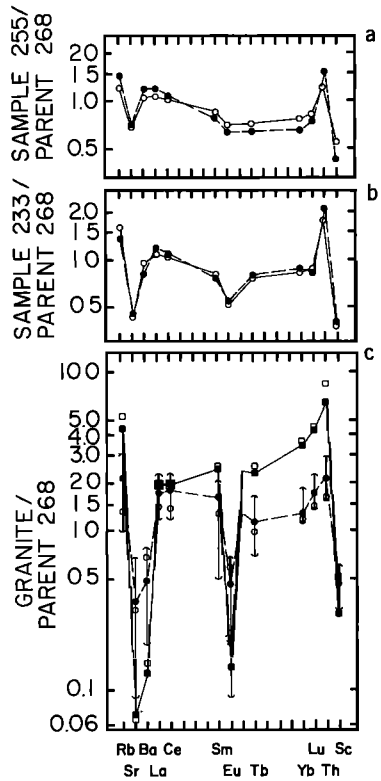

Fig. 7. (*a*) The measured (solid circle) and predicted (open circle) trace element contents of the presumed differentiate 255 from the Silvermine granite is compared to the presumed parent 268. The model assumes about 20% fractional crystallization of plagioclase/biotite/hornblende/magnetite/apatite/zircon/sphene in a ratio of 0.70/0.10/0.15/0.04/0.005/0.003/0.007. (*b*) The measured (solid circle) and predicted (open circle) trace element content of the presumed differentiate 233 from the Silvermine granite is compared to the presumed parent 268. The model assumes about 20% further fractional crystallization from a melt similar in composition to 255. (*c*) The measured (solid circle with bars to indicate the range of observed trace elements) and predicted (open circle) trace element content of the presumed differentiate of the average Butler Hill Granite is compared to the presumed parent 268. The model assumes about 40% fractional crystallization of plagioclase/biotite/hornblende/magnetite/spinel in a ratio of 0.70/0.20/0.068/0.037/0.003. Also the measured (solid square) and predicted (open square) trace element content of the presumed differentiate (open square) trace element content of the presumed differentiate of the Graniteville granite formed from differentiation from average Butler Hill granite is compared. The samples are again normalized to 268. The model assumes about 70% fractional crystallization of quartz/K-feldspar/plagioclase/biotite/hornblende/allanite/magnetite/apatite in a ratio of 0.33/0.39/0.21/0.03/0.03/0.0005/0.01/0.005 from average Butler Hill-type liquid to Graniteville granite.

and less hornblende, zircon, or sphene crystallization to increase the HREE. For example, about 20% further crystallization of plagioclase/biotite/magnetite/apatite/zircon/sphene in the ratio of 0.70/0.25/0.04/0.005/0.0006/0.005 from a liquid similar to BSF 255 will give the trace element characteristics of sample BSF 233 (Figure 7*b*). These mineral ratios are again similar to those ratios suggested in part 1 by *Bickford et al.* [this issue] to explain the major element trends.

Fractional crystallization to produce the higher-silica plutons. The higher-silica plutons appear to represent more extreme differentiates of undifferentiated Silvermine, Knoblick, or Slabtown-type granites in the order Butler Hill granite, Breadtray facies of the Butler Hill granite, and perhaps Graniteville granite. Element changes are regular through most of this sequence, suggesting that similar minerals have precipitated to cause the differentiation trends. The ratios of minerals crystallizing to explain the trace element trends are the same as those needed to explain the major element trends discussed in part 1.

Several examples of trace element models to explain these trends will be summarized below. One example will consider crystallization from medium-grained Silvermine (BSF 268) to average Butler Hill granite, and the second example will consider crystallization from average Butler Hill granite to Graniteville granite. Medium-grained Silvermine liquid can precipitate about 40% plagioclase/biotite/hornblende/magnetite/spinel in a ratio of 0.71/0.20/0.068/0.037/0.003 and produce the range of trace element contents in the Butler Hill granite (Figure 7*c*). This model is consistent with the mineralogy of the samples and with the major element model presented in part 1 except that the major elements require derivation of Butler Hill magma from Silvermine magma in two steps. Average Butler Hill-type liquid can precipitate about 70% quartz/K-feldspar/plagioclase/biotite/hornblende/allanite/magnetite/apatite in a ratio of 0.33/0.39/0.21/0.03/0.03/0.0005/0.01/0.005 and produce the trace element content of the Graniterville granite (Figure 7*c*). This model is again consistent with the mineralogy of the samples and the major element model for this differentiation.

Some samples of the Breadtray facies of the Butler Hill granite have very low contents of Rb and K, and a few even appear to have anomalously high contents of Ce relative to La (Figures 1 and 2). All anomalous samples are located in what is believed to have been the upper portion of the magma chamber, so they may have been altered by processes related to evolution of a separate fluid phase. Miarolitic cavities containing quartz, alkalic feldspar, and fluorite are abundant in this portion of the pluton. Certainly roof rock contamination does not seem very probable, since few roof rock inclusions are found in this area and the roof for the magma chamber in this area is rhyolitic ejecta of similar composition to the magmatic rocks.

The high Ce content relative to La does not appear to be an

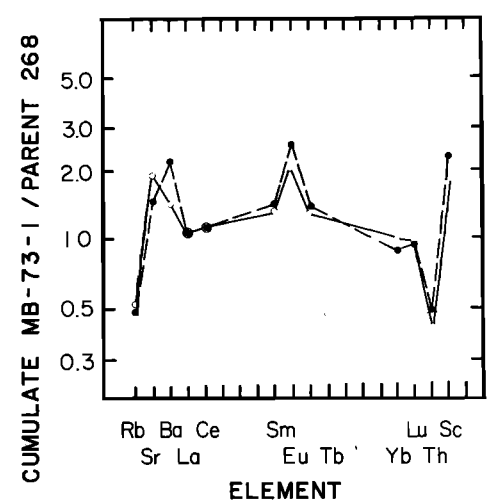

Fig. 8. The ratio of element contents in the presumed cumulate MB-73-1 is normalized to the presumed parent melt 268 (solid circle, dashed line). The predicted cumulate (open circle, solid line) obtained from parent 268 after about 40% crystallization of plagioclase/biotite/hornblende/apatite/zircon/sphene/magnetite = 0.65/0.20/0.10/0.009/0.001/0.005/0.04 compares fairly well with the observed values.

analytical problem. For example, high U contents could produce high apparent Ce values, yet the U content of the anomalous samples is no different from the samples that are not anomalous (R. Cullers and M. E. Bickford, unpublished data, 1981). Perhaps the conditions became very oxidizing in this portion of the batholith so that the usual Ce^{3+} ion became oxidized to Ce^{4+} so that Ce could be fractionated relative to the other REE. For example, apatite from igneous rocks in the Black Forest is depleted in Ce relative to La [*Puchelt and Emmermann,* 1976]. Precipitation of such apatite could produce enriched Ce relative to La in residual liquids.

Gneissoid granodiorite of the Hawn Park area. The granodiorite of the Hawn Park area contains mainly plagioclase and lesser hornblende, biotite, and quartz. Small amounts of apatite, zircon, sphene, and opaques are also present. The mineralogy and chemistry of this body make it the only candidate in the complex for a large accumulation of cumulus phases (Figure 8). For example, the trace element abundances in the predicted cumulate obtained from the presumed parent BSF 268 after about 40% crystallization of plagioclase/biotite/hornblende/apatite/zircon/sphene/magnetite in the ratio of 0.65/0.20/0.10/0.009/0.001/0.005/0.04 is fairly close to the observed trace element contents of the granodiorite of Hawn Park. The body is also located to the northeast of the shallow plutons and associated volcanics in the part of the batholith that is presumed to represent greater depth [*Sides et al.,* this issue].

Volcanic Rocks

The volcanic rocks of the complex have not been sampled or analyzed in detail so only the most general comments can be discussed. The volcanic rocks are most similar in composition to the high-silica plutons associated with the Butler Hill caldera, but there are significant differences between these plutonic and volcanic rocks. A notable difference is the much larger Fe content of the volcanic rocks compared to the plutonic rocks of similar SiO_2 content.

Crystallization models for the production of some volcanic rocks from average Butler Hill granite are consistent with the major element but not the trace element trends [*Bickford et al.,* this issue]. For example, about 50% crystallization of plagioclase/K-feldspar/quartz/biotite/magnetite in a ratio of 9.4/22.3/16.6/1.4/0.06 from average Butler Hill-type melt could produce the major element content of the Grassy Mountain ignimbrite. This model, however, is not consistent with the Eu anomaly size. Crystallization of large amounts of feldspar from the Butler Hill-type liquid should produce a much larger negative Eu anomaly in the residual liquid, but the size of the negative anomaly in the Butler Hill granite and the Grassy Mountain ignimbrite is the same. Thus, the volcanic rocks may not be derived from liquids of exactly the same chemical composition as the plutonic rocks currently exposed but rather from liquids of slightly different chemistry.

We do not feel, however, that the conclusions based on the limited trace element data on the volcanic rocks necessarily negates the conclusions based on the major elements. For example, the silicic ash flow tuffs could have been derived by a sudden expulsion of material that could have been drastically zoned in trace element contents, as described in the Bishop Tuff [*Hildreth,* 1979]. A detailed sampling of the volcanic stratigraphy is being planned so that a better comparison of the composition of the volcanic rocks to the plutonic rocks can be made.

TABLE A1. REE, Th, Co, and Sc Contents of Rocks From the St. Francois Mountains Igneous Complex

Unit and Sample Number	La	Ce	Sm	Eu	Gd*	Tb	Yb	Lu	∑REE†	Eu/Sm	La/Lu‡	Th	Co	Sc
Hawn Park gneissoid granodiorite														
MB-73-1-I	31.8	69.3	8.73	3.71	—	1.74	4.30	0.61	194	0.42	5.4	3.3	17.1	19.0
Knoblick granite														
BSF-35	28.1	53	4.86	1.30	—	0.98	3.40	0.48	140	0.27	6.1	7.2	19.3	10.5
Silvermine granite														
BSF-268	30.4	60.5	6.10	1.44	—	1.26	4.90	0.63	156	0.24	5.0	6.8	15.4	8.3
BSF-255	36.4	65	4.60	0.91	—	0.82	3.12	0.51	154	0.20	7.4	10.3	—	3.5
BSF-233	35.6	66.8	4.63	0.73	—	1.02	4.20	0.53	157	0.15	7.1	14.2	20	2.9
Slabtown granite														
BSF-258	44.9	98.1	11.1	2.5	—	1.5	6.5	1.15	254	0.23	4.0	10.2	20.4	18.6
BSF-259	42.2	75.1	9.30	2.1	—	1.3	—	0.70	205	0.23	6.2	7.6	—	14.1
Stono Mountain granite														
N 6976	39.0	93.6	9.44	1.56	—	1.84	6.77	0.93	242	0.17	4.3	8.8	21.8	12.8

Butler Hill granite														
12-5-9	69.9	136	11.0	0.91	8.9	1.67	7.82	1.23	329	0.082	5.9	—	—	—
BSF-155	54.9	117	9.4	0.59	11.1	1.34	6.22	1.18	273	0.063	4.8	22.6	—	4.2
BSF-42	54.8	102	10.1	0.64	—	1.42	6.47	1.22	258	0.063	4.6	15.2	25.7	4.7
Mo-22	64.4	136	12.6	0.80	13	1.96	7.95	1.47	333	0.064	4.5	—	—	—
Mo-23	57.7	116	11.4	0.96	10	1.72	6.42	1.19	289	0.084	5.0	—	—	—
Ans20	65.9	129	9.0	0.48	12.4	1.56	8.87	1.44	303	0.053	4.7	26.3	38.7	2.7
5-5-17	44.2	87	5.7	0.47	5.1	0.75	5.92	0.92	203	0.082	5.0	—	—	—
Breadtray granite														
N 3475	53.8	131	10.5	0.18	—	1.73	7.70	1.09	307	0.017	5.1	22.1	41.5	3.1
N 575	65.1	133	11.6	0.21	—	1.56	8.72	1.07	328	0.018	6.3	24.2	56.6	3.0
12-5-3	66.5	123	10.4	0.57	11.6	1.48	8.28	1.36	301	0.054	5.1	—	—	—
N 4175g	71.5	140	9.1	0.40	—	1.60	8.50	1.09	333	0.044	6.8	23.2	70	2.7
BSF-284	58.2	110	8.6	0.35	—	—	—	—	—	0.041	—	25.5	24.4	3.8
12-5-5	45.9	136	8.0	0.49	6.5	1.04	7.32	1.29	290	0.061	3.7	25.0	—	—
12-5-6	85.2	140	12.7	0.63	15.4	2.07	8.40	1.34	359	0.049	6.6	—	—	—
5-5-13	51.3	105	10.9	0.68	11.0	1.58	8.07	1.25	269	0.062	4.2	22.7	—	—
12-5-17	17.6	84.3	5.08	0.30	9.7	1.30	9.52	1.48	187	0.059	1.2	—	—	—
N 5276	32.4	74.8	10.2	0.31	—	1.37	8.01	1.15	209	0.030	2.9	21.7	40.4	2.8
12-5-7	18.2	86.2	4.06	0.26	6.4	1.02	8.75	1.38	179	0.070	1.4	22.7	16.5	3.2
N 2775g	7.6	71	3.1	0.10	—	2.2	9.7	1.16	167	0.030	0.7	30	25	3.7
Graniteville granite														
BSF-242	59.2	124	15.6	0.27	20.4	2.71	16.8	3.31	361	0.017	1.9	42	25.4	1.9
BSF-243	58.7	130	16.6	0.12	—	3.49	15.6	2.90	365	0.007	2.1	44.5	28.8	2.5
BSF-246	54.5	98.3	10.8	0.23	10.3	2.10	14.3	2.74	283	0.021	2.1	40	42.5	2.4
Buford Mountain granite porphyry														
BSF-293	60.3	120	13.7	2.78	—	2.30	7.8	1.18	309	0.22	5.3	14.2	27.4	9.0
Carver Creek granite														
Car. CK.	54.0	116	14.2	1.90	14.2	2.30	9.17	1.15	312	0.13	3.6	—	—	—
Munger granite														
6-28-1	44.4	78.5	8.47	1.65	7.1	1.06	4.1	0.75	200	0.20	6.1	9.1	21.1	6.4
6-28-7	31.4	51.4	5.76	1.47	—	1.12	3.7	0.66	145	0.26	4.9	7.0	13.7	4.8
6-28-8	48.9	80.7	7.90	1.81	—	1.15	4.2	0.75	212	0.23	6.7	10.8	22.0	6.2
6-28-3	43.3	75.5	7.50	1.37	—	1.28	4.6	0.76	204	0.18	5.9	9.0	5.8	5.5
6-28-6	55.4	100	9.70	2.21	—	1.39	6.0	0.98	256	0.23	5.8	—	—	—
6-28-10	43.7	76.3	8.25	1.89	8.87	1.21	4.4	0.74	204	0.23	6.1	9.6	17.4	6.1
6-28-14	42.7	77.5	8.65	1.50	6.59	1.20	4.5	0.87	205	0.17	5.1	—	—	—
6-15-9	40.6	75.3	7.75	1.56	6.6	1.10	4.6	0.84	195	0.20	5.0	9.3	36	7.8
Inclusions														
BSF-279	16.6	57.0	14.6	0.49	—	3.01	16.0	2.3	227	0.034	0.8	2.6	11.2	13.3
BSF-28b	31.6	77	8.5	1.14	—	1.50	5.5	0.86	199	0.13	3.8	8.3	31.6	26.6
BSF-30a	32.7	80.3	10.1	1.37	—	2.06	6.4	0.94	223	0.14	3.6	5.3	28.1	27.5
Ironton Hollow rhyolite														
12-5-33	19.7	38.4	7.3	0.93	9.6	1.48	6.8	1.09	134	0.13	1.9	—	—	—
6-5-21	17.9	31.7	6.9	1.1	—	2.48	12.7	2.2	148	0.16	0.8	4.8	12.7	2.9
Grassy Mountain ignimbrite														
6-4-19	33.8	66.4	7.2	0.63	—	1.78	7.86	1.02	192	0.088	3.4	10.9	17.9	4.1
6-5-8	91.0	151	15.2	1.24	15.4	2.18	7.02	1.10	393	0.082	8.5	—	—	—
Lake Killarney felsite														
7-5-38	62.8	125	13.5	0.61	—	1.95	8.1	1.28	328	0.045	5.1	—	—	—
12-5-21	56.1	92	9.73	0.66	—	1.81	6.77	1.09	251	0.068	6.9	10.9	10.2	3.7

All values are in ppm.

* Samples analyzed by radiochemical activation analysis have Gd values. Samples analyzed by instrumental activation do not have Gd values.

† ∑REE includes all the REE but not Y. Estimates of REE not analyzed were made from chondrite-normalized curves.

‡ La/Lu ratios are chondrite-normalized ratios.

TABLE A2. D.C. Used for the Modeling in This Paper

Element	Quartz	Alkali Feldspar	Plagioclase	Mica	Hornblende	Clinopyroxene	Allanite	Garnet	Apatite	Zircon	Sphene
Rb	0.001	0.036	0.034	5.5(2.2)+	0.011	0.038	...	0.0085	...	...	...
Sr	0.001	3.9	9(4.4)†	0.12	0.058	0.10	...	0.015	...	...	...
Ba	0.001	6.1(5)†	0.033	8.0	0.049	0.061	...	0.017	...	...	...
Ce	0.001	0.044	0.24	0.037	0.86	0.29	1400	0.35	35	2.6	139
Sm	0.001	0.018	0.13	0.058	4.15	0.93	220	2.7	63	3.1	70
Eu	0.001	1.13	2.1	0.15	3.2	0.87	50	1.5	230	3.1	61
Lu	0.001	0.006	0.062	0.19	2.97	1.05	low	29.6	20	323	21
Th	0.001	0.02	0.020	0.3	0.01?	0.013	...	...	30*	30*	30*
Co	0.001	0.01	0.10	20	10	5	...	2.5	0.2	...	...
Sc	0.001	0.06	0.06	11	15	15	...	15	0.5	...	...

From *Arth and Hanson* [1975] and *J. L. Anderson and R. Cullers* [1978]. Only a few REE values are included that represent the D.C. of the REE used. Dashes indicate the values are not known but that the D.C. are probably less than one.

* These minerals concentrate Th, but D.C. are arbitrarily assigned since they are unknown. J. Stuckless (personal communication, 1981) suggests that D.C. for Th in apatite might be closer to 1–5.

† Values in parentheses are used in fractional crystallization models if they are different than for the melting models.

TABLE A3. Range of Tonalites, Graywackes, and Arkoses Used for the Partial Melting Models

Element	Tonalites*	Subgraywackes, Graywackes, or Arkoses†
Rb	60–200	20–200
Sr	300–940	45–700(150–720)
Ba	900–2000	30–1070(200–1100)
La	58–110	15–180
Ce	50–90	12–150
Sm	13–40	7–65
Eu	12–36	6–40
Gd	11–32	5–52
Tb	10–29	4.5–53
Yb	6.7–20	2.8–60
Lu	6–18	2.5–62
Th	4–11	1–15
Co	1–43	3–32
Sc	1–46	2–25

The REE are normalized to chondrites; the rest are in ppm.

* As summarized by *Anderson and Cullers* [1978] (R. Cullers and J. L. Anderson, unpublished data, 1981, of Penokean tonalites).

† The range of these are obtained from many sources; the range of graywackes and arkoses are similar for all elements except Sr and Ba; arkoses tend to have larger Sr and Ba contents that graywackes; the ranges of Sr and Ba used in arkoses are in parentheses.

Acknowledgments. Support for this research was provided by a National Science Foundation grant EAR 76-03769 in geology. Special thanks go to Steve Lange, Sam Chaudhuri, Steve Massie, and Bob Cook for some analyses and special help. Richard Koch did the analytical work for part of his M.S. thesis at Kansas State. We thank John Stuckless for his constructive criticism of the manuscript, Bob Barnett for doing the drafting of the figures, and Renée Hambleton for typing the manuscript.

REFERENCES

Anderson, J. L., and R. Cullers, Geochemistry and evolution of the Wolf River batholith, a Late Precambrian rapakivi massif in north Wisconsin, U.S.A., *Precambrian Res., 7,* 287–324, 1978.

Anderson, J. L., R. Cullers, and W. R. Van Schmus, Anorogenic metaluminous and peraluminous granite plutonism in the mid-Proterozoic of Wisconsin, U.S.A., *Contrib. Mineral. Petrol., 74,* 311–328, 1980.

Anderson, R. E., Ash-flow tuffs of Precambrian age in southeast Missouri, *Rep. Invest. Mo. Geol. Surv., 46,* 50 pp., 1970.

Arth, J. G., and G. N. Hanson, Geochemistry and origin of the early Precambrian crust of northeastern Minnesota, *Geochim. Cosmochim. Acta, 39,* 325–362, 1975.

Berry, AW., Precambrian volcanic rocks associated with the Taum Sauk caldera, St. Francois Mountains, Missouri, Ph.D. thesis, 147 pp., Univ of Kansas, Lawrence, 1970.

Berry, A.W., Jr., Proposed stratigraphic column for Precambrian volcanic rocks, western St. Francois Mountains, Missouri, in *Studies in Precambrian Geology of Missouri,* edited by E. B. Kisvarsanyi, *Rep Invest Mo. Geol. Surv., 61,* 80–90, 1976.

Bickford, M. E., and D. G. Mose, Geochronology of the Precambrian rocks in the St. Francois Mountains, southeastern Missouri, *Spec. Pap. Geol. Soc. Am. 165,* 48, pp., 1975

Bickford, M. E., J. R. Sides, and R. L. Cullers, Chemical evolution of magmas in the Proterozoic terrane of the St. Francois Mountains, Southeastern Missouri, 1. Field, petrographic, and major element data, *J. Geophys. Res.,* this issue.

Condie, K. C., Geochemistry of Proterozoic granitic plutons from New Mexico, U.S.A., *Chem. Geol., 21,* 131–149, 1978.

Cullers, R. L., and Graf, J., Rare-earths in the continental crust: Intermediate and silicic rocks, in *Rare Earth Geochemistry,* edited by P. Henderson Elsevier, New York in press, 1981.

Cullers, R. L., L. Yeh, S. Chaudhuri, and C. V. Guidotti, Rare-earth elements in Silurian pelitic schists from N. W. Maine, *Geochim, Cosmochim. Acta, 38,* 389–400, 1974

Cullers, R. L., S. Chaudhuri, N. Kilbane, and R. J. Koch, The rare-earth contents in different size fractions and whole rocks from Pennsylvanian and Permian platform sediments from the mid-continent of the U.S.A., *Geochim. Cosmochim. Acta, 43,* 1285–1307, 1979.

Denechaud, E. B., P. A. Helmke, and L. A. Haskin, Analysis for the rare-earth elements by neutron activation and Ge(Li) spectrometry, *J. Radioanal. Chem., 6,* 97–113, 1970.

Gast, P. W., Trace-element fractionation and the origin of tholeiitic and alkaline magma types, *Geochim. Cosmochim. Acta, 32,* 9057–1086, 1968.

Gordon, G. E., K. Randle, G. G. Goles, J. B. Corliss, M. H. Beeson, S. S. Oxley, and O. E. Gram, Instrumental activation analysis of standard rocks with high resolution detectors, *Geochim. Cosmochim. Acta, 32,* 369–396, 1968.

Greenland, L. P., An equation for trace element distribution during magmatic crystallization, *Am Mineral. 55,* 455–465, 1970.

Hanson, G. N., The application of trace elements to the petrogenesis of igneous rocks of granitic composition, *Earth Planet, Sci. Lett., 38,* 26–43, 1978.

Haskin, L. A., F. A. Frey, R. A. Schmitt, and R. H, Smith, Meteoritic, solar, and terrestrial rare-earth distributions, *Phys. Chem. Earth, 7,* 167–321, 1968.

Haskin, L. A., R. O. Allen, P. A. Helmke, T. P. Paster, M. R. Anderson, R. S. Korotev, and K. A. Zweifel, Rare earths and other trace elements in Apollo 11 lunar samples, *Proc. Lunar Sci. Conf. 1st,* 1213–1231, 1970.

Hertogen, J., and R. Gijbels, Calculation of trace element fractiona-

tion during partial melting, *Geochim, Cosmochim. Acta, 40,* 313–322, 1976.

Hildreth, W.,The Bishop Tuff: Evidence for the origin of compositional zonation in silicic magma chambers, in *Ash Flow Tuffs,* edited by C. E. Chapin and W. E. Elston, *Spec. Pap. Geol. Soc. Am., 180,* 43–75, 1979.

Jacobs, J. W., R. L. Korotev, D. P. Blanchard, and L. A. Haskin, A well tested procedure for instrumental neutron activation analysis of silicate rocks and minerals, *J. Radianal. Chem., 40,* 93–114, 1977.

McCarthy, T. S., And R. A. Hasty, Trace element distribution patterns and their relationship to the crystallization of granitic melts, *Geochim. Cosmochim. Acta, 40,* 1351–1358, 1976.

Puchelt, H., and R. Emmermann, Bearing of rare-earth patterns of apatites from igneous and metamorphic rocks, *Earth Planet. Sci. Lett., 31,* 279–286, 1976.

Scully, E. M., Petrogenesis of the Silver Mine granite, M. S. thesis, 45 pp., Univ. of Kansas, Lawrence, 1978.

Shaw, D. M., Trace element fractionation during anatexis, *Geochim. Cosmochim. Acta, 34,* 237–243, 1970.

Sides, J. R., M. E. Bickford, R. D. Shuster, and R. L. Nusbaum, Calderas in the Precambrian terrane of the St. Francois Mountains, southeastern Missouri, *J. Geophys. Res.,* this issue.

Tolman, C., and F. Robertson, Exposed Precambrian rocks in southeast Missouri, *Rep. Invest. Mo. Geol. Surv., 44,* 68 pp., 1969.

Wenner, D. B., and H. P. Taylor, Jr., Oxygen and hydrogen isotope studies of a Precambrian granite-rhyolite terrane, St. Francois Mountains, southeastern Missouri, *Geol. Soc. Am. Bull., 87,* 1587, 1976.

(Received October 31, 1980;
revised April 30, 1981;
accepted May 20, 1981.)

JOURNAL OF GEOPHYSICAL RESEARCH, VOL. 86, NO. B11, PAGES 10402–10410, NOVEMBER 10, 1981

Contrasting Evolution of Calc-Alkalic Volcanic and Plutonic Rocks of Western Chihuahua, Mexico

W. C. BAGBY,[1] K. L. CAMERON, AND M. CAMERON[2]

Board of Earth Sciences, University of California at Santa Cruz, Santa Cruz, California 95064

Two sequences of continental arc igneous rocks occur in the Batopilas area of the Sierra Madre Occidental of northwestern Mexico. The older includes late Cretaceous to (?) early Cenozoic granitoids, and the younger is a mid-Tertiary andesite to rhyolite series that is represented largely by voluminous ignimbrites. The latter sequence contains rocks varying from 54 to 78 wt.% SiO_2 whereas the granitoids have a more restricted range in SiO_2, 57–68 wt %. The major element chemistry of the two sequences is generally similar; however, the older granitoids have lower Zr/Nb, and higher Nb/Y and K/Rb compared to volcanic rocks. In addition, the granitoids have generally smaller Eu anomalies, lower concentrations of REE, and higher $(Ce/Yb)_N$ (4.6–7.2 versus 3.8–4.0) than the volcanic rocks. The intermediate rocks of the two sequences, quartz diorites and andesites, had similar petrogenetic histories, and both may have originated by fractionation of mantle-derived basaltic magmas. In contrast, the more silicic rocks, granodiorites on one hand and dacites and rhyolites on the other, evolved very differently. The granodiorites may have originated from a crustal source leaving a residue of amphibolite or garnet granulite, whereas the rhyolites were the product of protracted fractional crystallization of mantle-derived melts.

INTRODUCTION

The early Mesozoic to Late Tertiary igneous rocks of western Mexico are the expression of arc magmatism associated with an eastward-dipping Benioff zone. A significant proportion of the magmatism was silicic, and products include the voluminous (> 250,000 km^3) mid-Tertiary rhyolitic ignimbrites of the Sierra Madre Occidental and the Mesozoic and Cenozoic granitoids of mainland Mexico and Baja California. Throughout the period of subduction the locus of igneous activity was not stationary but migrated back and forth between Baja California and west Texas (Figure 1). The best documented evidence of the oldest arc magmatism is that for northern Sonora, where lower and middle Jurassic (180–150 m.y. old) plutonic and volcanic rocks are widespread [*Anderson and Silver,* 1978]. Late Triassic to middle Jurassic granitoids of southern Chihuahua and adjacent Durango may represent a southern extension of this Sonoran arc [*Clark et al.,* 1979]. About 140 m.y. B.P., the locus of magmatic activity shifted westward to the Pacific margin of the Peninsula Ranges Batholith of Southern and Baja California [*Silver,* 1979]. Magmatism remained static there for ~ 30 m.y. and then migrated eastward, reaching central Sonora in mid-Cretaceous time, about 80 m.y. ago. Mid- to late Cretaceous plutonic rocks occur in Sonora [*Silver et al.,* 1975], extreme western Chihuahua [*Bagby,* 1979], Sinaloa [*Henry,* 1975], and Durango [*Clark et al.,* 1979]. *Clark et al.* [1979] and *Clark and Foster* [1979] concluded that the magmatic arc continued to sweep eastward during late Cretaceous to mid-Tertiary time, traversing Chihuahua and eventually reaching west Texas, where igneous activity peaked 40–31 m.y. B.P. [*McDowell,* 1978]. After about 35 m.y. B.P. magmatism spread rapidly westward again, crossing the present area of the Sierra Madre Occidental about 35–28 m.y. B.P. and reaching eastern Baja California by 22–17 m.y. B.P. [*Gastil et al.,* 1979]. The Cretaceous to mid-Tertiary eastward sweep of magmatism may have been the result of shallowing of the angle of subduction [*Henry,* 1975; *Coney and Reynolds,* 1977], whereas the following westward expansion of volcanism may reflect steepening of the Benioff zone or detachment and floundering of the slab.

In this paper we compare the petrogenesis of two sequences of igneous rocks from the Batopilas area of the Sierra Madre Occidental (Figure 1). These two sequences, mid-Tertiary volcanic rocks and older plutonic rocks, represent two pulses of arc magmatism, one associated with the late Cretaceous–early Tertiary eastward sweep and the other with the mid-Tertiary westward expansion. The plutonic rocks are members of a volcano-plutonic complex, the oldest unit exposed in the region. Volcanic rocks in this older complex are predominantly intermediate in composition but are pervasively altered and are not discussed in this report. The granitoids described include approximately a dozen small epizonal plutons that are exposed within a 50-km radius of Batopilas. A geological map of the Batopilas area and locations of the samples analyzed can be found in a work by *Bagby* [1979]. The plutonic rocks form a bimodal population of quartz diorites and granodiorites, approximately equal in abundance. One granodiorite yielded biotite and hornblende K-Ar ages of about 83 m.y., but plutonic activity probably extended into the Cenozoic [*Bagby,* 1979]. The granodioritic plutons are cross cut by quartz dioritic dikes and vice versa; thus the field evidence suggests that the two compositional groups are coeval, although the time span represented by the plutonic rocks is not well constrained. The mid-Oligocene volcanic rocks discussed here are members of the Upper Volcanic sequence, which overlies the volcano-plutonic complex. This younger sequence is approximately 1000 m thick and is composed predominantly (~80%) of rhyolitic ash flow tuff, but lava flows ranging in composition from basaltic andestite to rhyolite occur interlayered with the tuffs. The Upper Volcanic sequence in the Batopilas region was emplaced about 30 m.y. B.P. Rocks of this sequence are discussed only to the extent required to allow meaningful comparison with the older plutonic rocks. They are described in detail by *Cameron et al.* [1980], *Lanphere et al.* [1980] and *Cameron and Hanson* [1981].

[1] Now with the Homestake Mining Company, Exploration Division, Napa, California 94558.

[2] Now with the School of Geology and Geophysics, University of Oklahoma, Norman, Oklahoma 73019.

Copyright © 1981 by the American Geophysical Union.

Paper number 1B0752.
0148-0227/81/001B-0752$01.00

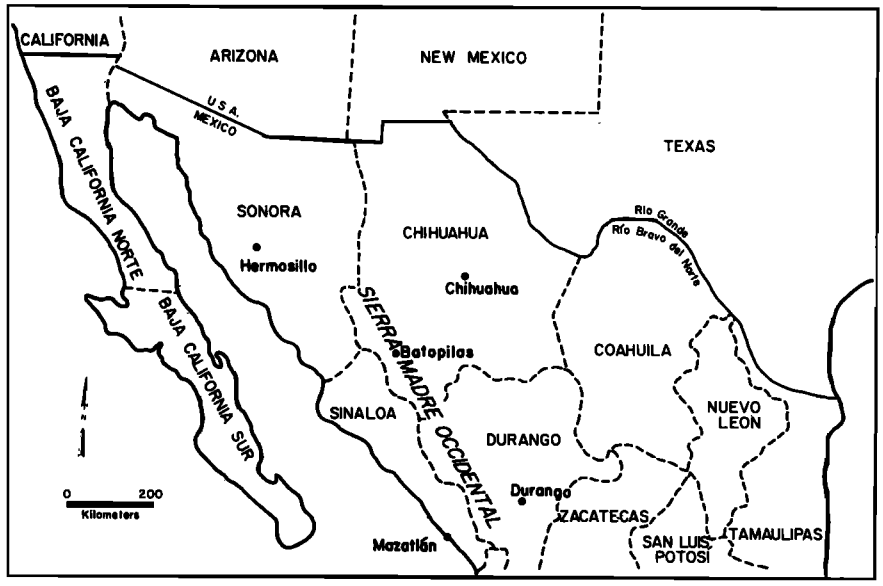

Fig. 1. Location map showing towns and geographic areas mentioned in text.

PETROGRAPHY AND MINERALOGY

The plutonic rocks of the Batopilas region are divided into two groups, quartz diorites and granodiorites, on the basis of texture and chemical composition. Our grouping, while not corresponding perfectly to the IUGS classification (Figure 2), appears to have petrogenetic significance for the Batopilas region. Characteristically, the quartz diorites are fine-grained and nonporphyritic with an average grain size of ~0.4 mm. Flow alignment of plagioclase crystals in some rocks produced a strongly developed foliation. Rocks of the second group, which is composed of granodiorites and one tonalite, are nonfoliated, equigranular, and have an average grain size of 2–3 mm. Augite ($\sim Wo_{45}En_{40}Fs_{15}$) and hypersthene ($En_{70-60}$) are common in the quartz diorites, but both are absent from the granodiorites (Table 1). Hornblende, which appears relatively late in the paragenetic sequence of the quartz diorites, is subhedral to anhedral and commonly occurs as reaction rims on pyroxene. In contrast, the hornblende in the granodiorites is prismatic and typically euhedral. Mafic inclusions are rare in rocks of both groups. The fine-grained texture of the quartz diorites, the presence of euhedral hornblende in the granodiorites, and the paucity of mafic inclusions indicate that both plutonic groups crystallized from magmatic liquids and that restite [*White and Chappel*, 1977] is not an important component of either.

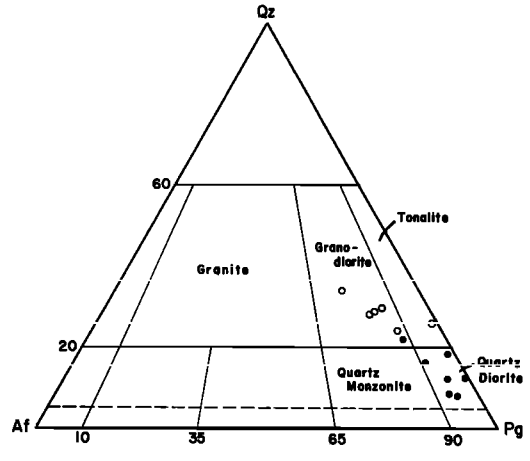

Fig. 2. Modal compositions of plutonic rocks from the Batopilas area. The rocks represented by solid circles constitute the quartz diorite group of this paper.

Plagioclase is a ubiquitous phenocryst in rocks of the Upper Volcanic sequence. Few rocks contain phenocrysts of alkali feldspar, and quartz phenocrysts are usually restricted to high silica (≥ 75% SiO_2) rhyolites. The characteristic ferromagnesian phenocrysts are augite and hypersthene, whereas hornblende and biotite are generally present only in the high silica rhyolites. The ferromagnesian minerals are Mg-rich, and all pyroxenes, even those from the most silicic rocks, have compositions that lie in the ranges reported for the quartz diorites. The most mafic rock from the sequence, a basaltic andesite with 54 wt. % SiO_2, crystallized from a hybrid magma formed by mixing of basaltic and andesitic magmas; there is, however, no clear evidence of magma mixing in the other volcanic rocks [*Cameron et al.*, 1980]

GEOCHEMISTRY

Samples from the Upper Volcanic sequence range from 54 to 78 wt. % SiO_2 (Figure 3). By far the most voluminous of the volcanic rocks are rhyolitic ignimbrites, which generally contain 70–75% SiO_2. Most volcanic rocks outside of this silica range are lavas, which are greatly over-represented in Figure 3 compared to their true relative abundance. The quartz diorites (SiO_2 = 57–63%; Figure 3) overlap in silica content with andesites from the Upper Volcanic sequence, and the granodiorites and tonalite (SiO_2 = 66–68; Figure 3) lie within the silica range of the dacites.

On major element silica variation diagrams, the chemical trends of the volcanic and plutonic sequences generally coincide (Figure 3), but the plutonic rocks may have slightly higher Al_2O_3 and slightly lower TiO_2, P_2O_5, and total Fe. Moreover, the quartz diorites contain somewhat higher K_2O than the andesites, about 1.5 versus 1.0 wt. % K_2O at SiO_2 = 60 wt. %. The two sequences are calcic according to *Peacock*'s [1931] classification as both have an alkali-lime index of 62.5. However, we describe them as calc-alkalic because of

TABLE 1. Major and Trace Element Contents* and Modal Mineralogy of Plutonic Rocks from the Batopilas Region, Chihuahua, Mexico

	Rock Type† and Rock Number												
	Qd, MXU7609	Qd, MXB7704	Qd, M93	Qd, MXV7611	Qd, MXU7602	Qd, MXB7677	Qd, MXB7668	Gd, MXB7665	Gd, MXB7678	Gd, MXB7703	Gd, MXU7607	Gd, MX7539	Ton, MXV7606
						Major Elements, wt % Anhydrous							
SiO_2	57.21	56.93	57.69	59.21	58.85	60.36	62.81	65.65	66.93	66.96	67.03	67.61	66.24
TiO_2	0.90	0.93	0.95	0.83	0.85	0.96	0.73	0.50	0.45	0.43	0.46	0.44	0.50
Al_2O_3	16.95	18.06	17.83	18.14	18.16	17.26	16.68	17.01	16.36	16.22	16.18	15.89	16.81
Fe_2O_3‡	2.44	2.45	2.48	2.35	2.37	2.49	2.25	2.05	1.97	1.95	1.98	1.97	2.04
FeO	5.66	5.01	4.66	4.24	4.16	4.28	3.38	1.82	1.57	2.09	2.13	1.86	2.29
MnO	0.16	0.12	0.11	0.13	0.12	0.13	0.10	0.07	0.08	0.10	0.08	0.10	0.09
MgO	4.92	4.09	4.38	3.16	3.17	2.72	2.55	2.17	1.69	1.33	1.80	1.41	1.96
CaO	7.80	7.48	7.04	6.86	7.18	6.26	5.51	3.47	4.45	4.27	4.38	4.55	4.62
Na_2O	2.78	3.41	3.27	3.38	3.73	3.88	3.71	4.65	4.14	3.87	3.57	3.56	3.85
K_2O	1.03	1.33	1.39	1.50	1.20	1.45	2.09	2.42	2.22	2.62	2.27	2.46	1.44
P_2O_5	0.15	0.19	0.20	0.20	0.22	0.21	0.18	0.18	0.14	0.14	0.12	0.13	0.15
L.O.I.§	1.42	0.88	1.82	0.88	0.21	0.92	0.48	2.66	1.06	1.11	1.19	1.78	1.64
						Trace Elements, ppm							
Y	26	20	19	21	19	24	22	14	16	17	18	17	15
Sr	380	494	466	527	577	499	457	652	479	466	395	442	520
Rb	38	38	34	46	29	38	61	80	65	78	75	76	51
Th	3	3	ND‖	5	4	4	2	6	6	9	7	8	6
Pb	37	13	12	18	12	12	14	15	17	18	51	17	24
Nb	10	10	10	10	10	11	11	9	10	11	11	11	9
Zr	112	119	133	124	120	122	149	117	92	108	121	104	102
						Modal Mineralogy, Volume %							
Plagioclase	54.3	62.6	56.6¶	62.4	46.4	60.8	56.1	55.9	52.0	51.1	52.2	42.3	64.2
Alkali feldspar	0.3	5.0	3.3	3.3	4.3	1.2	8.1	7.9	10.6	11.4	8.9	13.9	0.0
Quartz	7.5	6.0	8.0	5.3	9.6	13.8	17.5	19.6	25.5	24.6	25.9	28.4	22.9
Biotite	0.0	4.8	10.0	12.4	5.6	11.6	7.5	8.7	6.6	6.1	0.0	7.5	10.9
Hornblende	34.5	0.5	13.3	12.2	0.0	8.1	8.8	7.0	4.2	5.3	12.3	6.7	0.9
Pyroxene	0.0	18.3	4.8	0.1	25.1	2.7	0.0	0.0	0.0	0.0	0.0	0.0	0.0
Opaque**	3.3	2.8	4.0	4.3	9.0	1.9	1.8	0.9	1.0	1.4	0.6	1.1	1.1

* Analyses by X ray fluorescence; see *Bagby*, [1979] for details.
† Qd = quartz diorite; Gd = granodiorite; Ton = tonalite.
‡ Fe_2O_3 calculated to be no greater than TiO_2 + 1.5%.
§ Loss on ignition at 1000°C.
‖ Not determined.
¶ Mode from sample MX7541 from the same outcrop.
** Also includes trace amounts of apatite and zircon.

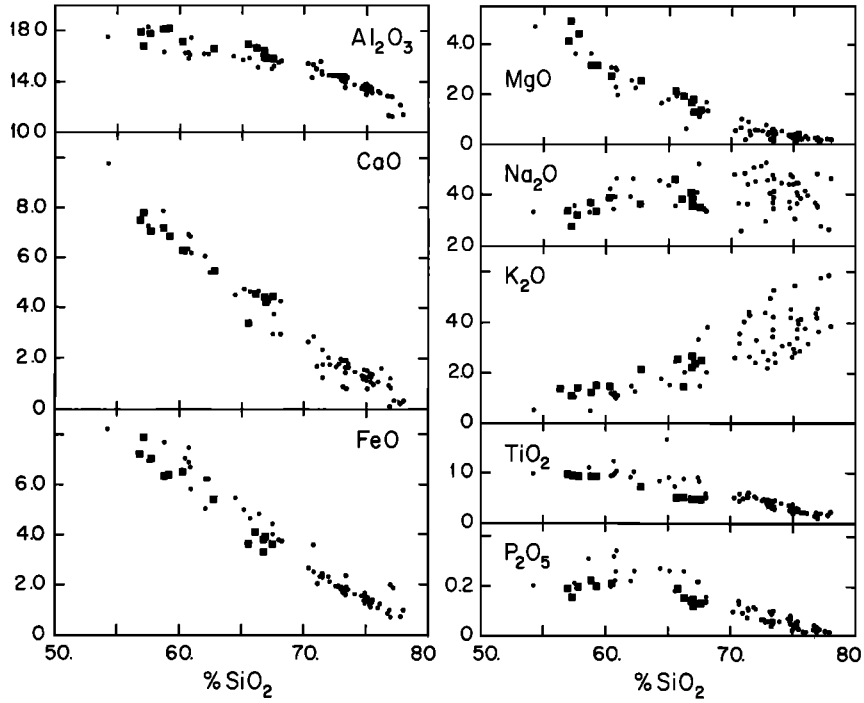

Fig. 3. Major element silica variation diagrams. Squares and solid circles represent the plutonic and Upper Volcanic sequences, respectively. Total Fe is reported as FeO. Volcanic rock names are based on SiO_2 content. Basaltic andesites contain 53–56% SiO_2, andesites 56–63% SiO_2, dacites 63–70% Si_2, and rhyolites > 70% SiO_2. Data on volcanic rocks are from *Cameron et al.* [1980].

their low iron enrichment. Both groups plot in the calc-alkalic field on *Miyashiro*'s [1974] FeO*/MgO versus SiO_2 diagram.

Although the major element chemistry of the volcanic and plutonic sequences is generally similar, important differences exist both in the abundances of some trace elements and in interelement ratios (Figures 4–7). For example, the plutonic rocks have higher K/Rb (Figure 5) and Nb/Y (Figure 6) and lower Zr/Nb (Figure 7) than volcanic rocks with similar SiO_2 contents. Within the plutonic sequence the K/Rb and Zr/Nb ratios are similar but the granodiorites have higher Nb/Y than the quartz diorites (Figure 6). Zr and Y exhibit contrasting trends in the plutonic rocks and in the intermediate (< 70 wt % SiO_2) volcanic rocks. Both elements decrease slightly with increasing SiO_2 in the plutonic sequence, but increase slightly in the intermediate volcanic rocks (Figure 4). In spite of the different trends, the Zr/Y ratios of the two sequences are similar (Figure 6).

The rare earth element (REE) patterns of the plutonic and volcanic rocks also display important differences. All of the volcanic rocks have negative Eu anomalies, and on the average the total concentrations of REE increase in the series andesite-dacite-rhyolitic ignimbrite (Figure 8). Ignimbrite 10 is somewhat aberrant to this trend because its concentrations of middle and heavy REE lie within the andesitic range. The general shape of the REE patterns of the volcanic rocks does not change greatly with increasing silica except for the size of

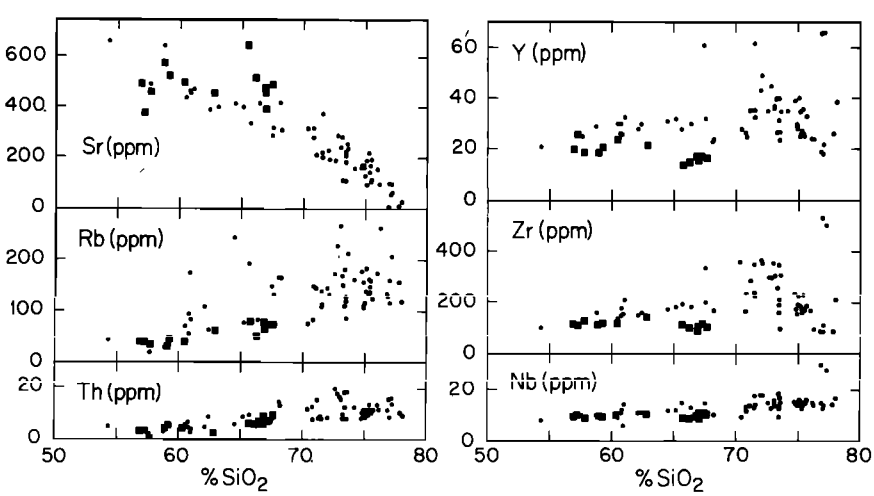

Fig. 4. Trace element silica variation diagrams. Square and solid circles represent the plutonic and Upper Volcanic sequences, respectively. Data on volcanic rocks are from *Cameron et al.* [1980].

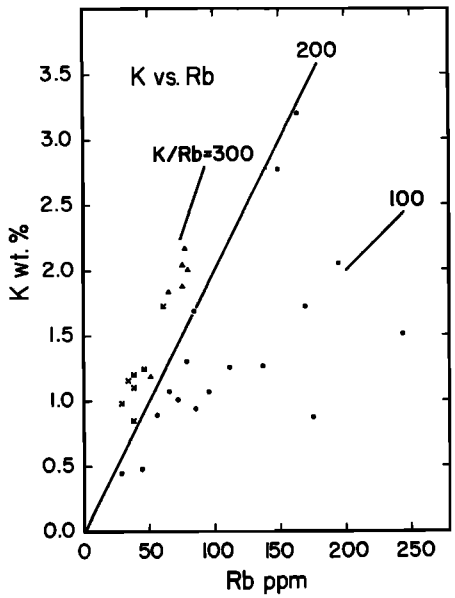

Fig. 5. K versus Rb. Crosses represent quartz diorites, triangles represent granodiorites, and solid circles represent intermediate rocks (<70 wt % SiO_2) from the Upper Volcanic sequence.

the Eu anomaly. In contrast, the plutonic rocks have lower concentrations of REE and higher $(Ce/Yb)_N$ than the volcanic rocks (Figure 9, Table 2). Within the plutonic sequence the concentrations of REE decrease from quartz diorite to granodiorite and the shapes of the REE patterns of the two groups of rocks are quite different. The granodiorites have

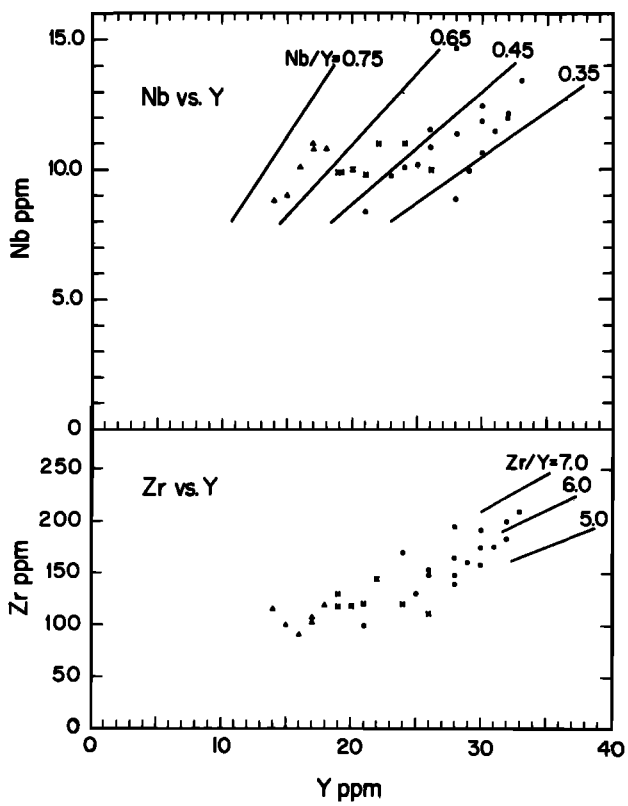

Fig. 6. Nb versus Y and Zr versus Y. Symbols are the same as in Figure 5.

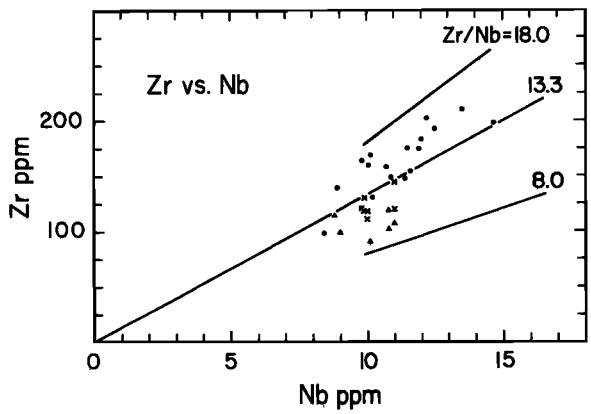

Fig. 7. Zr versus Nb. Symbols are the same as in Figure 5.

REE patterns that are distinctly concave upward in the heavy REE, and they have smaller Eu anomalies than the quartz diorites.

The initial $^{87}Sr/^{86}Sr$ ratios of rocks from the Upper Volcanic sequence have a median value of 0.7046 [*Lanphere et al.*, 1980], and the ratios do not vary significantly with silica content (Figure 10). All but one of the quartz diorites have higher initial ratios than the intermediate volcanic rocks, whereas two of the three granodiorites have ratios similar to those of the volcanic rocks (Figure 10, Table 3).

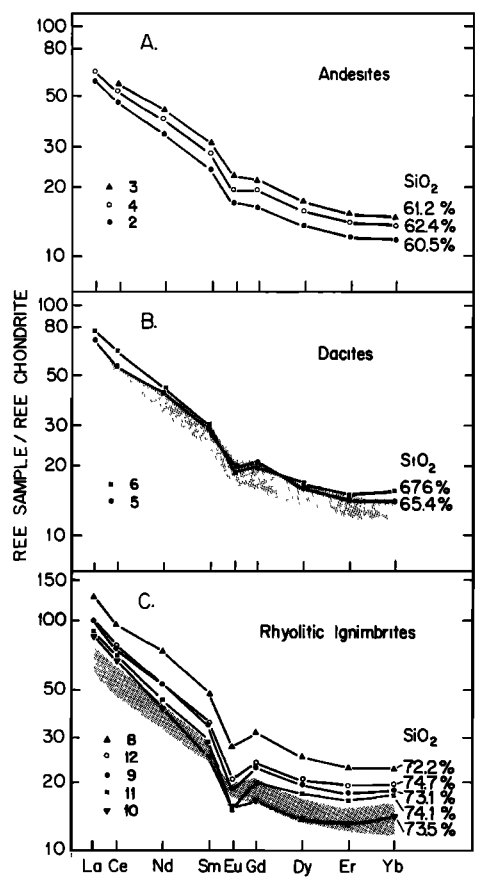

Fig. 8. Chondrite-normalized REE patterns of rocks from the Upper Volcanic sequence of the Batopilas area. Data are from *Cameron and Hanson* [1981]. (*a*) Andesites (*b*) Dacites: field of andesite stippled. (*c*) Rhyolitic ignimbrites: field of andesites and dacites stippled.

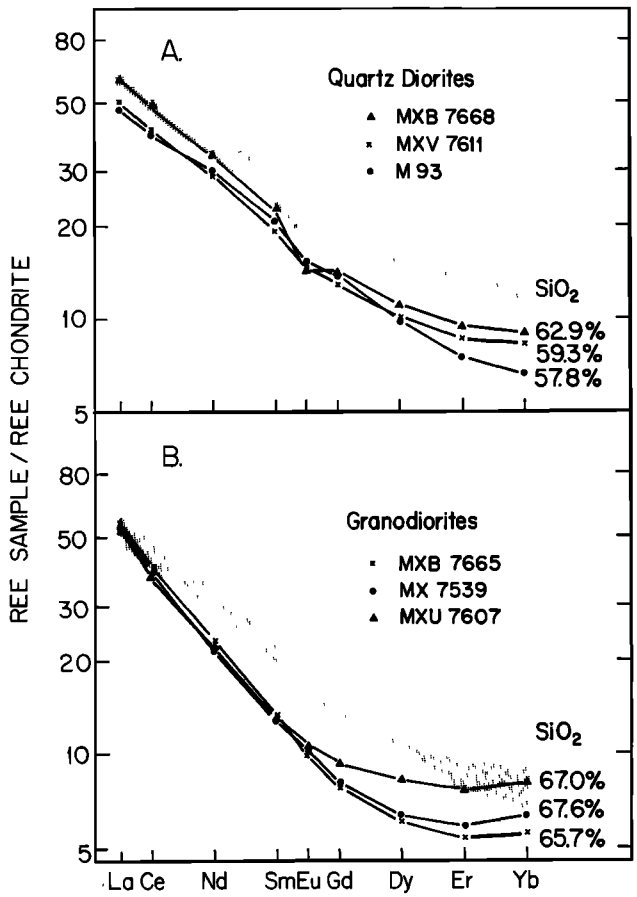

Fig. 9. Chondrite-normalized REE patterns of plutonic rocks from the Batopilas area. (*a*) Quartz diorites: field of andesites from Figure 8 stippled. (*b*) Granodiorites: field of quartz diorites stippled. Patterns are normalized to the Leedy chondrite [*Masuda et al.*, 1973] divided by 1.2.

DISCUSSION

The Crust Beneath Western Mexico

A knowledge of the nature of the crust beneath western Mexico is important in evaluating hypotheses for the origin of the plutonic and volcanic sequences. All inferences made in this section regarding the chemical characteristics of the crust are based upon the age and composition of relatively few outcrops of basement rock, upon the few $^{87}Sr/^{86}Sr$ data available, and upon tectonic models for the evolution of western Mexico.

Between Hermosillo and Mazatlán, exposures of basement terrain are very limited. That closest to Batopilas occurs about 100 km to the southwest in northern Sinaloa (Figure 1). The basement rocks, known as the Francisco Gneiss, consist of mafic and felsic gneisses interlayered on a scale of a few millimeters to a few meters [*Mullan*, 1978]. The mafic gneisses are generally basaltic in composition (~ 50% SiO_2) and have amphibolite mineralogy, whereas the felsic gneisses range in composition from diorite to leucocratic tonalite and are composed of varying proportions of plagioclase, quartz, biotite, and hornblende with little or no garnet [*Mullan*, 1975]. Mullan suggested that the Francisco Gneiss is Precambrian in age, but the limited geochronological data now available indicate a late Paleozoic or early Mesozoic age (T. H. Anderson, personal communication, 1980).

Strontium isotopic compositions have been used in numerous petrogenetic studies of granitoids and silicic volcanic rocks to document the degree of interaction between magmas and radiogenic crustal rocks. For example, in studies of the mid-Tertiary San Juan Mountains volcanic field, *Lipman et al.* [1978] noted a positive correlation between initial $^{87}Sr/^{86}Sr$ ratio and SiO_2 content of the Oligocene rocks. The initial Sr isotopic ratios, which increased from ~0.7054 in andesites to ~0.7070 in rhyolites, were interpreted as evidence of interaction between the silicic magmas and radiogenic upper crust. Basaltic rocks have generally high Sr contents and therefore are relatively insensitive to contamination by radiogenic crustal Sr. Thus their initial isotopic ratios may approach those of mantle source regions more closely than ratios of silicic rocks with lower Sr contents. The only data published on basalts of western Mexico are two analyses of rocks collected ~100 km northeast of Batopilas [*McDowell et al.*, 1978]. The initial $^{87}Sr/^{86}Sr$ ratios, 0.7043 ± 0.0004 and 0.7047 ± 0.0006, are similar to those of some late Cenozoic basalts from the San Juan Mountains volcanic field that presumably were derived from continental lithosphere [*Lipman et al.*, 1978].

Kistler and Peterman [1973, 1978] and *Armstrong et al.* [1977] recognized a line in the western United States, west of which Mesozoic granitoids have initial Sr ratios less than 0.706 and east of which the initial ratios are higher. They interpreted this line as the approximate edge of the Precambrian craton. The plutonic and volcanic rocks from the Batopilas area of Mexico all have initial Sr isotopic ratios less than

TABLE 2. Rare Earth Element Analyses of Plutonic Rocks From the Batopilas Region, Chihuahua, Mexico

	Rock Number					
	M93	MXV7611	MXB7668	MXB7665	MXU7607	MX7539
La, ppm	15.2	15.9	18.9	17.6	16.4	17.0
Ce	32.5	33.2	39.9	32.6	30.3	31.6
Nd	17.7	17.3	20.3	13.8	13.0	12.9
Sm	3.99	3.71	4.27	2.57	2.70	2.44
Eu	1.08	1.05	1.03	0.705	0.773	0.741
Gd	3.55	3.34	3.68	2.03	2.44	2.09
Dy	3.21	3.27	3.56	1.96	2.68	2.07
Er	1.59	1.83	2.01	1.14	1.64	1.25
Yb	1.37	1.72	1.96	1.16	1.69	1.32
Eu/Eu*	0.88	0.91	0.78	0.95	0.93	1.00
$(Ce/Yb)_N$	6.1	5.0	5.2	7.2	4.6	6.1

Analyses by isotope dilution. Analytical precision for La and Gd is better than 5% and about 1% for the other REE. See *Hanson* [1976] for discussion of techniques.

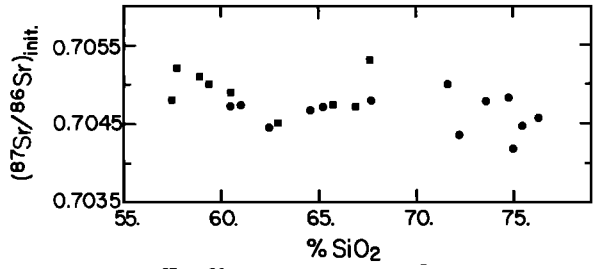

Fig. 10. Initial $^{87}Sr/^{86}Sr$ ratios versus SiO_2. Squares and solid circles represent the plutonic and Upper Volcanic sequences, respectively. Data on the Upper Volcanic sequence are from *Lanphere et al.* [1980].

0.706 (Figure 10); thus if a '0.706 line' exists in Mexico, it must lie to the north or east of Batopilas. Such a position is in accord with *Anderson and Silver* [1975], who suggested that the southern limit of the Precambrian craton may lie along an east–west line not far north of Hermosillo (Figure 1). Complicating this rather simple picture are a few silicic rocks from western Mexico with initial $^{87}Sr^{86}Sr$ ratios higher than 0.706. Three lava flows collected 60–100 km north of Batopilas have ratios of 0.7055, 0.7063, and 0.7074 [*Lanphere et al.*, 1980]. *McDowell et al.* [1978] reported Sr isotope analyses of eight rhyolites collected near and to the west of Durango. The rhyolites have a median initial $^{87}Sr/^{87}Sr$ ratio of 0.7048, but individual values range from 0.7033 to 0.7062. *Henry* [1975] reported Sr isotopic data on six granitoids between Maztlán and Durango; five of the six lie in the range 0.7030–0.7063, but one has an initial ratio greater than 0.710.

In summary, the meager data presently available suggest that the crust is composed largely of Mesozoic arc deposits as *Anderson and Silver* [1978] concluded. Because the crust appears to be intermediate in composition and relatively young, its average $^{87}Sr/^{86}Sr$ ratio probably is not much higher than that of the mantle. For example, the $^{87}Sr/^{86}Sr$ ratio of early Jurassic crust with a Rb/Sr ratio of 0.08 would increase only 0.0004 by late Cretaceous and 0.0005 by mid-Tertiary time. Nevertheless, local pockets of radiogenic crust, capable to producing or contaminating magmas, must exist.

Behavior of Selected Trace Elements

The REE and K, Rb, Zr, Nb, and Y have bulk crystal/liquid distribution coefficients (D) less than 1.0 for the assemblage plagioclase (>50%) + orthopyroxene + clinopyroxene + Fe Ti oxides. These minerals compose the early crystallizing assemblage of the quartz diorites and intermediate volcanic rocks, and in addition, they could also occur in a granulite facies, crustal source region. For this assemblage K, Rb, Zr, and the light REE have $D \leq 0.1$. [*Arth*, 1976; *Pearce and Norry*, 1979], and thus the ratios of their concentrations should not change substantially even when the concentrations vary as a result of different degrees of partial melting or fractional crystallization. In contrast, ratios of Nb, Y, and the heavy REE may be sensitive to such variations or to the modal proportions of minerals. Nb is enriched in Fe-Ti oxides [*McCallum and Charette*, 1978], and Y and the heavy REE in clinopyroxene. For the plagioclase-dominated assemblage given above, they may have $D \sim 0.1$–0.5.

Hornblende and garnet, which have distribution coefficients > 1.0 for Y, Zr, Nb, and the heavy REE, could substantially affect ratios involving these elements. Hornblende is relatively ineffective in lowering K/Rb [*Hanson*, 1978], and the K/Rb of the intermediate rocks should be similar to that of the source provided that mica and K-feldspar are not residual phases.

Petrogenesis of the Plutonic Rocks

The uniformly fine-grained texture of the quartz diorites indicates that they crystallized from magmas containing few, if any, cumulate or restite crystals. Their origin, therefore, must be examined in light of the numerous models proposed for the genesis of orogenic andesites. The moderately fractionated REE patterns (Figure 9) indicate that garnet may have been an accessory or minor phase in the residue remaining in the ultimate source region of the magmas. If it were a major phase, however, the heavy REE would probably be more strongly depleted. Thus the REE data eliminate eclogite and garnet-rich granulite as possible residues. Although the $Mg/(Mg + Fe^{2+})$ values of the quartz diorites are relatively high, six of the seven are in the range 0.63–0.57. The values are too low for the magmas to have been derived directly from mantle peridotite [*Nicholls*, 1974]. The presence of negative Eu anomalies (Table 2) in the REE patterns of all three quartz diorites suggest that plagioclase was involved, at least to a limited extent, in the evolution of the magmas. One possible petrogenetic model involves derivation of the quartz diorites by crystal fractionation of basaltic magmas. In fact, the REE pattern of M93 can be duplicated by fractionation of plagioclase, olivine, and clinopyroxene from a model basaltic melt. The REE composition of the model basalt was calculated using a lherzolite nodule from San Carlos, Arizona, as the source [*Bagby*, 1979]. The residue from partial melting of the source would include olivine, clinopyroxene, and orthopyroxene. In addition, patterns similar in shape to those of the quartz diorites can be produced by partial melting of *Taylor's* [1969] average andesite, leaving a granulite residue of plagioclase, orthopyroxene, and clinopyroxene [*Bagby*, 1979]. It is not possible to choose between the fractional crystallization and crustal anatexis models with confidence. Perhaps the only argument against crustal anatexis is that melts with a composition similar to that of the quartz diorites have liquidus temperatures near 1000°C, even under water saturation conditions [*Wyllie*, 1977]. Crustal temperatures this high re-

TABLE 3. Sr Isotopic Compositions of Plutonic Rocks from the Batopilas Region, Chihuahua, Mexico

Sample Number	$^{87}Rb/^{86}Sr$*	$^{87}Sr/^{86}Sr$, Measured†	$^{87}Sr/^{86}S$, Initial‡
Quartz Diorites			
MXU7609	0.280	0.7051 ± 2	0.7048
M93	0.211	0.7054 ± 2	0.7052
MXU7602	0.141	0.7053 ± 2	0.7051
MXV7611	0.246	0.7053 ± 2	0.7050
MXB7677	0.214	0.7051_5 ± 2	0.7049
MXB7668	0.378	0.7049_5 ± 2	0.7045
Granodiorites			
MXB7665	0.351	0.7051_5 ± 2	0.7047_5
MXU7607	0.538	0.7053 ± 3	0.7047
MX7539	0.495	0.7058_5 ± 3	0.7053

* Rb and Sr concentrations measured by X ray fluorescence; see Table 1.

† $^{86}Sr/^{88}Sr$ ratios normalized to a value of 0.1194. Average of three determinations for NBS987 = 0.7101_5. The uncertainties are standard deviations of analytical precision. The subscripts refer to the fifth decimal place.

‡ Initial ratios calculated using an age of 83 m.y.

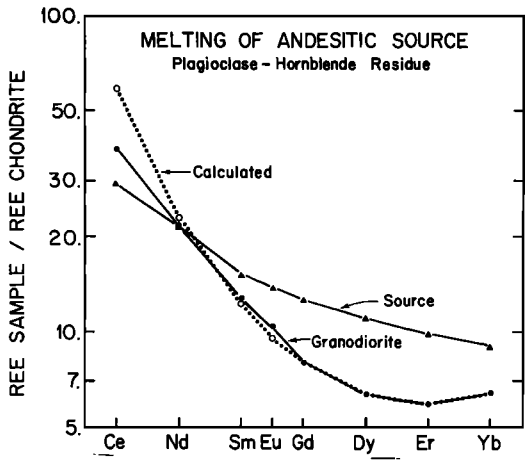

Fig. 11. Model REE pattern of a granodiorite. Solid lines show the REE patterns of *Taylor's* [1969] average andesite (source) and granodiorite MX 7539. The dotted line is a model REE pattern calculated for 15% model melting [e.g., *Arth*, 1976] of the average andesite with a residue of 70% plagioclase and 30% hornblende. Distribution coefficients from *Hanson* [1980].

quire a substantial volume of mantle-derived magma for a heat source [*Wells*, 1980].

The granodiorites cannot be related to the quartz diorites by fractionation of plagioclase and pyroxene, the near-liquidus phases in the quartz diorites. Removal of these phases increases the concentrations of the REE and Y, as well as the size of the Eu anomaly in the melt fraction. The granodiorites have lower concentrations of the middle and heavy REE and Y than the quartz diorites (Figure 9), and they have only small Eu anomalies (Table 2). On the other hand, fractionation of hornblende, which appears petrographically to be a near-liquidus phase in the granodiorites, could explain the observed variations. This hypothesis, however, is not favored. Major element *Wright and Doherty* [1970] calculations indicate that derivation of the granodiorites from the quartz diorites would require removal of ~60–65 wt. % crystals in the proportions 0.60 plagioclase, 0.35 hornblende, and 0.05 magnetite. This amount of fractionation would significantly increase the concentration of Nb and lower the Zr/Nb ratio. If Nb had a $D \approx 0.3$ and 60 wt. % crystals were removed from a quartz dioritic melt with a Nb content of 10 ppm, the residual liquid would contain ~21 ppm Nb, a factor of two higher than the concentrations observed in the granodiorites (Figures 4, 7). This weakness in the fractional crystallization model makes a direct crustal anatexis model attractive. The shape of the REE patterns of the granodiorites can be modelled closely, except for La and Ce, by partial melting of an intermediate source leaving a residue with amphibolite mineralogy (Figure 11). The general shape of the REE patterns can also be modelled, but not as well, by partial melting of a garnet granulite. If the quartz diorites were mantle-derived, they would conveniently provide a heat source to produce the granodiorites by crustal anatexis and would account for the bimodal composition of the plutonic sequence in the Batopilas area.

Petrogenesis of the Upper Volcanic Sequence

The andesites of the Upper Volcanic sequence and the quartz diorites were probably mantle peridotite, there were and the petrogenetic arguments against an eclogite or garnet-rich granulite residue, against a crustal source, and against equilibrium with mantle peridotite for the quartz diorites also apply to the andesites. Our preferred model for the origin of the Batopilas andesites is that they were derived by fractional crystallization of a mantle-derived basaltic magma, but an origin by direct anatexis of garnet-free granulite is also consistent with the geochemical data. The single basaltic andesite (54 wt. % SiO_2; Figures 3 and 4) collected to date clearly represents a mixture of basaltic and andesitic magmas [*Cameron et al.*, 1980; *Cameron and Hanson*, 1981], and thus it provides evidence for the existence of mid-Tertiary calc-alkalic basaltic magmas.

Although the ultimate source regions for the andesites and quartz diorites were probably mantle peridotite, there were significant geochemical differences and perhaps minor mineralogic differences between the two. The source region for the andesites appears to have had a lower K/Rb (Figure 5) than the source region of the quartz diorites. The higher of Zr/Nb (Figure 7) and lower Nb/Y (Figure 6) of the andesites compared to the quartz diorites may reflect differences in trace element ratios in the sources and/or the presence of minor garnet in the residue of the quartz diorites. The andesites represent at least the second pulse of mantle-derived arc magmatism in the Batopilas region. Their source region, however, was not necessarily 'more depleted' by traditional criteria (e.g., higher K/Rb) than the source of the quartz diorites.

The petrogenesis of the rhyolitic ignimbrites of the Upper Volcanic sequence is discussed in detail by *Cameron et al.* [1980] and *Cameron and Hanson* [1981], and their conclusions are briefly summarized here. In contrast to the quartz diorite-granodiorite sequence, the andesite to rhyolite series of the Upper Volcanic sequence is believed to be co-magmatic. Changes in the REE patterns (Figure 12) and concentrations of other trace elements can be closely modelled using the Rayleigh fractionation equation and mineral proportions generated by major element *Wright and Doherty* [1970] calculations. The resultant mineral proportions are similar to modal abundances of phenocrysts in the volcanic rocks. The intermediate rocks in the series were formed by fractionation of plagioclase, pyroxene, and Fe-Ti oxides in approximately model proportions. Within the rhyolites two groups were recognized: lower Y rhyolites and higher Y rhyolites that are separated by a Y concentration of 32 ppm [*Cameron et al.*, 1980; *Cameron and Hanson*, 1981]. These authors concluded that

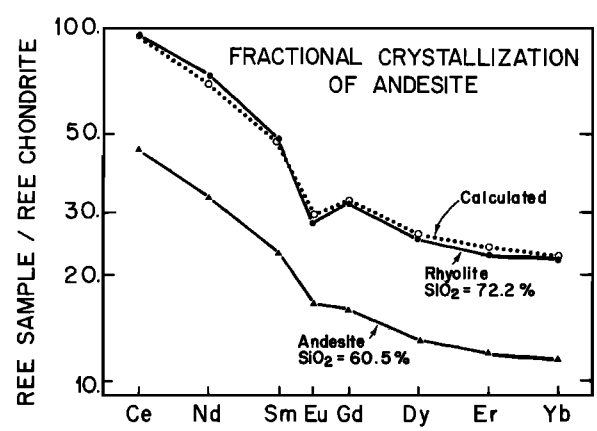

Fig. 12. Model REE pattern of a rhyolitic ignimbrite, after *Cameron et al.* [1980]. Data from *Cameron and Hanson* [1981]. Dashed line was calculated with the Rayleigh fractionation equation and by removal of 57 wt. % crystals (plagioclase, orthopyroxene, clinopyroxene, and Fe-Ti oxides in the wt. proportions 63:11:17:9) from the andesite.

pyroxene was the principal ferromagnesian phase fractionating from the higher Y rhyolites, the most common variety of ignimbrite (samples 8, 9, 11, 12; Figure 8), whereas hornblende was important in the fractionation of the lower Y rhyolites (e.g., sample 10, Figure 8). This model is generally, but not invariably, consistent with the phenocryst assemblages of the two varieties of rhyolites. The voluminous ignimbrites represent no more than 20% of the original mass of the mafic parental magmas. Although the possibility of interaction between the silicic magmas and crust cannot be ruled out, no such interaction is needed to explain the geochemical data.

Acknowledgments. REE and Sr isotopic analyses were made in G. N. Hanson's laboratory at the State University of New York at Stony Brook. The field work on which this study is based benefited greatly from the hospitality of Jeff Candler, La Bufa, Chihuahua. W. C. Bagby also thanks D. De Cristoforo and D. Krier for their able assistance during field work. This research was supported by the Petroleum Research Fund, administered by the American Chemical Society, and by National Science Foundation Grant EAR77-09006.

REFERENCES

Anderson, T. H., and L. T. Silver, Extent and development of the craton under part of the Sierra Madre Occidental, northwestern Mexico, *Geol. Soc. Am. Abstr. Programs, 7,* 141, 1975.

Anderson, T. H., and L. T. Silver, Jurassic magmatism in Sonora, Mexico, *Geol. Soc. Am. Abstr. Programs, 10,* 359, 1978.

Armstrong, R. L., W. H. Taubeneck, and P. O. Hales, Rb-Sr and K-Ar geochronometry of Mesozoic granitic rocks and their Sr isotopic compositions, Oregon, Washington, and Idaho, *Geol. Soc. Am. Bull., 88,* 397–411, 1977.

Arth, J. G., Behavior of trace elements during magmatic processes—A summary of theoretical models and their applications, *J. Res. U. S. Geol. Surv., 4,* 41–47, 1976.

Bagby, W. C., Geology, geochemistry, and geochronology of the Batopilas region, Sierra Madre Occidental, Chihuahua, Mexico, Ph.D. dissertation, 271 pp., Univ. of Calif., Santa Cruz, 1979.

Cameron, K. L., and G. N. Hanson, Rare-earth element evidence concerning the origin of voluminous mid-Tertiary rhyolitic ignimbrites and related volcanic rocks, Sierra Madre Occidental, Chihuahua, Mexico, submitted to *Geochim. Cosmochim. Acta,* 1981.

Cameron, M., W. C. Bagby, and K. L. Cameron, Petrogenesis of voluminous mid-Tertiary ignimbrites of the Sierra Madre Occidental, Mexico, *Contrib. Mineral. Petrol., 74,* 271–284, 1980.

Clark, K. F., and C. T. Foster, Composition variations in Cenozoic mineral deposits located in subduction related magmatic arcs in western Mexico, *Geol. Soc. Amer. Abstr. Programs, 11,* 402, 1979.

Clark, K. F., P. E. Damon, S. R. Schutter, and M. Shattigullah, Magmatismo en el norte de Mexico en relacion a los Yacimientos metaliferos, paper presented at XIII Convención Nacional, Asociación de Ingenieros de Minas, Metalurgistas y Géologos de México, Acapulco, Guerrero, Mexico, 1979.

Coney, P. J., and S. J. Reynolds, Cordilleran Benioff zones, *Nature, 270,* 403–405, 1977.

Gastil, G., D. Krummenacher, and J. Minch, The record of Cenozoic volcanism around the Gulf of California, *Geol. Soc. Am. Bull., 90,* 839–857, 1979.

Hanson, G. N., Rare earth element analyses by isotope dilution, *NBS Spec. Publ. U. S., 422,* 937–49, 1976.

Hanson, G. N., The application of trace elements to the petrogenesis of igneous rocks of granitic composition, *Earth Planet. Sci. Lett., 38,* 26–43, 1978.

Hanson, G. N., Rare earth elements in petrogenetic studies of igenous systems, *Ann. Rev. Earth Planet, 8,* 371–406, 1980.

Henry, C. D., Geology and geochronology of the granitic batholitic complex, Sinaloa, Mexico, Ph.D. dissertation, Univ. of Tex., Austin, 1975.

Kistler, R. W., and Z. E. Peterman, Variations in Sr, Rb, K, Na, and initial Sr^{87}/Sr^{86} in Mesozoic granitic rocks and intruded wall rocks in central California, *Geol. Soc. Am. Bull. 84,* 3489–3512, 1973.

Kistler, R. W., and Z. E. Peterman, Reconstruction of crustal blocks of California on the basis of initial strontium isotopic compositions of Mesozoic granitic rocks, *Geol. Surv. Prof. Pap. U.S., 1071,* 1978.

Lanphere, M. A., K. L. Cameron, and M. Cameron, Sr isotope geochemistry of voluminous rhyolitic ignimbrites and related rocks, Batopilas area, western Mexico, *Nature, 286,* 594–596, 1980.

Lipman, P. W., B. R. Doe, C. E. Hedge, and T. A. Steven, Petrologic evolution of the San Juan volcanic field, southwestern Colorado: Pb and Sr isotope evidence, *Geol. Soc. Am. Bull. 89,* 59–82, 1978.

Masuda, A., N. Nakamura, and T. Tanaka, Fine structures of mutually normalized rare earth patterns of chondrites, *Geochim. Cosmochim. Acta, 37,* 239–248, 1973.

McCallum, I. S., and M. P. Charette, Zr and Nb partition coefficients implications for the genesis of Mare basalts, KREEP and seafloor basalts, *Geochim, Cosmochim. Acta, 42,* 859–869, 1978.

McDowell, F. W., Potassium-argon dating in Trans-Pecos Texas volcanic field, in *Cenozoic Geology of the Trans-Pecos Volcanic Field of Texas, Guideb. 19,* edited by A. W. Walton and C. D. Henry, pp. 9–18, Bureau of Economic Geology, Austin, Texas, 1978.

McDowell, F. C., T. W. Duex, C. D. Henry, and L. E. Long, Age and strontium isotope chemistry of the Sierra Madre Occidental volcanic province, western Mexico, *U.S. Geol Surv. Open File Rep., 78-701,* 289–295, 1978.

Miyashiro, A., Volcanic rock series in island arcs and active continental margins, *Am. J. Sci., 274,* 321–355, 1974.

Mullan, H. S., The West Mexico Batholith and its envelope in the El Fuerte region, Sinaloa, Mexico, Ph.D. dissertation, 308 pp., University of Liverpool, Liverpool, England, 1975.

Mullan, H. S., Evolution of part of the Nevadan Orogen in northwestern Mexico, *Geol. Soc. Am. Bull., 89,* 1175–1188, 1978.

Nicholls, I. A., Liquids in equilibrium with peridotitic mineral assemblages at high water pressures, *Contrib. Mineral. Petrol., 45,* 289–316, 1974.

Peacock, M. A., Classification of igneous rock series, *J. Geol., 39,* 54–67, 1931.

Pearce, J. A., and M. J. Norry, Petrogenetic implications of Ti, Zr, Y, and Nb variations in volcanic rocks, *Contrib. Mineral. Petrol., 69,* 33–47, 1979.

Silver, L. T., Peninsular Ranges Batholith: A case study in continental margin magmatic arc setting, characteristics, and evolution, *Geol. Soc. Am. Abstr. Programs, 11,* 517, 1979.

Silver, L. T., T. O. Early, and T. H. Anderson, Petrological, geochemical and geochronological asymmetries of the Peninsular Ranges batholith, *Geol. Soc. Am. Abstr. Programs, 7,* 375–376, 1975.

Taylor, S. R., Trace element chemistry of andesites and associated calc-alkaline rocks, *Bull. Oregon Dep. Geol. Miner. Ind. 65,* 1969.

Wells, P. R. A., Thermal models for the magmatic accretion and subsequent metamorphism of continental crust, *Earth Planet. Sci. Lett., 46,* 253–265, 1980.

White, A. J. R., and B. W. Chappell, Ultrametamorphism and granitoid genesis, *Tectonophysics, 43,* 7–22, 1977.

Wright, T. L., and P. C. Doherty, A linear programming and least square computer method for solving petrologic mixing problems, *Geol. Soc. Am. Bull., 81,* 1995–2008, 1970.

Wyllie, P. J., Crustal anatexis: An experimental review, *Tectonophysics, 43,* 41–71, 1977.

(Received October 27, 1980;
revised February 25, 1981;
accepted April 22, 1981.)

JOURNAL OF GEOPHYSICAL RESEARCH, VOL. 86, NO. B11, PAGES 10412–10422, NOVEMBER 10, 1981

Phase Relationships of I-Type Granite With H_2O to 35 Kilobars: The Dinkey Lakes Biotite-Granite From the Sierra Nevada Batholith

CHARLES R. STERN

Department of Geological Sciences, University of Colorado, Boulder, Colorado 80309

PETER J. WYLLIE

Department of Geophysical Sciences, University of Chicago, Chicago, Illinois 60637

The Dinkey Lakes biotite-granite from the Sierra Nevada batholith was reacted (with varying percentages of H_2O in sealed platinum capsules) in a piston-cylinder apparatus between 10 and 35 kbar. The results were combined with the results from previously published experiments to provide comprehensive phase relationships for an I-type granite: a P-T diagram with excess H_2O; isobaric T-X_{H_2O} diagrams at 25, 30, and 35 kbar showing H_2O-undersaturated relations; the H_2O-undersaturated liquidus surface mapped with contours for constant H_2O contents and fields for near-liquidus minerals; and the solubility of H_2O in granite liquids to 35 kbar. Results and their implications show: (1) The solidus temperature decreases from 680°C at 2 kbar to 620°C at 10 kbar, then increases to 700°C at 35 kbar because of changes from less dense to more dense subsolidus mineral assemblages. (2) The melting interval with excess H_2O, which is only 35°C at 2 kbar, increases to 105°C at 10 kbar and 150°C at 35 kbar because the liquidus minimum in the complex rock system departs from granite composition with increasing pressure. (3) The solubility of H_2O in granite liquid is 27 ± 2.5 weight percent at 35 kbar and 850°C, indicating that a miscibility gap persists between H_2O-saturated silicate magmas and aqueous vapor phase, at least to pressures corresponding to 120-km depth in the mantle. Dissolution of alkali feldspar (20% of rock) in the subsolidus aqueous vapor phase indicates that deep-seated aqueous fluids are concentrated solutions. (4) Quartz and coesite are the liquidus minerals at mantle pressures for all H_2O contents, indicating that granites and rhyolites cannot be primary magmas from mantle peridotite or subducted oceanic gabbroic crust. (5) The liquidus surface at crustal pressures, with plagioclase and quartz as primary minerals, indicates that primary liquids of granite composition with moderate H_2O contents can be generated in the crust at reasonable temperatures; these liquids could rise to near surface levels without vesiculation. Granite liquid together with residual crustal minerals could constitute plutonic magmas of intermediate composition.

INTRODUCTION

Chappell and White [1974] identified two distinctly different types of granitoid rocks in southeastern Australia that they designated I-type and S-type. *White and Chappell* [1977] discussed their derivation by partial melting of igneous or sedimentary source rocks, respectively. The granitoid rocks of the Sierra Nevada batholith, with abundant hornblende [*Bateman et al.*, 1963], correspond to the I-type.

The Dinkey Lakes biotite-granite is one of a series of four rocks from the central Sierra Nevada batholith (with a tonalite and two granodiorites) that were studied in the presence of excess H_2O by *Piwinskii* [1968*a*, 1973], initially to 3 kbar and then to 10 kbar. Additional results on the tonalite were presented by *Lambert and Wyllie* [1974]—excess H_2O relationships to 30 kbar and 850°C; *Stern and Wyllie* [1973*b*, 1978]—30 kbar results for H_2O contents from 0% to excess; *Stern et al.* [1975]—completed PT diagram with excess H_2O to 30 kbar and the H_2O-undersaturated liquidus surface. Additional results on the granite have been presented by *Boettcher and Wyllie* [1968*a*]—near-solidus results with excess H_2O from 10–30 kbar; *Stern and Wyllie* [1973*a*, *b*]—completed PT diagram with excess H_2O to 35 kbar, preliminary results for 25 kbar with variable H_2O content, and results at 30 kbar with 5% H_2O; *Stern et al.* [1975]— the H_2O-undersaturated liquidus surface.

In this paper we present the complete phase relationships for the Dinkey Lakes biotite-granite (consolidated from the scattered publications) together with previously unpublished run data, as representative for an I-type granite. Similar data for a muscovite granite, with mineralogy corresponding to an S-type granite, are presented in a companion paper [*Huang and Wyllie*, 1981].

THE DINKEY LAKES BIOTITE-GRANITE

The porphyritic biotite granite from the Dinkey Lakes region of the Sierra Nevada was provided by P. C. Bateman and F. C. Dodge of the U. S. Geological Survey. The geology of the area and the mineralogy and petrology of the granitic rocks were summarized by *Bateman et al.*, [1963]. The rock is number HL-29 in the account by *Kistler et al.* [1965] and number 104 in the system of *Piwinskii* [1968*a*].

Table 1 provides a chemical analysis for the rock, its CIPW norm, and its mode as determined by F. C. Dodge using stained slabs. *Piwinskii* (1968*b*) listed the Niggli value and Differentiation Index. The rock consists of nearly equal proportions of quartz, alkali feldspar, and plagioclase, with less than 5 volume percent mafic minerals, dominantly biotite. The alkali feldspar has the composition $Or_{79}Ab_{21}$, and the plagioclase is zoned form $An_{16}Ab_{84}$ to An_8Ab_{92} [*Piwinskii*, 1968*b*].

EXPERIMENTAL PROCEDURES

With measured amounts of distilled and deionized water the powdered rock sample (passed through 200 mesh) was sealed within platinum capsules and reacted in a single-stage piston-cylinder apparatus [*Boyd and England*, 1960], using a half-inch diameter tungsten carbide pressure chamber with

Copyright © 1981 by the American Geophysical Union.

Paper number 1B0412.
0148-0227/81/001B-0412$01.00

TABLE 1. Chemistry and Mineralogy of Dinkey Creek Biotite-Granite #104

Chemical Analysis		CIPW Norm	
SiO_2	75.4	Qz	31.6
TiO_2	0.15	Or	27.2
Al_2O_3	13.5	Ab	34.1
Fe_2O_3	0.0	An	5.0
FeO	0.64	Hy	0.6
MnO	0.04	Il	0.3
MgO	0.10	Mode	
CaO	1.0		
Na_2O	4.0	Quartz	34.8
K_2O	4.6	K-feldspar	29.0
H_2O^+	0.35	Plagioclase	31.5
H_2O^-	0.04	Mafic minerals, mostly biotite	4.7
P_2O_5	0.07		
CO_2	<0.05		
Total	99.94		

Sample provided by P. C. Bateman and F. C. Dodge.

hardened steel liner and talc sleeves and cylinders in the furnace assembly. Grease-base 'Molykote-G' (MoS_2) served as a lubricant between the pressure chamber and the furnace assembly, which was jacketed with lead foil. All runs were brought to final pressure by the hot piston-out procedure [*Boyd et al.*, 1967]: pressure was raised 5 to 7 kbar above run pressure, the sample was heated to the run temperature, and the pressure was released to the run value. The nominal pressure without friction correction is considered accurate to ± 5% [*Huang and Wyllie*, 1975]. Thermocouples used were chromel-alumel ($T \leq 850°C$) and Pt/Pt 10 Rh ($T > 850°C$), with no correction for pressure effects on output emf. Temperatures are precise to ±5°C, and probably accurate to within ±13°C at 1000°C, 30-kbar pressure, considering pressure effects on thermocouple emf [*Getting and Kennedy*, 1971; *Merrill and Wyllie*, 1975]. The oxygen fugacity imposed on the reactants by the furnace assembly was slightly below the Ni/NiO buffer [*Merrill and Wyllie*, 1975].

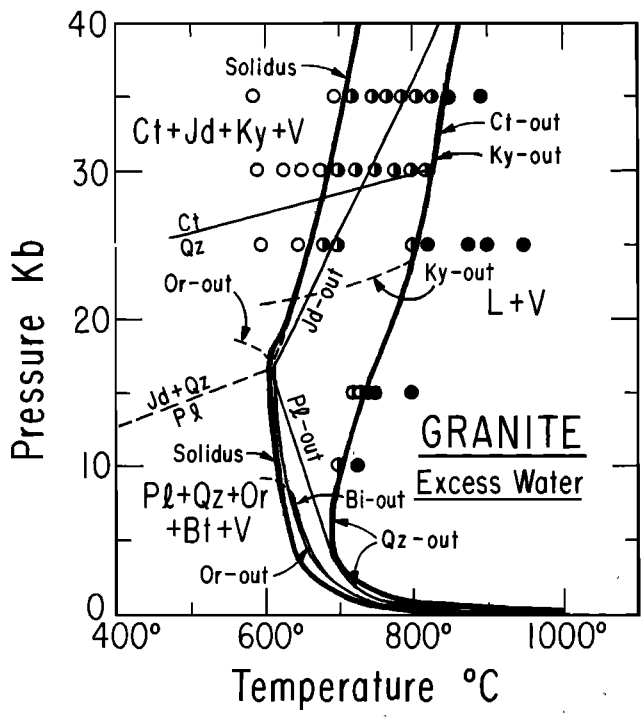

Fig. 1. Phase relations for biotite-granite (#104) with excess water. Definitive experiments are listed in Table 2. Phase boundaries below 3 kbar are from *Piwinskii* [1968*a*], and those between 3 and 25 kbar incorporate the results of *Piwinskii* [1973] and *Boettcher and Wyllie* [1968*a*]. Solid circles are runs above the liquidus, empty circles are subsolidus runs, and half-filled circles represent crystals + liquid. Dashed lines: phase boundaries estimated or uncertain. Abbreviations: Pl, plagioclase; Qz, quartz; Or, orthoclase; Bt, biotite; Jd, jadeite; Ct, coesite; Ky, kyanite; L, liquid; V, vapor. At low pressures, a single feldspar would replace Ab + Or at temperatures above the solvus.

Boettcher and Wyllie [1968*a*] found that above 15.3 kbar, metastable melting of this granite could occur below the solidus unless the high pressure mineral assemblage was used. Therefore, most runs above 15 kbar were performed in two stages. First, the sample was held below the metastable extension of the solidus curve long enough to produce the high-pressure mineral assemblage, and then the temperature was raised to the required level for the run. These two stages are indicated by pairs of rows in the run tables. Normal, single-stage runs were used at near-liquidus temperatures, above 950°C.

The reversibility of some phase boundaries was established by two-stage runs that were first held at temperature above the phase boundary, and then the temperature was lowered to the required level for the run. Details of problems and procedures for establishing reversibility of phase boundaries for rock samples within narrow temperature intervals were reviewed by *Stern and Wyllie* [1975].

Runs were quenched rapidly by switching off the power to the furnace. The capsules were recovered, tested for leaks by the application of gentle heat, and the sample was recovered and crushed for examination.

Identification of Phases

Phase assemblages were determined by optical and X ray studies of the quenched materials, as described by *Piwinskii* [1968*a*, 1973] and *Boettcher and Wyllie* [1968*a*]. Phases present at run conditions included crystals, silicate liquid containing dissolved H_2O, and a dense aqueous fluid phase containing dissolved solid components. Original crystals were preserved during the quench; liquids quenched to glasses; and the vapor phase quenched to water and a variety of precipitated solids.

Minerals encountered include quartz, coesite, plagioclase, jadeite, kyanite, garnet, and orthoclase-hydrate. Plagioclase and orthoclase-hydrate were positively identified only with X ray powder diffraction patterns. Euhedral prisms of quartz and coesite were easily identified. Jadeite occurred as small distinctive acicular prisms, while kyanite formed larger needles and clear euhedral prisms, often curved, with low birefringence and near-parallel extinction. Positive identification of kyanite was achieved with the electron microprobe. Small grains of garnet were easily identified optically.

All runs in the vapor-present region contained deposits from vapor such as quench mica and brown aggregates, which were described by *Boettcher and Wyllie* [1968*a*]. Glasses in the H_2O-saturated region were filled with cavities, as were some glasses in the vapor-absent region, indicating that exsolution of vapor from liquids occurred during the quench. Many runs in the vapor-absent region contained glasses with no cavities. The glasses from any one run usually appeared to be homogeneous.

TABLE 2. Definitive Experimental Runs for Granite #104 With Excess Water

Run	Pressure, kbar	Temperature, °C	Water Added, wt %	Time, hours	Phases Present
93	10	700	50	75	Qz, L, V
50	10	725	50	20	L, V
56	15	720	50	23	Qz, L, V
70	15	730	50	18	Qz, L, V
48	15	740	50	24	L, V
102	15	745	25	13	L, V
46	15	800	50	10	L, V
60R	15	900	50	6	Qz, L, V
		675	—	16	
44R	22.5	900	50	8	—
		750	—	15	Qz, Ky, L, V
53T	25	595	50	7	
		750	—	16	Qz, Ky, L, V
57T	25	595	50	7	—
		775	—	16	Qz, Ky, L, V
51T	25	595	50	6	—
		800	—	14	Ky, L, V
49T	25	595	50	6	—
		850	—	16	Ky, L, V
90T	25	595	50	6	—
		925	—	12	Ky, L, V
89T	25	595	50	6	—
		950	—	12	L, V
64	25	595	25	6	Qz, Jd, Ky, V
88T	25	595	25	6	—
		645	—	16	Qz, Jd, Ky, V
62T	25	595	25	8	—
		680	—	12	Qz, Jd, Ky, L, V
79T	25	595	25	6	—
		700	—	16	Qz, Ky, L, V
99T	25	595	25	6	—
		800	—	16	Qz, Ky, L, V
106T	25	595	25	6	—
		825	—	15	L, V
97T	25	595	25	6	—
		875	—	13	L, V
96T	25	595	25	6	—
		900	—	12	L, V
95T	25	595	25	5	—
		950	—	8	L, V
222T	30	590	33	6	—
		725	—	14	Ct, Jd, Ky, L, V
218	30	800	33	14	Ct, Ky, L, V
233	30	590	30	6	Ct, Jd, Ky, V
267T	30	590	30	6	—
		675	—	14	Ct, Jd, Ky, V
81T	30	590	26	6	—
		700	—	16	Ct, Jd, Ky, L, V
221T	30	590	26	6	—
		725	—	14	Ct, Jd, Ky, L, V
185T	30	590	26	6	—
		750	—	16	Ct, Ky, L, V
219T	30	590	26	6	—
		775	—	16	Ct, Ky, L, V
290T	30	590	25	6	—
		625	—	12	Ct, Jd, Ky, V
278T	30	590	25	6	—
		650	—	12	Ct, Jd, Ky, V
216	30	800	25	12	Ct, Ky, L, V
215	30	820	25	12	Ct, Ky, L, V
85T	35	585	50	6	—
		780	—	14	Ct, Ky, L, V
71T	35	585	50	6	—
		800	—	16	Ct, Ky, L, V
73T	35	585	50	6	—
		825	—	17	Ky, L, V
61T	35	585	50	10	—
		850	—	12	Ky, L, V
91T	35	585	50	6	—
		950	—	11	L, V
126T	35	585	30	6	—
		785	—	16	Ct, Jd, Ky, L, V

TABLE 2. (continued)

Run	Pressure, kbar	Temperature, °C	Water Added, wt %	Time, hours	Phases Present
123T	35	585	30	6	—
		805	—	16	Ct, Ky, L, V
118T	35	585	28	6	—
		825	—	16	Ct, Ky, L, V
119T	35	585	28	6	—
		850	—	16	L, V

All runs conducted in Pt capsules. Abbreviations: Qz, quartz; Ct, coesite; Jd, jadeite; Ky, kyanite; L, liquid; V, vapor. Runs occupying double rows were completed in two stages: T—after holding the sample at subsolidus conditions indicated in the first row, it was transferred to conditions indicated in the second row. R—after holding the sample above the liquidus at conditions indicated in the first row, it was transferred to conditions indicated in the second row.

EXPERIMENTAL RESULTS

Phase Relationships With Excess H_2O

Figure 1 shows the P-T projection for the melting interval of the granite with excess water; definitive runs from this study are listed in Table 2. The melting relations with excess water at 1, 2, 3, 5, and 10 kbar were determined by *Piwinskii* [1968*a*, 1973]. The near-solidus relations at 10, 15, and 20 kbar, determined and discussed in detail by *Boettcher and Wyllie* [1968*a*], were incorporated. Dashed lines are drawn where interpretation is uncertain.

The subsolidus mineral assemblage at crustal pressure corresponds to that of the natural rock, two feldspars, quartz, and a trace of biotite. At high pressures, for temperatures just below the solidus and with between 25 and 50 wt % H_2O, the subsolidus mineral assemblage is jadeite + coesite + kyanite. The change is caused by the breakdown of plagioclase to yield jadeite + quartz at about 17 kbar [*Boettcher and Wyllie*, 1968*b*]; by the transition of quartz to coesite at about 27 kbar [*Kitahara and Kennedy*, 1964]; by the disappearance of orthoclase and biotite at about 18 and 8 kbar, respectively, which is due to their solution in the large percentage of vapor [*Boettcher and Wyllie*, 1968*a*; *Piwinskii*, 1973; see discussion below for relationships with less H_2O]; and by the appearance of kyanite. No kyanite was found in a reexamination of the run products at 20 kbar of *Boettcher and Wyllie* [1968*a*]. The formation of kyanite might be expected to result in part from the breakdown of biotite and the anorthite component of the plagioclase, but the kyanite boundary is separated from those for biotite and plagioclase, and the presence of kyanite is probably due more to the preferential solubility of alkalis in the vapor as compared to alumina and possibly silica (see discussion below for H_2O-undersaturated conditions).

The solidus is identical (within the limits of experimental error) with that determined for a muscovite-granite by *Huang and Wyllie* [1973] and the melting curve for the eutectic and liquidus minimum in the system Ab-Or-Qz-H_2O [*Merrill et al.*, 1970; *Huang and Wyllie*, 1975]. The muscovite-granite solidus at 35 kbar is somewhat higher than the other two. The solidus determinations of *Boettcher and Wyllie* [1968*a*] are consistent with Figure 1 at 25 kbar, but somewhat higher in temperature at 30 kbar. Below 17-kbar pressure, increasing solubility of H_2O in the silicate liquid with increasing pressure lowers the solidus temperature. At about 17 kbar the solidus passes through a minimum and begins to increase in temperature with increasing pressure. This kind of change has been predicted through consideration of progressive change in the values of the partial molar volume of H_2O in vapor and liquid phases [for example, discussion by *Carmichael et al.*, 1974], but in this example it is evidently due to the breakdown of plagioclase and the formation of the dense assemblage jadeite + quartz, as discussed by *Boettcher and Wyllie* [1967].

At 3 kbar, plagioclase is the liquidus mineral [*Piwinskii*, 1968*a*]. Between 5 kbar and 20 kbar, quartz is the liquidus mineral. At higher pressures, quartz (or coesite above 28 kbar) and kyanite occur together on the liquidus for H_2O-saturated liquids, but for higher H_2O contents, kyanite is the liquidus mineral (see Figure 2).

The liquidus boundary with excess H_2O has been reversed with 50°C brackets for quartz at 15 kbar (run 60, Table 2) and for quartz and kyanite at 22.5 kbar (run 44, Table 2). *Huang and Wyllie* [1973] reported pairs of runs reversing the corresponding liquidus boundaries in a muscovite-granite within 25°C brackets for quartz and kyanite at 15 and 25 kbar respectively. Water at pressures greater than 10 kbar has a remarkable kinetic effect on silicate reactions, as demonstrated for granite-H_2O systems at 10 kbar by *Piwinskii and Martin* [1970]. These facts suggest that the phase boundaries above 10 kbar in Figure 1 are not far from their equilibrium positions, but proof of this in multimineral felsic systems is extraordinarily difficult.

At pressures below 5 kbar, the melting interval is narrow, and the granite behaves as a eutectic-like composition. This is consistent with the fact that its composition, projected onto the system Ab-Or-Qz, is not far removed from the quartz-feldspar cotectic boundary for low pressures. The melting interval increases significantly at pressures above 5 kbar; it is 35°C at 2 kbar, 100°C at 10 kbar, and 150°C at 35 kbar. This is caused by the increasing temperature of the quartz-out curve and is consistent with change of the minimum-melting composition in the Synthetic Granite System, Ab-Or-Qz, away from SiO_2 towards $NaAlSi_3O_8$, both with excess H_2O and in the dry system [*Luth et al.*, 1964; *Luth*, 1969; *Huang and Wyllie*, 1975].

Phase Relationships With Variable H_2O Content

Figure 2 shows the phase relations determined at 30 kbar with varying weight percentages of water and interpolated to estimated results for the anhydrous rock composition (Tables 2 and 3). Phase boundaries are labeled through the melting interval. Figures 3*a* and 3*b* show similar, but less detailed, diagrams for results at 25 and 35 kbar, respectively, with dashed-line boundaries estimated according to determinations in Figures 1 and 2 (Tables 2 and 3). The granite itself contains 0.35 wt % H_2O, mostly in biotite, and this rock composition plots at

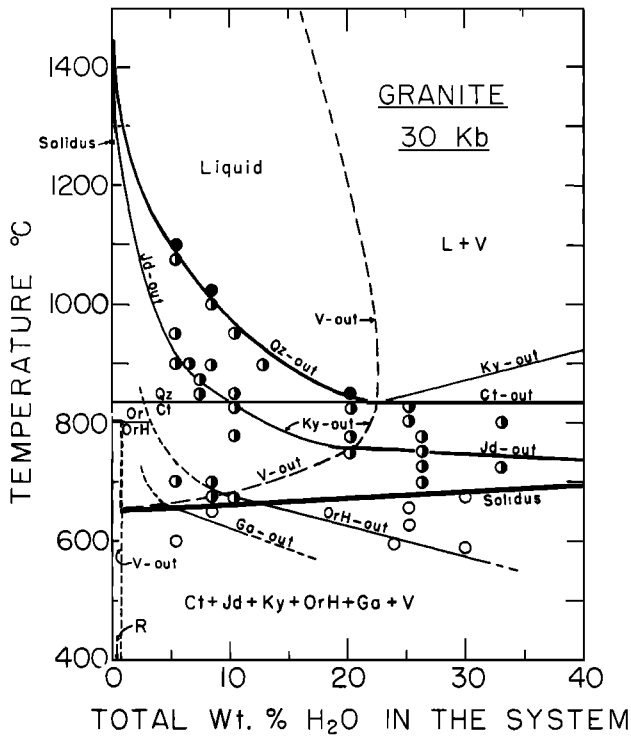

Fig. 2. Phase relationships for granite #104 with varying H_2O contents at 30 kbar. Definitive runs are listed in Tables 2 and 3. R on the horizontal axis represents the composition of the granite (0.35% H_2O contained in biotite). For abbreviations, see Figure 1, and OrH = orthoclase-hydrate, Ga = garnet.

the point marked R. The excess H_2O runs at 25, 30, and 35 kbar shown in Figure 1 are the runs plotted in Figures 2, 3*a*, and 3*b* with between 25 and 40 wt % H_2O (Table 2).

The H_2O-saturation boundary (V-out, Figure 2) separates the phase fields wth vapor present from those with vapor absent. The position of this boundary has not been experimentally determined but its approximate position is known from the analysis of *Robertson and Wyllie* [1971]. In runs from all fields labeled vapor present, there are deposits from the quenched vapor. Similar deposits also occur in some runs from the vapor-absent areas, and we believe that these derive from vapor that exsolved from liquid during the quench, as discussed above in connection with cavities in quenched glass. The process was discussed by *Boettcher and Wyllie* [1968*a*], and interpretation of the observed products in similar systems at lower pressures was reviewed in detail by *Whitney* [1975*a*].

For low H_2O contents (<5%) or low temperatures in the subsolidus region, which minimizes the effects of the solution of solids in the vapor, the high-pressure subsolidus assemblage is jadeite + coesite + kyanite + orthoclase-hydrate + garnet (Figure 2). This assemblage results from the subsolidus reactions discussed for H_2O-excess conditions and, in addition, the transition of orthoclase to orthoclase-hydrate [*Seki and Kennedy*, 1964] and the breakdown of biotite to produce garnet.

At low pressures the vapor phase composition is almost pure H_2O, but with increasing pressure, increasing amounts of rock dissolve in the vapor (see Figure 4). The high solubility of solids in the vapor at 30 kbar is indicated by the subsolidus disappearance of orthoclase-hydrate (Figure 2). Granite 104 contains 29% orthoclase, all of which presumably would form orthoclase-hydrate, given enough H_2O. At a given temperature the amount of orthoclase-hydrate, as determined from the relative strengths of X ray peaks, decreases with increasing amounts of H_2O until it disappears. At 590°C it disappears with 27% H_2O. The phase relationships show that all K_2O has dissolved in vapor at this stage, but we cannot determine the distribution of Al_2O_3 and SiO_2 between vapor and residual minerals. The limited data available indicate that the solution reaction is strongly dependent on temperature (Figure 2).

The subsolidus dissolution of 29% alkali feldspar, congruently or incongruently, indicates that at pressures of 15 kbar and above (Figure 1) the aqueous fluids coexisting with granitic materials are very concentrated solutions [*Boettcher and Wyllie*, 1968*a*; *Stern and Wyllie*, 1973*a*]. The position of the boundary in Figure 3*a* limiting the subsolidus existence of alkali feldspar is assumed to be similar to that for orthoclase-hydrate at 30 kbar (Figure 2). Solution in the vapor phase also limits the subsolidus field of garnet (Figure 2). Preferential solubility of alkalis compared with alumina and possibly silica is shown by the development of an increasing area of kyanite stability with increasing H_2O content in the vapor-present region (Figures 2, 3*a*, and 3*b*). A segment of the kyanite-out curve (Figure 2) is drawn coincident with the saturation boundary. This curve connects the determined kyanite-out curves in the vapor-present region and in the vapor-absent region (which is coincident with the jadeite-out curve within experimental limits of detection).

At low pressures, where the vapor-phase composition is nearly pure H_2O, the phase boundaries for vapor-present conditions are isothermal. At high pressures, where the vapor is a concentrated solution, these phase boundaries are not isothermal, although this may not be detectable within the limits of experimental measurement [*Robertson and Wyllie*, 1971]. Figures 2, 3*a*, and 3*b* show that in the system granite-H_2O at 25 kbar or higher pressure, the vapor-present phase boundaries do depart measurably from isothermal lines. At 30 kbar the solidus rises 25°C between 8% and 25% H_2O; at 30 and 35 kbar the quartz-out and coesite-out curves drop 25°C between 25% and 50% H_2O; and at 35 kbar the jadeite-out curve drops 25°C between 25% and 50% H_2O.

There are three solidus reactions shown in Figure 2, depending on the amount of water present. In an anhydrous rock containing no hydrous minerals, the solidus is high, near 1250°C, as estimated from the results of *Luth* [1969] and *Huang and Wyllie* [1975] in the dry synthetic granite system. *Green and Ringwood* [1968] estimated 1300°C for the anhydrous solidus temperature of a rhyolite with 70% silica at 30 kbar. For low H_2O contents (0.7%) all H_2O may be structurally bound in orthoclase-hydrate, and the beginning of melting would be the temperature on the breakdown of orthoclase-hydrate, near 800°C at 30 kbar [*Huang and Wyllie*, 1974]. For a rock with more than 0.7% H_2O and a free vapor phase, the solidus is between 660° and 690°C, depending on the H_2O content, as discussed bove.

In the vapor-absent region the upper stability temperature of quartz, jadeite, kyanite, orthoclase-hydrate, and garnet increase with decreasing H_2O content. The phase boundary for quartz has been reversed within a 25°C bracket at 30 kbar with 12.5% H_2O (run 200, Table 3). The estimated liquidus temperature for the anhydrous granite is taken from *Green and Ringwood* [1968].

For a rock containing 5% H_2O at 30 kbar, melting begins at 670°C, garnet having already dissolved in the vapor phase just below the solidus. A few degrees above the solidus, the H_2O is completely dissolved in the liquid. With increasing

TABLE 3. Definitive Experimental Runs for Granite #104 With Amounts of Water Less Than Required to Saturate the Liquid

Run	Pressure, kbar	Temperature, °C	Water Added, wt %	Time, hours	Phases Present
109T	25	595	20	6	—
		825	—	15	L
108T	25	595	20	6	—
		850	—	21	L
107T	25	595	20	6	—
		875	—	12	L, (V)
100T	25	595	18	6	—
		800	—	16	Qz, L
113T	25	595	16	6	—
		850	—	18	Qz, L
112T	25	595	16	6	—
		875	—	14	L
111T	25	595	16	6	—
		900	—	14	L
229	25	595	6	6	Qz, Jd, Ky, Or, Ga, V
129	25	1000	6	6	Qz, L
133	25	1040	6	8	L
294	30	590	24	12	Ct, Jd, Ky, OrH, V
220T	30	590	20	6	—
		750	—	14	Ct, Jd, Ky, L
217T	30	590	20	6	—
		775	—	14	Ct, (Ky), L
187	30	825	20	11	Qz, L
186	30	850	20	11	L
200R	30	1050	12.5	6	—
		900	—	14	Qz, L
297T	30	590	10	4	—
		675	—	12	Ct, Jd, Ky, OrH, L, V
191T	30	590	10	6	—
		775	—	12	Ct, Jd, Ky, L, V
193T	30	590	10	6	—
		825	—	12	Ct, Jd, Ky, L
212T	30	590	10	6	—
		850	—	14	Qz, L
192	30	950	10	12	Qz, L
242T	30	590	8	6	—
		650	—	6	Ct, Jd, Ky, OrH, V
297T	30	590	8	4	—
		675	—	12	Ct, Jd, Ky, OrH, L, V
244T	30	590	8	6	—
		700	—	6	Ct, Jd, Ky, L
195T	30	590	8	6	—
		900	—	14	Qz, L
196	30	1000	8	8	Qz, L
198	30	1025	8	8	L
208T	30	590	7	6	—
		850	—	14	Qz, Jd, Ky, L
203T	30	590	7	6	—
		875	—	14	Qz, Jd, Ky, L
209T	30	590	6	6	—
		900	—	14	Qz, L
236	30	590	5	6	Ct, Jd, Ky, OrH, Ga, V
299T	30	590	5	5	—
		700		12	Ct, Jd, Ky, OrH, L
298T	30	590	5	5	—
		900	—	6	Qz, Jd, Ky, L
201	30	950	5	12	Qz, L
214	30	1075	5	8	Qz, L
194	30	1100	5	8	L
103T	35	585	25	6	—
		825	—	14	Ct, Ky, L, V
114T	35	585	25	6	—
		850	—	14	L
98T	35	585	25	6	—
		890	—	14	L, V
66	35	585	22.5	6	Ct, Jd, Ky, V
86T	35	585	22.5	6	—
		690	—	14	Ct, Jd, Ky, V
83T	35	585	22.5	6	—
		720	—	14	Ct, Jd, Ky, L, V

Table 3. (continued)

Run	Pressure, kbar	Temperature, °C	Water Added, wt %	Time, hours	Phases present
75T	35	585	22.5	6	—
		745	—	14	Ct, Jd, Ky, L, V
74T	35	585	22.5	6	—
		765	—	14	Ct, Jd, Ky, L, V
115T	35	585	22.5	6	—
		785	—	14	Ct, Jd, Ky, L, V
124	35	900	22.5	8	L
125	35	900	20	8	Ct, L
120	35	975	14	11	Ct, L
121	35	1025	12.5	8	L

All runs conducted in Pt capsules. Abbreviations and symbols as in Table 2 and Ga, garnet; Or, orthoclase; OrH, orthoclase-hydrate; ( ) indicates trace amounts.

temperature, first, orthoclase-hydrate, then jadeite and kyanite, and finally quartz, at 1090°C, dissolve in the liquid. Equilibrium crystallization of a granite liquid containing 5% dissolved H_2O proceeds in exactly the reverse sequence, with a free vapor phase separating from the liquid only at a very late stage of crystallization.

The liquidus boundary changes slope at its point of intersection with the vapor-saturation boundary, and this point gives the solubility of H_2O in the liquid [*Robertson and Wyllie*, 1971]. We have determined the position of the change in slope of the liquidus in Figures 2, 3*a*, and 3*b* as a measure of H_2O solubility. Figure 4 shows the solubility of H_2O in a granite liquid with increasing pressure, as determined from these diagrams and previously published results up to 8 kbar [*Clark*, 1966], as well as previously published results for the solubility of H_2O in basaltic and andesitic liquids and in the eutectic composition in the Residua System up to 8 kbar. The solubility of albite in aqueous vapor up to 10 kbar is also given. The high-pressure results are consistent with the approximate values and limits determined for albite composition by *Boettcher and Wyllie* [1969]. The brackets are wide, but they demonstrate that solubility of H_2O in granite liquids is limited with increasing pressure. Complete miscibility between liquid and vapor has been reported in the system SiO_2-H_2O at pressures above the second critical endpoint near 10 kbar [*Kennedy et al.*, 1962], but the results in Figures 2, 3*a*, 3*b*, and 4 show that a miscibility gap persists between H_2O-saturated granite liquid and aqueous vapor at least to 35 kbar. The solubility relationships in silicate magma-H_2O systems thus appear to correspond more closely to the type predicted by *Smith* [1963, Figure 12-35] than to the type with critical endpoints, at least to mantle depths of 120 km, as discussed by *Boettcher and Wyllie* [1968*a*].

The H_2O-Undersaturated Liquidus Surface

Figure 5 shows the H_2O-undersaturated liquidus surface for the granite, extending from the dry liquidus (estimated from *Green and Ringwood* [1968]) to the H_2O-saturated liquidus (from Figure 1). The H_2O content of the saturated liquid increases from 0% at 1 bar to 27% at 30 kbar, as shown in Figure 4.

The surface is contoured by lines of constant H_2O content drawn from the known points on the excess-H_2O boundary (Figure 4) through corresponding points on the liquidus boundaries determined from the rock-water isobars at 15, 25 (Figure 3*a*), 30 (Figure 2), and 35 kbar (Figure 3*b*). The values at 15 kbar are consistent with results of *Huang and Wyllie* [1973] for a muscovite granite. The map of the surface in P-T-X_{H_2O} space shows the fields for the liquidus and near-liquidus minerals based on the results shown in Figures 1, 2, 3*a*, and 3*b*, and it takes into account the results of H_2O-deficient experiments on similar compositions below 10 kbar [*Eggler and Burnham*, 1973; *Whitney*, 1975*a*]. Kyanite, a minor accessory mineral in Figures 1, 3, 3*a*, and 3*b* has been omitted from Figure 5 because kyanite does not appear on the liquidus for H_2O-undersaturated conditions (Figures 2, 3*a*, and 3*b*). Although the positions of the boundaries and the shape of the liquidus surface in Figure 5 may change with changes in some chemical parameters, the relative positions of the phase boundaries are correct for most rocks called granites and rhyolites. As far as the major minerals are concerned, the liquidus for all H_2O contents is dominated at high pressure by quartz or coesite and at pressures below 10 kbar corresponding to crustal depths, by quartz and plagioclase.

DISCUSSION

The phase relationships for a single rock summarized here provide constraints about its origin, but they do not provide an adequate basis for detailed discussion of the petrogenesis of I-type granitoids. It is necessary to consider, in addition, the phase relationships of the other rocks constituting a batholithic series as well as the field relationships and the geochemistry of trace elements and isotopes.

The phase relationships can be used to determine the conditions under which granite #104 could be a primary magma form various source rocks. The near-liquidus minerals for a primary magma must correspond to major minerals in the source rock at the depth and temperature of origin. The liquidus mineralogy of the granite is dominated by quartz or coesite at pressures above about 10 kbar (Figure 5), and no other mineral crystallizes through a considerable temperature interval below the liquidus (Figures 1, 2, and 3). The only candidates for source rocks above 10 kbar are mantle peridotite, subducted oceanic crust, and deep continental crust. Neither of the first two potential source rocks could yield granite liquid and residual quartz or coesite, and there are few deep crustal rocks likely to leave residual quartz. At pressures below 10 kbar, quartz on the liquidus is joined or replaced by plagioclase (Figures 5 and 1), and this is consistent with derivation of the granite liquid by partial fusion of continental rocks of varied composition.

The eutecticlike character of granite #104 with excess H_2O exists only up to pressures of about 5 kbar (Figure 1). At higher pressures the melting interval increases, indicating that

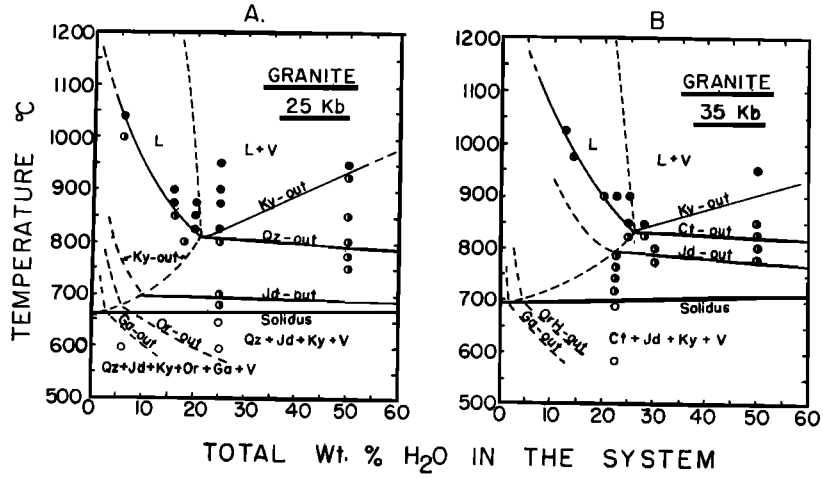

Fig. 3. Phase relationships for granite #104 at 25 and 35 kbar, with varying H_2O contents. Definitive runs are listed in Tables 2 and 3. Symbols and abbreviations as in Figures 1 and 2.

the compositions of liquids produced by partial melting of rocks of granitic composition depart progressively from the low-pressure eutectic composition. This has been demonstrated in synthetic systems [*Luth et al.*, 1964; *Luth*, 1969; *Huang and Wyllie*, 1975]. Therefore, we would not expect liquids of granite composition to be derived by partial melting of quartzo-feldspathic rocks at very high pressures.

The eutecticlike character of granite exists only for the conditions of excess H_2O. If there is less H_2O present than that required to saturate the liquid, there is a wide temperature interval for crystals plus liquid between liquidus and solidus. Figures 2 and 3 illustrate the phase relationships for high pressures, and the same general picture exists at lower crustal pressures [*Robertson and Wyllie*, 1971; *Whitney*, 1975*a*]. This is illustrated in Figure 6 for another biotite granite studied by *Maaløe and Wyllie* [1975] at 2 kbar. The melting interval with excess H_2O at 2 kbar is higher than that for granite #104 (Figure 1) because the ratio of plagioclase/quartz is higher. The interval between solidus and liquidus for H_2O content of 1% is about 400°C, and H_2O-undersaturated liquid coexists with quartz, plagioclase, and alkali feldspar through 200°C. Considering source rocks with realistically low proportions of aqueous pore fluid, it is evident that this fluid dissolves within a few degrees of the solidus. Note in Figure 6 that without aqueous pore fluid, the solidus temperature of the biotite granite is considerably higher. Melting begins where biotite reacts to release H_2O for the liquid phase. The normal product of partial fusion of a wide range of crustal rocks is H_2O-undersaturated granite liquid [*Piwinskii and Wyllie*, 1970; *Brown and Fyfe*,, 1970; *Robertson and Wyllie*, 1971; *Wyllie*, 1977*a*].

According to Figure 5, granite #104 at 40-km depth would be completely liquid at 1000°C with 2% H_2O, and at 860°C with 5% H_2O. Therefore, primary garnite melts with moderate H_2O contents could be generated in the crust at temperatures attained during regional metamorphism [*Turner*, 1968]. These magmas could reach near-surface levels before vesiculating where their paths crossed the excess-H_2O boundary (Figure 5).

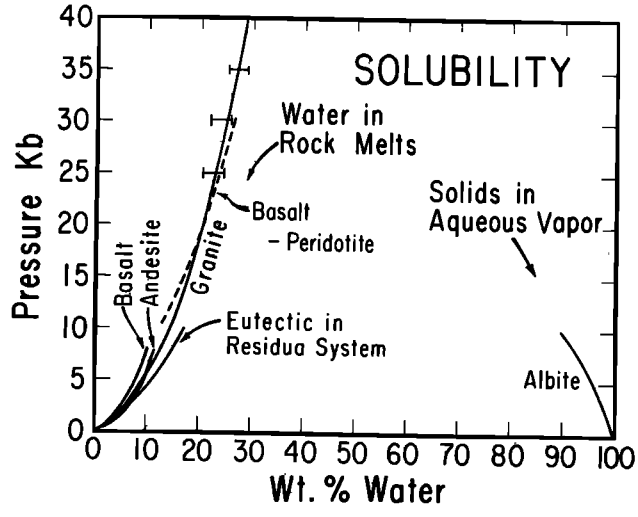

Fig. 4. The solubilities of H_2O in silicate liquids and of dissolved solid components in aqueous vapor, as a function of pressure. Brackets for the solubility in granite at 25, 30, and 35 kbar are from the experimental data in Figures 2, 3*a*, and 3*b*. The curve for basalt-peridotite is from *Green* [1973]. The data below 10 kbar are from the compilation by *Clark* [1966].

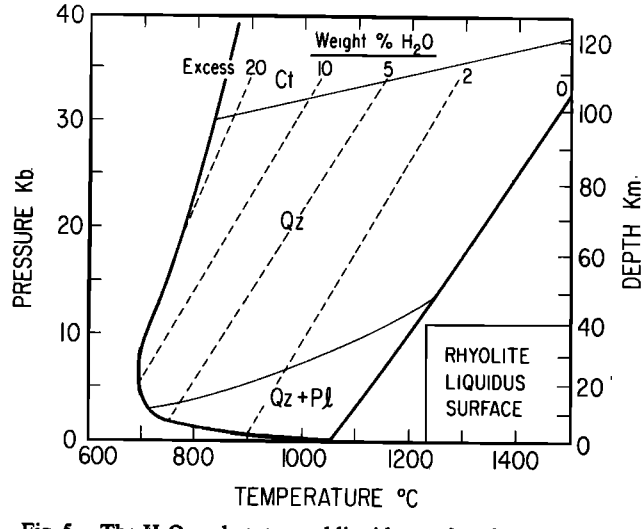

Fig. 5. The H_2O-undersaturated liquidus surface for granite #104 (rhyolite liquidus surface) connecting the H_2O-saturated liquidus (from Figure 1) with the dry liquidus. The surface is contoured by lines of constant H_2O content and mapped with areas of liquidus and near-liquidus minerals.

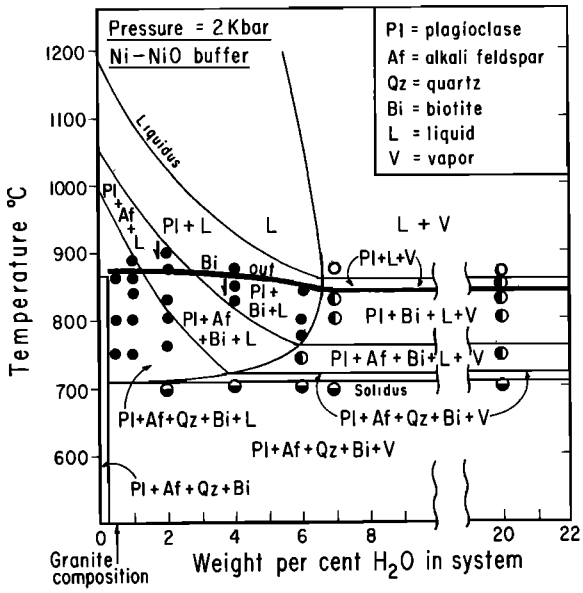

Fig. 6. Phase relationships for a biotite granite with varying H_2O contents at 2 kbar, with oxygen fugacity buffered [*Maaløe and Wyllie,* 1975]. Note the boundary between the phase fields with vapor and those without vapor (run circles filled). The heavy line is the upper stability limit of biotite, which intersects the phase boundaries for quartz and the feldspars in the vapor-absent region.

Maaløe and Wyllie [1975] concluded on the basis of granite petrography and experiments that most large bodies of granitic magma initially contained relatively low H_2O contents, probably less than 1.5%, and that most batholiths remained H_2O-undersaturated through most of their histories. H_2O-saturation and evolution of vapor occurs either as a result of uprise to lower pressures (Figure 5; *Whitney* [1975*b*]) or through crystallization (Figure 6; *Jahns and Burnham* [1969]). *Robertson and Wyllie* [1971] pointed out that although most granitic magmas evolve aqueous vapors only in the late stages of crystallization, insoluble volatile components, such as CO_2, may be concentrated in a vapor phase at an earlier stage together with a small proportion of H_2O. The consequences of this behavior were explored by *Holloway* [1976].

It has been established in experimental studies on granitoid rock sequences tonalite-granodiorite-granite-H_2O that the rocks consist of two groups of minerals with different characteristics. The minerals of the residua system, quartz, orthoclase, and the sodic portion of plagioclase feldspar melt together to produce a euteticlike granite liquid that coexists with the more refractory assemblage of calcic plagioclase, biotite, and amphibole, with little exchange of components among coexisting phases through a wide temperature interval [*Piwinskii,* 1968*a*, 1973; *Piwinskii and Wyllie,* 1968, 1970; *Gibbon and Wyllie,* 1969]. A wide range of granitoid magmas can be developed by combinations of granite liquid and suspended minerals of the more refractory group. The mafic inclusions in many batholiths are composed of the refractory mineral group with compostions consistent with the hypothesis that the magmas represent mixtures of granite liquid and residual minerals from the source rocks [e.g., *Piwinskii,* 1968*b*]. The designation of granite #104 as a eutecticlike granite liquid of I-type is based on the association of granite #104 with I-type granodiorities and tonalites [*Piwinskii,* 1968*a*, 1973].

For more detailed reviews of these and other experimental results relevant to the I-type granitoid series, including the phase relationships of amphibole in the rocks and some discussion of the involvement of material from mantle and subducted oceanic crust, see *Piwinskii and Wyllie* [1968], *Stern et al.* [1975], *Wyllie et al.* [1976], *Wyllie* [1977*a*, *b*], and *Stern and Wyllie* [1978].

Johannes [1980] presented detailed studies on melting reactions in the synthetic granite system with excess H_2O at 5 kbar and raised an important question. To what extent is it valid to apply metastable experimental results to natural processes? He reviewed some of the previous attempts to test for equilibrium in experiments on similar systems. He concluded that overinterpretation of granitic systems should be carefully avoided and that controversies about the formation of granites and migmatites are due to contradictory experimental data and inconsistent interpretations of the data. Johannes' results indicate that solidus curves determined for crystalline materials with excess H_2O are close to equilibrium but that other melting curves may be considerably below stable temperatures. He demonstrated that plagioclase of intermediate composition melts almost stoichiometrically, producing too much liquid enriched in (Ca + Al)/(Na + Si) compared with the equilibrium amount and composition. Under these conditions the whole system is metastable, and the positions of phase boundaries for other minerals must also be metastable. He estimated that it would take 10^{14} years to reach compositional equilibrium at 665°C. Therefore, he concluded, the separation of melts with metastable compositions may occur during anatexis, just as the occurrence of zoned plagioclase illustrates disequilibrium between plagioclase and melt during crystallization.

We agree that the attainment and demonstration of reversible equilibrium within narrow temperature intervals in many parts of multimineral granitic systems is impossible [*Stern and Wyllie,* 1975; *Wyllie,* 1977*b*]. From our experience with granitic systems at crustal pressures we would consider any applications claiming to use precise temperatures or compositions of feldspars and liquid to be suspect because of the clear evidence that equilibrium values cannot be attained experimentally [*McDowell and Wyllie,* 1971; *Johannes,* 1980].

Reaction rates improve with increasing temperature, with increasing pressure in the presence of H_2O, and in PT regions where feldspars are unstable. Note the two-stage runs required at pressures above 15 kbar to remove feldspar from the starting material in order to avoid metastable melting (Table 2). Even at high pressures, the demonstration of reversible brackets narrower than 50°C is difficult [*Stern and Wyllie,* 1975]. In general it appears that the phase relationships best approaching equilibrium conditions are at the solidus and near the liquidus. At crustal pressures, particularly within the vapor-absent region, details of the phase relationships within the crystallization interval are unreliable. Conditions are greatly improved at pressures above about 15 kbar, but there are many examples of metastability at temperatures below 800°–900°C.

We endorse *Johannes'* [1980] conclusion and hope that we do not overinterpret our data. Metastable conditions are most prevalent in the H_2O-undersaturated region illustrated in Figure 6, the region most applicable to natural granites. Because the phase compostions in experiments are certainly not equilibrium values, the positions of the phase boundaries are not precisely located. Only the biotite-out boundary could be reversed [*Maaløe and Wyllie,* 1975], but because the liquid composition was metastable, even the biotite phase boundary

could represent metastable equilibrium. However, from the available experimental data and interpolation between dry and excess-H_2O conditions [*Robertson and Wyllie,* 1971], it is evident that the general pattern illustrated in Figure 6 is valid. To that extent it is appropriate to draw petrogenetic conclusions about processes and changes in sequence of crystallization as a function of changes in H_2O content. Overviews of the phase relationships for series of related granitic rocks [e.g., *Piwinskii,* 1968*a*, 1973; *Piwinskii and Wyllie,* 1968, 1970; *Gibbon and Wyllie,* 1969] illustrate sufficient consistency, within a given series and from one series to another, that we feel confident in the broad pattern of phase relationships that emerges, which we have applied in the cited papers and outlined above.

Acknowledgments. This research was supported by the Earth Sciences Section of the National Science Foundation, NSF Grant EAR 76-20413. For review of earlier versions of parts of the manuscript we thank A. T. Anderson, A. J. Irving,and R. C. Newton.

REFERENCES

Bateman, P. C., L. C. Clark, H. R. Huber, J. G. Moore, and C. D. Rhinehart, The Sierra Nevada batholith—A synthesis of recent work across the central part, *U. S. Geol. Surv. Prof. Pap. 414D,* p. 46, 1963.

Boettcher, A. L., and P. J. Wyllie, Hydrothermal melting curves in silicate-water systems at pressures above 10 kilobars, *Nature, 216,* 572–573, 1967.

Boettcher, A. L., and P. J. Wyllie, Melting of granite with excess water to 30 kilobars pressure, *J. Geol., 76,* 235–244, 1968*a*.

Boettcher, A. L., and P. J. Wyllie, Jadeite stability measured in the presence of silicate liquids in the system $NaAlSiO_4$-SiO_2-H_2O, *Geochim. Cosmochim. Acta, 32,* 999–1012, 1968*b*.

Boettcher, A. L., and P. J. Wyllie, Phase relationships in the system $NaAlSiO_4$-SiO_2-H_2O to 35 kilobars pressure, *Am. J. Sci., 267,* 875–909, 1969.

Boyd, F. R., and J. L. England, Apparatus for phase-equilibrium measurements at pressures up to 50 kilobars and temperatures up to 1750°C, *J. Geophys. Res., 65,* 741–748, 1960.

Boyd, F. R., P. M. Bell, J. L. England, and M. C. Gilbert, Pressure measurement in single-stage apparatus, *Year Book Carnegie Inst. Washington, 65,* 410–414, 1967.

Brown, G. C., and W. S. Fyfe, The production of granite melts during ultrametamorphism, *Contrib. Mineral. Petrol., 28,* 235–244, 1970.

Carmichael, I. S. E., F. J. Turner, and J. Verhoogen, *Igneous Petrology,* McGraw-Hill, New York, 1974.

Chappell, B. W., and A. J. R. White, Two contrasting granite types, *Pacific Geol., 8,* 173–174, 1974.

Clark, S. P., Handbook of physical constants, *Geol. Soc. Am. Mem., 97,* 587, 1966.

Eggler, D. H., and W. C. Burnham, Crystallization and fractionation trends in the system andesite-H_2O-CO_2-O_2 at pressures to 10 kb, *Geol. Soc. Am. Bull., 84,* 2517–2532, 1973.

Getting, I. C., and G. C. Kennedy, The effect of pressure on the E. M. F. of thermocouples, in *Accurate Characterization of the High-Pressure Environment,* pp. 77–80, edited by E. C. Lloyd, *Spec. Pub. 326,* U. S. Nat. Bur. Stand., Washington, D. C. 1971.

Gibbon, D. L., and P. J. Wyllie, Experimental studies of igneous rock series: The Farrington Complex, North Carolina, and the Star Mountain Rhyolite, Texas, *J. Geol., 77,* 221–239, 1969.

Green, D. H., Contrasted melting relations in a pyrolite upper mantle under midoceanic ridge, stable crust, and island arc environments, *Tectonophysics, 17,* 285–297, 1973.

Green, T. H., and A. E. Ringwood, Genesis of the calc-alkaline igneous rock suite, *Contr. Mineral. Petrol., 18,* 105–162, 1968.

Holloway, J. R., Fluids in the evolution of granitic magmas: Consequences of finite CO_2 solubility, *Geol. Soc. Am., Bull. 87,* 1513–1518, 1976.

Huang, W. L., and P. J. Wyllie, Melting relations of muscovite-granite to 35 kbar as a model for fusion of metamorphosed subducted oceanic sediments, *Contrib. Mineral. Petrol., 42,* 1–14, 1973.

Huang, W. L., and P. J. Wyllie, Melting relations of muscovite with quartz and sanidine in the system K_2O-Al_2O_3-SiO_2-H_2O to 30 kilobars and an outline of paragonite melting relations, *Am. J. Sci., 274,* 378–395, 1974.

Huang, W. L., and P. J. Wyllie, Melting reactions in the system $NaAlSi_3O_8$-$KAlSi_3O_8$-SiO_2 to 35 kilobars, dry and with excess water, *J. Geol., 83,* 737–748, 1975.

Huang, W. L., and P. J. Wyllie, Phase relationships of S-type granite with H_2O to 35 kilobars: The Harney Peak muscovite-granite from South Dakota, *J. Geophys. Res.,* this issue, 1981.

Jahns, R. H., and W. C. Burnham, Experimental studies of pegmatite genesis, 1, A model for the derivation and crystallization of granitic pegmatites, *Econ. Geol., 64,* 843–864, 1969.

Johannes, W., Metastable melting in the granite system Qz-Or-Ab-An-H_2O, *Contrib. Mineral. Petrol., 72,* 73–80, 1980.

Kennedy, G. C., G. J. Wasserburg, H. C. Heard, and R. C. Newton, The upper three-phase region in the system SiO_2-H_2O, *Am. J. Sci., 260,* 501–521, 1962.

Kistler, R. W., P. C. Bateman, and W. W. Brannock, Isotopic ages of minerals from granitic rocks of the Central Sierra Nevada and Inyo Mountains, California, *Geol. Soc. Am. Bull., 76,* 155–164, 1965.

Kitahara, S., and G. C. Kennedy, The quartz-coesite transition, *J. Geophys. Res., 69,* 5395–5400, 1964.

Lambert, I. B., and P. J. Wyllie, Melting of tonalite and crystallization of andesite liquid with excess water to 30 kilobars, *J. Geol., 82,* 88–97, 1974.

Luth, W. C., The system $NaAlSi_3O_8$-SiO_2 and $KAlSi_3O_8$-SiO_2 to 20 kb and the relation between H_2O content, P_{H_2O}, and P_{total} in granitic magma, *Am. J. Sci., Schairer Vol. 267-A,* 325–341, 1969.

Luth, W. C., R. H. Jahns, and O. F. Tuttle, The granite system at pressures of 4 to 10 kilobars, *J. Geophys. Res., 69,* 759–773, 1964.

Maaløe, S., and P. J Wyllie, Water content of granite magma deduced from the sequence of crystallization determined experimentally with water undersaturated conditions, *Contrib. Mineral. Petrol., 52,* 175–191, 1975.

McDowell, S. D., and P. J. Wyllie, Experimental studies of igneous rock series: The Kungnat syenite cmplex of southwest Greenland, *J. Geol., 79,* 173–194, 1971.

Merrill, R. B., and P. J. Wyllie, Kaersutite and kaersutite-eclogite from Kakanui, New Zealand-Water-excess and water-deficient melting at 30 kilobars, *Geol. Soc. Am. Bull., 86,* 555–570, 1975.

Merrill, R. B., J. K. Robertson, and P. J. Wyllie, Melting relations in the system $NaAlSi_3O_8$-$KAlSi_3O_8$-SiO_2-H_2O to 20 kilobars compared with results for other feldspar-quartz-H_2O and rock-H_2O systems, *J. Geol., 78,* 558–569, 1970.

Piwinskii, A. J., Experimental studies of igneous rock series: Central Sierra Nevada Batholith, California, *J. Geol., 76,* 548–570, 1968*a*.

Piwinskii, A. J., Studies of batholithic feldspar, Sierra Nevada, California, *Contrib. Mineral. Petrol., 17,* 204–223, 1968*b*.

Piwinskii, A. J., Experimental studies of igneous rock series, Central Sierra Nevada batholith, California: Part II, *Neues Jahrb. Mineral. Monatsh., 5,* 193–215, 1973.

Piwinskii, A. J., and R. F. Martin, On experimental study of equilibrium with granitic rocks at 10 kb, *Contrib. Mineral. Petrol., 29,* 1–10, 1970.

Piwinskii, A. J., and P. J. Wyllie, Experimental studies of igneous rock series: A zoned pluton in the Wallowa Batholith, Oregon, *J. Geol., 76,* 205–234, 1968.

Piwinskii, A. J., and P. J. Wyllie, Experimental studies of igneous rock series: Felsic body suite from the Needle Point pluton, Wallowa Batholith, Oregon, *J. Geol., 78,* 52–76, 1970.

Robertson, J. K., and P. J. Wyllie, Experimental studies on rocks from the Deboullie Stock, northern Maine, including melting relations in the water-deficient environment, *J. Geol., 79,* 549–571, 1971.

Seki, Y., and G. C. Kennedy, The breakdown of potassium fledspar, $KAlSi_3O_8$, at high temperatures and pressures, *Am. Mineral., 49,* 1688–1706, 1964.

Smith, F. G., *Physical Geochemistry,* p. 691, Addison-Wesley, Reading, Mass., 1963.

Stern, C. R., and P. J. Wyllie, Water-saturated and undersaturated melting relations of a granite to 35 kilobars, *Earth Planet. Sci. Lett., 18,* 163–167, 1973*a*.

Stern, C. R., and P. J. Wyllie, Melting relations of basalt-andesite-rhyolite-H_2O and a pelagic red clay at 30 kbar, *Contrib. Mineral. Petrol., 42,* 313–323, 1973*b*.

Stern, C. R., and P. J. Wyllie, Effect of iron abosrption by noble-

metal capsules on phase boundaries in rock-melting experiments at 30 kilobars, *Am. Mineral., 42,* 681–689, 1975.

Stern, C. R., and P. J. Wyllie, Phase compositions through crystallization intervals in basalt-andesite-H_2O at 30 kbar with implications for subduction zone magmas, *Am. Mineral., 63,* 641–663, 1978.

Stern, C. R., W. L. Huang, and P. J Wyllie, Basalt-andesite-rhyolite-H_2O: Crystallization intervals with excess H_2O and H_2O-undersaturated liquidus surfaces to 35 kilobars, with implications for magma genesis, *Earth Planet. Sci. Lett., 28,* 189–196, 1975.

Turner, F. J., *Metamorphic Petrology,* 403 p., McGraw Hill, New York, 1968.

White, A. J. R., and B. W. Chappell, Ultrametamorphism and granitoid genesis, *Tectonophysics, 43,* 7–22, 1977.

Whitney, J. A., The effects of pressure temperature and X_{H_2O} on phase assemblages in four synthetic rock compositions, *J. Geol., 83,* 1–31, 1975*a*.

Whitney, J. A., Vapor generation in a quartz monzonite magma: A synthetic model with application to prophyry copper depostis, *Econ. Geol., 70,* 346–358, 1975*b*.

Wyllie, P. J., Crustal anatexis: An experimental review, *Tectonophysics, 43,* 41–71, 1977*a*.

Wyllie, P. J., From crucible through subduction to batholiths, in *Energetics of Geological Processes,* edited by S. K. Saxena and S. Battacharji, pp. 389–433, Springer-Verlag, New York, 1977*b*.

Wyllie, P. J., W. L. Huang, C. R. Stern, and S. Maaløe, Granitic magmas: Possible and impossible sources, water contents, and crystallization sequences, *Can. J. Earth Sci., 13,* 1007–1019, 1976.

(Received October 20, 1980;
revised March 2, 1981;
accepted March 5, 1981.)

JOURNAL OF GEOPHYSICAL RESEARCH, VOL. 86, NO. B11, PAGES 10423–10430, NOVEMBER 10, 1981

The Redskin Granite: Evidence for Thermogravitational Diffusion in a Precambrian Granite Batholith

STEVE LUDINGTON

U. S. Geological Survey, Reston, Virginia 22092

The 1000-Ma-old composite Pikes Peak batholith consists largely of medium- to coarse-grained biotite granite but is intruded by several smaller granite plutons. Two of these, the Tarryall Mountains batholith and the Redskin Granite (Hawley, 1969; Hawley and Wobus, 1977), are here interpreted as cupolas atop the main mass of the Pikes Peak batholith.

Chemical analysis for 38 elements in rocks from the Redskin Granite, the Tarryall Mountains batholith, and the biotite granite of the Pikes Peak batholith support the contention that the compositions of the smaller plutons are unlikely to have evolved from that of the main mass of the batholith by crystal fractionation. It is believed that these compositions arose through liquid-state fractionation processes, possibly the convection-aided thermogravitational model of Shaw et al. (1976).

It is important to recognize that the chemical signature of this fractionation process can be discerned in holocrystalline rocks as well as in their glassy equivalents because the process may be instrumental in the formation of some kinds of lithophile ore deposits.

INTRODUCTION

Recent papers by *Shaw et al.* [1976], *Hildreth* [1976, 1979], *Smith* [1979], *Smith and MacDonald* [1979], and others have created considerable interest in alternatives to the crystal fractionation process to explain the origin of chemically zoned magma chambers. Although it is not perfectly understood, the process termed thermogravitational diffusion (TGD) by *Shaw et al.* [1976] seems to be a viable alternative. The TGD model emphasizes the combined effects of convective circulation and Soret diffusion which develop chemical gradients within the thermal and gravitational fields existing in magma chambers. Those desiring an explicit description of the TGD theory are referred to *Hildreth* [1979, and this volume].

This paper grew out of an earlier study of the mineralogical residence of selected trace elements in the Redskin Granite, a late differentiate of the 1000-Ma-old composite Pikes Peak batholith [*Desborough et al.* 1980]. Recognition of the significance of major- and trace-element compositional variation among the various satellitic plutons of the Pikes Peak batholith led to these further geochemical studies. This study would have been impossible without the previous geologic and geochemical work of *Hawley* [1969], *Barker et al.* [1975], *Barker et al.* [1976], and *Hawley and Wobus* [1977]. A comprehensive geochemical study of the Pikes Peak batholith remains to be done. Much of it has not been mapped in detail, and more ancillary plutons, such as the Redskin Granite probably remain to be discovered. The purpose here is to point out the possibility for discerning evidence for liquid-state differentiation in crystalline plutonic rocks.

GEOLOGIC SETTING

The bulk of the Pikes Peak batholith (Figure 1) is composed of medium-coarse-grained biotite and biotite-hornblende granite; petrographic descriptions are found in *Barker et al.* [1975] and *Hawley and Wobus* [1977]. This granite commonly contains subequal amounts of quartz and plagioclase and somewhat larger amounts of potassium-rich alkali feldspar. Other rock types in the Pikes Peak batholith are not considered here.

The Tarryall Mountains batholith (Figure 1) is thought to be slightly younger than most of the Pikes Peak batholith on the basis of poorly exposed field relations and chemical composition [*Hawley and Wobus*, 1977]. The batholith is texturally zoned and consists of three main granite units: homogeneous coarse porphyritic granite (innermost), coarse subequigranular granite (medial), and a heterogeneous unit termed medium- to coarse-gained granite (outermost) [*Hawley and Wobus*, 1977, Figure 18]. The mineralogy of all three

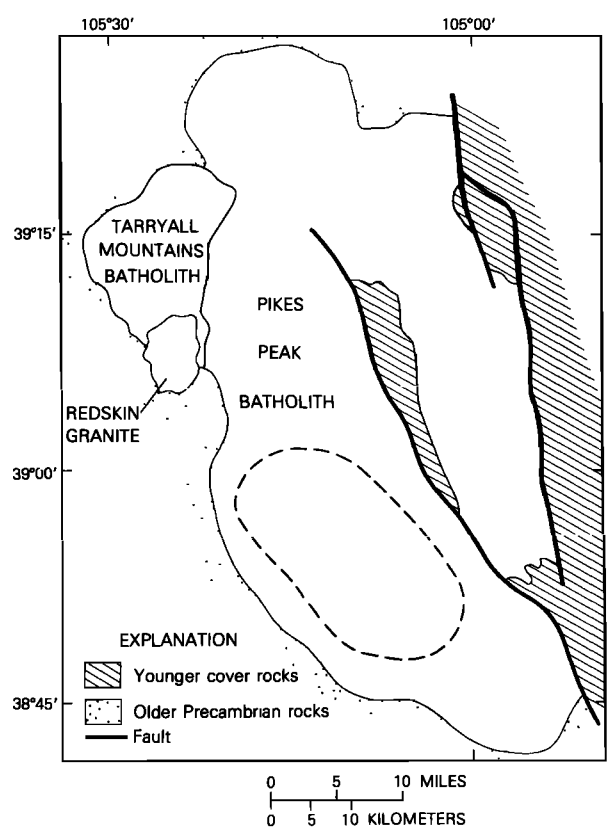

Fig. 1. Index map of the Pikes Peak batholith, showing areal relations of the three plutons of this report. The dashed line shows the size and shape of the Long Valley caldera (source of the Bishop Tuff).

This paper not subject to U. S. copyright. Published in 1981 by the American Geophysical Union

Paper number 1B0493.

TABLE 1. Average Major Element Content of RSG, TMB, and PPG

	RSG	TMB	PPG
SiO_2	74.5	74.2	72.6
Al_2O_3	13.2	12.9	13.4
TiO_2	0.10	0.19	0.28
FeO*	1.5	2.0	2.5
MgO	0.05	0.07	0.14
CaO	0.71	0.91	1.18
Na_2O	4.00	3.34	3.31
K_2O	4.88	5.42	5.60
P_2O_5	0.01	0.02	0.05
MnO	0.04	0.05	0.07
Cl	0.01	0.03	0.05
F	0.46	0.46	0.35
$H_2O(+)$	0.27	0.33	0.35

FeO* is total iron, reported as FeO. These numbers are averages, arrived at in the following manner: (1) RSG composition is the average of 13 analyses from *Hawley and Wobus* [1977]. (2) TMB composition is the average of 10 analyses from *Hawley and Wobus* [1977]. (3) PPG composition is the average of 19 analyses from *Barker et al.* [1975].

units is similar to the biotite granite described above, with the exception of the presence of traces of muscovite and generally greater amounts of fluorite.

The Redskin Granite (Figure 1) lies to the south of and intrudes the Tarryall Mountains batholith. It is also a texturally zoned pluton, consisting of three main granite units: fine-grained equigranular granite (innermost), fine-grained porphyritic granite (medial), and coarse-grained granular granite (outermost) [*Hawley and Wobus,* 1977, Figure 24]. Fluorine-rich, strongly phengitic muscovite and fluorite are abundant, along with biotite. Accessory minerals include zircon, fluocerite, ilmenorutile, columbite, magnetite, and hematite. Thorite, monazite, xenotime, cassiterite, and topaz are rare [*Desborough et al.,* 1980].

A fine-grained granite-aplite unit cuts earlier facies of the Redskin and is associated with beryllium- and tin-bearing greisens. Trace-element concentrations for one sample of the granite-aplite (SL007) are reported in the Appendix, but from its chemical composition the sample appears to be hydrothermally altered, so the results are not considered in any interpretations.

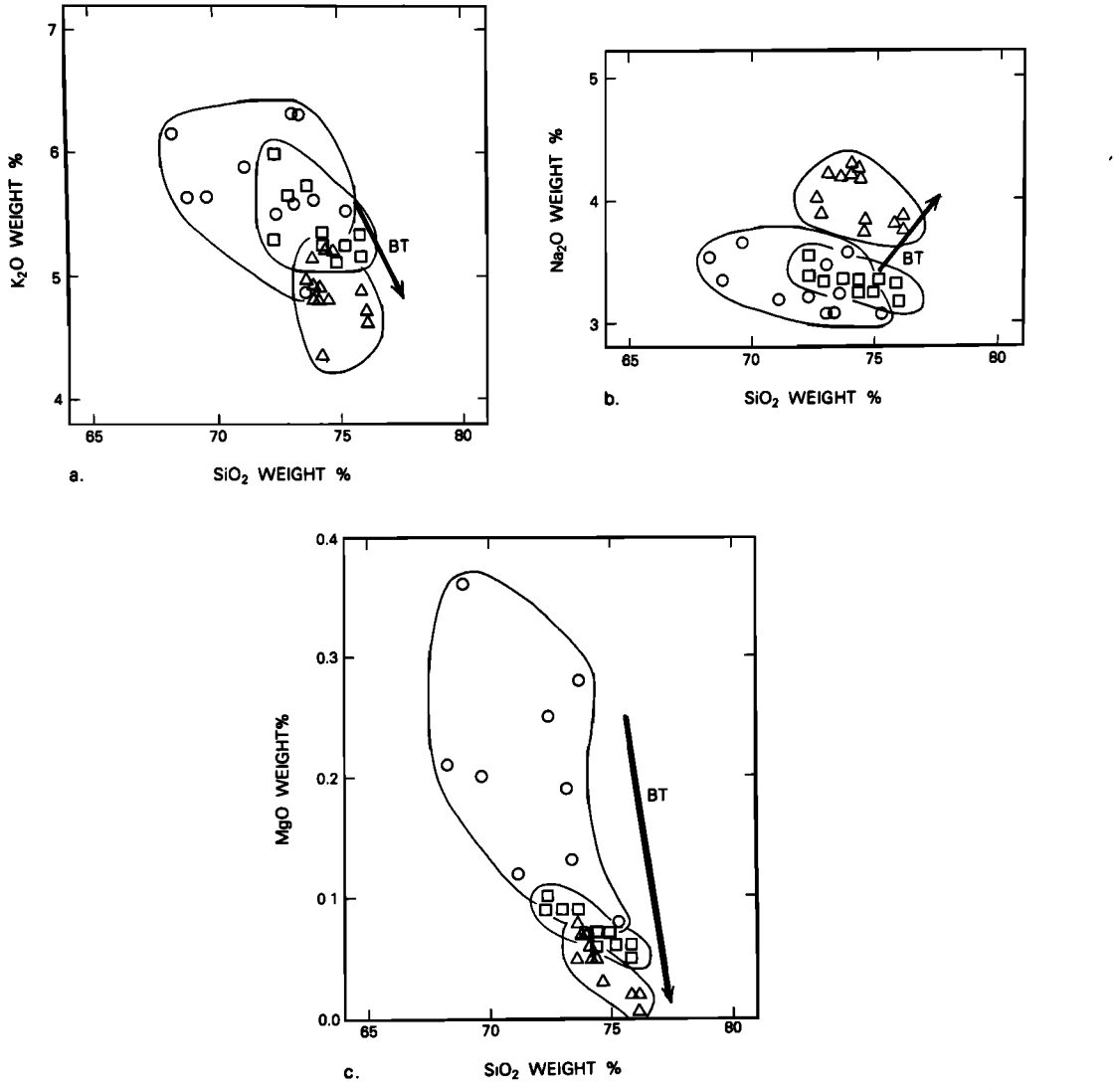

Fig. 2. Plot of (*a*) K_2O, (*b*) Na_2O, and (*c*) MgO against SiO_2 for PPG (circles), TMB (squares), a RSG (triangles). Arrow labeled BT represents range of compositions of Bishop Tuff, with the point of the arrow representing the most-evolved portion.

TABLE 2. Average Trace Element Content of RSG, TMB, and PPG

	RSG	TMB	PPG
Sc	3.7	—	2.9
Mn	180	—	560
Co	0.47	—	1.3
Zn	70	60	80
Rb	460	330	240
Sr	25	60	130
Y	95	80	75
Zr	210	250	330
Nb	95	70	40
Sn	25	9	6
Cs	3.8	—	2.7
Ba	260	630	1160
La	70	—	110
Ce	160	—	240
Nd	63	—	110
Sm	12	—	22
Eu	0.75	—	2.5
Tb	2.2	—	2.5
Dy	16	—	14
Yb	14	—	9
Lu	2.5	—	1.5
Hf	9.2	—	13
Ta	13	—	4.5
Pb	<20	40	40
Th	53	—	25
U	7.3	—	5.2

— indicates no data

In the interest of brevity, the biotite granite of the Pikes Peak batholith, granites of the Tarryall Mountains batholith, and the Redskin Granite will be abbreviated as PPG, TMB, and RSG, respectively. These abbreviations refer to the rocks specified, not to the batholiths and plutons. The Pikes Peak batholith, especially, contains many other diverse, though volumetrically minor, rock types [see *Barker et al.*, 1975], and indeed, the TMB and RSG are part of the 'greater' Pikes Peak batholith.

The data in this paper are interpreted in terms of a model that views the Redskin Granite and the Tarryall Mountains batholith as cupolas atop the main mass of the Pikes Peak batholith. There may well have been more cupolas, including some atop the center of the batholith, but if they existed, erosion has removed them, or else mapping has not revealed them. By analogy with a subcaldera magma chamber, these plutons are believed to have evolved chemically because of the thermal and gravitational fields imposed on them after intrusion but while they were still largely in the liquid state. The plutons are thought to merge imperceptibly at depth into the PPG, which represents a large, unevolved parent magma. Structural and age considerations are permissive to this model, and as shown later, development of RSG and TMB by fractional crystallization from the PPG seems unlikely.

Analytic Data

For this study, 28 granite samples (11 PPG, 10 TMB, 7 RSG) were analyzed by energy-dispersive X ray fluorescence for Zn, Rb, Sr, Y, Zr, Nb, and Pb (^{109}Cd excitation source) and Sn, Ba, La, and Ce (^{241}Am excitation source). Natural and synthetic standards were used, and the analytical precision is approximately ±5% of the amount present. In addition, seven samples of RSG were analyzed by INAA for REE and other trace elements by D. M. McKown of the U. S. Geological Survey. All new analytic results are tabulated in the appendix.

Localities and major element analyses of PPG samples may be found in *Barker et al.* [1975], and of TMB analyses in *Hawley and Wobus* [1977]. Localities for the RSG samples are shown in *Desborough et al.* [1980], while major element analyses of other samples of the Redskin are given in *Hawley and Wobus* [1977]. Previous trace-element analyses of PPG are referenced in *Barker et al.* [1976].

Chemical Variations

Utilizing the model that considers the Redskin Granite and the Tarryall Mountains batholith to be cupolas atop the main mass of the Pikes Peak batholith, major- and trace-element variations among the plutons show a remarkable parallelism to those exhibited within the magma chamber of the Pleistocene Bishop Tuff of California [*Hildreth*, 1976, 1979].

Table 1 summarizes the differences in major-element composition among the three plutons considered, while Figure 2 portrays some trends on silica variation diagrams. Both the tabular data and the illustrations suggest that RSG is more

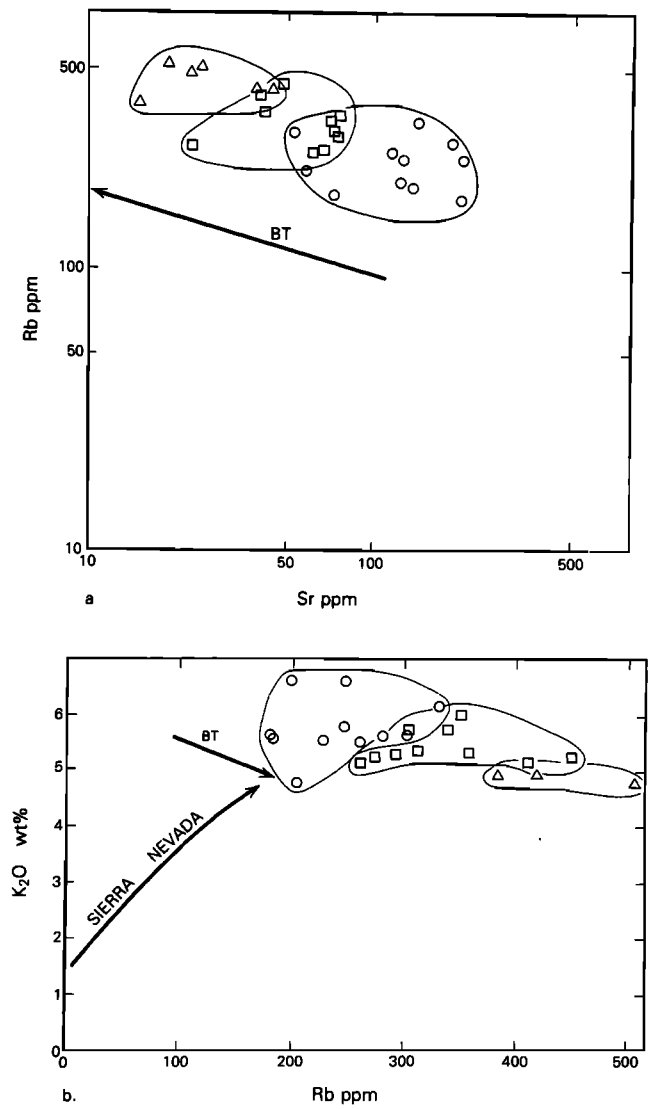

Fig. 3. Plot of (*a*) Rb against Sr and (*b*) K_2O against Rb for PPG (circles), TMB (squares), and RSG (triangles). Arrow labeled BT represents range of compositions of Bishop Tuff, with the point of the arrow representing the most-evolved portion. Arrow labeled Sierra Nevada was constructed using the data of *Kistler and Peterman* [1973].

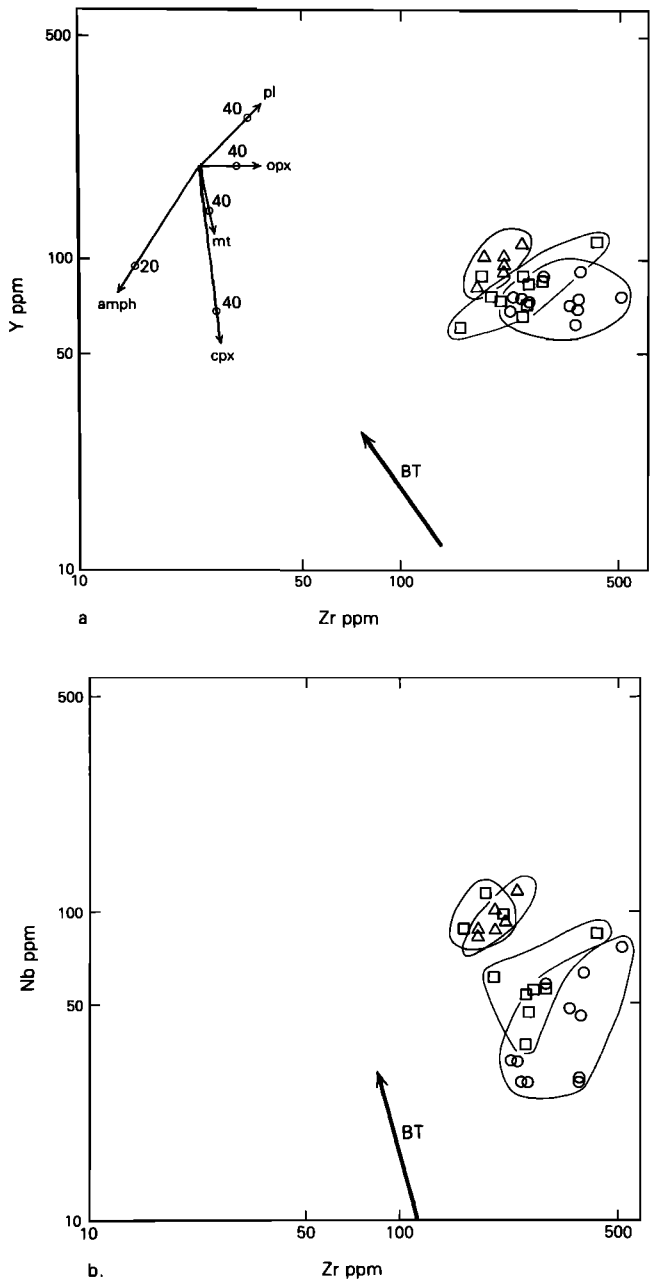

Fig. 4. Plot of (*a*) Y against Zr and (*b*) Nb against Zr in PPG (circles), TMB (squares), and RSG (triangles). In (*a*), arrows indicate change in composition of melts as a result of fractional crystallization of: pl, plagioclase; opx, orthopyroxene; cpx, clinopyroxene; mt, magnetite; amph, amphibole. Circles on arrows describe the amount of change caused by the removal of the labeled percentages of phenocrysts. In both diagrams, arrow labeled BT represents range of composition of Bishop Tuff, with the point of the arrow representing the most-evolved portion. Fractionation vectors for Zr-Y taken from *Walsh et al.* [1979].

highly evolved in relation to PPG than is TMB, but both RSG and TMB seem to be related to PPG in the same way. Of particular interest is the concomitant increase in Na and decrease in K with increasing evolution, a diagnostic feature of diffused systems (those affected by TGD). Another striking feature, particularly apparent with regard to Na, is that the variation between plutons appears to be distinctly different from the variation within plutons. Figure 2*b* shows that, within each of the three plutons, increasing silica content is accompanied by a decrease in Na_2O, while the average compositions of the two evolved plutons both exhibit higher Na_2O than PPG, mimicking the trend shown for the Bishop Tuff. This feature is also seen on trace element diagrams. This suggests that crystal fractionation may have been operating at particular levels of the magma chambers, but it may also represent scatter caused by insufficient sample size.

Table 2 summarizes differences in trace-element concentrations for the plutons studied. The data are of somewhat uneven quality, particularly the INAA data, which, though done in the same laboratory, represent three separate analytical runs as much as 5 years apart. Thus an element-by-element discussion comparing these data to Hildreth's for the Bishop Tuff seems inappropriate. Only a few interelement variation diagrams are presented.

There are some subtle chemical differences between the textural facies in both the Redskin and Tarryall Mountain plutons, but they are small, and difficult to attribute to any particular process. The inner zone of the Tarryall Mountains batholith, for example, has the highest SiO_2 and the lowest MgO, while the inner zone of the Redskin Granite has the lowest SiO_2 and the highest MgO. In the absence of consistency of sample collection, treatment, and analytical techniques, it is probably not wise to attempt to interpret these small differences.

Figure 3*a* shows that Rb/Sr ratios for RSG are approximately 20 times those in PPG and that the magnitude of this increase is very close to that exhibited by the Bishop Tuff. As noted by *Hildreth* [1979], this degree of Rb concentration would require removal of large amounts of feldspar, were it to have occurred by crystal fractionation. Figure 3*b* illustrates a distinctive characteristic of diffused systems (those affected by TGD)—the concomitant increase in Rb with decrease in K, a

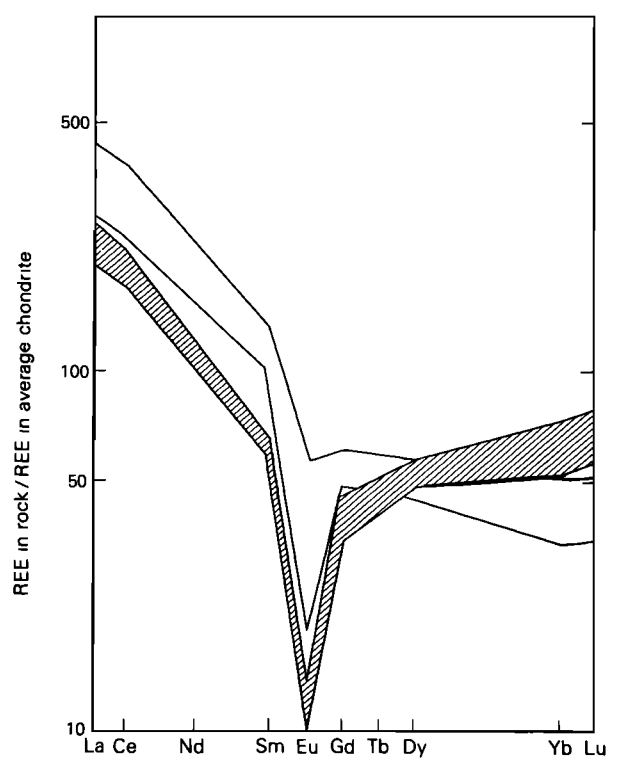

Fig. 5. Chondrite-normalized REE patterns for PPG (hachured) and RSG (stippled).

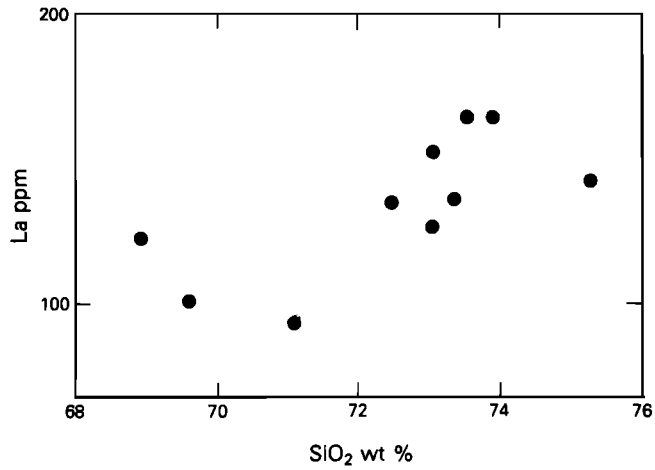

Fig. 6. Plot of La against SiO_2 for PPG.

trend generally opposite to that exhibited by magma systems controlled by crystal fractionation. It is possible, however, that removal of significant amounts of K-rich alkali feldspar has contributed to the increase in Rb/Sr and Na/K.

Figure 4*a*, which compares Zr to Y, illustrates progressive enrichment in Y with depletion of Zr among the three granites studied. The Rayleigh fractionation vectors plotted show that no combination of phases considered could yield the interpluton trends that exist, even though variations in modal plagioclase could account very nicely for much of the variation shown within each of the three plutons. Figure 4*b*, which relates Nb to Zr, is very similar to the Zr-Y diagram and suggests the same conclusion, i.e., that the RSG and TMB did not evolve through fractional crystallization.

Figure 5 compares REE patterns of RSG with those of PPG. The collateral depletion in light REE, enrichment in heavy REE, and the large increase in negative europium anomaly are features shown by other diffused magma systems [*Smith and MacDonald,* 1979] and are extremely difficult to explain via crystal fractionation. Figure 6, which shows the variation of La with silica for PPG, illustrates again that variation within plutons is diametrically opposed to that between plutons. La increases with silica in PPG, yet RSG, with approximately 76% silica, contains only 75–100 ppm La. This suggests that the Redskin REE patterns did not arise by settling into PPG of a phase rich in heavy REE.

Figure 7 is a summary plot comparing all the available chemical data for RSG and PPG with comparable data for the Bishop Tuff. Remarkably few discrepancies exist with respect to direction of concentration or depletion of the 38 elements for which good data are available. In addition to the elements on Figure 7, data in *Hawley et al.* [1966] show that Li and Be, both upward-migrating elements in the Bishop Tuff, are enriched in RSG relative to TMB, lending additional support to the TGD hypothesis.

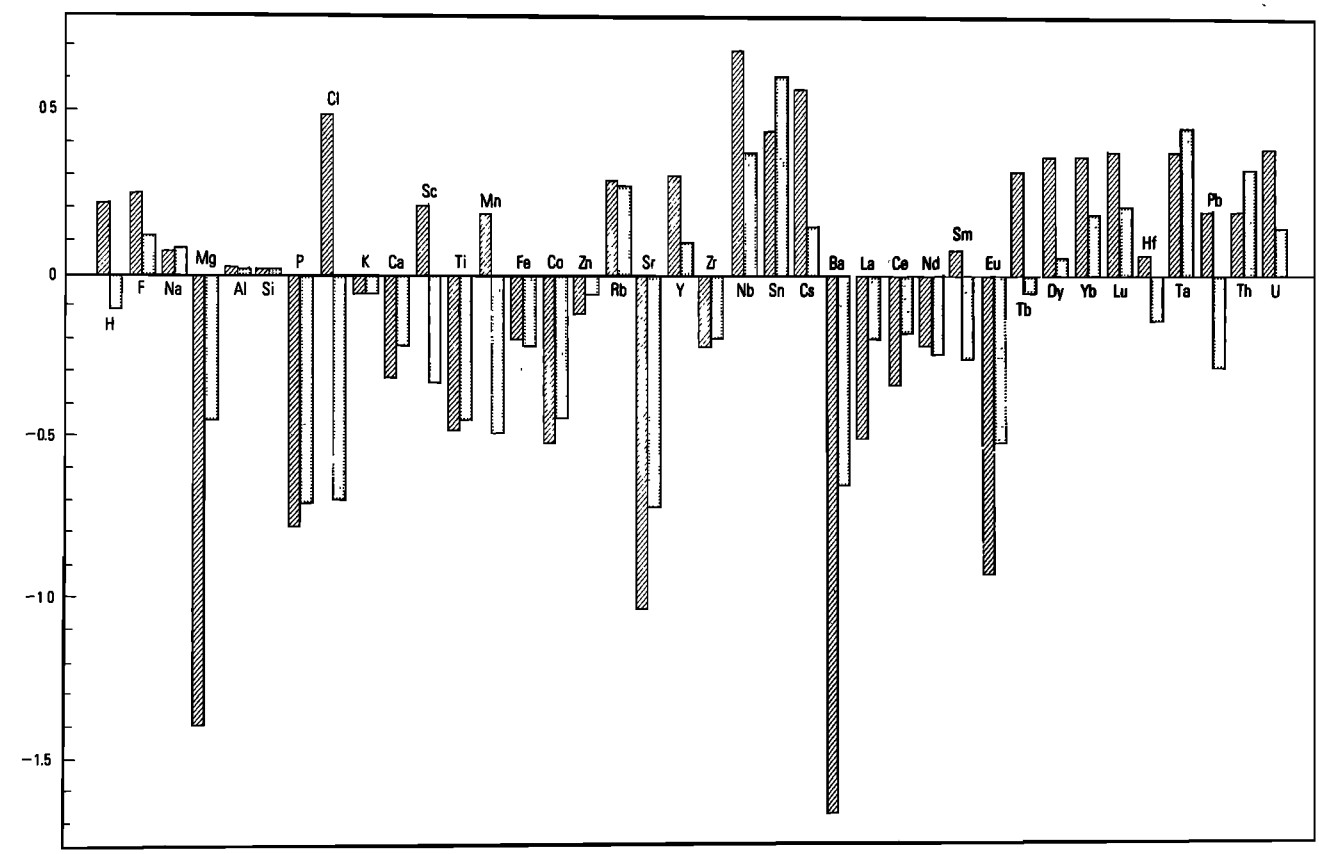

Fig. 7. Enrichment factors for 38 elements for the PPG-RSG system (stippled bars) compared to those for the erupted portion of the Bishop Tuff magma chamber (clear bars) by *Hildreth* [1979]. Arranged by atomic number, the factors are simply the logarithm of the ratio of the concentrations from the most highly evolved portion of the system (RSG and roof zone of Bishop Tuff magma chamber) to those of the deeper, less-evolved portion (PPG and lower part of the Bishop Tuff magma chamber). Bars are shown only for those elements for which reliable data exist for both systems.

Chlorine and hydrogen show opposite trends in the two systems. This is very likely due to loss of these elements from RSG to a fluid phase. The crossover point for the intermediate REE is different, but the overall pattern, as shown in Figure 5, is closely similar. Scandium, manganese, hafnium, and lead were apparently concentrated in the roof of the Bishop Tuff magma chamber but appear to be depleted in RSG. No convincing explanation for these aberrations is apparent, but it may well be that substantial amounts of many of the upward-concentrating elements have been removed from RSG in an exsolved aqueous phase. Perhaps Mn, Sc, and Pb are simply three elements for which this postdiffusion scavenging has proceeded so far as to cause actual concentration ratio reversal. For Hf, the raw data for the Bishop Tuff are scattered; both systems exhibit an approximately 30% reduction in the Zr/Hf ratio. Also, the migration direction of elements undergoing TGD may vary with the bulk chemistry of the system. For example, in the Mt. Rosa Granite Pikes (Peak batholith, S. Ludington, unpublished data, 1979), the McDermitt caldera [*Rytuba and Conrad,* 1979] and the Sierra la Primavera [*Mahood,* 1979], peralkaline-diffused rocks are characterized by Zr enrichment, not depletion. Presumably, as more systems are studied, more departures in detail from the Bishop Tuff pattern will be discovered.

Perhaps it should be less surprising to see a few differences than to see so much similarity. The Redskin Granite is host, at its present level of erosion, to numerous greisen pipes carrying subeconomic quantities of Be and Sn, but also large amounts of Si, K, Rb, and F. If substantial amounts of these elements have been removed from even lower in the magma chamber to create these mineral deposits, one can only speculate on how much the composition of RSG has been moified at its exposed level by loss of elements to a magmatic fluid phase.

IMPLICATIONS

The compositional trends outlined in this paper suggest that the chemical differences between the cupolalike plutons atop the Pikes Peak batholith and the bulk of the batholith did not form by crystal fractionation, though crystal fraction may well have operated within individual plutons. The trends do not prove that TGD was operating, because, lacking experimental and theoretical evidence, it is not certain that TGD as formulated is a viable physicochemical process for magmas. However, it seems probable that the process operating in Colorado in the Precambrian was the same or very similar to that responsible for vertical zonation of elements in the magma chamber of the Bishop Tuff and other recently documented examples of zoned magmas [*Mahood,* 1979; *Rytuba and Conrad,* 1979; *Crecraft et al.,* 1979; *Bacon et al.,* 1979]. With this qualification in mind, I would like to comment on a few implications of the probable operation of TGD in these large Precambrian magma chambers.

These magmas must have had a low (<50%?) crystal content at the time of emplacement. Otherwise, the viscosity of the bulk magma would have been too high for TGD to operate, no matter what the viscosity of the melt phase. It is tempting to imagine, for example, that the fine-grained, innermost facies of the Redskin Granite was nearly totally molten at the time of intrusion. This suggests high, but unknown, temperatures. Without knowledge of depths of intrusion and of the original volatile element content of the magma, precise speculation is unwarranted. It is interesting to note that mineral chemistry [*Desborough et al.,* 1980] suggests relatively low intrusion temperatures or else prolonged cooling and subsolidus reequilibration for the Redskin. The only was to resolve these observations would be a lowered liquidus and/or large crystallization interval for highly evolved, volatile-rich granites like the Redskin.

The cooling of the Redskin Granite would seem to have occurred fast enough to preserve the TGD signature throughout the pluton at the present level of exposure. This conclusion is forced by the observation that, at the level now exposed, striking textural zonation is preserved in the absence of striking chemical zonation. The significance of this observation awaits more precise estimation of the time scale on which TGD may operate, estimated by *Smith* [1979] to be measured in hundreds of thousands of years.

Because the tops of the Redskin Granite and the Tarryall Mountain batholith have been removed by erosion, it seems possible, even likely, that original chemical gradients were even more extreme than those outlined in this paper. This would be remarkable because, for some of the upward-concentrated elements, the rocks discussed in this paper already represent truly exceptional compositions. Few igneous rocks contain more Rb, Cs, Y, Nb, Ta, Sn, and F than the Redskin Granite.

The possibility of the existence of tops of silicic magma chambers greatly enriched in lithophile metals has strong implications for the genesis of, and exploration for, ore deposits of these metals. The list of elements concentrated by TGD is remarkably similar to the list of elements concentrated in granites associated with tin deposits [*Tischendorf,* 1974]. There is growing evidence that stockwork molybdenum deposits are largely the result of magmatic processes and that most of the constituents of the deposits came from a subjacent, evolved granite intrusive [*Gunow et al.,* 1981; *Mutschler et al.,* 1981; *White et al.,* 1981]. The presence of plutons with the TGD chemical signature may serve as a guide to nearby ore deposits.

An important question to be studied with respect to these ore deposits is the way in which elements move from the cooling magma into the surrounding wall rock. Distribution coefficients between melt and aqueous fluid for evolved granite compositions are sorely lacking, and until they are known, it is extremely difficult to evaluate how representative of the magmatic composition a holocrystalline rock is. The tantalizing proposition remains that systems like the Redskin Granite represent the eroded roots of ore-producing igneous systems.

APPENDIX

Table A1 presents new energy-dispersive X ray fluorescence data collected for this study. Samples were excited with a ^{109}Cd source for analysis of Zn, Rb, Sr, Y, Zr, Nb, and Pb, and with ^{241}Am source for analysis of Ba, Sn, La, and Ce. Standards are synthetic for most elements, but natural materials analyzed by isotope dilution were used to calibrate Rb and Sr. Repeated analysis of USGS rock standards [*Flanagan,* 1976] show that accuracy is generally within ± 5%.

Table A2 presents new INAA data collected for this study. These were done by standard methods used by the Branch of Isotope Geology, Denver, Colorado.

TABLE A1. X Ray Fluorescence Analyses of Rocks From the Redskin Granite, the Tarryall Mountains Batholith, and the Biotite Granite of the Pikes Peak Batholith

	Zn	Rb	Sr	Y	Zr	Nb	Pb	Ba	Sn	La	Ce
					RSG						
SL001 (fp)	70	490	20	100	190	80	<20	240	30	80	170
SL002 (fe)	50	420	40	95	220	100	<20	340	15	80	175
SL003 (fe)	80	420	45	90	220	85	<20	400	25	100	190
SL004 (fp)	50	500	25	80	180	85	<20	230	30	75	155
SL005 (cg)	100	380	15	110	250	115	<20	140	15	105	185
SL006 (fp)	60	520	20	100	220	100	<20	200	25	75	155
SL007 (ga)	250	400	5	75	80	65	150	45	15	25	65
					TMB						
FP-5 (mc)	60	270	20	70	260	50	40	240	7	110	240
M1-58 (cs)	60	350	75	85	250	55	40	920	10	170	350
M2-81 (cs)	60	260	65	65	250	35	40	840	7	100	180
M1-50 (cs)	60	300	70	85	270	55	40	850	<6	185	350
TR-74 (cs)	110	290	75	115	430	75	40	760	9	220	400
TR-63 (cs)	70	260	60	85	290	45	—	690	7	145	280
LP-3 (cs)	—	340	70	75	200	60	—	730	<6	85	135
M2-36 (cp)	50	360	40	60	160	90	40	430	<6	85	210
M3-156 (cp)	50	450	50	70	220	100	50	460	20	130	240
M1-36 (cp)	50	410	40	90	190	120	40	390	9	115	270
					PPG						
M4-241	120	280	190	70	350	50	40	1670	<6	100	175
TR-58	60	300	50	85	290	60	50	500	<6	165	290
PP-14a	80	330	140	75	510	65	50	1290	9	165	350
CC-18	100	180	200	70	380	30	40	1740	<6	120	220
CC-1	60	200	120	75	240	35	50	880	<6	110	220
PPG-12	100	180	70	75	380	45	50	760	<6	150	280
PP-8	50	260	110	75	250	30	50	930	6	135	260
PP-4	60	200	140	70	260	30	40	1260	6	135	250
SPD-1	—	230	60	90	390	65	—	500	<6	140	300
PP-11	—	250	130	65	230	35	—	1220	8	125	230
S71-P3	90	250	210	50	380	30	40	2070	14	90	175

All results are in parts per million. Analyzed by Ross A. Yeoman. — denotes no data. Textural facies of RSG and TMB are denoted in parentheses: For RSG, fe, fine-grained equigranular granite (innermost); fp, fine-grained porphyritic granite (medial); cg, coarse-grained granular granite (outermost); and ga, granite-aplite. For TMB, cp, coarse-grained subequigranular granite (medial); and mc, medium- to coarse-grained granite (outermost).

TABLE A2. INAA Analyses of Rocks From the Redskin Granite

	Sc	Mn	Co	Cs	La	Ce	Nd	Sm	Eu	Tb	Dy	Yb	Lu	Hf	Ta	Th	U
SL001 (fp)	3.7	160	0.60	3.6	71	150	63	12	0.75	2.4	17	16	2.8	8.6	15	62	9.7
SL002 (fe)	2.5	90	0.59	2.8	65	150	59	11	0.79	2.2	17	13	2.3	9.2	13	46	8.5
SL003 (fe)	3.8	220	0.67	4.0	78	175	67	11	0.93	2.0	15	13	2.3	8.4	13	54	8.9
SL004 (fp)	3.5	130	0.42	3.7	68	145	59	11	0.74	1.8	15	13	2.3	7.9	16	58	7.4
SL005 (cg)	3.9	240	0.27	3.7	81	165	64	12	0.63	2.5	17	14	2.5	11.2	9	46	4.7
SL006 (fp)	5.0	220	0.26	4.7	64	145	65	12	0.67	2.3	15	14	2.6	9.6	13	49	4.7
SL007 (ga)	3.1	100	0.68	1.7	23	70	41	10	0.12	1.7	11	13	2.5	8.0	6	32	5.7

Textural units noted in parentheses; fe, fine-grained equigranular granite (innermost); fp, fine-grained porphyritic granite (medial); cg, coarse-grained granular granite (outermost); and ga, granite-aplite.

Acknowledgments. I would like particularly to thank George Desborough for his continuing interest in this project, Dave McKown for the new INAA analyses, Bill Sharp for helping me with field relations and identification of rock type of samples previously collected by others, Ross Yeoman for performing most of the energy-dispersive X ray fluorescence analyses and helping write the software by which the raw XRF data were quantified, and finally, Fred Barker for encouraging me to actually write the paper.

REFERENCES

Bacon, C. R., R. McDonald, and J. Meta, Petrogenesis of the Quaternary high-silica rhyolites of the Coso Range geothermal area, California, *Geol. Soc. Am. Abstr. Programs, 11,* (7), 382, 1979.

Barker, F., D. R. Wones, W. N. Sharp, and G. A. Desborough, The Pikes Peak batholith, Colorado Front Range, and a model for the origin of the gabbro-anorthosite-potassic granite suite, *Precambrian Res., 2,* 97–160, 1975.

Barker, F., H. T. Millard, C. E. Hedge, and J. R. O'Neil, Pikes Peak batholith: Geochemistry of some minor elements and isotopes and implications for magma genesis, in Studies in Colorado Field Geology, edited by R. C. Epis and R. J. Weimer, *Prof. Contrib. 8,* pp. 44–56, Colorado School of Mines, Golden, Colo., 1976.

Crecraft, H. R., W. P. Nash, and S. H. Evans, Jr., Chemical evolution and development of compositional gradients in a silicic magma, *Geol. Soc. Am. Abstr. Programs, 11,* (7), 406, 1979.

Desborough, G. A., S. Ludington, and W. N. Sharp, Redskin Granite: A rare-metal-rich Precambrian pluton, *Mineral. Mag., 43,* 959–966, 1980.

Flanagan, F. J., Description and analyses of eight new USGS rock standards, *U. S. Geol. Surv. Prof. Pap. 840,* 192 pp., 1976.

Gunow, A. J., S. Ludington, and J. L. Munoz, Fluorine in micas from

the Henderson molybdenite deposit, Colorado, *Econ. Geol., 75,* 1127–1137, 1981.

Hawley, C. C., Geology and beryllium deposits of the Lake George (or Badger Flats) beryllium area, Park and Jefferson counties, Colorado, *U. S. Geol. Surv. Prof. Pap. 608-A,* 44 pp., 1969.

Hawley, C. C., and R. A. Wobus, General geology and petrology of the Precambrian crystalline rocks, Park and Jefferson counties, Colorado, *U. S. Geol. Surv. Prof. Pap. 608-B,* 77 pp., 1977.

Hawley, C. C., C. Huffman, Jr., J. C. Hamilton, and L. F. Rader, Jr., Geologic and geochemical features of the Redskin Granite and associated rocks, Lake George beryllium area, Colorado, *Geol. Surv. Prof. Pap. 550-C,* C138–C147, 1966.

Hildreth, E. W., The magma chamber of the Bishop Tuff: Gradients in temperature, pressure, and composition, Ph. D. thesis, 328 pp., Univ. of Calif., Berkeley, 1976.

Hildreth, E. W., The Bishop Tuff: Evidence for the origin of zoned magma chambers, *Geol. Soc. Am. Spec. Pap. 180,* 43–72, 1979.

Kistler, R. W., and Z. E. Peterman, Variations in Sr, Rb, K, Na, and initial Sr^{87}/Sr^{86} in Mesozoic granitic rocks and intruded wall rocks in central California, *Geol. Soc. Am. Bull., 84,* (11), 3489–3512, 1973.

Mahood, G., Contrasting trace element behavior in rhyolitic ash flows and lavas, Sierra la Primavera (SLP), Mexico, *Geol. Soc. Am. Abstr. Programs, 11,* (7), 471, 1979.

Mutschler, F. E., E. G. Wright, S. Ludington, and J. T. Abbott, Granite molybdenite systems, *Econ. Geol., 76*(5), 1981.

Rytuba, J. J., and W. K. Conrad, Structural petrologic associations of uranium deposits within the McDermitt caldera complex, Nevada-Oregon, *Geol. Soc. Am. Abstr. Programs, 11,* (7), 508–509, 1979.

Shaw, H. R., R. L. Smith, and W. Hildreth, Thermogravitational mechanisms for chemical variations in zoned magma chambers, *Geol. Soc. Am. Abstr. Programs, 8* (7), 1102, 1976.

Smith, R. L., Ash-flow magmatism, *Geol. Soc. Am. Spec. Pap. 180,* 5–27, 1979.

Smith, R. L., and R. MacDonald, Rhyolitic volcanism and its relationship to granite plutonism, *Geol. Soc. Am. Abstr. Programs, 11* (7), 520, 1979.

Tischendorf, G., Geochemical and petrographic characteristics of silicic magmatic rocks associated with rare-element mineralization, in *Metallization Associated With Acid Magmatism,* edited by M. Stemprok, pp. 41–96, Geological Survey of Czechoslovakia, Prague, 1974.

Walsh, J. N., R. D. Beckinsdale, R. R. Skelhorn, and R. S. Thorpe, Geochemistry and petrogenesis of Tertiary granitic rocks from the Island of Mull, northwest Scotland, *Contrib. Mineral. Petrol., 71,* 99–116, 1979.

White, W. H., et al., Character and origin of the climax-type molybdenum deposits, *Econ. Geol., 75th Anniv. Vol.,* in press, 1981.

(Received November 3, 1980;
revised March 9, 1981;
accepted March 20, 1981.)

JOURNAL OF GEOPHYSICAL RESEARCH, VOL. 86, NO. B11, PAGES 10431-10469, NOVEMBER 10, 1981

Chemistry of Rock-Forming Minerals of the Cretaceous-Paleocene Batholith in Southwestern Japan and Implications for Magma Genesis

GERALD K. CZAMANSKE

U.S. Geological Survey, Menlo Park, California 94025

SHUNSO ISHIHARA

Geological Survey of Japan, 1-1-3 Higashe, Yatabe, Ibaraki, 305 Japan

STEVEN A. ATKIN

U.S. Geological Survey, Menlo Park, California 94025

Petrographic descriptions and electron microprobe analyses of minerals are presented for 35 specimens from seven suites chosen to examine the transition from magnetite series to ilmenite series granitoids along two transects across the Cretaceous-Paleocene Inner Zone batholith of southwestern Japan. Regularities in chemical compositions of amphiboles, biotites, and feldspars suggest that fundamentally similar processes produced the magmas that formed the two series. Constant or decreasing Fe/(Fe+Mg) for biotites and amphiboles with increasing host rock silica content, coupled with the absence of early formed magnetite and sphene, suggest that magnetite series rocks may have become oxidized during crystallization near the level of intrusion, through the processes of second boiling and differential loss of hydrogen. For the Daito-Yokota, magnetite series suite, Fe/(Fe+Mg) for biotites decreased from 0.48 to 0.37 as SiO_2 content of the host rock increased from 55.3 to 75.5 wt %; for an ilmenite series suite from the Takanawa Peninsula, Fe/(Fe+Mg) for biotites increased from 0.51 to 0.77 with an increase in host rock SiO_2 from 53.4 to 75.5. Detailed consideration of amphibole chemistry shows predominance of edenitic and tschermakitic substitution schemes as well as coupling between substitutions of Ti in octahedral sites and Al^{IV}. Interrelations between amphibole and biotite chemistry show that Fe/(Fe+Mg) and Mn contents can be interpreted in terms of equilibration, whereas Ti content cannot. The chemistry of chlorites correlates well with that of biotites; primary and secondary muscovites are distinct in composition. Plagioclase in all studied suites shows igneous zoning appropriate to host rock composition; perthitic alkali feldspars in all samples have lost albite component, and temperatures based on the two-feldspar geothermometer are low. The biotite-apatite geothermometer is also inoperative for this group of samples because fully fluorinated apatites typically occur in biotites of modest F content. Whereas magnetites have reequilibrated, analyses of ilmenites for the representative Daito-Yokota and Takanawa suites corroborate biotite compositional data and suggest that f_{O_2} probably differed by 2 to 3 orders of magnitude during crystallization of silica-rich magnetite and ilmenite series granites. Whole-rock chemistry supports mineral chemistry in suggesting that the studied granitoids have crystallized from magmas generated in a lower crustal environment in which mantle-derived magmas partially melted source materials with igneous characteristics.

INTRODUCTION

The largest batholith in the Japanese islands occurs in the Inner Zone of southwestern Japan. This batholith, here referred to as the Inner Zone batholith, is about the same size as the Sierra Nevada batholith in California. Rb-Sr whole-rock and K-Ar mineral ages indicate that the Inner Zone batholith was formed from Cretaceous to Paleogene time and generally is younger toward the northwest. It is composed mostly of granodiorite and granite, which intrude basement rocks and coeval volcanic strata, and may thus be considered a volcano-plutonic complex.

Regional variations across the batholith have been established by numerous workers, but especially through the concentrated efforts of S. Ishihara. The most distinct regional variations seen in the chemistry of the batholith are in whole-rock Fe_2O_3/FeO and Mo/W of related mineralization [*Ishihara*, 1971*a*, 1973], both of which increase toward the northern, marginal sea side. Variation of Fe_2O_3/FeO correlates with magnetite content [*Tsusue and Ishihara*, 1974; *Ishihara*, 1979]. Granitoids in the south are typically low in Fe-Ti oxide content and contain only ilmenite, whereas, in general, magnetite content tends to increase toward the north. *Ishihara* [1977, 1978, 1979] has discussed the batholith in terms of ilmenite series granitoids in the south and magnetite series granitoids in the north, with a poorly defined zone of weakly magnetic rocks between those two (see Figures 1 and 2). Isotopic studies have shown that, typically, from north-to-south, initial strontium ratios increase [*Shibata and Ishihara*, 1979*a*], $\delta^{34}S$ changes from positive to negative values [*Sasaki and Ishihara*, 1979], and whole-rock $\delta^{18}O$ (at 74 wt % SiO_2) increases from values near +7‰ to +11‰ [*Ishihara and Matsuhisa*, 1977; Y. Matsuhisa and S. Ishihara, unpublished data, 1980).

Chemical compositions of major rock-forming minerals have been studied for individual granitoid plutons [e.g., *Murakami*, 1969; *Kanisawa*, 1972, 1976], and regional zoning patterns in silicate chemistry have been considered by Japanese geologists in recent years [e.g., *Murakami*, 1977, 1979; *Tainosho et al.*, 1979; A. Tsusue, personal communication, 1981]; yet there are no systematic studies of mafic silicate chemistry that attempt to evaluate intensive parameters during crysallization or to interpret mineral chemistry in the light of isotopic studies. Moreover, the weakly magnetic granitoids have been little studied. For this paper, samples of fresh, representative

Copyright © 1981 by the American Geophysical Union.

Paper number 1B0705.
0148-0227/81/001B-0705$01.00

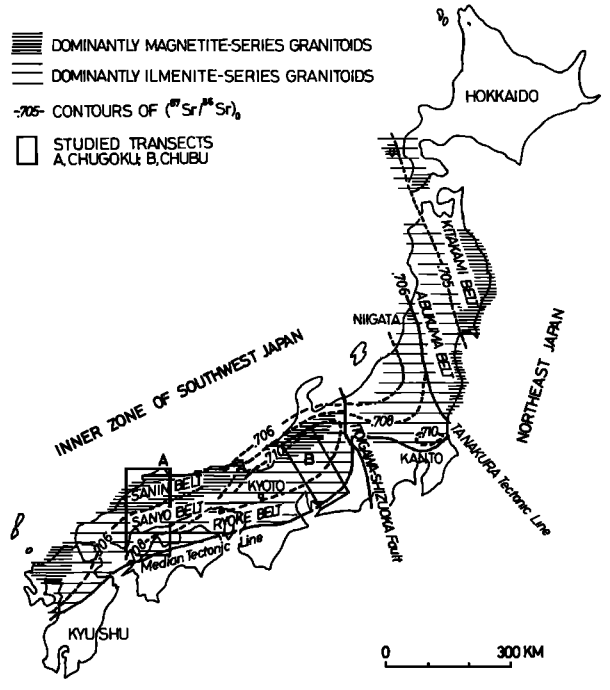

Fig. 1. Index map of the Japanese islands showing locations of the two studied transects. The index map relates the transects to the overall patterns of magnetite and ilmenite series terranes; the Sanin, Sanyo, and Ryoke belts; and $(^{87}Sr/^{86}Sr)_0$ for Cretaceous-Paleocene granitic and gabbroic rocks.

granitoids were selected along two transects where mapping, major and minor rock chemistry, and reconnaissance isotopic studies are complete. The studied transects are named the Chubu (ca. 137°E) and the Central Chugoku (ca. 132°45'E) and are shown in Figure 2. The nature of outcrop is such that rock interrelations are sometimes obscure, and the pattern of intrusive bodies within the Inner Zone batholith is such that simple, demonstrably comagmatic, zoned plutons are rare. Samples were chosen to cover a broad range in SiO_2 content and to be representative of the major plutonic 'suites' constituting the batholith. In some instances, the most mafic rock types within a suite occur as inclusions within more extensive silicic units, and one of our goals for this study has been to see if mineral chemistry can clarify the question of possible genetic relation between host rocks and inclusions. Mafic plutonic rocks are of limited occurrence in the Japanese island arc; quartz diorite, tonalite, granodiorite, and monzogranite predominate.

Chubu Transect

This transect is in the eastern part of the batholith and is identical to that called the Shirakawa-Toki-Okazaki transection by *Ishihara and Terashima* [1977*a*]. Granitoids of this transect can be grouped into three suites from north to south; Shirakawa granitoids, Toki-Naegi plutons, and Ryoke granitoids. The Shirakawa granitoids are high level, have small exposed dimensions, and are fine grained [*Ishihara*, 1971*a*]. Granitoids of the other two suites have larger exposed areas and are composed of medium- and coarse-grained rocks [*Suzuki and Ishihara*, 1969]. Nomenclature adopted for rocks in this paper is that recommended by the IUGS subcommission on the systematics of igneous rocks [*Streckeisen*, 1973].

Shirakawa granitoids of the Sanin belt include amphibole-biotite quartz monzodiorite and granodiorite but consist largely of biotite monzogranite. They intrude Cretaceous rhyodacitic pyroclastic rocks called the Nohi rhyolite and, in part, Hida metamorphic rocks. They are generally magnetite series granitoids, but the Awaradani pluton is weakly magnetic to magnetite free [*Ishihara*, 1979]. Samples RS-87, RS-88, and RS-91 represent the compositional zones characteristic of the largest pluton, Hatogaya. Granodiorites from the typical magnetite series Mihoro pluton (RS-69) and magnetite-free Awaradani pluton (RS-57) were also studied. The Hatogaya pluton has a whole-rock Rb-Sr age of 65.6 Ma and an $(^{87}Sr/^{86}Sr)_0$ of 0.7100 [*Shibata and Ishihara*, 1979*a*, *b*].

The Toki-Naegi granitoids of the Sanyo belt to the south, largely composed of amphibole-biotite granodiorite and biotite or biotite-muscovite monzogranite, discordantly intrude Paleozoic sedimentary rocks and Nohi rhyolite. They belong to the ilmenite series and contain no magnetite. The Toki pluton (T-25 through T-44), which is slightly zoned, has a whole-rock Rb-Sr age of 72.3 Ma and an $(^{87}Sr/^{86}Sr)_0$ of 0.7106 [*Shibata and Ishihara*, 1979*a*, *b*]. Sample 6511-213 is a medium-grained representative of monzogranite from the Naegi pluton which also contains a coarser-grained variant and aplitic phases with abundant pegmatites to 50 cm wide.

The Ryoke granitoids intrude discordantly and concordantly into a terrane of Paleozoic metamorphic rocks which increase in grade toward the south from biotite schists, through cordierite-bearing gneisses, into sillimanite gneisses. The Ryoke granitoids are continuously exposed but can be subdivided from north to south into zones I to III [*Ishihara and Terashima*, 1977*a*]. Zone I granitoids, intruded into the biotite schist zone, are largely amphibole-biotite granodiorite and biotite monzogranite (T-94, T-97, and T-145). Typical Ryoke granitoids in zones II (T-75, T-128, T-165, and T-168) and III (T-76, T-79, T-133, and T-173B), occurring respectively in the cordierite-bearing gneiss and sillimanite gneiss zones, are foliated and relatively heterogeneous. They consist mostly of amphibole-biotite granodiorite, with less abundant tonalite and biotite granite, and contain numerous mafic inclusions. Quartz diorite specimen T-165 is from a lens-shaped mafic inclusion (0.7 × 1 m) in granodiorite represented by T-75; in addition to such large inclusions, the granodiorite often hosts swarms of small lensoid inclusions (3 × 20 cm). T-168 is from a salic phase of the granodiorite associated with T-165. Whereas current geologic maps show T-128 and T-75 to be representative of the same pluton, pre-1950 maps showed separate plutons; T-128 is a notably finer-grained, less foliated rock. Muscovite-biotite monzogranite and biotite granodiorite constituting the Busetsu pluton are dominant in zone III. The granodiorite (T-76) tends to occur along the northern margin of the pluton, and monzogranite (T-133 and T-173B) crops out extensively in the core. The Busetsu pluton contains very few mafic inclusions, trace amounts of garnet throughout, and sillimanite in some localities [*Koide*, 1958]; it has been considered to have a sedimentary source [*Ishihara*, 1973], although chemical compositions do not fulfill the requirements of the Australian S type. In contrast, the Kamihara tonalite (T-79) in zone III is thought to have a deep igneous origin because of its composition and lack of variation in Th/U [*Ishihara et al.*, 1969]. Complete absence of coeval volcanic rocks and the intimate relations of the granitoids with migmatite and high-grade metamorphic rocks lead to estimates of 5 kbar for emplacement of the Ryoke granitoids. This pressure is also compatible with extrapolation of geobarometric studies on sphalerite in Sanin and Sanyo belt skarns [*Shimizu and Shimazaki*, 1979]. The Busetsu pluton has an $(^{87}Sr/^{86}Sr)_0$ of 0.7096 and has been dated at 82.5 Ma by the whole-rock Rb-Sr isochron

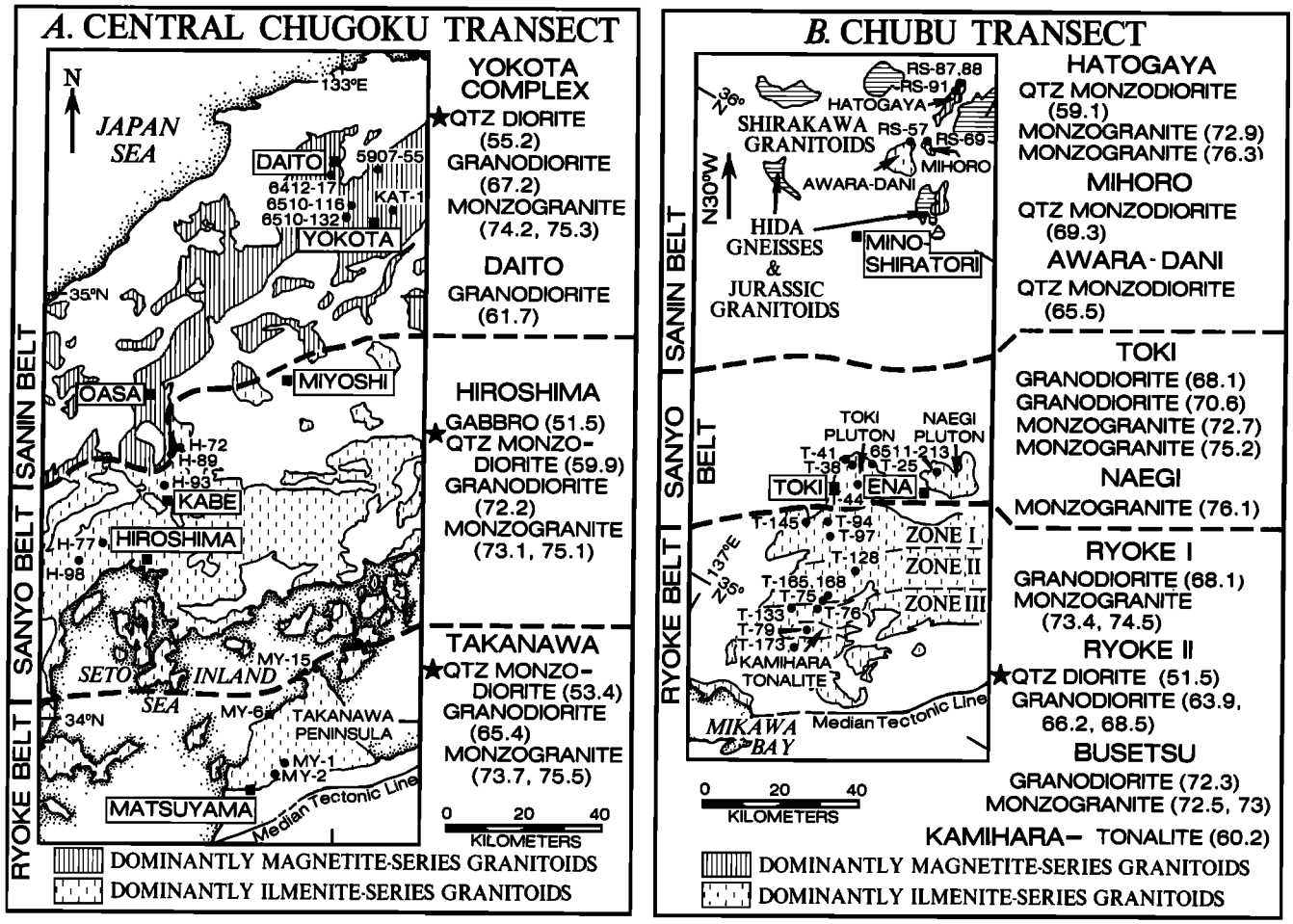

Fig. 2. Strip maps for the Chubu and Central Chugoku transects showing sample locations and generalized geology. Blank areas include Cenozoic volcanic and sedimentary rocks, undifferentiated; coeval volcanic rocks; Permo-Triassic sedimentary rocks; and minor unclassified granitoids. Legend to the right of each transect indicates the rock name and silica content of each sample. Stars highlight variants which occur as small masses or inclusions.

method [*Shibata and Ishihara*, 1979*a*, *b*]. The amphibole-bearing Kiyosaki and Mitsuhashi granodiorites in the Dando area, located about 15 km to the east of the Chubu transect, have an $(^{87}Sr/^{86}Sr)_0$ of 0.7075 and ages of 75.6 Ma [*Ozima et al.*, 1967].

Central Chugoku Transect

In the central part of Chugoku district, the Cretaceous-Paleogene granitoids are widely exposed as medium- to coarse-grained rocks. The granitoids are mostly granodiorite and monzogranite in the northern, Sanin belt, but they are largely monzogranite, known as the Hiroshima granite, in the Sanyo belt to the south. Granodiorite is predominant in the Ryoke belt. Gabbro and diorite are sparsely distributed throughout the three belts, but mafic inclusions are fairly common, especially in granodiorite.

Granitoids of the Sanin belt have K-Ar mineral ages of 30–65 Ma, but granitoid ages in the other two belts are 65–95 Ma. The age discordance is sharp just north of Oasa township. Rb-Sr whole-rock ages are generally 4–9 Ma older than K-Ar mineral ages [*Shibata and Ishihara*, 1979*a*]. Values of $(^{87}Sr/^{86}Sr)_0$ gradually increase toward the south, being about 0.7055 in the Sanin belt, and ranging from 0.7068 to 0.7082 in the Sanyo and the Ryoke belts [*Shibata and Ishihara*, 1979*b*].

Granitoids of the Daito-Yokota area, from which samples of the Sanin belt were selected (Katsura 1 through 5907-55), are large batholithic bodies of coarse-grained amphibole-biotite granodiorite and biotite monzogranite, which commonly show fine-grained marginal facies against intruded volcanic rocks. They are the type examples of the magnetite series, and magnetite has been mined from the weathered parts of intrusions ranging in composition from quartz gabbro through monzogranite [*Tsusue and Ishihara*, 1974]. The granitoids are depleted in lithophile elements in contrast to those of Sanyo belt. The Daito granodiorite (6412-17 [*Ishihara*, 1971*b*]) is elongated in an east-northeasterly direction (30 × 10 km) and contains abundant mafic inclusions. The other four samples are from the 12-km-wide Yokota granitic complex which is also elongated in an east-northeasterly direction, the common tectonic lineament in Cretaceous time. This complex is largely composed of monzogranite (6510-132, 5907-55) but grades into granodiorite in some places. Sample 6510-116 was taken from a small mass (2×4 km) of granodiorite. Quartz diorite (Katsura 1) occurs as a xenolithic block (500 m wide) exposed between the granodiorite and monzogranite and was intruded by them.

The Hiroshima granite (H-72 through H-98) is a huge batholithic complex composed of varoius felsic granitoids but mainly of biotite monzogranite. In addition to being richer in lithophile elements than the Sanin granitoids, its K/Na ratio is somewhat higher [*Ishihara*, 1971 and unpublished data, 1980], although this is not shown well in our samples. The

granite is weakly magnetic in its northern part but typically is magnetite free in the southern part; the studied samples are mostly of the weakly magnetic intermediate type. North of Hiroshima, the Hiroshima granite tends to crop out with northeasterly distribution, following tectonic lineaments. In contrast to granitoids in the Daito-Yokota area of the Sanin belt, roof rocks are well preserved. The intruded rocks are mainly late Cretaceous rhyodacitic pyroclastic rocks and upper Paleozoic-early Mesozoic sedimentary rocks. Samples H-72, H-89, and H-93 are from the northern part of Kabe township where the granite is exposed in a 20-km-wide zone. Gabbro (H-72) and quartz monzodiorite (H-89) were collected from a huge, zoned, xenolithic block (±1 km) that is intruded by the host granite (H-93). Monzogranite samples H-77 and H-88 were taken about 30 km to the southwest in an extension of the Hiroshima granite.

Granitoids of the Ryoke belt (MY-15 through MY-1) were selected from the Takanawa peninsula. The granitoids contain no magnetite and belong to the ilmenite series. Small syenite bodies among these granitoids are considered to have a replacement origin. Ryoke granitoids of the Takanawa peninsula are continuously exposed, whereas Ryoke metamorphic rocks are rarely seen; thus the spatial relation between grade of metamorphism and type of the granitoids cannot be established. However, biotite-muscovite granitoids do not occur in the peninsula, and the highest-grade Ryoke metamorphic rocks seem to run to the north of the peninsula in the Seto Inland Sea area. The granitoids themselves constitute an amphibole-biotite suite and are somewhat similar to granitoids of the Ryoke I zone in the Chubu transect. Granodiorite (MY-6), commonly foliated, is the most common rock on the peninsula; it contains lens-shaped mafic inclusions as well as blocks of quartz monzodiorite (MY-15) several hundred meters across which appear to be floating in their host. The southern part of the granodiorite is intruded by small monzogranite stocks (MY-1 and MY-2). Mafic rocks of the peninsula have recently been considered as cumulates of an earlier mafic plutonism (O. Ujike, personal communication, 1980).

CHEMISTRY OF THE MAFIC SILICATES

Analytical Methods

Mafic silicates in polished thin sections were analyzed using a three-channel ARL EMX-SM electron microprobe with an accelerating potential of 15 kV and a sample current of 0.02μA on benitoite. Elements were anaylzed in the sequence Mg+K+Fe, Al+Si+Ti, F+Cl+Ca, and Na+Mn. All analyzed grains were photographed to permit relocation for those samples in which grains are zoned. Six to twelve points per grain, or distinct portion of a grain, were typically analyzed for count intervals (~10 s) fixed by beam current termination. The selected amphibole, biotite, and pyroxene described by *Czamanske and Wones* [1973] were used as standards for most elements for the appropriate mineral species. Supplementary standards were Mn_2O_3 for Mn, a synthetic fluor-phlogopite for F (9.01 wt %), a natural crocidolite for Na (6.24 wt %), and a natural sodalite for Cl (6.82 wt %). Count data were stored and analyses computed on-line using the data reduction scheme FRAME [*Yakowitz et al.*, 1973]. As is too often the case, we have not determined Li in the mafic phases. Whole-rock Li contents average 16 to 50 ppm for individual suites and show little relation to SiO_2 content.

Whenever possible, biotite and amphibole separates were obtained for wet chemical determination of ferrous iron content, using magnetic and heavy liquid techniques; chloritic alteration posed the principal difficulty in separation. All analyzed separates were ultimately purified by hand under a binocular microscope.

Biotites

Biotite was analyzed in each of the 35 specimens; separates suitable for ferrous iron determination were obtained for all but eight. In five specimens for which ferrous iron was determined, secondary biotite is present as subordinate overgrowths on primary cores. With one exception, this secondary biotite is distinctly lower in Ti content; it shows no other typical chemical characteristic. On an individual basis, increases in Si, Al, or Mg seem to predominate in balancing loss of Ti. The absence of substantial change in Fe/(Fe+Mg) and Al^{IV} content suggests that even in those samples in which two biotites can be recognized, they do not record significant changes in crystallization history.

Biotite analytical and structural data are presented in Table 1. Biotite, amphibole, and chlorite structural data in this report were entered in a computer, and more than 50 plots were produced to test chemical correlations within and between these mineral groups. Some of these plots are presented; many others form the basis for statements concerning elemental correlations. The biotite data are summarized in the ternary diagrams $Fe^{3+} - Fe^{2+} - Mg$ and $Mg - (Al^{VI}+Fe^{3+}-Ti) - (Fe^{2+}+Mn^{2+})$ (Figures 3*a* and 3*b*). (For Figures 3*a* and 3*b* alone, only those analyses have been plotted for which ferrous iron has been determined. Where two analyses are reported in Table 1, the predominant core composition has been plotted.) In terms of octahedral-site occupancy, the majority of the biotites form a coherent grouping near *Foster*'s [1960] divalent cation limit to the Mg and Fe^{2+} biotite fields (Figure 3*b*). Biotites in T-25 and T-44 from the Toki pluton are siderophyllites, and the biotites coexisting with primary muscovite in T-173B, T-76, and T-133 from the Ryoke III zone Busetsu pluton are distinct by virtue of their high Al^{VI} contents. Figure 3*a*, which relates the biotite compositions to the three common oxygen buffers, quartz-fayalite-magnetite, Ni-NiO, and Fe_3O_4-Fe_2O_3, is rather surprising, not so much because these biotites as a group are more reduced in character than those from the Sierra Nevada batholith [*Dodge et al.*, 1969] but because there is relatively little distinction in content of Fe^{3+} between biotites from these magnetite and ilmenite series rocks. The relations of Figure 3*a* are fully compatible with *Ishihara*'s [1977] concepts of the reduced character of the ilmenite series granitoids and with earlier data of *Honma* [1974*b*, Figure 7] for biotites from the Yanai district. Only biotites from the most siliceous of the ilmenite series rocks plot above the Ni-NiO buffer curve.

The most significant aspect of biotite chemistry is the decreasing or constant Fe/(Fe+Mg) which accompanies increasing SiO_2 content in the host rocks of the magnetite series suites. This trend is best shown by the granitoids of the Daito-Yokota suite, where increase in host rock SiO_2 content from 55.3 to 75.5 wt % is accompanied by a decrease in Fe/(Fe+Mg) from 0.48 to 0.37 (Figure 4). The trend can also be seen in the two magnetite-

bearing samples of the Hiroshima granite (H-72 and H-89). For the magnetite series Shirakawa granitoids, Fe/(Fe+Mg) is nearly constant rather than decreasing. The most striking example of this type of trend has been documented for the Finnmarka complex, Norway, by *Czamanske and Wones* [1973], who ascribed it to progressive oxidation during magmatic crystallization. A similar but less regular and pronounced trend has been documented by *Murakami* [1969] for rocks of the Tamagawa cauldron, located in the Sanin magnetite series belt just west of our Central Chugoku transect. Although many Japanese writers have remarked upon the relatively Mg-rich character of biotites from the magnetite series granitoids and discussed this terrane in terms of relatively high oxygen fugacity, our Daito-Yokota data show the most pronounced and regular trend of Fe impoverishment in biotite with increasing host rock SiO_2 content. It is possible that much of the magmatic activity within *Ishihara*'s [1977] magnetite series belt along the Japan Sea side of southwest Japan has been characterized by progressive oxidation during crystallization and magmatic differentiation. To our knowledge, no similar terrane has been identified elsewhere.

$Fe^{2+}/(Fe^{2+}+Fe^{3+})$ for biotites in magnetite series rocks is in the range 0.85 to 0.89, whereas the range for the Ryoke belt is 0.91 to 0.96 (Table 1 and Figure 5*a*). No significant change in $Fe^{2+}/(Fe^{2+}+Fe^{3+})$ accompanies decreasing iron content within biotites of the Daito-Yokota granitoids, and we conclude that the oxidation consumed Fe^{2+} but that $Fe^{2+}/(Fe^{2+}+Fe^{3+})$ was buffered by mineral equilibria. Figure 3*b* shows that this process evolved biotites which are poorer in Fe^{3+} than those from the Sierra Nevada but richer in Mg. Figure 5*a* shows that the range of 0.85 to 0.89 in $Fe^{2+}/(Fe^{2+}+Fe^{3+})$ for magnetite series biotites contrasts with a range of 0.32 to 0.87 for host rock $Fe^{2+}/(Fe^{2+}+Fe^{3+})$; data for ilmenite series rocks plot in a cluster, with $Fe^{2+}/(Fe^{2+}+Fe^{3+})$ ranging from 0.87 to 0.96 for biotites and 0.68 to 0.92 for host rocks. This cluster suggests a relatively fixed or buffered environment of biotite crystallization in these rocks also. For ilmenite series specimens, there is a good correlation between Fe/(Fe+Mg) for biotites and host rocks (Figure 6). As might be expected, biotites from magnetite series rocks do not show this correlation and show no increase in Fe/(Fe+Mg) as this ratio increases in host rocks. (On this and all subsequent plots of data, lines are drawn for visual reference only; fitting of regression lines was not considered appropriate.) For these biotites Fe/(Fe+Mg) does not correlate with either Al^{VI} or (Al^{VI}+Ti); for 31 specimens, Fe/(Fe+Mg) ranges from 0.37 to 0.89 for Al^{VI} contents between 0.0 and 0.22 and (Al^{VI}+Ti) contents between only 0.21 and 0.38. (Biotites from 6511-213, T-173B, T-76, and T-133 have higher Al^{VI} contents (0.406–0.593 atoms) and are displaced and noncorrelative on these and other plots.) Ti does not correlate with Si or Al^{VI} content or with total octahedral-site occupancy, (M_1-M_2); Ti shows a weak correlation with Mg content, but the range in Mg cations (0.11–1.55) far exceeds that of Ti (0.01–0.28). Thus, the situation is similar to that found by *Wones* [1980] in that we cannot specify the mechanism of Ti substitution. There is no correlation between total Al and Na+K, although the five biotites richest in Al have high Na+K contents, matched by only two other biotites. Unit-cell contents of Al exceed Na+K for all biotites.

In most suites, Mn content and Mn/(Mn+Fe) for biotites increase significantly with increasing SiO_2 content of the host rock. There is no correlation between Mn and either Ti content or Fe/(Fe+Mg). Ca contents for these biotites are typically low, in accord with our belief that older biotite analyses commonly include CaO contained in mineral impurities. Na contents are also low; only one sample contains over 0.19 wt % Na_2O. Cl and F data for these biotites are discussed in a later section.

Czamanske and Wones [1973], *de Albuquerque* [1973], and others have discussed correlation of biotite composition with mafic mineral association. Although our sample population is not large, Table 2 reveals no distinction between our magnetite, intermediate-type, and ilmenite series examples for the assemblages amphibole + biotite and biotite alone; this suggests that there has been no fundamental difference in the evolution of these suites. In contrast, biotites associated with muscovite have the expected compositional distinctions from other biotites. Our distinction between secondary and primary muscovites on textural and chemical grounds is clearly reflected in the high Al^{IV} and consistently high Al^{VI} contents of biotite associated with primary muscovite in the Busetsu pluton (e.g., Figure 14).

Although their data are not compelling, *Tainosho et al.* [1979] maintain that biotites from the Sanin magnetite series belt are poorer in Al^{IV} than those from the Sanyo and Ryoke belts to the south. Our data do not support this contention or show correlations involving Al^{VI}. However, excluding the three examples of biotite-muscovite association, a weak positive correlation exists between F/(Fe+Mg) and total Al site occupancy; all magnetite series biotites have Fe/(Fe+Mg) below 0.57, and all magnetite series and Hiroshima granite specimens contain less than 1.30 atoms of Al. This correlation is in keeping with considerations of tetrahedral and octahedral layer articulation presented by *Hazen and Wones* [1972].

Amphiboles

A total of 80 discrete amphibole analyses were obtained by electron microprobe from the 21 specimens which contain this mineral; these data are represented by the 30 analyses of Table 3. For nine specimens in Table 3, the analyses (most commonly, averages of analyses) are considered representative of core and late (rims or patches) amphibole compositions; both compositions are carried forward to amphibole data plots. Data for remaining samples have been averaged because no consistent patterns could be distinguished among data for three or more elements—maximum variation in SiO_2, Al_2O_3, FeO, or MgO within these averaged data does not exceed 2.06, 2.19, 2.14, and 1.97 wt %, respectively; variation is notable in Ti, Na, and Mn contents. We were able to obtain clean separates for ferrous iron analysis from only 12 of the 21 amphibole-bearing samples; of these 12 separates, only four represent homogeneous amphiboles. Therefore, although we report available wet chemical FeO values, we have, for purposes of uniformity, chosen to base discussions of amphibole chemistry on the midpoint values of FeO and Fe_2O_3 estimated by the computer program of *Papike et al.* [1974]. For the four homogeneous amphiboles for which a wet chemical FeO value is available (6412-17, 6510-116, H-93, and T-165), calcu-

TABLE 1. Electron Microprobe Analyses and Structural Formulae for Biotites From the Chubu and Central Chugoku Transects, Japan

	KAT-1 (3)*	6412-17 (3)	6510-116 (3)	6510-132 (4)	5907-55 (4)	H-72 Core(3)	H-72 Late(2)	H-89 (3)	H-93 (3)	H-77 (3)	H-98 Core(2)	H-98 Late(2)	MY-15 (3)
SiO_2	36.6	37.8	37.9	38.1	38.3	37.0	36.7	37.2	36.0	35.3	34.9	35.7	36.6
Al_2O_3	14.3	13.7	13.5	14.3	14.8	13.9	13.7	13.5	13.6	13.8	13.8	14.0	15.0
FeO^T	19.4	17.3	16.3	15.2	14.6	21.4	22.8	20.0	26.1	27.4	28.9	28.5	20.2
$Fe_2O_3^C$	3.28	2.63	2.10	2.53	2.41	2.30	2.46**	2.00***	2.36	3.24	4.23	4.17**	2.03
FeO^M	16.43	14.92	14.38	12.91	12.43	19.30	20.61**	18.17***	23.99	24.46	25.04	24.69**	18.37
MgO	12.0	12.6	13.2	14.0	14.0	10.2	9.07	11.4	6.81	6.05	5.37	5.91	10.8
MnO	0.32	0.28	0.42	0.63	0.74	0.12	0.13	0.19	0.76	0.78	0.98	1.00	0.13
TiO_2	3.11	4.10	3.84	3.39	3.42	4.70	4.82	3.92	3.06	3.04	2.82	1.87	3.45
CaO	0.00	0.00	0.00	0.00	0.00	0.00	0.01	0.00	0.00	0.00	0.03	0.04	0.00
Na_2O	0.12	0.11	0.10	0.12	0.18	0.23	0.28	0.19	0.13	0.08	0.12	0.08	0.19
K_2O	9.48	9.83	9.70	9.83	9.69	9.35	9.22	9.30	9.31	9.41	9.23	9.20	9.53
Cl	0.10	0.06	0.04	0.04	0.05	0.24	0.26	0.21	0.11	0.12	0.21	0.19	0.02
F	0.23	0.26	0.45	1.12	1.42	0.23	0.21	0.23	0.77	0.90	0.98	1.09	0.23
	95.97	96.29	95.63	96.97	97.44	97.57	97.47	96.31	96.90	97.18	97.71	97.94	96.35
Si	2.779	2.833	2.856	2.830	2.833	2.791	2.788	2.821	2.825	2.783	2.761	2.806	2.779
Al	1.221	1.167	1.144	1.170	1.167	1.209	1.212	1.179	1.175	1.217	1.239	1.194	1.221
Al	0.059	0.041	0.050	0.083	0.119	0.026	0.017	0.030	0.080	0.068	0.047	0.102	0.117
Ti	0.178	0.231	0.217	0.190	0.190	0.267	0.276	0.224	0.181	0.180	0.168	0.111	0.197
Fe^{3+}	0.188	0.148	0.119	0.142	0.134	0.131	0.141	0.114	0.139	0.192	0.252	0.247	0.116
Fe^{2+}	1.044	0.935	0.906	0.803	0.769	1.219	1.311	1.154	1.574	1.614	1.658	1.623	1.166
Mn	0.021	0.018	0.027	0.040	0.046	0.008	0.008	0.012	0.051	0.052	0.066	0.067	0.008
Mg	1.353	1.406	1.478	1.551	1.538	1.143	1.029	1.295	0.797	0.712	0.634	0.693	1.217
$\Sigma(M_1-M_2)$	2.842	2.780	2.797	2.808	2.797	2.792	2.782	2.829	2.821	2.818	2.824	2.841	2.822
Ca	0.000	0.000	0.000	0.000	0.000	0.000	0.001	0.000	0.000	0.000	0.003	0.003	0.000
Na	0.018	0.016	0.015	0.017	0.026	0.034	0.041	0.028	0.020	0.012	0.018	0.012	0.028
K	0.919	0.940	0.932	0.933	0.914	0.901	0.895	0.901	0.932	0.947	0.932	0.923	0.923
$\Sigma(A)$	0.937	0.956	0.947	0.950	0.940	0.935	0.937	0.929	0.952	0.959	0.953	0.938	0.951
F	0.055	0.062	0.107	0.263	0.332	0.055	0.051	0.055	0.191	0.225	0.245	0.271	0.055
Cl	0.013	0.008	0.005	0.005	0.006	0.031	0.034	0.027	0.015	0.016	0.028	0.025	0.003
X_{phlog}	0.48	0.51	0.53	0.55	0.55	0.41	0.37	0.46	0.28	0.25	0.22	0.24	0.43
X_{ann}	0.28	0.31	0.31	0.26	0.24	0.34	0.37	0.34	0.41	0.39	0.40	0.40	0.27
X_{sid}	0.25	0.19	0.16	0.19	0.21	0.25	0.26	0.21	0.31	0.36	0.38	0.36	0.30
F/F+OH	0.028	0.031	0.054	0.132	0.166	0.027	0.025	0.028	0.096	0.112	0.123	0.135	0.028
Fe/Fe+Mg	0.477	0.435	0.410	0.379	0.370	0.542	0.585	0.495	0.682	0.717	0.751	0.730	0.513
Mn/Mn+Fe	0.0168	0.0163	0.0257	0.0406	0.0485	0.0059	0.0055	0.0094	0.0289	0.0280	0.0334	0.0346	0.0062
$Mg/Mg+Fe^{2+}$	0.56	0.60	0.62	0.66	0.67	0.48	0.44	0.53	0.34	0.31	0.28	0.30	0.51

	MY-6 Core(3)	MY-6 Late(1)	MY-2 (3)	MY-1 (2)	RS-88 (2)	RS-57 (3)	RS-69 (5)	RS-87 (2)	RS-91 (3)	T-41 (3)	T-38 (3)	T-44 Core(3)	T-44 Late(1)
SiO_2	35.7	35.6	35.8	33.8	35.5	36.9	37.3	36.5	36.7	35.5	36.2	35.1	34.7
Al_2O_3	14.8	15.3	13.8	15.1	14.2	14.1	13.3	13.2	13.5	14.1	13.8	14.4	15.6
FeO^T	24.2	24.2	27.5	28.9	23.0	22.3	19.9	21.1	21.5	23.1	25.5	32.4	32.7
$Fe_2O_3^C$	2.32	2.32**	2.13	2.18***	2.81***	2.94	2.37	2.58***	2.63***	1.80***	2.10	5.66	5.70**
FeO^M	22.13	22.08**	25.54	26.93***	20.50***	19.69	17.81	18.79***	19.12***	21.50***	23.60	27.33	27.57**
MgO	7.90	8.63	6.00	4.80	10.1	9.68	11.1	9.85	9.62	6.74	7.37	2.39	2.36
MnO	0.36	0.37	0.87	1.10	0.53	0.26	0.57	0.54	1.89	0.40	0.74	1.13	1.16
TiO_2	3.34	2.27	2.82	2.50	3.42	4.05	3.99	4.66	2.99	3.61	3.52	3.12	1.28
CaO	0.02	0.01	0.00	0.05	0.10	0.00	0.00	0.00	0.00	0.00	0.01	0.00	0.00
Na_2O	0.09	0.08	0.08	0.08	0.11	0.12	0.12	0.14	0.16	0.13	0.17	0.06	0.04
K_2O	9.65	9.52	9.44	9.38	8.15	9.63	9.50	9.29	9.73	8.90	9.60	9.15	9.11
Cl	0.06	0.01	0.03	0.01	0.15	0.11	0.18	0.16	0.15	0.22	0.15	0.09	0.03
F	0.50	0.53	0.20	0.30	0.61	0.39	0.88	0.58	1.84	0.62	0.65	0.54	0.58
	96.87	96.72	97.71	96.23	96.18	97.87	97.12	96.29	97.33	93.52	97.91	98.97	98.13
Si	2.761	2.758	2.817	2.709	2.740	2.790	2.831	2.803	2.820	2.840	2.801	2.759	2.750
Al	1.239	1.242	1.183	1.291	1.260	1.210	1.169	1.197	1.180	1.160	1.199	1.241	1.250
Al	0.115	0.151	0.096	0.137	0.028	0.047	0.024	0.000	0.048	0.165	0.063	0.091	0.209
Ti	0.195	0.132	0.167	0.151	0.199	0.230	0.228	0.269	0.173	0.217	0.205	0.184	0.076
Fe^{3+}	0.135	0.135	0.126	0.131	0.163	0.167	0.135	0.149	0.152	0.108	0.122	0.335	0.340
Fe^{2+}	1.434	1.430	1.682	1.804	1.325	1.244	1.131	1.208	1.230	1.439	1.527	1.795	1.828
Mn	0.024	0.024	0.058	0.075	0.035	0.017	0.037	0.035	0.123	0.027	0.048	0.075	0.077
Mg	0.912	0.996	0.704	0.573	1.167	1.090	1.254	1.128	1.103	0.804	0.850	0.280	0.279
$\Sigma(M_1-M_2)$	2.814	2.869	2.833	2.871	2.917	2.795	2.808	2.789	2.828	2.761	2.815	2.760	2.810
Ca	0.002	0.001	0.000	0.004	0.008	0.000	0.000	0.000	0.000	0.000	0.001	0.000	0.000
Na	0.014	0.012	0.012	0.012	0.016	0.018	0.018	0.021	0.024	0.020	0.025	0.009	0.006
K	0.954	0.941	0.948	0.958	0.804	0.928	0.920	0.911	0.954	0.909	0.947	0.917	0.922
$\Sigma(A)$	0.970	0.954	0.960	0.974	0.828	0.946	0.938	0.932	0.978	0.929	0.973	0.926	0.928
F	0.122	0.130	0.299	0.076	0.149	0.093	0.211	0.141	0.447	0.157	0.159	0.134	0.145
Cl	0.008	0.001	0.004	0.001	0.020	0.014	0.023	0.021	0.020	0.030	0.020	0.012	0.004
X_{phlog}	0.32	0.35	0.25	0.20	0.40	0.39	0.45	0.40	0.39	0.29	0.30	0.10	0.10
X_{ann}	0.30	0.27	0.41	0.30	0.30	0.34	0.35	0.37	0.37	0.36	0.39	0.42	0.33
X_{sid}	0.37	0.38	0.34	0.50	0.30	0.27	0.20	0.22	0.24	0.35	0.31	0.48	0.57
F/F+OH	0.061	0.065	0.149	0.038	0.075	0.047	0.106	0.070	0.224	0.078	0.079	0.067	0.073
Fe/Fe+Mg	0.632	0.611	0.720	0.772	0.560	0.564	0.502	0.546	0.556	0.658	0.660	0.884	0.886
Mn/Mn+Fe	0.0151	0.0151	0.0311	0.0373	0.0230	0.0119	0.0284	0.0251	0.0817	0.0172	0.0283	0.0340	0.0343
$Mg/Mg+Fe^{2+}$	0.39	0.41	0.30	0.24	0.47	0.47	0.53	0.48	0.47	0.36	0.36	0.14	0.13

TABLE 1. (continued)

	T-25 (4)	6511-213 Core(3)	6511-213 Late(2)	T-97 (3)	T-94 (4)	T-145 (3)	T-165 (3)	T-128 (3)	T-75 (3)	T-168 (4)	T-79 (3)	T-173B (4)	T-76 (3)	T-133 (3)
SiO_2	3.54	36.2	36.4	36.3	35.5	36.1	35.8	36.4	36.1	36.2	36.7	34.9	35.1	35.3
Al_2O_3	15.3	17.0	18.8	14.2	14.3	14.4	15.5	15.2	15.4	15.5	15.5	19.8	19.0	19.5
FeO^T	31.2	28.8	28.6	24.0	27.7	27.3	24.5	23.4	25.5	24.3	19.1	24.3	23.2	23.3
$Fe_2O_3{}^C$	4.29	3.84***	3.81**	1.66	3.61	2.44	1.58	2.12	2.68	2.43***	0.99	2.73	0.97	1.42
FeO^M	27.34	25.34***	25.13**	22.49	24.49	25.13	23.05	21.46	23.04	22.13***	18.24	21.84	22.32	22.02
MgO	2.50	0.95	1.00	7.73	5.75	5.50	7.79	8.73	6.84	7.69	10.9	5.37	6.05	5.57
MnO	1.09	0.81	0.84	0.42	0.97	1.35	0.18	0.35	0.34	0.41	0.23	0.55	0.33	0.50
TiO_2	2.09	2.04	0.24	4.23	3.25	2.72	3.67	3.66	3.75	3.49	3.07	2.75	2.77	2.09
CaO	0.00	0.00	0.00	0.00	0.00	0.00	0.02	0.00	0.00	0.00	0.01	0.03	0.01	0.00
Na_2O	0.07	0.18	0.18	0.10	0.07	0.07	0.15	0.10	0.12	0.10	0.15	0.15	0.17	0.14
K_2O	9.33	9.50	9.59	9.44	9.55	9.49	9.44	9.82	9.64	9.70	9.81	9.84	9.80	9.77
Cl	0.16	0.28	0.30	0.02	0.06	0.04	0.08	0.01	0.04	0.01	0.09	0.00	0.00	0.00
F	1.03	2.38	2.67	0.50	1.14	1.71	0.25	0.32	0.68	0.40	0.24	0.53	0.35	0.92
	98.60	98.52	98.96	97.09	98.69	98.95	97.51	98.17	98.63	98.06	95.93	98.49	96.87	97.23
Si	2.792	2.858	2.856	2.795	2.765	2.815	2.744	2.760	2.756	2.760	2.793	2.643	2.691	2.708
Al	1.208	1.142	1.144	1.205	1.235	1.185	1.256	1.240	1.244	1.240	1.207	1.357	1.309	1.292
Al	0.219	0.438	0.593	0.088	0.076	0.140	0.141	0.115	0.138	0.148	0.182	0.411	0.406	0.474
Ti	0.124	0.121	0.014	0.245	0.190	0.160	0.212	0.209	0.216	0.200	0.176	0.157	0.160	0.121
Fe^{3+}	0.255	0.228	0.225	0.096	0.212	0.143	0.091	0.121	0.154	0.139	0.057	0.156	0.056	0.082
Fe^{2+}	1.804	1.672	1.650	1.449	1.595	1.640	1.479	1.360	1.473	1.410	1.160	1.384	1.433	1.413
Mn	0.073	0.054	0.056	0.027	0.064	0.089	0.012	0.022	0.022	0.026	0.015	0.035	0.021	0.032
Mg	0.294	0.112	0.117	0.888	0.668	0.640	0.891	0.986	0.779	0.874	1.233	0.606	0.692	0.637
$\Sigma(M_1-M_2)$	2.768	2.625	2.655	2.794	2.804	2.813	2.825	2.812	2.782	2.797	2.821	2.745	2.770	2.759
Ca	0.000	0.000	0.000	0.000	0.000	0.000	0.002	0.000	0.000	0.000	0.001	0.002	0.001	0.000
Na	0.011	0.028	0.027	0.015	0.011	0.011	0.022	0.015	0.018	0.015	0.022	0.022	0.025	0.021
K	0.939	0.956	0.960	0.928	0.949	0.945	0.924	0.949	0.940	0.943	0.952	0.951	0.960	0.956
$\Sigma(A)$														
F	0.257	0.594	0.663	0.122	0.281	0.422	0.061	0.077	0.164	0.096	0.058	0.127	0.085	0.223
Cl	0.021	0.037	0.040	0.003	0.008	0.005	0.010	0.001	0.005	0.001	0.012	0.000	0.000	0.000
X_{phlog}	0.11	0.04	0.04	0.32	0.24	0.23	0.32	0.35	0.28	0.31	0.44	0.22	0.25	0.23
X_{ann}	0.36	0.31	0.21	0.36	0.37	0.39	0.28	0.29	0.31	0.29	0.24	0.11	0.14	0.12
X_{sid}	0.53	0.65	0.74	0.33	0.39	0.39	0.41	0.36	0.41	0.40	0.32	0.67	0.61	0.64
F/F+OH	0.129	0.297	0.331	0.061	0.140	0.211	0.030	0.038	0.082	0.048	0.029	0.063	0.042	0.112
Fe/Fe+Mg	0.875	0.944	0.941	0.635	0.730	0.736	0.638	0.600	0.676	0.639	0.497	0.718	0.683	0.701
Mn/Mn+Fe	0.0342	0.0276	0.0290	0.0172	0.0342	0.0475	0.0076	0.0146	0.0133	0.0165	0.0122	0.0222	0.0139	0.0210
$Mg/Mg+Fe^{2+}$	0.14	0.06	0.07	0.38	0.30	0.28	0.38	0.42	0.35	0.38	0.52	0.31	0.33	0.31

The structural formulae for Table 1 have been calculated using the computer program of S. Ludington (personal communication, 1979) using the option of setting the sum of the positive charges equal to 22. The program also was used to calculate F/(F+OH) (using a reconstructed OH^-), X_{phlog} = Mg/total octahedral cations, X_{sid} = (3-Si/Al)/1.75, and X_{ann} = 1 − (X_{phlog} + X_{sid}). FeO^T values are electron microprobe values for iron expressed as FeO; FeO^M values are wet chemical determinations of FeO made by S. Neil of the Branch of Analytical Laboratories, U.S. Geological Survey (except see below); $Fe_2O_3{}^C$ values are by difference or calculation (see below).

*Number in parentheses indicates the number of discrete analyses averaged to obtain the values in the column below. A 'discrete analysis' may represent a grain, a group of grains, or a 'late' rim of second generation biotite that is distinct in composition.

**Indicates that FeO^M and $Fe_2O_3{}^C$ values are calculated by assuming (1) that the wet chemical value for FeO^M for the bulk biotite concentrate applies to the dominant phase, and (2) that the proportions of FeO^M and $Fe_2O_3{}^C$ in the 'late' phase are equal those in the dominant 'core' phase.

***Indicates that both FeO^M and $Fe_2O_3{}^C$ values are simply based on a 'best estimate' of their relative proportion, considering other biotites in the suite for which separates could be obtained and analyzed.

lated midpoint FeO values deviate by +10, −8, +10, and −2%, respectively, from the measured values.

For no single specimen have we been compelled to report two compositions for both biotite and amphibole. Second-generation amphibole compositions show much more dramatic contrasts with core compositions than do secondary biotites (Tables 1 and 3). Secondary amphibole generally contains less Al (principally Al^{IV}), Ti, and Na, but more Si and Mg.

Correlation between Fe/(Fe+Mg) for amphiboles and host rocks is so similar to that shown for biotites (Figure 6) that a separate figure is not justified; again, the most deviant points are for five representatives of the two magnetite series suites for which Fe/(Fe+Mg) for the rock markedly exceeds that in the amphibole. Because of the uncertainty introduced by the calculation of Fe^{3+}, it is tenuous to make much of the fact that $Fe^{2+}/(Fe^{2+}+Fe^{3+})$ for the amphiboles as a group appears to show a better relation to rock $Fe^{2+}/(Fe^{2+}+Fe^{3+})$ than $Fe^{2+}/(Fe^{2+}+Fe^{3+})$ for the biotites: magnetite series and Ryoke series granitoids are well separated (Figure 5*b*). In part, the better correlation may simply reflect the fact that amphiboles do not occur in the most oxidized high-silica rocks. As shown in Figure 5*b*, amphiboles from individual suites and zoned amphiboles do not follow this apparent trend.

The data of Table 3 show that amphibole compositions have been significantly influenced by magmatic oxidation state (e.g., Figure 4). Fe/(Fe+Mg) for the amphiboles decreases regularly and significantly with increase in host rock SiO_2 for the Daito-Yokota and Shirakawa suites and between magnetite-bearing specimens H-72 and H-89. Because amphibole is not present in 14 of the siliceous granites, the data base is not as extensive as that for biotites. However, the data strongly suggest that the amphiboles record progressive magmatic oxidation or variation in intrinsic oxidation state just as well as the biotites [cf. *Czamanske and Wones,* 1973].

Most common types of solid solution in amphiboles may be represented by the generalized formula

$$(Na+K)_x Ca_2^{2+}(R_{5-y-z}^{2+}R_y^{3+}R_z^{4+}) \cdot (Al_{x+y+2z})(Si_{8-x-y-2z})O_{22}(OH)_2$$

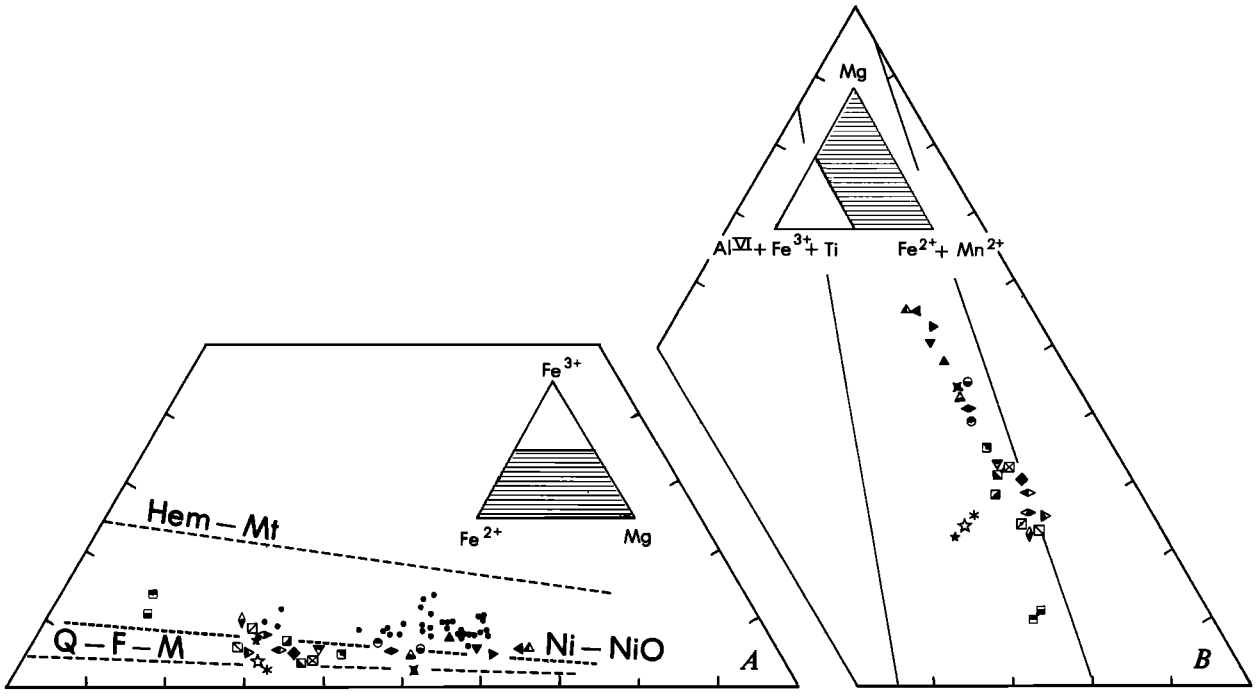

Fig. 3. (*a*) The relation of biotite compositions in terms of octahedral Fe^{3+} – Fe^{2+} – Mg, in relation to the buffer curves HM, Ni–NiO, and QFM. Data from *Dodge et al.* [1969] are shown by small dots. (In this and subsequent figures, symbols relate data points to the tabulated data of this paper. This and all subsequent figures are based on atomic proportions unless otherwise noted.) (*b* Biotite compositions in terms of *Foster*'s [1960] breakdown of octahedral occupancy into Mg – $(Al^{VI}+Fe^{3+}+Ti)$ – $(Fe^{2+}+Mg^{2+})$.

where Na^+ and K^+may occupy the otherwise vacant A-site; R^{2+} = Mg^{2+}, Fe^{2+}, Mn^{2+}; R^{3+} = Al^{3+}, Fe^{3+}; x = A-site occupancy; y = sum of Al^{VI} + Fe^{3+}; and z = Ti^{4+}.

Within the amphibole structure, in addition to simple substitutions such as Fe^{2+} for Mg, there are at least six possible schemes of coupled substitution which involve charge balancing and lead to idealized end members [e.g., *Czamanske and Wones,* 1973]. As noted by *Robinson et al.* [1971] and implicit in the generalized formula, substitutions of Na^+ or K^+ in the A-site and Al^{3+}, Fe^{3+}, or Ti^{4+} in octahedral sites, compensated by substitution of Al for Si in tetrahedral sites, should result in Al^{IV} = A-site occupancy + $(Al^{3+}+Fe^{3+})^{VI}$ + $2Ti^{4+}$. Figure 7*a* shows that these substitutions dominate the chemistry of this group of Japanese amphiboles including the evolution of core-to-late amphibole compositions. The relation shown is nearly identical to that found in amphiboles from the granodiorite at Finnmarka [*Czamanske and Wones,* 1973]; specifically, Al^{IV} is slightly deficient for satisfaction of the equation. An inadvertent plotting error revealed that, on the average, the relation is almost ideally satisfied if Ti is treated as a trivalent ion. Specifically, the average Al^{IV} content for the amphiboles of Table 3 is 1.060 cations, and the average for A-site occupancy + $(Al+Fe^{3+})^{VI}$ + Ti^{4+} is 1.057 cations; the average sum utilizing $2Ti^{4+}$ is 1.195. Thus, discounting the possibility that Ti is trivalent in these amphiboles, 88% of the charge excess due to octahedral and A-site substitution is typically offset by Al^{IV} substitution.

According to recognized substitutional schemes, the remaining average excess octahedral and A-site charge of about 12% should be balanced by substitution of Na for Ca in the M4 site. Plots were made of Na^{M4} versus Al^{VI}, Fe^{3+}, $Al^{VI}+Fe^{3+}$, and Ti. These typically show poor correlation for the total data set, for individual suites, or in response to formation of secondary amphiboles. Thus, in large measure, excess octahedral and A-site charge is unaccounted for by our analysis. Only for a few of the Ryoke series samples are correlations apparent; these can be summarized as follows: Na^{M4}–Ti, good correlation for specimens T-97, T-128, T-75, and T-79 from the Chubu transect; Na^{M4}–Al^{VI}, Na^{M4}–Fe^{3+}, and Na^{M4}–$(Al^{VI}+Fe^{3+})$, correlation only, but in each case, for T-97 and T-79.

A similar situation is revealed by plotting Na^{M4} versus Na in the A-site for investigation of richterite-type coupled substitution. (The plot of Na^{M4} versus total A-site occupancy is virtually identical.) Richeritic substitution is not operative for the amphiboles as a group, for individual suites, or for zoned

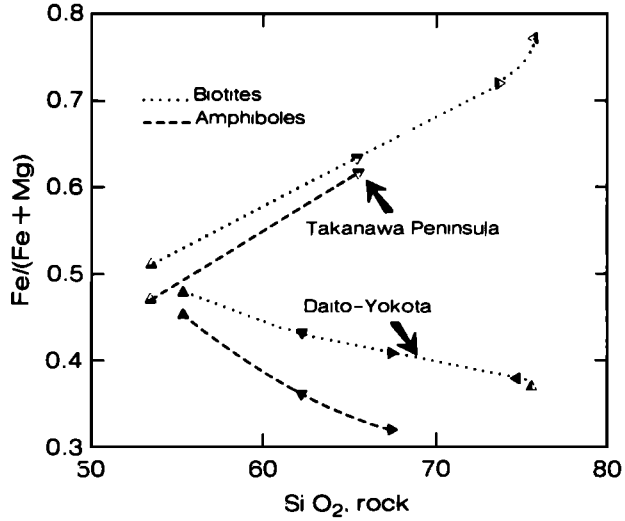

Fig. 4. Plot of whole-rock SiO_2 versus Fe/(Fe+Mg) for biotites and amphiboles from magnetite and ilmenite series suites from the Central Chugoku transect.

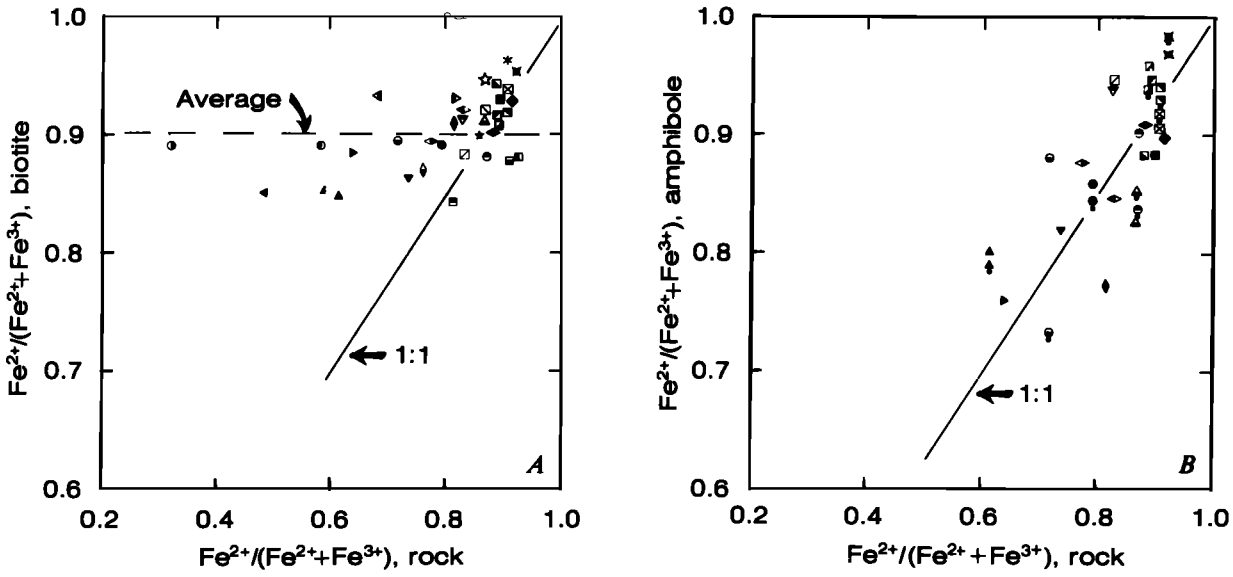

Fig. 5. (*a*) The relation of rock and biotite compositions in terms of $Fe^{2+}/(Fe^{2+}+Fe^{3+})$. (*b*) The relation of rock and amphibole compositions in terms of $Fe^{2+}/(Fe^{2+}+Fe^{3+})$.

amphiboles from the Daito-Yokota, Shirakawa, or Takanawa suites. However, there is good evidence of coupling between Na in the M4 and A site for the zoned amphiboles in T-97, T-128, T-75, and T-79.

Further insight into the relative contributions of the various coupled substitution schemes is possible through consideration of Figures 7*b*, 7*c*, and 7*d*. A component of edenite-type substitution of Al^{IV} plus Na or K in the A-site for Si^{4+} plus A-site vacancies is indicated by Figure 7*b*, in which subtraction of Na^{M4} has removed richterite-type coupled substitution. The reference line for a 1:1 relation between Al^{IV} and A-site − Na^{M4} fits the data set reasonably well and shows that removal of edenite-type substitution can account for the typically lower Al^{IV} and Na contents of secondary amphiboles. The intercept at ~0.6 Al^{IV} cations for 0.0 (A-site − Na^{M4}) cations establishes a substantial residual of Al^{IV} substitution, unrelated to A-site occupancy, that reflects coupling with Al^{3+}, Fe^{3+}, and Ti in octahedral sites. (A plot of Al^{IV} versus total A-site occupancy shows good correlation, the data falling between limiting reference lines of 2:1 and 3:1.) Coupling between Al^{IV} and octahedral Ti in a ratio between 4:1 and 5:1 is suggested by Figure 7*c*. The substantial loss of Ti commonly associated with development of secondary amphiboles can be understood in terms of this coupled substitution and the well-documented, decreasing Ti saturation limit in amphiboles with decreasing temperature [cf. *Anderson*, 1980]. Good correlation between total A-site and Ti contents reflects the combined influence of both substitution schemes.

For this group of amphiboles, Al^{IV} content shows little correlation with total Fe or Fe^{3+} content, and secondary amphibole formation typically involves substantial loss of Al^{IV}, with relatively little change in unit-cell content of total Fe and irregular change in calculated Fe^{3+}. Figure 7*d* shows that these amphiboles have contents of Al^{VI} that (1) exceed Al^{IV} content, (2) correlate poorly with total Al content, and (3) show a disproportionately small decrease, relative to Al^{IV}, during secon dary amphibole formation. All of these considerations combine to suggest that there is a persistent, tschermakite-type, coupled substitution of Al^{IV} plus Al^{VI}, for Mg plus Si, that is relatively unaffected by Al content or alteration. Lower contents of Al^{IV}, Na+K in the A-site, and Ti, typical of the secondary amphiboles, are well accounted for by the edenite- and tchermakite-type substitutional schemes. Neither Al^{IV} nor total Al contents of amphiboles are characteristic for magnetite and ilmenite series terranes (Table 3 and Figures 7*d* and 7*e*), findings contrary to *Murakami* [1977, 1979] and *Tainosho et al.* [1979]. Murakami held that all granites in the Sanin, magnetite series belt contain Al-poor amphibole, whereas Tainosho et al. maintained that amphiboles from the Sanin belt are poor in Al^{IV} as compared to those from the Sanyo and Ryoke ilmenite series belts. In contrast, Figures 7*d* and 7*f* show that amphiboles from the ilmenite series suites contain, on the average, more Al^{VI} than those from the two magnetite series suites and the Hiroshima granite. This result is also contrary to *Murakami* [1977], who found no detectable difference in Al^{VI} among the three belts. A corollary of the higher Al^{VI} contents of many of the Ryoke belt amphiboles is that in them

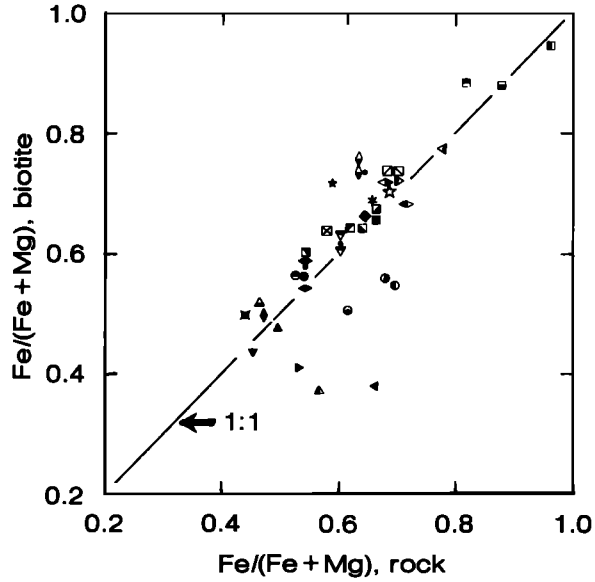

Fig. 6. The relation of rock and biotite compositions in terms of Fe/(Fe+Mg).

TABLE 2. Variation of Al^{IV}, Al^{VI}, and $\Sigma(M_1 - M_2)$ Contents With Paragenesis and Intrusive Suite for Biotites From the Chubu and Chugoku Transects, Japan

	All Examples	Magnetite Series Suites		Intermediate-Type Suites		Ilmenite Series (Ryoke) Suites		All Examples	
	P + A + B (4)	A + B (7)	B (2)	A + B (4)	B (2)	A + B (7)	B (3)	B + SM (3)	B + PM (3)
Al^{IV}	1.179–1.240	1.144–1.260	1.167–1.180	1.160–1.217	1.239–1.241	1.205–1.256	1.185–1.291	1.142–1.208	1.292–1.357
Al^{VI}	0.026–0.115	0.000–0.059	0.048–0.119	0.030–0.165	0.047–0.091	0.076–0.182	0.096–0.140	0.083–0.438	0.406–0.474
$\Sigma(M_1\text{-}M_2)$	2.792–2.329	2.780–2.917	2.792–2.828	2.761–2.321	2.760–2.864	2.782–2.825	2.813–2.871	2.625–2.808	2.749–2.770

P, pyroxene; A, amphibole; B, biotite; SM, secondary muscovite; PM, primary muscovite. Number in parentheses is the number of samples.

Fe^{3+} exceeds Al^{VI} content. The characteristically higher Al^{VI} contents of amphiboles from our Ryoke belt samples may reflect higher pressures of crystallization, as suggested by *Thompson* [1947]. In further comparison to previous studies, in Figures 7*e* and 7*f* we show the relation between Al^{IV} and Al^{VI}, and Fe/(Fe+Mg). Our Figure 7*e* is similar to Figure 12 of *Tainosho et al.* [1979] but markedly different from Figure 10 of *Murakami* [1977] which shows a good correlation between Al^{IV} and Fe/(Fe+Mg). On the other hand, Figure 7*f* shows good correlation between Al^{VI} and Fe/(Fe+Mg) for individual suites and for primary and secondary amphiboles.

Nonsubstitutional correlations have been examined for the following pairs: Mn–Ti, Mn–total Fe, Mn–total Al, Ti–total Fe, A-site K–A-site Na, A-site K–Na^{M4}, and A-site K–total Na. No significant correlation exists for any of these pairs except between A-site K and either total or A-site Na. We have elected to show the correlation of A-site K and Na as Figure 8. Because A-site Na is the larger portion of total Na, the poor correlation between A-site K and Na^{M4} is overwhelmed, and a nearly equal correlation is found between A-site K and total Na. The basis for the correlation is not clear, but it holds just as well for individual suites and the reaction of primary to secondary amphiboles as it does for the amphiboles as a group.

In the terminology of *Leake* [1978], all but one of the studied amphiboles are members of the calcic amphibole group, with Ca ranging from 1.569 to 1.919 and Na from 0.091 to 0.564 cations. (The core amphibole composition of RS-69 belongs to the sodic-calcic group, with Ca = 1.760 and Na = 0.753.) Following Figure 3 of Leake, at least nine names might properly be ascribed to these amphiboles, the majority being magnesio- or ferro-hornblendes, edenites, ferro-edenites, edenitic hornblendes, or ferro-edenitic hornblendes. Magnesio-hornblendes are more typical of magnetite series suites and ferro-edenitic hornblendes of the Ryoke belt.

Interrelations

Some interrelations among rock, biotite, and amphibole chemistry have already been noted; others are more conveniently discussed now. A plot of rock Fe/(Fe+Mg) versus rock $Fe^{2+}/(Fe^{2+}+Fe^{3+})$ shows no overall correlation for our specimens, but a fair separation at $Fe^{2+}/(Fe^{2+}+Fe^{3+}) = 0.8$, with lower ratios dominated by specimens from the magnetite series suites and the Hiroshima granite. For the two magnetite series suites, $Fe^{2+}/(Fe^{2+}+Fe^{3+})$ ranges more widely than Fe/(Fe+Mg), whereas the remaining suites show substantially more range in Fe/(Fe+Mg). For individual suites, Fe/(Fe+Mg) typically increases irregularly with increasing SiO_2 content; the largest and most regular changes in ratio are for the Takanawa suite (0.46 to 0.78), the Toki-Naegi granitoids (0.66 to 0.96), and the Ryoke III zone granitoids (0.44 to 0.69). $Fe^{2+}/(Fe^{2+}+Fe^{3})$ typically shows modest variation and little change with SiO_2 content except for the Shirakawa granitoids in which it decreases strongly (0.79 to 0.32) with increasing silica content.

Al^{IV} contents of primary amphiboles range from 0.46 to 1.72 cations as compared to a range of only 1.14 to 1.36 cations for Al^{IV} contents of biotites. Correspondingly, $X_{Al^{IV}}{}^{A}$ ranges from 0.045 to 0.215, but $X_{Al^{IV}}{}^{B}$ only ranges between 0.286 and 0.315. Our data therefore plot above and with lesser slope than *Gorbatschev*'s [1970] proposed equilibrium curve for $X_{Al^{IV}}{}^{A}$ versus $X_{Al^{IV}}{}^{B}$; moreover, as at the Pliny Range [*Czamanske et al.*, 1977], primary and secondary amphiboles are not readily distinguished by this plot. Following *Ste-*

phenson [1977], we have related $K_{D(Al^{IV}/(Al^{IV}+Si))}{}^{B/A}$ to $K_{D(Al^{VI}+Ti+Fe^{3+})}{}^{B/A}$ (Figure 9*a*) and $X_{AL^{IV}}{}^{A}$ (Figure 9*b*). The relation shown by Figure 9*a* was not found by Stephenson and that depicted by Figure 9*b* was by no means so regular. The limited range in $X_{Al^{IV}}{}^{B}$ is significant to the regularity of Figure 9*b*, and instrumental therefore in suggesting that both of these plots invariably will be dominated by amphibole substitutional relations involving Al^{IV} and highly charged octahedral cations. $Fe^{2+}/(Fe^{2+}+Fe^{3+})$ shows a much greater range for amphiboles than biotites, as noted in our earlier observations in which we compared this ratio in minerals and rocks. A range of 0.85 to 0.95 for biotites corresponds to a range of 0.73 to 0.98 for amphiboles. These data may support *Stephenson* [1977], who suggested that $Fe^{2+}/(Fe^{2+}+Fe^{3+})$ may be more sensitive to variations in oxygen fugacity for amphiboles than for biotites. No correlation exists for specimens within individual suites or for the entire data set, but in magnetite series specimens both minerals tend to have relatively low $Fe^{2+}/(Fe^{2+}+Fe^{3+})$. The opportunity to generate plots by computer encouraged us to examine the relation between Fe and Mg contents in amphiboles and biotites in four ways: $Fe/(Fe+Mg)_{Amp} - Fe/(Fe+Mg)_{Bio}$; $Fe/(5+Xoct)_{Amp} - Fe/(M_1-M_2)_{Bio}$; $Mg/(5+Xoct)_{Amp} - Mg/(M_1-M_2)_{Bio}$; and $Mg/Mg+Fe^{2+})_{Amp} - Mg/(Mg+Fe^{2+})_{Bio}$. The second and fourth plots are shown as Figures 10*a* and 10*b*. (We have elected to consider total octahedral site occupancy for amphiboles to be (5+Xoct), believing that Xoct could be a function of calculation scheme.) The second plot (Figure 10*a*) is least similar to the other three in tending to compress the data to a more linear relation. We interpret this to reflect the effect of octahedral Ti^{4+}, which is present in significant amount in both minerals ($\simeq Fe^{3+}$) and will compete most directly for structural sites with Fe^{3+}. The fact that the fourth plot (Figure 10*b*), using calculated values for Fe^{2+}, is virtually indistinguishable from plots that do not rely on assignment of iron valence lends support to the use of calculated ferric-ferrous data for amphiboles in other places in this report.

Both Figures 10*a* and 10*b* show that as Mg content increases, amphiboles tend to contain a higher proportion of Mg in octahedral sites than is characteristic of coexisting biotites; a similar relation was obtained by *Honma* [1974*b*, Figure 6]. *Stephenson* [1977] has used distribution coefficients to explore in depth the influence of compositional factors on $Fe^{2+}-Mg$ distribution in coexisting amphiboles and biotites. Whereas for gneisses he finds correlations between values of $K_D{}^{B/A}$ for $Fe^{2+}/(Fe^{2+}+Mg)$ versus $(Al^{VI}+Ti+Fe^{3+})$, $Fe^{2+}/(Fe^{2+}+Mg)$ versus $Al^{IV}/(Al^{IV}+Si)$, and $Mg/\Sigma oct$ versus $(Al^{VI}+Ti+Fe^{3+})$, these correlations are not shown by our data for plutonic rocks, although there is a weak, inverse relation between the latter two distribution coefficients. Our data can be explained if, on a codistributional basis, the smaller M_2 sites in amphiboles are preferred sites for Mg occupancy, in contrast to the more nearly equivalent character of the M_1 and M_3 sites in amphiboles and the M_1 and M_2 sites in biotites.

In seven of nine cases, formation of secondary amphibole causes $Mg/(Mg+Fe^{2+})$ for amphibole and biotite to diverge; the greatest changes are seen for magnetite series specimens Katsura-1, RS-88, RS-57, and RS-69 in which the secondary amphiboles are notably enriched in Mg. If Fe^{2+} is being depleted by oxidation, these data suggest that amphiboles can more readily recrystallize and reflect the late-stage magmatic environment than biotites.

K_D values for the distribution of Mn and Ti between coexisting amphiboles and biotites have been calculated on the basis of the mole fraction of each element in the six-coordinated sites, less Al^{VI} [*Kretz*, 1960], although calculation has shown that our K_D values are not materially affected by inclusion of Al^{VI}. Following our earlier argument, we have added Xoct (Table 3) to the octahedral-site cations for amphiboles; for biotites we have not considered octahedral-site vacancies. Figure 11*a* shows that the distribution of Mn between amphibole and biotite is quite regular for our specimens, with no distinction between magnetite and ilmenite series suites in either K_D or Mn concentration. *Stephenson* [1977] discusses such complexities for Mn codistribution as (1) increasing temperature favoring the amphibole lattice, and (2) correlation of higher values of $K_D{}^{B/A}$ with higher Mn content. Our data might support the second possibility, but in approaching $K_D{}^{B/A} = 0.5$ (Figure 11*a*), they do not appear to support the first; Stephenson found mean values of 0.53 and 0.44, respectively, for amphibolite-and granulite-facies gneisses. For comparison with the data of *Greenland et al.* [1968], who utilized Mn weight percentages, an average K_D value of 1.69 represents our data; this is similar to their average for the southern California batholith. It is of interest that (1) $K_D{}^{B/A}$ increases in five of nine cases where second generation amphibole was analyzed, and (2) in seven of nine cases, $K_D{}^{D/A}$ for secondary amphibole is further removed from 0.5 than $K_D{}^{B/A}$ for primary amphibole in the samples. We hesitate to make any interpretation of these observations.

As shown by Figure 11*b*, the distribution of Ti between amphibole and biotite is a much more complex relation; we interpret this to reflect the involvement of Ti in coupled substitutions and the related fact that its charge and size do not allow it to substitute as readily for Fe as does Mn. Even disregarding the loss of Ti by secondary amphiboles, Figure 11*b* shows no consistent pattern to Ti codistribution for individual suites or for the entire group of samples. Because there are so many other indications of equilibration between the mafic silicate phases, our data add to the evidence that Ti codistribution is an unreliable index of equilibrium between amphiboles and biotites. Our data support the general tendency [cf. *Czamanske et al.*, 1977] for relative enrichment of Ti in biotite and Mn in amphibole, with formation of secondary phases of each mineral involving little change in Mn content but substantial decrease in Ti content.

It is timely to return to the question of the relation between those mafic rocks that occur as inclusions and their more silicic hosts; these are T-165 in T-75; Katsura-1 intruded by granodiorite and monzonite; H-72 and H-89 in H-93; and MY-15 in MY-6. There appears to be no distinction in bulk rock or mineral chemistry which would lead us to suspect that any of these inclusions could not represent the most mafic phase of a magmatic sequence. The type of data herein reported which lead to this conclusion is not insensitive to revealing intrusive complexity, as evidenced by study of the Pliny Range in New Hampshire [*Czamanske et al.*, 1977; *Loiselle*, 1978]. However, proof of the consanguinity of inclusions and host would require gathering of isotopic and trace element data along the lines suggested in the epilogue to this paper.

The earlier raised question of the relation between the units sampled as T-75 and T-128 cannot be answered conclusively from our mafic silicate data, but these data and other data which follow show that there are greater distinctions than expected on the basis of respective SiO_2 contents and suggest that the specimens represent different plutons.

Another point can be made with regard to specimen T-

TABLE 3. Electron Microprobe Analyses and Structural Formulae for Amphiboles and Pyroxenes From the Chubu and Central Chugoku Transects, Japan

AMPHIBOLES

	KAT-1 Core	KAT-1 Late*(2)**	6412-17 Av(3)	6510-116 Av(2)	H-72 Av(2)	H-89 Av(3)	H-93 Av(4)	H-77 Av(4)	MY-15 Core(2)	MY-15 Late	MY-6 Av(3)	RS-88 Core
SiO_2	43.9	48.5	48.3	48.8	50.4	47.8	44.1	43.1	44.2	48.3	44.9	42.1
Al_2O_3	9.82	6.31	6.08	5.65	3.47	6.10	7.85	8.63	9.95	6.55	8.84	10.3
FeO^T	16.5	15.1	14.1	12.5	22.5	15.9	25.1	24.7	17.1	17.2	21.4	20.52
FeO^M	12.44***	12.44***	10.53	10.34	---	---	19.34	---	15.31	15.31	---	15.77
FeO^{CM}	13.23	11.92	11.56	9.49	20.40	12.29	21.21	21.61	14.06	14.64	20.14	17.60
FeO^{CL}	10.90	9.47	9.01	6.48	19.01	8.64	17.32	18.54	11.04	12.05	18.84	15.33
$Fe_2O_3^{CM}$	3.68	3.54	2.83	3.35	2.34	4.05	4.31	3.40	3.35	2.88	1.44	3.25
MgO	11.2	13.3	13.8	15.0	9.84	13.3	6.15	5.92	10.9	11.9	7.50	8.05
MnO	0.60	0.56	0.51	0.78	0.50	0.26	1.53	1.22	0.30	0.41	0.64	0.92
TiO_2	2.43	1.05	1.28	1.10	0.08	1.26	1.07	1.28	2.49	1.05	1.16	1.86
CaO	11.5	11.6	11.5	11.3	10.7	10.7	10.2	10.3	11.1	10.8	11.4	11.1
Na_2O	1.45	0.83	1.07	1.19	0.39	1.54	1.69	1.85	1.33	0.80	1.05	1.61
K_2O	0.52	0.49	0.49	0.48	0.17	0.53	0.83	1.05	0.74	0.40	1.13	0.91
Cl	0.02	0.02	0.04	0.09	0.00	0.06	0.07	0.10	0.02	0.01	0.03	0.14
F	0.09	0.10	0.16	0.26	0.10	0.45	0.49	0.58	0.11	0.10	0.23	0.34
	98.44	98.22	97.62	97.49	98.39	98.34	99.50	99.04	98.55	97.84	98.46	98.18
Si	6.502	7.080	7.086	7.121	7.537	7.022	6.767	6.670	6.542	7.127	6.823	6.442
Al	1.498	0.920	0.914	0.879	0.463	0.978	1.233	1.330	1.458	0.873	1.177	1.558
Al	0.218	0.168	0.137	0.094	0.149	0.079	0.188	0.245	0.276	0.266	0.408	0.291
Fe^{3+}	0.411	0.390	0.312	0.368	0.263	0.448	0.499	0.397	0.373	0.319	0.164	0.374
Fe^{2+}	1.639	1.457	1.418	1.159	2.550	1.510	2.724	2.797	1.738	1.806	2.561	2.250
Mg	2.467	2.886	3.017	3.266	2.192	2.919	1.408	1.365	2.404	2.605	1.699	1.834
Mn	0.075	0.069	0.063	0.097	0.063	0.032	0.199	0.160	0.038	0.051	0.082	0.119
Ti	0.271	0.115	0.141	0.121	0.009	0.139	0.124	0.149	0.277	0.117	0.133	0.214
XOCT	0.081	0.085	0.088	0.105	0.226	0.127	0.142	0.113	0.106	0.164	0.047	0.082
Ca	1.825	1.818	1.805	1.770	1.717	1.691	1.675	1.701	1.762	1.712	1.859	1.823
Na	0.094	0.097	0.107	0.125	0.057	0.182	0.183	0.186	0.132	0.124	0.094	0.095
Na	0.323	0.138	0.197	0.211	0.057	0.256	0.320	0.369	0.249	0.104	0.215	0.383
K	0.098	0.091	0.092	0.090	0.032	0.099	0.163	0.207	0.140	0.075	0.219	0.178
Σ(A)	0.421	0.229	0.289	0.301	0.089	0.355	0.483	0.576	0.389	0.179	0.434	0.561
Fe/Fe+Mg	0.454	0.390	0.364	0.319	0.562	0.401	0.696	0.701	0.468	0.449	0.616	0.589
Na/Na+K	0.810	0.721	0.768	0.789	0.781	0.816	0.755	0.728	0.731	0.752	0.585	0.729
Mn/Mn+Fe	0.0353	0.0360	0.0351	0.0597	0.0219	0.0161	0.0582	0.0477	0.0177	0.0234	0.0292	0.0434
$Mg/Mg+Fe^{2+}$	0.60	0.66	0.68	0.74	0.46	0.66	0.34	0.33	0.58	0.59	0.40	0.45

	RS-88 Late(4)	RS-57 Core	RS-57 Late	RS-69 Core	RS-69 Late(3)	T-41 Av(2)	T-38 Av(5)	T-97 Core(3)	T-97 Late(2)	T-94	T-165 Av(4)	T-128 Core(2)
SiO_2	47.8	45.0	49.4	41.7	47.7	47.2	45.3	45.5	49.7	42.4	44.9	46.7
Al_2O_3	5.75	8.20	4.90	11.4	6.11	6.32	7.74	7.91	4.54	9.06	9.61	7.56
FeO^T	17.5	18.4	17.8	16.6	16.2	22.2	21.4	21.3	21.9	24.1	22.0	18.9
FeO^M	15.77	14.33	14.33	---	---	---	---	18.20	18.20	---	19.85	17.10
FeO^{CM}	14.81	16.62	14.77	14.54	11.84	19.59	19.16	19.25	20.06	22.73	19.38	17.71
FeO^{CL}	12.08	14.81	11.78	12.53	7.49	16.97	16.95	17.22	18.44	21.32	16.78	16.56
$Fe_2O_3^{CM}$	3.03	2.01	3.31	2.23	4.84	2.90	2.45	2.24	2.03	1.56	2.89	1.27
MgO	11.2	10.1	12.1	10.2	12.9	8.15	7.86	7.92	9.04	5.08	7.22	9.34
MnO	1.05	0.50	0.59	0.67	1.08	0.65	1.08	0.74	0.71	1.50	0.51	0.51
TiO_2	1.01	1.71	0.76	2.76	1.17	0.60	1.29	1.59	0.25	1.37	1.26	1.51
CaO	11.0	11.2	11.2	10.9	9.94	9.96	10.7	10.7	11.8	10.7	10.7	11.2
Na_2O	1.10	1.60	0.85	2.58	1.75	1.09	1.42	1.31	0.53	1.85	1.24	1.10
K_2O	0.44	0.97	0.40	0.65	0.42	0.57	0.88	0.80	0.43	1.14	0.61	0.76
Cl	0.05	0.08	0.04	0.03	0.08	0.10	0.19	0.08	0.02	0.13	0.04	0.06
F	0.39	0.24	0.20	0.53	0.52	0.41	0.45	0.28	0.23	0.80	0.14	0.19
	97.63	98.23	98.52	98.19	98.36	97.54	98.52	98.32	99.34	98.32	98.50	97.91
Si	7.144	6.770	7.271	6.282	7.032	7.194	6.894	6.900	7.408	6.655	6.779	7.013
Al	0.856	1.230	0.729	1.718	0.968	0.806	1.106	1.100	0.593	1.345	1.221	0.987
Al	0.158	0.226	0.121	0.298	0.093	0.329	0.285	0.313	0.205	0.332	0.488	0.351
Fe^{3+}	0.341	0.227	0.367	0.253	0.536	0.333	0.281	0.255	0.228	0.184	0.328	0.143
Fe^{2+}	1.851	2.092	1.818	1.831	1.459	2.496	2.442	2.439	2.500	2.985	2.445	2.223
Mg	2.500	2.262	2.643	2.291	2.829	1.851	1.785	1.789	2.007	1.189	1.623	2.089
Mn	0.133	0.064	0.074	0.086	0.135	0.084	0.139	0.095	0.090	0.200	0.065	0.065
Ti	0.114	0.194	0.084	0.313	0.130	0.069	0.148	0.181	0.028	0.162	0.143	0.170
XOCT	0.097	0.065	0.107	0.072	0.182	0.162	0.080	0.072	0.058	0.052	0.092	0.041
Ca	1.767	1.804	1.771	1.760	1.569	1.626	1.747	1.742	1.877	1.804	1.727	1.803
Na	0.136	0.131	0.122	0.168	0.249	0.212	0.173	0.186	0.065	0.144	0.181	0.156
Na	0.183	0.336	0.120	0.585	0.251	0.109	0.246	0.200	0.088	0.420	0.182	0.164
K	0.084	0.186	0.075	0.125	0.079	0.111	0.171	0.155	0.082	0.228	0.117	0.146
Σ(A)	0.267	0.522	0.195	0.710	0.330	0.220	0.417	0.355	0.170	0.648	0.299	0.310
Fe/Fe+Mg	0.467	0.506	0.453	0.476	0.414	0.604	0.604	0.601	0.576	0.727	0.631	0.531
Na/Na+K	0.792	0.715	0.763	0.858	0.864	0.743	0.710	0.713	0.651	0.712	0.756	0.687
Mn/Mn+Fe	0.0572	0.0269	0.0328	0.0396	0.0634	0.0288	0.0486	0.0341	0.0319	0.0594	0.0229	0.0267
$Mg/Mg+Fe^{2+}$	0.57	0.52	0.59	0.56	0.66	0.43	0.42	0.42	0.45	0.28	0.40	0.48

TABLE 3. (continued)

	T-128 Late(2)	T-75 Core(3)	T-75 Late	T-168 Av(4)	T-79 Core(3)	T-79 Late(2)
SiO_2	47.6	43.4	43.1	44.8	48.5	51.9
Al_2O_3	7.06	9.94	11.3	9.41	6.29	3.70
FeO^T	19.8	23.0	23.4	21.4	15.5	14.6
FeO^M	17.10	19.93	19.93	—	13.89	13.89
FeO^{CM}	18.27	22.01	21.94	20.20	14.99	14.30
FeO^{CL}	16.77	20.97	20.70	19.00	14.49	14.03
$Fe_2O_3^{CM}$	1.66	1.14	1.59	1.33	0.55	0.29
MgO	9.09	5.85	5.35	7.11	11.6	13.1
MnO	0.62	0.60	0.52	0.65	0.42	0.35
TiO_2	0.83	1.40	0.27	1.10	1.35	0.20
CaO	11.4	11.1	11.5	11.2	11.7	12.2
Na_2O	0.82	1.30	0.97	1.09	0.75	0.32
K_2O	0.69	1.27	1.11	1.11	0.61	0.29
Cl	0.04	0.10	0.02	0.06	0.04	0.00
F	0.19	0.38	0.32	0.23	0.15	0.12
	98.27	98.49	97.99	98.29	96.95	96.77
Si	7.126	6.682	6.645	6.816	7.217	7.640
Al	0.874	1.318	1.355	1.184	0.783	0.360
Al	0.374	0.487	0.703	0.502	0.320	0.282
Fe^{3+}	0.187	0.133	0.185	0.152	0.062	0.032
Fe^{2+}	2.290	2.835	2.829	2.569	1.866	1.761
Mg	2.030	1.343	1.230	1.611	2.566	2.868
Mn	0.079	0.078	0.068	0.084	0.053	0.044
Ti	0.094	0.162	0.031	0.126	0.151	0.022
XOCT	0.054	0.038	0.046	0.044	0.018	0.009
Ca	1.824	1.830	1.903	1.828	1.866	1.919
Na	0.122	0.132	0.051	0.128	0.116	0.072
Na	0.116	0.256	0.239	0.193	0.100	0.019
K	0.132	0.250	0.218	0.215	0.116	0.055
Σ(A)	0.248	0.506	0.457	0.408	0.216	0.074
Fe/Fe+Mg	0.550	0.688	0.710	0.628	0.429	0.385
Na/Na+K	0.643	0.608	0.571	0.599	0.651	0.623
Mn/Mn+Fe	0.0309	0.0256	0.0221	0.0229	0.0268	0.0240
$Mg/Mg+Fe^{2+}$	0.47	0.32	0.30	0.39	0.58	0.62

	PYROXENES H-72(2)	H-72(6)	H-89	H-89	MY-6(3)	T-128(3)
SiO_2	51.5	52.5	52.6	51.7	51.6	52.3
Al_2O_3	0.93	0.70	0.37	2.16	0.36	0.38
FeO^T	29.7	14.2	28.4	9.50	15.9	14.4
$Fe_2O_3^C$	1.06	0.44	0.0	1.69	0.43	0.0
FeO^C	28.73	13.75	28.43	7.98	15.53	14.36
MgO	16.8	11.7	17.8	15.0	8.73	9.46
MnO	0.75	0.37	1.05	0.27	0.96	0.88
TiO_2	0.25	0.10	0.04	0.51	0.00	0.00
CaO	1.80	20.9	1.02	20.4	22.5	22.5
Na_2O	0.04	0.22	0.03	0.26	0.17	0.13
K_2O	0.06	0.00	0.00	0.05	0.06	0.00
	101.92	100.68	101.34	100.02	100.34	100.01
Si	1.958	1.983	1.995	1.924	1.992	2.001
Al	0.042	0.017	0.005	0.076	0.008	0.000
Al	0.000	0.015	0.011	0.019	0.008	0.017
Fe^{2+}	0.913	0.435	0.902	0.249	0.501	0.461
Fe^{3+}	0.030	0.013	0.000	0.047	0.012	0.000
Mg	0.950	0.660	1.006	0.831	0.502	0.541
Mn	0.024	0.012	0.034	0.009	0.031	0.029
Ti	0.007	0.003	0.001	0.014	0.000	0.000
Ca	0.073	0.847	0.041	0.812	0.932	0.925
Na	0.003	0.016	0.002	0.019	0.013	0.010
Σ	2.001	2.001	1.998	2.000	2.000	1.982
Fe/Fe+Mg	0.498	0.404	0.473	0.263	0.505	0.460
Mn/Mn+Fe	0.025	0.026	0.036	0.030	0.057	0.059
$Mg/Mg+Fe^{2+}$	0.51	0.60	0.53	0.77	0.50	0.54
QUAD	95.83	97.01	98.77	91.96	97.93	98.28
WO	3.79	43.62	2.13	42.92	48.15	48.02
EN	49.04	33.90	51.60	43.94	25.95	28.07
FS	47.17	22.39	46.27	13.14	25.90	23.91

The structural formulae for Table 3 have been calculated using the program of *Papike et al.* [1974] based on 23 oxygen atoms. For the amphiboles, FeO^{CM} and $Fe_2O_3^{CM}$ were the values utilized (and are the values included in the oxide totals); for the pyroxenes, FeO^C and $Fe_2O_3^C$. For the amphiboles, FeO^M values are wet chemical determinations of FeO, whereas FeO^{CL} values are minimum FeO contents calculated by the program. Wet chemical determinations of FeO content were made by S. Neil, Branch of Analytical Laboratories, U.S. Geological Survey. For both minerals, FeO^T values represent electron microprobe determinations of total iron expressed as FeO. See text for clarification. Note that the pyroxene program does not accept K_2O, so that the minor amounts found are neglected in the calculations.

*Late is used paragenetically; it is preferred to 'rim' or other textural terms because some 'late' amphibole may occur as uniform, whole grains. See the appendix and the text for elucidation.

**Number in parentheses indicates the number of discrete analyses (separate grains) included in the composition presented. 'Av(3),' as a column heading, signifies that the analysis represents the average of three, relatively homogeneous grains of essentially similar composition. No numerical entry indicates a single analysis.

***The wet chemical FeO value determined for the mineral separate is listed for both 'core' and 'late' compositions.

173B. *Ishihara and Terashima* [1977*a*, Figure 3] were impressed by the heterogeneity of the Ryoke granitoids at their location 43, as evidenced by 7- to 10-cm-wide bands that are relatively poor (T-173B) or rich (T-173A) in biotite as well as showing notable distinctions in modal content of plagioclase and K-feldspar. Microprobe analyses of biotites from the two facies are identical; thus, the bands are presumably in equilibrium, whatever their origin. Additional, mineralogical data were obtained only for T-173B.

Pyroxenes

Pyroxenes are present in only four of the specimens studied; their analyses are reported in the lower part of Table 3. Structural formulae, partitioning of iron, and QUAD components have been calculated with the program of *Papike et al.* [1974]. The orthopyroxenes in Hiroshima granite specimens H-72 and H-89 lie near the ferrohypersthene limit of hypersthene composition. They have significantly higher Fe/(Fe+Mg) than associated clinopyroxenes. The clinopyroxenes are uniformly high in CaO and low in Al_2O_3 and TiO_2. As expected, Fe/(Fe+Mg) is lower for clinopyroxenes than for coexisting amphiboles. Mn/(Mn+Fe) is higher in clinopyroxenes than in coexisting amphiboles, in agreement with the observations of *Czamanske and Wones* [1973]. These Japanese pyroxenes display a linear relation between unit cell contents of Ti and Al^{IV}, similar to that noted by Czamanske and Wones, but the atomic ratio is near 1 Ti to 6 Al^{IV} rather than 1 Ti to 3 Al^{IV}.

Chlorites

Chlorite replacing biotite (filling voids in 6510-132 and 5907-55) has been analyzed from all but specimen 6511-213 in which a phase that appeared to be chlorite proved to be a late green biotite. Chlorite analyses were made concurrently with the biotite analyses for each sample, using the same standards. Where possible, two chlorite analyses were obtained for each sample, but for 10 samples only one good analysis was practical. Fifteen pairs of analyses differed in SiO_2, Al_2O_3, and FeO^T by averages of only 0.33, 0.49, and 0.34 wt %, respectively; for these, one analysis was chosen for presentation. For eight samples (so noted in Table 4), averages were made because one or more among SiO_2, Al_2O_3, and FeO^T differed by up to 2.00, 2.29, and 1.82 wt %, respectively. Sample 6510-132

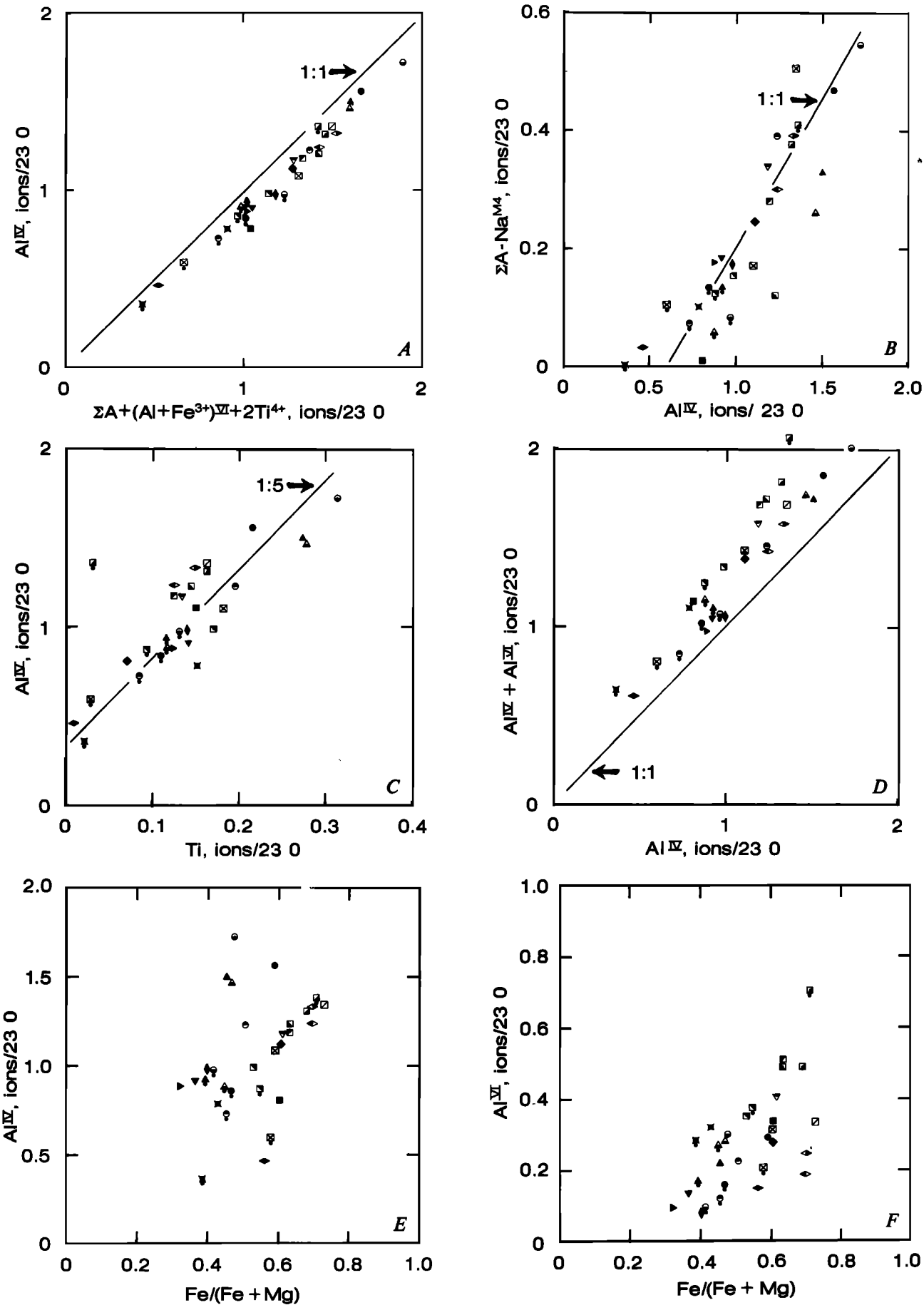

Fig. 7. Presentation of compositional relations for amphiboles from the Chubu and Central Chugoku transects, based on atoms/23 oxygens. (*a*). A-site occupancy + $Al^{VI} + Fe^{3+} + 2Ti^{4+}$ versus Al^{IV}. (*b*) Al^{IV} versus A-site occupancy minus Na^{M4}. (*c*). Ti versus Al^{IV}. (*d*) Al^{IV} versus $Al^{IV} + Al^{VI}$. (*e*). Fe/(Fe+Mg) versus Al^{IV}. (*f*) Fe/(Fe+Mg) versus Al^{VI}.

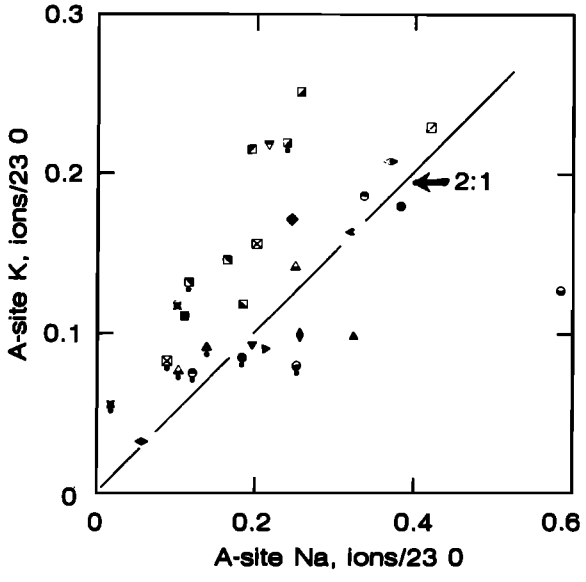

Fig. 8. Relation between contents of Na and K in the amphibole A-sites.

is exceptional in that it contains chlorite with both the lowest and highest Fe/(Fe+Mg) observed. Petrographic study gives no obvious clue to a unique origin for the high-iron chlorite, although it appears to be the less abundant variety; it shows up as aberrant on most data plots. The analytical data show that there is nothing particularly distinctive among any of these chlorites and that they are composed essentially of Si, Al, Fe, Mg, Mn, F, and (OH). On the one hand, therefore, these data support the position of *Albee* [1962] and *Deer et al.* [1971] that Ca, K, and Na typically occur in impurities in chlorite; on the other hand, these microprobe analyses suggest that sometimes these elements are adsorbed or occur as interlayer cations. The analyses also suggest that Ti is not typically an important constituent of chlorite. A plot of Fe/(Fe+Mg) for biotites versus chlorites (Figure 12) shows that this ratio is well preserved by the chlorites. The correlation between Fe/(Fe+Mg) of rocks and chlorites is much poorer, producing a plot quite similar to Figure 6. Nearly as well maintained is the relation between Mn content of biotites and chlorites. This relation is evident in plots of $Mn/(M_1-M_2)$, Mn/(Mn+Fe), and $Mn/(Mn+Fe^{+2})$ for biotites versus, respectively, Mn/Σ, Mn/(Mn+Fe), and Mn/(Mn+Fe) for chlorites; the latter is shown as Figure 13. Note that specimens representing individual suites follow the general trend fairly well. The plot of Mn/(Mn+FE) for both biotites and chlorites is quite similar in aspect, but a best fit line would be slightly displaced toward relatively higher Mn/(Mn+Fe) in chlorite. There is thus the suggestion, also seen in Figure 12, that relative to Mn and Mg, the chlorites are slightly depleted in total (principally ferric) iron in relation to their biotite precursors. Si contents of the chlorites range from 5.274 to 6.031 and, combined with Fe/(Fe+Mg) ranging from 0.378 to 0.990, lead to classification as pycnochlorites, ripidolites, brunsvigites, and daphnites [*Deer et al.*, 1971]. There is no correlation of chlorite Si content with whole-rock silica content or with Fe/(Fe+Mg) of the chlorite. There is little correlation between the Si contents of biotite and derived chlorite and only a weak, general correlation between the total Al contents of these two phases (Figure 14); specimens from the Busetsu pluton containing primary muscovite are a notable exception. The data of Table 4 show that Al in six-fold positions always exceeds that in four-fold coordination; respective averages are 2.603 and 2.383 cations; a plot of the data shows that this spread is independent of total Al content. Fe^{3+} and (OH) have not been (and cannot be) determined for this group of chlorites, and a detailed discussion of structural chemistry in the sense of *Albee* [1962] is unwarranted. Even among apparently superior, complete analyses, Albee found many deviations from ideality. Nonetheless, it is intriguing that a good inverse correlation exists between the sum of octahedral cations (Σ) and $Al^{VI} - Al^{IV}$ (Figure 15). The correlation is well shown for the two chlorites in 6510-132. The sum of the octahedral cations averages 11.845; this average total site deficiency of 0.155 compares to the average Al^{VI} excess of 0.220 cations. These values suggest that (1) the excess of Al^{VI} over Al^{IV} is at least partially balanced by octahe-

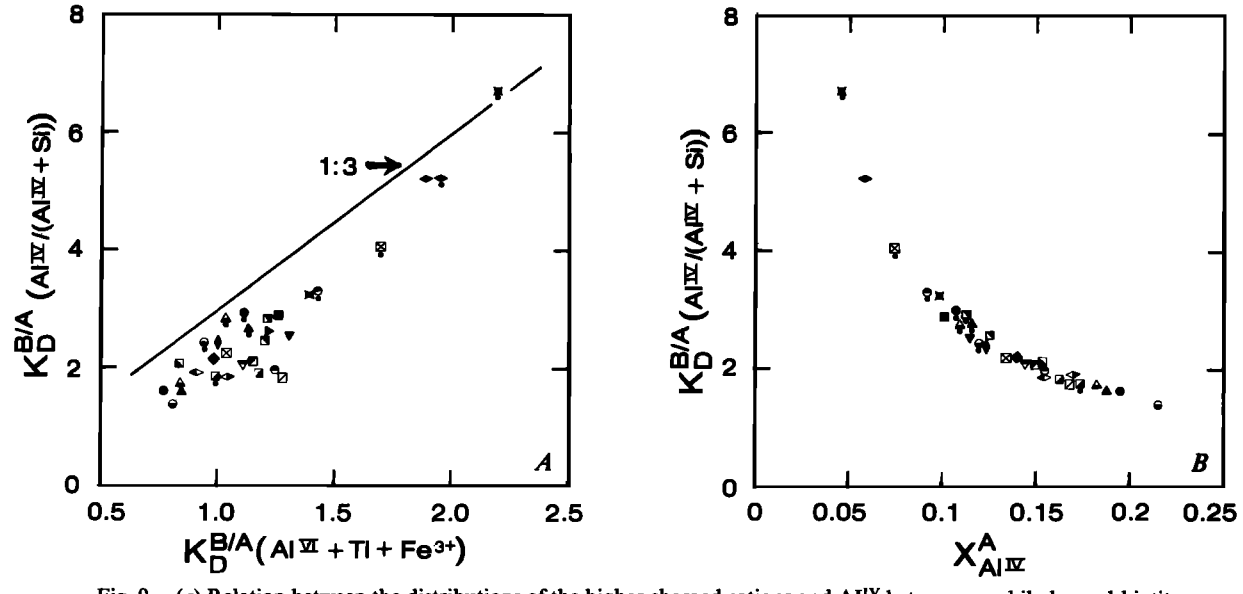

Fig. 9. (*a*) Relation between the distributions of the higher charged cations and Al^{IV} between amphiboles and biotites. (*b*) Relation between the mole fraction of Al^{IV} in amphiboles and the distribution of Al^{IV} between amphiboles and biotites.

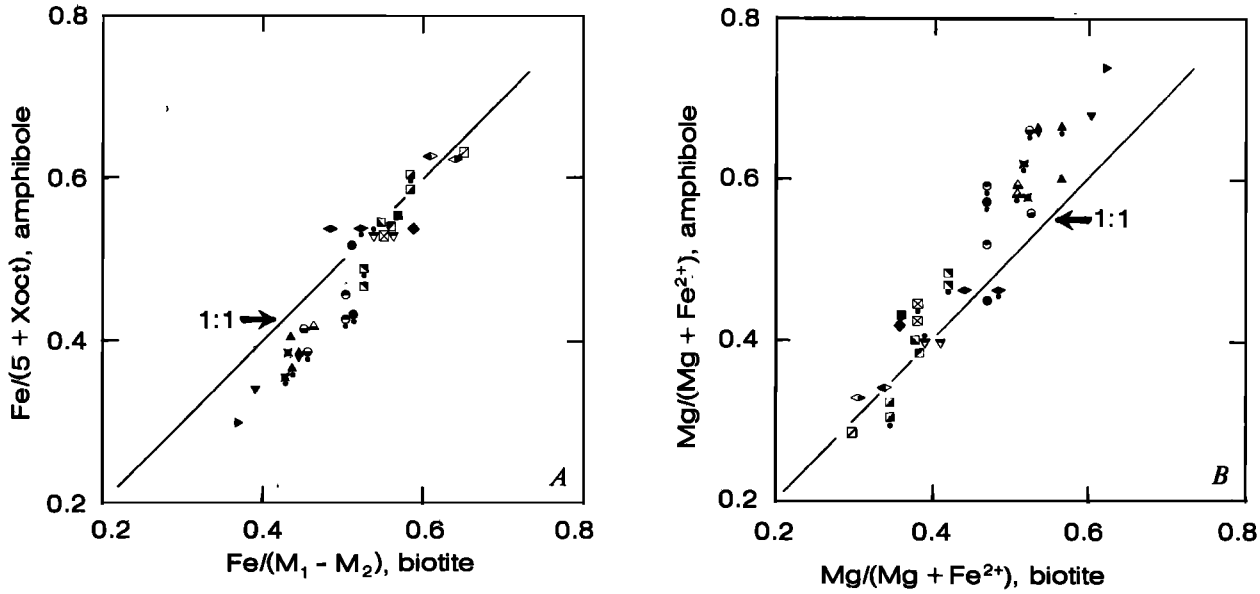

Fig. 10. (*a*) Relation between $Fe/(M_1-M_2)$ in biotites and Fe/(5+Xoct) in amphiboles. (*b*). Relation between Mg/Mg+Fe^{2+}) for biotites and amphiboles.

dral site vacancies, and (2) the ferric iron contents of these chlorites are low and fairly uniform. If the overall quality of the analyses is as high as we would hope, there is also the suggestion that some of the excess Al^{VI} must be balanced by deficiency of H [cf., *Albee*, 1962]. It is notable that formation of chlorite has been accompanied by total removal of Cl, whereas all chlorites contain minor F, although not in amounts that correlate well with those contained in their biotite precursors.

Muscovites

Procedures used for analysis of the mafic silicates were followed for muscovite with the exception that grains from an analyzed sample of Methuen muscovite were used as the standard for Al, K, and Si. Muscovite is present in six of the specimens studied (Table 4) but on petrographic grounds [e.g., *Miller et al.*, 1981] is considered to have been a stable, solidus phase only in samples T-173B, T-76, and T-133 from the Busetsu pluton of the Ryoke III zone of the Chubu transect. The estimated emplacement pressure of 5 kbar for the Busetsu pluton is well within the stability limit of muscovite [*Day*, 1973]. For three samples, consistent chemical distinction has led us to report data for cores and rims of grains.

There are significant differences in the chemistry of the primary and secondary muscovites. The primary muscovites are markedly lower in FeO^T, despite their occurrence in rocks which contain less SiO_2 and, on the average, more total iron; they also contain less MnO and K_2O and more Al_2O_3, TiO_2, and Na_2O. In each case where two compositions are reported for a specimen, evolution has produced muscovites that contain more FeO^T, MgO, and F. Although the data base is small, it is notable that most of the chemical distinctions between primary and secondary muscovites are not mimicked by those between two generations of muscovite in a single specimen.

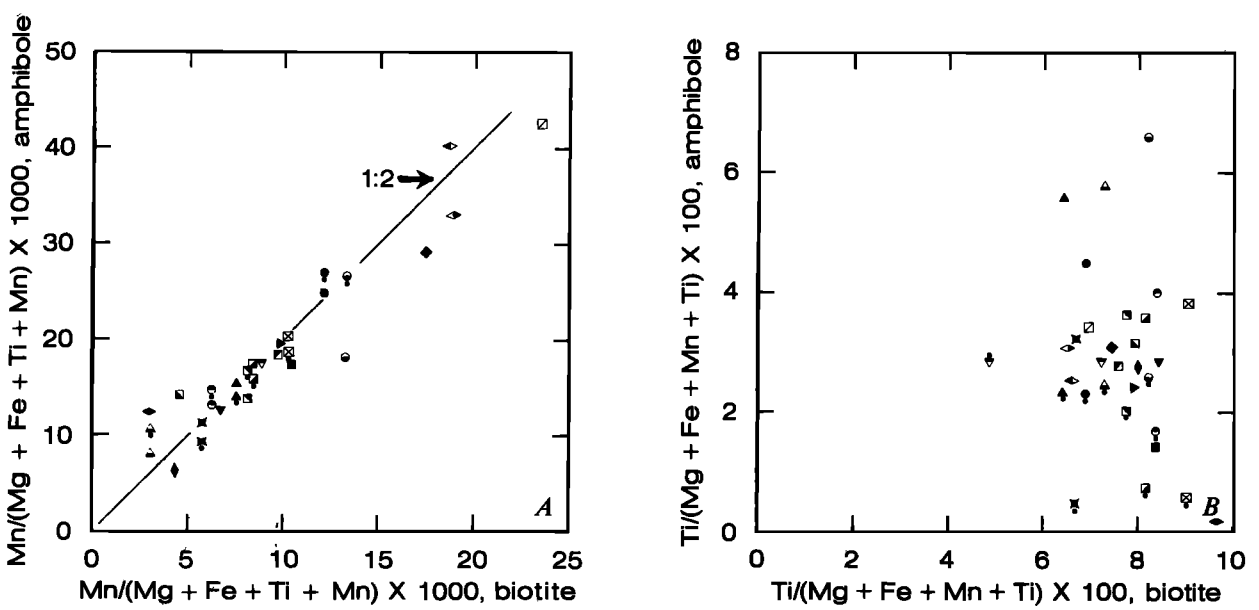

Fig. 11. (*a*) Distribution of manganese between amphiboles and biotites. (*b*) Distribution of titanium between amphiboles and biotites.

In a recent report, *Miller et al.* [1981] characterize primary muscovites as richer in Ti, Na, and Al and poorer in Mg and Si than secondary muscovites. Our data and those of Miller et al. are thus in agreement with regard to those elements enriched in primary muscovites, but we have not found lower concentrations of MgO and SiO_2.

Feldspars

Stormer [1975] refined a practical, two-feldspar geothermometer which has been used with success on granitic and high-grade metamorphic rocks [e.g., *Whitney and Stormer*, 1976; *Bohlen and Essene*, 1977]. Subsequently, *Whitney and Stormer* [1977] extended the use of the geothermometer by consideration of ordered, lower temperature alkali feldspars such as may be involved in slow crystallization of granitic plutonic rocks. We have analyzed the feldspars in all units in an attempt to obtain equilibration temperatures and to glean information relevant to the cooling histories of the diverse suites. Accurate data for Ca, K, and Na content were obtained using wavelength-dispersive spectrometers and well-characterized feldspar standards; Al and Si counts were simultaneously gathered on an EDS system to allow correction of the alkali data. Typically, analyses were obtained for three pairs of contiguous alkali feldspar and plagioclase grains. Plagioclase grains were analyzed at intervals from core to rim with a well-focused beam. The typically perthitic alkali feldspars were analyzed by actively traversing a defocused beam about 30 μm wide along parallel paths over large parts of the grains for ten 20-s count intervals. Recrystallized rims on plagioclase and alkali feldspar were avoided, although analyses of presumed late albite rims on plagioclase grains are reported for several specimens in the appendix, where feldspar textural relations are given for all specimens. (Numerical ranges for Or content of alkali feldspar and Ab and Or content of plagioclase are also given in the rock descriptions of the appendix. An content of all analyzed alkali feldspars falls in the range 0.3 to 1.2 mol %.)

Data for all analyzed feldspars are represented on Figure 16 as fields in relation to isotherms photocopied from *Stormer* [1975] and based on disordered alkali feldspar. Rock suites have been plotted on diagrams appropriate to estimated confining pressures. These estimates are based on sphalerite geobarometry [*Shimizu and Shimazaki*, 1979] and the fact that primary muscovite is only stable above 3–4 kbar [*Day*, 1973]. Considering the labor required to produce Figure 16, the result is disappointing, though not entirely unexpected. None of our suites faithfully retains solidus feldspar relations even if ordered alkali feldspars were involved in $NaAlSi_3O_8$ codistribution. Figure 16 suggests that, in general, the feldspars throughout both transects have undergone similar significant amounts of alkali exchange and reequilibration despite the shallower levels of intrusion indicated for the Sanin belt. One important revelation of our feldspar study is that plagioclase from all suites is zoned, with some zoning for silicic Ryoke specimens far in excess of what might be expected for magmas generated by high-level partial melting. Moreover, for all suites the compositional range of zoning is congruent with host rock composition.

Cl and F

We accepted *Ludington*'s [1978] challenge to investigate the halogen contents of apatites and the mafic silicate minerals in the hope of obtaining magmatic equilibration temperatures. This goal was not attained, but the data are of petrologic interest and bear on the crystallization histories of the rock suites. As noted, natural sodalite (PSU-4-296-8, 6.82 wt % Cl) was used as the Cl standard; fluorine contents for amphiboles, biotites, and chlorites are standardized to a synthetic fluorphlogopite (9.01 wt % F), those for apatites to Wilberforce apatite (3.67 wt % F). Typically, the three to five apatite grains chosen for analysis were contained with analyzed biotites. Several of the samples contain apatites whose F contents appear to exceed the theoretical maximum (3.77 wt %). We are unable to explain this but have communicated with several others who have obtained similar results [e.g., *Wones*, 1980].

Our data show that the Cl contents of amphiboles and biotites in these rocks are comparable and low (<0.3 wt %) and that chlorite typically contains no chlorine. In contrast, F is typically present in chlorite (total range 0.06–0.30 wt %), and biotites contain significantly more F than coexisting amphiboles. Where two amphibole or biotite compositions are reported for a sample, there are no regular or significant differences in Cl and F content. There appears to be no significant distinction among the eight suites in halogen content of the mafic silicates, a rather surprising result. However, within individual suites, F contents of biotites and amphiboles typically increase with SiO_2 content, whereas Cl contents show little change or decrease. Associated apatites show the same trends (Table 5) though less pronounced for F and more extreme for Cl. It is striking that aside from the two magnetite series suites, only (and all) rocks with $\leq$60 wt % SiO_2 contain apatite with significant Cl content. Equally impressive is the fact that Cl is present in apatites representing the full range of rock compositions from the two magnetite series suites which have crystallized in a progressively more oxidizing environment. Our additional evidence for high Cl activity as a distinction of magnetite series from ilmenite series magmas supports the concepts of *Ishihara and Terashima* [1977*b*] and *Burnham and Ohmoto* [1980], who relate the characteristics of sulfide mineralization and Cl activity for these suites. *Fuge* [1977] has suggested that although F concentrations are highest in late stage differentiates, Cl concentrations are highest in earlier differentiates. Our data for amphiboles, biotites, and apatites indicate that the behavior of Cl is less regular than he suggests but may be predictable. *Ishihara and Terashima* [1977*b*] and others have considered that the F content of magmas may be important in controlling chemical variation and associated mineralization. Granitoids rich in Cl and F are found to contain polyphase inclusions and fluorite [*Ishihara and Terashima*, 1977*b*; *Terashima and Ishihara*, 1980], and mineralization may be related to late-stage concentration of Cl and F.

Highly fluorinated apatite compositions and modest fluorine contents of biotite for our specimens combine to indicate equilibration temperatures that are typically of the order of 300°C or less. Possible explanations for these data are that (1) biotites have lost F, or (2) apatites have become enriched in F. Equilibrium cooling in a closed system ($\log f_{H_2O}/f_{HF}$ = constant) would essentially be a variant of explanation 1 in that F loss from biotite would predominate. It is difficult for us to imagine that apatites within biotite grains would take up fluorine preferentially, and our first inclination was to make the more conventional assumption that low-equilibration temperatures reflect substantial loss of F from biotite. A corollary of this position is that fluorine-rich magmas have been involved in each of the suites we have studied. However, consideration of F/(F+OH) versus X_{phlog} relations in biotites suggests

that the anomalous relation between fluorine contents of apatites and biotites should not be oversimplified.

The f_{H_2O}/f_{HF} of a coexisting gas phase can be estimated from the F content of an unreacted biotite if its Mg content is known [*Munoz and Ludington*, 1974]. Figure 17 is a plot of F/(F+OH) versus X_{phlog} (Table 1) for the Japanese biotites we have studied; contours are drawn for selected temperatures at values of log f_{H_2O}/f_{HF} equal to 3, 4, and 5. The dilemma that we have discussed is readily apparent: many of studied biotites are indicated to have crystallized at a relatively high log f_{H_2O}/f_{HF} of 4.5 to 5, yet contain fully fluorinated apatites. The tendency for biotites from individual suites to fall near one another is often more a function of X_{phlog} than of F/(F+OH). It is notable, however, that for most suites there is indication of decreasing log f_{H_2O}/f_{HF} with increasing SiO_2 content. Figure 17 is quite similar to Figure 7 of *Kanisawa et al.* [1979] in that biotites from the Sanin belt, the Naegi granites, and the Ryoke belt are similarly situated.

Oxides

Previous experience with Fe, Ti-oxide phases in plutonic rocks [e.g. *Czamanske and Mihalik*, 1972; *Czamanske et al.*, 1977] has shown that reequilibration is common, and studies by *Tsusue and Ishihara* [1974] and *Tainosho et al.* [1979] show this to be typical for the Japanese granitoids. Nonetheless, a reconnaissance was made of Fe, Ti-oxide phase compositions in rocks of the Daito-Yokota and Takanawa Peninsula suites which show the most regular and opposing trends in X_{annite} for biotites (Table 1 and Figure 4) with increasing silica content. Electron microprobe analyses (for analytical techniques, see *Czamanske and Mihalik* [1972]) show that ilmenites are commonly variable in composition within a given specimen and

TABLE 4. Electron Microprobe Analyses and Structural Formulae for Chlorites and Muscovites From the Chubu and Central Chugoku Transects, Japan

CHLORITES

	KAT-1*	6412-17	6510-116	6510-132		5907-55	H-72	H-89	H-93	H-77	H-98	MY-15	MY-6	MY-2	MY-1
SiO_2	26.0	27.1	27.9	26.6	22.6	27.1	27.8	28.1	26.6	24.9	25.1	26.1	24.6	25.7	23.9
Al_2O_3	20.2	19.0	17.3	20.7	22.1	20.6	16.3	17.7	16.0	18.4	18.8	20.1	20.6	19.4	20.2
FeO^T	22.9	21.1	21.9	19.8	40.4	21.0	29.1	22.7	32.5	34.8	36.5	27.4	31.3	34.7	37.3
MgO	16.8	17.9	17.6	18.2	0.22	17.2	13.5	17.5	9.37	7.12	7.27	14.1	10.4	7.22	5.84
MnO	0.82	0.59	0.84	0.90	1.85	1.07	0.25	0.30	1.14	1.55	0.91	0.24	0.70	0.85	1.39
TiO_2	0.01	0.00	0.01	0.06	0.00	0.00	0.04	0.00	0.08	0.00	0.03	0.00	0.02	0.16	0.08
CaO	0.00	0.00	0.00	0.00	0.01	0.00	0.07	0.00	0.16	0.00	0.03	0.02	0.00	0.00	0.06
Na_2O	0.04	0.02	0.03	0.04	0.06	0.05	0.01	0.01	0.01	0.00	0.03	0.01	0.01	0.02	0.02
K_2O	0.00	0.00	0.00	0.00	0.00	0.00	0.00	0.00	0.00	0.00	0.00	0.00	0.01	0.01	0.00
Cl	0.00	0.00	0.00	0.00	0.00	0.00	0.00	0.00	0.00	0.00	0.00	0.00	0.00	0.00	0.00
F	0.06	0.06	0.16	0.27	0.10	0.30	0.12	0.11	0.21	0.19	0.11	0.10	0.10	0.12	0.16
	86.83	85.77	85.74	86.57	87.34	87.32	87.19	86.42	86.07	89.96	88.78	88.07	87.74	88.18	88.95
Si	5.494	5.714	5.926	5.526	5.274	5.611	6.012	5.919	5.998	5.640	5.590	5.530	5.376	5.680	5.359
Al	2.506	2.286	2.074	2.474	2.726	2.389	1.988	2.081	2.002	2.360	2.410	2.470	2.624	2.320	2.641
Al	2.508	2.443	2.240	2.597	3.336	2.643	2.171	2.306	2.252	2.544	2.508	2.563	2.674	2.735	2.688
Fe	4.044	3.730	3.893	3.428	7.867	3.627	5.272	4.004	6.120	6.596	6.805	4.858	5.727	6.419	6.976
Mg	5.272	5.621	5.577	5.642	0.076	5.310	4.349	5.483	3.144	2.405	2.413	4.448	3.400	2.379	1.945
Mn	0.147	0.105	0.150	0.158	0.365	0.188	0.046	0.054	0.217	0.296	0.171	0.043	0.130	0.160	0.264
Ti	0.002	0.000	0.001	0.009	0.000	0.000	0.007	0.000	0.014	0.000	0.005	0.000	0.003	0.026	0.014
Ca	0.000	0.000	0.000	0.000	0.002	0.000	0.016	0.000	0.038	0.000	0.007	0.004	0.000	0.000	0.014
Na	0.015	0.006	0.011	0.016	0.027	0.017	0.002	0.004	0.003	0.002	0.009	0.006	0.002	0.007	0.007
K	0.000	0.000	0.000	0.000	0.000	0.000	0.000	0.000	0.000	0.001	0.000	0.000	0.002	0.002	0.000
Σ	11.988	11.905	11.872	11.850	11.673	11.785	11.863	11.851	11.788	11.844	11.918	11.922	11.938	11.728	11.908
F	0.038	0.042	0.104	0.174	0.073	0.197	0.080	0.075	0.151	0.132	0.073	0.064	0.071	0.087	0.111
Fe/Fe+Mg	0.434	0.399	0.411	0.378	0.990	0.405	0.548	0.422	0.661	0.733	0.738	0.522	0.628	0.730	0.782
Mn/Mn+Fe	0.0351	0.0274	0.0371	0.0441	0.0443	0.0493	0.0086	0.0133	0.0342	0.0429	0.0245	0.0088	0.0222	0.0243	0.0365

	RS-88	RS-37	RS-69	RS-87	RS-91	T-41	T-38	T-44	T-25	T-97	T-94	T-145	T-165	T-128	T-75
SiO_2	26.7	27.2	27.4	26.0	27.5	25.9	26.4	23.8	23.5	25.6	25.8	25.5	25.7	26.0	25.3
Al_2O_3	17.9	18.8	17.6	18.7	16.7	19.1	17.9	20.4	20.9	20.0	18.6	19.0	20.1	20.0	20.3
FeO^T	28.3	27.2	26.2	27.4	27.8	30.1	32.2	40.4	40.7	30.9	35.0	34.6	34.1	30.0	33.4
MgO	12.8	14.1	14.9	12.7	11.7	9.33	9.51	2.87	3.12	10.5	7.81	7.01	9.52	12.2	8.89
MnO	0.51	0.46	0.81	0.74	2.26	0.68	0.96	2.02	1.42	0.67	0.89	1.65	0.26	0.62	0.64
TiO_2	0.06	0.07	0.08	0.01	0.04	0.03	0.07	0.07	0.03	0.00	0.22	0.10	0.01	0.04	0.04
CaO	0.07	0.01	0.08	0.00	0.01	0.02	0.03	0.00	0.03	0.01	0.02	0.02	0.00	0.04	0.04
Na_2O	0.04	0.01	0.04	0.04	0.11	0.03	0.03	0.04	0.01	0.02	0.01	0.00	0.01	0.02	0.02
K_2O	0.00	0.11	0.00	0.00	0.07	0.22	0.00	0.05	0.00	0.00	0.01	0.00	0.00	0.00	0.00
Cl	0.00	0.00	0.00	0.00	0.00	0.00	0.00	0.00	0.00	0.00	0.00	0.00	0.00	0.00	0.00
F	0.21	0.14	0.12	0.12	0.21	0.14	0.20	0.08	0.13	0.12	0.21	0.13	0.09	0.11	0.16
	86.59	88.10	87.23	85.71	86.40	85.55	87.30	89.73	89.84	87.82	88.57	88.01	89.79	89.03	88.79
Si	5.807	5.765	5.843	5.705	6.031	5.767	5.828	5.377	5.305	5.555	5.689	5.679	5.539	5.539	5.506
Al	2.193	2.235	2.157	2.295	1.969	2.233	2.172	2.623	2.695	2.445	2.311	2.321	2.461	2.461	2.494
Al	2.388	2.449	2.276	2.524	2.350	2.781	2.483	2.823	2.853	2.687	2.532	2.672	2.631	2.567	2.709
Fe	5.140	4.812	4.676	5.027	5.099	5.618	5.946	7.652	7.679	5.616	6.468	6.432	6.141	5.346	6.096
Mg	4.164	4.460	4.748	4.145	3.818	3.098	3.127	0.970	1.050	3.405	2.570	2.325	3.056	3.864	2.887
Mn	0.094	0.082	0.147	0.136	0.419	0.128	0.180	0.387	0.271	0.123	0.166	0.311	0.048	0.112	0.119
Ti	0.010	0.012	0.013	0.002	0.007	0.006	0.012	0.012	0.006	0.000	0.036	0.017	0.005	0.006	0.006
Ca	0.017	0.002	0.019	0.000	0.002	0.004	0.008	0.000	0.007	0.002	0.006	0.005	0.001	0.008	0.010
Na	0.016	0.005	0.016	0.018	0.045	0.014	0.014	0.016	0.003	0.010	0.006	0.001	0.005	0.006	0.010
K	0.000	0.032	0.000	0.000	0.021	0.062	0.000	0.014	0.000	0.000	0.001	0.000	0.000	0.000	0.000
Σ	11.829	11.854	11.895	11.852	11.761	11.711	11.770	11.874	11.869	11.951	11.785	11.763	11.887	11.909	11.837
F	0.144	0.094	0.084	0.080	0.147	0.096	0.138	0.058	0.093	0.081	0.146	0.089	0.068	0.073	0.108
Fe/Fe+Mg	0.553	0.519	0.496	0.548	0.572	0.645	0.655	0.888	0.880	0.623	0.716	0.735	0.668	0.581	0.679
Mn/Mn+Fe	0.0180	0.0168	0.0305	0.0263	0.0759	0.0223	0.0294	0.0481	0.0341	0.0214	0.0250	0.0461	0.0078	0.0205	0.0191

TABLE 4. (continued)

	T-168	T-79	T-173B	T-76	T-133	MUSCOVITES								
						6510-132 (1)**	T-25 Core(2)	T-25 Rim(2)	6511-213 (1)	T-173B Core(2)	T-173B Rim(2)	T-76 (3)	T-133 Core(2)	T-133 Rim(2)
SiO_2	25.4	25.7	24.4	24.5	24.5	SiO_2 46.8	45.3	44.2	45.3	45.7	46.1	45.4	46.0	45.7
Al_2O_3	20.5	21.3	21.9	20.8	21.8	Al_2O_3 30.8	31.8	33.2	33.3	36.1	34.7	35.9	36.4	35.7
FeO^T	32.0	23.7	34.1	32.4	32.7	FeO^T 4.76	4.06	6.38	6.76	1.27	1.89	1.38	1.24	1.62
MgO	10.1	15.2	8.00	8.95	7.99	MgO 1.54	0.41	0.45	0.28	0.51	0.85	0.60	0.54	0.71
MnO	0.71	0.47	0.87	0.50	0.65	MnO 0.06	0.19	0.20	0.22	0.03	0.04	0.02	0.02	0.04
TiO_2	0.00	0.00	0.02	0.00	0.03	TiO_2 0.34	0.04	0.00	0.01	0.53	0.35	0.45	0.35	0.51
CaO	0.00	0.00	0.02	0.00	0.02	CaO 0.00	0.00	0.00	0.00	0.00	0.00	0.00	0.00	0.08
Na_2O	0.02	0.05	0.02	0.03	0.05	Na_2O 0.14	0.26	0.24	0.40	0.59	0.42	0.54	0.61	0.60
K_2O	0.00	0.00	0.00	0.02	0.00	K_2O 11.02	11.09	10.99	10.70	10.80	10.87	10.69	10.48	10.66
Cl	0.00	0.00	0.00	0.00	0.00	Cl 0.00	0.00	0.02	0.06	0.00	0.00	0.01	0.00	0.04
F	0.13	0.10	0.18	0.10	0.21	F 0.20	0.65	0.82	2.23	0.17	0.25	0.08	0.24	0.58
	88.86	86.52	89.51	87.30	87.95	95.66	93.80	96.50	99.26	95.70	95.47	95.07	95.88	96.24
Si	5.497	5.444	5.287	5.411	5.366	Si 3.167	3.124	3.000	3.020	3.036	3.077	3.034	3.042	3.026
Al	2.503	2.556	2.713	2.589	2.634	Al 0.833	0.876	1.000	0.980	0.964	0.923	0.966	0.958	0.974
Al	2.706	2.763	2.888	2.825	2.989	Al 1.627	1.712	1.660	1.563	1.862	1.811	1.866	1.875	1.808
Fe	5.770	4.199	6.198	5.976	6.003	Fe 0.270	0.230	0.368	0.377	0.071	0.106	0.077	0.069	0.090
Mg	3.244	4.806	2.589	2.945	2.611	Mg 0.156	0.042	0.046	0.028	0.051	0.086	0.060	0.054	0.070
Mn	0.129	0.084	0.160	0.093	0.120	Mn 0.003	0.011	0.012	0.012	0.002	0.003	0.001	0.001	0.002
Ti	0.000	0.000	0.003	0.000	0.005	Ti 0.017	0.002	0.000	0.001	0.027	0.017	0.023	0.018	0.025
Ca	0.000	0.000	0.004	0.000	0.004	Σ 2.073	1.997	2.086	1.981	2.013	2.023	2.027	2.017	1.995
Na	0.001	0.019	0.008	0.012	0.022									
K	0.001	0.000	0.000	0.005	0.000	Ca 0.000	0.000	0.000	0.000	0.000	0.000	0.000	0.000	0.010
Σ	11.851	11.871	11.850	11.856	11.754	Na 0.019	0.035	0.032	0.052	0.076	0.054	0.065	0.079	0.076
						K 0.951	0.976	0.953	0.911	0.915	0.926	0.912	0.884	0.900
F	0.091	0.069	0.122	0.071	0.148	Σ 0.970	1.011	0.985	0.963	0.991	0.980	0.977	0.963	0.986
Fe/Fe+Mg	0.640	0.466	0.705	0.670	0.697									
Mn/Mn+Fe	0.0219	0.0196	0.0252	0.0153	0.0196	F 0.043	0.141	0.176	0.471	0.037	0.053	0.014	0.050	0.121

The structural formulae for Table 4 have been calculated on the basis of 28 oxygen equivalents for chlorites and 22 oxygen equivalents for muscovites. For both minerals only FeO^T, based on electron microprobe analysis, can be reported. Two distinct analyses are presented for specimen 6510-132. For all other specimens we report a single analysis (see text).
*A bar above the last part of the specimen number indicates that somewhat divergent analyses have been averaged.
**Number in parentheses indicates the number of discrete analyses represented by the values in the column below.

contain increasing amounts of Mn as host rock SiO_2 content increases (Table 6). In contrast, magnetites in all specimens from the Daito-Yokota suite have reequilibrated and contain minor elements in the following weight percent ranges: Al_2O_3, 0.1–0.3; MgO, 0.1–0.7; MnO, 0.0–0.15; TiO_2, 0.1–0.5; and V_2O_3, 0.2–0.6. More V-rich magnetites are found in the two more mafic rocks; more Mn-rich magnetites in the more siliceous rocks.

Study of the ilmenite series suite from the Takanawa Peninsula (MY-1 to MY-15) underscores the fact that rocks of the ilmenite series are low in oxide mineral content—no more than two ilmenite grains (the largest 120 × 180 μm) were found in 2.5-cm-diameter polished thin sections of the three more siliceous specimens. Ilmenites in all members of the suite appear to be free of exsolution or alteration features. Although only two grains were present in the section of MY-6, ilmenites in MY-6 and MY-15 may be of relatively uniform composition. As indicated by the data of Table 6, ilmenites are not of uniform composition in MY-2, and, most likely, in MY-1. The ilmenite grain in MY-2 containing 9.2 wt % MnO is surrounded by a reaction rim of sphene. There is a close association of ilmenite with mafic silicates in each of these rocks.

Oxide phases in specimens from the Daito-Yokota suite are more abundant, and it is not uncommon to find a small sulfide droplet in either ilmenite or magnetite grains. Ilmenites in all specimens show exsolution textures, and analyses reported in Table 6 were made using a 10-μm beam that was scanned over areas comprising the bulk of grains that showed the least coarse and complex exsolution. A small percentage of the magnetite grains in 6510-116 and 6510-132 contain a few narrow hematite lamellae. This feature is more notable in 5907-55 in which magnetite grains may also be peripherally altered to hematite. Typical, larger (up to 300 μm) ilmenite grains in Katsura-1 are mildly exsolved [e.g., *Czamanske and Mihalik,* 1972, Plate 1, Figure A] with a few larger lamellae at grain boundaries and are represented by the averaged analysis of Table 6. Two smaller grains contain 6.7 and 8.0 wt % MnO; the reported analysis is of a grain 20 × 80 μm that wraps half way around a magnetite grain twice its size. Sample 6412-17 from the Daito pluton contains less ilmenite in proportion to magnetite, and analyses for the only two grains found are reported in Table 6. It is notable that variations in $(FeO+MnO)/TiO_2$ and MgO are comparable to those found in Katsura-1 and that the contrast is again between a larger isolated grain and a smaller grain bound to a magnetite grain twice its size. A 200 × 250 μm grain of magnetite in biotite is overgrown by five hematite laths, the largest of which is 30 × 250 μm. Although it was possible to find ilmenite grains in 6510-116, 6510-132, and 5907-55 that show minor, coherent exsolution, grains in each of these three specimens show incipient stages of patchy reaction to hematite + rutile related to strongly oxidizing environments [e.g., *Czamanske and Mihalik,* 1972]. MnO contents of ilmenite vary substantially in 6510-116 but seem to be less variable among closely associated grains. We chose to report in Table 6 an analysis for a Mn-poor ilmenite (30 × 70 μm) trapped in plagioclase, along with the average of two grains at the high end of Mn content. Three isolated ilmenite grains in 6510-132 contain an average of 12.4 wt % MnO, whereas two grains in contact with magnetite contain 21.6 and 29.0 wt % MnO; an analysis of the latter and an average of the three are reported in Table 6. MnO contents of five ilmenites in 5907-55 vary unsystematically from 14.5 to 21.0 wt %; we have selected an intermediate analysis for presentation.

The study of *Czamanske and Mihalik* [1972] presents a model for the development of Mn-rich ilmenites in oxidizing magma systems, and the occurrence of Mn-rich ilmenites in

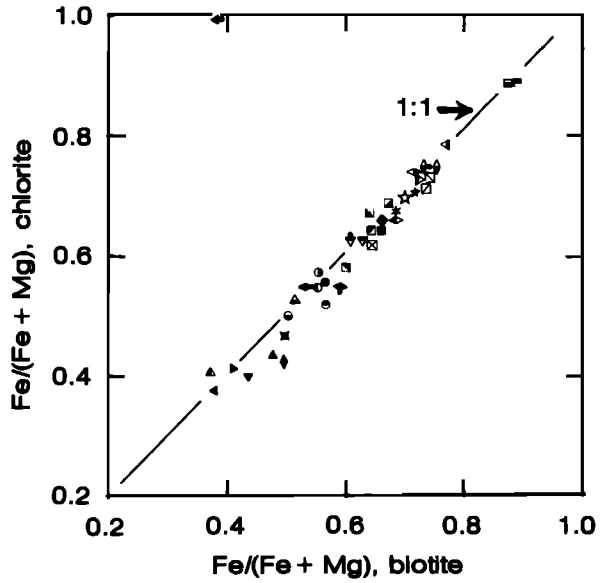

Fig. 12. Relation between Fe/(Fe+Mg) in biotites and chlorites.

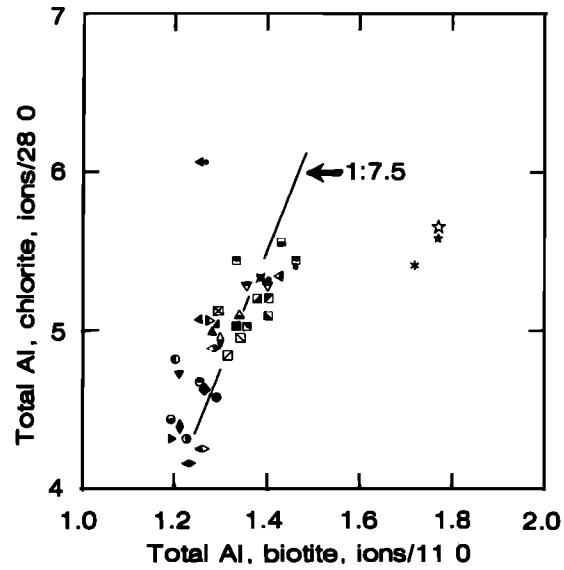

Fig. 14. Relation of total Al contents in biotites and chlorites.

the Sanin belt was reported by *Tsusue and Ishihara* [1974, Table 4]. To our knowledge, Mn-rich ilmenites have not been reported heretofore from the Ryoke belt. Whole-rock Mn contents for both the Daito-Yokota and Takanawa suites decrease from about 0.17 to 0.04 wt %. Thus, under the relatively reducing conditions of Ryoke belt crystallization, Mn enrichment in ilmenite, biotite, and amphibole within more SiO_2-rich rocks appears to be simply related to accomodation of Mn in a steadily decreasing concentration of host phases, of which ilmenite is preferred [*Czamanske et al.*, 1977, p. 1102].

Tainosho et al. [1979] report magnetite analyses for 17 samples and ilmenite analyses for nine; all but three of the magnetites are reequilibrated. Their single Ryoke belt ilmenite contains only 0.75 wt % Fe_2O_3, whereas the range for six Sanyo belt ilmenites is 0.75 to 10.02 (average 4.39) and two Sanin belt ilmenites contain 5.51 and 8.47 wt % Fe_2O_3. *Tsusue and Ishihara* [1974] report 1.6 and 3.8 wt % Fe_2O_3 for ilmenite in Ryoke belt sample T-165 of this study, and a range of 0.9 to 4.0 (average 3.0) for ilmenites in two Sanyo belt samples. Most interesting are their data for Sanin belt samples that are closely related to the Daito-Yokota suite of this study. Ilmenites with exsolved hematite lamellae in three samples have bulk Fe_2O_3 contents of 8.8 to 20.7 (average 12.9). For two of these samples, however, ilmenites coexisting with magnetite contain only 2.3 (average 4.1) wt % Fe_2O_3. Some of the implications of the three sets of ilmenite compositional data are addressed in the folowing section of f_{O_2}-T.

The f_{O_2}-T Relations

The importance of relative oxygen fugacities to development of the magnetite and ilmenite series terranes mandates some attempt to quantify f_{O_2}-T relations for representative suites, despite our difficulty in obtaining data that could be used confidently to proceed with such an endeavor. For Figure 18 we have gathered data for the Yokota and Takanawa suites to allow a subjective presentation. Our data in Table 6 show a clear distinction between ilmenite compositions for the two suites, such that Hem_{15} and Hem_3 may be chosen as rep-

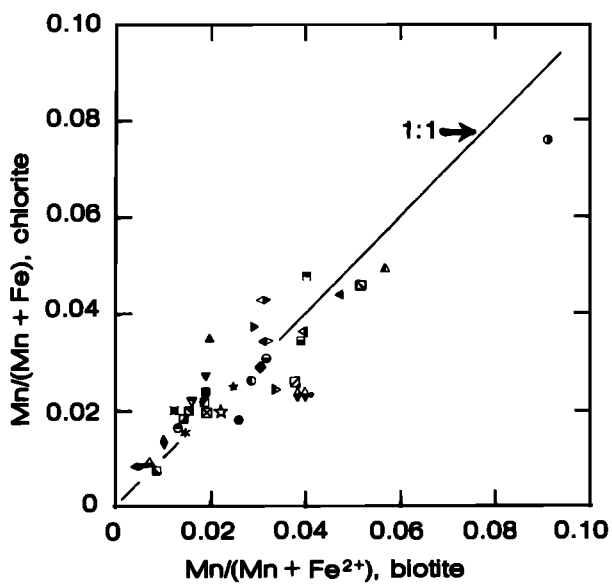

Fig. 13. Relation between $Mn/(Mn+Fe^{2+})$ in biotites and Mn/(Mn+Fe) in chlorites.

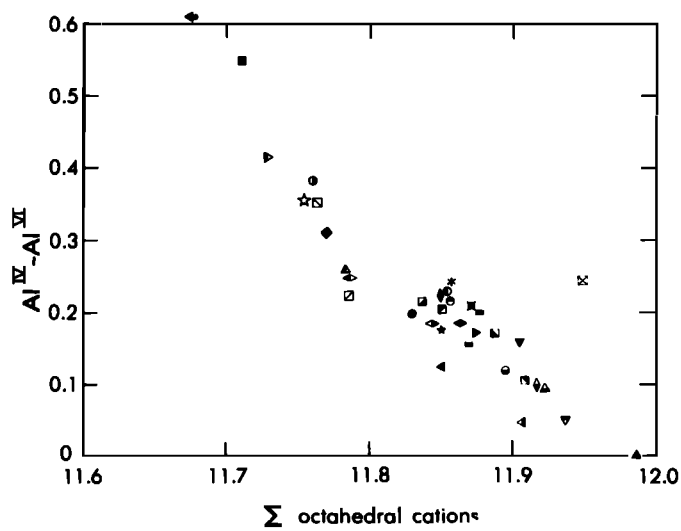

Fig. 15. Relation between the sum of the octahedral cations and $Al^{VI} - Al^{IV}$ in chlorites.

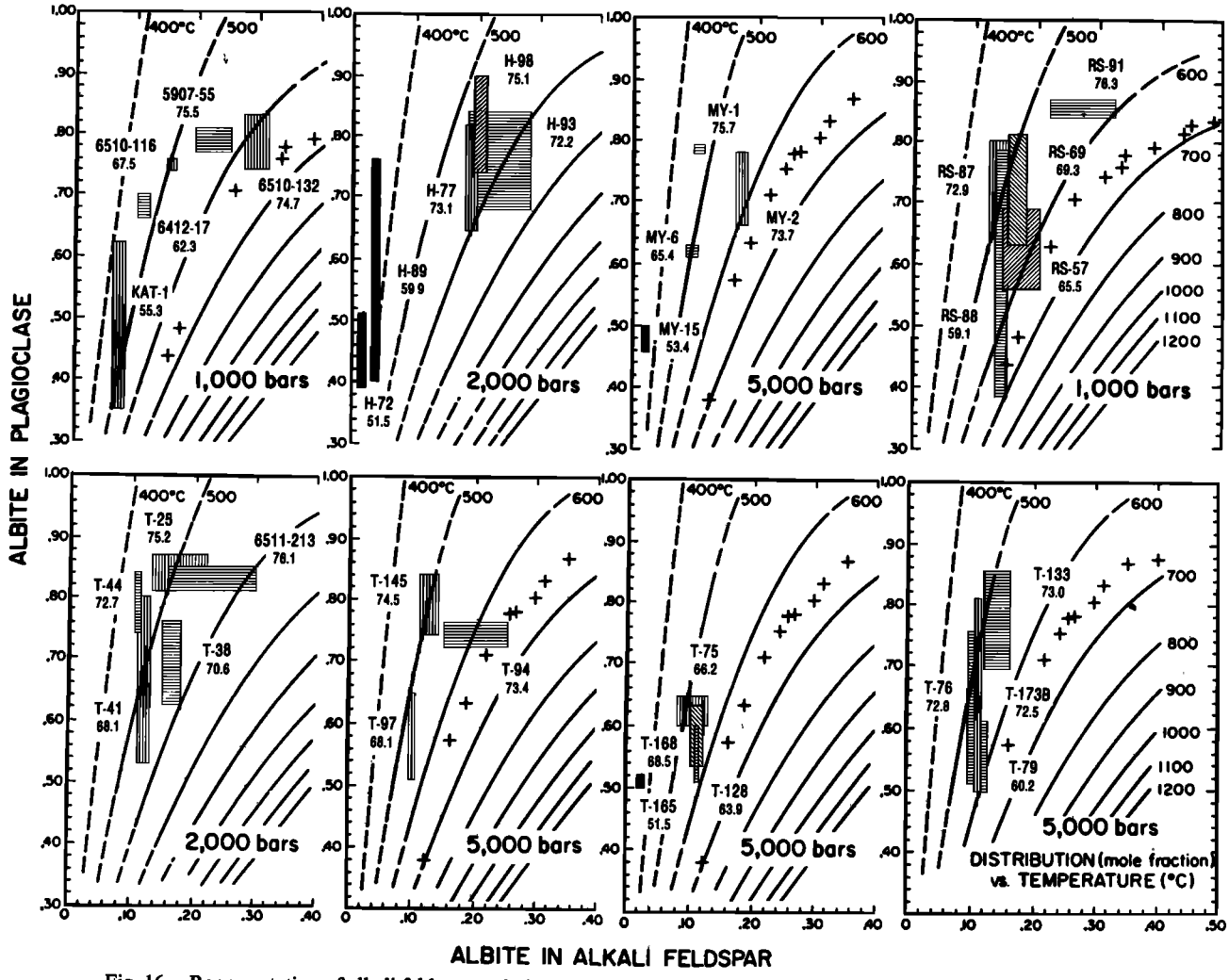

Fig. 16. Representation of alkali feldspar and plagioclase compositions for individual suites on diagrams for appropriate pressures [from *Stormer*, 1975]. Black bars represent ranges of plagioclase composition for four units which contain no alkali feldspar. Host rock SiO_2 contents are given below specimen numbers. Plus symbols were Stormer's for representation of experimental data.

resentative. Upper limits of biotite stability can be calculated from the equation used by *Czamanske and Wones* [1973]:

$$-1/2 \log f_{O_2} = (7409/T) + 4.25 - \log f_{H_2O} + 3 \log X_{Fe_{2+}} + 2 \log X_{OH} - \log a_{KAlSi_3O_8} - \log a_{Fe_3O_4},$$

where $X_{Fe^{2+}}$ is the number of ferrous iron atoms divided by three, the total number of octahedral sites; and X_{OH} is the inverse of F/(F+OH) (Table 1). The respective values for Katsura-1, 5907-55, MY-15, and MY-1 are 0.35 and 0.97; 0.26 and 0.83; 0.39 and 0.97; 0.60 and 0.96. These values reflect the opposing Mg and Fe enrichment trends shown by biotites and amphiboles, as well as F enrichment in the Yokota granitoids. On the basis of our microprobe analyses (Figure 16 and the appendix), we have taken $X_{KAlSi_3O_8}$ as 0.9 for Katsura-1 and MY-1, and 0.8 for 5907-55. *Waldbaum and Thompson* [1969] show that activity of $KAlSi_3O_8$ is approximately equal to mole fraction in this composition range, whereas between 600° and 800°C, $a_{KAlSi_3O_8} = 0.6$ for $X_{KAlSi_3O_8}$ from 0.25 to 0.75. Hence, loss of albite component during cooling can have lowered our calculated curves by no more than 0.17 log unit. My-15 contains neither alkali feldspar or magnetite, a circumstance to be considered shortly, and for the purposes of calculation we set $a_{KAlSi_3O_8} = 0.9$ assuming communication with the main magma body. Activity of Fe_3O_4 is taken as 1.0 for the magnetite series specimens and, arbitrarily, as 0.2 for the ilmenite series specimens. Elsewhere we have based discussion on typical crystallization pressures of 1 and 5 kbar for magnetite and ilmenite series suites. If P_{H_2O} is equal to total pressure, then corresponding values of f_{H_2O} average 810 and 4500 bars over the temperature range 660° to 910°C [*Burnham et al.* 1969]. The assumption that P_{H_2O} equaled total pressure appears reasonable for the Yokota granitoids, whereas the absence of fluid inclusions in rocks of the Takanawa suite (M. Watanabe, personal communication, 1981) suggests that water saturation was not attained. Accordingly, we have taken f_{H_2O} as 3500 bars for calculation of MY-15 and MY-1 biotite stabilities. Sources for appropriate 1-atm buffer curves are cited in the caption to Figure 18; separate figures have not been drafted for 1000 and 5000 bars total pressure because, for example, the Ni-NiO and QFM curves are shifted up by only 0.25 and 0.6 log units, respectively, at 5000 bars pressure, whereas the ilmenite series biotite stability curves are more sensitive to assumptions regarding $a_{Fe_3O_4}$, f_{H_2O}, and $a_{KAlSi_3O_8}$.

Consideration of Figure 18 suggests that our set of assumptions leads to a reasonable cartoon, though we note that other

TABLE 5. Fluorine and Chlorine Contents of Apatites, Central Chugoku and Chubu Transects, Japan

Sample	F	Cl
Katsura 1	2.0–2.4	0.39–0.51
6412-17	2.3–2.5	0.26–0.33
6510-116	3.0–3.1	0.08–0.10
6510-132	3.5–3.6	0.02–0.07
5907-55	3.5–3.6	0.12–0.14
H-72	2.1–2.2	0.35–0.69
H-89	1.6–2.4	0.49–1.3
H-93	3.4–3.5	<0.01
H-77	3.5–3.7	<0.01
H-98	3.4–3.8	<0.01
MY-15	2.0–2.6	0.17–0.31
MY-6	3.1–3.3	<0.01
MY-2	1.9*	<0.01
MY-1	3.3–3.4	<0.01
RS-88	3.0–3.3	0.10–0.15
RS-57	2.8–3.2	0.05–0.10
RS-69	3.4–3.5	0.12–0.25
RS-87	2.9–3.2	0.08–0.11
RS-91	3.5–3.6	<0.03
T-41	3.5–3.8	<0.03
T-38	3.3–3.7	<0.03
T-44	3.6–4.1	<0.01
T-25	3.8–4.2**	<0.02
6511-213	3.6–3.9	<0.01
T-97	3.2–3.4	<0.01
T-94	3.7–3.8	<0.01
T-145	3.6–3.8	<0.01
T-165	2.7–2.9	0.04–0.07
T-128	2.8–3.1	<0.03
T-75	3.4–3.5	<0.01
T-168	3.1–3.3	<0.02
T-79	2.2–2.5	0.18–0.22
T-173B	3.2–3.6	<0.01
T-76	3.1–3.4	<0.02
T-133	3.4–3.5	<0.01

Weight percent.
* Only one apatite grain found.
** Associated fluorite.

sets of assumptions are by no means disproven. Many authors [e.g., *Bowles,* 1977; *Anderson,* 1980] have suggested that bulk ilmenite compositions in plutonic rocks are reasonable indicators of crystallization oxygen fugacity, even when coexisting magnetites have recrystallized and geothermometry is not possible. The ilmenite stability curves of Figure 18 differ in f_{O_2} by 2.1 to 3 orders of magnitude over the temperature range 600° to 900°C, and one may conclude that at some point in time a similar difference in f_{O_2} characterized crystallization in the two studied magnetite and ilmenite series suites. As noted by *Czamanske et al.* [1977], the absolute positioning of these stability curves is in doubt because of uncertainties in dealing with the $MnTiO_3$ component; however, ilmenites from the two granitoid series are similar in Mg and Mn content, and their relative positioning should be reasonably accurate. Our assumptions have led to a similar difference of 2.5 log units in the stabilities of biotites in the 75 wt % SiO_2 granites from each suite. Moreover, the biotite stability curves for the two ilmenite series specimens make reasonable intersections with the buffer and ilmenite stability curves. The rather broad shaded fields of Figure 18 are suggestive of f_{O_2}–T conditions during crystallization of MY-15 and MY-1. Biotite compositional data (Figure 3*a*) also suggest that the ilmenite series suites crystallized under f_{O_2} less than that defined by Ni-NiO. The upper temperature limits for the fields may be closer to the QFM buffer if manganese stabilizes ilmenites at higher oxygen fugacities [*Czamanske et al.,* 1977].

It is somewhat more difficult to characterize the f_{O_2}–T environment of crystallization for Yokota granitoids Katsura-1 and 5907-55, but perhaps the clue can be taken from the data of *Tsusue and Ishihara* [1974] that indicate an average composition of Hem_6 for ilmenites coexisting with magnetite in some Daito-Yokota samples. If these data reflect f_{O_2} conditions during an early stage of magmatic evolution, the proximity of the stability curves for biotites in Katsura-1 and MY-15 (Figure 18) becomes comprehensible, and credibility is added to our assumptions regarding the biotite stability calculations. Moreover, the intersection at 700°C of the Hem_{15} and Katsura-1 biotite stability curves is anomalously low and would be pushed even lower if ilmenites are stabilized by Mn. The intersection of the stability curves for Hem_{15} and biotite in 5907-55 is at about 900°C and would be lowered to a more reasonable temperature if ilmenites are stabilized by Mn. Hematite occurs in magnetite series granites because the hematite-magnetite stability curve is intersected at well over 500°C, where reaction rates are appreciable (Figure 18).

The oxide compositional data, in combination with the oxide and biotite stability relations, suggest that magnetite and ilmenite series melts began crystallization under conditions of similar f_{O_2}, but by the time of crystallization of the silica-rich granites, f_{O_2} differed by over 2 orders of magnitude. In specimens from the Daito-Yokota area studied by *Tsusue and Ishihara* [1974], ilmenites from both environments are preserved; ilmenites from the more reduced environment were not noted in the specimens studied for this report.

The System Q-Ab-Or-H_2O

One of the most important contributions of the classic work of *Tuttle and Bowen* [1958] was the revelation that the minimum melting compositions of crystallizing granitic melts, represented by the system Q-Ab-Or-H_2O, reflect pressure of crystallization. Relevant, subsequent studies that have evaluated the effects of higher pressure, absence of an aqueous phase, and addition of An component are cited in the caption to Figure 19. Representation of the studied Japanese granitoids in Figure 19 shows that the more mafic rocks typically lie within

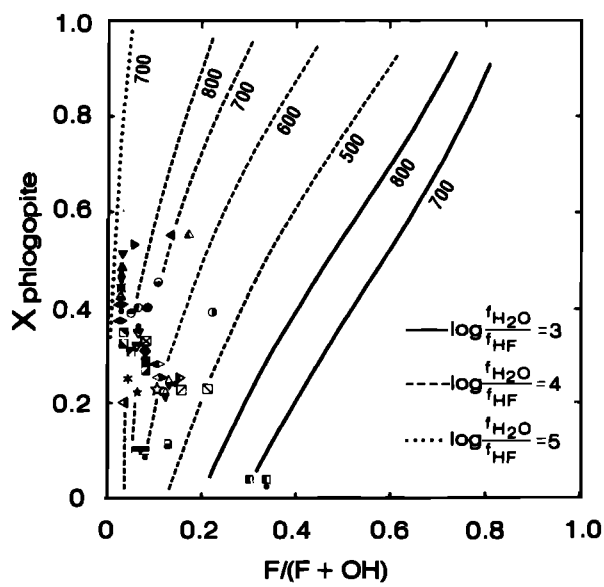

Fig. 17. Plot of F/(F+OH) versus X_{phlog} for biotites from the Chubu and Central Chugoku transects. Values are temperatures in °C [see *Munoz and Ludington,* 1974].

TABLE 6. Representative Ilmenite Compositions From Selected Specimens From the Central Chugoku Transect, Japan

	Katsura-1		6412-17		6510-116		6510-132		5907-55	MY-15	MY-6	MY-2		MY-1
	(3)*	(1)*	(1)*	(1)*	(1)*	(2)*	(3)*	(1)*	(1)*	(2)*	(2)*	(1)*	(1)*	(1)*
FeO	49.7(0.7)**	41.2	47.4	40.6	51.6	39.6(0.1)	39.1(0.6)	22.0	30.2	45.0(0.3)	42.6(0.2)	37.6	31.1	33.6
MnO	2.37(0.6)	8.04	5.54	7.10	2.50	9.55(0.4)	12.4(0.5)	29.0	18.5	2.25(0.25)	4.35(0.1)	9.2	15.9	13.1
TiO_2	44.6(0.7)	47.5	44.0	48.7	42.0	48.7(0.2)	46.3(0.6)	48.1	48.3	51.0(0.1)	51.0(0.1)	50.8	50.4	51.0
MgO	0.63(0.25)	2.53	0.37	2.34	1.92	0.30(0.06)	0.12(0.06)	0.17	0.10	0.57(0.07)	0.35(0.1)	0.25	0.10	0.10
$FeTiO_3$	77.26	63.49	70.33	68.49	67.19	70.94	60.95	28.66	51.77	89.91	86.24	75.85	61.33	68.45
$MnTiO_3$	5.04	17.10	11.78	15.10	5.32	20.31	26.37	61.67	39.34	4.78	9.25	19.56	33.81	27.86
$MgTiO_3$	1.88	7.54	1.10	6.98	5.73	0.89	0.36	0.51	0.30	1.70	1.04	0.75	0.30	0.30
Fe_2O_3	14.58	12.38	15.67	9.09	21.99	6.68	11.39	9.37	6.32	2.70	1.97	1.87	2.29	1.33
Total R_2O_3	98.76	100.51	98.88	99.66	100.23	98.82	99.07	100.21	97.33	99.09	98.50	98.03	97.73	97.94
$Fe_2O_3/(Fe_2O_3+FeTiO_3)$***	15.21	15.63	17.47	11.20	23.72	8.21	15.08	23.70	10.39	2.77	2.12	2.29	3.43	1.81

Al_2O_3 and V_2O_3 contents for all grains less than 0.1 and 0.2 wt %, respectively. Calculations according to *Anderson* [1968].
* Indicates number of grains averaged in column below.
** Value in parentheses reflects plus and minus range necessary to include all values averaged; it is not the standard deviation.
*** Mole ratio.

the field of primary plagioclase precipitation, whereas those rocks containing more than 70 wt % SiO_2 generally cluster in a region expected for crystallization at pressures of the order of 1 kbar and normative An contents less than or equal to 3 wt %. Thus, Figure 19 is doubly perplexing. On the one hand, normative An contents for 18 specimens containing over 70 wt % SiO_2 average 6.60 wt % (range 2.84 to 12.21; mode 5.90) even before normalization to (Q+Ab+Or+An) = 100. Experimental studies (see Figure 19) suggest that crystallization of such An-rich compositions should have been at minima poorer in Ab component. On the other hand, it is remarkable that there is no reflection in Figure 18 of the higher pressures of crystallization thought characteristic of the Ryoke belt. A similar pattern is suggested by the data of *Honma* [1974*a* Figure 4] for Ryoke belt granitic rocks of the Yanai district. A partial explanation for both problems is suggested in Figure 19 by the experimental data which reveal that the effects of raising P_{H_2O} and increasing An content move melt minima in opposing directions. No additional insight into the problem is revealed by consideration of the normative data in terms of the system An-Ab-Or.

DISCUSSION

Granitoid rocks have been the subject of intense interest for decades, and since 1970 an IGCP project on Circum-Pacific Plutonism has focused particular attention on the granites of the Circum-Pacific region. Questions regarding source materials and pressure-temperature conditions in the regions of magma formation have attracted considerable attention. In addition to the many sophisticated isotopic studies that have addressed these problems, there has been substantial emphasis on using whole-rock chemistry and mineralogy to indicate source materials. Since the publication of a brief note by *Chappell and White* [1974], much discussion has been in terms of I- and S-type granites, depending on whether derivation of

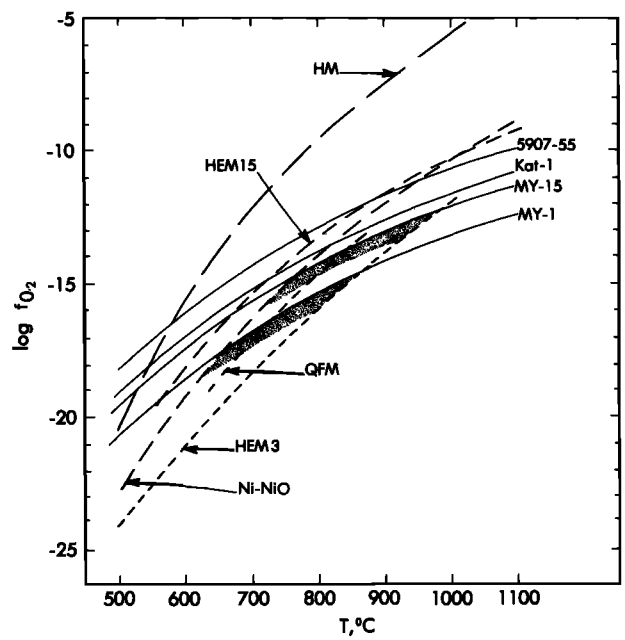

Fig. 18. Ilmenite and biotite stability relations in f_{O_2}–T space, in relation to the buffer assemblages hematite-magnetite [*Chou*, 1978], Ni-NiO [*Huebner and Sato*, 1970], and quartz-fayalite-magnetite [*Hewitt*, 1978]. The stability curves for Hem_3 and Hem_{15} are taken from *Buddington and Lindsley* [1964].

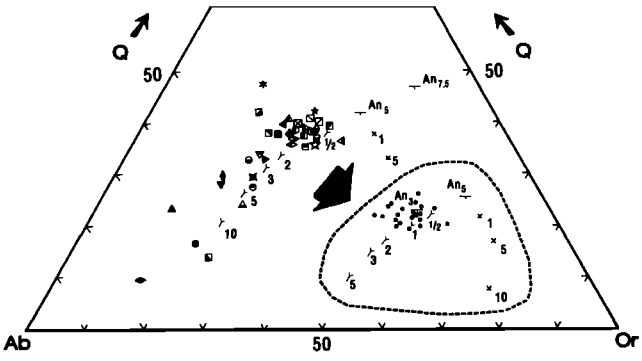

Fig. 19. Representation of bulk compositions of the Japanese granitoids in terms of normative Q+Ab+Or. Data for 21 specimens are replotted as dots in the insert more clearly to show relation to minima at indicated pressures (in kilobars) as follows: Y are taken from *Luth et al.* [1964] and relate to the 'granite' system, SiO_2-$NaAlSi_3O_8$-$KAlSi_3O_8$-H_2O, where $P_{H_2O} = P_{total}$; T are from *James and Hamilton* [1969] and relate to addition of 3, 5, and 7.5 wt % An to the 'granite' system at $P_{H_2O} = P_{total} = 1$ Kbar; x are for the dry, 'granite' system where $P_{H_2O} = O$ [*Luth*, 1969].

magma by partial melting of igneous or sedimentary source materials was indicated. Using similar criteria for distinguishing these two types, *Murakami* [1974], *Oba* [1974], *Ishihara* [1973], and others speculated as to the nature of the source materials for Japanese granitoids. *Ishihara* [1977] emphasized the mineralogical distinction between magnetite and ilmenite series granitoids, and *Takahashi et al.* [1980] have made a comprehensive effort to use whole-rock chemical criteria to resolve the relation between magnetite series/ilmenite series and I-type/S-type granitoids. Currently, Japanese magnetite series granitoids are considered to be I-types and the ilmenite series granitoids to be of both I- and S-type, though dominantly I-type.

In distinguishing between I- and S-type or magnetite and ilmenite series granitoids, emphasis has been placed on field relations, mineral assemblages, whole-rock chemistry, and isotopic composition [e.g., *Chappell and White*, 1974; *White et al.*, 1976; *Hine et al.*, 1978; *Griffen et al.*, 1978, *O'Neil and Chappell*, 1977; *Ishihara*, 1977, 1979; *Takahashi et al.*, 1980]. Relatively few papers have considered the mineral chemistry of suites of related granitoid rocks of I- and S-type, or of magnetite and ilmenite series for which I- and S-type character is in question.

Let us consider those characteristics of the studied Japanese granitoids that suggest I- or S-type affinity, noting at the outset that the evidence, on balance, strongly favors designation of the studied suites as I-type. One of the principal reasons that S-type character has been considered for some of the Ryoke, ilmenite series granitoids stems from their field relations. They intrude rocks of a metamorphic complex, and biotite-muscovite granitoids are emplaced in the highest grade rocks exposed, sillimanite gneisses. Moreover, the granitoids are in places concordant and are generally foliated and relatively heterogeneous. The presence of abundant mafic inclusions within Ryoke belt granitoids other than the Busetsu pluton is one respect in which field relations do not support S-type source derivation.

According to current thinking, one of the strongest indications of I-type for the studied suites lies in their mineralogy. For example, noting that the Sierra Nevada and southern California batholiths are hornblende bearing, *Griffen et al.* [1978, p. 235] flatly state 'Thus the change in K across these batholiths is a change within I-types. . .' Amphibole is present in each of our samples containing less than 72.5 wt % SiO_2 and is present in two rocks containing 73.1 wt % SiO_2. On the other hand, aluminum silicates and cordierite are not found in our Ryoke belt specimens. Among the samples we have studied, only the presence of primary muscovite and traces of garnet in three specimens from the Busetsu pluton of the Ryoke III zone of the Chubu transect give mineralogical indication of possible sedimentary source. As noted in the appendix, sphene is present in 10 samples and allanite in 20; rocks tend to contain either sphene or allanite. There is no pattern of distribution of these two phases among magnetite series, intermediate-type, or ilmenite series rocks. The suggestion of *Hine et al* [1978] that allanite may be favored by high oxidation state does not find support from our study and conflicts with our expectation [cf. *Czamanske and Wones*, 1973].

Turning to major element rock chemistry, it is sobering to quote from *Griffen et al.* [1978]. Concluding their comparison of two I-type granitoids representing eastern and western extremes across the Lachlan Fold Belt in Australia, they state [*Griffen et al.*, 1978, p. 246] 'In general, the chemical differences between the two areas are perhaps less than might be expected and certainly different from that which would have been predicted.' *White et al.* [1976] considered the I-S line in the Lachlan Fold Belt (east of which there are no S-type granites) to probably coincide with the eastern margin of a very thick block of continental crust, possibly crystalline shield. Across the Lachlan Fold Belt the K contents of the two I-type suites are indistinguishable [*Griffen et al.*, 1978]. One can readily imagine influence of thick continental crust across the Sierra Nevada and southern California batholiths, and change in K content is conspicuous, but S-type granitoids are not common.

The major elements that have been found most useful in distinguishing between I- and S-type granitoids are visually represented for the Chubu and Central Chugoku transects in the several diagrams of Figure 20. (Full chemical data for our samples from the Chubu transect were reported by *Ishihara and Terashima* [1977*a*]; those for the Central Chugoku transect are presented in Table 7.) SiO_2 content ranges widely for all suites except the Toki-Naegi and Ryoke I and III zone suites of the Chubu transect; restricted SiO_2 contents are typical of S-type suites. Plots of CaO, K_2O, Na_2O, TiO_2, and molar $Al_2O_3/(Na_2O+K_2O+CaO)$ against SiO_2 and of Na_2O against K_2O show no tendencies toward the distinct groupings held by *Chappell and White* [1974], *Hine et al.* [1978], and *Griffen et al.* [1978] to be bases for distingushing I- and S-type granitoids. Our data generally show overall linear or near-linear variation, a characteristic of I-type granitoids. Previous workers have not presented plots of $Al_2O_3/(Na_2O+K_2O+CaO)$ versus SiO_2, and for our data, this plot shows a rather regular trend with strong dependency on SiO_2 content. Only four samples display the S-type characteristic of $Al_2O_3/(Na_2O+CaO) > 1.1$, and the highest value is 1.1345.

Considering that *Bateman and Dodge* [1970] and *Baird et al.* [1974] show that K_2O increases (at constant SiO_2) from west to east across the Sierra Nevada and southern California batholiths, it is impressive that the relation between K_2O and SiO_2 contents for these transects of the Inner Zone batholith is so regular that there is complete overlap of suites and transects. Na_2O content is intermediate [cf. *Hines et al.*, 1978; *Griffen et al.*, 1978] and quite constant over a broad range of SiO_2

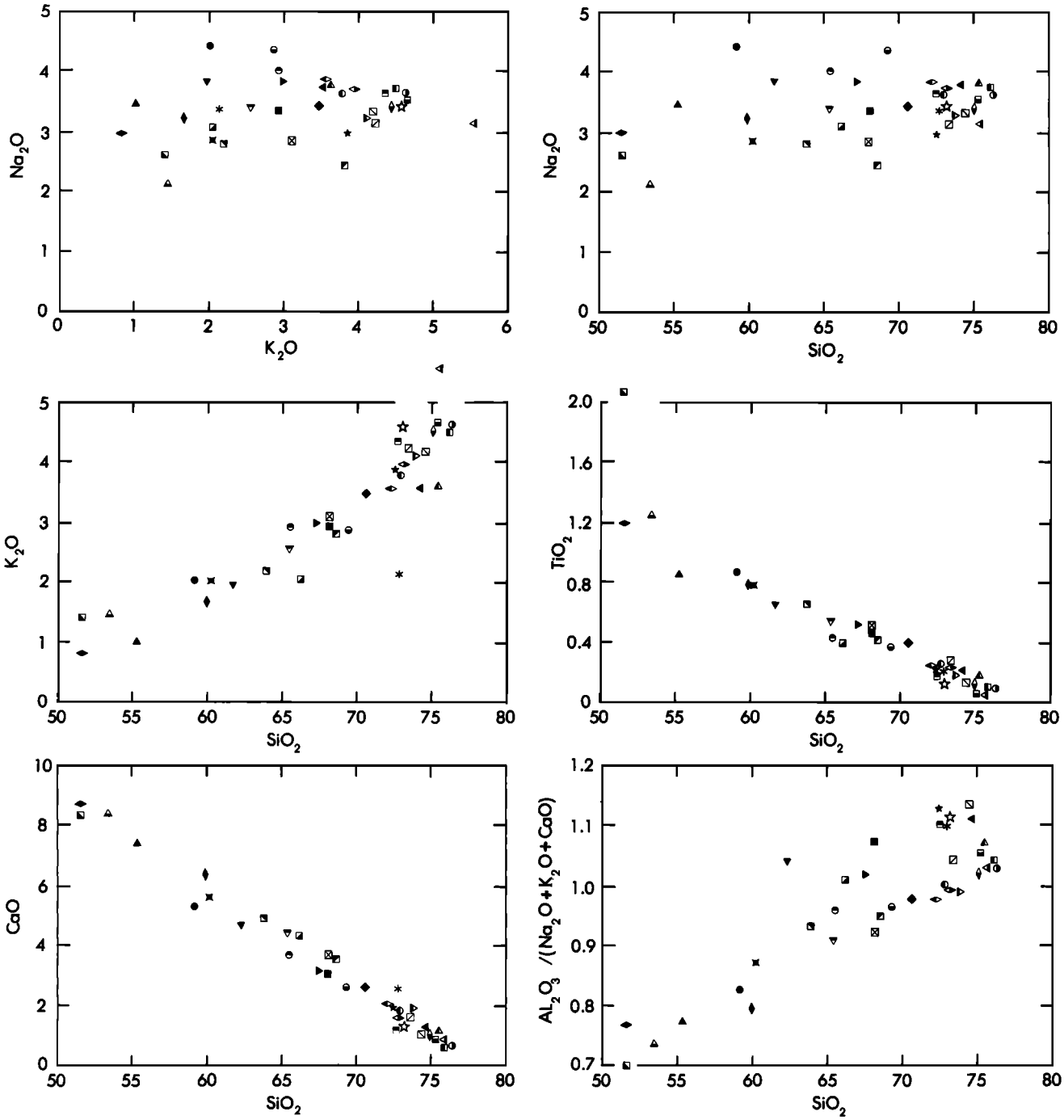

Fig. 20. Relations between oxide concentrations in whole rocks from the Chubu and Central Chugoku transects. All data in weight percent except $Al_2O_3/(Na_2O+K_2O+CaO)$, which is in mole percent.

contents. Ryoke belt suites tend to be less sodic than the others, but Na_2O is not a discriminator for these rocks in the sense proposed by *Chappell and White* [1974]. Similarly, although normative corundum averages 2.63 in the more comprehensive Ryoke III granitoid suite considered by *Ishihara and Terashima* [1977*a*], it averages only 0.8 in our suite of rocks from the Takanawa peninsula (MY-1 thru MY-15), and normative corundum contents >2.4 are found in some magnetite series and weakly magnetic, intermediate-type granitoids.

Additional means for considering the relation between I- and S-type versus magnetite and ilmenite series granitoids on the basis of rock chemistry have been explored and recently presented by *Takashashi et al.* [1980]. Whereas they show that proportionately more ilmenite series than magnetite series granitoids do possess S-type chemical characteristics, the majority of the Japanese ilmenite series granitoids can clearly be classed as I-type. Perhaps attempts to categorize granitoids on the basis of whole-rock chemistry and mineralogy, e.g., I- and S-type and magnetite and ilmenite series, although useful in the field, can divert attention from the types of isotopic and trace element study capable of definitively constraining theories of granitoid genesis and evolution (see the epilogue).

The Inner Zone batholith provides a particularly good area

TABLE 7. Chemical Analyses and CIPW Norms for Studied Samples From the Central Chugoku Transect

	Kat-1	6412-17	6510-116	6510-132	5907-55	H-72	H-89	H-93	H-77	H-98	MY-15	MY-6	MY-2	MY-1
SiO_2	55.20	61.68	67.15	74.16	75.28	51.52	59.87	72.20	73.06	75.09	53.35	65.38	73.66	75.48
TiO_2	0.85	0.66	0.52	0.22	0.19	1.19	0.78	0.25	0.24	0.12	1.24	0.55	0.19	0.07
Al_2O_3	17.90	19.53	16.83	14.39	13.58	19.14	16.84	14.30	13.95	13.09	17.32	16.51	13.66	13.49
Fe_2O_3	4.18	1.76	1.68	0.96	0.68	1.85	1.71	0.59	0.71	0.48	1.82	1.15	0.55	0.36
FeO	3.70	2.73	1.65	0.50	0.54	7.65	4.20	1.58	1.37	0.86	6.58	3.05	1.33	0.43
MnO	0.18	0.08	0.08	0.04	0.06	0.19	0.11	0.07	0.06	0.06	0.15	0.07	0.06	0.02
MgO	3.48	2.51	1.30	0.30	0.40	4.14	3.27	0.43	0.46	0.37	4.94	1.37	0.40	0.10
CaO	7.37	4.67	3.17	1.32	1.15	8.64	6.35	2.03	1.68	1.07	8.35	4.43	1.80	0.89
Na_2O	3.46	3.83	3.83	3.78	3.80	2.98	3.22	3.83	3.70	3.40	2.12	3.40	3.25	3.12
K_2O	1.01	1.96	2.98	3.54	3.60	0.82	1.66	3.56	3.94	4.53	1.45	2.56	4.15	5.56
P_2O_5	0.15	0.14	0.20	0.10	0.06	0.33	0.20	0.09	0.10	0.08	0.19	0.17	0.07	0.04
S	0.50	0.02	0.03	0.01	...	0.01	<0.01	<0.01	<0.01	<0.01	<0.01	<0.01	<0.01	<0.01
CO_2	0.06	...	...	...	...	0.01	0.03	0.02	<0.01	<0.01	0.09	...	...	...
$H_2O(+)$	1.58	0.10	0.06	0.16	0.46	0.98	1.12	0.62	0.39	0.39	1.57	0.81	0.53	0.30
$H_2O(-)$	0.28	0.30	0.36	0.42	0.02	0.28	0.32	0.10	0.20	0.12	0.24	0.12	0.04	0.05
Total	99.90	99.97	99.84	99.90	99.82	99.73	99.67	99.67	99.86	99.66	99.41	99.57	99.69	99.91
F, ppm	n.d.	370	380	230	220	260	240	360	380	360	370	500	560	70
Cl, ppm	n.d.	160	95	135	90	195	250	115	80	85	185	160	85	60
Q	10.75	17.36	24.88	35.63	36.40	3.25	15.27	30.59	31.71	34.86	8.31	22.99	33.80	33.92
C	...	2.95	2.02	2.18	1.48	...	...	0.67	0.78	0.84	...	0.50	0.72	0.82
OR	5.97	11.58	17.61	20.92	21.27	4.85	9.81	21.04	23.28	26.77	8.57	15.13	24.53	32.86
AB	29.28	32.41	32.41	31.99	32.15	25.22	27.25	32.41	31.31	28.77	17.94	28.77	27.50	26.40
AN	30.33	22.25	14.42	5.90	5.31	36.43	26.59	9.48	7.68	4.79	33.46	20.87	8.47	4.15
WO-DI	2.19	...	...	...	...	1.79	1.50	...	...	...	2.57	...	...	...
EN-DI	1.58	...	...	...	...	0.86	0.87	...	...	...	1.44	...	...	...
FS-DI	0.41	...	...	...	...	0.91	0.56	...	...	...	1.03	...	...	...
EN-HY	7.09	6.25	3.24	0.75	1.00	9.46	7.27	1.07	1.15	0.92	10.87	3.41	1.00	0.25
FS-HY	1.86	2.62	0.93	...	0.23	10.00	4.66	2.13	1.64	1.10	7.78	3.87	1.79	0.41
MT	6.06	2.55	2.44	1.10	0.99	2.68	2.48	0.86	1.03	0.70	2.64	1.67	0.80	0.52
HM	...	...	...	0.20	...	...	...	...	...	...	...	...	...	...
IL	1.61	1.25	0.99	0.42	0.36	2.26	1.48	0.47	0.46	0.23	2.36	1.04	0.36	0.13
AP	0.35	0.32	0.46	0.23	0.14	0.76	0.46	0.21	0.23	0.19	0.44	0.39	0.16	0.09
Femic total	21.16	12.99	8.05	2.69	2.70	28.71	19.29	4.74	4.51	3.13	29.32	10.39	4.10	1.41

for the study of island arc magma genesis because, as noted by *Ishihara* [1978, 1979], granitoids are most continuously exposed there. (There are also profound tectonic breaks in the Japanese islands at the Tanakura and Median Tectonic Lines (Figure 1) such that northwest Japan and the Outer Zone of southwest Japan must in some ways be regarded as quite separate entities.) In recent years Ishihara has collaborated on regional isotopic studies (O, *Ishihara and Matsuhisa* [1977]; S, *Sasaki and Ishihara* [1979, 1980]; and Sr, *Shibata and Ishihara* [1979*a*, *b*] in an organized attempt to understand the derivation of the diverse suites of Japanese granitoids. In four recent papers derivative from these studies [*Ishihara*, 1978, 1979; *Sasaki and Ishihara*, 1979; *Shibata and Ishihara*, 1979*b*], a relatively consistent model has been presented for the Inner Zone batholith for the transition from magnetite to ilmenite series and for the regional isotopic patterns; namely, that the data can best be explained by the depth of generation of the magmas and the extent of crustal interaction. Despite its metallogenic emphasis, *Ishihara*'s [1978] paper provides the most comprehensive geologic perspective and lucid exposition of his model, the others provide more specific detail. The magnetite series granitoids, typically displaying low $(^{87}Sr/^{86}Sr)_0$, low $\delta^{18}O$, and positive $\delta^{34}S$ values, are thought to reflect a predominant, upper mantle source, with possible reaction and further magma generation in the lowest crust. *Sasaki and Ishihara* [1979] suggest that the characteristic heavy sulfur ($\delta^{34}S \simeq +5‰$) of magnetite series granitoids indicates the contribution of marine sulfate from a subducted oceanic plate. The higher $(^{87}Sr/^{86}Sr)_0$ and $\delta^{18}O$ and negative $\delta^{34}S$ values typical of ilmenite series granitoids are thought to reflect magma generation in the environment of the middle to lower continental crust, and their reduced, magnetite-free nature to be caused by mixing with carbon-bearing sedimentary and metamorphic rocks at some stage in their igneous history. At times there seems to be a bias toward the alternative of shallow crustal assimilation into magmas of deeper origin, whereas *Ishihare* [1979, p. 521] envisions the possibility of '... A zone-melting type emplacement with short distance of magma migration...' A fundamental factor in the distinctive styles of plutonism is presumed to be that the magnetite series magmas of the Japan Sea side were emplaced in an inner-arc tensional zone of sustained, vertical block movement, whereas the ilmenite series magmas were emplaced in an outer-arc compressional environment characterized by thrusting and reverse faulting. In some respects the two orogenic environments could thus be classed as Andinotype and Hercynotype [*Pitcher*, 1979]. *Ishihara* [1978] considered that magnetite series granitic magmas are related to major subduction, whereas those of the ilmenite series need not be.

Ishihara's thoughts on magma genesis in southwestern Ja-

pan are based on more than a decade of intimate familiarity with field relations and intense pursuit of mineralogic, chemical, and isotopic data that would help to develop and refine a comprehensive framework for understanding metallogenesis. The data of this paper compel one to consider the granitoids of the Inner Zone batholith as having more similarities than dissimilarities in mode of origin. Taking that view, it seems appropriate to review available evidence and, from a slightly different perspective, to offer reasoned alternatives to aspects of Ishihara's model.

At the outset, let us briefly discuss the conditions that appear necessary for development of magnetite-free and magnetite-bearing granitoids. Most mantle-derived magmas are only slightly more oxidized than QFM and, if they remain as essentially closed systems, will crystallize as magnetite-free, ilmenite-bearing plutonic or volcanic rocks. Moreover, if mantle-derived magma interacts with, and assimilates, crustal material that has not undergone oxidation during or subsequent to intrusion, the hybrid magmas will still be magnetite free, but perhaps with higher $(^{87}Sr/^{86}Sr)_0$ values. Finally, significant incorporation of graphite from remelted crustal rocks will insure that derivative magmas are reduced and magnetite free. On the other hand, magnetite-bearing rocks owe that characteristic to crustal processes. Magnetite-bearing rocks may result from shallow level intrusion of relatively reduced magmas, followed by devolatilization (H_2O saturation) and differential loss of H_2; their $(^{87}Sr/^{86}Sr)_0$ values will depend upon whether material has been assimilated in the lower crust and on the age and Rb content of such material. Alternatively, magmas of magnetite-bearing character may develop in a lower crustal environment if mantle-derived melts interact with materials that have been oxidized at the earth's surface. Such magmas can be thought of as being intrinsicially oxidized and, in contrast to the preceding case, rocks derivative from them should show evidence of early crystallization of magnetite and sphene. Depending upon absolute age, chemical character, and proportions of juvenile volcanic versus weathered sedimentary material in lower crustal source regions, values of $(^{87}Sr/^{86}Sr)_0$ for intrinsically oxidized magmas could range widely. On the basis of these considerations, it is not surprising that there are a few magnetite-free plutons in the magnetite series terrane and some magnetite-bearing granitoids in the Ryoke belt.

Magnetite-bearing rocks from the Sierra Nevada batholith are considered to have been intrinsically oxidized because early formed magnetite and sphene are typically included within plagioclase and amphibole grains [e.g., *Noyes*, 1978]. In contrast, petrographic study of the Finnmarka complex [*Czamanske and Wones*, 1973] and of our Daito-Yokota magnetite series specimens (see the appendix) shows that magnetite and sphene are typically late, interstitial to plagioclase, and intergrown with, but seldom included in, amphibole. Earlier discussion has shown that ilmenite compositions in some magnetite series specimens may reflect both relatively reduced (early) and oxidized (late) environments. The Shirakawa magnetite series suite contrasts with the Daito-Yokota suite in having nearly constant rather than decreasing Fe/(Fe+Mg) for amphiboles and biotites and a virtual absence of sphene; both characteristics suggest a more weakly oxidizing environment. Biotites from our magnetite series specimens have higher $Fe^{2+}/(Fe^{2+}+Fe^{3+})$ than those characteristic of magnetite-bearing granitoids from the Sierra Nevada (Figure 3*a*) [*Dodge et al.*, 1969], and on the basis of these and Finnmarka data, we suggest that $Fe^{2+}/(Fe^{2+}+Fe^{3+})$ for biotites may be high in magmatic systems that undergo oxidation late in their crystallization history. Analyses of other biotites from the magnetite series terrane of southwestern Japan [*Murakami*, 1977] show a greater proportion of ferric iron, and a study of plutons throughout the terrane might show that some were intrinsically oxidized. In fact, *Murakami* [1969, Figures 7 and 8] has sketched the two modes of magnetite occurrence that we discuss. He noted that the most Mg-rich biotites are associated with interstitial magnetite but does not discuss relation of magnetite occurrence to $Fe^{2+}/(Fe^{2+}+Fe^{3+})$ in biotite.

One of the goals of this study was to gain insight into the nature of the weakly magnetic granitoids of southwestern Japan, represented by the northern part of the Hiroshima granite. With respect to many of the criteria we have considered, there is little that distinguishes these samples, but compositional data for biotites and amphiboles suggest that the Hiroshima granite shows greater affinities to ilmenite series suites. Field relations show that these granitoids were typically emplaced at deeper levels than granitoids of the Sanin belt, that they are accompanied by less hydrothermal alteration, and that sphene is absent; all of these facts are compatible with the interpretation that there was less opportunity for near-surface oxidation in the Sanyo belt. Observation of magnetite included in relic clinopyroxene in H-72 and H-89 leads to the more tenuous suggestion that some weakly magnetic granitoids may have derived their magnetite-bearing character from their source regions, i.e., were more intrinsically oxidized but incorporated carbon-bearing sediments.

Shibata and Ishihara [1979*a*, *b*] have determined $(^{87}Sr/^{86}Sr)_0$ values for about 80 rocks in an attempt to characterize the source materials and understand the evolution of the plutonic rocks of Japan. The $(^{87}Sr/^{86}Sr)_0$ data exhibit just those complexities that we have anticipated, magnetite and ilmenite series rocks are each characterized by a broad range of $(^{87}Sr/^{86}Sr)_0$. Among magnetite series plutons, the Daito-Yokota granitoids of the Central Chugoku transect have $(^{87}Sr/^{86}Sr)_0$ of ~0.7055, whereas $(^{87}Sr/^{86}Sr)_0$ is 0.7100 for the Hatogaya pluton of the Chubu transect. Similarly, whereas the Busetsu pluton has $(^{87}Sr/^{86}Sr)_0$ of 0.7096, this value is only 0.7068 to 0.7082 for ilmenite series granitoids of the Central Chugoku transect, and granitoids in the far western part of the ilmenite series terrane north of Kyushu are characterized by $(^{87}Sr/^{86}Sr)_0$ values in the range 0.7050 to 0.7062. Nonetheless, $(^{87}Sr/^{86}Sr)_0$ data are fundamental in terms of constraining models of magma derivation. Within southwest Japan, $(^{87}Sr/^{86}Sr)_0$ values are systematically low toward the inland, Japan Sea side, but correlate well with "thickness of the continental crust" as deduced from the Bouguer gravity anomaly. *Kistler and Peterman* [1973, 1978] have shown similar relations between $(^{87}Sr/^{86}Sr)_0$, crustal thickness, and Bouguer anomaly for the Sierra Nevada batholith and have 'seen through' the batholith with sufficient resolution to propose a detailed crustal 'map' and reconstruction. *De Paolo* [1980, this issue] has used Nd/Sm isotopic studies based on the same specimens of Sierra Nevada granitoids to confirm the validity of Kistler and Peterman's interpretation. *Shibata and Ishihara* [1979*b*] discuss the possibility that segments of Precambrian basement underlie southwest Japan but do not specifically attempt to outline these fragments in the manner of Kistler and Peterman because of the complexity of the Japanese basement, as shown by $(^{87}Sr/^{86}Sr)_0$ data for younger rocks. The contoured $(^{87}Sr/^{86}Sr)_0$ data of Figure 1 (taken from *Shibata and Ishihara* [1979*b*, Figure 1]) allow two segments of thickened crust to be outlined and suggest that our Chubu and Central Chugoku transects over-

lie differing crustal profiles. The $(^{87}Sr/^{86}Sr)_0$ values for granitoids of the more westerly, Central Chugoku transect increase regularly, from north to south, from 0.7055 to 0.7082, whereas granitoids across the entire Chubu transect have $(^{87}Sr/^{86}Sr)_0 = 0.710 \pm 0.006$. A regular increase in $(^{87}Sr/^{86}Sr)_0$ is again found farther to the east, between Niigata and Kanto, where values of 0.7124 are reached. The major, northward indentation in the Median Tectonic Line at the Itoigawa-Shizuoka fault may therefore be related to pre-Cretaceous fragmentation of older, thick crust into a smaller eastern 'splinter' and a larger western segment, correlative with the $(^{87}Sr/^{86}Sr)_0$ high northeast of Kyoto. The data of Figure 1 show a strong increase in $(^{87}Sr/^{86}Sr)_0$ from northern Kyushu northeastward toward the 'Kyoto high,' and values of $(^{87}Sr/^{86}Sr)_0$ south of this high appear to fall off again. Thick, old crustal segments beneath southwest Japan have apparently contributed to values of $(^{87}Sr/^{86}Sr)_0 > 0.710$; in peripheral areas underlain by thinner and younger crust, granitoids with significantly lower initial ratios were emplaced from 70 to 120 Ma.

The presence of older, continental-type crust is compatible with studies of oxygen and sulfur isotopes. *Ishihara* [1978] has shown that for both Cretaceous-Paleocene and Miocene granitoids, whole-rock $\delta^{18}O$ at 74 wt % SiO_2 increases from +6 or +7‰ to +10 or +11‰ as one crosses southwest Japan from north to south. *Matsuhisa et al* [1972], *Honma and Sakai* [1975, 1976], and *Kagami and Honma* [1979] also document this increase in $\delta^{18}O$ with data for quartz, biotites, amphiboles, and whole rocks. Because $\delta^{18}O$ in mantle sources is taken to be $+6.0 \pm 0.5$‰ and sedimentary rocks are enriched in ^{18}O, high $\delta^{18}O$ values for plutonic rocks are considered to reflect crustal involvement in magma generation. Indeed, O'Neil and Chappell [1977] and *O'Neil et al.* [1977] present a strong case for being able to distinguish I- and S-type granites in the Australian Berridale and New England batholiths on the basis that S-type granites have $\delta^{18}O$ values >10, whereas I-type granites have lesser values. On this basis most of the granitoids we have studied would be considered I-type.

Honma and Sakai [1975] relate the heavier oxygen of the Ryoke series granitoids to fluid interaction between the magmas and surrounding metamorphic rocks, enhanced by the structural deformation accompanying Ryoke metamorphism. *Matsuhisa et al.* [1972] specifically reject the assimilation of metasedimentary rocks as the cause of enrichment in ^{18}O for typical Ryoke belt granites. Yet, these workers show that $\delta^{18}O$ fractionations between mineral pairs retain magmatic values. The absence of anomalous isotopic fractionations convinced *Masi et al.* [1981] that most of the whole-rock $\delta^{18}O$ values they have obtained for Mesozoic granites of California and Oregon are primary.

Masi et al. [1981] discuss a peculiarity of the central part of the Sierra Nevada batholith that is similar to the Inner Zone batholith and rare among granitoids, the association of relatively low $\delta^{18}O$ values of +7 to +9 with $(^{87}Sr/^{86}Sr)_0$ values of 0.706 to 0.707. Such isotopic signatures have been observed for volcanic rocks from the Banda arc of Indonesia and the Peruvian Andes [*Margaritz et al.*, 1978]. These isotopic characteristics are satisfied by derivation of magma from altered oceanic crust, or mafic crust in general, logical components of the Japanese island basement adjacent to the inferred, thick crustal segments. For their Banda arc samples, Margaritz et al. find precisely the correlation between $\delta^{18}O$ and $(^{87}Sr/^{86}Sr)_0$ that characterizes the Central Chugoku transect and call upon mixing between mantle and crustal components. *Yanagi* [1975] has used a detailed consideration of Rb and Sr contents and $(^{87}Sr/^{86}Sr)_0$ values to arrive at a similar conclusion; namely, that the chemical and isotopic characteristics of the Japanese granites are best understood in terms of partial melting of an earlier formed "primary crust" by additional, mantle-derived melt.

Sasaki and Ishihara [1979, 1980] provide S-isotopic data for a broad range of granitoids, gabbroids, and ores of granitic affinity from the Japanese islands. Their results show that magnetite and ilmenite series suites have distinct, characteristic ranges of $\delta^{34}S$; the isotopic composition of sulfur in magnetite series granitoids averages about +5‰ (range, 0 to +9‰) and that in ilmenite series granitoids about −5‰ (range, −11 to +2‰). On the average, the gabbroids show less sulfur isotopic distinction, but the ore sulfur from both series is about 3‰ lighter than the host granitoid sulfur. $\delta^{34}S$ values for the Cretaceous-Paleocene granitoids of the Inner Zone often show a good, inverse correlation with $(^{87}Sr/^{86}Sr)_0$, e.g., our Chugoku transect; but because $\delta^{34}S$ and $(^{87}Sr/^{86}Sr)_0$ need not be interdependent, this correlation is not always found.

Coleman [1977] and *Ohmoto and Rye* [1979] review evidence that $\delta^{34}S$ values for mafic rocks cluster around 0‰ and typically range between −3 and +3‰; Ohmoto and Rye suggest that partial melting of average crustal rocks will produce melts with a similar range of values. Thus, there are two problems to be addressed with regard to $\delta^{34}S$ data for the Inner Zone batholith: (1) an explanation for the distinct bimodal distribution between magnetite- and ilmenite-series terranes, and (2) consideration as to why typical values for granitoids from each terrane are more than 3‰ removed from 0‰. The simplest explanation for both aspects of the sulfur isotope data is to assume that $\delta^{34}S$, like $(^{87}Sr/^{86}Sr)_0$ and $\delta^{18}O$, reflects the character of magmatic source regions in the lower crust—light, biogenic, sulfide sulfur being derived from the continental-type crustal segments, and the peripheral, more primitive crust on the Japan Sea side being characterized by heavier (sulfate?) sulfur. *Sasaki and Ishihara* [1979] show that isotopically light S is characteristic of several fundamental sedimentary units of the Japanese island arc and cite several cases for ilmenite series plutons in which lower $\delta^{34}S$ is correlative with higher S concentrations. They prefer to explain positive $\delta^{34}S$ values (to +9‰) by incorporation of marine sulfate from a subducting plate into magnetite series magmas but entertain the possibility that associated high values of $(^{87}Sr/^{86}Sr)_0$ and $\delta^{34}S$ for magnetite series plutons of the Chubu transect may result from incorporation of sulfate layers in the lower crust. Evidence from basalt-seawater interaction experiments and ocean floor basalts [see *Ohmoto and Rye*, 1979] suggests that island arc volcanic sediments could be characterized by heavy $\delta^{34}S$.

Ohmoto and Rye [1979] review the theory and evidence for large isotopic fractionations of sulfur during geologic processes. However, fractionations at magmatic temperatures are small, and were it not for two somewhat puzzling studies, one would discount the possibility that the +5‰, $\delta^{34}S$ character of the magnetite series granitoids could be related in some way to their oxidized nature. In a study of German basalt suites, *Schneider* [1970] found that $\delta^{34}S$ values varied slightly with oxidation state, as deduced from mineral phase relations. *Coleman* [1979] measured $\delta^{34}S$ for a number of Australian granites and found that oxidized I-types have positive values, whereas reduced S-types generally have negative values. Coleman's data for the Stanthorpe leucogranites show evidence for

modification of inherited $\delta^{34}S$ by oxidation; as Fe_2O_3/FeO for biotites in leucogranite samples increases from 0.1 to 0.2 to 0.3, $\delta^{34}S$ values first decrease from +2.5‰ to −5‰ and then dramatically increase to +5‰. Coleman suggests that the interrelation is caused by loss of water from water-rich, oxidized, I-type melts, and that [*Coleman*, 1979 p. 133] '... This same mechanism may account for the positive sulfur isotope values in the magnetite-series granitoids described by Sasaki and Ishihara (1979)...'

Coleman's 'mechanism' is unclear, and the oxidation we document is thought to relate principally to loss of H_2 rather than H_2O; moreover, whereas Coleman cites the heavy $\delta^{18}O$ character of the most oxidized Stanthorpe leucogranites as evidence for loss of H_2O; the magnetite series granitoids of Japan have relatively light $\delta^{18}O$. In fact, the heavy $\delta^{18}O$ character of the leucogranite and the evidence of this paper and *Czamanske and Wones* [1973] that magmatic oxidation does not involve a decrease in $Fe^{2+}/(Fe^{2+}+Fe^{3+})$ for biotites combine to suggest that the Stanthorpe leucogranite underwent postmagmatic oxidation by meteoric water.

Sulfur exists in hydrous silicate melts principally as HS^- but in the aqueous phase as SO_2 and H_2S; the high f_{O_2} and low confining pressure typical of magnetite series plutons will not only promote a high SO_2/H_2S, but also a high $\Sigma S^{aq}/\Sigma S^{m}$ because of the low solubility of SO_2 in hydrous magmas [*Burnham and Ohmoto*, 1980]. This effective extraction of sulfur from magnetite series melts as SO_2, and subsequent hydrolysis or reaction of SO_2 to form H_2S, is a fundamental factor in the typical association of sulfide ore deposits with magnetite series suites. Our evidence that a strong oxidizing trend in these suites, caused by aqueous fluid separation and H_2 loss, has reversed the normal Fe/(Fe+Mg) evolutionary trend in the major rock-forming silicates suggests that kinetic and disequilibrium isotopic effects could be significant for an element such as S which is in low abundance (0.00X to 0.0X wt %). However, in this oxidizing environment we can visualize no equilibrium or nonequilibrium process that would evolve gabbroids and granitoids that are heavy in $\delta^{34}S$ because SO_2 should always be heavier than the HS^- remaining in the melt and any sulfides that might separate from the melt would also be enriched in ^{34}S. In fact, there is no magmatic environment involving H_2S, HS^-, and SO_2 for which preferential removal of ^{32}S is predicted [*Ohmoto and Rye*, 1979, Figure 10.6].

The problem is interesting enough that it should be pursued through careful, further study of comagmatic, magnetite series suites. Specifically, the gabbroid data are presently so few and loosely related to the granitoid data that it is not clear whether $\delta^{34}S$ for granitoids is actually heavier than rather than similar to those of associated gabbroids. The demonstration that $\delta^{34}S$ could increase during magmatic evolution would require reevaluation of current thinking regarding sulfur isotope systematics in the magmatic regime. The fact that sulfide ores associated with granitoids in magnetite and ilmenite series terranes show a similar, bimodal distribution, averaging about 3‰ lighter than the host granitoids, is considered to reflect the isotopic distinction of the magmas themselves and is a limitation on models proposed to explain the S-isotopic character of the magnetite series suites.

Because one of the main contributions of our study of mafic silicate and oxide chemistry is the documentation of an oxidizing trend during differentiation of the studied magnetite series suites, it is appropriate to discuss the importance of H_2O and depth of emplacement of magma evolution. Our analytical data show that there was sufficient water present at endstage crystallization of all suites to lower the albite content of perthitic feldspar and reduce the F and Na contents of biotite. However, lack of miarolitic cavities, pegmatites, and contact alteration show that little water separated from Ryoke belt granitoids. Granitoids in the Sanyo belt contain miarolitic cavities, and drusy small pegmatites are well developed in aplitic marginal phases of the plutons. Nonetheless, rather narrow hornfels zones around granitoids of the Sanyo belt contrast with the wide, hydrothermal contact alteration zones characteristic of Sanin belt granitoids. *Burnham [1979] and Burnham and Ohmoto* [1980] summarize many of the relevant theoretical concepts. They note that to depths of 70 km, melts generated from mafic amphibolite must contain at least 2.7 wt % H_2O and that the amount of melt generated will depend upon the H_2O content of the source rock. Presence of amphibole in both magnetite and ilmenite series rocks requires that the melts contained at least 3 wt % water, perhaps 4 wt % water when amphibole was an early crystallizing phase. As such a melt moves upward in the crust, minerals will crystallize from it and eventually cause the residual melt to reach H_2O saturation and undergo a second-boiling reaction. The percentage of the melt that will have crystallized when this reaction commences and the overall effect of the reaction will be critically dependent on the depth of emplacement of the magma. Emplacement at less than 4-km depth (about 1100 bars) will result in release of mechanical energy sufficient to cause strong fracturing or explosive eruption; of equal importance is the fact that second-boiling reaction will take place when less than one third of the magma mass has crystallized. In the absence of early formed magnetite and sphene, crystallization of a substantial fraction of the original magma under circumstances in which an aqueous phase has separated and diffusive loss of H_2 can take place through fractured roof rocks is the means we suggest to account for the oxidizing trend that appears to characterize the entire magnetite series terrane of the Japan Sea side of the Inner Zone batholith. The tensional environment of the inner arc is presumed to have been of profound importance in allowing high-level plutonic emplacement.

Field relations in the Cretaceous ilmenite series terranes of southwestern Japan indicate that magmas which developed only minor gabbroic phases were emplaced at depths of 13 to 17 km (4 to 5 kbar). In the Ryoke II zone of the Chubu transect, conditions were such that granodiorites were the most siliceous rocks evolved. Typical ilmenite series melts may have contained a smaller upper mantle component and reflect their origin in crust with a larger metasedimentary component. Emplacement into an outer arc compressional environment must have restricted their upward mobility. Moreover, melts generated in a Precambrian crustal environment where micaceous metasediments are logical constituents will contain substantially more H_2O than melts generated in amphibolitic crust and, because of their high H_2O content and origin at relatively low temperature, do not possess the requisite thermal energy to attain high-level, subvolcanic emplacement. Having moved perhaps half the distance to the surface, they are emplaced at such great depth that (1) the mechanical energy released upon second boiling produces only weak fracturing, and (2) a fluid phase does not separate until the magma is largely crystalline. Associated mineralization is of a higher pressure, oxide-type (e.g., Sn and W). Any sulfide-forming components that might have once characterized such magma

systems would have typically been bled away to higher levels and been removed by erosion.

Ishihara [1977] has shown that a substantial proportion of Fe and Ti are bound in oxide phases in the magnetite series suites, whereas in the oxide-poor, ilmenite series suites these elements are principally carried in biotite and amphibole. The fact that there are so few significant distinctions in mafic silicate chemistry between the two contrasting suites strongly suggests that there is no significant difference in the process of generation of magnetite and ilmenite series magmas. Specifically, compositional characteristics of the mafic silicates appear to exclude the possibility that relatively low-temperature, midcrustal assimilation is an important process in the generation of ilmenite series magmas. They are also in keeping with petrographic evidence for late oxide crystallization in studied magnetite series rocks. We suggest that depth of magma generation is not the most significant variable and that both magnetite and ilmenite series magmas originate through the reactive and assimilative action of mantle-derived melt in the lower crust. This suggestion is supported by several further lines of evidence.

1. Chemical disequilibrium, reaction textures, restite, and other features are absent, and instead, suites of rocks are remarkably similar in chemistry, mineralogy, and apparent crystallization history.

2. Cretaceous-Paleocene gabbroic rocks of the Inner Zone have $(^{87}Sr/^{86}Sr)_0$ values that do not differ significantly from those of the granites [*Shibata and Ishihara*, 1979*b*].

3. The age-independent character of oxide and isotopic characteristics is most compatible with deep magma derivation.

A tenable model for magma genesis cannot be time dependent because values of $(^{87}Sr/^{86}Sr)_0$, $\delta^{34}S$, and $\delta^{18}O$ as well as oxide mineralogy are regionally characteristic for both Cretaceous-Paleocene and Miocene plutonism. In fact, magnetite-bearing character was typical of the Japan Sea side from the Triassic onward, as evidenced by the Funatsu granitoids. The age independence of granitoid characteristics may also be used to argue against the importance of subduction or a subducting plate to models of magma genesis in the Japanese islands because of their mobility and the probable changing relations of subducting motion to them.

EPILOGUE

In their paper on S-isotopic compositions of the magnetite series and ilmenite series granitoids, *Sasaki and Ishihara* [1979] point out that the geologic background of Japan might be "unique" and acknowledge the possibility that the dramatic distinction between the sulfur isotopic data of the two series could be a 'mere peculiarity' of the Japanese island arc. The batholithic terranes of North America, South America, and Australia each have their unique features, and it seems likely that the Japanese islands present an environment for generation of granitic magmas characterized by a distinctive suite of crustal materials. A great deal of tectonic mobility is reflected in their framework, and the source regions for generation of magmas beneath Japan may well be more diverse in chemical and isotopic characteristics than the source regions for the North American and Australian batholiths. Continental crust, oceanic crust, volcanic complexes, and volcanogenic sediments that have not been long exposed to surficial chemical weathering are logical, major crustal components.

Pankhurst et al. [1976], *Carter et al.* [1978], *Anderson and Cullers* [1978], *McCulloch and Wasserburg* [1978], *Taylor et al.* [1979], *Foland and Friedman* [1977], *Hawkesworth and Vollmer* [1979], *Perfit et al.* [1980], and others have shown that application of radiogenic (strontium and neodymium) and stable (oxygen and hydrogen) isotopic systematics, with trace and rare-earth element chemistry can be exceedingly powerful in developing comprehensive petrogenetic models and in distinguishing between a wide variety of magmatic and assimilative processes (e.g., fractional crystallization, magma mixing, liquid immiscibility, anatexis, bulk assimilation, reaction melting, and subsolidus hydrothermal exchange). Crucial questions regarding the temporal and spatial evolution of the Inner Zone batholith require resolution of questions regarding the nature of the source region and of where, when, and how "crustal contamination" may have occurred. Ishihara has realized the importance of isotopic studies, and reconnaissance data are available for all relevant isotopes except Nd, Pb, and H. However, until thorough, well-orchestrated studies of isotopic and rare-earth element systematics are applied to representative granitoid suites of the Japanese islands, adequate understanding of the evolution of those granitoid rocks and of the broader problem of crustal evolution will be elusive. Conversely, such comprehensive studies would contribute substantially to understanding the framework of the Japanese islands in its broadest sense and to establishing a type example for the characteristics of granitoid evolution in island arc systems.

APPENDIX: DESCRIPTIONS OF THIN SECTIONS

RS-88: 36°19′10″N 136°53′53″E (sample location in latitude and longitude coordinates), a medium crystalline quartz monzodiorite (59.10; 60.4; 591; 1) (the first number in parentheses is the silica content, the second the differentiation index [*Thornton and Tuttle*, 1960] for the rock unit, the third is the magnetic susceptibility in (emu/q) $\times 10^{-6}$, and the fourth is that used by *Ishihara and Terashima* [1977*a*] to report data for specimens from the Chubu transect; Ishihara has classified rocks with magnetic susceptibility less than 100 as ilmenite series), composed of poikilitic quartz, potassium feldspar, plagioclase, biotite, and amphibole. Potassium feldspar (to 3 mm; Or_{85-87}) and quartz enclose smaller plagioclase laths (to 1 mm), amphibole, and chloritized biotite. Plagioclase (to 1.5 mm) is broadly zoned (Ab_{39-79}; $Or_{2.1-1.9}$) with finely twinned, recrystallized, corroded, and sericitized cores or reaction rings, and untwinned, locally myrmekitic rims. Abundant, zoned amphibole (olive green to green cores and pleochroic green rims) occurs both as slender poikilitic rods (to 2.7 mm) enclosing small plagioclase laths and magnetite and as smaller subhedral grains (to 1 mm) in which the rim composition predominates. Biotite occurs primarily as small, ragged grains (pleochroic light tan to amber brown) replacing amphibole and to a lesser extent as individual anhedral grains (to 0.6 mm, pleochroic light tan to dark brown). Commonly, chlorite partially replaces both types of biotite. Fine-grained magnetite is rather uniformly distributed and typically intergrown with amphibole and the rims of plagioclase grains.

RS-57: 36°08′58″N 136°50′49″E, a porphyritic quartz monzodiorite (65.46; 71.8; 22; 8) composed of phenocrysts of plagioclase (to 6 mm, averaging 3 mm), perthitic potassium feldspar (to 3mm), anhedral quartz (to 2 mm), glomeroporphyritic clusters of anhedral to subhedral amphibole (individual crystals to 2 mm), euhedral allanite, and anhedral biot-

ite (to 2 mm) set in an interstitial, fine-grained, aplitic groundmass of interlocking anhedral grains of quartz, plagioclase, potassium feldspar, biotite, and amphibole. Phenocryst potassium feldspar (Or_{90-86}) may be twinned after the microcline law and is perthitic. Poikilitic potassium feldspar enclosed grains of amphibole and plagioclase and, along with twinned potassium feldspar grains, may include an interior ring of fine, round groundmass grains. Potassium feldspar, along with quartz, exhibits irregular, intergrown boundaries with the aplitic groundmass. Phenocryst plagioclase exhibits fine oscillatory zoning (Ab_{56-69}; $Or_{1\ 2-1.6}$) and thin, discontinuous albitic rims adjacent to potassium feldspar grains. Large amphibole grains (pleochroic green to olive cores, and green rims) are zoned, with bleached and fibrous cores surrounded by more pristine, igneous rims. Larger biotite grains (pleochroic tan to red brown) are often bent, are rimmed by and include fine nets of rutile, and are moderately altered to chlorite.

RS-69: 36°09′45″N 136°53′27″E, a porphyritic quartz monzodiorite (69.34; 80.8; 552; 7) with phenocrysts of lath-shaped plagioclase (to 5 mm), quartz (to 3 mm), amphibole (to 3.8 mm) and biotite (to 1.25 mm), in an allotriomorphic-granular groundmass mosaic of quartz, potassium feldspar, plagioclase, euhedral to anhedral amphibole, biotite, chloritized biotite, and accessory magnetite. Phenocryst plagioclase is broadly zoned (Ab_{63-81}; $Or_{2\ 0-2\ 9}$) with either fine oscillatory zoning or polysynthetic twinned) cores and smooth, untwinned rims. A fine dusting of sericite is common in the cores of both the larger plagioclase phenocrysts and the smaller (to 1.5 mm) anhedral plagioclase grains of the groundmass. Irregular quartz phenocrysts are poikilitic, enclosing groundmass grains of potassium feldspar. Turbid, perthitic potassium feldspar (Or_{82-85}), confined to the groundmass, often contains fine grains of albitic plagioclase (to 0.05 mm), especially along perthite-perthite grain boundaries. Long, slender amphibole phenocrysts (pleochroic light greenish tan to green) often enclose anhedral plagioclase laths and magnetite grains and commonly are partially replaced by ragged, secondary biotite (pleochroic tan to dark brown) and/or overgrown and enclosed by more well-developed igneous biotite (pleochroic tan to dark brown). Amphibole is zoned, with the late phase apparently more dominant, and locally chloritized, although the chlorite may be replacing secondary biotite. Amphibole grains in the groundmass are generally subhedral to anhedral and, as in the case of the amphibole phenocrysts, partially replaced or overgrown by biotite. Phenocryst biotite includes fine-grained rutile or sphene, especially at grain boundaries, and, along with groundmass biotite, is often partially replaced by chlorite and epidote. In contrast to RS-57, the groundmass makes up a much larger percentage of the rock, as it is not confined to interstices between otherwise contiguous grains. Magnetite is restricted to the groundmass, where it is randomly intergrown with both felsic and mafic phases.

RS-87: 36°19′10″N 136°53′53″E, a medium crystalline, hypidiomorphic-granular monzogranite (72.86; 87.0; 276; 2), composed of a mosaic of intergrown poikilitic potassium feldspar, anhedral quartz, plagioclase grains, and minor biotite. Potassium feldspar (up to 3.5 mm; Or_{85-88}) is only weakly perthitic and may enclose grains of plagioclase, quartz, and biotite. Plagioclase (to 2.5 mm), is broadly zoned (Ab_{64-80}; $Or_{2.1-2.3}$) with the discontinuous, narrow, more albitic rims best developed on grains enclosed within the poikilitic potassium feldspar. Individual plagioclase grains lack well-developed, polysynthetic twinning, are locally myrmekitic, and have a weak dusting of fine-grained sericite. Unlike RS-88, which was included in RS-87 as a xenolithic block, amphibole is extremely rare, the primary mafic phase being a ragged, moderately chloritized biotite (to 1 mm; pleochroic amber or with better crystalline grains, pleochroic light tan to brown). Magnetite occurs intergrown with potassium feldspar, plagioclase, and quartz. Rare sphene and allanite are accessories.

RS-91: 36°18′05″N 135°53′49″E, an equigranular, fine-to-medium crystalline, allotriomorphic-granular monzogranite (76.28; 94.7; 262; 3). This unit, intrusive into both RS-87 and RS-88, is composed of interlocking grains of perthite (to 2.5 × 1.8 mm), quartz, and plagioclase (to 2 mm) with accessory biotite (pleochroic tan to brown), allanite, and magnetite. The perthite is inhomogeneous (Or_{69-79}) and strongly exsolved, with individual lamellae exhibiting well-developed, polysynthetic twinning. Perthite-perthite contacts are highly irregular and include fine, albitic plagioclase grains, suggestive of late albite migration. Plagioclase grains are weakly zoned (Ab_{84-87}; $Or_{3\ 8-2\ 2}$) and finely twinned, with broad, irregular albitic rims ($Ab_{96.5}$) adjacent to perthite. Fine biotite (to 1 mm; pleochroic tan to brown) is moderately altered to chlorite. Magnetite occurs intergrown with potassium feldspar, plagioclase, and quartz.

T-41: 35°25′44″N 137°10′06″E, a medium crystalline, hypidiomorphic-granular granodiorite (68.10; 74.2; 17; 11), composed primarily of intergrown plagioclase, potassium feldspar, anhedral quartz, and biotite. Plagioclase (to 5 mm) is strongly zoned (Ab_{53-80}, locally reversed; $Or_{3.3.-1.6}$), with well-developed, fine polysynthetic twinning and occasional oscillatory zoning in the cores, and untwinned rims. Larger plagioclase grains may have recrystallized cores and thin albitic rims when in contact with potassium feldspar. Potassium feldspar (to 4 mm; Or_{87-89}) is only mildly perthitic, with scattered, exsolved blebs and discontinuous, irregular, albitic lamellae. It is locally twinned, after the microcline law, and commonly encloses euhedral to subhedral quartz, plagioclase, and biotite. Quartz, other than the well-preserved, euhedral to subhedral, hexagonal inclusions in the poikilitic potassium feldspar, is anhedral and itself often encloses smaller plagioclase and biotite grains. The section studied contained only small (0.5 mm) amphibole grains (pleochroic green), including a single skeletal grain; the primary mafic phase is biotite. Euhedral to anhedral biotite (to 1 mm) is weakly zoned (pleochroic light brown to dark red brown, with more greenish pleochroism toward the rims) and moderately chloritized. Zoned, euhedral allanite is a common accessory phase.

T-38: 35°25′24″N 137°11′27″E, a hypidiomorphic-granular granodiorite (70.57; 79.7; 17; 12), composed of a mosaic of larger, intergrown poikilitic grains of potassium feldspar, quartz, and to a lesser extent plagioclase, with biotite and minor amphibole. Mildly perthitic potassium feldspar grains (to 4.5 mm, Or_{82-85}) enclose plagioclase laths, amphibole, and biotite, are twinned, and often, when in contact with other potassium feldspar grains, contain small, irregular, albitic patches along grain boundaries. Quartz is also poikilitic, enclosing plagioclase and biotite grains, and occurs primarily as clusters of large intergrown, irregular grains with interstitial quartz and potassium feldspar fillings. Plagioclase (to 4 mm) is zoned (Ab_{62-76}; $Or_{2.5-3.0}$), including cores which exhibit fine polysynthetic twinning and delicate oscillatory (occasionally reversed) zoning and broad, untwinned rims. Plagioclase grains occurring as inclusions within, or as contiguous grains

adjacent to, potassium feldspar generally have sutured contacts with thin, irregular, more albitic rims. Minor, subhedral amphibole, including a single, large skeletal grain (1.25 mm) is zoned (pleochroic olive brown to light green cores and green to light greem rims). Biotite (pleochroic brown to light tan) occurs both as fine grains replacing amphibole or as individual subhedral to anhedral grains (to 1.7 mm). Minor chlorite (primarily after biotite), allanite, and sericite (after plagioclase and potassium feldspar) are accessories.

T-44: 35°23′23″N 137°14′19″E, unlike T-41 and T-38, both of which are from the granodioritic phase of the Toki pluton, is a sample from the porphyritic monzogranitic phase of the body (72.72; 88.7; 16; 13). Phenocrysts of plagioclase, perthite, quartz, and biotite are set in a fine-grained (to 1 mm), allotriomorphic-granular matrix of quartz, plagioclase, potassium feldspar, and biotite. Large, turbid potassium feldspar phenocrysts (to 2.7 mm; Or_{87-90}) are twinned, strongly exsolved, and poikiliticly enclose smaller plagioclase laths and subhedral quartz hexagons. Potassium feldspar of the groundmass is turbid and much less perthitic, although exsolved albite within and along grain boundaries is common. Quartz phenocrysts occur as clusters of individual, intergrown grains which often enclose plagioclase laths and euhedral to subhedral potassium feldspar grains. Plagioclase phenocrysts (to 4.5 mm) are zoned (Ab_{74-84}; $Or_{3.6-2.0}$), with strongly corroded and, in part, recrystallized cores. Matrix plagioclase is also zoned with turbid and weakly sericitized cores. Two distinct biotites (to 1.75 mm) are present: an early Ti-rich phase (pleochroic dark brown to tan) and a later Ti-poor variety (pleochroic dark green to olive). Low Ti biotite occurs around the edges of the Ti-rich biotite, with rutile and/or sphene plus epidote as a possible replacement product, and, as individual grains with epidote and chlorite, filling interstices. Rare chlorite occurs as an interstitial phase and replacing biotite. Allanite is a minor accessory.

T-25: 35°27′02″N, 137°14′31″E like T-44, is from the monzogranitic phase of the Toki pluton (75.18; 92.0; 16; 16). It is a medium crystalline, hypidiomorphic-granular rock composed of a mosaic of quartz, perthite, plagioclase, and strongly chloritized biotite. Turbid potassium feldspar (to 3.5 mm; Or_{78-87}) is strongly exsolved, showing twinned, albitic lamellae and blebs and fine-grained albite along perthite grain boundaries. Plagioclase (to 3 mm) is only weakly zoned (Ab_{81-87}; $Or_{4.2-2.2}$) but shows well-defined, albitic rims (Ab_{97}) when adjacent to potassium feldspar. Individual, anhedral quartz grains (to 4 mm) are intergrown with plagioclase and potassium feldspar. Biotite (to 1.7 mm) is zoned with an earlier Ti-rich phase (pleochroic dark brown to tan) and a later Ti-poor phase (pleochroic dark green to olive green) that occurs both as rims on Ti-rich cores and as individual grains. Chlorite occurs on the edges of pleochroic green biotite, completely replacing previous biotite grains, with magnetite plus sphene or rutile, and intergrown with muscovite and quartz, filling scattered interstices. Allanite occurs within biotite grains and as corroded remnants in chloritized biotite. Minor fluroite also occurs in biotite.

6911-213: 35°30′22″N, 137°24′29″E a hypidiomorphic-granular to allotriomorphic-granular monzogranite (76.12; 94.1; 16; 19), composed of intergrown grains of perthite, quartz, plagioclase, and minor biotite. Turbid potassium feldspar grains (to 6 mm; Or_{70-84} are strongly exsolved), (as in T-25), including twinned exsolution lamellae and blebs of plagioclase within the perthite grains and small chains of albitic plagioclase along perthite grain boundaries; they are commonly twinned and poikilitic, enclosing abundant subhedral quartz hexagons and plagioclase laths. Plagioclase (to 3 mm) is weakly zoned (Ab_{81-85}; $Or_{3.0-1.5}$) with well-developed, albitic rims (Ab_{96}) adjacent to potassium feldspar grains and, as with potassium feldspar, partially encloses euhedral to subhedral quartz grains. Quartz generally occurs as intergrown clusters of individual, anhedral crystals. Biotite (to 1 mm) occurs as zoned grains with Ti-rich cores (pleochroic red brown to tan) and Ti-poor rims (pleo-chroic green to light green or tan) or as homogeneous grains composed solely of the Ti-poor phase. Rare chlorite partially replaces biotite or, with quartz and minor muscovite, fills scattered interstices.

T-97: 35°14′48″N 137°15′03″E, a hypidiomorphic-granular granodiorite (68.06; 71.1; 17; 22), composed of plagioclase grains (to 5.4 mm) intergrown with poikilitic potassium feldspar (to 3.5 mm) and irregular quartz grains (to 3 mm). Potassium feldspar and quartz enclose small plagioclase laths, euhedral to subhedral biotite, and amphibole grains. Potassium feldspar (Or_{90}) is weakly perthitic. Plagioclase is zoned (Ab_{57-65}), occasionally reversed; $Or_{1.5-1.0}$), commonly with fine oscillatory zoning and corroded and recrystallized cores. Euhedral to subhedral amphibole (to 1.5 mm) is zoned (pleochroic olive brown to olive green cores and green to light tanish green rims) and occasionally encloses small plagioclase laths. Biotite (to 2.5 mm; pleochroic tan to red brown) is partially chloritized along cleavage planes. Allanite and sphene are accessories, along with interstitial chlorite plus calcite.

T-94: 35°16′57″N 137°12′55″E, an allotriomorphic-granular monzogranite (73.42; 86.5; 13; 27), composed of an interlocking mosaic of perthite, quartz, plagioclase, and biotite. Potassium feldspar (to 6.5 mm; Or_{75-85}) is strongly exsolved, containing albitic plagioclase as blebs within individual grains and along perthite grain boundaries; grains are often twinned, following both the carlsbad and microcline laws, and may enclose smaller plagioclase laths and anhedral biotite. Plagioclase (to 2 mm) is weakly zoned over a narrow composition range (Ab_{72-76}; $Or_{1.0-1.2}$) with thin sodic rims (Ab_{94}), especially well-developed adjacent to perthite grains. Quartz is generally anhedral (to 5 mm), although it can be subhedral when enclosed by potassium feldspar. Two small grains of amphibole (to 0.2 mm; pleochroic green to light green tan) were analyzed; however, biotite is by far the dominant mafic phase. Biotite (to 1 mm) includes two compositionally distinct phases, a dominant Ti-rich phase (pleochroic brown to light tan) and a less common, Ti-poor phase (light green to tan). The later phase occurs as faint rims on, or more extensive replacement of, the more Ti-rich phase. Minor chlorite (replacing biotite), allanite, rutile, ilmenite, and sphene are accessory phases.

T-145: 35°14′44″N 137°10′18″E, an allotriomorphic-granular monzogranite (74.54; 89.3; 12; 29), composed of larger plagioclase grains (to 2 mm), poikilitic potassium feldspar (to 2.75 mm), and patches of intergrown quartz grains in a mosaic matrix of plagioclase, potassium feldspar, quartz, and biotite. Potassium feldspar (Or_{86-89}) is mildly perthitic; larger grains enclose small plagioclase laths and irregular, exsolved plagioclase blebs. Plagioclase is zoned (Ab_{74-84}; $Or_{1.2-1.6}$) with distinct, broad, more albitic rims, often including fine myrmekitic intergrowths. Biotite (to 1 mm) is zoned (as in T-94), with an earlier Ti-rich phase (pleochroic brown to tan) and a second phase lower in Ti (pleochroic green). Chlorite may partially or completely replace biotite and often occurs with ilmenite and rutile. Chlorite and allanite are accessories.

T-165: 35°07′31″N 137°19′36″E, a strongly foliated, porphyritic quartz diorite (51.46; 35.7; 14; 36), composed of plagioclase megacrysts (to 7.5 mm) with plagioclase (to 3.6 mm) and quartz (to 4.5 mm) phenocrysts set in a matrix of planar oriented plagioclase (to 1 mm), biotite, quartz, and amphibole. Plagioclase phenocrysts are weakly zoned (Ab_{50-52}; $Or_{0.8-0.7}$), occasionally with corroded cores, and often enclose small euhedral amphibole grains. Plagioclase grains of the groundmass are similar in composition. Anhedral quartz phenocrysts are intimately intergrown with and surround plagioclase, amphibole, and biotite grains. Amphibole (pleochroic deep green to olive) occurs in elongate clusters of euhedral to anhedral grains (to 0.5 mm) intergrown with and enclosing plagioclase, quartz, and abundant ilmenite. Biotite (to 2 mm; pleochroic brown to tan), often poikilitically encloses groundmass plagioclase, quartz, and ilmenite and lacks the pronounced orientation developed in amphibole and plagioclase grains. Chlorite occurs after biotite as a minor phase.

T-128: 35°12′05″N 137°21′36″E, a hypidiomorphic-granular granodiorite (63.92; 60.1; 17; 31), composed of plagioclase, quartz, and poikilitic potassium feldspar, intergrown with clinopyroxene, amphibole, and abundant biotite. Potassium feldspar (to 4 mm; Or_{89}) is homogeneous, often interstitial, and may enclose small plagioclase, quartz, and biotite grains. Plagioclase (to 1.7 mm) is zoned (Ab_{51-60}; $Or_{1.2-1.0}$) often with delicate oscillations and recrystallized cores. Quartz (to 5mm) is also often poikilitic and, in part, interstitial. Clinopyroxene (to 3.5 mm) is generally anhedral, often corroded, and, especially in the case of larger grains, replaced or overgrown by amphibole and to a lesser extent biotite. Zoned amphibole grains (to 4 mm; pleochroic brown to light green cores and green to light green rims) are often intergrown with or replace clinopyroxene; are occasionally poikilitic, enclosing small, rounded quartz, ilmenite, plagioclase, and biotite grains, and, though often intergrown with, may rarely be in part replaced by ragged biotite. Biotite (to 3 mm) is generally anhedral and most often occurs in clusters alone or with amphibole or py- . Rare chlorite after biotite and sphene are accessory phases.

T-75: 35°06′31″N 137°19′15″E, is a sheared, hypidiomorphic-granular granodiorite (66.16; 66.4; 47; 32). Within shear zones, quartz is recrystallized and elongated roughly parallel to shearing, plagioclase twin lamellae are bent, and potassium feldspar is recrystallized. Brown biotite is strongly bent and recrystallized and intergrown with more brittle amphibole, contorted plenochroic green biotite, minor calcite, and sphene; it is often sheathed in a thin, sinuous, amorphous to locally opaque rim. In undeformed areas between shear zones, potassium feldspar (to 4 mm; Or_{88-92}) is only mildly perthitic and encloses scattered grains of biotite, plagioclase, and amphibole. Plagioclase (to 3 mm), often with bent twin lamellae while still several millimeters removed from zones of maximum shearing, is weakly zoned (Ab_{60-65}, locally reversed; $Or_{1.0-1.4}$). Quartz, most commonly with irregular extinction and locally recrystallized, even away from shear zones, is irregular and occasionally interstitial. Amphibole (to 1.7 mm) is generally anhedral and strongly zoned (pleochroic olive green to brown cores and aqua to green rims). Biotite (to 1 mm; pleochroic reddish brown to tan) often occurs with amphibole in glomeroporphyritic clusters; however, where the pleochroic brown biotite occurs in shear zones, it grades into a second biotite phase (not analyzed; pleochroic light green to light tan) and then into chlorite. Chlorite primarily replaces pleochroic green biotite in shear zones and, to a lesser extent, replaces pleochroic brown biotite along cleavage planes outside of the zone of shearing. Rare allanite, apatite, and rutile are accessory phases.

T-168: 35°07′31″N 137°19′36″E, the host pluton enclosing the xenolith from which T-165 was collected, is a medium-grained, hypidiomorphic-granular granodiorite (68.54; 72.0; 17; 37) composed of a mosaic of plagioclase, potassium feldspar, quartz, amphibole, and biotite. Plagioclase (to 2 mm; Ab_{53-63}; $Or_{1.3}$) is broadly zoned with occasional myrmekitic rims and often with oscillatory zoning and recrystallization in the cores; it is commonly finely twinned. Potassium feldspar (to 7.5 mm; Or_{88-90}) is only mildly perthitic and commonly encloses plagioclase laths, subhedral quartz, and biotite. Quartz is generally anhedral and may be recrystallized where associated with plagioclase exhibiting bent twin lamellae. Minor amphibole grains are subhedral to anhedral (to 1.8 mm; pleochroic green to light green) and locally enclose small plagioclase laths. Biotite (pleochroic red brown to tan) is anhedral (to 3 mm) and occasionally bent and structurally distorted as in T-75. Rare, pleochroic green biotite is developed on the edges of contorted biotite grains as in T-75. Minor chlorite after biotite and rare allanite are accessory phases.

T-79. 35°01′44″N 137°19′46″E, a medium crystalline, allotriomorphic-granular tonalite (60.24; 51.9; 29; 39), composed of interlocking plagioclase, quartz, minor potassium feldspar, and intergrown clusters of biotite and subordinate amphibole. Plagioclase (to 4 mm) is zoned (Ab_{50-61}; $Or_{1.5}$), with fine oscillatory zoning and corroded and occasionally sericitized cores. Quartz (to 4 mm) is irregular and in part interstitial. Potassium feldspar (Or_{88}) is restricted to interstices between plagioclase grains and may show pronounced albitic rims. Amphibole (to 3.3 mm) is zoned (pleochroic olive brown to light green cores, green to light green rims) and encloses small plagioclase laths and quartz grains; it generally occurs as irregular grains. Biotite (to 2.25 mm; pleochroic amber brown to tan) is irregular and generally occurs in glomeroporphyritic clusters intergrown with amphibole and surrounding amphibole grains as overgrowths. Rare chlorite (replacing biotite), sphene (developed as fine intergrowths along biotite grain boundaries), minor ilmenite, and allanite are accessory phases.

T-173-2: 34°58′35″N 137°19′57″E, a fine-to-medium crystalline, allotriomorphic-granular, muscovite-biotite monzogranite (72.49; 86.5; 19; 45), composed of a mosaic of irregular, interlocking grains of quartz, plagioclase, potassium feldspar, muscovite, and smaller biotite. Plagioclase (to 1 mm) is broadly zoned (Ab_{50-81};$Or_{1.4-1.3}$) with distinct turbid cores, often containing coarse sericite, and broad smooth rims. Potassium feldspar (to 1 mm; Or_{88-89}) is irregular and homogeneous. Quartz (to 3 mm) is irregular to interstitial and occasionally encloses plagioclase and biotite. Muscovite (to 1.5 mm) is zoned, and in the case of the larger grains, encloses small plagioclase, quartz, and biotite grains. Biotite (pleochroic amber brown to tan) is generally fine-grained (to 1 mm), interstitial, and moderately chloritized along cleavage planes.

T-76: 35°04′55″N 137°19′49″E, a medium crystalline, allotriomorphic-granular, muscovite-biotite granodiorite (72.28; 79.4; 15; 42), composed of a mosaic of plagioclase, poikilitic potassium feldspar, and quartz, with fine-grained biotite and muscovite. Plagioclase (to 1.7 mm) is strongly zoned (Ab_{51-76};

$Or_{1.1-1.5}$), with distinct and occasionally corroded cores and broad, locally myrmekitic, often oscillatory zoned rims. Potassium feldspar (to 2.7 mm; Or_{89-90}) is generally irregular and commonly encloses rounded quartz grains, plagioclase laths, and biotite. Quartz is irregular, often enclosing small grains of biotite and plagioclase. Biotite (to 1.2 mm; pleochroic brown to light tan) is commonly irregular and interstitial and may be partially or completely replaced by chlorite.

T-133: 35°02′21″N 137°00′15″E, a medium crystalline, allotriomorphic- to hypidiomorphic-granular, muscovite-biotite monzogranite (72.99; 88.7; 16; 48), composed of plagioclase laths of varying sizes intergrown with irregular, poikilitic potassium feldspar, and quartz, with interstitial biotite and muscovite. Plagioclase (to 3.8 mm; Ab_{69-85}; $Or_{1.5-1.3}$) displays distinct, turbid, and often corroded cores and smooth broad rims, often enclosing small, rounded quartz grains. Plagioclase is locally myrmekitic and, when adjacent to potassium feldspar, may also include a pronounced, discontinuous albitic rim. Irregular to interstitial potassium feldspar (to 2.7 mm; Or_{84-88}) is moderately perthitic and poikilitic, enclosing quartz, plagioclase, and biotite grains. Quartz is irregular, possibly recrystallized, and locally interstitial. Biotite (pleochroic brown to tan) is fine-grained (to 1 mm); weakly zoned muscovite (to 1 mm) is intergrown with and often encloses biotite. Chlorite may partially or completely replace biotite.

Katsura 1: 35°12′39″N133°08′56″E, a fine-to-medium crystalline, hypidiomorphic-granular quartz diorite (55.20; 47.2; 2475), composed of plagioclase laths (to 3.2 mm, but averaging less than 1.5 mm), intergrown with quartz (to 3 mm), minor interstitial potassium feldspar (Or_{92-94}), subhedral amphibole, and biotite. Plagioclase is strongly zoned (Ab_{35-62}; $Or_{0.5-1.2}$) with distinct, corroded, recrystallized, and locally sericitized cores and broad, generally smooth rims. Quartz encloses plagioclase laths, subhedral amphibole grains, and to a lesser extent biotite. Amphibole (to 2.5 mm) is zoned (pleochroic olive to tan cores, green to tan rims), commonly encloses plagioclase laths and subhedral magnetite grains, and is frequently intergrown with irregular to subhedral sphene grains (to 0.7 mm × 0.5 mm). Amphibole is intergrown with large biotite grains (to 3 mm) and, in several instances, appears also to be in part replaced by ragged biotite. Large, poikilitic biotite grains (pleochroic dark brown to tan) enclose plagioclase laths, to a lesser extent quartz, and occasionally apatite and magnetite. Biotite is weakly to moderately chloritized. Fine-grained magnetite is rather uniformly distributed and typically intergrown with the rims of plagioclase and amphibole grains, but included in biotite. Sphene is typically interstitial to euhedral plagioclase (more rarely to euhedral amphibole) and is often intergrown with amphibole. Large apatite grains are accessory.

6412-17: 35°17′19″N 132°58′08″E, a medium crystalline, hypidiomorphic-granular granodiorite (61.68; 61.6; 603), composed of plagioclase, potassium feldspar, quartz, amphibole, and biotite. Plagioclase (to 4.2 mm; Ab_{66-70}; $Or_{2.0-1.9}$) shows weak oscillatory zoning, and patchy, recrystallized, locally corroded, and mildly sericitized cores. Potassium feldspar (to 4 mm; Or_{88-90}) is irregular and encloses plagioclase, amphibole, and to a lesser extent quartz and biotite grains; it may be included in plagioclase. Quartz is irregular to interstitial, often intergrown with adjacent grains, and encloses plagioclase, amphibole, biotite, and potassium feldspar. Amphibole (to 2 mm) is commonly subhedral, zoned (pleochroic light olive green to tan cores, green to tan rims), and intergrown with magnetite and sphene. Biotite (pleochroic dark brown to tan) most common occurs as large poikilitic grains (to 2.5 mm) enclosing plagioclase, quartz, and subordinate amounts of apatite and magnetite, and is intergrown with and overgrown around amphibole grains. Chlorite occurs as a minor alteration product after biotite as well as an interstitial filling associated with amphibole. Magnetite is typically interstitial to, or intergrown with, amphibole or included in biotite or quartz. Sphene is interstitial to euhedral amphibole and plagioclase. Apatite and rare allanite are accessory.

6510-116: 35°13′23″N 133°01′34″E, a medium-to-coarse crystalline, hypidiomorphic-granular granodiorite (67.15; 75.4; 869), composed of large, perthitic potassium feldspar (to 7 mm) and plagioclase grains (to 4.5 mm) in a finer matrix of quartz, plagioclase, potassium feldspar, amphibole, and biotite. Both large and small plagioclase grains are zoned but over a narrow compositional range (Ab_{74-76}; $Or_{1.8}$). Most grains exhibit fine oscillatory zoning in their rims; their cores are marked by a sharp resorption ring, inside which the feldspar is strongly recrystallized and reequilibrated to a composition similar to that of the rims. Plagioclase grains in contact with potassium feldspar often have a discontinuous albitic rim that may be myrmekitic. Large potassium feldspar grains (Or_{84-86}) enclose euhedral quartz, plagioclase laths, and subhedral amphibole and biotite grains, and toward their margins are intergrown with interstitial quartz. Contacts between perthite grains are commonly sutured and include fine albitic plagioclase. Quartz is commonly interstitial to plagioclase and potassium feldspar, though larger grains do occur. Amphibole (commonly pleochroic light green to greenish tan) occurs as scattered, large grains (to 1 mm) or clusters of smaller grains intergrown with biotite and magnetite. Biotite occurs as ragged grains, partially replacing amphibole and as individual grains (to 0.8 mm) often enclosing or partially enclosing plagioclase and magnetite. Scattered grains of chlorite occur both replacing biotite and also as a late stage, interstitial filling. Subhedral magnetite is intergrown with the phases of the finer-grained matrix. A single, 160-mm-long cluster of sphene grains is wholly enclosed within interstitial potassium feldspar.

6510-132: 35°10′54″N 133°00′50″E, a medium-to-coarse crystalline, allotriomorphic-granular monzogranite (74.16; 89.2; 358), composed of anhedral quartz, plagioclase, perthite, and minor biotite and magnetite. Plagioclase grains (to 3 mm; Ab_{74-83}; $Or_{2.3-1.4}$) ar broadly zoned, often with corroded and weakly sericitized cores; larger grains commonly have recrystallized or partially recrystallized cores. Where plagioclase is in contact with potassium feldspar, grains include a discontinuous, though well-defined, locally myrmekitic, albitic rim. Large, irregular potassium feldspar grains (to 6 mm; Or_{69-73}), are strongly exsolved, twinned, and distinctly zoned [*McTaggart*, 1979]; potassium feldspar often encloses plagioclase and subhedral quartz, more rarely magnetite and biotite. Contacts between perthite grains are generally serrate, include small albite grains, and are myrmekitic. Quartz occurs as large, irregular grains or clusters of smaller grains and is often intimately intergrown with potassium feldspar in interstices. Scattered biotite (to 1.7 mm; pleochroic brown to tan) is ragged, moderately chloritized, and intergrown with magnetite. A late magmatic, zoned chlorite + muscovite + epidote assemblage fills rare interstices. Magnetite is interstitial to euhedral plagioclase grains or associated with biotite. Trace sphene is interstitial.

5907-55: 35°18′44″N 133°06′21″E, a medium crystalline, allotriomorphic-granular monzogranite (75.28; 90.4; 328),

composed predominantly of large, intergrown grains of perthite, quartz, and plagioclase, with minor biotite and magnetite. The rock contains scattered, fine-grained (to 1-mm) clusters of turbid, weakly sericitized plagioclase, potassium feldspar, epidote, quartz, muscovite, chlorite, and calcite which occur as "islands" in the otherwise granitic host. Plagioclase grains (to 2.5 mm; Ab_{77-81}; $Or_{2.7-1.0}$) display occasional, subtle, oscillatory zoning, and generally have turbid, weakly sericitized cores; plagioclase in contact with potassium feldspar has a discontinuous albitic rim (Ab_{96}). Perthite grains (to 4.8 mm; Or_{75-81}) are irregular to interstitial and enclose subhedral quartz, plagioclase, and scattered biotite grains; contacts between perthite grains show well-developed zones of irregular, albitic grains. Irregular to interstitial quartz grains are intimately intergrown with potassium feldspar and occasionally enclose or partially enclose small plagioclase grains; in a single instance, small, rounded grains of quartz occur within a large plagioclase grain. Biotite (pleochroic brown to tan) occurs as scattered, small (to 1 mm), poorly crystalline grains and commonly is partially to completely chloritized. Magnetite is usually intergrown along the margins of potassium feldspar, plagioclase, or quartz. Within the fine-grained assemblage, magnetite is interstitial to anhedral plagioclase.

H-72: 34°38′26″N 132°33′15″E, a medium crystalline, hypidiomorphic-granular, gabbro (51.52; 33.8; 731), composed of plagioclase and interstitial quartz, with partially uralitized and chloritized clinopyroxene and orthopyroxene, remnant primary amphibole, and biotite. Plagioclase (to 2.7 mm; Ab_{39-57}; $Or_{1.6-1.4}$), shows subtle oscillatory zoning and patchy recrystallization. Quartz is restricted to interstices between plagioclase laths. The mafic phases are extensively altered. Euhedral, columnar crystals and relict grains of orthopyroxene (to 1.7 mm) and sievy, anhedral grains of clinopyroxens (to 2 mm) are partially or completely replaced by fibrous sheaves and felted bundles of secondary amphibole and chlorite. Relict clinopyroxene grains are zoned. Remnant igneous amphibole (pleochroic tan to light green) is rare, and partially or completely replaced by fibrous phases; where present, it occurs as overgrowths on earlier pyroxene grains. Biotite (pleochroic brown to light tan) occurs as (1) large poikilitic grains (to 2.4 mm) intergrown with and enclosing magnetite and fibrous amphibole-chlorite, the later presumably after pyroxene and/or amphibole, and (2) small, ragged grains now surrounded by fibrous amphibole-chlorite mats, the biotite presumably having replaced igneous amphibole prior to uralitization. Rare chlorite has replaced biotite along cleavage planes; the extent to which the fibrous amphibole-chlorite phase has replaced biotite, especially along the margins of the poikilitic biotite grains is difficult to judge. Coarse blades of the fibrous phases fill angular interstices between plagioclase laths, suggesting a possible, later magmatic origin for both replacement and interstitial uralite. Large, anhedral magnetite grains are associated with mafic clusters, where they occur within clinopyroxene and amphibole grains, though more typically interstitial to amphibole. Magnetite may also be interstial to euhedral plagioclase, and enclose apatite.

H-89: 34°37′52″N 132°31′24″E, a fine-to-medium crystalline, hypidiomorphic-granular quartz monzodiorite (59.87; 53.3; 489), composed of interlocking plagioclase laths and interstitial quartz with partially altered pyroxene, amphibole, minor biotite, and magnetite. Plagioclase (to 2.2 mm, though commonly less; Ab_{40-76}; $Or_{1.1-3.4}$) occurs as (1) grains with broad, compositionally uniform, often corroded and locally recrystallized cores, bounded by a sharp reaction ring and surrounded by a smooth, more variable rind with subtle oscillatory zoning, (2) grains lacking a corroded core, exhibiting instead more uniform variation from the interior of the grain toward the edge, with local oscillations in the zoning patterns, and (3) grains displaying multiple, concentric reaction rings. Potassium feldspar occurs as unanalyzable (to 0.5 mm) turbid, interstitial, myrmekitic intergrowths with quartz. Quartz fills the intersticies between plagioclase laths, and commonly partially encloses plagioclase as well as occasional biotite and amphibole grains. Corroded clinopyroxene (to 2 mm) and rare orthopyroxene (to 0.2 mm) are universally enclosed in the larger amphibole grains. Amphibole (to 2.5 mm; pleochroic light tan to olive green) is subhedral in the smaller grains, generally anhedral in the larger grains. Some larger amphibole grains have been completely altered to felted mats of fibrous amphibole-chlorite similar to those observed in H-72; other large amphiboles have retained igneous rims, and have been altered to a more fibrous phase only in the core area, presumably after former pyroxene. Minor biotite (pleochroic dark brown to tan) occurs as small (to 0.4 mm), irregular grains intergrown with amphibole and magnetite or as small, ragged grains replacing amphibole. An epidote mineral commonly occurs with chlorite after biotite or amphibole, or as individual, interstitial grains. Magnetite is principally found in the mafic clusters, commonly intergrown with amphibole, but also as inclusions in clinopyroxene, amphibole, and biotite.

H-93. 34°33′29″N 132°31′02″E, a porphyritic granodiorite (72.20; 85.0; 75), composed of large crystals of plagioclase (common synneusis twins to 5 mm) and irregular quartz in a groundmass of perthite, quartz, and plagioclase, with fine amphibole and biotite. Both phenocryst and the groundmass plagioclase (to 2 mm; Ab_{68-84}; $Or_{2\,5\text{-}2\,1}$) display weak oscillatory zoning and occasional recrystallization. Turbid potassium feldspar (to 2 mm; Or_{72-82}) is moderately exsolved, irregular to interstitial, and often intergrown with quartz; boundaries between perthite grains are marked by chains of fine albitic grains. Large quartz grains (to 6 mm) often include irregular blebs of potassium feldspar, especially near their rims. Amphibole (to 1.2 mm; pleochroic dark green to light greenish brown) generally occurs as anhedral grains. Biotite (to 1.4 mm; pleochroic dark brown to tan) occurs as scattered anhedral grains occasionally intergrown with amphibole; it is only weakly chloritized. Magnetite is randomly distributed as intergrowths between quartz, potassium feldspar, and plagioclase. Allanite is a rare accessory. An aplitic mass composed of anhedral quartz, plagioclase, potassium feldspar, biotite, and amphibole occupies a small rounded area of the thin section.

H-77: 34°25′25″N 132°19′58″E, a medium crystalline, slightly porphyritic monzogranite (73.06; 86.9; 77), containing scattered, large plagioclase grains (to 7 mm) in a allotriomorphic to hypidiomorphic-granular groundmass of plagioclase, turbid potassium feldspar, quartz, biotite, and amphibole. Plagioclase (Ab_{65-82}; $Or_{3.3-2.5}$) often shows multiple, concentric, reaction rings, including some which mark abrupt shifts in composition, others which coincide with zones of reverse zonation, and others which bear no relation to compositional variation. Potassium feldspar (to 3.7 mm; Or_{80-82}) is mildly exsolved, irregular to interstitial, and encloses or partially enclosing smaller plagioclase laths. Chains of small, albitic grains are present along contacts between perthite grains. Quartz ranges from clusters of individual, more equant grains (to 5 mm) to irregular interstitial fillings between plagioclase laths. Amphibole (pleochroic olive brown to blue green or

tan) occurs as scattered, large subhedral grains (to 2.8 mm) and smaller, generally anhedral grains. Biotite (pleochroic dark brown to tan) occurs as individual, larger grains (to 1.3 mm) as well as overgrowths surrounding and replacing amphibole. Chlorite occurs replacing biotite along cleavage planes. Rare, pleochroic green biotite fringes on brown biotite, epidote intergrown with biotite, and interstitial fillings of epidote-green biotite-chlorite suggest a late magmatic event. Two small magnetite grains are included in potassium feldspar. Allanite is as an accessory phase.

H-98: 34°22′34″N 132°16′02″E, a fine-to-medium grained, allotriomorphic-granular monzogranite (75.09; 91.2; 18), composed of a mosaic of plagioclase, potassium feldspar, quartz, and biotite. Plagioclase (to 2 mm; Ab_{74-90}; $Or_{2.4-1.7}$) is smoothly zoned; however, adjacent to potassium feldspar grains, individual plagioclase grains exhibit discontinuous, often myrmekitic, more albitic rims (Ab_{94}). Equant, turbid potassium feldspar grains (to 2.5 mm; Or_{79-81}) are mildly perthitic, commonly include small albitic grains along contacts between perthite grains, and, though intergrown with quartz along grain boundaries, rarely enclose quartz. Quartz occurs as relatively equant grains (to 2 mm). Biotite (to 1 mm; pleochroic dark brown to tan cores, green to greenish tan rims) is commonly zoned and chloritized, with some grains completely altered to chlorite plus epidote. There appears to be a more or less continuous evolution from the pleochroic brown (Ti-rich) biotite cores, to pleochroic green (Ti-poor) rims, to chlorite. Allanite and ilmenite are rare accessory phases.

MY-15: 34°08′16″N 132°56′41″E, a layered, hypidiomorphic-granular quartz monzodiorite (53.35; 35.7; 19), with distinct fine-grained and medium-grained facies, is composed of plagioclase, quartz, amphibole, biotite, and ilmenite. Plagioclase (Ab_{46-50}; $Or_{0.9-0.8}$; to 1 mm in the fine-grained facies and 3 mm in the coarse-grained facies) is distinctly zoned and in some instances exhibits reverse zoning. Zoning in the case of the larger grains includes broad, corroded, locally sericitized, and recrystallized cores and narrow, smoothly zoned rims. Zoning in submillimeter-sized plagioclase includes a narrow, corroded, and sericitized core similar to but smaller than that in the larger grains and a narrow, smooth rim of approximately the same width as that on the larger grains. Quartz occurs as large (to 3 mm), irregular poikilitic and interstitial grains commonly enclosing amphibole, biotite, and smaller plagioclase grains. Amphibole is zoned (pleochroic tan to olive green cores and tan to green rims) and occurs as large subhedral grains (to 1.5 mm) occasionally enclosing small plagioclase laths and ilmenite. Biotite (to 2.4 mm; pleochroic brown to tan) occurs as individual grains often intergrown with and perhaps replacing amphibole, and partially enclosing and intergrown with small plagioclase grains and poikilitic quartz. Biotite is partially altered to chlorite plus sphene or epidote; amphibole is locally recrystallized to a second amphibole phase (pleochroic light green) and occasionally altered to a fibrous secondary phase.

MY-6: 34°01′23″N 132°49′33″E, a medium crystalline, allotriomorphic-granular granodiorite (65.38; 67.8; 16), composed of plagioclase, quartz, interstitial potassium feldspar, and primarily glomeroporphyritic clusters of pyroxene, biotite, and minor amphibole. Plagioclase (to 3.4 mm; Ab_{61-63}; $Or_{2.0-1.5}$) is locally myrmekitic. Potassium feldspar (to 1.7 mm; Or_{90-93}) occurs as an interstitial phase between plagioclase grains. Quartz occurs as large grains (to 5 mm) enclosing plagioclase, pyroxene, amphibole, and biotite and smaller interstitial grains. Clinopyroxene (to 1.9 mm) is generally rounded and corroded and is overgrown by amphibole. Amphibole (to 2 mm; pleochroic tan to light green) is a relatively minor phase, most commonly developed surrounding pyroxene. Biotite is zoned (to 1.8 mm; pleochroic tan to brown cores and tan to green rims); commonly occurs in clusters intergrown with pyroxene, amphibole, and minor sphene; and is only weakly chloritized.

MY-2: 33°52′21″N 132°50′18″E, a medium-to-coarse crystalline, allotriomorphic-granular monzogranite (73.66; 86.6; 14), composed of intergrown perthite, plagioclase, quartz, and minor biotite. Plagioclase grains, including large synneusis twinned clusters (to 5 mm; Ab_{66-78}; $Or_{1.1-1.0}$), display oscillatory zoning and sericitized reaction rings and cores. Potassium feldspar (to 5 mm; Or_{83-84}) shows strongly exsolved, albitic lamellae, irregular blebs within individual perthite grains, and albitic grains along twin planes and contacts between perthite grains. Plagioclase grains, included within potassium feldspar grains or in contact with them, often have distinctly more albitic rims which locally extend as lobate forms into the adjacent perthite. Quartz occurs primarily as large clusters of grains (to 6 mm) intergrown with potassium feldspar. Biotite (pleochroic tan to brown) occurs both as clusters of smaller grains and individual larger grains (to 1.9 mm), weakly chloritized along cleavage planes; several grains include a sievy, corroded, pleochroic fringe of green biotite. Allanite is accessory.

MY-1: 33°54′11″N 132°51′48″E, a medium crystalline, allotriomorphic-granular monzogranite (75.48; 93.6; 13), composed of an interlocking mosaic of plagioclase, potassium feldspar, quartz, and minor biotite. Plagioclase (to 2.5 mm) shows little compositional variation (Ab_{78-79}; $Or_{1.4-1.3}$), yet some grains show distinct cores. Plagioclase grains in contact with potassium feldspar display a well-developed, locally myrmekitic, albitic rim (Ab_{97}). Potassium feldspar (Or_{89-90}) is mildly perthitic, commonly twinned, and occurs both as irregular interstitial grains and distinctly larger grains (to 3.5 mm). Quartz (to 2 mm) is irregular, interstitial, and often includes and is intimately intergrown with potassium feldspar. Biotite (to 1.5 mm; pleochroic amber to tan) is partially or completely altered to chlorite; a minor, pleochroic green biotite may be the precursor to chloritic alteration. Allanite is accessory.

Acknowledgments. For perceptive and encouraging reviews we thank Ronald Kistler, David Wones, Marc Loiselle, and J. C. Stormer, Jr. The stratigraphic nomenclature in this report has not been reviewed for conformity with U.S. Geological Survey standards.

REFERENCES

Albee, A. L., Relationships between mineral association, chemical composition and physical properties of the chlorite series, *Am. Mineral., 47*, 851–870, 1962.

Anderson, A. T., Oxidation of the LaBlache Lake titaniferous magnetite deposit, Quebec, *J. Geol., 76*, 528–547, 1968.

Anderson, J. L., Mineral equilibria and crystallization conditions in the late Precambrian Wolf River rapakivi massif, Wisconsin, *Am J. Sci., 280*, 298–332, 1980.

Anderson, J. L., and R. L. Cullers, Geochemistry and evolution of the Wolf River batholith, a late Precambrian rapakivi massif in north Wisconsin, U.S.A., *Precambrian Res., 7*, 287–324, 1978.

Baird, A. K., K. W. Baird, and E. E. Welday, Chemical trends across

Cretaceous batholithic rocks of southern California, *Geology, 2,* 493–495, 1974.

Bateman, P. C., and F. C. W. Dodge, Variations of major chemical constituents across the central Sierra Nevada batholith, *Geol. Soc. Am. Bull., 81,* 409–420, 1970.

Bohlen, S. R., and E. J. Essene, Feldspar and oxide thermometry of granulites in the Adirondack Highlands, *Contrib. Mineral. Petrol., 62,* 153–169, 1977.

Bowles, J. F. W., A method of tracing the temperature and oxygen-fugacity histories of complex magnetite-ilmenite grains, *Mineral. Mag., 41,* 103–109, 1977.

Buddington, A. F., and D. H. Lindsley, Iron-titanium oxide minerals and synthetic equivalents, *J. Petrol.,5,* 310–357, 1964.

Burnham, C. W., Magmas and hydrothermal fluids, in *Geochemistry of Hydrothermal Ore Deposits,* 2d ed., edited by H. L. Barnes, pp. 71–136, John Wiley, New York, 1979.

Burnham, C. W., and H. Ohmoto, Late-state processes of felsic magmatism, *Min. Geol. Spec. Issue, 8,* 1–11, 1980.

Burnham, C. W., J. R. Holloway, and N. F. Davis, Thermodynamic properties of water to 1,000°C and 10,000 bars, *Spec. Pap. Geol. Soc. Am., 132,* 96 pp., 1969.

Carter, S. R., N. M. Evenson, P. J. Hamilton, and R. K. O'Nions, Neodymium and strontium isotope evidence for crustal contamination of continental volcanics, *Science, 202,* 743–747, 1978.

Chappell, B. W., and A. J. R. White, Two contrasting granite types, *Pac. Geol., 8,* 173–174, 1974.

Chou, I. M., Calibration of oxygen buffers at elevated P and T using the hydrogen fugacity sensor, *Am. Mineral., 63,* 690–703, 1978.

Coleman, M. L., Sulfur isotopes in geology, *J. Geol. Soc. London, 133,* 593–608, 1977.

Coleman, M. L., Isotopic analysis of trace sulphur from some S- and I-type granites: Heredity or environment?, in *Origin of Granite Batholiths, Geochemical Evidence,* edited by M. P. Atherton and J. Tarney, pp. 129–148, Shiva Publishing, Orpington, Kent, England, 1979.

Czamanske, G. K., and P. Mihalik, Oxidation during magmatic differentiation, Finnmarka complex, Oslo area, Norway, 1, The opaque oxides, *J. Petrol., 13,* 493–509, 1972.

Czamanske, G. K., and D. R. Wones, Oxidation during magmatic differentiation, Finnmarka complex, Oslo area, Norway, 2, The mafic silicates, *J. Petrol., 14,* 349–380, 1973.

Czamanske, G. K., D. R. Wones, and J. C. Eichelberger, Mineralogy and petrology of the intrusive complex of the Pliny Range, New Hampshire, *Am. J. Sci., 277,* 1073–1123, 1977.

Day, H. W., The high temperature stability of muscovite plus quartz, *Am. Mineral., 58,* 255–262, 1973.

de Albuquerque, C. A. R., Geochemistry of biotites from granitic rocks, Northern Portugal, *Geochim. Cosmochim. Acta, 37,* 1779–1802, 1973.

Deer, W. A., R. A. Howie, and J. Zussman, *Rock-Forming Minerals,* vol. 3, *Sheet Silicates,* p. 270, Longman, London, 1971.

De Paolo, D. J., Sources of continental crust: Neodymium isotope evidence from the Sierra Nevada and Peninsular Ranges, *Science, 209,* 684–687, 1980.

De Paolo, D. J., A. neodymium and strontium isotopic study of the Mesozoic calc-alkaline granitic batholiths of the Sierra Nevada and Peninsular Ranges, California, *J. Geophys. Res.,* this issue.

Dodge, F. C. W., V. C. Smith, and R. E. Mays, Biotites from granitic rocks of the central Sierra Nevada batholith, *J. Petrol., 10,* 250–271, 1969.

Foland, K. A., and I. Friedman, Application of Sr and O isotope relation to the petrogenesis of the alkaline rocks of the Red Hill complex, New Hampshire, USA, *Contrib. Mineral. Petrol., 65,* 213–225, 1977.

Foster, M. D., Interpretation of the composition of trioctahedral micas, *U.S. Geol. Surv. Prof. Pap., 354-B,* 48 pp., 1960.

Fuge, R., On the behaviour of fluorine and chlorine during magmatic differentiation, *Contrib. Mineral. Petrol, 61,* 245–249, 1977.

Gorbatschev, R., Distribution of tetrahedral Al-Si in coexisting biotite and amphibole, *Contrib. Mineral. Petrol., 28,* 251–258, 1970.

Greenland, L. P., D. Gottfried, and R. I. Tilling, Distribution of manganese between coexisting biotite and hornblende in plutonic rocks, *Geochim. Cosmochim. Acta, 32,* 1149–1163, 1968.

Griffen, T. J., A. J. R. White, and B. W. Chappell, The Moruya batholith and geochemical contrasts between the Moruya and Jindabyne suites, *J. Geol. Soc. Aust., 74*(4), 235–247, 1978.

Hawkesworth, G. J., and R. Vollmer, Crustal contamination versus enriched mantle: $^{143}Nd/^{144}Nd$ and $^{87}Sr/^{86}Sr$ evidence from the Italian volcanics, *Contrib. Mineral. Petrol., 69,* 151–165, 1979.

Hazen, R. M., and D. R. Wones, The effect of cation substitution on the physical properties of trioctahedral micas, *Am. Mineral., 57,* 103–129, 1972.

Hewitt, D. A., A redetermination of the fayalite-magnetite-quartz equilibrium between 650° and 850°C, *Am. J. Sci., 278,* 715–724, 1978.

Hine, R., I. S. William, B. W. Chappell, and A. J. R. White, Contrasts between I- and S-type granitoids of the Kosciusko batholith, *J. Geol. Soc. Aust., 25,* 217–232, 1978.

Honma, H., Major element chemistry of metamorphic and granitic rocks of the Yanai District in the Ryoke Belt, *J. Jpn. Assoc. Mineral. Petrol. Econ. Geol., 69,* 193–204, 1974*a*.

Honma, H., Chemical features of biotites from metamorphic and granitic rocks in the Yanai District in the Tyoke Belt, Japan, *J. Jpn. Assoc. Mineral. Petrol. Econ. Geol., 69,* 390–402, 1974*b*.

Honma, H., and H. Sakai, Oxygen isotope study of metamorphic and granitic rocks of the Yanai District in the Ryoke Belt, Japan, *Contrib. Mineral. Petrol., 52,* 107–120, 1975.

Honma, H., and H. Sakai, Zonal distribution of oxygen isotope ratios in the Hiroshima granite complex, Southwest Japan. *Lithos, 9,* 173–178, 1976.

Huebner, J. S., and M. Sato, The oxygen fugacity-temperature relationships of manganese oxide and nickel oxide buffers, *Am. Mineral., 55,* 934–952, 1970.

Ishihara, S., Modal and chemical composition of the granitic rocks related to the major molybdenum and tungsten deposits in the Inner Zone of southwest Japan, *J. Geol. Soc. Jpn., 77,* 441–452, 1971*a*.

Ishihara, S., Major molybdenum deposits and related granitic rocks in Japan (in Japanese), *Rep. Geol. Surv. Jpn., 239,* 1–178, 1971*b*.

Ishihara, S., The Mo-W metallogenic provinces and related granitic provinces (in Japanese), *Min. Geol. Tokyo, 23,* 13–32, 1973.

Ishihara, S., The magnetite-series and ilmenite-series granitic rocks, *Min. Geol. Tokyo, 27,* 293–305, 1977.

Ishihara, S., Metallogenesis of the Japanese island arc system, *J. Geol. Soc. London, 135,* 389–406, 1978.

Ishihara, S., Lateral variation of magnetic susceptibility of the Japanese granitoids, *J. Geol. Soc. Jpn., 85,* 509–523, 1979.

Ishihara, S., and Y. Matsuhisa, The magnetite-series and ilmenite-series granitoids and their $^{18}O/^{16}O$ isotope ratios (in Japanese), *Abstr. Issue Annual Meet. Geol. Soc. Jpn., 84th,* 82, 1977.

Ishihara, S., and S. Terashima, Chemical variation of the Cretaceous granitoids across southwestern Japan—Shirakawa-Toki-Okazaki-transection, *J. Geol. Soc. Jpn., 83,* 1–18, 1977*a*.

Ishihara, S., and S. Terashima, Chlorine and fluorine contents of granitoids as indicators for base metal and tin mineralizations (in Japanese), *Min. Geol. Tokyo, 27,* 191–199, 1977*b*.

Ishihara, S., S. Sekine, and T Mochizuki, Contents of uranium and thorium in granitic rocks and their petrogenetic significance (in Japanese), *Rept. Geol. Surv. Japan,* no. 232, p. 170–219, 1969.

James, R. S., and D. L. Hamilton, Phase relations in the system $NaAlSi_3O_8$-$KAlSi_3O_8$-$CaAl_2Si_2O_8$-SiO_2 at 1 kilobar water vapor pressure, *Contrib. Mineral. Petrol., 21,* 111–141, 1969.

Kagami, H., and H. Honma, Oxygen isotope study of the granites in eastern Chugoku, Southwest Japan (in Japanese), *Mem. Geol. Soc. Jpn., 17,* 93–98, 1979.

Kanisawa, S., Coexisting biotites and hornblendes from some granitic rocks in southern Kitakami Mountains, Japan, *J. Jpn. Assoc. Mineral. Petrol. Econ. Geol., 67,* 332–344, 1972.

Kanisawa, S., Chemistry of biotites and hornblendes of some granitic rocks in the San'in Zone, southwest Japan, *J. Geol. Soc. Jpn., 82,* 543–548, 1976.

Kanisawa, S., H. Tanaka, and Y. Nakai, Behaviour of fluorine in granitic rocks from the Abukuma Plateau, the Ryoke zone, and the San-in zone, Japan, *J. Geol. Soc. Jpn., 85,* 123–134, 1979.

Kistler, R. W., and Z. E. Peterman, Variations in Sr, Rb, K, Na, and initial Sr^{87}/Sr^{86} in Mesozoic granitic rocks and intruded wall rocks in central California, *Geol. Soc. Am. Bull., 84,* 3489–3512, 1973.

Kistler, R. W., and Z. E. Peterman, Reconstruction of crustal blocks of California on the basis of initial strontium isotopic compositions of Mesozoic granitic rocks, *U.S. Geol. Surv. Prof. Pap., 1071,* 17 pp., 1978.

Koide, H., *Dando Granodioritic Intrusives and Their Associated Meta-*

morphic Complex, 311 pp., Japanese Society for Promotion of Science, Tokyo, 1958.

Kretz, R., The distribution of certain elements among coexisting calcic pyroxenes, calcic amphiboles and biotites in skarns, *Geochim. Cosmochim. Acta, 20*, 161–191, 1960.

Leake, B. E., Nomeclature of amphiboles, *Can. Mineral., 16*, 501–520, 1978. (Also *Am. Mineral., 63*, 1023–1052, 1978.)

Loiselle, M., Geochemistry and petrogenesis of the Belknap Mountains complex and Pliny Range, White Moutain Series, New Hampshire, Ph.D. thesis, 302 pp., Mass, Inst. of Technol., Cambridge, 1978.

Ludington, S., The biotite-apatite geothermometer revisited, *Am. Mineral., 63*, 551–553, 1978.

Luth, W. C., The systems $NaAlSi_3O_8$-SiO_2 and $KAlSi_3O_8$-SiO_2 at 20 kb and the relationship between H_2O content, P_{H_2O}, and P_{total} in granitic magmas, *Am. J. Sci., 267-A*, 325–341, 1969.

Luth, W. C., R. H. Jahns, and O. F. Tuttle, The granite system at pressures of 4 to 10 kilobars, *J. Geophys. Res., 69*, 759–773, 1964.

Margaritz, M., D. J. Whitford, and D. E. James. Oxgen isotopes and the origin of high $^{87}Sr/^{86}Sr$ andesites, *Earth Planet. Sci. Lett., 40*, 220–230, 1978.

Masi, U., J. R. O'Neil, and R. W. Kistler, Stable isotope systematics in Mesozoic granites of central and northern California and southwestern Oregon, *Contrib. Mineral. Petrol., 76*, 116–126, 1981.

Matsuhisa, Y., H. Honma, O. Matsubaya, and H. Sakai, Oxygen isotopic study of the Cretaceous granitic rocks in Japan, *Contrib. Mineral. Petrol., 37*, 65–74, 1972.

McCulloch, M. T., and G. H. Wasserburg, Sm-Nd and Rb-Sr chronology of continental crust formation, *Science, 200*, 1003–1011, 1978.

McTaggart, K. C., 'Qone perthite' from southern British Columbia, *Can. Mineral., 17*, 27–32, 1979.

Miller, C. F., E. F. Stoddard, L. J. Bradfish, and W. A. Dollase, Composition of plutonic muscovite: Genetic implications, *Can. Mineral., 19*, 25–34, 1981.

Munoz, J. L., and S. D. Ludington, Fluoride-hydroxyl exchange in biotite, *Am. J. Sci., 274*, 396–413, 1974.

Murakami, N., Two contrastive trends of evolution of biotite in granitic rocks, *J. Jpn. Assoc. Mineral. Petrol. Econ. Geol., 62*, 223–248, 1969.

Murakami, N., Some problems concerning late Mesozoic to early Tertiary igneous activity on the inner side of southwest Japan, *Pac. Geol., 8*, 139–151, 1974.

Murakami, N., Compositional variations of some constituent minerals of the late Mesozoic to early Tertiary granitic rocks of southwest Japan, *Bull. Geol. Soc. Malays., 9*, 75–89, 1977.

Murakami, N. (Ed)., Mesozoic acid igneous activity in Japan. *Mem. Geol. Soc. Jpn., 17*, 302 pp., 1979.

Noyes, H. J., Petrogenesis of Sierran plutons: A petrologic and geochemical investigation into the origin and differentiation of granodioritic plutons in the central Sierra Nevada batholith, Ph.D. thesis, 324 pp., Mass. Inst. of Technol., Cambridge, 1978.

Oba, N., Petrographic provinces and the contamination-effects on granitic rocks of Japanese islands, *Pac. Geol., 8*, 153–157, 1974.

Ohmoto, H., and R. O. Rye, Isotopes of sulfur and carbon, in *Geochemistry of Hydrothermal Ore Deposits*, 2d ed., edited by H. L. Barnes, pp. 509–567, John Wiley, New York, 1979.

O'Neil, J. R., and B. W. Chappell, Oxygen and hydrogen isotope relations in the Berridale batholith, *J. Geol. Soc. London, 133*, 559–571, 1977.

O'Neil, J. R., S. E. Shaw, and R. H. Flood, Oxygen and hydrogen isotope compositions as indicators of granite genesis in the New England batholith, Australia, *Contrib. Mineral. Petrol., 62*, 313–328, 1977.

Ozima, M., N. Ueno, N. Shimizu, and H. Kuno, Rb-Sr and K-A isotopic investigations of Sidara granodiorites and the associated Ryoke metamorphic belt, central Japan, *Jpn. J. Geol. Geogr., 38*, 159–162, 1967.

Pankhurst, R. J., R. D. Beckinsale, and C. K. Brooks, Strontium and oxygen isotope evidence relating to the petrogenesis of the Kangerdlugssuaq alkaline intrusion, East Greenland, *Contrib. Mineral. Petrol., 54*, 17–42, 1976.

Papike, J. J., K. L. Cameron, and K. Baldwin, Amphiboles and pyroxenes: Characterization of *other* than quadrilateral components and estimates of ferric iron from microprobe data, *Geol. Soc. Am. Abstr. Programs, 6*, 1053–1054, 1974.

Perfit, M. R., H. Brueckner, J. R. Lawrence, and R. W. Kay, Trace element and isotopic variations in a zoned pluton and associated volcanic rocks, Unalaska Island, Alaska: A model for fractionation in the Aleutian calcalkaline suite, *Contrib. Mineral. Petrol., 73*, 69–87, 1980.

Pitcher, W. S., Comments on the geological environments of granites, in *Origins of Granite Batholiths, Geochemical Evidence*, edited by M. P. Atherton and J. Tarney, pp. 1–8, Shiva Publishing, Orpington, Kent, England, 1979.

Robinson, P., M. Ross, and H. W. Jaffe, Composition of the anthophyllite-gedrite series, comparison of gedrite-hornblende, and the antophyllite-gedrite solvus, *Am. Mineral., 56*, 1005–1041, 1971.

Sasaki, A., and S. Ishihara, Sulfur isotopic composition of the magnetite-series and ilmenite-series granitoids in Japan, *Contrib. Mineral. Petrol., 68*, 107–115, 1979.

Sasaki, A., and S. Ishihara, Sulfur isotope characteristics of granitoids and related mineral deposites in Japan, in *Proceedings of the Fifth Quadrennial IAGOD Symposium*, pp. 326–335, International Association for the Geology of Ore Deposits, Stuttgart, Germany, 1980.

Schneider, A., The sulfur isotope composition of basaltic rocks, *Contrib. Mineral. Petrol., 25*, 95–124, 1970.

Shibata, K., and S. Ishihara, Rb-Sr whole-rock and K-Ar mineral ages of granitic rocks in Japan, *Geochem. J., 13*, 113–119, 1979*a*.

Shibata, K., and S. Ishihara, Initial $^{87}Sr/^{86}Sr$ ratios of plutonic rocks from Japan, *Contrib. Mineral. Petrol., 70*, 381–390, 1979*b*.

Shimizu, M., and H. Shimazaki, Estimation of formation pressure of skarn-type deposits using sphalerite geobarometry (in Japanese) (abstract), *Min. Geol. Tokyo, 29*, 54–55, 1979.

Stephenson, N. C. N., Coexisting hornlendes and biotites from Precambrian gneisses of the south coast of Western Australia, *Lithos, 10*, 9–27, 1977.

Stormer, J. C., Jr., A practical two-feldspar geothermometer, *Am. Mineral., 60*, 667–674, 1975.

Streckeisen, A. L., Plutonic rocks: Classification and nomenclature recommended by the IUGS Subcommission on the Systematics of Igneous Rocks, *Geotimes, 18*, 26–30, 1973.

Suzuki, Y., and S. Ishihara, Modal compositions of granitic plutons of Toki-Okazaki region, central Japan, *Rep. Geol. Surv. Jpn., 232*, 155–168, 1969.

Tainosho, Y., H. Honma, and K. Tazaki, Mineral chemistry of granitic rocks in eastern Chugoku, Southwest Japan (in Japanese), *Mem. Geol. Soc. Jpn., 17*, 99–112, 1979.

Takahashi, M., S. Aramaki, and S. Ishihara, Magnetite-series/ilmenite-series vs. I-type/S-type granitoids. *Min. Geol. Spec. Issue, 8*, 13–28, 1980.

Taylor, H. P., B. Giannetti, B. Turi, Oxygen isotope geochemistry of the potassic igneous rocks from Roccamonfina volcano, Roman comagmatic region, Italy, *Earth. Planet. Sci. Lett., 46*, 81–106, 1979.

Terashima, S., and S. Ishihara, Anomalous chlorine contents of Miocene granitoids from Tsushima, Japan, *J. Jpn. Assoc. Mineral. Petrol. Econ. Geol., 75*, 62–67, 1980.

Thompson, J. B., Role of aluminum in the rock forming silicates (abstract), *Geol. Soc. Am. Bull., 58*, 1232, 1947.

Thornton, C. P., and O. F. Tuttle, Chemistry of igneous rocks, I, Differentiation index, *Am. J. Sci., 258*, 664–684, 1960.

Tsusue, A., and S. Ishihara, The iron-titanium oxides in the granitic rocks of Southwest Japan (in Japanese), *Min. Geol. Tokyo, 24*, 13–30, 1974.

Tuttle, O. E., and N. L. Bowen, Origin of granite in light of experimental studies, *Mem. Geol. Soc. Am., 74*, 142 pp., 1958.

Waldbaum, D. R., and J. B. Thompson, Jr., Mixing properties of sanidine crystalline solutions, IV, Phase diagrams from equations of state, *Am. Mineral., 54*, 1274–1298, 1969.

White, A. J. R., I. S. Williams, and B. W. Chappell, The Jindabyne Thrust and its tectonic, physiographic and petrogenetic significance, *J. Geol Soc. Aust., 23*, 105–112, 1976.

Whitney, J. A. and J. C. Stormer, Jr., Geothermometry and geobarometry in epizonal granite intrusions: A comparison of iron-titanium oxides and coexisting feldspars, *Am. Mineral., 61*, 751–761, 1976.

Whitney, J. A., and J. C. Stormer, Jr., The distribution of $NaAlSi_3O_8$ between coexisting microcline and plagioclase and its effect on geothermometric calculations, *Am. Mineral., 62*, 687–691, 1977.

Wones, D. R., Contributions of crystallography, mineralogy, and pe-

trology to the geology of the Lucerne pluton, Hancock County, Maine, *Am. Mineral.*, *65*, 411–437, 1980.
Yakowitz, H., R. L. Myklebust, and K. F. J. Heinrich, FRAME: An on-line correction procedure for quantitative electron probe analyses, *NBS Tech. Note*, *796*, 1973.
Yanagi, T., Rubidium-strontium model of formation of the continental crust and the granite at the island arc, *Mem. Fac. Sci., Kyushu Univ., Ser. D.*, *22*, 1–31, 1975.

(Received December 8, 1980;
revised March 30, 1981;
accepted April 21, 1981.)

JOURNAL OF GEOPHYSICAL RESEARCH, VOL. 86, NO. B11, PAGES 10470–10488, NOVEMBER 10, 1981

A Neodymium and Strontium Isotopic Study of the Mesozoic Calc-Alkaline Granitic Batholiths of the Sierra Nevada and Peninsular Ranges, California

DONALD J. DEPAOLO

Department of Earth and Space Sciences, University of California, Los Angeles, California 90024

Plutonic igneous rocks of the Sierra Nevada batholith exhibit a range of Nd isotopic composition described by $\varepsilon_{Nd} = +6.5$ to -7.6. Similar rock types from the Peninsular Ranges have $\varepsilon_{Nd} = +8.0$ to -6.4. In both batholiths, ε_{Nd} correlates strongly with initial $^{87}Sr/^{86}Sr$. Decreasing ε_{Nd} values are accompanied by increasing $^{87}Sr/^{86}Sr$ and increasing $\delta^{18}O$; the correlation with $\delta^{18}O$ being more pronounced for the Peninsular Ranges. The ε_{Nd} values show regular geographic variations, as was found previously for initial $^{87}Sr/^{86}Sr$. Three metasedimentary country rock samples from the Sierra Nevada region have low ε_{Nd} values (-11 to -16) and Precambrian model Sm-Nd ages (1.5 to 1.9 Æ). The country rock ε_{Nd} values, and those of primitive oceanic island arcs ($\varepsilon_{Nd} = +8$), bracket the data for the batholith rocks. The Nd, Sr, and O isotopic data can be explained if the batholiths are mixtures of island arc and metasedimentary components, the latter being of both Paleozoic and early Proterozoic age. This model appears to be consistent with existing Pb isotopic data. Consideration of O-Sr isotopic relations and the variation of $^{147}Sm/^{144}Nd$ with ε_{Nd} suggests that assimilation of crustal rocks by magmas rising from the mantle and undergoing fractional crystallization could have been the major process responsible for the mixing of crustal- and mantle-derived components. The isotopic data, when combined with assumptions about the structure of the crust beneath the batholiths, suggest that about 50% of the crustal material presently within the geographic boundaries of the batholiths and above the Moho represents juvenile crust derived from the mantle in the Mesozoic. The remaining material appears to be mostly derived from 1.8-Æ crust, yielding an average crust formation age of nearly 1 Æ for this section of the crust. This result, which may apply to large portions of the Cordillera, suggests that the average age of the North American continent may be greater than previously estimated. The concentration of Nd correlates well with ε_{Nd} in the batholith rocks and supports the conclusion that juvenile continental crust is derived from mantle reservoirs that are depleted in incompatible elements. A 1.5-Æ Sm-Nd model age for sedimentary rocks of the Mesozoic(?) Calaveras Formation indicates that the Nd in this "oceanic" terrain is dominated by continental detritus and demonstrates the potential of Sm-Nd isotopic studies for aiding in construction of tectonic models.

INTRODUCTION

The initial isotopic composition of Nd and Sr and the concentrations of K, Rb, Sr, Sm, and Nd have been measured in 35 samples of plutonic, volcanic, and metasedimentary rocks of the Mesozoic Sierra Nevada and Peninsular Ranges composite batholiths in California and Baja California. The purpose of this study is to determine the Nd and Sr isotopic characteristics of recently formed continental crust, as represented by the batholith terrains, in order to clarify the petrogenesis of these large volumes of granitic rock and to better understand the process of continental growth, the chemical composition of the continental crust, and the structure and evolution of the earth's mantle.

Current models of post-Archean crustal evolution hold that the production of new continental crust occurs in island arcs in association with the subduction of oceanic lithosphere. It has been argued that batholith belts represent a deeper level of erosion of mature island arcs [cf. *Dickinson,* 1970]. Hence, since the batholiths are now found welded to the margins of older continental crust (e.g., the western margin of North America), it follows that they should represent the final product of the continental accretion process. However, many of the batholiths apparently formed above subduction zones that dipped beneath the margins of previously existing continental crust [*Bateman,* 1981]. In the continental margin environment, the sedimentary apron surrounding the continent or the crystalline basement may become involved in the subduction-related magmatism. The igneous rocks produced may therefore represent melted continental crust rather than new additions to the crust from the mantle. Consequently, it becomes difficult to determine newly added crust from 'reconstituted' crust. Previous work, using Sr isotopes, has shown this to be a serious problem for the Sierra Nevada and, by inference, for all continental margin magmatic arcs [*Kistler and Peterman,* 1973, 1978; *Armstrong et al.,* 1977].

This investigation has therefore been directed at the following questions on the Sierra Nevada and Peninsular Ranges batholiths. First, do these seemingly new increments added to continental margins contain a component that can be identified as oceanic island-arc-type material newly extracted from the mantle, and second, what proportion of the apparent total volume is composed of this new material and what proportion is older crust. These questions then raise a third; if there is a mixture of crustal- and mantle-derived components, how is this mixing achieved, and how does it relate to the petrologic characteristics of the rocks? Answers to these questions are necessary to understand the age and evolutionary history of continental crust, a key datum for reconstructing the earth's physical and chemical evolution.

An additional question concerns the nature of the mantle source of new crust. Recently proposed models [*DePaolo,* 1980*a*; *Wasserburg and DePaolo,* 1979] predict that successive increments of continental crust have been extracted from the same, limited volume of the upper mantle. These extractions caused the upper mantle to change in composition through time. This change should also be reflected by the chemical composition of the new additions to the crust. This model differs distinctly from those proposed by *Ringwood* [1975] and *Dickinson and Luth* [1971] which hold that differentiation of the mantle is a one-time-only process and imply that crust is

Copyright © 1981 by the American Geophysical Union.

Paper number 1B0530.
0148-0227/81/001B-0530$01.00

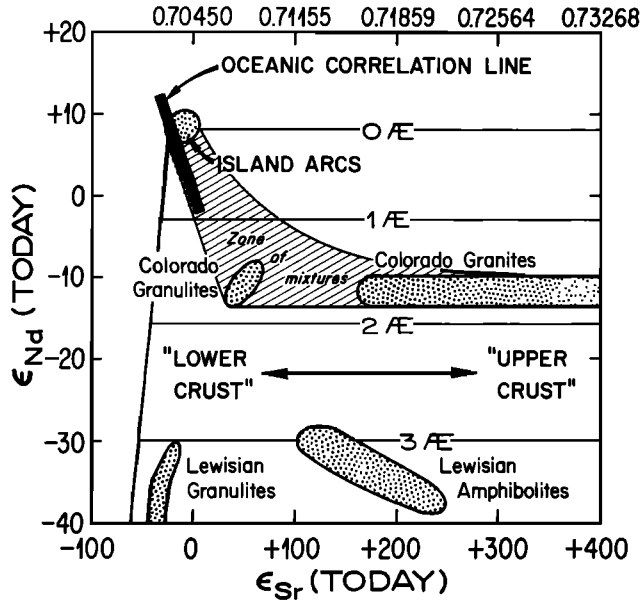

Fig. 1. Generalized isotopic model for present-day ϵ_{Nd} and ϵ_{Sr} values in the mantle (oceanic correlation line) and the crust, as a function of crustal age (modified from *DePaolo and Wasserburg,* [1979]). Differences between Rb-depleted 'lower crust' and Rb-enriched 'upper crust' are exemplified by measurements on metamorphic and igneous basement rocks from the Lewisean gneisses of Scotland [*Hamilton et al.,* 1979] and the Front Range of Colorado [*DePaolo,* 1981*a*]. Equivalent $^{87}Sr/^{86}Sr$ ratios for zero-aged rocks are given at the top.

always produced from previously undifferentiated parts of the mantle. This question can be addressed by investigating certain trace element characteristics of the batholith rocks and their relation to isotopic composition.

Preliminary results based on a much more restricted sampling [*DePaolo,* 1980*b*] showed for the Sierra Nevada a large range of Nd isotope composition consistent with large-scale mixing of mantle and crustal components. In the present work, new data from both the Sierra Nevada and Peninsular ranges are presented, and they are integrated with other isotopic and chemical data to create a more comprehensive geochemical model for the origin of the batholiths and to enumerate the implications for crustal evolution.

Previous Work

The Sierra Nevada and Peninsular ranges have been chosen for study because they have been the subject of extensive petrologic, geochronologic, geochemical, and field studies [cf. *Bateman and Wahrhaftig,* 1966; *Larsen,* 1948; *Gastil et al.,* 1975; *Silver et al.,* 1963; *Presnall and Bateman,* 1973; *Piwinskii,* 1968, *Saleeby,* 1981]. An extensive chemical and Sr isotopic study of the Sierra Nevada batholith has been carried out by *Kistler and Peterman* [1973, 1978]. They noted that geographic variations of $^{87}Sr/^{86}Sr$ were regular and that they correlated with paleogeographic boundaries. In particular, they suggested that a value of 0.7060 for $^{87}Sr/^{86}Sr$ was a dividing point between plutons found in regions underlain by Precambrian basement (higher $^{87}Sr/^{86}Sr$) and those found outside the limits of the basement (lower $^{87}Sr/^{86}Sr$). Plutons with $^{87}Sr/^{86}Sr < 0.7040$, on the other hand, were associated with oceanic-type crust, including ultramafic bodies, which were found exclusively on the western edge of the batholith. They concluded that the granitic magmas formed by melting in a depth range that intersected both upper mantle and lower crust, and that all of the source reservoirs for the magmas, had been formed 1.7 Æ ago (Æ ≡ 10^9 years), or at the time of Late Proterozoic rifting. They could not identify with certainty any component that represented newly derived material from the mantle and that would be geochemically analogous to oceanic island arcs located far from continental crust.

Isotopic and geochronologic studies of the Peninsular Ranges batholith have shown that the plutonic rocks are oldest at the western edge and youngest eastward, with ages ranging from 130–90 m.y. [*Silver et al.,* 1975]. Similar east-west asymmetries were found for initial $^{87}Sr/^{86}Sr$, which ranges from 0.7030 to 0.7080 west to east [*Early and Silver,* 1973], and $\delta^{18}O$, which ranges from +6 to +13 [*Taylor and Silver,* 1978]. Rare-earth element (REE) patterns also change across the batholith, with the easternmost rocks having stronger light-REE enrichment in relation to heavy REE; they are also depleted in heavy REE relative to western rocks [*Gromet,* 1979]. *Taylor and Silver* [1978] have interpreted O and Sr isotope data in terms of a mixed source, including a mantle-derived component and crustal, possibly metasedimentary, components of two types. In general, the Peninsular Ranges batholith appears to be less complicated than the Sierra Nevada in terms of its geometry, tectonics, and intrusive history. For example, several intrusive epochs have been identified in the Sierra Nevada that range in age from at least 210 m.y. to 79 m.y. ago [*Evernden and Kistler,* 1970]. Furthermore, the loci of intrusive centers define linear, subparallel, but intersecting trends, so that younger intrusives can be found both to the east and west of older plutons at different latitudes. This complex geometry of intrusive trends presumably reflects the rather complex Mesozoic tectonic history of California [cf. *Ernst,* 1981]. In contrast, the Peninsular Ranges intrusives formed over a much narrower time interval and show a regular, progressive decrease in age west to east [*Silver et al.,* 1975]. More recent work on the Sierra Nevada [*Saleeby,* 1981] suggests that the Cretaceous age patterns of the intrusives may be more regular than previously thought, approximating the pattern found in the Peninsular Ranges. In general, the geochemical west and east asymmetries that are displayed so convincingly in the Peninsular Ranges are seen in the Sierra Nevada also but are less pronounced. For instance, O isotope data show no regular west to east variation [*Masi et al.,* 1981], but $^{87}Sr/^{86}Sr$ ratios are generally higher on the east side [*Kistler and Peterman,* 1973].

Isotopic Models

In this study the systematics of Sr and Nd isotope variations in crustal and mantle rocks are used to attempt to answer the questions posed above. The model employed is summarized in Figure 1, which is adapted from *DePaolo and Wasserburg* [1979*a*]. This figure shows the expected distribution of present-day values of $^{143}Nd/^{144}Nd$ and $^{87}Sr/^{86}Sr$, expressed here as ϵ_{Nd} and ϵ_{Sr} (see data representation section below). Typical mantle values of ϵ_{Nd} and ϵ_{Sr}, as defined by oceanic basalt samples, fall along a linear trend with a slope $d\epsilon_{Nd}/d\epsilon_{Sr} = -0.37$, as shown by the heavy solid line in the upper left corner. This trend will hereafter be referred to as the oceanic correlation line (OCL). The vast majority of oceanic samples has positive ϵ_{Nd}. The values of ϵ_{Nd} and ϵ_{Sr} in crustal rocks depend upon their age and the relative enrichment of Sm/Nd and Rb/Sr. Most crustal rocks have low Sm/Nd and initial ϵ_{Nd} values of zero to +5. Their ϵ_{Nd} values today are negative, with absolute values roughly proportional to age. For Rb-Sr, rocks of the

lower crust (e.g., granulites) have low Rb/Sr, while rocks of the upper crust (e.g. shales, granites) have high Rb/Sr. Consequently, rocks of the same age from the 'upper' and 'lower' crust can have drastically different values of ε_{Sr} but similar ε_{Nd}. This pattern is shown in Figure 1. The data for the 2.9-Æ-old Lewisian gneisses [*Hamilton et al.*, 1979] and from the 1.8-Æ-old Colorado, Front Range basement [*DePaolo*, 1980*c*] exhibit the characteristics predicted by this model.

Simple mixtures of mantle and crustal components will define curves linking the end members whose shapes are dependent on the ratio of Sr/Nd in the end members [cf. *DePaolo and Wasserburg*, 1979*a*]. Negative curvature ($d^2\varepsilon_{Nd}/d\varepsilon^2_{Sr} < 0$) results when Sr/Nd in the crustal component is higher than in the mantle component. This type of curve might be expected if the crustal component is composed of plagioclase-rich rocks which have high Sr/Nd. Positive curvature would result if the crustal component has very low Sr/Nd. Generally, crustal igneous rocks do not have Sr/Nd much different from mantle-derived rocks, but clastic sediments (and metasediments), especially those that have been through more than one weathering cycle, very often are greatly depleted in Sr and enriched in Nd [cf. *McCulloch and Wasserburg*, 1978]. Therefore, pronounced positive curvature of this sort could be considered indicative of sediment involvement. More complicated mixing effects can also result [*Taylor*, 1980; *DePaolo*, 1981*b*]. These will be discussed below in conjunction with a discussion of the data. The zone of isotopic compositions that could be generated by mixtures of components resembling island arcs and 1.8-Æ-old crust is also shown. Note that there is no reason to expect mixtures to follow a well-defined line because of the Sr isotopic variability of the old crustal rocks.

The effect of exchange of material between seawater and rocks, as can take place during hydrothermal alteration of rocks in the oceanic environment, has been discussed by *DePaolo and Wasserburg* [1977] and *Hawkesworth et al.* [1977]. Seawater contains a considerable amount of dissolved Sr but essentially no Nd, so this exchange will affect only ε_{Sr}. Since ε_{Sr} of seawater Sr is +30 to +64 [*Peterman et al.*, 1970], the effect will be to displace ε_{Sr} of altered rocks to the right, away from the oceanic correlation trend. This type of displacement has been observed in some island arc lavas and has been attributed to their being derived by melting of subducted oceanic basalt that had been hydrothermally altered prior to subduction [*DePaolo and Johnson*, 1979].

Samples

The Sierra Nevada (SNB) samples analyzed in this study are the same samples analyzed by *Kistler and Peterman* [1973, 1978], who give the exact locations, descriptions, and ages for the rocks. Major-element chemical analyses and oxygen isotopic compositions [*Masi et al.*, 1981] have been measured for all of the samples. Samples numbered 73-3, 5, 14, 26, and 28 have been measured for rare-earth element abundances by G. N. Hanson (unpublished data, 1977). The plutonic rock samples numbered with the prefix SNB-73 correspond to the sample numbers in *Kistler and Peterman* [1973]; those numbered SNB-78 are from *Kistler and Peterman* [1978]. Sample number FD-33 is a volcanic composite from west of the Melones fault zone; FD-39 is a composite of metasedimentary rocks from the Calaveras Formation, a terrain of metamorphosed hemipelagic sediments and interlayered volcanic rocks of Permian(?) or Jurassic(?) age that comprises part of the Sierra Nevada western metamorphic belt [*Saleeby*, 1981]. Sample

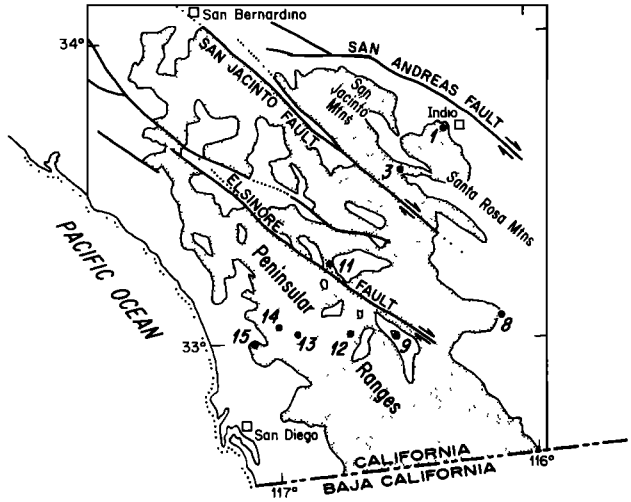

Fig. 2. Locations of Peninsular Ranges batholith (PRB) samples analyzed in this study. [See *DePaolo*, 1980*b*; *Kistler and Peterman*, 1973, 1978, for other sample locations.]

B37 is a granulite-facies metamorphic xenolith from a Tertiary volcanic stock (R. W. Kistler, personal communication, 1980) in the central Sierra Nevada; RRPV-1 is a composite of metamorphosed sedimentary and volcanic rocks from the Ritter Range roof pendant; PC-30a is a Precambrian schist. The nonplutonic samples are described in *Kistler and Peterman* [1973].

The Peninsular Ranges samples numbered PRB-1 through 15 were collected for this study by the author along an east-west transect of the batholith, at approximately latitude 33°N (Figure 2). Samples 1 and 3 lie to the northeast of the San Jacinto fault zone, an area called the 'San Jacinto-Santa Rosa Mountain Block' by *Taylor and Silver* [1978], who found it to be anomalous in terms of oxygen and strontium isotope relationships. Exact locations of the samples are given in the Appendix. No other analytical data exist for these samples, but the sample localities correspond closely to those of *Taylor and Silver* [1978]. *Gromet* [1979] has also done an extensive study of rare-earth abundance patterns in the same area. Samples SM, WM, and RL are from the type localities of San Marcos gabbro, Woodson Mountain granodiorite, and Rubidoux leucogranite [*DePaolo*, 1980*b*]; PRB-800 and 805 are from the San Telmo pluton in Baja California [*DePaolo et al.*, 1975; *Gromet and Silver*, 1977]. This pluton is an eipzonal ring complex of gabbro, tonalite (800), and granophyre (805) intruded into gently dipping volcanic rocks. It is located at the extreme western edge of the batholith at latitude 31°N [*DePaolo*, 1980*b*]. Samples DG-1 and 3 are volcanic country rocks. The granophyre is apparently a thin sheet near the roof of the pluton. It exhibits abundant petrographic evidence for hydrothermal alteration after emplacement and contains turbid alkalifeldspar that is drastically out of oxygen isotopic equilibrium with coexisting quartz (D. J. DePaolo and H. P. Taylor, unpublished data, 1974). It contrasts with sample 800, which is petrographically pristine and shows no oxygen isotope disequilibrium between constituent minerals. The San Telmo area samples differ from all other PRB samples analyzed in that they lie in the 'western high-$\delta^{18}O$' zone of *Taylor and Silver* [1978], which has been interpreted as a more 'oceanic' environment compared to the continental margin environment of southern California.

Age data exist only for samples 800 and 805 [*DePaolo et al.*,

TABLE 1. Normal Nd Isotopic Ratios

	$^{142}Nd/^{144}Nd$	$^{145}Nd/^{144}Nd$	$^{146}Nd/^{144}Nd$	$^{148}Nd/^{144}Nd$
This work*	1.138332 ± 14	0.348945 ± 7	0.724127	0.243064 ± 8
Caltech†	1.138331 ± 10	0.348954 ± 4	0.724108 ± 7	0.243067 ± 5

* Measured as Nd^+; normalized to $^{146}Nd/^{142}Nd = 0.63613$.

† Measured as NdO^+; corrected for oxygen isotopes, using $^{18}O/^{16}O = 0.00210$ and $^{17}O/^{16}O = 0.000384$; normalized to $^{150}Nd/^{142}Nd = 0.209600$ [*DePaolo*, 1978].

1975]. Ages for the other PRB samples have been inferred from the work of *Silver et al.* [1975] and are estimated to be correct to about ±10 m.y., an uncertainty that corresponds to negligible error in the calculated initial isotopic ratios. Sample PRB-11 has been dated during the course of this work by a Rb-Sr biotite-whole rock 'isochron' at 93.9 ± 0.2 m.y. (λ_{Rb} = 0.0139 AE^{-1}).

Analytical techniques

For the Sierra Nevada samples, 500-mg splits of previously analyzed powders were used for analysis. For the Peninsular Ranges samples, 1-kg chunks of rock were crushed and ground, and 500-mg splits were analyzed. The chemical procedures used for Nd and Sr isotopic analysis are described in detail by *Papanastassiou et al.* [1978] and *DePaolo* [1978]; K, Rb, Sr, Sm, and Nd concentrations were determined by taking a 1%–2% aliquot of the sample solution, spiking with ^{41}K, ^{87}Rb, ^{84}Sr, ^{147}Sm, and ^{150}Nd, and then loading a small aliquot (about 20–40 μg equivalent of rock) directly onto a single Re filament for mass spectrometric analysis. Total blank levels for Nd and Sm were about 1 ng and 0.2 ng, respectively, at the beginning of this investigation. During the course of the study the blanks dropped to 0.10 ng for Nd and 0.02 ng for Sm, as a result of refinement of the procedure for making high-purity HCl. The Sr blank is about 1 ng.

Sr isotopic data on the Sierra Nevada samples are from *Kistler and Peterman* [1973, 1978]. Three samples were remeasured during the current study, and the results agreed to within about 0.0001 for the calculated initial $^{87}Sr/^{86}Sr$ ratio. All trace-element concentrations were remeasured for this study. The XRF data of *Kistler and Peterman* [1973, 1978] are in good agreement with the new isotope dilution results. Samples for which Nd isotopic data have been previously reported [*DePaolo*, 1980*b*] were analyzed in the Lunatic Asylum at the California Institute of Technology. All other data were analyzed in a newly constructed laboratory at UCLA, using a recently purchased Micromass 54E mass spectrometer. The mass spectrometric procedures used differ somewhat from those described previously and are briefly summarized here.

Sr isotopic measurements were made by first loading 0.5–1.0 μg of Sr onto an unoxidized single, flat, Ta filament (Rembar Ta), using HCl medium. After evaporating the HCl from the filament, the dried sample was covered with 1 μl of 10%–20% H_3PO_4, and the filament was heated to a dull red color by passing a 3-A current through it for 10 to 15 s. This procedure yields an ^{88}Sr ion beam of 4–6 × 10^{-11} A for several hours in the mass spectrometer. The ion beam intensities were measured using a Micromass Digital integrator which was equipped with a 10^{10}-ohm feedback resistor in the remote head. Data were collected by using either of two procedures. The first, using software provided by VG Micromass, measures ion beam intensities at the following masses (in order) 88, 86.5, 84, 86.5, 85, 86, 87.5, 87. The second procedure, using software written at UCLA, measures ion beam intensities in the order 88.3, 88, 87.7, 87.3, 87, 86.7, 86.3, 86, 85.7, 84.3, 84, 83.7. This latter method is identical to that used in the Lunatic Asylum [*Wasserburg et al.*, 1969]. For both procedures ion beams are integrated for 1 s. A 1.5-s delay between readings allows the electromagnet to slew and lock-in to the next field setting; it also provides settling time for the electronics.

For the second data collection procedure, the background reading at mass 87.7, measured after integrating the peak at 88, is higher than the background reading at mass 88.3 by only ≤1 × 10^{-5} of the 88 peak. Four analyses of strontium isotopic standard NBS987 gave a mean value of 0.71028 ± 3. The mean measured value of $^{84}Sr/^{88}Sr$, measured in every run, is 0.0067454 ± 15. Rubidium interference at mass 87 was negligible for all analyses.

Neodymium was analyzed by loading 200–1000 ng of Nd on the side filaments of a triple Re filament bead and was run as the species Nd^+. The procedure yields a $^{144}Nd^+$ ion beam of 0.6 to 3.0 × 10^{-11} A, which lasts for several hours. In each run, five isotopes were measured, with the ion beam intensities integrated in the sequence 144, 143, 142, 146, 145. For each isotope, background readings are taken at ±0.4 amu in a manner analogous to procedure two for Sr. Nd isotope ratio measurements are made by using a 10^{11}-ohm feedback resistor in the remote head of the digital integrator. The background readings after each peak are displaced upward by about 6 × 10^{-5} for the 10^{11}-ohm resistor.

During a Nd mass spectrometer run, possible interferences caused by Ce and Sm are monitored at masses 140 and 152, respectively; interferences occur at mass 142 (Ce) and at mass 144 (Sm). The magnitude of the interferences relative to the intensity of the Nd peak affected is generally 2 to 4 × 10^{-5} for ^{142}Nd and ≤10^{-5} for ^{144}Nd. If no corrections were made for these interferences, the effect on the $^{143}Nd/^{144}Nd$ ratio would be ≤2 × 10^{-5}; smaller than the analytical uncertainty of ±3 to 5 × 10^{-5}. With the corrections incorporated, any systematic error is totally negligible. In order to compare the data from the Micromass 54E with previously measured data from the Lunatic Asylum, all seven Nd isotopes have been measured in some runs. The mean values measured at UCLA are compared to those measured by the author at Caltech in Table 1. The Caltech data are those summarized by *DePaolo* [1978], but they have been corrected to account for the fact that the measurements are made on NdO^+ at Caltech as opposed to Nd^+ at UCLA. This correction is necessary because the measured oxygen isotope ratios in the NdO^+ ion beam differ somewhat from those originally chosen for use in the oxide corrections [cf. *DePaolo*, 1978; *Papanastassiou et al.*, 1977]. The Caltech numbers in Table 1 are the best estimates given by *DePaolo* [1978], using the measured oxygen isotope ratios. The Caltech data are normalized to $^{150}Nd/^{142}Nd = 0.2096$ to eliminate the effects of instrumental fractionation. The UCLA data are normalized to $^{146}Nd/^{142}Nd = 0.63613$, which is essentially equivalent. The table shows that all of the isotopic ratios agree to within 2 to 3 × 10^{-5} between the two labs. The fact

that exactly the same results are obtained through the use of two completely different mass spectrometers strongly suggests that the ratios measured are accurate at a level comparable to the precision. The $^{143}Nd/^{144}Nd$ ratios measured at UCLA should therefore be comparable to those measured at Caltech within about 2 parts in 10^5.

To test the accuracy of the estimate obtained from in-run statistics for the 95% uncertainty limits on the $^{143}Nd/^{144}Nd$ measurements, the ratio $^{145}Nd/^{144}Nd$ has also been measured on every rock sample. This ratio can be measured to a precision comparable to that obtained for $^{143}Nd/^{144}Nd$ and does not change in nature. Its reproducibility gives an internal check on the accuracy of the $^{143}Nd/^{144}Nd$ measurements. A histogram of $^{145}Nd/^{144}Nd$ measurements for 34 runs made between April and August 1980 is shown in Figure 3 along with the average statistical estimate of the 95% confidence level uncertainty ($2\sigma_m$), which in this case is about $\pm 0.65 \times 10^{-4}$ as a fraction of the ratio measured. Of the 34 measurements, 31, or 92% are within the average $\pm 2\sigma_m$. The in-run error estimates for each individual run overlap the grand mean for 30 of the 34 measurements. Two others miss by only 0.08×10^{-4}. Thus the statistical estimate of the 95% confidence level appears to be correct to as well as can be determined by the limited number of runs. The average $2\sigma_m$ for $^{143}Nd/^{144}Nd$ is about 0.5×10^{-4}, expressed as a fraction of the $^{143}Nd/^{144}Nd$ ratio. The data also show that long-term drift in the measured ratio is negligible.

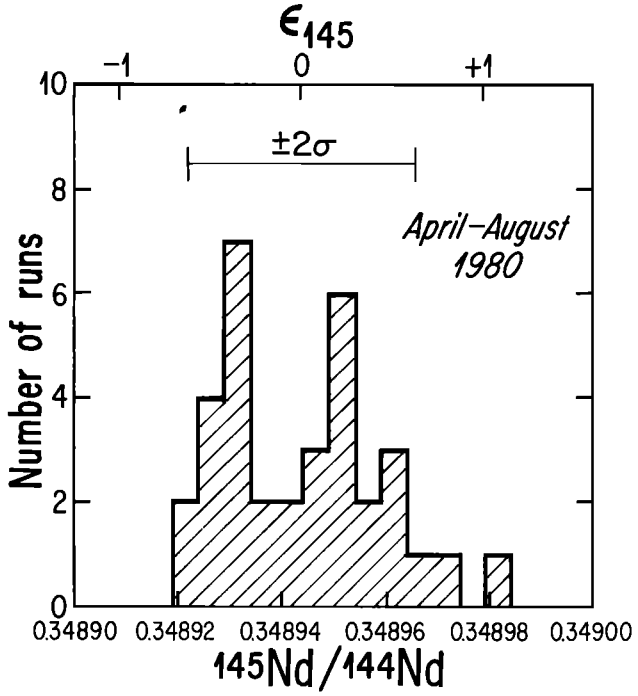

Fig. 3. Histogram of $^{145}Nd/^{144}Nd$ ratios measured at UCLA during the time of this investigation, showing the reproducibility and the correspondence between the statistically estimated 95% confidence level ($\pm 2\ \sigma_m$) and the distribution of the measured values. Measurement of $^{145}Nd/^{144}Nd$ in every rock sample provides an internal check for the presence of artifacts in the $^{143}Nd/^{144}Nd$ measurements.

Data Representation

Isotopic data for Nd and Sr are presented in terms of the parameters ε_{Nd} and ε_{Sr} as previously defined [*DePaolo and Wasserburg*, 1976, 1977]; ε_{Nd} is the deviation in parts in 10^4 of a rock's initial $^{143}Nd/^{144}Nd$ ratio from the ratio of $^{143}Nd/^{144}Nd$ in a model chondritic reservoir (CHUR):

$$\varepsilon_{Nd}(T) = 10^4 \left[\frac{^{143}Nd/^{144}Nd_{ROCK}(T)}{^{143}Nd/^{144}Nd_{CHUR}(T)} - 1 \right] \quad (1)$$

The ratio $^{143}Nd/^{144}Nd_{CHUR}(T)$ is given by the following expression:

$$^{143}Nd/^{144}Nd_{CHUR}(T) = 0.511836 - 0.1967\ [\exp(\lambda_{Sm}T) - 1] \quad (2)$$

where $\lambda_{Sm} = 0.00654\ AE^{-1}$, T is time measured backward from the present (age), and the numbers given are $^{143}Nd/^{144}Nd_{CHUR}(0)$ and $^{147}Sm/^{144}Nd_{CHUR}(0)$, respectively. The latter number differs from the value used previously. It has been revised following the results of a careful study of chondritic meteorites by *Jacobsen and Wasserburg* [1980]; ε_{Sr} is the deviation in parts in 10^4 of a rock's initial $^{87}Sr/^{86}Sr$ ratio from the ratio in a model reservoir thought to be representative of the total earth (UR) (it is not a chondritic reservoir):

$$\varepsilon_{Sr}(T) = 10^4 \left[\frac{^{87}Sr/^{86}Sr_{ROCK}(T)}{^{87}Sr/^{86}Sr_{UR}(T)} - 1 \right] \quad (3)$$

The ratio $^{87}Sr/^{86}Sr_{UR}(T)$ is given by:

$$^{87}Sr/^{86}Sr_{UR}(T) = 0.7045 - 0.0839\ [\exp(\lambda_{Rb}T) - 1] \quad (4)$$

where $\lambda_{Rb} = 0.0139\ AE^{-1}$, and the numbers are $^{87}Sr/^{86}Sr_{UR}(0)$ and $^{87}Rb/^{86}Sr_{UR}(0)$, respectively. Oxygen isotopic data are discussed using the parameter $\delta^{18}O$, defined:

$$\delta^{18}O = 10^3 \left[\frac{^{18}O/^{16}O_{ROCK}}{^{18}O/^{16}O_{STD}} - 1 \right] \quad (5)$$

where the standard is mean ocean water [*Craig*, 1961].

The model Sm-Nd age T_{DM} represents the time when a rock sample would have had the same value of ε_{Nd} as the depleted upper mantle [*DePaolo*, 1981*a*]. The ε_{Nd} of the model depleted mantle is given to sufficient accuracy by

$$\varepsilon_{Nd}^{DM}(T) = 0.25T^2 - 3T + 8.5 \quad (6)$$

where T is in Æ (10^9 yr). The ε_{Nd} of a rock sample at a time T in the past is given by

$$\varepsilon_{Nd}^{ROCK}(T) = \varepsilon_{Nd}^{ROCK}(0) - f_{Sm/Nd}Q_{Nd}T \quad (7)$$

where $\varepsilon_{Nd}(0)$ is the measured value, $Q_{Nd} = 25.1AE^{-1}$, and $f_{Sm/Nd}$ is the Sm/Nd enrichment factor, defined:

$$f_{Sm/Nd} = (^{147}Sm/^{144}Nd_{ROCK}/0.1967) - 1 \quad (8)$$

The T_{DM} model age is obtained by equating (6) and (7), that is, solving for T to satisfy

$$\varepsilon_{Nd}^{ROCK}(T) = \varepsilon_{Nd}^{DM}(T) \quad (9)$$

The model Rb-Sr age T_{UR} represents the time when a rock sample would have had $\varepsilon_{Sr} = 0$ [*DePaolo and Wasserburg*, 1979*b*].

RESULTS

1. *Metasedimentary and Volcanic Rocks*

All trace element and isotopic data are presented in Tables 2–5. The isotopic parameters for samples SN-FD-33, 39, and 46, composites of volcanic and sedimentary rocks from the central western Sierra Nevada are plotted on Figure 4. The volcanic composite (FD-33) plots close to the ε_{Nd}-ε_{Sr} oceanic basalt correlation line but has ε_{Nd} somewhat more negative than typical oceanic island arcs. This slightly lowered ε_{Nd} ap-

TABLE 2. Sierra Nevada Batholith Trace Element Concentrations and Ratios

Sample	Type	K, %	Rb	Sr	Sm	Nd	$^{87}Rb/^{86}Sr$	$^{147}Sm/^{144}Nd$	Sr/Nd
SNB-73-2	Granodiorite	3.66	65.1	620	2.91	15.4	0.304	0.114	40.3
SNB-73-3	Granodiorite	2.58	89.1	726	3.82	20.9	0.356	0.111	34.8
SNB-73-5	Granodiorite	2.24	125.5	332	4.53	20.0	1.094	0.137	16.6
SNB-73-9	Granodiorite	3.87	138	552	6.88	37.2	0.723	0.112	14.8
SNB-73-14	Granite	2.90	140	597	3.12	20.9	0.678	0.090	28.6
SNB-73-15	Granite	2.36	91	312	4.29	27.4	0.844	0.095	11.4
SNB-73-25	Quartz monzonite	4.06	154	301	5.51	35.2	1.480	0.095	8.6
SNB-73-26	Granodiorite	1.57	80.5	409	3.61	17.7	0.570	0.123	23.1
SNB-73-28	Quartz diorite	0.60	10.3	482	2.44	13.2	0.062	0.112	36.5
SNB-73-29	Granodiorite	1.70	48.5	428	2.94	15.6	0.328	0.114	27.4
SNB-78-3	Quartz diorite	1.47	37.9	460	2.52	13.9	0.239	0.110	33.1
SN-FD-46	Metasediment	2.24	91.8	96	3.59	18.0	2.767	0.120	5.3
SN-FD-39	Metasediment	2.16	94.6	109	4.26	22.6	2.511	0.114	4.8
SN-RRPV-1	Volc.-sed. composite	3.11	151.3	213	2.78	15.9	2.055	0.106	13.4
SN-PC-30a	Schist	2.09	88.3	164	8.87	47.0	1.557	0.114	3.5
SN-B37	Granulite xenolith	1.63	56.1	186	7.56	38.6	0.873	0.118	4.8

Concentrations in ppm except for K; isotopic ratios are atomic ratios, Sr/Nd is weight ratio.

TABLE 3. Peninsular Ranges Batholith Trace Element Concentrations and Ratios

Sample	Type	K, %	Rb	Sr	Sm	Nd	$^{87}Rb/^{86}Sr$	$^{147}Sm/^{144}Nd$	Sr/Nd
PRB-1	Quartz monzonite	3.34	117.6	446	3.94	20.6	0.763	0.116	21.6
PRB-3	Granodiorite	2.37	97.9	530	5.61	30.7	0.535	0.111	17.3
PRB-8	Granodiorite	2.48	122.1	407	4.24	20.9	0.868	0.123	19.5
PRB-9	Tonalite	0.92	35.0	546	4.39	18.2	0.185	0.146	30.0
PRB-11	Tonalite	1.68	83.0	319	2.80	10.6	0.753	0.160	30.1
PRB-12	Quartz diorite	1.48	61.2	325	5.73	27.3	0.193	0.127	1.9
PRB-13	Quartz gabbro	0.75	20.3	302	3.89	15.1	0.195	0.156	20.0
PRB-14	Quartz monzonite	2.80	52.5	177	4.20	16.6	0.859	0.153	10.6
PRB-15	Granodiorite	1.8	40	253	4.14	15.4	0.457	0.163	16.4
PRB-SM-1	Gabbro	0.23	4.1	451	1.25	4.95	0.027	0.153	91.1
PRB-WM-1	Granodiorite	2.19	65.7	158	1.70	7.2	1.203	0.143	21.9
PRB-RL-1	Granite	4.54	223	104	2.84	11.5	6.203	0.149	9.0
PRB-800	Tonalite	0.83	13.8	74.7	3.40	10.5	0.535	0.196	7.1
PRB-805	Granophyre	2.83	32.0	55.3	4.06	14.3	1.674	0.172	3.9
PRB-DG-1	Basalt	0.32	2.3	227	3.23	11.2	0.030	0.174	20.3
PRB-DG-3	Keratophyre	2.06	16.4	33.3	8.38	31.1	1.425	0.163	1.1

Concentrations in ppm except for K; isotopic ratios are atomic ratios; Sr/Nd is weight ratio.

TABLE 4. Sierra Nevada Isotopic Data

Sample	T, m.y.*	$^{143}Nd/^{144}Nd_{meas}$†	$^{87}Sr/^{86}Sr_{meas}$‡	$\varepsilon_{Nd}(T)$	$\varepsilon_{Sr}(T)$	$\delta^{18}O$§
SNB-73-2	121	0.512037 ± 26	0.7041	+5.1	−10	+7.5
SNB-73-3	88	0.511850 ± 24	0.7052	+1.2	+6	+8.2
SNB-73-5	90	0.511932 ± 28	0.7058	+2.5	−1	—
SNB-73-9	210	0.511542 ± 28	0.7073	−3.5	+13	+8.2
SNB-73-14	84	0.511460 ± 17	0.7074	−6.3	+30	+8.2
SNB-73-15	107	0.511548 ± 20	0.7061	−3.9	+23	+8.3
SNB-73-25	79	0.511396 ± 26	0.7098	−7.6	+54	+11.0
SNB-73-26	86	0.511828 ± 32	0.7056	+0.6	+7	+7.8
SNB-73-28	126	0.512105 ± 17	0.7033	+6.5	−16	+9.2
SNB-73-29	103	0.511949 ± 20	0.7050	+3.3	0	—
SNB-78-3	120	0.512076 ± 25	0.7036	+6.0	−16	+7.3
SNB-78-4	90	0.511651 ± 27	0.7089	−2.4	+25	+9.4
SNB-78-17	90	0.511456 ± 18	0.7069	−6.3	+31	+10.2
SN-FD-33	Jurassic	0.512022 ± 23	0.7047	+4.6	−9	—
SN-FD-46¶	Permian(?)	0.511445 ± 25	0.7159	−6.6	+108	—
SN-FD-39¶	Permian(?)	0.511230 ± 34	0.7171	−10.8	+131	—
SN-RRPV-1¶	Permian	0.511663 ± 22	0.7115	−2.2	+60	—
PC30a[d]	Precambrian	0.510987 ± 25	0.7383	−15.6	+450	—
SN-B37[d]	?	0.511195 ± 26	0.7162	−11.5	+150	+14.8

* Ages from *Kistler and Peterman* [1973, 1978].

† Uncertainties at the 95% confidence level.

‡ Data from *Kistler and Peterman* [1973, 1978]. Samples 73-3, 73-15, and 78-3 were remeasured at Caltech or UCLA, yielding identical results.

¶ ε_{Nd} and ε_{Sr} values calculated for $T = 100$ m.y.

§ Data from *Masi et al.* [1981].

TABLE 5. Peninsular Ranges Isotopic Data

Sample	T, m.y.*	$^{143}Nd/^{144}Nd_{meas}$†	$^{87}Sr/^{86}Sr_{meas}$†	$\varepsilon_{Nd}(T)$	$\varepsilon_{Sr}(T)$	$\delta^{18}O$‡
PRB-1	90	0.511486 ± 24	0.70872 ± 4	−5.9	+48	+9.4
PRB-3	90	0.511455 ± 38	0.70847 ± 4	−6.4	+49	+9.8
PRB-8	90	0.511586 ± 25	0.70736 ± 5	−4.1	+27	+10.8
PRB-9	100	0.511901 ± 24	0.70481 ± 14	+1.9	+2	+9.7
PRB-11	94¶	0.511775 ± 35	0.70564 ± 4	−0.8	+3	+9.2
PRB-12	100	0.512083 ± 18	0.70458 ± 4	+5.7	−8	+8.5
PRB-13	110	0.511972 ± 18	0.70439 ± 7	+3.2	−4	+7.8
PRB-14	110	0.512070 ± 26	0.70523 ± 8	+5.1	−6	+6.3
PRB-15	120	0.512087 ± 34	0.70431 ± 4	+5.4	−12	<+5.5
PRB-SM-1	120	0.512045 ± 30	0.70338 ± 5	+4.7	−15	—
PRB-WM-1	110	0.511977 ± 27	0.70542 ± 5	+3.6	−11	—
PRB-RL-1	110	0.511868 ± 24	0.71353 ± 6	+1.3	−2	+8.0
PRB-800	110	0.512237 ± 23	0.70334 ± 11	+7.8	−15	+6.5
PRB-805	110	0.512224 ± 24	0.70700 ± 4	+7.9	+2	+9.2
PRB-DG-1	120	0.512179 ± 22	0.70425 ± 10	+7.0	−3	—
PRB-DG-3	120	0.512230 ± 26	0.70637 ± 6	+8.2	−5	+12.0

* All ages estimated from regional variations described by *Silver et al.* [1975].

† Uncertainties are at the 95% confidence level.

‡ Estimated from geographic contours of *Taylor and Silver* [1978], except for samples 800, 805, and DG-3 (DePaolo and Taylor, unpublished).

¶ Rb-Sr biotite-whole rock age (λ_{Rb} = 0.0139 AE^{-1}).

pears to be characteristic of continental margin arc-type volcanic rocks in general [cf. *Carmichael and DePaolo,* 1980]. This effect may be due to a small crustal component in the magma source or to contamination of mantle-derived magma at relatively shallow levels. This datum suggests that the 'island arc' accreted to the western margin of North America in mid-Mesozoic time [*Saleeby,* 1981; *Dickinson,* 1981] was of continental margin type and may have formed close to its present position. The datum is also consistent with more exotic models [*Schweikert and Snyder,* 1981] which have the arc forming far to the west but on a continental sedimentary terrane that was rifted away earlier. The sedimentary composites (FD-39 and 46) have large negative ε_{Nd} values. The model ages T_{DM} are 1.54 Æ and 1.29 Æ, respectively. These data indicate that the detrital fraction of the Calaveras formation in this area contains a large component derived from the Precambrian continental crust to the east and a relatively small component (<20%) derived from contemporaneous(?) arc volcanics with compositions similar to FD-33. This is strong evidence that throughgoing, westward-directed dispersal systems existed in the Sierra Nevada region in the Late Paleozoic (or Mesozoic). If Paleozoic in age, the Calaveras could represent a distal facies of the Paleozoic continentally derived sedimentary section to the east of the Sierra Nevada ('Cordilleran geosyncline') [cf. *King,* 1977], as proposed by *Bateman and Wahrhaftig* [1966]. However, even if it was formed farther to the west and was allochthonous, it apparently was close enough to the continent to receive significant amounts of continental detritus [cf. *Saleeby,* 1981]. The Sr isotope data on FD-39 and 46, in contrast to the Nd data, indicate model ages (T_{UR}) of only 375 and 307 m. y., much closer to the estimated Permian or younger sedimentation age. This effect of low Sr model ages in comparison to Nd model ages has been observed previously in sedimentary rocks [*McCulloch and Wasserburg,* 1978]. It is probably due to redistribution of Rb and Sr during diagenesis, involving an increase of Rb/Sr as a result of Rb retention in phyllosilicates in preference to Sr, to a lowering of ε_{Sr} in the sediment caused by exchange with Sr dissolved in seawater, or both. The high Rb/Sr of FD-39 (FD-46 also) caused its ε_{Sr} to increase rapidly subsequent to the rock's formation. This is shown on Figure 4, where the ε_{Nd}-ε_{Sr} composition is plotted as a function of age from 270 to 90 m. y. a. The ε_{Nd} does not change much over this time interval.

Sample B37 had ε_{Nd}-ε_{Sr} coordinates similar to those of the Calaveras sample in mid-Cretaceous time (Figure 4). Its Sm-Nd model age T_{DM} is 1.62 Æ. This datum demonstrates the existence of metasedimentary material within the geographic boundaries of the Sierra Nevada and below the shallow granitic rocks which has isotopic characteristics that adhere to the model shown in Figure 1. This sample has low Rb/Sr and a greater Rb-Sr model age (T_{UR} = 1.2 Æ) than the Calaveras samples. The low Rb/Sr can be plausibly assumed to be the result of granulite facies metamorphism during the Mesozoic. The $\delta^{18}O$ for this sample is +14.8 (R. W. Kistler, personal communication, 1980).

The Ritter Range sample (RRPV-1) is a composite of a mixed volcanic and sedimentary terrane and exhibits properties that are intermediate between those of FD-33 and FD-39.

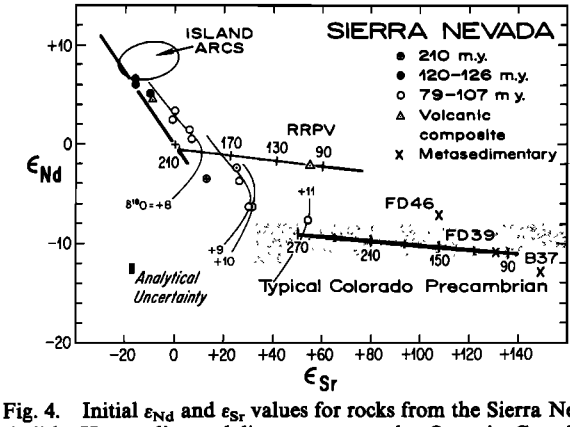

Fig. 4. Initial ε_{Nd} and ε_{Sr} values for rocks from the Sierra Nevada batholith. Heavy diagonal line represents the Oceanic Correlation Line. Stippled region gives the isotopic composition of typical 1.8-Æ-old basement rocks of Colorado [*DePaolo,* 1981*a*]. Samples RRPV, FD39, FD46, and B37 are metamorphic wallrock samples. The isotopic parameters for two of the samples are shown as a function of time (e.g., 90, 150, 210, 270 m.y. ago for FD39). Both FD39 and FD46 (Calaveras Formation) and B37 (granulite xenolith) have ε_{Nd} and ε_{Sr} coordinates similar to the 1.8-Æ crust, indicating cratonic provenance. Contours are for $\delta^{18}O$ [*Masi et al.,* 1981] in the plutonic samples.

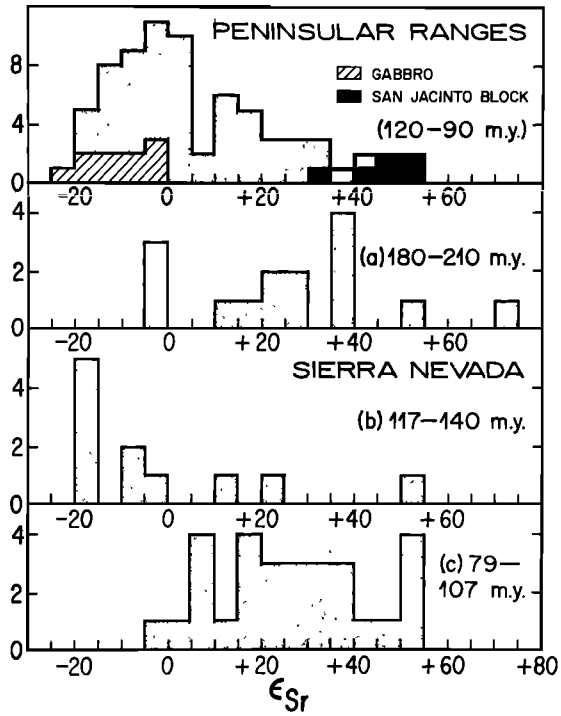

Fig. 5. Histogram of ϵ_{Sr} values for the Peninsular Ranges and three separate time intervals for the Sierra Nevada [data from *Taylor and Silver*, 1978; *Kistler and Peterman*, 1973, 1978]. 'San Jacinto block' refers to the area bounded by the San Jacinto and San Andreas faults (Figure 2).

At the time of the oldest plutonic rocks formed (Triassic) this sample had ϵ_{Nd}-ϵ_{Sr} coordinates that lay on the oceanic correlation line. Subsequently, because of its high Rb/Sr, its ϵ_{Sr} has increased rapidly. At 90 million years ago its composition was distinctly different from any of the Sierra Nevada plutonic rocks.

The Precambrian pelitic schist (PC-30a) has isotopic properties that are substantially different from the other country rock samples. It has an extremely large ϵ_{Sr} (+450) and a model Rb-Sr age of about 1.6 Æ [*DePaolo*, 1980*b*], suggesting that the sedimentation age may be early Proterozoic. The ϵ_{Nd} value is a large negative number (−15.6), and the sample has a model T_{DM} age of 1.9 Æ. This age is slightly older than the age of the crust in this region (≲1.8 Æ) and could indicate that this sediment contains a small amount of detritus derived from the Wyoming Archean terrane. This would be consistent with the presence, in some igneous rocks of the southern Sierra Nevada, of inherited zircons that yield ages in excess of 2.0 Æ [*Chen*, 1976]. This sample and the metasedimentary composites have distinctly low Sr/Nd, a characteristic of mature clastic sedimentary rocks.

The volcanic rocks from the San Telmo area (DG-1, DG-3) have the highest ϵ_{Nd} values of any of the samples measured. As shown on Figure 6, they plot within or close to the field of primitive oceanic island arcs [*DePaolo and Johnson*, 1979]. Like many other arc-type volcanics they have ϵ_{Sr} values that are displaced to the right of the OCL. For these samples, this displacement in ϵ_{Sr} could be a characteristic of the magma source or it could be due to hydrothermal exchange with a seawaterlike pore fluid during low grade metamorphism. Sample DG-3, for example, is classified as keratophyre because its plagioclase has been thoroughly altered to albite. A feldspar separate yielded $\delta^{18}O = +12$, indicative of extensive low-temperature exchange with water of approximately seawater composition ($\delta^{18}O \approx 0$ to +3) (D. J. DePaolo and H. P. Taylor, unpublished data, 1974). The ϵ_{Nd} data are consistent with the proposal by *Silver et al.* [1963] and by *Silver and Anderson* [1974] that the western Peninsular Ranges batholith at this latitude represents a Cretaceous oceanic island arc.

2. *Sierra Nevada Plutonic Rocks*

Nd and Sr isotopic data on the Sierra Nevada plutonic rocks are shown on Figure 4. The points define a slightly curved trend extending from $\epsilon_{Nd} = +6.5$ to −7.6 with a corresponding range of ϵ_{Sr} from −16 to +54. The new data presented here fill in the gap in the trend inferred by *DePaolo* [1980*b*]. The data array extends from the field of primitive oceanic island arcs to the field of continental crustal rocks that have ages equal to that of the crustal rocks in eastern California (~1.8 Æ old today, but the same rocks would have been ~1.7 Æ old in mid-Cretaceous time). As evidenced by samples FD-39 and 46 and B37, the Paleozoic sedimentary rocks of the Sierra Nevada region also have isotopic compositions similar to the old crustal rocks. Mixtures of either of these with a mantle component having a composition at the intersection of the OCL and the island arc field would lie along curves which would closely follow the data array (Figure 1). The volcanic composite FD-33 falls along the same trend.

Kistler and Peterman [1973] showed that the Sr isotopic compositions of the Sierra Nevada plutonic rocks exhibit regular geographic variations that can be areally contoured and reflect geologic structures that have existed in California since the Precambrian. As expected, considering the correlation between ϵ_{Nd} and ϵ_{Sr}, such regional variations also hold for Nd isotopes, and the ϵ_{Nd} values follow the contours drawn by Kistler and Peterman quite closely. The positive ϵ_{Nd} values are generally restricted to the western side and the northern end of the batholith. These are the areas that are farthest from any outcrops of Precambrian rocks or Paleozoic shelf-type sedimentary rocks and, hence, can be assumed also to be farthest from the Paleozoic continental margin.

Most of the samples analyzed have mid-Cretaceous ages. The limited sampling of intrusives of other ages give no indication that they would define a different trend. The distribution of values along the trend, however, may vary between rocks of different age groupings. This is shown on Figure 5, using the more abundant Sr isotopic data of *Kistler and Peterman* [1973, 1978]. The age groups shown are arbitrary; they do not correspond exactly to the identified intrusive epochs of *Evernden and Kistler* [1970]. Assuming that the samples analyzed are approximately representative, it appears that the rocks of each age group span most of the total range of ϵ_{Sr}—and by inference ϵ_{Nd}. It may be noteworthy, however, that the lowest ϵ_{Sr} value in rocks of the oldest and youngest groups is about −5, whereas the rocks with ages near the Jurassic-Cretaceous boundary reach values as low as about −17, with a large proportion of the values being less than −5. The data indicate that the late Jurassic-early Cretaceous magmatic arc was isotopically most like a typical oceanic island arc. This is primarily a result of the geographic position. The locus of magmatism at this time was mainly near the western edge of the present batholith exposures and, hence, farthest from continental materials, as opposed to more easterly (inland) loci for both the older and younger intrusives. As noted by Kistler and Peterman, the Sr isotopic values are mostly a function of

geographic position, independent of age. This is also true of the ε_{Nd} values.

Contours of $\delta^{18}O$ (data from *Masi et al.* [1981]) are also shown on Figure 4. The $\delta^{18}O$ values generally increase in the direction of decreasing ε_{Nd} and increasing ε_{Sr} with several exceptions. There is also a suggestion of an increase in $\delta^{18}O$ that is related to shifts in ε_{Sr} away from the OCL, but there are insufficient data to fully document the effect. The sample with the highest ε_{Nd} is notably anomalous, having $\delta^{18}O = +9.2$.

3. *Peninsular Ranges Plutonic Rocks*

The data for the plutonic rocks, shown on Figure 6, define a trend that is almost identical to that shown by the Sierra Nevada data, with the exception of the San Telmo samples, which have somewhat higher ε_{Nd} and tend to lie to the right of the OCL. Also, the PRB data exhibit more scatter in ε_{Sr} among the samples with positive ε_{Nd} but extend over almost the same range of both ε_{Nd} and ε_{Sr} as do the Sierra data. They also show a fairly regular west to east decrease in ε_{Nd}. The samples from the San Jacinto block, which are anomalous in terms of their O and Sr isotopic characteristics [*Taylor and Silver,* 1978], are the most extreme in terms of ε_{Nd} and ε_{Sr} but do not appear to be anomalous to the extent that they lie along essentially the same trend defined by both the other PRB data and the SNB data. The distribution of values along the ε_{Nd}-ε_{Sr} trend can be inferred from the histogram of ε_{Sr} values shown in Figure 5 (data from *Taylor and Silver* [1978]). The data appear to indicate a lower average value of ε_{Sr} in the PRB. However, this could be due to a sampling bias in the SNB away from the rocks from the northern part of the batholith, which tend to have lower values than those from the southern, more heavily studied, part.

The contours of $\delta^{18}O$ given by *Taylor and Silver* [1978] have been used to estimate $\delta^{18}O$ of the samples analyzed in this study (Table 5). The results are shown by the $\delta^{18}O$ contours in Figure 6. The $\delta^{18}O$ values increase steadily as a function of decreasing ε_{Nd} and increasing ε_{Sr}, except for the San Jacinto block samples, as expected. There is also an increase in $\delta^{18}O$ in samples that lie to the right of the OCL. The $\delta^{18}O$ values converge to the mantle value of about +6 at the point where the island arc field overlaps the OCL on the ε_{Nd}-ε_{Sr} plot. Note that for the PRB, the $\delta^{18}O$ values are higher than those of the SNB rocks for the same ε_{Nd}, ε_{Sr} coordinates.

The plutonic rocks from the San Telmo pluton, Baja California, like the volcanic rocks from the same area, lie close to the primitive island arc field. Their higher ε_{Nd} values distinguish them from the other PRB rocks. The close correspondence in ε_{Nd} with oceanic arcs supports the inferred continental-to-oceanic transition from Southern California to Baja California [*Taylor and Silver,* 1978].

As mentioned previously, the $\delta^{18}O$ variations in the samples whose ε_{Nd}-ε_{Sr} coordinates lie close to the island arc field are, in general, more complicated than indicated by the $\delta^{18}O$ contours on Figure 6. These rocks, which occur at the western margin of the batholith, have been shown by *Taylor and Silver* [1978] to have interacted with meteoric water or seawater, probably near the roof of the batholith. The $\delta^{18}O$ values may be either increased or decreased from the mantle value, depending on the type of fluid involved and the temperature at which oxygen exchange took place.

The effects on ε_{Sr} and ε_{Nd} that accompany the interactions with surface waters may be demonstrated by the San Telmo samples (Baja California). Tonalite sample 800 shows no petrographic evidence for hydrothermal alteration and lies close to the OCL in Figure 6. Granophyre sample 805, on the other hand, exhibits both petrographic and $\delta^{18}O$ evidence for postcrystallization low-temperature hydrothermal alteration. It has ε_{Nd} identical to sample 800 but greatly elevated ε_{Sr}, causing it to plot to the right of the OCL. Similarly, volcanic wallrock sample DG-3 has elevated $\delta^{18}O$ (feldspar $\delta^{18}O = +12$) and also plots to the right of the OCL. These data confirm the resistance of ε_{Nd} values to changes induced by hydrothermal alteration, in contrast to ε_{Sr}. The other possible explanation of the ε_{Sr} shift is that the magmas were originally derived from subducted seafloor basalt that had suffered hydrothermal alteration prior to subduction [*DePaolo and Johnson,* 1979]. This possibility could apply also to the other samples from the PRB with positive ε_{Nd} values which show smaller but recognizable shifts to the right of the OCL. The correlation between the ε_{Sr} shift and the petrographic evidence for postcrystallization alteration at San Telmo suggest that the largest ε_{Sr} shifts are partly the result of postemplacement phenomena. The smaller effects may have been inherited from the magma sources, indicating that at least near the western margin, materials derived from subducted oceanic crust could have contributed to the batholith. By contrast, the Sierra Nevada data show much less evidence for comparable ε_{Sr} shifts.

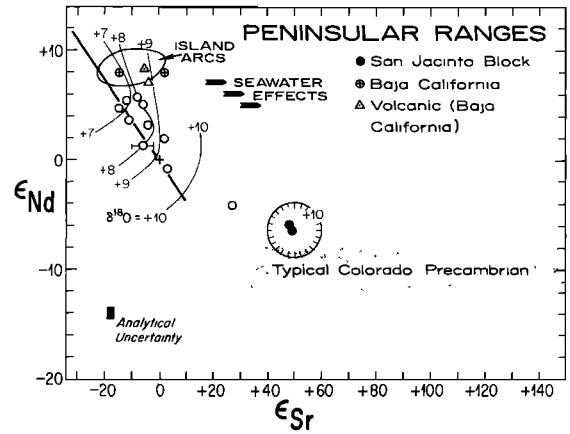

Fig. 6. Initial ε_{Nd} and ε_{Sr} values for rocks from the Peninsular Ranges batholith. Heavy diagonal line represents the Oceanic Correlation Line. Contours are for $\delta^{18}O$ values inferred from geographic variations described by *Taylor and Silver* [1978]. Stippled region is the average composition of 1.8-Æ-old basement rocks from the Colorado Front Range, shown for comparison. Both the Peninsular Ranges and the Sierra Nevada exhibit concurrently increasing ε_{Sr} and $\delta^{18}O$ and decreasing ε_{Nd}.

Taylor and Silver [1978] also noted a 'gap' in $\delta^{18}O$ values near $\delta^{18}O = +8.5$ to +9.0 but found no corresponding gap for $^{87}Sr/^{86}Sr$. The $\delta^{18}O$ gap appears in Figure 6 as the closeness of the +8 and +9 contours. For ε_{Nd}, there is an apparent dearth of ε_{Nd} values in the range 0 to −2 for both batholiths. This corresponds roughly to $\delta^{18}O = +9$, but additional data would be needed to confirm any such relationship between the two parameters.

DISCUSSION

The data presented above require that petrogenetic models for the Sierra Nevada and Peninsular Ranges batholiths account for concurrent variations of ε_{Nd}, ε_{Sr}, and $\delta^{18}O$. The simple patterns displayed in Figures 4 and 6 strongly suggest a mixing process between two relatively homogeneous end members. The geographic patterns in the isotopic data must

also be explained. Because they correlate so well with paleogeographic boundaries, there is a strong suggestion that crustal rocks are one of the components, as argued convincingly by *Kistler and Peterman* [1973]. In this section it will be shown that all of the data can be explained by mixing of mantle-derived magmas and/or volcanic rocks with sedimentary and metasedimentary rocks that were derived from Precambrian continental crust or were part of the Precambrian crystalline basement itself. Furthermore, there exists no other plausible model that is consistent with all of the data. We will proceed by first examining geologic data on the material available at the site of the batholiths which could have acted as the source of the magmas as well as other isotopic evidence for mixing and the nature of the end members. This will be followed by a discussion of possible mixing processes.

An excellent discussion of many of the geologic, geochemical and geophysical constraints on magma genesis for the SNB has been previously presented by *Kistler and Peterman* [1973], with specific reference to Sr isotopic data patterns. Their arguments will not be repeated here except where needed. In general, the new data strongly support the conclusions of Kistler and Peterman, but when considered also with the $\delta^{18}O$ data, they suggest more specific models for the generation of the batholiths.

Constraints on Possible Magma Source Materials

Current models of the paleogeography and evolution of the western margin of North America can be found in *Ernst* [1981]. With respect to the batholiths, the southern Sierra Nevada occupies a position at the approximate western edge of the pre-Phanerozoic North American continent. Paleozoic sedimentary rocks to the east of the southern SNB are miogeoclinal and are underlain by ~1.8-Æ-old metamorphic crystalline basement. The character of the prebatholithic sedimentary rocks changes to eugeoclinal (smaller proportions of carbonate and quartzite) in the central SNB, and north of about latitude 30°N there is no evidence of sialic crystalline basement [*King,* 1979]. Most of the Paleozoic geoclinal sediments were probably derived from the east, from continental crust of 1.8-Æ or 2.7-Æ age, with the eugeoclinal series having some materials derived from Paleozoic 'arc' terrains [*Dickinson,* 1981]. If the Calaveras Formation is representative, even the eugeoclinal rocks may contain mostly continentally derived clastic material. Hence, it can be concluded that the SNB terrain was occupied by continentally derived sedimentary rocks along its entire length. The sediments were floored by Precambrian crust to the south and east and presumably by oceanic crust to the north and west. The nature of the Precambrian crust in the Sierra Nevada region is unknown, but based on the exposures north of the Garlock Fault, east of the SNB, many of the Precambrian metamorphic rocks could also be characterized as broadly 'metasedimentary,' in terms of their geochemical characteristics. They consist of schist (e.g., sample PC-30a) and two-mica granite gneiss [*Lanphere et al.,* 1963]. For example, the augen gneiss and granite of the Panamint Range are highly siliceous (71% SiO_2) and rich in alkalies (4% to 5% K_2O). They are depleted in Sr (60–80 ppm), highly enriched in Rb (240–350 ppm), and have extremely high ε_{Sr} (+2000 to +5000). Oxygen isotopic data are lacking but presumably would show elevated $\delta^{18}O$. Thus the term 'metasedimentary' is used here in an artificially broad sense to include not only metamorphosed sedimentary rocks but also granitic rocks that have certain geochemical properties resembling metasediments and may, of course, be anatectic products of sedimentary rocks. Precambrian metasedimentary rocks differ isotopically from the Paleozoic sediments mainly in their extreme ε_{Sr}, because the Paleozoic sediments (e.g. FD-39) should generally have more modest ε_{Sr} values of +100 to +200. The $\delta^{18}O$ and ε_{Nd} values should be similar to the Paleozoic rocks. Precambrian granulites and other 'lower crustal' type rocks could also have been present. In addition to Phanerozoic sedimentary rocks, abundant volcanic rocks of both Paleozoic and Mesozoic age are evident in roof pendants and in the western metamorphic belt [*Bateman,* 1981].

Precambrian crystalline rocks are also found nowhere within the limits of outcrop of the Peninsular Ranges batholith but are found just across the San Andreas fault to the east (and in the Transverse Ranges west of the fault) [*Ehlig,* 1981]. The PRB also appears to have formed near the western margin of the continent in a geoclinal environment [*Gastil et al.,* 1975]. Unlike the SNB, however, it is remote from any crust older than 1.8 Æ, so it is likely that the Paleozoic and Mesozoic sediments that comprise the wallrocks in the eastern half of the batholith contain little or no detritus carried from 2.7-Æ crust. In the western part of the batholith the prebatholithic rocks are mainly volcanic [*Larsen,* 1948; *Silver et al.,* 1963; *Gastil et al.,* 1975]. The materials available in the Peninsular Ranges are therefore sediments derived from crust 1.8 Æ old or younger, volcanic rocks that are only slightly older than the batholith, and the underlying oceanic crust and mantle.

The Nd and Sr isotopic character of the prebatholithic crustal rocks can be inferred from the model shown in Figure 1, with confirmation provided by samples FD-39, FD-46, B37, PC-30a, FD-33 for the SNB, and DG-1 and 3 for the PRB. The $\delta^{18}O$ values can likewise be inferred from general considerations [cf. *Taylor,* 1980] to be high (+10 to +20), and measurements in the northern PRB bear this out [*Turi and Taylor,* 1970]. The isotopic properties of the mantle reservoirs can also be estimated. Basalts from midocean ridges and intraplate islands exhibit a large range of ε_{Nd}, mostly from +4 to +12 [*O'Nions et al.,* 1977; *DePaolo and Wasserburg,* 1979*a*] falling along the trend indicated in Figures 1, 4, and 6. Continental flood basalts, and some alkalic oceanic islands, extend the range of commonly observed values down to −2. These data indicate that a relatively large range of ε_{Nd} can be found in typical mantle reservoirs. However, Figures 1, 4, and 6 show the field of ε_{Sr} and ε_{Nd} in oceanic island arcs [*DePaolo and Johnson,* 1979]. The relatively narrow range of ε_{Nd} observed indicates that the mantle reservoirs accessed in island arcs have a well-defined ε_{Nd} compared to the total range observed in mantle-derived basalt; ε_{Sr} values are more variable because of effects related to the involvement of ocean water. The average ε_{Nd} of island arcs (+8) lies midway between the average for midocean ridges (+10) and that for intraplate islands (+6). Neither this fact nor the uniformity of values is presently understood in terms of models of mantle structure, but for purposes of this discussion the ε_{Nd} of magmas generated from the mantle or subducted oceanic crust, in oceanic island arc settings, can be considered to be narrowly defined (+8 ± 1.5). This is confirmed by the data from the San Telmo area of Baja California. No crustally derived materials were present in that area, and ε_{Nd} values for four samples fall in the narrow range of +7 to +8.2.

Recently, evidence has emerged that some parts of the subcontinental mantle may have ε_{Nd}-ε_{Sr} characteristics similar to

crustal rocks [*Menzies and Murthy*, 1979]. It appears that such 'enriched' mantle reservoirs may be restricted to subcratonic areas and can remain isolated from the oceanic-type mantle for time periods up to the age of the overlying crust [*DePaolo*, 1981*b*]. If this is the case, an additional reservoir that must be considered here is 'enriched subcontinental mantle.' Because of the hypothesized restriction of such material to subcratonic areas, its involvement as a magma source could be expected to correlate with paleogeographic features, as required by the isotopic data from the batholiths. Thus a 'mixture' of island-arc type mantle and enriched mantle could possibly generate the ε_{Nd}-ε_{Sr} trends of Figures 4 and 6 if the isotopic composition of the enriched mantle were appropriate. However, since no differences in $\delta^{18}O$ are expected for the two types of mantle, the two-mantle mixing model cannot in itself explain the data.

Materials carried down with sinking lithosphere represent another possible source for the magmas. Two categories of subducted material have been considered with regard to explanation of isotopic data in island arc settings: (a) hydrothermally altered oceanic crust and (b) deep sea or continental margin sediments. Both of these materials can be dismissed as being primarily responsible for the trends shown in Figures 4 and 6. The former material can have elevated $\delta^{18}O$ and ε_{Sr}, as compared to typical mantle values, but it has ε_{Nd} values which do not vary from those expected for mantle-derived magmas [*McCulloch et al.*, 1980; *Jacobsen and Wasserburg*, 1979]. The negative ε_{Nd} values that accompany the elevated $\delta^{18}O$ and ε_{Sr} therefore rule out melting of hydrothermally altered oceanic crust as an explanation for the overall trends displayed by the data in Figures 4 and 6 [*DePaolo*, 1980*a*]. As discussed previously, smaller-scale variations of ε_{Sr} and $\delta^{18}O$ may be related to this process. Deep-sea sediments are unlikely to be involved since there is no evidence that they are important in oceanic island arcs, where their involvement would be equally likely [*Meijer*, 1976; *DePaolo and Wasserburg*, 1977], except to the extent that they may be responsible for the shift of 1 to 2 ε_{Nd} units between island arc basalts and MORB [*Nohda and Wasserburg*, 1981]. All subducted materials appear to be poor candidates for the source of the batholiths on the basis that the data would require the largest contributions of subducted materials in the magmas emplaced farthest from the trench (eastern side of the batholiths) and essentially no contribution in the magmas emplaced closest to the trench. Furthermore, the fact that the geographic patterns in the isotopic data are related to paleogeographic boundaries rather than to the loci of magmatic intrusion also argues against the subduction models [*Kistler and Peterman*, 1973]. The lack of correspondence between the isotopic trends and the intrusive belts is prominently displayed in the Sierra Nevada, where paleogeographic boundaries diverge sharply from the intrusive trends [*Kistler and Peterman*, 1973, 1978], but is presumably masked in the Peninsular Ranges, where the paleogeographic boundaries almost exactly parallel the magmatic front [*Gastil et al.*, 1975, p. 12, and 1981].

Oxygen and Strontium Isotopic Constraints

The Sr and O isotopic data are plotted in Figure 7. Also shown is the main trend defined by the Peninsular Ranges data of *Taylor and Silver* [1978]. The shaded field at the lower left represents the composition of the mantle, mantle-derived magmas, and mantle-derived volcanic rocks of essentially zero age. In the upper right is a shaded box representing the isotopic composition of Paleozoic sedimentary rocks. The $\delta^{18}O$ range shown for the sedimentary rocks represents typical values; a larger range is possible. Simple mixtures of mantle-derived materials and sedimentary rocks describe a curved zone connecting the end members that closely follows the main PRB trend. The curvature is a result of the lower value of Sr/O assumed for the sedimentary rocks as compared to the mantle-derived end members. Mixtures of these two components would also be perfectly consistent with the ε_{Nd}-ε_{Sr} trends (Figures 4 and 6), as noted above.

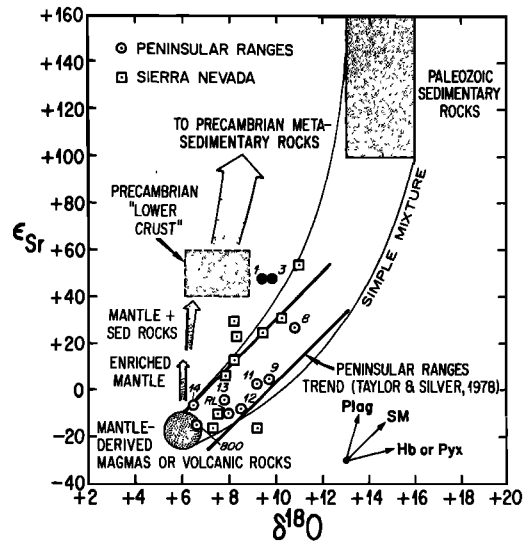

Fig. 7. ε_{Sr}-$\delta^{18}O$ systematics of mixtures and plutonic rock samples from the Peninsular Ranges and the Sierra Nevada. Filled symbols represent San Jacinto-Santa Rosa Mountain block samples. Simple mixtures of Paleozoic sedimentary rocks and mantle-derived mafic magmas closely follow the Peninsular Ranges trend and would also be consistent with the ε_{Nd}-ε_{Sr} data in Figures 4 and 6. Mixtures involving other end members would generally produce trends of steeper slope. Although these are not likely to be the primary mixing processes, such end members could explain the deviations of some rocks from the Peninsular Ranges trend. Arrows at lower right show the effects of crystal fractionation concurrent with wallrock assimilation on the mixing curves. Relative to the simple mixing curve (SM), plagioclase fractionation would cause steeper trends, while hornblende or pyroxene fractionation would produce less steep mixing lines.

An alternative process for mixing crustal and mantle components would be that proposed by *Kistler and Peterman* [1973], which is that the zone of melting intersects both the mantle and lower crust. In its simplest form this would be equivalent to physically mixing mantle and crust and then forming a magma by a partial melt of the mixture. In order to account for the elevated $\delta^{18}O$ it would be required that the crustal material have a sedimentary protolith. The mixing trend for this process is indicated on Figure 7. The steep slope is due to the low Sr/O ratio of the mantle in comparison with that of the crustal rocks. This mixing model does not appear to be consistent with the O-Sr data; it is, however, consistent with the ε_{Nd}-ε_{Sr} data.

Mixtures involving Precambrian rocks would also produce steeply sloping trends on Figure 7 as a consequence of their higher values of ε_{Sr} compared to those of $\delta^{18}O$ [*Taylor and Silver*, 1978]. Precambrian metasedimentary rocks (e.g., sample PC-30a) would tend to have extreme ε_{Sr} values. Rocks similar to the Colorado granulites (Figure 1) would tend to have lower ε_{Sr} values but also would be expected to have relatively low $\delta^{18}O$. These 'lower crustal' type rocks would tend to plot

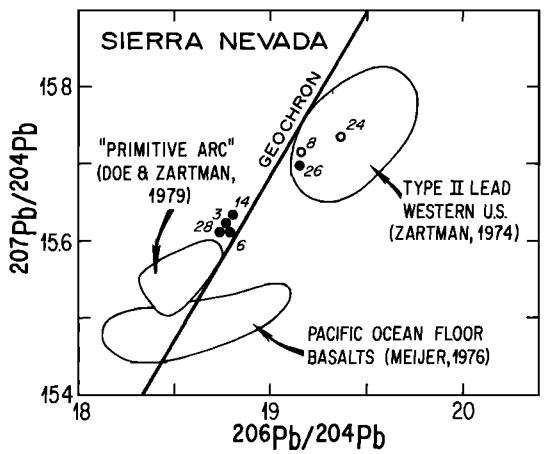

Fig. 8. Sierra Nevada Pb isotopic data from *Doe and Delevaux* [1973], showing their relationship with primitive arc Pb and the Type II Pb as defined by *Zartman* [1974]. Field of ocean floor basalts is shown for comparison. The Sierra Nevada Pb data are consistent with mixing of island arc and continental margin components as represented by the Type II Pb.

near the field indicated on Figure 7. Hence where Precambrian rocks are involved, the result would be to move the ϵ_{Sr} of the resulting granitic rock off the PRB trend toward higher ϵ_{Sr} or lower $\delta^{18}O$ values. This effect is observed in the samples from the San Jacinto-Santa Rosa block (1 and 3) and in many of the SNB samples. All of the samples that plot above the PRB trend are found in regions where Precambrian (early Proterozoic) rocks are thought to have existed prior to the formation of the batholiths. These include most of the analyzed SNB samples. Thus the $\delta^{18}O$-ϵ_{Sr} data support a model whereby the parent material for the granitic magmas is a mixture of mantle-derived materials and either or both of (1) Paleozoic sedimentary and metasedimentary rocks and (2) Precambrian craton. Where Precambrian craton is not present the PRB-type trend is obtained. Where Precambrian crust is present the data deviate from the PRB trend in the expected fashion. These generalizations are supported by extensive O and Sr isotopic data from the SNB [*Masi et al.*, 1981]. In particular, only the data from the northern SNB closely follow the PRB trend. This is as expected because the region was sufficiently far removed from the edge of the craton. Data from the southern and central SNB scatter about the PRB trend in a manner similar to that shown in Figure 7.

The deviations from the PRB trend could also be due to tapping of enriched mantle sources, which would be expected to be present only beneath the Precambrian crust. Direct mixing of mantle and crust as proposed by *Kistler and Peterman* [1973] would also produce the same effect and might be expected to be more important where crystalline crust exists because the base of the crust is more likely to be deep enough to be at the zone of melting. Nevertheless, for both of these alternatives, a sedimentary component is necessary to produce elevated $\delta^{18}O$ values.

Pb Isotopes

Lead isotope analyses on SNB rocks taken from the literature [*Doe and Delevaux*, 1973] are shown in Figure 8. Five of the samples shown (3, 5, 14, 26, 28) [*Kistler and Peterman*, 1973] are the identical rocks analyzed for Nd isotopes in this study. The data form two clusters, but all of the points fall within or between the fields of primitive island arc lead [*Doe and Zartman*, 1979] and 'Type II' lead from the western U.S. as defined by *Zartman* [1974]. Type II lead is that characteristic of ore deposits found in the Paleozoic geoclinal area of the northern and central Great Basin. The lead isotopes in this region are notable for their radiogenic character (high $^{207}Pb/^{204}Pb$ and high $^{206}Pb/^{204}Pb$) and relative uniformity. These properties are just those expected for sedimentary rocks eroded from old crust that have never been metamorphosed to the high grades typical of the base of the continental crust in orogenic zones. The homogeneity is thought to be a result of the averaging over diverse source areas that takes place during sedimentary rock formation at continental margins. There are numerous possible explanations for the Pb data, but because they fall in a zone between arc lead and Type II lead, they must be considered to be at least qualitatively consistent with the model of mixing of a mantle-derived component with a sedimentary component derived from old crust. The amounts of each component that would be inferred from the lead isotope data do not correspond well with the ϵ_{Nd} and ϵ_{Sr} data for all samples (e.g., 14 and 26). This is not unexpected because of the probable presence of retarded leads in the Precambrian cratonic rocks, which could plot off Figure 8 to the lower left. However, samples 3, 5, and 28 would appear to have small contributions of sedimentary lead consistent with the positive ϵ_{Nd} values measured (Table 4). Samples 8 and 24 would have larger sedimentary contributions consistent with their high ϵ_{Sr} values (+26 and +53) [*Kistler and Peterman*, 1973]. It is notable, however, that the steeply sloping trend of the SNB data, corresponding to a Pb-Pb age of 2.9 Æ [*Doe and Delevaux*, 1973], even when interpreted as a mixing line, as proposed here, is not simply explainable in terms of models of crust-mantle evolution. Open-system behavior of the mantle of the type discussed by *Dupré and Allegre* [1980], or some other mechanism, seems necessary to produce this. The lead isotope data of *Chen and Tilton* [1978] differ somewhat from those of *Doe and Delevaux* [1973], but they also suggest the presence of a 1.8-Æ-old crustal component in the SNB.

Mixing Processes

The precise nature of the mixing processes responsible for generating the isotopic trends is problematical. Consideration of the data discussed above leads to the conclusion that the end members of the mixing process are (1) 'mantle end-member'—magmas rising from the mantle or subducted oceanic crust, or mantle-derived volcanic rocks that are only slightly older than the batholith rocks; (2) 'crustal end-member'—Paleozoic and Mesozoic sedimentary rocks derived from early Proterozoic crust with admixtures of early Proterozoic cratonic rocks, or melts derived from these sources.

In terms of the relationship between the mixing process and the petrogenesis of the batholith the possibilities can be separated into three overlapping categories: (1) Mixing of source materials prior to the melting events that produced the granitic magmas, e.g. interlaying of mantle-derived volcanic rocks with sedimentary rocks; (2) Contamination of mantle-derived magmas by crustal materials as the magmas rise through the crust; and (3) Mixing of magmas derived from the end-member sources.

Alternative (1) would require the magma source to be entirely within the crust. Since it is clear that in island arcs magmas are derived from mantle depths, this alternative is unlikely to be the sole mixing process, but could be important. Process (2), contamination of mantle-derived magmas, must

be expected to occur to some degree. The primary questions as regards contamination are whether it can occur to the extent necessary to generate the large isotopic shifts observed and whether the process is compatible with the overall petrologic characteristics of the rocks. These questions are discussed in detail below. Process (3) is also likely since crustal materials generally melt at lower temperatures than mantle peridotite at the same pressure, so that a geotherm could intersect a 'crustal solidus' at the base of the crust and the mantle solidus at much greater depths. Melts rising from the mantle could then mix with the crustally derived melts.

Isotopic trends generated by mixing processes (1) and (3) can be approximated by simple mixing equations [*Vollmer*, 1976; *Langmuir et al.*, 1978; *DePaolo and Wasserburg*, 1979]. These have been diagrammed in Figures 1 and 7 and can be considered to be compatible with the data. Magma contamination, on the other hand is somewhat more complex. *Bowen* [1928] discussed at length the effects of assimilation on silicate liquids and concluded that the process could be important, considering that the heat necessary for heating and melting the wallrocks could be supplied by the heat of fusion of crystallizing minerals. Spme isotopic effects of assimilation accompanied by fractional crystallization have been discussed by *Taylor* [1980]. The shift of isotopic composition caused by assimilation for a simple model of concurrent assimilation and fractional crystallization (AFC) is given by [*DePaolo*, 1981*b*]:

$$\frac{\Delta\varepsilon_m}{\varepsilon_a - \varepsilon_m^0} = \frac{(1 - F^{-z})r/(r-1)}{(1 - F^{-z})r/(r-1) + F^{-z}zC_m^0/C_a} \tag{10}$$

where $\Delta\varepsilon_m$ is the shift of ε_{Nd}, ε_{Sr}, or $\delta^{18}O$; ε_a, ε_m^0 are isotopic values for assimilated material and original magma, respectively; $r = \dot{M}_a/\dot{M}_c$ is the ratio of mass rate of assimilation to mass rate of crystal fractionation; $z = (r + D - 1)/(r - 1)$, where D is the bulk crystal/liquid distribution coefficient for the element in the fractionating phases; F is the mass of magma remaining as a fraction of the mass of the original magma; and C_a, C_m^0 are the concentrations of the element in assimilated material and the original magma, respectively.

For plots of two isotopic parameters (Figures 1, 4, 6, 7) the mixing curves for the AFC model depend upon the values of D for the two elements involved. If the D values are equal, the mixing trend for AFC will follow the simple mixture curves. If the D values are greatly different, the AFC trend will diverge from the simple mixture trend. This effect is illustrated in Figure 7 for the Sr and O isotopic parameters. The value of D_O is approximately 1 for all likely fractionating species. The value of D_{Sr}, however, is about 2 for plagioclase and ≤ 0.1 for clinopyroxene and hornblende. Hence, if plagioclase alone is fractionating, ε_{Sr} will shift relatively more quickly than $\delta^{18}O$ because the liquid is being depleted in Sr. The opposite is true for pyroxene or hornblende fractionation, as shown in an exaggerated manner in Figure 7.

Another aspect of AFC which is different from simple mixing is a built-in limit to the shift ($\Delta\varepsilon_m$) that is possible as a result of contamination when D values are less than unity. This limit is a function of the heat balance between crystallization and assimilation expressed through the parameter r. When $(r + D) < 1$, the largest possible shift is given by ($f \to 0$):

$$\frac{\Delta\varepsilon_m(\max)}{\varepsilon_a - \varepsilon_m^0} = \left[1 - \frac{r + D - 1}{r}(C_m^0/C_a)\right]^{-1} \tag{11}$$

There are several reasons why assimilation is a plausible explanation of the data. These will be discussed here, using the above relationships as guides. For Nd, the total range of ε_{Nd} values observed (+7 to −8 for the SNB and +8 to −6 for the PRB) is about 60%–80% of the total difference in ε_{Nd} between the end-member values of +8 for the mantle component and −10 to −16 for the crustal components. The minimum value of r necessary to generate the most negative ε_{Nd} can be estimated from (7), although since assimilation is not likely to continue at the same rate up to the point where the magma is completely solid, r values substantially larger than this minimum would in fact be required. Typical values for the other parameters in (7) are $C_{Nd,m}^0 = 12$ ppm (island arc tholeiitic basalt), $C_{Nd,a} = 35$ (typical shale), and $D_{Nd} = 0.1$ (clinopyroxene/liquid or plagioclase/liquid) [*Arth and Hanson*, 1975]. Setting the right hand side of (7) equal to 0.6 or 0.8 gives $r =$ 0.3 to 0.5. In order to evaluate whether r values of this magnitude or larger are reasonable, an estimate of the temperatures of the country rock is needed [*Taylor*, 1980]. *Schwarz* [1969], in a study of regional metamorphic rocks of the northern peninsular ranges, concluded that regional temperatures up to 750°C were reached at depths of 7 to 15 km (2.5- to 4-kbar pressure) at the time of intrusion of the batholith. He also noted evidence of increasing temperature gradients to the east. If the temperature gradient increased eastward, then clearly temperatures of 1000°C or more, close to magmatic temperatures, are probable at crustal depths (<30 km) in the eastern part of the batholith, where the isotopic shifts are largest. For this situation the heat necessary to melt 1 g of wallrock already at its fusion temperature can be supplied by crystallization of less than 1 g of magma at 1200°C. Thus r values of 0.3 to 0.5 or greater would indeed be possible. Because the temperature differential between magma and wallrock would be minimal, heat loss by conduction would be small, and r values of 1 or greater might be possible. For $r = 1$, (7) does not apply because the mass of magma remains constant. For this case and for D small the following approximation holds [*DePaolo*, 1981*b*]:

$$\frac{\Delta\varepsilon_m}{\varepsilon_a - \varepsilon_m^0} \approx (1 + C_m^0 M_m/C_a M_a)^{-1} \tag{12}$$

where M_m is the mass of the magma, and $M_a/M_m = 0.5$ to 1 would be required in order to generate the maximum effects observed. This amount of assimilation is not implausible and would also be approximately that required by the O isotope data. On the other hand, to shift ε_{Nd} by 5 units, M_a/M_m need only be 0.1 or less, i.e., the magma need assimilate only 10% of its original mass.

For strontium, typical parameters would be $C_{Sr,m}^\circ \approx 250$ ppm, $C_{Sr,a} = 120$ ppm, and assuming that plagioclase is not the primary fractionating phase, $D_{Sr} = 0.2$. Using the r values deduced for Nd gives for the equivalent maximum ε_{Sr} shift:

$$\frac{\Delta\varepsilon_{Sr,m}}{\varepsilon_{Sr,a} - \varepsilon_{Sr,m}^0} = 0.22 \text{ to } 0.44 \tag{13}$$

The most extreme shifts in $\varepsilon_{Sr,m}$ are therefore expected to be substantially less than the total range spanned by mantle and crustal reservoirs as a result of the assumed low Sr concentration of the contaminant. This is consistent with the observations, since the total range exhibited by the batholith rocks is about 70 εU compared to the total range in mantle and crustal materials of 150 to about 450 εU. The assimilation model provides a possible explanation of why ε_{Sr} values as high as the

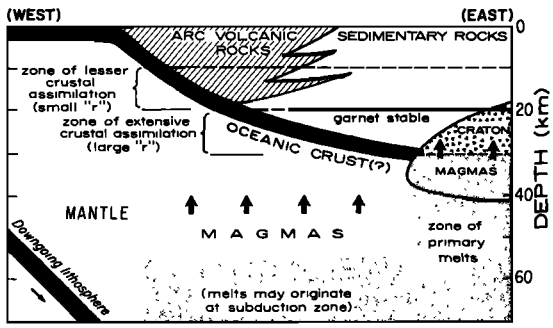

Fig. 9. Schematic representation of inferred prebatholithic structural elements and Mesozoic magma sources along an arbitrary transverse section through the batholiths. Primary (basaltic) melts originate at mantle depths as a consequence of subduction. Advection of magmas and hot (or partially molten) mantle to shallower depths may eventually raise the temperature of the base of the craton above its solidus also. All rising magmas will interact extensively with the deepest, hottest parts of the crust by assimilation with concurrent crystallization. Assimilation is less important at shallower depths because the country rocks are relatively cool. Plutons emplaced in the upper crust represent petrologically complex mixtures of mantle and crustal components and are underlain by intensely metamorphosed remains of the prebatholithic crust with admixed cumulates composed partly of mantle-derived materials. The isotopic composition of the plutons reaching the upper crust reflects the nature of the crustal column they traversed. Trace element patterns in the plutons will be affected by the liquidus mineralogy of the magmas, and by the mineral assemblages in the crust if crustal melting is taking place. The stability of garnet, represented crudely as depth dependent on the figure, will be particularly important in determining rare-earth element patterns. The parameter r refers to the relative importance of assimilation as opposed to fractional crystallization in the evolution of the magmas traversing the crust (equation 10).

country rock values are not observed in the batholith [*Kistler and Peterman,* 1973]. Conversely, the observation that any plutonic rock has isotopic values greatly different from its immediate wallrocks does not in any way prove that the magma has not assimilated a substantial amount of that wallrock or some other rock type deeper in the crust.

These calculations are intended as support for the abundant qualitative and suggestive evidence for the role of assimilation. For the Peninsular Ranges, and presumably also for the Sierra Nevada, the eastward increase in the amount of assimilation is consistent with increasing prebatholithic crustal thickness [*Gromet,* 1979] and increasing temperature gradients in the same direction [*Schwarz,* 1969]. Furthermore, the western parts of the prebatholithic terrane probably contained a sizable proportion of volcanic rocks with mantlelike isotopic compositions (e.g., SNB-FD33, DG-1, 3), so that even an equal amount of assimilation on the west side could result in smaller isotopic shifts. The more differentiated character of the eastern batholithic rocks [*Gromet,* 1979] is broadly consistent with the necessary relationship between assimilation and crystallization. The same processes could account for the observation [*Early and Silver,* 1973; *Taylor and Silver,* 1978] that gabbro bodies in the PRB tend to have lower ε_{Sr} and $\delta^{18}O$ than nearby tonalite and granodiorite plutons. Also, the overall predominance of relatively silicic rock types over gabbro suggests that assimilation has been important [*Larsen,* 1948], since assimilation of any silica-rich rock tends to increase the proportion of late differentiates [*Bowen,* 1928].

It is probable that the bulk of assimilation occurs in relatively basic magmas at deep crustal levels where the wallrock is hot, where crystallizing minerals have the highest heats of fusion (olivine, pyroxenes, calcic plagioclase) and the magma is sufficiently dense that it will tend to rise very slowly through the crust, and stoped blocks may sink slowly or even float. Indeed, gabbro bodies in the PRB do exhibit substantial shifts in isotopic ratios [*Taylor and Silver,* 1978]. Assimilation will tend to diminish as the magma rises into cooler country rocks at shallower levels and as differentiation proceeds, especially if the magma becomes a crystal-rich mush where high viscosity [*Shaw,* 1965] might provide a barrier to the incorporation of substantial amounts of foreign material. One might, therefore, expect noticeable isotopic differences between gabbro and tonalite but insignificant or minor differences between tonalite, granodiorite, and granite in a given area.

Whether the assimilation-fractional crystallization model can adequately account for the major and trace element compositions of the batholith rocks is difficult to test. In order to properly model the process one needs to know the liquidus mineral phases and their proportions in a magma that is evolving in composition (including H_2O content) at the same time it is moving through pressure and temperature space. The problem is further complicated by uncertainties as to whether plagioclase, which has a density similar to that of basic magma, will fractionate as readily as ferromagnesian phases, which have much higher densities. In addition, there is the problem of reliable trace element partition coefficients, considering the pressure-temperature-composition changes, and the questionable role of minor phases. However, calculations show that the gross characteristics of the trace and major elements can be modeled (W. C. Luth and D. J. DePaolo, unpublished data, 1980). A particular problem cited by *Kistler and Peterman* [1973] is that some of the Sierra Nevada rocks having Sr isotopic compositions that might suggest crustal contamination also have elevated Sr concentrations, just the opposite of what would be expected for a simple mixture, because the contaminant should have a low Sr concentration and high $^{87}Sr/^{86}Sr$. For simple mixing there should be a correlation between high $^{87}Sr/^{86}Sr$ and low Sr concentration, which is not observed. For the AFC process this correlation would not necessarily be expected. For example, if plagioclase fractionation is minor during assimilation, the AFC process will tend to enrich later differentiates in Sr, even though the assimilated material may have a lower Sr concentration than the magma [cf. *Kistler and Peterman,* 1973; *Gromet,* 1979, for discussions of Sr abundances]. In conjunction with this it is noteworthy that the experimental studies of *Yoder and Tilley* [1962] demonstrate that high water pressure, as might be expected in wet island-arc-type magmas at lower crustal depths, suppresses plagioclase crystallization in favor of pyroxenes in basaltic magmas [cf. *DePaolo,* 1981*b*]. A schematic cross section is given in Figure 9 that summarizes the inferred crustal structure, magma source regions, and depth zones where crustal assimilation occurs.

Fraction of New Crust Added to the Continent

In the context of the petrogenetic mixing processes discussed, the isotopic data can be used to estimate the fraction of the batholith terranes that represent material newly added to the crust from the mantle. At the present level of exposure the fraction of newly added mantle-derived material would appear to decrease from west to east across each batholith. To obtain rough estimates of the average isotopic composition of each batholith, the abundant Sr isotopic data can be used [*Kistler and Peterman,* 1973, 1978; *Taylor and Silver,* 1978].

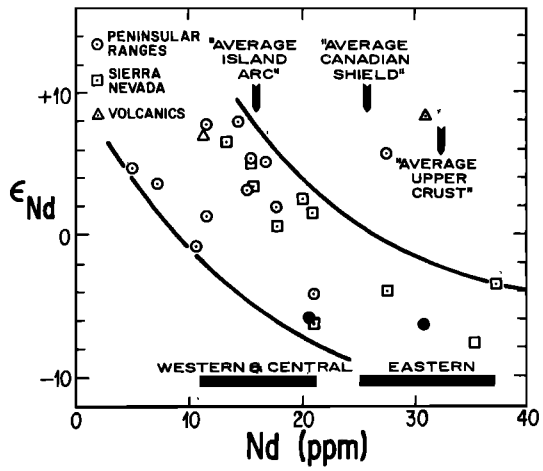

Fig. 10. Nd concentrations and ϵ_{Nd} values showing a rough correlation. Typical metasedimentary wallrock samples would have $\epsilon_{Nd} = -11$ to -16 and Nd = 25–50 ppm (Table 2). Heavy solid bars refer to typical ranges of Nd concentration measured in plutonic rocks of the Peninsular Ranges by *Gromet* [1979]. Rocks with $\epsilon_{Nd} > 0$ have Nd mostly less than 20 ppm and an average concentration similar to average island arcs [*Taylor*, 1977]. Rocks with $\epsilon_{Nd} < 0$ have Nd > 20 ppm, similar to average Canadian shield [*Shaw et al.*, 1976] or average upper crust [*Taylor*, 1977]. Filled symbols are samples from the San Jacinto-Santa Rosa Mountain block.

These are summarized in Figure 5. Using the correlations of Figures 4, 6, and 7, and the geographic contouring, average values of $\epsilon_{Sr} \approx +10$, $\epsilon_{Nd} \approx -1$ and $\delta^{18}O \approx +9$ are computed. The averages are approximately the same for both batholiths. The O and Nd data give the most straightforward indication of the proportions of mantle and crustal components because their concentrations in both end members can be estimated with some confidence. If the mantle component has $\delta^{18}O = +6$ and the crustal component $\delta^{18}O = +15$, it is calculated that two thirds of the batholith is mantle component and one third is crustal component. For Nd, if the crustal component ($\epsilon_{Nd} \approx -12$) is assumed to have a Nd concentration 2 to 3 times greater than the mantle component, a crustal contribution of 20% to 30% is calculated, in reasonable agreement with the estimate from O isotopes. These estimates are not precise since they depend upon the eastern and western boundaries specified for the batholiths. The SNB, for instance, may extend for some distance west beneath the Great Valley in central California. Cretaceous intrusives also are found inland for large distances over the entire length of both batholiths and could represent eastward extensions of the batholiths.

The question of the average age of the crust in the region of the batholiths is somewhat more difficult to address because it involves assumptions about the makeup of the lower crust. The present thickness of granitic rocks is probably no more than 10–15 km, based on heat flow [*Lachenbruch*, 1968]. Considering that mafic differentiates may comprise some fraction of the lower crust, it is likely that the igneous rocks of the batholith represent about 50% of the total crustal section. A plausible estimate of the rock types of the prebatholithic terrane might be a 1/3–2/3 mix of mantle-derived volcanic rocks and crustally derived sediments (and some crystalline basement). Thus, overall it appears that about half the volume of material within the geographic confines of the batholiths, and above the Moho, probably represents juvenile crust, with a crust formation age of about 0.1 Æ. The remaining half appears to have an average age close to that of the adjoining craton (1.8 Æ).

In the western U.S., extensive geochronological studies allow the ages of the old cratonic and the young magmatic arc components to be specified with some certainty. The average age of the plutonic province gives little additional information nad has no significance in terms of any geologic event. It is, however, of interest to determine to what extent the Sm-Nd isotopic data give information about the average crust-formation age of the province.

Taking the average ϵ_{Nd} of -1 and an $^{147}Sm/^{144}Nd$ of 0.125 (Figure 9), a T_{DM} model age of 0.8 Æ is calculated. Thus, the batholith average Sm-Nd isotopic characteristics give a surprisingly reasonable estimate of the crust formation age, considering the Sm/Nd fractionation that occurs during magma evolution, the mixing processes and the presence of the remaining country rocks.

Mantle Evolution and the Chemical Composition of Continental Crust

In Figure 10 is shown Nd concentration data (Tables 2 and 3) and their relations to ϵ_{Nd} in the batholiths. The Nd concentration can be taken to be representative of the light REE. As ϵ_{Nd} decreases there is a marked tendency toward higher Nd abundances: The batholith rocks with ϵ_{Nd} values close to the mantle values exhibit Nd concentrations similar to island arcs. These concentrations are about 40% lower than typical values for Archean crust as represented by Canadian Shield composites [*Shaw et al.*, 1976]. On the other hand, those rocks with negative ϵ_{Nd} values and containing large contributions from older continental crust are more enriched in Nd and show no depletion relative to the Canadian Shield average. The data from this study are confirmed by the more extensive measurements of REE abundances carried out by *Gromet* [1979] on the Peninsular Ranges batholith.

Figure 11 shows the relationship between ϵ_{Nd} and $^{147}Sm/$

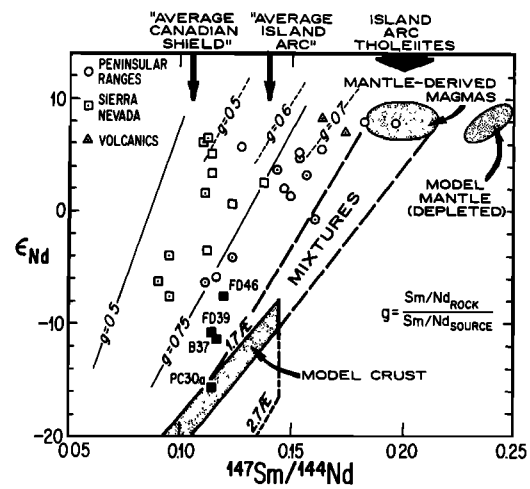

Fig. 11. ϵ_{Nd} versus $^{147}Sm/^{144}Nd$, showing fields of crust and depleted mantle for a continuous depletion model for the upper mantle [*DePaolo*, 1980*a*]. Simple mixtures of island arc tholeiites (basalts) and Precambrian crust do not fall near the plutonic data. This indicates that igneous differentiation, which decreases $^{147}Sm/^{144}Nd$, took place after mixing or concurrently with mixing processes.

Values of g shown with solid lines are relative to the 'mixtures;' those shown with dashed lines are relative to the mantle. The average $^{147}Sm/^{144}Nd$ ratios of samples with $\epsilon_{Nd} > 0$ are close to island arc values, while samples with $\epsilon_{Nd} < 0$ have lower $^{147}Sm/^{144}Nd$ ratios.

^{144}Nd; the latter being an indication of the degree of fractionation within the rare-earth group of elements. In a manner analogous to the Nd concentration data, the average $^{147}Sm/^{144}Nd$ value is close to island arc values for the samples with positive ε_{Nd}. The relationship between the rock ratios and those of the deduced source materials is indicated by the solid lines contouring the fractionation factor g. The dashed contours of g represent the fractionation factor relative to the model depleted mantle. Note that the fractionation factors for almost all of the rocks are within the range 0.5 to 0.7 relative to the ultimate sources, which are represented by the mantle and crustal fields. The average Sm/Nd fractionation factor of about 0.6 indicated by the data confirms that the value assumed in recent mathematical modeling of crust-mantle evolution is appropriate [*DePaolo,* 1980*a; Jacobsen and Wasserburg,* 1979].

As noted previously [*DePaolo,* 1980*b*], the upper limit ε_{Nd} value of the batholiths indicates that the mantle source is depleted in incompatible elements, including light REE, relative to the abundances expected in the mantle for an earth with chondritic REE abundances. Figures 10 and 11 show relationships between chemical features of the rocks and their Nd isotopic compositions. The rocks with ε_{Nd} values approaching the upper limit of about +8 have relatively low Nd (light REE) and relatively high $^{147}Sm/^{144}Nd$, features expected in rocks derived from light-REE-depleted mantle reservoirs. The comparisons with the Canadian Shield composites as possible representatives of Archean crust are only tentative, since at present no sound estimate for the composition of average Archean crust exists. Nevertheless, the data do illuminate possible problems in determining whether the composition of the crust has changed through time. If the Mesozoic rocks with $\varepsilon_{Nd} > 0$ are compared to the Canadian Shield average, there is a suggestion of a change toward lower light-REE concentrations and higher $^{147}Sm/^{144}Nd$ toward the present. This shift would be consistent with the idea that the upper mantle today is more depleted than it was in the early Archean. This, in turn, would mean that the volume of continental crust has grown substantially since the time just prior to when most of the Canadian Shield rocks were first derived from the mantle—about 2.7 Æ ago [*McCulloch and Wasserburg,* 1978]. Furthermore, since the data would suggest that the materials being added to the continents in relatively recent times have a different chemical makeup from the older parts of the crust, there is an implication that the crust has been changing in composition through time toward less light-REE enrichment, tracking the light-REE depletion of the upper mantle. On the other hand, if the Mesozoic rocks with $\varepsilon_{Nd} < 0$ are compared to the Canadian Shield rocks, no such trend would be evident. These data demonstrate that comparisons of crustal composition at different points in time cannot be done without attention to the petrogenesis of the rocks as revealed by isotopic data. In this case, the light-REE contents of many of the batholith rocks have been augmented by assimilation of old, light-REE-enriched crustal material and consequently are not representative of what is being added to the crust but rather are a reflection of what is already in the crust.

In a study of shales of different ages, *Nance and Taylor* [1976, 1977] found that REE abundances increase in younger formations. They also concluded that the crust may have changed in composition since the Archean—toward greater enrichments of REE toward the present, just the opposite of what is suggested by Figures 10 and 11. The Sierra Nevada provides a case-in-point, showing that such inferences from data on sedimentary rocks may be suspect. Sediments shed from the Sierra Nevada have received a biased sampling of the batholith. The regions that have been eroded most deeply and stand topographically highest today are just those regions that have the lowest ε_{Nd} values (and highest ε_{Sr}) [*Kistler and Peterman,* 1973]. Consequently, considering the relationship between REE concentration and ε_{Nd} (Figure 9), the REE concentrations in those sediments would most likely be a poor representation of the 'new' crust formed during the Mesozoic. The REE depletion evident in the batholith rocks with positive ε_{Nd} would not be reflected very well by the sedimentary rocks ultimately derived from the Sierra Nevada by erosion. The interpretation of the shale data of *Nance and Taylor* [1976, 1977] is a more difficult problem because the sediments they studied were formed in a variety of different tectonic environments. Nevertheless, the situation encountered in the Sierra Nevada may not be uncommon in the geologic record. Clearly, care must be exercised in relating sedimentary rock trace element data to the trace element content of the crust.

Concerning the petrologic models for the batholiths, the relationships shown on Figures 10 and 11 are compatible with any of the mixing models which are considered to be viable. The data demonstrate, however, that a simple mixture of mantle-derived materials and old crust will not in general yield products that will plot where most of the samples do. The rocks tend to have low Sm/Nd compared to any simple mixtures. This supports petrogenetic models where differentiation postdates, or is contemporaneous with, mixing. Both mixing of source materials, followed by Sm/Nd fractionation during melting, and assimilation accompanied by fractional crystallization are consistent with the data. The SNB samples tend to be more fractionated (lower $^{147}Sm/^{144}Nd$) than the PRB samples. This suggests a basic difference between the petrogenesis of the SNB samples studied here and the PRB rocks. This difference is manifested in the overall REE patterns. For the PRB, *Gromet* [1979] has shown that amphibole did not play a major role, either as a fractionating phase or a residual phase, in the generation of the batholith. The REE data for the SNB, although limited (G. N. Hanson, unpublished data, 1977), suggest a greater role for amphibole and could explain the lower $^{147}Sm/^{144}Nd$ ratios of the SNB. Whether this difference is a consistent feature that distinguishes the two batholiths is not determinable on the basis of existing data. The probable existence of Paleozoic volcanic belts in the Sierra Nevada region [*Dickinson,* 1981], and a lack of counterparts in the Peninsular Ranges, could help explain the difference. If a thick section of older, hydrated metavolcanic rocks occupied parts of the prebatholithic Sierra Nevada terrain, partial melting of that material (amphibolite) could have caused the amphibole signature in the REE patterns of some of the SNB plutonic rocks.

CONCLUSIONS

The regular and systematic variations of ε_{Nd}, ε_{Sr}, and $\delta^{18}O$ in the batholiths of the Sierra Nevada and Peninsular Ranges strongly suggest a simple, qualitative, nonmechanistic model for their formation as mixtures of a mantle-derived island-arc-type component and crustal components with ages equal to that of nearby cratonic areas [*DePaolo,* 1980*b*]. The relatively coherent covariation of ε_{Nd} and ε_{Sr} is facilitated by the homogeneity of the end members—a result of homogenization during sedimentation (both Precambrian and Paleozoic) and the

limited variability of crustal $^{147}Sm/^{144}Nd$ in the case of the crustal end-member and a result of, as yet poorly understood, dynamical processes in the upper mantle in the case of the mantle end-member. These intensive isotopic parameters see through the inevitably multifaceted petrological and chemical processes associated with the geologic evolution of subcontinental scale provinces. They provide evidence that an island-arc-type magmatic province superimposed upon a preexisting continental margin results in magmatic products that are blends of mantle-derived and crustally derived materials, as would be predicted a priori.

As noted by *Taylor and Silver* [1978] the heat energy needed to drive this mixing process is most likely supplied by magmas rising from the mantle. The petrologic nature of the mixing process may be complex, but plausible mechanisms include assimilation of crustal rocks accompanied by fractional crystallization, in accord with the suggestions of *Larsen* [1948]. Trace element data [*Gromet,* 1979] may require, in addition, differing depths of magma genesis, which could be related to the inferred relationship of the magmatism to subduction of oceanic lithosphere.

The mantle source for the batholiths is characterized by incompatible element depletion, as evidenced by $\varepsilon_{Nd} \approx +8$ and by the abundance data for light rare-earth elements. These data clearly indicate that continental crust is presently being formed by tapping the same limited volume of the mantle that has acted as a source for continental crust in the past and has become depleted in incompatible elements through earth history. The mantle source of continental crust (island arcs) appears to be surprisingly homogenous with respect to Nd isotopic composition, more so than mid ocean ridge and intraplate oceanic island basalts. This could be a result of contributions to the other basalts from deeper, undepleted mantle reservoirs [*DePaolo and Wasserburg,* 1979*b*]. In contrast, orogenic zones may access only shallow mantle reservoirs. This characteristic suggests that initial Nd isotopic compositions of continental crustal rocks may provide a clear indication of mantle evolution through time. It also suggests that the general lack of preserved Precambrian oceanic crust provides no impediment to studies of the Precambrian mantle, as has been heretofore supposed. However, as with the Sierra Nevada and Peninsular Ranges, in all cases the highest value of ε_{Nd} observed will be of most significance. Consequently, precise age determinations, using multiple methods, coupled with precise Nd isotopic measurements, will be necessary in order to estimate the mantle ε_{Nd} values from studies of older rock suites. Whole-rock Sm-Nd isochrons alone will be generally insufficient, since small variations in initial ε_{Nd} may result in only small scatter of points about a quasi-isochron which represents the approximate age of the rock suite.

The mixing model, combined with some assumptions about the thickness of the batholiths and the composition of the prebatholithic rocks, results in an estimate of about 50% for the fraction of material now found within the geographic boundaries of the batholiths that represent juvenile crust derived from the mantle during the Mesozoic. The estimated average 'crust-formation age' is close to 1 AE, which is far older than the geologic age. If the regions studied are typical, then it is likely that much of the western margin of North America is actually older than previously thought [cf. *Faure,* 1977, p. 120] and hence that the average age of the continent is also considerably older. This general statement is supported by the Sm-Nd isotopic data of *McCulloch and Wasserburg* [1978] from the Canadian Shield and, for example, by their analysis of one sample of Birch Creek Schist from Alaska, which gives a T_{DM} crust-formation age of 2.5 AE. Consequently, the crustal growth curves suggested by *Hurley and Rand* [1969] should be reevaluated when more Sm-Nd data become available.

The evidence presented here for assimilation of crustal material in continental margin magmatic arcs must be considered in any models for the petrologic evolution of calc-alkaline batholiths, and of continental magmatic arcs in general. Mineralogical and chemical characteristics of these arcs could be in large part due to assimilation effects. The major element, and even the trace element, effects of assimilation may be subtle, but important differences in alkali contents, especially K, could be expected. It is notable, for instance, that the type localities of the 'calc-alkaline differentiation trend,' showing lack of Fe-enrichment on an alkalies-Fe-Mg diagram [*Poldervaart,* 1949], are all continental margin arcs [cf. *Ringwood,* 1975]. Purely oceanic arcs tend to be more tholeiitic in character [*Ewart et al.,* 1973; *Baker,* 1968]. Assimilation of relatively alkali-enriched materials concurrent with fractional crystallization can account for this difference. The Peninsular ranges batholith is distinctly calc-alkaline in this regard [cf. *Carmichael,* 1974]. The assimilation model is also consistent with the abundant high-silica rock types, compared to differentiated tholeiitic intrusions. In this regard, it is noteworthy that Andean andesites from Chile and Peru exhibit $\varepsilon_{Nd} - \varepsilon_{Sr}$ values that lie precisely on the trend defined by the batholith data [cf. *Hawkesworth et al.,* 1979]. An andesite and rhyolite from Peru also show evidence of contamination [*DePaolo and Wasserburg,* 1977], although they tend to have lower ε_{Nd} values for the same values of ε_{Sr}, indicating a different type of crustal component; Pb isotope data on the Andean lavas also show convincing isotope evidence for contamination [*Tilton and Barreiro,* 1980].

APPENDIX

Peninsular Ranges Sample Locations

PRB 1. Roadcut on Hwy. 111 at Point Happy, 1.5 km east of Indian Wells. Palm Desert 15′ quad. 116°17′50″W, 33°43′00″N.

PRB 3. Small roadcut on Hwy. 74 at Spring Crest, 50 m east of Palm Canyon Trail head. Idyllwild 15′ quad. 116°30′33″W, 33°34′04″N.

PRB 8. Quarry, SE end of Borrego Mountain, 1.5 km NW of Ocotillo Wells. Borrego Mountain 7.5′ quad. 116°09′00″W, 3°09′35″N.

PRB 9. Roadcut on Hwy. 78, in Valle de San Felipe, 6 km east of Banner. Borrego 15′ quad. 116°29′50″W, 33°05′20″N.

PRB 11. Roadcut on Hwy. S7, elevation 3600′. Palomar Observatory 7.5′ quad. 116°46′13″W, 33°15′34″N.

PRB 12. Roadcut on Hwy. 78, 1.5 km south of Witch Creek. Santa Ysabel 15′ quad. 116°43′10″W, 33°04′10″N.

PRB 13. Roadcut on Hwy. 78 in Clevenger Canyon, 1 km south of Santa Ysabel Creek. San Pasqual 15′ quad. 116°54′10″ W, 33°04′50″N.

PRB 14. Small roadcut on Hwy. 78, 1 km east of Cloverdale Road. Escondido 7.5′ quad. 117°00′45″W, 33°05′54″N.

PRB 15. Roadcut on Hwy. S6 (Del Dios Road) at Del Dios. Escondido 7.5′ quad. 117°07′15″W, 33°04′24″N.

Acknowledgments. Ron Kistler provided well-characterized rock samples from the Sierra Nevada, unpublished data, incisive questions, seasoned ideas, and a few chuckles, all of which were invaluable. The advice and suggestions of Dmitri Papanastassiou were enormously valuable in the design and construction of the mass spectrometry labs at UCLA. A careful review of an earlier version of this manuscript by Joe Wooden resulted in substantial improvements. Some of the isotopic and trace element data reported here was obtained in the Lunatic Asylum at Caltech. This work has been supported by National Science Foundation grants EAR78-12966, EAR78-18006, and EAR76-22494.

REFERENCES

Armstrong, R. L., W. H. Taubeneck, and P. O. Hales, Rb-Sr and K-Ar geochronometry of Mesozoic granitic rocks and their Sr isotopic composition, Oregon, Washington, Idaho, *Geol. Soc. Am. Bull., 88,* 397–411, 1977.

Arth, J. G., and G. N. Hanson, Geochemistry and origin of the early Precambrian crust of northeastern Minnesota, *Geochim. Cosmochim. Acta, 39,* 325–362, 1975.

Baker, P. E., Comparative volcanology and petrology of the Atlantic island arcs, *Bull. Volcanol, 32,* 189–206, 1968.

Bateman, P., Geologic and geophysical constraints on models for the origin of the Sierra Nevada batholith, in *The Geotectonic Development of California,* edited by W. G. Ernst, Prentice-Hall, Englewood Cliffs, N.J., 1981.

Bateman, P. C., and C. Wahrhaftig, Geology of the Sierra Nevada, *Geology of Northern California,* edited by E. H. Bailey, *Bull. 190,* 105–172, Calif. Div. Mines Geol., Sacramento, 1966.

Bowen, N. L., *Evolution of the Igneous rocks,* 322 pp., Princeton Univ. Press, Princeton, N. J., 1928.

Carmichael, I. S., F. J. Turner, and J. Verhoogen, *Igneous Petrology,* 739 pp., McGraw Hill, New York, 1974.

Carmichael, I. and D. J. DePaolo, Nd and Sr isotopes in the lavas of Colima, Mexico, *Geol. Soc. Am. Abstr. With Programs, 12,* 398, 1980.

Chen, J. H., U-Pb isotopic ages of the southern Sierra Nevada batholith and Independence dike swarm, California, *Geol. Soc. Am. Abstr. With Programs, 8,* 810, 1976.

Chen, J. H., and G. R. Tilton, Lead and strontium isotopic studies of the southern Sierra Nevada batholith, California, *Geol. Soc. Am. Abstr. With Programs, 10,* 99, 1978.

Craig, H. Standards for reporting concentrations of deuterium and oxygen-18 in natural waters, *Science, 133,* 1833–1834, 1961.

DePaolo, D. J., Study of magma sources, mantle structure and the differentiation of the earth using variations of $^{143}Nd/^{144}Nd$ in igneous rocks, Ph.D. thesis, 360 pp., Calif. Inst. of Technol., 1978.

DePaolo, D. J., Crustal growth and mantle evolution: Inferences from models of element transport and Nd and Sr isotopes, *Geochim. Cosmochim, Acta, 44,* 1185–1196, 1980*a*.

DePaolo, D. J., Sources of continental crust: Neodymium isotope evidence from the Sierra Nevada and Peninsular Ranges, *Science, 209,* 684–687, 1980*b*.

DePaolo, D. J., Nd in the Colorado Front Range and implications for crust formation and mantle evolution in the Proterozoic, *Nature, 291,* 193–196, 1981*a*.

DePaolo, D. J., Trace element and isotopic effects of combined wallrock assimilation and fractional crystallization, *Earth Planet. Sci. Lett., 53,* 189–202, 1981*b*.

DePaolo, D. J., and R. W. Johnson, Magma genesis in the New Britain island-arc: Constraints from Nd and Sr isotopes and trace-element patterns, *Contrib. Mineral. Petrol., 70,* 367–379, 1979.

DePaolo, D. J., and G. J. Wasserburg, Nd isotopic variations and petrogenetic models, *Geophys. Res. Lett., 3,* 249–252, 1976.

DePaolo, D. J., and G. J. Wasserburg, The sources of island arcs as indicated by Nd and Sr isotopic studies, *Geophys. Res. Lett., 4,* 465–468, 1977.

DePaolo, D. J., and G. J. Wasserburg, Neodymium in flood basalts from the Siberian Platform and inferences about their mantle sources, *Proc. Nat. Acad. Sci., 76,* 3056–3060, 1979*a*.

DePaolo, D. J., and G. J. Wasserburg, Petrogenetic mixing models and Nd-Sr isotopic patterns, *Geochim. Cosmochim. Acta, 43,* 615–627, 1979*b*.

DePaolo, D., P. Gromet, R. Powell, and L. T. Silver, San Telmo ring complex, Peninsular Ranges batholith, Northwest Baja California, Mexico, *Geol. Soc. Am. Abstr. with Programs, 7,* 309–310, 1975.

Dickinson, W. R., Relation of andesites, granites, and derivative sandstones to arc-trench tectonics, *Rev. Geophys. Space Phys., 8,* 813–860, 1970.

Dickinson, W. R., Plate tectonics and the continental margin of California, in *The Geotectonic Development of California,* edited by W. G. Ernst, Prentice-Hall, Englewood Cliffs, N.J., 1981.

Dickinson, W. R., and W. C. Luth, A model for plate tectonic evolution of mantle layers, *Science, 174,* 400–404, 1971.

Doe, B. R., and M. H. Delevaux, Variations in lead isotopic compositions in Mesozoic granitic rocks of California—A preliminary investigation, *Geol. Soc. Am. Bull., 84,* 3513–3526, 1973.

Doe, B. R., and R. E. Zartman, Plumbotectonics: The Phanerozoic, in *Geochemistry of Hydrothermal Ore Deposits, 2nd ed.,* edited by H. L. Barnes, 798 pp., John Wiley, New York, 1979.

Dupré, B., and C. J. Allegre, Pb-Sr-Nd isotopic correlation and the chemistry of the North Atlantic mantle, *Nature, 286,* 17–22, 1980.

Early, T. O., and L. T. Silver, Rb-Sr isotopic systematics in the Peninsular Ranges batholith of southern and Baja California: *Eos Trans. AGU, 54,* 494, 1973

Ehlig, P., Origin and tectonic history of the basement terrane of the San Gabriel Mountains, central Transverse Ranges, in *The Geotectonic Development of California,* edited by W. G. Ernst, Prentice-Hall, Englewood Cliffs, N.J., 1981.

Ernst, W. G. (Ed.), *The Geotectonic Development of California,* Prentice-Hall, Englewood Cliffs, N.J., 1981.

Evernden, J. F., and R. W. Kistler, Chronology of emplacement of Mesozoic batholithic complexes in California and western Nevada, *U.S. Geol. Surv. Prof. Pap. 623,* 42 pp., 1970.

Ewart, A., W. B. Bryan, and J. Gill, Mineralogy and geochemistry of the younger volcanic islands of Tonga, S. W. Pacific, *J. Petrol., 14,* 429–465, 1973.

Faure, G., *Isotope Geology,* 464 pp., John Wiley, New York, 1977.

Gastil, R. G., R. P. Phillips, and E. C. Allison, Reconnaissance geology of the state of Baja California, *Geol. Soc. Am. Mem., 140,* 170 pp., 1975.

Gastil, R. G., G. J. Morgan, and D. Krummenacher, The tectonic history of peninsular California and adjacent Mexico, in *The Geotectonic Development of California,* edited by W. G. Ernst, Prentice-Hall, Englewood Cliffs, N. J., 1981.

Gromet, L. P., Rare earth's abundances and fractionations and their implications for batholithic petrogenesis in the Peninsular Ranges batholith, California, USA, and Baja California, Mexico, Ph.D. Thesis, Calif. Inst. of Technol., 1979.

Gromet, L. P., and L. T. Silver, Trace element and isotopic variations in the San Telmo ring complex, N.W. Baja California del Norte, Mexico, *Geol. Soc. Am. Abstr With Programs, 9,* 427, 1977.

Hamilton, P. J., N. M. Evensen, R. K. O'Nions, and J. Tarney, Sm-Nd systematics of Lewisian gneisses: Implications for the origin of granulites, *Nature, 277,* 25–28, 1979.

Hawkesworth, C. J., R. K. O'Nions, R. J. Pankhurst, P. J. Hamilton, and N. M. Evensen, A geochemical study of island-arc and back-arc tholeiites from the Scotia Sea, *Earth Planet, Sci. Lett., 36,* 253–262, 1977.

Hawkesworth, C. J., M. J. Norry, J. C. Roddick, P. E. Baker, P. W. Francis, and R. S. Thorpe, $^{143}Nd/^{144}Nd$, $^{87}Sr/^{86}Sr$, and incompatible element variations in calc-alkaline andesites and plateau lavas from South America, *Earth Planet, Sci. Lett., 42,* 45–57, 1979.

Hurley, P. M., and J. R. Rand, Pre-drift continental nuclei, *Science, 164,* 1229–1242, 1969.

Jacobsen, S. B., and G. J. Wasserburg, The mean age of mantle and crustal reservoirs, *J. Geophys. Res., 84,* 7411–7428, 1979.

Jacobsen, S. B., and G. J. Wasserburg, Sm-Nd isotopic systematics of chrondrites, *Lunar Planet, Sci., XI,* 502–504, 1980.

King, P. B., *The Evolution of North America,* 197 pp., Princeton Univ. Press, Princeton, N. J., 1977.

Kistler, R. W., and Z. E. Peterman, Variations in Sr, Rb, K, Na, and initial Sr^{87}/Sr^{86} in Mesozoic granitic rocks and intruded wall rocks in Central California, *Geol. Soc. Am. Bull., 84,* 3489–3512, 1973.

Kistler, R. W., and Z. E. Peterman, A study of regional variation of initial strontium isotopic composition of Mesozoic granitic rocks in California, *U.S. Geol. Surv. Prof. Pap. 1071,* 1978.

Lachenbruch, A. H., Preliminary geothermal model of the Sierra Nevada, *J. Geophys. Res., 73,* 6977–6989, 1968.

Langmuir, C. H., R. D. Vocke, Jr., and G. N. Hanson, A general mix-

ing equation with applications to Icelandic basalts, *Earth Planet. Sci. Lett., 37,* 380–392, 1978.

Lanphere, M. A., G. J. Wasserburg, A. L. Albee, and G. R. Tilton, Redistribution of strontium and rubidium isotopes during metamorphism, World Beater complex, Panamint Range, California, in *Isotopic and Cosmic Chemistry,* edited by H. Craig et al., pp. 269–320, North-Holland, Amsterdam, 1963.

Larsen, E. S., Batholith and associated rocks of the Corona, Elsinore, and San Luis Rey quadrangles, southern California, *Geol. Soc. Am. Mem., 29,* 1–182, 1948.

Masi, U., J. R. O'Neil, and R. W. Kistler, Stable isotope systematics in Mesozoic granites of Central and Northern California and Southwestern Oregon, *Contrib. Mineral. Petrol., 76,* 116–126, 1981.

McCulloch, M. T., and G. J. Wasserburg, Sm-Nd and Rb-Sr chronology of continental crust formation, *Science, 200,* 1003–1011, 1978.

McCulloch, M. T., R. T. Gregory, G. J. Wasserburg, and H. P. Taylor, A neodymium, strontium and oxygen isotopic study of the Cretaceous Samail ophiolite and implications for the petrogenesis and seawater-hydrothermal alteration of ocean crust, *Earth. Planet. Sci. Lett., 46,* 201–211, 1980.

Meijer, A., Pb and Sr isotopic data bearing on the origin of volcanic rocks from the Mariana island-arc system, *Geol. Soc. Am. Bull., 87,* 1358–1369, 1976.

Menzies, M., and V. R. Murthy, Enriched mantle: Nd and Sr isotopes in diopsides from Kimberlite nodules, *Nature, 283,* 634, 1980.

Nance, W. B., and S. R. Taylor, Rare earth element patterns and crustal evolution, 1, Australian post-Archean sedimentary rocks, *Geochim. Cosmochim Acta, 40,* 1539–1551, 1976.

Nance, W. B., and S. R. Taylor, Rare earth element patterns and crustal evolution, 2, Archean sedimentary rocks from Kalgoorlie, Australia, *Geochim. Cosmochim. Acta, 41,* 225–231, 1977.

Nohda, S., and G. J. Wasserburg, Nd and Sr isotopic study of volcanic rocks from Japan, *Earth Planet. Sci. Lett., 52,* 264–276, 1981.

O'Nions, R. K., P. J. Hamilton, and N. M. Evensen, Variations in $^{143}Nd/^{144}Nd$ and $^{87}Sr/^{86}Sr$ ratios in oceanic basalts, *Earth Planet. Sci. Lett., 34,* 13–22, 1977.

Papanastassiou, D. A., D. J. DePaolo, and G. J. Wasserburg, Rb-Sr and Sm-Nd chronology and genealogy of mare basalts from the Sea of Tranquility, *Proc. Lunar Sci. Conf. 8th,* 1639–1672, 1977.

Peterman, Z. E., C. E. Hedge, and H. A. Tourtelot, Isotopic composition of strontium in seawater throughout Phanerozoic time, *Geochim. Cosmochim. Acta, 34,* 105–120, 1970.

Piwinski, A. J., Experimental studies of igneous rock series, central Sierra Nevada batholith, California, *J. Geol., 76,* 548–570, 1968.

Poldervaart, A., Three methods of graphic representation of chemical analyses of igneous rocks, *Trans. R. Soc. S. Africa, 32,* 177–188, 1949.

Presnall, D. C., and P. C. Bateman, Fusion relations in the system $NaAlSi_3O_8$-$CaAl_2Si_2O_8$-$KAlSi_3O_8$-SiO_2-H_2O and generation of granitic magmas in the Sierra Nevada Batholith, *Geol. Soc. Am. Bull., 84,* 3181–3202, 1973.

Ringwood, A. E., *Composition and Petrology of the Earth's Mantle,* 618 pp., McGraw-Hill, New York, 1975.

Saleeby, J., Ocean floor accretion and volcano-plutonic arc evolution of the Mesozoic Sierra Nevada, in *The Geotectonic Development of California,* edited by W. G. Ernst, Prentice-Hall, Englewood Cliffs, N. J., 1981.

Schwarz, H. P., Pre-Cretaceous sedimentation and metamorphism in the Winchester area, Northern Peninsular ranges, California, *Geol. Soc. Am. Spec. Pap. 100,* 1969.

Schweikert, R. A., and W. S. Snyder, Paleozoic plate tectonics of the Sierra Nevada and adjacent regions, in *The Geotectonic Development of California,* edited by W. G. Ernst, Prentice-Hall, Englewood Cliffs, N. J., 1981.

Shaw, D. M., J. Dostal, R. R. Keays, Additional estimates of continental surface Precambrian shield composition in Canada, *Geochim. Cosmochim. Acta, 40,* 73–83, 1976.

Shaw, H. R., Comments on viscosity, crystal settling, and convection in granitic magmas, *Am. J. Sci., 263,* 120–152, 1965.

Silver, L. T., and T. H. Anderson, Possible left-lateral early to middle Mesozoic disruption of the southwestern North American craton margin, *Geol. Soc. Am. Abstr. With Programs, 6,* 955, 1974.

Silver, L. T., F. G. Stehli, and C. R. Allen, Lower Cretaceous prebatholithic rocks of northern Baja California, Mexico, *Bull. Am. Assoc. Petrol. Geol., 47,* 2054–2059, 1963.

Silver, L. T., T. O. Early, and T. H. Anderson, Petrological, geochemical, and geochronological asymmetries of the Peninsular Ranges batholith, *Geol. Soc. Am. Abstr. with Programs, 7,* 375–376, 1975.

Taylor, H. P., Oxygen and hydrogen isotope studies of plutonic granitic rocks, *Earth Planet. Sci. Lett., 38,* 177–210, 1978.

Taylor, H. P., The effects of assimilation of country rocks by magmas on $^{18}O/^{16}O$ and $^{87}Sr/^{86}Sr$ systematics in igneous rocks, *Earth Planet. Sci. Lett., 47,* 243–254, 1980.

Taylor, H. P., and L. T. Silver, Oxygen isotope relationships in plutonic igneous rocks of the peninsular ranges batholith, Southern and Baja California, *U.S. Geol. Surv. Open-File Rep. 78-701,* 423–436, 1978.

Taylor, S. R., Island arc models and the composition of the continental crust, in *Island Arcs, Deep Sea Trenchs and Back-Arc Basins,* edited by M. Talwani and W. C. Pitman, pp. 325–336, American Geophysical Union, Washington, D. C., 1977.

Tilton, G. R., and B. A. Barreiro, Origin of lead in Andean calc-alkaline lavas, southern Peru, *Science, 210,* 1245–1247, 1980.

Turi, B., and H. P. Taylor, An oxygen and hydrogen isotope study of a granodiorite pluton from the Southern California batholith, *Geochim. Cosmochim. Acta, 35,* 383–406, 1971.

Vollmer, R., Rb-Sr and U-Th-Pb systematics of alkaline rocks: The alkaline rocks from Italy, *Geochim. Cosmochim. Acta, 40,* 283–295, 1976.

Wasserburg, G. J., and D. J. DePaolo, Models of earth structure inferred from Neodymium and Strontium isotopic abundances, *Proc. Nat. Acad. Sci., 76,* 3594–3598, 1979.

Wasserburg, G. J., D. A. Papanastassiou, E. V. Nenow, and C. A. Bauman, A programmable magnetic field mass spectrometer with on-line data processing, *Rev. Sci. Instr., 40,* 288–295, 1969.

Yoder, H. S., and C. E. Tilley, Origin of basaltic magmas: An experimental study of natural and synthetic rock systems, *J. Petrol., 3,* 342–532, 1962.

Zartman, R. E., Lead isotopic provinces in the Cordillera of the western United States and their geologic significance, *Econ. Geol., 69,* 792–805, 1974.

(Received November 6, 1980;
revised March 13, 1981;
accepted March 25, 1981.)

JOURNAL OF GEOPHYSICAL RESEARCH, VOL. 86, NO. B11, PAGES 10489–10501, NOVEMBER 10, 1981

Petrology and Geochronology of Metamorphosed Volcanic Rocks and a Middle Cretaceous Volcanic Neck in the East-Central Sierra Nevada, California

RONALD W. KISTLER

U.S. Geological Survey, Menlo Park, California 94025

SAMUEL E. SWANSON

Geology/Geophysics Program, University of Alaska, Fairbanks, Alaska 99701

Metamorphosed Mesozoic volcanic rocks from the east-central Sierra Nevada range in composition from basalt to rhyolite and have ages, based on whole rock Rb-Sr and U-Pb zircon dating, of about 237–224, 185, 163, 134, and 100 m.y. The major plutons of the batholith in this area are of Triassic (215–200 m.y.) and Cretaceous (94–80 m.y.) ages. Initial $^{87}Sr/^{86}Sr$ values for the metamorphosed volcanic rocks of the area are in the range from 0.7042 to 0.7058 and are generally different from the values for the surrounding batholithic rocks (0.7056–0.7066). A circular, zoned granitic pluton, with an outcrop area of 2.5 km^2, similar in appearance to a ring dike complex, was apparently a conduit for some or possibly all of the middle-Cretaceous metamorphosed volcanic rocks exposed about 5 km to the south in the western part of the Ritter Range. Samples from the metamorphosed volcanic rocks and the pluton yield a Rb-Sr whole rock isochron age of 99.9 ± 2.2 m.y. with an initial $^{87}Sr/^{86}Sr$ of 0.7048 ± 0.0001. Major element variation diagrams of the pluton and volcanic rocks define coincident compositional trends. The pluton, intruded into Early Jurassic metamorphosed volcanic rocks (Rb-Sr whole rock isochron age of 185 ± 6 m.y., initial $^{87}/^{86}Sr = 0.70474 \pm 0.00009$), is composed of a central body of granite that is intruded into and almost completely surrounded by a crescent-shaped outer rim of quartz monzodiorite. Contact relations between the granitic rocks, intrusive in some places and completely gradational at other places, indicate that the quartz monzodiorite was not completely crystallized prior to the intrusion of the granite. Modal minerology within the pluton is also consistent with this inferred crystallization history. The granitic rock textures are cataclastic, characterized by a groundmass of feldspar and quartz that surrounds larger grains of feldspar, hornblende, and biotite. Widely spaced aplite dikes from the granite intrude the quartz monzodiorite along the contact between the granitic rocks. The aplite dikes and interstitial alkali feldspar associated with myrmekite in the pluton, being undeformed, indicate crystallization of a small amount of silicate liquid after cataclasis. Aplite compositions suggest a minimum crystallization pressure of 0.5 kb (1–2 km); this depth is consistent with crystallization near the base of a large stratovolcano. The pluton is characterized by steep, linear features, defined by mineral clots and inclusions, that probably formed during the upward movement of the nearly crystallized magma in the volcanic conduit. The ages of volcanic events relative to the ages of the major intrusive epochs and the major element and isotopic compositions of the volcanic rocks relative to the major plutons indicate that the volcanic rocks are not simply or directly related to the major plutons in the Sierra Nevada.

INTRODUCTION

Metamorphosed volcanic rocks are found in a series of roof pendants along the eastern margin of the central portion of the Sierra Nevada batholith [*Erwin*, 1934; *Rinehart and Ross*, 1957, 1964; *Moore*, 1963; *Huber and Rinehart*, 1965; *Bateman*, 1965; *Kistler*, 1966*a*,*b*; *Chesterman*, 1975; *Brook*, 1977; *Fiske et al.*, 1977; *Keith and Seitz*, 1981]. The rocks are predominantly of intermediate composition but range from rhyolite to basalt. Relict clastic and pyroclastic textures are much more common than flow features. Regional metamorphism has produced mineral assemblages corresponding to the high greenschist or low epidote-amphibolite facies [*Kistler*, 1966*a*; *Fiske and Tobisch*, 1978]. Locally, granitoid plutons have metamorphosed the volcanic rocks under conditions of the hornblende-hornfels facies of contact metamorphism.

Ages of volcanism in the eastern Sierra Nevada are very poorly known. Fossils have been found in only two localities in associated metamorphosed sedimentary rocks, and they indicate an Early Jurassic age [*Rinehart et al.*, 1959]. Because of the lack of fossils, structural studies [*Kistler*, 1966*a*] and U-Pb and Rb-Sr isotopic studies have been used to help determine the history of the rocks in the roof pendants. *Kistler* [1966*a*] reported a Permian(?) age (256 ± 26 m.y.) for the lower part of the volcanic section, and *Brook* [1977] reported a Permian age (250 ± 25 m.y.) for a rhyodacite-andesite unit in the Saddlebag Lake roof pendant based on whole rock Rb-Sr isochrons. *Fiske and Tobisch* [1978] used isotopic ages to distinguish three zones that are progressively younger from east to west in the metamorphic volcanic rocks of the Ritter Range. The easternmost (oldest) zone is chiefly crystal-lithic tuff and tuff breccia, dated at 250 m.y. by a Rb-Sr whole rock isochron and 186 to 214 m.y. by U-Pb ages of zircons. Age relations in the intermediate zone are unclear, because tuffs found near to marbles with Early Jurassic fossils have Late Jurassic U-Pb ages from zircons of 153 and 158 m.y. [*Fiske and Tobisch*, 1978]. The westermost zone is a caldera fill complex of rhyolitic ash flows and volcanic tuff breccia that was deposited unconformably on volcanic flows and sediments. The age of the caldera fill complex is 101 m.y. by U-Pb on zircons and 99.9 ± 2.2 m.y. by Rb-Sr whole-rock dating; the volcanic flows unconformably beneath the caldera fill are dated at 127 m.y. (U-Pb, zircon) and 134 ± 13 m.y. (Rb-Sr whole-rock) [*Fiske et al.*, 1977; *Fiske and Tobisch*, 1978; this report].

The relationship between the Mesozoic plutons and volcanic rocks in the Sierra Nevada has been difficult to decipher. *Hamilton and Myers* [1967] suggested that the volcanic

Copyright © 1981 by the American Geophysical Union.

Paper number 1B0903.
0148-0227/81/001B-0903$01.00

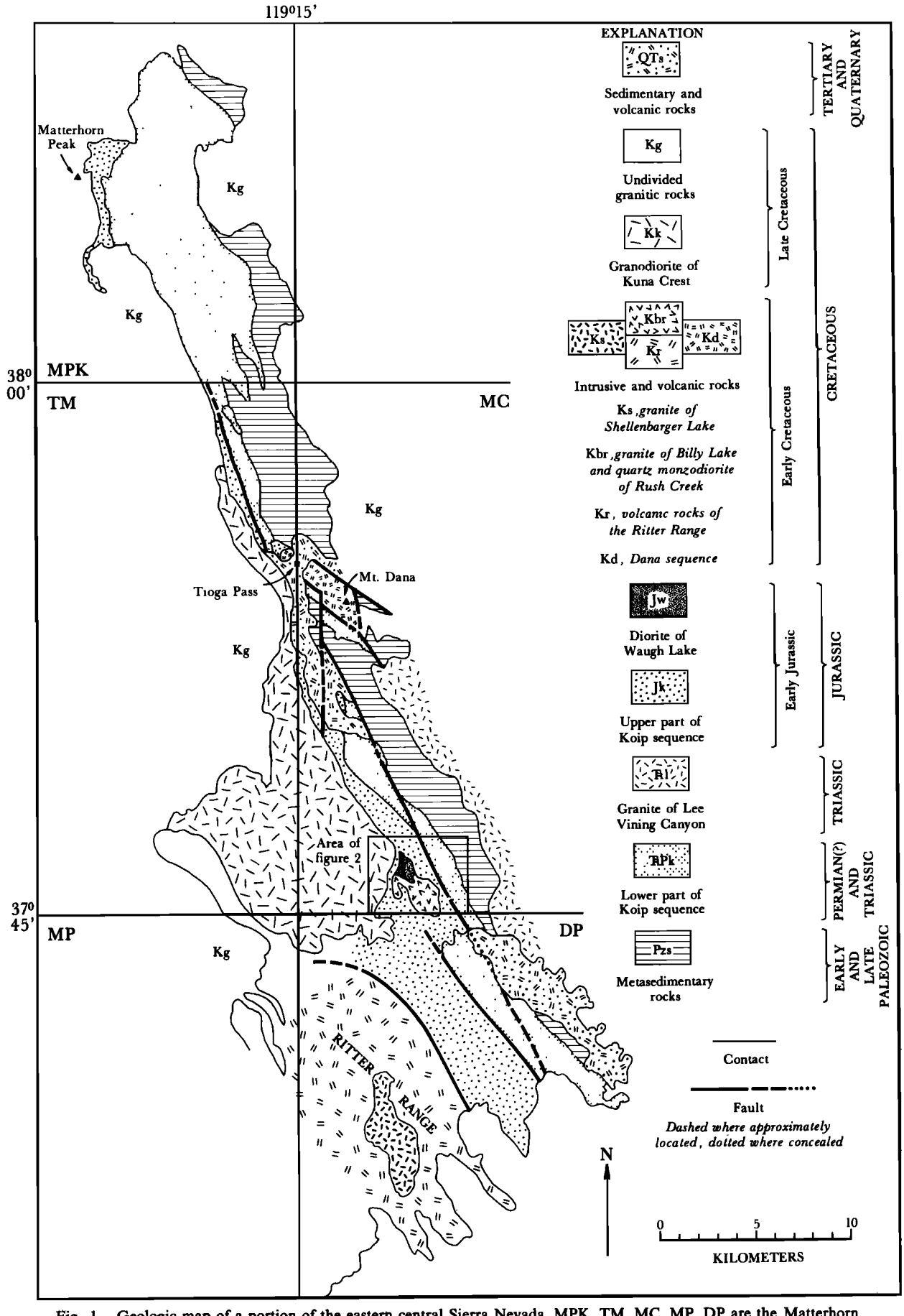

Fig. 1. Geologic map of a portion of the eastern central Sierra Nevada. MPK, TM, MC, MP, DP are the Matterhorn Peak, Tuolumne Meadows, Mono Craters, Merced Peak, and Devils Postpile quandrangles, respectively.

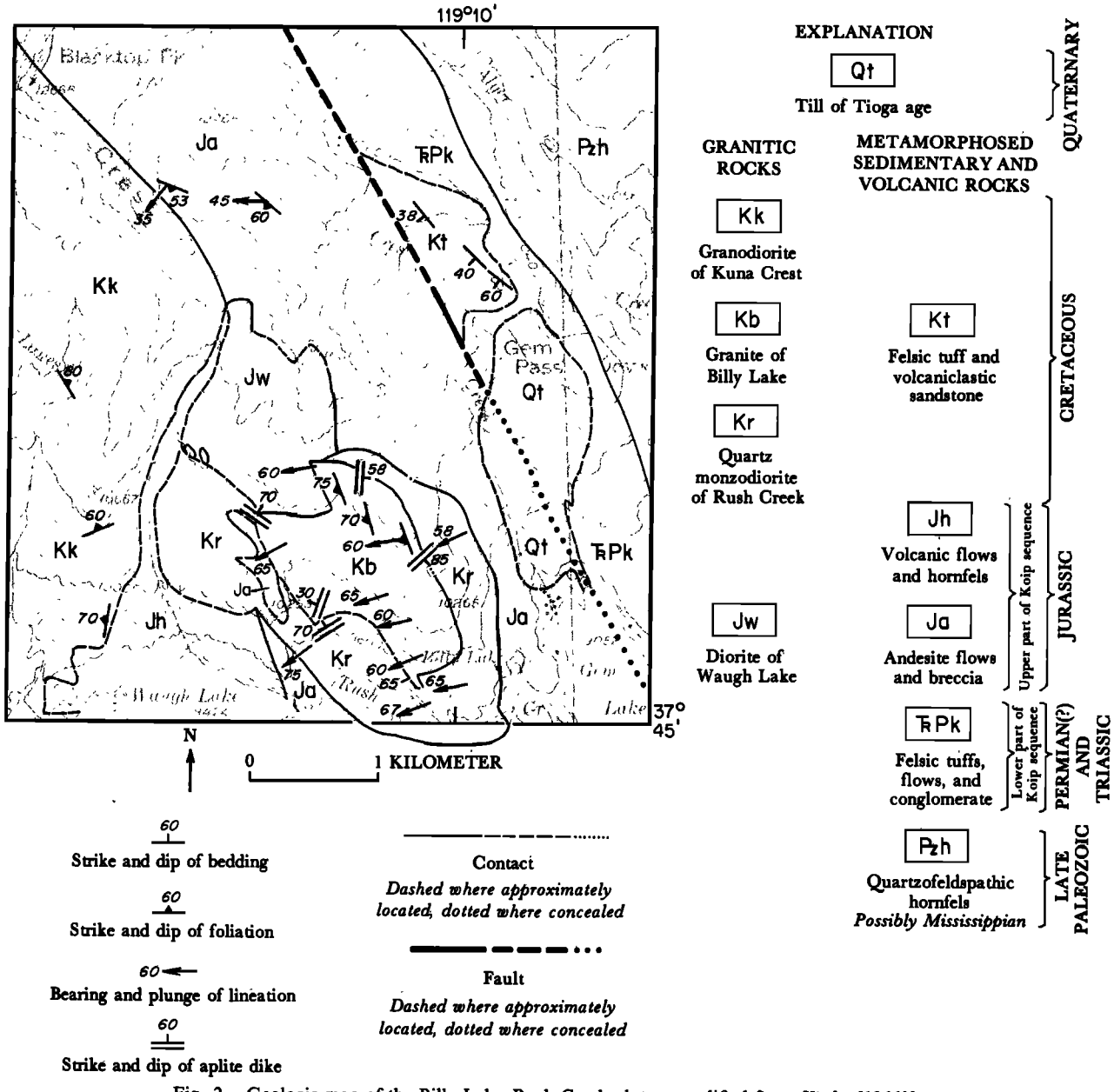

Fig. 2. Geologic map of the Billy Lake–Rush Creek pluton, modified from *Kistler* [1966*b*].

rocks are directly related to the plutons and simply represent facies that vented all the way to the surface. The ages of the volcanic rocks occurring in roof pendants, however, do not coincide with ages of the major plutonic epochs [*Kistler*, 1978]. This paper presents more chemical and geochronological data for the metavolcanic rocks and describes a small zoned granitic pluton that, unlike the major plutons of the batholith, probably actually was a middle Cretaceous volcanic feeder.

Analytical Methods

Major element chemical analyses were made by the rapid method of *Shapiro and Brannock* [1962] or by X ray fluorescence. Rubidium and strontium concentrations were measured either by isotope dilution or by X ray fluorescence using a direct comparison method with standard samples of similar bulk compositions [*Doering*, 1968]. Strontium isotope ratios were determined on a 30.5-cm-radius, 90° sector mass spectrometer, using a triple rhenium filament mode of ionization, automatic peak switching, and digital output. The $^{86}Sr/^{88}Sr$ ratios were normalized to 0.1194, and the $^{87}Sr/^{86}Sr$ ratios were further adjusted to an Eimer and Amend $SrCO_3$ value of 0.7080. The decay constant of ^{87}Rb used is $\lambda_\beta = 1.42 \times 10^{-11}$ yr^{-1}. The abundance ratio of $^{85}Rb/^{87}Rb = 2.59265$ in normal Rb and atomic weight of Rb = 85.46776 were used. Uncertainties in the Rb/Sr ratios determined by X ray fluorescence are about ± 3%, whereas those determined by isotope dilution are about ±1%. Duplicate analyses completed during this study indicate a standard deviation of ±0.00011 for $^{87}Sr/^{86}Sr$. Isochrons were calculated using the least squares regression technique of *York* [1969]. The goodness of fit of data points about the isochron is reported as MSWD (mean square of weighted deviates). It is a statistical index (sums/N-2) that compares the observed scatter to that accounted for by analytical error only [*Brooks et al.*, 1972; *Roddich*, 1978]. When this parameter exceeds approximately 2.5, the observed variation

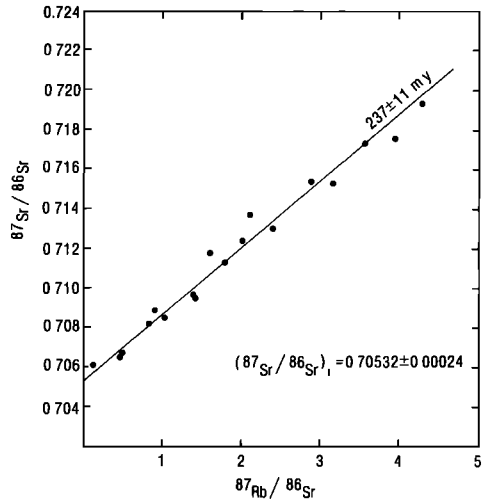

Fig. 3. RB-Sr whole rock isochron of metamorphosed volcanic rocks from the lower part of the Koip sequence of *Kistler* [1966*a*]. Analytical data are given in Tables 1 and 2. Age = 237 ± 11 m.y., r_i = 0.70532 ± 0.00024; MSWD = 5.695.

about the best fit line is larger than can be accounted for solely by analytical uncertainty, and some geologic source of scatter is probable at the 95% level of confidence.

METAMORPHOSED VOLCANIC ROCKS

The distribution of groups of metamorphosed volcanic rocks ranging in age from Permian(?) and Triassic to middle Cretaceous in the east central Sierra Nevada (Figure 1) was determined using the previously mentioned isotopic age studies, the geologic mapping of *Peck* [1964], *Huber and Rinehart* [1965], *Kistler* [1966*b*], *Chesterman* [1975], *Brook* [1977], *Fiske and Tobisch* [1978], and *Keith and Seitz* [1981], and data reported here. Lithologic descriptions of many of these volcanic rock units have been published previously [*Huber and Rinehart,* 1965; *Kistler,* 1966*a*; *Brook,* 1977; *Fiske and Tobisch,* 1978] and so will be discussed only briefly. The volcanic neck, discussed below, is shown in Figure 2.

TABLE 1. Rb-Sr Data for the Lower part of Koip Sequence South of Latitude 38° N

Samples	Rb, ppm	Sr, ppm	Atomic Ratio $^{87}Rb/^{86}Sr$	Atomic Ratio $^{87}Sr/^{86}Sr$
SL-1V*	158	129	3.57	0.7173
SrV-17	50	1133	0.127	0.7061
SL-3Va*	83	501	0.48	0.7065
SL-3Vd*	109	638	0.50	0.7067
SL-10V*	60	207	0.84	0.7082
D 118†	100	320	0.915	0.7089
D 122†	128	207	1.81	0.7113
MC-304†	120	173	2.02	0.7124
SL-11V*	120	164	2.12	0.7137
SrV-7	149	149	2.89	0.71542
SL12-73	173	158	3.17	0.71530
SL-13V*	144	97	4.30	0.7193
MD-24	179	131	3.96	0.71757
F73-1	137	279	1.43	0.7095
F73-5	131	270	1.40	0.7097
F73-7	131	157	2.41	0.7130
F70-18	207	574	1.04	0.7085
F65-127	150	270	1.61	0.7118

Age = 237 ± 11 m.y., r_i = 0.70532 ± 0.00024, MSWD = 5.7.
* From *Brook* [1977].
† From *Kistler* [1966*a*].

TABLE 2. Chemical Analyses and norms of Two Volcanic Rocks of the Lower Part of Koip Sequence, Mono Craters Quadrangle

Samples	Chemical Analyses, wt % SrV-17*	SrV-7*
SiO_2	50.64	70.30
Al_2O_3	18.18	14.46
Fe_2O_3	3.21	0.64
FeO	5.69	2.68
MgO	5.45	0.60
CaO	4.97	0.68
Na_2O	5.05	4.21
K_2O	1.26	4.90
H_2O^+	2.97	0.43
H_2O	0.12	0.06
TiO_2	1.07	0.25
P_2O_5	0.20	0.08
MnO	0.15	0.87
CO_2	0.92	0.17
Rb	49.9	149
Sr†	1133	149
Sum	99.88	100.33
Rb/Sr	0.044	1.00
K/Rb	210	273
CIPW Norms, wt %		
q		23.7
c	2.2	1.6
or	7.7	29.2
ab	44.1	36.0
an	18.1	1.8
di		
hy	12.6	5.7
ol	5.7	
mt	4.8	0.9
hm		
il	2.1	0.5
ap	0.5	0.2
cc	2.2	0.4
Total	100.0	100.0

* Analyst, R. Espos.
† Concentrations reported in parts per million.

Permian(?) and Triassic Volcanic Rocks

The oldest Phanerozoic igenous rocks in the area are Permian(?) and Triassic metamorphosed volcanic rocks which lie

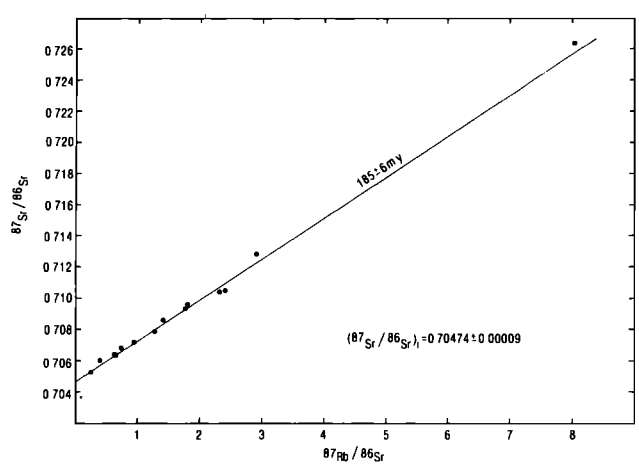

Fig. 4. Rb-Sr whole rock isochron of metamorphosed volcanic rocks from the upper part of the Koip sequence of *Kistler* [1966*a*]. Analytical data are given in Tables 3 and 5. Age = 185 ± 6 m.y., r_i = 0.70474 ± 0.00009; MSWD = 1.672.

TABLE 3. Rb-Sr Data for the Upper Part of Koip Sequence

Samples	Rb, ppm	Sr, ppm	Atomic Ratio	
			$^{87}Rb/^{86}Sr$	$^{87}Sr/^{86}Sr$
SrV-8	70	313	0.644	0.70639
SL-7-73	129	596	0.627	0.70645
SrV-14	177	693	0.740	0.70681
SrV-15	192	394	1.41	0.70861
SrV-20	52	84	1.77	0.70935
SrV-16	120	197	1.80	0.70967
SL-9-73	167	165	2.90	0.71288
SrV-18	214	77	8.01	0.72638
Sr-4-77*	84	448	0.399	0.70604
F-65-158	39	447	0.255	0.7053
F-65-159	158	486	0.94	0.7072
F-65-161	318	384	2.40	0.7103
F-70-26	116	264	1.27	0.7079
HT	154	194	2.31	0.7104

* Sample from the diorite of Waugh Lake.

unconformably on late Paleozoic metamorphosed sedimentary rocks. *Kistler* [1966*a*] called these rocks the Koip sequence and reported a Permian(?) age for them based on a Rb-Sr whole rock isochron of 256 ± 26 m.y. A similar age (Rb-Sr whole rock isochron of 250 m.y.) was reported for metamorphosed volcanic rocks lying unconformably on late Paleozoic sedimentary rocks in the Saddlebag Lake roof pendant, just north of Tioga Pass [*Brook,* 1977]. Specimens from the stratigraphically lowest volcanic unit in the Ritter Range also yield a Rb-Sr whole rock isochron age of 250 m.y., but U/Pb zircon ages are 214 to 186 m.y. [*Fiske and Tobisch,* 1978]. We collected more samples from the Koip sequence of *Kistler* [1966*a*] in the Mono Craters quadrangle and from the Saddlebag Lake roof pendant. The new data and those already published, eighteen specimens, in the lower part of the Koip sequence to the south of latitude 38° N., yield a whole-rock isochron age of 237 ± 11 m.y. (Figure 3, Table 1). If the data of 17 specimens from the Matterhorn Peak area [*Keith and Seitz,* 1981] (Figure 1) are combined with the 18 specimens just mentioned, the indicated ischron age is 224 ± 14 m.y. and is thus Triassic. However, the estimated uncertainties of these isochrons do not preclude a Permian age on the basis of currently accepted time scales [*Harland et al.,* 1964] and the entire lower part of the Koip sequence is considered as Permian(?) and Triassic in age.

The lower part of the Koip sequence, interbedded with or underlain by conglomerate, is made up of metamorphosed sedimentary and volcanic rocks. The latter are dominated by the equivalents of felsic pyroclastic rocks in the southern part of the area shown in Figure 1 [*Kistler,* 1966*a*; *Brook,* 1977; *Fiske and Tobisch,* 1978] and by mafic flows and breccias in the northern part [*Keith and Seitz,* 1981]. Chemical analyses indicate metamorphosed dacite or rhyodacite (sample Sr V-7) and basalt (sample SrV-17) (Table 2). Partial analyses from the Saddlebag Lake area in the Tuolumne Meadows quadrangle show that these volcanic rocks are andesite and rhyodacite [*Brook,* 1977].

Jurassic Rocks

Jurassic metamorphosed volcanic rocks (upper Koip) occur in a belt just west of the Permian(?) and Triassic rocks of the lower Koip sequence (Figure 1). *Kistler* [1966*a*, *b*] believed the upper Koip rocks in the Mono Craters quadrangle to be of Permian(?) age, but new Rb-Sr whole rock data yield an isochron age of 185 ± 6 m.y. (Figure 4, Table 3); that is, Jurassic. Fossiliferous, stratigraphically continuous sedimentary rocks in the southern part of the Ritter Range in the Devils Postpile quadrangle [*Huber and Rinehart,* 1965] are early Jurassic, and Rb-Sr whole rock data from associated volcanic rocks plot on the 185 ± 6 m.y. isochron. Furthermore, a sample of the diorite of Waugh Lake (Figure 2) plots on the 185 m.y. isochron (sample Sr-4-77, Table 3). The diorite intruded the Jurassic volcanic rocks, but the small outcrop size and similar age suggests that the diorite is a hypabyssal intrusive rock related to the volcanism; therefore the diorite of Waugh Lake will be discussed along with the upper part of the Koip sequence.

The metamorphosed volcanic rocks of the upper part of the Koip sequence are dominated by rhyolite and dacite tuffs in the Ritter Range [*Erwin,* 1934; *Huber and Rinehart,* 1965; *Fiske and Tobisch,* 1978]; there are subordinate amounts of andesite and basalt lava flows. Fossiliferous marine carbonate of Early Jurassic age makes up part of this section [*Rinehart et al.,* 1959]. To the north this unit is composed of andesite and basalt flows and breccias, with minor rhyodacite tuffs and volcanic sediments [*Kistler,* 1966*a*,*b*]. The lower contact of this unit is a fault in most places (Figure 1), and the original depositional relationships between upper and lower Koip are equivocal. The lower Koip sequence was folded before being intruded by the granite of Lee Vining Canyon of 212 ± 8 m.y. age [*Kistler,* 1966*a*] (Table 4). Since volcanic rocks in the upper Koip are only 185 m.y. old, the lower Koip sequence must have been dformed before the deposition of the upper Koip sequence.

Chemical analyses from the upper part of the Koip sequence (Table 5) correspond to andesite with a wide range of silica content (SiO_2 = 54 to 65 wt %), or to rhyolite (SiO_2 = 76 wt %).

The 185 m.y. old diorite of Waugh Lake has an outcrop of about 1½ km². It intruded the metamorphosed Jurassic volcanic rocks, and is intruded by a late cretaceous pluton called the granodiorite of Kuna Crest, by the quartz monzodiorite of Rush Creek, and by the granite of Billy Lake (Figure 2). The contact of the diorite with the granodiorite of Kuna Crest is ambiguous, but inasmuch as there is a marked increase in quartz and alkali feldspar in the diorite near the contact, we believe that this material was introduced from the granodiorite, which is therefore the younger rock. The granite of Billy Lake contains inclusions of the diorite near the contact.

Outcrops of the diorite of Waugh Lake are dark gray, and in hand specimens small plagioclase phenocrysts can be seen in a fine-grained groundmass. In thin sections, the diorite is

TABLE 4. Rb-Sr Data for the Granite of Lee Vining Canyon

Samples	Rb, ppm	Sr, ppm	Atomic Ratio	
			$^{87}Rb/^{86}Sr$	$^{87}Sr/^{86}Sr$
Sr1	56	146	1.11	0.70962
Sr3	131	344	1.10	0.70956
Sr4	140	136	3.00	0.71435
Sr5	112	209	1.55	0.71028
Sr6	114	161	2.05	0.71262
I-340*	160	140	3.31	0.7168
I-157*	156	86	5.28	0.7219
I-337*	185	86	6.21	0.7251

Age = 212.4 ± 8 m.y.; r_i = 0.70614 ± 0.00017; MSWD = 2.57.
* From *Kistler* [1966*a*].

TABLE 5. Chemical Analyses and Norms of Rocks of the Upper Part of Koip Sequence in the Mono Craters Quad

Samples*	SrV-8	Sr4-77†	SrV-15	SrV-14	SrV-18	SrV-16
			Chemical Analyses, wt %			
SiO_2	53.64	55.89	60.14	64.05	75.69	75.75
Al_2O_3	17.49	17.06	16.22	16.56	11.39	11.86
Fe_2O_3	2.68	2.12	2.17	3.28	0.48	1.16
FeO	6.46	5.25	4.14	1.57	1.65	1.30
MgO	4.28	4.26	3.09	2.19	0.52	0.15
CaO	7.81	6.66	2.42	1.43	1.44	1.21
Na_2O	2.54	3.56	3.72	4.78	0.19	3.71
K_2O	2.61	2.25	4.75	3.59	6.20	3.62
H_2O^+	1.13	0.82	1.32	1.03	1.15	0.02
H_2O^-	0.10	0.05	0.21	0.14	0.10	0.08
TiO_2	0.88	1.00	0.67	0.43	0.05	0.12
P_2O_5	0.17	0.24	0.19	0.18	0.02	0.04
MnO	0.18	0.12	0.12	0.01	0.08	0.08
CO_2	0.06	0.01	0.06	0.03	1.44	0.12
Rb‡	69.6	84	192	177	214	120
Sr‡	313	448	394	693	77.3	197
Sum	100.03	99.29	99.22	99.36	100.4	99.22
Rb/Sr	0.222	0.187	0.487	0.255	2.77	0.609
K/Rb	311	222	205	168	240	250
$\delta^{18}O$ SMOW	7.27 ‰			6.91 ‰		
δD SMOW	−123 ‰			−138 ‰		
			CIPW Norms, wt %			
q	4.4	5.4	9.2	17.1	49.3	37.3
c			1.2	2.8	4.4	
or	15.6	13.5	28.7	21.6	37.0	21.4
ab	21.8	30.6	32.7	41.2	1.6	31.4
an	29.0	24.3	10.6	5.8		5.0
di	7.2	6.2				
hy	15.9	14.3	12.9	5.6	4.0	1.8
ol						
mt	3.9	3.1	3.2	4.2	0.7	1.7
hm				0.40		
il	1.7	1.9	1.3	0.86	0.1	0.2
ap.	0.4	0.6	0.5	0.4	0.1	0.1
cc	0.1	0.0	0.1	0.1	2.5	0.3
Total	100.0	99.9	99.9	100.0	99.7	99.2

* Analyst, R. Espos.
† Diorite of Waugh Lake.
‡ Concentration reported in parts per million.

seen to be prophyritic with phenocrysts of plagioclase (An_{33-54}, 1.0 to 2.5 mm in longest dimension) and hornblende. The fine-grained matrix is composed of anhedral crystals of biotite, hornblende, and feldspar in variable abundances. Plagioclase is unaltered to slightly altered, and it is generally normally zoned. Alkali feldspar occurs as small anhedra in the groundmass, and most of it has grid twinning. Hornblende is pleochroic (dark green to yellow green) with occasional cores

TABLE 6. Rb-Sr Data for Upper Jurassic Volcanic Rocks of the Upper Part of Koip Sequence

Samples	Rb, ppm	Sr, ppm	Atomic Ratio $^{87}Rb/^{86}Sr$	Atomic Ratio $^{87}Sr/^{86}Sr$
F65-154	203	96	6.1	0.7190
F65-162	225	114	6.46	0.7206
F70-25	72	200	1.03	0.7079
F70-29	179	127	4.01	0.7154
F70-23	84	912	0.27	0.7064
F70-22	102	926	0.32	0.7061

Age = 163 ± 5 m.y., r_i = 0.7055 ± 0.00012, MSWD = 1.9.

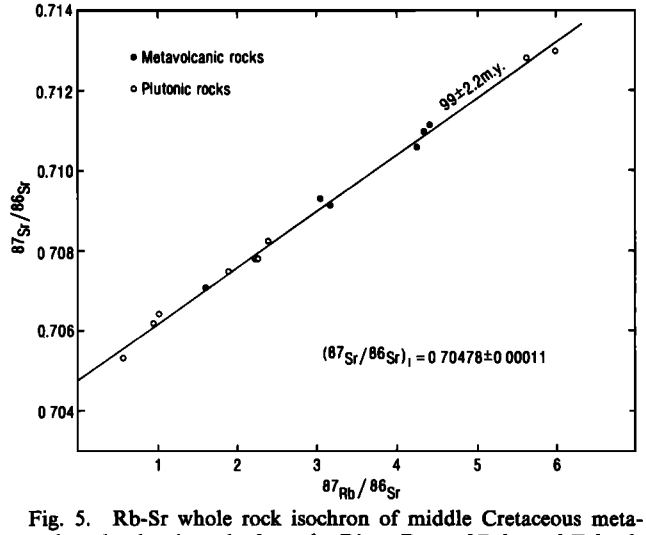

Fig. 5. Rb-Sr whole rock isochron of middle Cretaceous metamorphosed volcanic rocks from the Ritter Range [*Fiske and Tobisch*, 1978] and the Billy Lake–Rush Creek pluton (Figure 2). Analytical data are given in Tables 7, 10, and 11. Age = 99.9 ± 2.2 m.y., r_i = 0.70478 ± 0.00011; MSWD = 0.7355.

TABLE 7. Rb-Sr Data for Middle Cretaceous Metavolcanic Rocks from the Ritter Range, the Quartz Monzodiorite or Rush Creek, Granite of Billy Lake, Aplite, and Granite of Shellenbarger Lake

Samples	Rb, ppm	Sr, ppm	Atomic Ratio $^{87}Rb/^{86}Sr$	Atomic Ratio $^{87}Sr/^{86}Sr$
F70-11	111	200	1.60	0.7071
F65-144	159	206	2.23	0.7078
F70-36	125	118	3.05	0.7093
F73-10	127	116	3.17	0.70914
F65-151	148	101	4.25	0.7106
F70-16	177	118	4.34	0.7110
F70-35	144	94	4.41	0.7113
Sr-13*	90	462	0.565	0.70532
Sr-21*	123	373	0.95	0.70620
Sr-22*	128	368	1.01	0.70643
Sr-12†	187	287	1.89	0.70749
Sr-9†	200	255	2.26	0.70781
Sr-10†	209	252	2.40	0.70825
EG‡	190	92	5.98	0.71300
MC-14B§	128	66	5.62	0.71282

Age = 99.9 ± 2.2 m.y.; r_i = 0.70478 ± 0.00011; MSWD = 0.74.
* Quartz monzodiorite of Rush Creek.
† Granite of Billy Lake.
‡ Granite of Shellenbarger Lake.
§ Aplite.

of colorless augite ($2V_z$ = 60°). Biotite is pleochroic (dark brown to pale brown) and occurs as isolated, ragged crystals or associated with and replacing hornblende. Chlorite was observed in one thin section. Accessory minerals are magnetite, apatite, and sphene. Chemically, the diorite of Waugh Lake (Table 5) is similar to the andesites in the upper part of the Koip sequence.

In the Ritter Range, *Fiske and Tobisch* [1978] reported ages of 153–158 m.y. on zircons from tuffs in the Jurassic volcanic rocks in their intermediate zone (which are included in but not differentiated in the upper part of the Koip sequence of Figure 1). Specimens of the volcanic rocks from which the zircons were dated yield a Rb-Sr whole-rock isochron age of 163 ±5 m.y. (Table 6). No other volcanic rocks of this age have been found in the area of Figure 1. The distribution of the rocks of this age indicates that they are repeated in the intermediate zone by unrecognized folds and faults.

Cretaceous Rocks

Two units comprise the western part of the metamorphosed volcanic rocks in the Ritter Range. The younger unit, which lies unconformably on the older unit, is middle Cretaceous in age based on U-Pb zircon ages of 101 and 98 m.y. [*Fiske and Tobisch*, 1978]. Samples of this unit, the granite of Shellenbarger Lake, and a small zoned pluton to be discussed below define a whole-rock Rb-Sr isochron age of 99.9 ±2.2 m.y. (Figure 5, Table 7). Rocks from the lower unit of this youngest part of the section have a U-Pb zircon age of 127 m.y. [*Fiske and Tobisch*, 1978], and a Rb-Sr whole-rock age of 134 ±13 m.y. (Table 8, Figure 6). Rocks in the Cretaceous part of the section are much less deformed than is the older Koip sequence. The Cretaceous rocks are faulted against the Koip sequence, and their upper contact is with late Cretaceous plutons [*Fiske and Tobisch*, 1978].

TABLE 8. Rb-Sr Data for the Lower Unit of the Cretaceous Metamorphosed Volcanic Rock Section in Ritter Range and Lower Part of Dana Sequence

Samples	Rb, ppm	Sr, ppm	Atomic Ratio $^{87}Rb/^{86}Sr$	Atomic Ratio $^{87}Sr/^{86}Sr$
MD-18*	155	149	3.01	0.70995
F70-30	113	163	2.00	0.7082
F70-32	183	201	2.63	0.7092
F73-9	146	220	1.92	0.70775

Age = 134 ± 13 m.y.; r_i = 0.70424 ± 0.0006; MSWD = 0.52.
* Dana sequence.

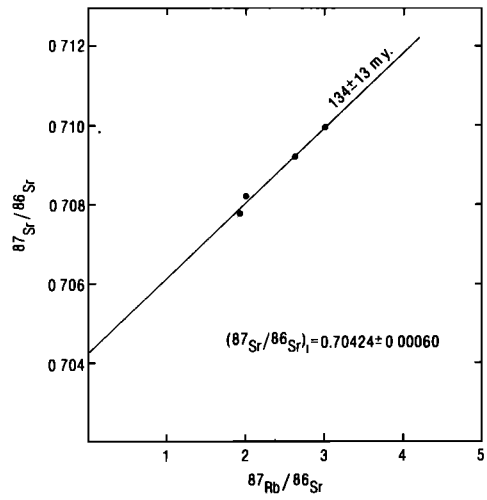

Fig. 6. Rb-Sr whole rock isochron of Early Cretaceous metamorphosed volcanic rocks from the Ritter Range. Analytical data are given in Table 8. Age = 134 ± 13 m.y., r_i = 0.70424 ± 0.00060; MSWD = 0.5204.

North of the Ritter range, *Kistler* [1966*a*,*b*] defined the Dana sequence to include a group of moderately deformed metamorphosed volcanic and associated sedimentary rocks. These rocks likewise do not exhibit as much or as many deformations as the underlying metamorphosed volcanic rocks of the Koip sequence. *Kistler* [1966*a*] assigned the Dana sequence an Early Jurassic age on the basis of lithologic similarity to Lower Jurassic rocks in west central Nevada [*Ferguson and Muller*, 1949], but Rb-Sr whole rock analyses from a vol-

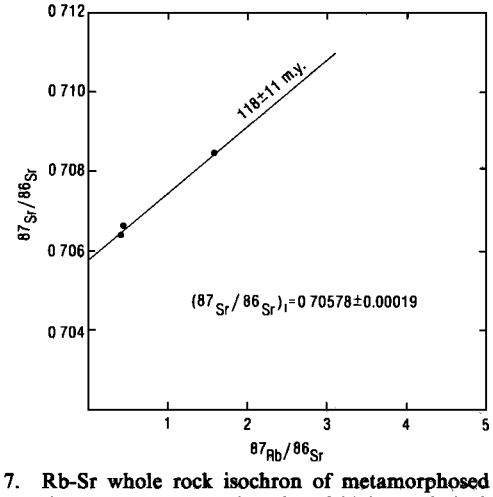

Fig. 7. Rb-Sr whole rock isochron of metamorphosed volcanic rock from the Dana sequence [*Kistler* 1966*a*]. Analytical data are given in Table 6. Age = 118 ± 11 m.y.,; r_i = 0.70578 ± 0.00019, MSWD = 0.5696.

TABLE 9. Rb-Sr Data for Metamorphosed Tuff From the Uppermost Part of the Dana Sequence

Samples	Rb, ppm	Sr, ppm	Atomic Ratio $^{87}Rb/^{86}Sr$	Atomic Ratio $^{87}Sr/^{86}Sr$
MD-12D	67	466	0.42	0.70639
MD-12E	80	519	0.45	0.70663
MD-12	109	199	1.59	0.70844

Age = 118 ± 11 m.y.; r_i = 0.70578 ± 0.00019; MSWD = 0.57.

canic unit in the uppermost part of the Dana sequence indicate middle Cretaceous age of 118 ±11 m.y. (Figure 7, Table 9). Rb-Sr whole rock data for a specimen of a tuff from the lower part of the Dana sequence lies on the 134 m.y. isochron of Figure 6. These data are sufficient only to demonstrate that the Dana sequence is composed of Cretaceous rocks. Some of the lithologically similar rocks in west central Nevada have also been found to be of Cretaceous age [*Speed and Kistler*, 1980]. The Dana sequence lies unconformably above the Koip sequence [*Kistler*, 1966*a*; *Russell*, 1977]. Chemical analyses from the Ritter Range (Table 10) correspond to dacite-rhyodacite (66–74 wt % SiO_2).

The metamorphosed volcanic rocks of middle-Cretaceous age in the Ritter Range are thought to have formed in association with a caldera called the Minarets caldera [*Fiske et al.*, 1977]. In the upper part of the section is a thick breccia unit that could be the result of caldera collapse [*Fiske and Tobisch*, 1978]. Volcanic rocks in the Dana sequence are not abundant, and most of the sequence is composed of volcaniclastic sedimentary rocks [*Kistler*, 1966*a*,*b*; *Russell*, 1977].

GRANITOID CRETACEOUS VOLCANIC CONDUIT

Most of the granitic rocks in the area of Figure 1 are Triassic (215–200 m.y.) and Cretaceous (94–80 m.y.) [*Evernden and Kistler*, 1970] and are thus not the same age as the metamorphosed volcanic rocks in the area. An exception to this rule is a composite pluton (Figure 2), with an outcrop pattern suggestive of a ring dike with a core of granite and a rim of quartz monzodiorite. *Kistler* [1966*b*] mapped the pluton as two separate masses—the quartz monzodiorite of Rush Creek and the granite of Billy Lake—based on cross-cutting contacts showing the granite to be younger. However, the contact is gradational in some places. This observation and the chemical

TABLE 10. Chemical Analyses and Norms of the Middle Cretaceous Metavolcanic Rocks from the Ritter Range in the Devils Postpile Quadrangle

Samples*	F65-144	F70-16	F70-11	F70-36	F65-151	F73-10	F70-35
			Chemical Analysis, wt %				
SiO_2	65.9	66.6	68.7	72.6	73.5	73.6	74.1
Al_2O_3	15.5	14.8	15.1	13.2	13.6	13.3	13.0
Fe_2O_3	0.60	0.30	0.80	0.80	0.30	0.30	0.40
FeO	4.2	5.2	3.8	3.3	2.8	2.3	3.0
MgO	1.5	0.59	0.85	0.21	0.30	0.15	0.15
CaO	2.8	1.7	2.0	1.7	1.0	0.69	0.80
Na_2O	3.4	4.6	4.5	4.6	3.7	4.0	4.2
K_2O	4.1	5.1	3.6	4.4	4.9	4.6	4.8
H_2O^+	0.5	0.65	0.80	0.33	0.74	0.31	0.27
H_2O^-	0.14	0.02	0.06	0.02	0.8	0.26	0.03
TiO_2	0.56	0.24	0.42	0.12	0.09	0.15	0.08
P_2O_5	0.10	0.04	0.08	0.02	0.02	0.05	0.01
MnO	0.08	0.09	0.07	0.03	0.08	0.09	0.04
CO_2	0.06	0.54	0.02	0.04	0.02	0.06	0.08
Rb†	159	177	111	125	198	127	144
Sr†	206	118	200	118	101	116	94.3
Sum	99.44	100.47	100.80	101.37	101.13	99.86	100.96
Rb/Sr	0.772	1.50	0.555	1.06	1.96	1.14	1.53
K/Rb	214	239	269	292	275	301	277
$\delta^{18}O$ SMOW			6.23 ‰	2.11 ‰			2.25 ‰
δD SMOW			−137 ‰	−108 ‰			−110 ‰
			CIPW Norms, wt %				
q	19.7	13.3	20.9	24.1	28.5	29.6	27.5
c	0.8		0.4		0.5	0.7	
or	24.2	30.1	21.3	26.0	29.0	27.2	28.4
ab	28.8	38.9	38.1	38.9	31.3	33.8	35.5
an	12.9	4.7	9.3	2.4	4.7	2.7	2.4
di		0.1		5.0			0.8
hy	10.2	10.5	7.9	3.2	5.6	4.3	5.0
ol							
mt	0.9	0.4	1.2	1.2	0.4	0.4	0.6
hm							
il	1.1	0.5	0.8	0.2	0.2	0.3	0.2
ap	0.2	0.1	0.2				
cc	0.1	1.2		0.1		0.1	0.2
Total	98.9	99.8	100.1	101.1	100.2	99.2	100.6

* Analyst, Lowell Artis.

† Concentration reported in parts per million.

TABLE 11. Chemical Analyses and Norms of the Middle Cretaceous Plutonic Rocks in the Mono Craters Quadrangle

	Quartz Monzodiorite of Rush Creek			Granite of Billy Lake			Aplite
Samples*	Sr-13	MC-29	Sr-22	Sr-12	MC-14A	Sr-10	MC-14B
			Chemical Analyses, wt %				
SiO_2	60.0	63.37	64.5	68.1	68.99	69.0	76.12
Al_2O_3	17.0	15.87	16.2	15.0	15.22	14.7	12.77
Fe_2O_3	2.4	1.77	2.1	1.5	1.12	1.2	0.36
FeO	4.0	3.40	3.2	2.7	1.90	2.4	0.27
MgO	2.4	1.95	1.6	1.2	1.02	0.92	0.02
CaO	4.8	3.83	3.1	2.7	2.60	2.3	0.72
Na_2O	4.2	3.67	4.0	3.5	3.54	3.4	2.85
K_2O	2.9	3.64	3.6	4.5	3.92	4.7	5.99
H_2O^+	0.59	0.61	0.79	0.55	0.34	0.45	0.07
H_2O^-	0.28	0.10	0.31	0.28	0.04	0.25	0.06
TiO_2	0.80	0.72	0.68	0.58	0.42	0.47	0.11
P_2O_5	0.25	0.18	0.22	0.16	0.10	0.12	0.02
MnO	0.10	0.1	0.09	0.07	0.06	0.06	0.013
CO_2	0.02	0.02	0.07	0.06	0.01	0.04	0.02
Rb†	90.1	140	128	187	143	209	128.4
Sr†	462	283	368	287	293	252	66.2
Sum	99.74	99.23	100.46	100.84	99.28	100.01	99.39
Rb/Sr	0.195	0.495	0.347	0.652	0.488	0.829	1.08
K/Rb	267	216	233	200	228	187	371
$\delta^{18}O$ SMOW	7.10 ‰			6.23 ‰		7.80 ‰	
δD SMOW	−115 ‰			−131 ‰		−111 ‰	
			CIPW Norms, wt %				
q	10.2	16.4	17.9	22.2	26.0	24.3	35.4
c			0.8		0.7	0.2	0.4
or	17.3	21.8	21.4	26.6	23.4	28.0	35.7
ab	35.9	31.5	34.1	29.6	30.3	29.0	24.3
an	19.2	16.3	13.6	11.9	12.3	10.4	3.3
di	2.6	1.3					
hy	9.1	8.1	7.2	5.9	4.6	5.1	0.1
ol							
mt	3.5	2.6	3.1	2.2	1.6	1.8	0.5
hm							
il	1.5	1.4	1.3	1.1	0.8	0.9	0.2
ap	0.6	0.4	0.5	0.4	0.2	0.3	0.1
cc	0.1	0.1	0.2	0.1		0.1	0.1
total	100.0	99.9	100.1	100.0	99.9	100.1	100.0

* Analyst, R. Espos.
† Concentration reported in parts per million.

and isotopic data indicate that these granitic rocks are not only comagmatic, but that they are plutonic equivalents of some of the volcanic rocks in the Ritter Range to the south. Also significant in this regard is the appearance of the granite of Shellenbarger Lake (Figure 1), whose miarolitic cavities and a granophyric texture are generally attributed to the subvolcanic intrusive environment [*Erwin*, 1934; *Huber and Rinehart*, 1965; *Fiske and Tobisch*, 1978].

Petrography of the Granitic Rocks

Quartz monzodiorite of Rush Creek. The quartz monzodiorite of Rush Creek (Figure 2) intruded metamorphosed volcanic rocks of the Koip sequence and the diorite of Waugh Lake and is intruded by the granite of Billy Lake [*Kistler*, 1966*b*]. This small pluton surrounds the granite of Billy Lake on three fourths of its perimeter. The western part of the quartz monzodiorite contains inclusions of volcanic rocks and the diorite of Waugh Lake. Much of the contact between the diorite and the quartz monzodiorite is diffuse and poorly defined. This and the gradational mineralogy of the quartz monzodiorite in this area (Figure 8), suggests homogenization of the diorite and quartz monzodiorite along the contact zone. The contact is better defined along the extreme western edge, where inclusions of metamorphosed volcanic rocks are between the diorite and quartz monzodiorite.

In thin section, the quartz monzodiorite appears porphyritic with rounded subhedra of plagioclase in a fine-grained cataclastic matrix of ragged feldspar and quartz recrystallized by subsequent contact metamorphism. Plagioclase (An_{40}) is mostly zoned with cores of labradorite. Hornblende is pleochroic, and some crystals have small granular augite ($2V_z = 60°$) cores. Biotite has replaced some hornblende. Chlorite, associated with biotite, was found in about half of the sections. Accessory minerals are sphene, magnetite, and apatite.

Alkali feldspars show a considerable amount of textural diversity, and modal amounts vary from 0 to as much as 46% along the contact between the granite and the quartz monzodiorite (Figure 8). Alkali feldspar is generally anhedral and interstitial, but in samples containing more than 20% alkali

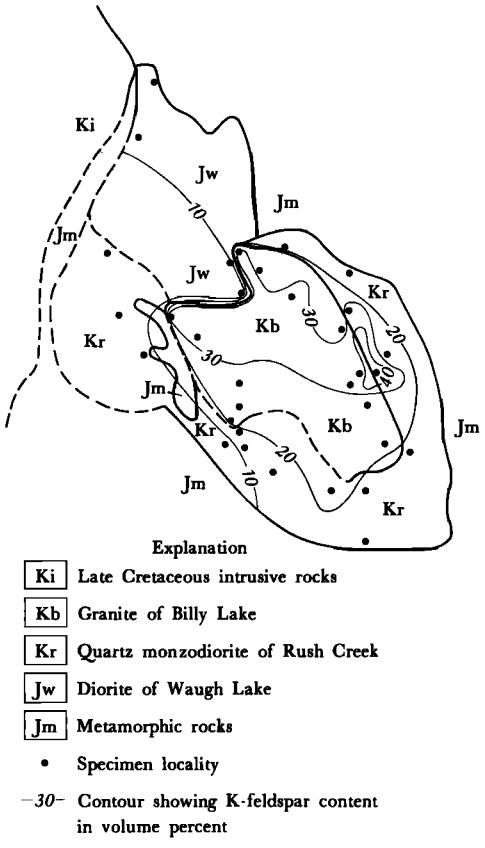

Fig. 8. Distribution of K-feldspar in the Billy Lake–Rush Creek pluton. Contours are in volume percent.

feldspar, the grains are commonly subhedral and coarse (to 6 mm). The distribution of alkali feldspar (Figure 8) suggests that it was introduced from the granite. Where alkali feldspar is interstitial, individual grains are undeformed and commonly rimmed by semiradial myrmekitic intergrowths of plagioclase and quartz which appear to have grown from a small mass of silicate liquid. Alkali feldspar, the last phase to crystallize in the rock, forms an interstitial mass between the myrmekite grains. Chemical analyses of the quartz monzodiorite of Rush Creek (Table 11) range from 60 to 65 wt % SiO_2 in no obvious areal pattern.

Granite of Billy Lake. The outcrop area of the white or light gray granite of Billy Lake totals a little more than one square kilometer (Figure 2). The small pluton intruded metamorphosed volcanic rocks of the upper part of the Koip sequence, the diorite of Waugh Lake, and the quartz monzodiorite of Rush Creek. the contact between the granite and the quartz monzodiorite is abrupt on the west and east sides, but gradational along the south, indicating limited mixing. Aplite dikes, emanating from the granite, sharply intrude the quartz monzodiorite (Figure 2). Thus the crystallization of the quartz monzodiorite barely preceded the crystallization of the last of the granite.

In thin section the granite is seen to be porphyritic with subhedral crystals of plagioclase ($An_{31,32}$), alkali feldspar, or hornblende in a matrix of ragged crystals of the same minerals and biotite. Even though broken phenocrysts are seldom found, the matrix has a recrystallized cataclastic appearance. Plagioclase and alkali feldspar are in phenocrysts up to 7 mm long. Alkali feldspar is subhedral with grid twinning. The mafic minerals have the same physical characteristics as those in the quartz monzodiorite of Rush Creek, but pyroxene was observed in the core of hornblende in only one sample of the granite. Accessory minerals are magnetite, sphene, and zircon. Chlorite replaces biotite in nearly all samples of the granite. Chemical analyses of the granite of Billy Lake (Table 11) show little variation in SiO_2 (68–69 wt %).

Aplite dikes. Light-colored, fine-grained, allotriomorphic-granular dikes from 0.01 to 2 m wide occur along the contact between the quartz monzodiorite and granite (Figure 2) only where the contact is sharp. The dikes can be traced for only short distances into the granite. Within the granite the margins of the dikes become diffuse and ill-defined and finally merge into the hypidiomorphic-granular granite.

The dikes contain alkali feldspar, plagioclase, and quartz with minor biotite and traces of chlorite, apatite, and magnetite. Grain size is rather uniform, from 1 to 2 mm. All of the minerals in the dikes are anhedral, making it difficult to determine a crystallization history. Textures show no evidence of deformation. Chemical composition of one of the dikes is given in Table 11. The silica content, over 74 wt %, is the highest of any intrusive unit associated with the ring dike complex. The modal mineralogy of one specimen of the dikes plots in the quartz syenite field (Figure 9).

Structures and textures. Both the granite of Billy Lake and the quartz monzodiorite of Rush Creek have pronounced lineations which trend westward and plunge steeply (Figure 2). The lineation consists of spindle-shaped mafic clots as much as a meter long and streaks and trains of biotite and hornblende. At the highest elevations along the eastern granite-quartz monzodiorite contact, the lineation merges into a north-trending foliation with a steep westerly dip. The transition from lineation to foliation with increasing elevation may reflect a constriction in flow at the roof or sides of the intrusion during emplacement.

Thin sections show that the quartz monzodiorite and granite are characterized by a cataclastic groundmass composed of anhedral feldspar and quartz that surrounds larger, less deformed grains of feldspar, hornblende, and biotite. This tex-

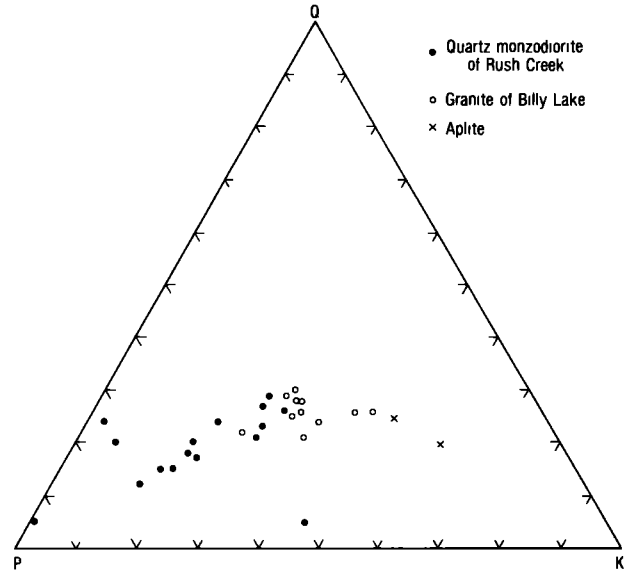

Fig. 9. Modal quartz—plagioclase—K-feldspar diagram for the middle Cretaceous plutonic rocks. 1000 data points on stained slabs.

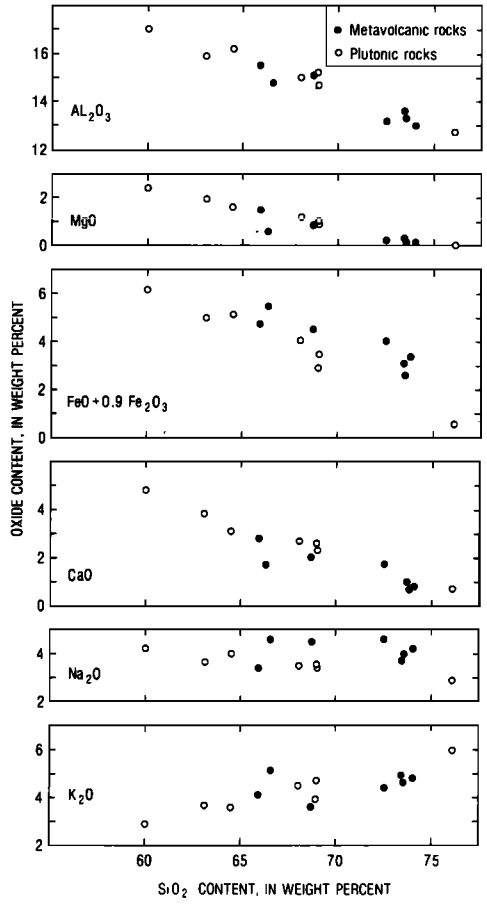

Fig. 10. SiO_2-oxide variation diagrams for the middle Cretaceous plutonic and volcanic samples.

ture is present throughout both plutons, except near the inclusion of metamorphic rock north of Waugh Lake and in the aplite dikes associated with the rim of the granite. The deformation that produced the crushing must have occurred after much of the magma had crystallized, since the late-crystalliz-

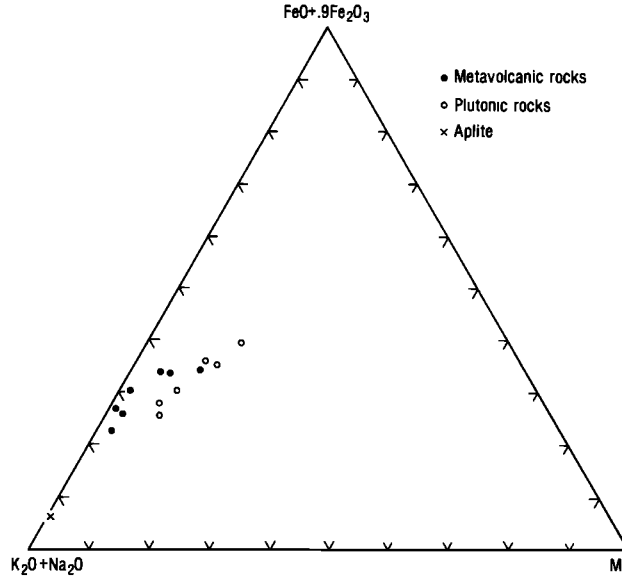

Fig. 11. AFM variation diagram for the middle Creataceous plutonic and volcanic samples.

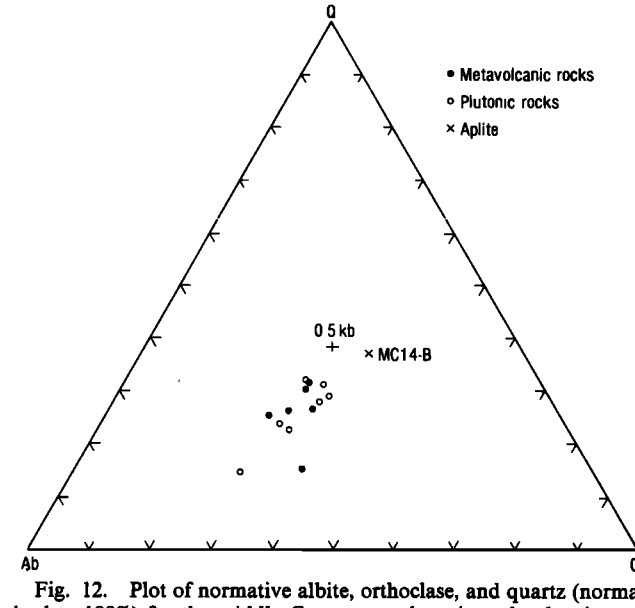

Fig. 12. Plot of normative albite, orthoclase, and quartz (normalized to 100%) for the middle Cretaceous plutonic and volcanic samples. Also shown is the 0.5-kb minimum in the system $NaAlSi_3O_8$–$KAlSi_3O_8$–SiO_2–H_2O after *Tuttle and Bowen* [1958]. Sample MC-14b, from an aplite dike, plots close to this minimum.

ing minerals alkali feldspar and quartz are included within the deformed groundmass. The presence of at least some silicate liquid subsequent to the deformation is indicated by the undeformed myrmekite-alkali feldspar masses in the quartz monzodiorite and aplite dikes.

Petrogenesis of the Intrusive Rocks

A standard quartz-plagioclase-alkali feldspar diagram (Figure 9) allows but does not prove that the granite and quartz monzodiorite are comagmatic and that the aplite dikes repre-

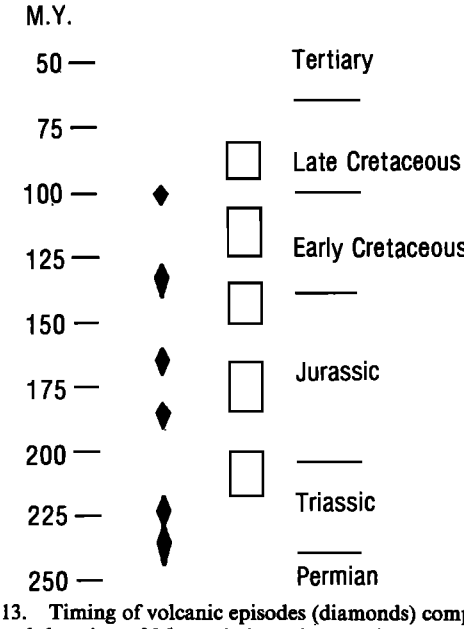

Fig. 13. Timing of volcanic episodes (diamonds) compared to the timing and duration of Mesozoic intrusive epochs (rectangles) in the Sierra Nevada. Period boundaries are from time scale adopted by the U.S. Geological Survey in 1980.

sent the last magma to crystallize. The mineralogical relationships and field evidence establish rather firmly that the sequence was quartz monzodiorite-granite-aplite.

The radial distribution of the aplite dikes is probably a response to a stress field produced by a vertical movement of magma just prior to solidification, followed by a relaxation of sinking. Likely a caldera once lay overhead, and the radial fractures served as conduits for residual silicate liquid. Thus the plutons would have a cataclastic texture whereas the dikes would not. Both the aplite dikes in the granite and the interstitial masses of alkali feldspar and myrmekite in the quartz monzodiorite are post-deformational crystallization products. Both features are composed of Ab-rich plagioclase, alkali feldspar, and quartz. The same deformation that broke and deformed crystals may have squeezed the silicate liquid in intersticies, where it crystallized.

Isotopic relationships also suggest that the intrusive rocks are related. The Rb-Sr data define a single isochron with a common age (99.9 ± 2.2 m.y.) and common initial $^{87}Sr/^{86}Sr$ (0.7048 ± 0.0001) (Figure 5). Significantly, the analyses of the mid-Cretaceous volcanic rocks of the Ritter Range and of the granite at Shellenbarger Lake plot on the same isochron. Inasmuch as the volcanic rocks are more than 5 km from the Rush Creek and Billy Lake bodies, a direct field relation cannot be demonstrated; the granite of Shellenbarger Lake is intruded directly into the middle Cretaceous volcanic rocks (Figure 1). The composition of some middle Cretaceous metamorphosed volcanic rocks from the Ritter Range (Figures 10, 11, and 12) show that, although chemical data from the volcanic rocks and plutonic rocks plot on similar trends, there is some scatter in the volcanic rock data. This pattern has been found in other areas of comagmatic volcanic rocks and plutonic rocks [*Tilling*, 1974]. In ash flows, *Walker* [1972], *Sparks and Walker* [1977] and *Flood et al.* [1980] have shown that, during eruption, selective loss of fine vitric fragments can be as much as 35% by weight of the vitric component of the original material. This process would both increase the phenocryst/glass ratio in the ash flows and lead to scatter on chemical variation diagrams. The light oxygen-isotope compositions of two of the volcanic rocks (Table 10) indicate a significant exchange of oxygen from meteoric water, which could be additional reason for the scatter.

The composition of the aplite dikes may be used to estimate the depth of intrusion of the pluton [*Putman and Alfors*, 1965]. *Tuttle and Bowen* [1958] recognized a systematic shift with pressure in silicate liquid composition of the ternary minimum point in the system $NaAlSi_3O_8$–$KAlSi_3O_8$–SiO_2–H_2O. Silicate liquids in equilibrium with quartz, alkali feldspar, and vapor in the synthetic system show a progressive shift with increasing pressure to more Na-rich compositions. Presence of small amounts of Ca to the system causes the depth estimates based on the Ca-free system to be minimum values [*Swanson*, 1978]. The normative composition of the analyzed aplite (Table 11) from the granite plots near the 0.5 kb minimum (Figure 12), corresponding to a minimum estimate of depth in the 1-2 km range. This depth too is consistent with the position of a shallow volcanic conduit in the base of a large stratovolcano, as already suggested for the quartz monzodiorite of Rush Creek and the granite of Billy Lake.

DISCUSSION

A history of Mesozoic volcanism spanning about 125 m.y. has been documented in the eastern Sierra Nevada. During the same span of time the composite Sierra Nevada batholith was intruded in five major epochs of magma generation and emplacement, each separated by about 30 m.y., [*Evernden and Kistler*, 1970]. Ages of eruption of the Mesozoic volcanic rocks (Figure 13) occur close to the beginning of, or in the intervals between, the intrusive epochs. Most, but not all, of the volcanic rocks are more alkalic and have lower initial strontium isotopic compositions than the plutonic rocks that intrude them [*Kistler and Peterman*, 1973]. The subvolcanic quartz monzodiorite of Rush Creek and granite of Billy Lake have a peacock index of 54, are alkali-calcic, and have initial $^{87}Sr/^{86}Sr$ of 0.7048, whereas the Triassic and Late Cretaceous plutons in the area are calc-alkalic with initial $^{87}Sr/^{86}Sr$ values of 0.7056 to 0.7066 [*Kistler*, 1974]. Thus we see that the volcanic rocks are not simply or directly related to the major plutons. Instead, the principal silicic volcanic episodes apparently occurred during brief periods of relaxation during an overall compressive regime along the American continental margin, or during times when the direction or rate of plate convergence was changing [*Kistler*, 1978]. The quartz monzodiorite of Rush Creek and granite of Billy Lake are an exceptional case of plutons that apparently can be related to some of the Mesozoic volcanic rocks. They are distinct in size, texture, composition, and isotopic signature from the predominant plutons of the batholith, which apparently did not vent volcanic facies in significant volumes.

Acknowledgments. Richard S. Fiske and Othmar T. Tobisch collected the specimens from the Ritter Range. Useful comments on an early draft of the manuscript were made by F. C. W. Dodge and Robert J. Fleck of the U.S. Geological Survey. Later comments by M. E. Bickford and especially Leon E. Long were extremely helpful.

REFERENCES

Bateman, P. C., Geology and tungsten mineralization of the Bishop district, California, *Geol. Surv. Prof. Pap. U.S., 470*, 1965.

Brook, C. A., Stratigraphy and structure of the Saddlebag Lake roof pendant, Sierra Nevada, California, *Geol. Soc. Am. Bull., 88*, 321–334, 1977.

Brooks, C., S. R. Hart, and I. Wendt, Realistic use of two-error regression treatments as applied to rubidium-strontium data, *Rev. Geophys. Space Phys., 10*, 551–577, 1972.

Chesterman, C. W., Geology of the Matterhorn Peak Quadrangle, Mono, and Tuolumne Counties, California, Map, Sheet 22, Calif. Div. Mines and Geol., 1975.

Doering, W. P., A rapid method for measuring the Rb/Sr ratio in silicate rocks, *Geol. Surv. Prof. Pap. U.S., 600-C*, C164–C168, 1968.

Erwin, H. D., Geology and mineral resources of northeastern Madera County, California, *Calif. J. Mines Geol., 30*, 7–78, 1934.

Evernden, J. F., and R. W. Kistler, Chronology of emplacement of Mesozoic batholithic complexes in California and western Nevada, *Geol. Surv. Prof. Pap. U.S., 623*, 1970.

Ferguson, H. G. and S. W. Muller, Structural geology of the Hawthorne and Tonopah quadrangles, Nevada, *Geol. Surv. Prof. Pap. U.S., 216*, 1949.

Fiske, R. S., and O. T. Tobisch, Paleogeographic significance of volcanic rocks of the Ritter Range pendant, central Sierra Nevada, California, in *Mesozoic Paleogeography of the western United States*, pp. 209–222, edited by D. G. Howell and K. A. McDougall, Society of Economic Paleontologists and Mineralogists, Pacific Sec tion, Los Angeles, Calif., 1978.

Fiske, R. S., O. T. Tobisch, R. W. Kistler, T. W. Stern, and M. Tatsumoto, Minarets caldera: A Cretaceous volcanic center in the Ritter Range pendant, central Sierra Nevada, California, *Geol. Soc. Am. Abstr. Programs, 9*, 975, 1977.

Flood, R. H., S. E. Shaw, and B. W. Chappell, Mineralogical and chemical matching of plutonic and associated volcanic units, New England batholith, Australia, *Chem. Geol., 29*, 163–170, 1980.

Hamilton, W., and W. B. Myers, The nature of batholiths, *Geol. Surv. Prof. Pap. U.S., 554-C*, 1967.

Harland, W. B., A. C. Smith, and B. Wilcock, The Phanerozoic time scale—A symposium dedicated to Professor Arthur Holmes, *Q. J. Geol. Soc. London*, suppl., *1205*, 1964.

Huber, N. K., and C. D. Rinehart, Geologic map of the Devils Postpile quadrangle, California, geological quandrangle, *GQ-437*, U.S. Geol. Surv, Reston, Va., 1965.

Keith, W., and J. Seitz, Geologic map of the Hoover Wilderness and adjacent study area, Mono and Tuolumne Counties, California, scale 1:125,000 *Map M-F1185-A*, U.S. Geol. Surv., Reston, Va., 1981.

Kistler, R. W., Structure and metamorphism in the Mono Craters quadrangle, Sierra Nevada, California, *Geol. Surv. Bull. U.S., 1221-E*, 1966*a*.

Kistler, R. W., Geologic map of the Mono Craters quadrangle, Mono and Tuolumne Counties, California, geological quadrangle, *GQ-462*, U.S. Geol. Surv., Reston, Va., 1966*b*.

Kistler, R. W., Phanerozoic batholiths in western North America: A summary of some recent work on variations in time, space, chemistry, and isotopic compositions, *Ann Rev. Earth Planet. Sci., 2*, 403–418, 1974.

Kistler, R. W., Mesozoic paleography of California: A viewpoint from isotope geology, in *Mesozoic Paleogeography of the Western United States*, vol. 2, pp. 75–84, edited by D. G. Howell and K. A. McDougall, Society of Economic Paleontologists and Minereralogists, Pacific Section, Los Angeles, Calif., 1978.

Kistler, R. W., and Z. E. Peterman, Variations in Sr, Rb, K, Na, and initial Sr^{87}/Sr^{86} in Mesozoic granitic rocks and intruded wall rocks in central California, *Geol. Soc. Am. Bull., 84*, 3489–3512, 1973.

Moore, J. G., Geology of the Mount Pinchot quadrangle, southern Sierra Nevada, California, *Geol. Surv. Bull. U.S., 1130*, 1963.

Peck, D. L., Preliminary geologic map of the Merced Peck quadrangle, California, Mineral investigation field studies map, *MF-281*, U.S. Geol Surv., Reston, Va., 1964.

Putman, G. W., and J. T. Alfors, Depth of intrusion and age of the Rocky Hill stock, Tulare County, California, *Geol. Soc. Am. Spec. Pap., 120*, 1965.

Rinehart, C. D., and D. C. Ross, Geology of the Casa Diablo Mountain quadrangle, California, geological quadrangle, *GQ-99*, U.S. Geol Surv., Reston, Va., 1957.

Rinehart, C. D., and D. C. Ross, Geology and mineral deposits of the Mount Morrison quadrangle, Sierra Nevada, California, *Geol. Surv. Prof. Pap. U.S., 385*, 1964.

Rinehart, C. D., D. C. Ross, and N. K. Huber, Paleozoic and Mesozoic fossils in a thick stratigraphic section in the eastern Sierra Nevada, California, *Geol. Soc. Am. Bull., 70*, 941–945, 1959.

Roddich, J. C., The application of isochron diagrams in ^{40}Ar-^{39}Ar dating—A discussion, *Earth Planet. Sci. Lett., 41*, 233–244, 1978.

Russell, S. J., Structural and stratigraphic relationships of Mesozoic metavolcanic rocks in the vicinity of Mt. Dana, Yosemite National Park, California, M.S. thesis, Calif. State Univ., Fresno, Calif., 1977.

Shapiro, L., and W. W. Brannock, Rapid analyses of silicate, carbonate, and phosphate rocks, *Geol. Survey Bull. U.S., 1144-A*, 1962.

Sparks, R. S. J., and G. P. L. Walker, The significance of vitric-enriched air-fall ashes associated with crystal-enriched ignimbrites, *J. Volcanol. Geotherm. Res., 2*, 329–341, 1977.

Speed, R. C., and R. W. Kistler, Cretaceous volcanism, Excelsior Mountains, Nevada, 1, *Geol. Soc. Am. Bull., 91*, 392–398, 1980.

Swanson, S. E., Petrology of the Rocklin pluton and associated rocks, western Sierra Nevada, California, *Geol. Soc. Am. Bull., 89*, 679–686, 1978.

Tilling, R. I., Composition and time relations of plutonic and associated volcanic rocks, Boulder Batholith region, Montana, *Geol. Soc. Am. Bull., 85*, 1925–1930, 1974.

Tuttle, O. F., and N. L. Bowen, Origin of granite in the light of experimental studies in the system $NaAlSi_3O_8$–$KAlSi_3O_8$–SiO_2–H_2O, *Geol. Soc. Am. Mem., 74*, 1958.

Walker, G. P. L., Crystal concentrations in ignimbrites, *Contrib. Mineral. Petrol., 36*, 135–146, 1972.

York, D., Least-square fitting of a straight line with correlated errors, *Earth Planet. Sci. Lett., 5*, 320–324, 1969.

(Received November 11, 1980;
revised May 6, 1981;
accepted May 20, 1981.)

JOURNAL OF GEOPHYSICAL RESEARCH, VOL. 86, NO. B11, PAGES 10502-10514, NOVEMBER 10, 1981

CALEDONIAN PLUTONISM IN BRITAIN: A SUMMARY

G. C. Brown, J. Cassidy, and C. A. Locke

Department of Earth Sciences, The Open University,
Milton Keynes, MK7 6AA, United Kingdom

J. A. Plant

Institute of Geological Sciences (NERC),
London, EC1R 4DU, United Kingdom

P.R. Simpson

Institute of Geological Sciences (NERC),
London, WC1X 8NG, United Kingdom

Abstract. The Caledonian granites of Britain are a wide-ranging suite of pretectonic and posttectonic tonalite-granodiorite-granite intrusions which were emplaced in the time interval 650-380 Ma ago. The volume of magmatic products and the frequency of intrusions increased with time as closure of the Iapetus ocean occurred across the Caledonide belt in the British Isles. Early pretectonic and posttectonic intrusions (older than about 410 Ma) are distinguished from a later (post-410 Ma) group using geophysical (gravity, aeromagnetic, and heat production) and geochemical data. The evidence is interpreted in terms of a trend with time from relatively local thermal and crust-dominated melting events to a final widespread melting event at deeper levels. The latter event produced abundant intrusions with characteristics that resemble the calc-alkaline batholiths of modern destructive margins. Finally, we propose that crustal growth during the Caledonian period took place by northward lateral accretion of the European continental foreland and by vertical accretion of continental crust on both margins by underplating and by later intrusive magmatism.

Structural and Geological Framework

In Britain, the most important period of magmatic activity and crustal growth is recorded by calc-alkaline igneous tonalites, granodiorites, and granites and by metasedimentary greywackes, cherts, and black shales of Caledonian age (650-380 Ma) which crop out throughout most of the northern and western parts of the country. The igneous rocks (Figure 1) are mainly intrusive and resemble suites from modern ocean-continent covergence zones; therefore, they are interpreted as having evolved during the closure of the former Iapetus ocean along a zone from Greenland and Scandinavia through Britain to the Appalachians. In Britain, a wide variety of evidence indicates that suturing took place in Silurian times approximately through southern Scotland and central Ireland (SS in Figure 1) (Leggett et al., 1979; Phillips et al., 1976). In this way the pre-450 Ma 'American' and 'European' plates, which had different crustal structure, were brought together and some features of the Caledonian intrusions reflect this contrast.

Referring to Figure 1, the northern province is characterized by 2900 Ma old Lewisian basement (Hamilton et al., 1979) which crops out as mainly refractory granulites in the extreme northwest. This basement or its younger equivalent is overlain to the south by late Precambrian-lower Palaeozoic greenschist facies Moine and Dalradian metasedimentary cover rocks of the orthotectonic Caledonides (Watson and Plant, 1979). Downthrow on the southern side of the Highland Boundary Fault obscures these older rocks beneath a further cover of younger sediments that postdate the Caledonian metamorphism. But seismic data (Bamford et al., 1978) and the evidence of granulite xenoliths in Carboniferous volcanic vents indicated in Figure 1 (Upton et al., 1976) suggest that Proterozoic basement continues at depth to the Southern Uplands Fault and possibly farther south in Ireland. Therefore, there is good evidence that the northern Caledonide province in Britain is founded on ancient continental crust.

In contrast, there is no evidence of continental basement older than of late Precambrian (early Caledonian) age beneath the southern Caledonides. According to the isotopic data for European Precambrian crystalline rocks summarized by Zwart and Dornsiepen (1978) the early Proterozoic continental foreland (2000-2600 Ma age) must lie to the south, beneath southern Britain or continental Europe: igneous rocks of this age are known from the Channel Islands and northern France but not from southern Britain (more detailed summaries of the available evidence may be found in works by Brown et al. (1979b) and Thorpe (1979, 1981)). These authors proposed that the exposed low-grade and strongly folded greywacke-shale sequences with interbedded calc-alkaline volcanics of the southern paratectonic Caledonides (Figure 1) are the exposed part of thickened accretionary prisms of marginal and back arc basin sediments. These prisms are thought to overlie directly the metabasalts of the Iapetus ocean crust, as in models for the evolution of the Southern Uplands and central England-Wales regions by McKerrow et al. (1977)

Copyright 1981 by the American Geophysical Union.

Paper number 1B0704.
0148-0227/81/001B-0704$01.00

and Thorpe [1981], respectively. To summarize, a case can be made that the continental crust of the southern British Caledonides was formed during late Precambrian-lower Palaeozoic times.

In this paper we evaluate the role of intrusive igneous complexes in the evolution of the Caledonide crust in Britain: these complexes are numerous at outcrop (Figure 1) and, in many cases, are thought to be more extensive at depth. Until recently, they were regarded as the products of simple crustal anatexis, intrusion, and recrystallisation. But for various reasons, such as the inadequate volume of suitable source materials in the crust, the lack of high temperature assemblages in some eroded regions, the apparent immaturity of the continental crust in the southern region, and the combined evidence of different isotopic techniques, this view is now regarded as oversimplified. Although there is not universal agreement about the source of the Caledonian magmas, most workers postulate that at least some relatively juvenile material, possibly of direct mantle derivation, contributed to their formation.

Age Relations and Petrological Range

Attempts to classify the Caledonian intrusive complexes on the basis of age and petrology have been numerous and while most workers agree that several major episodes of magmatism took place, there has been some debate about how many subgroups should be identified. The most detailed attempt to unravel the history of magmatism by Read [1961], based on the relationship of the intrusions to the deformation of their host rocks, has dominated later attempts to fit radiometric ages into an evolutionary sequence (see recent summaries by Leake [1978], Pankhurst and Sutherland [1981], and Plant et al. [1980]).

It is now clear that Read's 'older granites', comprising pretectonic intrusions and vein complexes, predate the climax of Caledonian metamorphism at 485-500 Ma in the cover rocks of the northern province. These intrusions are relatively small in outcrop area and are generally concentrated (though not exclusively so) in northern Scotland (Figure 1); they are dominated by biotite-hornblende gneisses, often with augen texture and adamellite to diorite compositions, with occasional alkaline complexes. There are many associated migmatite complexes (for example, the most northerly Strath Halladale complex of mainland Scotland) in which it is often difficult to distinguish intrusive contacts between deformed plutons and high grade country rocks.

Postmetamorphic 'newer granites' were subdivided by Read [1961] into an earlier 'forceful' suite around which country rock deformation due to the intrusive process and occasional contact aureoles may be traced (e.g. Rogart, Figure 1), and a later 'permitted' suite of discordant granites with low pressure aureoles (e.g. the Cairngorm and Etive complexes in Figure 1). Most of the newer granites vary internally from dioritic to adamellitic or granitic facies, although there is a trend with time from mainly dioritic to more granitic intrusions on average. For example, the forceful Rogart and Foyers intrusions are zoned granodiorites with significant marginal tonalites and cores of biotite adamellite [Soper, 1963; Marston, 1970], whereas some of the permitted discordant intrusions, such as Cairngorm [Harry, 1965] and Shap [Locke and Brown, 1978] are relatively felsic, varying only in the range adamellite to granite. These features are not simply a function of erosion level because intrusions which contrast petrologically (e.g. Foyers and Cairngorm) are known from field evidence to be exposed at similar levels. Thus there appears to be a definite petrological change with time and an intermediate stage is represented by the Loch Doon pluton (Figure 1) [Brown et al. 1979a], which is mainly quartz monzonite at outcrop but has cumulate hypersthene diorite margins and a residual granite core. The implication that crystal fractionation has occurred is fundamental in studies of magmatic evolution in all such zoned Caledonian plutons.

In keeping with their relatively unmetamorphosed fabrics, the newer granites all have radiometric ages younger than about 460 Ma and so were emplaced during or after the closure of Iapetus [Phillips et al. 1976]. But whereas most of the forceful intrusions are indeed older, radiometrically, than most of the permitted intrusions, there are exceptions and it is possible [cf. Pankhurst and Sutherland, 1981] that changes in the style of emplacement took place at different times in different places in response to local factors. However, with the exception of some early Ordovician (c. 460 Ma old) intrusions that are concentrated in northeast Scotland, two main age groups are represented among the newer granites of both the northern and southern Caledonide provinces.

1. Pre-410 Ma intrusions of mid-Ordovician and early Silurian age such as the Strontian (435 Ma [Pidgeon and Aftalion, 1978]), Helmsdale and Foyers (420 and 415 Ma [Brown et al. 1968]) intrusions of Figure 1.
2. Post-410 Ma Siluro-Devonian intrusions, such as those of the Southern Uplands of Scotland (392-408 Ma [Halliday et al. 1980]), Etive (400 Ma [Flett Brown, 1972]) and Shap (394 Ma [Wadge et al. 1978]) in Figure 1.

Geophysical and geochemical data (Tables 1-3) show that the boundary between groups 1 and 2, as defined above, is associated with an important change in magma volumes, types, evolution, and, possibly, provenance. Therefore, we bracket group 1 intrusions with the older granites of Read [1961] as a pre-410 Ma suite (pre-mid-Silurian) which, in Figure 1, is distinguished from the later, post-410 Ma (Siluro-Devonian) group of intrusions.

Geophysical Characteristics of Caledonian Intrusions

The residual gravity, aeromagnetic, and filtered aeromagnetic expressions of British Caledonian intrusions have been assessed from the Bouguer gravity and magnetic anomaly maps of the Institute of Geological Sciences:

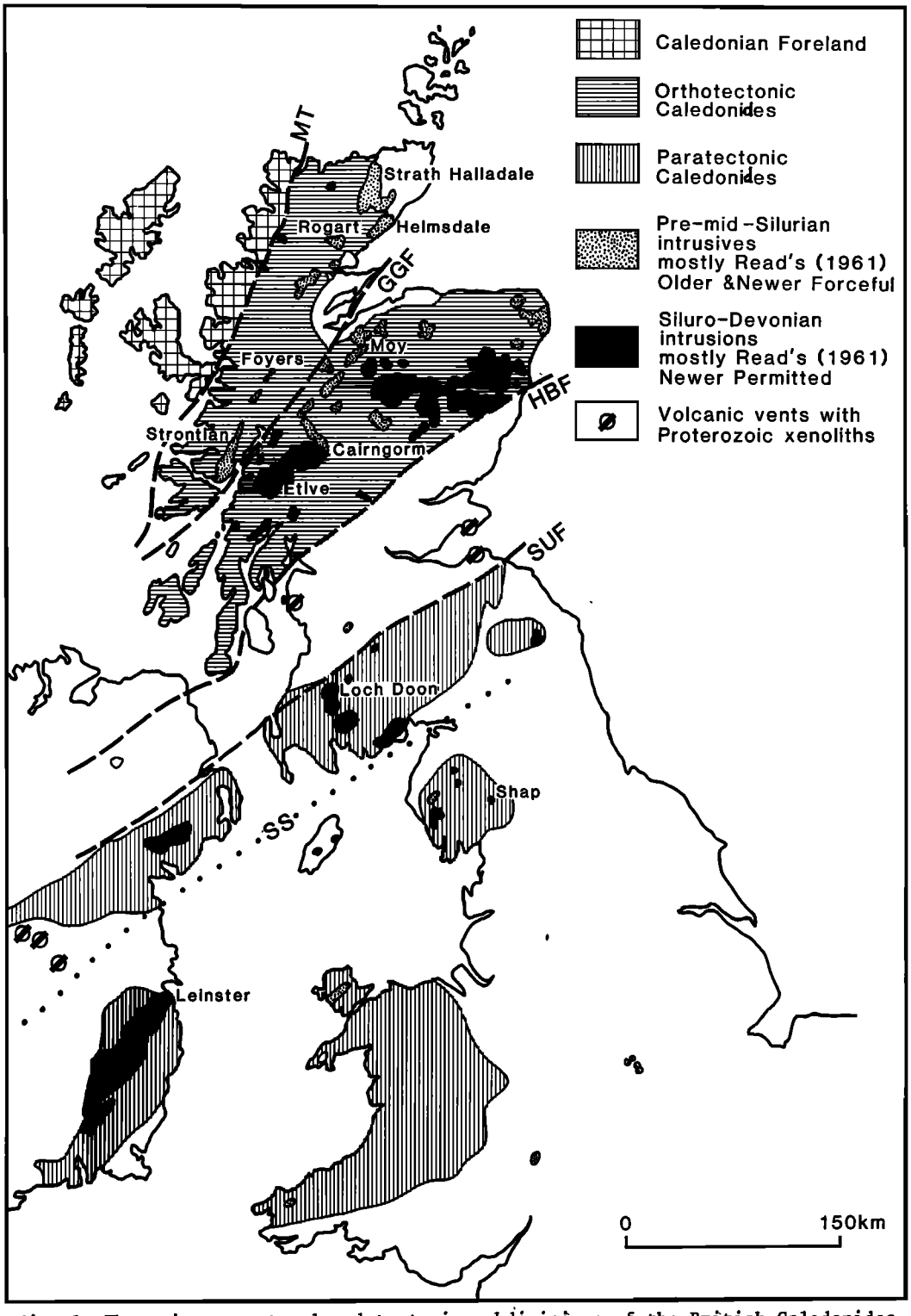

Fig. 1. The major structural and tectonic subdivisions of the British Caledonides including the main intrusive complexes which are differentiated in the text. Named intrusions received particular attention in the geophysical and geochemical data sections. MT, Moine Thrust; GGF, Great Glen Fault; HBF, Highland Boundary Fault; SUF, Southern Upland Fault; and SS, Solway-Shannon line.

summaries of these data are given in Table 1 and full details of the source data may be found in the works by Brown and Locke (1979) and Locke (1980).

Gravity characteristics. Of the pre-mid-Silurian (group 1 newer and older) intrusions assessed, 58% have no residual gravity anomaly, 16% have positive anomalies, and 26%

TABLE 1a. Summary of the Residual Gravity Expressions of British Caledonian Intrusions

Group	Number of Intrusions	Number With No Significant Residual Anomaly	Number With Positive Residual Anomaly	Number With Negative Residual Anomaly	Number With Negative Residual Anomaly of Magnitude ≥ 100 gu	Number With No Data
Northern Province						
Pre-mid-Silurian	28	15	5	7	0	1
Siluro-Devonian	30	9	0	16	10	5
Southern Province						
Pre-mid-Silurian	5	3	0	1	0	1
Siluro-Devonian	9	0	0	9	8	0
Southern Uplands						
Siluro-Devonian	4	1	0	3	3	0

TABLE 1b. Summary of the Aeromagnetic Expressions of British Caledonian Intrusions

Group	Number of Intrusions	Number With No Significant Magnetic Anomaly	Number With Positive Magnetic Anomaly	Number With Positive Anomaly of Magnitude ≥200nT	≥300nT	Number With Negative Magnetic Anomaly	Number With Negative Anomaly of Magnitude ≥200nT	≥300nT	Number With No Data
Northern Province									
Pre-mid-Silurian	28	10	14	11	0	2	1	0	2
Siluro-Devonian	30	3	14	11	4	2	1	0	11
Southern Province									
Pre-mid-Silurian	5	3	2	0	0	0	0	0	0
Siluro-Devonian	9	2	5	3	0	1	0	0	1
Southern Uplands									
Siluro-Devonian	4	3	1	1	0	0	0	0	0

TABLE 1c. Summary of the Filtered Aeromagnetic Expressions of British Caledonian Intrusions

Group	Number of Intrusions	Number With No Significant Smoothed Magnetic Anomaly	Number With Positive Smoothed Magnetic Anomaly	Number With Positive Smoothed Magnetic Anomalies of Magnitude ≥100nT	Number With Negative Smoothed Magnetic Anomaly	Number With Negative Smoothed Magnetic Anomalies of Magnitude ≥100nT	Number With No Data
Northern Province							
Pre-mid-Silurian	28	23	3	3	0	0	2
Siluro-Devonian	30	9	8	5	2	0	11
Southern Province							
Pre-mid-Silurian	5	5	0	0	0	0	0
Siluro-Devonian	9	7	1	1	0	0	1
Southern Uplands							
Siluro-Devonian	4	4	0	0	0	0	0

have negative anomalies (Table 1a). Positive anomalies range up to +130 gravity units (gu) over the Foyers intrusion; negative anomalies vary down to -90 gu over the Moy intrusion (Figure 1). In contrast, of the Siluro-Devonian (group 2 newer) intrusions assessed, 25% have no significant residual anomaly, none has a positive residual anomaly, and no less than 75% have significant negative residual anomalies, most of which are more intense than -100 gu. These negative anomalies range down to -320 gu over the Etive complex. Thus there is a significant difference between granites emplaced before and after mid-Silurian times according to gravity data. There is no question that the sizes of gravity anomalies over the Caledonian intrusions correlate significantly with depth

TABLE 2. Summary of Uranium, Thorium and Heat Production Data for British Caledonian Intrusions

Group	Number of Intrusions Analysed	Uranium, ppm		Thorium, ppm		Heat Productivity $\mu W\ m^{-3}$	
		Range	Mean	Range	Mean	Range	Mean
Pre-mid-Silurian	6	0.7-8.7	3.8	4.0-15.0	9.6	0.8-3.4	2.0
Siluro-Devonian (excluding Southern Uplands)	14	2.2-13.0	6.0	8.0-34.0	19.0	1.7-4.7	3.2
Southern Uplands	3	3.9-4.6	4.4	16.0-25.0	19.0	2.5-3.3	2.8

There are no systematic differences between the northern and southern provinces which, therefore, are not separately identified.

of erosion or the nature of the country rock: newer granites of groups 1 and 2 exposed near their roof zones have contrasting gravity expressions irrespective of their erosion level or the nature of their host rocks (Locke, 1980).

Although a simple unique interpretation of gravity data cannot be made, some constraints can be put on the causative body for each intrusion. For example, a positive residual gravity anomaly may characterize an intrusion where relatively basic rocks of greater density underlie a thin layer of granite. The positive anomaly over Foyers has been modeled as a basic body extending to a depth of 13 km beneath a 2-km-thick layer of granite (Kneen, 1973). The Rogart intrusion has no residual gravity anomaly, although its surface density of 2520 kg m^{-3} contrasts with that of the host Moine rocks (density 2700 kg m^{-3} (Locke, 1980); this body is probably very thin. A negative gravity anomaly indicates a low density intrusion; the magnitude of the anomaly depends on both the size of the intrusion and the density contrast with the country rocks which, of course, may not be constant with depth. However, in the case of the large anomaly Siluro-Devonian intrusions, a vast volume of low density material must be present to account for each anomaly, even if there were a decrease in density with depth within the intrusion. Examples of these intrusions have been modeled (Locke, 1980): Cairngorm and its neighboring intrusions extend at least to 12 km below the surface and have outward sloping margins; similarly, the Leinster intrusion extends at least to 8-km depth. These are large volumes, and clearly, a source for prodigious volumes of low density magma must be a part of any petrogenetic model.

Aeromagnetic characteristics. Many (58%) of the pre-mid-Silurian intrusions have aeromagnetic expressions (Table 1b), the largest of which is + 250 nT over the Strontian intrusion. Most of these anomalies are complex, comprising many small closed anomalies and components of different wavelengths (Brown and Locke, 1979). Significantly more (85%) of the northern province Siluro-Devonian intrusions have aeromagnetic expressions (Table 1b), reaching a maximum of + 650 nT over Etive, while fewer (58%) of the southern province Siluro-Devonian intrusions are associated with such anomalies.

These characteristics are emphasized by the filtered aeromagnetic map which reveals those anomalies with component wavelengths greater than about 13 km (Hall and Dagley, 1970): an analysis of these data appears in Table 1c. Few of the pre-mid-Silurian intrusions have expressions on this filtered map and only one of the southern province Siluro-Devonian intrusions is associated with an anomaly. However, many of the northern province Siluro-Devonian intrusions have expressions on the filtered aeromagnetic map. The origin of these anomalies must be due to deep or wide sources and is unlikely to be within the intrusions, for the magnetization parameters of most Caledonian intrusive rocks tend to be low (Kneen, 1973; Locke, 1980; Robson and Green 1980). The short wavelength, shallow-source anomalies such as those at Shap (Locke and Brown, 1978) are known to be generated by contact metamorphism around the intrusion, but the interpretation of the longer wavelength anomalies is not unique. It could be argued that a vertically inhomogeneous intrusion, increasing in magnetic components with depth would produce such an anomaly, but the implied increase in iron content necessitates an increase in density which cannot easily be reconciled with the gravity data. Therefore, it appears that the source of these anomalies may be associated magnetization of the basement through which the magmas rose from deep crustal or subcrustal levels. Thus, the difference in the filtered aeromagnetic expressions of the Siluro-Devonian intrusions of the northern province, on the one hand, and those of the Southern Uplands and the southern province on the other (Table 1c) is further evidence that there are differences between these regions in the properties of the deep crust (see earlier discussion of seismic and other contrasts).

To summarize, geophysical studies have identified: (1) variations with age: there is a significant increase in the amplitude of both gravity and aeromagnetic (northern province only) anomalies of Caledonian intrusions with decreasing age, (2) variation between provinces: the aeromagnetic expressions associated with Siluro-Devonian intrusions differ between northern and southern provinces,

TABLE 3. Summary of Age, Isotopic and Selected Trace Element Geochemical Data for British Caledonian Intrusions

Group	Age Ma	Initial $^{87}Sr/^{86}Sr$	Initial $^{143}Nd/^{144}Nd$	Inherited Zircon	Li, ppm	Y, ppm	Zr, ppm	Rb, ppm	Sr, ppm	Ba, ppm
Northern Province										
Pre-mid-Silurian	>410	0.704-0.717	0.5114-0.5121	present	2-55	4-50	60-800	55-250	300-2000	500-5000
Siluro-Devonian	400-410	0.704-0.708	0.5116-0.5118	trace or absent	2-200	2-100	20-200	200-900	60-200	50-800
Southern Province										
Pre-mid-Silurian	>410	0.704-0.708	no data	minor	no data	10-60	70-400	40-400	60-800	100-1200
Siluro-Devonian	390-410	0.705-0.708	0.5120*	trace or absent	no data	10-70	50-400	200-700	80-500	100-800
Southern Uplands										
Siluro-Devonian	392-408	0.704-0.708	no data	minor or absent	no data	10-45	50-350	80-500	60-700	150-1200

All data quoted as ranges of results presently available. Further details can be found in the source references quoted in the text.
* One value only available.

possibly reflecting a difference in basement characteristics beneath the two provinces, and (3) the Southern Uplands intrusions: the lack of Proterozoic basement beneath the margin of the northern Caledonide province in the Southern Uplands is apparently reflected in the geophysical characteristics of the intrusions in this region (see separate entries in Table 1).

Radioelements and Heat Production

Regional interintrusion and local intra-intrusion K, U, and Th distributions reflect both magma provenance and subsequent magmatic evolution. Although most Caledonian intrusions are not mineralized with respect to radioelements, many members of the Siluro-Devonian group show enrichments of these elements compared with the earlier pre-mid-Silurian group [Simpson et al. 1979; Watson and Plant, 1979]. For example, typical ranges of uranium concentrations in these groups are 2.2-13 ppm and 0.7-8.7 ppm, respectively (Table 2).

Radioelement-enriched granites can be identified readily using in situ gamma ray spectrometry. This technique allows the rapid mapping of K, U, and Th and is widely used as a uranium exploration tool [Lovborg, 1973; Duval, 1977]. Detailed field radioelement studies of the Loch Doon intrusion, for example [Cassidy, 1981], have proved that radioelement distributions correlate with magmatic trends and reflect the differentiation history of this intrusion. Fission track studies indicate that most of the U-Th-enriched Siluro-Devonian intrusions carry uranium, at least, mainly in primary accessory minerals such as zircon, apatite, sphene, and allanite [Bowie et al. 1973; Simpson et al. 1979]. These observations and the fact that the zircons of most Siluro-Devonian intrusions (analyzed for U-Pb isotopes by Pidgeon and Aftalion [1978]) are of Caledonian rather than of Proterozoic age suggest that radioelements, like their host zircons, are primary constituents of intrusions such as Etive and Cairngorm (Figure 1). In addition, it is improbable that remelting of Proterozoic basement rocks under the northern Caledonides contributed in any major way to the relevant magmas, for then inherited zircons would be identified. However, many of the earlier Caledonian intrusions (including Helmsdale, Foyers, and Strontian, Figure 1) do carry inherited zircons, indicating that ancient continental crust was involved in their magmagenesis.

Earlier, we noted that some of the larger Siluro-Devonian intrusives are relatively unfractionated at outcrop. To this can now be added the evidence from gravity and radiometric data indicating their large volumes and relatively high heat production (Table 2). This raises the question of whether the surface radioelement enrichments are preserved at depth, in which case there might be corresponding heat flow anomalies over these intrusions. In the one case where heat flow has been measured (95 mW m^{-2} at Weardale [England et al., 1980]) this has proved to be true. Thus, in regions where ancient hydrothermal convection systems,

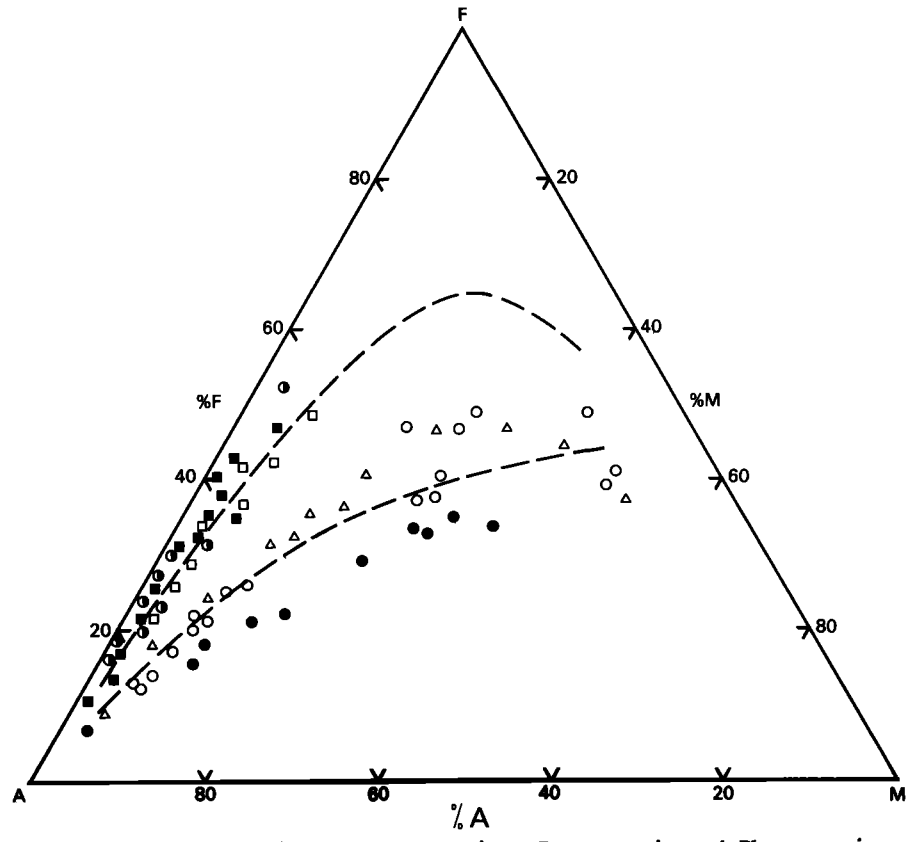

Fig. 2. AFM diagram with data for various Proterozoic and Phanerozoic intrusive suites as follows:- open circles, SW Finland trondhjemites (Arth et al. 1978); triangles, Ben Ghnema batholith, Libya (Ghuma and Rogers, 1978); solid circles, British Caledonides (Brown et al. 1979a) ; half solid circles, Pikes Peak batholith, Colorado (Barker et al. 1975) ; open squares, Fennoscandian rapakivi granites (Vorma, 1971) ; and solid squares, Nigerian younger granites (Jacobson et al. 1958) . Dashed lines indicate the limits of AFM variation for volcanic rocks of modern magmatic arcs. Further details of source and discussion in the work by Brown (1981).

leading to metalliferous mineralization, were established, such radioelement-enriched intrusions may have acted as important heat-focusing agents (Brown et al. 1980). Associations of uraniferous Caledonian granites with postintrusive metalliferous mineralization in northern England emphasize the potential importance of these ideas. Although specific uranium mineralization is not generally encountered in the British Caledonides, secondary uranium enrichments, up to 0.3%, have been located in intrusions such as Helmsdale (Figure 1) which have been affected by fluid flow along fault systems. Thus, heat production determinations in Caledonian intrusions not only reinforce the age groupings described earlier but also highlight potential sites for related metalliferous mineralization.

Geochemical Characteristics

Before considering the geochemical variations between several intrusions, first we emphasize that the Siluro-Devonian intrusions, known to have large subsurface volumes, are, in geochemical terms, typically calc-alkaline; many of these intrusions resemble the batholiths of modern ocean-continent convergence zones, such as those of the western Americas (Bateman and Dodge, 1970; Pitcher, 1978). In Figure 2, some representative Caledonian rocks are compared, on an AFM diagram, with several other major granite-bearing suites of Proterozoic and Phanerozoic age. This diagram focuses attention on the calc-alkaline, iron-depleted nature of compression zone suites, including those of the British Caledonides, which contrast with the relatively iron and alkali-enriched intrusive rocks of extension zones (further details from Brown (1981) and Petro et al. (1979)). Geochemical and isotopic data for these intrusive suites usually indicate juvenile origins, implying major contributions from within subducted ocean crust or, more likely, within the overlying mantle wedge (Saunders et al. 1980). In general terms, we favor such a model for the origin of the late Caledonian granites, as developed in detail by Simpson et al. (1979), although we note that there are some unanswered questions about a possible role of continental crust in magma genesis resulting from different interpretations of isotopic data for these intrusions (papers by Harmon and Halliday (1980), Hamilton et al. (1980), and Pankhurst and Sutherland (1981) take different views of

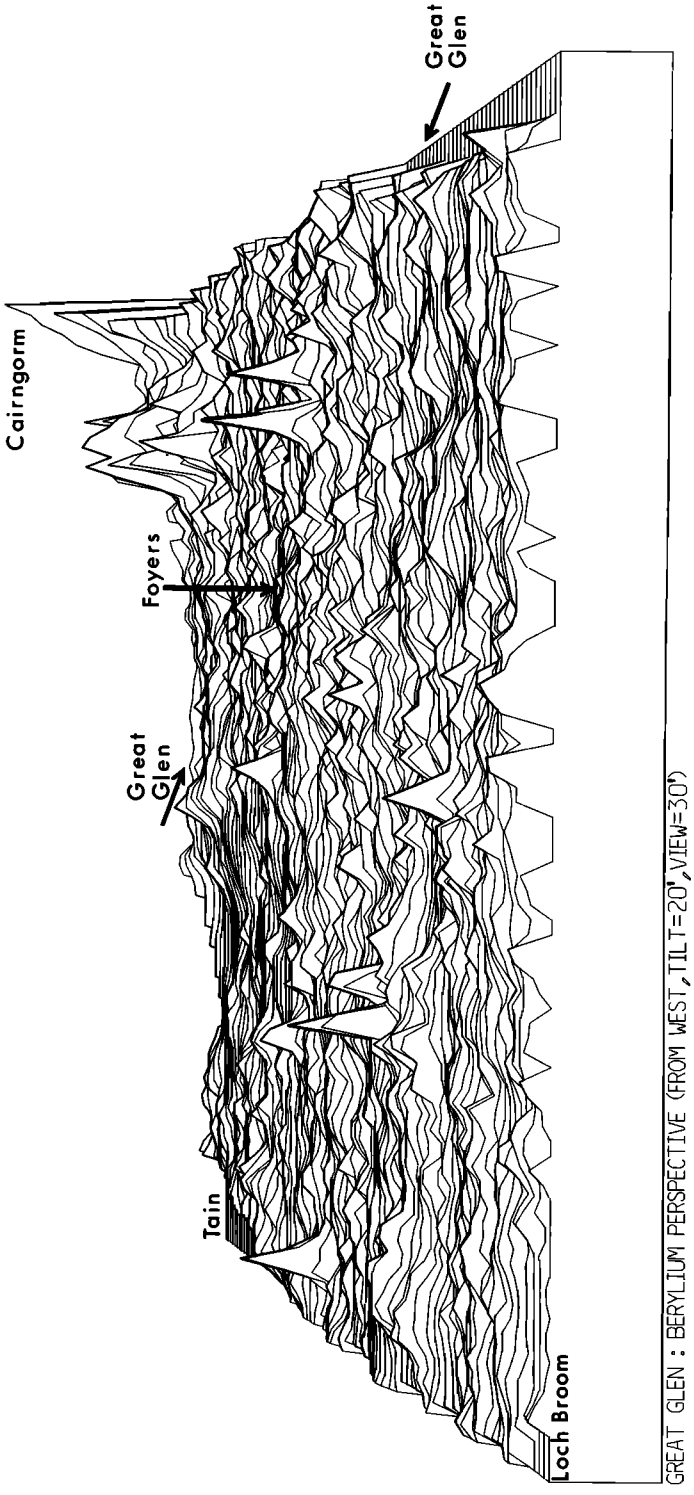

Fig. 3. Beryllium distribution over the IGS 1:250,000 scale map of the Great Glen area viewed from the west (after Johnstone et al. 1979).

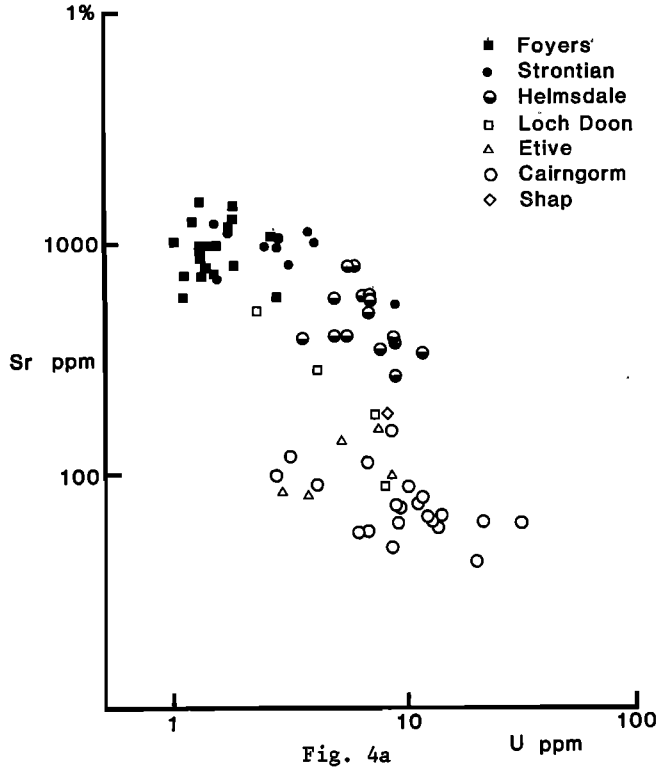

Fig. 4a

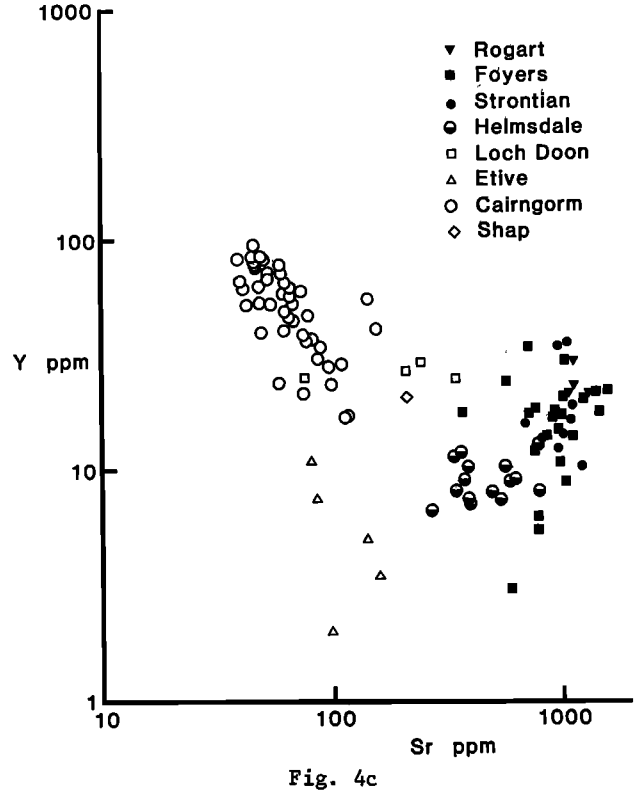

Fig. 4c

Fig.4. Selected interelement relationships for named Caledonian instrusives. (a) Strontium-uranium. (b) Barium-rubidium. (c) Yttruim-strontium. Data mainly from Plant et al.(1980), supplemented from Brown et al.(1979a) .

this problem). Some of these data are summarized in Table 3 from which it is clear that, apart from some of the early northern province intrusions, initial strontium isotope ratios are low, suggesting a strong contemporary mantle imprint. Yet the low initial neodymium ratios and the presence of small amounts of

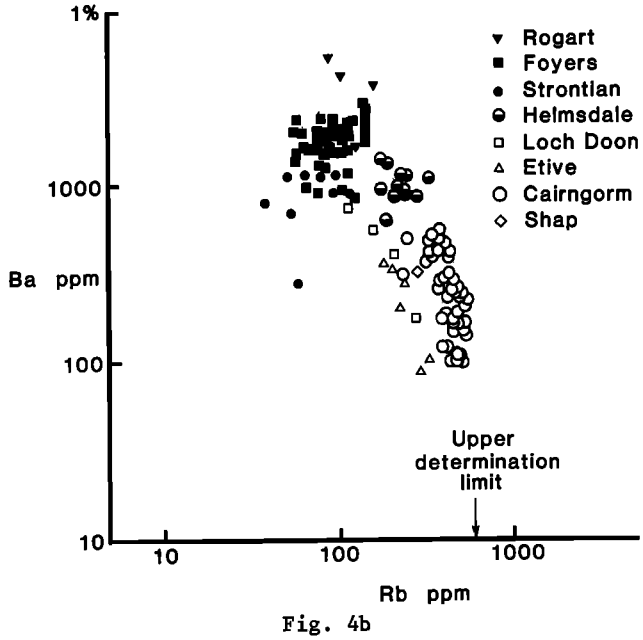

Fig. 4b

inherited Proterozoic zircon in many intrusions argue, in contrast, for an important crustal contribution to magma genesis. Despite these complications, most isotope geochemists agree that the later magmas to be emplaced may have contained a larger mantle-derived component than the earlier Caledonian granite magmas (for example, initial strontium isotope ratios and the abundance of inherited zircons are both generally lower in the Siluro-Devonian intrusions of the northern province than in the pre-mid-Silurian intrusions, Table 3). More detailed discussions of these isotopic data can be found in the references cited above; here we present additional geochemical data that relate to the question of magma genesis.

Regional geochemical maps (published by the Institute of Geological Sciences) have recently become available for a large area containing Caledonian intrusions in northern Scotland (see description by Watson and Plant (1979)). Many of the largest and most persistent anomalies on these maps occur over Siluro-Devonian granites and result from extreme enrichments of many large-ion lithophile (LIL) trace elements such as uranium, thorium (see Table 2), potassium, rubidium, caesium, and other incompatible elements such as lithium, beryllium, and molybdenum. For example, Figure 3 provides striking evidence of the enrichment of beryllium over the Cairngorm granite compared with the surrounding region, which includes the newer group 1 intrusion at Foyers. Plant et al. (1980) have drawn attention to the geochemical similarity between the pre-mid-Silurian intrusions (mainly the forceful granite suite) and their host metasediments including, in places, inliers

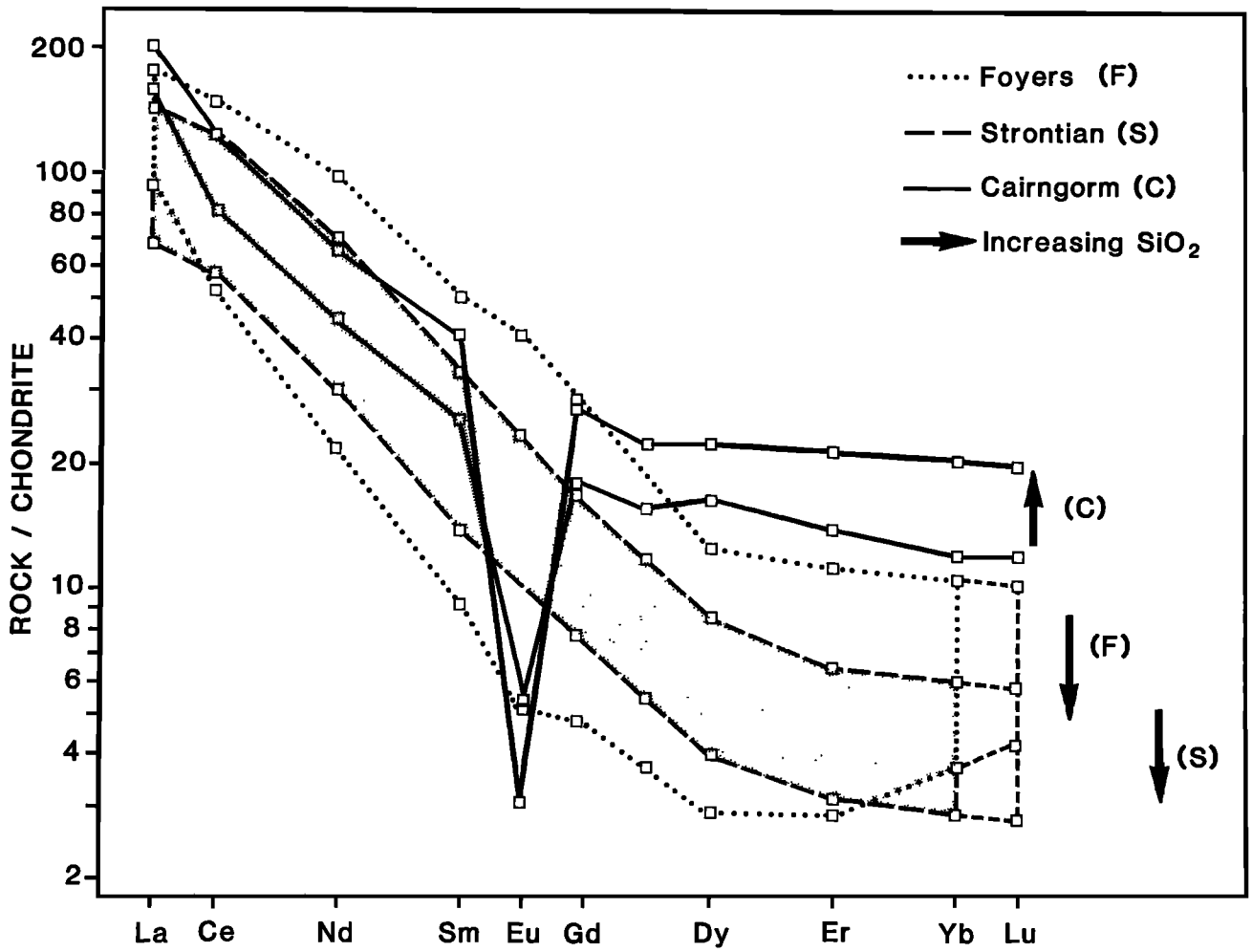

Fig. 5. Chondrite normalised rare-earth element abundances for Strontian, Foyers, and Cairngorm (data from Pankhurst [1979] and Plant et al. [1980]).

of Proterozoic basement. They argued that this reinforces the view that partial melting of crustal rocks could have provided a suitable source for these bodies but that such an origin for the geochemically anomalous Siluro-Devonian suite would have to be accompanied by improbably large amounts of crystal fractionation to yield the necessary trace element enrichments.

The clear geochemical distinction between the group 1 and 2 newer granites also appears in some critical trace element variation diagrams (Figure 4). For clarification, in the northern province, Rogart and Strontian are interpreted as relatively deeply eroded intrusions, whereas Foyers and Helmsdale are exposed at a high level; all four are pre-mid-Silurian in age. The four other intrusions in Figure 4 are Siluro-Devonian in age and are not deeply eroded; Etive and Cairngorm are emplaced in the northern province, Loch Doon is in the Southern Uplands, and Shap is in the southern province. Figure 4 indicates that the four younger intrusions are relatively enriched in uranium, rubidium, and yttrium and relatively depleted in strontium and barium (see also Tables 2 and 3). Bearing in mind that the geochemical signature of the Helmsdale intrusion has been affected by postintrusive mineralization leading, in particular, to uranium-enrichment, the two groups of newer granites (indicated by closed and open symbols) show little overlap. However, the four data points for Loch Doon bridge the gap between the two types of intrusion on most plots. This reaffirms the transitional nature of this, the oldest of the Southern Uplands intrusions [Brown et al. 1979a; Halliday et al. 1980].

Another important point to note from Figure 4 is that geochemical differences between intrusions do not seem to be a function of erosion level. Thus, Foyers and Strontian, exposed at different levels, have overlapping geochemical properties, whereas Cairngorm and Foyers, exposed at the same level, contrast geochemically. This point is amplified by recent rare-earth element (REE) data for these three intrusions (Figure 5 and Pankhurst [1979]). All three intrusions are strongly enriched in light REEs, but whereas Cairngorm shows normalized Ce/Yb ratios similar to those of calc-alkaline suites from modern ocean-continent margins [Tarney and Saunders, 1979], the REE profiles for Strontian and Foyers are most

strongly fractionated and their total REE abundances decrease with increasing SiO_2 (Pankhurst, 1979), suggesting rather a typical compatible behavior during crystallisation. The contrasting incompatible behavior of REEs in the Cairngorm intrusion (see also Y in Figure 4c), coupled with a strong negative europium anomaly (Figure 5), suggests refractory feldspar residua in the melt zone or cumulate feldspar at depth (the former is favored because geochemical parameters do not change with erosion level, see earlier).

To summarize, geochemical data have identified quite different characteristics for the early (group 1) and the late (group 2) Caledonian intrusions. As predicted from the tectonic interpretation, the two suites were produced from different magmas: the Siluro-Devonian suite shows most features in common with the batholiths of ancient and modern zones of crustal convergence, such as calc-alkaline major element geochemistry, incompatible behavior of LIL and RE elements, etc. The earlier, pre-mid-Silurian suite also has calc-alkaline affinities, but these intrusions are more varied in composition both internally (i.e., they are more heavily zoned) and in regional terms. Yet they lack the characteristic incompatible element enrichments mentioned above and, in the two cases shown in Figure 5, even have compatible REE characteristics.

Concluding Discussion

The closure of the Iapetus ocean across the British Caledonides was associated with the emplacement of three intrusive suites:

1. A pretectonic group of mainly dioritic plutons with associated migmatites and with isotopic ages exceeding 460 Ma.
2. A posttectonic, mainly forcefully emplaced group of zoned granodiorites with ages ranging from 410 to 460 Ma (pre-mid-Silurian).
3. A posttectonic, mainly discordant group of granites and granodiorites with ages ranging from 390 to 410 Ma.

The geophysical and geochemical evidence discussed in this contribution suggests that, apart from their relative states of deformation, the first two groups have many features in common. These include a lack of prominent gravity anomalies, probably indicating small volumes of magma; generally low levels of LIL trace elements which are reminiscent of average crustal rocks in the region; and variable isotopic characteristics which, nevertheless, generally include some evidence of a partly crustal derivation. Two important potential heat sources were available at the time of magma generation:
(1) increased heat flow from the mantle due either to fluid flow or rise of magmas from above a subduction zone and (2) increased crustal heat production due to tectonic activity (frictional heating) and the overthrusting of insulating, heat producing upper crustal metasedimentary layers. Taken together with the often forceful mode of emplacement of the earlier granite suites and their close temporal relationship to the climax of Caledonian metamorphism, there seems little difficulty in accepting that local crustal melting may have been involved. A simple basement source is unlikely, however, as in the northern province, crustal isotopic residence times are younger than the age of potential Lewisian sources (Hamilton et al. 1980) and a multicomponent origin, involving various crustal and juvenile sources, seems most acceptable (as argued also by Pankhurst and Sutherland, (1981)).

In contrast with the conclusions of Pankhurst and Sutherland (1981), however, our data (Tables 1 and 2 and Figures 3-5) clearly show different trends for the later group of Siluro-Devonian, mainly 'permitted' granites, as typified by the Cairngorm intrusion. From the gravity data, there is little doubt that large amounts of magma were involved, much more than could simply be produced by partially melting the available underlying crust (for example, the Cairngorm massif is at least 12 km thick and the entire continental crust, much of it comprising older refractory granulites, is only 30 km thick in this region). The evidence from detailed radioelement and geochemical studies suggests also that the marked enrichments of certain incompatible elements in these intrusions may require an LIL-enriched source region. It is unlikely that these enrichments arose from major fractionation of intermediate parental magmas, as this would necessitate either hornblende-dominated or plagioclase-pyroxene-rich cumulates at depth, both of which would be more dense than the Cairngorm granite, for example, and so would be difficult to reconcile with the gravity evidence. It is true that Cairngorm has a europium anomaly (Figure 5) that most probably indicates feldspar removal, but we suggest (as argued more fully by Plant et al. (1980)) that this implies that, rather than having been subject to massive removal, feldspar was a refractory phase in the melt zone.

Following this line of reasoning, we propose, therefore, a two-stage origin for the Siluro-Devonian intrusive magmas (see also, Simpson et al. 1979). There is little evidence that normal calc-alkaline magmas were erupted or emplaced in the crust in large volumes during most of the subduction history of the Iapetus ocean. It is true that the early intrusions represent local thermal events, but they are not on the scale of, and do not correspond geochemically to, normal calc-alkaline batholiths. If subduction was taking place in the time interval preceding suturing, it seems inconceivable that no magmas were generated, however, and we suggest that large volumes of basaltic andesite magmas were formed but were trapped by underplating beneath the ancient crustal basement of the northern province and beneath the young accreting margin to the south of Iapetus. As the ocean closed and the adjacent continental margin entered a phase of postcollisional relaxation, it is suggested that the underplated material remelted by adiabatic decompression (see Brown (1981) for discussion of phase relations). By this time it would already have undergone intense volatile fluxing and consequent LIL enrichments (as in the model of Saunders et al.

(1980)), so providing an ample source for the large volumes of typical arc-type magmas which were then emplaced in one relatively short episode.

In conclusion, there is little doubt that important crustal growth took place during the events described here: progressive northward lateral accretion of the European foreland during the Lower Palaeozoic now seems well established, but vertical accretion of the continental crust, first perhaps by underplating and later by intrusive magmatism has also been suggested. Further information is still required to complete this analysis; in particular, new geochemical and isotopic data for a wider range of Caledonian plutons will be a useful test of this model and will, no doubt, lead to further refinements.

Acknowledgments. We are grateful to our colleagues and to two anonymous reviewers for comments that improved the ideas presented here. This paper is published with the permission of the Director of the Institute of Geological Sciences.

References

Arth, J.G., F. Baker, Z.E. Peterman, and I. Friedman, Geochemistry of the gabbro-diorite tonalite-trondhjemite suite of south west Finland and its implications for the origin of tonalitic and trondhjemitic magmas, J. Petrol., 19, 289-316, 1978.

Bamford, D., K. Nunn, C. Prodehl, and B. Jacob, LISPB-IV: Crustal structure of northern Britain, Geophys. J. R. Astron. Soc., 54, 43-60, 1978.

Barker, F., D.R. Wones, W.N. Sharp, and G.A. Desbrough, The Pikes Peak batholith, Colorado Front Range, and a model for the origin of the gabbro-anorthosite-syenite-potassic granite suite, Precambrian Res., 2, 97-160, 1975.

Bateman, P.C., and F.C.W. Dodge, Variations of major chemical constituents across the central Sierra Nevada batholith, Geol. Soc. Am. Bull., 81, 409-420, 1970.

Bowie, S.H.U., P.R. Simpson, and C.M. Rice, Application of fission-track and neutron activation methods to geochemical exploration, in Geochemical Exploration, edited by M.J. Jones, pp.359-372, Institute of Mining Metallurgy, London, 1973.

Brown, G.C., Space and time in granite plutonism, Philos. Trans. R. Soc. London, 301, 321-336 1981.

Brown, G.C., and C.A. Locke, Space-time variations in British Caledonian granites: Some geophysical correlations, Earth Planet. Sci. Lett., 45, 69-79, 1979.

Brown, G.C., J. Cassidy, A.G. Tindle, and D.J. Hughes, The Loch Doon granite: An example of granite petrogenesis in the British Caledonides, J. Geol. Soc. London, 136, 745-753, 1979a.

Brown, G.C., J. A. Plant, and R.S. Thorpe, Plutonism in the British Caledonides: Space time and geochemistry, in The Caledonides in the U.S.A., edited by D.R. Wones, Mem. 2 pp.157-166, Dep. of Geol. Sci.Va. Polytech. Inst. and State Univ. Blacksburg, 1979b.

Brown, G.C., J. Cassidy, E.R. Oxburgh, J. Plant, P.A. Sabine, and J.V. Watson, Basement heat flow and metalliferous mineralisation in England and Wales, Nature, 288, 657-659, 1980.

Brown, P.E., J.A. Miller, and R.L. Grasty, Isotopic ages of late Caledonian granitic intrusions in the British Isles, Proc. Yorks Geol. Soc., 36, 251-276, 1968.

Cassidy, J., Techniques of field gamma-ray spectrometry, Min. Mag. in press 1981.

Duval, J.S., High sensitivity gamma-ray spectrometry - State of the art and trial application of factor analysis. Geophysics, 42(3), 549-559, 1977.

England, P.C., E.R. Oxburgh, and S.W. Richardson, Heat refraction and heat production in and around granite plutons in north-east England, Geophys. J. R. Astron. Soc., 62, 439-455, 1980.

Fleet Brown, J., Rb-Sr studies and related chemistry on the Caledonian calc-alkaline igneous rocks of north-west Argyllshire, Ph.D. thesis, Univ. of Oxford, Oxford, England, 1972.

Ghuma, M.A., and J.J. W. Rogers, Geology, geochemistry, and tectonic setting of the Ben Ghnema batholith, Tibetsi massif, southern Libya, Geol. Soc. Am. Bull., 89, 1351-1358, 1978.

Hall, D.H., and P. Dagley. Regional magnetic anomalies: Analysis of the smoothed aeromagnetic maps of Great Britain and Northern Ireland, Rep. Inst. Geol. Sci. U.K., 70-10, 8 pp., 1970.

Halliday, A.N., W.E. Stephens, and R.S. Harmon, Rb-Sr and O isotopic relationships in 3 zoned Caledonian granitic plutons, Southern Uplands, Scotland: Evidence for varied sources and hybridisation of magmas, J. Geol Soc. London, 137, 329-348, 1980.

Hamilton, P.J., N.M. Evensen, R.K. O'Nions, and J. Tarney, Sm-Nd systematics of Lewisian gneisses: implications for the origin of granulites, Nature, 277, 25-28, 1979.

Hamilton, P.J. R.K. O'Nions, and R.J. Pankhurst, Isotopic evidence for the provenance of some Caledonian granites, Nature, 287, 279-284, 1980.

Harmon, R.S., and A.N. Halliday, Oxygen and strontium isotope relationship in the British late Caledonian granites, Nature, 283, 21-25, 1980.

Harry, W.T., The form of the Cairngorm granite pluton, Scott. J. Geol., 1, 1-8, 1965.

Jacobson, R.R.F., W.N. MacLeod, and R. Black, Ring-complexes in the Younger Granite Province of northern Nigeria, Geol. Soc. London. Mem., 1, 72 pp., 1958.

Johnstone, G.S., J. Plant, and J.V. Watson, Regional geochemistry in northern Scotland, in The Caledonides of the British Isles - reviewed, edited by A.L. Harris, C.H. Holland, and B.E. Leake, Spec. Publ. Geol. Soc. London, 8, 117-128, 1979.

Kneen, S.J., The magnetic properties and subsurface structures of certain Caledonian granites, Ph.D.thesis, Univ. of Liverpool, Liverpool, England. 1973.

Leake, B.E., Granite emplacement: The granites

of Ireland and their origin, in Crustal Evolution in northwestern Britain and adjacent Regions, edited by D.R. Bowes, and B.E. Leake, Geol. J., Spec. Issue, 10, 221-248, 1978.

Leggett, J.K., W.S. McKerrow, J.H. Morris, G.J.H. Oliver, and W.E.A. Phillips, The north-western margin of the Iapetus ocean, in The Caledonides of the British Isles-reviewed, edited by A.L. Harris, C.H. Holland, and B.E. Leake, Spec. Publ. Geol. Soc. London, 8, 499-512, 1979.

Locke, C.A., Geophysical investigations of Caledonian granites within a regional classification, Ph.D.thesis, Univ. of Liverpool, Liverpool, England. 1980.

Locke, C.A. and G.C. Brown, Geophysical constraints on structure and emplacement of Shap granite, Nature, 272, 526-528, 1978.

Lovborg, L., Future development in the use of gamma-ray spectrometry for uranium prospecting on the ground, in Uranium Exploration Methods, pp.141-153, IAEA, Vienna, 1973.

Marston, R.J., The Foyers granitic complex, Inverness-shire, Scotland, Q. J. Geol. Soc. London, 126, 331-368, 1970.

McKerrow, W.S., J.K. Leggett, and M.H. Eales, Imbricate thrust model of the Southern Uplands of Scotland, Nature, 267, 237-239, 1977.

Pankhurst, R.J., Isotope and trace element evidence for the origin and evolution of Caledonian granites in the Scottish Highlands, in Origin of granite batholiths: geochemical evidence, edited by M.P. Atherton, and J. Tarney, Shiva Publishing, Orpington, Kent, pp. 18-33, 1979.

Pankhurst, R.J., and D.S. Sutherland, Caledonian granites and diorites of Scotland and Ireland, in Igneous Rocks of the British Isles, edited by D.S. Sutherland, John Wiley, New York, in press, 1981.

Petro, W.L., T.A. Vogel, and J.T. Wilband, Major-element chemistry of plutonic rock suites from compressional and extensional plate boundaries, Chem. Geol., 26, 217-235, 1979.

Phillips, W.E.A., C.J. Stillman, and T. Murphy, A Caledonian plate tectonic model, J. Geol. Soc. London, 132, 579-609, 1976.

Pidgeon, R.T., and M. Aftalion, Cogenetic and inherited zircon U-Pb systems in Palaeozoic granites from Scotland and adjacent regions, in Crustal evolution in northwestern Britain and adjacent regions, edited by D.R. Bowes, and B.E. Leake, Geol. J., Spec. Issue, 10, 183-220, 1978.

Pitcher, W.S., The anatomy of a batholith,; J. Geol. Soc. London, 135, 157-182, 1978.

Plant, J.A., G.C. Brown, P.R. Simpson, and R.T. Smith, Signatures of metalliferous granites in the Scottish Caledonides, Trans. Inst. Min. Metall., 89, B198-B210, 1980.

Read, H.H. Aspects of Caledonian magmatism in Britain, Liverpool Manchester Geol. J. 2, 653-683, 1961.

Robson, D.A., and A.G. Green, A magnetic survey of the aureole around the Cheviot granite, Scott. J. Geol., 16, 11-27, 1980.

Saunders, A.D., J. Tarney, and S.D. Weaver, Transverse geochemical variations across the Antarctic Peninsula: Implications for the genesis of calc-alkaline magmas, Earth Planet. Sci. Lett., 46, 344-360, 1980.

Simpson, P.R., G.C. Brown, J.A. Plant, and D. Ostle, Uranium mineralisation and granite magmatism in the British Isles, Philos. Trans. R. Soc. London, 291A, 385-412, 1979.

Soper, N.J., The structure of the Rogart igneous complex, Sutherland, Scotland, Q. J. Geol. Soc. London, 119, 445-478, 1963.

Tarney, J., and A.D. Saunders, Trace element constraints on the origin of cordilleran batholiths, in Origin of Granite Batholiths: geochemical evidence, edited by M.P. Atherton, and J. Tarney, Shiva Publishing, Orpington, Kent, pp. 90-105, 1979.

Thorpe, R.S., Late Precambrian igneous activity in Southern Britain, in The Caledonides of the British Isles - reviewed, edited by A.L. Harris, C.H. Holland, and B.E. Leake, Spec. Publ. Geol. Soc. London, 8, 579-584, 1979.

Thorpe, R.S., Precambrian igneous rocks of England, Wales and Southeast Ireland, in Igneous Rocks of the British Isles, edited by D.S. Sutherland, John Wiley, New York, in press, 1981.

Upton, B.G.J., P. Aspen, A. Graham, and N.A. Chapman, The pre-Palaeozoic basement of the Scottish Midland Valley, Nature, 260, 517-518, 1976.

Vorma, A., Alkali feldspars of the Wiborg rapakivi granite in southeastern Finland, Bull. Comm. Geol. Finl., 246, 72 pp. 1971.

Wadge, A.J., N.H. Gale, R.D. Beckinsale, and C.C. Rundle, A Rb-Sr isochron for the Shap granite, Proc. Yorks. Geol. Soc., 42, 297-305, 1978.

Watson, J.V., and J. Plant, The regional geochemistry of uranium as a guide to deposit formation, Philos. Trans. R. Soc. London, 291A, 321-338, 1979.

Zwart, H.J., and U.F. Dornsiepen, The tectonic framework of central and western Europe, Geol. Mijnbouw, 57, 627-654, 1978.

(Received November 5, 1980;
revised April 8, 1981;
accepted April 20, 1981.)

JOURNAL OF GEOPHYSICAL RESEARCH, VOL. 86, NO. B11, PAGES 10515-10529, NOVEMBER 10, 1981

Phase Relationships of S-Type Granite With H_2O to 35 kbar: Muscovite Granite From Harney Peak, South Dakota

W. L. HUANG

Exxon Production Research, Houston, Texas 77001

P. J. WYLLIE

Department of Geophysical Sciences, University of Chicago, Chicago, Illinois 60637

Muscovite granite (13.8% muscovite, 4.8% normative corundum) was reacted, with varying percentages of H_2O, in cold-seal vessels at 2 kbar and in piston-cylinder apparatus between 10 and 35 kbar. The diagrams illustrating melting/crystallization relationships are: P-T sections with both excess H_2O and with no H_2O added (0.66% H_2O in rock); T-X_{H_2O} sections at 15 kbar and 25 kbar showing H_2O-undersaturated conditions; the H_2O-undersaturated surface for the crystallization of quartz/coesite (small amounts of aluminosilicate minerals persist to higher temperatures). Glass compositions measured by electron microprobe from samples with 5% H_2O at 15 kbar confirm that liquids are syenitic through at least 100°C above the solidus, as predicted from the effect of pressure on the Residua System. Results are explained successfully by phase relationships involving muscovite, quartz, and orthoclase in K_2O-Al_2O_3-SiO_2-H_2O, with reactions depicted in a P_{total}-$P_{e_{H_2O}}$-T model, with special reference to the divariant surfaces in the region $P_{e_{H_2O}} < P_{total}$. With reduced $P_{e_{H_2O}}$ (or a_{H_2O}), produced either by small amounts of H_2O (and H_2O-undersaturation) or by CO_2 + H_2O mixtures, subsolidus dehydration reaction temperatures decrease, vapor-present solidus temperatures increase, and muscovite stability in presence of liquid increases. In general, muscovite, biotite, and amphibole can be precipitated from magmas containing only a few tenths per cent H_2O (although the H_2O-undersaturated liquids coexisting with crystals may contain 3% or more dissolved H_2O). This particular granite cannot be a primary magma from mantle or subducted oceanic crust. It is a possible product of partial fusion of pelitic rocks between about 20 km and 40 km depth given sufficient H_2O, and xenocrystal muscovite or sillimanite from the source rocks. The phase relationships are consistent with the idea of S-type granites, but not sufficient to prove the origin of this rock. Additional tests require phase relationships of other associated granitic rocks, and details of geochemistry, geophysics, and field relationships.

INTRODUCTION

According to *Chappell and White* [1974] and *White and Chappell* [1977], granitic rocks derived by the partial melting of sedimentary rocks contain muscovite and biotite, with no hornblende. These S-type granites contrast with I-type granites, which are derived from igneous source material and characteristically have hornblende more abundant than biotite in mafic samples.

The muscovite granite from Harney Peak, South Dakota, contains abundant muscovite with traces of biotite and no hornblende, and is therefore considered to be of S-type. Phase relationships for this granite have been determined to 35 kbar, with H_2O contents varying from excess to low values. Phase diagrams and some applications have been presented by *Huang and Wyllie* [1973] and *Huang* [1977]. As a basis for interpretation of the phase relationships in the complex rock system, the phase relationships for assemblages of muscovite, sanidine and quartz, with and without aqueous vapor, were determined in the sytem K_2O-Al_2O_3-SiO_2-H_2O [*Huang et al.*, 1973; *Huang and Wyllie*, 1974].

In this paper, we compile the complete phase relationships for the muscovite granite, together with unpublished run data, as representative for an S-type granite. The phase relationships are compared with results from the synthetic system, with special reference to conditions of H_2O-undersaturation. Phase relationships for a biotite granite with mineralogy (and associated granitoid sequences) corresponding to an I-type granite are presented in a companion paper [*Stern and Wyllie*, this issue].

MUSCOVITE GRANITE FROM HARNEY PEAK

The crushed rock sample was kindly supplied by J. J. Norton and R. T. McLaughlin of the U.S. Geological Survey. Table 1 provides a chemical analysis of the rock, its CIPW norm, and a partial mode. Table 2 lists the compositions of alkali and plagioclase feldspar, and muscovite, measured by electron microprobe on grains picked randomly from the crushed rock. The detailed mineralogy and petrology of related pegmatites have been presented by *Norton* [1970].

EXPERIMENTAL PROCEDURES

The powdered rock sample, after passing through 200-mesh sieve, was ground by hand under acetone to grain sizes of 40–60 microns. The sample was dried at 120°C for more than 24 hours before experiments. Samples were sealed within capsules (gold at 2 kbar, silver-palladium or platinum at higher pressures, except for one group of runs in gold at 15 kbar, Table 6) with measured amounts of distilled and deionized water, and reacted in pressure vessels. Runs at 2 kbar were completed in Rene-41 cold-seal pressure vessels with filler rods using standard experimental methods [*Piwinskii and Wyllie*, 1968; *Boettcher and Kerrick*, 1971]. Pressures are accurate to ±5%, and temperatures precise to ±5°C and accurate to ±10°C. Runs at higher pressures were completed in single-stage piston-cylinder apparatus, using the procedures described by *Stern and Wyllie* [this issue], but with some talc

Copyright © 1981 by the American Geophysical Union.

Paper number 1B0494.
0148-0227/81/001B-0494$01.00

TABLE 1. Chemistry, Norm, and Partial Mode of Muscovite Granite (L26) Supplied by J. J. Norton and R. T. McLaughlin

Chemical Composition*	%
SiO_2	74.66
TiO_2	0.03
Al_2O_3	15.55
Fe_2O_3	0.17
FeO	0.42
MnO	0.07
MgO	0.02
CaO	0.42
Na_2O	4.29
K_2O	3.08
H_2O+	0.66
H_2O-	0.04
P_2O_3	0.15
F	0.04
CO_2	0.02
	99.62
O ≡ F	−0.02
Total	99.60
Norm	**%**
Quartz	37.16
Orthoclase	18.20
Albite	36.28
Anorthite	0.98
Hypersthene	0.52
Corundum	4.80
Magnetite	0.25
Ilmenite	0.06
Apatite	0.36
Calcite	0.05
Water	0.70
Partial Mode	**wt %**
Feldspar + quartz	85.2
Muscovite	13.8
Biotite	0.1
Accessory minerals (garnet + apatite + opaque minerals)	0.9

* J. C. DeVine and J. B. Bodkin, analysts.

pieces in the furnace assembly replaced at higher temperatures by pyrex glass to avoid talc dehydration and embrittlement. Pressures are considered accurate to ±5%, and temperatures precise to ±5°C, and accurate to within ±13°C.

In order to avoid metastable melting of the low-pressure mineral assemblage, near-solidus runs at pressures above 15 kbar were performed in two stages, which are indicated in the run tables by pairs of rows. In the first stage the sample was converted to the high-pressure mineralogy, and the temperature was then raised to require run conditions for the second stage. Other two-stage runs from high to low temperatures represent tests for reversibility of the reactions.

Phase assemblages were determined by optical and X ray studies of the quenched materials, using criteria described by *Stern and Wyllie* [this issue]. Muscovite, sillimanite, corundum, and garnet are additional minerals from runs with this rock. Muscovite forms irregular crystal plates about 60 microns in diameter. Sillimanite forms small needles. The high relief of corundum is distinctive. Distinction between alkali feldspar and albitic plagioclase is difficult. The occurrence of two ($\bar{2}01$) peaks on X ray diffraction patterns was taken as evidence for the occurrence of two feldspars. The ($\bar{2}01$) peaks were too weak and broad to be used for estimation of feldspar composition(s). The rare grains of garnet were irregular, about 10–30 microns diameter, similar to those in the original rock. They may represent unreacted original garnets.

Electron microprobe analyses were performed on an ARL EMX electron microprobe at 15 KV, 0.02 micro-amp, and with counting time of 10 s, following the procedures of *Smith* [1965]. The beam size was about 2 micrometers diameter.

MUSCOVITE-ORTHOCLASE-QUARTZ MELTING RELATIONSHIPS

The system K_2O-Al_2O_3-SiO_2-H_2O includes the minerals muscovite, orthoclase, and quartz, and it therefore provides a good model for the natural granite, which is composed of muscovite, two feldspars, and quartz. *A. B. Thompson* [1974] has evaluated theoretically the effect of adding albite as a component to the mica-orthoclase reactions in this system.

Figure 1 shows univariant reactions for the dissociation and melting of muscovite in association with quartz, alkali feldspar, and aluminous minerals in the system K_2O-Al_2O_3-SiO_2-H_2O. The dehydration curve for muscovite extends through Q_3 and Q_4 to Q_2, and that for muscovite + quartz terminates at Q_1. Melting begins at Q_2 and Q_1, respectively.

There are three melting reactions involving muscovite that rise to higher pressures from Q_2, and three melting reactions involving muscovite and quartz that rise from Q_1. The lowest-temperature reactions associated with each of these invariant points has the familiar shape for silicate-H_2O melting curves, with significant depression of melting temperatures caused by increase in pressure. Above each invariant point muscovite is stable, but below each invariant point the corresponding melting curve has muscovite replaced by anhydrous products of the dehydration reactions. The highest-temperature melting reaction associated with each invariant point is the vapor-absent fusion of muscovite, or of muscovite + quartz, which extends above the invariant point with little change in slope compared with the corresponding dehydration reaction at lower pressures and temperatures. The equivalent melting reactions with excess H_2O occur at somewhat lower temperatures, but with the same positive slope (dP/dT).

The estimated compositions of liquids for the vapor-present reactions were illustrated by *Lambert et al.* [1969] and *Wyllie*

TABLE 2. Average Electron Microprobe Analyses for Feldspars and Muscovite in Muscovite Granite (L26)

Minerals	Alkali-Feldspar (4 Grains)	Plagioclase (4 Grains)	Muscovite (2 Grains)
SiO_2	64.6	67.7	45.6
TiO_2	<0.05	<0.05	0.06
Al_2O_3	18.6	20.3	36.0
FeO	0.4	0.3	1.7
MgO	0.05	<0.05	0.7
CaO	0.05	0.8	<0.05
Na_2O	0.8	10.8	0.5
K_2O	16.2	0.05	10.8
Total	100.7	100.0	95.3*
Mole %			Mole %
An	0.3	5.1	Ms 93.3
Ab	6.4	94.3	Pa 6.7
Or	93.2	0.6	

Abbreviations: An—anorthite, Ab—albite, Or—orthoclase, Ms—muscovite, Pa—paragonite.

* H_2O contents in muscovite are not included in total.

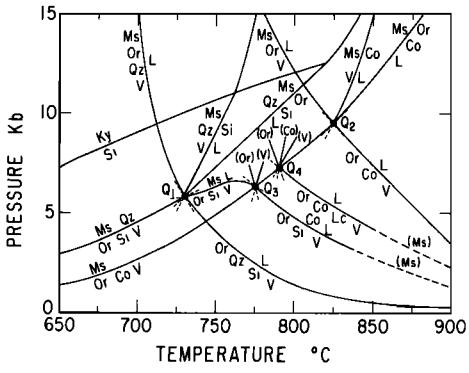

Fig. 1. Univariant reactions in the K_2O-Al_2O_3-SiO_2-H_2O according to *Huang and Wyllie* [1974, Figure 3], incorporating the experimental results of *Huang et al.* [1973]. The reactions of interest in this paper are the dehydration and melting reactions around invariant points Q_1 and Q_2. Abbreviations for Figure 1 and other figures and tables: Ms = muscovite, Qz = quartz, Or = orthoclase, or alkali feldspar, or any polymorph of $KAlSi_3O_8$, Si = sillimanite, Ky = kyanite, Co = corundum, L = liquid, V = vapor, Pl, Ab = plagioclase, Fsp = feldspar, Jd = jadeite, Ga = garnet, Ct = coesite, OrH = orthoclase hydrate.

[1977*a*, Figure 2]. The H_2O-saturated liquid coexisting with orthoclase + quartz + muscovite occurs at a slightly lower temperature than the H_2O-saturated liquid coexisting with orthoclase + quartz [*Huang and Wyllie*, 1974], and it contains a small excess of Al_2O_3 compared with the latter liquid.

For bulk compositions with sufficient H_2O to form muscovite, but with none left over for a vapor phase, melting begins at temperatures higher than the vapor-present reactions. The muscovite reacts to release H_2O which generates H_2O-undersaturated liquid.

Experimental Results

Phase Relationships With Excess H_2O

The runs listed in Table 3 bracket boundaries for the phase diagram in Figure 2. The main features correspond closely to those described and reviewed for biotite granite by *Stern and Wyllie* [this issue, Figure 1], with addition of the muscovite-out curve instead of the biotite-out curve, and of fields for kyanite and metastable corundum.

The subsolidus assemblage at crustal pressures corresponds to that of the natural rock, two feldspars, quartz, and muscovite, with a trace of garnet. At high pressures, this becomes jadeite + coesite + muscovite via reactions plotted in Figure 2. Orthoclase disappears by reaction with aqueous solution between 15 kbar and 25 kbar. Similarly, in the biotite granite, biotite dissolves in the subsolidus vapor between 5 kbar and 10 kbar. in contrast, the muscovite in our rock exists to the highest pressures attained. The traces of accessory garnet were not observed in runs at pressures of 20 kbar or higher, nor in runs more than 25°C above the solidus, but we have not determined a phase boundary that we could draw with confidence.

The solidus curve is identical within the limits of experimental error with those for biotite granite and the synthetic granite system [*Huang and Wyllie*, 1975] to 30 kbar, but it is somewhat higher at 35 kbar. The solidus temperature at high pressures varies as a function of H_2O content (see Figure 5), which might be responsible for the temperature difference.

At 10 kbar and 30 kbar the muscovite-out curve is at 25°C and 40°C, respectively, below the univariant melting curve for muscovite + quartz with excess H_2O, which is explained by the paragonite component of the natural mica (Table 2). At 2 kbar, however, the muscovite persisted in 4-month runs to temperatures about 50°C higher than the maximum stability limit of muscovite + quartz (Figure 1; *Huang and Wyllie* [1974, Figure 2]. This is testimony to slow reaction rates in granitic systems at crustal pressures.

Quartz or coesite is the liquidus phase for the biotite granite, and the corresponding boundary for muscovite granite is shown by the heavy line in Figure 2. Kyanite and sillimanite are produced near the muscovite-out boundary, and traces of kyanite, sillimanite, and corundum occupy large fields above the heavy line. Traces of corundum at 10 kbar and 15 kbar, instead of or accompanying the Al_2SiO_5 polymorph, are considered to be metastable. Corundum, once formed metastably, persists indefinitely in the synthetic muscovite system [*Huang and Wyllie*, 1974].

The change in slope of the solidus curve is associated with the formation of jadeite from plagioclase. The change in slope of the liquidus curve and the increasing width of the melting interval with increasing pressure are functions of the change in composition of the eutectic liquid away from SiO_2. These observations were reviewed in detail by *Stern and Wyllie* [this issue].

Details of the problems and procedures for establishing reversibility of phase boundaries for rock samples within narrow temperature limits were reviewed by *Stern and Wyllie* [1975]. We have discussed the persistence of metastable muscovite at 2 kbar, and the formation and persistence of metastable corundum at 10 kbar and 15 kbar. At higher pressures reaction rates are improved. At 15 kbar, the quartz and muscovite boundaries were reversed within 25°C (Table 3, runs 231, 229, and 242R). At 25 kbar, the kyanite boundary was reversed within 25°C (Table 3, runs 212, 209, 215R, and 217R).

Phase Relationships With No Added H_2O

The runs listed in Table 4 bracket boundaries for the phase diagram in Figure 3. The subsolidus assemblage below the jadeite reaction boundary is the same as in Figure 2, but without vapor. With increasing pressure, plagioclase and quartz are replaced by jadeite and coesite, respectively. Alkali felspar remains stable to high pressures in the absence of vapor. The original garnet was detected in all subsolidus runs.

Melting begins where muscovite reacts releasing H_2O for solution in a small amount of H_2O-undersaturated liquid. The muscovite dissolves completely within 20°C above the solidus, and the melting curve for synthetic muscovite + quartz without vapor is about 25°C higher (Figure 1). This temperature difference is explained by paragonite in the natural muscovite (Table 2). The solidus curve (and the narrow interval for the melting of muscovite) occurs at a temperature higher than the vapor-present muscovite-out curve in Figure 2, and the divergence increases with increasing pressure. This difference corresponds to the difference between fusion curves for muscovite + quartz with and without vapor in Figure 1.

According to Figure 2, the muscovite + quartz dehydration reaction crosses the granite-H_2O solidus near 2 kbar and 660°C. By analogy with the reactions near Q_2 in Figure 1, both solidus and muscovite-out curve for vapor-absent granite should also occur near 660°C and 2 kbar. In fact, the muscovite does not react to produce liquid until 725°C (Table 4), even after runs of 7 months duration. We attribute this to slow reaction at these low pressures in the nearly dry system (see

TABLE 3. Experimental Runs for Muscovite Granite (L26) With Sufficient Water for Vapor to be Present

Run	Pressure, kbar	Temperature, °C	Wt. %, H_2O	Duration, Hours or Months (m)	Results *V* in Every Run
10	2	650	7.2	4 (m)	Qz, Ab, Or, Ms, Ga
12	2	675	9.4	4 (m)	Qz, Ab, Or, Co, (L), Ms?
17	2	700	8.6	3 (m)	Qz, Ab, L, (Si)?
13	2	725	8.1	2 (m)	Qz, L, (Si)?
15	2	750	8.8	2 (m)	Qz, L, (Si)?
14	2	775	8.4	2 (m)	L, (Si)?
16	2	800	8.9	1.5 (m)	L, (Si)?
11	2	850	8.5	1 (m)	L, Co?
225	10	605	31	9	Qz, Ab, Or, Ms, Ga
214	10	615	31	9	Qz, Ab, Or, Ms, Ga
202	10	625	22	11	Qz, Ab, Ms, Ga, L
228	10	700	38	26	Qz, Ms, L
224	10	725	27	25	Co, L, (Si)?
222	10	750	32	21	(Co), L, (Si)?
203	10	800	28	21	(Co), L
201	10	850	27	9	(Co), L
220	10	900	33	12	(Co), L
226	15	600	27	9	Qz, Ab, Or, Ms, Ga
227	15	610	29	9	Qz, Ab, (Or), Ms, Ga, (L)
270	15	635	38	16	Qz, Ab, Ms, (Ga), L
271	15	660	35	16	Qz, Ms, L
240R	15	825	36.3	6	...
	15	700	...	16	Qz, Ms, L
231	15	725	32	26	Qz, Ms, L
242R	15	825	37.3	6	...
	15	725	...	18	Qz, (Ms), L
229	15	750	40	24	Co, (Ky), L
395	15	750	43	12	Co, (Ky), L
219	15	775	46	21	Co, (Ky), L
223	15	800	32	21	(Co), L
210	15	825	45	13	(Co), L
328	20	750	40	24	Qz, Ms, L
321	20	775	40	24	Qz, Ky, L
235	20	800	40	24	Ky, L
208	20	875	46	11	L
213	20	900	52	39	L
237	25	595	24.5	6	Qz, Jd, (Or), Ms
327	25	655	25	13	Qz, Jd, (Or), Ms
248T	25	595	25	6	...
	25	675	...	11.5	Qz, Jd, Ms, (L)
250T	25	595	25	6	...
	25	690	...	10	Qz, Jd, Ms, L
349	25	715	25	19	Qz, Ms, L
317T	25	595	25	6	...
	25	720	...	16	Qz, Ms, L
244T	25	595	25	6	...
	25	745	...	10	Qz, Ms, L
366	25	770	50	24	Qz, Ms, Ky, L
243T	25	595	46	6	...
	25	790	...	18	Qz, Ky, L
381	25	810	32	8	Ky, L
376	25	835	32	13	Ky, L
380	25	840	50	13	Ky, L
304	25	855	33	18	Ky, L
207	25	875	42	13	Ky, L
373	25	900	28	15	Ky, L
212	25	900	50	19	Ky, L
314	25	900	32	15	L
215R	25	975	45	6	...
	25	900	...	16	Ky, L
209	25	925	47	11	L
217R	25	975	55	5	...
	25	925	...	15	L
211	25	950	51	10	L
221	25	975	48	5	L
333T	35	575	20	4	...
	35	700	...	20	Ct, Jd, (OrH), Ms
334T	35	575	20	4	...
	35	725	...	4	Ct, Jd, (OrH), Ms
335T	35	575	20	4	...
	35	750	...	7.5	Ct, Jd, Ms, (L)
350T	35	575	25	18	...
	35	775	...	24	Ct, Jd, Ms, Ky, L
332	35	800	45	18	Ct, Ky, L

TABLE 3. (continued)

Run	Pressure, kbar	Temperature, °C	Wt. %, H_2O	Duration, Hours or Months (m)	Results *V* in Every Run
364T	35	575	49	4	...
	35	825	...	18	Ct, Ky, L
331	35	875	45	10	Ct, Ky, L
399	35	890	35	6	Ct, Ky, L
336	35	900	40	25	Ct, Ky, L
330	35	925	45	10.5	(Ky), L

Abbreviations: see Figure 1. ( ) indicates trace amounts of phase. Runs occupying double rows were completed in two states: T—after holding the sample at subsolidus (or near-solidus) conditions indicated in the first row, it was transferred to conditions at higher temperature indicated in the second row. R—after holding the sample above the liquidus at conditions indicated in the first row, it was transferred to conditions indicated in the second row.

the variety of published curves for muscovite + quartz dehydration in *Huang and Wyllie* [1974, Figure 2]). The solidus at 2 kbar is therefore drawn through the bracket determined by the vapor-present runs of Figure 2, which established that muscovite + quartz should release H_2O for melting at this temperature.

The dashed line is a solidus between 3 kbar and 10 kbar presented by *Brown and Fyfe* [1970] for a granite with 10% and 50% muscovite added to it. The muscovite was slightly more sodic than that in our rock. The agreement in position of the solidus is good.

At 35 kbar, no liquid could be detected in runs up to about 100°C higher than the muscovite-out curve, indicating that the H_2O released from muscovite did not become available for melting. The reaction curve for the formation of $KAlSi_3O_8 \cdot H_2O$ [*Seki and Kennedy*, 1964] fits the experimentally determined solidus at 35 kbar. Therefore, although we could not detect sanidine hydrate in the subsolidus runs, we conclude that H_2O from the muscovite did react with the orthoclase to produce this mineral. The solidus curve therefore follows the sanidine hydrate reaction curve about 32 kbar, and melting begins where this mineral releases H_2O, as shown by the heavy line.

Only a trace of liquid is formed near the solidus. The plagioclase-out curve gives the limit for the coexistence of two feldspars, which are replaced by a single alkali feldspar at higher temperatures. There is no significant increase in amount of liquid through an interval of about 250°C, until the alkali feldspar dissolves, near the Fsp-out curve. Note the distribution of kyanite and metastable corundum produced from the muscovite melting reaction (quartz and corundum are incompatible, see Figure 1). The heavy line representing the liquidus is defined at temperatures where there is a significant decrease in the percentage of quartz. Very small, scattered

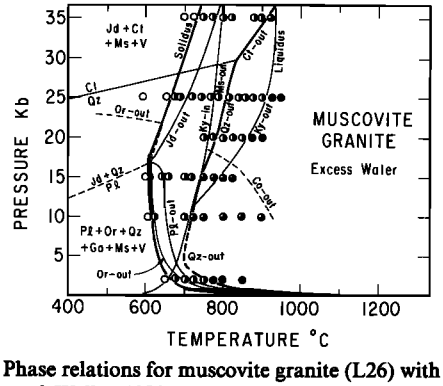

Fig. 2. Phase relations for muscovite granite (L26) with excess water [*Huang and Wyllie*, 1973]. Experiments are listed in Table 3. At pressures below about 1 kbar, a single feldspar should replace Pl + Or at temperatures above the solidus. Abbreviations: see Figure 1.

grains of quartz persist above this boundary, as well as traces of corundum. We interpret this as incomplete reaction in a sluggish system with liquid containing a maximum of 0.6% H_2O. Attempts to reverse the liquidus boundary were unsuccessful (Table 4, runs 263 and 296R), which is disappointing but not unexpected.

Phase Relationships With Variable H_2O Content

The runs listed in Table 5, together with runs from Tables 3 and 4, bracket boundaries for isobaric T-X_{H_2O} sections for the rock-H_2O system at 15 kbar and 25 kbar, as illustrated in Figures 4 and 5. These diagrams show the relationships between the two limits of excess and no additional H_2O illustrated in Figures 2 and 3, and the results are extrapolated further towards the anhydrous rock composition. The composition of the rock is shown by the arrow, at 0.6% H_2O.

The subsolidus phase assemblage at 15 kbar corresponds to the original rock mineralogy, but plagioclase would be replaced by jadeite below about 525°C. At 25 kbar, the jadeite field has expanded to exceed the solidus, and none of the original garnet or orthoclase was observed in runs contining 5% or more H_2O (Figure 5). The capability of only 5% H_2O to dissolve all of the orthoclase (probably incongruently) is remarkable. For H_2O contents less than the 0.6% stored in muscovite, the rock would exist as a vapor-absent assemblage separated by a vertical phase boundary from the vapor-present assemblage.

The vapor-absent assemblage melts at a higher temperature than the vapor-present assemblage (compare Figures 3 and 2) as predicted from the synthetic system (Figure 1). For each pressure, for the anhydrous rock composition, there is a third solidus temperature in the region of 1125°C at 15 kbar, and 1210°C at 25 kbar [*Huang and Wyllie*, 1975]. At low pressures, where the vapor phase composition is almost pure H_2O, the vapor-present solidus curve and other phase boundaries are isothermal. At high pressures, where the vapor contains significant amounts of dissolved rock, they are not quite isothermal, as shown in Figure 5, and by *Stern and Wyllie* [this issue, Figures 2 and 3]. For discussion see *Robertson and Wyllie* [1971] and *Whitney* [1975].

The H_2O-saturation boundary separates phase fields with vapor from those without vapor. In the vapor-absent region, the upper stability limits for quartz, feldspars, jadeite and garnet decrease considerably with increasing H_2O content. The muscovite breakdown temperature increases with decreasing H_2O content, reaching the very low H_2O contents where muscovite granite melts in the absence of vapor. The crystallization of muscovite from melts containing little H_2O is consistent with phase relationships in synthetic systems (Figure 1; *Yoder and Kushiro* [1969]; *Modreski and Boettcher* [1972,

TABLE 4. Experimental Runs for Muscovite Granite (L26) With No Water Added

Run	Pressure, kbar	Temperature, °C	Duration, Hours or Months (m)	Estimated % Liquid	Results Phases Present
23	2	650	4 (m)	0	Qz, Ab, Or, Ms, (Si), (Co), Ga
19	2	675	4 (m)	0	Qz, Ab, Or, Ms, (Si), (Co), Ga
25	2	700	7 (m)	0	Qz, Ab, Or, (Ms), (Si), (Co), Ga
21	2	725	3.5 (m)	<1	Qz, Ab, Or, (Si), (Co), Ga, (L)
393	10	725	12	0	Qz, Ab, Or, Ms, Ga
369	10	750	24	<1	Qz, Ab, Or, Ms, Ga, (L)
233	10	775	24	<1	Qz, Ab, Or, Ms, (Co), Ga, (L)
232	10	800	24	2	Qz, Ab, Or, Co, Ga, L
344	10	1025	23	40	Qz, Fsp, (Ky), Co, L
345	10	1075	24	80	Qz, Co, L
259	10	1150	10	80	Qz, (Si), (Co), L
258	10	1200	10	98	(Qz), (Si), (Co), L
262	10	1250	2.5	99	(Qz), Si?, (Co), L
257	15	800	23	0	Qz, Ab, Or, Ms, Ga
236	15	825	23	1	Qz, Ab, Or, (Ms), (Co), Ga, (L)
230	15	875	25	3	Qz, Fsp, Co, Ga, L
241	15	1000	3	5	Qz, Fsp, Co, Ga, L
269	15	1000	43	8	Qz, Fsp, Co, L
266	15	1050	42	25	Qz, Fsp, (Ky), Co, L
265	15	1100	47	75	Qz, Ky?, Si?, (Co), L
263	15	1200	37	80	Qz, Si, L
296R	15	1315	5	...	...
	15	1200	5	99.5	Co?, L
247	15	1250	5	96	(Qz), (Si), Co, L
254R	15	1315	5	...	...
	15	1240	5	98	(Si), (Co), L
249	15	1300	5	99	(Co), L
252	25	850	20	0	Qz, Jd, Or, Ms, Ga
396	25	875	12	...	Qz, Jd, Or, Ms, Ga
253	25	900	22	1	Qz, Fsp, (Ky), Co, Ga, (L)
356	25	950	10	2	Qz, (Ab), Fsp, Ms, (Ky), (Si), Co, Ga, L
351	25	1000	8	2	Qz, Fsp, (Ky), Co, Ga, L
338	25	1100	8	25	Qz, Fsp, (Ky), Co, L
339	25	1150	9	35	Qz, Fsp, (Ky), Co, L
326	25	1200	6.5	70	Qz, Ky, Co, L
256	25	1300	4	90	Qz, Ky, Co, L
255	25	1350	4	99	(Qz), (Co), L
260	35	925	20	0	Ct, Jd, Or, Ms, (Co), (Ga)?, OrH?
261	35	975	20	0	Ct, Jd, Or, (Ky), Co, OrH?
267	35	1025	23	0	Ct, Jd, Or, (Ky), Co
346T	35	900	6	...	...
	35	1075	18	1	Ct, Jd, Or, (Ky), Co, (L)
347T	35	900	6	...	...
	35	1150	26	10	Ct, Jd, (Fsp), (Ky), Co, L
341	35	1200	8	70	Qz, (Fsp), (Ky), Co, L
340	35	1250	14	80	Qz, (Ky), Co, L
268	35	1350	8.5	95	Qz, Ky, Co, L
345	35	1400	2	90	Qz, Ky, Co, L
364	35	1450	1/2	90	Qz, Ky, Co, L

Abbreviations: see Figure 1 and Table 3.

1973]). At 15 kbar, the orthoclase-out boundary terminates at about 860°C, where two coexisting feldspars are replaced by a single feldspar. At 25 kbar, the critical temperature occurs just above the reaction of jadeite. With increasing temperature, the feldspathic components exist as orthoclase + jadeite, orthoclase + albite through a narrow temperature interval, followed in turn by a single alkali feldspar.

At 15 kbar, traces of kyanite and metastable corundum exist above the heavy line marking the quartz-out boundary. At 25 kbar, kyanite phase fields extend from the muscovite-out boundary to temperatures of 100°C or more above the quartz-out boundary. The temperature of the kyanite-out boundary decreases as H_2O content decreases from 55% to 30% H_2O, which probably reflects the preferential solubility of alkalies in the vapor, compared with alumina and silica. Because kyanite is present only in trace amount, it seems appropriate to consider the upper stability limit of quartz as the liquidus, for comparison with the phase relationships of biotite-granite. The solubility of H_2O in the granite liquid, estimated by the intersections of the H_2O-saturation boundaries with the quartz liquidus, is 23±3% at 15 kbar, and 29±2% at 25 kbar.

Reactions can be reversed in the presence of H_2O-undersaturated liquids at 15 kbar and above. The quartz-out boundary with 9.5% H_2O at 15 kbar was reversed as shown in runs 284, 288, 382, and 289R, in the presence of traces of metastable corundum. The albite-jadeite reaction with 3-4.6% H_2O at 15 kbar was reversed as shown in runs 319, 315, and 322T.

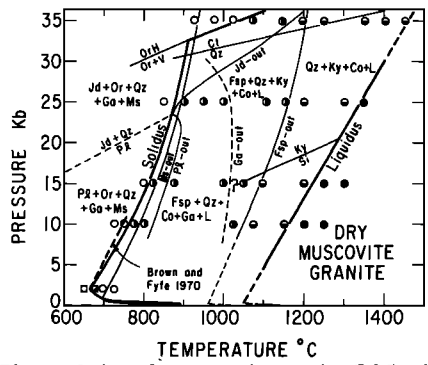

Fig. 3. Phase relations for muscovite granite (L26) with no water added, but 0.66% H_2O in the rock, stored in muscovite [*Huang and Wyllie,* 1973]. Experiments are listed in Table 4. The 2 kbar runs marked with square symbols were with excess H_2O. The dashed line is the solidus for a similar rock reported by *Brown and Fyfe* [1970]. Abbreviations: see Figure 1.

H_2O-Undersaturated Liquidus Surface

The liquidus surface corresponding to the quartz(coesite)-out phase boundary, neglecting the traces of kyanite, sillimanite, and corundum at higher temperatures, is given in Figure 6, with contours for constant H_2O contents. The limiting boundary for excess H_2O was taken from Figure 2, the contour for 0.6% H_2O was taken from Figure 3, and the dry liquidus boundary was estimated by taking the same slope as the 0.6% H_2O contour. The H_2O contours were passed through points from 15 kbar (squares) and 25 kbar (circles) taken directly from the quartz-out boundaries in Figures 4 and 5, respectively. The contours terminate on the excess-H_2O liquidus at crosses. The crosses were interpolated between the 15 kbar and 25 kbar solubilities determined at 15 kbar and 25 kbar, and calculated for lower pressures by *Huang* [1977], following the method of *Wasserburg* [1957] and using the data of *Burnham et al.* [1969] and *Burnham and Davis* [1971, 1974].

Muscovite coexists with quartz at or just below the liquidus with excess H_2O between about 5 kbar and 15 kbar, but with increasing pressure the quartz liquidus migrates to higher temperatures than the muscovite-out curve (Figure 2). Muscovite as a near-liquidus mineral does not extend across the H_2O-undersaturated liquidus surface, because of the divergence between the muscovite and quartz boundaries with decreasing H_2O content (Figures 4 and 5). At all pressures above 5 kbar, and probably at lower pressures where we have no results, kyanite, or sillimanite, or metastable corundum occurs on and above the H_2O-undersaturated quartz/coesite liquidus surface (Figures 2, 3, 4, and 5).

Microprobe Analyses of Phases at 15 kbar With 5% H_2O Added

Table 6 lists a series of runs conducted in gold capsules at 15 kbar specifically to prepare polished charges for electron microprobe determination of phase compositions for the 5% H_2O composition in Figure 4. The phases coexisting with glass are listed, according to the results given in Figure 4 and Table 5, and the average composition of glass determined from several analyses is given for each temperature.

The glasses analyzed were clear, free of minerals, and the consistency among analyses indicates that they were homogeneous. The glass compositions change fairly regularly with increasing temperature. The result at 800°C departs somewhat from the main trends, which are as follows. At 650°C and 700°C, SiO_2 is low, Al_2O_3 is high, and K_2O is high compared with the composition of the granite (Table 1). The glass compositions (anhydrous) are similar to that of syenite, which is consistent with the pressure effect on the composition of the eutectic in the residua system [*Huang and Wyllie,* 1975]. Between 700°C and 800°C, SiO_2 increases significantly towards granitic values, and Al_2O_3 drops markedly. Between 800°C and 900°C, the plagioclase dissolves, and Na_2O increases. If the difference between the total analyses and 100% is equated approximately to the H_2O content of the glass, and thus to that of the original H_2O-undersaturated liquid, the results indicate that dissolved H_2O changed from about 11–13% between 650°C and 800°C, with a decrease to about 7–8% associated with the increased melting where plagioclase and muscovite disappear between 800°C and 900°C. According to Figures 4 and 6, and 23% H_2O is required for saturation of the liquid at 15 kbar.

The average compositions of plagioclase crystals were determined at 650°C (6 analyses) and 700°C (10 analyses). The results in mole per cent anorthite were 5.9 at 650°C, and 5.1 at 700°C, essentially unchanged compared with the 5.1% in the original granite. The paragonite contents of muscovite from runs at 700°C and 750°C are, respectively, 5.9 and 3.7 mole per cent, compared with 6.7% in the muscovite of the original granite.

MUSCOVITE AND SILICATE-H_2O LIQUIDS

Phase relationships in the synthetic system K_2O-Al_2O_3-SiO_2-H_2O and the natural muscovite granite system illustrate the process of partial fusion of a rock containing a hydrous mineral but no free vapor, and outline the range of conditions under which muscovite will crystallize from H_2O-undersaturated silicate liquids. Figure 7 compares schematic phase relationships in T-X_{H_2O} diagrams at 2 kbar and 15 kbar for three different bulk compositions of increasing complexity: muscovite (invariant point Q_2 in Figure 1), muscovite + quartz (invariant point Q_1 in Figure 1) and muscovite granite (Figure 4). The amounts of H_2O stored in the crystalline assemblages are marked on the horizontal axes. For starting compositions with less H_2O than that required to constitute the maximum amount of muscovite, the vapor-absent assemblage includes muscovite and the products of the dehydration reaction.

At low pressures, muscovite dissociates at temperatures lower than the solidus, and melting begins for the anhydrous crystalline assemblage in the presence of H_2O vapor, with $P_{e_{H_2O}} = P_{total}$ (*Greenwood* [1961] for definition of $P_{e_{H_2O}}$). In Figures 7*a*, 7*b*, and 7*c* the point *a* gives the solubility of H_2O in the saturated liquid with composition of the mineral assemblage. The solidus reactions are univariant in Figures 7*a* and 7*b* (compare Figure 1), and melting is completed isothermally in the presence of vapor. For the muscovite granite in Figure 7*c*, vapor-present melting occurs through a temperature interval above the solidus. For mixtures with H_2O contents less than *a*, the assemblage passes through a vapor-absent region with $P_{e_{H_2O}} < P_{total}$. This region begins at the solidus for the univariant reactions, and at a temperature higher than the solidus for the more complex system (Figure 7*c*), the temperature interval increasing with H_2O content of the starting composition.

TABLE 5. Experimental Runs for Muscovite Granite (L26) at 15 kbar and 25 kbar With Water Contents Low Enough to Delineate the Vapor-Absent Regions

Run	Pressure, kbar	Temperature, °C	Wt. % H_2O	Duration, Hours	Results Phases Present
359	15	635	12	20	Qz, Ab, Ms, (Co), (Ga), L
357	15	660	9	22	Qz, Ab, Ms, L
353	15	660	12	23	Qz, Ms, L
374	15	700	1	23	Qz, Ab, Or, Ga, L
307	15	700	5	41	Qz, Ab, Ms, Ga, L
310	15	700	10	27	Qz, Ms, L
282	15	750	15	20	Qz, Ms, (Co), L
299	15	750	23	24	Qz, Ms, (Co), L
386	15	750	24	12	Qz, Ms, Co, L
301	15	750	25	22	Qz, (Ms), Co, L
293	15	775	15	22	Qz, Co, L
337	15	775	20	22	(Qz), Co, L
325	15	775	23	27	Ky, Co, L
303	15	795	5	20	Qz, Ab, Ms, Co, L
283	15	800	15	20	Qz, (Co), L
302	15	820	5	20	Qz, Ab, (Ms), Co, L
306	15	820	9	22	Qz, Co, L
292	15	825	15	23	Qz, Co, L
280	15	850	14	20	Co, L
388	15	850	3.2	18	Qz, Ab, Co, (Ga), L
390	15	875	2.7	10.5	Qz, Fsp, Co, Ga, L
382	15	875	5	10	Qz, Co, L
289R	15	940	9.5	9	...
	15	875	...	11	Qz, Co, L
288	15	900	9.5	11	Qz, Co, L
279	15	900	15	20	Co, L
284	15	925	9.5	9	(Si)?, Co, L
354	15	950	5	23	Qz, (Si)?, (Co), L
363	15	1000	5	5	Qz, Co, L
501	15	1125	1.6	23	Qz, Co, L
502	15	1175	1.6	23	Co, L
392T	25	595	5	5	...
	25	630	...	6	Qz, Jd, Ms
389T	25	595	10	5.5	...
	25	630	...	6	Qz, Jd, Ms
379T	25	595	10	5	...
	25	650	...	15	Qz, Jd, Ms, (L)
377	25	675	10	15	Qz, Jd, Ms, L
504	25	725	5	32	Qz, Jd, Ms, L
360	25	720	16	20	Qz, Jd, Ms, L
372	25	750	1.6	21	Qz, Jd, (Or), Ms, L
320T	25	595	3	6	...
	25	750	...	39	Qz, Jd, Ms, L
313T	25	595	10	11.5	...
	25	725	...	5	...
	25	750	...	21	Qz, Jd, Ms, L
318T	25	595	13	6	...
	25	750	...	18	Qz, Jd, Ms, L
397	25	770	20	13	Qz, (Ky), L
352	25	770	25	20	Qz, (Ms), Ky, L
362	25	775	15	11	Qz, Ms, L
316T	25	595	15	15	...
	25	800	...	25	Qz, Ky, L
503	25	820	5	24	Qz, Jd, Ms, L
391	25	825	0.5	10.5	Qz, Jd, Or, Ms, L
315	25	850	4.6	24	Qz, Jd, Ms, L
368	25	855	25	18	Ky, L
319	25	875	4.5	24	Qz, Ab, (Ms), Ky, L
298	25	875	20	18	Qz, Ky, L
295	25	875	25	15	Ky, L
322T	25	850	3	24	...
	25	885	...	24	Qz, Ab, (Ms), Ky, L
297	25	900	20	15	Ky, L
394	25	910	3.3	5.5	Qz, Fsp, Ky, L
291	25	925	20	15	Ky, L
309	25	925	25	16	Ky, L
378	25	950	5	19	Qz, Ms, L
375	25	950	7.3	18	Qz, Ky, L
311	25	950	25	15	(Ky), L
286	25	975	10	6	Qz, Ab, Ky, L
287	25	1025	9.5	6	Qz, Ky, L
371	25	1025	23	22	(Ky), L

TABLE 5. (continued)

Run	Pressure, kbar	Temperature, °C	Wt. % H_2O	Duration, Hours	Results Phases Present
294	25	1050	10	10	Ky, L
290	25	1075	10	6	Ky, L
398	25	1075	21.5	12	(Ky), L
365	25	1100	5	5	Qz, Ky, L
308	25	1125	10	0.5	Qz, (Ky), Co, L
312	25	1125	10	6	Ky, L
367	25	1225	10	10	Co?, L

Abbreviations: see Figure 1 and Table 3.

At the pressures corresponding to the invariant points in Figure 1, the temperature of a dehydration reaction reaches that of a solidus reaction. The shaded areas in Figure 7 show where at higher pressures the muscovite is stable at temperatures above the solidus. At 15 kbar, the vapor-absent melting reactions in Figures 7*d* and 7*e* are located at temperatures higher than the vapor-present reactions, following the univariant reactions in Figure 1. The same condition exists for the muscovite granite in Figure 7*f*, as determined in Figures 2, 3, and 4.

Each melting reaction in Figures 7*d* and 7*e* is univariant, but dissociation products of muscovite occur at temperatures above each reaction. The vapor-present solidus reactions produce liquid saturated with H_2O. For mixtures with more H_2O than that represented by points *a* muscovite melts completely at the solidus, but for mixtures with less H_2O muscovite persists with other minerals and H_2O-undersaturated liquid through an interval extending to the vapor-absent solidus temperature. The muscovite-out boundaries *ab* connect the two solidus reactions through the vapor-absent region, with $P_{e_{H_2O}} < P_{total}$. For the muscovite granite at 15 kbar (Figure 7*f*), the vapor-absent region is bounded below by a line diverging from the solidus with increasing H_2O content (as in Figure 7*c*), and by the muscovite-out curve rising through the vapor-absent region to the vapor-absent solidus reaction. Muscovite persists through a considerable temperature interval above the vapor-present solidus. The liquid produced by the melting of vapor-absent muscovite granite is H_2O-undersaturated, corresponding to the liquid associated with points *b* in Figures 7*d* and 7*e*.

It is not necessary for a silicate liquid to be sautrated with H_2O in order to precipitate muscovite, or any other hydrous mineral. The assemblage H_2O-undersaturated liquid + muscovite + other minerals exists in the shaded areas in Figure 7. Therefore, muscovite can be precipitated from an initial liquid with very low H_2O contents (compare biotite in *Stern and Wyllie* [this issue, Figure 6], after *Maaløe and Wyllie* [1975]).

The vapor-absent regions in synthetic and natural systems are illustrated in Figure 7. However, because $P_{e_{H_2O}}$ can vary from P_{total} to zero in these regions, it would be useful to map them in terms of $P_{e_{H_2O}}$. In natural systems, reactions may occur in the presence of multicomponent pore fluids, so that even in vapor-present systems, $P_{e_{H_2O}}$ may be much lower than P_{total}. Detailed theoretical treatments for dissociation reactions have been presented by *J. B. Thompson* [1955] and *Greenwood* [1961, 1967], but there is little information about melting reactions because of the paucity of thermodynamic data for liquids.

Dissociation and Melting of Muscovite With $P_{e_{H_2O}} < P_{total}$

Greenwood [1961] constructed a generalized three-dimensional P_{total}-$P_{e_{H_2O}}$-T model for the dissociation reactions of hydrous minerals. Figure 8 is a similar phase diagram constructed to illustrate the dissociation and melting reactions of muscovite around the invariant point Q_2 in Figure 1, with $P_{e_{H_2O}}$ as an additional independent variable. Figure 9 gives projections of the surfaces from within the model, contoured in terms of $P_{e_{H_2O}}$. *Greenwood*'s [1961] thermodynamic treat-

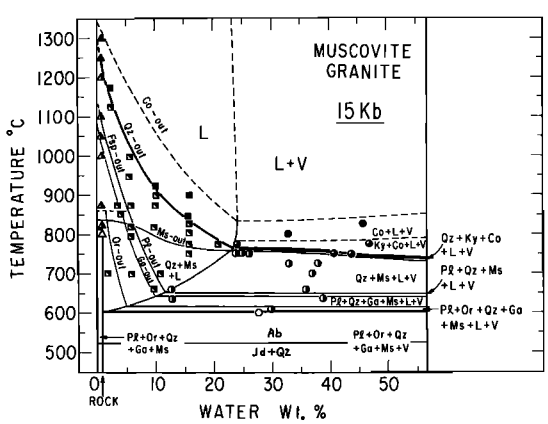

Fig. 4. Phase relations for muscovite granite (L26) with varying H_2O contents at 15 kbar (modified after *Huang and Wyllie* [1973]). Experiments are listed in Tables 3, 4, and 5. Abbreviations: see Figure 1. Circles—vapor present; squares and triangles—vapor absent; triangles—dry rock starting material.

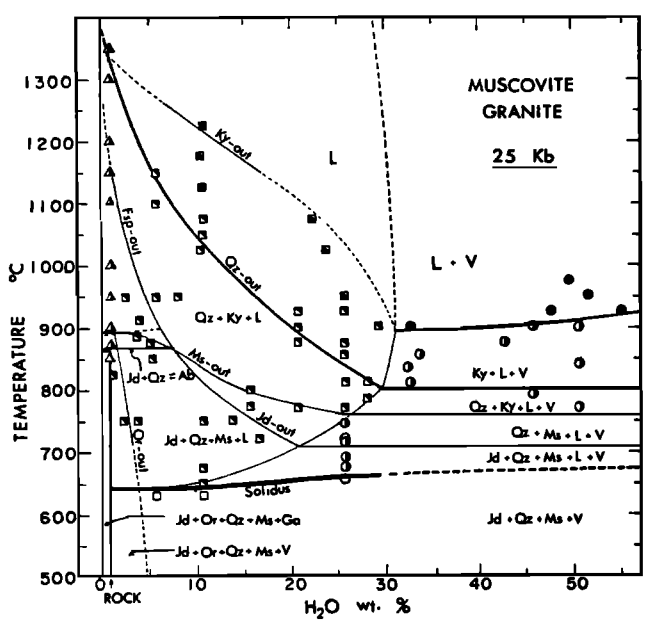

Fig. 5. Phase relations for muscovite granite (L26) with varying H_2O contents at 25 kbar [after *Huang*, 1977]. Experiments are listed in Tables 3, 4, and 5. Abbreviations: see Figure 1. Symbols: see Figure 4.

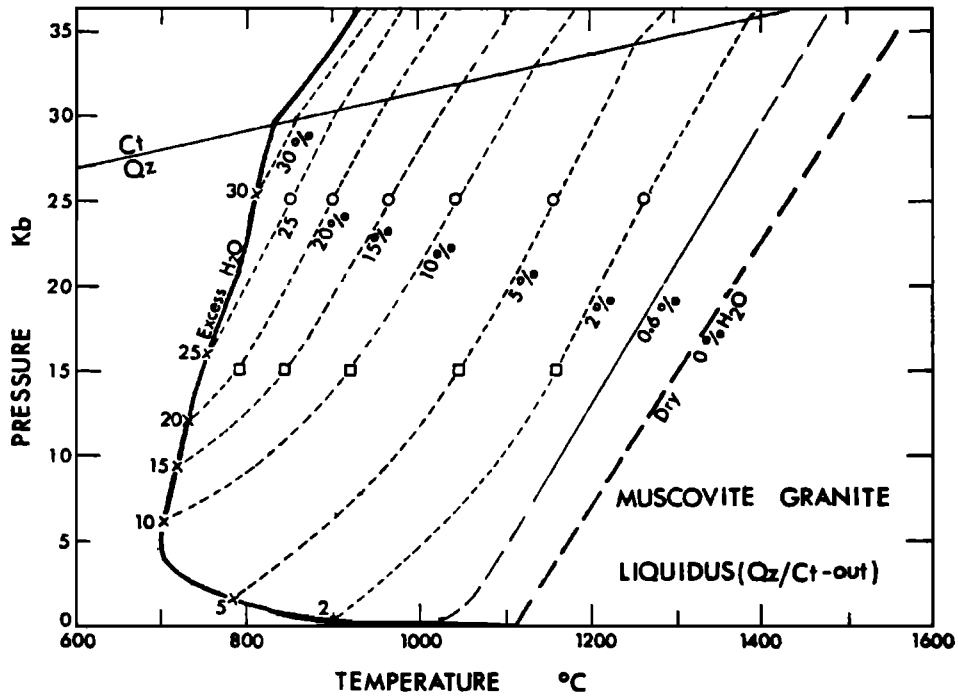

Fig. 6. The H_2O-undersaturated liquidus surface for muscovite granite (L26), neglecting the small amounts of aluminosilicate minerals existing at higher temperatures (Figures 2, 4, and 5). The surface connects the excess-H_2O quartz/coesite-out boundary (Figure 2) with the estimated position of the anhydrous liquidus. The surface is contoured by lines of constant H_2O content, and mapped with areas of primary crystallization of quartz and coesite. Muscovite is almost coincident with the excess-H_2O boundary between 5 kbar and 10 kbar (Figure 2). Abbreviations: see Figure 1.

ment of $P_{e_{H_2O}}$ involved an osmotic system. In the system K_2O-Al_2O_3-SiO_2-H_2O, $P_{e_{H_2O}}$ can be varied independently only if P_{vapor} can be reduced relative to P_{total}. This condition exists with vapor-absent H_2O-undersaturated liquid.

In Figure 8*c*, the univariant reactions around Q_2 are reproduced from Figure 1, together with the anhydrous fusion curve for Or + Co. The five phases Ms + Or + Co + L + V coexist at point Q_2. Each reaction curve involves four of these

TABLE 6. Electron Microprobe Analyses of Glass From Runs on Granite (L26) With 5 wt % Water Added at 15 kbar, Using Gold Capsules

Run	506	509	505	507	508	510
Temperature, °C	1000	950	900	800	700	650
Duration, hours	9	7	25	48	102	141
No. of analyses	4	5	6	7	5	4
Coexisting phases	Qz, Co	Qz, (Co)	Qz, Co	Ms, Pl, Qz, Co	Ms, Pl, Qz, Ga	Ms, Pl, Qz, Ga
SiO_2	71.8	70.9	69.5	70.8	54.0	56.9
TiO_2	...	...	...	...	...	0.06
Al_2O_3	12.9	13.0	14.3	11.7	23.5	19.3
Cr_2O_3	...	...	...	...	...	...
FeO	0.3	0.4	0.4	0.8	1.1	1.3
MnO	...	...	...	...	...	...
MgO	...	...	...	...	...	...
CaO	0.6	0.5	0.5	0.7	0.6	0.6
Na_2O	3.7	4.1	4.5	1.8	2.5	3.2
K_2O	3.1	3.1	3.5	3.10	6.3	5.5
Total	92.3	92.1	92.7	88.9	88.0	86.9
	Recalculated to 100% Total					
SiO_2	77.8	77.1	75.0	79.6	61.4	65.5
TiO_2	...	...	...	...	...	0.07
Al_2O_3	14.0	14.1	15.4	13.2	26.7	22.2
Cr_2O_3	...	...	...	...	...	...
FeO	0.3	0.5	0.4	0.9	1.3	1.5
MnO	...	...	...	...	...	...
MgO	...	...	...	...	...	...
CaO	0.6	0.6	0.6	0.8	0.7	0.7
Na_2O	4.0	4.5	4.9	2.0	2.8	3.7
K_2O	3.3	3.3	3.7	3.5	7.2	6.3

Abbreviations: see Figure 1 and Table 3.

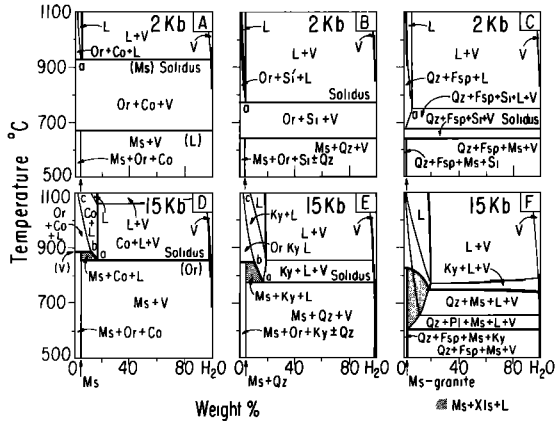

Fig. 7. Isobaric diagrams comparing the geometry of the melting relationships for muscovite-H_2O and muscovite+quartz-H_2O with that for muscovite-granite-H_2O at 2 kbar and 15 kbar (compare Figure 4). Abbreviations: see Figure 1.

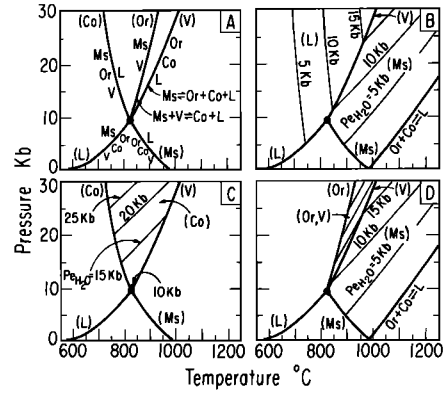

Fig. 9. P_{total}-T projections of the divariant surfaces from within the model of Figure 8*a*, illustrated by the contours for constant $P_{e_{H_2O}}$. The surface (Or, V) connects the reactions *a* and *b* in Figure 8*c*, and corresponds to the vapor-absent phase boundary *a-b* in Figure 7*a*. Abbreviations: see Figures 1 and 8.

phases, and it is identified by the fifth, missing phase, placed in parentheses. The reactions (Or) and (V) are the reactions identified by *a* and *b*, respectively, in Figure 7*d*. The five reactions around Q_2 are plotted in Figure 8*a* in a model with $P_{e_{H_2O}}$ as a third orthogonal axis, and with the diagonal plane representing the condition $P_{e_{H_2O}} = P_{total}$. The four reactions with excess vapor from Figure 8*c* are situated on this diagonal plane, as illustrated in the projection in Figure 8*b*. The vapor-absent melting curve for muscovite, (V), extends upwards from Q_2 into the region where $P_{e_{H_2O}} < P_{total}$, as shown clearly in projection in Figure 8*b*, and somewhat less clearly in Figure 8*a*.

The vapor-absent fusion curve for muscovite, (V), is connected to each of the other three univariant fusion curves by divariant surfaces within the model of Figure 8*a*. The divariant surface (L) extending from the subsolidus dehydration reaction also terminates along the line (V). These four surfaces are situated within the volume for $P_{e_{H_2O}} < P_{total}$ (Figures 8*a* and 8*b*), and their geometrical positions can be illustrated by contours for constant values of $P_{e_{H_2O}}$, as shown in Figure 8*a*. In Figure 9, the four divariant reaction surfaces are more clearly distinguished in projections; each univariant reaction is identified in Figure 9*a*, and each corresponding contoured surface from Figure 8*a* is projected onto the front P_{total}-T face of the model.

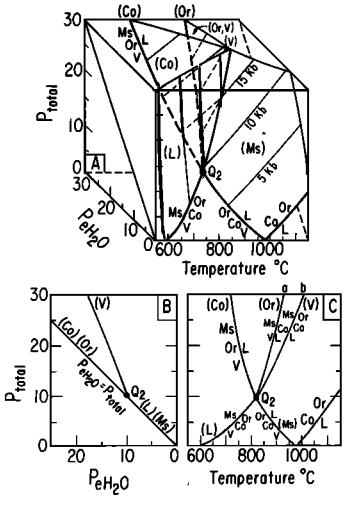

Fig. 8. Schematic diagram showing dehydration and melting reactions involving muscovite in the system K_2O-Al_2O_3-SiO_2-H_2O, including the conditions $P_{e_{H_2O}} < P_{total}$. Abbreviations: see Figure 1. Parentheses identify a phase assemblage in terms of the phase(s) absent from the invariant 5-phase assemblage at Q_2. Pressure axis is in kilobars. (*a*) P_{total}-$P_{e_{H_2O}}$-T diagram, showing the diagonal surface for $P_{e_{H_2O}} = P_{total}$. (*b*) Projection of univariant reactions, showing that reactions (Co), (Or), (Ms), and (L) coincide with projection of the $P_{e_{H_2O}} = P_{total}$ plane, whereas the vapor-absent reaction (V) is inclined to the plane. (*c*) Projection of univariant reactions onto the P_{total}-T face (compare Figure 1), together with the anhydrous melting curve.

Figure 9*b* shows the projection of the two divariant surfaces (L) and (Ms) together with curve (V), along which they intersect. The slopes of $P_{e_{H_2O}}$ contours for (L) are assumed to be similar to those presented for the dissociation of muscovite + quartz by *Kerrick* [1972]. The intersections of these contours with the reaction curve (V) gives $P_{e_{H_2O}}$ values along (V). The $P_{e_{H_2O}}$ contours for the reaction (Ms) were drawn assuming the same slope as that for a syenite solidus surface [*Millhollen*, 1971] which is intermediate between results calculated for granite by *Kerrick* [1972] and for albite by *Burnham and Davis* [1974]. Contours on the surfaces (Co) and (Or, V) were drawn to connect values on the reaction curve (V) to the corresponding P_{total} pressures on the univariant curves (Co) and (Or), respectively (Figures 9*c* and 9*d*).

The divariant dehydration surface (L) in Figures 8*a* and 9*b* shows how reduction of $P_{e_{H_2O}}$ lowers the dissociation temperature at a given total pressure. The univariant reactions (Ms) and (Co) in Figure 8 show the beginning of melting in the system with excess H_2O, for the melting of assemblages Or + Co and Or + Ms. The divariant surfaces (Ms) in Figures 9*b* and 9*d*, and (Co) in Figure 9*c*, show how reduction of $P_{e_{H_2O}}$ increases the temperature of beginning of melting at a given total pressure. All H_2O is dissolved at these surfaces, giving H_2O-undersaturated liquids.

The vapor-absent divariant melting surface (Or, V) of Figures 8*a* and 9*d* is the liquidus for the assemblage Ms + Co. The line *ab* in Figure 7*d* corresponds to the 15 kbar section through this surface. At constant pressure, Figure 9*d* shows that $P_{e_{H_2O}}$ decreases, as the maximum temperature stability of Ms + Co + L increases from the H_2O-saturated melting of muscovite (Or) to its vapor-absent melting reaction (V). This is accompanied by a decrease in H_2O content of the liquid (Figure 7*d*).

The effect of decreasing $P_{e_{H_2O}}$ on muscovite stability therefore differs depending on the reaction. For subsolidus dehydration, (L), the temperature of muscovite reaction is lowered

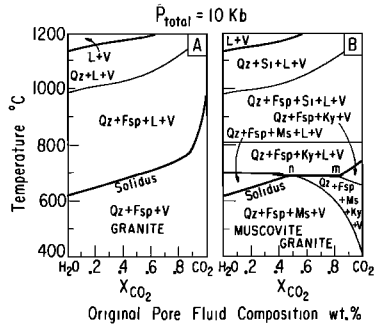

Fig. 10. The effect of H_2O-CO_2 mixtures on the melting relationships of granite at 10 kbar in a closed system, with initial subsolidus vapor phase compositions given by the horizontal axis, and initially 2% vapor present. Partly schematic: see text for method of construction. It is assumed that CO_2 solubility in granitic liquids is negligible [*Wyllie and Tuttle*, 1959; *Mysen et al.*, 1976]. Abbreviations: see Figure 1. (*a*) Simple granite without hydrous minerals. (*b*) Muscovite granite. The dissociation of muscovite enriches the vapor in H_2O, lowering the solidus towards the CO_2 side compared with the simple granite. Compare *Kerrick* [1972, Figure 5].

(Figure 9*b*); for vapor-absent melting, (Or, V), the temperature of muscovite stability is increased (Figure 9*d*).

The divariant reactions shown in Figures 8 and 9 are valid for the plotted values of $P_{e_{H_2O}}$, whatever the mechanism for producing these values. During metamorphism, the condition $P_{e_{H_2O}} < P_{total}$ is commonly achieved by the presence of a mixed pore fluid, such as H_2O-CO_2. Conditions on the dehydration surface, all three fusion surfaces, and the univariant reaction (V) can therefore be attained in the presence of vapor of appropriate compositions.

Buffering Effect of Muscovite on the Solidus of Granite-H_2O-CO_2

Figure 10 compares the phase relationships for granite and muscovite granite in closed systems at 10 kbar, with $P_{e_{H_2O}} < P_{total}$ achieved by diluting H_2O with CO_2. Each system has 2% pore fluid at low temperatures, with the original pore fluid composition given by the horizontal axis. With increasing temperature, melting or dissociation begins, and the vapor phase then changes in composition and amount and is no longer represented by the horizontal scale. The solidus and liquidus for pure H_2O are taken from Figures 2 and 6 (2% H_2O contour for H_2O-undersaturated liquidus surface).

The solidus in Figure 10*a* is based on calculation of $P_{e_{H_2O}}$ at the corresponding P_{total}, temperature, and mole fraction of H_2O in H_2O-CO_2 mixtures, from the thermodynamic properties of H_2O [*Burnham et al.*, 1969], following the method of *Millhollen* [1971]. The calculations assume ideal mixing of H_2O and CO_2, negligible solubility of CO_2 in the silicate melt, and no carbonate phases stable. The slope of the solidus curve is intermediate between that calculated for granite melting by *Kerrick* [1972] and for albite by *Burnham and Davis* [1971, 1974]. The solidus for granite-CO_2 is high, effectively the same as that for granite alone. Figure 10*a* shows that addition of very little H_2O to the pore fluid is sufficient to cause a large depression of the solidus temperature. In contrast, the addition of CO_2 to an aqueous pore fluid is much less effective in raising the solidus temperature.

The solidus for muscovite granite in Figure 10*b* with pore fluids from H_2O to *n* is effectively the same as that in Figure 10*a* [compare *Stern and Wyllie*, this issue; *Huang and Wyllie*, 1975]. For pore fluids richer in CO_2 than point *n*, however, muscovite begins to dissociate at temperatures below the solidus. Dehydration of muscovite in a close system changes the pore fluid compsoition towards H_2O. The muscovite dissociates through an isobaric divariant interval, beginning along the curve which intersects the solidus at point *n*. For a rock with original pore fluid composition between *n* and *m*, dissociation of muscovite drives the pore fluid composition to *n*, at which point melting begins. This is represented by the isothermal solidus line *n*-*m*. For original pore fluids with more CO_2 than point *m*, all muscovite is dissociated with pore fluid composition richer in CO_2 than point *n*, and the solidus temperature is therefore at some higher temperature than *n*, corresponding to a point on the solidus of Figure 10*a*. The solidus temperature never reaches the high values for granite-CO_2 shown in Figure 10*a*, because the dissociation of muscovite maintains a relatively high value of H_2O/CO_2 in the pore fluid.

For muscovite granite in the presence of pore fluids with a range of compositions (*n*-*m* in the specific example of Figure 10), the solidus temperature is buffered by the muscovite dehydration. The conditions for the beginning of melting are defined by the temperature and pore fluid composition at the intersection point, *n*. The locus of point *n* in *P*-*T*-*X* space is a univariant vapor-buffered curve on the solidus surface for muscovite-granite-H_2O-CO_2, representing the intersection of the divariant solidus surface for the rock with the divariant subsolidus dehydration surface for muscovite in this assemblage. The geometry and principles are the same as those described for solidus reactions buffered by amphibole, phlogopite, and dolomite in the system peridotite-H_2O-CO_2 [*Wyllie*, 1977*b*, 1978, 1979; *Eggler*, 1978].

The principle of the involvement of muscovite in granite melting is illustrated in terms of $P_{e_{H_2O}}$ (regardless of mechanism for reducing $P_{e_{H_2O}}$ relative to P_{total}) by the intersection of two divariant surfaces in Figure 8*a*. For the condition $P_{e_{H_2O}} < P_{total}$, the subsolidus dehydration of muscovite is represented by the surface (L). This surface meets the muscovite-bearing solidus surface (Co) along the univariant vapor-absent reaction (V). In Figure 10*b*, the corresponding isobaric curves for the solidus and muscovite dehydration (with $P_{e_{H_2O}} < P_{total}$ achieved by diluting H_2O with CO_2) meet at the isobaric invariant point *n*. The muscovite-absent solidus curve rising from *m* in Figure 10*b* corresponds to a portion of the solidus surface (Ms) extending from (V) in Figure 8*a*. Values of $P_{e_{H_2O}}$ on curve (V) in Figure 8 define the values in the H_2O-CO_2 fluids on the corresponding vapor-present buffered solidus curve. At higher temperatures, because of the artificial conditions set up for Figure 10, further analogy with Figure 8 becomes complicated.

The variations in X_{H_2O} and $P_{e_{H_2O}}$ illustrated in Figures 7, 8, 9, and 10 can also be expressed in terms of activity of H_2O (a_{H_2O}). *A. B. Thompson and Algor* [1977] have calculated *P*-*T*-a_{H_2O} paths for melting and crystallization in systems modelling muscovite granite and pelitic rocks, with particular reference to the effect of excess Al_2O_3 relative to the residua system, Ab-Or-Qz-H_2O.

Discussion

Much of the discussion of *Stern and Wyllie* [this issue] for the biotite granite is directly applicable to this muscovite granite, because the phase relationships are basically similar. The main difference is associated with the 4.8% normative co-

rundum in this rock, compared with none in the biotite granite, and with the differing reactions of 13.8% muscovite compared with only 4.7% biotite.

With excess H_2O, the solidus and the interval to the quartz/coesite-out boundary are almost the same in both rocks. The biotite survives through only a short temperature above the solidus and only at pressures below 10 kbar. The muscovite is a near-liquidus mineral between about 5 kbar and 10 kbar, and persists to at least 35 kbar, the highest pressure of experiments.

The H_2O-undersaturated liquidus surface for the biotite granite, dominated by quartz/coesite with plagioclase present only at low pressures and high temperatures, is similar in position and shape to the quartz/coesite surface in the muscovite granite. In the latter rock, kyanite or sillimanite and metastable corundum are produced in addition to quartz/coesite surface.

Stern and Wyllie [this issue] reviewed the eutectic-like character of biotite granite with excess H_2O up to about 5 kbar, and the loss of this character at higher pressures. Figure 2 illustrates the same characteristics for the muscovite granite. Note, however, that the melting interval at low pressures is about 100°C, which is not strictly 'eutectic' behavior. The determination that liquids at 650°C and 700°C at 15 kbar are syenitic (Table 6) confirms the explanation of this change in terms of migration of the eutectic composition in the feldspar-quartz Residua System away from SiO_2 with increasing pressure [*Huang and Wyllie,* 1975].

Stern and Wyllie [this issue] also emphasized that the eutectic-like condition exists only with excess H_2O. With less H_2O present than that required to saturate the liquid, there is a wide temperature interval between solidus and liquidus, as illustrated for the muscovite granite in Figures 3, 4, and 5.

Experimental results for both granites confirm that biotite and muscovite can be precipitated from H_2O-undersaturated liquids in magmas (liquid + crystals) with very low H_2O contents, at pressures ranging from low values where the hydrous mineral stability curve crosses the excess-H_2O solidus, to the highest pressures where the hydrous mineral is stable above the solidus. A significant H_2O limit is given by the geometrical boundary for the subsolidus tie-figure including the hydrous mineral without vapor. This amount of H_2O is marked in Figures 4, 5, and 7 by the vertical lines separating vapor-absent from vapor-present subsolidus assemblages. For magmas with H_2O contents less than this limit, a trace of hydrous mineral is produced as the vapor-absent liquid solidifies. The details depend on whether the hydrous mineral melts congruently or incongruently in the mineral assemblage [*Robertson and Wyllie,* 1971]. For magmas with H_2O contents greater than this limit, precipitation of the hydrous mineral is followed through a temperature interval by the coprecipitation of other minerals from the vapor-absent assemblage until vapor exsolution occurs, followed by crystallization of the H_2O-saturated liquid at the vapor-present solidus.

There is a misconception prevalent in the literature that hydrous minerals can be precipitated only from magmas with several per cent of H_2O. In his discussion of the crystallization of hydrous minerals from silicate melts, *Burnham* [1979, pp. 90–91] wrote: 'Therefore, the minimum value of X_m^w at which hornblende can exist stably with melt in this system is approximately 0.3 which is roughly equivalent to 3.0 wt. % H_2O. This minimum H_2O content is almost independent of magma composition, and, from the work of *Yoder and Kushiro* [1969], also appears to hold for biotite.' This does not mean that an original liquid must contain at least 3% H_2O in order to precipitate hydrous minerals within the crystallization interval, a view maintained by some petrologists. Using Figure 7*e* as an example, it means that the H_2O content of the H_2O-undersaturated liquid associated with the assemblage Ms + Or + Ky + L at temperature *b* is at least 3% (compare the corresponding reaction for muscovite granite in Figure 7*f*). Consider the phase assemblage at a temperature just above *b*. Because the assemblage Or + Ky + L contains H_2O content given by point *b*, the vapor-undersaturated liquid contains somewhat more H_2O than *b*, the precise amount depending on the proportion of liquid to crystals. It is this liquid which then precipitates muscovite. This is the liquid discussed by *Burnham* [1979], with the limit of at least 3% H_2O. This is a liquid within a magma composed to liquid + crystals, but note from Figure 7*e* that this assemblage can be derived from original high-temperature liquids with H_2O contents ranging from *b* to almost 0%. What varies with original H_2O content is the percentage of H_2O-undersaturated liquid of defined composition at the temperature *b*.

Whether the activity of H_2O is reduced to low levels by small amounts of H_2O in a vapor-absent system, or by high CO_2/H_2O in a vapor-present system, the preceding discussion demonstrates how muscovite, biotite, or amphibole can be precipitated from normal silicate magmas with H_2O contents certainly as low as 0.5% (corresponding to the subsolidus boundary for maximum hydration). At the stage of initial precipitation, *Burnham's* [1979] work indicates that the H_2O content of the H_2O-undersaturated liquid in the magma exceeds 3%. This limit must vary as a function of pressure and bulk composition (and hence mineralogy).

Figures 7, 8, 9, and 10 permit some generalizations about the melting and stability of hydrous minerals such as muscovite, biotite, and amphibole if a_{H_2O} or $P_{e_{H_2O}}$ is decreased by increasing the ratio of CO_2/H_2O in the vapor phase: (1) the temperature of beginning of melting of mineral assemblages is increased, (2) the temperature of subsolidus dehydration of hydrous minerals is decreased, (3) the stability temperature of hydrous minerals coexisting with liquid is increased (to the maximum value where CO_2/H_2O gives a_{H_2O} corresponding to the vapor-absent melting reaction). For further examples, see *Eggler* [1972], *Holloway* [1973], *Eggler and Burnham* [1973], *Allen and Boettcher* [1978], and *Allen et al.* [1975].

The phase relationships can be used to test for conditions under which the muscovite granite could be a primary magma from various source rocks. The near-liquidus minerals for a primary magma must correspond to the major minerals in the source rock at the depth and temperature of origin. The liquidus minerals are sillimanite or kyanite, but there is a well-defined sub-liquidus surface for the coexistence of these minerals with quartz or coesite (Figures 2 to 6). Quartz or coesite crystallizes without feldspar through a considerable interval below the liquidus. The candidates for source rocks are mantle peridotite, subducted oceanic crust, and continental crust. Neither of the first two sources could yield granitic liquid with prominent, residual quartz/coesite. *Huang and Wyllie* [1973] used results for the muscovite granite to model the partial melting of marine sediments during subduction, and concluded that the products would not be primary granites or rhyolites. This conclusion is now confirmed by the analyses of glass from the partly melted rock at mantle pressures (Table 6).

It is well-established that H_2O-undersaturated granite liquid is a normal product of regional metamorphism of varied crustal rocks [e.g., *Wyllie, 1977a*]. For this muscovite granite to be a primary melt from the crust, it would have to be derived from a source rock leaving residual sillimanite. It could possibly represent a primary melt leaving residual muscovite and quartz under specific conditions (Figure 2): at depth corresponding to pressures between 5 kbar and 10 kbar, temperature of 700°C to 725°C, with sufficient H_2O to saturate the liquid with 9–16 wt. % H_2O (depending on the pressure, Figure 6). In fact, the high muscovite content (reflected in the high normative corundum) is sufficient to disqualify this bulk composition as a candidate for a primary melt from the crust. The available evidence suggests that only a few percent of muscovite is soluble in granite liquids at crustal pressures [*Lambert et al.*, 1969, Figure 5; *Wyllie, 1977a*, Figure 2]. Therefore, the mineralogy of this particular granite indicates either that it represents a granite melt with additional muscovite (possibly derived from restite material), or that it represents a melt from which a vapor phase has leached alkalies [e.g., *Tuttle and Bowen*, 1958, pp. 89–91; *Norton*, 1970].

The phase relationships for granitic and related rocks are consistent with the ideas of I-type and S-type granites [*Chappell and White*, 1974; *White and Chappell*, 1977], but the major-element relationships are not adequate to exclude alternative processes. Additional experiments related to the origin of S-type granites include those with pelitic sediments by Winkler and associates (see *Winkler* [1976] for a review), *Wyllie and Tuttle* [1961], *Kilinc* [1972], and *Green* [1976]. *Wyllie and Tuttle* [1961] melted five standard shales from Pennsylvania, varying widely in chemical composition, in the presence of excess H_2O at pressures up to 3 kbar. The solidus curves were 20°C to 40°C higher than the corresponding curve for granites. About 150°C above the solidus curves the shales were about 50% melted, and the refractive indices of the quenched glasses indicated that the liquid compositions were in the range granite-granodiorite. The melts were accompanied by residual refractory minerals including quartz, cordierite, hypersthene, muscovite, mullite, and calcic plagioclase.

Green [1976] tested the proposal that specific S-type granites were derived by partial melting of pelitic rocks. He confirmed that the fusion of pelitic rocks with 2% and 5% H_2O pressures of 4 kbar, 7 kbar, and 10 kbar produces granitic liquids. He compared Fe/Mg ratios in the liquids and residual cordierite and garnet with partition relationships in natural S-type granites, and concluded that the results were consistent with magma generation from the pelitic rocks at 800 ± 20°C (below the maximum stability of biotite), at depths greater than 25 km for garnet-bearing granites, and less than 25 km for cordierite-bearing granites (compare Figures 2 and 6 at 800°C and 7 kbar = 25 km).

The phase relationships for a single rock summarized in this paper provide constraints about its origin, but they do not provide an adequate basis for the petrogenesis of S-type granitoids. It is necessary to consider in addition the phase relationships of other rocks constituting a batholithic series, as well as the field relationships and the geochemistry of trace elements and isotopes. There is growing evidence from geochemistry and geophysics that few granites have a simple origin [e.g., *Atherton and Tarney*, 1979], and many batholiths contain evidence for the involvement of material from subducted oceanic crust, mantle, and continental crust [e.g., *Hamilton and Myers*, 1967; *Wyllie, 1977c*; *Burnham*, 1979].

Johannes [1980] concluded that most experimental results on granitic rocks at crustal pressures were metastable, and he raised an important question: To what extent is it valid to apply metastable experimental results on granitic rocks to natural processes? *Stern and Wyllie* [this issue] reviewed this topic, and agreed that the attainment and demonstration of reversible equilibrium is impossible in many parts of the multi-mineral granite systems. The failure to reach equilibrium with muscovite granite at 2 kbar in runs of 4 and 7 months duration is confirmed in Figures 2 and 3 (Tables 3 and 4). Some phase boundaries were reversed within 25°C at 15 kbar and 25 kbar, but metastable corundum was widely distributed. We endorse *Johannes'* [1980] conclusion, but we feel satisfied that the patterns of phase relationships that have emerged from many experimental studies on many compositions are applicable to petrological processes. They help to distinguish between possible and impossible processes. When it comes to tracing the specific compositions of feldspars and liquids in the low-pressure H_2O-undersaturated regions most directly applicable to the emplacement and crystallization of batholiths, however, experiments have not yet provided definitive information.

Another aspect of the equilibrium question, and the applicability of experimental data to real magmas, is provided by the crystal growth experiments of *Naney and Swanson* [1980] using model granitic compositions with added Fe-Mg components. They found that the mafic minerals (orthopyroxene, clinopyroxene, biotite, hornblende, epidote, and magnetite) nucleated and grew outside of their thermal stability fields as defined by equilibrium phase diagrams. In the undercooling crystal growth experiments, the nucleation of feldspars and quartz was greatly inhibited by the presence of Fe and Mg in the systems. They suggested that the border zones of granitic plutons may become enriched in mafic minerals by their more rapid nucleation and early crystallization rather than other processes of differentiation commonly proposed. *Johannes* [1980] suggested from his results with the felsic components that reaction rates are so slow that we should expect non-equilibrium processes to occur in the generation of granites as well as during their crystallization.

Acknowledgments. This research was supported by the Earth Sciences Section of the National Science Foundation, NSF grant EAR 76-20413. For review of earlier versions of parts of the manuscript we thank V. C. Juan, D. M. Kerrick, R. C. Newton, and Y. Wang.

REFERENCES

Allen, J. C., and A. L. Boettcher, Amphiboles in andesite and basalt, II, Stability as a function of P–T–f_{H_2O}–f_{O_2}, *Am. Mineral., 63*, 1074–1087, 1978.

Allen, J. C., A. L. Boettcher, and G. Marland, Amphiboles in andesite and basalt, I, Stability as a function of P–T–f_{O_2}, *Am. Mineral., 60*, 1069–1085, 1975.

Atherton, M. P., and J. Tarney (Eds.), *Origin of Granite Batholiths, Geochemical Evidence*, 148 pp., Shiva Publishing, Orpington, 1979.

Boettcher, A. L., and D. M. Kerrick, Temperature calibration in cold-seal vessels, in *Experimental Techniques in Non-Condensed Systems*, edited by G. C. Ulmer, pp. 178–193, Springer-Verlag, New York, 1971.

Brown, G. C., and W. S. Fyfe, The production of granite melts during ultrametamorphism, *Contrib. Mineral. Petrol., 28*, 235–244, 1970.

Burnham, C. W., Magmas and hydrothermal fluids, in *Geochemistry of Hydrothermal Ore Deposits*, 2nd ed., edited by H. L. Barnes, pp. 71–136, John Wiley, New York, 1979.

Burnham, C. W., and N. F. Davis, The role of H_2O in silicate melts, I,

P–V–T relations in the system $NaAlSi_3O_8$–H_2O to 10 kilobars and 1000°C, *Am. J. Sci., 270,* 54–79, 1971.

Burnham, C. W., and N. F. Davis, The role of H_2O in silicate melts, II, Thermodynamics and phase relations in the system $NaAlSi_3O_8$-H_2O to 10 kilobars, 700° to 1100°C, *Am. J. Sci., 274,* 902–940, 1974.

Burnham, C. W., J. R. Holloway, and N. F. Davis, The specific volume of water in the range of 1000 to 8900 bars, 20° to 900°C, *Am. J. Sci., 267-A,* 70–95, 1969.

Chappell, B. W., and A. J. R. White, Two contrasting granite types, *Pac. Geol., 8,* 173–174, 1974.

Eggler, D. H., Water-saturated and undersaturated melting relations in a Paricutin andesite and an estimate of water content in the natural magma, *Contrib. Mineral. Petrol., 34,* 261–271, 1972.

Eggler, D. H., The effect of CO_2 upon partial melting of peridotite in the system Na_2O-CaO-Al_2O_3-MgO-SiO_2-CO_2 to 35 kb, with an analysis of melting in a peridotite-H_2O-CO_2 system, *Am. J. Sci., 278,* 305–343, 1978.

Eggler, D. H., and W. C. Burnham, Crystallization and fractionation trends in the system andesite-H_2O-CO_2-O_2 at pressures to 10 kb, *Geol. Soc. Am. Bull., 84,* 2517–2532, 1973.

Green, T. H., Experimental generation of cordierite- or garnet-bearing granitic liquids from a pelitic composition, *Geology, 4,* 85–88, 1976.

Greenwood, H. J., The system of $NaAlSi_2O_6$-H_2O-argon: Total pressure and water pressure in metamorphism, *J. Geophys. Res., 66,* 3923–3946, 1961.

Greenwood, H. J., Mineral equilibria in the system MgO-SiO_2-H_2O-CO_2, in *Researches in Geochemistry,* vol. 2, edited by P. H. Abelson, pp. 542–567, John Wiley, New York, 1967.

Hamilton, W., and W. B., Myers, The nature of batholiths, *U.S. Geol. Surv. Prof. Pap., 554-C,* 30 pp., 1967.

Holloway, J. R., The system pargasite-H_2O-CO_2: A model for melting of a hydrous mineral with a mixed-volatile fluid, I, Experimental results to 8 kilobars, *Geochim. Cosmochim Acta, 37,* 651–666, 1973.

Huang, W. L., Melting and crystallization of hydrous granite at crust and mantle pressures, *Acta Geol. Taiwan., 19,* 13–28, 1977.

Huang, W. L., and P. J. Wyllie, Melting relations of muscovite-granite to 35 kbar as a model for fusion of metamorphosed subducted oceanic sediments, *Contrib. Mineral. Petrol., 42,* 1–14, 1973.

Huang, W. L., and P. J. Wyllie, Melting relations of muscovite with quartz and sanidine in the system K_2O-Al_2O_3-SiO_2-H_2O to 30 kilobars and an outline of paragonite melting relations, *Am. J. Sci., 274,* 378–395, 1974.

Huang, W. L., and P. J. Wyllie, Melting reactions in the system $NaAlSiO_3O_8$-$KAlSi_3O_8$-SiO_2 to 35 kilobars, dry and with excess water, *J. Geol., 83,* 737–748, 1975.

Huang, W. L., J. K. Robertson, and P. J. Wyllie, Melting relations of muscovite to 30 kbars in the system $KAlSi_3O_8$-Al_2O_3-H_2O, *Am. J. Sci., 273,* 415–427, 1973.

Johannes, W., Metastable melting in the granite system Qz-Or-Ab-An-H_2O, *Contrib. Mineral. Petrol., 72,* 73–80, 1980.

Kerrick, D. M., Experimental determination of muscovite + quartz stability with $P_{H_2O} < P_{total}$, *Am. J. Sci., 272,* 946–958, 1972.

Kilinc, I. A., Experimental study of partial melting of crustal rocks and formation of migmatites, *Proc. Int. Geol. Congr. 24th, Sect. 2,* 109–113, 1972.

Lambert, I. B., J. K. Robertson, and P. J. Wyllie, Melting reactions in the system $KAlSi_3O_8$-SiO_2-H_2O to 18.5 kilobars, *Am. J Sci., 267,* 609–626, 1969.

Maaløe, S., and P. J. Wyllie, Water content of granite magma deduced from the sequence of crystallization determined experimentally with water undersaturated conditions, *Contrib. Mineral. Petrol., 52,* 175–191, 1975.

Millhollen, G. L., Melting to nepheline syenite with H_2O and H_2O + CO_2, and the effect of dilution of the aqueous phase on the beginning of melting, *Am. J. Sci., 270,* 244–254, 1971.

Modreski, P. J., and A. L. Boettcher, The stability of phlogopite and enstatite at high pressures: A model for mica in the interior of the earth, *Am. J. Sci., 272,* 852–869, 1972.

Modreski, P. J., and A. L. Boettcher, Phase relationships of phlogopite in the system K_2O-MgO-CaO-Al_2O_3-SiO_2-H_2O to 35 kilobars: A better model for micas in the interior of the earth, *Am. J. Sci., 273,* 385–414, 1973.

Mysen, B. O., D. H. Eggler, M. G. Seitz, and J. R. Holloway, Carbon dioxide in silicate melts and crystals, I, Solubility measurements, *Am. J. Sci., 276,* 455–479, 1976.

Naney, M. T., and S. E. Swanson, The effect of Fe and Mg on crystallization in granitic systems, *Am. Mineral., 65,* 639–653, 1980.

Norton, J. J., Composition of a pegmatite, Keystone, South Dakota, *Am. Mineral., 55,* 981–1002, 1970.

Piwinskii, A. J., and P. J. Wyllie, Experimental studies of igneous rock series: A zones pluton in the Wallowa Batholith, Oregon, *J. Geol., 76,* 205–234, 1968.

Robertson, J. K., and P. J. Wyllie, Experimental studies on rocks from the Deboullie Stock, northern Maine, including melting relations in the water-deficient environment, *J. Geol., 79,* 549–571, 1971.

Seki, Y., and G. C. Kennedy, The breakdown of potassium feldspar, $KAlSi_3O_8$, at high temperatures and pressures, *Am. Mineral., 49,* 1688–1706, 1964.

Smith, J. V., X-ray-emission microanalysis of rock-forming minerals, I, Experimental techniques, *J. Geol., 73,* 830–864, 1965.

Stern, C. R., and P. J. Wyllie, Effect of iron absorption by noble-metal capsules on phase boundaries in rock-melting experiments at 30 kilobars, *Am. Mineral., 42,* 681–689, 1975.

Stern, C. R., and P. J. Wyllie, Phase relationships of I-type granite with H_2O to 35 kbar: The Dinkey Lakes biotite-granite from the Sierra Nevada Batholith, *J. Geophys. Res.,* this issue.

Thompson, A. B., Calculation of muscovite-paragonite-alkali feldspar phase relations, *Contrib. Mineral. Petrol., 44,* 173–194, 1974.

Thompson, A. B., and J. R. Algor, Model systems for anatexis of pelitic rocks, I, Theory of melting reactions in the system $KAlO_2$-$NaAlO_2$-Al_2O_3-SiO_2-H_2O, *Contrib. Mineral. Petrol., 63,* 247–269, 1977.

Thompson, J. B., Jr., The thermodynamic basis for the mineral facies concept, *Am. J. Sci., 253,* 65–103, 1955.

Tuttle, O. F., and N. L. Bowen, Origin of granite in the light of experimental studies in the system $NaAlSi_3O_8$-$KAlSi_3O_8$-SiO_2-H_2O, *Geol. Soc. Am. Mem., 74,* 153 pp., 1958.

Wasserburg, G. J., The effect of H_2O in silicate systems, *J. Geol., 65,* 15–23, 1957.

White, A. J. R., and B. W. Chappell, Ultrametamorphism and granitoid genesis, *Tectonophysics, 43,* 7–22, 1977.

Whitney, J. A., The effects of pressure temperature and X_{H_2O} on phase assemblages in four synthetic rock compositions, *J. Geol., 83,* 1–31, 1975.

Winkler, H. G. F., *Petrogenesis of Metamorphic Rocks,* 4th ed., Springer-Verlag, New York, 1976.

Wyllie, P. J., Crustal anatexis: An experimental review, *Tectonophysics, 43,* 41–71, 1977*a*.

Wyllie, P. J., Mantle fluid compositions buffered by carbonates in peridotite-CO_2-H_2O, *J. Geol., 85,* 187–207, 1977*b*.

Wyllie, P. J., From crucible through subduction to batholiths, in *Energetics of Geological Processes,* edited by S. K. Saxena and S. Battacharji, pp., 389–433, Springer-Verlag, New York, 1977*c*.

Wyllie, P. J., Mantle fluid compositions buffered in perioditite-CO_2-H_2O by carbonates, amphibole, and phlogopite, *J. Geol., 86,* 687–713, 1978.

Wyllie, P. J., Magmas and volatile components, *Am. Mineral., 64,* 469–500, 1979.

Wyllie, P. J., and O. F. Tuttle, Effect of carbon dioxide on the melting of granite and feldspar, *Am. J. Sci., 257,* 648–655, 1959.

Wyllie, P. J., and O. F. Tuttle, Hydrothermal melting of shales, *Geol. Mag., 98,* 56–66, 1961.

Yoder, H. S., and I. Kushiro, Melting of a hydrous phase: Phlogopite, *Am. J. Sci., 267-A,* 558–582, 1969.

(Received October 8, 1980;
revised March 19, 1981;
accepted March 20, 1981.)

JOURNAL OF GEOPHYSICAL RESEARCH, VOL. 86, NO. B11, PAGES 10530–10544, NOVEMBER 10, 1981

The New England Batholith, Eastern Australia: Geochemical Variations in Time and Space

S. E. SHAW AND R. H. FLOOD

School of Earth Sciences, Macquarie University, North Ryde, New South Wales, 2113, Australia

The New England Batholith, Australia, is part of the Upper Paleozoic New England Fold Belt, with most plutons intruded into the deformed trench-complex metasedimetary rocks in the southeast part of the Fold Belt. The Batholith was emplaced in two major periods of plutonism, the first during the Upper Carboniferous and the second during the Upper Permian and Triassic, with a major phase of metamorphism and deformation including westward overthrusting of the trench-complex sedimentary rocks between the two periods. On the basis of petrography, geochemistry and isotopic characteristics, the granitoids of the Batholith are subdivided into five named intrusive suites and a group of leucoadamellites. The differences between the six groups are considered to reflect differences in their source-rock types. The Carboniferous granitoids are peraluminous S-type and are divided into the Bundarra Plutonic Suite, a belt of very coarse-grained adamellites with cordierite ± garnet, and the Hillgrove Plutonic Suite, a belt of biotite-rich ± garnet deformed adamellites and granodiorites. Both suites have $\delta\ ^{18}O$ greater than 10, negative $\delta^{34}S$, $^{87}Sr/^{86}Sr$ initial ratios about 0.706, are ilmenite-bearing and have low FeO_3 ratios. The Bundarra Plutonic Suite, however, is consistently SiO_2-rich (greater than 70%), contains cordierite and has higher $\delta^{18}O$ than the Hillgrove Plutonic Suite. The two S-type suites are inferred to have formed by partial melting of the deepest parts of a wedge of trench-complex sedimentary rocks oceanwards of an 'Andean' volcanic chain to the west, analagous to the lower Tertiary S-type plutons of the Sanak-Baranof plutonic belt of southern Alaska. Of the remaining four groups of plutons emplaced during the Upper Permian and Triassic, two are metaluminous I-type granitoids, one the Clarence River Plutonic Suite (new name), a group of K-poor granodiorites and tonalites with low $^{87}Sr/^{86}Sr$ initial ratios (average 0.7035), and the other the Moonbi Plutonic Suite, a group of K-rich adamellites with low $^{87}Sr/^{86}Sr$ initial ratios (average 0.7045), $\delta^{18}O$ less than 10 and $\delta^{34}S$ positive. The Clarence River Plutonic Suite is inferred to have formed from the partial melting of a large-ion lithophile element-poor (gabbro?) source region and the Moonbi Plutonic Suite from a large-ion lithophile element-rich (shoshonite?) source region. A third group, the Uralla Plutonic Suite, is less metaluminous, has higher $^{87}Sr/^{86}Sr$ initial ratios (average 0.706), $\delta^{18}O$ only just less than 10 and negative $\delta^{34}S$, and is considered to have formed in a region containing a physical mixture of metaluminous and peraluminous source rocks (gabbro and metasedimentary rocks?). Plutons of the fourth group are leucoadamellites, largely emplaced after the other suites, with low $\delta^{18}O$ indicating an I-type source. It is argued that this group has resulted from low degrees of 'dry' partial metling of an I-type source region that had undergone an earlier melting event. These four groups of plutons are largely confined to a narrow belt parallel to, but 100 km west of, the present rifted margin of Australia. Their origin may be related to crustal thickening attendant on the overthrusting that occurred early in the Permian and/or a temperature increase in the lower crust due to the recovery of normal continental geotherms following the cessation of subduction.

INTRODUCTION

The New England Batholith of northeastern New South Wales and southern Queensland, Australia, includes all of the granitoids in the southern part of the New England Fold Belt [*Leitch*, 1974] (Figure 1 inset) and is one of the largest of the Paleozoic and upper Mesozoic batholiths in eastern Australia. This Batholith, with an outcrop area of 15,000 km^2, is composed of 80% adamellite, 18% grandiorite, 1% diorite and tonalite, 1% quartz-bearing monzonite and less than 0.2% gabbro [*Wilkinson*, 1969; *Pogson and Hitchins*, 1973; *O'Neil et al.*, 1977] (classification after *Streckeisen* [1973] modified by *Chappell* [1978] to retain adamellite for those quartz-rich granitoids with subequal amounts of plagioclase and K-feldspar). Beginning with the studies of *Binns et al.* [1967] and followed by *Flood* [1971], *Flood and Shaw* [1975, 1977], *O'Neil et al.* [1977] and results herein, it has been shown that the plutons, numbering over one hundred, can be grouped into five suites on the basis of geochemical, mineralogical and isotopic characteristics, particularly of the more mafic adamellites and granodiorites. Two of these suites have S-type characteristics, whereas the remainder are I-type, following the scheme of *Chappell and White* [1974]. A group of leucoadamellites that is difficult to classify into any of the five suites is considered separately.

This paper presents data that characterize the five suites and the group of leucoadamellite plutons. It also discusses the distribution of the granitoids in time and space and evaluates the number and type of different source rocks required to produce the observed geochemical variations within the Batholith.

REGIONAL SETTING

The country rocks surrounding the New England Batholith are part of the New England Fold Belt that extends from Newcastle in New South Wales to Townsville in Queensland. Recent descriptions of the geology of this Belt have been provided by *Leitch* [1974], *Korsch* [1977], *Day et al.* [1978] and *Evans and Roberts* [1979], with perhaps the most concise summary by *Leitch* [1975]. The main point that emerges is that the sedimentary and metasedimentary rocks can be divided into a western belt of gently folded Devonian, Carboniferous and Permian rocks, largely deposited on an east-facing continental shelf (Zone A of *Leitch* [1974]) and an eastern belt of similar age but more deformed and having characteristics indicative of a deep marine origin (Zone B of *Leitch* [1974]). The Peel

Copyright © 1981 by the American Geophysical Union.

Paper number 1B0576.
0148-0227/81/001B-0576$01.00

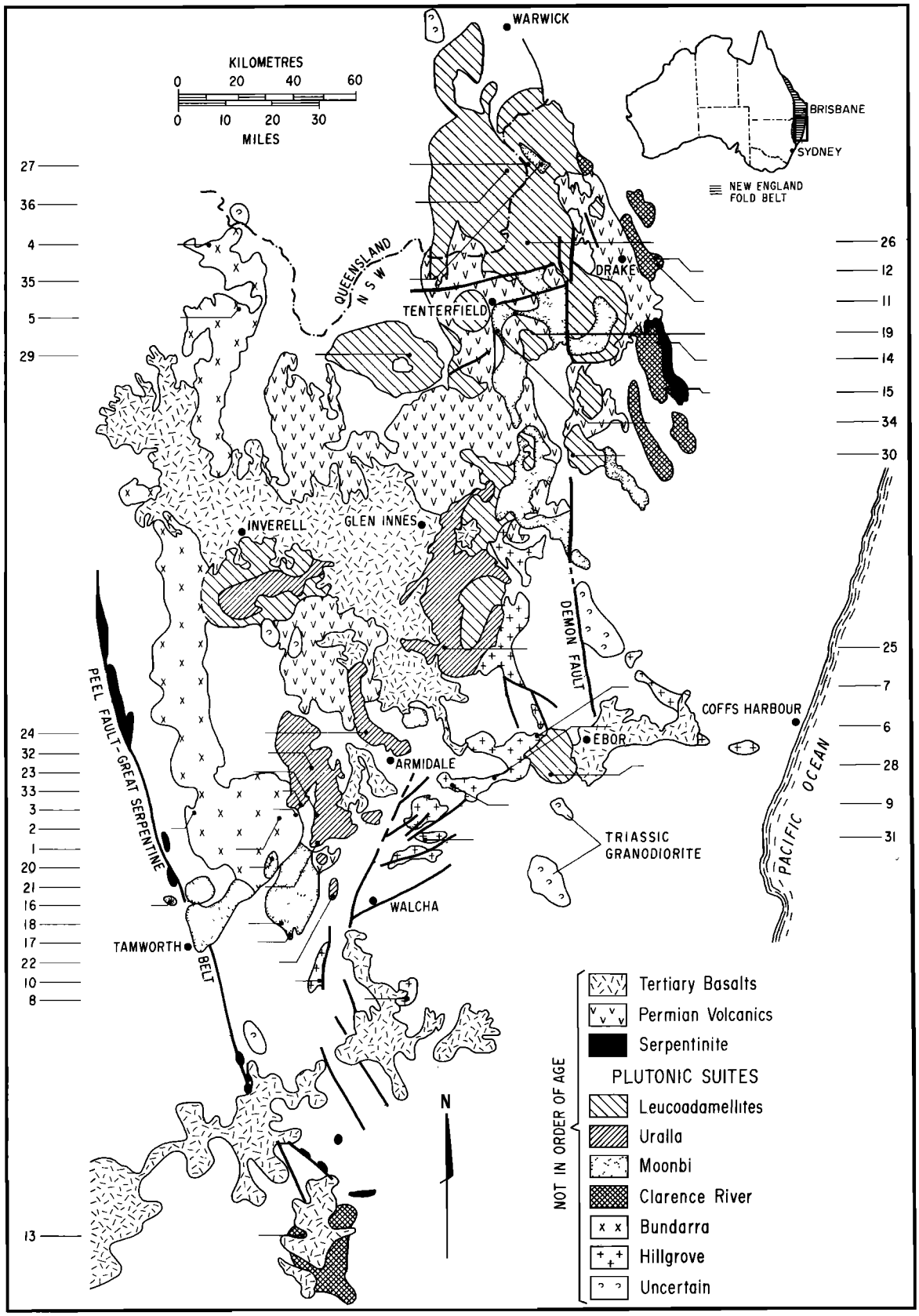

Fig. 1. The distribution of the plutonic suites and leucoadamellites in the New England Batholith. Numbered points refer to the specimen numbers in Tables 2 and 3.

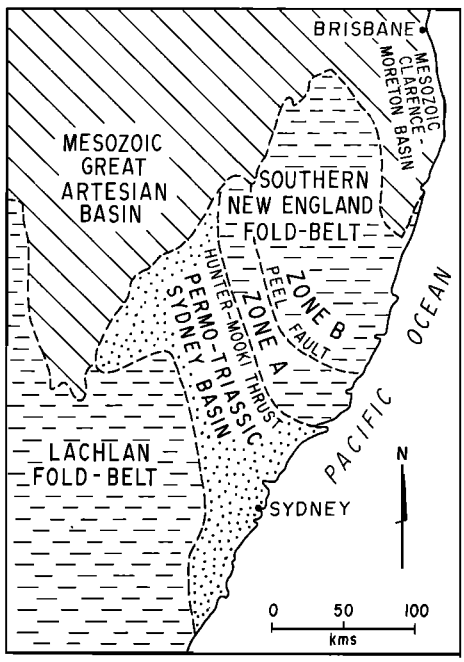

Fig. 2. Structural elements of the southern New England Fold Belt and surrounding areas.

Fault/Great Serpentine Belt (Figure 1) forms the boundary between the two sequences. The western margin of Zone A is defined by the easterly-dipping Hunter Mooki Thrust System [*Carey and Osborne,* 1939] along which the rocks of Zone A have been thrust westward over the Permian sedimentary rocks of the Sydney Basin (Figure 2).

The sequence of rocks of the western part of Zone A includes terrestrial and shallow marine volcaniclastic material derived from source regions further to the west [*A. H. White,* 1966]. Rocks on the eastern side of Zone A are of marine shelf and perhaps deeper water marine origin. Rocks of Zone B east of the Great Serpentine Belt are of deep water marine origin and include chert, jasper and siliceous mudstone of the Woolomin Association, greywacke and mudstone trench-fill of the Sandon Association and a monotonous sequence of feldspathic greywacke and mudstone of the Coffs Harbour Association [*Korsch,* 1977]. These units are only sparsely fossiliferous and are considered to have formed on oceanic crust, fragments of which are now represented by the dismembered ophiolites of the Great Serpentine Belt. What little fossil evidence is available suggests a largely Devonian and Lower Carboniferous age [*Korsch,* 1977; *Evans and Roberts,* 1979] for these Zone B sedimentary rocks. Unconformably overlying these rocks types are remnants of Upper Permian silicic volcanic rocks co-magmatic with the New England Batholith [*Flood et al.,* 1977, 1980]. These volcanics, which are not accompanied by basaltic units, occur on the topographically higher parts of the New England Plateau and may have once been much more extensive in the south.

All major movements on the Peel Fault/Great Serpentine Belt, which separates Zone A from Zone B, must have preceded the emplacement of the Upper Permian plutons that cut across the Fault near Tamworth (Figure 1). Some (and perhaps all) movement did occur during the Permian, as slivers of Lower Permian sedimentary rocks have been truncated adjacent to the Fault. Radiometric K/Ar ages of 279 to 286 Ma on nephrite regarded as having formed during emplacement of the serpentinite along the Peel Fault system [*Lanphere and Hockley,* 1976] also indicate Permian fault activity.

The hundred or so plutons of the Batholith range in age from Upper Carboniferous to Triassic [*Evernden and Richards,* 1962; *Flood and Shaw,* 1977; *Kleeman,* 1975] and with only three exceptions are confined to the complexly deformed deep-water metasedimentary rocks of Zone B (Figure 1). Of the three exceptions, one pluton, the Moonbi Adamellite [*Chappell,* 1978], intrudes across the Peel Fault and the other two are within a few kilometers of the fault (Figure 1).

Recognition of Granitoid Suites

Following accepted Australian usage, the term New England Batholith includes all of the Upper Paleozoic and Mesozoic granitoids in the southern portion of the New England Fold Belt. Major subdivisions within the Batholith are termed suites following *O'Neil et al.* [1977] and the recommendations of the Stratigraphic Commission [*Sohl,* 1977]. The basis of suite subdivision in the New England Batholith involves the recognition of groups of plutons with distinct mineralogical, geochemical, isotopic and age characteristics. The suites thus defined tend to occupy elongate but narrow belts.

We see suite recognition as an attempt to identify the major source-rock types and as such is an extension of the two-fold subdivision of granitoids into S- and I-type, as proposed by *Chappell and White* [1974]. As documented by *Tuttle and Bowen* [1958], the composition of most felsic granites is strongly controlled by the granite minimum and as such these igneous rocks tend to be poor indicators of source-rock type. More mafic granitoids that result from either a higher degree of partial melting and/or a greater retention of refractory source material will carry stronger indications of parental rock type. From an examination of the Berridale Batholith of southeastern Australia, *Chappell and White* [1974] saw indications of two contrasting source-rock types: one group of plutons were potassic, strongly peraluminous (corundum-normative) and had a high $^{87}Sr/^{86}Sr$ initial ratio (greater than 0.708), while the other group was more sodic, metaluminous (diopside-normative) and had lower initial ratios (less than 0.706). *Chappell and White* [1974] interpreted these differences as indicating a sedimentary source-region for the peraluminous group (S-type) and an igneous source-region for the metaluminous group (I-type). The studies on the oxygen isotopes of the Berridale Batholith [*O'Neil and Chappell,* 1977] and the New England Batholith [*O'Neil et al.,* 1977] also support the suggestion of two contrasting source-rock types. Values of $\delta^{18}O$ ($\delta^{18}O$ is the enrichment of the sample in ^{18}O relative to ^{16}O compared with Standard Mean Ocean Water and expressed in per mil) of materials that have equilibrated under low temperature surface weathering and deposition conditions are high (10–30) relative to mantle-derived igneous rocks (5–7). Partial melts of metasedimentary rocks (S-type) will therefore inherit the enriched $\delta^{18}O$ characteristics, in contrast to the melts derived from sources that have not undergone a surficial weathering stage (I-type).

Metasedimentary and metaigneous rocks also have different sulphur isotopic ratios. Basalts and other mantle-derived igneous rocks have $\delta^{34}S$ ($\delta^{34}S$ is the enrichment of the sample in ^{34}S relative to ^{32}S compared with troilite sulphur from the Canon Diablo meteorite and expressed in permil) ranging from zero to slightly positive [*Nielsen,* 1979]. Sulphur deposited in a sedimentary environment as sulphide (generally as pyrite) typically has negative values of $\delta^{34}S$ [*Nielsen,* 1979]

TABLE 1. Subdivision of the New England Batholith

Association	Area km²	Area %	Lithology
Bundarra Plutonic Suite	3,400	23	Adamellite, leucoadamellite, minor granite
Hillgrove Plutonic Suite	1,650	11	Subequal adamellite and granodiorite
Clarence River Plutonic Suite	910	6	Granodiorite and tonalite
Moonbi Plutonic Suite	1,800	12	Adamellite and minor monzonite
Uralla Plutonic Suite	1,700	11	Adamellite, granodiorite, minor tonalite and diorite
Leucoadamellites	4,440	30	Leucoadamellite
Triassic Granodiorite	300	2	Granodiorite
Unspecified Plutons	750	5	?
Total	14,950	100	

and as sulphide constitutes the major sulphur-bearing phase in pelitic sedimentary rocks, these rocks also generally have low $\delta^{34}S$ values. Magmas derived from igneous or metasedimentary source regions would be expected to reflect the different sulphur isotopic abundances, I-type granitoids having $\delta^{34}S$ values around zero or slightly positive and S-type granitoids around zero to slightly negative. *Sasaki and Ishihara* [1979] have interpreted the low $\delta^{34}S$ values of some Japanese ilmenite-bearing granitoids as reflecting the involvement of light biogenic sulphur from continental metasedimentary sources.

S-type granitoids have lower bulk rock and biotite Fe_2O_3/FeO ratios and contain ilmenite as the opaque oxide phase. The I-type granitoids typically have higher Fe_2O_3/FeO bulk rock and biotite ratios and many contain magnetite and/or ilmenite. *Flood and Shaw* [1975] have argued that the consistently 'reduced' character of the S-types reflects the presence in the metasedimentary source rocks of organically-derived carbonaceous material.

Although the criteria for distinguishing I- and S-type granitoids in the Berridale Batholith may not be exactly applicable elsewhere, the major I-S subdivision can still be recognized. The characteristics we would regard as having general applicability to the I-S subdivision are as follows:

1. The presence of cordierite with or without a Ca-poor almandine-pyrope garnet, andalusite (or sillimanite or kyanite) is indicative of S-types, while the presence of hornblende with or without augite is indicative of I-types. Biotite typically occurs in both types but is more aluminous in S-types.

2. The $^{87}Sr/^{86}Sr$ initial ratios of S-types is generally greater than 0.708 and is unlikely to be much less than 0.706 [*Peterman et al.*, 1967; *Flood and Shaw*, 1977]. Initial ratios of I-types tend to be less than 0.706, although higher ratios do occur [*Black*, 1980].

3. Bulk-rock $\delta^{18}O$ values in the absence of substantial groundwater interaction can be used to distinguish type: for S-types the $\delta^{18}O$ value is greater than 10 and for I-types it is less than 10.

4. Bulk-rock $\delta^{34}S$ values tend to be positive in I-type granitoids and negative in those granitoids that have a sedimentary component in the source region. Whereas distinction of I- and S-types on the basis of $\delta^{18}O$ can be made in even the most evolved granitoids, the extremely low sulphur abundances in leuco-granitoids restrict the use of $\delta^{34}S$ to the more mafic types.

Figure 1 shows, as far as possible, the subdivision of the Batholith into various plutonic suites, the leucoadamellites, plutons of unknown affinities, and volcanic cover-rocks. This paper does not attempt to deal with all of the small stocks and dykes of uncertain age and affinity that compositionally vary from gabbro to leucogranite but collectively form only a minor part of the Batholith. The areas occupied by the various granitoids, together with their dominant lithologies, are listed in Table 1. Where K/Ar and Rb/Sr ages are given in this paper, they have been recalculated to the new constants of *Steiger and Jager* [1977]. The recalculated Phanerozoic Time Scale for the Carboniferous-Permian boundary is 288 Ma, that of the Permian-Triassic 242 Ma and that of the Triassic-Jurassic 212 Ma [*Armstrong*, 1978].

UPPER CARBONIFEROUS–LOWER PERMIAN PLUTONISM

The two suites of granitoids recognised as belonging to this first period of plutonism are the Bundarra Plutonic Suite, identified by *Flood* [1971] and documented by *Flood and Shaw* [1975] as a group of cordierite-bearing adamellites occurring along the western margin of the Batholith, and the Hillgrove Plutonic Suite, first defined by *Binns et al.* [1967], but as restricted by *Flood and Shaw* [1977] to biotite-bearing granodiorite and adamellite plutons, some of which contain almandine-rich garnet, that forms a northeast-trending belt along the southeastern margin of the Batholith (Figure 1).

Although K/Ar dating of the Hillgrove Plutonic Suite gives a range of Upper Permian ages from 275 to 258 Ma [*Cooper et al.*, 1963; *Binns*, 1966], a Rb/Sr bulk-rock isochron age for the Suite is 289 ± 25 Ma and an $^{87}Sr/^{86}Sr$ initial ratio of 0.7064 ± 0.0009 [*Flood and Shaw*, 1977]. A bulk-rock Rb/Sr age for the Bundarra Plutonic Suite is 286 ± 13 Ma with an initial ratio of 0.7057 ± 0.0014 [*Flood and Shaw*, 1977]. The Rb/Sr data are considered to best approximate the intrusive ages, but differ somewhat from the K/Ar ages of biotite from the massive Bundarra Plutonic Suite [*Kleeman*, 1975]. The deformed nature of the Hillgrove Plutonic Suite precludes the use of biotite for determining intrusive ages.

Bundarra Plutonic Suite

This elongate north-south belt of leucocratic granitoids extends along the western margin of the Batholith and consists mainly of adamellites, although *Chappell* [1978] has documented a small granite pluton in the southern part. To date no

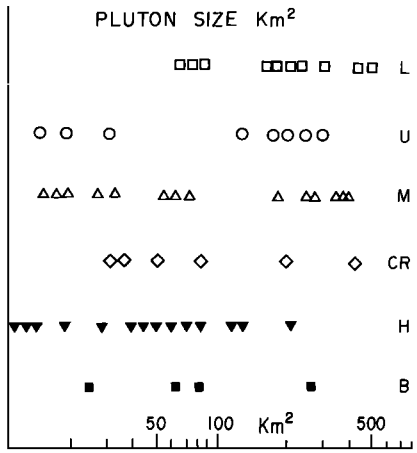

Fig. 3. Outcrop area of individual plutons from the plutonic suites and the leucoadamellites. Approximately 50 small plutons, each less than 10 km², are not plotted. Symbols for the plutonic suites are: Bundarra (B), solid squares; Hillgrove (H), solid triangles; Clarence River (CR), diamonds; Moonbi (M), open triangles; Uralla (U), circles; leucoadamellites (L), open squares.

volcanic equivalents of this Suite have been found. Recognition of individual plutons is difficult, but in the southern part data of *Chappell* [1978] suggest that plutons are up to 250 km² (Figure 3). Thermal metamorphic aureoles up to hornblende-hornfels facies and foliated contact rocks occur around the plutons of this Suite.

The massive grey adamellites and minor granites are exceptionally coarse-grained. The grain size of even-grained adamellite commonly exceeds 10 mm and, in porphyritic adamellite, K-feldspar megacrysts are up to 80 mm long. Mineralogically the granitoids are characterized by euhedral 20 mm-long cordierite crystals, traces of almandine-rich garnet in the more mafic rocks, red-brown aluminous biotite, ilmenite, microcline with moderate triclinicity, and slightly opalescent blue quartz. Tourmaline and secondary muscovite are accessory phases. The SiO_2 range is restricted with most granitoids exceeding 70% (Table 2, analyses 1–5) and variable amounts of normative corundum up to a maximum of 2% in the more mafic adamellites (Figure 4). The average bulk-rock $\delta^{18}O$ value is 12.4 [*O'Neil et al.*, 1977] (Figure 5) and the average $\delta^{34}S$ is about −5 [*Coleman*, 1979]. Rare earth element (REE) patterns (Table 3, Figure 6) show light REE (LREE) enrichments between 50 and 100 times chondrite, LREE/HREE fractionation of about 4 and only a small *−ve* Eu anomaly. The Suite has an indicated range in $^{87}Sr/^{86}Sr$ initial ratios of from 0.706 to 0.707 (Figure 7). As suggested by *Flood and*

TABLE 2. Chemical Analyses of Granitoids, New England Batholith

	Bundarra Plutonic Suite					Hillgrove Plutonic Suite					Clarence River Plutonic Suite				
	1* FS420†	2* FS106†	3* BAN1†	4* FS138†	5* FS132†	6* FS35†	7* FS231†	8* FS252†	9* FS246†	10* KL69†	11* FS1601†	12* FS1603†	13* B.TOPS†	14* FS1594†	15* FS1593†
SiO_2	72.39	72.70	72.94	73.46	74.59	65.26	66.65	68.59	70.09	71.35	60.42	62.51	63.46	67.80	72.93
TiO_2	0.34	0.32	0.26	0.29	0.19	0.73	0.80	0.55	0.55	0.50	0.73	0.69	0.73	0.38	0.25
Al_2O_3	14.50	14.16	13.86	13.54	13.37	15.07	15.34	14.68	14.12	13.76	15.50	14.85	15.65	15.14	13.72
Fe_2O_3	0.20	0.29	0.20	0.20	0.28	0.25	0.81	0.50	0.37	0.23	2.64	2.15	1.80	1.93	1.29
FeO	2.00	1.67	1.42	1.70	1.24	4.72	4.21	3.05	2.71	2.20	3.85	3.76	3.56	2.35	1.22
MnO	0.01	0.04	0.03	0.05	0.03	0.09	0.10	0.11	0.07	0.05	0.14	0.11	0.12	0.12	0.09
MgO	0.77	0.63	0.66	0.62	0.46	2.39	1.78	1.73	1.19	0.80	3.93	3.07	2.39	2.02	0.78
CaO	1.98	1.57	1.57	1.28	0.95	2.66	2.28	2.36	2.08	1.73	6.54	5.44	5.07	4.22	2.63
Na_2O	2.44	3.13	3.38	3.21	3.33	3.14	3.39	3.50	3.14	3.48	3.16	3.09	3.88	3.79	3.82
K_2O	4.05	4.43	4.71	4.57	4.61	3.31	3.17	3.43	4.19	4.42	1.79	2.37	1.70	1.73	2.50
P_2O_5	0.15	0.16	0.15	0.14	0.16	0.17	0.17	0.12	0.09	0.10	0.10	0.09	0.14	0.06	0.04
H_2O^+	0.76	0.62	0.58	0.55	0.48	1.56	0.85	0.80	0.63	0.76	1.35	0.96	1.00	0.61	0.38
H_2O^-	0.14	0.08	0.17	0.09	0.12	0.17	0.13	0.09	0.16	0.21	0.07	0.10	0.15	0.10	0.09
Total	99.73	99.80	99.93	99.70	99.81	99.52	99.68	99.51	99.39	99.59	100.22	99.19	99.65	100.25	99.74

	Moonbi Plutonic Suite					Uralla Plutonic Suite					Leucoadamellites				
	16* M1†	17* MG2†	18* FS870†	19* 229†	20* M105†	21* FS33†	22* E33†	23* FS942†	24* FS241†	25* FS1576†	26* D352†	27* FS205†	28* FS233†	29* FS214†	30* FS1626†
SiO_2	57.52	59.37	64.40	69.09	76.21	54.24	59.73	63.09	66.49	67.71	74.07	75.75	75.96	76.68	77.21
TiO_2	0.86	1.00	0.68	0.43	0.06	1.20	0.95	0.76	0.60	0.50	0.21	0.05	0.07	0.10	0.06
Al_2O_3	16.03	15.15	14.73	14.94	12.89	14.16	16.14	15.16	14.79	15.01	13.19	13.28	12.18	12.19	12.33
Fe_2O_3	2.06	1.29	1.55	1.06	0.29	1.40	1.11	1.20	0.55	0.97	0.23	0.04	0.32	0.26	0.34
FeO	3.91	4.93	2.63	1.38	0.84	6.98	4.96	3.75	3.21	2.62	1.31	0.87	0.81	1.10	0.16
MnO	0.11	0.13	0.07	0.06	0.07	0.17	0.13	0.11	0.08	0.09	0.05	0.05	0.05	0.01	0.01
MgO	4.37	4.55	3.23	1.19	0.05	7.96	4.15	3.80	2.26	1.73	0.30	0.16	0.12	0.06	0.16
CaO	6.20	6.08	3.93	2.38	0.69	7.85	5.84	4.30	3.20	3.18	0.88	0.45	0.55	0.40	0.36
Na_2O	3.19	2.65	3.19	3.77	3.77	2.30	3.12	2.93	3.38	3.29	3.90	4.02	3.98	3.39	3.96
K_2O	3.26	3.80	4.34	4.83	4.72	2.20	2.80	3.50	4.02	4.24	4.81	4.51	4.66	4.76	4.67
P_2O_5	0.43	0.34	0.30	0.16	0.01	0.27	0.29	0.21	0.18	0.12	0.04	0.01	0.01	0.02	0.01
H_2O^+	1.07	0.65	0.72	0.56	0.27	1.15	0.87	0.95	1.04	0.62	0.27	0.41	0.23	0.27	0.32
H_2O^-	0.16	0.09	0.08	0.11	0.05	0.13	0.11	0.13	0.09	0.09	0.16	0.22	0.11	0.13	0.10
Total	99.17	100.03	99.85	99.96	99.92	100.01	100.20	99.89	99.89	100.17	99.42	99.82	99.05	99.37	99.69

Analyses by Shaw and Flood except analyses 16 and 20 from *Chappell* [1978, Table 2]. All analyses by XRF following the method of *Norrish and Chappell* [1977] except for Na_2O, FeO, H_2O^+ and H_2O^- which were done by conventional methods. Average sample size 10 kg.

* Figure 1 number.

† Field number.

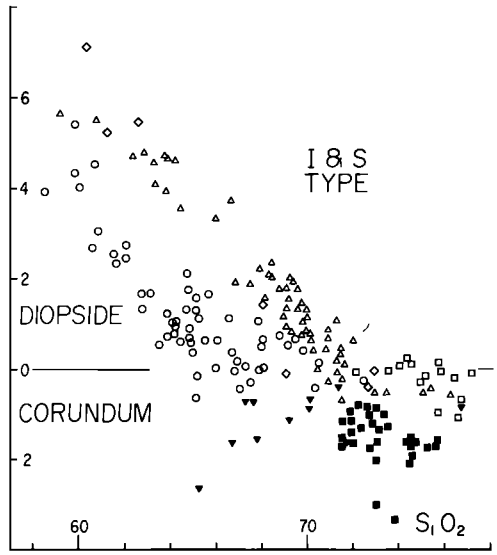

Fig. 4. Normative corundum/diopside versus SiO_2. The leucoadamellites and the most leucocratic members of all plutonic suites have over 70% SiO_2 and most are just corundum-normative. The Uralla Plutonic Suite (circles) at any SiO_2 value generally has less normative diopside than the Moonbi Plutonic Suite (open triangles). Other symbols for the plutonic suites are: Bundarra, solid squares; Hillgrove, solid triangles; Clarence River, diamonds; leucoadamellites, open squares.

Shaw [1975] and Chappell (1978), this Suite of granitoids has strong S-type characteristics, except for the low $^{87}Sr/^{86}Sr$ initial ratios which, as discussed by *Flood and Shaw* [1975], would be consistent only with a relatively young, volcanically-derived, metasedimentary source-material.

Hillgrove Plutonic Suite

This Suite includes all the Upper Carboniferous biotite-rich granodiorite and adamellite plutons that form a northeast-southwest trending belt over 200 km long and centred 20 km southeast of Armidale. The 20 or so small plutons of this Suite (Figures 1, 3) have been texturally modified by a deformation that in some has imparted a mylonitic foliation (R. H. Vernon, personal communication, 1980) and has variously faulted both the pluton contacts and the metamorphic aureoles that surround them. Two plutons have well-developed regional aureoles [*Binns*, 1966; *Gunthorpe*, 1970] with migmatites and cordierite-K-feldspar-garnet gneisses at the highest grades. The remaining plutons seem to have neither regional nor well-developed contact aureoles, although this may in part be attributable to the effects of later deformation. The range of upper Permian K/Ar ages of biotite from these granitoids of 275 to 258 Ma could represent partial resetting by the deformation/metamorphism and/or the thermal event accompanying the

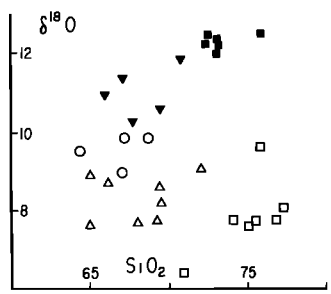

Fig. 5. Bulk rock $\delta^{18}O$ [*O'Neil et al.*, 1977] versus SiO_2. The S-type suites (solid symbols) have a similar SiO_2 range to the I-type suites (open symbols) but have $\delta^{18}O$ values greater than 10. Symbols for the plutonic suites are: Bundarra, solid squares; Hillgrove, solid triangles; Moonbi, open triangles; Uralla, circles; leucoadamellites, open squares.

TABLE 3. Rare Earth Elements in Granitoids, New England Batholith (in ppm)

Figure 1 Number	Field Number	La	Ce	Nd	Sm	Eu	Yb	Lu
			Bundarra Plutonic Suite					
5	FS132	12.6	27.2	18.2	4.56	1.33	2.78	0.57
1	FS420	24.9	49.4	22.1	5.75	1.25	3.04	0.58
			Hillgrove Plutonic Suite					
31	FS250	34.9	57.3	31.4	6.72	0.97	3.28	0.64
8	FS252	24.9	45.2	38.2	7.09	1.44	2.92	0.78
			Uralla Plutonic Suite					
32	FS237	28.8	45.4	31.6	5.64	0.83	2.67	0.69
33	BDN5	20.4	34.3	23.1	4.80	0.97	2.40	0.42
			Moonbi Plutonic Suite					
34	FS199	35.6	66.5	30.6	6.60	1.77	2.59	0.46
35	FS204	34.3	67.4	35.6	6.19	1.77	2.70	0.53
			Leucoadamellites					
36	FS206	30.9	60.8	41.8	6.92	0.57	5.45	1.15
28	FS233	36.6	72.0	42.5	9.94	0.46	6.50	1.40

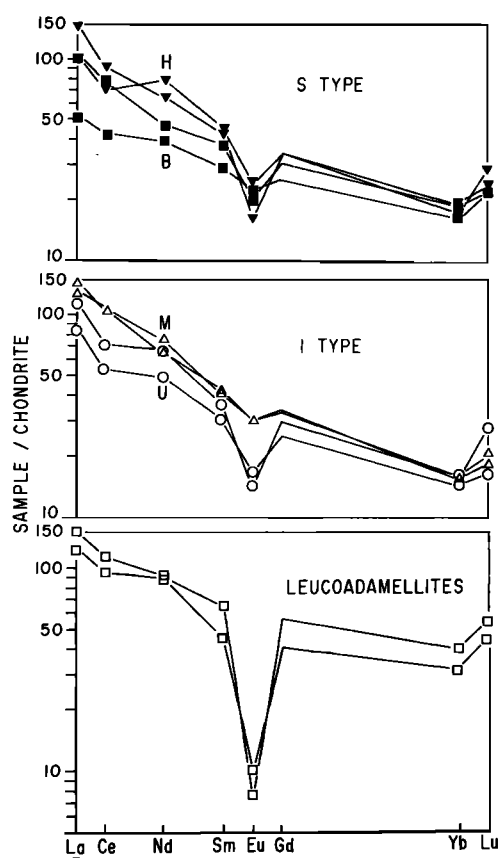

Fig. 6. Chondrite-normalized (to the values of *Evensen et al.* [1978]) REE patterns for two samples from each of the plutonic suites: Bundarra (B), solid squares; Hillgrove (H), solid triangles; Moonbi (M), open triangles; Uralla (U), circles; and the leucoadamellites, open squares. Gd values inferred from the join Sm-Yb. Neutron activation analyses at Oregon State University by R. Schmitt.

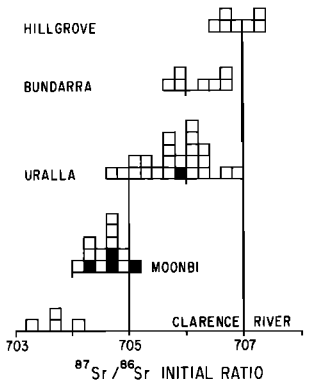

Fig. 7. $^{87}Sr/^{86}Sr$ initial ratios for the five plutonic suites [*Flood and Shaw,* 1977; S. E. Shaw and R. H. Flood, unpublished data, 1980]. In general low $\delta^{18}O$ (Figure 5) is associated with low initial ratios. The intermediate character of the Uralla Plutonic Suite is indicated by initial ratios between the other I-types and the two S-types. Solid areas on the diagram are for volcanic rocks associated with the plutonic suites. Each square represents a calculated initial ratio based on the age of the suite, present-day $^{87}Sr/^{86}Sr$ and the Rb and Sr content.

emplacement of the Upper Permian I-type plutons discussed below.

As well as being biotite-rich and foliated, these adamellites and granodiorites are characterized by a blue-grey color when fresh, due mainly to abundant opalescent blue quartz. They have a medium grain-size, some with megacrysts of microcline up to 20 mm long. The biotite is russet-red in color, is aluminous and contains elongate needles of exsolved rutile. Minor mafic phases that occur in some plutons are almandine-rich garnet [*Flood and Shaw,* 1977], actinolitic amphibole and cummingtonite. K-feldspar in the more deformed plutons is near maximum microcline [*Binns,* 1966; *Flood,* 1971].

The rocks are generally more silica-poor than those of the Bundarra Plutonic Suite and range from 65 to 72% SiO_2 (Table 2, analyses 6–10). In common with the Bundarra Plutonic Suite, the more mafic plutons are the most corundum-normative (Figure 4). The average $\delta^{18}O$ value (Figure 5) at 11.0 is 1.4 lower than the average of the Bundarra Plutonic Suite and the $\delta^{34}S$ value of −10 [*Coleman,* 1979] is much lower. The $^{87}Sr/^{86}Sr$ initial ratios overlap or are higher than those from the Bundara Plutonic Suite (Figure 7). REE patterns (Figure 6) show higher LREE enrichments (100 to 150 times chondrite), a higher LREE/HREE fractionation of about 6, and a similar small *-ve* Eu anomaly as compared with the Bundarra Plutonic Suite.

Although the Hillgrove Plutonic Suite differs from the Bundarra Plutonic Suite in being more mafic, containing no cordierite and having slightly lower $\delta^{18}O$ and $\delta^{34}S$ values, both share the geochemical and mineralogical characteristics that, together with the low $^{87}Sr/^{86}Sr$ initial ratios (for S-types), suggest a young volcanically-derived metasedimentary source-rock type.

Upper Permian and Triassic Plutonism

The second and major period of plutonism began about 255 Ma ago with the intrusion of the main I-type hornblende-biotite plutons and continued at least until 225 Ma ago when the last of the large leuconadamellites were emplaced [*Evernden and Richards,* 1962; *Binns,* 1966; S. E. Shaw, unpublished data, 1980]. Reported K/Ar ages of biotite from three small plutons situated within the eastern part of the Batholith vary from 215 to 185 Ma [*Thomson,* 1974]. This probably indicates that minor igneous activity extended into the Jurassic, although the reported alteration of some of the samples used cast doubt on the significance of these young dates. The age data presently available suggest that plutonism was relatively continuous within the period 255 to 225 Ma but that most of the I-type plutons were emplaced early in the intrusive period and that the relatively few, but volumetrically large, leucoadamellite plutons were emplaced late. This intrusive period beginning with mafic adamellites and granodiorites and becoming progressively more leucocratic is analogous to that observed in the 'Super Units' of the Coastal Batholith of Peru [*Pitcher,* 1978]. Three geochemically distinct I-type suites are recognized from this intrusive period, the Moonbi and Uralla Plutonic Suites of *O'Neil et al.* [1977] and a new suite, the Clarence River Plutonic Suite, which is characterized by lower K_2O and lower $^{87}Sr/^{86}Sr$ initial ratios than either of the other I-type suites. These three suites lie in a north-northeasterly-trending belt approximately 300 km by 60 km that extends from Tamworth in the south to east of Warwick in the north. Faulting in the northeast part of the belt has displaced granitoids that lie to the east of the north-south-trending Demon Fault [*Shaw,* 1969] to the south (Figure 1).

The leucoadamellites have not been included with any of the three I-type suites unless they form part of suite-recognizable zoned plutons. The problem of the leucoadamellites is not so much one of determining whether they are I- or S-type, as *O'Neil et al.* [1977] on the basis of oxygen isotopes (average $\delta^{18}O$ 7.8) showed they had I-type affinities, but one of assigning them to a specific suite in the absence of diagnostic mineralogy and geochemistry, paucity of xenoliths and inability to determine accurate $^{87}Sr/^{86}Sr$ initial ratios.

Clarence River Plutonic Suite

In a northeastern portion of the Batholith, near a serpentinite belt southeast of Drake (Figure 1) and still partly covered by the Mesozoic Clarence-Moreton Basin, are granodiorite and tonalite plutons that are the most K_2O-poor intrusions of the Batholith (Figure 1). We propose the name Clarence River Plutonic Suite for this group of plutons. Rock types are K_2O-poor granodiorite and tonalite, although trondjhemitic and dioritic variants occur. Mapping has not necessarily revealed the full extent of this Suite, and other plutons near the Great Serpentine Belt to the southwest could also belong to the

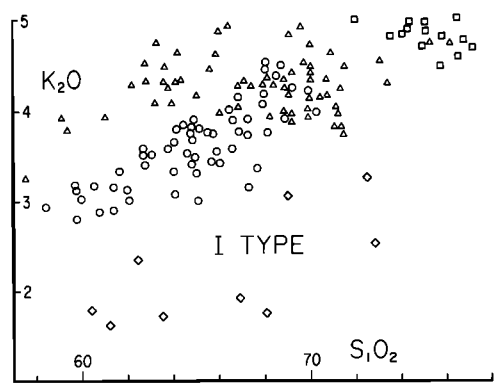

Fig. 8. K_2O versus SiO_2, used to distinguish the three I-type plutonic suites: Moonbi (triangles) most potassic, Uralla (circles) intermediate, Clarence River (diamonds) least potassic. Leucoadamellites (squares) are indistinguishable from the extensions of the Moonbi and Uralla trends.

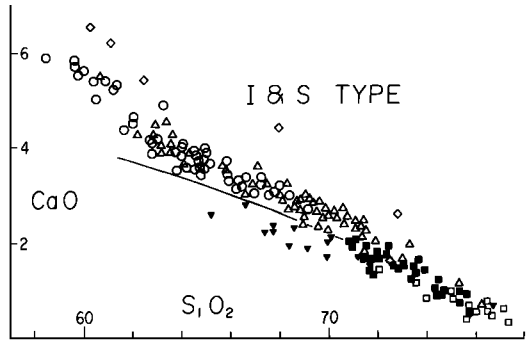

Fig. 9. CaO versus SiO_2 showing the division (solid line) between the lower CaO S-types (solid symbols) and the higher CaO I-types (open symbols) at SiO_2 values less than 70%. Symbols for the plutonic suites are: Bundarra, solid squares; Hillgrove, solid triangles; Clarence River, diamonds; Moonbi, open triangles; Uralla, circles; and leucoadamellites, open squares.

Suite. We tentatively include the Barrington Tops Granodiorite, which is the most southerly in the Batholith (Figure 1), despite the 300 or so km that separate it from the major members of this Suite.

Typically the rocks are fine-to medium-, even-grained and are commonly pink to grey in color, with some specimens showing the effects of post-intrusive deformation. Whether this group of plutons has volcanic equivalents in the extensive volcanics to the northeast has yet to be investigated. The mafic minerals are hornblende and augite (largely replaced by fibrous green amphibole), minor biotite and magnetite. Texturally K-feldspar, quartz and the ferro-magnesian minerals mound around larger zoned plagioclase euhedra. The granitoids of this Suite have, for a given SiO_2 value (Table 2, analyses 11–15), the lowest K_2O (Figure 8) and highest CaO (Figure 9) contents of the New England granitoids. Despite the high CaO content, Sr (Figure 10) is lower than in most of the other I-types. Based on four whole rock samples, the $^{87}Sr/^{86}Sr$ initial ratio has an average value of 0.7037 (Figure 7) which is the lowest in the New England Batholith and low for granitoids in general. This suite of plutons is chemically similar to the major K_2O-poor granodiorites and tonalties of the western part of the Cordilleran Batholiths in North America [*Moore*, 1959], where gabbros and quartz-diorites form significant parts of the intrusive sequence.

Two Triassic granodiorite plutons that give concordant hornblende and biotite K/Ar ages of 228 Ma [*Leitch and McDougall*, 1979] have $^{87}Sr/^{86}Sr$ initial ratios and major element chemical variations similar to those of the Clarence River Plutonic Suite. As these Triassic plutons, which are situated in the southeastern part of the Batholith (Figure 1), are considerably younger than the Clarence River Suite and contain ilmenite rather than magnetite, they are left as granitoids of uncertain affinities.

Moonbi Plutonic Suite

Most plutons of this Suite were recognised as a coherent group by *Andrews and Mingaye* [1907], who noted the presence of large pink orthclase megacrysts and sphene euhedra. They range in size from about 20 to 400 km^2 (Figure 3) and mainly occur in the southwest of the Batholith near Tamworth and in the north around Glen Innes and Tenterfield (Figure 1). Texturally the granitoids are massive, apart from a variable degree of alignment of K-feldspar megacrysts, and detailed mapping has revealed that some plutons are compositionally zoned to central leucocratic types (cf. Johnson Granite Porphyry, of the Tuolumne Intrusive Series of the Sierra Nevada Batholith [*Bateman and Chappell*, 1978]). The plutons in the region between Glen Innes and Tenterfield are intruded into a comagmatic series of silicic ignimbrite sheets [*Flood et al.*, 1977, 1980]. In the south the plutons are intrusive into the metasedimentary Sandon Association of *Korsch* [1977] and are surrounded by hornfels ridges that, adjacent to intrusive contacts, contain cordierite–K-feldspar–biotite assemblages commonly with a strong schistosity parallel to the contacts.

K/Ar ages for the Attunga Creek Adamellite and the Inlet Monzonite [*Chappell*, 1978] included in the Moonbi Plutonic Suite are 250 Ma [*Cooper et al.*, 1963]. They compare closely with 247 Ma [*Evernden and Richards*, 1962] obtained from biotite in a sample of the co-magmatic silicic ignimbrite sheets in southern Queensland. Our unpublished Rb/Sr data on bulk-rock and biotite samples confirm an Upper Permian age for other plutons of the Suite. A possible anomaly is the Undercliffe Falls Adamellite [Philipps, 1969], where concordant K/Ar ages for hornblende and biotite are 226 and 230 Ma, respectively (Evernden and Richards, 1962). We are unsure whether this means that the intrusion of the Moonbi Plutonic Suite extended into the Triassic or whether the K/Ar ages of the Undercliffe Falls Adamellite are the result of thermal resetting by the enclosing Triassic Stanthorpe Adamellite of *Shaw* [1969].

Magnesio-hornblende, biotite, minor augite, sphene and magnetite are the common mafic minerals in the more mafic plutons and, in the felsic plutons or the felsic parts of zoned plutons, the mafic minerals are biotite or biotite with minor iron-rich tschermakitic hornblende. The most mafic rocks are monzonites (e.g., the Inlet Monzonite of *Chappell* [1978]) and the most leucocratic members are leucoadamellite. High K_2O (Figure 8), Sr (Figure 10), BaO and Fe_2O_3/FeO ratios characterize members of this Suite (Table 2, analyses 16–20). The $^{87}Sr/^{86}Sr$ initial ratios range from 0.704 to 0.705 and only slightly overlap the lower initial ratios of the Clarence River Plutonic Suite (Figure 7). The $\delta^{18}O$ averages 8.5 [*O'Neil et al.*, 1977] and $\delta^{34}S$ from the same rock samples averages +2 [*Coleman*, 1979]. The two samples analysed for REE from this

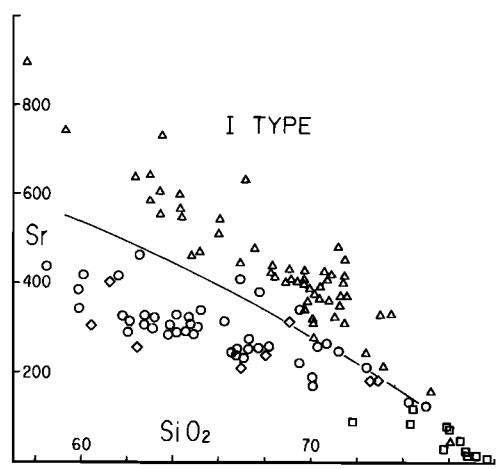

Fig. 10. Sr (ppm) versus SiO_2, used to distinguish the Sr-rich Moonbi Plutonic Suite (open triangles) from the Clarence River Plutonic Suite (diamonds) and the Uralla Plutonic Suite (circles). Leucoadamellites (squares) are indistinguishable from the extensions of the I-type suites.

Suite (Figure 6) show LREE enrichment up to 150 times chondrite, similar to that found in the S-type suites but different in that they have only minor *−ve* Eu anomalies and steeper LREE/HREE fractionation of about 8. The REE pattern of the Moonbi Plutonic Suite is similar to that of shoshonites and calc-alkaline rocks of island arcs [*Morrison,* 1980] except that the REE abundances are about twice as high as those of the Moonbi Plutonic Suite.

Uralla Plutonic Suite

The Upper Permian plutons that do not fit readily into the Clarence River or Moonbi Plutonic Suites have K_2O values intermediate between the two and $^{87}Sr/^{86}Sr$ initial ratios higher than both. Some contain only ilmenite as an opaque phase, whereas others have both ilmenite and magnetite. In general the granitoids from these plutons are equigranular but porphyritic variants with large white K-feldspar megacrysts do occur. Although the distribution of plutons considered as belonging to the Uralla Plutonic Suite (Figure 1) is much the same as that initially proposed by *O'Neil et al.* [1977], we have found a greater range of mineralogical and geochemical variation than anticipated and have extended the definition. We believe that the diversity of this Suite is a result of physical mixtures of the other recognizable source-rock types. Dominant mafic phases are actinolitic amphibole, biotite and lesser amounts of orthopyroxene and clinopyroxene.

The large asymmetrically-zoned Uralla Granodiorite [*Flood and Shaw,* 1979], used as the type example for the Uralla Plutonic Suite [*O'Neil et al.,* 1977], has along with other plutons of the Suite (Table 2, analyes 21–25) many characteristics intermediate between the low K_2O Clarence River Plutonic Suite and the S-type Hillgrove Plutonic Suite. For example, the high $\delta^{18}O$ [*O'Neil et al.,* 1977] (Figure 5), negative $\delta^{34}S$ [*Coleman,* 1979], CaO contents (Figure 9) and the amount of normative diopside or corundum (Figure 4) all indicate the intermediate I-S-type characteristics of the Uralla Plutonic Suite. In contrast with the other two I-type suites, the large pyroxene crysals occurring in the more mafic variants are hypersthene and the ignimbrities associated with the Uralla pluton are dactitic, with phenocrysts of plagioclase, hypersthene, lesser amounts of augite and minor ilmenite. The high normative hypersthene to normative diopside ratios of this pluton are reflected modally as abundant biotite similar to the S-type Hillgrove Plutonic Suite. The REE patterns (Figure 6) are similar to those of the S-type suites and differ from the Moonbi Plutonic Suite in having a marked *-ve* Eu anomaly and a less pronounced LREE/HREE enrichment.

Leucoadamellites

Most of the leucoadamellites of the New England Batholith are of Triassic age [*Evernden and Richards,* 1962; *Binns,* 1966; S. E. Shaw, unpublished data, 1980] and occur as large plutons mainly in the northern part of the Batholith (Figure 1). All leucoadamellites contain biotite which in a few plutons is accompanied by minor iron-rich tschermakitic hornblende or muscovite. Accessory minerals include zircon and metamict allanite and in the muscovite-bearing leucoadamellites, fluorite and cassiterite also occur. The leucoadamellites contain 74 to 77% SiO_2 (Table 2, analyses 26–30) and most are slightly corundum-normative (Figure 4). The high Rb/Sr ratios (greater than 10) preclude the determination of precise $^{87}Sr/^{86}Sr$ initial ratios for an indication of source-rock type. REE patterns of two samples (Figure 6) show large *−ve* Eu anomalies, LREE of about 150 times chondrite and a flatter REE slope than the analyzed members of the granitoid suites. The $\delta^{18}O$ values around 7.5 [*O'Neil et al.,* 1977] suggest an I-type affinity, whereas only 4 of the 6 leucoadamellites analyzed [*Coleman,* 1979] have positive $\delta^{34}S$ values similar to the I-type Moonbi Plutonic Suite. Because of the extremely low sulphur abundances in these rocks, there will be a greater possibility of isotopic variations due to reaction by late-stage hydrothermal activity, analytical difficulties and the high Fe_2O_3/FeO ratios. For these reasons $\delta^{34}S$ is not considered as diagnostic as for the more mafic-rich I-and S-type suites.

SOURCE-ROCK TYPES

Carboniferous S-Type Plutonic Suites

As discussed earlier, the presence of cordierite, the moderate amounts of normative corundum, the low Fe_2O_3/FeO ratios and the high $\delta^{18}O$ values of the Bundarra Plutonic Suite indicate a derivation from a peraluminous metasedimentary source. The quartz-rich character of even the most mafic and most corundum-normative samples (Figure 4) suggests that the source rocks were also quartz-rich.

The low $^{87}Sr/^{86}Sr$ initial ratios of this Suite around 0.706 are interpreted as reflecting a source region derived from a young volcanic terrain. In order to maintain low $^{87}Sr/^{86}Sr$ ratios in the source rocks, deposition, burial and partial melting to provide the Bundarra Plutonic Suite must have occurred rapidly. The Devonian and Carboniferous metasedimentary rocks, deposited under deep water conditions and which surround the Bundarra Plutonic Suite, are generally fine-grained apart from where they are contact metamorphosed to form assemblages containing quartz-cordierite-K-feldspar-biotite-oligoclase ± garnet. The calculated $^{87}Sr/^{86}Sr$ ratios of these metasedimentary rocks during the Upper Carboniferous (unpublished data) suggest they could form suitable source material provided they extend to the zone of partial melting.

The Hillgrove Plutonic Suite does not contain cordierite and the most important mineralogical indications of its S-type character are the abundant quartz and aluminous biotite and the presence of minor almandine-rich garnet. Unlike the Bundarra Plutonic Suite, the most mafic and most corundum-rich granitoids of the Hillgrove Plutonic Suite have only 65% SiO_2. Minor cummingtonite (perhaps replacing hypersthene) is consistent with a sedimentary source, and actionolitic amphibole in several plutons could be derived from calcareous nodules within the source rocks, similar to those found in the surrounding sedimentary rocks.

The metasedimentary rocks that form a narrow (less than 4 km) 'regional metamorphic aureole' around the Abroi Granodiorite, a pluton of the Hillgrove Plutonic Suite, contain the assemblage garnet–fibrolitic sillimanite–oligoclase–K-feldspar ± cordierite [*Binns,* 1966] in addition to quartz-feldspar gneisses and migmatites. The metasedimentary rocks that form the high-grade parts of the aureole could provide suitable source-rocks types assuming they were originally at the depth of magma generation. The problem of how these narrow, high-grade aureoles are surrounded by low-grade metasedimentary rocks has been discussed by *Flood and Vernon* [1978] who explained the required high thermal gradient across such a narrow regional metamorphic zone. Using the Cooma Gneiss as an example, they suggested that both the pluton and its surrounding source rock must have been dia-

pirically emplaced at higher levels in the crust. The model implies that while the high-grade gneisses and migmatites are part of the source region dragged up by the intruding magma, the same is not necessarily true of the low-grade rocks.

The bulk rock $\delta^{18}O$ values for the Hillgrove Plutonic Suite are slightly lower than those of the Bundarra Plutonic Suite (Figure 5) but are still above 10, the lower value that distinguishes peraluminous (S-type) plutons from metaluminous (I-type) plutons in eastern Australia [*O'Neil and Chappell,* 1977; *O'Neil et al.,* 1977]. *Gulson and Godbeer* [1979] have shown that the Cs contents of the two S-type suites in New England are similar to the Cs contents of the S-type plutons in the Berridale Batholith, southeastern Australia [*Chappell and White,* 1974].

We see both New England S-type suites as being derived by partial melting of young, volcanically-derived metasedimentary rocks and although depth of exposure and degree of partial melting could partly account for the different compositions, there are indications of two source materials, one relatively quartz- and cordierite-rich but feldspar-poor and the other feldspar-rich and relatively quartz- and cordierite-poor.

Upper Permian and Triassic I-Type Plutonic Suites

Partial melting of coarse volcaniclastic sediments (I-type) was once considered a viable model for generating the I-type magmas in New England [*Shaw,* 1964; *Flood,* 1971]. Several lines of evidence now suggest that models involving a significant sedimentary component in the source region cannot be justified for the Clarence River and Moonbi Plutonic Suites. These are as follows:

1. The Moonbi and Clarence River Plutonic Suites (and the two Triassic granodiorites) have $^{87}Sr/^{86}Sr$ initial ratios between 0.703 and 0.705, which is lower than most sedimentary rocks.

2. The complexly deformed region into which the plutons are intruded contains few sedimentary rocks that are diopside-normative (based on the presence of hornblende in contact aureoles). Even in the less distal sedimentary rocks to the west of the Peel Fault, mudstones are much more abundant than coarse volcaniclastic sandstones and on average are too aluminous to have formed suitable source rocks.

3. The low bulk-rock and mineral $\delta^{18}O$ values of the Moonbi Plutonic Suite have been interpreted by *O'Neil et al.* [1977] as indicating a source rock that has not undergone surfical weathering and is therefore I-type. Although no oxygen isotopic studies have been done for the Clarence River Plutonic Suite, petrological data would indicate low $\delta^{18}O$ values and hence on I-type source.

4. Although ilmenite (in the absence of magnetite) is not a sufficient criterion for indicating a metasedimentary source, we do not believe that any Paleozoic sedimentary pile is sufficiently free of carbon to produce magmas with the high Fe_2O_3/FeO ratios and magnetite that characterize the Moonbi and Clarence River Plutonic Suites.

5. The K_2O content of the Clarence River Plutonic Suite is too low and the CaO content of the Moonbi Plutonic Suite is too high for these suites to have been derived from a peraluminous metasedimentary source.

The K_2O-poor granodiorites and tonalites of the Clarence River Plutonic Suite require a gabbroic or dioritic parent because of the nature of their chemistry, mineralogy and texture. Whether these plutons were derived by partial melting of preexisting deep crustal plutons or by crystal fractionation of basaltic liquids is as yet unclear. A close examination of the more mafic plutons for fine-grained chilled margins and/or fine-grained dykes or stocks might resolve this question. The more mafic plutons have the doleritic textures (i.e., sub-ophitic) which characterize crystallization from liquids, suggesting that the magmas giving rise to the Clarence River Plutonic Suite were not rich in restite material.

Chappell [1978] has suggested that the Moonbi Plutonic Suite near Tamworth was derived by partial melting of K_2O-rich source rocks, with SiO_2 values between 55 and 65%, that underplated the crust from an earlier subduction event. An alternative model proposed by *Johnson et al.* [1978] to explain the more mafic, but similarly high potassic, lavas in Papua New Guinea involves the partial melting of mantle lithosphere previously modified by fluids rich in large-ion lithophile elements during an earlier period of subduction. The selective enrichment of mantle lithosphere in large-ion lithophile elements would explain the high Cs abundance of the Moonbi Plutonic Suite [*Gulson and Godbeer,* 1979]. The underplating model of *Chappell* [1978] and the mantle modification model of *Johnson et al.* [1978] could be complementary provided the mantle derived potassic magnas which gave rise to the Papua New Guinea type of volcanism also formed deep crustal plutons that at a later stage became the source rock for the Moonbi Plutonic Suite. Whether or not this two-stage model is required is debatable. Fine- to medium-grained stocks associated with the Moonbi Plutonic Suite that have SiO_2 values of 60% and have only small euhedral plagioclase and pyroxene phenocrysts indicate that some of the less silicic Moonbi Suite magmas were largely liquid and contained little, if any, restite. Whether or not the adamellites of the Moonbi Plutonic Suite were derived from largely liquid magmas of the composition of the stocks or from an unmixing of near-minimum melt and restite, remains a problem.

Although a metasedimentary source region can be discounted for the Clarence River and Moonbi Plutonic Suites, the Uralla Plutonic Suite and especially the Uralla Granodiorite [*Flood and Shaw,* 1979] is different. Although the Uralla Granodiorite is I-type with subaluminous hornblende and alumina-poor biotite as the major mafic minerals and $\delta^{18}O$ values [*O'Neil et al.,* 1977] less than 10, the transitional character of its source rocks is suggested by: (1) abundant biotite and ilmenite (without magnetite); (2) $^{87}Sr/^{86}Sr$ initial ratios (Figure 7) that overlap the initial ratios of the S-type suites; (3) the presence of numerous small metasedimentary xenoliths as well as I-type xenoliths; (4) values of $\delta^{18}O$ that are only just less than 10 and intermediate between the S-types and the Moonbi Plutonic Suite (Figure 5); and (5) bulk rock $\delta^{34}S$ values slightly negative and intermediate between the positive $\delta^{34}S$ values of the Moonbi Plutonic Suite and the more negative $\delta^{34}S$ values of the Carboniferous S-type suites.

Three possible explanations of the origin of the Uralla Plutonic Suite are as follows:

1. An original I-type magma of the Moonbi or Clarence River Plutonic Suite that was contaminated by pelitic material during ascent and emplacement.

2. Partial melting of a young volcaniclastic metasedimentary pile.

3. Partial melting of an interface region consisting of pelitic metasedimentary rocks of the type that gave rise to the S-type suites and a metaigneous source region of the type that

gave rise to the Moonbi and/or Clarence River Plutonic Suites.

The Moonbi, Clarence River and Uralla Plutonic Suites all consist of plutons of approximately the same range in size, shape and age and were all emplaced into Zone B rocks of the New England Fold Belt, yet the Uralla Plutonic Suite is the only suite that has transitional I-S characteristics. Marginal contamination of the three I-type suites is absent both in respect of metasedimentary material and the incorporation of I-type material from other suites. Because it would be unusual for only the Uralla Plutonic Suite to have selectively incorporated a metasedimentary component and to show no marginal evidence of such incorporation, we do not favor the contamination explanation.

While it might be possible for the diopside-normative granitoid magmas of the Uralla Plutonic Suite to have been produced from labile volcaniclastic metasedimentary rocks, we do not accept this explanation because:

1. Zone B, the region into which the granitoids of the New England Batholith were intruded, is composed of a sequence of deep marine, pelagic and distal turbidites deposited on an oceanic crust during the Middle Paleozoic. As such, Zone B would be unlikely to contain large volumes of relatively unmodified volcanic detritus with sufficiently few clay-rich interbeds to provide a composition which on average would be a suitable source material for the horblende-bearing Uralla Plutonic Suite.

2. Even in the unlikely situation that a large volcaniclastic pile did exist in Zone B (and there is no evidence of this) we would predict that although the $^{87}Sr/^{86}Sr$ ratios of granitoid melts could reflect the original igneous material, the oxygen isotopes will not. The $^{87}Sr/^{86}Sr$ ratios of a volcaniclastic metasediments at the time of partial melting will depend on the initial ratio of the magma that gave rise to the volcanic material, the increase in ^{87}Sr with time due to the breakdown of radiogenic Rb between eruption and partial melting, and the degree with which the weathered material equilibrates with sea water. It has been shown [*Peterman et al.*, 1967] that volcaniclastic piles will on partial melting give rise to magmas whose $^{87}Sr/^{86}Sr$ initial ratios will have increased little from the original igneous material providing melting takes place within about 30 Ma of deposition. On the other hand the large reservoir of oxygen in groundwater and/or ocean water would ensure that all low temperature secondary minerals will be enriched in $^{18}O/^{16}O$ by 10–30‰ compared with the primary igneous minerals. Thus the volcaniclastic sequences that have suitable Sr isotopic chemistry for I-type source regions could well be sufficiently enriched in $^{18}O/^{16}O$ to give partial melts with $\delta\ ^{18}O$ greater than 10.

We therefore favor the third mixed-source model. Sediment of the type that gave rise to the S-type suites would certainly have $^{87}Sr/^{86}Sr$ values greater than 0.706 by Upper Permian times. Mixtures of this material and the material that gave rise to the Clarence River Plutonic Suite (initial ratio about 0.704) might well produce magmas with $^{87}Sr/^{86}Sr$ initial ratios near 0.706. The $\delta^{18}O$ values (Figure 5) are also consistent with a mixed source-region origin. Thus the Uralla Plutonic Suite is seen as having source-rock regions, possibly as physical mixtures along interfaces, intermediate in composition between the S-types that gave rise to the Upper Carboniferous peraluminous suites and the I-types that gave rise to the low K_2O Clarence River and high K_2O Moonbi Plutonic Suites.

Whereas subequal aluminous and metaluminous metasedimentary mixes might provide a suitable source rock for the Uralla Granodiorite, other plutons of the Uralla Plutonic Suite that are much closer in composition to the Moonbi Plutonic Suite, even to the extent of containing magnetite, are explicable as being derived from an I-type source with only minor amounts of infolded or admixed metasedimentary rocks. As the plutons of the Uralla Plutonic Suite have $\delta^{18}O$ less than 10 and have a mineralogy basically similar to the other I-type suites, we classify this suite as I-type even though we envisage the source to be a physical mixture of metasedimentary and metaigneous material.

Two Triassic granodiorites [*Leitch and McDougall*, 1979] (Figure 1) have low $^{87}Sr/^{86}Sr$ initial ratios and are K_2O-poor like the Clarence River Plutonic Suite, but differ in that they contain ilmenite rather than magnetite. The low K_2O and low $^{87}Sr/^{86}Sr$ initial ratios (unpublished) are consistent with an I-type source having low oxygen activity, but until REE and oxygen isotope data are available, it is not possible to fully evaluate the source-rock types for these plutons.

Upper Permian and Triassic Leucoadamellites

The leucoadamellites have low $\delta^{18}O$ values that suggest an I-type source-rock [*O'Neil et al.*, 1977] but the high Rb/Sr ratios of these plutons preclude the precise determination of $^{87}Sr/^{86}Sr$ initial ratios. Based on the low $\delta^{18}O$ values, the presence of minor hornblende in some plutons, the near-minimum melt composition and the suggested high level of emplacement, *O'Neil et al.* [1977] argued that these plutons were derived by a 'dry' partial melting of an I-type source that had undergone a previous melting episode. The flatter REE patterns for these plutons (Figure 6) can also be explained using this model. If, as argued by *Frey et al.* [1978], the high LREE/HREE enrichment patterns of the Tuolumne Intrusive Series result from hornblende fractionation, then the resitite and/or cumulate will contain hornblende (and pyroxene) that is HREE-enriched [*Hanson*, 1978]. Subsequent partial melting of this HREE-enriched source could give rise to the rather flatter and greatly enriched HREE patterns of the New England leucoadamellites. Additionally, the breakdown of pargasitic amphibole during partial melting would leave less-aluminous pyroxenes as restite and could explain the corundum-normative character of most of these leucoadamellites as an alternative to the production of corundum-normative melts by the hornblende-fractionation model of *Cawthorn and O'Hara* [1976]. Certainly low degrees of partial melting and/or high degrees of fractionation involving significant feldspar extraction is indicated by the large *−ve* Eu anomalies (Figure 6). The muscovite-bearing Triassic leucoadamellite that occurs as irregular masses within the large Stanthorpe Adamellite [*Shaw*, 1969] might well have had alkalis selectively removed by chloride-rich aqueous fluids [*Burnham*, 1979] when the magma became water-saturated and vented to the surface, producing a medium-grained, pressure-quenched, Sn-bearing muscovite leucoadamellite.

TECTONIC RECONSTRUCTION

In a discussion of the age and low $^{87}Sr/^{86}Sr$ initial ratios of the New England S-type suites [*Flood and Shaw*, 1977], we suggested that tectonically they are more closely related to the Andean margin I-type volcanoes that flanked the western margin of the New England Fold Belt in the Upper Carboni-

ferous [*Wilkinson,* 1971; *Jakes and White,* 1972] than to the Upper Permian I-type plutons with which they are spatially associated. The S-type suites were emplaced in Zone B at about the time when the Andean volcanism in Zone A was replaced by coal-basin sedimentation and basaltic volcanism.

With the emplacement of the S-type plutons, the western part of Zone B became emergent as a non-volcanic outer arc [*Leitch,* 1975]. Although to date no volcanics of S-type have been positively identified, we are unsure whether this implies an initially nonvolcanic region, subsequent removal of any volcanics by erosion, or failure as yet to recognise S-type volcanics among the large areas of exposed silicic volcanics.

Recently, *Hudson et al.* [1979] have described a belt of Lower Tertiary 'anatectic' (S-type) plutons that form mainly an island chain about 100 km south or oceanwards from the Gulf of Alaska margin. These plutons provide an excellent analogue for the New England S-type plutons. Points of similarity include: (1) the Bundarra Plutonic Suite (and in the reconstruction of *Flood and Shaw* [1977] also the Hillgrove Plutonic Suite) is parallel to the outcrops of Andean margin volcanics about 100 km to the west; (2) the granitoids are developed in a trench complex; (3) the granitoids have S-type mineralogical characteristics but have only moderately high $^{87}Sr/^{86}Sr$ initial ratios (about 0.706); (4) some plutons in both areas have migmatitic regional aureoles of the type considered by *Flood and Vernon* [1978] to result from the source rocks being dragged up around diapirically-emplaced anatectic granite magmas; and (5) both had plutons developing while marine sedimentation probably continued on both sides of the zone of plutonism.

Hudson et al. [1979] conclude that the Sanak-Baranof plutonic belt formed when subduction ceased and the base of the trench-complex sediments gradually heated up. The Lower Tertiary age of these plutons does correspond to the change in direction of movement of the Pacific plate from due north (i.e., directly towards the Gulf of Alaska) to northwest (i.e., obliquely past the Gulf) as recorded by the dog-leg in the Hawaiian-Emperor sea-mount chain. As the Sanak-Baranof belt of plutons closely parallels the shape of the continental margin, it would appear inappropriate to use the direction of elongation of the New England S-type suites to assign a direction of plate motion in the same way that the Hawaiian chain has been interpreted.

Between the Upper Carboniferous S-type plutonism and the Upper Permian and Triassic I-type plutonism, the New England region underwent a major period of deformation [*Leitch,* 1975] that resulted in significant movement on both the Peel Fault and Hunter-Mooki Thrust (Figure 2). The intrusion of I-type granitoids within Zone B has been regarded as post-orogenic [*Day et al.,* 1978]. Apart from the plutons along the eastern margin of the Batholith that have been slightly offset by the dextral movement on the Demon Fault (Figure 1), the Upper Permian and Triassic plutons are unaffected by faulting. Further evidence that the region had generally stabilized from the Upper Permian onward is seen by the presence of shallow marine and terrestrial sedimentation in the Sydney Basin during the Permian and Triassic and in the Clarence-Moreton Basin during the Triassic (Figure 2). A few basaltic lava flows occur in the lower parts of both basins and these basins reflect a change from compressional to perhaps tensional tectonics in the upper crust during emplacement of the I-type plutons.

The present coastline of eastern Australia is a rift margin formed when the submarine Lord Howe Rise separated from the continent during the Tertiary [*Jones,* 1971]. As the I-type plutons lie only 100 km inland from the present continental margin and as little is known of the inferred Paleozoic basement of the Lord Howe Rise, it is difficult to assess the tectonic development of eastern New England during the Upper Permian and Triassic. Of particular note, however, is the north-north-east trend of the main I-type granitoid belt which parallels the present coastline (Figure 1).

Although it has not been previously suggested that the I-type granitoids occupy a graben-like structure, the preservation of co-magmatic silicic volcanics along much of the I-type belt does suggest some subsidence. Whether it is a graben with general subsidence along the whole length or local subsidence associated with caldera collapse is yet to be determined. There is no evidence of bi-modal basaltic and rhyolitic activity that might indicate a major rift zone, such as the Rio Grande Rift [*Elston and Bornhorst,* 1979]. Equally, the tectonic stability of southeastern Australia during the Upper Permian and Triassic suggests that if it still formed part of a convergent plate margin, then the subduction zone trench must have situated far to the east of the present coastline.

Whatever the tectonic model proposed for the Upper Permian and Triassic plutonism, it must be capable of explaining the change from S-type plutonism in the Upper Carboniferous to I-type plutonism in the Upper Permian and Triassic. It must also explain why almost all of the plutons are restricted to Zone B. Our explanation involves the partial melting of I-type source rocks in the lower crust underlying the continental margin that resulted from the combined effects of an increase in temperature of the lower crust due to the recovery of normal continental geotherms following the cessation of subduction, and crustal thickening with attendant sinking of the lower crust as a result of over-thrusting of the upper parts of the trench complex (Zones A and B) over the continental margin.

Although over-thrusting of east over west is known to have occurred on the Hunter-Mooki Thrust [*Carey and Osborne,* 1939], the presence of Permian rocks adjacent to and on both sides of the Thrust suggests that movement was limited and we are therefore forced to argue that the major part of the movement was along the Peel Fault and associated faults in Zone B. Large-scale thrusting and reverse faulting along the Peel and associated faults implies that the dip of the fault surfaces shallow at depth, although field and geophysical evidence on the Peel Fault suggests that this does not happen for at least several kilometers below the present surface [*Ramsay and Stanley,* 1976]. East-over-west thrusting would have several effects. Firstly, it would move the upper crustal rocks including the S-types plutons westward onto or further over the continental margin, the lower parts of which may constitute suitable source rocks for the later I-type plutonism. Secondly, this over-thrusting would produce continental thickening and result in isostatic subsidence of the lower parts of the continental crust.

The emplacement of the I-type granitoids next to the earlier trench-complex S-type plutons could simply result from the thrusting of the upper parts of the trench complex (and the emplaced S-type granitoids) westward over the continental margin between the two episodes of plutonism. Alternatively, the trench-complex sedimentary wedge could have been partly obducted onto and partly subducted under the continental margin. This latter possibility would imply that the

early subduction-complex S-type granitoids were derived from partly subducted metasedimentary rocks and rose as magmas through the edge of the continental crust to be finally emplaced into the obducted parts of the same metasedimentary complex.

We are unwilling to speculate on whether the lower crustal source rocks were developed or modified during the Carboniferous subduction event or were produced during an earlier stage of continental development.

CONCLUSIONS

In the New England Batholith, the Upper Carboniferous S-type plutons occupy two narrow linear belts along the edge of the Batholith (Figure 1) that may have been offset by mid-Permian faulting. The upper Permian I-type plutons occupy a north-east-trending belt some 60 km wide and 300 km long in the centre of the Batholith. The Triassic plutons also form a diffuse belt, mainly along the eastern margin of the Batholith. The period of I-type plutonism in the Upper Permian and Triassic consists mainly of early mafic adamellites and granodiorites (255–240 Ma) and late leucoadamellites (230–220 Ma). This mafic to felsic evolution is similar to that of the 'super-units' of the Coastal Batholith, Peru [*Pitcher,* 1978].

We suggest that the peraluminous S-type plutonism in the New England Batholith occurred in a wedge of trench-complex sedimentary rocks during the waning stages of Andean volcanism further to the west. That is, plutonism occurred on the ocean side of the coeval I-type volcanism and this relationship seems to match the lower Tertiary S-type plutons that are along the margin of the Gulf of Alaska [*Hudson et al.,* 1979]. The low $^{87}Sr/^{86}Sr$ initial ratio subduction-complex S-type granitoid suites in New England may not have the same tectonic significance as the high $^{87}Sr/^{86}Sr$ initial ratio S-type granitoids of the Lachlan Fold Belt inferred by *A. J. R. White et al.* [1976] as occurring above pre-existing continental crust on the continental side of most I-type plutons.

The change from entirely S-type plutonism to mainly I-type plutonism in the same region may result from the thrusting of the subduction-complex sediments (and the S-type plutons emplaced in them) westward over the deeper parts of the earlier subduction zone that is inferred to have modified the upper mantle and/or lower crust to produce suitable source rocks for the later I-type plutons by either underplating the crust [*Chappell,* 1978] or chemically modifying the upper mantle [*Ringwood,* 1974; *Johnson et al.,* 1978].

Deformation of the subduction-complex sediments and the emplaced S-type plutons occurred prior to the I-type plutonism in the Upper Permian and Triassic. The I-type plutons range from low-K_2O to high-K_2O types similar to volcanics of convergent plate-margins. One of the diopside-normative (hornblende-bearing) suites, the Uralla Plutonic Suite, has mineralogical and isotopic features intermediate between the S-type suites and the I-type Clarence River and Moonbi Plutonic Suites. The Uralla Plutonic Suite is inferred to have been derived from the interface region between the I- and S-type source regions where the two types might be physically intermixed. Except for these mixed I-S granitoids, little sedimentary material seems to have been involved in the genesis of the Moonbi and Clarence River Plutonic Suites.

In contrast to the Berridale Batholith [*Chappell and White,* 1974], the $^{87}Sr/^{86}Sr$ initial ratios of the corundum-normative S-types and the diopside-normative I-types in New England overlap. This results both from the low initial ratios of the S-types derived from the young, volcanically-derived sedimentary rocks and from the presence of the diopside-normative plutons with mixed I-S characteristics.

Although all S-type plutons contain ilmenite and not magnetite, so too do some of the diopside-normative mixed I-S-type of the Uralla Plutonic Suite and the two I-type Triassic granodiorites (Figure 1) that have no S-type characteristics. Thus, while all S-type, plutons contain ilmenite, not all plutons containing ilemnite are S-type, suggesting that the correlation between I-type and magnetite and S-type and ilmenite (e.g., the ilmenite series and the magnetite series granitoids of Japan [*Ishihara,* 1977]) is not simple.

In New England, the leucoadamellites of both I- and S-type suites tend towards normative-corundum compositions, as indicated by *A.J.R. White and Chappell* [1977]. Whereas S-type granitoids evolve from moderate to only slightly corundum-normative compositions as a function of the decreasing abundance of alumino-silicate minerals, the I-type granitoids evolve from diopside-normative (hornblende-bearing) to slightly corundum-normative (biotite-bearing) composition. The production of more strongly corundum-normative muscovite-bearing I-type leucoadamellites is best explained by the loss of alkalis in the chloride-rich aqueous fluids by near-surface venting. The fine grain-size of these rocks is consistent with fluid release and subsequent 'pressure quenching.'

Acknowledgments. We wish to thank the following institutions for providing facilities and results used in this project: the United States Geological Survey, Denver, and in particular Z. Peterman and C. Hedge; the Commonwealth Scientific and Industrial Research Organization, North Ryde, New South Wales, and in particular G. Riley; Oregon State University, Corvallis, Oregon, and in particular R. Schmitt. The work was supported by Macquarie University Research grants and the Australian Research Grants Committee (E7815488). We are grateful to R. H. Vernon and E. C. Leitch for commenting on the manuscript, B. W. Chappell for his encouragement, and R. H. Moench for his valuable critical review.

REFERENCES

Andrews, E. C., and J. C. H. Mingaye, The geology of the New England Plateau with special references to the granites of northern New England, 4, Petrology, *Rec. Geol. Surv. N. S. W.,* 196–238, 1907.

Armstrong, R. L., Pre-Cenozoic Phanerozoic time scale—computer file of critical dates and consequences of new and in-progress decya-constant revisions, in *Studies in Geology, No. 6,* edited by G. V. Cohee, M. F. Glaessner, and H. D. Hedberg, pp. 73–91, American Association of Petroleum Geologists, Tulsa, Okla., 1978.

Bateman, P., C., and B. W. Chappell, Crystallization, fractionation, and solidification of the Tuolumne Intrusive Series, Yosemite National Park, *U.S. Geol. Surv. Prof. Pap., 160,* 120–129, 1978.

Binns, R. A., Granitic intrusions and regional metamorphic rocks of Permian age from the Wongwibinda District, north-eastern New South Wales, *J. Proc. R. Soc. N. S. W., 99,* 5–36, 1966.

Binns, R. A., et al., Geological map of New England—New England Tableland—Southern part, with explanatory text, scale 1:250,000, Univ. of New England, Armidale, New South Wales, Australia, 1967.

Black, L. P., Rb-Sr systematics of the Claret Creek ring complex and their bearing on the origin of Upper Palaeozoic igneous rocks in northeast Queensland, *J. Geol. Soc. Aust., 27,* 157–166, 1980.

Burnham, C. W., Magmas and hydrothermal fluids, in *Geochemistry of Hydrothermal Ore Deposits,* edited by H. L. Barnes, pp. 71–136, John Wiley, New York, 1979.

Carey, S. W., and G. D. Osborne, Preliminary note on the nature of

stresses involved in the late Palaeozoic diastrophism in New South Wales, *J. Proc. R. Soc. N. S. W., 72,* 199–208, 1939.

Cawthorn, R. G., and M. J. O'Hara, Amphibole fractionation in calc-alkaline magma genesis, *Am. J. Sci., 276,* 309–329, 1976.

Chappell, B. W., Granitoids from the Moonbi district, New England Batholith, eastern Australia, *J. Geol. Soc. Aust. 25,* 267–283, 1978.

Chappell, B. W., and A. J. R. White, Two contrasting granite types, *Pac. Geol., 8,* 173–174, 1974.

Coleman, M. L., Isotopic analysis of trace sulphur from some S- and I-type granites: Heredity or environment?, in *Origin of Granite Batholiths: Geochemical Evidence,* edited by M. P. Atherton and J. Tarney, pp. 129–133, Shiva Publishing, Orpington, Kent, United Kingdom, 1979.

Cooper, J. A., J. R. Richards, and A. W. Webb, Some potassium-argon ages in New England, New South Wales, *J. Geol. Soc. Aust., 10,* 313–316, 1963.

Day, R. W., C. G. Murray, and W. G. Whitaker, The eastern part of the Tasman orogenic zone, *Tectonophysics, 48,* 327–364, 1978.

Elston, W. E., and T. J. Bornhorst, The Rio Grande Rift in context of regional post-40 m.y. volcanic and tectonic events, in *Rio Grande Rift: Tectonics and Magmatism,* edited by R. E. Riecker, pp. 416–438, AGU, Washington, D. C., 1979.

Evans, P. R., and J. Roberts, Evolution of central eastern Australia during the late Palaeozoic and early Mesozoic, *J. Geol. Soc. Aust., 26,* 325–340, 1979.

Evensen, N. M., P. J. Hamilton, and R. K. O'Nions, Rare-earth abundances in chondritic meteorites, *Geochim. Cosmochim. Acta, 42,* 1199–1212, 1978.

Evernden, J. F., and J. R. Richards, Potassium-argon ages in eastern Australia. *J. Geol. Soc. Aust., 9,* 1–50, 1962.

Flood, R. H., A study of part of the New England Batholith, New South Wales, Ph.D. thesis, Univ. of New England, Armidale, New South Wales, Australia, 1971.

Flood, R. H., and S. E. Shaw, A cordierite-bearing granite suite from the New England Batholith, N.S.W., Australia, *Contrib. Mineral. Petrol., 52,* 157–164, 1975.

Flood, R. H., and S. E. Shaw, Two 'S-type' granite suites with low initial $^{87}Sr/^{86}Sr$ ratios from the New England Batholith, Australia, *Contrib. Mineral. Petrol., 61,* 163–173, 1977.

Flood, R. H., and S. E. Shaw, K-rich cumulate diorite at the base of a tilted granodiorite pluton from the New England Batholith, Australia, *J. Geol., 87,* 417–425, 1979.

Flood, R. H., and R. H. Vernon, The Cooma granodiorite, Australia: An example of in situ crustal anatexis?, *Geology, 6,* 81–84, 1978.

Flood, R. H., R. H. Vernon, S. E. Shaw, and B. W. Chappell, Origin of pyroxene-plagioclase aggregates in a rhyodacite, *Contrib. Mineral. Petrol., 60,* 299–309, 1977.

Flood, R. H., S. E. Shaw, and B. W. Chappell, Mineralogical and chemical matching of plutonic and associated volcanic units, New England Batholith, Australia, *Geology, 29,* 163–170, 1980.

Frey, F. A., B. W. Chappell, and S. D. Roy, Fractionation of rare-earth elements in the Tuolume Intrusive Series, Sierra Nevada batholith, California, *Geology, 6,* 239–242, 1978.

Gulson, B. L., and W. Godbeer, Caesium as a possible discriminant between felsic rocks of different origins from eastern Australia, *J. Geol. Soc. Aust. 26,* 11–15, 1979.

Gunthorpe, R. J., Plutonic and metamorphic rocks of the Walcha-Nowendoc-Yarrowitch district, northern New South Wales, Ph.D. thesis, Univ. of New England, Armidale, New South Wales, Australia, 1970.

Hanson, G. N., The application of trace elements to the petrogenesis of igneous rocks of granitic composition, *Earth Planet. Sci. Lett., 38,* 26–43, 1978.

Hudson, T., G. Plafker, and Z. E. Peterman, Paleogene anatexis along the gulf of Alaska margin, *Geology, 7,* 573–577, 1979.

Ishihara, S., the magnetite-series and ilmenite-series granitic rocks, *Min. Geol. J., 27,* 293–305, 1977.

Jakes, P., and A. J. R. White, Hornblendes from calc-alkaline volcanic rocks of island arcs and continental margins, *Am. Mineral., 57,* 887–902, 1972.

Johnson, R. W., D. E. Mackenzie, and I. E. M. Smith, Delayed partial melting of subduction-modified mantle in Papua New Guinea, *Tectonophysics, 46,* 197–216, 1978.

Jones, J. G., Australia's Caenozoic drift, *Nature, 230,* 237–239, 1971.

Kleeman, J. D., Geological age measurements using fission tracks, A.A.E.C. Journal, *Atomic Energy in Australia, 18,* 3–8, 1975.

Korsch, R. J., A framework for the Palaeozoic geology of the southern part of the New England geosyncline, *J. Geol. Soc. Aust., 24,* 339–355, 1977.

Lanphere, M. A., and J. J. Hockley, The age of nephrite occurrences in the Great Serpentine Belt of New South Wales, *J. Geol. Soc. Aust., 23,* 15–17, 1976.

Leitch, E. C., The geological development of the southern part of the New England Fold Belt, *J. Geol. Soc. Aust., 21,* 133–156, 1974.

Leitch, E. C., Plate tectonic interpretation of the Paleozoic history of the New England Fold Belt, *Geol. Soc. Am. Bull., 86,* 141–144, 1975.

Leitch, E. C., and I. McDougall, The age of orogenesis in the Nambucca slate belt: A K-Ar study of low-grade regional metamorphic rocks, *J. Geol. Soc. Aust., 26,* 111–119, 1979.

Moore, J. G., The quartz diorite boundary line in the western United States, *J. Geol., 67,* 198–210, 1959.

Morrison, G. W., Characteristics and tectonic setting of the shoshonite rock association, *Lithos, 13,* 97–108, 1980.

Nielsen, H., Sulfur isotopes, in *Lectures in Isotope Geology,* edited by E. Jäger and J. C. Hunziker, pp. 283–312, Springer-Verlag, Berlin, 1979.

Norrish, K., and B. W. Chappell, X-ray fluorescence spectrometry, in *Physical Methods in Determinative Mineralogy,* 2nd ed., edited by J. Zussman, pp. 201–272, Academic, New York, 1977.

O'Neil, J. R., and B. Chappell, Oxygen and hydrogen isotope relations in the Berridale batholith, *J. Geol. Soc. London, 133,* 559–571, 1977.

O'Neil, J. R., S. E. Shaw, and R. H. Flood, Oxygen and hydrogen isotope compositions as indicators of granite genesis in the New England Batholith, Australia, *Contrib. Mineral. Petrol., 62,* 313–328, 1977.

Peterman, Z. E., C. E. Hedge, R. G. Coleman, and P. D. Snavely, Jr., $^{87}Sr/^{86}Sr$ ratios in some eugeosynclinal sedimentary rocks and their bearing on the origin of granitic magma in orogenic belts, *Earth Planet. Sci. Lett., 2,* 433–439, 1967.

Phillips, E. R., The adamellites of the Liston area, The Geology of New South Wales, *J. Geol. Soc. Aust., 16,* 290–294, 1969.

Pitcher, W. S., The anatomy of a batholith, *J. Geol. Soc. London, 135,* 157–182, 1978.

Pogson, D. J., and B. L. Hitchins, The New England geological sheet, Scale 1:500,000, Geol. Surv. of New South Wales, Sydney, Australia, 1973.

Ramsay, W. R. H., and J. M. Stanley, Magnetic anomalies over the western margin of the New England foldbelt, northeast New South Wales, *Geol. Soc. Am. Bull., 87,* 1421–1428, 1976.

Ringwood, A. E., The petrological evolution of island arc systems, *J. Geol. Soc. London, 130,* 183–204, 1974.

Sasaki, A., and S. Ishihara, Sulfur isotopic composition of the magnetite-series and ilmenite-series granitoids in Japan, *Contrib. Mineral. Petrol., 68,* 107–115, 1979.

Shaw, S. E., The petrology of portion of the New England Batholith, New South Wales, Ph.D. thesis, Univ. of New England, Armidale, New South Wales, Australia, 1964.

Shaw, S. E., Granitic rocks from the northern portion of the New England Batholith, The Geology of New South Wales, *J. Geol. Soc. Aust., 16,* 285–290, 1969.

Sohl, N. F., Stratigraphic commission note 45—Application for amendment concerning terminology for igneous and high grade metamorphic rocks, *Am. Assoc. Petrol. Geol. Bull., 61,* 248–251, 1977.

Steiger, R. H., and E. Jager, Subcommission on geochronology: Convention of the use of decay constants in geo- and cosmochronology, *Earth Planet. Sci. Lett., 36,* 359–362, 1977.

Streckeisen, A. L., Plutonic rocks: Classification and nomenclature, *Geotimes, 18,* 26–30, 1973.

Thomson, J., Results of radiometric programme 1971–1973, *Rec. Geol. Surv. N. S. W., 16,* 239–244, 1974.

Tuttle, O. F., and N. L. Bowen, Origin of granite in the light of experimental studies in the system $NaAlSi_3O_8$-$KAlSi_3O_8$-SiO_2-H_2O, *Geol. Soc. Am. Mem., 74,* 153 pp., 1958.

Voisey, A. H., The New England region: Geological history, The Geology of New South Wales, *J. Geol. Soc. Aust., 16,* 307–310, 1969.

White, A. H., An analysis of Upper Devonian and Carboniferous sedimentation in part of the Western Foreland of the New England Eugeosyncline, Ph.D. thesis, Univ. of New England, Armidale, New South Wales, Australia, 1966.

White, A. J. R., and B. W. Chappell, Ultrametamorphism and granitoid genesis, *Tectonophysics, 43,* 7–22, 1977.

White, A. J. R., I. S. Williams, and B. W. Chappell, The Jindabyne thrust and its tectonic, physiographic and petrogenetic significance, *J. Geol. Soc. Aust., 23,* 105–112, 1976.

Wilkinson, J. F. G., Intrusive rocks: The New England Batholith, The Geology of New South Wales, *J. Geol. Soc. Aust. 16,* 271–278, 1969.

Wilkinson, J. F. G., The petrology of some vitrophyric calc-alkaline volcanics from the Carboniferous of New South Wales, *J. Petrol., 12,* 587–619, 1971.

(Received December 1, 1980;
revised March 19, 1981;
accepted April 3, 1981.)

JOURNAL OF GEOPHYSICAL RESEARCH, VOL. 86, NO. B11, PAGES 10545-10568, NOVEMBER 10, 1981

MANASLU LEUCOGRANITE: A COLLISION SIGNATURE OF THE HIMALAYA A MODEL FOR ITS GENESIS AND EMPLACEMENT

Patrick Le Fort

Centre de Recherches Pétrographiques et Géochimiques
54501 Vandoeuvre-lès-Nancy Cedex, France

Abstract. The Manaslu pluton is one of 10 leucogranites that formed in the overthrusted Higher Himalaya after the Indo-Eurasian collision. Field and analytical data indicate that the underlying migmatites of the Tibetan Slab may be where the leucogranitic melts were generated. The Himalayan crustal thrusting of a hot slab over a rather cold volcano-sedimentary pile [Le Fort, 1975a] provides the necessary release of fluids. These fluids cross the Main Central Thrust (MCT), induce the partial anatexis of the overheated Tibetan Slab, and produce a leucogranitic magma. The emplacement of the magma at first is located along the main disharmonic plane above the MCT, between the infrastructure and the superstructure. There it generates a convective hydrothermal system extending very far laterally according to the stratification of permeabilities. Progressive emplacement of the granite proceeds as the convected fluids, including the fluids released by the saturated magma, dissolve the mainly calcareous host rocks of Tibetan sedimentaries. A frozen image of this 'caving out' progression is given by the extensive network of granitic dikes outside the pluton. The two quite independant fluid cycles of the generation and of the emplacement were triggered or guided by the tectonics due to collision. This two-fold model, dominated by fluid activity, may be of importance for other leucogranites and granites.

Et ma prérogative sur les mers
est de rêver pour vous ce rêve du réel...
Saint-John Perse (Amers)

Introduction

The Manaslu pluton is located in the Higher Himalaya of central Nepal. It is one of the 10 or so plutons which are very irregularly scattered along 2000 km of the Himalayan range from the Nanga Parbat massif in Pakistan to Bhutan [Le Fort, 1973a, 1975b]. These plutons form the main part of some of the highest peaks of the world (Everest, Lhotse, Makalu, Manaslu, Shisha Pangma, etc.).

From their description in the literature (principally Heim and Gansser [1975], Misch [1949], Bordet [1961], Gansser [1964], Wager [1965], Hagen [1969], and Le Fort [1973a] it appears that all the plutons have similar characteristics: they are very homogeneous leucogranites of the same mineralogy and chemical composition, the same texture, and the same relations to the surrounding rocks. Intruding Jurassic rocks in Bhutan [Nautiyal et al., 1969] and Cretaceous rocks in Nepal, their age is generally thought to be post-Eocene and pre-Pliocene, probably Miocene. It has been proposed from their field location, from the metamorphic and structural pattern of the surrounding rocks, and from the general geodynamic history of the Himalaya that they are typical anatectic products of a thick and isolated continental crust [Le Fort, 1975a].

Although relatively small (about 400 km^2 in area, as compared to some 8000 km^2 for all of the Himalayan granites) the Manaslu pluton is a good representative of these leucogranites [Le Fort, 1973a, 1975b].

Geology of the Manaslu Granite

Geological Setting

Previous descriptions of the Manaslu granite have been given by Le Fort [1973a, 1975b,d]. The surrounding formations have been dealt with by Le Fort [1975a,c], Colchen [1975a,b], and Pêcher [1978]. A geological map of central Nepal at a scale of 1/200,000 has been published [Colchen et al., 1980] (Figures 1 and 2). From these descriptions, let us recall the salient features:

The Manaslu pluton forms a large laccolith or lenticular sheet dipping to the NNE (Figures 1-3). The main part is an elliptic body having an area of some 300 km^2 and a maximum thickness of some 10 km, from which a sheet a few hundred of meters thick and some 60 km long stretches towards the ESE: the *arm* or Chhokang sheet of the Manaslu pluton. Farther east, this *arm* seems to join the Shisha Pangma pluton, which is like the Manaslu body. West of the granite in the region of Chago, in the valley of Nar (Figure 2), an astonishingly large aplopegmatitic network of dikes appears in the metamorphic limestones at the base of the Tibetan sedimentaries (Figure 4 and from Le Fort [1975d, Figure 31]. This network extends out of the granite for at least some 10 km.

The base of the pluton- main body as well as the arm -lies in a constant lithologic (Figures 1 and 2) and structural position. It is located a few hundred meters to 1 km above the top of the augen gneisses of Formation III of the Tibetan Slab, in pyroxene marbles that contain intercalations of micaschists (Figure 5a). This location corresponds to the change in tectonic style between the isoclinally folded infrastructure of the Tibetan Slab and the more open folding of the superstructure of the Tibetan sedimentary series (Figure 6).

The top of the main body intrudes higher and higher levels of the Tibetan sedimentary series as its thickness increases: from Cambro-Ordovician to Upper Triassic in the Noir and Blanc glaciers region (Figures 3 and 4). The Tibetan sedimentary rocks are platform deposits of Atlantic margin type in which limestones dominate [Colchen, 1975a].

The base of the pluton is in metamorphic equilibrium with the surrounding rocks (diopside marbles, sillimanite gneisses). The top of the pluton develops a thin (∿50 m) metamorphic aureole

Copyright 1981 by the American Geophysical Union.

Paper number 1B0986.
0148-0227/81/001B-0986$01.00

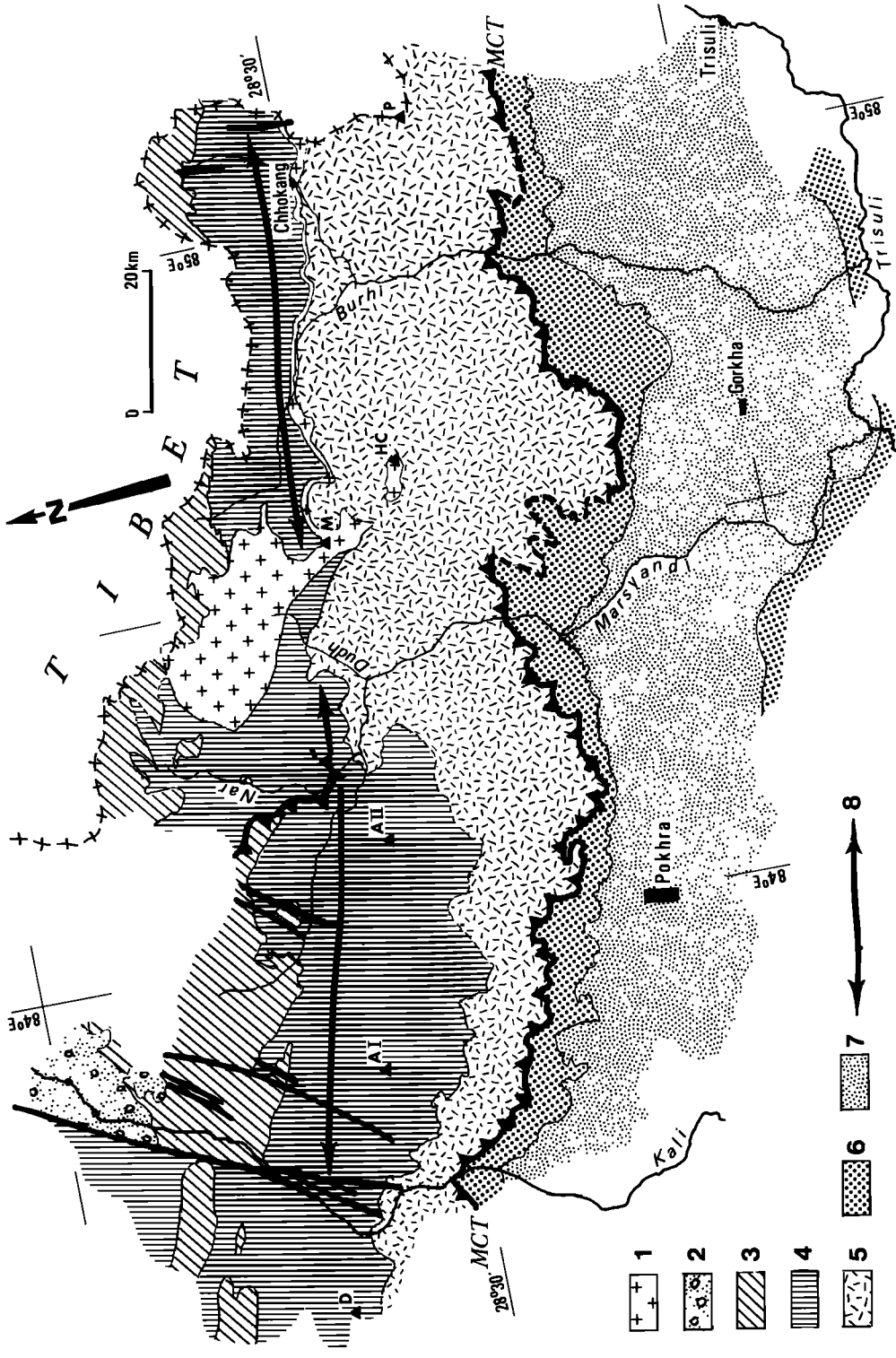

Fig. 1. Geological sketch map of central Nepal [from Colchen, Le Fort and Pêcher, 1980]. 1, Manaslu granite; 2 to 4, Tibetan sedimentary series; 2, Cenozoic Thakkhola series; 3, Mesozoic series; 4, Paleozoic series; 5, Tibetan Slab; 6, Upper Midland formations; 7, Lower Midland formations; 8, Nilgiri or Annapurna northward recumbent anticlinal. AI and AII, Annapurna I and II peaks; D, Dhaulagiri; HC, Himal Chuli; M, Manaslu; P, Pabil (Ganesh Himal).

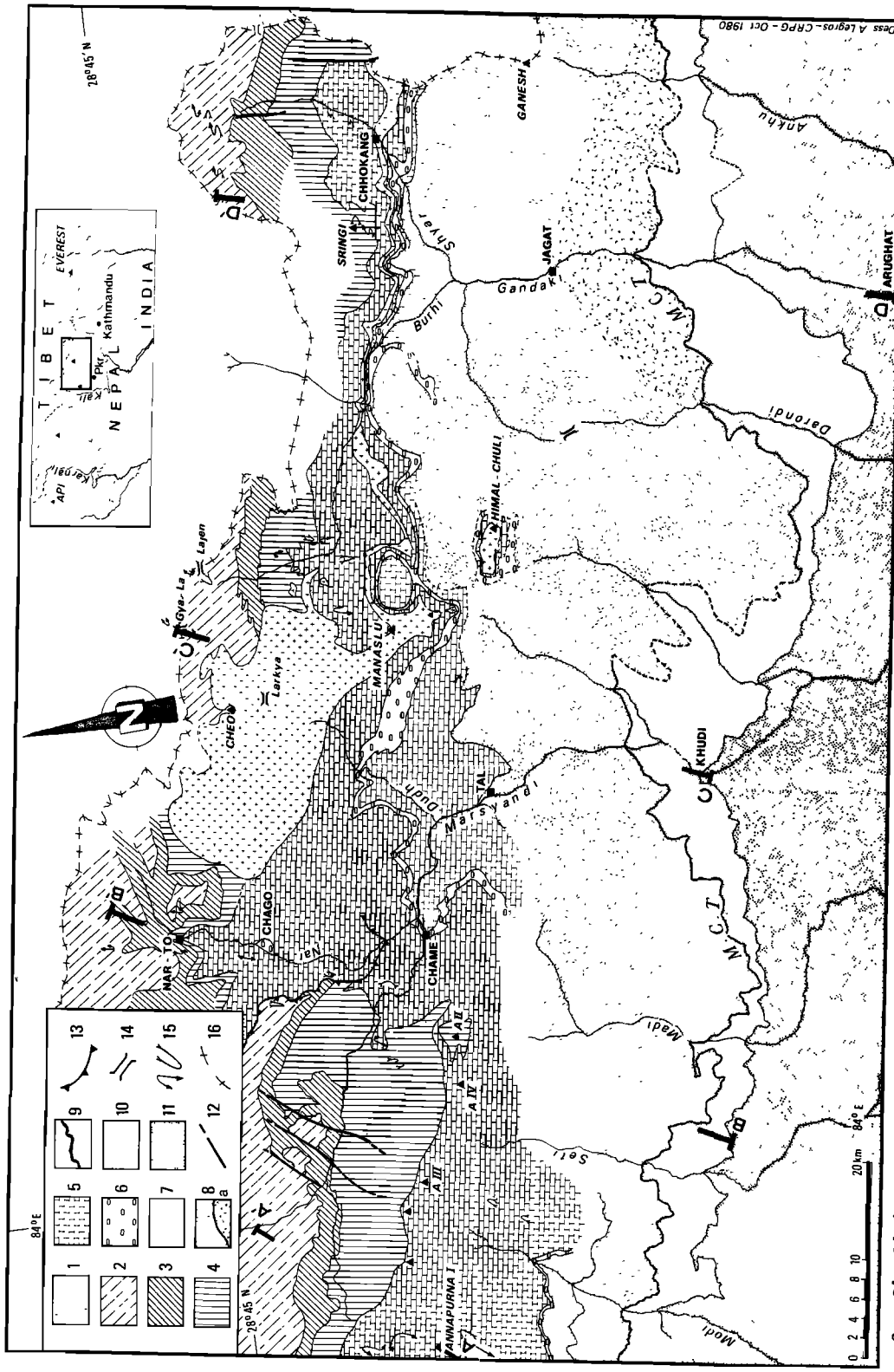

Fig. 2. Simplified geological map of north-central Nepal [after Colchen, Le Fort and Pêcher, 1980] showing the extension of the Manaslu pluton in Nepal. 1, Manaslu granite; 2 to 5, Tibetan sedimentary series; 2, Mesozoic series (Triassic and Jurassic); 3, Permo-Carboniferous series; 4, Siluro-Devonian series; 5, Lower Paleozoic series, mainly metamorphosed limestones; 6 to 8, Tibetan Slab; 6, Formation III augen gneisses; 7, Formation II marbles and calc-silicate gneisses; 8, Formation I alternances of metasandstones and metapelites more or less migmatized (mainly quartzites where dots are added); 9, Main Central Thrust (MCT); 10 and 11, Midland metasedimentary and metavolcanic group; 10, Upper formation; 11, Lower formation; 12, faults; 13, other thrust; 14, main pass; 15, anticlinal or synclinal fold; 16, Nepal border. AA' to DD' refer to the cross sections of Figure 6.

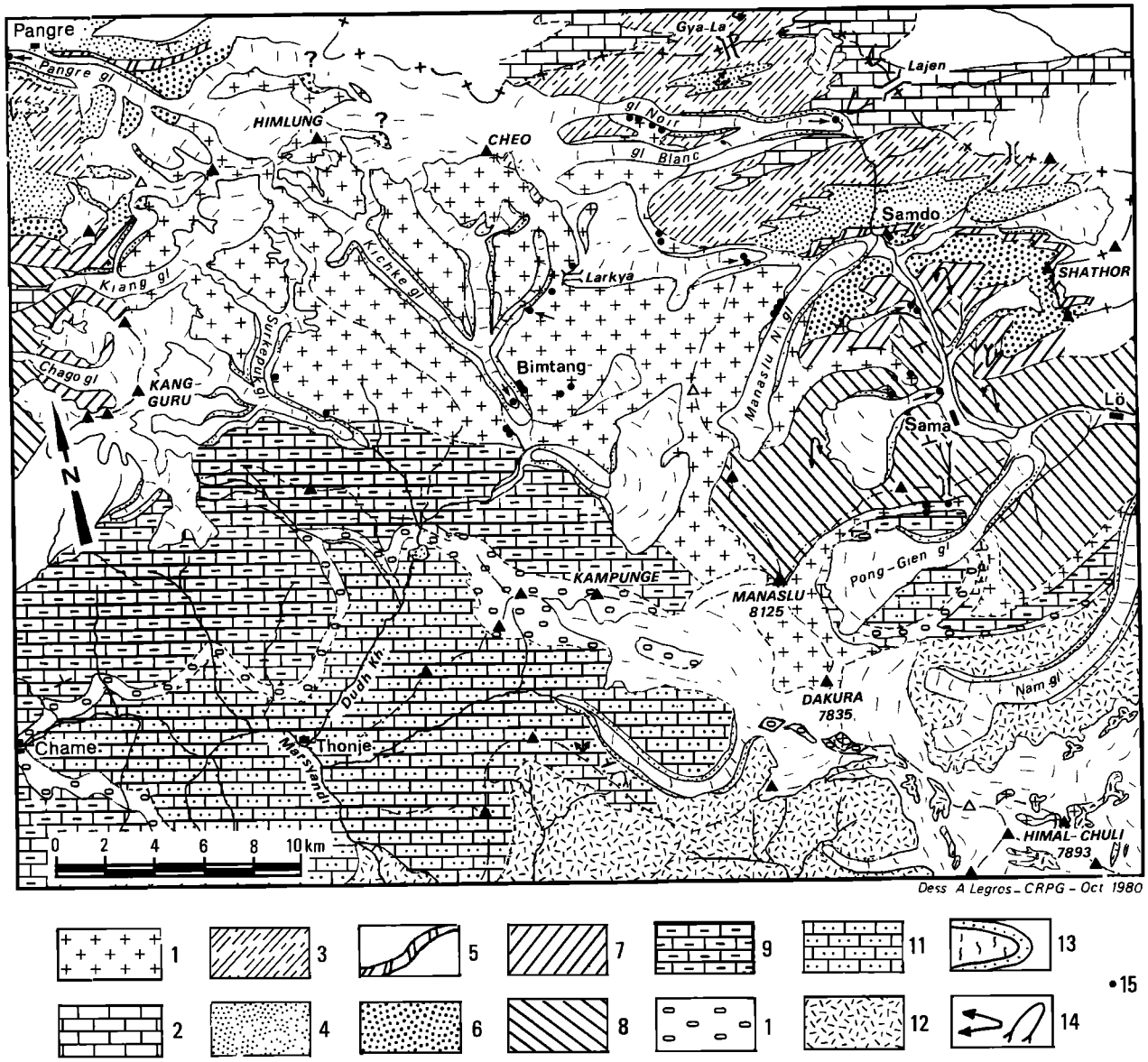

Fig. 3. Simplified geological map of the main body of the Manaslu granite [after Colchen, Le Fort and Pêcher, 1980]. 1, Manaslu granite; 2, Jurassic series; 3, Triassic series; 4, Permian white quartzites and black shales; 5, Carboniferous limestones and shales; 6, Devonian series; 7, Silurian shales; 8, Ordovician limestones and quartzites; 9, Annapurna yellow formation (Cambro-Ordovician ?); 10, Formation III augen gneisses of the Tibetan Slab; 11, Formation II marbles and calc-silicate gneisses; 12, Formation I alternances of metasandstones and metapelites more or less migmatized; 13, glaciers and moraines; 14, anticlinal and synclinal folds; 15, location of the geochemical samples of the Manaslu granite.

especially at the contact with the Upper Paleozoic and Mesozoic series (Figures 5b and 5c).

The pluton clearly cuts some of the major folds of the Tibetan sedimentaries (Figures 1 and 6, section CC'), but it has been observed at several places that the main cleavage of the surrounding rocks (S_2 of Le Fort [1975a] and Pêcher [1978]) may enter the granite and pass into its foliation. Also, some of the minerals from the contact aureole in the sedimentary series- in particular, staurolite -show typical synkinematic internal structures. Misch [1949] arrived at the same conclusion in the Nanga Parbat region. The granite is synkinematic to latekinematic.

The granite

In the Manaslu pluton, one may distinguish the main part of the granite (the core) from its rim or border facies and from the western network of dikes. The granite core forms most of the main body and the arm of Chhokang. It has a very constant mineralogical and chemical composition (Table 1). It is a leucocratic rock devoid of inclusions. The grain size is generally medium (0.5 to 1 mm). The micas and, in particular, the muscovite have a planar disposition defining the foliation. It is made up of quartz (32%), of subhedral, weakly zoned (An_{16} to An_6) plagioclase

(37%), of perthitic potassium feldspar which is a mixture of predominating orthoclase and intermediate triclinic microcline (21%), of largely euhedral muscovite (7%) and associated orange-brown, more-or-less altered biotite (3%). Sillimanite may fringe or underline flexures in muscovite crystals. Accessory minerals (apatite, zircon, opaques) are sparse. These minerals have constant characteristics and compositions throughout the massif [see Colchen et al., 1980]. Alteration is very limited.

Tourmaline (black schörl) is not actually part of the mineral assemblage of the granite itself. It is found in the innumerable dikes, veinlets, patches, and nodules of aplites and pegmatites that pervade the granite.

The border facies are developed mainly at the base of the pluton for a distance of a few hundred meters. They are made up of a dense and intricate network of dikes of granite, aplite, and pegmatite with numerous xenoliths of the surrounding metamorphic formations. Foliation is almost absent. Tourmaline is abundant and garnet is frequent. The rest of the mineral assemblage is very similar to that of the granite itself; however, the minerals show small differences such as a more Ab-rich plagioclase. The chemical composition of the border facies is very little affected by the nature of the rocks it intrudes (mica-schist, quartzite, marble).

Chemical analyses of the granite itself corroborate the very constant composition of the Manaslu granite (Table 1 and Figure 7). Extremely leucocratic, the granite is also aluminum- and alkali-rich (sodium-rich, in general). The main variations occur in the relative proportions of sodium and potassium, which give a negative correlation such that $K_2O + Na_2O \sim 8.5$ wt % (Figure 8). Compared to the average of 1148 analyses of uranium-bearing French two-mica granites and leucogranites (the Granites Uranifères Français (GUF) file of the Centre de Recherches Pétrographiques et Géochimiques (CRPG) in Nancy), the Manaslu granite is typically more sodic and less ferruginous (Table 1). The weight loss on ignition, which is also much smaller, is a measure of the good state of preservation and the weak alteration of the granite. To find similar compositions elsewhere, one has to look for peculiar and rather evolved types or portions of granite bodies. Four from Western Europe Hercynian plutons are listed in Table 1. These are generally given a crustal anatectic origin; in particular, the Mont-Pilat pluton is considered by Ravier and Chenevoy [1966] to result in part from the in situ melting of rhyolitic letynites. These peculiar plutons, except for the Mont-Pilat, are in general, associated with tin and/or uranium mineralizations. Tin mineralizations are, in fact, preferentially linked with the sodic character [La Roche et al., 1980].

Occurrences of base metals and pegmatites bearing other mineralizations (Cu, Zn, Pb, Bi, Mo,...) have been observed in the Manaslu pluton. But no tin has been found so far, and it is only due to a confusion with the Lesser Himalayan granites that Mitchell [1978] attributes tin to Manaslu-type granite.

The Himalayan leucogranites crosscut the Cretaceous of the Tibetan series but are included as boulders in Pliocene sediments. Their age lies between the Eocene (youngest sediments of the Tibetan series [Bassoullet et al., 1977]) and the Pliocene. Paleogeographic considerations would favor a Miocene age. K/Ar measurements on biotites [Krummenacher et al., 1978], on biotites and muscovites [Wager, 1965] of the Everest-Makalu granite, and on muscovites of the Mustang granite [Krummenacher, 1971] give, respectively, 19 ± 1, 14.1 to 16.6, and 15 to 24 m.y. A recent Rb/Sr whole rock isochron has been proposed for the tourmaline-muscovite granite of Cabug (?) at 42.95 ± 2.6 m.y. with a high Sr initial ratio of 0.748 [Wang et al., 1980]. But whole rock Rb/Sr isotopic analyses of the Manaslu granite have not given an isochron (from Vidal [1978] and Figure 9). Three whole rock plus muscovite ages of 16 to 20.5 m.y. have been found and further considerations could bracket the age between 26 and 20 m.y. (Ph. Vidal et al., manuscript in preparation, 1981).

The Roots of the Granite: The Tibetan Slab Migmatites

It has already been suggested [Le Fort, 1973a, b, 1975b,d] that the Higher Himalaya leucogranites have an anatectic origin and that they are rooted in the migmatitic zone of the Formation I of the Tibetan Slab.

Geological evidence. Below the Manaslu pluton, to the SSW of it, Formation I of the Tibetan Slab shows widespread anatexis (Figures 6 and 2). This anatexis begins in the kyanite zone but develops mainly in the sillimanite zone (Figure 4). Field and petrological descriptions of the anatectic zone have been given for this region by Le Fort [1975c] and Pêcher [1978].

Owing to the very special feature of the Himalayan inverted metamorphism [Le Fort, 1975a, 1976; Pêcher, 1978], these migmatites are the only ones to appear in the 20 to 25 km thick section of the crust visible below the pluton (Figure 6).

Laterally, Formation I presents large variations of thickness: from 1,400 m in the Kali Gandaki section [Le Fort, 1971] to some 10,000 m south of the Manaslu [see also Le Fort, 1975c]. Where Formation I is at its thinnest, sillimanite grade is hardly reached [Le Fort, 1971], anatexis is poorly developed, and no granite appears higher up (Figures 1, 2, and 6, AA'). As the thickness increases anatexis develops and the network of dikes becomes progressively developed (Figures 2 and 6, BB'). Finally, granite appears with increasing amount of migmatite (Figures 2 and 6, CC'). The Burhi Gandaki section (Figures 2 and 6, DD') is a peculiar case: although Formation I lies almost entirely in the sillimanite grade, the first half is mainly quartzitic and unfit for anatexis. There is, of course, no strict proportionality between the thickness of Formation I and of the granite sheet.

Below the Main Central Thrust (MCT), the Midland formations present an inverted metamorphic pattern [Le Fort, 1975a; Pêcher, 1978] (Figure 11), but the highest grade reached by these formations seems to be a function of the thickness of the overlying Tibetan Slab as well as of the more or less downdip position. This maximum varies between biotite-garnet and kyanite grades.

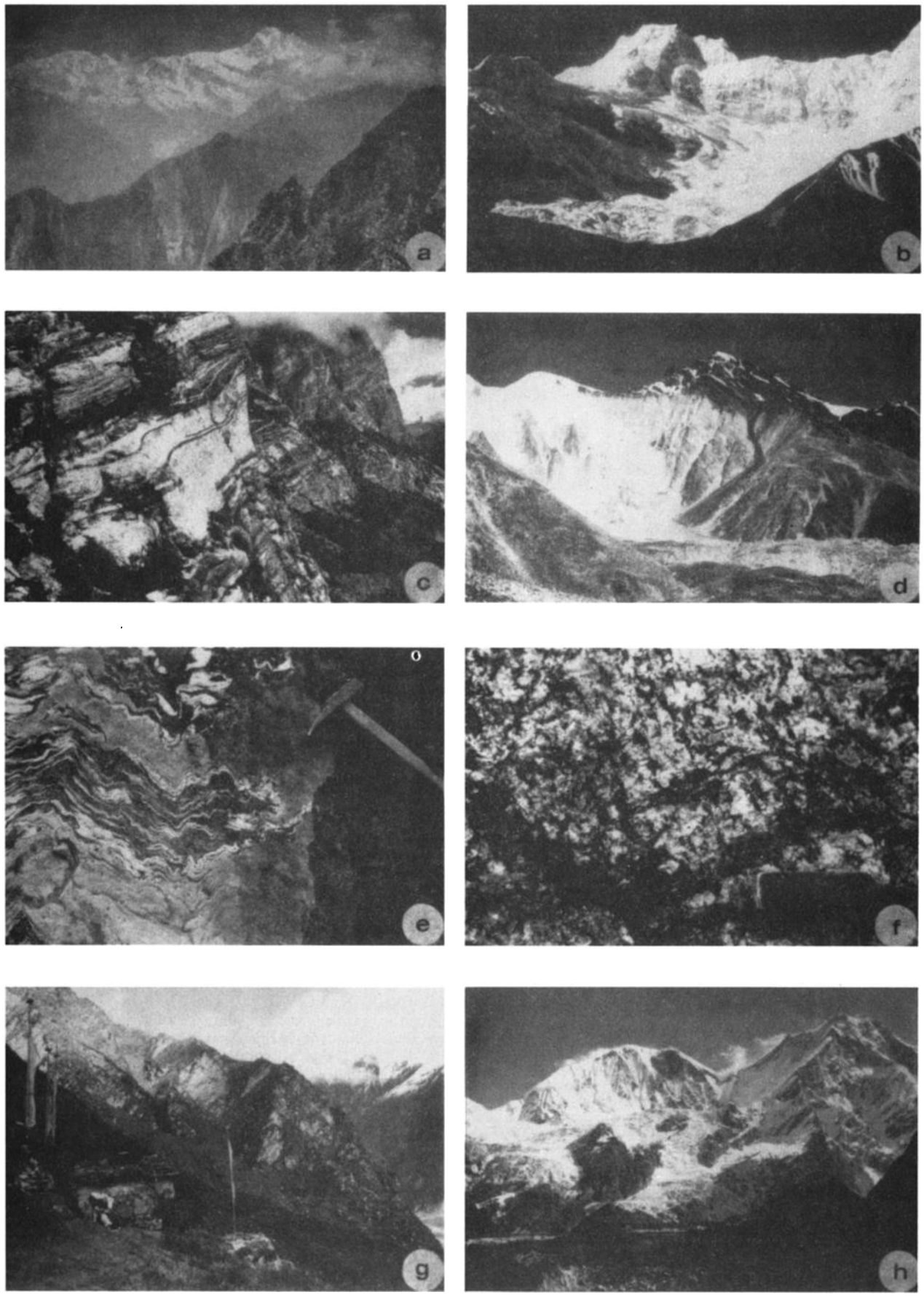
a
b
c
d
e
f
g
h

This and the fact that the maximum of the P T conditions lie within the Tibetan Slab indicate that the observed metamorphic pattern depends mainly upon conductive redistribution of heat from the hot upper slab, even if shear heating may have generate a nonnegligible amount of heat [Graham and England, 1976]. In other words, the metamorphism of the Midland formations is a sort of dynamic contact aureole of the Tibetan Slab.

In the migmatitic zones of Formation I, the mobilization takes place in an irregular way [see Le Fort, 1975c]. When reaching the nebulitic zones, leucosome dominates over melanosome. Analysis of similar migmatization in the equivalent Darjeeling gneisses has been given by Ghose and Singh [1977]. In addition to the biotite-garnet-rich melanosome which they describe, we have found abundant quartz-fibrolite associations that probably represent a peculiar type of restite left by the departure of granitic melts. On the contrary, the lenticular inclusions of clinopyroxene and hornblende bearing rocks are not restites, as suggested by Ghose and Singh [1977] but, according to our observation, belong to levels of metamorphosed limestones interbedded in the Formation I and affected by boudinage during deformation.

It is to be noticed that according to the available information, all the other Higher Himalaya leucogranites occur in the same position, above a thick zone of migmatitic gneisses: the Vaikrita gneisses of Kumaon [Valdiya, 1973], the Barun gneisses and migmatites of Eastern Nepal [Bordet, 1961], the Darjeeling gneisses of Sikkim, and the Takhtsang gneisses of Bhutan [Gansser, 1964].

The age of the anatexis is 'alpine' (Himalayan) and not Paleozoic or Precambrian, as some authors propose. In fact, the Tibetan Slab is part of the MCT zone [Pêcher, 1978; Brunel et al., 1979] and is thoroughly deformed by the P_2 phase. Further, K/Ar ages on minerals of the Tibetan Slab have given a young Cenozoic age: 15.5 m.y. for biotite and muscovite of a finely banded gneiss of the Kali Gandaki valley [Krummenacher, 1971, sample KA 108] and from 18 to 9 m.y. and even younger on biotites of 10 different gneisses above the main central thrust in eastern Nepal [Krummenacher et al. 1978], but this is already part of the geochemical evidence.

Geochemical evidence. Some 67 samples from Formation I of the Tibetan Slab have been analyzed for major and some trace elements. As stated by Pêcher [1978, p. 51, and Figures 19 and 20], the nonmigmatized samples of Formation I consist of a variable mixture of rather immature and poorly sorted sediments. It is dominated by a detrital contribution of greywackes and sandstones with subordinate amounts of shales (Figure 7). Very few carbonate horizons are intercalated, and they have not been taken into account.

Figure 7 illustrates how starting from this sedimentary 'crescent', lines of anatexis converge toward the granite area, leaving behind rocks enriched in ferromagnesian and aluminous minerals. The degree of anatexis is progressive because intermediate compositions exist along the lines.

According to the experiments quoted by Winkler [1979], melting of greywackes produces melts of high Na/K ratio, whereas the melting of shales produces melts of lower Na/K ratio. Thus the predominance of greywackes over shales could explain the sodic- but not the aluminous -character of the granite.

Rb/Sr isotopes have been analyzed in 11 samples from Formation I that show a small degree of anatexis (Ph. Vidal et al., manuscript in preparation, 1981). The extremely scattered results reflect the sedimentary mixture of greywackes and pelites that has not been homogeneized by metamorphism. If one compares the isotopic evolution lines as a function of time with the possible initial isotopic ratios of the Manaslu granite and if the granitic melts have the same isotopic ratios as the source material, one finds that they correspond rather well (Figure 10).

Vidal has also measured the isotopic composition of lead in three samples of the Manaslu granite, in two samples of micaschists, and in two

Fig. 4. (Opposite) (a) Himal-Chuli (7893 m) seen from the east (Shyar valley). The crest in the foreground, right bank of the Burhi Gandaki, is mainly made of Formation I gneisses. The glaciated crest at the rear shows the gentle north dip of the Tibetan Slab and the compact mass of the Manaslu granite. The black cliffs in the center correspond to the well-bedded marbles of Formation II and augen gneisses of Formation III. (b) The Dakura (7835 m) and Dakura to Manaslu granitic crest seen from the Pong-Gien valley. Formation III augen gneisses crop out from the glacier. The regular north dip of the Tibetan Slab is still visible in the granite. This scene lies north of Figure 4a. (c) The cliffs right bank of the Nar valley. Aplo-pegmatitic dykes in white thoroughly intrude marbles of the Annapurna formation in grey. The total height approximates a thousand meters. The dikes are dominantly interbedded, although they crosscut the marbles at every scale. (d) The upper contact of the Manaslu granite, north-east of the Larkya pass, sharp against the dark upper Triassic sedimentaries. Contact metamorphism is 30 to 50 m thick (pyroxene marbles, garnet-muscovite quartzites, staurolite, garnet micaschists). (e) Formation I migmatitic gneisses in the Shyar valley (Tsum). The granitic portion is white: the darker micaceous portion is isoclinally folded, refolded, and loaded with quartz-feldspar pegmatitic lenses. Sillimanite is present. (f) Coarse grain Manaslu granite (northern Manaslu glacier). The strong foliation is given by the muscovite (in grey). (g) Upper contact of the Manaslu arm just above Chhokang. The contact more or less follows the grass band in the middle of the picture. The limestones on top are metamorphosed into pyroxene marbles with aplite and pegmatites leucogranitic dikes. Nests of wollastonite occur for the first 50 cm (cf. Figure 3). The Tibetan border lies along the crest in the background. Prayer flags float in the foreground. View is NNE. (h) Manaslu seen from the north-west. The summit (8125 m) is on the extreme right, and the upper contact of the granite outcrops a few meters below. The rounded summit in the center of the picture is entirely made of metasedimentaries, and the contact lies in the glaciers zone. Note the strong foliation visible in the NW pillar of the Manaslu.

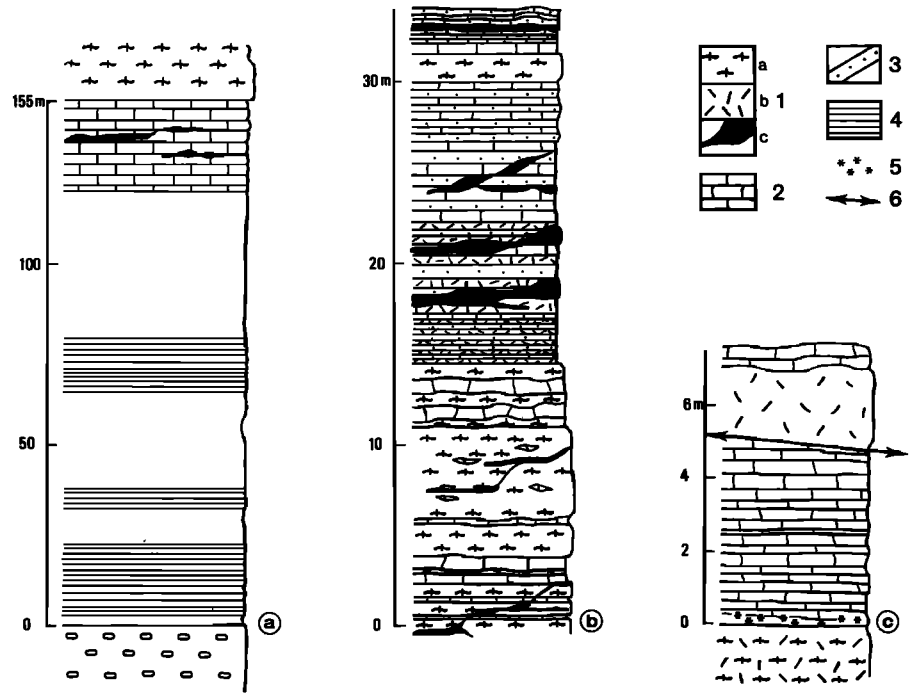

Fig. 5. Contacts of the Manaslu granite with the surrounding rocks. Three schematic lithologic columns measured in the field. (a) The banded gneisses ('gneiss en plaquettes') separating the Formation III augen gneisses of the Tibetan Slab from the granite sheet of Chhokang (left bank of the Pong-Gien glacier around Pong-Gien Gompa, about 4000 m). They occur with the same lithologic and petrologic characteristics all along the Chhokang sheet. (b) Detail of the upper contact of the Manaslu main body with the Upper Triassic series on the left bank of the glacier Blanc around 4900 m of elevation. The section begins with the first level of marble and gives a section of the 35 m thick metamorphic aureole in the Upper Triassic limestones and sandstones transformed into pyroxene marbles and muscovite garnet quartzites. The abundance of granitic and pegmatitic dikes diminishes away from the granite. (c) Detail of the upper contact of the Chhokang sheet on the slope north-east of the village (left bank of the Shyar river) about 3300 m. The granite contact is sharp and slightly discordant to the overlying pyroxene marbles. Nests of wollastonite appear in the first 50 cm from the contact. 1, granite and granitic dike (Figure 5a), aplitic dikes (Figure 5b) and pegmatitic dikes (Figure 5c); 2, pyroxene marble; 3, quartzites; 4, banded gneisses ('gneiss en plaquettes'); 5, wollastonite; 6, fault.

granitic samples from the Formation I (Ph. Vidal et al., manuscript in preparation, 1981). The $^{207}Pb/^{204}Pb$ ratios of these seven samples are identical. However, the $^{208}Pb/^{204}Pb$ and $^{206}Pb/^{204}Pb$ ratios of one of the micaschists are not compatible with a direct involvement in the genesis of the Manaslu granite unless the different batches of melt from the Tibetan Slab have been mixed and homogeneized.

In a preliminary study of the oxygen and hydrogen isotopes of the granite (S.M.F. Sheppard, unpublished data, 1980) the whole rock $\delta^{18}O$ and δ D ratios were found to be, respectively, within the range 11 to 12.5‰ and -75 to -90‰ SMOW. The high $\delta^{18}O$ values are similar to those obtained on Hercynian two-mica granites from the Cornubian batholith [Sheppard, 1977] and the Pyrénées [Michard-Vitrac et al., 1980]. Compared with many other fresh granites, the whole rock δ D values are low, reflecting the deuterium depletion of both the muscovites (range -72 to -82) and the biotites (-97 to -106). The high ^{18}O values, which are comparable to the rhyolitic volcanic ^{18}O-rich magmas of Tuscany, Italy [Taylor and Turi, 1976], clearly point to the 'melting, assimilation and/or exchange with argillaceous rich metasediments at depth' [Sheppard, 1977]. Altogether, the joint use of major elements as well as Sr, Pb, O, and H isotopes corroborates the idea that the Manaslu granite may well be the melting product of gneisses of Formation I of the Tibetan Slab.

Conditions of Formation of the Magma

Two quite independent though indirect ways may be followed to evaluate the pressure-temperature-fluid composition conditions of the formation of the magma. The first way is to follow the field evidence of the migmatitic zone of the Tibetan Slab; the second is to use the available experimental data on the granite system.

P T Conditions of the Migmatitic Zone of the Tibetan Slab

After Le Fort [1975a], these conditions were discussed and evaluated by Pêcher [1978]. The in-

fluence of the presence of CO_2 in the fluid phase as reported from the fluid inclusions [Leroy and al., 1975; Pêcher, 1978, 1979] has also been taken into account.

The results are shown in Figure 11. Starting from the Lesser Himalaya formations, the metamorphic evolution curve brings us to the staurolite-kyanite grade close to the MCT, the minimum pressure being indicated by the stability of zoisite in the presence of plagioclase, quartz ± kyanite (equilibrium Zo + Ky + Q = An + V [Boettcher, 1970] and Zo + Q = An + Gr + Mag + V [Liou, 1973]). Anatexis starts above the MCT in rocks of kyanite grade. Higher up in the Formation I, in the sillimanite grade zone, anatexis spreads progressively. The maximum temperature is probably reached within the Tibetan Slab when muscovite starts to react with plagioclase [Pêcher, 1978, Figure 17] according to the equilibrium: Mu + Pl = Fk + Sil + L [Thompson and Algor, 1977]. This reaction apparently does not go to completion, and the higher temperature reaction of disappearance of the muscovite, Mu + Q = Fk + Sil + L, is not reached. When anatexis stops, sillimanite is still present, and kyanite and staurolite only appear higher up in the beginning of the Tibetan sedimentary series.

Most of the equilibrium curves are displaced or modified by the addition of CO_2 to the fluid phase (Figure 11). However, the change in P T conditions for the anatexis would not be very large [Kerrick, 1972; Thompson and Algor, 1977].

Thus the temperature of the migmatitic zone can be estimated to have been between 660° and 710°C, and the pressure between 6 and 8.5 kbar. The actual anatectic roots of the visible part of the pluton probably lie farther to the north, directly under the pluton, and, according to the P T model proposed by Le Fort [1975a], would have reached higher temperature and pressure. However, the gentle dip of the MCT and the spacing of the temperature isograds occasion a limited increase of the P T maximum attained.

Experimental Results on Granites and Granitic Systems

As stated by Steiner et al. [1975], the bulk composition of a granite is not enough to define its origin and history and to estimate the pressure, temperature, and fluid conditions under which the rock was formed. However, if we take into account what we know of the occurrence of the Manaslu granite, the experimental results on both natural and synthetic rocks can be indicative of what probably occurred in nature.

Huang and Wyllie [1973] have experimented with the melting relations of a natural muscovite granite whose chemical composition is very close to that of the Manaslu granite (Table 1), though small differences exist for potassium and perhaps also for aluminium and magnesium. With excess water, the solidus of this granite is, within the limits of experimental error, identical to that for the biotite granites studied by Boettcher and Wyllie [1968], Piwinskii [1968], and Stern and Wyllie [1973] as well as the melting curve for the eutectic and liquidus minimum in the Ab-Or-Q-H_2O system [Merrill et al., 1970]. Figure 12 gives some of the main solidus and liquidus curves for these systems.

Owing to the slope inversion of the wet liquidus curve, geologically reasonable melting conditions of a granite such as the Manaslu granite lie somewhere between 5 and 8 kbar at 700° to 730°C in the presence of excess water.

Provided the granite has the same composition as the entirely liquid magma (except for volatile components), the wet liquidus corresponds to minimum conditions of entire melting of the granite. Addition of halogens and/or boron, etc., of course, may shift these curves to lower temperatures. This is particularly true for boron: adding 2, 5, or 13% B_2O_3 (weight percent to solution) lowers the solidus temperature respectively by 35°, 70°, or 115° ± 5°C at 1 kbar [Pichavant, 1979, 1981b] (Figure 12). On the contrary, addition of carbon dioxide noticeably increases the melting temperatures of granite (see Novgorodov and Shkodzinskiy [1974], and Eggler and Kadik [1979], for results for albite).

Comparison of the Manaslu norm with that of the minimum melts and eutectics (Figure 13) shows that the Manaslu composition is close to that of minimum melts of the haplogranitic system at about 2 kbar of fluid pressure. It also lies on the HCl rather than on the CO_2 side of the minimum curve. In the Q-Or-Ab-An-H_2O system, it lies close to the projection of the melt compositions on the Q-Ab-Or triangle for 5 kbar with Ab/An = 7.2, equivalent to an anorthite content of approximately 12% [Winkler et al., 1975], although the Manaslu normative compositions hardly exceed 4% An (Table 1). Because our field observations show that the sedimentary cover of the Manaslu pluton reached some 6 km, 2 kbar is about the minimum emplacement pressure of this body. Thus obtaining such compositions for the entire pluton probably necessitates higher pressures, a few An percent normative and small percentages of HCl in the granite.

The Fluid Content of the Magma

Fluids in general and water in particular are often considered to be rather abundant constituents of leucogranitic magmas [Lameyre, 1973]. This component, long removed from the system, is generally considered to have left a strong imprint on the granites and on the surrounding rocks, such as large pegmatitic networks, hydrothermal muscovitization, greisenization, and kaolinization.

In fact, a pegmatitic network is very well developed in the vicinity of the Manaslu granite, but hydrothermal alteration seems to be rather limited. Other arguments, however, point to a relatively abundant and complex fluid phase.

Muscovite. It is difficult to prove that muscovite belongs to the primary magmatic paragenesis and is not of secondary origin. If such primary muscovite exists, at least some from the Manaslu granite is a good candidate, in particular when it exhibits perfect hexagonal shapes up to 2 cm in diameter (Figure 4). In fact, muscovitization of the feldspars is very limited, and the muscovites of the Manaslu do not seem to grow at the expense of other minerals. They show occasional syneusis textures with quartz.

If muscovite did crystallize as a primary phase in addition to alkali feldspar or quartz, the

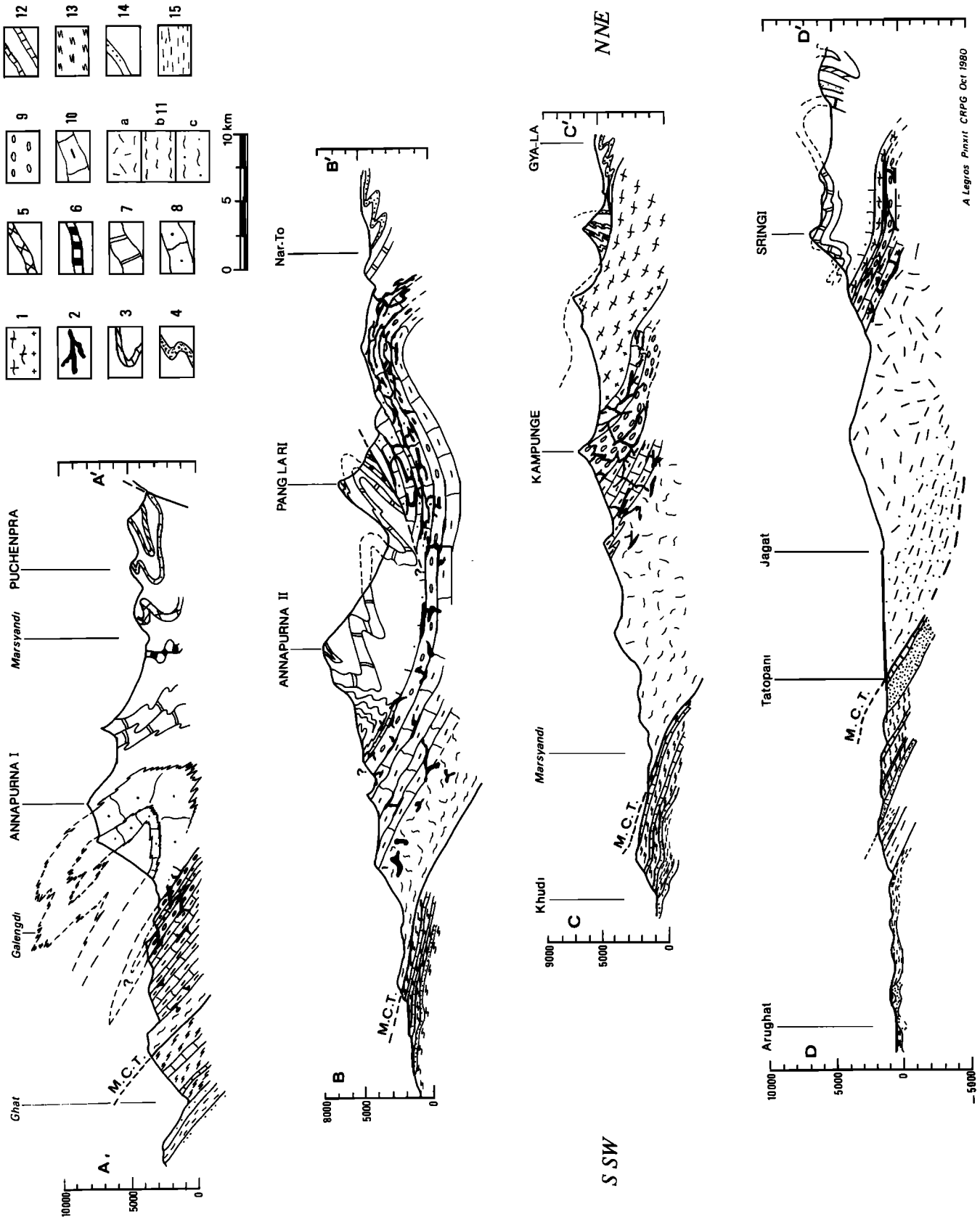
1
2
3
4
5
6
7
8
9
10
a
b 11
c
12
13
14
15
0
5
10 km
A
A'
Ghat
Galengdi
Marsyandi
ANNAPURNA I
PUCHENPRA
M.C.T.
10000
5000
0
B
B'
Nar.To
PANG LA RI
ANNAPURNA II
M.C.T.
8000
5000
0
SSW
NNE
C
C'
Khudi
Marsyandi
KAMPUNGE
GYA-LA
M.C.T.
9000
5000
0
D
D'
Arughat
Tatopani
Jagat
SRINGI
M.C.T.
10000
5000
0
-5000
A Legros Pinxit CRPG Oct 1980

Fig. 6. Four sections through the Himalaya of central Nepal (see Figure 2 for their location). These sections clearly illustrate the link between the thickness of Formation I and the production of granite as well as the disharmony that is very favourable for the emplacement of the granitic magma produced. AA' is a section 40 km west of the Manaslu granite. The thickness of the Formation I of the Tibetan Slab is very reduced, and sillimanite grade is hardly reached. Only a few granitic dikes appear at the top of the Tibetan Slab. The disharmony between the infrastructure of the Tibetan Slab and the suprastructure of the Tibetan sedimentary series is particularly conspicuous in this section, where the huge Annapurna recumbent, refolded fold developed mainly in the Lower Palaeozoic Annapurna yellow limestones formation. BB' lies just west of the Manaslu granite. Formation I is already thicker; the upper part is in the sillimanite grade, and anatexis is well-developed. Farther to the north, the augen gneisses of Formation III reappear at the top of the Chago dome with a pervasive network of granitic and aplopegmatitic dikes that invade the overlying marbles. CC' section shows the Tibetan Slab at about its maximum thickness. The granite lies conformably on it and at the top cuts the vertical Upper Triassic beds part of the eastward prolongation of the north vergent Annapurna fold. However, in the region of Gya La, the south vergent folds have the same axial plane cleavage as the foliation of the granite. The slab of granite has been folded in a broad movement together with the surrounding rocks. DD' is a section more than 70 km long from the middle of the Lesser Himalaya (in the Lower Kunchha formation) up to the Tibetan Jurassic series at the border. The Tibetan Slab shows a particularly thick Formation I; however, the first half of it is essentially made of quartzites (dotted) that show very little anatexis. It is the region in which the arm of the Manaslu granite is always located at the boundary between infrastructure and suprastructure. The huge fold of the Sringi corresponds to that of the Annapurna in section AA'. Parts of the sections in the Lesser Himalaya are from Pêcher [1978]. 1, Manaslu granite with border facies at the base; 2, aplite and pegmatite dikes; 3, a Rhetian horizon; 4, a Permian quartzite; 5, a Carboniferous limestone; 6, a Devonian horizon; 7, an Ordovician limestone; 8, Annapurna yellow formation; 9 to 11, Tibetan Slab; 9, Formation III augen gneisses; 10, Formation II marbles and calc-silicate gneisses; 11, Formation I alternating metasandstones and metapelites (Figure 6b), more or less migmatized (Figure 6a), mainly quartzitic (Figure 6c); 12 to 15, Midland formation; 12, dolomitic limestones; 13, carbonaceous shales and schists; 14, quartzites; 15, shales.

P_{H_2O} of the water-saturated melt was more or less above 4 kbar [Chatterjee and Johannes, 1974], which would imply some 10% (weight percent) [Burnham, 1967] of dissolved water.

Carbon dioxide. A search for CO_2 retained in the fluid inclusions of the Manaslu samples has been negative, but one knows how difficult it is to observe primary inclusions in igneous rocks. CO_2-rich inclusions have only been found in late mineralized pegmatites at the top of the pluton.

Although CO_2 has not been observed in the fluid inclusions of the granite itself, the fluid inclusions of the Formation I of the Tibetan Slab have a high CO_2 content [Leroy et al., 1975; Pêcher, 1978, 1979; M. Cuney and P. Le Fort, unpublished data, 1978]. This suggests that CO_2 was present in appreciable quantities during anatexis. Again, above the Formation I, the pyroxene-scapolite marbles of Formation II must have liberated very large amounts of CO_2 during their metamorphism. The same observation is also valid for the pyroxene marbles at the base of the Tibetan sedimentaries.

However, study of the fluid inclusions shows that if the content of CO_2 in the fluid phase increases with grade, the very high CO_2 contents of as much as 70% and even 95% weight percent of fluid inclusions close to the MCT [Leroy et al., 1975; Pêcher, 1978, 1979] represents the maximum composition of the fluid at the peak of the metamorphism. The mobility of CO_2 is less than that of H_2O and Pêcher [1979] suggests among other hypotheses that CO_2 is left as a sort of 'fluid restite,' accumulated in the mesozonal rocks metamorphosed under the MCT. Furthermore, in the most migmatized part of the Tibetan Slab, pegmatitic lenses have a smaller CO_2 content than those in nonmigmatized rocks [Pêcher, 1979].

The solubility of CO_2 in granitic magma is relatively small, even at elevated pressure; the amount of CO_2 available in the anatectic source region was therefore probably sufficient to saturate the magma, and a fluid phase consisting of H_2O and CO_2 probably coexisted with the magma [Holloway, 1976]. At decreasing pressure, the CO_2 solubility in the magma also decreases and the partitioning of H_2O between the magma and fluid will increase in favor of the latter. It is possible, however, that the CO_2 fluid will be preferentially retained because of limited mobility in the upward ascent of the magma [see Touret, 1980]. Results on calcite stability in the Q-Ab-Or-An-H_2O-CO_2 system also suggest that if a CO_2-rich fluid is present in the magmatic source region, it is left (or escapes) before the magma is emplaced [Swanson, 1979].

Boron. Tourmaline is very abundant in the late crystallization stages of the granite, and boron must have been a fairly abundant minor component of the magma. I suspect that boron was part of the initial fluid that provoked the anatexis. Actually, tourmaline is a common accessory mineral of the Lower Midland formation.

We do not know yet the influence of boron on the composition of the minimum melts (M. Pichavant, personal communication, 1980). We know that it will lower the solidus [Pichavant, 1979, 1981a], increase the amount of melt above solidus, and probably make the magma less viscous [Bruckner and Navarro, 1966]. If a fluid phase

TABLE 1. Chemical Composition of the Manaslu Granite (Core: Average of 36 Analysis; Arm: Average of 23 Analysis) and Comparison With Seven Similar Granites

	Manaslu Granite		GUF Two-Mica Granites	Mont de Blond Leucogranite	Mont Pilat Leucogranite	Guérande Sodic Leucogranite	Hingston Down Leucogranite	La Bérarde Leucogranite	Muscovite Granite	CIPW-Lacroix	Manaslu	
	Core	Arm									Core	Arm
SiO_2	74.04	73.94	72.53	73.85	73.06	72.43	73.22	75.24	74.66	Q	31.48	31.19
	0.59	*0.92*	*1.80*								*0.97*	*2.03*
Al_2O_3	14.67	14.76	14.77	14.56	15.23	14.90	14.67	12.69	15.55	Or	26.59	26.52
	0.34	*0.40*	*0.72*								*1.53*	*2.40*
Fe_2O_{3T}	0.84	0.81	1.41	1.63	1.17	0.90	0.82	1.14	0.64	Ab	34.35	34.96
	0.14	*0.17*	*0.65*								*2.29*	*2.77*
MnO	0.02	0.02	0.03	0.00	0.06	0.01	0.01	0.05	0.07	An	2.50	2.30
	0.01	*0.01*	*0.02*								*0.79*	*0.82*
MgO	0.18	0.13	0.34	0.15	0.34	0.21	0.23	0.22	0.02	Mag	0.20	0.19
	0.11	*0.10*	*0.31*								*0.03*	*0.06*
CaO	0.50	0.46	0.69	0.27	0.46	0.57	0.45	0.53	0.42	Ilm	0.14	0.13
	0.16	*0.16*	*0.38*								*0.13*	*0.12*
Na_2O	4.06	4.14	3.27	4.07	4.16	3.89	3.85	3.86	4.29	Hyp	1.41	1.21
	0.27	*0.33*	*0.50*								*0.33*	*0.46*
K_2O	4.50	4.48	4.89	4.52	4.52	4.43	4.75	4.54	3.08	Cor	2.19	2.25
	0.26	*0.41*	*0.58*								*0.28*	*0.48*
TiO_2	0.07	0.07	0.20	0.11	0.09	0.12	0.06	0.10	0.03			
	0.07	*0.06*	*0.12*									
P_2O_5	0.14	0.13	n.d.	n.d.	0.41		0.18	n.d.	0.15	Q'	34.06	33.66
											0.97	*2.17*
i.L.	0.79	0.72	1.47	(1.37)	0.95	1.49	1.19	0.65	(0.76)	Or'	28.78	28.62
	0.25	*0.12*	*0.44*								*1.84*	*2.60*
										Ab'	37.16	37.72
Total	99.81	99.66	99.60	100.53	100.45	98.95	99.43	99.02	99.65		*2.25*	*2.83*
F	1110	940					1300		400			
Cl	15	22										
B	from <50	to 820					410					
Ba	192	128		69								
Co	49	50										
Cr	<10	<10										
Cu	<10	<10		3								
Ni	<10	<10		3								
V	<10	<10										
U	10.8	7.1		7.5								
Sr	76	41		<31								
Rb	385	-										

GUF is an average of 1148 two-mica granites and leucogranites from the GUF file ('granites uranifères français') CRPG (Nancy) analysis and data bank. The Mont de Blond two-mica leucogranite [Barbier, 1967] has a tin-bearing annular structure made of three different leucogranite types; this composition is an average of six analysis from the coarse grain type. The Mont Pilat leucogranite [Ravier and Chenevoy, 1966] seems to be devoid of mineralization; it is made of segregations and lenses in leptynitic gneisses; this composition is an average of five analysis. The Guérande sodic leucogranite from South Brittany in France has shown tin mineralizations; this composition is an average of six unpublished CRPG analysis. The Hingston Down leucogranite is a small sodic occurrence of the Cornubian batholith [Hall, 1973]; this analysis corresponds to a fresh sample. The La Bérarde-Promontoire leucogranite from the Hercynian crystalline of the Alps [Le Fort, 1973b] is the central pluton of the Haut-Dauphiné associated with molybdenite and sometimes scheelite mineralization; this composition is an average of seven analysis. The muscovite granite is the one experimented on by Huang and Wyllie [1973]. The Manaslu samples have been analyzed by mass spectrometry (CRPG, Nancy, quantometric analysis by K. Govindaraju) with the exception of P_2O_5, F, Cl and B (wet chemistry by M. Vernet on ten samples of the core and two of the arm), U (wet chemistry by C. Kosztolanyi on seven samples of the core and two of the arm) and Rb (isotope-dilution analysis) on four samples by Vidal [1978]. Mean standard deviation is given below the major elements value of the Manaslu and GUF. I.L. stands for ignition loss, n.d. for not determined.

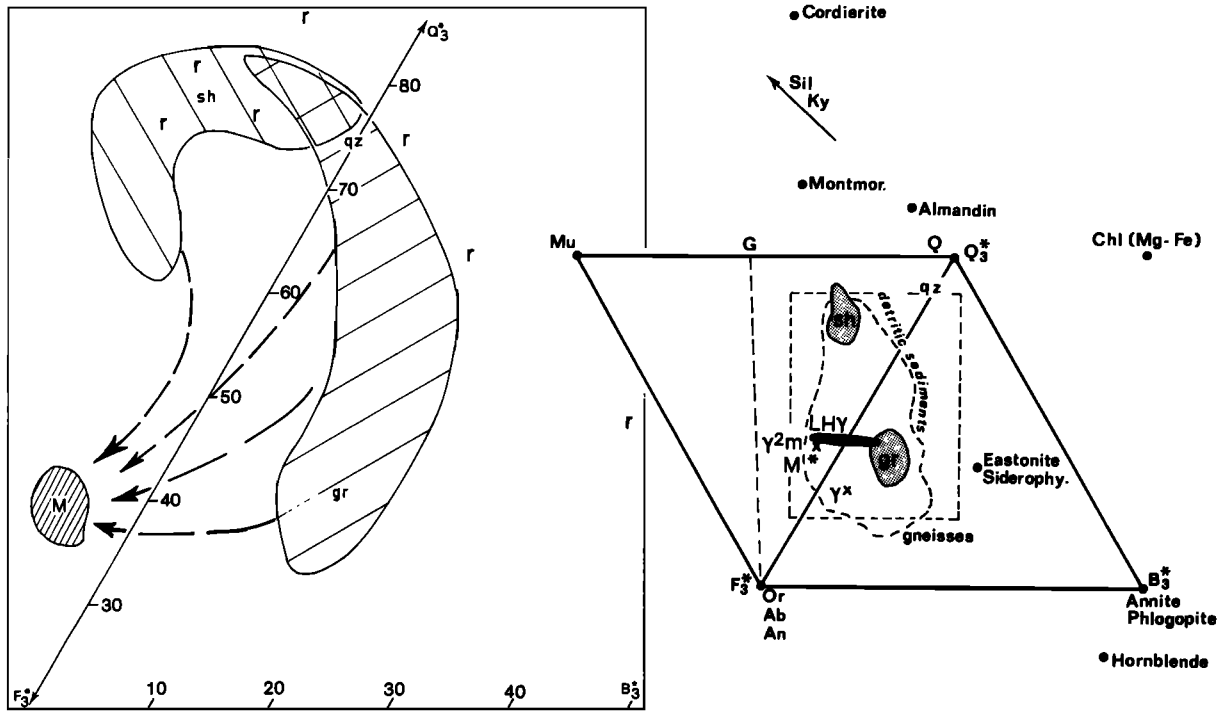

$$Q_3 = Si + 7\,Al/2 - 9\,Ca - 13\,(Na + K)/2 \quad ; \quad Q^*_3 = 100\,Q_3/\Sigma$$
$$B_3 = -7\,Al/2 + 7\,Ca + 7\,(Na + K)/2 + 8\,(Mg + Fe + Ti)/3 \quad ; \quad B^*_3 = 100\,B_3/\Sigma$$
$$F_3 = + Al + 3\,Ca + 4\,(Na + K) - 5\,(Mg + Fe + Ti)/3 \quad ; \quad F^*_3 = 100\,F_3/\Sigma$$
$$\Sigma = Si + Al + Ca + (Na + K) + (Mg + Fe + Ti) \qquad \Sigma^* = 100$$

Fig. 7. Analyzed samples from the Manaslu granite and from Formation I of the Tibetan Slab in the quartz-muscovite-feldspars-biotite rhombus of La Roche [1980]. This diagram [see also La Roche et al., 1980], which is useful for genetic typology, helps to correlate and identify the source materials. It associates the Q^*_3 B^*_3 F^*_3 coordinates ($Q^*_3 = Q_3/\Sigma$, etc.) obtained from the chemical analysis with the principal mineral paragenesis. The opposition of muscovite to biotites and of quartz to feldspars is very useful in examining continental crust rocks. Granites occupy a central area of this chemical representation. The Manaslu granite samples are remarkably clustered, the more so as there is no differential vector for Na and K. There is an abundance of muscovite (hence the aluminous character is shown by the location of the granite to the left of the Q^*_3 - F^*_3 line) in the muscovite field of the diagram. The area covered by the primary sediments of Formation I stretches all the way from the greywackes (gr) up to the quartzites fields (qz). There the shale field (sh) overlaps and extends to the left toward the clay minerals location. Anatexis of these sediments seems to produce mobilized rocks with a composition following the trends shown; (r) shows some restite compositions of highly mobilized rocks. Shales and greywackes fields from the flysch-molasse file, gneisses field from the gneiss-migmatite file (CRPG). Granite (γ) after the CLAIR file [Le Maître, 1976]. Two mica granite (γ2M) after the GUF file (CRPG). Lesser Himalayan cordierite granite trend (LHγ) after Le Fort et al. [1980].

exists, boron will concentrate in it and will help to dissolve Na preferentially in it. Finally, it may allow primary magmatic muscovite to crystallize directly from the melt at much lower pressures than in a pure H_2O system [Pichavant, 1981a,b].

Other volatiles. The fluid phase also must have contained phosphorus and fluorine, as shown by the chemical analysis (Table 1). The partitioning of chlorine being strongly in favour of the aqueous solution, the actual Cl content of the granite may be only a small fraction of that of the original magma [Burnham, 1967]. The presence of abundant scapolite in the calcsilicate gneisses and marbles of Formation II [Le Fort, 1975c] also suggests that chlorine and other volatiles were present in the fluids that equilibrated with the Tibetan Slab and partly joined the magma.

Manaslu granite homogeneity. The composition of major and most trace elements of the Manaslu granite as well as of its constituting minerals appear to be very constant. This sets a problem that I cannot satisfactorily solve; but I think that it implies that the original anatexis cannot have developed in rocks of highly variable composition; otherwise melting would have produced large heterogeneities. Thus saturation has proba-

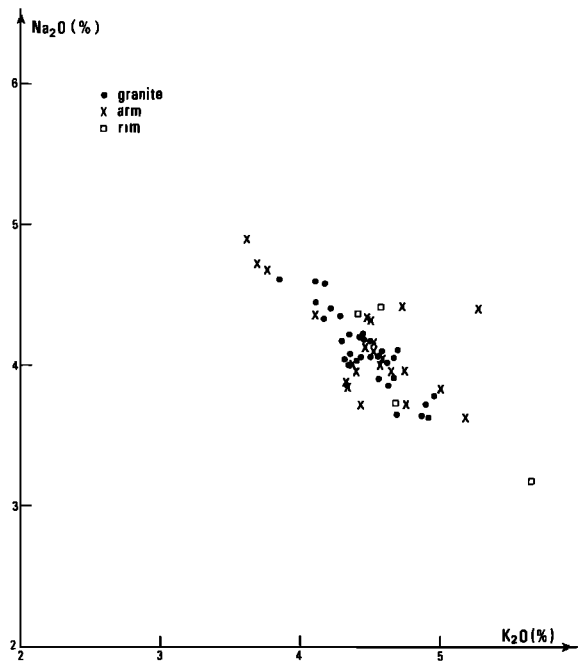

Fig. 8. Na_2O versus K_2O (weight percent) diagram for the Manaslu granite showing the negative correlation between the two oxides. The sum remains more or less constant. There appears no important difference between the granite itself, the Chhokang arm, or the rim facies.

bly not been attained at the anatexis level.

The only significant variations in the granite composition concern the K/Na ratio. In rocks of different An content, the 'minimum melt' compositions will considerably vary in Ab and Or content according to the Ab/An ratio [Winkler, 1979] (Figure 13). Thus, variable K/Na ratios in the granite may reflect nonhomogeneized 'minimum anatectic melt' compositions. This again would indicate a nonsaturated magma.

Potassium versus rubidium. Figure 14 demonstrates the absence of a correlation between the Rb and the K content of the Manaslu granite. This type of behaviour is called the 'pegmatitic-hydrothermal trend' by Shaw [1968] and emphasizes the part played by the fluid phase. It is very similar to the trend observed in the Hercynian leucogranites of the Marche orientale by Gauthier [1974], who claims little differentiation and much fluid circulation.

Rare-earth elements patterns. Seven samples from the Manaslu granite (four from the core, one from the arm, one from the rim, and one from an aplitic dike outside the granite) and four samples from the Formation I of the Tibetan Slab (two nonmigmatized and two orthogneisses) have been analyzed for rare-earth elements by Cocherie [1977, 1978]. Three of the granitic samples analyzed by Cocherie and five new samples (two from the core and three from dikes outside) have been reanalyzed [Fourcade et al., 1977]. The results from duplicate samples are in good agreement.

The rare-earth element contents are small for rocks of granitic composition (Figure 15). The nonmigmatized gneisses are richer (50×chondritic); the granite varies from 25×chondritic for a sample from the core to 8×chondritic for the samples of the rim and even 3×chondritic for one of the dikes. All the patterns show an enrichment in light REE compared to the heavy REE (La/Yb > 10, generally). A clear negative anomaly in Eu is shown by nearly all the samples (except for the orthogneisses, the rim, and one or two dikes). Similar patterns seem to be characteristic of granitoids said to be of anatectic origin [Cocherie, 1978].

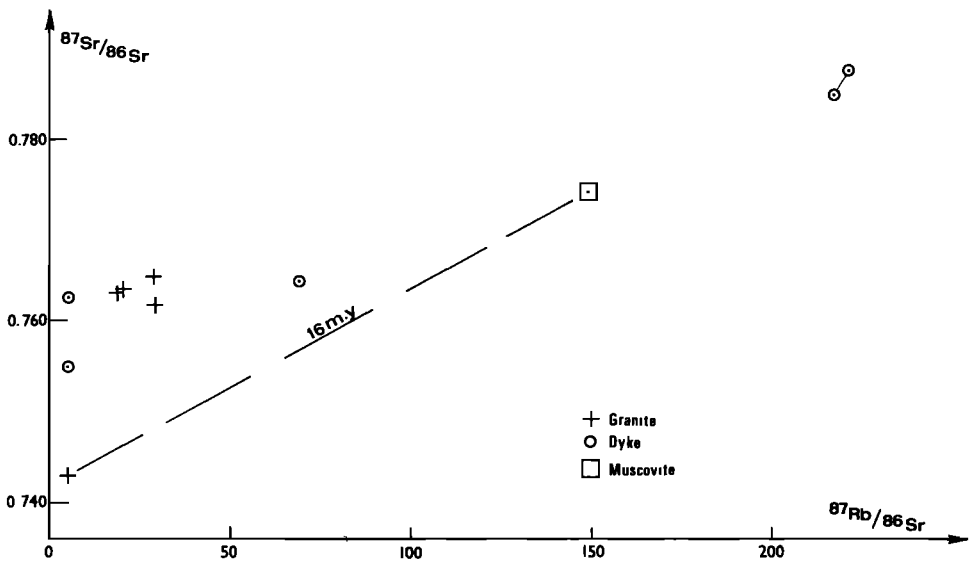

Fig. 9. Rb/Sr isotopic analysis of five whole rock samples of granite, four samples of aplitic dikes and one muscovite of the granite [Vidal, 1978; Ph. Vidal et al., manuscript in preparation, 1981]. There is definitely no whole rock isochron. The muscovite-whole rock age of sample D 22 is very close to the result obtained on micas of other Himalayan leucogranites by K-Ar method [Krummenacher, 1971; Krummenacher et al., 1978]. $^{87}Sr/^{86}Sr$ values are fairly high.

To explain the low REE contents of the granite by equilibrium anatexis would require impossibly low REE concentrations in the source rocks. Other melting models were unable to produce the observed patterns. It may be important that thorium concentrations in the Manaslu granite are also abnormally low. An early precipitation of monazite (REE and thorium phosphate) could partly explain the observed patterns (Ph. Vidal et al., manuscript in preparation, 1981), but the reason for such process is not clear.

Actually, a large circulation of fluid probably played an important part in the establishment of the present REE patterns. In experiments with H_2O saturated melts, addition of chlorine and fluorine in pure water increases the partitioning of rare earths into the fluid phase, while CO_2 does not [Flynn and Burnham, 1978]. It also induces a large positive europium anomaly in the fluid. Aplites or pegmatites that are aqueous fluids derived from melts have such significantly low REE concentrations [Hanson, 1980].

This observation, added to the known Rb/Sr isotopic inhomogeneity, leads me to think that both characteristics result from the same large fluid circulation in the magma. Rough calculations show that the REE patterns may be explained by rather important chlorine-bearing solutions (Ph. Vidal et al., manuscript in preparation,1981).

Conclusion. We are brought to the tentative conclusion that if the melt was not initially water-saturated, it became so before emplacement. At the temperature and pressures envisaged above, even saturated magma can still move a good distance upward with a constant H_2O content before being completely crystallized because of the positive dP/dT slope of the wet liquidus of the muscovite granite of Huang and Wyllie [1973] (Figure 12).

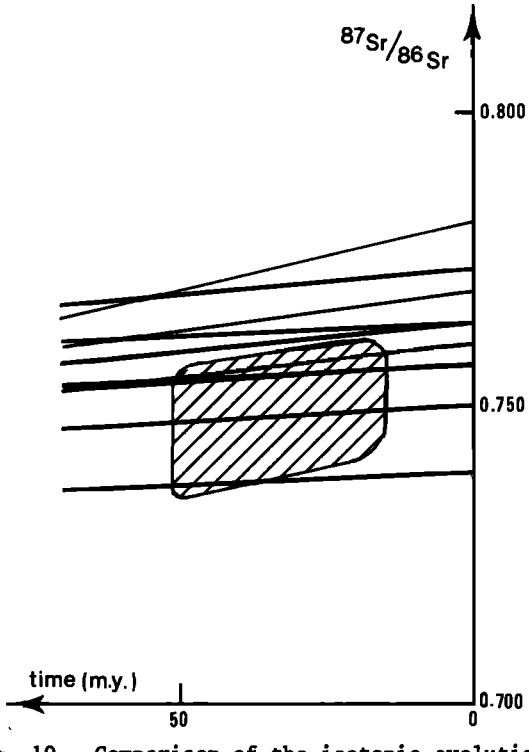

Fig. 10. Comparison of the isotopic evolution lines $^{87}Sr/^{86}Sr = f(t)$ for samples of the Formation I of the Tibetan Slab with the area of the possible initial Sr isotopic ratios of the Manaslu granite (Ph. Vidal, et al., manuscript in preparation, 1981).

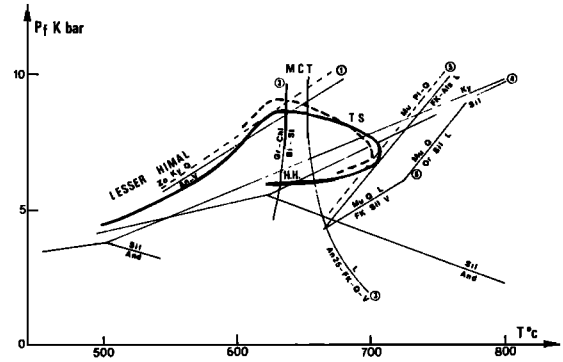

Fig. 11. Pressure-temperature diagram showing the final state of the metamorphic evolution through the MCT and the Tibetan Slab [after Pêcher, 1978]. 1, Zo + Ky + Q = An + V [Boettcher, 1970]; 2, Gr + Chl = Bi + St [Thompson, 1976]; 3, anatexis curve [after Winkler, 1979]; 4, aluminosilicates polymorphs [Holdaway, 1971; Richardson et al., 1969]; 5, Mu + Pl = Fk + Als + L [Thompson and Algor, 1977]; 6, Mu + Q + L = Fk + Sil + V and Mu + Q = Or + Sil + L [Thompson and Algor, 1977]. Dashed curves correspond to CO_2 added to the fluid (X_{H_2O} in the order of 0.8). MCT: main central thrust. TS: Tibetan Slab. HH: Higher Himalaya.

Once saturated, an aqueous phase will separate, and the magma will start to boil off the dissolved fluid, beginning with chloride enriched solutions [Burnham, 1967]. Bubbles of fluid will rise at significant rates through the magma and may concentrate large lithophile ions and other incompatible trace elements.

A Model to Generate the Manaslu Magma

Field and geochemical data indicate that the migmatites of the Tibetan Slab that lie below the Himalayan leucogranites are quite adequate to yield a magma of Manaslu granite type. The production of large volumes of magma of very uniform composition and the timing of melting are the major problems. There are three possibilities to initiate melting in large quantities:

1. The first is to increase the temperature of the Tibetan Slab. Shear stress heating during the Main Central Thrust movement produced a rise in temperature. Its importance is very difficult to estimate, as it depends on the viscosity, the thickness of the shear zone, and the relative velocity of the movement. Such a hypothesis of magma generation by shear melting has been proposed by Shaw [1969] and could well have played a part here. But the actual disposition of the metamorphic and temperature isograds across the MCT [Le Fort, 1975a] with cooling of the base of the Tibetan Slab due to the overthrusting of a cold plate rules out this possibility as the major factor that initiated melting.

2. The second is to modify the pressure

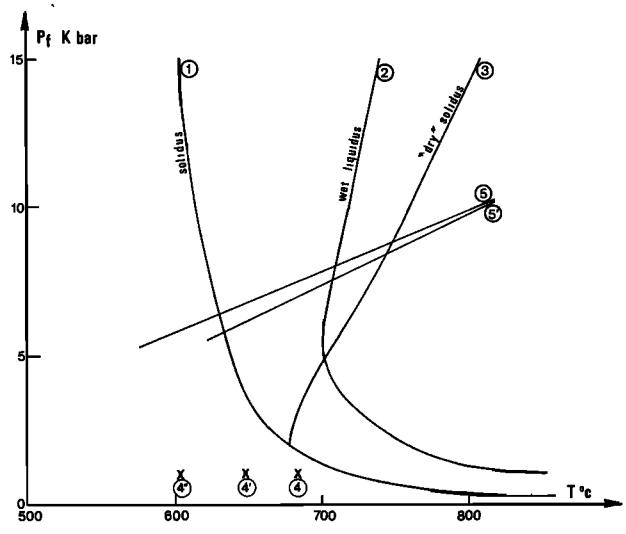

Fig. 12. Pressure-temperature section with curves for melting of the granite system. 1, Solidus for the system granite - H_2O [after Piwinskii, 1968; Boettcher and Wyllie, 1968], the system Ab-Or-Q-H_2O [after Merrill et al., 1970], and the muscovite granite [after Huang and Wyllie, 1973]; 2 and 3, wet liquidus and dry solidus of the muscovite granite of Huang and Wyllie [1973]; 4, 4', and 4'', solidus at 1 kbar with 2, 5, and 13% B_2O_3 added, respectively (in weight percent added to the solution) [after Pichavant, 1979; 1981b]; 5, 5', kyanite-sillimanite equilibrium curve [after Holdaway, 1971; Richardson et al., 1969].

strongly. Because of the steep dP/dT slope of the beginning of anatexis curve, the variation in pressure has to be very large in order to accomplish the required melting. Overpressure may only be local and could hardly explain the regional extent of anatexis. Of course, folding of the Tibetan sedimentary series may thicken the rock column a limited amount. In fact, this thickenning is opposed by a certain amount of flattening and by the dewatering of the Tibetan sediments. Altogether the mineral assemblages and, in particular, the sillimanite-muscovite occurrence in the migmatites of the Tibetan Slab do not indicate abnormally high pressure or an important change in pressure during the metamorphic history of the rock.

3. The third is to introduce a free fluid phase in large amounts in an already heated and rather dry mass of rocks. In fact, the thrusting of the Tibetan Slab over the little or nonmetamorphosed Lesser Himalayan sediments induces in them a prograde inverted metamorphism [Le Fort, 1975a; Pêcher, 1978] with the corresponding dehydration reactions. This metamorphism reaches the garnet and even the kyanite grade. Even after the loss of pore water during diagenesis and the beginning of metamorphism, sediments may contain about 5% by weight of chemically bound water, 60 to 80% of which is lost during the defluidization reactions of the metamorphism up to 500° or 600°C. Altogether, in the 150° - 600°C range, the sediment will lose some 10 to 20% volume as fluids [Fyfe et al., 1978]. In the case of the Manaslu massif, the thickness of the Lesser Himalayan formations under the MCT down to the biotite isograd (450°C) varies from 8 to 12 km [Pêcher, 1978, Fig. 42] and may have produced between 0.6 to 1.5 x 10^6 kg m^{-2} of fluid (~0.1 g/cm^3 of rock).

Actually, water will not be the only component of the fluid. The released water will react with the rock and dissolve salts. Prograde metamorphic reactions will later also release CO_2 in the carbonate-bearing rocks- particularly in the Upper Midland Group.

The fluids produced during prograde metamorphism only move when sufficient porosity and permeability are generated. The generation of fluids builds up the fluid pressure until it reaches a value approximately equal to the geostatic load; it also enables the rock pile to be water-weakened and to react to the existing tectonic stress of the system [Fyfe et al., 1979]. This is in part the reason for the continuous cleavage generation described by Pêcher [1978, p. 274]. The cleavage planes form a direction of relatively easy migration with a possible average dip around 30° that facilitates the upward movement of the fluids. The very numerous quartz veins and quartz lenses are the trace of this fossil migration. Vertical fractures also will help the fluid drainage. Although the fluids are produced in pulses, the downward propagation of the dehydration reactions will provide a continuous flow or a wavy flux of fluids.

When the fluid, crossing the MCT, reaches the Tibetan Slab, it initiates melting as soon as the temperature of the gneisses is above the solidus (Figure 16). As the temperature still increases above, the amount of anatectic melt formed is directly dependent on the amount of water present. An important character of this melt is that it will be 'superheated' with regard to the solidus temperature. Being well above this temperature, even if the magma soon becomes saturated, it will not prevent the magma's moving upward a significant distance. A crude calculation shows that the average thickness of melt that must be extracted from the Tibetan Slab, below the Manaslu granite, may be estimated to be between 1 and 2 km, which is of the order of 10 to 15% of Formation I.

Extrapolation of the normal metamorphism of the Tibetan sedimentaries before thrusting would give an estimated temperature of approximately 800°C at the base of Tibetan Slab in central Nepal [Pêcher, 1978, p. 305]. Such an elevated temperature requires a thin and hot lithosphere, reflecting a regional and durable anomaly that could date back to the Upper Paleozoic at the time of the northern rifting of the Indian continent, when Tethys was given birth and abundant basaltic flows spread over northern India. Also, shear heating may have contributed an amount which is difficult to evaluate at these elevated temperatures [Graham and England, 1976]. In particular, it could help to provide the required enthalpy of melting. Finally, one cannot also completely forget the possibility of heating by isenthalpic decompression [Waldbaum, 1971].

Emplacement of the Manaslu Granite

Once the melt is generated, it collects through channels a system of cleavage planes and vertical fractures, and begins its buoyant ascent in the upper Tibetan Slab. During this slow rise, the confining rocks remain ductile. Where and how

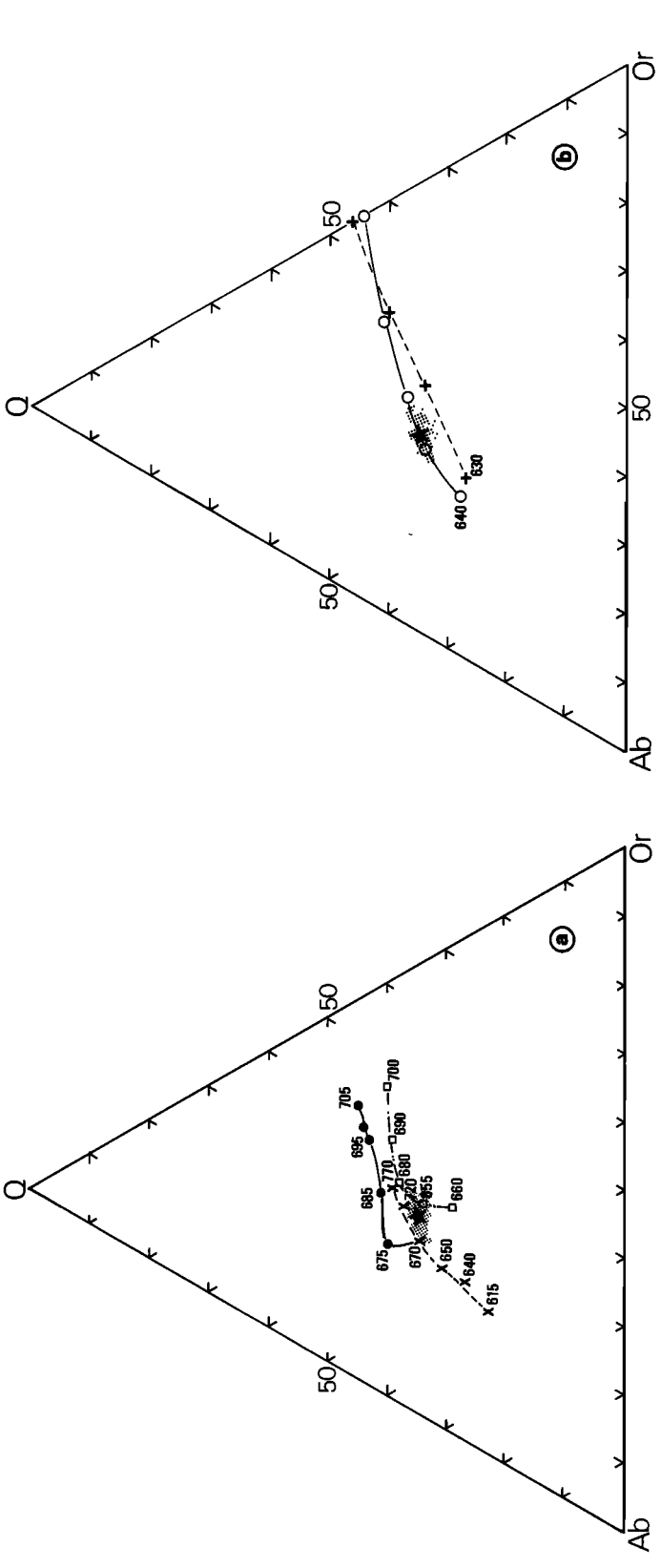

Fig. 13. Minimum melts or eutectics in a simplified granitic system (data from Winkler [1979] and Winkler et al. [1975]) compared to the Manaslu CIPW-Lacroix normative composition. (a) Crosses are minima or eutectics for 0.5, 1, 2, 4, 5 and 10 kbar in the system Q-Ab-Or-H_2O (from right to left). Dots are minimum melt compositions at 2 kbar for an Ab/An ratio of 7.8, 5.2, 3.8, 2.9, 1.8 (from left to right). Squares are minimum melt compositions at 2 kbar with 0.05 mol/l HCl added and Ab/An ratios of ∞, 7.8, 5.2, 3.8, 1.8 (from left to right). The star corresponds to the Manaslu granite solid rock normative composition (93% of the rock) (Table 1). The shaded area corresponds to its extension (main body and arm). (b) Open circles are minimum melts compositions at 5 kbar for Ab/An ratios of 11.7, 7.2, 3.0, 1.1, and 0. Plus (+) are minimum melts compositions at 7 kbar for Ab/An ratios of 12.2, 3.7, 1.9, and 0.

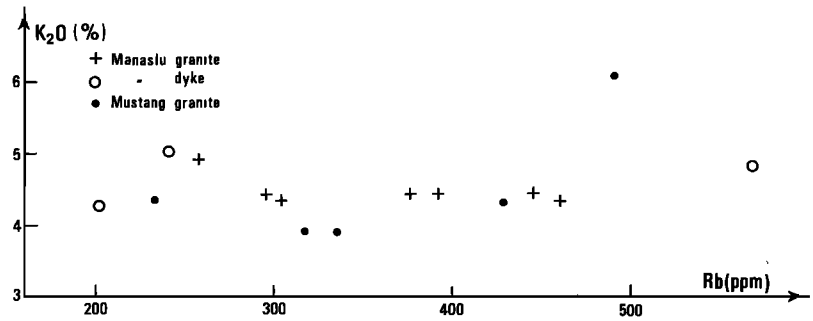

Fig. 14. K_2O versus Rb diagram for 10 samples of the Manaslu granite and five of the westward, nearest Mustang granite. The rather widespread rubidium content is independant of the potassium content ('pegmatitic hydrothermal trend' of Shaw [1968]).

the magma finally emplaced itself is the last question addressed.

Disharmony at the Top of the Tibetan Slab: a Favourable Initial Location

Above the MCT, the main tectonic surface lies at the top of the Tibetan Slab just below the Tibetan sedimentary series. This sharp zone corresponds to the end of the isoclinally folded unit: the infrastructure, and the sudden appearance of open recumbent folds: the superstructure [Le Fort, 1975a]. It lies approximately on the metamorphic isograd of the disappearance of pyroxene in metamorphic limestones. This boundary is a zone of disharmony and weakness clearly visible on the sections of Figure 6.

When the rising magma reaches this zone of differential movement and easy fluid circulation, it begins to build up a small lenticular mass. At the transition between the regions of ductile and brittle behaviour of the two units, the magma finds a very favourable site at which to gather.

The problem of how the Manaslu pluton finds the room to emplace itself can be summerized as follows. The leucogranite takes the place of a dominantly carbonated series (limestones occupy some 60% of the Palaeozoic and Triassic series of Nyi-Shang according to the detailed logs published by Colchen [1975b] and Bassoullet and Mouterde [1977]). The leucogranite shows absolutely no sign of endomorphism but cuts out and replaces the sedimentary series (Figures 2, 4 and 6). The major tectonic feature of the Nilgiri northward recumbent fold can be traced on both sides of the pluton with no displacement (Figure 1). Similarly, the sedimentary columns show no important difference on the two sides of the pluton, and there seems to be no reason to make the pluton take the place of a sudden lack of deposition when the Tibetan sedimentaries are known to occur in broadly similar thicknesses and facies for several hundred kilometers along the Himalaya. Detailed investigations east, west, and on top of the granite show that the room produced by an anticlinal, diapiric upwelling is small.

The only alternative is that the granitic material has taken the place of the more or less metamorphosed sedimentary series that the previous rocks have been expelled. As no purely mechanical ejection can be seen, one is left with the presumption that the rock has been corroded by fluid solutions, dissolved, and carried away just before the magma was emplaced, in a sort of dissolution front preceding the magma.

The first estimate needed is the quantity of fluid necessary to achieve this dissolution. This is made difficult because of our poor knowledge of the supercritical behaviour of water and because we do not know the initial composition of the fluid, particularly its content of halogens, boron, phosphorus, etc. Yet the amount by weight of fluid is necessarily of an order of magnitude greater than that of the granite. Thus the fluid dissolved and liberated during the ascent and the

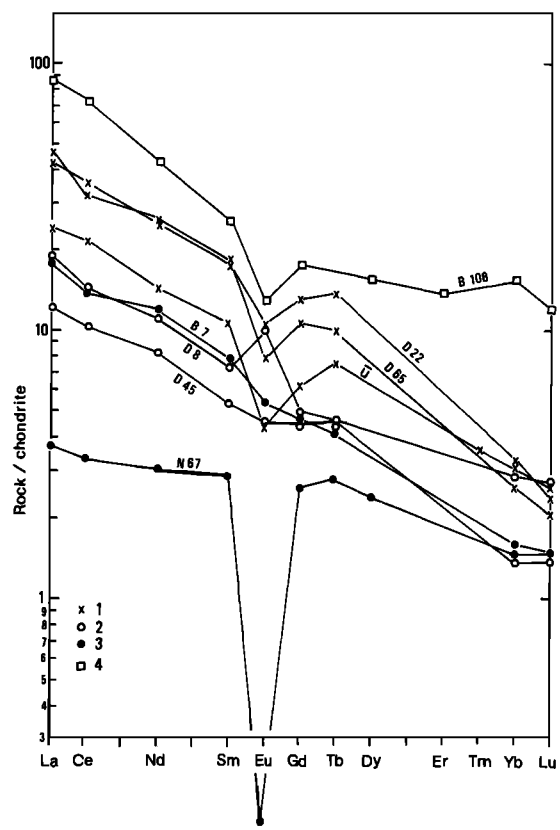

Fig. 15. Chondrite-normalized rare-earth patterns for the Manaslu granite: 1, six samples from the core ($\bar{U}$ is an average of four samples); 2, two samples from the rim; 3, two samples of dikes; 4, one sample of nonmobilized gneiss of the Formation I (data from Cocherie [1977, 1978] and Fourcade et al. [1977]).

crystallization of the magma cannot match alone this amount; neither could dehydration reactions of the metamorphosed Himalayan rocks produce the necessary quantity of fluid. Although meteoric water could attain the required volume (the Manaslu region has a present rainfall of the order of 0.5 x 10^8 kg/cm^2 m.y.), recycling of the fluid in a convective system could more easily match it.

Birth of a Fluid Convective System

From the study of Norton and Knight [1977], which takes into account to a certain extent real fluid and rock properties, we know that 'fluid circulation is an inevitable consequence of the emplacement of magmas within the upper (part) of the Earth's crust.' The considerable extent of these fluid circulations generates convective heat fluxes where host rock permeabilities exceed 10^{-14} cm^2.

This study and others [Norton, 1978, 1979] are of direct significance for the Manaslu pluton. Although they only envisage the case of an instantaneous emplacement of a pluton in a two-dimensional region of the crust, most of their conclusions are of direct application to the Manaslu. The continuous feeding of magma, for a certain period of time, will maintain the growing pluton at a more or less constant temperature for a longer period. The emplacement of such a magma body immediately results in a thermal perturbation which is dispersed by a combination of heat conduction and inevitable fluid circulation, the building of a hydrothermal system. In the different examples cited by Norton, the size of the stocks and plutons is much smaller than the Manaslu granite; the life span of the hydrothermal system is of the order of 10^5 to several million years, although our interest lies mainly in the precrystallization period.

The magnitude of the fluid circulation generated by convective heat fluxes depends on the permeability of the host rocks. The permeability of rocks can only be estimated in general; it is a poorly known quantity. Norton and Knapp [1977] suggest that permeabilities to depths of 10 to 15 km may be significantly greater than 10^{-14} cm^2, which is conducive to the circulation of fluids in pluton environments. The permeability of crystalline rocks is very low despite their relatively high total porosity. The sedimentary rocks in which the Manaslu granite is emplaced, although mainly limestones, have a permeability probably well above 10^{-14} cm^2. Fracturing related to the stress conditions of the magma emplacement and to the differential thermal expansion will augment the permeability around the pluton. Norton and Knight [1977] give a permeability of 10^{-10} cm^2 to a sedimentary rock layer 2.6 to 5.5 km deep, and Norton [1979] gives a permeability of 2×10^{-11} cm^2 to Palaeozoic limestones, dolomites, and evaporites from the southern Arizona-New Mexico region at depths of 2.5 to 6.5 km. Such a relatively high permeability for the deep-seated sedimentaries surrounding the Manaslu would be an important characteristic and may be extended to all the other Himalayan leucogranites.

Apart from the permeability of the host rock, the magnitude of the fluid circulation will also depend on the temperature and on the volume of

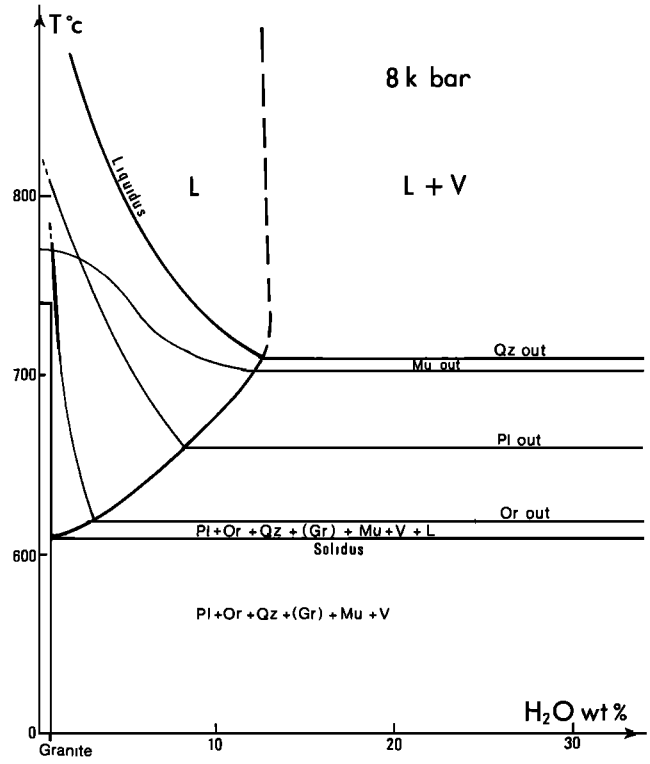

Fig. 16. Isobaric schematic diagram of the melting relations of a muscovite granite [Huang and Wyllie, 1973] at 8 kbar and varying water contents. The position of the saturated melt is taken from Huang and Wyllie [1975].

the magma emplaced (the Manaslu pluton is comparatively very large, about an order of magnitude larger than the plutons proposed by Norton and Knight [1977] as well as on the permeability of the pluton itself. In favorable systems, the magnitude of the fluid circulation may reach enormous values. The mass of fluids circulated through such systems for 10^5 years may reach in the most permeable regions some 2×10^6 g cm^{-2} and the fluid fluxes range from 10^{-4} to 10^{-8} g cm^{-2} sec^{-1}.

The geometries of the fluid circulation and of the isotherms are directly linked to the general architecture of the surrounding rocks and, in particular, to the distribution of the permeabilities. Strong vertical variations in permeability of the stratified host rocks, as is the case of the Manaslu pluton, have a determining influence on the disposition of isotherms toward the sides of the pluton (see P_4 simulation of Norton and Knight [1977] and Norton [1978]). Stratified permeabilities restrict pathline movement to the formations having larger permeability. The layered formations force the circulation toward the pluton. Fluids in host rocks convect toward and eventually into the pluton, depending on its permeability. Also, the convex top pattern tends to decrease the tendency for secondary cells of fluid circulation to develop.

The minor amounts of hydrothermal alteration products as well as the absence of calcite precipitation in the Manaslu may be taken as an indication of the absence of fluid circulation from the carbonated surrounding rocks into the pluton

[Villas and Norton, 1977]. In other words, the permeability of the Manaslu pluton probably remained very low even after crystallization; the tourmaline-rich border facies prove anyhow that a shell of magma remained for a long time, isolating the crystalline core. Such a low permeability acts as a barrier that enhances circulation in the vicinity of the pluton. Thus the fluid flow was probably deflected upward at the side contacts of the pluton.

The origin of the fluids is restricted to the surrounding rocks and the cooling plutons in most of the models presented by Norton because the conductive boundary condition with no flow through the top of the systems is imposed. When it is not, the contribution of the surface fluid may become important, depending among other factors on the depth of the pluton and on the distribution of permeabilities; this contribution is balanced by the development of hot springs. The source regions of the fluid may extend to a distance of some 15 km, and the fluid may be cycled several times. This explains how average fluid to rock mass ratios of 0.4 and as high as 0.9 may be realized in such hydrothermal systems for the entire thermal anomaly. However depending upon the location of the sample of rock, these ratios may be increased by several order of magnitude.

Fluid circulation involves the redistribution of enormous quantities of fluid. Along the fluid flow paths, changes in temperature, pressure, and host rock composition produce dramatic changes in the solvent properties of the fluid and subsequent broad chemical interaction between the fluid and the host rock. In the model of Norton and Knight [1977] the circulating fluids are assumed not to react with the enclosing rocks. Of course, this is not realistic but the nature of fluid-rock reactions may be predicted if the variables are known. Unfortunately, the irreversible mass transfer between the circulating fluid and rocks has been studied mainly in plutonic rock systems [Villas and Norton, 1977].

Dissolution Possibilities

Continuous reactions take place between the fluid and the rock along the pathlines of the convective system. The fluid flow is probably slow enough that equilibrium is generally attained.

The temperature of fluids moving toward the pluton will increase, particularly in the vicinity of the pluton where the solvent properties of the water-dominated fluid will be maximum for a certain number of minerals, among which quartz is the most important [Holland, 1967]. But quartz probably is only the second most abundant mineral in the surrounding sedimentary rocks; calcite is the most abundant, particularly in the Lower Palaeozoic Annapurna and Nilgiri formations.

Solubility of calcite. The solubility of calcite in pure water markedly decreases with increasing temperature. From the available data, this 'retrograde solubility' dominates other factors like increase of P_{CO_2} and addition of NaCl, at least up to 300°C and low pressure [Fyfe et al., 1978].

At 600°C, 1.4 kbar, and 1.9% CO_2, the maximum conditions in the experiments by Sharp and Kennedy [1965], calcite has a solubility of 6.8 mg/kg of solution. This means that even at higher pressures, with 10 mg/kg solubility, for example, the water contained in 1 kg of saturated magma under crustal PT conditions could only dissolve 0.5 to 1.5 mg of calcite.

In other words, a simple calculation shows that the water contained in a saturated granite batholith with a thickness like the Manaslu granite could dissolve a bed of pure limestone some 10 cm thick!

Departure from ideality of the system CO_2-H_2O above the miscibility gap has been analyzed thermodynamically by Flowers [1979] and Flowers and Helgeson [1981]. Walther and Helgeson [1980] examined the geochemical and petrologic consequences of nonideality. Nonideality induces dramatic effects on saturation limits and stability field boundaries among minerals and fluids in the system CaO-MgO-SiO_2-HCl-CO_2-H_2O, HCl being assumed dilute so that it will not introduce a miscibility gap at relatively high pressure and temperature [Walther and Helgeson, 1980, p. 586]. Above 300°C the system CO_2-H_2O (+HCl) is above the critical composition curve and forms a single fluid phase. Above this miscibility gap, the activity of H_2O may depart appreciably from unity with increasing CO_2 concentrations. However, as temperature increases to 600°C, the thermodynamic behaviour of the fluid approaches ideality, although the presence of high concentrations of NaCl in the fluid may well cause the CO_2-H_2O miscibility gap to extend to temperatures greater than 600°C at high pressures (H.C. Helgeson, personal communication, 1981).

Walther and Helgeson deduce that in H_2O-rich fluids coexisting with calcite, quartz, and diopside at 2 kbar and temperatures above 500°C, $a_{Ca^{2+}}$ is about 4 orders of magnitude greater than $a_{Mg^{2+}}$ and 'the total concentration of calcium may be several orders of magnitude greater than that of magnesium... which may then be essentially conserved among solids during metasomatic reactions of the fluid phase with its mineralogical environment.' Similar conclusions were also reached for the system CaO-MgO-SiO_2-H_2O-HCl by Popp and Frantz [1979].

The observation on fluid inclusions in calc-silicate rocks from the upper amphibolite facies terrane of Prince Rupert, British Columbia [Crawford et al., 1979], have revealed aqueous brines with high salinities and a high proportion of $CaCl_2$ (around 12 to 15 wt % of dissolved $CaCl_2$). Similar contents are known from some brines of present hydrothermal areas, such as the Salton Sea geothermal system [White, 1968].

That the fluid phase may contain up to several percents of total calcium in peribatholitic conditions and limestone environments is of utmost importance in the case of the Himalaya, where the limestones form a major part of the intruded sedimentary rocks and are very low in magnesium content [Le Fort, 1975c; Pêcher, 1978].

Conclusion. Taking into account these possibilities and the enormous flux of fluid generated by the progressive emplacement of the Manaslu granite, it becomes possible to envisage that the granite itself indirectly generated the necessary room for its progression. The 'caving out' of the surrounding rocks by dissolution becomes an integral part of the granite emplacement.

The very low permeability of the pluton at the

magmatic stage prevents entrance of fluids into it. On the contrary, its crystallization releases large amounts of fluid that join the outward convective system.

Minerals and species dissolved in the vicinity of the pluton will be deposited farther along the continuing pathlines in veins and lenses of mainly calcite and quartz as appear in the Tibetan sedimentaries. But also, fluids may ultimately reach the surface in a region of hot springs above the pluton, where large amounts of dissolved species may precipitate. However, if such rocks were deposited, they have been eroded away.

The Example of the Nar Network of Dikes

As often referred to, 10 km west of the Manaslu pluton, the valley of Nar (Figures 1 and 2) shows outcrops of a surprisingly large aplopegmatitic and granitic network of dikes (Figure 4), [Le Fort, 1975d, Fig. 31]. This network represents up to about 30% by volume of the pyroxene metamorphic zone, here almost exclusively thick-bedded marbles. It has a remarkable variety of shapes that are preferentially organized along to the bedding or the cleavage. However, a study of the detailed geometry shows that emplacement of the network cannot be accounted for by a simple swallowing of the limestone beds but that there is an effective substitution of the marble by the granitic material. The rims of the granitic dikes show metasomatic reactions at most on a scale of a few millimeters into the host rock. The proportion of granitic dikes increases toward the pluton, where they finally join into the border facies of the Manaslu.

Misch [1949] describes a very similar situation for the Nanga-Parbat region interpreted as 'lit-par-lit remplacement,' involving infiltration and replacement of the country rock.

The point here is to illustrate what I think happened during the emplacement of the Manaslu. The progression of the granitic dikes follows the pathlines of the fluid circulation and the accompanying dissolution. The system has been congealed, frozen in its advance at the end of the Manaslu activity, but it is probably a good image of what happened previously, during the several million years of the emplacement of the Manaslu pluton.

Conclusion

Overthrusting of more highly metamorphozed rocks on less metamorphozed ones is a typical feature of intracontinental orogeny. It is a very favourable situation for the release of large quantities of fluids and the initiation or enhancement of anatexis. Fluid-rich leucogranitic magma may rise to upper levels of the crust, where it is likely to generate large convection systems in metasedimentary rocks. Although the optimum conditions for the generation and emplacement of a maximum volume of leucogranite may be difficult to realize, such a production of leucogranite seems to be a symptom of postcollisional basement thrusting.

The model presented in this paper tries to constrain in one sequence of events the generation and the emplacement of a very special type of granite in a very special environment. Two successive independent cycles happen, each being dominated by a genuine fluid beginning. The entire history of this granite, from birth to maturity, rise, emplacement, crystallization, and finally postmagmatic stages, is, above all, the story of these lost fluids. Just as the sediments hardly speak of the mother sea, the now dry Manaslu granite hardly speaks of its lost fluid genitors and progeny.

Such a model illustrates the often doubted third possibility of generating melts in continental crust environment, neither by temperature nor pressure variation but by an addition of volatiles, a volatile fluxing [Yoder and Tilley, 1962] that occurs when P and T are in the proper range. It is also a type of generation entirely restricted to continental crust.

This model is an alternative to the two main types of emplacement of granitic magmas classically adopted: the forceful and the passive granites [Read, 1961; Lameyre, 1980]. In a way and with the help of enormous amounts of liberated fluids, it is a self-sufficient granite.

The conjunction of the two more or less independent fluid cycles of the generation and of the emplacement is noteworthy. By the large hydrothermal and magmatic overlap involved, it may help to reconcile supporters of the 'naked', or relatively dry, magmatism with those of the more insidious metasomatic way. This model may be of importance not only for other leucogranites but, as well, for other granites.

Notation

T	temperature, °C.
P	total pressure, kbar.
P_i	partial pressure of species i.
fl	fluid.
L	liquid.
V	vapor.
Q	quartz.
Fk	potassium feldspar.
Pl	plagioclase.
Ab	albite.
An	anorthite.
Mu	muscovite.
Bi	biotite.
Als	aluminium silicate.
Ky	kyanite.
Sil	sillimanite.
Gr	garnet.
St	staurolite
Zo	zoisite.
Mag	magnetite.

Acknowledgements. I am very grateful to M. Cuney, F. Debon, A. Pêcher, M. Pichavant, Cl. Ramboz, S. M. F. Sheppard, J. M. Stussi, and Ph. Vidal for the innumerable discussions and for their suggestions concerning different parts of the manuscript. The study has also benefited from the review of H. C. Helgeson, H. D. Holland, H. de La Roche, D. Norton and E-an Zen. The text has been greatly improved by F. Barker. Field work has been supported by the Centre National de la Recherche Scientifique under the RCP 253 and GRECO 12: 'Himalaya - Karakorum.' Laboratory work was mainly supported by the Centre de Recherches Pétrographiques et Géochimiques, Nancy. His Majesty's Nepal Bureau of Mines and Geology very

kindly helped us to obtain the necessary permissions. Careful typing and drawing was assumed by J. Gerbaut and A. Legros.

References

Barbier, J., Etude pétrographique et géochimique du granite à deux micas des Monts de Blond (Limousin, France), *Sci. Terre*, Nancy, Fr., 12, 183-206, 1967.

Bassoullet, J. P., and R. Mouterde, Les formations sédimentaires mésozoïques du domaine tibétain de l'Himalaya du Népal, Ecologie et géologie de l'Himalaya, Vol. Sci. de la Terre, *Colloq. Int. Centre National de la Recherche Scientifique*, 268, 53-60, 1977.

Bassoullet, J. P., M. Colchen, and R. Mouterde, Esquisse paléogéographique et essai sur l'évolution géodynamique de l'Himalaya, *Mém. Hors Sér. Soc. Géol. Fr.*, 8, 213-234, 1977.

Boettcher, A. L., The system $CaO-Al_2O_3-SiO_2-H_2O$ at high pressures and temperatures, *J. Petrol.*, 11, 337-379, 1970.

Boettcher, A. L., and P. J. Wyllie, Melting of granite with excess water to 30 kbars pressure, *J. Geol.*, 76, 235-244, 1968.

Bordet, P., *Recherches géologiques dans l'Himalaya du Népal, région du Makalu*, 275 pp., Centre National de la Recherche Scientifique, Paris, 1961.

Bruckner, R., and J. F. Navarro, Physicalisch-chemische Untersuchungen im System $B_2O_3-SiO_2$, *Glastech. Ber.*, 39, 283-293, 1966.

Brunel, M., M. Colchen, P. Le Fort, G. Mascle, and A. Pêcher, Structural analysis and tectonic evolution of the central Himalaya of Nepal, in *Structural Geology of the Himalaya, edited by P. S. Saklani*, 247-264, Today & Tomorrow's, New Delhi, India, 1979.

Burnham, C. W., Hydrothermal fluids at the magmatic stage, in *Geochemistry of Hydrothermal Ore Deposits, edited by H. L. Barnes*, 670 pp., Holt, Rinehart and Winston, New York, 1967.

Chatterjee, N. D., and W. Johannes, Thermal stability and standard thermodynamic properties of synthetic $2M_1$-muscovite, $K\,Al_2\,[Al\,Si_3\,O_{10}\,(OH)_2]$, *Contrib. Mineral. Petrol.*, 48, 89-114, 1974.

Cocherie, A., Données préliminaires sur la géochimie des terres rares dans le massif leucogranitique du Manaslu (Népal central), Ecologie et géologie de l'Himalaya, Vol. Sci. de la Terre, *Colloq. Int. Centre National de la Recherche Scientifique*, 268, 93-110, 1977.

Cocherie, A., Géochimie des terres rares dans les granitoïdes, *Spec. thesis*, 116 pp., Univ. of Rennes, France, 1978.

Colchen, M., Palaeogeographic and structural evolution of the Tibetan area of the Nepal Himalaya (Annapurna region), *Himalayan Geol.*, 5, 83-103, 1975a.

Colchen, M., Les séries tibétaines, in *Recherches géologiques dans l'Himalaya du Népal, région du Nyi-Shang*, pp. 67-97, Centre National de la Recherche Scientifique, Paris, 1975b.

Colchen, M., P. Le Fort, and A. Pêcher, Carte géologique Annapurna-Manaslu-Ganesh, Himalaya du Népal 1/200.000, *Centre National de la Recherche Scientifique, Paris*, 1980.

Crawford, M. L., D. W. Kraus, and L. S. Hollister, Petrologic and fluid inclusion study of calc-silicate rocks, Prince Rupert, British Columbia, *Am. J. Sci.*, 279, 1135-1159, 1979.

Eggler, D. H., and A. A. Kadik, The system $NaAlSi_3O_8 - H_2O - CO_2$ to 20 kbar pressure, I, Compositional and thermodynamic relations of liquids and vapors coexisting with albite, *Am. Mineral.*, 64, 1036-1048, 1979.

Flowers, G. C., Corrections of Holloway's (1977) adaptation of the modified Redlich-Kwong equation of state for calculations of the fugacities of molecular species in supercritical fluids of geologic interest, *Contrib. Mineral. Petrol.*, 69, 315-318, 1979.

Flowers, G. C., and H. C. Helgeson, Equilibrium and mass transfer during progressive metamorphism of siliceous dolomites, *Am. J. Sci.*, in press, 1981.

Flynn, R. T., and C. W. Burnham, An experimental determination of rare earth partition coefficients between a chloride containing vapor phase and silicate melts, *Geochim. Cosmochim. Acta*, 42, 685-701, 1978.

Fourcade, S., J. Hamet, and C. J. Allègre, Données de la méthode rubidium-strontium et détermination des Terres Rares dans le leucogranite du Manaslu: implications pour l'orogenèse himalayenne, *C.R. Hebd. Séances Acad. Sci. (Paris)*, 284, 717-720, 1977.

Fyfe, W. S., N. J. Price, and A. B. Thompson, *Fluids in the Earth's Crust: Their Significance in Metamorphic, Tectonic and Chemical Transport Processes*, 383 pp., Elsevier, New York, 1978.

Gansser, A., *Geology of the Himalayas*, 289 pp., Interscience, New York, 1964.

Gauthier, J. C., Evolution granitique, développement des granites à deux micas et géochimie des alcalins dans la Marche orientale (Massif Central français), géochimie des alcalins rares, *Sci. Terre*, Nancy, Fr., 19(2), 119-151, 1974.

Ghose, N. C., and N. K. Singh, Experimental study of granitic rocks of Darjeeling (West Bengal, India) and its application to the origin of Himalayan granites, *Tectonophysics*, 43, 23-40, 1977.

Graham, C. M., and P. C. England, Thermal regimes and regional metamorphism in the vicinity of overthrust faults: An example of shear heating and inverted metamorphic zonation from Southern California, *Earth Planet. Sci. Lett.*, 31, 142-152, 1976.

Hagen, T., Report on the geological Survey of Nepal, vol. I, Preliminary reconnaissance, *Mem. Soc. Helv. Sci. Nat.*, 86(1), 185 pp., 1969.

Hall, A., Géochimie des granites varisques du Sud-Ouest de l'Angleterre, *Bull. Soc. Géol. Fr.*, XV(3-4), 229-238, 1973.

Hanson, G. N., Rare earth elements in petrogenetic studies of igneous systems, *Am. Rev. Earth Planet. Sci.*, 8, 371-406, 1980.

Heim, A., and A. Gansser, *Central Himalaya: Geological Observations of the Swiss Expedition 1936*, reprint of 1939 ed., 245 pp., *Hindustan Publishing Delhi*, 1975.

Holdaway, M. J., Stability of andalusite and the aluminium silicate phase diagram, *Am. J. Sci.*, 271, 97-131, 1971.

Holland, H. D., Gangue minerals in hydrothermal deposits, in *Geochemistry of Hydrothermal Ore Deposits, edited by H. L. Barnes*, pp. 382-436, Holt, Rinehart and Winston, New York, 1967.

Holloway, J. R., Fluids in the evolution of gra-

nitic magmas: consequences of finite CO_2 solubility, *Geol. Soc. Am. Bull.*, 87, 1513-1518, 1976.

Huang, W. L., and P. J. Wyllie, Melting relations of muscovite-granite to 35 kbar as a model for fusion of metamorphosed subducted oceanic sediments, *Contrib. Mineral. Petrol.*, 42, 1-14, 1973.

Huang, W. L., and P. J. Wyllie, Melting reactions in the system $NaAlSi_3O_8$ - $KAlSi_3O_8$ - SiO_2 to 35 kilobars, dry and with excess water, *J. Geol.*, 83, 737-748, 1975.

Kerrick, D. M., Experimental determination of muscovite + quartz stability with PH_2O < P tot., *Am. J. Sci.*, 272, 946-958, 1972.

Krummenacher, D., Géochronométrie des roches de l'Himalaya, in *Recherches géologiques dans l'Himalaya du Népal, Région de la Thakkhola*, 279 pp., chap. VI, pp. 187-202, Centre National de la Recherche Scientifique, Paris, 1971.

Krummenacher, D., A. M. Basett, F. A. Kingery, and H. F. Layne, Petrology, metamorphism and K/Ar age determinations in Eastern Nepal, in *Tectonic Geology of the Himalaya, edited by P. S. Saklani*, pp. 151-166, Today & Tomorrow's, New Delhi, India, 1978.

Lameyre, J., Les marques de l'eau dans les leucogranites du Massif Central français, *Bull. Soc. Géol. Fr.*, XV(3-4), 288-295, 1973.

Lameyre, J., Les magmas granitiques: leurs comportements, leurs associations et leurs sources, *Mém. Hors Sér. Soc. Géol. Fr.*, 10, 51-62, 1980.

La Roche, H. de, Granite's chemistry through multicationic diagrams, *Sci. Terre, Sér. Inf. Géol.*, Nancy, Fr., 13, 67-88, 1980.

La Roche, H. de, J. M. Stussi, and L. Chauris, Les granites à deux micas hercyniens francais: Essais de cartographie et de corrélations géochimiques appuyés sur une banque de données, implications pétrologiques et métallogéniques, *Sci. Terre*, Nancy, Fr., 24(1), 5-121, 1980.

Le Fort, P., Les formations cristallophylliennes de la Thakkhola, in *Recherches géologiques dans l'Himalaya du Népal, région de la Thakkhola*, chap. 3, pp. 41-81, Centre National de la Recherche Scientifique, Paris, 1971.

Le Fort, P., Les leucogranites à tourmaline de l'Himalaya sur l'exemple du granite du Manaslu (Népal central), *Bull. Soc. Géol. Fr.*, XV, 555-561, 1973a.

Le Fort, P., Géologie du Haut-Dauphiné cristallin (Alpes françaises): Etude pétrologique et structurale de la partie occidentale, *Sci. Terre*, Nancy, Fr., *Mém.*, 25, 373 pp., 1973b.

Le Fort, P., Himalaya: the collided range. Present knowledge of the continental arc, *Am. J. Sci.*, 275A, 1-44, 1975a.

Le Fort, P., The Anatectic Himalayan Leucogranites with emphasis on the Manaslu Tourmaline granite, in *Recent Researches in Geology*, vol. II, pp. 76-90, *Hindustan Publishing Delhi*, 1975b.

Le Fort, P., Les formations cristallophylliennes de la "Dalle du Tibet" en Marsyandi, in *Recherches géologiques dans l'Himalaya du Népal, région du Nyi-Shang*, chap. II, pp. 21-47, Centre National de la Recherche Scientifique, Paris, 1975c.

Le Fort, P., Le granite du Manaslu, in *Recherches géologiques dans l'Himalaya du Népal, région du Nyi-Shang*, chap. III, pp. 49-65, Centre National de la Recherche Scientifique, Paris, 1975d.

Le Fort, P., A thermal model of intracontinental subduction: Explanation of the Himalayan inverted metamorphism, in *Geotettonica Delle Zone Orogeniche del Kashmir Himalaya (Roma, 1974)*, pp. 209-213, *Accademia Nazionale dei Lincei, Rome*, 1976.

Le Fort, P., F. Debon, and J. Sonet, The "Lesser Himalayan" cordierite granite belt: Typology and age of the pluton of Manserah (Pakistan), in *Proceedings of the International Geodynamic Conference, Peshawar, Nov.-Dec. 1979, Geol. Bull. Univ. Peshawar*, 13, 51-61, 1980.

Le Maitre, R. W., The chemical variability of some common igneous rocks, *J. Petrol.*, 17, 589-637, 1976.

Leroy, J., P. Le Fort, and B. Poty, Some quartz crystals and their fluid inclusions from the Nepal Himalaya, *Himalayan Geol.*, 5, 139-152, 1975.

Liou, J. G., Synthesis and stability relations of epidote, $CaAl_2Fe_1$, *J. Petrol.*, 14(3), 381-413, 1973.

Merrill, R. B., J. K. Robertson, and P. J. Wyllie, Melting reactions in the system $NaAlSi_3O_8$ - $KAlSi_3O_8$ - SiO_2 - H_2O to 20 kilobars compared with results for other feldspar-quartz-H_2O and rock - H_2O systems. *J. Geol.*, 78, 558-569, 1970.

Michard-Vitrac, A., F. Albarède, C. Dupuis, and H. P. Taylor Jr., The genesis of Variscan (Hercynian) plutonic rocks: Inferences from Sr, Pb and O studies on the Maladeta igneous complex, Central Pyrenées (Spain), *Contrib. Mineral. Petrol.*, 72, 57-72, 1980.

Misch, P., Metasomatic granitization of batholitic dimensions, *Am. J. Sci.*, 247, 209-245, 372-406, 673-705, 1949.

Mitchell, A. H. G., Geosynclinal and plate-tectonic hypotheses : significance of late-orogenic Himalayan tin granites and continental collision, paper presented at *the Eleventh Commonwealth Mining and Metallurgical Congress, Hong Kong*, May 1978.

Nautiyal, S. P., B. S. Jangpangi, Pushkar Singh, T. K. Guha Sarkar, V. D. Bhate, M. R. Raghavan, and T. N. Sahai, A preliminary note on the geology of Bhutan Himalaya, *Int. Geol. Congr. Rep. Sess. 22nd 1964*, part II, 1-14, 1969.

Norton, D., Sourcelines, sourceregions and pathlines for fluids in hydrothermal systems related to cooling plutons, *Econ. Geol.*, 73, 21-28, 1978.

Norton, D., Transport phenomena in hydrothermal systems: The redistribution of chemical components around cooling magmas, *Bull. Minéral.*, 102, 471-486, 1979.

Norton, D., and R. Knapp, Transport phenomena in hydrothermal systems: The nature of porosity, *Am. J. Sci.*, 277, 913-936, 1977.

Norton, D., and J. Knight, Transport phenomena in hydrothermal systems: Cooling plutons, *Am. J. Sci.*, 277, 937-981, 1977.

Novgorodov, P. G., and V. S. Shkodzinskiy, Experiments on melting of granite in H_2O - CO_2 mixtures and some problems of granite formation, *Geochem. Int.*, 522-531, 1974.

Pêcher, A., Déformations et métamorphisme associés à une zone de cisaillement. Exemple du grand chevauchement central himalayen (M.C.T.), transversale des Annapurnas et du Manaslu,

Népal, *Thèse ès science*, 354 pp., Univ. Grenoble, France, 1978.

Pêcher, A., Les inclusions fluides des quartz d'exsudation de la zone du M.C.T. himalayen au Népal central : données sur la phase fluide dans une grande zone de cisaillement crustal, *Bull. Minéral.*, 102, 537-554, 1979.

Pichavant, M., Etude expérimentale à haute température et 1 Kbar du rôle du bore dans quelques systèmes silicatés: Intérêt pétrologique et métallogénique, *Thèse spéc.*, 201 pp., *Inst. Natl. Polytech. de Lorraine, Nancy, France*, 1979.

Pichavant, M., Application des données expérimentales aux conditions de genèse et de cristallisation des leucogranites à tourmaline, *C.R. Hebd. Séances Acad. Sci. (Paris)*, Sér. B, 292, 851-854, 1981a.

Pichavant, M., An experimental study of the effect of boron on a water saturated haplogranite at 1 Kbar vapour pressure; geological applications, *Contrib. Mineral. Petrol.*, 76(4), 430-439, 1981b.

Piwinskii, A. J., Experimental studies of igneous rock series: Central Sierra Nevada batholith, California, *J. Geol.*, 76, 548-570, 1968.

Popp, R. K., and J. D. Frantz, Mineral solution equilibria, II, An experimental study of mineral solubilities and the thermodynamic properties of aqueous $CaCl_2$ in the system CaO-SiO_2-H_2O-HCl, *Geochim. Cosmochim. Acta*, 43, 1777-1790, 1979.

Ravier, J., and M. Chenevoy, Les granites à muscovite du Mont-Pilat (Massif Central), *Bull. Soc. Géol. Fr.*, VIII, 133-149, 1966.

Read, H. H., Aspects of Caledonian magmatism in Britain, *Liverpool Manchester Geol. J.*, 2, 653-683, 1961.

Richardson, S. W., M. C. Gilbert, and P. M. Bell, Experimental determination of kyanite - andalusite and andalusite - sillimanite equilibria; the aluminium silicate triple point, *Am. J. Sci.*, 257, 259-272, 1969.

Sharp, W. E., and G. C. Kennedy, The system CaO - CO_2 - H_2O in the two phase region calcite + aqueous solution, *J. Geol.*, 73, 391-403, 1965.

Shaw, D. M., A review of K/Rb fractionation trends by covariance analysis, *Geochim. Cosmochim. Acta*, 32, 573-601, 1968.

Shaw, H. R., Rheology of basalt in the melting range, *J. Petrol.*, 10, 510-535, 1969.

Sheppard, S. M. F., The Cornubian batholith, SW England: D/H and $^{18}O/^{16}O$ studies of kaolinite and other alteration minerals, *J. Geol. Soc. London*, 133, 573-591, 1977.

Steiner, J. C., R. H. Jahns, and W. C. Luth, Crystallization of alkali feldspar and quartz in the haplogranite system $NaAlSi_3O_8$ - $KAlSi_3O_8$ - SiO_2 - H_2O at 4 Kb, *Geol. Soc. Am. Bull.*, 86, 83-98, 1975.

Stern, C. R., and P. J. Wyllie, Water-saturated and undersaturated melting relations of a granite to 35 Kbars, *Earth Planet. Sci. Lett.*, 18, 163-167, 1973.

Swanson, S. E., The effect of CO_2 on phase equilibria and crystal growth in the system $KAlSi_3O_8$ - $NaAlSi_3O_8$ - $CaAl_2Si_2O_8$ - SiO_2 - H_2O - CO_2 to 8000 bars, *Am. J. Sci.*, 279(6), 703-720, 1979.

Taylor, H. P., Jr., and B. Turi, High - ^{18}O igneous rocks from the Tuscan magmatic province, Italy, *Contrib. Mineral. Petrol.*, 55, 33-54, 1976.

Thompson, A. B., Mineral reactions in pelitic rocks, II, Calculations of some P-T-X (Fe-Mg) phase relations, *Am. J. Sci.*, 276, 425-454, 1976.

Thompson, A. B., and J. R. Algor, Model systems for anatexis of pelitic rocks, *Contrib. Mineral. Petrol.*, 63, 247-269, 1977.

Touret, J., Le métamorphisme régional: régime des fluides et grilles pétrogénétiques, *Mém. hors sér. Soc. géol. Fr.*, 10, 63-70, 1980.

Valdiya, K. S., Lithological subdivision and tectonics of the "central crystalline zone" of Kumaon Himalaya, in *Seminar on Geodynamics of the Himalayan Region*, pp. 204-205, *National Geophysical Research Institute, Hyderabad*, 1973.

Vidal, Ph., Rb-Sr systematics in granite from central Nepal (Manaslu): Significance of the Oligocene age and high $^{87}Sr/^{86}Sr$ ratio in Himalayan orogeny: Comment, *Geology*, 6(4), 196, 1978.

Villas, R. N., and D. Norton, Irreversible mass transfer between circulating hydrothermal fluids and the Mayflower stock, *Econ. Geol.*, 72, 1471-1504, 1977.

Wager, L. R., Injected granite sheets of the Rongbuk valley and the north face of Mt Everest, in *D.N. Wadia Commemorative Volume*, pp. 358-379, *Min. Geol. and Metall. Inst. India*, 1965.

Waldbaum, D. R., Temperature changes associated with adiabatic decompression in geological processus, *Nature*, 232, 545-547, 1971.

Walther, J. V., and H. C. Helgeson, Description and interpretation of metasomatic phase relations at high pressures and temperatures, 1, Equilibrium activities of ionic species in non-ideal mixtures of CO_2 and H_2O, *Am. J. Sci.*, 280, 575-606, 1980.

Wang, J., X. Gui, Z. Chen, and R. Xu, Rb-Sr isotopic studies of some intermediate-acidic plutons in Southern Xizang, (abstract), in *Symposium on Qinghai-Xizang (Tibet) Plateau, Academia Sinica*, Pekin, May 1980.

White, D. E., Environments of generation of some base-metal ore deposits, *Econ. Geol.*, 63(4), 301-335, 1968.

Winkler, H. G. F., *Petrogenesis of metamorphic rocks*, 5th ed., 348 pp., Springer-Verlag, New York, 1979.

Winkler, H. G. F., M. Boese, and Th. Marcopoulos, Low temperature granitic melts, *Neues Jahrb. Mineral. Monatsh.*, 6, 245-268, 1975.

Wyllie, P. J., Crustal anatexis: An experimental review, *Tectonophysics*, 43, 41-71, 1977.

Yoder, H. S., Jr., and C. E. Tilley, Origin of basalt magmas: An experimental study of natural and synthetic rock systems, *J. Petrol.*, 3, 342-532, 1962.

(Received November 5, 1980;
revised June 10, 1981;
accepted June 12, 1981.)

JOURNAL OF GEOPHYSICAL RESEARCH, VOL. 86, NO. B11, PAGES 10569-10590, NOVEMBER 10, 1981

HYBRID GRANODIORITES INTRUDING THE ACCRETIONARY PRISM, KODIAK, SHUMAGIN, AND SANAK ISLANDS, SOUTHWEST ALASKA

Malcolm Hill[1]

Earth Sciences Board, University of California, Santa Cruz, California 95064

Julie Morris

Center for Geoalchemy, Department of Earth and Planetary Sciences, Massachusetts Institute of Technology, Boston, Massachusetts, 02139

Joseph Whelan

Isotope Branch, U.S. Geological Survey, Denver, Colorado 80225

Abstract. A narrow belt of tonalite-granodiorite-granite plutons and batholiths intruded the accretionary prism in southwestern Alaska about 60 m.y. ago, simultaneously with plutonism over 100 km north along the main arc axis. The presence of metasedimentary xenoliths, kyanite, and garnet within the intrusions exposed on the Kodiak, Shumagin and Sanak islands establishes the presence of a crustal component. Extremely high values of $\delta^{18}O$, from +10.9 to +13.2 o/oo, require a crustal origin for much of the oxygen in the intrusions. Open-system alteration has disrupted whole-rock Rb-Sr systematics in some samples from the Sanak pluton and Shumagin batholith. Mineral isochrons using unaltered minerals yield an age of 58.7 ± 1.2 m.y. and $^{87}Sr/^{86}Sr_i$ = 0.70534 ± 10 for the Shumagin batholith, and ages of 62.7 ± 1.2 m.y. and $^{87}Sr/^{86}Sr_i$ = 0.70523 ± 14 for the Sanak pluton. Comparison of the isotopic data for the intrusions with those of sedimentary rocks in the Kodiak and Shumagin formations requires that a low-$\delta^{18}O$, low-$^{87}Sr/^{86}Sr$ component be present as well. Mixing models combining $^{87}Sr/^{87}Sr$ and Sr contents of various kinds of mafic magmas with partial melts of metasedimentary wall rocks suggest that three types of mafic magmas can satisfactorily duplicate the oxygen isotope signature of the intrusions: (1) a mid ocean ridge (MORB)-like magma, (2) a magma derived by partial fusion of altered MORB, or (3) an arc basalt. The MORB model predicts abundances of Rb, Sr, Ba, and rare earth elements which are similar to those in the intrusions, while the altered MORB model does not. The arc magma model provides a better trace element match than the remelted MORB model, but is not as successful as the MORB model. These intrusions were preceded by a pulse of mafic to intermediate volcanism near or within the accretionary prism, recorded in the Paleocene Ghost Rocks Formation. This volcanism is probably the heat and mass source of the mafic component within the intrusions, and may be related to activity of the Kula-Farallon ridge approximately 60 m.y. ago.

Introduction

A narrow arcuate belt of plutons intruded Upper Cretaceous sedimentary rocks along the continental margin of southwest Alaska 60 m.y. ago. The intrusions range from biotite tonalite to granite and vary in size from the small pluton on Sanak Island to batholiths on Kodiak and the Shumagin islands (Figure 1). Here we attempt to determine the source rocks which melted to form these intrusions. In order to do this, it is necessary to distinguish between characteristics imposed by the source material(s) and those caused by other processes such as fractional crystallization, hydrothermal exchange with wall rocks, and postcrystallization alteration or metamorphism.

To separate these effects we have determined major and trace element concentrations, Sr and O isotopic compositions for whole rocks, and Sr isotopic compositions for mineral separates from selected samples. Trace elements can be used as sensitive indicators of fractionation processes, postsolidification alteration, and, if these effects can be thoroughly evaluated, source characteristics. Sr isotope ratios do not change during fractional crystallization, and so give information on the nature of the source(s) assuming that alteration effects can be 'seen through', if present. In this study, some alteration has occurred, and we use the mineral isochrons to help evaluate its extent. Oxygen isotopes are not appreciably fractionated during fractional crystallization (less than about 2o/oo [Matsuhisa et al., 1973]). At the high temperatures required for partial melting, the $\delta^{18}O$ of the magma will be similar to that of its source rocks. This signature can be affected by post-intrusion hydrothermal exchange, but intrusions which have suffered extensive exchange with their wall rocks typically display concentric zonation of $\delta^{18}O$ [Taylor, 1978]; samples chosen for geographic coverage across an intrusion can help evaluate this possibility.

Field Relations and Age

Volcanic and plutonic rocks have been generated at intervals throughout the Mesozoic and Cenozoic in southwest Alaska [Burk, 1965; Reed and Lanphere, 1969, 1973; Hudson, 1979], presumably in relation to the subduction of oceanic

[1]Now at Earth Sciences Department, 14-HO, Northeastern University, Boston, Massachusetts 02115.

Copyright 1981 by the American Geophysical Union.

Paper number 1B0904.
0148-0227/81/001B-0904$01.00

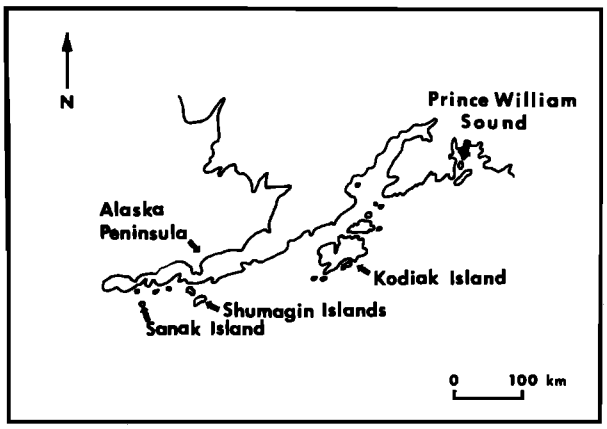

Fig. 1. General location map of southwestern Alaska showing the locations of the Kodiak and Shumagin batholiths and the Sanak pluton.

lithosphere. Most of this activity occurred along and north of the present-day belt extending from Sanak Island northeast through the Shumagin and Kodiak islands toward Prince William Sound (Figure 1), and lie more than 100 km nearer the axis of the presumed early Tertiary subduction zone than coeval intrusions along the magmatic arc axis. Our samples, from the southwestern part of this belt, were collected by J. C. Moore during mapping of the Sanak and Shumagin islands, and by the senior author along Three Saints Bay on Kodiak Island (Figure 2). Hudson et al. [1979] describe plutons from the northeastern part of this belt, near Prince William Sound.

The Kodiak, Shumagin, and Sanak islands consist largely of a series of probably accreted terranes ranging from Early Jurassic to Eocene in age [Burk, 1965; Connelly, 1978; J. C. Moore, 1973a, b, 1974a, b; G. W. Moore, 1967, 1969; Fisher and Holmes, 1980]. Structural deformation is complex in all accreted units, yielding broken formations and tectonic melange. Formations generally are fault-bounded. The trend of regional tectonic structures, including major faults and foliation within the deformed units, is parallel to the present-day continental margin.

The three intrusions we have studied intrude Upper Cretaceous (Maestrichtian, 73-66 m.y. [Lanphere and Jones, 1978]) graywacke and argillite of the Kodiak Formation on Kodiak Island and the correlative Shumagin Formation on the Shumagin and Sanak islands [Connelly, 1978; Nilsen and Moore, 1979; J. C. Moore, 1974a, b]. Small satellite plutons, probably related to the Kodiak batholith, intrude the graywacke-, argillite-, and greenstone-bearing Ghost Rocks Formation of Kodiak Island [Connelly, 1978; G. W. Moore, 1967, 1969; Reid and Gill, 1980], which contains fossils tentatively dated as Paleocene [Nilsen and Moore, 1979] (approximately 65-45 m.y. [Hardenbol and Berggren, 1978]). K-Ar biotite and muscovite ages for the Kodiak, Shumagin, and Sanak intrusions are generally concordant in samples where both have been analyzed, and cluster around 60 m.y. [Burk, 1965; Kienle and Turner, 1976; Turner et al., 1973]. These ages suggest that the Ghost Rocks Formation was deposited in the earliest Paleocene, between 60 and 65 m.y. ago. This point becomes important when we consider the origin of the intrusions.

The contacts of the Tertiary intrusions on the Kodiak, Shumagin and Sanak islands are locally

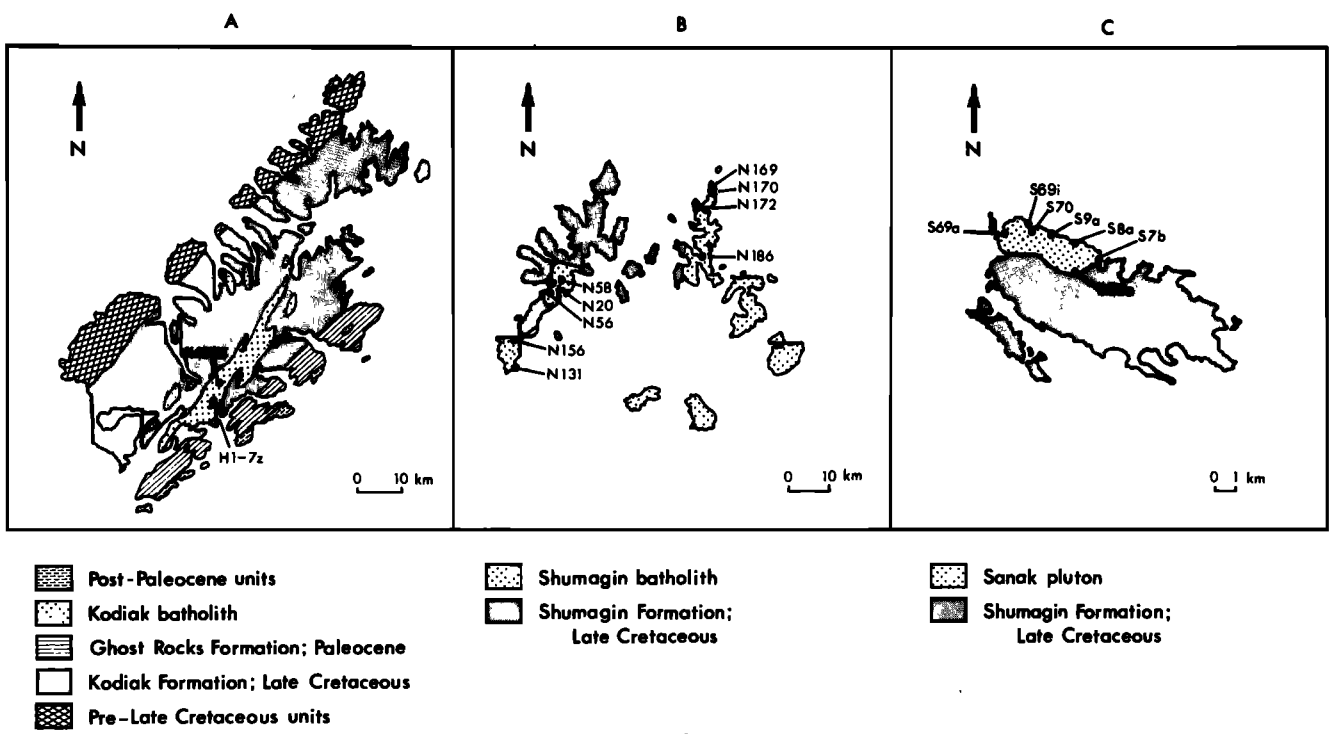

Fig. 2. Generalized geologic maps of the (a) Kodiak, (b) Shumagin, and (c) Sanak islands with sample locations for intrusive rocks. Geology is after G. W. Moore [1967], Connelly, [1978], Connelly and Moore [1977], Grantz [1963], and J. C. Moore [1974a, b].

discordant with the trends of fold axes in the country rocks [J. C. Moore, 1974a, b]. However, on a regional scale both the Kodiak batholith and its smaller satellite plutons are elongate parallel to the regional tectonic grain, suggesting structural control of the shapes of the intrusions. No strong foliation or protoclastic fabric was observed in any of the intrusions. The Kodiak and Shumagin formations have been metamorphosed to biotite- and andalusite-bearing hornfels within about 500 m of the contacts (T. Byrne, personal communication, 1980). Regional metamorphism away from the intrusions has not been extensively studied; the Shumagin Formation contains laumontite and prehnite [J. C. Moore, 1973b and personal communication, 1980], and Connelly [1978] described prehnite and pumpellyite from the Ghost Rocks Formation.

Petrography

The intrusions are composed of biotite tonalite, biotite granodiorite, and biotite granite (Table 1) (International Union of Geological Sciences (IUGS) classification [Streckeisen, 1973]). The samples in the IUGS granite field would fall in the quartz monzonite field of Bateman et al. [1963]. Biotite is the sole ferromagnesian silicate. Muscovite, where present, generally replaces biotite, plagioclase, or orthoclase. Rarely, muscovite forms euhedral, possibly primary crystals. In all sections, FeTi oxides, apatite, and zircon occur as inclusions in most minerals. Most samples have been sericitized, and locally biotite has been chloritized. The freshest samples were chosen for detailed geochemical studies, but none are completely free of these effects.

Xenocrysts and partially digested inclusions of probably metasedimentary origin are common in all three intrusions. The inclusions range in size from less than 1 cm to more than 6 cm in diameter. They contain the same minerals present as phenocrysts in the intrusions: biotite, plagioclase, quartz, perthitic orthoclase, and some muscovite. In addition, some contain garnet and kyanite. Kyanite xenocrysts are surrounded by reaction rims of a fine-grained, high-relief mineral which may be sillimanite; kyanite should not be stable at magmatic temperatures. The garnets have no reaction rims but are anhedral. We consider the clots and kyanite and garnet xenocrysts to be relicts of partially digested amphibolite-grade metamorphic rocks, which could represent either residual material not melted in the source region or accidental contaminants derived from the wall rocks. In either case, the xenocrysts and inclusions establish the presence of a metasedimentary component in the intrusions.

Geochemistry

Samples from the Kodiak and Shumagin batholiths, the Sanak pluton, graywacke and argillite from the Kodiak and Shumagin formations, and greenstones from the Ghost Rocks Formation have been analyzed for major and trace elements, and selected samples for Sr and O isotopes, by methods described below. Additional major and trace element analyses for plutonic, volcanic and sedimentary rocks from this area are given in the works by Hill [1979] and Reid and Gill [1980].

Analytical methods. Major and minor elements were analyzed by X ray fluorescence (XRF) on a Phillips PW1410 spectrometer at the University of California at Santa Cruz, using glass pellets prepared after Norrish and Hutton [1969] and Harvey et al. [1973]. Pressed powder pellets were used for XRF determination of Na and trace elements (Zr, Y, and some Ba analyses in Table 2). Additional trace elements (Cs, Ba, rare earth elements (REE), Ta, Hf, Sc, Co) were obtained by instrumental neutron activation at the NASA-Johnson Space Center in Houston (samples S70, N20, H1-7z, K4033, U13a, M5c, and 15-2e), the U.S. Geolological Survey in Denver (S7b, S8a, S69a, S72d, S89d, and S233b), and at the Massachusetts Institute of Technology (MIT) in Cambridge (N131, N170, and N186). Methods used are similar to those described by Jacobs et al. [1977].

Oxygen isotopes were determined at the U.S. Geological Survey in Denver following standard techniques [Clayton and Mayeda, 1963]. Using a CO_2-H_2O fractionation factor of 1.0412, 14 analyses of NBS-28 [Friedman and Gleason, 1973] during the study gave a mean value of 9.97 ± 0.11 o/oo (1σ).

Rb and Sr contents and Sr isotope ratios were analyzed at the Department of Earth and Planetary Sciences at MIT on a 9", 60° spectrometer using techniques given by Hart and Brooks [1977]. A Rb decay constant of 1.42×10^{-11} yr^{-1} [Steiger and Jaeger, 1977] was used for all calculations. All $^{87}Sr/^{86}Sr$ ratios are normalized to $^{86}Sr/^{88}Sr = 0.1194$ and are reported relative to Eimer and Amend $SrCO_3 = 0.70800$. Reported uncertainties are 2σ of the mean.

Major and trace elements. SiO_2 varies from 64.5 to 72.7% in the Sanak pluton, from 61.3 to 75.9% in the Shumaggin batholith, and three samples from the Kodiak batholith range from 63.8 to 68.6% (Table 2). On a normative Q-Ab-Or diagram, rocks from the three intrusions occupy different but partially overlapping fields near the minimum melting compositions for $P_{H_2O} < 4$ kbar in the granite system [Tuttle and Bowen, 1958; Luth et al., 1964]. All samples are peraluminous with normative corundum from 0.4 to 4.4%. Na_2O/K_2O ratios are close to 1, and K/Rb ratios are between 249 and 273. Compositions vary more or less regularly within each intrusion and between different intrusions. For example, in Figure 3 note that the Kodiak batholith has the least K_2O and the Sanak pluton the most K_2O at a given SiO_2 content, with Shumagin samples falling between the two.

All of these granitic rocks are light rare earth element (LREE) enriched (Figure 4). Although the magnitude of the europium anomaly increases smoothly with increasing SiO_2, total rare earths increase, then decrease with increasing SiO_2 for the Sanak and Shumagin intrusions (too few data are available for the Kodiak batholith to establish any trends). The REE contents of the sedimentary rocks of the Kodiak and Shumagin formations are also shown in Figure 4, with the Haskin et al. [1966] average of 40 North American shales for comparison. There is no systematic difference in REE contents between the graywacke and argillite samples, or between the sedimentary rocks from different islands.

Oxygen isotopes. Oxygen isotope data for the

TABLE 1. Sample Locations and Petrographic Descriptions of Analyzed Plutonic Samples

Sample	N. Latitude	W. Longitude	Description
		Sanak pluton	
S8a	54°28'28"	162°43'48"	Biotite granodiorite; 0.271 qtz + 0.394 plg. + 0.079 ksp + 0.231 bio + 0.01 ox + tr. ap + tr. zir + tr. ky + tr. gar
S9a	54°28'48"	162°45'07"	Biotite granodiorite; 0.301 qtz + 0.346 plg + 0.059 ksp + 0.213 bio + 0.007 ox + 0.003 ap + tr. zir + 0.004 mus + tr. ky
S69i	54°29'12"	162°46'52"	Biotite granodiorite; 0.242 qtz + 0.408 plg + 0.080 ksp + 0.246 bio + 0.002 ox + tr. ap + tr. zir + tr. gar + tr. mus
S70	54°29'09"	162°46'47"	Biotite granodiorite; 0.260 qtz + 0.44 plg + 0.07 ksp + 0.21 bio + 0.001 ox + 0.02 mus + tr. ap + tr. zir
S20a	54°27'08"	162°43'00"	Biotite granodiorite; 0.33 qtz + 0.38 plg + 0.07 ksp + 0.19 bio + 0.01 ox + 0.002 ap + 0.002 zir + 0.004 mus
S69a	54°28'46"	162°49'00"	Biotite granite; 0.29 qtz + 0.33 plg + 0.20 ksp + 0.16 bio + 0.003 ox + 0.002 ap + 0.002 zir + 0.01 mus
S7b	54°27'43"	162°41'38"	Biotite granite; 0.32 qtz + 0.32 plg + 0.29 ksp + 0.07 bio + 0.002 ox + tr. ap + tr. zir
S7a	54°27'43"	162°41'38"	Biotite granodiorite; 0.227 qtz + 0.445 plg + 0.183 ksp + 0.108 bio + 0.007 ox + 0.002 ap + 0.001 zir + tr. mus
		Shumagin batholith	
N131	54°52'48"	160°11'43"	Biotite tonalite; qtz + plg + bio + ox + tr. ap + tr. zir
N58	55°03'54"	160°02'38"	Biotite granodiorite; 0.196 qtz + 0.564 plg + 0.138 ksp + 0.080 bio + 0.004 ox + tr. ap + tr. zir
N186	55°06'12"	159°33'21"	Biotite granodiorite; 0.282 qtz + 0.521 plg + 0.062 ksp + 0.115 bio + 0.004 ox + 0.004 ap + 0.001 zir + 0.011 chl
N172	55°11'28"	159°32'17"	Biotite granodiorite; 0.272 qtz + 0.470 plg + 0.153 ksp + 0.101 bio + 0.001 ox + tr. ap + tr. zir
N20	55°02'40"	160°05'21"	Biotite granite; 0.436 qtz + 0.308 plg + 0.180 ksp + 0.070 bio + 0.002 ox + tr. ap + tr. zir + tr. chl + tr. mus
N56	55°02'04"	160°05'40"	Biotite granite; 0.221 qtz + 0.334 plg + 0.398 ksp + 0.044 bio + tr. ox + 0.002 ap + tr. zir
N156	55°56'00"	160°11'53"	Biotite granodiorite; 0.216 qtz + 0.476 plg + 0.239 ksp + 0.069 bio + tr. ox + tr. ap + tr. zir + tr. chl
N169	55°14'27"	159°39'19"	Biotite granite; 0.362 qtz + 0.294 plg + 0.272 ksp + 0.072 bio + tr. ox + tr. ap + tr. zir + tr. mus + tr. chl
N170	55°14'38"	159°30'38"	Granophyric granite; qtz, ksp, and zoned plg in granophyric intergrowth; tr. bio, ox, ap, zir
		Kodiak batholith	
H1-7z	57°10'46"	153°30'44"	Biotite tonalite; 0.28 qtz + 0.45 plg + 0.04 ksp + 0.20 bio + 0.003 ox + 0.008 ap + tr. zir + tr. mus
K4033			Biotite granodiorite; 0.27 qtz + 0.40 plg + 0.17 ksp + 0.13 bio + 0.001 ox + 0.002 ap + 0.003 zir + 0.02 mus

Abbreviations: ap = apatite; bio = biotite; chl = chlorite; gar = garnet; ksp = k-feldspar; ky = kyanite; mus = muscovite; ox = Fe-Ti oxide; plg = plagioclase; qtz = quartz; tr. = trace; zir = zircon.

Table 2a. Major Element Analyses of Sanak Pluton and Kodiak Batholith, Alaska

	Sanak Pluton								Kodiak Batholith	
	S8a	S9a	S69i	S70	S20a	S7a	S69a	S7b	H1-7z	K4033
SiO_2	64.54	64.97	65.22	65.45	66.01	66.18	68.90	72.74	65.76	68.56
TiO_2	0.90	0.82	0.79	0.82	0.79	0.72	0.54	0.20	0.63	0.52
Al_2O_3	15.71	15.83	15.57	15.41	15.64	15.47	14.85	13.66	15.91	15.80
Fe_2O_3*	6.55	6.24	5.87	5.89	5.87	5.37	4.13	2.26	4.22	2.82
MnO	0.10	0.09	0.09	0.08	0.10	0.09	0.07	0.05	0.08	0.07
MgO	1.96	1.77	1.66	1.74	1.63	1.43	0.93	0.29	2.29	1.19
CaO	2.37	2.10	2.26	2.30	2.10	2.09	1.63	0.85	3.40	2.63
Na_2O	2.82	2.86	2.81	3.20	2.58	2.74	3.18	4.16	2.49	2.99
K_2O	3.06	3.28	3.19	3.24	3.54	3.82	4.18	4.64	2.49	2.91
P_2O_5	0.26	0.23	0.23	0.24	0.22	0.21	0.20	0.18	0.20	0.20
LOI	1.19	1.28	1.75	1.36	1.09	1.23	1.18	1.24	1.03	0.83
Total	99.46	99.47	99.44	100.13	99.57	99.35	99.79	100.27	98.50	98.52

*Total iron as Fe_2O_3.
LOI = Loss on Ignition. All other data by XRF.

intrusive and sedimentary rocks are presented in Table 3 and summarized in Figure 5. In the intrusive rocks, $\delta^{18}O$ ranges from +10.9 to +13.2 o/oo. These are extremely high values for igneous rocks and require a crustal source for much of the oxygen in the intrusions [Taylor, 1978]. Although the data scatter, samples with greater SiO2 and lower TiO2 and total Fe tend to have slightly higher positive $\delta^{18}O$ values, perhaps due to fractional crystallization. Except for one sample from the very edge of the Sanak pluton (S7b), there is no systematic zonation of $\delta^{18}O$ within the intrusions. We conclude that the high positive $\delta^{18}O$ of the intrusive rocks is a primary feature of the magma and is not the result of postintrusion, hydrothermal exchange with the sedimentary wall rocks.

Graywackes from the Upper Cretaceous wall rocks partly overlap the $\delta^{18}O$ range for the intrusions, but extend to higher values. Argillites have even heavier oxygen, as expected from their higher clay mineral contents [Savin and Epstein, 1970].

Strontium isotopes. Rb, Sr, and Sr isotopic compositions for 21 granitic whole rocks, four sets of mineral separates, and 11 sedimentary rocks are presented in Table 3. The granitic samples were chosen to give geographic coverage of the intrusions and to cover the range of major and trace element variation.

The whole rock data for the intrusions are plotted in Figure 6. The Shumagin batholith samples scatter somewhat, defining an 'errorchron' with an apparent age of 59.8 m.y. and an initial $^{87}Sr/^{86}Sr$ of 0.70482. The Sanak pluton shows less scatter, but gives an 'age' of 49.5 m.y., substantially younger than the 60 m.y. K-Ar ages reported [Burk, 1965; J. C. Moore, 1974b]. The scatter of points about the best fit lines and the young age for the Sanak pluton suggest that closed system models cannot be applied to these intrusions. Alteration and (or) initial isotopic heterogeneity could explain this behavior.

In an attempt to explain the scatter of data and the young age for the Sanak pluton, we analy-

Table 2b. Major Element Analyses of Shumagin Batholith, and a Greenstone from the Ghost Rocks Formation, Alaska

	Shumagin Batholith									Greenstone, Ghost Rocks Formation
	N131	N58	N186	N172	N20	N56	N156	N169	N170	15-2e
SiO_2	61.32	67.78	68.03	69.60	73.24	73.32	74.54	74.79	75.94	52.14
TiO_2	1.07	0.42	0.63	0.50	0.24	0.24	0.18	0.21	0.08	0.91
Al_2O_3	16.81	15.53	15.36	14.79	13.87	13.72	13.49	13.34	12.87	15.41
Fe_2O_3*	7.15	3.00	4.38	3.72	2.24	2.27	2.15	1.84	1.42	7.74
MnO	0.11	0.06	0.07	0.06	0.04	0.04	0.05	0.04	0.04	0.12
MgO	2.73	1.37	1.46	1.07	0.45	0.41	0.16	0.38	0.02	7.42
CaO	3.94	2.84	2.69	2.39	1.27	1.13	1.16	0.73	0.51	7.08
Na_2O	2.86	4.03	3.54	3.53	4.13	4.27	4.13	3.95	3.84	4.10
K_2O	2.19	2.91	3.95	3.51	4.01	4.01	4.00	4.42	4.72	0.27
P_2O_5	0.24	0.10	0.13	0.12	0.08	0.08	0.08	0.09	0.07	0.14
LOI	0.91	1.67	1.08	0.85	0.94	1.04	0.63	0.97	0.73	3.92
Total	99.33	99.71	100.32	100.15	100.51	100.53	100.57	100.76	100.24	99.25

*See footnotes for Table 2a.

Table 2c. Major Element Analyses of Mesozoic Sedimentary Rocks, Kodiak, Shumagin and Sanak Islands, Alaska

	Kodiak Formation		Shumagin Formation (Shumagin Islands)						Shumagin Formation (Sanak Island)				
	Graywacke	Argillite	Graywacke				Argillite		Graywacke			Argillite	
	U13a	M5c	N16a	N18b	N62	N65	NY90	N42b	N135	S84f	S72d	S233b	S33e	S89d
SiO_2	71.62	61.30	65.08	61.09	70.05	63.86	66.77	59.37	58.55	61.50	61.39	63.93	60.79	58.88
TiO_2	0.63	0.84	0.60	0.69	0.53	0.71	0.68	0.76	0.81	0.72	0.79	0.67	0.82	0.81
Al_2O_3	11.72	15.94	14.87	15.65	12.78	15.99	14.34	17.87	23.19	17.22	15.47	13.38	16.58	16.60
Fe_2O_3*	3.95	6.83	5.69	5.78	4.47	5.35	4.40	7.49	5.44	5.76	6.20	5.66	6.75	6.92
MnO	0.05	0.10	0.11	0.12	0.06	0.10	0.10	0.10	0.11	0.12	0.15	0.12	0.10	0.10
MgO	1.54	2.32	1.87	2.66	1.59	2.20	1.57	3.09	2.13	1.99	1.89	2.09	2.62	2.57
CaO	1.35	1.02	2.69	3.61	1.34	2.81	2.17	1.09	0.40	2.00	1.93	2.83	1.63	1.34
Na_2O	3.01	1.19	2.84	3.24	2.47	3.46	4.20	0.76	1.51	4.29	4.39	3.10	1.79	2.07
K_2O	0.93	2.50	1.20	1.43	2.36	1.67	1.46	2.91	3.73	1.45	1.45	0.95	2.62	2.74
P_2O_5	0.13	0.23	0.14	0.23	0.15	0.19	0.19	0.18	0.15	0.17	0.17	0.14	0.22	0.22
LOI	3.21	5.53	3.21	3.11	2.65	3.22	2.13	4.52	4.23	3.20	2.77	5.32	5.05	5.31
Total	98.14	97.80	98.30	97.61	98.25	99.56	98.01	98.14	100.25	98.42	97.60	98.19	98.97	97.56

*See footnotes for Table 2a.

zed mineral separates from four whole rocks. The whole rocks were chosen to provide examples of samples which plot on the whole rock isochron (N20, S70) and ones which fall off the isochron (N131, S9a).

Compared with fresh plagioclase, sericitized plagioclase has greater Rb and Sr contents, as well as higher $^{87}Sr/^{86}Sr$ ratios. The Rb/Sr ratio of the altered plagioclase is higher in two out of three cases. These relationships can be seen in the mineral isochrons (Figure 7), which show that the samples differ greatly in degree of open-system behavior. N131 shows no alteration effects (there is no altered plagioclase), and the two minerals and the whole rock define a good isochron. N20 shows greater alteration, having sericitized plagioclase and cloudy K-feldspar; no three points lie on the same line for this sample. The initial $^{87}Sr/^{86}Sr$ ratio defined by N131 (0.70534 ± 10) is different at the 95% confidence level from that obtained from the whole rock errorchron (0.70482 ± 18). From the present data we cannot evaluate whether all of the Sr isotope heterogeneity for the Shumagin batholith reflects secondary alteration or whether some is due to initial heterogeneity inherited from the source(s). It is clear from sample N20 that secondary, open-system behavior is responsible for at least some of the variability. Nonetheless, the ages determined from the mineral isochrons (approximately 60 m.y.) are in good agreement with K-Ar results and with geologic relationships.

The situation for the Sanak samples is somewhat different, as the mineral isochrons give older ages than the whole rock isochrons. This would seem to indicate closed-system behavior for the minerals, but open-system relations for the whole rocks, exactly the opposite of the systematics usually described [Faure, 1977].

We have considered several possible explanations for these anomalous whole rock:mineral relationships. A real thermal event of 49 m.y. age is not a suitable explanation, as it would reset the mineral isochrons as well as those for the whole rocks. Alternatively, if the whole rock points defined a line of negative slope on a $(^{87}Sr/^{86}Sr)_o$ vs. Rb/Sr (pseudoisochron) diagram, the rotation of the isochrons through time would produce an apparent age for the whole rock isochron which is less than the real age. This suggests that the sources for the granitic rocks lay along a mixing line; however, this model runs into difficulties because of the implausibility of and end-member component which is mafic in character with Rb/Sr > 1.25 and $^{87}Sr/^{86}Sr$ < 0.7045.

A third model involves partial alteration of the whole rocks. This needs to be a systematic alteration or it would produce the random scatter about the isochron seen in the Shumagin case, rather than rotation of the whole rock isochron from a steeper to a shallower slope, corresponding to an apparent young age, as seen in Sanak. An alteration of this sort, affecting grain boundaries and some altered minerals, would not show up in a mineral isochron based on analysis of fresh minerals. Mechanisms for this include loss of common Sr recently or loss of radiogenic Sr through time.

These results suggest that alteration, primar-

Table 2d. Trace Element Analyses of Tertiary Intrusives, Kodiak, Shumagin, and Sanak Islands, Alaska

	Sanak Pluton				Shumagin Batholith				Kodiak Batholith	
	S8a	S70	S69a	S7b	N131	N186	N20	N170	H1-7z	K4033
Cs	5.5	6.8	6.5	2.8	4.0	6.2	7.9	9.0	6.8	2.9
Ba	898.	851.	898.	421.	917.	866.	—	603.	874.	721.
U	3.28	3.40	5.85	5.19	1.73	—	3.37	3.26	—	—
Th	6.84	11.2	8.18	5.55	5.0	11.6	8.7	6.7	7.3	7.8
Y	36.	35.	32.	17.	24.	46.	35.	28.	17.	24.
La	24.9	31.9	24.3	10.6	21.0	31.1	23.1	10.82	23.0	21.4
Ce	48.9	74.	48.4	22.44	48.	75.	52.1	28.9	48.5	45.5
Nd	26.0	—	26.0	13.8	23.	31.	—	14.	—	—
Sm	6.8	7.8	5.69	2.92	5.33	7.17	6.0	3.87	5.2	5.3
Eu	1.29	1.24	0.861	0.384	1.50	1.33	0.7	0.183	0.83	0.67
Gd	6.95	—	6.61	3.50	—	—	—	—	—	—
Tb	1.10	1.17	1.13	0.664	0.84	1.24	0.97	0.76	0.76	0.88
Tm	0.512	—	0.526	0.234	—	—	—	—	—	—
Yb	2.42	3.33	2.52	1.19	2.47	4.43	3.13	3.45	2.50	2.90
Lu	0.389	0.54	0.391	—	0.393	0.680	0.52	0.505	0.40	0.46
Ta	0.990	1.16	1.33	0.962	0.81	0.69	1.2	0.70	0.74	0.76
Zr	204.	210.	204.	110.	215.	232.	—	85.	—	—
Hf	5.47	7.1	6.02	3.08	6.7	7.0	5.1	2.8	5.7	4.2
Sc	16.0	15.3	10.5	6.98	21.71	13.59	11.0	4.27	14	9.5
Co	13.3	11.8	7.66	3.44	17.92	9.71	3.0	1.18	11.0	6.6
K/Rb	262.	269.	267.	360.	289.	373.	256.	231.	262.	249.
Rb/Sr	0.49	0.49	0.82	1.05	0.28	0.45	1.33	4.36	0.40	0.62
Ba/Rb	9.26	8.51	6.91	3.93	14.56	9.84	—	3.55	11.00	7.43
Ba/Sr	4.49	4.15	5.65	4.13	4.02	4.40	—	15.46	4.46	4.59
Th/U	2.09	3.29	1.40	0.94	2.89	—	2.58	2.06	—	—

Concentrations are in parts per million.
Ba (sample S70) and all Y and Zr data by XRF. Rb and Sr data from Table 3. All other trace elements by neutron activation.

Table 2e. Trace Element Analyses of Mesozoic Sedimentary Rocks and a Tertiary Greenstone, Kodiak and Sanak Islands, Alaska

	Shumagin Formation (Sanak Island)				Kodiak Formation		Ghost Rocks Formation
	Graywacke		Argillite		Graywacke	Argillite	Greenstone
	S72d	S233b	S33e	S89d	U13a	M5c	15-2e
Cs	0.32	2.6	5.3	5.2	1.7	6.3	0.22
Ba	968.	237.	923.	892.	352.	780.	---
U	1.52	1.35	2.46	2.54	---	---	---
Th	3.21	2.95	6.31	5.83	4.4	7.6	1.59
Y	24.	18.	25.	9.	20.	27.	5.
La	15.2	30.5	23.1	22.1	19.9	25.1	6.0
Ce	28.9	50.1	49.3	42.7	44.1	58.	15.7
Nd	23.7	25.0	26.0	18.1	---	---	---
Sm	3.36	3.78	5.22	4.63	4.01	5.5	2.8
Eu	1.15	1.00	1.25	1.30	0.98	1.38	0.77
Gd	4.30	3.76	4.46	4.21	---	---	---
Tb	0.76	0.52	0.75	0.78	0.53	0.88	0.70
Tm	0.450	0.337	0.446	0.484	---	---	---
Yb	2.07	1.32	1.90	2.47	1.85	2.88	2.34
Lu	0.281	0.154	0.304	0.258	0.312	0.48	0.36
Ta	1.05	1.13	0.846	0.734	0.55	0.9	0.25
Zr	---	---	---	---	---	---	86.
Hf	4.28	3.06	4.03	3.84	5.3	4.9	2.32
Sc	22.7	17.7	23.2	26.3	10.2	18.1	30.3
Co	32.3	29.6	24.2	27.6	14.2	18.3	28.5
K/Rb	502.	292.	275.	274.	266.	250.	320.
Rb/Sr	0.06	0.10	0.49	0.45	0.21	0.82	0.05
Ba/Rb	40.33	8.78	11.68	10.75	12.14	9.40	---
Ba/Sr	2.51	0.91	5.73	4.85	2.50	7.72	---
Th/U	2.11	2.19	2.57	2.30	---	---	---

Concentrations are in parts per million.
Ba (samples U13a, M5c) and all Y and Zr data by XRF. Rb and Sr data from Table 3. All other trace element data by neutron activation.

ily, rather than source heterogeneity, is responsible for the deviation from closed-system behavior. Heterogeneity, if present, is a minor effect. In later sections, we will model the Sanak pluton as an isotopically homogeneous body.

The data for the sedimentary rocks of the Kodiak and Shumagin formations are presented in Table 3. The graywacke Rb contents vary from 24 to 54 ppm, Sr from 136 to 492 ppm, and $^{87}Sr/^{86}Sr$ (calculated for 60 m.y.) from 0.70455 to 0.70498. The argillite Rb contents range from 86 to 125 ppm, Sr from 165 to 190 ppm, and $^{87}Sr/^{86}Sr$ (calculated for 60 m.y.) from 0.70607 to 0.70892. In addition to these differences controlled by lithology, there are also systematic differences in isotopic composition between samples from different islands. Ratios are highest for Kodiak sediments and become progressively lower westward along the arc.

The Causes of Major and Trace Element Variations Within the Intrusions

In this section, we examine the data in more detail in order to explain the geochemical variations within the intrusions. The intrusions display a number of common characteristics. Their trends on an Na-Ca-K diagram (Figure 8) are similar to many calc-alkaline intrusions. Projections of the trends of CaO vs. SiO2 and (Na2O + K2O) vs. SiO2 intersect in Peacock's [1931] calc-alkali (Sanak) and calcic (Shumagin, Kodiak) fields. Most elements display smooth trends on variation diagrams (Figure 3). K, Rb, Cs, Rb/Sr, and Ba/Sr are positively correlated with SiO2, while Fe, Mg, Sc, Co, (Cr), Eu, Eu/Eu* (europium anomaly), Sr, and (Ba) are negatively correlated with SiO2. The highly charged cations Zr, Hf, Ta, Th, U, and REE (except Eu) rise, then fall with increasing SiO2. Of the samples analyzed, the maximum abundances for these highly charged cations (except Ta) occur at 65.5% and 68.0% SiO2 for the Sanak pluton and the Shumagin batholith, respectively.

Several of the trends within the Sanak pluton and Shumagin batholith (increasing Rb, Sr, and Rb/Sr, and decreasing Eu/Eu* and ferromagnesian elements with increasing SiO2) are qualitatively consistent with fractional crystallization involving plagioclase + biotite ± Fe-Ti oxide. However, the behavior of the highly charged cations is not explained using major minerals alone, and no combinations of major and accessory minerals (apatite, zircon) have been found which can explain all of the trace element variations simultaneously. The negative correlation between REE and SiO2 in the Sanak and Shumagin intrusions is not uncommon in granitic rocks [Creasy et al., 1979; Crecraft et al., 1979; Frey and Chappell,

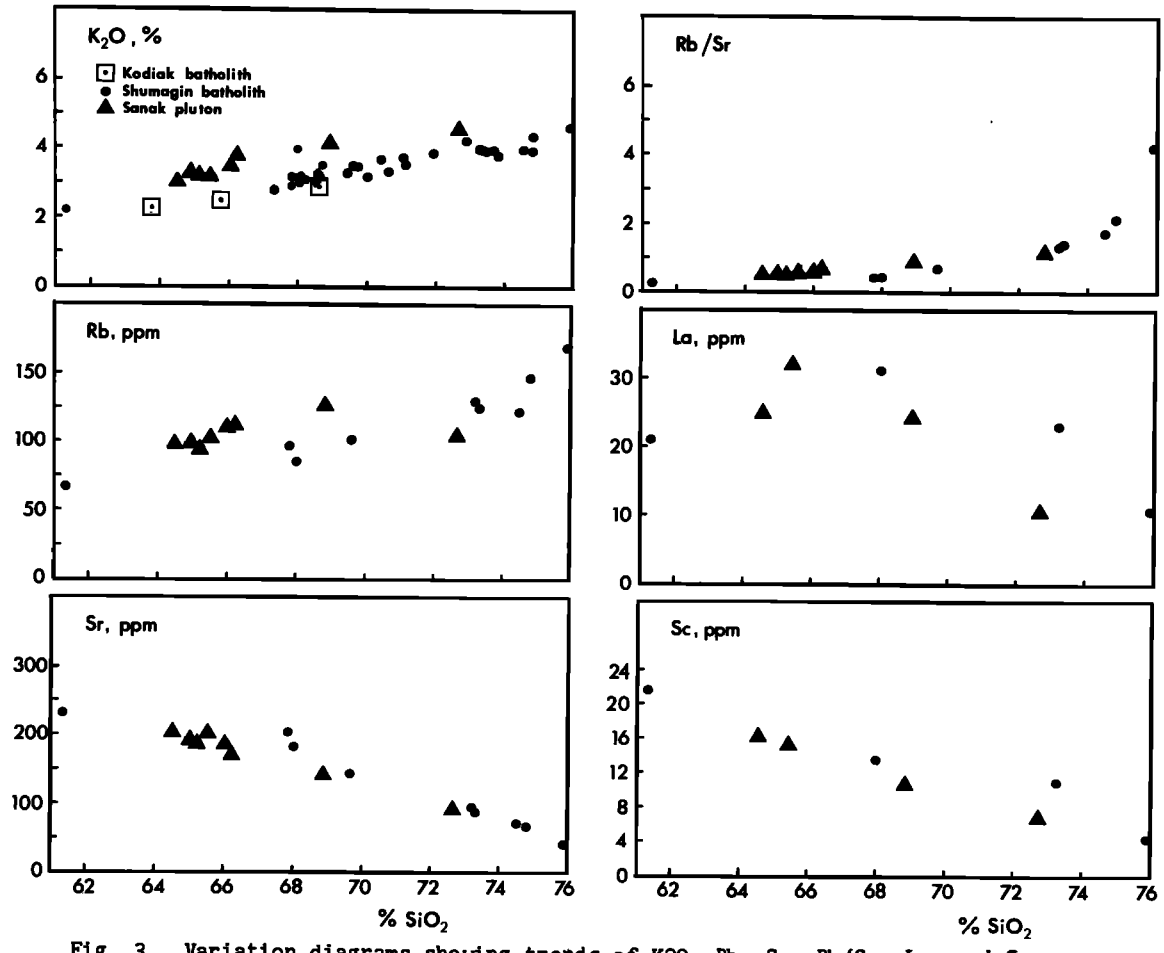

Fig. 3. Variation diagrams showing trends of K2O, Rb, Sr, Rb/Sr, La, and Sc vs. SiO2 for intrusive rocks from the Kodiak, Shumagin, and Sanak intrusions. K2O data are from Table 2 and Hill [1979]; remaining data are from Tables 2 and 3. Kodiak trace element data have been omitted for clarity.

1979; Luddington et al., 1979; Miller and Mittlefehldt, 1979], and no general solution has yet been provided to explain it.

We believe that crystal fractionation is responsible for generating most of the within-intrusion variations described above, modified by alteration as described in the previous section. Other processes which could conceibably generate these variations include (1) alteration alone; (2) mixing of two or more magmas without crystal fractionation; (3) local contamination with wall rocks; and (4) varying degrees of separation of melt from restite [White and Chappell, 1977].

Although the alkalies and (or) alkaline earths have been sufficiently mobile in some samples to obscure age information, the regular trends evident in Figure 3 argue against the hypothesis that alteration has had a dominant effect in establishing the observed element variations. Alteration would tend to increase the scatter of initially regular arrays of data, and it is improbable that alteration of unrelated samples would produce such regular variation patterns as those observed. Process 2 alone is unlikely because three different magmas would have to combine to explain the variations observed in the highly charged cations (La vs. SiO2, Figure 3). Since the Sanak pluton and Shumagin batholith show similar distributions of these elements, it would be necessary for the same kinds of magmas to combine in similar ways in two areas separated by more than 100 km.

While local wall rock contamination is probably responsible for the higher $\delta^{18}O$ of Sanak pluton sample S7b, process 3 fails as a general explanation for the regular geochemical trends because occasional assimilation of heterogeneous sedimentary rocks (Table 2) would produce random scatter on variation diagrams. This process might account for some of the fine-scale variations in Figure 3, but it cannot be responsible for the overall trends.

Finally, unless the accretionary prism was homogenized with respect to Sr isotopes prior to melting, process 4 cannot reconcile the variations observed in major and trace elements with the apparent Sr isotope homogeneity of the Sanak pluton. The most likely explanation for the chemical variations within the intrusions involves a melting event which produced an isotopically homogeneous magma, followed by fractional crystallization which changed the abundances of major and trace elements. More extensive isotopic anlysis of mineral separates from the Shumagin batholith is necessary to establish isotopic homogeneity for that body.

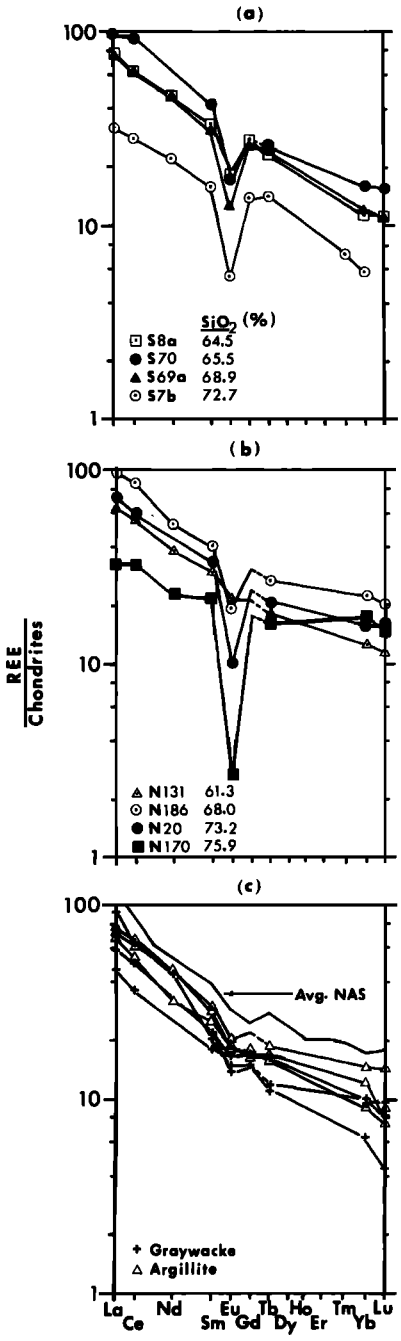

Fig. 4. Chondrite-normalized rare earth diagrams for (a) Sanak pluton, (b) Shumagin batholith, and (c) Upper Cretaceous graywacke and argillite of the Kodiak and Shumagin formations from Kodiak and Sanak islands. Avg. NAS is average of 40 North American shales from Haskin et al. [1966]. Kodiak batholith samples have been omitted for clarity.

Source Materials for the Intrusions

Hudson et al. [1979] proposed that the 50 m.y. old granodiorite intrusions near Prince William Sound, as well as those on the Kodiak, Shumagin, and Sanak islands, formed solely by melting within the accretionary prism. We disagree with this view, and argue below that an additional mafic or intermediate magma component, derived from beneath the accretionary prism, is also required. Our conclusions are based on a comparison of $\delta^{18}O$, Sr contents, and Sr isotopic compositions of the intrusions vs. potential sources in the prism. The models are discussed in a later section. In the following two sections we describe possible sources within and beneath the accretionary prism.

Sources within the accretionary prism. The oldest dated formation in the Kodiak-Shumagin-Sanak belt is the Upper Triassic greenstone- and graywacke-bearing Shuyak Formation [Connelly, 1978], exposed in the northern Kodiak Islands (Figure 2). One allocthonous block of Permian limestone occurs in the Uyak Complex [G. W. Moore, 1969], a tectonic melange which was emplaced after the mid-Early Cretaceous but before the Maestrichtian Kodiak Formation. The major point here is that ancient granitic or metamorphic crust is not likely to be present at depth: the nearest known Precambrian rocks are exposed well north of the Alaska Peninsula [Beikman, 1978]. The thin crust [Berg, 1973; Shor, 1962; Fisher and Holmes, 1980] further supports this conclusion.

Accretion in subduction zones apparently proceeds by the addition of younger units beneath older units [Karig and Sharman, 1975]. Assuming that this geometry applies to the Kodiak-Shumagin-Sanak area at 60 m.y. (and further, that the intrusions rose nearly vertically or at least did not form much nearer the Alaska Peninsula), it seems unlikely that the intrusions would have 'seen' any units within the accretionary prism older than the oldest ones they intrude at the surface - the Upper Cretaceous Kodiak and Shumagin formations. The only other unit which would have been in place 60 m.y. ago is the Ghost Rocks Formation, exposed on Kodiak Island. Accordingly, we have determined the geochemical characteristics of sediments from the Kodiak and Shumagin formations and a greenstone from the Ghost Rocks Formation (Tables 2 and 3).

It is important to estimate the relative proportions of greenstone, graywacke, and argillite in the accretionary prism. Unfortunately, no comprehensive studies of rock proportions exist for this area. Nilsen and Moore [1979] estimate sand:shale ratios of 1:1 to 1:5 for most of the Kodiak Formation, and ratios down to 1:30 for parts of it. The Ghost Rocks Formation may contain as much as 10% volcanic rocks, but very little greenstone or tuff occurs in the much more extensive Kodiak and Shumagin formations.

The Sr contents, $\delta^{18}O$, and $^{87}Sr/^{86}Sr$ ratios for Sanak Island graywacke and argillite used in Table 4 are taken from Table 3. We assume that the range of trace element and Sr and O isotopic variation we observe in the low-grade, metasedimentary rocks presently exposed at the surface would prevail through metamorphism to amphibolite facies at depth [Shaw, 1956; Sighinolfi and Gorgoni, 1978; Dostal and Capedri, 1978].

The concentrations of Sr and other trace elements in melts derived from metasediments depend on the values of D (distribution coefficient) for (bulk solid/liquid) chosen. Without experimental melting studies of graywacke and argillite which provide residual phase identities and proportions, comparable to those of Helz

Table 3. Rb and Sr Contents, and Sr and O Isotope Ratios For Tertiary Granitic and Mesozoic Sedimentary Rocks, Kodiak, Shumagin and Sanak Islands, Alaska

Sample		Rb ppm	Sr ppm	$^{87}Rb/^{86}Sr$	$^{87}Sr/^{86}Sr \pm 2\sigma$	$\delta^{18}O$ o/oo
Granitic Rocks						
Kodiak batholith						
H1-7z	w.r.	80.88	194.2	1.206	0.70651 ± 5	---
K4033	w.r.	99.7	157.0	1.839	0.70700 ± 7	---
Shumagin batholith						
N131	w.r.	65.5	231.0	0.821	0.70605 ± 6	11.4
	plag, fresh	3.95	459.2	0.025	0.70534 ± 4	---
	biotite	315.8	18.38	49.76	0.73914 ± 21	---
N58	w.r.	97.4	203.6	1.385	0.70544 ± 6	11.5
N186	w.r.	86.19	181.3	1.377	0.70610 ± 6	11.0, 10.8
N172	w.r.	103.1	145.1	2.058	0.70657 ± 4	11.3
N20	w.r.	129.5	95.7	3.919	0.70812 ± 9	12.0, 12.2
	plag, fresh	4.78	33.3	0.416	0.70443 ± 6	---
	plag, altered	108.9	166.9	1.890	0.70618 ± 6	---
	kspar	239.7	103.1	6.734	0.71012 ± 5	---
	biotite	626.3	12.69	142.9	0.82555 ± 36	---
N56	w.r.	126.0	88.0	4.147	0.70819 ± 8	12.9
N156	w.r.	123.3	70.9	5.040	0.70908 ± 5	11.5
N169	w.r.	148.2	68.2	6.291	0.71021 ± 5	12.1
N170	w.r.	170.0	40.2	12.25	0.71540 ± 4	12.5, 12.6
Sanak pluton						
S8a	w.r.	98.3	201.3	1.399	0.70662 ± 5	11.8, 12.0
S9a	w.r.	99.3	191.2	1.501	0.70684 ± 6	11.3
	plag, fresh	7.76	187.2	0.120	0.70559 ± 6	---
	plag, altered	13.08	442.	0.276	0.70567 ± 6	---
	kspar	78.6	339.8	0.670	0.70605 ± 6	---
	biotite	340.9	37.85	26.08	0.72521 ± 16	---
S69i	w.r.	97.3	187.1	1.506	0.70668 ± 7	11.2
S70	w.r.	102.4	200.7	1.478	0.70670 ± 6	11.8
	plag, fresh	19.33	369.8	0.151	0.70543 ± 6	---
	plag, altered	30.15	423.1	0.206	0.70558 ± 8	---
	kspar	140.2	289.1	1.404	0.70642 ± 7	---
	biotite	332.3	22.46	42.85	0.74346 ± 23	---
S20a	w.r.	111.5	182.5	1.770	0.70696 ± 5	12.0
S7a	w.r.	113.7	173.0	1.902	0.70700 ± 4	11.8
S69a	w.r.	126.9	143.8	2.556	0.70747 ± 6	11.4
S7b	w.r.	110.6	93.0	3.444	0.70810 ± 8	13.2, 13.2, 13.3
Sedimentary Rocks						
Kodiak Formation						
M5c	argillite	83.9	105.5	2.304	0.71088 ± 6	---
U13a	graywacke	28.9	136.4	0.614	0.70738 ± 7	---
Shumagin Formation, Shumagin Islands						
N135a	argillite	125.3	190.0	1.910	0.70905 ± 6	14.9
N42b	argillite	93.9	171.4	1.586	0.70790 ± 5	13.5
N62	graywacke	54.0	246.0	0.635	0.70552 ± 4	12.9
NY90	graywacke	30.8	471.2	0.189	0.70471 ± 5	---
N16a	graywacke	31.44	405.8	0.224	0.70497 ± 7	13.4
N18b	graywacke	---	---	---	-----	12.8
N65	graywacke	---	---	---	-----	12.1
N233b	graywacke	---	---	---	-----	12.4
Shumagin Formation, Sanak Island						
S33e	argillite	97.2	164.9	1.706	0.70760 ± 7	14.8
S89d	argillite	85.9	181.5	1.370	0.70724 ± 4	14.6, 14.7

TABLE 3. (continued)

Sample	Rb ppm	Sr ppm	$^{87}Rb/^{86}Sr$	$^{87}Sr/^{86}Sr$ ± 2σ	$\delta^{18}O$ o/oo
S72d graywacke	24.5	407.2	0.175	0.70484 ± 5	11.6
S84f graywacke	33.76	492.3	0.199	0.70476 ± 6	13.2
Greenstone					
Ghost Rocks Formation, Kodiak Island 15-2e	7.0	142.0	---	-----	---

w.r. is whole rock.
Rb and Sr concentrations by isotope dilution for all samples except 15-2e (XRF).
Sr isotopes normalized to $^{86}Sr/^{88}Sr$ = 0.1194 and reported relative to Eimer & Amend SrCO3 = 0.70800.

[1973, 1976] for amphibolite melting, it is difficult to make firm estimates of melt compositions. In our models, we use D(Sr) = 1 and 2 to cover a range of likely residual mineral contents. Other authors concerned with modelling sediment melting have used similar figures [Arth and Hanson, 1975].

To consider the effects of melting amphibolite which may be intercalated with metasediments at depth in the prism, we use the Sr data from Hudson et al. [1979] for amphibolites in the Cretaceous Valdez Group near Prince William Sound (Figure 1), which may be in part correlative with the Kodiak and Shumagin formations. This parent is Amphibolite I in Table 4. Because the Sr contents of these amphibolites are quite low for basaltic rocks (58 ppm), we also consider a model amphibolite with a typical mid ocean ridge basalt (MORB) Sr content (135 ppm) (Amphibolite II in Table 4). D(Sr) will not be 1 for partial melting of amphibolite. Using Arth's basalt-andesite distribution coefficients and the residual phases reported by Helz [1976] for partial melting of Picture Gorge Basalt at 970°C, 5 kbar P_{H2O} (57% melt), we calculate D(Sr) = 0.24. Batch melts of amphibolite under these conditions will have Sr = 85 ppm (Amphibolite I) or 200 ppm (Amphibolite II). Basalt-related or -derived melts having more than or equal to 200 ppm Sr require negative sediment contributions for melting of metasedimentary rocks with D(Sr) = 1; thus we use Sr = 190 ppm for Amphibolite II in Table 4, which allows positive sediment contributions. No $\delta^{18}O$ data are available for the Alaskan amphibolites or greenstones. We have taken the mean $\delta^{18}O$ (+10.6 o/oo) of Franciscan Formation (California) metabasalts from Magaritz and Taylor [1976] for these amphibolite models, as examples of metabasalts within an accretionary prism.

Sources beneath the prism. Possible sources beneath the prism include ascending magmas from either the subducted slab (either MORB or remelted MORB) or the mantle wedge between the slab and the prism (arc magmas).

Ocean ridge basalt magma could be injected into the prism during subduction of an active ridge [Marshak and Karig, 1977] or perhaps by extrusion along a number of subducted, leaking transform faults. Alternatively, arc magma may have formed anomalously near the trench. Typical Sr and O data for MORB and arc magmas are given in Table 4. Remelted MORB would likely be in the amphibolite facies (ignoring the difficulties in melting basalt at shallow depth along the top of the subducted slab), and it would likely have suffered low-temperature alteration by exchange with seawater. Sr contents of altered seafloor basalts need not change, whereas both $^{87}Sr/^{86}Sr$ and $\delta^{18}O$ increase during low-temperature alteration [Hart, 1972; Hart et al., 1974; Muehlenbachs and Clayton, 1972; Spooner and Fyfe, 1973]. These effects have been taken into account in the Altered MORB end member in Table 4. The Sr content in the remelted, Altered MORB was determined as described above for the Amphibolite I and II models.

One additional effect must be noted. As they rise through the accretionary prism and begin to

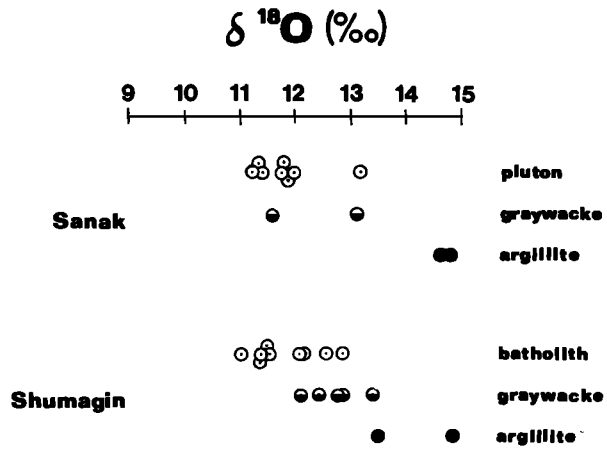

Fig. 5. Variations in $\delta^{18}O$ for intrusions and Shumagin Formation graywacke and argillite from the Sanak and Shumagin islands.

melt their wall rocks, these magmas must crystallize [Bowen, 1928; Taylor, 1978, 1980]; thus it is especially important to our models to estimate the change in Sr content as this occurs. We assume that D(Sr) = 1 for these magmas, which is not unreasonable. For example, Ewart et al. [1973] calculated that Tongan dacites were related to andesites by fractional crystallization of phenocryst assemblages which yield D(Sr) = 1.08 and 1.09 using Arth's [1976] distribution coefficients. Gill [1978] reached similar conclusions, noting the nearly constant Sr contents in several arc suites.

For other trace elements, the distribution coefficients will not be 1, so we must estimate the degree of fractionation required to produce a given amount of sediment melt. Taylor [1980] estimated that for hot wall rock, ratios of cumulates to assimilated wall rocks might approach 1:1, while for cool wall rock, ratios would exceed 3.25:1. We have no direct evidence on the thermal state of the accretionary prism 60 m.y. ago in the Kodiak-Shumagin-Sanak area. Hudson et al. [1979] described amphibolite-grade metamorphic rocks from the Chugach Mountains which correlate with the Kodiak and Shumagin formations. If that area represents a deeper section through the accretionary wedge, it is possible that the wall rocks to the intrusions may have been heated. This is not the normal case for subduction zones, but we are dealing with an anomalously situated igneous belt, which requires an unusual thermal regime.

Byrne [1979] suggested that the Kula-Farallon spreading ridge may have been quite close and parallel to the accretionary prism in the early Tertiary. If so, subduction of hot oceanic lithosphere may have generated unusually high temperatures in the overlying accretionary prism [DeLong et al., 1979]. We assume that the wall rocks were preheated to amphibolite grade, and that one part of basalt (by weight) must fractionate to form one part of sediment-derived melt.

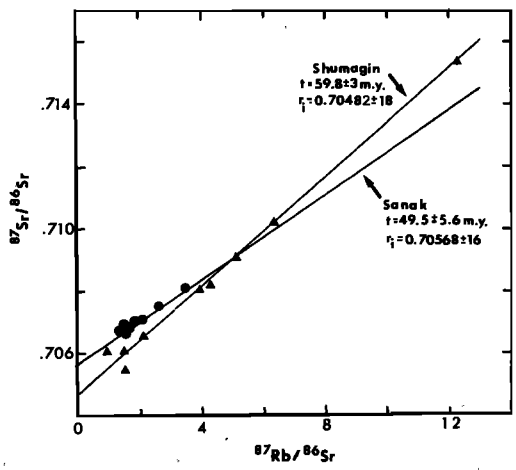

Fig. 6. Whole rock isochrons for the Shumagin batholith (triangles) and the Sanak pluton (circles) showing age and initial ratio. Reported uncertainties are 2σ of the mean. Analytical uncertainties of individual analyses are less than or equal to the size of the symbols.

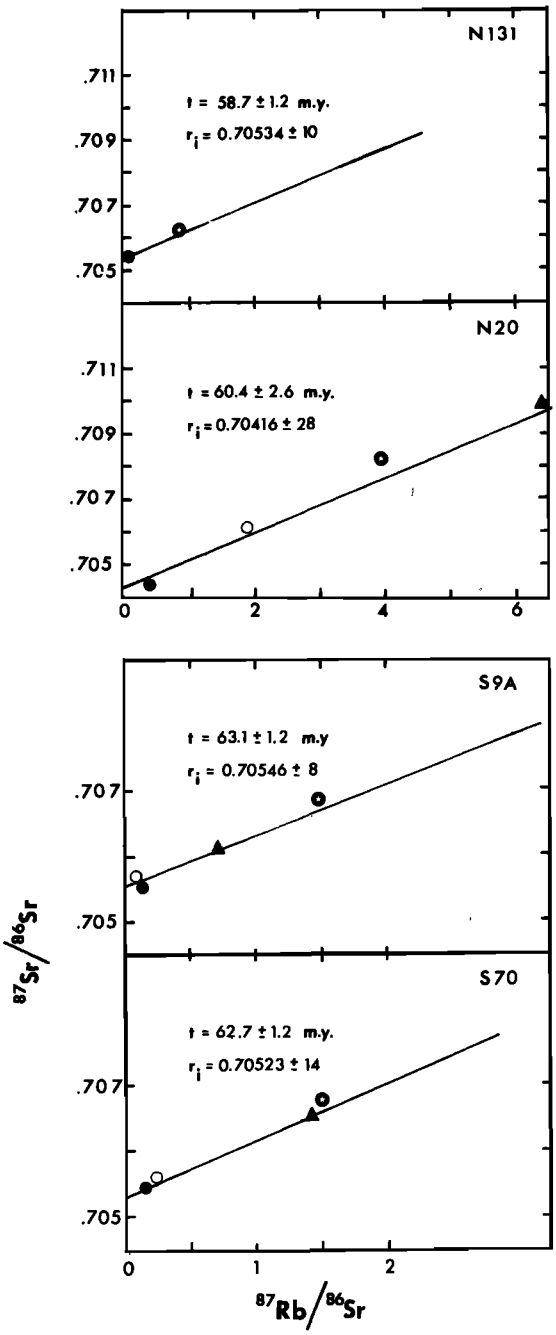

Fig. 7. Mineral isochrons for two samples from the Shumagin batholith (N131, N20) and two from the Sanak pluton (S9a, S70). Symbols used are fresh plagioclase (solid circles), altered plagioclase (open circles), K-feldspar (triangles), and whole rock (encircled stars). Isochrons are fitted using fresh minerals only, and all isochrons pass through biotite (not shown). Reported values are age and initial ratios; uncertainties are 2σ of the mean. Analytical uncertainties for individual analyses are less than or equal to the size of the symbol.

A last point to consider for the thermal effects, which may have a bearing on deciding between models involving 'primary' vs. remelted basalt, is the relative temperatures of MORB vs.

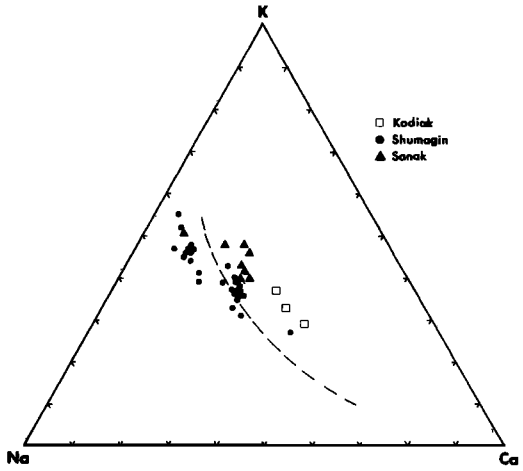

Fig. 8. Ca-Na-K diagram for Kodiak, Shumagin, and Sanak intrusions. Data are from Table 2 and Hill [1979]. Dashed line is average calc-alkaline trend, after Barker and Arth [1976].

remelted-MORB magmas. The liquidus temperature of ocean ridge tholeiite is approximately 1200°C [Tilley et al., 1972]. The temperatures of melts derived from water-saturated amphibolite would be much lower, up to 1000°C [Helz, 1976]. Therefore, a first-cycle basalt should be a more efficient melting agent within the prism than a second-cycle basalt, and would be more likely to be able to cause widespread melting to form batholiths.

We have used measured values where possible and typical analyses from the literature where necessary to characterize the Sr contents, $\delta^{18}O$, and $^{87}Sr/^{86}Sr$ of potential source materials which may have combined to form the intrusions exposed on the Kodiak, Shumagin and Sanak islands. These values, for graywacke, argillite, and amphibolite from within the prism, and for MORB, arc magma, and remelted-MORB from below the prism, are presented in Table 4a. In the following section we use these values and other trace element data to constrain the origin of the intrusions.

Origin of the Intrusions

Sr and O isotope constraints. In this section we will use the isotopic data to model the origin of the Sanak and Shumagin intrusions. Sr and O isotope correlations have been used by several workers to establish mixing models for igneous rocks [Magaritz et al., 1978; James, 1980; Taylor and Silver, 1978; Michard-Vitrac et al., 1980; Halliday et al., 1980; Taylor, 1980]. Theoretical calculations [Langmuir et al., 1978] indicate that samples related by simple mixing should form a smooth curvilinear array with, in the case of Sr vs. O, a positive correlation.

Data for the Shumagin batholith and the Sanak pluton are plotted on a $(^{87}Sr/^{86}Sr)_o$ vs. $\delta^{18}O$ diagram in Figure 9. The two intrusions define essentially horizontal arrays with limited variation in $\delta^{18}O$. The fact that the whole-rock samples are not positively correlated means that the samples do not represent mixing of different proportions of the same end members. Instead, the data are consistent with a model that generates each intrusion from a single batch melting or mixing process which yields a well mixed, homogeneous magma which is subsequently modified by fractional crystallization and alteration.

This is demonstrated again in Figure 10, where $(^{87}Sr/^{86}Sr)_o$ is plotted against (1/Sr). On this diagram, simple two-component end-member mixing is represented by a straight line. The effect of plagioclase fractionation is to shift samples horizontally to lower Sr contents, as indicated on the diagram. The purpose of this diagram is to illustrate that MORB, or melts derived from MORB or Amphibolite II can be mixed with melts derived from sediments of various graywacke: argillite ratios to produce melts with $^{87}Sr/^{86}Sr$ ratios and Sr contents typical of the least fractionated (lowest SiO2, highest Sr) Sanak and Shumagin intrusive samples. A similar set of lines could be drawn between the 'arc basalt magma' and the sediments if a different bulk D(Sr) were used for melting of the sediments.

In order to evaluate and quantify these models, we have carried out a series of calculations for the Sanak pluton. Compositions of possible end members, discussed in a previous section, are presented in Table 4a. The mixing proportions, listed in Table 4b, were determined by simultaneously solving two mass balance equations, one in terms of Sr contents and one for $^{87}Sr/^{86}Sr$ ratios equivalent to those of the least fractionated Sanak pluton sample. Thus, all combinations listed in Table 4b satisfy the constraints imposed by Sr contents and isotopic compositions (i.e., it is the numerical equivalent of Figure 10).

We tested all of these models by calculating the $\delta^{18}O$ that would result from mixing the end members in the proportions indicated. These values are listed in the column headed 'predicted $\delta^{18}O$' in Table 4b. Models are considered acceptable if they match the observed average $\delta^{18}O$ of the Sanak pluton (+11.6 o/oo) within ±10%. This allows a range in $\delta^{18}O$ of +10.4 to +12.8 o/oo.

Models 1, 2, and 3 in Table 4b refer to melting of sources within the accretionary prism. Model 1, melting of sediments only, clearly is unsatisfactory, because it yields $\delta^{18}O$ far higher than observed in the intrusions. Model 2, melting of sediments plus Amphibolite I, satisfies the oxygen constraints if a graywacke-rich sediment melts. Model 3, melting of sediments plus Amphibolite II, produces acceptable $\delta^{18}O$ for all sediment compositions tested.

The final test of any model is that it conform with geologic observations. In this case, we require that the end-member proportions be consistent with the observed geology of the accretionary prism. Both models 2 and 3 fail on this basis, because they require an accretionary wedge which is 50-92% amphibolite (making the simple assumption that amphibolite and metasediments would melt in proportion to their abundance in the prism - probably not true in reality).

We next consider models 4 through 6, which combine sediment melts with magmas derived from beneath the prism. Model 4, melting of sediments by an ascending, remelted MORB magma, matches the oxygen constraints if the sediments are argillite-rich. Model 5, melting of sediments by an ascending MORB-like magma, produces satisfactory

Table 4a. Sr Contents and Sr and O Isotopic Compositions of Possible End Members, With Sanak Pluton Data for Comparison

Component	Sr ppm	$^{87}Sr/^{86}Sr$	$\delta^{18}O$ o/oo
Sources within the prism			
Average graywacke, Sanak Is.	450.	0.70464	12.0
Average argillite, Sanak Is.	173.	0.70611	14.7
Amphibolite I[a]	58.5 (87. in melt)	0.7046	10.6
Amphibolite II	135. (190. in melt)	0.7046	10.6
Sources beneath the prism			
Altered MORB[b]	135. (190. in melt)	0.7039	8.8
MORB[c]	135.	0.7029	5.5
Arc basalt[d]	385.	0.7032	5.5
Sanak pluton	200.	0.70535	11.6

[a] Amphibolite I data from Hudson et al. [1979] and Magaritz and Taylor [1976].
[b] Altered MORB data from Spooner and Fyfe [1973] and Muehlenbachs and Clayton [1972].
[c] MORB data from Hart [1971], Hart and Brooks [1977], and Pineau et al. [1976].
[d] Arc basalt data from Kay [1977].

results for all but the 1:1 G:A mixture. Model 6, melting of sediments by an arc magma, was constructed using bulk D(Sr) = 2 for sediment melting (otherwise, the sediment melts have too much Sr to allow any match to be made). All models (1 through 6) were tested using both D(Sr) = 1 and 2. Models 1 through 5 (having a low-Sr mafic end member) require D(Sr) ≈ 1 for melting of the metasediments in order to satisfy the twin constraints of Sr contents and isotopic composition, while model 6 (having a high-Sr mafic end member) requires that D(Sr) ≈ 2 for metasediment melting.

Table 4b. Sr and O Model Calculations[a]

End Members	Mixing Proportions		Predicted $\delta^{18}O$
1. Sediments only	9.8% Graywacke	90.2% Argillite	14.5
2. Sediments plus Amphibolite I			
1:1 G:A[b]	50.3% Sediments	49.7% Amphibolite	12.1
1:3 G:A	72.9% Sediments	27.1% Amphibolite	13.2
1:5 G:A	85.7% Sediments	14.3% Amphibolite	13.8
3. Sediments plus Amphibolite II			
1:1 G:A	7.9% Sediments	92.1% Amphibolite	10.8
1:3 G:A	18.6% Sediments	81.4% Amphibolite	11.2
1:5 G:A	33.7% Sediments	66.3% Amphibolite	11.8
4. Sediments plus Altered MORB			
1:1 G:A	7.9% Sediments	92.1% MORB	9.2
1:3 G:A	18.6% Sediments	81.4% MORB	9.8
1:5 G:A	33.7% Sediments	66.3% MORB	10.7
5. Sediments plus MORB			
1:1 G:A	36.5% Sediments	63.5% MORB	8.4
1:3 G:A	60.3% Sediments	39.7% MORB	10.7
1:5 G:A	77.3% Sediments	22.7% MORB	12.3
6. Sediments plus Arc Basalt[c]			
1:3 G:A	86.1% Sediments	13.9% Basalt	12.8
1:5 G:A	80.1% Sediments	19.9% Basalt	12.5

[a] See text for details of models.
[b] G:A - graywacke:argillite ratio in the sedimentary component.
[c] Requires D(Sr) = 2 for melting of sedimentary component.

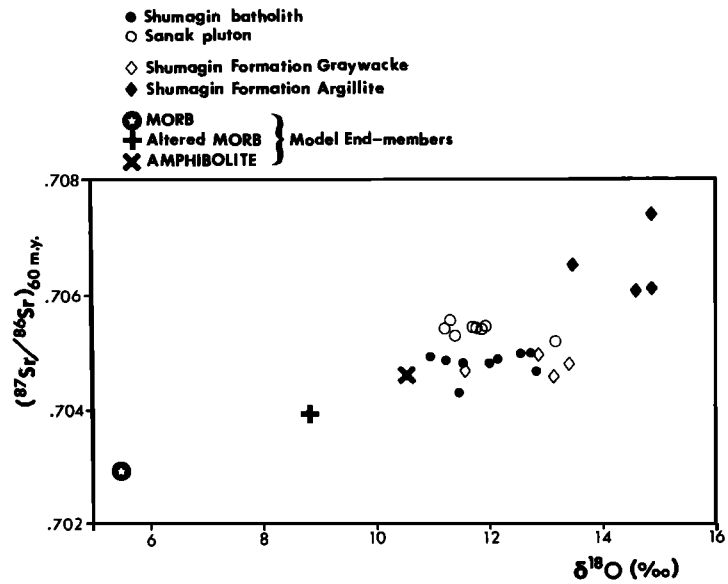

Fig. 9. $^{87}Sr/^{86}Sr$ (calculated for 60 m.y.) vs. $\delta^{18}O$ for the Sanak and Shumagin intrusions, Shumagin Formation sediments, and the end-member compositions chosen for melting models (taken from Table 4). See text for discussion.

Model 6 also provides a satisfactory match to the observed values of $\delta^{18}O$ in the intrusions.

Thus, all three models which involve a magma derived from beneath the prism are acceptable on the basis of the isotope modelling. None of them require a sediment composition which is inconsistent with the surface geology. In the context of the anomalous tectonic setting proposed for this region, all three mafic end members could be geologically reasonable. Therefore, all three models are considered acceptable at this stage, and will be tested against other trace elements in the following section.

Trace element constraints. In this section we examine the three preferred models from the preceding discussion using Rb, Sr, Ba, and the REE. In general, metasediment residues which contain major amounts of biotite, garnet, or hornblende are precluded because they retain too much Rb, Ba, and heavy rare earth elements (HREE). We focus on residues dominated by quartz and plagioclase, with minor garnet and trace

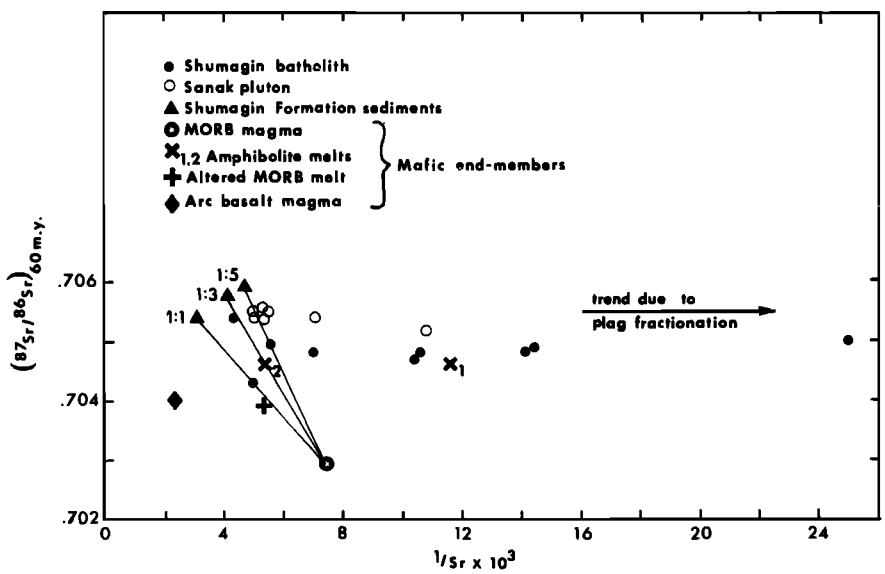

Fig. 10. Mixing diagram showing samples from the Sanak pluton, the Shumagin batholith, and various model end members. The Shumagin Formation sediments are labeled to indicate graywacke:argillite ratios. Values used for mafic end members are taken from Table 4. Straight lines are drawn from MORB to the three sediment mixtures to illustrate our model of MORB magma mixing with sediment melts to form a homogeneous mixture which is subsequently modified by plagioclase separation.

Table 5. Trace Element Compositions of Model Melts

	Starting Compositions				Model 4					Model 5			Model 6			Target Values	
	1	2	3	4	5	6	7	8	9	10	11	12	13	14	15	16	17
Rb	3.	10.	29.	92.	5.	11.	48.	150.	52.	7.	77.	104.	23.	110.	111.	97.	66.
Sr	135.	328.	450.	174.	180.	185.	450.[D(Sr)=1]	174.	197.	138.	193.	201.	305.	192.	186.	200.	231.
							321.[D(Sr)=2]	124.									
Ba	13.	115.	603.	908.	17.	38.	916.	1379.	464.	28.	771.	1013.	253.	1123.	1093.	898.	917.
La*	8.8x	29.1x	69.4x	68.5x	13.0x	29.4x	96.8x	95.6x	51.8x	20.0x	64.6x	78.6x	66.3x	91.8x	89.9x	75.5x	63.6x
Sm	14.4x	22.1x	19.7x	27.2x	17.0x	32.9x	24.4x	33.6x	32.6x	27.8x	28.2x	31.1x	46.4x	33.4x	34.9x	37.6x	29.5x
Eu	14.5x	18.8x	15.5x	18.4x	17.2x	29.0x	14.1x	16.8x	24.7x	24.6x	18.0x	18.2x	34.1x	18.6x	19.9x	18.7x	21.7x
Gd	13.4x	16.1x	16.2x	17.4x	15.0x	27.5x	16.8x	18.1x	24.3x	24.6x	19.0x	19.4x	32.8x	19.9x	20.9x	27.9x	21.0x
Yb	13.2x	13.5x	8.5x	11.0x	16.4x	30.0x	5.5x	7.0x	22.2x	24.1x	12.1x	10.7x	27.0x	9.5x	10.8x	12.1x	12.4x

Columns are described as follows.

1) MORB - sample 13-E, Kay et al. [1970]; Sr from Table 3 for continuity.
2) High alumina basalt, Taylor [1969].
3) Average graywacke, Sanak Island.
4) Average argillite, Sanak Island.
5) 63% melt of MORB using phase proportions from Helz [1976] and basalt D's from Arth [1976].
6) 60% crystallization of (5), using (0.5 plagioclase + 0.5 clinopyroxene); basalt D's from Arth [1976].
7) and 8) 60% melt of graywacke and argillite, respectively. Values shown for bulk D(Sr) = 1 and 2. Other trace elements calculated using rhyolite D's from Arth [1976] residue = (0.47 plagioclase + 0.47 quartz + 0.055 garnet + 0.005 apatite + 0.002 zircon). Apatite and zircon proportions after Hanson [1980].
9) Pluton predicted from model 4: (0.337 sediment melt from a 1:5 G:A source) + (0.663 fractionated, MORB remelt).
10) MORB from (1), 60 % crystallized using (0.5 plagioclase + 0.5 clinopyroxene), basalt D's from Arth [1976].
11) Pluton predicted from model 5: (0.603 sediment melt from a 1:3 G:A source) + (0.337 fractionated MORB).
12) Pluton predicted from model 5: (0.773 sediment melt from a 1:5 G:A source) + (0.227 fractionated MORB).
13) High alumina basalt from (2), 60% crystallized using (0.3 clinopyroxene + 0.06 orthopyroxene + 0.57 plagioclase + 0.07 oxide) after Ewart et al. [1973]; basalt D's from Arth [1976].
14) Pluton predicted from model 6: (0.861 sediment melt from a 1:3 G:A source) + (0.139 fractionated high alumina basalt).
15) Pluton predicted from model 6: (0.801 sediment melt from a 1:5 G:A source) + (0.199 fractionated high alumina basalt).
16) Least evolved sample, Sanak pluton (S8a).
17) Least evolved sample, Shumagin batholith (N131).

* Rare earths have been normalized to the chondrite average of Haskin et al. [1966].
Rb, Sr, and Ba data are in parts per million.

apatite and zircon. We have assumed 60% melting of the metasedimentary source, which requires 60% crystallization of the ascending mafic magmas, as discussed earlier. The results of our calculations are given in Table 5.

The ascending amphibolite melt (model 4) must be derived by at least 60% fusion; otherwise the melt will be so silicic that dacite amphibole D's are required, which yield very low HREE contents in the melt [Arth, 1976; Helz, 1976; Hanson, 1980]. An eclogite residue is not acceptable, again because the HREE in the melt would be too low. Fractionating either (plagioclase + clinopyroxene) or (plagioclase + hornblende) from this melt will yield generally similar trace element contents in fractionated liquids if basalt-andesite D's apply. This model does not give a satisfactory trace element match with the intrusions (compare column 9 with columns 16 and 17, Table 5), because of the large basalt component imposed by the higher $\delta^{18}O$ of the altered basalt parent.

Calculated trace elements for fractionated MORB mixing with melts derived from 1:3 and 1:5 G:A ratios are given in columns 11 and 12 of Table 5. This model yields a good overall match with the real intrusions (columns 16 and 17).

Finally, columns 14 and 15 of Table 4 show that a typical arc basalt (column 2, Table 4) can fractionate and mix with argillite-rich metasediment melts to form a generally satisfactory trace element match to the intrusions, although Ba and the LREE are somewhat high in the model plutons. Nevertheless, in view of the many estimates needed to construct the model, we feel that the results are close enough to make this a viable possibility for explaining the origin of the intrusions.

In summary, comparison of the Sr and O relationships in the intrusions vs. probable source materials rules out the possibility that the intrusions formed solely within the accretionary prism. Metasediments alone are not a suitable source. The high $\delta^{18}O$ of metabasalt in accretionary prisms forces a high proportion of this end member in the intrusions, which makes it impossible to match the abundances of other trace elements in the intrusions. Similar arguments rule out remelted MORB as a source. A magma with an isotopic and trace element content similar to MORB forms a close match in all respects. If the bulk $D(Sr) \approx 2$ during sediment melting, then an arc magma having typically higher Sr than MORB is a possible source, although it does not form as close a match for all trace elements. In the following section we briefly review possible reasons for this magmatic activity.

Tectonic Implications

It is probably not a coincidence that major episodes of both basaltic volcanism and intermediate plutonism occurred in or near the accretionary belt of southern and southwestern Alaska in early Tertiary time. The Paleocene Ghost Rocks Formation on Kodiak Island [G. W. Moore, 1969; Connelly, 1978; Hill, 1979; Reid and Gill, 1980] and the Paleocene and Eocene (?) Orca Group in Prince William Sound [Tysdal et al., 1977] contain abundant mafic to intermediate volcanic rocks intercalated with subaqueous clastic sediments ranging from conglomerate to graywacke and argillite. It is important to note that volcanism and coarse clastic sedimentation occurred simultaneously in these units, indicating that the source of the volcanism was active quite near the continental margin and, by inference, the subduction zone.

The cause of the volcanism remains uncertain, if indeed a single mechanism can explain all of it. Most of the rocks have been metamorphosed, which makes it difficult to interpret their source. Tysdal et al. [1977] suggested that the Orca Group represents volcanism along a leaky transform fault. Reid and Gill [1980] described two groups of volcanics within the Ghost Rocks Formation, one tholeiitic and one calc-alkaline. Sample 15-2e (Table 1) is from the latter group, and calculations (not shown) suggest that this sample has suitable trace element concentrations to act as the mafic component in the granitic intrusions. We feel that the origin of the intrusions will not be completely understood until the origin of the Ghost Rocks Formations volcanism is explained, a study of which is in progress (M. Reid, manuscript in preparation, 1981).

Although Marshak and Karig [1977] suggested that the early Tertiary intrusions within the accretionary prism formed when the Kula-Farallon ridge was subducted at a high angle to the trench, Byrne [1979] reinterpreted the magnetic anomalies in the northeast Pacific to suggest that the ridge was adjacent and subparallel to the continental margin of southwestern Alaska. Whether or not the Kula-Farallon ridge was actually subducted as an active ridge, we believe that the volcanics of the Ghost Rocks Formation and the Orca Group are probably related to Kula-Farallon ridge activity and that the Kodiak, Shumagin, and Sanak intrusions represent hybrids formed when similar magma from the same source intruded the prism.

The Ghost Rocks Formation is intruded by satellites of the Kodiak batholith [Hudson et al., 1979; Hill, 1979], and thus it predates the intrusion. The short time period between emplacement of the Ghost Rocks Formation and intrusion of the Kodiak batholith, discussed earlier, is sufficiently short to allow a genetic relationship, perhaps not by the same pulse which formed the Ghost Rocks Formation flows but of similar material produced at most 3 to 5 m.y. later.

Some such anomalous source is required to explain the early Tertiary magmatism in the accretionary prism because 'normal' (?) arc magmatism, which was centered on and north of the Alaska Peninsula throughout the active periods of the Mesozoic and Cenozoic, occurred there simultaneously with the activity in the accretionary belt [Hudson 1979]. The Paleocene to Eocene Tolstoi Formation on the Alaska Peninsula contains abundant volcanic flows and detritus [Burk, 1965], suggesting that volcanism was coincident with this accretionary pulse. A temporary outward shift of the subduction zone to explain the magmatism within the accretionary belt, proposed by Kienle and Turner [1976] and G. W. Moore [1980], does not explain the continuity of 'normal' arc activity in its accustomed place during the time the 'anomalous' igneous rocks were being emplaced in the accretionary terrane.

Any models which attempt to reconcile the geology of southwestern Alaska in the early Tertiary with the position of ridges, etc., in the northeastern Pacific encounter a major problem, in that the exact location or orientation of southwestern Alaska 60 m.y. ago is not known. Much of Alaska south of the Denali fault consists of a number of allocthonous blocks, which formed somewhere to the south before being emplaced against northern Alaska [Jones et al., 1977; Hillhouse, 1977; Packer and Stone, 1974; Packer et al., 1975; Stone and Packer, 1977]. The work of Packer, Stone, and coworkers suggests that southwestern Alaska has had a complex history beginning far to the south of its present location, finally being emplaced against northern Alaska perhaps in post-Eocene time. While it seems clear that the Kodiak-Shumagin-Sanak accretionary terrane and the Alaska Peninsula arc terrane were part of the same block 60 m.y. ago, we must await more detailed paleomagnetic studies of Paleocene and Eocene rocks from this region before we can be sure how to relate the nature and timing of events within the arc and accretionary terranes with inferred positions of seafloor features.

Implications for I- vs. S-Type Granitoids

Chappell and White [1974] and O'Neil et al. [1977] listed criteria to distinguish between granitic rocks formed by melting igneous materials (I-type) and those formed by melting sedimentary materials (S-type) in eastern Australia. The intrusions we report possess both S-type and I-type characteristics. Among the S-type traits are the lack of hornblende and sphene, the presence of sedimentary-derived xenoliths which contain aluminosilicates and garnet, and $\delta^{18}O$ values > +10.0 o/oo. Among the I-type traits are the rarity of primary muscovite, linear variation diagrams for some elements, relatively high Na2O contents, and $^{87}Sr/^{86}Sr < 0.706$. Not all samples have >1% normative corundum, as in the S-type definition. This ambiguity results from the hybrid nature of the intrusions, in that both I-type ('basalt') and S-type material is present. To add to the complexity, much of the Upper Cretaceous Kodiak and Shumagin formations is composed of young volcanogenic detritus; thus, the S component itself has a significant I component. These complexities suggest that, although the I vs. S concept may be a useful one, blind application of the limits defined in one area may lead to spurious conclusions in another.

Summary

The 60 m.y. intrusions on the Kodiak, Shumagin, and Sanak islands represent an anomalous magmatic event which occurred over 100 km nearer the trench than the contemporaneous main locus of arc activity, centered on and north of the Alaska Peninsula. The metamorhpic xenocrysts and xenoliths suggest the presence of a crustal component within the intrusions. The strontium and oxygen isotope compositions and strontium contents require that an additional component, having lower $^{87}Sr/^{86}Sr$ and $\delta^{18}O$, be present as well if the crustal component was similar to the presently exposed Upper Cretaceous sedimentary rocks of the accretionary prism. Basalt is an obvious choice for this component, either as first-cycle magma generated from the mantle or as second-cycle, remelted basalt derived from the subducted slab. Partial melting models using proportions of end members deduced from the Sr and O relations suggest that first-cycle basalt better explains the trace element patterns observed in the intrusions. MORB is a suitable parent, as is the Paleocene Ghost Rocks Formation sample 15-2e. Typical arc basalts having Sr > 200 ppm may be suitable if the bulk D for Sr during metasediment melting was approximately 2. The mafic volcanics of the Ghost Rocks Formation and the Kodiak-Shumagin-Sanak intrusions may be genetically related, both ultimately derived from the Kula-Farallon ridge activity. This ridge may have been adjacent to or subducted beneath the accretionary prism 60 m.y. ago.

Acknowledgments. Part of this work was submitted by Hill in partial fulfillment of Ph.D. requirements at the University of California at Santa Cruz, and part was undertaken during Hill's tenure as National Research Council Postdoctoral Fellow with the U.S. Geological Survey. Work in Alaska and at Santa Cruz was supported by NSF grant EAR74-13266A01, ACS grant PRF-2884-G3, and grants from Exxon, Union Oil Company, the Chancellor's Patent Fund of the University of California, and the Penrose Bequest Fund of the Geological Society of America. The Alaska Branch of the U.S. Geological Survey provided logistical support in the field. The Sr isotopic data were acquired in Stan Hart's lab, supported by NSF grant 7803342-EAR. Casey Moore kindly provided the Sanak and Shumagin samples analyzed in this study. Jim Gill's expertise in setting up the Santa Cruz XRF lab and in supervising Hill's thesis are appreciateed. Fred Frey, L.A. Haskin, and Hugh Millard provided access to their neutron activation labs, and Doug Blanchard, Joyce Brannon, Jeff Jacobs, and Roy Knight made room in their busy schedules to help get the data out. We are grateful to each of these people and institutions for their support. Discussions with or critical reviews by Fred Barker, G. C. Brown, Tim Byrne, Fred Frey, Jim Gill, Stan Hart, Travis Hudson, Bob Kay, Casey Moore, Zell Peterman, Mary Reid, and Nobu Shimizu have helped focus our thinking on these rocks.

References

Arth, J. G., Behavior of trace elements during magmatic processes - A summary of theoretical models and their applications, J. Res. U.S. Geol. Surv., 4, 41-47, 1976.

Arth, J. G., and G. N. Hanson, Geochemistry and origin of the early Precambrian crust of northeastern Minnesota, Geochim. Cosmochim. Acta, 39, 325-362, 1975.

Barker, F., and J. G. Arth, Generation of trondhjemite-basalt suites, Geology, 4, 596-600, 1976.

Bateman, P. C., L. D. Clark, N. K. Huber, J. G. Moore, and C. D. Rinehart, The Sierra Nevada batholith: A synthesis of recent work across the central part, U.S. Geol. Surv. Prof. Pap., 414-D, 46 pp., 1963.

Beikman, H., Preliminary geologic map of Alaska,

U.S. Geol. Surv., Reston, Va., 1978.
Berg, E., Crustal structure in Alaska, Tectonophysics, 20, 165-182, 1973.
Bowen, N. L., The Evolution of the Igneous Rocks, Princeton University Press, Princeton, N. J., 1928.
Burk, C. A., Geology of the Alaska Peninsula - Island arc and continental margin, parts 1, 2, 3, Mem. Geol. Soc. Am., 99, 1965.
Byrne, T., Late Paleocene demise of the Kula-Pacific spreading center, Geology, 7, 341-344, 1979.
Chappell, B. W., and A. J. R. White, Two contrasting granite types, Pac. Geol., 8, 173-174, 1974.
Clayton, R. N., and T. K. Mayeda, The use of bromine pentafluoride in the extraction of oxygen from oxides and silicates for isotopic analysis, Geochim. Cosmochim. Acta, 27, 43-52, 1963.
Connelly, W., Uyak Complex, Kodiak Islands, Alaska: A Cretaceous subduction complex, Geol. Soc. Am. Bull., 89, 755-769, 1978.
Connelly, W., and J. C. Moore, Geologic map of the northwestern side of the Kodiak Islands, Alaska, U.S. Geol. Surv. Open File Map, 77-382, 1977.
Creasy, J. W., G. N. Eby, and S. A. Wood, Geochemistry of the Hart Ledge Complex, White Mountain batholith, New Hampshire, Geol. Soc. Am. Abstr. Programs, 11, 406, 1979.
Crecraft, H. R., W. P. Walsh, and S. H. Evans, Jr., Chemical evolution and development of compositional gradients in a silicic magma, Geol. Soc. Am. Abstr. Programs, 11, 406, 1979.
DeLong, S., W. Schwarz, and R. Anderson, Thermal effects of ridge subduction, Earth Planet. Sci. Lett., 44, 239-246, 1979.
Dostal, J. and S. Capedri, Uranium in metamorphic rocks, Contrib. Mineral. Petrol., 66, 409-414, 1978.
Ewart, A., W. B. Bryan, and J. B. Gill, Mineralogy and geochemistry of the younger volcanic islands of Tonga, S.W. Pacific, J. Petrol., 14, 429-465, 1973.
Faure, G., Principles of Isotope Geology, John Wiley and Sons, New York, 1977.
Fisher, M. A., and M. L. Holmes, Large-scale structure of deep strata beneath Kodiak shelf, Alaska, Geol. Soc. Am. Bull., 91, 218-224, 1980.
Frey, F. A., and B. W. Chappell, Granites from southeast Australia: Constraints on source mineralogy and composition imposed by rare earth element abundances, Geol. Soc. Am. Abstr. Programs, 11, 428, 1979.
Friedman, I., and J. D. Gleason, A new silicate intercomparison standard for ^{18}O analysis, Earth Planet. Sci. Lett., 18, 124, 1973.
Gill, J. B., Role of trace element partition coefficients in models of andesite genesis, Geochim. Cosmochim. Acta, 42, 709-724, 1978.
Grantz, A., Aerial reconnaissance of the outer Shumagin Islands, Alaska, U.S. Geol. Surv. Prof. Pap., 475-B, B106-B109, 1963.
Halliday, A. N., W. E. Stephens, and R. S. Harmon, Rb-Sr and O isotopic relationships in three zoned Caledonian granitic plutons, Southern Uplands, Scotland: Evidence for varied sources and hybridisation of magmas, J. Geol. Soc. London, 137, 329-348, 1980.
Hanson, G. N., Rare earth elements in petrogenetic studies of igneous systems, Annu. Rev. Earth Planet. Sci., 8, 371-406, 1980.
Hardenbol, J., and W. A. Berggren, A new Paleogene numerical time scale, in Contributions to the Geologic Time Scale, AAPG Stud. in Geol. #6, pp. 213-234, Am. Assoc. Pet. Geol., Tulsa, 1978.
Hart, S. R., K, Rb, Cs, Sr and Ba contents and Sr isotope ratios of ocean floor basalts, Philos. Trans. R. Soc. London, Ser. A, 268, 573-587, 1971.
Hart, S. R., and C. Brooks, The geochemistry and evolution of the early Precambrian mantle, Contrib. Mineral. Petrol., 61, 109-128, 1977.
Hart, S. R., A. J. Erlank, and E. J. D. Kable, Seafloor basalt alteration: Some chemical and Sr isotopic effects, Contrib. Mineral. Petrol., 44, 219-230, 1974.
Harvey, P. K., D. M. Taylor, R. D. Hendry and K. Bancroft, An accurate fusion method for the analysis of rocks and chemically related materials by X ray fluorescence spectrometry, X-Ray Spectrom., 2, 33-44, 1973.
Haskin, L. A., F. A. Frey, R. A. Schmitt, and R. H. Smith, Meteoritic, solar and terrestrial rare-earth distributions, in Physics and Chemistry of the Earth, vol. 7, edited by L. H. Ahrens et al., pp. 167-321, Pergammon, New York, 1966.
Helz, R. T., Phase relations of basalts in their melting range at PH2O = 5 kb. as a function of oxygen fugacity, J. Petrol., 14, 249-302, 1973.
Helz, R. T., Phase relations of basalts in their melting range at PH2O = 5 kb., part II, Melt compositions, J. Petrol., 17, 139-193, 1976.
Hill, M. D., Volcanic and plutonic rocks of the Kodiak-Shumagin Shelf, Alaska: Subduction deposits and near-trench magmatism, Ph. D. thesis, Univ. of Calif., Santa Cruz, 1979.
Hillhouse, J. W., Paleomagnetism of the Triassic Nikolai Greenstone, McCarthy Quadrangle, Alaska, Can. J. Earth. Sci., 14, 2578-2592, 1977.
Hudson, T., Mesozoic plutonic belts in Southern Alaska, Geology, 7, 230-234, 1979.
Hudson, T., G. Plafker, and Z. E. Peterman, Paleogene anatexis along the Gulf of Alaska margin, Geology, 7, 573-577, 1979.
Jacobs, J. W., R. L. Korotev, D. P. Blanchard, and L. A. Haskin, A well-tested procedure for instrumental neutron activation analysis of silicate rocks and minerals, J. Radioanal. Chem., 40, 93-114, 1977.
James, D. E., Oxygen and strontium isotopic composition of Quaternary andesites from the Andes of S.W. Colombia, Year Book Carnegie Inst. Washington, 79, 452-455, 1980.
Jones, D. L., N. L. Silberling, and J. Hillhouse, Wrangellia - A displaced terrane in northwestern North America, Can. J. Earth Sci., 14, 2565-2577, 1977.
Karig, D. E., and G. F. Sharman, Subduction and accretion in trenches, Geol. Soc. Am. Bull., 86, 377-389, 1975.
Kay, R. W., Geochemical constraints on the origin of Aleutian magmas, in Island Arcs, Deep Sea Trenches and Back-Arc Basins, pp. 229-242, edited by M. Talwani and W. C. Pitman, AGU, Washington, D. C., 1977.
Kay, R. W., N. J. Hubbard, and P. W. Gast,

Chemical characteristics and origin of oceanic ridge volcanic rocks, J. Geophys. Res., 75, 1585-1610, 1970.
Kienle, J., and D. L. Turner, The Shumagin-Kodiak batholith - A Paleocene magmatic arc?, Geol. Rep. 51, pp. 9-11, Alaska Dep. of Nat. Res., Juneau, 1976.
Langmuir, C. H., R. D. Vocke, G. N. Hanson, and S. R. Hart, A general mixing equation with applications to Icelandic basalts, Earth Plan. Sci. Lett., 37, 380-392, 1978.
Lanphere, M. A., and D. L. Jones, Cretaceous time scale from North America, in Contributions to the Geologic Time Scale, AAPG Stud. in Geol. #6, pp. 259-268, Am. Assoc. Pet. Geol., Tulsa, 1978.
Luddington, S., W. N. Sharp, D. McKowan, and F. Barker, The Redskin granite - A Proterozoic example of thermogravitational diffusion?, Geol. Soc. Am. Abstr. Programs, 11, 469, 1979.
Luth, W. C., R. H. Jahns, and O. F. Tuttle, The granite system at pressures 4 to 10 kilobars, J. Geophys. Res., 69, 759-773, 1964.
Magaritz, M., and H. P. Taylor, Jr., Oxygen, hydrogen and carbon isotope studies on the Franciscan Formation, Coast Ranges, California, Geochim. Cosmochim. Acta, 40, 215-234, 1976.
Marshak, R. S., and D. E. Karig, Triple junctions as a cause for anomalously near-trench igneous activity between the trench and volcanic arc, Geology, 5, 233-236, 1977.
Matsuhisa, Y., O. Matsubaya, and H. Sakai, Oxygen isotope variations in magmatic differentiation processes of the volcanic rocks in Japan, Contrib. Mineral. Petrol., 39, 277-288, 1973.
Michard-Vitrac, A., F. Albarede, C. Dupuis, and H. P. Taylor, Jr., The genesis of Variscan (Hercynian) plutonic rocks: Inferences from Sr, Pb, and O studies on the Maldeta Complex, Central Pyrenees, Contrib. Mineral. Petrol., 72, 57-72, 1980.
Miller, C. F., and D. W. Mittlefehldt, Rare earth element depletion accompanying differentiation of felsic plutonic rocks, Geol. Soc. Am. Abstr. Programs, 11, 479-480, 1979.
Moore, G. W., Preliminary geologic map of Kodiak Island and vicinity, U.S. Geol. Surv. Open File Rep., 271, 1967.
Moore, G. W., New formations of Kodiak and adjacent islands, Alaska, U.S. Geol. Surv. Bull., 1274-A, A27-A35, 1969.
Moore, G. W., Arc-type volcanic rocks anomalously near oceanic trenches, Geol. Soc. Am. Abstr. Programs, 12, 142-143, 1980.
Moore, J. C., Complex deformation of Cretaceous trench deposits, southwestern Alaska, Geol. Soc. Am. Bull., 84, 2005-2020, 1973a.
Moore, J. C., Cretaceous continental margin sedimentation, southwest Alaska, Geol. Soc. Am. Bull., 84, 595-614, 1973b.
Moore, J. C., Geologic and structural map of the outer Shumagin Islands, southwestern Alaska, U.S. Geol. Surv. Misc. Invest. Ser. Map, I-815, 1974a.
Moore, J. C., Geologic and structural map of the Sanak Islands, southwestern Alaska, U.S. Geol. Surv. Misc. Invest. Ser. Map, I-817, 1974b.
Muehlenbachs, K., and R. N. Clayton, Oxygen isotope studies of fresh and weathered submarine basalts, Can. J. Earth Sci., 9, 172-184, 1972.
Nilsen, T. H., and G. W. Moore, Reconnaissance study of Upper Cretaceous to Miocene stratigraphic units and sedimentary facies, Kodiak and adjacent islands, Alaska, U.S. Geol. Surv. Prof. Pap., 1093, 34, 1979.
Norrish, K., and J. T. Hutton, An accurate X-ray spectrographic method for the analysis of a wide range of geological samples, Geochim. Cosmochim. Acta, 33, 431-453, 1969.
O'Neil, J. R., S. E. Shaw, and R. H. Flood, Oxygen and hydrogen isotope compositions as indicators of granite petrogenesis in the New England batholith, Australia, Contrib. Mineral. Petrol., 62, 313-328, 1977.
Packer, D. R., and D. B. Stone, Paleomagnetism of Jurassic rocks from southern Alaska, and their tectonic implications, Can. J. Earth Sci., 11, 979-997, 1974.
Packer, D. R., G. E. Brogan, and C. B. Stone, New data on plate tectonics of Alaska, Tectonophysics, 29, 84-102, 1975.
Peacock, M. A., Classification of igneous rocks, J. Geol., 39, 65-67, 1937.
Pineau, F., M. Javoy, J. W. Hawkins, and H. Craig, Oxygen isotope variations in marginal basin and ocean-ridge basalts, Earth Planet. Sci. Lett., 28, 299-307, 1976.
Reed, B. L., and M. A. Lanphere, Age and chemistry of Mesozoic and Tertiary plutonic rocks in south-central Alaska, Geol. Soc. Am. Bull., 80, 23-44, 1969.
Reed, B. L., and M. A. Lanphere, Alaska-Aleutian Range batholith - geochronology, chemistry and relation to circum-Pacific plutonism, Geol. Soc. Am. Bull., 84, 2583-2610, 1973.
Reid, M., and J. B. Gill, Near-trench volcanism, Kodiak Island, Alaska: Implications for ridge-trench encounter, Geol. Soc. Am. Abstr. Programs, 12, 148-149, 1980.
Savin, S. M., and S. Epstein, The oxygen and hydrogen isotope geochemistry of clay minerals, Geochim. Cosmochim. Acta, 34, 25-42, 1970.
Shaw, D. M., Geochemistry of pelitic rocks, part III, Major elements and general geochemistry, Geol. Soc. Am. Bull., 67, 25-42, 1956.
Shor, G. G., Jr., Seismic refraction studies off the coast of Alaska: 1956-1957, Bull. Seismol. Soc. Am., 52, 37-57, 1962.
Sighinolfi, G. P., and C. Gorgoni, Chemical evolution of high-grade metamorphic rocks - Anatexis and remotion of material from granulite terrains, Chem. Geol., 22, 157-176, 1978.
Spooner, E. T. C., and W. S. Fyfe, Sub-sea-floor metamorhpism, heat and mass transfer, Contrib. Mineral. Petrol., 42, 287-304, 1973.
Steiger, R. H., and E. Jaeger, Subcomission on geochronology: Convention on the use of decay constants in geo- and cosmo-chemistry, Earth Planet. Sci. Lett., 36, 359-362, 1977.
Stone, D. B., and D. R. Packer, Tectonic implications of Alaska Peninsula paleomagnetic data, Tectonophysics, 37, 183-201, 1977.
Streckeisen, A. L., Plutonic rocks - Calssification and nomenclature recommended by the IUGS subcommission on the systematics of igneous rocks, Geotimes, 18(10), 26-30, 1973.
Taylor, H. P., Jr., Oxygen and hydrogen isotope studies of plutonic granitic rocks, Earth Planet. Sci. Lett., 38, 177-210, 1978.
Taylor, H. P., Jr., and L. T. Silver, Oxygen isotope relationships in plutonic igneous rocks

of the Peninsular Ranges batholith, Southern and Baja California, U.S. Geol. Surv. Open-File Rep., 78-701, 423-426, 1978.

Taylor, S. R., Trace element chemistry of andesites and associated calcalkaline rocks, Proceedings of the Andesite Conference, edited by A. R. McBirney, State of Oregon, Dep. Geol. Miner. Res. Bull., 65, pp. 43-64, 1969.

Tilley, C. E., R. N. Thompson, and P. A. Lovenbury, Melting relations of some oceanic basalts, Geol. J., 8, 59-64, 1972.

Turner, D. L., R. B. Forbes, and C. W. Naeser, Radiometric ages of Kodiak Seamount and Giacomini Guyot, Gulf of Alaska - Implications for circum-Pacific tectonics, Science, 182, 579-581, 1973.

Tuttle, O. F., and N. L. Bowen, Origin of granite in the light of experimental studies in the system $NaAlSi_3O_8$-$KAlSi_3O_8$-SiO_2-H_2O, Geol. Soc. Am. Mem., 74, 1958.

Tysdal, R. G., J. E. Case, G. R. Winkler, and S. H. B. Clark, Sheeted dikes, gabbro and pillow basalt in flysch of coastal southern Alaska, Geology, 5, 377-383, 1977.

White, A. J. R., and B. W. Chappell, Ultrametamorphism and granitoid genesis, Tectonophysics, 43, 7-22, 1977.

(Received October 31, 1980;
revised May 4, 1981;
accepted May 19, 1981.)

JOURNAL OF GEOPHYSICAL RESEARCH, VOL. 86, NO. B11, PAGES 10591–10606, NOVEMBER 10, 1981

Petrogenesis of Garnet Two-Mica Granites in the Ruby Mountains, Nevada

R. W. KISTLER

U.S. Geological Survey, Menlo Park, California 94025

E. D. GHENT

Department of Geology, The University of Calgary Calgary Alberta, T2N 1N4, Canada

J. R. O'NEIL

U.S. Geological Survey, Menlo Park, California 94025

Garnet-two-mica granites of Jurassic (160 ± 3 m.y.) and Cretaceous (83 ± 1.3 m.y.) ages intrude amphibolite facies metasedimentary rocks of Precambrian age and lower Paleozoic sedimentary rocks in the northern part of the Ruby Mountains, Nevada. High initial $^{87}Sr/^{86}Sr$ and high values of $\delta^{18}O$ for minerals suggest a dominantly sedimentary source for the magmas. Total rare-earth contents are low and less fractionated ($Ce_N/Yb_N = 10$) than granitic rocks of similar composition in the Sierra Nevada and show a negative Eu anomaly ($Eu/Eu^* = 0.57$). These data are consistent with melting in the stability field of plagioclase with little contribution to the melt from refractory minerals such as zircon, sphene, and apatite. Minor euhedral garnets are manganese-rich and magnesium-poor ($al_{60}sp_{34}py_{3.6}gr_{2.8}$) compared to garnet ($al_{79}sp_6py_{13}gr_2$) in the intruded metamorphic rocks and show an increase in manganese and a decrease in calcium in the outer few microns. Fractionation of magnesium-iron between garnet and biotite, and of sodium-potassium between K-feldspar and plagioclase in the granites suggest submagmatic equilibration temperatures, in the range of 365° to 505°C, whereas oxygen isotope equilibration temperatures for two granites are higher at 480° and 570°C. The compositions of the granites plot near minimum melting compositions in the water-saturated quartz-albite-orthoclase system. Comparison of muscovite plus quartz stability, the water-saturated granite solidus, and experimental garnet-melt equilibria suggests pressures of crystallization no lower than about 3.5 kbar. This pressure is compatible with that estimated from garnet-plagioclase-sillimanite-quartz equilibria for the intruded metasedimentary rocks.

INTRODUCTION

The Ruby Mountains are a northerly trending range about 120 km long and 17 km wide within the Basin and Range province in east-central Nevada (Figure 1). The northern part of the range is an igneous and metamorphic complex that is separated from an essentially complete Paleozoic section of quartzites, carbonates, and shales in the southern part of the range by granitic rocks of Mesozoic and Cenozoic age [*Willden et al.*, 1967; *Willden and Kistler*, 1969, 1979; *Howard et al.*, 1979]. The age of the protolith of schists, quartzites, marbles, and gneisses that are exposed in the northern part of the range has been considered to be Precambrian by *King* [1878], *Blackwelder* [1935], *Misch* [1960], *Misch and Hazzard* [1962], *Snelson* [1957], and *Willden and Kistler* [1969, 1979] but has been assigned to the Paleozoic by *Hill* [1916], *Sharp* [1939, 1942], *Howard* [1966, 1971, 1980], and *Snoke* [1980]. In the roof pendants within the granitic rock complex in the east-central Ruby Mountains, the basal Cambrian Prospect Mountain quartzite lies depositionally with angular discordance on schists and impure quartzites [*Kistler and Willden*, 1969; *Willden and Kistler*, 1979]. Here a part of the protolith of the metamorphic complex can be shown in the field to be Precambrian.

Tertiary potassium-argon and rubidium-strontium mineral ages in the granitic and metamorphic rocks of the northern Ruby Mountains are not primary and can be shown to reflect the age of cooling during uplift, along a gently southwest plunging arch of regional extent with a trend of about N30°E. Formation of the arch began during emplacement of the 36 m.y. old Harrison Pass pluton that is exposed in the central part of the range [*Kistler and O'Neil*, 1975]. Petrologic and experimental geochemical data indicate that the crystalline terrane was at depths that ranged from about 13 to 8 km prior to uplift and erosion beginning 36 m.y. ago. Metamorphic facies and the youngest reduced mineral ages (Figure 1) indicate that rocks from the greatest depth are now exposed along the west side of the range. The Ruby Range represents the east flank of the uplift, the central part of which probably collapsed during late Cenozoic Basin and Range faulting and is buried beneath the alluvial valley to the west of the range.

Mesozoic granitoids exposed by erosion to these deep crustal levels in the Ruby Mountains are far to the east of the principal loci of the major composite batholiths of similar age like the Sierra Nevada in California [*Kistler et al.*, 1971]. Petrologic, chemical, and isotopic data are all compatible in suggesting that the Ruby Mountains plutons were emplaced as magmas that could have been derived from source materials like their enclosing wall rocks. In this respect, the plutons are unusual relative to most other Mesozoic plutons that occur in the major composite batholiths to the west. A reconnaissance chemical and isotopic study of the plutons and their wall rocks in the northern Ruby Mountains is the subject of this paper.

Copyright © 1981 by the American Geophysical Union.

Paper number 1B0834.
0148-0227/81/001B-0834$01.00

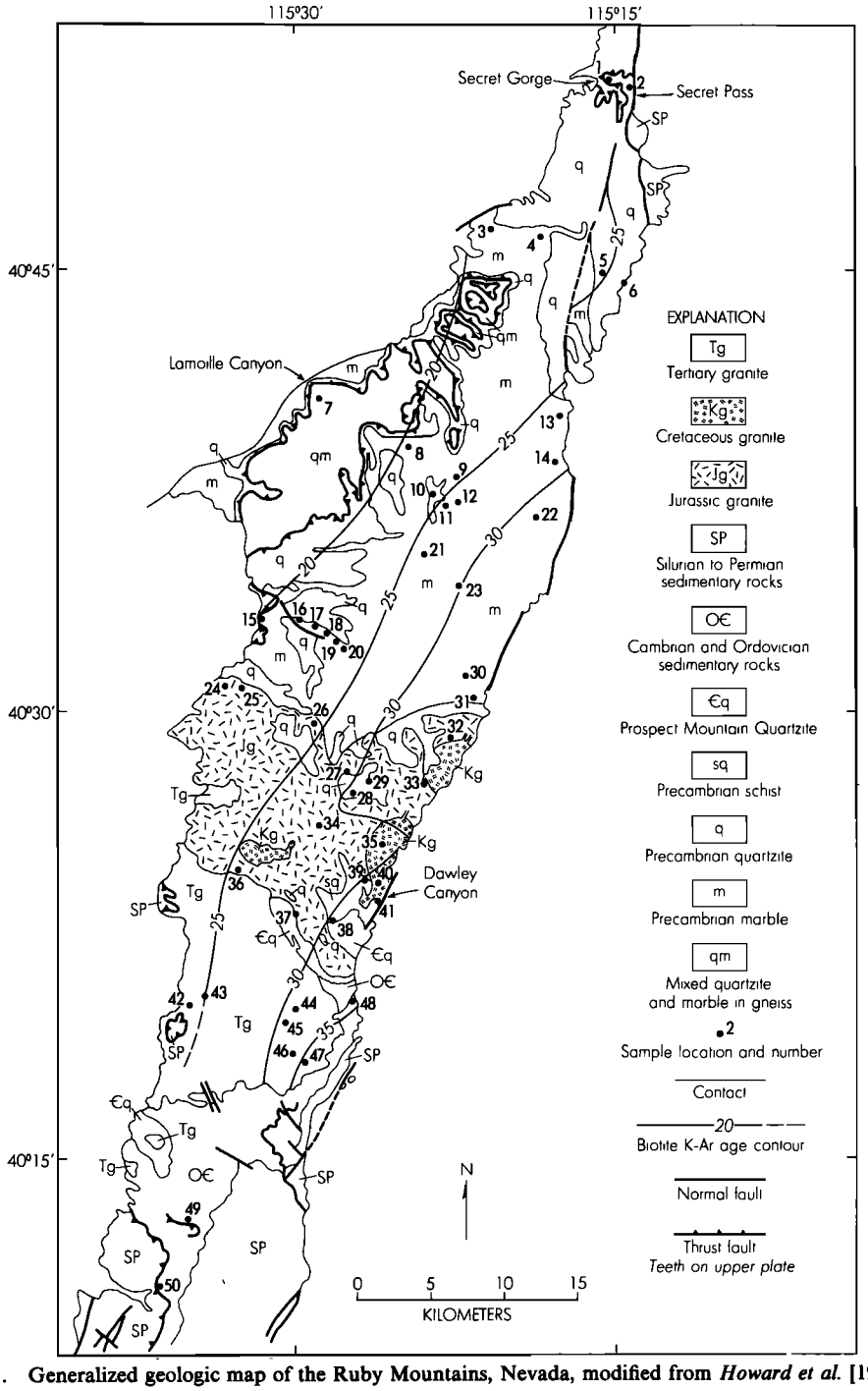

Fig. 1. Generalized geologic map of the Ruby Mountains, Nevada, modified from *Howard et al.* [1979].

ANALYTICAL TECHNIQUES

All chemical analyses for major elements were made by the rapid rock technique [*Shapiro and Brannock,* 1962]. Rubidium and strontium contents were determined by XRF, using a direct comparison method with standard samples of similar bulk compositions [*Doering,* 1968], or by standard isotope-dilution techniques. Strontium isotope ratios were determined on a 30.5-cm-radius, 90° sector mass spectrometer, using a rhenium triple filament mode of ionization, automatic peak switching, and digital output. The $^{86}Sr/^{88}Sr$ ratios were normalized to 0.1194. Replicate analyses of the Eimer and Amend $SrCO_3$ gave a mean $^{87}Sr/^{86}Sr$ value of 0.7081. Duplicate isotope dilution analyses of unknowns and analyses of U.S. Geological Survey (USGS) standard rocks indicate that rubidium and strontium abundances are known to ±1.0% and Rb/Sr is known to ±1.4%. The Rb/Sr values determined by XRF are known to ±3.0% [*Doering,* 1968]. The whole-rock isochron ages were computed using λ_β $^{87}Rb = 1.42 \times 10^{-11}$ yr^{-1} and by the least squares regression analysis of *York* [1969]. Analyses in duplicate of separate splits of unspiked whole-rock powders during this study show that the standard deviation of an individual $^{87}Sr/^{86}Sr$ value is ±0.0156%. For some samples, only a spiked isotope dilution analysis was made, and for these, the $^{87}Sr/^{86}Sr$ values were calculated. There is good agreement between $^{87}Sr/^{86}Sr$ values in those

specimens where both spiked and unspiked analyses were made (Table 2). Rare-earth element and Ba analyses are by isotope dilution using a fully automated 30.5-cm-radius, 90° sector and a 15-cm-radius, 60° sector National Bureau of Standards (NBS) (Shields) design mass spectrometers in the laboratory of G. N. Hanson, State University of New York, Stony Brook. The analytical precision for each REE is about 1%, but sample heterogeneity may cause larger variations in replicate analyses of these low concentration trace elements. Trace elements Cs, Zr, Th, and Ta determinations are by instrumental neutron activation analysis (INAA), using large Ge(Li) (12%) detector. Overall accuracy of these results is ±10% (J. J. Rowe, written communication, 1974). Electron probe analyses were made on an ARL-EMX-SM electron probe microanalyzer at the University of Calgary. Data were reduced using the correction procedures of *Bence and Albee* [1968] and *Albee and Ray* [1970] and the programs of *Nicholls et al.* [1977]. Oxygen isotope compositions were determined by the BrF_5 technique of *Clayton and Mayeda* [1963], using conventional isotope ratio mass spectrometry.

METAMORPHIC COMPLEX

The general features of the metamorphic complex are described by *Howard* [1966, 1971, 1980], *Snoke* [1980], and *Willden and Kistler* [1979]. Regional metamorphism reached amphibolite facies. The metamorphism can be subdivided into higher-grade sillimanite-almandine and lower grade staurolite-kyanite subfacies, and in the western part of the range the sillimanite isograd dips shallowly westward and crosscuts structure [*Howard,* 1966]. Retrograde metamorphism occurs in places in the west-central part of the range where muscovite replaces sillimanite, biotite, and K-feldspar. In the western part of the range and in the vicinity of Secret Pass, cataclastic and mylonite textures postdate the amphibolite facies crystallization [*Snoke,* 1980]. Locally above the cataclastic rocks are klippen of unmetamorphosed Paleozoic strata that were emplaced in the Tertiary [*Willden et al.,* 1967, *Snoke,* 1980].

The prograde amphibolite metamorphism of the northern Ruby Mountains can be classified as Mirashiro's low-pressure intermediate type [*Howard,* 1966] or belonging to bathozone 4 of *Carmichael* [1978]. The annealing of tectonite textures, retrograde metamorphism, cataclasis, and reduced mineral K-Ar, Rb-Sr, and U-Pb ages are all evidence of a very complicated thermal history in the range subsequent to the amphibolite facies metamorphism. Structural and stratigraphic studies in the southern Ruby Mountains [*Willden and Kistler,* 1967, 1979] indicate that the last folding in the range took place during the Late Ordovician. A Precambrian deformation in the metamorphic complex is indicated by the angular discordance between these rocks and the overlying basal Cambrian Prospect Mountain quartzite [*Kistler and Willden,* 1969; *Willden and Kistler,* 1979].

Chemical analyses of representative lithologies in the metamorphic complex are given in Table 1, and their locations are shown on Figure 1. Normative quartz, albite, and orthoclase of these specimens normalized to 100% are plotted on a ternary diagram in Figure 2.

Some of the analyzed specimens are known to have been magmas at one stage in their history on the basis of their field relations and textures. Specimen SP1-A is a coarse-grained leucosome enclosed in biotite schist SP2 in the Secret Pass area. Specimen 'Lam Can' is a biotite granite gneiss that intruded strongly deformed marble in Lamoille Canyon. Specimens RM-3-66, RM-40-66, RM-42-66, and RM-44-66 are granite gneisses that intruded quartzites and marbles exposed on the west side of the range. RM-24A-67 is a fine-grained porphyritic granite dike, and RM-24B-67 and RM-24D-67 are two specimens from an amphibolite that intruded carbonates, quartzites, and quartzofeldspathic schists in the Secret Gorge area. The other gneisses, quartzofeldspathic schists, and mica schists are compositionally equivalent to shale (SP-2), argillite (RM-27-66), and arkoses or graywacke (SP1-C, RM-19-67, RM-24F-67) [*Pettijohn,* 1963].

In outcrop, the quartzofeldspathic schist beds have a compositional layering manifested by garnet rich zones (RM19-67) or by variable mica contents (RM27-67). The central portion of the quartzofeldspathic schist beds are commonly aplite-pegmatites that apparently developed in place during a Cretaceous thermal event. Some layering of quartzofeldspathic schists in the limbs of large overturned isoclinal folds can be traced into hinge areas of the folds where it is obliterated as the rocks grade to pegmatite.

Rubidium, strontium, and $^{87}Sr/^{86}Sr$ for specimens of whole-rocks from the metamorphic complex are given in Table 2, and these data are plotted on a strontium evolution diagram in Figure 3. The data scatter widely on the evolution diagram, but two bounding reference isochrons of 1450 m.y. and 550 m.y. encompass the points.

Specimens that lie along the 1450 m.y. reference isochron include the two specimens from the diabase dike in the Secret Pass area (RM-24B-67, RM-24D-67), granitic augen gneiss specimens from the west-central part of the range (RM-3-66, RM-42-66, RM-45-66), and two quartzofeldspathic schist specimens from the Secret Pass area (RM-24F-67, SP1-C). To the north in Idaho, *Armstrong* [1975] has dated, at about 1450 m.y., a granitic rock body that intruded highly deformed and metamorphosed quartzites, argillites, and carbonates. The data for this granitic rock plot along the 1450 m.y. reference isochron for the Ruby Mountains specimens (Figure 3). *Evans and Zartman* [1981*a*] have dated Precambrian granites of almost this age in east-central Idaho.

Specimens that lie along the 550 m.y. reference isochron include two-mica granite (RM-37, 66, RM-9-66), quartzofeldspathic schist (RM-27-66), biotite granite gneiss from Lamoille Canyon ('Lam Can,' LC1, 5, 7, 8), quartzites from Secret Gorge (RM-24C-67, RM-24G-67), and biotite schist from the same area (SP-2). The biotite granite gneiss ('Lam Can') is a coarse-grained granitoid rock that intruded strongly folded marble. The dispersion of points for the specimens from this pluton, which were all collected from the same outcrop, about the reference isochron is indicative that the pluton has not been a closed chemical system since its emplacement. The apparent 550 m.y. age derived from the slope of the reference isochron that includes data from this pluton, therefore, is interpreted to represent an approximate time of metamorphism in the metamorphic complex.

To the north, near McCall, Idaho, *Armstrong et al.* [1977] dated by the Rb-Sr whole-rock technique, at about 550 m.y. age, gneisses from a granodiorite-granite unit. The data [*Armstrong et al.,* 1977] for this unit plot along the 550 m.y. reference isochron for the Ruby Mountains specimens (Figure 3). *Evans and Zartman* [1981*b*] have dated Cambrian granitoids as old as 540 m.y. in east-central Idaho. The crystalline complex of the northern Ruby Mountains has an igneous and metamorphic history similar to Precambrian crystalline complexes in central Idaho.

TABLE 1. Chemical analyses and C.I.P.W. Norms of Representative

	Granitoids, Diabase, and Metasediments of the Metamorphic Complex										Map
	9	2	25	20	37	18	17	1	1	1	2
Specimen	Lam Can	SPI-A	RM-3-66	RM-40-66	RM-9-66	RM-42-66	RM-44-66	RM-24A-67	RM-24B-67	RM24D-67	SPI-C
SiO_2	72.8	71.4	72.0	74.4	75.0	75.7	74.4	72.4	53.5	55.3	78.3
Al_2O_3	15.1	16.0	15.1	14.0	14.2	14.6	14.9	13.7	6.4	17.0	12.0
Fe_2O_3	0.08	0.10	0.20	0.30	0.18	0.27	0.20	0.23	0.66	2.0	00.00
FeO	1.2	1.0	1.1	0.92	0.84	0.64	1.0	2.2	7.6	5.8	1.2
MgO	0.21	0.07	0.36	0.23	0.16	0.11	0.05	0.35	15.3	3.3	0.07
CaO	1.4	0.98	1.9	1.0	1.0	1.8	1.7	1.4	11.5	5.9	0.95
Na_2O	3.6	3.6	3.6	3.0	2.6	4.5	4.5	3.0	1.1	3.3	3.0
K_2O	4.7	5.7	4.5	5.1	4.7	2.2	2.4	4.8	0.52	2.4	3.0
H_2O	0.04	0.12	0.45	0.07	0.07	0.06	0.09	0.60	0.37	0.54	0.17
H_2O^+	0.39	0.87	0.11	0.41	0.78	0.38	0.33	0.24	0.79	1.2	0.42
TiO_2	0.13	0.02	0.10	0.10	0.08	0.00	0.00	0.23	0.65	1.2	0.02
P_2O_5	0.05	0.07	0.33	0.09	0.07	0.04	0.04	0.12	0.09	0.35	0.02
MnO	0.00	0.06	0.01	0.00	0.02	0.00	0.04	0.02	0.20	0.13	0.02
CO_2	<0.05	<0.05	0.04	0.00	<0.05	0.00	0.01	0.11	0.04	0.10	<0.05
Sum	100	100	100	100	100	100	100	99	99	99	99
Rb	117	256	140	154	146	69	70	120	8	78	95
Sr	187	204	659	340	161	319	128	312	70	505	143
C.I.P.W. norms											
q	29.92	25.81	29.50	34.62	39.23	37.35	34.67	32.29	2.0	7.84	46.67
c	1.67	2.30	1.74	1.94	3.20	1.80	1.93	1.33	...	...	2.16
or	27.86	33.69	26.59	30.14	27.86	13.00	14.18	28.82	3.15	14.67	17.88
ab	30.55	30.47	30.46	25.38	22.07	37.23	38.08	25.78	9.54	28.88	25.60
an	6.64	4.40	7.02	4.37	4.52	8.67	8.11	6.26	11.27	25.32	4.62
di	...	...	...	...	...	...	...	...	37.37	2.13	...
en	0.53	0.17	0.90	0.57	0.40	0.27	0.13	0.89	25.66	7.94	0.18
fs	1.93	1.83	1.71	1.28	1.30	0.95	1.75	3.56	8.56	7.02	2.23
mt	0.12	0.15	0.29	0.44	0.26	0.39	0.29	0.34	0.98	3.0	...
il	0.25	0.04	0.19	0.19	0.15	...	...	0.44	1.27	2.36	0.04
ap	0.12	0.17	0.78	0.21	0.17	0.10	0.10	0.29	0.22	0.86	0.05
cc	...	...	0.09	...	...	...	0.02	0.25	0.09	0.23	...

Total Fe as Fe_2O_3.

The apparent metamorphic age of 550 m.y. in these metamorphic terranes has been enigmatic, but it is often detected; with occurrences in the Albion Range (536 m.y. hornblende, K-Ar [*Armstrong and Hills,* 1967]), in the Wasatch Range in Utah (559 to 535 m.y. biotite ages in the Precambrian Farmington Canyon Complex and a 560 m.y. hornblende age in the Precambrian Little Willow Series [*Hashad,* 1964]), biotite K-Ar ages of about 550 m.y. in the Precambrian metamorphic complex in northern Idaho [*Armstrong,* 1975], 550 m.y. age for gneiss near McCall, Idaho [*Armstrong et al.,* 1977], and in the Ruby Mountains [*Willden and Kistler,* 1969; this paper]. On an outline map of the western United States (Figure 4), these areas are shown relative to the position of the western margin of Precambrian sialic crust, as indicated by initial $^{87}Sr/^{86}Sr$ isotope compositions in Mesozoic and Cenozoic plutonic rocks [*Kistler and Peterman,* 1973, 1978; *Armstrong et al.,* 1977]. The boundary in Nevada and eastern California is modified from *Kistler and Peterman* [1978] on the basis of unpublished data in these areas [*Kistler et al.,* 1980; R. W. Kistler and D. E. Lee, unpublished data, 1979]. The margin developed during rifting of western North America during the late Precambrian [*Stewart,* 1972; *Kistler and Peterman,* 1978]. Both of the Idaho areas are in the continental crust along the margin, whereas the Ruby Mountains are 120 km and the Wasatch Range is 400 km into the continent from the margin, respectively. The 550 m.y. metamorphic age in these areas could represent the time of cooling, after heating prior to rifting of the continental crust in earliest Cambrian time, to temperatures low enough to permit rocks and minerals to retain radiogenic daughter products.

MESOZOIC AND CENOZOIC GRANITIC ROCKS

The metamorphic complex of the northern Ruby Mountains is pervasively invaded by Mesozoic and Tertiary granites. Emplacement of the granitic magmas was mostly passive, since lithologic sequences and structures in the gneisses, schists, quartzites, and carbonates have not been destroyed [*Howard,* 1971]. The predominant granitic rock type is two-mica garnet-bearing granite with widely variable texture from equigranular to pegmatitic. Geochronologic studies indicate that the plutons are of Jurassic, Cretaceous, and Oligocene age [*Willden et al.,* 1967; *Willden and Kistler,* 1969].

Jurassic Granite

Granite of Jurassic age intruded the metamorphic complex, and in the central Ruby Mountains a pluton of this age is well exposed (Figure 1). On the east side of the range the granite is predominantly an equigranular two-mica variety with considerable textural diversity grading to pegmatitic in diffuse pods and stringers. On the west side of the range, the two-mica granite is more coarse-grained, and pegmatitic facies are more abundant. An intrusive contact between the textural types could not be found in the field, and the granite is mapped as a single pluton. The pluton intruded subhorizontal sheetlike bodies of granite gneiss, and other inclusions or roof pendants are locally abundant and include quartzite, schist, granite

Igneous and Metamorphic Rocks of the Ruby Mountains, Nevada

Number				Jurassic Granite				Cretaceous Granite			Oligocene Granite	
39	1	2	23	24	36	37	37	41	35	Sierra Nevada	42	46
RM-19-67	RM-24F-67	SP-2-	RM-27-66	64W66	RM-47-66	RM-11-66	J1	RM-17-66	RM-19-66	S-SR4-73	63W51	RM-1-67
75.8	80.6	65.2	68.0	73.6	72.0	74.3	74.9	73.5	73.8	73.3	69.6	74.8
14.0	9.4	16.0	15.5	14.0	16.1	15.0	14.0	14.8	15.2	14.2	14.2	13.7
0.31	0.39	1.1	0.50	0.80	0.39	0.15	0.11	0.46	0.19	1.88[1/]	0.70	0.27
0.60	1.6	4.5	1.0	1.4	1.1	0.56	0.60	0.44	1.1		3.0	0.84
0.12	0.11	2.8	0.39	0.18	0.19	0.11	0.16	0.16	0.24	0.14	0.92	0.06
0.62	0.42	0.62	2.6	0.92	0.84	0.74	0.86	0.84	0.73	1.34	2.2	0.40
2.8	1.6	1.0	1.8	2.9	3.8	3.9	5.2	3.6	3.0	3.2	3.4	4.0
2.9	4.0	5.2	8.8	4.7	4.4	4.4	3.5	4.5	4.7	5.0	3.1	5.2
0.31	0.41	0.24	0.04	0.15	0.10	0.04	0.06	0.11	0.09	...	0.12	0.09
0.89	0.21	2.0	0.34	0.71	0.79	0.51	0.52	0.78	0.58	0.28	1.18	0.24
0.00	0.07	0.73	0.12	0.06	0.11	0.05	0.02	0.06	0.12	0.27	0.47	0.00
0.16	0.07	0.013	0.33	0.04	0.08	0.09	0.07	0.22	0.20	0.08	0.19	0.03
0.10	0.01	0.06	0.00	0.01	0.04	0.06	0.08	0.04	0.04	0.04	0.06	0.10
0.00	0.02	<0.05	0.12	0.00	0.05	<0.05	<0.05	<0.05	<0.05	0.00	0.03	0.00
99	99	100	100	100	100	100	100	100	100	99.58	99	100
316	85	207	212	204	188	232	199	283	274		110	344
108	168	63	479	173	126	91	33	86	112		406	26
46.89	54.91	31.63	18.79	35.79	30.50	32.89	28.84	33.90	36.22	32.98	30.85	30.09
5.51	1.87	7.94	...	2.57	3.75	2.69	0.26	3.02	4.33	1.27	1.78	0.84
17.14	24.06	30.86	52.00	27.77	26.02	26.02	20.67	26.72	27.78	29.60	18.32	30.73
23.69	13.78	8,50	15.23	24.54	32.17	33.03	43.97	30.61	25.39	23.98	28.77	33.84
2.03	1.66	2.24	8.22	4.30	3.65	3.09	3.81	2.74	2.31	5.62	9.48	1.79
...	...	...	...	...	...	...	...	...	...	...	...	...
0.30	0.28	7.00	0.65	0.45	0.47	0.27	0.40	0.40	0.60	0.41	2.29	0.15
1.03	2.56	6.29	0.82	1.83	1.59	0.93	1.13	0.41	1.74	1.51	4.27	1.51
0.45	0.58	1.60	0.73	1.16	0.57	0.22	0.16	0.67	0.28	0.68	1.02	0.39
...	0.14	1.39	0.23	0.11	0.21	0.10	0.04	0.11	0.23	0.51	0.89	...
0.38	0.17	0.31	0.78	0.10	0.19	0.21	0.17	0.52	0.47	0.19	0.45	0.07
...	0.05	...	0.27	...	...	...	...	...	...	...	0.07	...

gneiss, amphibolite, and calc-silicate rocks. The pluton, like all other rocks, is characterized by cataclastic texture in the westernmost part of the range.

In thin section, the granite texture varies from allotriomorphic to hypidiomorphic granular. Equally abundant oligoclase, microcline, and quartz are the major minerals. Muscovite occurs as embayed crystals intergrown with biotite and as oriented crystals in plagioclase. The muscovite appears to be in textural equilibrium in the granite and of magmatic origin. Brown to yellow brown biotite also occurs as discrete crystals. Accessory apatite occurs as discrete needlelike crystals in feldspar. Zircon, allanite, and garnet are the other accessory minerals. Opaque oxides are absent from the rock, and lines of minute fluid inclusions, some containing colorless cubic crystals, occur in the quartz.

Chemical analyses of three specimens of the granite and of a pegmatite dike (J-1) that emanates from the granite into the intruded rocks are given in Table 1, and the locations of the specimens are shown on Figure 1. Normative quartz, albite, and orthoclase of these specimens normalized to 100% are plotted on a ternary diagram in Figure 5. Electron microprobe analyses of muscovite, biotite, and garnet and of plagioclase and alkali feldspar from two specimens from this pluton are given in Tables 3, 4, 5, and 6, respectively.

The muscovite analyses are on an anhydrous basis with total iron expressed as FeO. Compared to other muscovites considered to be magmatic, these muscovites have lower Si contents than muscovites from the Monte Rosa granite, western Alps (6.13 to 6.16 atoms per formula unit versus 6.23 to 6.42 atoms per formula unit) [*Frey et al.*, 1976, p. 157]. Iron plus magnesium contents of muscovites from the Ruby Mountains Jurassic granite are comparable to those of the Monte Rosa granites reported by *Frey et al.*, [1976] and to those of the Murrumbidgee batholith reported by *Joyce* [1973].

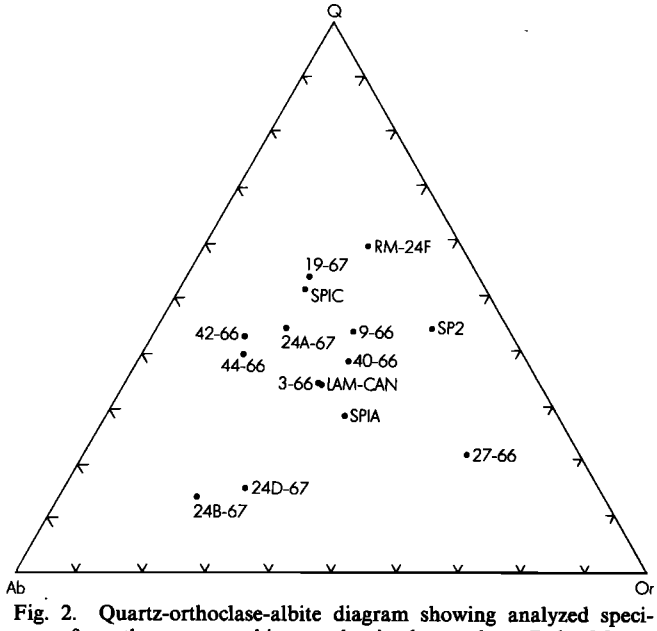

Fig. 2. Quartz-orthoclase-albite diagram showing analyzed specimens from the metamorphic complex in the northern Ruby Mountains, Nevada.

TABLE 2. Rubidium-Strontium Data for Representative Rocks of the Metamorphic Complex

Map Number	Specimen	Rock Type	Rb, ppm	Sr, ppm	Rb/Sr	$^{87}Rb/^{86}Sr$	$^{87}Sr/^{86}Sr$
9	'Lam Can'	granite	117.4	187.7 187.0	0.63	1.81	0.72328†
9	LC-1	granite	150	226.7	0.66	1.92	0.72050† 0.72056
9	LC-5	granite	135	192.8	0.70	2.03	0.72287† 0.72280
9	LC-7	granite	160	200.4	0.80	2.32	0.72522† 0.72534
9	LC-8	granite	173.2	237.3	0.73	2.11	0.72147
2	SPIA	pegmatite	256	203.9	1.26	3.66	0.74415†
25	RM-3-66	granite	140*	659*	0.21	0.61	0.71570†
37	RM-9-66	granite	146.1 146.5	161.2 159.5	0.91 0.92	2.67	0.72730†
27	RM-36-66	granite	176.7	141.4	1.25	3.63	0.74460† 0.74450
1	RM-24A-67	granite	120.4	312.8	0.38	1.12	0.71787†
1	RM-7B-67	granite	110.7	315.2	0.35	1.02	0.71728
1	RM6-67	granite	131	261.3	0.50	1.45	0.71800†
18	RM-42-66	granite	69*	319*	0.20	0.58	0.71714†
20	RM-40-66	granite	154*	340*	0.45	1.30	0.71782†
17	RM-44-66	granite	70*	128*	0.55	1.59	0.71753†
1	RM-24B67	diabase	8*	70*	0.14	0.33	0.70983†
1	RM-24D67	diabase	77.8	505.4	0.15_4	0.45	0.71318† 0.71336
29	RM-37-66	granite	201.	103	1.96	5.68	0.75132
19	RM-41-66	granite	93	234	0.40	1.15	0.71875
16	RM-45-66	granite	85	395	0.22	0.62	0.71615
2	SPI-C	quartzofeldspathic schist	94.9	143.2	0.66	1.91	0.74164† 0.74210
39	RM-19-67	quartzofeldspathic schist	316.0	160.8	1.96	5.72	0.76651† 0.76733
2	SP-2	mica-schist	207.1	63.0	3.29	9.58	0.78142† 0.78223
23	RM-27-66	quartzofeldspathic schist	211.7	478.9	0.44	1.28	0.71727
23	RM-12-68	quartzofeldspathic schist	158	350	0.45	1.31	0.71796
1	RM-24G-67	quartzite	24.5	20.1	1.21	3.51	0.73233† 0.73134
1	RM-24C-67	quartzite	50.2	62.2	0.81	2.34	0.72693
1	RM-7A-67	quartzofeldspathic schist	118.4	169.9	0.69	2.01	0.72792
1	RM-27F-67	quartzofeldspathic schist	85	168*	0.51	1.47	0.73519
1	RM-24H-67	granite	67	263	0.26	0.74	0.71262
14	RM-43-68	granite	144	233.4	0.62	1.79	0.72945† 0.72991

* Rb and Sr concentrations by XRF; all other Rb and Sr concentration by isotope dilution.
† $^{87}Sr/^{86}$ measured; all other $^{87}Sr/^{86}Sr$ calculated.

In granitic rocks, biotites coexisting with muscovites and garnet typically have higher total aluminum than biotites which coexist with hornblende or those which occur as the sole ferromagnesium mineral [*Nockolds*, 1947; *Joyce*, 1973]. The biotites from the granite show similar tetrahedral plus octahedral aluminum to the average values quoted by *Nockolds* [1947] for biotite coexisting with muscovite and have similar values to biotites coexisting with muscovites and garnets [*Brammall and Harwood*, 1932; *Joyce*, 1973].

Garnets from the granite are spessartine and almandine-rich with very low grossular and pyrope contents. Compared to garnet phenocrysts from silicic volcanic rocks (Figure 6), garnets from the granite have lower pyrope and grossular contents and higher Mn contents. Garnet compositions from other granites, e.g., Westerly muscovite granite, Australia [*Joyce*, 1973], are similar to garnet compositions in the Ruby Mountains granite. In compositional profiles of garnets from specimen RM-31-66, there is a sharp incresae in the MnO content in the outer 5-20 μm, whereas calcium, iron, and magnesium typically show a decrease in the outer 20 to 30 μm (Figure 7).

Electron microprobe and X ray determination of coexisting alkali feldspar and plagioclase in Jurassic granite specimen RM-11-66 indicate that the plagioclase is albite to sodic oligoclase and the alkali feldspar is microcline (Table 6).

Rubidium, strontium, the $^{87}Sr/^{86}Sr$ determined for the specimens of the granite pluton and for a granite dike that intruded granite gneiss specimen 'Lam Can' about 20 km to the north of the granite pluton are given in Table 7 and their locations are shown on Figure 1. These data are plotted on a stron-

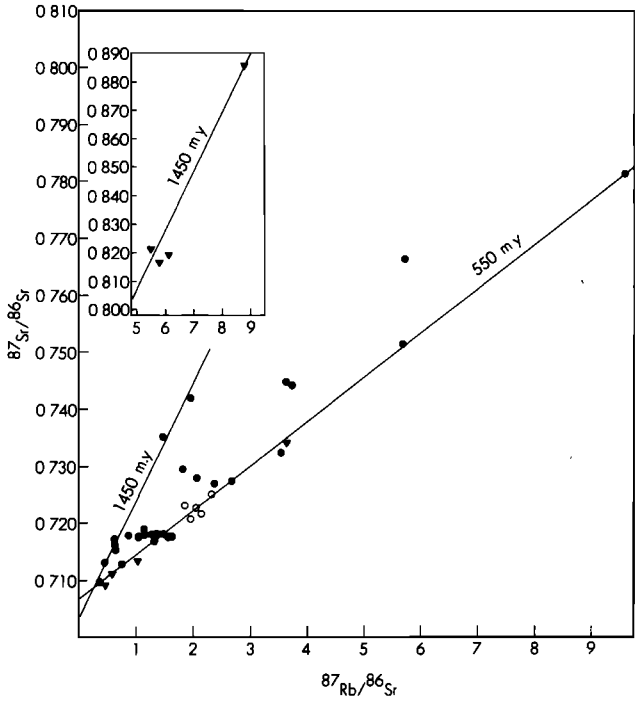

Fig. 3. Strontium evolution diagram for whole-rock specimens from the metamorphic complex in the northern Ruby Mountains, Nevada. Solid triangles are granitic (1450 m.y.) and metamorphic (550 m.y.) rocks from Idaho [*Armstrong,* 1975; *Armstrong et al.,* 1977]. Open circles are specimens of granite gneiss in Lamoille Canyon.

tium evolution diagram in Figure 8. Regression of the data for the granite pluton [*York,* 1969] yields a whole-rock isochron age of 159.7 ± 2.7 m.y. with an initial $^{87}Sr/^{86}Sr$ of 0.71366 ± 0.00036. The dike (LC2, LC6) is apparently the same age as indicated by the reference isochron through the two data points but has an initial $^{87}Sr/^{86}Sr$ of 0.7105. Therefore, the dike represents a contemporaneous but separate magma.

Zircon from one sample of this granitic rock yields highly discordant dates (Table 8) that reflect a complex history subsequent to the emplacement of the rock. The 1448 m.y. $^{207}Pb/^{206}Pb$ age indicates that the zircon was inherited from the source rocks of the granites.

Cretaceous Granite

Specimens of minerals from crystalline rocks in the Ruby Mountains that were dated by both the K-Ar and Rb-Sr technique in most cases have ages that reflect resetting during a Tertiary thermal event. However, Rb-Sr ages of muscovites from one Cretaceous granite pluton and coarse feldspars from a crosscutting pegmatite in the Ruby Mountains apparently have not been reset in the region where biotite K-Ar ages reach their maximum of 30 to 35 m.y.

Evidence for Cretaceous magmatism has been found along the length of the metamorphic complex in the range. Rubidium, strontium, and $^{87}Sr/^{86}Sr$ data for Cretaceous rocks are given in Table 9 and plotted on a strontium evolution diagram in Figure 9. Locations of the specimens are shown on Figure 1. Whole-rock specimens RM-2-79 A, C, and E are from a granite dike that intruded amphibolite, quartzofeldspathic schists, and marbles in the Secret Gorge area. Whole-rock specimen RM-45-68 and pegmatitic alkali-feldspar RM-45-68 K-spar are from a granite dike that intruded the folded carbonate section on the east side of the range. Whole-rock specimens RM-17-66, RM-19-66 and muscovites RM-17-66 and RM-19-66 are from the two-mica granite in the Dawley Canyon area. Whole-rock specimen J4a is from a dike in migmatite along the southern border zone of a biotite granite pluton. Specimens RM-15-67pl and K-spar are coarse (15 cm) plagioclase and microcline, respectively, from a tabular pegmatite that intruded the two-mica granite in the Dawley Canyon area. Specimen RM-19-67 is from an 1.5-m-thick quartzofeldspathic schist bed of Precambrian age that has a diffuse pegmatite center (RM-20-67). Regression of the whole-rock and muscovite data [*York,* 1969] for the two-mica granite in the Dawley Canyon area yields an age of 83.9 ± 1.25 m.y. and an initial $^{87}Sr/^{86}Sr$ ratio of 0.73723 ± 0.00061. Reference isochrons of this age are drawn through the data from the other related rocks and minerals in Figure 9. The large plagioclase and microcline crystals (RM-15-67) were separated from a pegmatite that intruded the two-mica granite in the Dawley Canyon area in order to extend the range of Rb/Sr in the analyzed specimens from this body and to improve the precision of the indicated age. The plagioclase-microcline pair have the same apparent age as that of the granite (Figure 9), but the initial $^{87}Sr/^{86}Sr$ for the pegmatite minerals is much higher than that for the granite. This indicates that the pegmatite magma was generated at the same time as the granite but from an entirely different source or that the pegmatite formed from a late fluid-rich phase of the granite that scavenged radiogenic strontium from the intruded Precambrian metamorphic rocks. In the contact zone of the two-mica granite, the Precambrian quartzofeldspathic schist (RM-19-67) and the diffuse pegmatitic core of the bed (RM-20-67) may be a clue to the formation process of the pegmatites. The apparent age of this pair (Figure 9) indicates strontium homogenization in the parent sediment and melt facies at the same time as in the Cretaceous granite. At the time of the formation of the pegmatitic fluid (specimen RM-20-67) there may not have been a sufficiently large fluid phase to permit formation of a crosscutting body.

The distribution of the known discrete major masses of Cretaceous granite in the central Ruby Mountains is shown on Figure 1. These plutons intruded the Jurassic granite and gneisses and metamorphosed sedimentary rocks of Precambrian age. One of these bodies, two-mica granite in the Dawley Canyon area, was investigated in more detail than the others. Exposures of the two-mica granite in the Dawley Canyon area are poor and occur as large, rounded inselbergs in a pediment surface. All exposures are deeply weathered and are characterized by a yellow-brown color, and samples from the body taken for analysis are from blasted outcrops. Contacts with the enclosing rocks are hard to find, but a sharp intrusive contact with the Jurassic two-mica granite was observed in some places. The Cretaceous granite does not have a fine-grained chilled contact zone, but the outer 2 cm of the rock is a mosaic of feldspar and quartz without the biotite or muscovite that characterize the rest of the pluton. Coarse-grained, tabular, beryl-bearing pegmatitic dikes are abundant in the Cretaceous granite. Some of these have been mined for muscovite and beryl [*Olson and Hinrichs,* 1960]. Inclusions of the intruded country rocks are locally abundant.

In hand specimen the granite is a medium-grained mosaic of feldspar and quartz anhedra with euhedra of biotite or

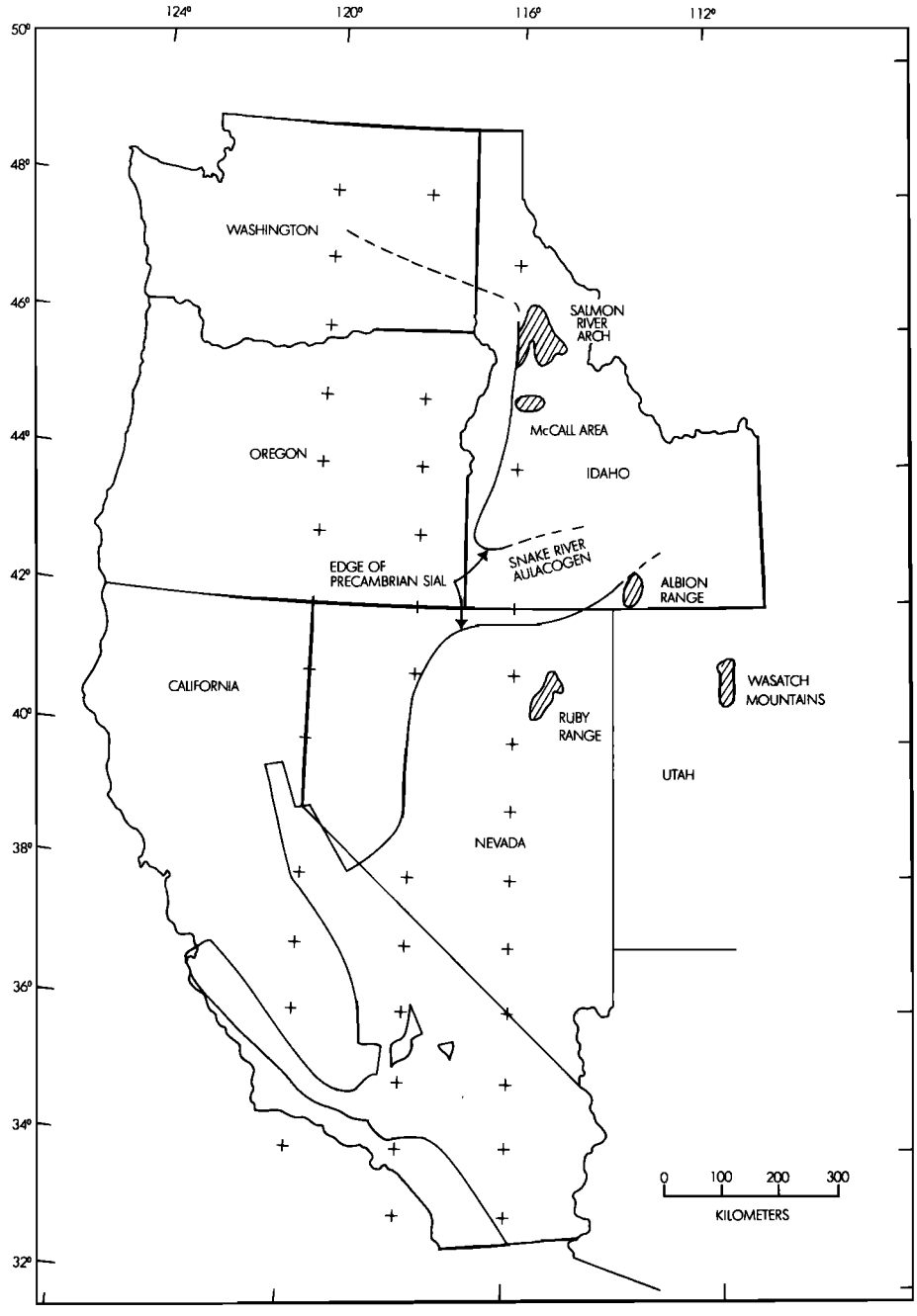

Fig. 4. Outline map of the western United States showing edge of Precambrian sialic crust as indicated by initial strontium isotopic composition of Mesozoic and Cenozoic plutons (modified from *Kistler and Peterman* [1978]). Areas that have yielded approximtely 550 m.y. metamorphic ages of rocks and minerals are hachured.

biotite and muscovite. Garnet and beryl are occasional accessory minerals.

In thin section, albite (30 to 35%), microcline (40 to 45%), and quartz (20 to 25%) are seen as generally 0.1 to 3 mm anhedral interlocking grains. Muscovite (1%) and/or biotite (2 to 4%) occur as anhedral crystals or as ragged crystals interstitial to the feldspar and quartz. Apatite inclusions in the feldspars are the most abundant and ubiquitous accessory mineral. Euhedral garnet, beryl, and zircon are minor accessory minerals. Opaque oxides are absent from the rock.

The chemical composition of two specimens of the two-mica granite in the Dawley Canyon area are given in Table 1, and their locations are shown on Figure 1. Normative albite, orthoclase, and quartz of these specimens normalized to 100% are plotted on a ternary diagram in Figure 5.

Electron microprobe analyses of muscovite, garnet, and both plagioclase and alkali feldspar from a specimen of the Cretaceous granite (RM-38-66) are given in Tables 3, 5, and 6, respectively. Biotite from this specimen was too altered to give a reliable analysis. The muscovite composition is the same as that in the Jurassic granite. The garnet is spessartine and almandine-rich with very low grossular and pyrope contents (Figure 6). The MnO zoning, however, is not as pronounced as the zoning in garnet RM-31-66 in the Jurassic granite. The plagioclase is albite, and X ray study indicates that the alkali feldspar is microcline and orthoclase.

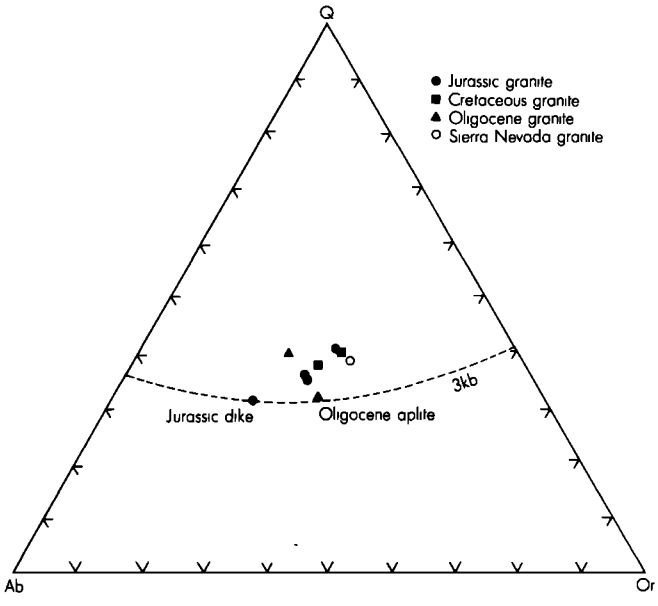

Fig. 5. Quartz-orthoclase-albite diagram for Mesozoic and Cenozoic granitic rocks in the Ruby Mountains, Nevada.

Oligocene Granite

The Harrison Pass pluton of Oligocene age [*Willden et al.*, 1967] crops out in the central part of the Ruby Mountains. The pluton ranges in composition from granodiorite to granite and intruded Cambrian and Ordovician sedimentary rocks and Jurassic granite. The pluton is poorly exposed, and outcrops are deeply weathered. Microcline magacrysts from 2.5 to 5 cm long occur sparsely at some places in the pluton. Aplite-pegmatite dikes locally intrude the granodiorite. The pluton is characterized by cataclastic texture and is locally overlain by klippen of unmetamorphosed Paleozoic sedimentary rocks at places in the western part of the range [*Willden et al.*, 1967; *Willden and Kistler*, 1969].

In thin section the granodiorite is hypidiomorphic granular with 1 to 5 mm crystals of orthoclase (40 to 45%), oligoclase (30 to 35%), quartz (20 to 25%), biotite (2 to 3%), and accessory apatite, hornblende, zircon, and opaque oxides.

Chemical analyses of a specimen of the granodiorite (63W51) and of a crosscutting aplite dike (RM-1-67) are given in Table 1. Normative albite, orthoclase, and quartz of these specimens normalized to 100% are plotted on a ternary diagram in Figure 5.

TABLE 3. Electron Microprobe Analyses of Muscovite

	Map Number				
	33	33	37	37	34
Sample	RM-38-68A Creataceous	RM-38-68B	RM-11-66A Jurassic	RM-11-66C	RM-31-66D Jurassic
SiO_2	46.00	46.11	45.69	45.86	45.79
Al_2O_3	34.79	34.64	34.59	34.21	34.49
TiO_2	0.38	0.41	0.49	0.42	0.15
FeO*	2.47	2.60	2.38	2.39	2.95
MnO	<0.04	<0.04	<0.04	<0.04	<0.04
MgO	0.57	0.62	0.70	0.83	0.42
CaO	nd	nd	nd	nd	nd
Na_2O	0.53	0.56	0.51	0.52	0.48
K_2O	11.08	10.83	11.00	11.15	11.05
BaO	<0.07	<0.08	<0.08	<0.08	<0.08
Sum	95.82	95.77	95.36	95.38	95.43
H_2O†	4.49	4.49	4.47	4.46	4.46
Sum	100.31	100.26	99.83	99.84	99.89
F	0.2	0.2	0.35	0.35	0.35
Number of atoms calculated on basis of 22 oxygens					
Si	6.15	6.16	6.13	6.16	6.16
Al	1.85	1.84	1.87	1.84	1.84
Σ	8.00	8.00	8.00	8.00	8.00
Al	3.63	3.61	3.61	3.58	3.63
Ti	0.04	0.04	0.05	0.04	0.02
Fe	0.28	0.29	0.27	0.27	0.33
Mn	0.00	0.00	0.00	0.00	0.00
Mg	0.11	0.12	0.14	0.17	0.08
Σ	4.06	4.06	4.07	4.06	4.06
Na	0.14	0.14	0.13	0.14	0.13
K	1.89	1.85	1.88	1.91	1.90
Ba	0.00	0.00	0.00	0.00	0.00
Σ	2.03	1.99	2.01	2.05	2.03

* Total Fe as FeO.

† Calculated on basis of $4OH^-$ per formula unit, % H_2O not determined separately.

TABLE 4. Electron Microprobe Analyses of Biotite From Jurassic Granite

	Map Number		
	37	37	34
Sample	RM-11-66A	RM-11-66C	RM-31-66D
SiO_2	35.86	34.94	33.64
Al_2O_3	19.19	19.61	19.29
TiO_2	2.04	2.09	1.34
FeO*	23.93	23.53	29.35
MnO	0.68	0.59	0.30
MgO	5.31	5.16	2.27
CaO	nd	nd	nd
Na_2O	0.10	0.10	0.08
K_2O	9.74	9.73	9.55
BaO	<0.08	<0.08	0.08
Sum	96.85	95.75	95.90
H_2O†	3.91	3.87	3.76
Sum	100.76	99.62	99.66
F	1.1	1.1	0.7
Number of atoms calculated on basis of 22 oxygens			
Si	5.50	5.42	5.37
Al	2.50	2.58	2.63
Σ	8.00	8.00	8.00
Al	0.96	1.00	1.00
Ti	0.24	0.24	0.16
Fe	3.07	3.05	3.92
Mn	0.09	0.08	0.04
Mg	1.21	1.19	0.54
Σ	5.57	5.56	5.66
Na	0.03	0.03	0.02
K	1.90	1.92	1.94
Ba	0.00	0.00	0.00
Σ	1.93	1.95	1.96

* Total Fe as FeO.

† Calculated on basis of $4OH^-$ per formula unit; % H_2O not determined separately.

Rubidium, strontium, and $^{87}Sr/^{86}Sr$ determined for two specimens of the Harrison Pass pluton and the crosscutting aplite dike are given in Table 10, and their locations are shown on Figure 1. These data are plotted on a strontium evolution diagram in Figure 10. Regression of the data [*York*, 1969] yields an age of 31.9 ± 1.2 m.y. with an initial $^{87}Sr/^{86}Sr$ of 0.71090 ± 0.00016. Biotite K-Ar dates of specimens from this pluton range from 30 to 37 m.y. [*Willden et al.*, 1967].

OXYGEN ISOTOPE COMPOSITIONS

The $\delta^{18}O$ values are defined as the relative difference in $^{18}O/^{16}O$ ratio between the sample and standard mean ocean water (SMOW) standard in per mil. Values of $\delta^{18}O$ in minerals from representative granitic and metamorphic rock types in the Ruby Mountains are given in Table 11. The $\delta^{18}O$ values of quartz from Precambrian granite gneiss RM-3-66 and 'Lam Can,' Jurassic granite J4b, and Cretaceous granite in the Dawley Canyon area RM-17-66 range from 12.3 to 14.8. These relatively high values indicate a significant sedimentary rock component in the parent materials for these igneous rocks [*O'Neil and Kistler*, 1972; *O'Neil and Chappell*, 1977; *O'Neil et al.*, 1977].

Except for the marble (RM-26-66) and one quartzite (RM-56-68), the $\delta^{18}O$ values of the metamorphic rocks examined are several per mil lower than those measured in the igneous rocks. This is the opposite of what is normally observed in other related suites of metamorphic and igneous rocks and further emphasizes the fact that the source materials for the granites were indeed relatively ^{18}O-rich. The magmas did not inherit their oxygen isotope signatures from the rocks they intruded. The metamorphic rocks exhibit some '^{18}O reversals' and have unusually low δD values. These features are interesting complications of the overall stable isotope geochemistry of the Ruby Mountains and are the subject of a separate report in preparation.

Oxygen isotope temperatures (Table 11) were calculated from the fractionations between quartz and mica, using the expressions of *Bottinga and Javoy* [1973]. Minimum temperatures of 480° to 570°C are obtained for the granites. These are clearly subsolidus but generally higher than those obtained from the chemical thermometers [*Kistler and O'Neil*, 1975]. This suggests that chemical migration between minerals may have continued after oxygen isotope exchange had ceased!

PETROGENESIS OF THE JURASSIC AND CRETACEOUS GRANITES

The garnets in the Mesozoic granites are considered to be magmatic because they do not show marginal alteration and/or resorption such as that displayed by many garnet phenocrysts in volcanic rocks; i.e., they are more or less in textural

TABLE 5. Average Microprobe Analyses of Ruby Mountains Garnets

	Map Number				
	33	37	37	34	34
Sample	RM-38-68-1A Cretaceous	RM-11-66-1A Jurassic	RM-11-66-A2 Jurassic	RM-31-66-D1 Jurassic	RM-31-66-D2 Jurassic
SiO_2	35.7	36.0	36.5	36.2	36.2
Al_2O_3	20.2	20.1	20.3	20.2	20.2
FeO	33.2	25.4	26.9	35.0	34.7
MnO	7.9	14.4	14.1	6.6	6.4
MgO	0.8	0.9	0.8	0.4	0.3
CaO	0.4	0.9	0.8	1.1	1.2
Sum	98.2	97.7	99.4	99.5	99.0
End-members, mol %					
Almandine	76.8	59.5	61.4	80.0	80.0
Spessartine	18.6	34.1	32.7	15.2	15.1
Pyrope	3.2	3.6	3.5	1.5	1.4
Grossular	1.3	2.8	2.4	3.3	3.5

TABLE 6. Average Electron Microprobe Analyses of Coexisting Feldspars From Ruby Mountains Granites

Map Number	Sample	Alkali Feldspar		Plagioclase	
		Average Or	Average Ab	Average Or	Average Ab
33	RM-38-68A Cretaceous	92	7.9	4.1	95
33	RM-38-68B Cretaceous	92.1	7.8	3.5	95.5
37	RM-11-66A Jurassic	92.1	7.8	12.5	86.7
37	RM-11-66C Jurassic	90.6	9.2	12.9	86.3
37	RM-11-66D Jurassic	93.1	6.8	8.5	90.5

equilibrium. The garnets are not likely to represent residual refractory metamorphic crystals because they do not contain inclusions similar to those in adjacent metamorphic rocks and they have radically different compositions ($al_{60}sp_{34}py_{3.6}gr_{2.8}$) from adjacent metamorphic garnets ($al_{79}sp_6py_{13}gr_2$) [*Ghent*, 1976]. The spessartine richer rims of the granitic rock garnets possibly reflect crystalline growth in a magma with increasing Mn/Ca+Mg+Fe. Since the other Fe–Mg phases are muscovite and biotite and these phases do not concentrate Mn relative to garnet, it is possible that crystallization of these minerals caused an increase in Mn/Ca+Fe+Mg in the magma. The same garnets (Rm-31-66) also show a decrease in Ca content in the outer 30 μm. *Green* [1977] has shown that while grossular content of magmatic garnet is controlled in part by bulk composition, for any given liquid composition the grossular content of the magmatic garnet increases with increasing pressure. The antipathetic relationship between Ca and Mn profiles suggests the possibility that the zoning reflects continued growth of garnet as the host magma rose to shallower levels [*Green*, 1977].

Estimates of the pressure of crystallization of the Mesozoic granites can be made from their mineral parageneses and compositions. According to *Green* [1977], addition of 1% MnO to granitic liquid permits garnet to crystallize at pressures as low as 3 kbar. Garnet experimentally crystallized at 4 kbar, 920°C contains 10.0 wt % MnO. The minimum average MnO content of the garnets from the Mesozoic granites is 6.4 wt %, suggesting the possibility that these garnets could have crystallized from granitic liquids at rather low pressures.

If muscovite in RM-38-68, RM-11-66, and RM-31-66 crystallized in equilibrium with a granitic melt, we can use experimental data on the stability of muscovite and quartz [*Chatterjee and Johannes*, 1974] and the water-saturated solidus of granite [*Piwinskii*, 1968; *Boettcher and Wyllie*, 1968] to set limits on the minimum pressure of crystallization of muscovite and quartz. On a pressure-temperature diagram the intersection of the muscovite quartz stability curve and the water-saturated granite solidus curve is at about 660°C and 3.4 kbar P_{H_2O}. If $P_{H_2O} < P_{total}$, both curves move in opposite directions driving the minimum pressure of crystallization of muscovite to higher pressures. The muscovites in these granites show significant substitution $(Mg,Fe)^{VI}(Si)^{IV} = (Al)^{VI}(Al)^{IV}$.

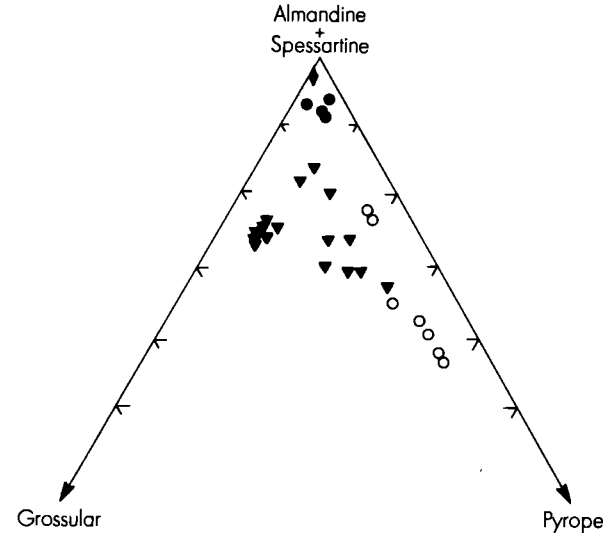

Fig. 6. Composition of garnets from Ruby Mountains. Mesozoic granites (solid circles) with compositions of garnets from andesite and dacite (open circles, *Fitton* [1972]), rhyolite (solid triangles, *Wood* [1973]), and the Westerly muscovite granite (solid diamond, *Joyce* [1973]).

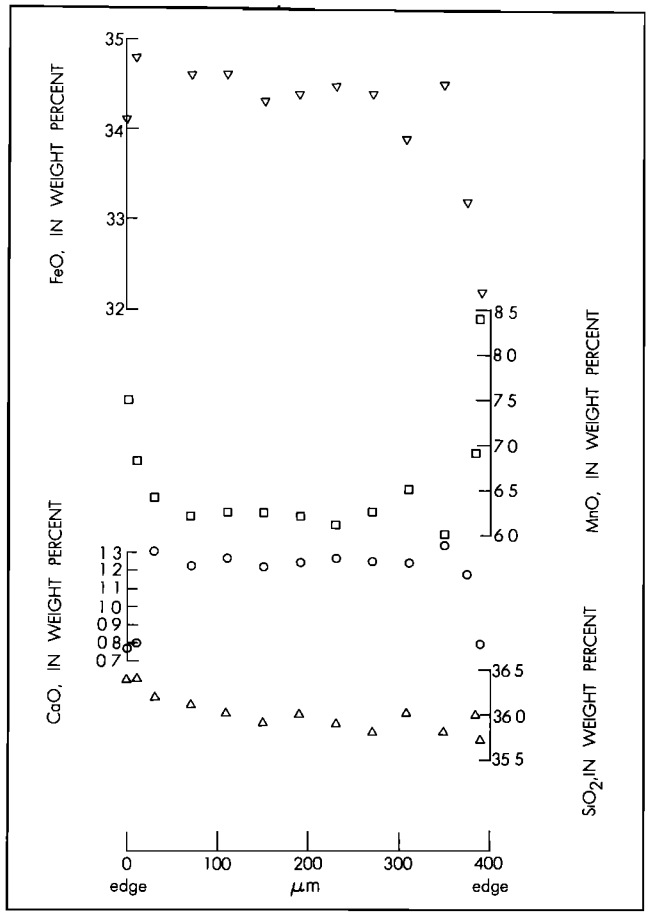

Fig. 7. Diagram showing compositional zoning in a representative garnet crystal from the Jurassic garnet-two-mica granite (RM-31-66) in the Ruby Mountains, Nevada.

TABLE 7. Rubidium-Strontium Data for Jurassic Granitoids

Map Number	Specimen	Rock Type	Rb, ppm	Sr, ppm	Rb/Sr	$^{87}Rb/^{86}Sr$	$^{87}Sr/^{86}Sr$
24	R1-65	granite	178.6	253.5	0.70	2.03	0.71683
24	R2-65	granite	209.7	204.5	1.03	2.98	0.72031
24	64W66	granite	204*	173*	1.18	3.42	0.71992†
37	RM-11-66	granite	232.2	90.6	2.57	7.45	0.73032
34	RM-31-66	granite	129.0	147.2	0.88	2.55	0.71952
36	RM-47-66	granite	187.5	125.8	1.49	4.32	0.72361
36	J4b	granite	262.0	48.0	5.46	15.82	0.74802
37	J1	granite	199.0	33.2	5.99	17.36	0.75301
37	RM-10-66	granite	152.0	286.7	0.53	1.54	0.71753
29	RM-38-66	schist	412.7	43.7	9.45	27.39	0.77741† 0.77840
9	LC-2	granite dike	245*	118.4*	2.07	8.00	0.72402†
9	LC-6	dike	276*	224.4*	1.13	3.27	0.71797†

* Rb and Sr concentrations by XRF; all other Rb and Sr concentrations by isotope dilution.
† $^{87}Sr/^{86}Sr$ measured; all other $^{87}Sr/^{86}Sr$ calculated.

This substitution should reduce the thermal stability of muscovite [*Velde*, 1965] and should also increase the minimum pressure necessary to crystallize celadonitic muscovite and quartz relative to pure muscovite plus quartz. For a contrary view, see *Miller et al.* [1980] and *Anderson and Rowley* [1980].

The distribution of Fe and Mg between coexisting garnet and biotite has been used as a geothermometer by *Thompson* [1976], and *Goldman and Albee* [1977] and others. The calibration of *Goldman and Albee* [1977] is based on oxygen isotope temperatures estimated from coexisting quartz and magnetite. They also estimated the effect of Ca and Mn in garnet and Fe, Ti and octhedral Al in biotite on the distribution coefficient, K_D-Mg/Fe garnet/Mg/Fe biotite. For Ruby Mountains samples we have measured $1nK_D$ for RM-11-66A and RM-31-66D. The values are $1nK_D = -1.83$ and -2.01 for RM-11-66A and -1.91 and -2.19 for RM-31-66D. Using equation 9 of *Goldman and Albee* [1977], we obtain temperatures of 505° and 465°C (RM-11-66A) and 405° and 365°C (RM-31-66D). The Mn content of Ruby Mountains garnets is far higher than that of the samples used in the Goldman and Albee calibration.

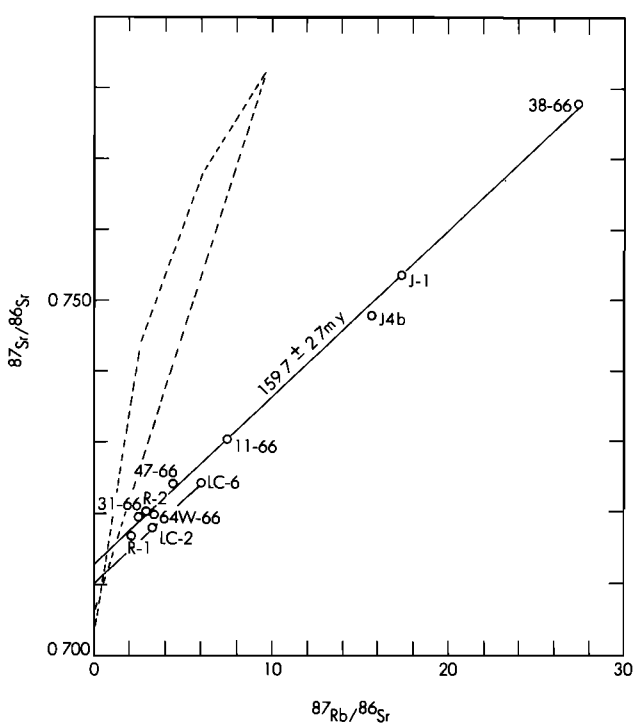

Fig. 8. Strontium-evolution diagram for Jurassic two-mica granite. Field of data of specimens from the metamorphic complex is enclosed in dashed lines.

These estimated equilibration temperatures for Ruby Mountains garnet-biotite pairs are clearly subsolidus (metamorphic). *Ferry* [1976] reported garnet-biotite Fe-Mg fractionation temperatures for granitic rocks in Maine which are significantly below magmatic temperatures.

Garnet crystals often show a slight decrease in Mg/Fe from core to rim. At constant pressure and constant Mg/Fe in biotite this would suggest a decrease in temperature from core to rim. A temperature estimate based on average Mg/Fe garnet is submagmatic (see above), and using the rim Mg/Fe garnet composition results in a still lower temperature.

Temperatures estimated from the compositions of the coexisting feldspars based on the feldspar geothermometer discussed by *Stormer* [1975] range from 380° to 410°C at 2 kbar. These temperatures are submagmatic and are similar to the temperatures based on garnet fractionation but somewhat

TABLE 8. U-Pb Data for Zircon From Jurassic Granite Specimen 64W66 (Map Number 24)

	Value
Th	116.2 ppm
U	2345 ppm
Pb	36.4 ppm
$^{206}Pb/^{238}U$	0.01462
$^{207}Pb/^{235}U$	0.15724
$^{206}Pb/^{204}Pb$	1101.2
$^{206}Pb/^{207}Pb$	10.988
$^{206}Pb/^{208}Pb$	8.7004
Age	
$^{206}Pb/^{238}U$	95 m.y.
$^{207}Pb/^{235}U$	150 m.y.
$^{207}Pb/^{206}Pb$	1448 m.y.
$^{208}Pb/^{232}Th$	471 m.y.

From T. W. Stern (written communication, 1969).

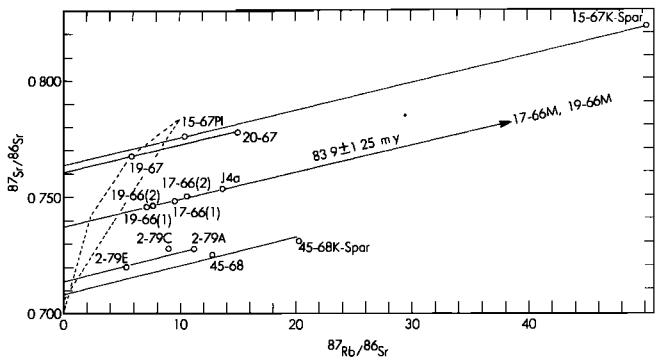

Fig. 9. Strontium-evolution diagram for Cretaceous granitoid rocks. Field of data of specimens from the metamorphic complex is enclosed in dashed lines.

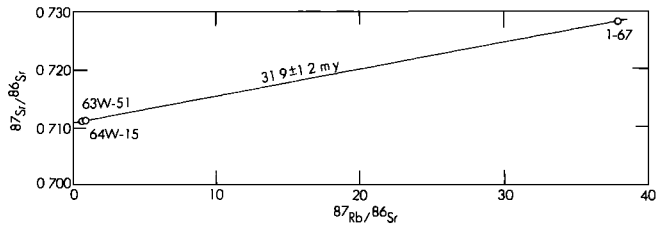

Fig. 10. Strontium-evolution diagram for Oligocene pluton.

lower than the mineral oxygen isotope equilibration temperatures.

The Mesozoic granitic rocks of the Ruby Mountains, Nevada, have field relationships, petrographic and mineral properties, chemical properties, and isotopic characteristics of granitic rocks with a significant sedimentary rocks component in their source material [*Chappell and White,* 1974; *O'Neil and Chappell,* 1977; *O'Neil et al.,* 1977; *Ghent et al.,* 1979*b*]. The field of data of analyzed metamorphosed rocks from the intruded metamorphic complex is shown on the strontium evolution diagrams of Jurassic (Figure 8) and Cretaceous (Figure 9) granites. These diagrams indicate that the Mesozoic granitic rocks could be minimum melt granites derived by partial melting of source rocks with Rb and Sr concentrations and $^{87}Sr/^{86}Sr$ values similar to those in the exposed metamorphic complex. The estimates of pressure of crystallization for the Mesozoic granites indicate that they crystallized at depths of about 10 to 13 km. The occurrence of staurolite-muscovite-sillimanite-quartz assemblages in the enclosing wall rocks suggests that metamorphic pressure did not exceed about 5 kbar [*Carmichael,* 1978, p. 776]. Estimates of pressure and temperature can be made for metamorphic wall rocks from Fe-Mg fractionation between coexisting garnet and biotite and garnet-plagioclase-sillimanite-quartz equilibria [see, e.g., *Ghent et al.,* 1979a]. These data suggest maximum metamorphic pressures and temperatures near 700°C and 6.5 kbar. These pressures estimated are only slightly higher than the minimum pressures estimated for crystallization of the granites. Comparison of these pressure estimates and the similarity in strontium and oxygen isotopic compositions of the Mesozoic granitic rocks and their enclosing wall rocks indicate that the depth of origin of the Mesozoic magmas could have been at intermediate crustal levels and need not have been at depths much greater than the maximum depths where they crystallized.

In the Sierra Nevada in California, the initial $^{87}Sr/^{86}Sr$ of Mesozoic plutons are much lower than these ratios in their intruded wall rocks, and the source materials of the magmas for these plutons have been interpreted to be in the upper mantle and lower crust [*Kistler and Peterman,* 1973]. In spite of the different source regions suggested for the plutons in the Sierra Nevada and in the Ruby Mountains, some granites in the Sierra Nevada have major element chemical compositions similar to those in the Ruby Mountains. The chemical analysis of one of the Sierra Nevada granites (SSr-4-73) is given in Table 1 for comparison with Ruby Mountains granite RM-17-66. This granite is from the southern Sierra Nevada, map 25 of *Kistler and Peterman* [1973].

Rare-earth element (REE), Li, Cs, Rb, Ba, Sr, Sn, Ta, Th, Zr, and Be concentrations, and initial $^{87}Sr/^{86}Sr$ in Ruby Mountains granite RM-17-66 and Sierra Nevada granite SSr-4-73 are given in Table 12. Total REE concentration is about 4 times greater in the Sierra Nevada granite than in the Ruby

TABLE 9. Rubidium-Strontium Data for Cretaceous Granitoids

Map Number	Specimen	Rock Type	Rb, ppm	Sr, ppm	Rb/Sr	$^{87}Rb/^{86}Sr$	$^{87}Sr/^{86}Sr$
41	RM-17-66(1)	granite	282.6	86.4	3.27	9.50	0.74831
41	RM-17-66(2)	granite	286.5	79.6	3.60	10.46	0.75065
35	RM-19-66(1)	granite	273.0	111.9	2.45	7.11	0.74603
35	RM-19-66(2)	granite	285.3	108.4	2.63	7.64	0.74608
36	J4a	granite	157.7	33.5	4.70	13.65	0.75314
35	RM-19-66M	muscovite	624	13.1	46.7	137.7	0.89194
41	RM-17-66M	muscovite	709.7	9.2	77.1	231.1	1.02694
40	RM-15-67P	plagioclase	126	35.4	3.56	10.36	0.77582
40	RM-15-67K	K-spar	1067	61.2	17.43	51.01	0.82249
39	RM-19-67	quartzo-feldspathic schist	316.0	160.8	1.96	5.72	0.76651* 0.76733
39	RM-20-67	pegmatite	172	33.6	5.14	15.00	0.77766
1	RM-2-79A	granite	298.8	77.4	3.85	11.19	0.72779
1	RM-2-79C	granite	284.1	91.5	3.10	9.0	0.72778
1	RM-2-79E	granite	184.5	99	1.86	5.4	0.71986
22	RM-45-68	granite	257.1	58.2	4.42	12.81	0.72530
22	RM-45-68K	K-spar	594.9	85.4	6.96	20.18	0.73094

All Rb and Sr concentrations by isotope dilution.
*$^{87}Sr/^{86}Sr$ measured; all other $^{87}Sr/^{86}Sr$ calculated.

TABLE 10. Rubidium-Strontium Data for Oligocene Granitoid

Map Number	Specimen	Rock Type	Rb, ppm	Sr, ppm	Rb/Sr	$^{87}Rb/^{86}Sr$	$^{87}Sr/^{86}Sr$
42	63W-51	granodiorite	110*	406*	0.27	0.78	0.71142†
43	64W-15	granodiorite	133*	391*	0.34	0.98	0.71120†
46	RM-1-67	aplite	344.2	26.3	13.09	37.90	0.72814

* Rb and Sr concentrations by XRF, other Rb and Sr concentrations by isotope dilution.
† $^{87}Sr/^{86}Sr$ measured; all other $^{87}Sr/^{86}Sr$ calculated.

Mountains granite. Relative to the Sierra Nevada granite the Ruby Mountains granite is enriched in Li, Cs, Rb, Sn, Be, Ta, and depleted in Ba, Zr, Th, and Sr. The initial $^{87}Sr/^{86}Sr$ value of the Ruby Mountains granite is much more radiogenic than that in the Sierra Nevada granite.

The high concentrations of alkali elements, in particular Li and Cs, Ta [*Wedepohl,* 1978], Sn, and Be, radiogenic initial $^{87}Sr/^{86}Sr$, and high $\delta^{18}O$ are compatible with a sedimentary source material for the Ruby Mountains granite in the Dawley Canyon area (RM-17-66). The low REE, Zr, and Th abundances indicate either that there was a very small contribution to the melt from refractory minerals with high REE concentrations like sphene, zircon, and apatite or that the source material had low Th and REE concentrations.

Exposed Archean crustal rocks and sediments derived from them have low REE and thorium abundances relative to post-Archean sedimentary rocks [*McLennan et al.,* 1980]. REE concentrations of Cretaceous Ruby Mountains granite (RM-17-66), Sierra Nevada granite (SSr-4-73), post-Archean North American shale composite [*Haskin and Paster,* 1979], and Archean average sedimentary rocks [*McLennan et al.,* 1980] normalized to chondritic values, divided by 1.2, of *Masuda et al.* [1973] are shown in Figure 11. Isotopic analysis of neodymium from the Sierra Nevada granite [*DePaolo,* 1980] and the Ruby Mountains granite (L. Farmer, written communication, 1980) yield initial εNd values of −7.6 and −9.7, respectively. These data give model ages for the source of the neodymium in the Sierra Nevada and Ruby Mountains of about 700 m.y. and 3000 m.y., respectively. In harmony with the strontium isotopic data, the neodymium isotopic data indicate source materials for both granites include old crustal material. The 3000 m.y. model age for neodymium in the Ruby Mountains granite suggests that its source material was either an Archean sediment or more likely a younger Precambrian sediment derived from crustal material of Archean age. Therefore, a sedimentary source material of Archean provenance

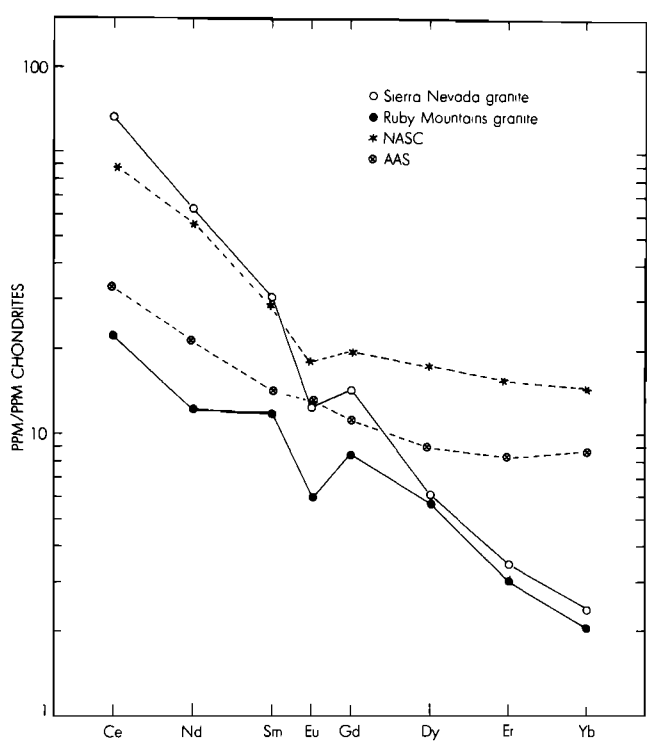

Fig. 11. Diagram showing chondrite-normalized REE pattern for Cretaceous granite in the Ruby Mountains (closed circles), Cretaceous granite in the Sierra Nevada (open circles), average post-Archean North America shale (NASC) (stars), average Archean sediment (AAS) (circled crosses). References are in text.

TABLE 11. $\delta^{18}O$ Values of Minerals and Oxygen Isotope Temperature of Granitoids and Intruded Wall Rocks in the Ruby Mountains, Nevada

Map Number	Specimen	Rock Type	Mineral	$\delta^{18}O$	T, °C
9	Lam Can	granite	quartz	+14.0	
		gneiss	K-spar	+12.3	
			plagioclase	+12.4	
			biotite	+7.7	470
25	RM-3-66	granite	quartz	+12.3	
		gneiss	K-spar	+11.0	
			plagioclase	+10.4	
			muscovite	+9.8	570
			biotite	+7.0	520
36	J4b	granite	quartz	+11.6	
		Jurassic	muscovite	+9.1	570
41	RM-17-66	granite	quartz	+14.9	
		Cretaceous	K-spar	+13.3	
			plagioclase	+13.0	
			muscovite	+11.5	480
			biotite	+9.6	530
8	RM-2-72	amphibolite	hornblende	+12.0	
			biotite	+9.0	
6	RM-20-68	mica schist	quartz	+10.1	
			muscovite	+7.6	570
			biotite	+5.2	550
23	RM-26-66	marble	actinolite	+13.5	
			phlogopite	+12.0	
5	RM-26-68	quartzite	quartz	+11.3	
			hornblende	+8.0	
			biotite	+5.4	490
5	RM-28-68	schist	quartz	+8.1	
			hornblende	+9.7	
			biotite	+0.6	413
3	RM-49-68	Biotite	quartz	+10.2	
		schist	biotite	+7.0	700
4	RM-50-68	gneiss	quartz	+10.9	
			biotite	−0.00	310
38	RM-56-68	quartzite	quartz	+13.9	
			muscovite	+10.4	460
			biotite	+7.7	470

TABLE 12. Selected Trace Element Concentrations in Granitic Rocks With Similar Major Element Concentrations in the Sierra Nevada and Ruby Mountains

Element	Specimen RM-17—66 (Ruby Mountains), ppm	Specimen S-Sr4 (Sierra Nevada), ppm
Ce	18.7	103
Nd	7.73	38.5
Sm	2.16	5.9
Eu	0.427	0.901
Gd	2.20	3.76
Dy	1.85	2.10
Er	0.625	0.751
Yb	0.434	0.497
Sum (REE)	34.13	155.41
Li	300	—
Cs	17.1	2.7
Rb	282.6	170.0
Ba	161	1348
Sr	86.4	343
Sn	15	—
Be	15	—
Zr	<95	185
Th	5.1	17.5
Ta	2.3	0.8
$(^{87}Sr/^{86}Sr)_i$	0.7372	0.7082

Dashes indicate not detected.

can account for the low REE and thorium concentrations in the granite. If the granite is a true minimum melt granite, its large negative europium anomaly indicates that the melting took place in a region of plagioclase stability or at a depth less than 40 km. The depletion in the granite of Nd and the heavy REE relative to the average Archean sediment (Figure 11) can be accounted for by residual garnet after partial melting of this possible source material.

SUMMARY AND CONCLUSIONS

Tertiary uplift and erosion has exposed relatively deep crustal levels, to about 13 km, in the Ruby Mountains, Nevada. The deepest levels of exposure are of a Precambrian igneous and metamorphic complex with lithologies and apparent age (>1450 m.y.) that are similar to Precambrian igneous and metamorphic complexes, in central Idaho [*Armstrong,* 1975, *Evans and Zartman,* 1981b].

Paleozoic rocks lie unconformably on the metamorphic complex in the Ruby Mountains. In the Paleozoic section in the Ruby Mountains, Cambrian and Ordovician rocks were folded in the Late Ordovician, and Silurian and younger strata lie unconformably on the older rocks. Evidence for subsequent folding is lacking since Silurian and younger Paleozoic rocks are homoclinal and dip shallowly to the east in the southern part of the range [*Willden and Kistler,* 1967]. This shallow dip is due to the Ruby Mountains being the east flank of a northeasterly trending arch that developed in Oligocene and younger time.

In spite of the apparent lack of Mesozoic deformation in the area of the Ruby Mountains, plutons of Jurassic (160 m.y.) and Cretaceous (84 m.y.) ages were emplaced into the metamorphic complex and lower Paleozoic rocks. This contrasts with the area to the west in the composite Sierra Nevada batholith where precontemporaneous deformation occurred in the intruded rocks during pluton emplacement [*Evernden and Kistler,* 1970].

Not only is there a contrast in tectonic character, but there is also a contrast in composition that apparently is due to different source materials for the Mesozoic plutons in the Ruby Mountains relative to most of the Mesozoic plutons to the west. The Ruby Mountains Mesozoic granites are without associated mafic facies and have strontium and oxygen isotopic characteristics that are similar to their wall rocks. The magmas that resulted in the Mesozoic plutons were apparently derived between 40 and 15 km depth. Pressure estimates in the enclosing metamorphic rocks and the isotopic similarities between plutons and wall rocks would favor magma generation at depths not much greater than the present deepest level of exposure which is about 13 km.

Acknowledgments. We appreciate the constructive, critical reviews of this paper by R. J. Fleck, G. K. Czamanske, F. K. Miller, and E-An Zen. Ghent acknowledges financial support from Natural Sciences and Engineering Research Council of Canada operating grant A-4379.

REFERENCES

Albee, A. L., and L. Ray, Correction factors for electron probe micronalysis of silicates, oxides, carbonates, phosphates, and sulfates, *Anal. Chem., 42,* 1408–1414, 1970.

Anderson, J. L., and M. C. Rowley, Infrastructural intrusion of garnetiferous two-mica adamellite, granodiorite, and tonalite associated with mylonitization in the autochton of the Whipple Mountains of S.E. California, *Geol. Assoc. Can. Program Abstr., 5,* 40, 1980.

Armstrong, R. L., Precambrian (1500 m.y. old) rocks of central Idaho—The Salmon River arch and its role in Cordilleran sedimentation and tectonics, *Am. J. Sci., 275-A,* 437–467, 1975.

Armstrong, R. L., and F. A. Hills, Rb-Sr and K-Ar geochronologic studies of mantled gneiss domes, Albion Range, southern Idaho, U.S.A., *Earth Planet. Sci. Lett., 3,* 114–124, 1967.

Armstrong, R. L., W. H. Taubeneck, and P. O. Hales, Rb-Sr and K-Ar geochronometry of Mesozoic granitic rocks and their Sr isotopic composition, Oregon, Washington and Idaho, *Geol. Soc. Am. Bull., 88,* 397–411, 1977.

Bence, A. E., and A. L. Albee, Empirical correction factors for the electron microanalysis of silicates and oxides, *J. Geol., 76,* 382–403, 1968.

Boettcher, A. L., and P. J. Wyllie, Melting of granite with excess water to 30 kilobars pressure, *J. Geol., 76,* 235–244, 1968.

Bottinga, Y., and M. Javoy, Comments on oxygen isotope geothermometry, *Earth Planet. Sci. Lett., 20,* 250–265, 1973.

Blackwelder, E., Summary of the Precambrian rocks of Utah and Wyoming, *Proc. Utah Acad. Sci. Arts Lett., 12,* 153–157, 1935.

Brammall, A., and H. F. Harwood, The Dartmoor granites: Their genetic relationships, *Q. J. Geol. Soc. London, 88,* 171–234, 1932.

Carmichael, D. M., Metamorphic bathozones and bathograds: A measure of the depth of post-metamorphic uplift and erosion on the regional scale, *Am. J. Sci., 278,* 769–797, 1978.

Chappell, B. W., and A. J. R. White, Two contrasting granite types, *Pac. Geol., 8,* 173–174, 1974.

Chatterjee, N. D., and W. Johannes, Thermal stability and standard thermodynamic properties of synthetic 2M muscovite, $KAl_2[AlSi_3O_{10}(OH)_2]$, *Contrib. Mineral. Petrol., 48,* 89–114, 1974.

Clayton, R. N., and T. K. Mayeda, The use of bromine penta-fluoride in the extraction of oxygen from oxide and silicates for isotopic analysis, *Geochim. Cosmochim. Acta, 27,* 43–52, 1963.

DePaolo, D. J., Sources of continental crust: Neodymium isotope evidence from the Sierra Nevada and Peninsula ranges, *Science, 209,* 684–687, 1980.

Doering, W. P., A rapid method for measuring the Rb/Sr ratio in silicate rocks, Geological Survey Research 1968. *U.S. Geol. Surv. Prof. Pap., 600C,* C164–C168, 1968.

Evans, K. V., and R. E. Zartman, U-Th-Pb zircon geochronology of Proterozoic Y granitic intrusions in the Salmon area, east-central Idaho, *Geol. Soc. Am. Abstr. Programs, 13*(4), 195, 1981*a*.

Evans, K. V., and R. E. Zartman, Evidence from U-Th-Pb zircon ages for Cambrian-Ordivician plutonism in east-central Idaho, *Geol. Soc. Am. Abstr. Programs,13*(4), 195, 1981*b*.

Evernden, J. F., and R. W. Kistler, Chronology of emplacement of Mesozoic batholith complexes in California and western Nevada, *U.S. Geol. Surv. Prof. Pap., 623,* 1970.

Ferry, J. M., Fluid interaction between granite and sediment during metamorphism, south-central Maine, *Year Book Carnegie Inst. Washington 75,* 764–771, 1976.

Fitton, J. G., The genetic significance of almandine pyrope phenocrysts in the calc-alkaline Borrowdule volcanic group, northern England, *Contrib. Mineral. Petrol., 36,* 231–248, 1972.

Frey, M., Hunziker, J. C., O'Neil, J. R., and Schwander, H. W., Equilibrium-disequilibrium relations in the Monte Rosa granite, western Alps; petrological, Rb-Sr, and stable isotope data, *Controb. Mineral. Petrol., 55,* 147–179, 1976.

Ghent, E. D., Plagioclase-garnet-Al_2SiO_5-quartz: A potential geobarometer-geothermometer, *Am. Mineral., 61,* 710–714, 1976.

Ghent, E. D., D. B. Robbins, and M. Z. Stourt, Geothermometry, geobarometry and fluid compositions of metamorphosed calc-silicates and pelites, Mica Creek, British Columbia, *Am. Mineral., 64,* 874–885, 1979*a*.

Ghent, E. D., R. W. Kistler, and J. R. O'Neil, Petrogenesis of Mesozoic garnet-two-mica granites of the Ruby Mountains, Nevada, *Geol. Soc. Am. Abstr. Programs 11*(7), 432, 1979*b*.

Goldman, D. S., and A. L. Albee, Correlation of Mg/Fe partition between garnet and biotite with $^{18}O/^{16}O$ partitioning between quartz and magnetite, *Am. J. Sci., 277,* 750–767, 1977.

Green, T. H., Garnet in silicic liquids and its possible use as a P-T indicator, *Contrib. Mineral. Petrol., 65,* 59–67, 1977.

Hashad, A. H., Geochronological studies in the central Wasatch Mountains, Utah, PhD thesis, Univ. of Utah, Salt Lake City, 1964.

Haskin, L. A., and T. P. Paster, Geochemistry and mineralogy of the rare earths, *Handb. Phys. Chem. Rare Earths, 3,* Chap. 21, 1979.

Hill, J. M., Notes on some mining districts in eastern Nevada, *U.S. Geol. Surv. Bull., 648,* 1916.

Howard, K. A., Structure of the metamorphic rocks of the northern Ruby Mountains, Nevada, Ph. D. dissertation, Yale Univ., New Haven, Conn., 1966.

Howard, K. A., Paleozoic metasediments in the northern Ruby Mountains, Nevada, *Geol. Soc. Am. Bull, 82,* 259–264, 1971.

Howard, K. A., Metamorphic infrastructure in the northern Ruby Mountains, Nevada, *Mem. Geol. Soc. Am., 153,* 1980.

Howard, K. A., R. W. Kistler, A. W. Snoke, and R. Willden, Geologic map of the Ruby Mountains, Nevada, 1:125,000, *Map I-1136,* U.S. Geol. Surv., Reston, Va., 1979.

Joyce, A. S., Chemistry of the minerals of the granitic Murrumbidgee batholith, Australian Capital Territory, *Chem. Geol., 11,* 271–296, 1973.

King, Clarence, U.S. Geological exploration of the 40th parallel, 1 Systematic geology, report, Chief of Eng. U.S. Dep. of War, 1878.

Kistler, R. W., and J. R. O'Neil, Fossil thermal gradients in crystalline rocks of the Ruby Mountains, Nevada, as indicated by radiogenic and stable isotopes, *Geol. Soc. Am. Abstr. Programs,*(3), 334–335, 1975.

Kistler, R. W., and Z. E. Peterman, Variations in Sr, Rb, K, Na, and initial $^{87}Sr/^{86}Sr$ in granitic rocks and intruded wall rocks in central California, *Geol. Soc. Am. Bull., 84,* 3489–3512, 1973.

Kistler, R. W., and Z. E. Peterman, Reconstruction of crustal blocks of California on the basis of initial strontium isotopic compositious of Mesozoic granitic rocks, *U.S. Geol. Surv. Prof. Pap., 1071,* 1978.

Kistler, R. W., and R. Willden, The Precambrian-Cambrian boundary in the Ruby Moluntains, Nevada, *Geol. Soc. Am. Abstr. Programs, 3,* 32, 1969.

Kistler, R. W., J. F. Evernden, and H. R. Shaw, The Sierra Nevada piutonic cycle, 1, The origin of composite batholiths, *Geol. Soc. Am. Bull., 82,* 853–868, 1971.

Kistler, R. W., A. C. Robinson, and R. J. Fleck, Mesozoic, right-lateral fault in eastern California; *Geol. Soc. Am. Abstr. Programs, 12*(3), 115, 1980.

Masuda, A., N. Nakamura, and T. Tanaka, Fine structures of mutually normalized rare-earth patterns of chondrites, *Geochim. Cosmochim. Acta, 40,* 1351–1358, 1973.

McLennan, S. M., W. B. Nance, and S. R. Taylor, Rare earth element-thorium correlations in sedimentary rocks, and composition of the continental crust, *Geochim. Cosmochim. Acta, 44,* 1833–1839, 1980.

Miller, C. F., E. F. Stoddard, L. J. Bradfish, and W. A. Dollase, Composition of plutonic muscovite: Genetic implications, *Geol. Assoc. Can. Program Abstr., 5,* 71, 1980.

Misch, P., Regional structural reconnaissance in central-northeast Nevada and some adjacent areas: Observations and interpretations, in *Guidebook to the Geology of East-Central Nevada,* pp. 17-42, Intermountain Association of Petroleum Geologists and Eastern Nevada Geological Society, 1960.

Misch, P., and J. C. Hazzard, Stratigraphy and metamorphism of late Precambrian rocks of central-northeast Nevada and adjacent Utah, *Am. Assoc. Pet. Geol. Bull, 46,* 289–343, 1962.

Nicholls, J., D. W. Fiesinger, and V. G. Ethier, Fortran IV programs for processing routine electron microprobe data, *Comput. Geosci., 3,* 49–83, 1977.

Nockolds, S. R., The relation between chemical composition and paragenesis in the biotite micas of igneous rocks, *Am. J. Sci., 245,* 401–420, 1947.

Olson, J. C., and E. N. Hinrichs, Beryl-bearing pegmatites in the Ruby Mountains and other areas in Nevada and northwestern Arizona, *U.S. Geol. Surv. Bull, 1082-D,* 1960.

O'Neil, J. R., and B. W. Chappell, Oxygen and hydrogen isotope relations in the Berridale batholith, *J. Geol. Soc., 133,* 559–571, 1977.

O'Neil, J. R., and R. W. Kistler, Isotopic investigations in the Ruby Mountains, Nevada, paper presented at the 4th All Union Symposium on Stable Isotope, Geochemistry, Moscow, 1972.

O'Neil, J. R., S. E. Shaw, and R. H. Flood, Oxygen and hydrogen isotope compositions as indicators of granite genesis in the New England batholith, Australia, *Contrib. Mineral. Petrol., 62,* 313–328, 1977.

Pettijohn, F. J., Chemical composition of sandstones—Excluding carbonate and volcanic sands, Date of Geochemistry, 6th ed., Chapter S, *U.S. Geol. Surv. Prof. Pap., 440-S,* 1963.

Piwinskii, A. J., Experimental studies of igneous rock series, central Sierra Nevada batholith, California, *J. Geol., 76,* 548–570, 1968.

Shapiro, L., and W. W. Brannock, Rapid analysis of silicate, carbonate, and phosphate rocks, *U.S. Geol. Surv. Bull, 1144-A,* 1962.

Sharp, R. P., Basin-Range structure of the Ruby-East Humboldt Range, northeastern Nevada, *Geol. Soc. Am. Bull., 50,* 881–920, 1939.

Sharp, R. P., Stratigraphy and structure of the southern Ruby Mountains, Nevada, *Geol. Soc. Am. Bull., 53,* 647–690, 1942.

Snelson, S., The geology of the northern Ruby Mountains and the east Humboldt Range, Elko County, Nevada, PhD thesis., 214 pp., Univ. of Wash., Seattle, 1957.

Snoke, A., The transition from infrastructure to superstructure in the northern Ruby Range, Nevada, *Mem. Geol. Soc. Am., 153,* 287–333, 1980.

Stewart, J. H., Initial deposits in the Cordilleran geosyncline: Evidence of a late Precambrian (850 m.y.) continental separation, *Geol. Soc. Am. Bull., 83,* 1345–1360, 1972.

Stormer, J. C. Jr., A practical two-feldspar geothermometer, *Am. Mineral., 60,* 667–674, 1975.

Thompson, A. B., Mineral reactions in pelitic rocks, II, Calculations of some P-T-X (Fe-Mg) phase relations, *Am. J. Sci., 276,* 425–454, 1976.

Velde, B., Phengite micas: Synthesis, stability and natural occurrence, *Am. J. Sci., 263,* 886–913, 1965.

Wedepohl, K. H., Tantalum, in *Handbook of Geochemistry,* vol. 2, edited by K. H. Wedepohl, Springer-Verlag, New York, 1978.

Willden, R., and R. W. Kistler, Ordovician tectonism in the Ruby Mountains, Elko County, Nevada, *U.S. Geol. Surv. Prof. Pap., 575-D,* 1967.

Willden, R., and R. W. Kistler, Geology of the Jiggs quadrangle, Elko county, Nevada, *Map GQ859,* U.S. Geol. Surv., Reston, Va., 1969.

Willden, R., and R. W. Kistler, Precambrian and Paleozoic stratigraphy in central Ruby Mountains, Elko County, Nevada, *Rep. RMAG-UGA-1979 Basin and Range Symposium,* pp. 221–243, Rocky Mountain Association of Geologists, Denver, Colo., 1979.

Willden, R., H. H. Thomas, and T. W. Stern, Oligocene or younger Thrust faulting in the Ruby Mountains, northeastern Nevada, *Geol. Soc. Am. Bull., 78,* 1345–1358, 1967.

Wood, C. P., Petrogenesis of garnet-bearing rhyolites from Canterbury, *New Zealand, N. Z. J. Geol. Geophys., 17,* 759–787, 1973.

York, D., Least-square fitting of a straight line with correlated errors, *Earth Planet. Sci. Lett., 5,* 320–324, 1969.

(Received November 20, 1980;
revised May 8, 1981;
accepted May 13, 1981.)

JOURNAL OF GEOPHYSICAL RESEARCH, VOL. 86, NO. B11, PAGES 10607–10616, NOVEMBER 10, 1981

Two-Mica Granites of Northeastern Nevada

DONALD E. LEE

U.S. Geological Survey, Denver, Colorado 80225

RONALD W. KISTLER

U.S. Geological Survey, Menlo Park, California 94025

IRVING FRIEDMAN AND RICHARD E. VAN LOENEN

U.S. Geological Survey, Denver, Colorado, 80225

The field settings are described and analytical data are presented for six two-mica granites from northeastern Nevada. High $\delta^{18}O$ and $^{87}Sr/^{86}Sr$ values indicate that all are S-type granites, derived from continental crust. The major element chemistry and accessory mineral contents of these rocks also are characteristic of S-type granites. Chemical, X ray, and other data are presented for the micas recovered from these granites. The muscovites are notably high in Fe_2O_3, FeO, and MgO. Except for one hydrobiotite, each of the biotites has an MgO content near 6.0 weight percent. Two different types of two-mica granites are recognized in the area of this study. One type is distinguished by the presence of many biotite euhedra within muscovite phenocrysts and by an unusual suite of accessory minerals completely devoid of opaque oxides. This type probably resulted from anatexis of late Precambrian argillites under conditions of relatively low oxygen fugacity, along a line that roughly coincides with the westward disappearance of continental basement. In the other textural type of two-mica granite the micas are equigranular and there is a greater variety of accessory minerals. The magmatic evolution of this type also appears to reflect the influence of late Precambrian argillites; there may be age differences between the two types of two-mica granites.

INTRODUCTION

During 1969–1976 one of us (D. E. Lee) visited more than 160 plutons while systematically sampling granitoid rocks in the Basin and Range Province of Nevada, Utah, California, and Arizona, Among these 160 plutons, three are two-mica granites that resemble each other and are unlike any of the other plutons observed during this study. These unusual granites occur along a N–S trend in northeastern Nevada and are distinguished in part by the presence of large phenocrysts of muscovite, many of which contain small inclusions of euhedral biotite. Three additional two-mica granites, with muscovite and biotite in separate grains, occur in the same general area. The purpose of this paper is threefold: (1) to present analytical data for these six rocks and their constituent micas, (2) to point up some of the differences among two-mica granites, and (3) to comment on the possible significance of the three most distinctive plutons noted above.

FIELD SETTING OF THE ANALYZED SAMPLES

Sample localities are shown in Figure 1 and are given by *Lee and Van Loenen* [1971] or listed in Table 1. A given rock and each of its constituent minerals are designated by the same number.

The three muscovite-phenocrystic two-mica granites are present in the Pole Canyon–Can Young Canyon area of the southern Snake Range, in the Kern Mountains, and in the Toana Range. Samples 120-MW-60, 226-MW-60, 122-DL-62, and 135-DL-62 are from the Pole Canyon–Can Young Canyon pluton and are included in a comprehensive field and laboratory study of granitoid rocks of the southern Snake Range, White Pine County, Nevada. The location, field setting, mineralogy, and chemistry of these rocks are described in detail by *Lee and Van Loenen* [1971, pp. 5, 38, 39], who attribute the distinctive nature of the pluton to assimilation of the upper Precambrian Osceola Argillite. Typically, phenocrysts of muscovite as large as 2 cm across contain small biotite euhedra that are easily visible with a hand lens. It is not uncommon to find as many as 20 biotite crystals included within a single large grain of muscovite. Petrographically, muscovite and biotite, both of which are very fresh looking, are seen to be associated and often intergrown. They appear to have formed in equilibrium. The muscovite contains no opaque inclusions, nor does it present any other evidence that it is secondary after biotite. Indeed, the rocks are devoid of magnetite and ilmenite, these minerals being undetected not only in thin section but also during systematic mineral separation work in preparation of the micas for analysis. Sample 244-MW-60, from the Kern Mountains of White Pine County, Nevada, is practically identical to the southern Snake Range rock just described. A complete analyses of the apatite from sample 244-MW-60 is presented by *Lee et al.* [1973*a*]. Sample 415, from the Toana Range of Elko County, Nevada, represents the third of the muscovite-phenocrystic two-mica granites noted in the introduction. The rock contains phenocrysts of muscovite as large as 1 cm across, and many of these muscovite phenocrysts contain small biotite euhedra. The Toana Range pluton is exposed in intrusive contact with Cambrian Prospect Mountain Quartzite (map of *Stewart and Carlson*, [1978]).

The three plutons of equigranular two-mica granites are present in the Lexington Creek, the Willard Creek, and the Silver Creek areas. Sample 378 was collected from the Lexington Creek intrusive, southern Snake Range, Nevada. The map of *Whitebread* [1969] shows this intrusive cut by a thrust fault;

This paper is not subject to U.S. copyright. Published in 1981 by the American Geophysical Union.

Paper number 1B0163.

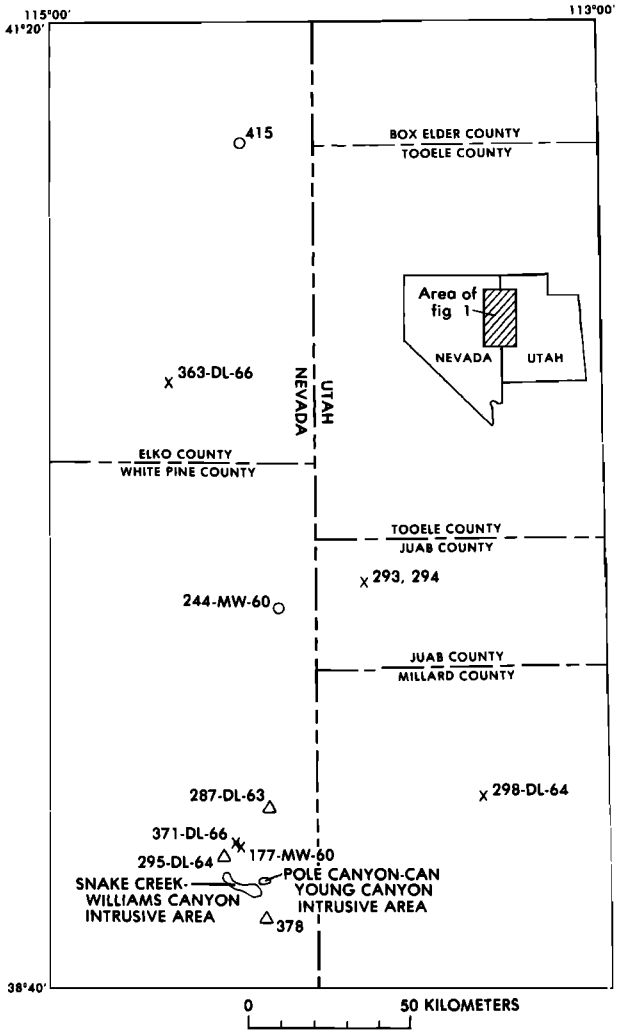

Fig. 1. Northeastern Nevada and northwestern Utah, showing locations of muscovite-phenocrystic two-mica granites (open circles), equigranular two-mica granites (open triangles), and biotites from calc-alkaline rocks (crosses) included in this study. The Pole Canyon–Can Young Canyon and Snake Creek–Williams Canyon intrusive areas are outlined; sample locations within these outlined intrusive areas are not shown for sake of simplicity. Sample site 493 is about 88 km east of the southeast corner of the map area.

Lee et al. [1980*a*, p. 24] suggest that the foliation noted by Whitebread and by *Drewes* [1958, p. 24] may have resulted from movement on the thrust before the pluton was completely crystallized. Whatever its cause, the development of the foliation appears to have been accompanied by a deuteric alteration that has left most of the original biotite chloritized and has otherwise obscured the original mineralogy of the pluton. However, it seems apparent that although muscovite and biotite coexisted in the original rock, biotite did not occur as euhedra within the muscovite as in the plutons discussed above. Sample 295-DL-64 was collected near the mouth of Willard Creek on the west side of the southern Snake Range from an area of intrusive rock referred to as the Osceola stock by *Armstrong* [1966]. In the vicinity of this sample site the stock is exposed in intrusive contact with upper Precambrian quartzitic and argillitic sediments (map of *Misch and Hazzard* [1962]). Sample 295-DL-64 is an equigranular rock in which biotite and muscovite are intimately associated, but biotite crystals are not present within the muscovite. Sample 287-DL-63 was collected in the bed of Silver Creek in the central Snake Range and is part of a pluton that is exposed in intrusive contact with Lower Cambrian quartzites and shales (map of *Hose and Blake* [1976]). The rock is equigranular, and although the biotite and muscovite are closely associated, biotite does not occur as euhedra within the muscovite.

THE MICA-BEARING ROCKS

Analyses of rock samples 120-MW-60, 226-MW-60, 122-DL-62, and 135-DL-62, all from the Pole Canyon–Can Young Canyon pluton of the southern Snake Range, are listed by *Lee and Van Loenen* [1971, p. 11, 18]. Analyses of the other two-mica granites discussed here are listed in Table 1. All of these rocks are peraluminous [*Shand*, 1951, p. 228]. That is, molecular $Al_2O_3 > (Na_2O + K_2O + CaO)$. Moreover, those analyses listed by Lee and Van Loenen contain 2.8–3.4 percent normative corundum; the analyses listed in Table 1, 1.48–2.72 percent. However, none of these rocks contains any of the aluminosilicates. Modal analyses listed by Lee and Van Loenen are similar to those in Table 1, where perhaps the most pronounced difference from sample to sample involves the plagioclase composition (An 7–An 28). The plagioclase from 135-DL-62 is approximately An 20 [*Lee et al.*, 1980*b*], probably representative of the plagioclase in the three other rock samples from the same area.

The Pole Canyon–Can Young Canyon pluton of the southern Snake Range contains a very distinctive suite of accessory minerals [*Lee and Van Loenen*, 1971, p. 39]. The apatite has a stubby habit, and almost all the zircon in the rock is present as tiny acicular inclusions within this apatite [*Lee et al.*, 1973*a*, p. 94]. The only other accessory minerals present are monazite [*Lee and Bastron*, 1967] and a few grains of an allanite-like mineral. Other accessory minerals were undetected not only in thin section but also during mineral separation work on the samples from this pluton. The great similarity of the Kern Mountains and Pole Canyon–Can Young Canyon two-mica granites extends to the details of the accessory mineral suites present in each, including even the same peculiar apatite-zircon relation just described. The third of the muscovite-phenocrystic two-mica granites discussed here, the Toana Range pluton, contains an accessory mineral suite similar, but not identical to that of the other two. The suite is similar in that it is sparsely distributed and is devoid of the opaque oxides, sphene, and most of the common accessory minerals. The dominant mineral present is apatite. There are a few tiny crystals of elongated zircon, but in contrast to the two plutons just discussed, these zircon crystals are discrete and not included in the apatite.

The equigranular two-mica granites contain a greater variety of accessory minerals. Sample 378, from the Lexington Creek intrusive of the southern Snake Range, contains apatite, zircon, fluorite, magnetite, and large amounts of epidote and zoisite. The character of the accessory mineral suite originally present in this rock is problematical because of the deuteric alteration noted earlier. Sample 295-DL-64, from the Willard Creek area of the southern Snake Range, contains monazite, ilmenite, magnetite, and sparse apatite, zircon, and garnet. Except for the magnetite present in sample 378, possibly secondary, this is the only one of the two-mica granites discussed here that contains any of the opaque oxides. Sample 287-DL-63, from the Silver Creek area of the central Snake Range, contains only very minor amounts of zircon, apatite, and an allanite-like mineral.

TABLE 1. Locations and Analyses of Granitoid Rocks From Which Analyzed Micas Were Recovered

	Sample Number, North Latitude, West Longitude				
	244-MW-60, 39°35′55″, 114°7′55″	415, 41°0′25″, 114°18′15″	295-DL-64, 30°01′58″, 114°22′22″	287-DL-63, 39°10′30″, 114°13′15″	378, 38°51′29″, 114°13′04″
	Chemical Analyses (Weight Percent)				
SiO_2	74.98	72.85	75.59	73.1	71.8
Al_2O_3	14.18	15.38	13.56	14.3	15.3
Fe_2O_3	0.25	0.75	0.31	0.50	1.1
FeO	0.63	0.25	0.72	1.0	0.48
MgO	0.26	0.19	0.22	0.37	0.43
CaO	1.53	1.04	0.81	1.7	1.8
Na_2O	3.17	4.07	3.50	3.5	3.3
K_2O	4.16	4.17	4.21	3.9	3.9
$H_2O(+)$	0.39	0.60	0.39	0.48	0.96
$H_2O(-)$	0.08	0.19	0.05	0.07	0.03
TiO_2	0.08	0.07	0.13	0.21	0.19
P_2O_5	0.07	0.06	0.05	0.08	0.12
MnO	0.02	0.03	0.06	0.10	0.10
CO_2	0.02	0.01	0.01	0.02	0.02
Cl	0.00	0.01	0.00	N. D.	N. D.
F	0.04	0.03	0.04	N. D.	N. D.
Subtotal	99.86	99.70	99.65	N. D.	N. D.
Less O	0.02	0.01	0.02	N. D.	N. D.
Total	99.84	99.69	99.63	99.	100.
	CIPW Norms				
Quartz	36.89	31.05	36.93	33.56	33.74
Corundum	1.90	2.46	1.92	1.48	2.72
Zircon	0.01	0.02	0.01	0.03	0.02
Orthoclase	24.63	24.76	24.98	23.21	23.16
Albite	26.88	34.61	29.73	29.83	28.06
Anorthite	7.02	4.73	3.64	7.84	8.06
Enstatite	0.65	0.48	0.55	0.93	1.08
Ferrosilite	0.86	N. D.	0.97	1.27	N. D.
Magnetite	0.36	0.70	0.45	0.73	1.33
Hematite	N. D.	0.27	N. D.	N. D.	0.19
Ilmenite	0.15	0.13	0.25	0.40	0.36
Apatite	0.17	0.14	0.12	0.19	0.29
Calcite	0.05	0.02	0.02	0.05	0.05
H_2O+F+Cl	0.51	0.83	0.48	0.55	0.51
Total	100	100	100	100	100
	Modal Analyses				
Quartz	31	35	35	33	35
Microcline	20	21	17	17	13
Plagioclase	35(An28)	36(An7)	38(An7)	38(An28)	33(An12)
Biotite	4	2	5	10	2
Muscovite	10	6	5	2	17
Total	100	100	100	100	100
	Semiquantitative Spectrographic Analyses (Weight Percent)				
Ba	0.2	0.2	0.2	0.15	0.2
Be	0.0001	0.0003	0.0003	0.0005	0.0005
Cr	0.0003	0	0	0	0
Cu	0	0	0	0.0005	0
Ga	0.002	0.005	0.002	0.003	0.003
Li	0	0	0	0.03	0
Nb	0	0.002	0.0015	0.001	0.0007
Ni	0.001	0	0	0	0
Pb	0.003	0.007	0.003	0.003	0.005
Sc	0	0	0.001	0	0
Sr	0.1	0.1	0.07	0.1	0.2
V	0	0	0.0007	0.002	0.002
Y	0	0.003	0.003	0.003	0.002
Yb	0	0.0003	0.0005	0.0003	0.0002
Zr	0.005	0.007	0.005	0.015	0.01

Samples 244-MW-60, 415, and 295-DL-64 analyzed by the chemical methods described by *Peck* [1964]. Elaine L. Munson Brandt was the analyst. Other samples were analyzed by P. Elmore and S. Botts, using methods similar to those developed by *Shapiro and Brannock* [1956]. Modal analyses were based on X ray diffraction patterns, following the procedure given by *Lee and Van Loenen* [1971, pp. 10, 11]. Semiquantitative spectragraphic analyses are by Leon A. Bradley. Method is described in text. N. D. means not determined or absent.

TABLE 2. Summary of Data on Accessory Minerals and $\delta^{18}O$ and Initial $^{87}Sr/^{86}Sr$ Values for Two-Mica Granites of Northeastern Nevada

Sample Number	Location of Intrusive	Accessory Minerals	$\delta^{18}O$	Initial $^{87}Sr/^{86}Sr$
		Granites with Biotite Present as Euhedra Within Muscovite Phenocrysts		
120-MW-60	Pole Canyon–Can Young Canyon	'Allanite' and monazite; acicular zircon in equant apatite	+10.9	0.7165
226-MW-60	Pole Canyon–Can Young Canyon	'Allanite' and monazite; acicular zircon in equant apatite	11.4	0.7165
122-DL-62	Pole Canyon–Can Young Canyon	'Allanite' and monazite; acicular zircon in equant apatite	11.0	0.7165
135-DL-62	Pole Canyon–Can Young Canyon	'Allanite' and monazite; acicular zircon in equant apatite	10.6	0.7165
244-MW-60	Kern Mountains	'Allanite' and monazite; acicular zircon in equant apatite	9.5	≃0.719
415	Toana Range	Apatite, zircon	9.1	0.7250
		Granites with Muscovite and Biotite Present as Discrete Grains		
378	Lexington Creek	Epidote, zoisite, apatite, zircon, fluorite, magnetite	10.6	0.7111
295-DL-64	Willard Creek	Monazite, ilmenite, magnetite, apatite, zircon, garnet	13.2	N. D.
287-DL-63	Silver Creek	'Allanite', zircon, apatite	12.4	N. D.

N. D. means not determined.

The accessory mineral suites are summarized in Table 2, along with data on the $^{18}O/^{16}O$ and $^{87}Sr/^{86}Sr$ ratios of these two-mica granites. These analytical results will be considered in relation to a classification of granites into S-types and I-types [*Chappell and White,* 1974]. Those granites derived from a largely pelitic source within the continental crust are S-types, while those derived from igneous materials are I-types.

There appears to be a systematic variation in $\delta^{18}O$ values from S-type to I-type granites, the division occurring at a $\delta^{18}O$ value of 10 [*O'Neil et al.,* 1977]. Lower values are characteristic of I-type granites, higher values of S-type. Except for samples 415 and 244-MW-60 the $\delta^{18}O$ values listed in Table 2 all are above 10, indicating S-type granites. Sample 415 (Toana range pluton) is a friable rock, and it is possible that the $\delta^{18}O$ value (+9.1) of this rock may have been lowered by late- or post-magmatic interaction with meteoric water. We will consider these $\delta^{18}O$ values further in a later section.

Data for muscovite 226-MW-60 [*Lee et al.,* 1970, p. D98] and our unpublished data for one sample of aplite and four samples of two-mica granite from the Pole Canyon–Can Young Canyon pluton of the southern Snake Range give an initial $^{87}Sr/^{86}Sr$ ratio of 0.7165 at an age of 79 m.y. A detailed discussion of these results is beyond the scope of this paper. However, we note here that this Cretaceous two-mica granite is separated from the Jurassic [*Lee et al.,* 1968, 1970] calc-alkaline rocks to the south only by a septum of sedimentary rocks about 2 km long and 300 m wide [*Lee and Van Loenen,* 1971, plate 1].

Whole-rock rubidium and strontium data for sample 244-MW-60 and for a nearby aplite give an apparent age of 71.6 m.y. and an initial $^{87}Sr/^{86}Sr$ ratio of 0.719 for the two-mica granite of the Kern Mountains [*Lee et al.,* 1980*a*, p. 22]. *Best et al.* [1974] found similarly high initial $^{87}Sr/^{86}S$ ratios and postulated a minimum age of 60 m.y. for this granite.

Sample 415, from the Toana Range pluton, gave an initial $^{87}Sr/^{86}Sr$ ratio of 0.7250 at a biotite K-Ar age of 128 m.y. Sample 378, from the Lexington Creek intrusive of the southern Snake Range, gave an initial $^{87}Sr/^{86}Sr$ ratio of 0.7111 at an assumed age of 150 m.y. This pluton may actually be younger, in which case the initial ratio would be somewhat higher. No $^{87}Sr/^{86}Sr$ ratios have been determined for samples 287-DL-63 and 295-DL-64.

Typical S-type granites have the highest initial $^{87}Sr/^{86}Sr$ ratios; typical I-type, the lowest. *Beckinsale* [1979, p. 37, 38] indicates that initial ratios higher than 0.708 are one characteristic of Phanerozoic S-type granites. All the initial ratios determined for the two mica-granites under discussion here are above 0.711 (Table 2), well within the range of S-type granites. The data in Table 2 are considered further in the closing discussion.

Despite the similarities among the six masses of two-mica granites considered here, plagioclase compositions show a rather wide range (An7–An28), no matter if we consider the entire group or only the three muscovite-phenocrystic rocks. The relatively sodic plagioclases in rocks 415 and 295-DL-64 (both An 7) indicate higher Na activity than in the others, and the Na_2O contents of their muscovites (each has Na_2O 0.80 percent) also indicate higher Na activity. In general, Na_2O contents of these muscovites tend to relate inversely to the An contents of the coexisting plagioclase. This same relation is not found between the biotites and their coexisting muscovites and plagioclases. That is to say, in regard to Na activity the biotites do not appear to be in very close equilibrium with their coexisting muscovites and plagioclases. Along with the density range exhibited by each of these biotites, as well as the different Fe_2O_3/FeO values of biotites from the two-mica granite of the Pole Canyon–Can Young Canyon area [*Lee and Van Loenen,* 1970], this may be interpreted as another indication that the biotites in these rocks were modified by late magmatic or post-magmatic processes.

MICA ANALYSES AND PHYSICAL PROPERTIES

The micas were prepared for analysis by methods described by *Lee and Van Loenen* [1970, p. D198]. Briefly, the final purification was by centrifuging in adjusted mixtures of methylene iodide and bromoform and by repeated passes through the magnetic separator. Generally, the muscovites fractionated over a very narrow density range, indicating a similarly small range of composition of the mineral in the rock. On the other hand, each biotite fractionated over a rather large density range, as indicated in Table 3, and the recovery of a homogeneous sample for analysis was difficult. Similar difficulties were encountered in the purification of the biotites discussed by *Lee and Van Loenen* [1970], who describe the problem in some detail.

Major elements were determined by the chemical methods described by *Peck* [1964] and calculated on the basis of 24 (O, OH, F, Cl) to the general mica formula $X_2Y_{4-6}Z_8O_{20}$ (OH, F, Cl)$_4$, using the computer program described by *Jackson et al.* [1967]. Calculated values for density and cell volume were determined by the same program.

Quantitative barium, rubidium, and strontium values were determined by X ray fluorescence. The methods for barium

TABLE 3. Analytical Data for Biotites From Two-Mica Granitoid Rocks of Northeastern Nevada

	Sample Number			
	244-MW-60	415	295-DL-64	287-DL-63
		Density		
Average	3.10	2.98	3.15	3.14
Range	3.06–3.13	2.95–3.01	3.11–3.19	3.11–3.17
		Index of Refraction (β)		
Average	1.646	1.672	1.652	1.653
Range	1.642–1.650	1.664–1.680	1.646–1.658	1.650–1.656
		Chemical Analyses (Weight Percent)		
SiO_2	35.61	34.52	34.29	35.76
Al_2O_3	18.17	18.59	17.99	17.78
Fe_2O_3	3.71	23.15	2.40	2.69
FeO	19.86	4.62	22.50	20.48
MgO	6.32	3.83	5.62	5.91
CaO	0.03	0.31	0.00	0.04
Na_2O	0.33	0.34	0.35	0.89
K_2O	8.96	6.10	8.95	9.40
$H_2O(+)$	3.20	5.61	3.37	2.93
$H_2O(-)$	0.14	0.89	0.11	0.07
TiO_2	2.20	1.21	2.53	3.02
P_2O_5	0.03	0.05	0.02	0.03
MnO	0.48	0.60	1.11	0.46
Cl	0.02	0.01	0.02	0.01
F	0.79	0.20	0.54	0.89
Subtotal	99.85	100.03	99.80	100.36
Less O	0.33	0.08	0.23	0.37
Total	99.52	99.95	99.57	99.99
		Quantitative Ba, Rb, Sr (Weight Percent)		
Ba	0.1188	0.0342	0.1494	0.0381
Rb	0.0699	0.0777	0.0782	0.1068
Sr	0.00076	0.00663	0.00122	0.00044
		Numbers of Ions on Basis of 24(O, OH, F, Cl)		
Z				
P^{5+}		0.01		
Si	5.50	5.06	5.37	5.54
Al^{IV}	2.50	2.93	2.63	2.46
Total	8.00	8.00	8.00	8.00
Y				
Al^{VI}	0.81	0.28	0.69	0.78
Fe^{3+}	0.43	2.55	0.28	0.31
Ti	0.26	0.13	0.30	0.35
Mg	1.46	0.84	1.31	1.36
Fe^{2+}	2.52	0.57	2.95	2.65
Mn	0.06	0.07	0.15	0.06
Total	5.59	4.44	5.68	5.51
X				
Ca	0.01	0.05	0.00	0.01
Na	0.10	0.10	0.11	0.27
K	1.77	1.14	1.79	1.86
Ba	0.01	0.00	0.01	0.00
Rb	0.01	0.01	0.01	0.01
Total	1.90	1.30	1.92	2.15
OH	3.30	5.39	3.52	3.03
F	0.39	0.09	0.27	0.44
Cl	0.01	0.00	0.01	0.00
Total	3.70	5.48	3.80	3.47
		Semiquantitative Spectrographic Analyses (Weight Percent)		
Be	0	0.001	0.0002	0
Co	0.0015	0	0.002	0.002
Cr	0.001	0.0002	0.003	0.002
Cu	0.002	0.002	0.003	0.0015
Ga	0.01	0.015	0.02	0.01
Li	0.07	0.1	0.05	0.2
Mo	0.0005	0.0005	0.0007	0.0005
Nb	0.002	0.005	0.005	0.005
Ni	0.0007	0.0005	0.001	0.0005
Pb	0	0.005	0.002	0.001
Sc	0.001	0.0005	0.007	0.005

TABLE 3. (continued)

	Sample Number			
	244-MW-60	415	295-DL-64	287-DL-63
	Semiquantitative Spectrographic Analyses (Weight Percent) (continued)			
Sn	0	0.002	0.003	0.003
V	0.01	0.001	0.015	0.03
Y	0.001	0.0015	0.003	0.002
Yb	0.0001	0.0002	0.0002	0.0005
Zn	0.1	0.1	0	0.05
Zr	0.002	0.005	0.01	0.01

Chemical analyses are by Elaine L. Munson Brandt. Quantitative Ba, Rb, and Sr analyses and by Willis P. Doering. Semiquantitative spectrographic analyses are by Leon A. Bradley. Methods of analyses are described in text.

and for rubidium and strontium are described by *Lee and Doering* [1974, 1980, respectively]. Results of semiquantitative spectrographic analyses are based on their identity with geometric brackets whose boundaries are 1.2, 0.83, 0.56, 0.38, 0.26, 0.18, 0.12, and so forth, and are reported arbitrarily as midpoints of these brackets: 1, 0.7, 0.5, 0.3, 0.2, 0.15, and 0.1, respectively. The precision of a reported value is approximately plus or minus one bracket at 69% confidence or two brackets at 95% confidence.

Analyses of biotites 120-MW-60, 122-DL-62, and 135-DL-62, from the Pole Canyon–Can Young Canyon area of the southern Snake Range, are listed by *Lee and Van Loenen* [1970]. We were unable to obtain an analysis of biotite 378 because of the deuteric alteration of the Lexington Creek intrusive noted earlier. Analyses of the other biotites from these two-mica granites are listed in Table 3.

Although MgO contents of the three Pole Canyon–Can Young Canyon biotites are in the range 6.03–6.18 percent, and most other major element contents also are similar from one of these biotites to another, Fe_2O_3/FeO values differ greatly [*Lee and Van Loenen,* 1970]. These writers interpreted the low and almost identical MgO values to indicate that these biotites were originally equilibrated with respect to the same (relatively low) oxygen fugacity. It was further suggested that localized conditions subsequent to magmatic crystallization may have altered Fe_2O_3/FeO values without modifying the overall mineralogy of the rock.

Except for 415 the biotites in Table 3 have MgO contents (5.62–6.32%) very similar to those just discussed. Moreover, there is some evidence to suggest that relatively low MgO contents may be a general characteristic of biotites coexisting with muscovites in plutonic rocks. *Nockolds* [1947, Table 1] lists four such biotites with MgO contents in the range 4.42–5.61% and three with MgO contents of 7.93–9.30%, *de Albuquerque* [1973, Table 1] presents five from northern Portugal with MgO contents of 6.32–8.38%, and *Guidotti et al.* [1975,

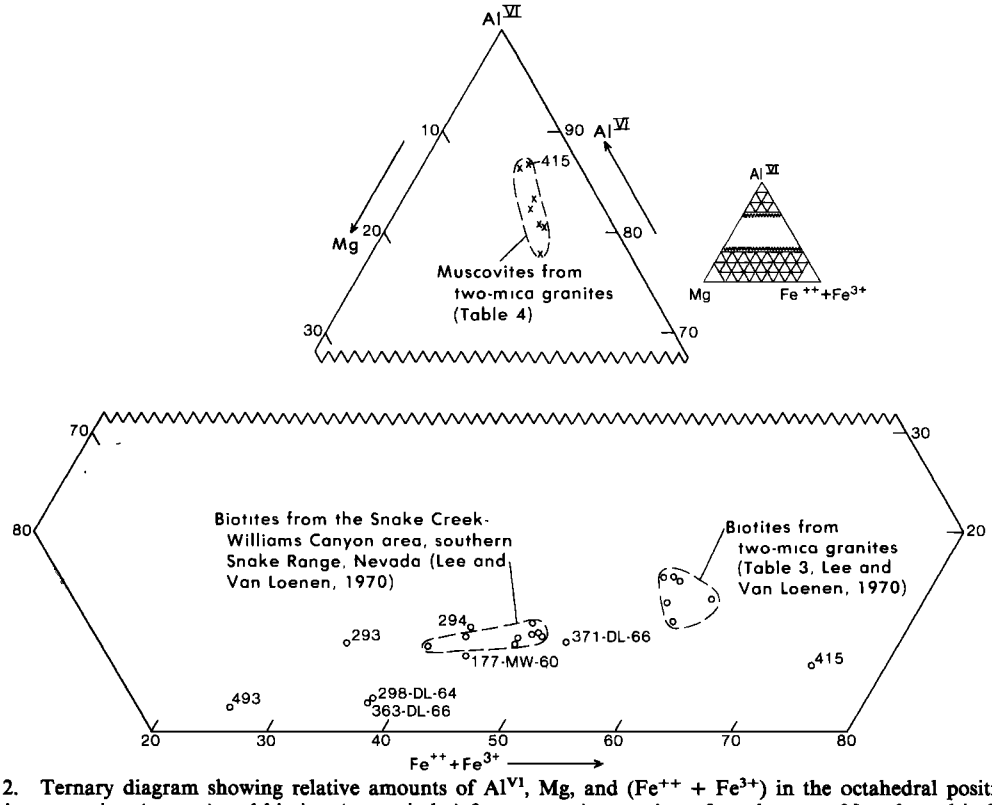

Fig. 2. Ternary diagram showing relative amounts of Al^{VI}, Mg, and (Fe^{++} + Fe^{3+}) in the octahedral position (Y group) in muscovites (crosses) and biotites (open circles) from two-mica granites of northeastern Nevada and in biotites (open circles) from various other granitoid rocks of eastern Nevada and western Utah (Figure 1). Biotites from the Snake Creek–Williams Canyon area of the Southern Snake Range, Nevada and (except for sample 415) biotites and muscovites from two-mica granites are not numbered for sake of simplicity.

TABLE 4. Analytical Data for Muscovites From Two-Mica Granitoid Rocks of Northeastern Nevada

	Sample Number							
	135-DL-62	122-DL-62	120-MW-60	226-MW-60	244-MW-60	415	295-DL-64	378
				Chemical Analyses (Weight Percent)				
SiO_2	46.11	46.03	46.25	46.28	45.79	46.07	45.76	46.54
Al_2O_3	31.90	31.16	30.88	31.12	33.72	33.48	32.37	30.12
Fe_2O_3	2.72	3.50	5.23*	3.15	1.85	1.51	2.18	4.26
FeO	1.46	1.53	N. D.	1.75	1.31	1.84	2.03	1.24
MgO	1.22	1.21	1.30	1.22	1.05	.83	1.07	1.54
CaO	0.00	0.00	0.00	0.03	0.00	0.00	0.00	0.04
Na_2O	0.57	0.63	0.60	0.68	0.49	0.80	0.80	0.46
K_2O	10.71	10.63	10.72	10.58	10.78	10.52	10.38	10.74
$H_2O(+)$	4.13	4.02	N. D.	4.12	4.15	4.17	4.04	4.10
$H_2O(-)$	0.05	0.08	0.02	0.06	0.09	0.09	0.04	0.04
TiO_2	0.76	0.77	0.74	0.66	0.53	0.33	0.77	0.64
P_2O_5	0.01	0.02	N. D.	0.05	0.01	0.01	0.02	0.01
MnO	0.05	0.07	N. D.	0.08	0.04	0.07	0.13	0.05
Cl	0.00	0.00	0.01	0.00	0.01	0.01	0.00	0.00
F	0.45	0.51	0.54	0.36	0.32	0.32	0.30	0.30
Subtotal	100.14	100.16	N. D.	100.14	100.14	100.05	99.89	100.08
Less O	0.19	0.21	N. D.	0.15	0.13	0.13	0.12	0.13
Total	99.95	99.95	N. D.	99.99	100.01	99.92	99.77	99.95
				Quantitative Ba, Rb, Sr (Weight Percent)				
Ba	0.0399	0.0491	0.0485	N. D.	0.1249	0.0766	0.0549	0.0760
Rb	0.0435	0.0465	0.0579	N. D.	0.0260	0.0373	0.0685	0.0668
Sr	0.00291	0.00383	0.00348	N. D.	0.00418	0.00235	0.00158	0.00645
				Numbers of Ions on Basis of 24(O, OH, F, Cl)				
Z								
P^{5+}			N. D.	0.01				
Si	6.22	6.24	N. D.	6.26	6.15	6.20	6.20	6.31
Al^{IV}	1.78	1.76	N. D.	1.73	1.85	1.80	1.80	1.69
Total	8.00	8.00	N. D.	8.00	8.00	8.00	8.00	8.00
Y								
Al^{VI}	3.30	3.22	N. D.	3.23	3.50	3.51	3.37	3.12
Fe^{3+}	0.28	0.36	N. D.	0.32	0.19	0.15	0.22	0.44
Ti	0.08	0.08	N. D.	0.07	0.05	0.03	0.08	0.07
Mg	0.25	0.24	N. D.	0.25	0.21	0.17	0.22	0.31
Fe^{2+}	0.17	0.17	N. D.	0.20	0.15	0.21	0.23	0.14
Mn	0.01	0.01	N. D.	0.01	0.01	0.01	0.02	0.01
Total	4.09	4.08	N. D.	4.08	4.11	4.08	4.14	4.09
X								
Ca	0.00	0.00	N. D.	0.00	0.00	0.00	0.00	0.01
Na	0.15	0.17	N. D.	0.18	0.13	0.21	0.21	0.12
K	1.84	1.84	N. D.	1.83	1.85	1.81	1.79	1.86
Ba	0.00	0.00	N. D.	N. D.	0.01	0.01	0.00	0.01
Rb	0.00	0.00	N. D.	N. D.	0.00	0.00	0.01	0.01
Total	1.99	2.01	N. D.	2.01	1.99	2.03	2.01	2.01
OH	3.72	3.63	N. D.	3.72	3.72	3.74	3.65	3.71
F	0.19	0.22	N. D.	0.15	0.14	0.14	0.13	0.13
Cl	0.00	0.00	N. D.	0.00	0.00	0.00	0.00	0.00
Total	3.91	3.85	N. D.	3.87	3.86	3.88	3.78	3.84
				Semiquantitative Spectrographic Analyses (Weight Percent)				
B	0.003	0	0.002	0	0	0	0	0
Be	0.0001	0.0002	0	0.0005	0	0.0002	0.0007	0.0005
Cr	0.0005	0.0007	0	0	0.0005	0.0002	0.0005	0.0005
Cu	0.0005	0.0007	0.0003	0.002	0.0002	0.0005	0.0005	0.0002
Ga	0.01	0.015	0.01	0.01	0.015	0.02	0.02	0.015
Li	0.05	0.05	0.07	0.07	0.02	0.07	0.05	0.02
Nb	0.003	0.005	0.005	0.005	0.001	0.002	0.005	0.001
Ni	0.0007	0.0005	0	0.0007	0	0	0	0
Pb	0	0	0	0	0.001	0.001	0.001	0.001
Sc	0.002	0.005	0.002	0.002	0.003	0.003	0.015	0.002
Sn	0.003	0.003	0	0.002	0	0.005	0.005	0.002
V	0.015	0.015	0.007	0.007	0.015	0.003	0.01	0.015
Y	0	0	0	0	0	0	0.002	0
Yb	0	0.0001	0	0	0	0	0.0002	0.0001
Zr	0	0.005	0.003	0.005	0	0	0.003	0.005

Chemical analyses are by Elaine L. Munson Brandt. Quantitative Ba, Rb, and Sr analyses are by Willis P. Doering. Semiquantitative spectrographic analyses are by Leon A. Bradley. Methods of analyses are described in text. N. D. means not determined.

* Total iron as Fe_2O_3.

TABLE 5. Properties of Analyzed Muscovites

	Sample Number							
	135-DL-62	122-DL-62	120-MW-60	226-MW-60	244-MW-60	415	295-DL-64	378
				Optical Properties				
β index	1.601	1.600	1.605	1.603	1.594	1.596	1.602	1.605
2V (−)	36°	34°	37°	35°	40°	42°	37°	38°
				Density				
Observed (±0.01)	2.87	2.88	2.88	2.88	2.86	2.87	2.89	2.88
Calculated	2.871	2.881	N. D.	2.872	2.868	2.871	2.884	2.887
				Cell Parameters Observed				
a(±0.005 Å)	5.200	5.202	5.201	5.212	5.196	5.195	5.194	5.205
b(±0.010 Å)	9.040	9.034	9.024	9.039	9.023	9.021	9.031	9.038
c(±0.010 Å)	20.049	20.045	20.035	29.039	29.065	20.046	20.043	20.028
β	95°45′	95°45′	95°46′	95°46′	95°49′	95°45′	95°47′	95°48′
Volume (±1.0 Å^3)	937.8	938.2	935.6	939.4	935.8	934.7	935.5	937.4
				Cell Volume Calculated				
Volume (Å^3)	934.78	938.55	N. D.	936.82	938.30	938.24	933.61	939.74

N. D. means not determined.

Table 5] list seven from northwestern Maine with MgO contents of 6.06–7.75%. Biotites coexisting with muscovite in plutonic rocks may tend to have relatively low MgO contents because muscovite-bearing rocks crystallize from felsic magmas likely to have low Mg/Fe.

In order to draw the distinction between biotites from two-mica granites and those from calc-alkaline rocks in the area of this study, we present Figure 2, showing relative amounts of Al^{VI}, Mg, and (Fe^{++} + Fe^{+++}) in the octahedral positions of the respective biotites. Biotites from both types of two-mica granites (except 415) plot in a relatively small field near the (Fe^{++} + Fe^{+++}) apex. The outlined field of eight biotites from the Snake Creek–Williams Canyon area are from the calc-alkaline rocks separated from the two-mica granites of the Pole Canyon–Can Young Canyon area only by a narrow septum of sedimentary rocks [*Lee and Van Loenen,* 1971, pl. 1]. Chemical data for the other biotites plotted on Figure 2 are unpublished, but locations and K-Ar age data are listed for 177-MW-60 and 371-DL-66 by *Lee et al.* [1970], a Pb/α age is listed for the zircon coexisting with biotite 298-DL-64 [*Lee et al.,* 1968], and a complete analysis is given for the apatite coexisting with 363-DL-66 [*Lee et al.,* 1973*a*]. Samples 293 and 294 are from the Deep Creek Range intrusive, Juab County, Utah, and sample 493 was collected in the Monroe Creek area, Sevier County, Utah.

Thus from the standpoint of the experimental work of *Wones and Eugster* [1965], biotites from the two-mica granites included in this study are distinguished by their low and very similar contents of MgO, indicating initial equilibration with respect to a relatively low oxygen fugacity. This is further substantiated by the complete lack of opaque oxides (Table 2) in the three muscovite-phenocrystic two-mica granites discussed here, and in sample 287 from the central Snake Range.

Biotite 415 (Table 3) is a hydrobiotite, with H_3O^+ substituting for K^+ in the interlayer X-group. If our earlier speculation that the $\delta^{18}O$ value of rock 415 (+9.1) may have been lowered by late- or post-magmatic interaction with meteoric water is correct, the same process may have caused the alteration of the biotite originally present in this rock. The analysis of biotite 415 is remarkably similar to that of a biotite from an alkali granite in the Velence Mountain of Hungary [*Gokhale,* 1967]. No additional information was reported for the Valence Mountain biotite.

All of the analyzed muscovites (Table 4, Figure 2) are $2M_1$ micas. As a group these igneous muscovites are notably high in Fe_2O_3, FeO, and MgO, and as such they represent solid solution between muscovite and celadonite and are phengitic micas [*Foster,* 1956]. It has been shown that high P and P_{H_2O} favor an increase in the phengitic content of muscovite [*Ernst,* 1963; *Velde,* 1965, 1967], and *Ramsay* [1973, p. 478] cites many previous studies and concludes that increased solid solution of celadonite in muscovite (that is, more phengitic muscovite) is favored by low temperature and high pressure. Such conditions suggest a low-grade metamorphic rather than an igneous environment.

However, *Guidotti* [1978] also has found phengitic muscovites in igneous rocks, the two-mica adamellites of northwestern Maine. The modal analyses listed [*Guidotti,* 1978, Table 1] for these two-mica adamellites resemble those of the two-mica granites included in the present study. Moreover, analyses of eight of the white micas present in the Maine adamellites [*Guidotti,* 1978, Table 2] are very similar to those of the muscovites recovered from the two-mica granites of northeastern Nevada (Table 4). Guidotti concluded that the celadonite content of the (igneous) muscovite from the Maine adamellites systematically changes with mineral assemblage in a pattern similar to that found in metamorphic parageneses. Results of the present study provide strong support for Guidotti's findings.

The ionic ratios of the analyzed muscovites in Table 4 are in rather good agreement with the ideal for dioctahedral mica. Properties of the analyzed micas are listed in Table 5, where there is good agreement between the observed and calculated values for density and cell volume. Data for muscovite 287 are not available, because this mineral was lost during the purification process.

DISCUSSION

As a group the six masses of two-mica granite considered here are similar in the following respects:

1. All of these masses have $\delta^{18}O$ values within or near the relatively high range presumably characteristic of S-type granites.

2. The four masses for which data are available all have relatively high initial $^{87}Sr/^{86}Sr$ ratios, well within the range characteristic of S-type granites.

3. All six masses are peraluminous, and modal analyses are similar.

4. The MgO contents of the constituent biotites are relatively low, and except for sample 415, a hydrobiotite, all fall in the restricted range of 5.62–6.32 percent. Moreover, results of previous workers already cited suggest that relatively low MgO contents may be a general characteristic of biotites coexisting with muscovites in igneous rocks.

5. The constituent muscovites all are phengitic and similar to one another and to the muscovites coexisting with biotites in the two-mica adamellites of northwestern Maine [*Guidotti*, 1978].

As noted in the introduction, the muscovite-phenocrystic two-mica granites of the Toana Range, the Kern Mountains, and the Pole Canyon–Can Young Canyon area of the southern Snake Range are different from all other plutons observed during systematic sampling of granitoid rocks in the Basin and Range Province of Nevada, Utah, California, and Arizona. In view of this, the locations of these three intrusive masses are rather striking. They are aligned along a north-south trend about 225 km long in northeastern Nevada (Figure 1). Moreover, the three equigranular two-mica granites discussed here are found along or near the same trend. Only a few other examples of two-mica granites were observed in the Basin and Range Province during the sampling program. Although all are within 'an inner Cordilleran muscovite-bearing plutonic belt' recognized by *Miller and Bradfish* [1980, p. 414, Figure 2], they are not otherwise arranged in any systematic fashion.

The north-south trend just described coincides roughly with the westward disappearance of a continental basement, as brought out in a summary of the regional geology and by the lead isotope data presented by *Stacey and Zartman* [1978]. *Stewart* [1972] suggests that a change occurred in the tectonic framework of western North America after the deposition of the Belt supergroup (850 to 1250 m.y.), and that this change marked the beginning of the Cordilleran geosyncline. In terms of plate tectonics theory, this change marks the time of a continental separation, with the subsequent accumulation of a thick sedimentary sequence along the stable continental margin. The resulting wedge of upper Precambrian and Lower Cambrian clastic sediments, having its maximum thickness near the edge of the continental basement, is diagramed by *Stewart* [1972, Figures 3 and 6]. We suggest that the two-mica granites of the Toana Range, the Kern Mountains, and the Pole Canyon–Can Young Canyon area of the southern Snake Range may have resulted from anatexis of some of this accumulation of upper Precambrian–Lower Cambrian clastic material near the westward disappearance of a continental basement delineated on the basis of lead isotopes by *Stacey and Zartman* [1978]. Based principally on their determination of variable and high initial $^{87}Sr/^{86}Sr$ ratios, *Best et al.* [1974] have suggested that the two-mica granite of the Kern Mountains formed from anatexis of old sialic basement rocks.

The origin suggested for these three masses of muscovite-phenocrystic two-mica granites would account for their peraluminous character, the types of accessory mineral suites observed, the $^{18}O/^{16}O$ and $^{87}Sr/^{86}Sr$ ratios determined, and the relatively low oxygen fugacity indicated by biotite compositions and the complete absence of opaque oxides. In other words, such an origin would be consistent with the locations and strongly S-type nature of these very unusual rocks.

From the field relations already discussed, it is likely that the magmatic evolution of the equigranular two-mica granites included in this study, the Lexington Creek, Willard Creek, and Silver Creek masses, also was strongly influenced by the great thickness of late Precambrian and Early Cambrian clastics noted above. Indeed, one or more of these masses may also have evolved through anatexis. The data presented (Table 2) for these rocks are more characteristic of S-type granites than I-type, except for the accessory mineral suite present in the Lexington Creek pluton. There may be systematic age differences between the muscovite-phenocrystic and equigranular types of two-mica granites discussed here, but data are still too few to check this possibility.

Based on this study, it appears that two-mica granites are characterized by phengitic muscovites and biotites with relatively low MgO content ($\simeq$ 6%), regardless of whether the biotite occurs as euhedra within muscovite phenocrysts or as discrete grains. Nonetheless, the three muscovite-phenocrystic two-mica granites emphasized throughout this paper would seem to have a special significance. To our knowledge no other such rocks are reported in the literature, while 'ordinary' two-mica granites have been reported from a number of localities, as is apparent from references cited earlier. Taken together, the two-mica granites of the Kern Mountains and the Pole Canyon–Can Young Canyon area of the southern Snake Range are of greatest interest, not only because the biotite is present as euhedra within muscovite but also because practically all of the zircon in these rocks is present as acicular inclusions within equant apatite.

The presence of biotite euhedra within muscovite phenocrysts would seem to result from some special relationship between the nucleation and growth rates of the two minerals. The presence of acicular zircon within apatite suggests that the two minerals formed in close equilibrium. Both are tetragonal minerals, but the orientation of zircon needles appears to be random and not related to the crystal structure of the apatite. Regardless of the validity of these speculations, we are unable to explain why these mineral textures are so rare, or what they might indicate regarding the evolution of the rocks in which they are found.

REFERENCES

Armstrong, R. L., K-Ar dating using neutron activation for Ar analysis, *Geochim. Cosmochim. Acta, 30,* 565–600, 1966.

Beckinsale, R. D., Granite magmatism in the tin belt of south-east Asia, in *Origin of Granite Batholiths: Geochemical Evidence,* edited by M. P. Atherton, and J. Tarney, Shiva Publishing, Ltd., 148 p., 1979.

Best, M. G., R. L. Armstrong, W. C. Graustein, G. F. Embree, and R. C. Ahlborn, Mica granite of the Kern Mountains pluton, eastern White Pine County, Nevada—Mobilized basement of the Cordilleran miogeosyncline?, *Geol. Soc. Am. Bull., 85,* 1277–1286, 1974.

Chappell, B. W., and A. J. R. White, Two contrasting granite types, *Pac. Geol., 8,* 173–174, 1974.

de Albuquerque, C. C. R., Geochemistry of biotites from granitic rocks, northern Portugal, *Geochim. Cosmochim. Acta, 37,* 1779–1802, 1973.

Drewes, H. D., Structural geology of the southern Snake Range, Nevada, *Geol. Soc. Am. Bull., 69,* 221–239, 1958.

Ernst, W. G., Significance of phengitic micas from low-grade schists, *Am. Mineralogist, 48,* 1357–1373, 1963.

Foster, M. D., Correlation of dioctahedral potassium micas on the basis of their charge relations, *Geol. Surv. Bull. U.S., 1036-D,* 57–67, 1956.

Gokhale, N. W., Alkali-poor biotites from the Velence Mountain granites, Hungary, *Curr. Sci., 36,* 578–579, 1967.

Guidotti, C. V., Muscovite and K-feldspar from two-mica adamellite in northwestern Maine: Composition and petrogenic implications, *Am. Mineral., 63,* 750–753, 1978.

Guidotti, C. V., J. T. Sheney, and P. D. Conatore, Interrelationship

between Mg/Fe ratio and octahedral Al content in biotite, *Am. Mineral., 60,* 849–853, 1975.

Hose, R. K., and M. C. Blake, Geology of White Pine County, Nevada, *Bull. Nev. Bur. Mines Geol., 85,* 1–35, 1976.

Jackson, E. D., R. E. Stevens, and R. W. Bowen, A computer-based procedure for deriving mineral formulas from mineral analyses, *Geol. Surv. Prof. Pap. U.S., 575C,* 23–31, 1967.

Lee, D. E., and H. Bastron, Fractionation of rare-earth elements in allanite and monazite as related to geology of the Mount Wheeler mine area, Nevada, *Geochim. Cosmochim. Acta, 31,* 339–356, 1967.

Lee, D. E., and W. P. Doering, Barium in hybrid granitoid rocks of the southern Snake Range, Nevada, *J. Res. U.S. Geol. Surv., 2,* 671–675, 1974.

Lee, D. E., and W. P. Doering, Rubidium and strontium in hybrid granitoid rocks, Southern Snake Range, Nevada, *Geol. Surv. Prof. Pap. U.S., 1158-A,* 1–7, 1980.

Lee, D. E., and R. E. Van Loenen, Biotites from hybrid granitoid rocks of the southern Snake Range, Nevada, *Geol. Surv. Prof. Pap. U.S., 700-D,* 196–206, 1970.

Lee, D. F., and R. E. Van Loenen, Hybrid granitoid rocks of the southern Snake Range, Nevada, *Geol. Surv. Prof. Pap. U.S., 668,* 1971.

Lee, D. E., T. W. Stern, R. E. Mays, and R. E. Van Loenen, Accessory zircon from granitoid rocks of the Mount Wheeler mine area, Nevada, *Geol. Surv. Prof. Pap., U.S., 600-D,* 197–203, 1968.

Lee, D. E., R. F. Marvin, T. W. Stern, and Z. E. Peterman, Modification of potassium-argon ages by Tertiary thrusting in the Snake Range, White Pine County, Nevada, *Geol. Surv. Prof. Pap. U.S., 700-D,* 92–102, 1970.

Lee, D. E., E. L. M. Brandt, R. E. Van Loenen, and H. J. Rose, Jr., The chemistry of five accessory rock-forming apatites, *J. Res. U.S. Geol. Surv., 1,* 267–272, 1973*a*.

Lee, D. E., R. E. Van Loenen, and R. E. Mays, Accessory apatite from hybrid granitoid rocks of the southern Snake Range, Nevada, *J. Res. U.S. Geol. Surv., 1,* 89–98, 1973*b*.

Lee, D. E., R. F. Marvin, and H. H. Mehnert, A radiometric age study of Mesozoic-Cenozoic metamorphism in eastern White Pine County, Nevada, and nearby Utah, *Geol. Surv. Prof. Pap. U.S., 1158-C,* 17–28, 1980*a*.

Lee, D. E., R. E. Van Loenen, and E. L. M. Brandt, Feldspars from hybrid granitoid rocks of the southern Snake Range, Nevada, *Geol. Surv. Open-File Rep. U.S., 80-322,* 1980*b*.

Miller, C. F., and L. J. Bradfish, An inner Cordilleran belt of muscovite-bearing plutons, *Geology, 8,* 412–416, 1980.

Misch, P., and J. C. Hazzard, Stratigraphy and metamorphism of Late Precambrian rocks in central northeastern Nevada and adjacent Utah, *Am. Assoc. Pet. Geol. Bull., 46,* 289–343, 1962.

Nockolds, S. R., The relation between chemical composition and paragenesis in the biotite micas of igneous rocks, *Am. J. Sci., 245,* 401–420, 1947.

O'Neil, J. R., S. E. Shaw, and H. H. Flood, Oxygen and hydrogen isotope compositions as indicators of granite genesis in the New England batholith, Australia, *Contrib. Mineral. Petrol., 62,* 313–328, 1977.

Peck, L. C., Systematic analysis of silicates, *Geol. Surv. Bull. U.S., 1170,* 1964.

Ramsay, C. R., Controls of biotite zone mineral chemistry in Archean metasediments near Yellowknife, Northwest Territories, Canada, *J. Pet., 14,* 467–488, 1973.

Shand, S. J., *Eruptive Rocks,* 488 pp., John Wiley, New York, 1951.

Shapiro, L., and W. W. Brannock, Rapid analysis of silicate rocks, *Geol. Surv. Bull. U.S., 1036-C,* 19–56, 1956.

Stacey, J. S., and R. E. Zartman, A lead and strontium isotopic study of igneous rocks and ores from the Gold Hill mining district, Utah, *Utah Geol., 5,* 1–15, 1978.

Stewart, J. H., Initial deposits in the Cordilleran geosyncline: Evidence of a late Precambrian (<850 m.y.) continental separation, *Geol. Soc. Am. Bull, 83,* 1345–1360, 1972.

Stewart, J. H., and J. E. Carlson, Geologic map of Nevada, U.S. Geol. Surv. with Nev. Bur. of Mines and Geol., Reno, Nev., 1978.

Velde, B., Phengitic micas: Synthesis, stability, and natural occurrence, *Am. J. Sci., 263,* 886–913, 1965.

Velde, B., Si^{+4} content of natural phengites: *Contrib. Mineral. Petrol., 14,* 250–258, 1967.

Whitebread, D. H., Geologic map of the Wheeler Peak and Garrison quadrangles, White Pine County, Nevada, and Milford County, Utah, *U.S. Geol. Surv. Misc. Geol. Invest., Map I-578,* 1969.

Wones, D. R., and H. P. Eugster, Stability of biotite—Experiment, theory, and application, *Am. Mineralogist, 50,* 1228–1272, 1965.

(Received October 27, 1980;
accepted January 22, 1981.)

JOURNAL OF GEOPHYSICAL RESEARCH, VOL. 86, NO. B11, PAGES 10617-10632, NOVEMBER 10, 1981

THE LATE ARCHAEAN QÔRQUT GRANITE COMPLEX OF SOUTHERN WEST GREENLAND

Michael Brown and C. R. L. Friend

Department of Geology and Physical Sciences, Oxford Polytechnic, Headington, Oxford OX3 OBP, United Kingdom

V. R. McGregor

Atangmik, 3912 Sukkertoppen, Greenland, Denmark
Geological Survey of Greenland, Copenhagen, Denmark

W. T. Perkins

Department of Geology and Physical Sciences, Oxford Polytechnic, Headington, Oxford OX3 OBP, United Kingdom

Abstract. Granites and granite pegmatites composing the ∿ 2550-Ma Qôrqut granite complex occur in a SSW-NNE trending linear belt >150 km long extending through the Buksefjorden-Ameralik-Godthåbsfjord region of southern West Greenland. The main body of the complex crops out over a distance of 50 km from Ameralik to Kapisigdlit kangerdluat and reaches a maximum outcrop width of 18 km between Storø and Qôrqut. Around Qôrqut the complex comprises three main groups of granites: early leucocratic granites, various grey biotite granites, and late aplogranite-granite pegmatites. Within the 1500-m vertical section available in this area the complex has a tripartite structure comprising a lower zone dominantly of polyphase granite, an intermediate zone where country rock occurs as rafts in polyphase granite with a complex sheeted structure, and an upper zone dominantly of country rock sheeted by granite. Fifty-two specimens of granite have been analyzed for major, minor, and some trace elements. Geochemical variation within the complex is consistent with either fractional crystallization or partial melting, but in both cases, feldspar + biotite must have been involved either as fractionating phases or as residual phases during melting to account for the trace element chemistry. Two possible models for the generation of the complex are either anatexis of granulite facies rocks in the lower crust following an influx of volatiles and heat from the mantle or melting at intermediate depths of amphibolite facies rocks with volatiles supplied by breakdown of hydrous phases.

Introduction

By far the most voluminous rocks in the Archaean of southern West Greenland are grey gneisses with tonalitic-trondhjemitic-granodioritic compositions. In the Godthåbsfjord-Ameralik-Buksefjorden region (Figure 1), two generations of grey gneisses have been recognized: the first comprising a major part of the ∿ 3700-Ma-old Amîtsoq gneisses; and the second comprising the ∿ 3000-Ma-old Nûk gneisses [McGregor, 1973, 1979]. A plausible model for the origin of these grey gneisses involves, first, partial melting of metabasaltic rocks followed by intrusion and differentiation of the resultant magmas under syntectonic conditions [O'Nions and Pankhurst, 1978; Compton, 1978b; McGregor, 1979]. It has been argued that the continental crust in this region was built up mainly of grey gneisses derived from the mantle by this two-stage process during two major episodes (termed accretion-differentiation superevents) approximately 3800-3600 Ma and 3100-2800 Ma ago [Moorbath, 1977, 1978; McGregor 1979]. During both of these crust-forming episodes, remelting of older sialic rocks is considered to have been, at most, only a minor factor in the production of the grey gneisses.

In contrast, potassic granites are much less abundant in the Archaean of southern West Greenland. Quartz-monzonitic augen gneiss occurs as a late phase in the Amîtsoq gneisses between Ameralik and Buksefjord [Bridgwater et al., 1976; Chadwick and Nutman, 1979]. This may be the product of partial melting of Amîtsoq grey gneisses under granulite facies conditions during the later part of the first accretion-differentiation superevent [McGregor, 1979; Griffin et al., 1980]. To the south of the Godthåbsfjord-Ameralik-Buksefjorden region, in the Sermilik-Fiskenaesset region, the ∿ 2800-Ma-old Ilivertalik granite [Kalsbeek and Myers, 1973; Myers, 1976; Pidgeon et al., 1976; Kalsbeek, 1976] has similar chemical characteristics to the Amîtsoq augen gneiss, for example high Fe/Mg ratios (see data of Hall [1977] and Compton [1978a] and compare those of McGregor [1979]). It, too, may be the product of partial melting of granulite facies grey gneisses [Compton, 1978b]. In the Godthåbsfjord-Ameralik-Buksefjorden region, the ∿ 2550-Ma-old Qôrqut granite complex represents the last major plutonic event in the Archaean history of southern West Greenland.

The occurrence of a discordant body of potassic granite at Qôrqut, a small branch of Godthåbsfjord (Figure 1), was first recorded by Noe-Nygaard and Ramberg [1961, p.7], but, presumably as the result of a drafting error, the granite was designated as homogeneous quartz dioritic to granodioritic gneiss on their map. McGregor made a reconnaissance of this granite in the area between Ameralik and Kapisigdlit kangerdluat (Figure 1) in 1965 and

Copyright 1981 by the American Geophysical Union.

Paper number 1B0461.
0148-0227/81/001B-0461$01.00

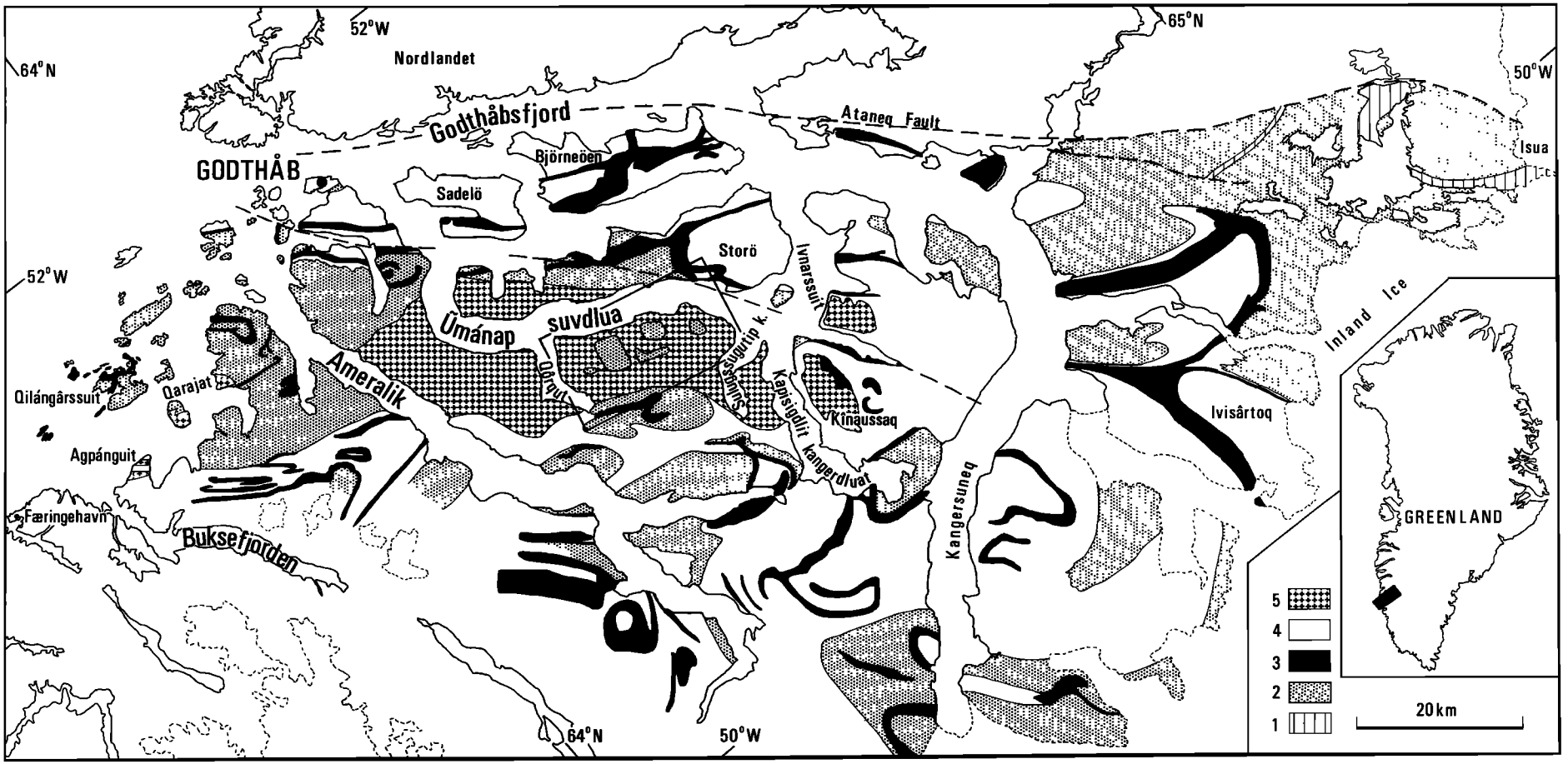

Fig. 1. Simplified geological map of the Godthåbsfjord-Ameralik-Buksefjorden region to show the location of the Qôrqut granite complex and of places referred to in the text. The area covered by Figure 2 is outlined. Key: 1 = Isua supracrustals; 2 = Amîtsoq gneisses; 3 = undifferentiated Malene supracrustals and anorthositic rocks; 4 = Nûk gneisses, including some areas of undifferentiated rocks; 5 = the main body of the Qôrqut granite complex.

1966, completed in 1978 and 1979, and named it the Qôrqut granite [McGregor, 1973].

Detailed mapping in the type area of the Qôrqut granite, around Qôrqut and as far north as Sulugssugutip kangerdlua, was undertaken during 1978 [Burwell and Friend, 1979] and 1979 [Brown and Friend, 1980a, b], and it is from this area that most of the information on the internal structure of the granite has been obtained. Much of the mapped Qôrqut granite between Ameralik and Kapisigdlit kangerdluat has in fact a highly complex internal structure with considerable amounts of country rock cut by sheets of many different phases of granite. It is misleading to think of the granitic rocks as forming a clearly defined pluton even in the type area around Qôrqut where granite is the dominant lithology. In order to avoid giving this impression and also to emphasize the polyphase nature of the granite, Brown and Friend [1980b] have suggested that the name be changed to the Qôrqut granite complex. Mapping by members of Exeter University team between 1972 and 1977 [Sharpe, 1975; Gibbs, 1976; Compton, 1978a; Coe et al., 1976; Chadwick, et al., 1978; Chadwick and Nutman 1979] has documented the existence of microgranite and banded aplite-pegmatite sheets along the extension of the axis of the main body of the Qôrqut granite complex to the south-southwest between Ameralik and Buksefjorden. Walton mapped the north-northeastern extension of the Qôrqut granite complex btween Kapisigdlit kangerdluat and Kangersuneq [Walton, 1976], but he included with the granite many rocks considered by us to be late-stage, relatively homogeneous phases of the Nûk gneisses. The extent of the Qôrqut granite complex in this area is, therefore, uncertain. Further to the northeast on Ivisârtoq, Friend and Hall mapped garnet-bearing granite and granite pegmatite sheets [Friend and Hall, 1977] that subsequent isotopic work (S. Moorbath, verbal communication, 1980) confirmed as being of the same age as the Qôrqut granite complex in the type area around Qôrqut.

Thus granites and associated granite pegmatites composing the Qôrqut granite complex are found in a linear belt, greater than 150 km long, that extends from the margin of the inland ice on Ivisârtoq, south-southwest at least as far as the outer coast at Faeringehavn (in Figure 1, only areas dominantly of granite are ornamented as Qôrqut granite complex).

This paper presents the current state of knowledge on the rather unusual late Archaean Qôrqut granite complex of southern West Greenland. Much of this material, including fifty-two chemical anlyses, is previously unpublished. We aim to give field and geochemical evidence which we interpret as showing that the Qôrqut granite complex represents a substantial example of reworking of sialic crustal rocks by anatexis to produce granite magmas.

Review of Isotope Geology

Rb-Sr, U-Pb, and Pb-Pb methods have been used in determining the age of the Qôrqut granite complex. Pankhurst et al. [1973] obtained a Rb-Sr mineral isochron age of 2520±30 Ma (recalculated using $\lambda = 1.42 \times 10^{-11}$ y^{-1}) on a late pegmatite from the south coast of Ameralik 5 km south-east of the contact of the main body of the Qôrqut granite complex. Moorbath and Pankhurst [1976] reported a Rb-Sr whole rock isochron age of 2460±90 Ma from seven granite samples from the north coast of Ameralik. Reanlysis of these samples and analysis of a further sixteen samples from Ûmanap suvdlua and Sulugssugutip kangerdlua has revised the whole rock Rb-Sr isochron age to 2530±30 Ma, the initial $^{87}Sr/^{86}Sr$ ratio being 0.7081±0.0007 [Moorbath et al., 1981]. The age agrees well with a Pb-Pb whole rock isochron age of 2580±80 Ma obtained by Moorbath et al [1981] on twenty-eight samples of Qôrcut granite and three pegmatitic K-feldspars, and with a U-Pb zircon age of 2530±30 Ma obtained by Baadsgaard [1976]. The high initial $^{87}Sr/^{86}Sr$ of the granite and the relatively unradiogenic nature of the contained Pb suggest that crustal anatexis was a major contributory factor in the genesis of the granites [Moorbath et al., 1981].

Regional Setting of the Qôrqut Granite Complex

The Qôrqut granite complex, whose age is taken to be 2550 Ma [Moorbath et al., 1981], was emplaced toward the end of a late Archaean period of plutonic activity 2700-2500 Ma ago. This activity affected not only parts of the Archaean craton but also areas to the north which subsequently became part of the early Proterozoic Nagssugtoqidian mobile belt. Large areas, especially in the northern part of the Archaean craton, escaped or were only weakly affected by this plutonic activity. In these areas, granulite facies mineral assemblages dating from the ∿ 2800-Ma metamorphic culmination [Black et al., 1973; Pidgeon and Kalsbeek, 1978] are widely preserved. Elsewhere, extensive retrogression of granulite facies mineral assemblages was caused by an influx of water and other mobile components such as Cl, K, Rb, and Si [Bridgwater, 1979].

Deformation in the period immediately preceding the formation of the Qôrqut granite complex appears to have been concentrated in SSW-NNE trending linear belts of intense ductile strain. Several linear belts of this type have been recognized in the Buksefjorden-Ameralik-Godthåbsfjord region [Sharpe, 1975; Chadwick and Nutman, 1979]. One such linear deformation belt is cut by the eastern contact zone of the Qôrqut granite complex on the north side of Ameralik. Another important linear deformation belt extends through southwestern Bjørneøen, Godthåb town, and the islands to the south-south west, some 10 km to the west of the Qôrqut granite complex. In this belt the foliation is generally steeply inclined, and both earlier structures and the lithological units are strongly attenuated. A strong extension lineation was produced that plunges regularly at 20°-30° to the SSW.

Widespread, but relatively minor, intrusion of granitic rocks occurred before and during the formation of these linear deformation belts.

On Bjørneøen and Sadelø, for example, a suite of thick granite pegmatites and thinner granite aplite dykes postdates the main fabric-forming deformation in the Nûk gneisses. The aplites are strongly deformed in the linear deformation belt exposed on south-western Bjørneøen. Zircons from an aplite belonging to this suite from south-eastern Bjørneøn have yielded a U/Pb concordia/discordia age of 2670 Ma [Baadsgaard and McGregor, 1981] which thus constrains the deformation within the linear belt which crosses southwestern Bjørneøen to the period immediately before the formation of the Qôrqut granite complex.

It appears, then, that shortly before the formation of the Qôrqut granite complex, the region was affected by activity that included the development of SSW-NNE trending linear belts of ductile deformation, the intrusion at the present level of erosion of small volumes of granitic magma, and the influx of aqueous fluids over large areas. Since the deeper parts of the crust in the Godthåbsfjord-Ameralik-Buksefjorden region can reasonably be assumed to have been depleted in H_2O during granulite facies regional metamorphism around the 2800-Ma metamorphic peak, the fluids must have come from below the crust.

One of the most interesting features of the Qôrqut granite complex is its location within a SSW-NNE trending linear belt at least 150 km long but no more than 18 km wide at the present level of erosion. The belt within which the Qôrqut granite complex was formed differs, however, from the linear deformation belts formed earlier in the same general period of activity in that a much larger volume of granite has been emplaced in it, at least at the present level of erosion, and that it does not appear to have been the site of significant ductile strain.

Field Relations

Country Rocks

Along much of its length the main body of the Qôrqut granite complex lies subparallel to the regional structure, although in detail at its margins the complex is usually sharply discordant. Around the northern part of Umanap suvdlua, however, the structure of the country rocks is more complicated than in the area to the south, and in its northern part the main body of the complex is strongly discordant to the regional structure.

Between Buksefjorden and the northern part of Umanap suvdlua the complex lies within a major unit of Amîtsoq gneisses (Figure 1). The country rocks around the main body of the complex, between Ameralik and Kapisigdlit kangerdluat, are almost entirely composed of Amîtsoq gneisses. Amîtsoq gneisses are recognized in the field by the presence of amphibolite layers. These layers are sometimes discordant to the gneissose banding but occur more commonly as strongly disrupted remnants. They have been derived from an abundant swarm of basic dykes — the Ameralik dykes [McGregor, 1973]. Commonly the rafts and enclaves of country rock gneisses which are found within the Qôrqut granite complex are seen to contain amphibolite layers or fragments, but these amphibolites do not cut the granites themselves. The striking similarity between the amphibolites in the rafts and enclaves and those found in the country rock Amîtsoq gneisses indicates that many of the rafts and enclaves within the complex are, in fact, derived from Amîtsoq gneisses.

Nûk gneisses, with enclaves of anorthositic rocks, crop out deep within the complex on the south side of the mouth of Qôrqut. Further north, between Sagdlia and Sulugssugutip kangerdlua (Figure 2), the lower levels of the complex contain rafts and enclaves of Nûk gneisses together with anorthositic rocks and amphibolites, the latter comparable in lithology to components of the Malene supracrustals [McGregor, 1973]. Within the area between Qôrqut and Sulugssugutip kangerdlua, the original configuration of the country rocks prior to granite emplacement is preserved as shown by careful mapping of the rafts and enclaves of country rock gneisses found within the granite complex (Figure 2). North of Kapisigdlit kangerdluat, the granites cut mainly Nûk gneisses, many of which contain enclaves and thin, semicontinuous units of anorthositic rocks.

Form and Internal Structure of the Qôrqut Granite Complex

Granite (as defined by Streckeisen [1976]) is the dominant lithology in an elongated area that extends for some 50 km from Ameralik to Kapisigdlit kangerdluat and which reaches a maximum width of 18 km from southern Storø to Qôrqut (Figure 1). The form of the complex in this area is difficult to establish because the margin of the complex in most places consists of a broad zone in which country rocks are cut by varying amounts of granite and granite pegmatite as sheets. There is generally no simple intrusive contact. Only on the south coast of Storø has a relatively sharp contact been observed. This contact is steeply inclined to the northwest and slightly discordant to the lithological boundaries and gneissose foliation in the country rocks (Figure 1). Compared with the margins of the complex elsewhere, there are relatively few angular, unmodified rafts and enclaves of country rock within the granite close to the contact and relatively few sheets of granite within the country rock outside the contact.

The granite complex appears to lie in the core of a broad antiformal structure that plunges 20°-30° to the south-southwest [McGregor, 1973; Bridgwater et al., 1976], parallel to the strike of the linear deformation belts. Four sets of joints are established from a stereographic analysis of joint orientations within the granites in the area north of Qôrqut. Two of these sets, oriented N050°E and N160°E, are symmetrically disposed about the SSW trending antiformal axis of the complex; one set, oriented N110°E, is perpendicular to this axis, and a fourth set, which is gently dipping and apparently randomly oriented, appears to be related to

the margins of randomly oriented shallowly inclined sheets of granite or composite aplogranite-granite pegmatite [Burwell and Friend, 1979]. This symmetrical arrangement of three sets of joints about the axial direction of the antiformal structure suggests some tectonic influence during the crystallization stage of the complex. The antiformal structure is probably the result of the diapiric rise of the granitic magmas which built up the complex.

In the area between Qôrqut and Sulugssugutip kangerdlua, the Qôrqut granite complex comprises three main groups of granites [Brown and Friend, 1980b]: early leucocratic granites which are often characterized by the presence of biotite schlieren and lamellae (group 1 granites); essentially homogeneous, grey biotite granites (group 2 granites); and composite aplogranite-granite pegmatite sheets (group 3 granites).

The early leucocratic granites contain discrete to diffuse enclaves of gneiss which exhibit a range of states of modification of their original textures and structures by segregation and disruption during anatexis. These modified enclaves are regarded by Brown and Friend [1980a] as fragments brought in by the leucocratic granites from a melting zone, rather than representing locally derived fragments of country rock gneisses, since clear examples of the latter are generally little modified after incorporation in the granite. The grey biotite granites, which are free of modified gneiss enclaves of the type found in the group 1 granites, occur as sheets from <1 m to >10 m in thickness which cut country rock rafts, the early leucocratic granites, and each other. At many localities, up to four penecontemporaneous phases of grey biotite granite occur, but although a consistent intrusive sequence occurs

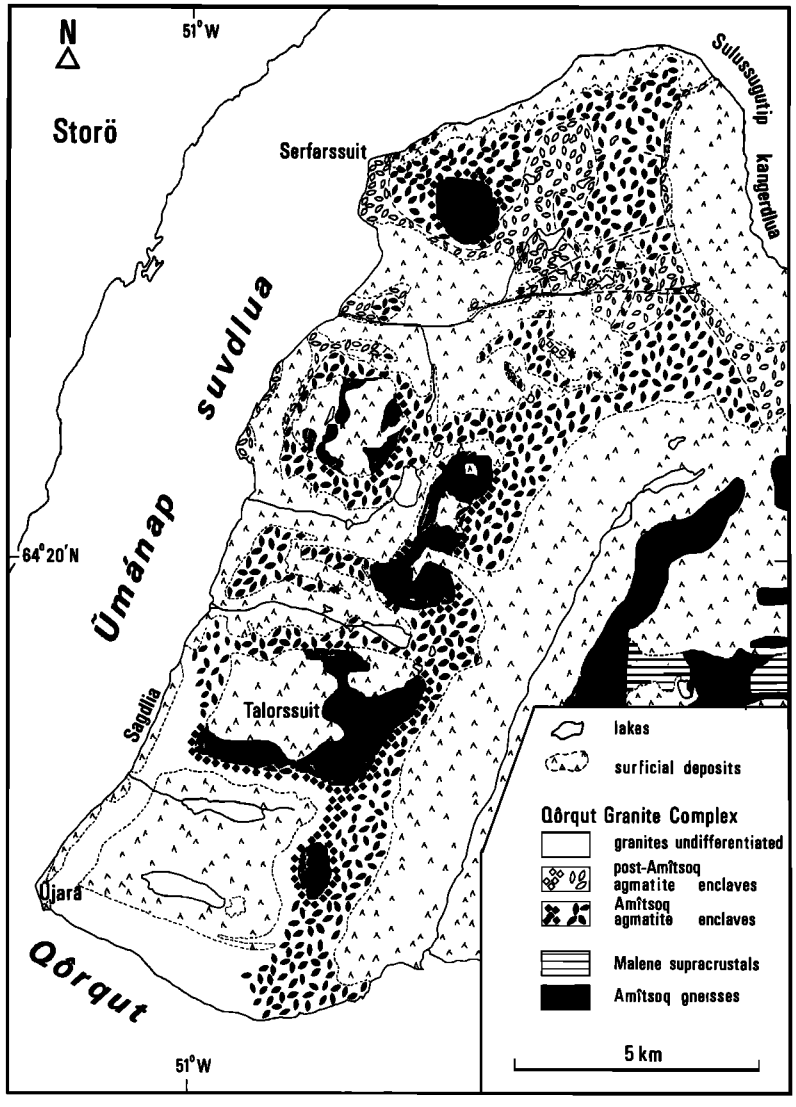

Fig. 2. Geological map (post Qôrqut granite complex dykes omitted) of the area east of Ûmánap suvdlua between Qôrqut and Sulugssugutip kangerdlua showing in detail part of the Qôrqut granite complex (the geology on Storø is not shown). Note that Talorssuit is 1490 m high; spot heights have been omitted for clarity but are shown in Figure 3.

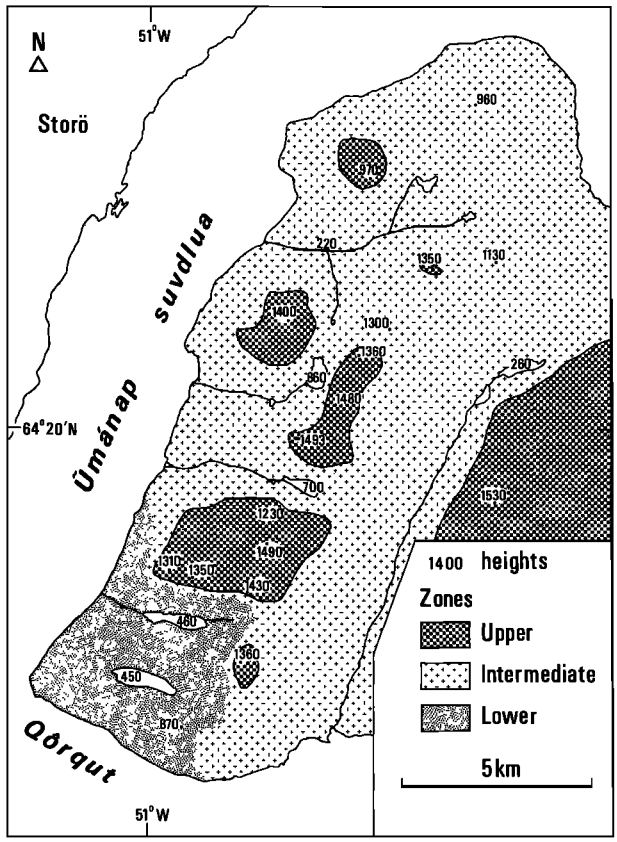

Fig. 3a. Map to show the three zones of the Qôrqut granite complex referred to in the text in the area east of Ûmánap suvdlua between Qôrqut and Sulugssugutip kangerdlua. Spot heights are used to illustrate the strongly dissected nature of the terrain which exposes the complex through approximately 1500 m of relief in this area.

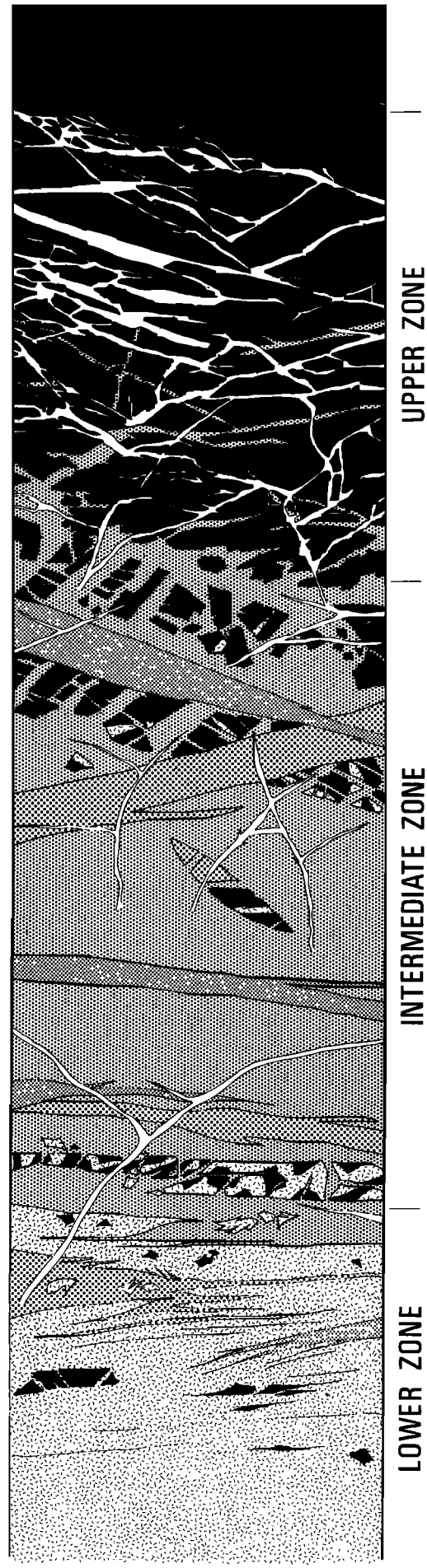

Fig. 3b. (Opposite) Composite section, about 2000 m thick, through the Qôrqut granite complex compiled from field data, field sketches, photographs, and photographic mosaics of steep to vertical fjord walls and mountain faces to show the internal structure of the complex and the three zones referred to in the text. Country rocks are shown in black, early leucocratic granites (group 1 granites) are shown in jackstraw ornament, grey biotite granites (group 2 granites) are shown in various dotted ornaments, and late aplogranite-granite pegmatite sheets (group 3 granites) are shown unornamented.

at some localities, it has not proved possible to construct an intrusive sequence of grey biotite granites applicable to the whole outcrop of the Qôrqut granite complex. The aplogranite-granite pegmatite sheets often show a distinct layering between biotite-bearing and biotite free types and between aplitic texture and pegmatitic texture. They cut through all of the earlier granites and become volumetrically the most important group at higher levels in the complex.

Within the 1500 m vertical section through the Qôrqut granite complex provided by the relief in this area, the complex exhibits a distinct tripartite structure [Brown and Friend, 1980b] (Figures 2 and 3) comprising (1) a lower zone dominantly of polyphase granite with group 1 granites commonly containing enclaves of modified gneiss but only rare enclaves of unmodified country rock cut by various group 2 granites and occasional group 3 granites, (2) an intermediate zone with a substantial proportion of country rock as rafts and enclaves in polyphase granite and with a complex sheeted structure dominantly of group 2 granites (shown semidiagrammatically in Figure 3), and (3) an upper zone dominantly of country rock cut by sheets of group 2 granite and of group 3 composite aplogranite-granite pegmatite (Figure 3, upper zone drawn from a number of photographic mosaics). The sheets in the upper zone fill what appear to be extension fractures rather than shear fractures, which suggests that on a regional scale the minimum principal compressive stress was acting vertically. On the steep sections through the complex provided by the mountain peaks, the upper zone is seen to comprise lozenge-shaped areas which consist of country rock cut by group 2 granites with the lozenge-shaped areas separated by anastomosing sheets of group 3 granites.

Between Qôrqut and Ameralik the internal structure of complex is broadly similar to that north of Qôrqut (described above), although it has not been studied in such detail. An upper zone, similar to that established north of Qôrqut, crops out on the tops of the mountains and on the slopes facing Ameralik. Country rocks, mainly Amîtsoq gneisses, are cut by sheets of grey granite and recut by a network of composite aplogranite-granite pegmatite sheets which generally dip broadly east or west at low to moderate angles. Granite sheets become thicker and more abundant downward, and an intermediate zone, some hundreds of meters thick, is dominated by more massive granite with subordinate rafts and enclaves of country rock. The deepest exposed part of the complex, along the coast of Ũmánap suvdlua north and south of the mouth of Qôrqut and on the southeast corner of Storø, is made up of polyphase granites including early leucocratic granites with abundant strongly modified rafts and enclaves of Amîtsoq gneisses. Nûk gneisses, virtually continuous and unmodified, crop out along the coast on the south side of the mouth of Qôrqut.

To the south the main body of the Qôrqut granite complex disappears down the plunge of the antiform as it crosses Ameralik. However, gently dipping sheets of microgranite and more variably inclined sheets of banded aplite-pegmatite, similar to those in the upper zone of the complex further north (described above), are common in a belt that extends to the south-southwest (see, for example, Chadwick and Nutman [1979]), suggesting that the complex extends at depth in this direction. More continuous areas of granite occur around Qarajat [Compton, 1978a], on the Agpanguit peninsula [Gibbs, 1976], and on Skinderhvalen, north of Faeringehavn, where the granite is thought to form an overthrust structure [Sharpe, 1975] (Figure 1).

North of Sulugssugutip kangerdlua the complex is poorly known. Polyphase granite is the dominant lithology on the peninsula between Sulugssugutip kangerdlua and Kapisigdlit kangerdluat. Along the north coast of Kapisigdlit kangerluat, around Kînaussaq, older rocks, mainly Nuk gneisses, are cut by only a few widely spaced granite sheets, although gently dipping granite sheets become progressively more abundant upwards on the mountain wall. To the northwest, rocks believed to be part of the Qôrqut granite complex crop out extensively on the plateau northeast of Ivnarssuit (A. Steenfelt, verbal communication, 1979) and reach the coast on the northwestern part of Ivnarssuit as a number of sheets several tens of meters thick that dip at moderate angles to the north-west. Structurally below these sheets, to the southeast, there is little Qôrqut granite in the gently dipping Nûk gneisses. Further northeast, on Ivisârtoq, bodies of aplitic and pegmatitic granite, which are part of the Qôrqut granite complex, have been emplaced into the core and along the limbs of an earlier antiformal structure [Friend and Hall, 1977].

Petrography

Although it is clear that the Qôrqut granite complex comprises a number of different types of granite throughout much of its outcrop, detailed mapping and subdivision of the granite has been attempted only in the area between Qôrqut and Sulugssugutip kangerdlua. For the purpose of this review, we offer some general petrographic remarks which apply to members of the complex as a whole. Table 1 gives a selection of representative modes of Qôrqut granite complex rocks.

Most of the rocks that make up the Qôrqut granite complex are medium grained (in the range 1-5 mm), although they vary from coarse-medium to fine-medium, with a texture which varies from hypidiomorphic-granular (common) to allotriomorphic-granular (rare). A porphyritic texture, with slightly larger plagioclase crystals, is occasionally developed. With the exception of a few thin, late tonalite dykes, the rocks examined in thin section are mostly granites but with some granodiorites (see Figure 4 and Table 1) and comprise quartz, sodic plagioclase, microcline, and biotite as the major phases. The plagioclase, which has a composition generally within the middle part of the oligoclase range, often has an albitic rim and occasionally is zoned, sometimes exhibiting patchy zoning. The microcline, which is often perthitic, is generally anhedral and slightly replacive toward quartz and plagioclase. Biotite (α = light brown, $\beta = \gamma$ = very dark green-brown) is the only mafic phase; it contains zircons and needles of rutile and may be fringed by opaques. Biotite is often closely associated

TABLE 1. Modes of Granites From the Qôrqut Granite Complex, Southern West Greenland

Specimen	Quartz	Plagio-clase	Micro-cline	Biotite	Others*
86619	24.0	39.2	20.4	12.6	3.8
79798	32.0	30.7	27.3	6.5	3.4
195322(1)	32.1	29.1	35.5	2.6	0.8
195337(1)	28.9	34.5	32.1	1.9	2.7
195352(1)	32.2	30.5	34.3	2.3	0.6
195360(1)	33.8	32.7	29.0	4.1	0.3
195361(1)	27.3	45.9	23.4	1.3	1.2
195304(2)	26.5	42.9	20.8	9.3	0.5
195309(2)	30.9	32.3	30.4	4.9	1.6
195317(2)	20.5	49.0	18.2	12.0	0.4
195325(2)	34.0	36.0	24.1	4.7	1.2
195329(2)	30.0	29.5	30.4	6.4	3.7
195338(2)	31.5	40.4	19.5	6.8	1.8
195339(2)	29.5	31.9	31.5	5.7	1.4
195344(2)	26.1	35.2	32.0	4.3	2.6
195350(2)	28.3	35.4	28.5	6.8	0.9
195359(2)	32.5	30.6	34.0	1.1	1.8
195363(2)	26.7	37.4	26.8	6.3	2.9
195390(2)	29.5	35.0	23.1	7.4	5.0
195377(3)	32.0	26.0	39.1	1.5	1.3
195397(3)	33.9	34.5	27.5	1.9	2.3
79635	24.6	35.0	35.6	1.9	3.0
79700	32.3	33.1	30.4	1.4	2.8
79701	28.5	38.6	24.9	3.3	4.7
79711	31.5	34.6	29.1	3.4	1.3
79712	27.7	35.8	27.7	5.5	3.3
79714	26.3	41.9	24.8	6.4	0.5
79717	36.4	31.4	26.6	4.0	1.7
79722	25.9	30.9	38.2	2.7	2.4

Specimen 86619 is a granite from along the north coast of Sulugssugutip kangerdlua. Specimens 79798 and 195304-195397 are granites from the area between Sulugssugutip kangerdlua and Qôrqut. The number in parenthesis refers to the groups established by Brown & Friend [1980b] in this area. Specimens 79635-79722 are granites which crop out in the mountains and along the coast on the north side of Ameralik.
*Others includes epidote, muscovite, allanite, magnetite, zircon, apatite, and sphene.

with muscovite and epidote, both of which appear to be secondary and associated with the alteration of plagioclase. Accessory minerals, which occur in virtually all rocks examined in thin section, are magnetite, allanite (commonly metamict), zircon, apatite, and sphene. Three main factors in the petrography of the granites account for much of the variation observed in the field between different phases. These factors are grain size variations; the appearance of the felsic minerals, which varies from translucent through cream to grey; and the modal amount of biotite, which, in homogeneous varieties of granite, varies from >12% down to <2%. There is some tendency for rocks with higher modal biotite to have a higher proportion of plagioclase feldspar relative to microcline; also, these rocks tend to be finer grained.

Textural relations in granitic rocks tend to be ambiguous and therefore difficult to interpret. Two general points may be stated, however, about those specimens of Qôrqut granite which we have examined in thin section. First, the biotite, especially in those rocks with higher modal biotite, often shows some evidence of instability and replacement. Second, there is some textural evidence of subsolidus reequilibriation between the felsic phases (for example, the occasional development of myrmekite). Bearing these two points in mind, the generalized crystallization sequence in many of the Qôrqut granite complex specimens, especially those with a hypidiomorphic-granular texture, is biotite with contained zircons and rutile needles, slightly before plagioclase followed closely by quartz; or, biotite with contained zircons and rutile needles slightly before quartz followed closely by plagioclase. In both cases, anhedral, slightly replacive microcline is clearly later. In some specimens, particularly those with an allotrimorphic-granular texture, quartz and microcline appear to have crystallized essentially simultaneously, but shortly after the appearance of plagioclase. No interstitial micrographic intergrowth of the felsic phases is found, and no miarolitic cavities have been found.

Geochemistry

A detailed geochemical study of the Qôrqut granite complex in the area between Qôrqut and Sulugssugutip kangerdlua is in progress at Oxford Polytechnic by W. T. Perkins. Compton [1978a, b] has analysed specimens of Qôrqut granite from the Buksefjorden area, but most of the data remain unpublished. At present, therefore, our knowledge of the chemical variation within the complex is based upon eighteen chemical analyses of specimens

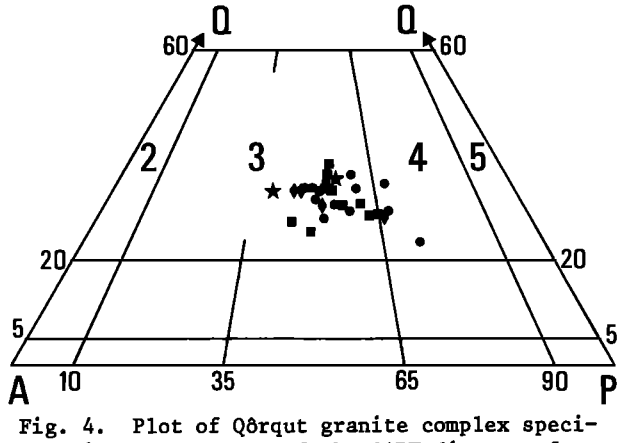

Fig. 4. Plot of Qôrqut granite complex specimens in the QAP part of the QAPF diagram of Streckeisen [1976]. Squares represent undifferentiated granites (collected before 1978), diamonds represent early leucocratic granites (group 1 granites), circles represent grey biotite granites (group 2 granites), and stars represent late aplogranite-granite pegmatite sheets (group 3 granites).

collected from the north coast of Sulugssugutip kangerdlua, from the sheets of Qôrqut granite which crop out along Ivnarssuit, and from the mountains and north coast of Ameralik (all collected before 1978, referred to as 'undifferentiated granites') and on thirty-four chemical analyses of specimens of group 1, group 2, and group 3 granites collected from the area between Qôrqut and Sulugssusutip kangerdlua which form part of a postgraduate study by one of us (W. T. Perkins).

Analytical Methods

Specimens 79701-79798 were analyzed by X-ray fluorescence (XRF), major and minor elements were determined at the Geological Survey of Canada, and trace elements at the University of Leeds, United Kingdom. Specimens 86606-86622 and 171933 -171955 were analyzed at the Greenland Geological Survey, Denmark, MgO and Na_2O were determined by atomic absorption spectrophotometry (AAS), and other elements by XRF. Specimens 195304-195399 were analyzed for major and minor elements at Oxford Polytechnic, United Kingdon, P_2O_5 was determined by colorimetry, and other elements by AAS; trace element determinations on these specimens were made by XRF analysis at the University of Nottingham, United Kingdom.

Discussion of the Geochemical Data

Major, minor and selected trace element contents of the fifty-two specimens analyzed are given in Table 2. Also tabulated for each specimen are a differentiation index (DI) value (where DI is the sum of the mesonormative components Q+Or+Ab) and the proportions of Qz:Ab:Or:An (the granite system of Winkler [1979]) based upon the mesonormative proportions for each specimen. On plots of oxide/element against the differentiation index, TiO_2, Al_2O_3, total FeO, MgO, CaO, Na_2O, and Sr all decrease with increasing values of DI, while Ba first increases with increasing values of DI to about DI 86 and then decreases, Rb shows little change, and K_2O shows a general increase with increasing values of DI (see Figure 5). This variation is consistent either with differentiation of a liquid of appropriate composition by fractional crystallization of a suitable phase or phases or with progressive fractional (batch) melting of an appropriate parent with a suitable residuum. The specimens have high contents of K_2O, Rb, Sr, and Ba, low K/Rb ratios, and high Rb/Sr and Ba/Sr ratios, features which mean that a basaltic parent (with typical contents K = 2100, Rb = 5.9, and Sr = 175, average values for Archaean basalts from Hart et al. [1970]), either as the parent liquid to be modified by fractional crystallization or as the source rock or progressive partial melting, may be considered unlikely [Hanson, 1978]. With increasing values of DI, K/Rb and Rb/Sr show a general increase, Ba/Sr increases to about DI 86 and then decreases, and Ba/Rb shows a general decrease (see Figure 5). The observed variations in K/Rb, Rb/Sr, Ba/Sr, and Ba/Rb combined with a consideration of the mineral/melt distribution coefficients for these elements in granitic rocks (Table 3) allow some assessment to be made of likely participating phases. It is clear that whether the process involved is fractional crystallization or partial melting, biotite and the feldspars must be important phases either as fractionating phases in crystallization or as residual phases in melting.

Plots of Ba against Rb and of Rb against Sr are given in Figure 6 together with vectors which indicate (1) the change in composition of a melt as a result of fractional crystallization (FC) of the named phenocryst phases in acid rocks and (2) the change in composition of a melt as a result of equilibrium partial melting (PM) of the named residual phases in acidic rocks. The vectors were constructed using the data on mineral/melt distribution coefficients given in Table 3 and the method summarized by Hanson [1978]. If fractional crystallization is the dominant process giving rise to the observed geochemical variation, then fractionation of biotite and/or K-feldspar is necessary to produce the observed trend of Ba against Rb, but fractionation of plagioclase and/or K-feldspar is necessary to produce the observed trend of Rb against Sr. Alternatively, if partial melting is the dominant process giving rise to the observed geochemical variation, then residual K-feldspar and/or biotite is required to produce the observed trend of Ba against Rb, and residual K-feldspar and/or biotite is required to produce the observed trend of Rb against Sr. The data appear to be more compatible with partial melting as the dominant process giving rise to the observed geochemical variation. The effect of fractional crystallization superimposed on different partial melts cannot be assessed by this qualitative approach but will be assessed by modeling of the trace element distributions as part of our planned future work on the Qôrqut granite complex.

Plots of oxide/element against height above sea level (not figured) exhibit no rational variation whatsoever, so that granite at a higher level in the complex need not be more fractionated than granite at lower levels.

Plots of mesonormative compositions for the Qôrqut granite specimens within the Qz-Ab-Or-An tetrahedron (the granite system) for conditions where PH_2O = P total = 5 kbar [Winkler et al., 1975] (note that this is the lowest value of PH_2O for which comprehensive experimental data are available) show that the granite compositions fall on a smooth curve close to the quartz saturation surface (see Figure 7, top diagram). Individual specimens plot either in the plagioclase primary phase volume or in the quartz primary phase volume or just below the two feldspar cotectic surface in the alkali feldspar primary phase volume. Since quartz or plagioclase was the first felsic phase to have crystallized in all specimens from the Qôrqut granite complex which have been examined in thin section, all of the specimens would be expected to plot above the two-feldspar cotectic surface in the Qz-Ab-Or-An tetrahedron. The two-feldspar cotectic surface is located closer to the base (the Qz-Ab-Or face) of the tetrahedron at lower values of PH_2O; thus it seems likely that PH_2O must have been less than 5 kbar at the time of crystallization of the Qôrqut granite complex magmas. The smooth curve

TABLE 2. Major(Percent), Minor(Percent), and Trace(parts per million) Element Compositions, Differentiation Index (Where DI= Mesonormative Q+Ab+Or) and Quaternary Qz, Or, Ab, and An Proportions of Granite Samples From the Qôrqut Granite Complex, Southern West Greenland

	171933	171937	171940	171949	171950	171951	171952	171955	86606	86615	86619	86622	79798
SiO_2	73.1	73.3	75.2	72.30	73.7	74.3	72.8	71.5	76.4	72.5	70.7	73.5	68.12
TiO_2	0.20	0.21	0.04	0.31	0.15	0.12	0.19	0.28	0.01	0.16	0.38	0.16	0.38
Al_2O_3	14.6	14.6	14.3	14.8	14.5	14.3	15.1	15.0	13.8	15.2	15.4	14.4	16.09
Fe_2O_3	0.3	0.1	-	0.1	-	0.2	-	0.7	0.1	-	-	-	0.07
FeO	1.3	1.2	0.5*	1.6	1.3*	0.9	1.6*	1.3	0.4	1.6*	2.4*	1.53*	2.27
MnO	0.01	0.02	0.01	0.02	0.01	0.01	0.01	0.01	0.00	0.01	0.03	0.01	0.05
MgO	0.56	0.45	0.27	0.67	0.52	0.37	0.55	0.72	0.16	0.48	0.84	0.43	0.89
CaO	1.63	1.31	1.40	1.63	1.30	1.19	1.32	1.64	1.01	1.34	2.00	1.29	2.14
Na_2O	3.6	3.2	3.6	3.4	3.3	3.4	3.3	3.4	3.0	3.4	3.6	3.3	4.94
K_2O	4.94	5.50	5.02	4.78	5.22	5.12	5.47	5.48	5.40	5.55	4.43	5.40	3.95
P_2O_5	0.10	0.08	0.03	0.12	0.08	0.05	0.11	0.10	0.05	0.08	0.15	0.08	0.13
H_2O	0.5	0.6	0.4	0.6	0.6	0.7	0.4	0.6	0.5	0.6	0.6	0.4	0.61
Total	100.84	100.57	100.77	100.33	100.68	100.66	100.85	100.73	100.83	100.92	100.53	100.50	99.64
Rb	250	240	200	250	170	170	170	200	220	200	260	250	207
Sr	200	190	250	250	80	160	170	210	220	220	230	140	275
Ba	820	1000	780	1200	750	620	840	740	n.d.	890	990	n.d.	1245
DI=Q+Ab+Or	86.86	88.27	90.61	85.00	87.85	89.75	86.81	86.01	92.30	87.11	80.98	88.09	81.72
Qz)	29.96	31.17	30.70	32.10	32.08	32.08	30.58	27.89	34.92	29.01	30.73	31.22	20.96
Or)	28.24	32.25	29.22	27.27	30.15	30.07	31.54	31.93	32.28	31.99	23.93	31.13	20.37
Ab)=100	34.59	30.94	33.27	33.75	31.95	32.38	32.25	33.11	27.97	32.98	36.68	31.88	49.28
An)	7.21	5.65	6.81	6.88	5.83	5.47	5.63	7.06	4.83	6.02	8.65	5.78	9.38

	195332	195337	195352	195360	195361	195362	195380	195385	195391	195304	195307	195309	195317
SiO_2	74.72	73.95	75.80	74.10	72.72	74.99	75.10	74.24	74.44	69.93	66.55	74.27	67.92
TiO_2	0.11	0.10	0.15	0.24	0.19	0.18	0.11	0.16	0.06	0.29	0.40	0.31	0.46
Al_2O_3	13.76	14.17	13.42	13.35	14.65	14.13	12.88	13.92	13.04	16.76	17.62	13.38	16.33
Fe_2O_3	0.13	0.48	0.02	0.17	0.12	0.02	0.55	0.56	0.13	0.29	0.56	0.32	0.44
FeO	0.74	0.80	0.57	1.20	1.11	0.38	0.79	1.19	0.46	2.07	1.93	1.21	2.19
MnO	0.01	0.02	0.01	0.02	0.02	0.02	0.02	0.03	0.01	0.03	0.03	0.03	0.04
MgO	0.12	0.10	0.12	0.34	0.28	0.09	0.24	0.37	0.04	0.83	0.97	0.31	1.02
CaO	1.07	1.16	0.97	1.42	1.61	1.58	1.13	1.29	1.24	2.12	2.62	1.21	2.69
Na_2O	3.31	3.66	3.34	3.10	3.49	3.53	2.96	2.97	3.13	4.11	5.04	3.32	4.12
K_2O	5.43	4.96	5.38	4.59	4.74	4.80	5.50	5.62	5.13	4.30	2.87	4.80	3.74
P_2O_5	0.01	0.01	0.02	0.05	0.03	0.02	0.08	0.04	0.03	0.13	0.14	0.05	0.17
H_2O	n.d.	n.d	n.d.	n.d.	n.d.	n.d.	n.d.	n.d.	n.d.	n.d.	n.d.	n.d.	n.d.
Total	99.41	99.41	99.80	98.58	98.96	99.74	99.30	100.39	79.71	100.86	98.73	99.21	99.12
Rb	205	217	178	169	163	144	205	186	149	218	169	211	198
Sr	104	95	111	186	184	188	116	264	159	261	367	123	375
Ba	197	283	300	710	707	756	287	942	475	1161	987	480	1892
DI=Q+Ab+Or	92.05	91.30	93.14	88.18	87.55	90.67	91.64	88.98	92.43	80.84	77.88	89.58	77.69
Qz)	31.50	30.36	32.59	36.14	30.87	31.45	33.73	32.50	33.19	26.29	22.40	34.43	26.12
Or)	32.33	29.63	31.95	27.10	27.86	28.53	32.89	33.14	32.21	23.22	14.19	28.36	19.54
Ab)=100	31.09	34.41	31.14	30.35	33.62	32.71	28.01	28.41	29.55	40.90	51.29	32.24	42.21
An)	5.08	5.59	4.32	6.41	7.65	7.31	5.37	5.95	6.04	9.60	12.12	4.97	12.13

Specimens 171933-171955 are undifferentiated granites from the Qôrqut granite complex sheets cutting Nûk gneisses along the coast of Ivnarssuit, north of the mouth of Kapisigdlit kangerdluat. Specimens 86606-86622 are undifferentiated granites from the Qôrqut granite complex which crops out along the north coast of Sulugssugutip kangerdlua. Specimen 79798 is an undifferentiated granite from the Qôrqut granite complex which crops out along the east coast of Umanap suvdlua at Serfarssuit.
*Total Fe as FeO.

TABLE 2. (continued)

	195325	195329	195338	195339	195344	195350	195363	195364	195365	195370	195372	195374	195381
SiO_2	74.88	73.08	72.81	72.38	71.70	71.35	72.04	72.99	71.38	73.88	74.45	67.25	68.16
TiO_2	0.22	0.32	0.16	0.17	0.29	0.32	0.51	0.40	0.32	0.16	0.21	0.51	0.26
Al_2O_3	13.37	13.91	13.40	14.11	13.93	14.65	14.20	13.95	14.59	13.88	13.79	15.74	15.00
Fe_2O_3	0.22	0.60	0.75	0.21	0.49	0.41	0.66	0.61	0.28	0.40	0.49	0.54	0.94
FeO	1.07	1.62	1.49	1.33	1.03	1.67	1.47	1.60	1.45	1.19	1.16	2.60	1.57
MnO	0.04	0.04	0.03	0.03	0.03	0.03	0.02	0.03	0.02	0.04	0.03	0.05	0.03
MgO	0.29	0.55	0.61	0.50	0.44	0.63	0.63	0.47	0.56	0.32	0.24	0.80	0.67
CaO	1.29	1.61	1.71	1.75	1.31	1.68	1.75	1.39	1.69	1.26	1.45	2.34	1.77
Na_2O	3.66	3.14	3.54	3.98	3.20	3.39	3.42	3.38	3.47	3.24	3.30	3.67	3.65
K_2O	4.39	4.67	4.20	5.19	4.79	4.80	4.84	5.08	4.82	5.21	4.89	4.57	5.25
P_2O_5	0.05	0.11	0.10	0.08	0.10	0.09	0.12	0.08	0.11	0.06	0.04	0.14	0.12
H_2O	n.d.	n.d.	n.d.	n.d.	n.d.	n.d.	n.d.	n.d.	n.d.	n.d.	n.d.	n.d.	n.d.
Total	99.48	99.65	98.80	99.73	97.31	99.02	99.66	99.98	99.69	99.64	100.05	98.21	98.42
Rb	303	223	200	168	176	196	174	190	179	220	190	182	235
Sr	129	260	251	220	223	205	286	260	237	181	177	262	195
Ba	639	1782	1632	1161	1099	789	1338	954	1269	606	588	918	631
DI=Q+Ab+Or	89.89	85.63	86.01	88.54	88.19	84.79	85.72	87.56	85.76	89.27	88.89	79.15	85.02
Qz)	33.85	34.88	33.33	26.24	33.46	31.06	31.22	31.78	30.33	32.43	33.17	25.95	24.36
Or)	25.51	27.13	23.94	29.84	29.17	27.74	28.20	29.66	28.07	30.73	28.77	25.54	31.18
Ab)=100	34.98	31.18	34.77	38.25	31.99	33.84	33.83	33.12	34.37	31.16	31.47	38.18	36.55
An)	5.65	6.81	7.96	5.68	5.38	7.37	6.74	5.44	7.23	5.68	6.59	10.33	7.91

	195382	195390	195396	195398	195316	195377	195397	79701	79711	79713	79714	79722	195399
SiO_2	71.50	71.51	72.32	75.34	77.31	75.20	76.70	73.64	73.63	73.43	71.63	71.69	71.88
TiO_2	0.19	0.40	0.20	0.09	0.10	0.15	0.10	0.15	0.15	0.09	0.31	0.20	0.32
Al_2O_3	14.05	14.63	14.06	13.50	13.92	13.49	13.46	14.08	13.81	13.66	14.45	14.42	13.78
Fe_2O_3	0.45	0.49	0.62	0.23	0.00	0.68	0.09	0.28	0.29	0.10	0.42	0.57	0.42
FeO	1.35	1.54	1.27	0.84	0.67	1.02	0.59	0.89	1.03	0.77	1.54	1.61	1.66
MnO	0.02	0.03	0.03	0.02	0.01	0.03	0.01	0.05	0.04	0.02	0.05	0.05	0.03
MgO	0.40	0.68	0.44	0.16	0.05	0.14	0.15	0.27	0.34	0.16	0.80	0.43	0.36
CaO	1.43	1.84	1.47	1.16	1.32	1.19	1.33	1.12	1.32	1.06	1.51	1.16	1.35
Na_2O	3.19	3.46	3.36	3.12	4.06	2.87	3.35	3.89	3.82	3.81	4.32	3.87	3.36
K_2O	5.27	4.47	5.10	5.06	3.51	5.62	4.59	4.87	4.68	5.17	4.77	5.14	5.12
P_2O_5	0.10	0.11	0.07	0.02	0.01	0.04	0.01	0.07	0.06	0.02	0.09	0.12	0.05
H_2O	n.d.	n.d.	n.d.	n.d.	n.d.	n.d.	n.d.	0.44	0.23	0.17	n.d.	0.78	n.d.
Total	97.95	99.16	98.94	99.54	101.16	100.43	100.38	99.75	99.40	98.46	99.87	100.04	98.34
Rb	216	168	214	159	118	158	170	263	292	203	242	204	245
Sr	198	229	156	116	89	178	156	112	159	86	194	156	143
Ba	690	1495	639	318	186	665	592	565	515	235	840	450	820
DI=Q+Ab+Or	87.83	84.19	87.85	90.89	90.75	90.74	90.94	91.09	89.86	92.53	87.00	88.84	87.95
Qz)	30.66	31.91	30.56	34.68	35.77	33.84	35.43	29.66	30.44	28.50	25.49	27.70	30.76
Or)	31.53	25.71	30.11	30.14	20.43	33.62	26.99	28.62	27.21	30.61	26.44	29.93	30.28
Ab)=100	31.46	34.58	32.68	29.57	37.50	27.15	31.17	36.88	36.37	35.84	41.80	37.72	33.18
An)	6.35	7.81	6.65	5.61	6.31	5.39	6.41	4.83	5.98	5.05	6.28	4.64	5.78

Specimens 195332, 195337, 195352, 195360, 195361, 195362, 195380, 195385, and 195391 are group 1 granites; specimens 195304, 195307, 195309, 195317, 195325, 195329, 195338, 195339, 195344, 195350, 195363, 195364, 195365, 195370, 195372, 195374, 195381, 195382, 195390, 195396, and 195398 are group 2 granites; and specimens 195316, 195377 and 195397 are group 3 granites, all from the area between Sulugssugutip kangerdlua and Qôrqut. Specimens 79701-79722 are undifferentiated granites from the Qôrqut granite complex which crops out in the mountains and along the coast on the north side of Ameralik. Specimen 195399 is an undifferentiated granite from the Qôrqut granite complex which crops out on the southwest side of Ameralik.

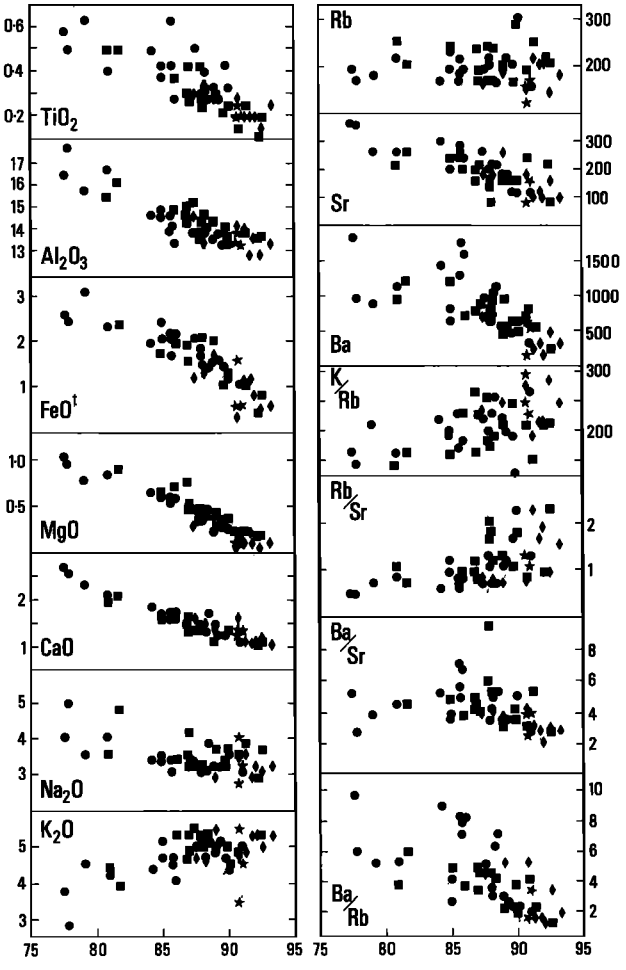

Fig. 5. Plots of selected oxides (in weight percent), trace elements (in parts per million), and element ratios against a differentiation index (where DI is the sum of the mesonormative components Q+Ab+Or) for the fifty-two analyzed specimens from the Qôrqut granite complex (symbols as in Figure 4).

defined by the Qôrqut granite complex specimens thus trends along the quartz saturation surface and terminates in the cotectic curve formed by the intersection of the quartz saturation surface and the two-feldspar cotectic surface.

The Qôrqut granite compositions seem likely to have been cotectic melts. Figure 7 also shows the mesonormative compositions of the Qôrqut granite complex specimens projected from An onto the Qz-Ab-Or face and projected from Qz onto the Ab-Or-An face of the Qz-Ab-Or-An tetrahedron. The Qôrqut rocks plot inside the projection of the 685°C isotherm determined by Winkler et al. [1975], and it is quite clear that they could represent low temperature granitic melts [Winkler and Breitbart, 1978] whether or not such melts are metastable [Johannes, 1980]. Plagioclase and/or quartz could be residual phases during melting of an appropriate source material, and plagioclase and/or quartz will be the first felsic phases expected to crystallize from liquids with compositions corresponding to the Qôrqut granite complex specimens, followed by alkali feldspar, either closely or after some crystallization of plagioclase and quartz; this accounts for the range in textures observed in these specimens from allotriomorphic-granular to hypidiomorphic-granular. If PH_2O approached P total during the production of the Qôrqut granites by crustal anatexis but was lower than 5 kbar, the maximum depth at which anatexis could have occurred is of the order of 15-20 km.

General Discussion

In the area between Ameralik and Kapisigdlit kangerdluat, the country rock geology is dominated by Amîtsoq gneisses at the present level of erosion. Around Qôrqut, some of the early leucocratic granites (group 1) carry schlieren of biotite and contain enclaves of modified gneiss thought originally to have been mostly amphibolite facies Amîtsoq gneisses. These enclaves are interpreted by Brown and Friend [1980a] as having been carried from the upper margin (?) of a zone of melting at a deeper level in the crust. Pegmatite increases in abundance upward through the exposed section of the Qôrqut granite complex, and composite aplogranite-granite pegmatite sheets (group 3 granites) are the most important granite component in the upper zone of the complex. Thus the granite magma or magmas from which the various granites composing the complex have been derived probably had a moderate content of water, although they may not have been water saturated.

TABLE 3. Mineral/Melt Distribution Coefficients for Common Rock-Forming Minerals From Dacitic and Rhyolitic Rocks

Element	Garnet	Ortho-pyroxene	Clino-pyroxene	Hornblende		Biotite			K-feldspar			Plagioclase		
						(1)	(2)	(3)	(1)	(2)	(3)	(1)	(2)	(3)
Rb	0.0085	0.0027	0.032	0.014	0.0077	3.26	2.24	3.0	0.659	0.34	0.8	0.041	0.048	0.04
Sr	0.015	0.0085	0.516	0.22	0.094	0.12	-	0.4	3.87	3.87	3.6	4.4	2.84	3.35
Ba	0.017	0.0029	0.131	0.044	0.054	6.36	9.7	10.0	6.12	6.12	6.0	0.308	0.36	0.4

Data for garnet, orthopyroxene, clinopyroxene, hornblende, biotite (1), K-feldspar (1) and plagioclase (1) are from the compilation by Hanson [1978]; data for biotite (2), K-feldspar (2) and plagioclase (2) are from the compilation by Arth [1976]; and data for biotite (3), K-feldspar (3) plagioclase (3) are from the compilation by McCarthy [1976].

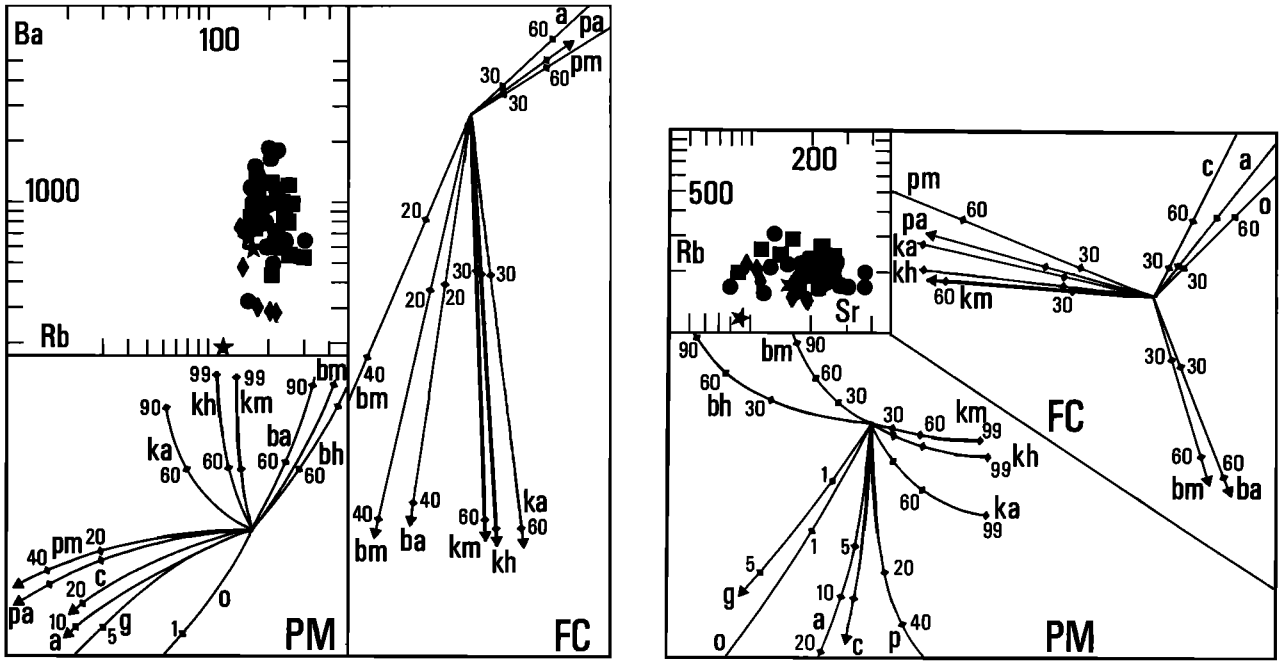

Fig. 6. Plots of Ba against Rb and Rb against Sr for the fifty-two analyzed specimens from the Qôrqut granite complex (symbols as in Figure 4). Also shown are vectors which indicate the change in composition of a melt as a result of fractional crystallization (FC) of the named phases in acid rocks and the change in composition of a melt as a result of equilibrium partial melting (PM) of the named phases in acid rocks. The percentage of fractional crystallization of the original melt or the percentage of partial melting of the original solid to produce corresponding changes in Ba and Rb and Rb and Sr is marked along the appropriate vectors. The vectors were calculated using the data in Table 3 and the method summarized by Hanson [1978]. Key: g = garnet, o = orthopyroxene, c = clinopyroxene, a = hornblende, bh = biotite [Hanson, 1978], ba = biotite [Arth, 1976], bm = biotite [McCarthy, 1976], kh = K-feldspar [Hanson, 1978], ka = K-feldspar [Arth, 1976], km = K-feldspar [McCarthy, 1976], ph = plagioclase [Hanson, 1978], pa = plagioclase [Arth, 1976], and pm = plagioclase [McCarthy, 1976]. Exceptions are Ba against Rb, for fractional crystallization (FC), a = hornblende, orthopyroxene, and garnet, since all three produce closely similar vectors, and for both fractional crystallization (FC) and partial melting (PM), pm = plagioclase for the data of Hanson [1978] and McCarthy [1976] which produce indistinguishable vectors; Rb against Sr, for fractional crystallization (FC), o = orthopyroxene and garnet, since both produce closely similar vectors, and pm = plagioclase for the data of Hanson [1978] and McCarthy [1976] which produce indistinguishable vectors, and for partial melting (PM), p = plagioclase for the data of Hanson [1978], Arth [1976], and McCarthy [1976] which produce closely similar vectors.

A high water content in such magmas places severe restrictions on their ability to move up through the crust [Tuttle and Bowen, 1958; Cann, 1970]. The form and internal structure of the Qôrqut granite complex, shown schematically in Figure 3, suggest emplacement at a relatively high level in the crust in a regime of brittle/semibrittle failure rather than one of ductile flow in response to deforming stresses. However, the absence of interstitial micrographic intergrowths between the felsic phases and miarolitic cavities places a restriction on the minimum thickness of overburden which must have been present at the time of granite emplacement. The geochemistry (this paper) and the isotope geology [Moorbath et al., 1981] of rocks from the Qôrqut granite complex strongly suggest that the granites were produced by partial melting of sialic continental crust. The position of mesonormative compositions of the analyzed Qôrqut granites in the Qz-Ab-Or-An tetrahedron and the inferred order of crystallization of the main phases established petrographically suggest a depth of generation of the parent magmas of less than 20 km at temperatures of up to 685°C if PH_2O approached P total.

Rocks with hornblende granulite facies mineral assemblages, produced during the metamorphic peak about 2800-Ma ago [Black et al., 1973], crop out extensively in the Archaean of West Greenland [Bridgwater et al., 1976; Allaart et al., 1977, 1978]. Rocks retrogressed from granulite facies mineral assemblages to amphibolite facies mineral assemblages crop out on the south coast of Ameralik just to the east of the Qôrqut granite complex, and it is likely that granulite facies conditions were reached at depth beneath the belt into which the complex was later emplaced.

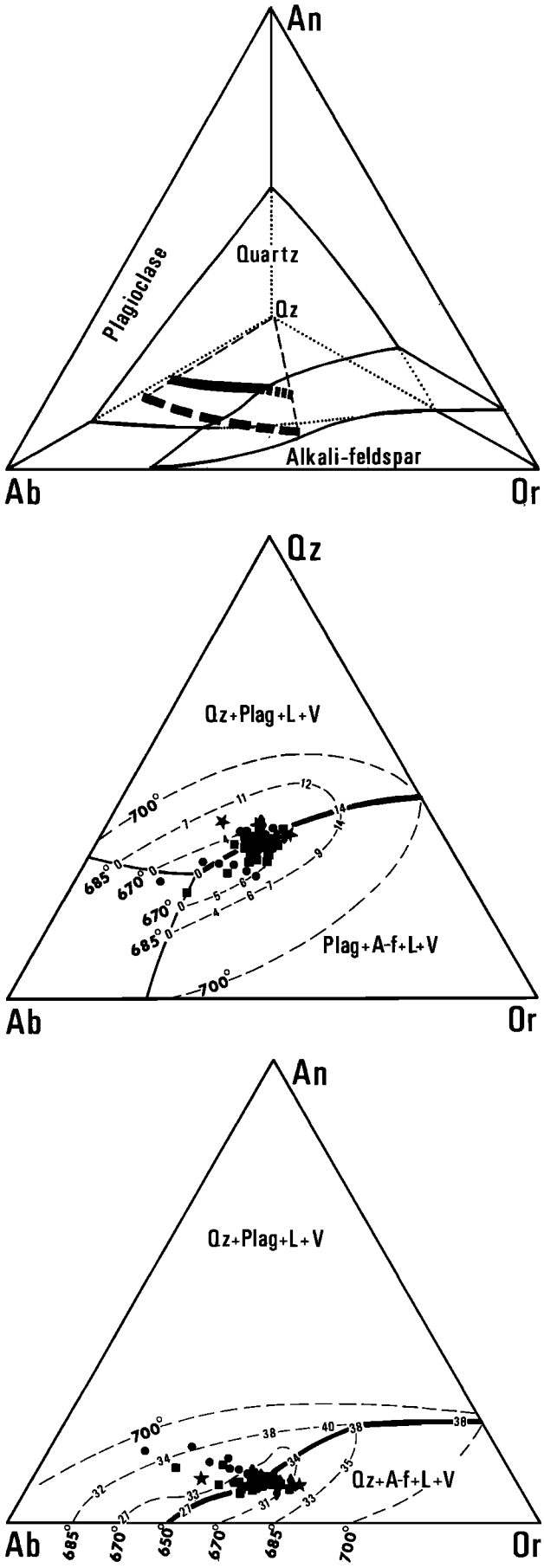

However, enclaves with preserved granulite facies mineral assemblages have not been found within the exposed part of the Qôrqut granite complex, and locally derived enclaves and rafts of country rocks within the complex and the country rocks immediately adjacent to the complex all have amphibolite facies mineral assemblages.

We do not at present have sufficient information to determine conclusively whether the source rocks in the crust from which the Qôrqut granite magmas have been derived by partial anatexis had amphibolite facies or granulite facies mineral assemblages. One of us (W. T. Perkins) is currently determining the rare earth element contents of a representative sample of 16 specimens from the Qôrqut granite complex, and we are hopeful that trace element modeling of these data will constrain further the likely mineralogy of the source rocks.

One possibility, given the regional setting of the Qôrqut granite complex, is that partial melting of granulite facies rocks deep in the crust could have occurred following an influx of volatiles. The rocks may have been sufficiently hot to melt in the presence of a volatile phase, or there may have been an enhanced heat flow accompanying the influx of volatiles. If this

Fig. 7. (Opposite) The top diagram shows the granite system of Winkler [1979] for conditions of PH_2O = 5 kbar. The quartz saturation surface separating the liquidus phase volume of quartz from that of either plagioclase or alkali feldspar is shown, and the two feldspar surface separating the liquidus phase volume of plagioclase from that of alkali feldspar is shown. The general trend of the Qôrqut granite complex specimens, plotted as mesonormative proportions, is shown as a solid curve above the two feldspar surface and is dotted below the two feldspar surface (see text for discussion). The projection of this general trend from Qz onto the Ab-Or-An face of the tetrahedron is also shown as a dashed curve. The middle and bottom diagrams show a Qz-Ab-Or plot of the Qôrqut rocks projected from An and an Ab-Or-An plot of the Qôrqut rocks projected from Qz in the Qz-Ab-Or-An tetrahedron. The cotectic lines shown are for the condition PH_2O = Ptotal = 5 kbar. The projection from An of the 670°C, 685°C, and 700°C isotherms on the quartz-plagioclase and plagioclase-alkali feldspar cotectic surfaces onto the Qz-Ab-Or face are shown, together with the An contents of liquid compositions lying on the cotectic surfaces or along the cotectic curve formed by the intersection of the two cotectic surfaces for conditions where PH_2O = Ptotal = 5 kbar [after Winkler et al., 1975]. On the Ab-Or-An face, the projection from Qz of the 670°C, 685°C, and 700°C isotherms on the quartz-plagioclase and quartz-alkali feldspar cotectic surfaces are shown, together with Qz contents of liquid compositions lying on the cotectic surfaces or along the cotectic curve formed by the intersection of the two cotectic surfaces for conditions where PH_2O = Ptotal = 5 kbar [after Winkler et al., 1975].

model is correct, the liquids produced by partial melting will need to have fractionated a substantial amount of feldspar (both alkali feldspar and plagioclase) and biotite to account for the trace element distributions, since phases such as biotite cannot normally be expected to have been present in a source with a granulite facies mineralogy. In such a model it is difficult to envisage a mechanism of emplacement of the granite sheets which make up the complex which will allow the apparent random observed sequence of intrusion of the fractionated liquids, which themselves define rational geochemical trends on variation diagrams, without postulating the presence of a cumulate granite (probably of tonalitic composition) at deeper levels in the crust than presently exposed. The proximity of the analyzed Qôrqut granite complex specimens to the quartz saturation surface in the granite system makes substantial fractional crystallization of plagioclase unlikely.

An alternative model is one in which the source material comprised amphibolite facies rocks at intermediate crustal depths. Sufficient water to permit melting to occur in the volumes necessary must have come from hydrates such as mica (biotite) and possibly amphibole (hornblende) once temperatures exceeded that on an appropriate equilibrium curve for melting. In this model, in rocks with a suitable mineral assemblage, alkali feldspar might be expected to melt out first, with mica (biotite) + plagioclase + quartz + amphibole (hornblende) contributing to the melt fraction. Hornblende in the residue has little effect on K_2O, Rb, Sr, or Ba but does deplete the middle and, to a lesser extent, the heavy rare earth elements and contributes to a positive Eu anomaly. With our present data we can neither establish nor exclude the possible involvement of hornblende in the generation of the Qôrqut granite complex magmas, but trace element modeling of rare earth element data should potentially confirm or deny such a possibility. However, the geochemical variations shown in Figures 5 and 6 are entirely consistent with a melting model and the distributions, in particular of K_2O, Rb, Sr, and Ba against DI and Rb/Sr and Ba/Sr, strongly suggest that in such a model alkali feldspar and biotite must have been involved as melting phases [see Hanson, 1978, p 35]. Thus a model which is based upon the generation of small batches of granite magma by partial melting of a largely similar source material with an amphibolite facies mineralogy is capable of explaining the observed geochemical variations and the random intrusive sequence required by the field observations.

Acknowledgments. We wish to thank the Director of the Geological Survey of Greenland for support in the field and for permission to publish this paper; D. Bridgwater for collecting the analyzed specimens from Ivnarssuit, for organising eighteen of the chemical analyses and, together with S. Moorbath, P. N. Taylor, J. Arth, A. D. M. Burwell, and C. G. Topley, for stimulating discussions on the nature and origin of the Qôrqut granite complex; P. E. Baker and P. K. Harvey for the use of XRF facilities at Nottingham University; and Anne Lloyd for typing the manuscript. Work in progress at Oxford Polytechnic on the Qôrqut granite complex is supported by research grants from the Oxford Polytechnic Research and Advanced Study Committee.

References

Allaart, J. H., S. B. Hensen, V. R. McGregor, and B. J. Walton, Reconnaissance mapping for the 1:500 000 map sheet in the Godthåb-Isua region, southern West Greenland, Rapp. Groenl. Geol. Unders., 85, 50-54, 1977.

Allaart, J. H., C. R. L. Friend, R. P. Hall, S. B. Jensen, and I. W. N. Roberts, Continued 1:500 000 reconnaissance mapping in the Precambrian of the Sukkertoppen region, southern West Greenland, Rapp. Grœnl. Geol. Unders., 90, 50-54, 1978.

Arth, J. G., Behaviour of trace elements during magmatic processes - A summary of theoretical models and their applications, J. Res. U.S. Geol. Surv. 4, 41-47, 1976.

Baadsgaard, H., Further U-Pb Dates on zircons from the early Precambrian rocks of the Godthåbsfjord area, West Greenland, Earth Planet. Sci. Lett., 33, 261-267, 1976.

Baadsgaard, H., and V. R. McGregor, The U-Th-Pb systematics of zircons from the type Nûk gneisses, Godthåbsfjord, West Greenland, Geochim. Cosmochim. Acta, 45, 1981

Black, L. P., S. Moorbath, R. J. Pankhurst, and B. F. Windley, $^{207}Pb/^{206}Pb$ whole rock age of the Archaean granulite facies metamorphic event in West Greenland, Nature Phys. Sci., 244, 50-53, 1973.

Bridgwater, D., Chemical and isotopic redistribution in zones of ductile deformation in a deeply eroded mobile belt, 1, Chemical redistribution, Geol. Surv. Open File Rep. U.S., 79-1239, 1-8, 1979.

Bridgwater, D., L. Keto, V. R. McGregor, and J. S. Myers, Archaean gneiss complex of Greenland, in Geology of Greenland, edited by A. Escher and W. S. Watt, pp. 18-75, Groenlands Geologiske Undersoegelse, Copenhagen, 1976.

Brown, M., and C. R. L. Friend, Field evidence concerning the origin of the early leucocratic granites within the Qôrqut granite complex in the area of Qôrqut, Rapp. Groenl. Geol. Unders., 100, 76-79, 1980a.

Brown, M., and C. R. L. Friend, The polyphase nature and internal structure of the Qôrqut granite complex east of Ûmánap suvdlua, Godthåbsfjord, southern West Greenland, Rapp. Groenl. Geol. Unders., 100, 79-83, 1980b.

Burwell, A. D. M., and C. R. L. Friend, Observations on the late Archaean Qôrqut granite, Qôrqut, Godthåbsfjord, southern West Greenland, Rapp. Groenl. Geol. Unders., 95, 76-79, 1979.

Cann, J. R., Upward movement of granitic magma, Geol. Mag., 107, 335-340, 1970.

Chadwick, B., and A. P. Nutman, Archaean structural evolution in the northwest of the Buksefjorden region, southern West Greenland, Precambrian Res., 9, 199-226, 1979.

Chadwick, B., K. Coe, and A. P. Nutman, Precambrian studies in the Buksefjorden region, southern West Greenland, Rapp. Groenl. Geol. Unders., 90, 60-64, 1978.

Coe, K., P. Compton, J. G. Stainforth, K. F. Vines, and P. R. A. Wells, Investigation of Precambrian rocks in the Buksefjorden region, southern West Greenland, Rapp. Groenl. Geol. Unders., 80, 77-82, 1976.

Compton, P. M., A study of the Nûk gneisses and Qôrqut granite in the Buksefjorden region, southern West Greenland, Ph.D. thesis, Univ. of Exeter, Exeter, United Kingdom, 1978a.

Compton, P. M., Rare earth evidence for the origin of the Nûk gneisses Buksefjorden region, southern West Greenland, Contrib. Mineral. Petrol., 66, 283-293, 1978b.

Friend, C. R. L., and R. P. Hall, Fieldwork on the Ivisârtoq area, inner Godthåbsfjord southern West Greenland, Rapp. Groenl. Geol. Unders., 85, 54-60, 1977.

Gibbs, A. D., Structural studies in part of the Buksefjorden region, southwest Greenland, Ph.D. thesis, Univ. of Exeter, Exeter, United Kingdom, 1976.

Griffin, W. L., V. R. McGregor, A. P. Nutman, P. N. Taylor, and D. Bridgwater, Early Archaean granulite-facies metamorphism south of Ameralik, West Greenland, Earth Planet. Sci. Lett., 50 59-74, 1980.

Hall. R. P., The Precambrian geology of the Kangangup tasia area, Fiskenaesset, southern West Greenland, M.Phil. thesis, Council for National Academic Awards at Portsmouth Polytechnic, Portsmouth, United Kingdom, 1977.

Hanson, G. N., The application of the trace elements to the petrogenesis of igneous rocks of granitic composition, Earth Planet. Sci. Lett., 38, 26-43, 1978.

Hart, S. R., C. Brooks, T. E. Krogh, G. L. Davis, and D. Nava, Ancient and modern volcanic rocks: a trace element model, Earth Planet. Sci. Lett., 10, 17-28, 1970.

Johannes, W., Metastable melting in the granite system Qz-Or-Ab-An-H_2O, Contrib. Mineral. Petrol., 72, 73-80, 1980.

Kalsbeek, F., Rb-Sr whole rock age of the Ilivertalik Granite and other rocks from the Fiskenaesset area, Bull. Geol. Soc. Denmark, 25, 85-88, 1976.

Kalsbeek, F., and J. S. Myers, The geology of the Fiskenaesset region, Rapp. Groenl. Geol. Unders., 51, 5-18, 1973.

McCarthy, T. S., Chemical interrelationships in a low-pressure granulite terrain in Namaqualand, South Africa, and their bearing on granite genesis and the composition of the lower crust, Geochim. Cosmochim. Acta, 40, 1057-1068, 1976.

McGregor, V. R., The early Precambrian gneisses of the Godthåb district, West Greenland, Phil. Trans. R. Soc. London, Ser. A, 273, 343-358, 1973.

McGregor, V. R., Archaean grey gneisses and the origin of the continental crust: Evidence from the Godthåb region, West Greenland, in Trondjemites, Dacites and Related Rocks, edited by F. Barker, pp. 169-204, Elsevier, New York, 1979.

Moorbath, S., Ages, isotopes and evolution of Precambrian continental crust, Chem. Geol., 20, 151-187, 1977.

Moorbath, S., Age and isotope evidence for the evolution of the continental crust, Phil. Trans. R. Soc. London, Ser. A, 288, 401-413, 1978.

Moorbath, S., and R. J. Pankhurst, Further rubidium-strontium age and isotopic evidence for the nature of the late Archaean plutonic event in West Greenland, Nature, 262, 124-126, 1976.

Moorbath, S., P. N. Taylor, and R. Goodwin, Origin of granitic magma by crustal remobilisation: Rb-Sr and Pb/Pb geochronology and isotope geochemistry of the late Archaean Qôrqut granite complex of southern West Greenland, Geochim. Cosmochim. Acta, 45, 1981.

Myers, J. S., Acid and intermediate intrusions, deformation and gneiss formation, north-east of Fiskenaesset, Rapp. Groenl. Geol. Unders., 73, 7-15, 1976.

Noe-Nygaard, A., and H. Ramberg, Geological reconnaissance map of the country between latitudes 60°N and 65°45'N, West Greenland, Medd. Groenl., 123(5), 9pp., 1961.

O'Nions, R. K., and R. J. Pankhurst, Early Archaean rocks and geochemical evolution of the earth's crust, Earth Planet. Sci. Lett., 38, 211-236, 1978.

Pankhurst, R. J., S. Moorbath, D. C. Rex, and G. Turner, Mineral age patterns in ca. 3700 my old rocks from West Greenland, Earth Planet. Sci. Lett., 20, 157-170, 1973.

Pidgeon, R. T., and F. Kalsbeek, Dating of igneous and metamorphic events in the Fiskenaesset region of southern West Greenland, Can. J. Earth Sci., 15, 2021-2025, 1978.

Pidgeon, R. T., M. Aftalion, and F. Kalsbeek, The age of the Ilivertalik granite in the Fiskenaesset area, Rapp. Groenl. Geol. Unders., 73, 31-33, 1976.

Sharpe, M. R., Anorthosites and serpentinites of the Faeringehavn area, southern West Greenland, Ph.D. thesis, University of Exeter, Exeter, United Kingdom, 1975.

Streckeisen, A. L., To each plutonic rock its proper name, Earth Sci. Rev., 12, 1-33, 1976.

Tuttle, O. F., and N. L. Bowen, Origin of granite in the light of experimental studies in the system $NaAlSi_3O_8$-$KAlSi_3O_8$-SiO_2-H_2O, Geol. Soc. Am. Mem., 74, 153 pp., 1958.

Walton, B. J., Mapping of Archaean rocks in the inner Godthåbsfjord region, southern West Greenland, Rapp. Groenl. Geol. Unders., 80, 72-77, 1976.

Winkler, H. G. F., Petrogenesis of Metamorphic Rocks, pp. 348, Springer-Verlag, New York, 1979.

Winkler, H. G. F., and R. Breitbart, New aspects of granitic magmas, Neues Jahrb. Mineral. Monatsh., 10, 463-480, 1978.

Winkler, H. G. F., M. Boese, and T. Marcopoulos, Low temperature granitic melts, Neues Jahrb. Mineral. Monatsh., 6, 245-268, 1975.

(Received November 18, 1980;
revised March 2, 1981;
accepted March 13, 1981.)

JOURNAL OF GEOPHYSICAL RESEARCH, VOL. 86, NO. B11, PAGES 10633–10638, NOVEMBER 10, 1981

Seismic Reflections From the Basal Contacts of Batholiths

HELOISE B. LYNN,[1] LAURA D. HALE, AND GEORGE A. THOMPSON

Stanford University, Geophysics Department, Stanford, California 94305

Although seismic reflection data in batholithic terranes are scarce, datasets available to us from three different regions show surprising similarities. All three profiles, one across Precambrian rocks in Texas, and two across Mesozoic batholiths in California and Nevada, show strong subhorizontal reflections at depths of 6–10 km. These reflections are interpreted to originate from the base of the batholiths, and indicate that these batholiths are tabular in shape. The large amplitudes of the reflections require a marked contrast in acoustic impedance (product of velocity and density) between the batholith and the underlying rocks. Two of the profiles show reflective zones having appreciable thicknesses (0.5–2.5 km), while the third profile shows a single continuous reflection. The four most favored candidates for sub-batholithic reflections are (1) underplated gabbro, (2) cumulate layers, (3) migmatites, and (4) thrust faults. Cumulate layering is the preferred interpretation where reflectors constitute a thick package and are laminated in appearance.

INTRODUCTION

It has long been known from seismic refraction studies in granitic terranes that velocities appropriate for granite are usually underlain at mid-crustal depths by higher velocities. Unfortunately, the refraction method does not have the resolution to determine whether batholiths have a distinct floor or grade irregularly downward into migmatites, gneisses or other rocks. Multichannel seismic reflection data, however, could answer this and related questions. We became interested in the problem in connection with our analysis of the Consortium for Continental Reflection Profiling (COCORP) seismic data in Hardeman County, Texas [*Lynn*, 1979; *Oliver et al.*, 1976]. We looked for reflection profiles in granitic terranes in other regions in order to check our inferences from the Hardeman profiles. Although reflection records in crystalline rocks are rare, because most reflection work is motivated by petroleum exploration in sedimentary rocks, we found significant data in two other areas, one in California and one in Nevada.

Two contrasting views of batholiths have held that they generally are thin, having spread out laterally at shallow depth [*Hamilton and Myers*, 1967], or that they are steep sided and thick [*Klepper et al*, 1971]. In the three widely separated regions of good reflection data, subhorizontal strong reflections at depths of 6–10 km support the idea of a tabular model for batholiths. Regardless of the model, however, the surprising observation of these reflections requires an explanation, which in turn may shed new light on the structure and origin of the continental crust.

BACKGROUND OF ALTERNATIVE EXPLANATIONS OF THE SEISMIC DATA

The principal features of interest are (1) the nearly horizontal attitude of the reflectors, (2) the contrast in acoustic impedance (velocity and/or density) required to produce the reflections, and (3) the thickness and laminated appearance of zones of reflectors at two of the sites. We cannot determine from the reflections whether the contrast in acoustic impedance is positive (as for gabbro below granite) or negative (as for sedimentary rocks below granite). Consequently, various interpretations are possible, and we summarize the four alternative explanations which we consider to be the most likely.

Among volcanologists the idea has been growing that at least some silicic magma systems (or epizonal batholiths) are underplated by basaltic magma [*Duffield et al*, 1980; *Eichelberger and Gooley*, 1977]. A key line of evidence is the long duration of some systems and hence the necessity for a continuing injection of basalt from the mantle to keep them hot [*Lachenbruch and Sass*, 1978]. The other line of evidence is more direct: the typical occurrence of basalt along with silicic extrusives. The underplating model invokes a density stratification of silicic above basaltic magma and thus explains basaltic eruptions around the periphery of silicic centers. As will be shown, the basaltic underplating model is capable of explaining both the strength and the subhorizontal attitude of reflectors but offers no ready explanation for the reflection zones with a laminated appearance.

A related but different model emphasizes reaction melting of crustal rocks by mantle basalt, with the formation of cumulate layers [*Barker et al*, 1975, 1982; *Chapman*, 1968]. *Taylor* [1980] has shown on the basis of strontium and oxygen isotopes that mixing of mantle-derived igneous rocks with crustal metamorphic rocks is very common. Moreover, the process of assimilation of country rocks by magmas requires crystallization of cumulates to explain the heat balance. Taylor suggests a ratio of cumulates to assimilated country rocks of at least 1:1 (for very hot country rocks) and more likely 5:1 or greater. Cumulate layers such as anorthosite and pyroxenite, if sufficiently thick (~100 m), could produce subhorizontal strong reflections with a laminated appearance.

Sub-batholithic migmatites constitute a third alternative explanation. Warren Hamilton (personal communication, 1980, 1981) emphasizes this idea. Migmatites may be candidate reflectors if they are composed of contrasting materials, i.e., amphibolite and granite gneiss, and the layers are of sufficient thickness (~100 m or more). As will be shown, the layering needs to be subhorizontal and fairly continuous. Hamilton would explain a subhorizontal attitude by widespread ductile flow in the crust.

Finally, a fourth possibility is that the reflectors represent tectonic contacts: subhorizontal thrust faults, perhaps underlain by sedimentary rocks in some instances.

Keeping in mind these alternative hypotheses, we now describe the seismic data.

[1]Present affiliation: Amoco Production Company, Houston, Texas 77001.

Copyright © 1981 by the American Geophysical Union.

Paper number 1B0709.
0148-0227/81/001B-0709$01.00

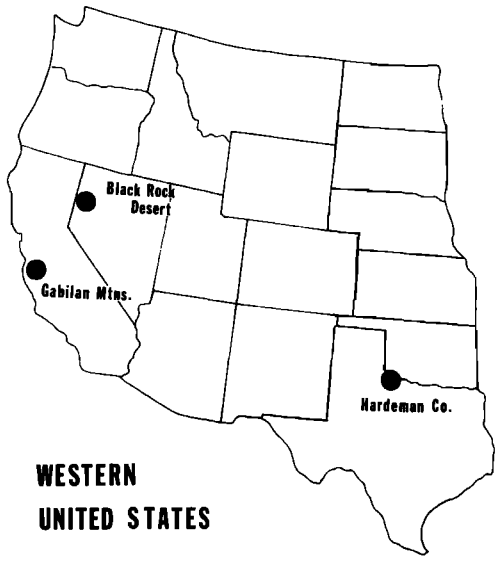

Fig. 1. Location map of reflection datasets.

PRECAMBRIAN ROCKS OF HARDEMAN COUNTY, TEXAS

In the Panhandle region of Texas, data from drillholes show that an extensive region of Precambrian rocks underlies a cover of Paleozoic sedimentary rocks. The most important Precambrian rock groups, as reported by *Flawn and Muehlberger* [1970], are (1) rhyolitic volcanics (Panhandle) about 1200 m.y. old, (2) an epizonal plutonic equivalent (Amarillo granite), (3) a complex of gabbro and diabase (Swisher) possibly also about 1200 m.y. old but perhaps younger, and (4) a metasedimentary group (Tillman) of Cambrian or Precambrian age consisting of graywacke, argillite, quartzite, and chert.

In this region (Figure 1) COCORP obtained deep seismic reflection data [*Oliver et al*, 1976]. Only one profile, which extends for 9 km in a east-west direction will be discussed here. The profile is shown in two versions, each of which brings out certain details. Figure 2 shows a twelve-fold stacked section as supplied by COCORP, and shows the same section after migration, a process which makes a more nearly correct image by collapsing diffractions and placing dipping reflectors in their correct geometric relations. The migration process was the Stolt-stretch F-K migration [*Stolt*, 1978] performed on a minicomputer at Stanford. Details of both the processing and interpretation are given in *Lynn* [1979].

Beneath the Paleozoic section the top of the basement, at 1.4 s on Figure 2, is known from drill data to be Precambrian rhyolite. The reflections from about 1.4 to 1.6 s (~0.5 km thick) are therefore interpreted to be layered rhyolitic tuffs that are well consolidated (seismic interval velocity 5.7 km/s). We interpret the seismically transparent zone from 1.6 to 2.8 s (~3.6 km thick) as a tabular pluton (seismic interval velocity 5.9 to 6.1 km/s) possibly comagmatic with the overlying rhyolite. The remarkably high amplitude of the two reflectors at 2.8 and 3.5 s (verified on true-amplitude playouts) demands a substantial contrast in seismic impedance. We were not able to resolve the velocities in these small intervals, except that the zone including both reflectors and the interval between has a velocity of about 6.5 km/s.

We tentatively interpret the entire section from the top of the basement (1.4 s) to about 3.7 s (~7 km thick) as layered Precambrian rhyolite underlain by a comagmatic tabular granitic pluton having two sill-like layers of higher velocity rock (each about 0.7 km thick) near its base. Because there is more than one layer and each appears to have internal sublayering, these reflectors fit the reaction cumulate model better than a model of simple basaltic underplating. At greater depth the seismic section shows mainly weaker, discontinuous reflectors which may originate from crude layering in gneisses, granulites and amphibolites of the deep crust.

An alternative explanation for the strong reflectors at 2.8 and 3.8 s has been proposed by Jon Brewer at Cornell University (oral communication, 1979, 1980). He suggests that they are part of a depositional sedimentary and possibly volcanic sequence in the Precambrian. We prefer our explanation based upon the evidence of regional Precambrian geology from drilling and the evidence of high seismic velocities.

MESOZOIC COAST RANGE BATHOLITH, GABILAN MOUNTAINS

Southeast of Monterey Bay, in San Benito County, California (Figure 1), the Mesozoic granitic batholith which comprises the Gabilan Mountains has been juxtaposed against the Franciscan Formation by the San Andreas Fault. Pre-Cretaceous metamorphosed limestones are found scattered throughout the batholith, and Miocene rhyolites and pyroclastic rocks are faulted against it.

Crustal refraction studies in this area have analyzed the velocity of the granitic batholith, the depth to which it extends, and the overall crustal thickness [*Stewart*, 1968; *Walter and Mooney*, 1981]. Velocities within the batholith are normal for granite (5.5 to 6.1 km/s). Deeper layers have velocities of 6.35 and 6.7 km/s. Crustal thickness estimates vary from 20–27 km.

In 1978, T. McEvilly of the University of California at Berkeley obtained an 18-km line of 24-fold deep crustal reflection data running SW-NE across the San Andreas Fault, approximately 2.5 miles north of the Pinnacles National Monument. Only the western portion of the line, crossing the granitic and rhyolitic terranes, is shown here. Figure 3 is the 24-fold stacked time section. The section was migrated with a 45-degree omega, finite difference algorithm [*Kjartansson*, 1979] which allows for lateral velocity variations as well as variations with depth (see *Lynn* [1979] for details).

Two striking features are apparent on the unmigrated section: a cluster of reflections at about 3 s and a band of reflectors which on the left side of the section extend from 6 to 8 s. Aside from scattered, discontinuous events, the remainder of the section is seismically transparent. Reflections from 6 to 8 s, approximately 18 to 24 km in depth, are interpreted as coming from the crust-mantle transition. They show an apparent dip in time because of a lateral velocity decrease toward the San Andreas fault zone (to the right of the section). Because velocities within the fault zone are approximately 20% lower than those in the unbroken granitic terrane, the reflections have been 'pulled down' about 1 s in time. The reflectors at about 3 s are interpreted as the base of the granitic batholith. The batholith itself is mostly nonreflective, implying acoustic homogeneity. The basal reflectors at 3 s are subhorizontal in the time section (Figure 3), suggesting a tabular shaped batholith. They extend from about 6.5 to 9.0 km and are much stronger than any surrounding events.

The migration process has located these 3-s reflectors at 6.5

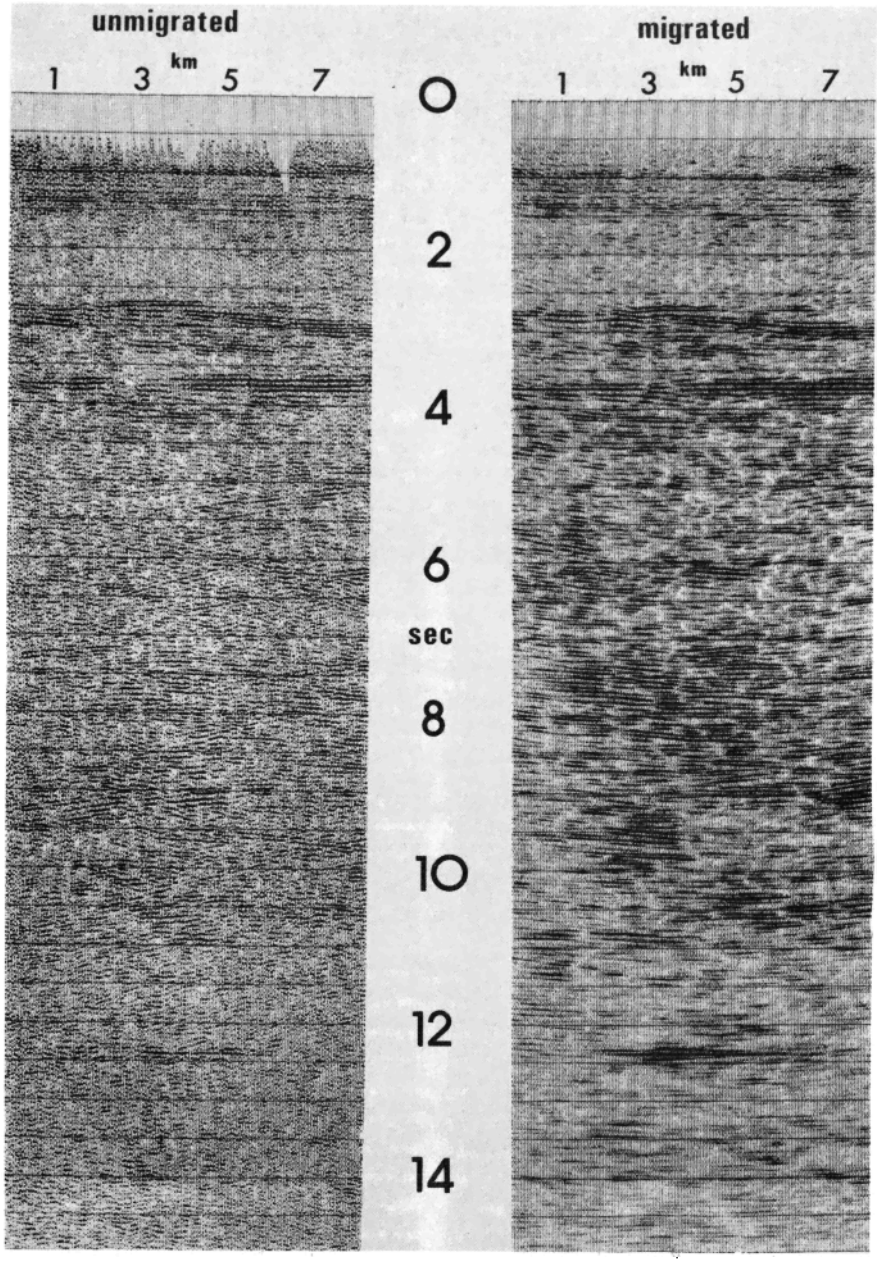

Fig. 2. COCORP seismic reflection profile, Line 2, Hardeman County, Texas; unmigrated and migrated versions. Line extends for 9 km from west (left) to east (right). Vertical scale is two-way travel time. Horizontal and vertical distance scales are approximately the same. In the migrated version diffractions have been collapsed and dipping reflectors have been moved laterally to show geometric relations more correctly. Interpretation: Precambrian rhyolite at 1.4 s, tabular pluton 1.6–2.8 s and 3.0–3.5 s, cumulate layers (?) 2.8 and 3.5 s.

to 9.0 km using a normal granite velocity of 6.1 km/s, while adjusting for lateral velocity gradients due to the proximity of the San Andreas Fault zone. The reflectors dip slightly to the southwest. The dip is due to the combination of subhorizontal reflectors in time with a lateral velocity change. The reflections evidently represent a boundary between granite and other rocks with a markedly different acoustic impedance.

Because of the transparent character of the section both over and under these reflectors, and because pre-batholithic rocks in the region are highly deformed and/or poorly stratified (Franciscan melange); it is difficult to interpret the reflectors as regularly bedded sediments or metasediments. We conclude that the strong reflectors at 6.5 to 9 km represent the lower boundary of a tabular batholith. The thickness (~2.5 km) and laminated appearance of the reflecting zone are most consistent with the hypothesis of cumulates formed by reaction melting. Note the resemblance to layering near the base of the crust.

CRETACEOUS BATHOLITH IN NORTHWESTERN NEVADA

Granitic rocks in the Black Rock Desert area of northwestern Nevada (Figure 1) resemble those of the Sierra Nevada batholith [*Grose and Sperandio*, 1978]. Their characteristics suggest emplacement at depths of 5–10 km. Older rocks, preserved as isolated roof pendants, are amphibolite, metasedimentary rocks, and metavolcanics (basalt and andesite), which are thought to be Permo-Triassic.

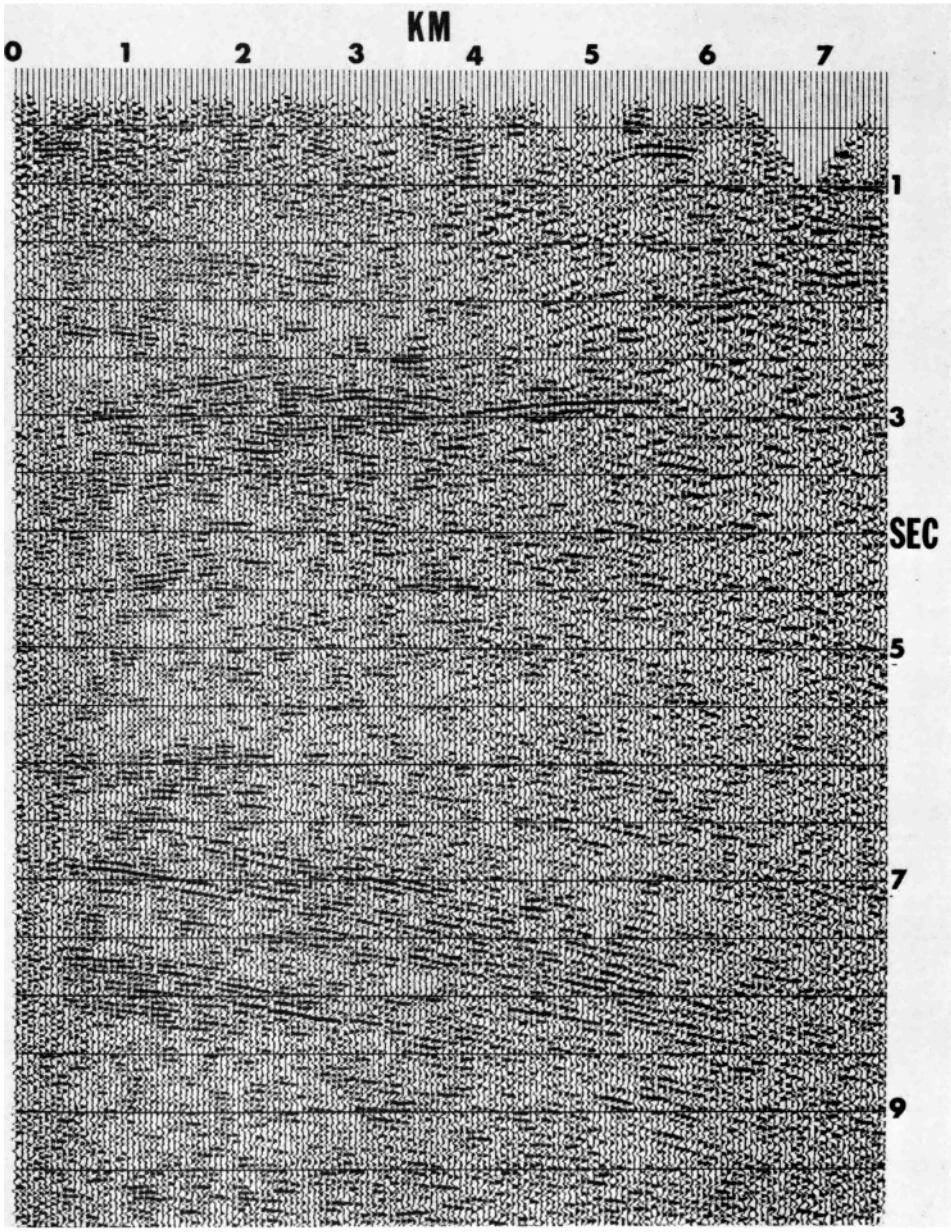

Fig. 3. Western (Pacific plate) portion of McEvilly's seismic profile across San Andreas fault. Section is 7.5 km long and vertical scale is two-way time in seconds; horizontally exaggerated roughly 3:1. Reflectors at about 3 s probably represent base of batholith and those at 6–8 s (on left side of section) the base of the crust.

A seismic reflection profile in this area [*Callaway*, 1978] extends for 27 km across the Black Rock Desert and Hualapai Flat from Trego Mountain at the southeast end to the Granite Range at the northwest end. The data are mostly single-fold with explosion sources, but along part of the line across the Black Rock Desert, six-fold coverage was shot. These six-fold stacked data are included in the left half of Figure 4.

As *Callaway* [1978] points out, the profile (Figure 4) shows prominent reflecting horizons at 0.5 s, 1.0 s, and 3.0 s. Interval velocities for the regions between these three reflections are 1.1 km/s, 2.2 km/s, and 5.4 (±0.5) km/s. The corresponding depths are 0.3, 0.8, and 6.2 km. The upper layer is interpreted by Callaway to be Quaternary lacustrine sediments and the second layer to be Cenozoic basin fill composed of volcanic and sedimentary rocks. The third layer is clearly "basement" and most likely consists of granitic rocks such as those forming the bulk of Trego Mountain to the southeast and the Granite Range to the northwest, but this layer may also include metamorphic rocks like those in the roof pendants.

We suggest that the strong reflector at 6.2 km represents the base of the batholith. No velocity was obtained for the region below the 5.4 km/s layer, and the original data are unobtainable.

Either gabbroic underplating of the batholith or cumulate layering at its base would explain the strength of the reflection and also its horizontal attitude. It appears to have an appreciable thickness, about 0.5 km, and internal layering which would favor the cumulate hypothesis. Alternative explanations include Callaway's suggestion that the 6.2 km reflector represents the base of a roof pendant. We think the regularity of the contact and the strength of the reflector, as well as the thickness of the required pendant, argue against

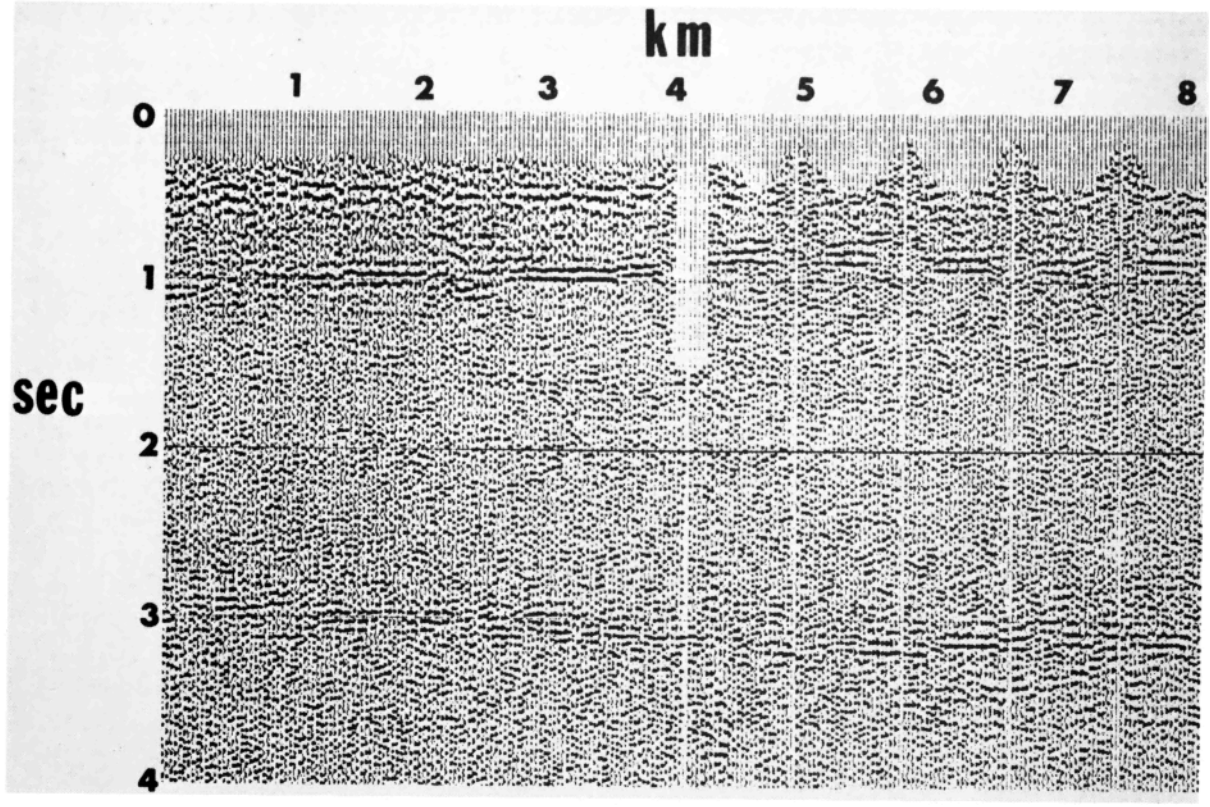

Fig. 4. Seismic profile in Black Rock Desert [*Callaway*, 1978]. Profile is 8 km long, single-fold on right half, six-fold stack on left half. Vertical scale is two-way time in seconds; horizontal exaggeration is roughly 1.5:1. Interpretation: base of Cenozoic basin fill, 1.0 s (0.8 km); granitic batholith 1.0–3.0 s (0.8–6.2 km).

this hypothesis. Another explanation, one that must remain open for the present, is that the reflector represents a thrust fault.

SUMMARY AND CONCLUSIONS

In three different provinces of granitic rocks, seismic reflectors at depths 6–10 km may represent the basal contacts of batholiths. The reflective zones are subhorizontal and have appreciable thicknesses (0.5–2.5 km).

These observations are generally consistent with a process of accumulation of granitic magma above higher density basaltic magma, but reflection zones of appreciable thickness favor the alternative hypothesis of reaction melting with formation of sub-batholithic cumulates. The third hypothesis, that the sub-batholithic reflectors are migmatites, is considered less likely.

Testing of these preliminary interpretations can be accomplished by comparative seismic reflection studies in other strategic locations and by refraction or wide-angle reflection experiments to resolve the velocities of rocks beneath batholiths. In the meantime, alternative explanations of the observed reflections, such as subhorizontal thrust zones or stratified sedimentary/volcanic rocks, should be kept in mind.

Acknowledgments. Tom McEvilly provided the California seismic data. Fred Barker alerted us to the importance of reaction melting and resultant cumulates. Several members of Jon Claerbout's Stanford Exploration Project helped generously with data processing. Discussions with many colleagues, including Warren Hamilton, the CO-CORP group at Cornell, and especially with Gail Mahood and Mary Lou Zoback, are gratefully appreciated. The work was supported by National Science Foundation grant EAR 78-22762.

REFERENCES

Barker, F., D. R. Wones, W. N. Sharp, and G. A. Desborough, The Pikes Peak batholith, Colorado Front Range, and a model for the origin of the gabbro-anorthosite-syenite-potassic granite suite, *Precambrian Res. 2*, 97–160, 1975.

Barker, F., J. G. Arth, and T. Hudson, Tonalites in crustal evolution, *Phil. Trans. R. Soc. London Ser. A*, in press, 1981.

Callaway, J., Reflection seismic traverse across Black Rock Desert and Hualapai Flat, Nevada, Studies of a Geothermal System in Northwestern Nevada, 1, *Colo. Sch. Mines Q., 73* (3), 65–72, 1978.

Chapman, C. A., A comparison of the Maine coastal plutons and the magmatic central complexes of New Hampshire, in *Studies of Appalachian Geology*, edited by E. Zen et al., pp. 385–396, John Wiley, New York, 1968.

Duffield, W. A., C. R. Bacon, and G. B. Dalrymple, Late Cenozoic volcanism, geochronology and structure of the Coso Range, Inyo County, California, *J. Geophys. Res., 85*, 2381–2404, 1980.

Eichelberger, J. C., and R. Gooley, Evolution of silicic magma chambers and their relationship to basaltic volcanism, in *The Earth's Crust, Geophys. Monogr. Ser. 20*, pp. 57–79, AGU, Washington, D.C., 1977.

Flawn, P. T., and W. R. Muehlberger, The Precambrian of the USA: South central United States, *The Precambrian*, vol. 4, edited by K. Rankama, pp. 74–144, Interscience, New York, 1970.

Grose, L. T., and R. J. Sperandio, Geology of the Gerlach–Hualapai Flat geothermal area, northwestern Nevada, Studies of a Geothermal System in Northwestern Nevada, 1, *Colo. Sch. Mines Q., 73* (3) 1–10, 1978.

Hamilton, W., and B. Myers, The nature of batholiths, *Geol Surv. Prof. Pap. U.S., 554-C*, C1–C30, 1967.

Kjartansson, E., Attenuation of seismic waves in rocks and applications in energy exploration, Ph.D. dissertation, Stanford Univ, Stanford, Calif., 1979.

Klepper, M. R., G. D. Robinson, and H. W. Smedes, On the nature of the Boulder batholith of Montana, *Geol. Soc. Am. Bull., 82*, 1563–1580, 1971.

Lachenbruch, A. H., and J. H. Sass, Models of an extending lithosphere and heat flow in the Basin and Range Province, *Geol. Soc. Am. Mem., 152,* 209–250, 1978.

Lynn, H. B., Migration and interpretation of deep crustal reflection data, Ph.D. dissertation, Stanford Univ., Stanford, Calif., 1979.

Oliver, J., M. Dobrin, S. Kaufman, R. Meyer, and R. Phinney, Continuous seismic profiling of the deep basement, *Geol. Soc. Am. Bull., 87,* 1537–1546, 1976.

Stewart, S. W., Preliminary comparison of seismic traveltimes and inferred crustal structure adjacent to the San Andreas Fault in the Diablo and Gabilan Ranges of central California, in *Proceedings of the Conference on Geologic Problems of San Andreas Fault System, Geol. Sci. 20,* edited by W. R. Dickinson and A. Grantz, pp. 218–230, Stanford University Press, Stanford, Calif., 1968.

Stolt, R., Migration by Fourier transform, *Geophysics, 43,* 23–48, 1978.

Taylor, H. P., Jr., The effects of assimilation of country rocks by magmas on $^{18}O/^{16}O$ and $^{87}Sr/^{86}Sr$ systematics in igneous rocks, *Earth Planet. Sci. Lett., 47,* 243–254, 1980.

Walter, A. W., and W. D. Mooney, Reinterpreting seismic data from central California, *Earthquake Notes, 52,* 51, 1981.

(Received November 3, 1980;
revised April 2, 1981;
accepted April 20, 1981.)